Lecture Notes in Electrical Engineering 262

Angui Li
Yingxin Zhu
Yuguo Li
Editors

Proceedings of the 8th International Symposium on Heating, Ventilation and Air Conditioning

Volume 2: HVAC&R Component and Energy System

Springer

Lecture Notes in Electrical Engineering

Volume 262

For further volumes:
http://www.springer.com/series/7818

Angui Li · Yingxin Zhu · Yuguo Li
Editors

Proceedings of the 8th International Symposium on Heating, Ventilation and Air Conditioning

Volume 2: HVAC&R Component and Energy System

Springer

Editors
Angui Li
Xi'an University of Architecture
and Technology
Xi'an
People's Republic of China

Yuguo Li
The University of Hong Kong
Hong Kong
People's Republic of China

Yingxin Zhu
Tsinghua University
Beijing
People's Republic of China

ISSN 1876-1100 ISSN 1876-1119 (electronic)
ISBN 978-3-642-39580-2 ISBN 978-3-642-39581-9 (eBook)
DOI 10.1007/978-3-642-39581-9
Springer Heidelberg New York Dordrecht London

Library of Congress Control Number: 2013945148

Printed on acid-free paper

Springer is part of Springer Science+Business Media (www.springer.com)

Preface

The 8th International Symposium on Heating, Ventilation, and Air Conditioning—ISHVAC2013 is held in Xi'an, China from October 19 to 21, 2013, organized by Xi'an University of Architecture and Technology and co-organized by Tsinghua University and The University of Hong Kong. The proceedings consist of over 220 peer-reviewed papers presented at the ISHVAC2013. We sincerely hope that the 8th International Symposium of Heating, Ventilation, and Air Conditioning will provide a good platform again to HVAC experts and researchers in China and elsewhere share their latest research findings and new technology development, and looking into the future of HVAC.

Xi'an has more than 3,000 years of history as one of the four great ancient capitals of China. Xi'an has now re-emerged as one of the important cultural, industrial, and educational centers in China. History tells us a lot. The history of HVAC is much shorter. Addington (2001) wrote, after the 1918–1919 influenza pandemic, which killed more people than World War I, "*Engineers and manufacturers were quick to capitalize on the public's concern with cleanliness, and pointed out that the air handler could produce 'manufactured weather' that was cleaner and purer than what nature provided (Carrier 1919). In spite of the continued work of open-air enthusiasts such as Winslow and Dr. Leonard Hill during the next several decades to challenge mechanical systems, most of the early ventilation laws remained in place and the air-handler-based system became the standard for conditioning interior environments*." The new revitalization of natural ventilation and new development of mixed-mode ventilation in the past 10 years confirms the wisdom of Winslow and Dr. Leonard Hill.

The success of HVAC is and will also be judged in the balance of providing people a comfortable and healthy indoor environment and using the minimum resources and energy. The key to the success of HVAC is in understanding the human physiological needs in thermal comfort and healthy air, and the roles played by human behavior, which is dynamical in nature. We cannot just focus on the HVAC technologies as we have done in the past 100 years.

Urbanization is a huge thing in rapidly developing countries such as in China. More than 50 % of the world's population now lives in cities. The urban population will reach 1 billion by 2030 in China. In the next 10 years, it is expected at least 1 % of the population will become urban dwellers every year. The expectation for better indoor environment is also on the rise in China and other

developing countries as the living standard rises. Building consumes a large proportion of our energy in the world. Efficient HVAC is the key in high performance buildings. Continuing urban warming has been observed and studied in many megacities in the world. Just imagine if you are asked to cool the air in a Mong Kok district in Hong Kong or Wang Fu Jing Street in Beijing by a few degrees, what would you do? When shall we design a city just like designing a building? What can HVAC engineers and researchers help?

Xi'an literally means "Peaceful in the West" in Chinese, and it was historically known as Chang An ("Perpetually Peaceful"). We also wish that the world will not only be peaceful, but also sustainable. The HVAC Engineers and Researchers have a great role to play.

Finally, the conference organizing and the high quality of the proceedings are the result of many people's hard work, dedication, and support. The first appreciation goes to the Members of the International Scientific Committee. Great appreciation should also go to many people who worked tirelessly on the Organizing Committee. We greatly appreciate all the sponsors and cooperators for their special contributions.

We also express our thanks to the authors who enthusiastically presented their work, ideas, and results.

Angui Li
Yingxin Zhu
Yuguo Li

International Scientific Committee

Yi Jiang (China)
Jiaping Liu (China)
Phillip J. Jones (UK)
Hazim B. Awbi (UK)
William Bahnfleth (USA)
Pradeep Bansal (NZ)
Mark Bomberg (USA)
Qingyan Chen (USA)
Zhenqian Chen (China)
Qihong Deng (China)
Shiming Deng (HK, China)
Lei Fang (DK)
Leon R. Glicksman (USA)
Yanling Guan (China)
Per Heiselberg (DK)
Jan Hensen (NL)
Sture Holmberg (SE)
Xiang Huang (China)
Shinsuke Kato (JP)
Angui Li (China)
Baizhan Li (China)
Xianting Li (China)
Yuguo Li (HK, China)
Zhiwei Lian (China)
Martin W. Liddament (UK)
John C. Little (USA)
Weiding Long (China)
Shuzo Murakami (JP)
Vincenzo Naso (IT)
Jianlei Niu (HK, China)
Bjarne W. Olesen (DK)
Saffa Riffat (USA)
Dirk Saelens (BE)
Jan Sundell (China)

Shin-ichi Tanabe (JP)
Kwok wai Tham (SG)
Peter V. Nielsen (DK)
Markku Virtanen (FI)
Fenghao Wang (China)
Ruzhu Wang (China)
Shengwei Wang (HK, China)
Yew Wah Wong (SG)
Hongxing Yang (HK, China)
Xudong Yang (China)
Yang Yao (China)
Harunori Yoshida (JP)
Hiroshi Yoshino (JP)
Shijun You (China)
Chuck Yu (UK)
Guoqiang Zhang (China)
Jensen Zhang (USA)
Xiaosong Zhang (China)
Xu Zhang (China)
Yinping Zhang (China)
Jianing Zhao (China)
Rongyi Zhao (China)
Xudong Zhao (UK)
Neng Zhu (China)
Yingxin Zhu (China)

Organizing Committee

Angui Li
Yingxin Zhu
Yuguo Li
Lei Zhao
Yi Wang
Yanfeng Liu
Zhiwei Wang
Yuesheng Fan
Qiuhui Yan
Xiaohong Nan
Xiong Liu
Qinghong Zheng

Contents

Part I
Energy System

Chapter 1
Net-Zero Energy Technical Shelter

Chen Zhang, Per Kvols Heiselberg and Rasmus Lund Jensen

Abstract Technical shelters are the basic structures for storing electronic and technical equipment, and commonly used for telecommunication base station, windmill, gas station, etc. Due to their high internal heat load density and special operation schedule, they consume more energy than normal residential or commercial buildings. On the other hand, it is a big challenge to power the technical shelter in remote area where the grids are either not available or the expansion of grid is expensive. In order to minimize the energy consumption and obtain a reliable and cost-efficient power solution for technical shelter, this study will apply the net-zero energy concept into the technical shelter design. The energy conservation can be achieved by proper design of building envelop and optimization of the cooling strategies. Both experiments and numerical simulations are carried out to investigate the indoor environment and energy performance of the technical shelter. Finally, a wind-solar hybrid energy system is designed as an alternative power solution for technical shelter, in order to achieve a net-zero energy target.

Keywords Technical shelter · Net-zero energy · Building envelop · Ventilative cooling · Hybrid energy system

1.1 Introduction

A net-zero energy building is a residential or commercial building with greatly reduced energy needs through highly efficient building system design while harvest energy on-site with renewable technologies. Technical shelters as the basic

C. Zhang (✉) · P. K. Heiselberg · R. L. Jensen
Department of Civil Engineering, Aalborg University, Sohngaardsholmsvej 57,
9000 Aalborg, Denmark
e-mail: cz@civil.aau.dk

A. Li et al. (eds.), *Proceedings of the 8th International Symposium on Heating, Ventilation and Air Conditioning*, Lecture Notes in Electrical Engineering 262,
DOI: 10.1007/978-3-642-39581-9_1,

structures for storing electronic and technical equipment are commonly used for telecommunication base station, windmill, gas station, etc. Compared with the normal residential or commercial buildings, technical shelters consume more energy due to their high inner heat density and special operating schedule. In addition, powering technical shelter is particularly challenge in remote areas where the grids are either not available or the expansion of grid is expensive. A 2,000 World Bank/UNDP study on rural electrification programs placed the average cost of grid extension per km at between $8,000 and 10,000, rising to around $22,000 in difficult terrains [1]. To minimize the energy consumption and provide reliable and cost-effective power solution of technical shelter, it's promising to apply net-zero energy concept into technical shelter design.

The previous studies show that energy conservation of technical shelter can be achieved by proper design of building envelop and improving the energy performance of air conditioning system. Nakao et al. [2] presented a thermal control wall combined exterior wall with cooling system, which can vary its heat transmission coefficient from one to ten times that for an ordinary wall and estimated to save 20 % of annual cooling energy. Zhang et al. [3] studied energy efficient envelop design for telecommunication base station in Guangzhou by considering heat transfer coefficient and solar absorptance. Nakao et al. [4] evaluated the impact of air flow systems on room air temperature distribution and ambient temperature of electric parts in telecommunication equipment rooms. Chen et al. [5] investigated the ventilative cooling technology by making full use of natural cooling resource. These studies analyze the impact of single influence factor on the energy performance of technical shelter. However, there are very rare studies making an exploration by combining these influencing factors, and exploring their impacts in different internal heat loads.

An alternative power solution for technical shelter is to use renewable energy resource [6]. Recent researches have shown the great potential of renewable energy to supplement or even replace conventional power systems in some locations where the grid is difficult to connect. The white paper [7] presents the state-of-art of sustainable power options, including wind, solar, fuel cell, and Pico hydro technologies. An advanced solution is to combine different renewable energy sources into a hybrid energy system [8].

The aim of this study is to design a net-zero energy technical shelter by improving the energy efficient of building systems and finding alternative power solution for technical shelter. Both experiments and numerical simulation are carried out to analyze the indoor environment and energy performance of technical shelter. Finally, an optimal hybrid energy system is design to provide reliable and economical power supply to the technical shelter.

1.2 Performance Investigation by Full-Scale Experiment

1.2.1 Experimental Method

The experiment is made in a full-scale typical technical shelter with the dimension of 3.82 m length, 2.27 m width, and 2.42 m height. The envelope of the technical shelter composes of three parts: wall and ceiling, foundation, and door. Wall and ceiling are made of sandwich constructions, with a core of expanded polystyrene and painted galvanized steel plate glued to the core. The thickness is 86 mm and U-value is 0.42 W/m^2 K. The foundation uses reinforced concrete, with the thickness of 150 mm and the U-value of 3.29 W/m^2 K. And the door is D-rated steel door with the thickness of 60 mm and U-value of 0.66 W/m^2 K. The tested technical shelter is located in a workshop, so no climate factor (solar and wind factors) are taken into account. A ventilative cooling system is installed in the tested technical shelter with flexible air intake, which aims to make full use of natural outdoor cooling resource. The air flow rate of ventilation system is controlled by fan speed, which depended on indoor and outdoor air temperature different (measured by the temperature sensors located indoor and outdoor). According to Fig. 1.1, the ventilated air supplied into the shelter through the filter bags, and exhausted by the blinded opening located in the upper zone of the shelter.

The aim of the experiment is to investigate the indoor environment and energy performance of the tested technical shelter in different internal heat load conditions. Thus, two heat load conditions are analyzed in the experiment: 1.5 and 3 kW. The indoor environment is evaluated by the vertical temperature profile, where air temperatures are measured in the middle of shelter in six different heights: 0.1, 0.5, 1.0, 1.5, 2.0, and 2.3 m, respectively, Fig. 1.2. In addition, supply and exhaust air temperatures as well as the ambient air temperature are measured in order to estimate the energy performance of technical shelter. All temperatures are measured by K-type thermocouples and recorded by data logger.

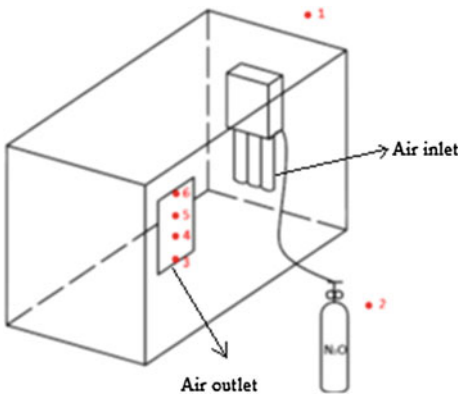

Fig. 1.1 Schema of the technical shelter and positions of tracer gas sensors

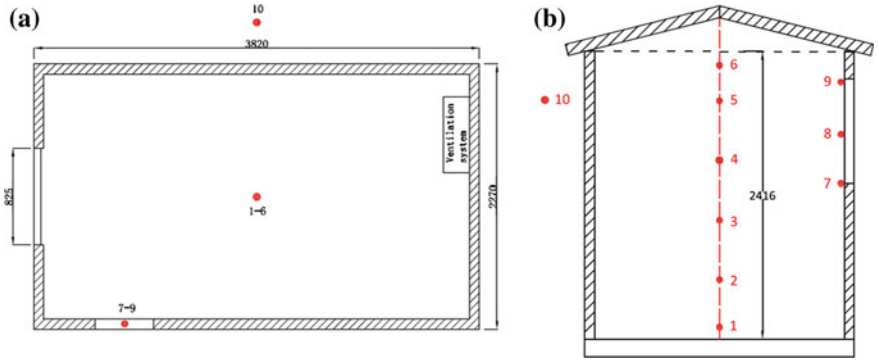

Fig. 1.2 **a** Plan view of technical shelter and positions of thermocouples; **b** cross-section of technical shelter and positions of thermocouples

The ventilation rate is measured by tracer gas technique. The constant injection method is used, where the equilibrium tracer concentration within a ventilated area is measured and this concentration can be related to the ventilation rate if the tracer release rate is known [9]. With regard to ventilation system, the pressure rise of the system is measured by a manometer and the electric power is measured by an AC power Analyzer.

1.2.2 Experimental Results

1.2.2.1 Performance of Ventilative Cooling System

In the ventilative cooling system, the cooling capacity is varied by changing air flow rate (VAV) and is controlled by fan's speed. The fan efficiency curve gives a clear indication of the energy performance of the ventilative cooling system, which is the ratio between power transferred to the air flow and the power consumed by the system. It is expressed by Eq. (1.1).

$$\eta = \frac{\Delta P \cdot q}{E} \tag{1.1}$$

where η is energy efficiency, ΔP is pressure rise across the fan (Pa), q is airflow rate (m^3/s), and E is electric power (W).

Figure 1.3 shows the fan efficiency curve of the tested ventilative cooling system as a function of air flow rate. The efficiency significantly increases with increased the airflow rate and reaches a peak efficiency of 78.95 % when the airflow rate is around 0.3 m^3/s. After that, efficiency gradually decreases with increased airflow rate until the airflow rate reaches the maximum value. It needs to notice that even when the airflow rate is zero, electric power of tested system is almost 13 W, which means that is quite inefficient to operate the system in this condition.

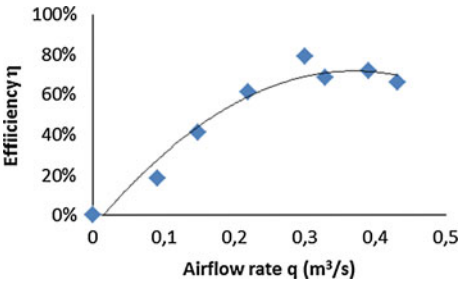

Fig. 1.3 Measured fan efficiency curve of the ventilative cooling system

1.2.2.2 Temperature Gradient

In this experiment, in order to keep the average indoor temperature around 30 °C, the ventilation system are running at 0.092 and 0.22 m^3/s air flow rate for 1.5 and 3 kW cases, respectively. Figure 1.4 shows the vertical temperature profiles for these two cases. In 1.5 kW case, the air temperature is almost constant from 0.1 to 1.0 m height, after that the temperature increases significantly with the height. This is because the heat source (1.5 kW) is too weak to generate great convection flow which causes completely mixing between cold supply air and the warm space air. So that high density cold air is trapped at the lower zone. On the contrary, in 3 kW case, the temperature linear increases with height at the lower zone while no large gradient from 1.5 to 2.3 m. This may be caused by the higher air flow rate generate higher supply air velocity, which enhances the turbulence level closed to supplied zone. However, in both of cases, the temperature gradient is large and the temperature difference reaches more than 10 °C between floor and ceiling level. This fact will be good for reducing the cooling need if the electric equipments are located at the lower zone. Even though the temperatures at the higher zone have exceeded the set point temperatures, the temperatures at the lower zone are still in an acceptable level. In addition, the period for people to stay in technical shelter for maintenance is very limited, so the discomfort caused by temperature gradient can be ignored in practice.

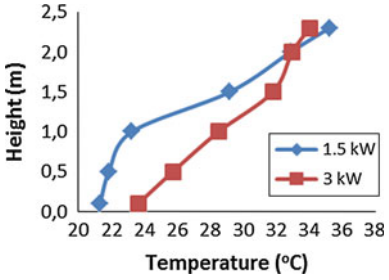

Fig. 1.4 Measured vertical temperature profiles for 1.5 and 3 kW cases

1.2.2.3 Energy Balance of the Technical Shelter

Generally, there are five heat sources or heat sinks in the technical shelter using a ventilative cooling system (Fig. 1.5): equipment heat load (Q_{eq}), heat transmission through envelops (Q_{trans}), infiltration (Q_{inf}), heat removed by ventilative cooling system (Q_{vent}), and solar radiation (Q_{sun}). Thus, the energy balance in the shelter can be expressed by Eq. (1.2).

$$Q_{eq} + Q_{trans} + Q_{vent} + Q_{inf} + Q_{sun} = 0 \tag{1.2}$$

Heat transmission through the building envelop can be expressed by the Eq. (1.3):

$$Q_{trans} = U \cdot A \cdot (T_{in} - T_{out}) \tag{1.3}$$

where U is the heat transfer coefficient of building envelop W/(m^2 K), A is the area of building envelop (m^2), T_{in} and T_{out} are indoor and outdoor air temperature (°C). Heat removed by ventilative cooling system has the definition below:

$$Q_{vent} = C_p \cdot \rho \cdot q \cdot \left(T_{ex} - T_{sup}\right) \tag{1.4}$$

where C_p is specific heat capacity of air (kJ/kg K), ρ is density of air (kg/m^3), q is airflow rate (m^3/s), T_{ex} and T_{sup} is exhaust and supply air temperature (°C).

However, the tested technical shelter is located in a workshop in this experiment, where no solar radiation is available and the temperature in the workshop keeps constant during measurement. Thus, the solar heat gain will be regardless in

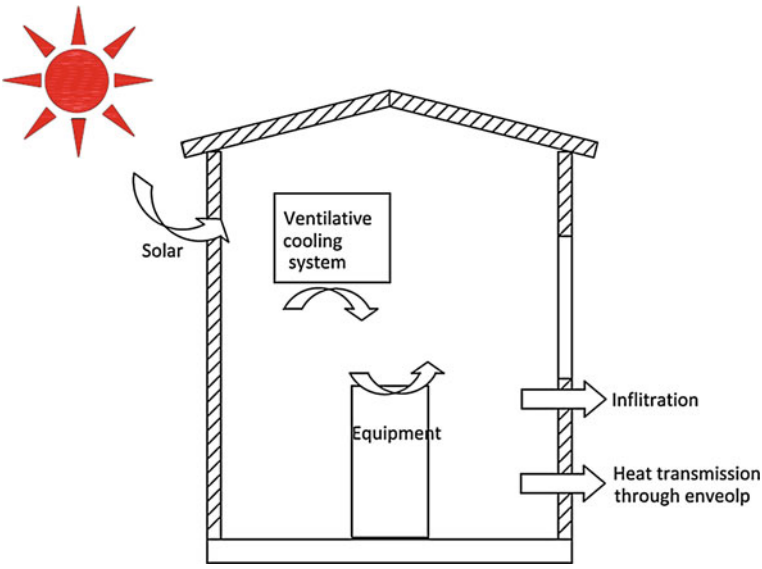

Fig. 1.5 Heat sources or heat sinks in the technical shelter

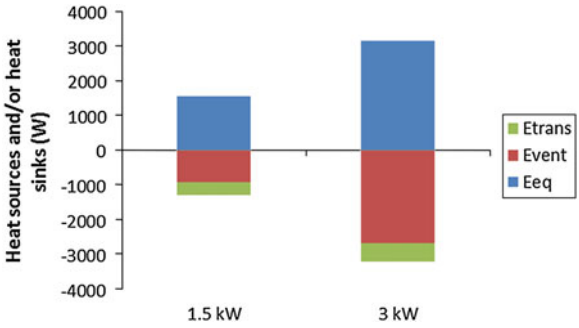

Fig. 1.6 Contribution of each heat sources or heat sinks

this case. In addition, the technical shelter are designed to be well sealed, thus the infiltration loss can be ignored if compared with the amount of ventilation.

In the measurement, two radiators serve as equipments to dissipate heat into the shelter. The powers of these two radiators are 1.52 and 1.59 kW, respectively. The outdoor temperature is kept around 19 °C during the measurement, and average indoor temperature is around 30 °C for both cases.

The contribution of each heat sources or heat sinks can be shown clearly in Fig. 1.6. Without any solar radiation, the electric equipment heat load (including the heat dissipation from the fan) is the only heat gain in our cases. Heat transmission through envelop and ventilative cooling are the main ways to remove heat from inside shelter. As indicated in Fig. 1.6, the calculated results by the simplified analysis method accord well with the energy balance, where the deviations of 1.5 and 3 kW cases are 13 and 2 %, respectively. This means no other unknown heat sources or heat sinks influence the energy performance of technical shelter. Thus, in order to reduce the energy consumption of technical shelter, it's important to perform energy efficiency envelops design and optimizes the control of ventilation system.

1.3 Performance Optimization by Numerical Simulation

1.3.1 Simulation Method

The aim of the numerical study is to evaluate the energy saving potential of the technical shelter by proper design of building envelope and application of an optimal ventilative and mechanical cooling strategy. The evaluation of the energy saving potential is carried out using a building thermal and energy simulation program. In this case, the BSim software is adopted to simulate the annual energy performance and indoor environment of a standard technical shelter [10].

The model created in BSim accords to the real plan of a standard technical shelter. The climate data of Copenhagen is used in the simulation based on the

Danish design reference year. And it is assumed that there are no other buildings in the neighborhood, thus no shadow from surroundings. Three equipment heat loads are analyzed: 1.5, 3, and 5 kW. In order to explore the optimal envelope solution, wall and ceiling are simulated with different insulation thicknesses. Four insulation thickness conditions are taken into account: 25, 50, 85, and 100 mm, and the corresponding *U*-values are 1.45, 0.72, 0.42, and 0.36 W/m^2 K, respectively. The set point temperature for cooling operation is 30 °C, while the set point temperature for heating operation is 10 °C. The cooling system composes of two parts: ventilative cooling system and an air-conditioner. The parameters of ventilative cooling system are set up according to the measurement results. The COP of the air conditioner is assumed to be 3 in this study.

1.3.2 Simulation Results

1.3.2.1 Impact of Envelope Insulation

Figure 1.7 shows the relationship between annual energy demand (heating/cooling) of the technical shelter and insulation thickness under three heat load conditions. For a normal building construction (office or residential building), the better insulation normally means higher energy saving potential. However, this concept is not applicable to technical shelter due to its high inner heat load density. As indicated in Fig. 1.7, the annual energy demand linearly rises while increasing insulation thickness. In addition, the simulation results show that cooling is the dominant energy demand in all cases. Heating is only needed in the case of 1.5 kW heat load with 25 mm insulation. However, the amount of the heating demand (27 kWh) can be ignored if compared with that of cooling (2,580 kWh), which taken only 1 % of total energy demand. Finally, as could be expected, the higher the heat load the more energy is needed.

The energy performance of the technical shelter and the contribution of different heat sources are also explored in four typical cases. The equipment runs continuously with a certain heat load, thus, the heat gain from equipment keeps

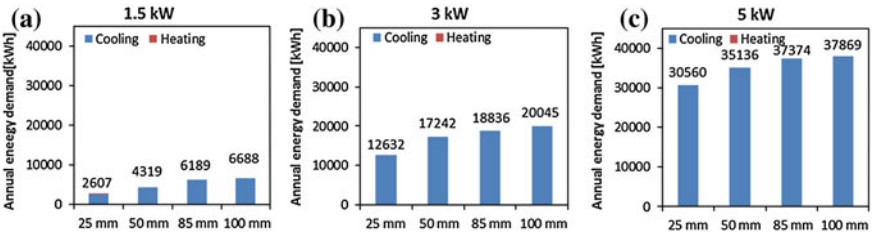

Fig. 1.7 Annual energy demands in different envelope insulation conditions. **a** 1.5 kW, **b** 3 kW, **c** 5 kW

constant during the whole year. The solar heat gain mainly depends on the solar radiation intensity, which has significant fluctuation between day and night. In most of the time, the envelope heat transmission help to dissipate the surplus heat load out of the shelter. The envelope with lower insulation thickness can transfer more heat to the outdoor environment, which is beneficial for reducing cooling demand. However, this will in return enhance the heating need potential in winter. As indicated in Fig. 1.8a, when the internal heat load is lower (1.5 kW), the envelop transmission not only remove all the heat load from the shelter in winter but also cause some heating demand when the indoor temperature is lower than 10 °C. On the other hand, in summer when the outdoor temperature is higher than indoor temperature, the envelop transmission will become heat gain which aggravates the cooling demand. During this period, the technical shelter with higher insulation thickness has better performance on preventing transmission heat gain, as indicated in Fig. 1.8b. For the technical shelter with higher internal heat load 5 kW, Fig. 1.8c, d, no heating is needed during the whole year. The envelope with higher insulation thickness 85 mm significantly reduces transmission loss and therefor increases the annual cooling demand.

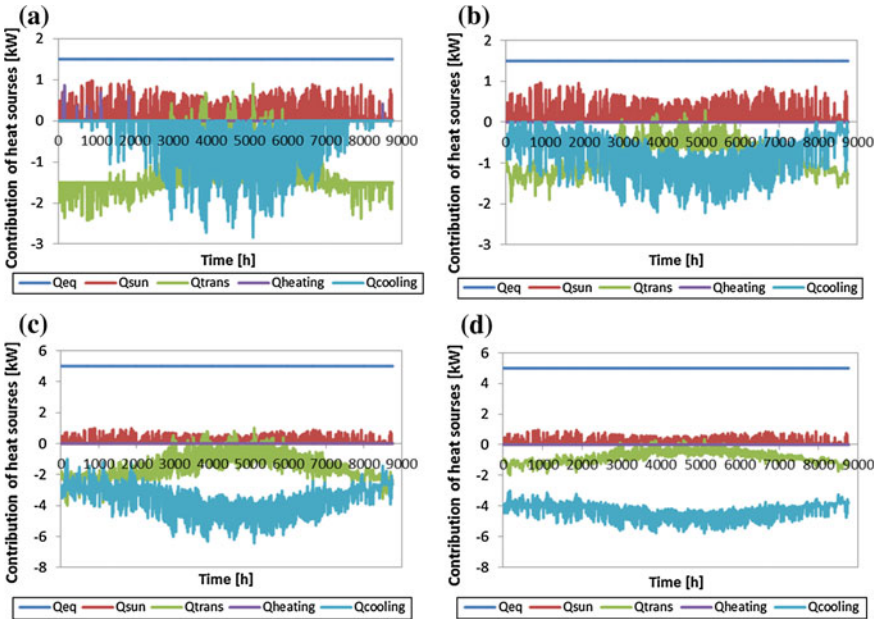

Fig. 1.8 Energy performance of the technical shelter with different internal heat loads and envelop insulation thicknesses. **a** 1.5 kW, 25 mm; **b** 1.5 kW, 85 mm; **c** 5 kW, 25 mm; **d** 5 kW, 85 mm

1.3.2.2 Cooling Strategies

If the ventilative cooling system can make full use of natural cooling resource of outdoor air, it can significantly reduce the cooling demand of the technical shelter. Normally, ventilation system consists of two types: natural ventilation and mechanical ventilation. Natural ventilation can be achieved by opening windows or doors to allow fresh cold air into the building. However, the technical shelter as a special building is normally designed without any window, and for the safety reasons, the door need to be closed during the whole year. Thus, the ventilation always achieved by applying a fan and the air change rate can be varied to meet the rising and falling heating gains or losses within the shelter.

The relationship between air change rate and annual cooling demand is analyzed by two cases: 85 mm, 1.5 kW and 85 mm, 5 kW. Figure 1.9 indicates that cooling demand can be significantly reduced by increasing air change rate. When the air change increases to 20 h^{-1} in 1.5 kW case and 50 h^{-1} in 5 kW case, the reduction of annual cooling demand reaches 90 % in both cases. After that, although air change rate continuous increases, the annual cooling load does not reduce significantly.

Controlling the indoor temperature in a safety range is very important for obtaining high performance and reliable operation of equipment. Thus, it's necessary to explore the effect of air change rate on indoor environment. Overheating hour is chosen as a key parameter to analyze how much time the indoor temperature exceeds set point temperature. As shown in Fig. 1.10a, c, overheating mainly occurs during summer season from May to September and reaches a peak in July. This is because ventilation cooling uses outdoor air as cooling sources, which greatly depend on the outdoor temperature and easily influenced by climate. As mentioned, when the air change rate reach 20 and 50 h^{-1} in 1.5 and 5 kW case, respectively, more than 90 % heat load can be eliminated. But the overheating hours still reach 500 and 1000 h in these situations, respectively. Even increasing air change rate to 100 and 150 h^{-1}, the overheating phenomenon cannot entirely disappear, because ventilative cooling does not work when the outdoor

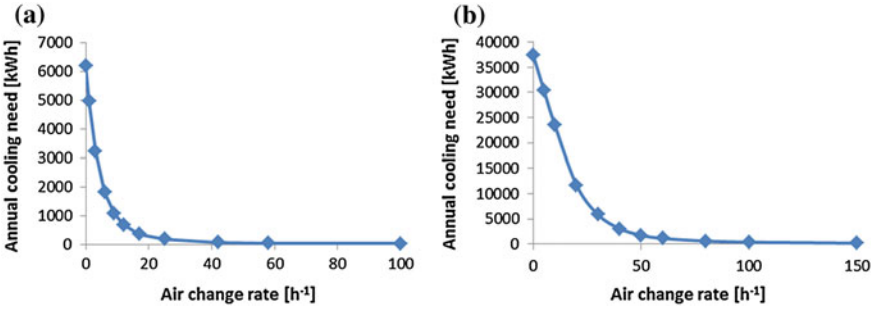

Fig. 1.9 Relationship between air change rate and annual cooling demand. **a** 85 mm, 1.5 kW; **b** 85 mm, 5 kW

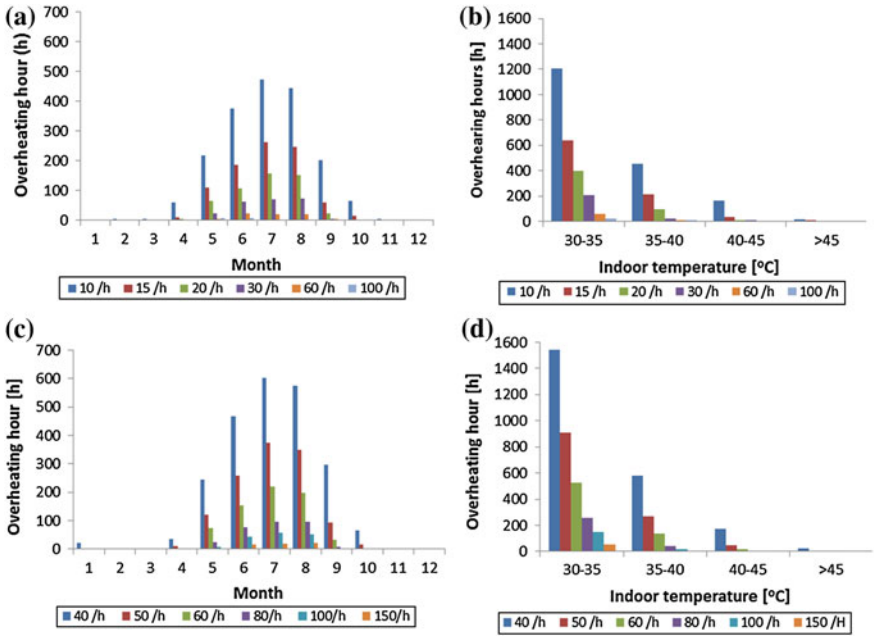

Fig. 1.10 Overheating hours for different ventilation rates. **a** Overheating hours per month, 85 mm, 1.5 kW; **b** overheating hours distribution of indoor temperature, 85 mm, 1.5 kW; **c** overheating hours per month, 85 mm, 5 kW; **d** overheating hours distribution of indoor temperature, 85 mm, 5 kW

temperature is higher than set point indoor temperature. Thus, it needs to cooperate with air conditioner to achieve the cooling target in this condition.

Figure 1.10b, d indicate the amounts of overheating hours in each temperature range. It's clear to find out that the overheating temperature is mainly in the range of 30–35 °C. The higher the ventilation rate, the less the overheating hour will be. The overheating temperature above 45 °C only last 10–20 h per year when the ventilation rate is 10 and 40 h^{-1} in 1.5 and 5 kW cases, respectively. And in other ventilation rate, overheating temperature is almost below 40 °C. Thus, it is essential to find out the temperature sensitivity of electric equipment in the technical shelter. The ventilation rate can be greatly reduced if the equipment can still work in the overheating condition for a certain period, so is the energy consumption of ventilation system. If the indoor temperature exceeds the permitted temperature of electric equipment for a long time, air-conditioner needs to work together with ventilative cooling system to discharge the internal heat, especially in the summer time.

As indicated in Fig. 1.9, an appropriate ventilation rate can meet the cooling demand in most time of the year. However, during summer, when the outdoor temperature increase, only increasing ventilation rate cannot achieve the target to remove all heat or it need huge ventilation rate to do so. Thus, another cooling

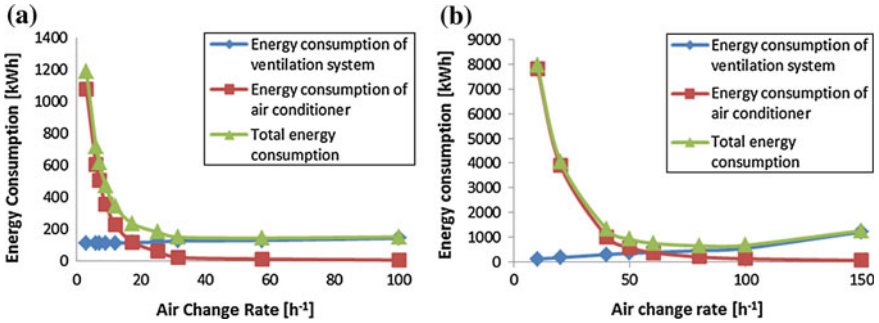

Fig. 1.11 Effect of air change rate on annual energy consumption. **a** 85 mm, 1.5 kW; **b** 85 mm, 5 kW

solution is to combine the ventilative cooling system with an air conditioner. How to reach an energy efficient combination is a crucial question for cooling system design.

Energy consumption of the cooling system composes of two parts: energy consumption of ventilative cooling system and energy consumption of air conditioner. Figure 1.11 shows the effect of air change rate on annual energy consumption. The energy consumption of air conditioner has the similar shape with annual cooling demand (Fig. 1.9), due to the linear relationship between these two parameters. The energy consumption of ventilative cooling system is the energy consumption of the fan, which increases with the air change rate. For 1.5 kW case, the total energy consumption decreases significantly, while the air change rate increases from 0 to 30 h^{-1}. As the air change rate continues increases to 100 h^{-1}, the total energy consumption keeps almost constant value. While for 5 Kw case, the total energy consumption reaches a bottom at 80 h^{-1}. After that, more energy is needed while increasing air change rate. Thus, if taken into account the economic factor, it is not advisable to combine air conditioner in the 1.5 kW case. But for 5 kW case, it recommends to use ventilative cooling system combined air conditioner.

1.4 Alternative Power Solutions for a Technical Shelter

Technical shelters in remote areas are often powered by diesel generators, continuing a reliance on fossil fuels and adding to greenhouse gas emissions. Thus, more and more attentions have been paid on seeking a sustainable solution for powering technical shelter. One of the promising solutions is to use renewable energy sources. Solar and wind energy are the most rapidly expanding sources of renewable energy in the world today. Due to the costs steadily falling of solar and wind technology, solar and wind power have significantly progressed in recent years where they can be considered as supplementary or even the primary power

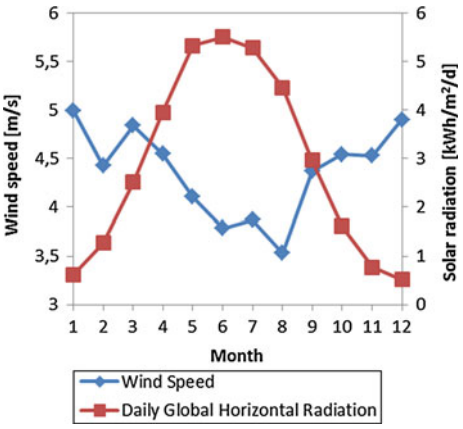

Fig. 1.12 Wind and solar energy resources for the site

sources in some locations where the grid is difficult to connect. However, wind and solar are intermittent energy resources, so some short-term storage is required to deliver reliable 24 h power supply. Wind and solar are often combined in a hybrid system because they complement each other on a daily and seasonal basis. Back-up generators are often necessary for larger sites.

Due to the large energy consumption of the technical shelter and intermittency of renewable energy resources, a hybrid energy system is designed to obtain a reliable and cost-effective power solution. HOMER [11] is used as energy modeling software for such a hybrid renewable energy system, which offers optimal design in terms of energy component size and economic cost.

The design is based on a standard technical shelter with a constant equipment heat dissipation rate of 1.5 kW. The predicted hourly energy consumption of the cooling systems is obtained by BSim simulation. The load demand in total is approximate 36.4 kWh/d and the peak load is 2.7 kW. The location of the technical shelter is Copenhagen, Denmark and the wind and solar energy resources are shown in Fig. 1.12 [12]. The life cycle cost of the hybrid energy system is calculated based on capital and operation and maintenance cost of each energy component. The capital cost of a wind turbine (under 100 kW) [13], PV cells [14] and diesel generators [14] are 3,000, 5,000, and 400 $/kW, respectively. The operation and maintenance cost of wind [13] and PV [14] are 0.015 and 0.01 $/kWh. The operation cost of diesel generator relies on fuel price, where the diesel price is 2.11 $/L (Demark 24th, Oct 2012) [15]. For a stand-alone hybrid system, battery and converter are needed to store electricity and convert DC power into AC power. The 6 V, 360 Ah, 2.16 kWh batteries connected in series or parallel are used in this study. The lifetime of all energy components is assumed to be 20 years and annual real interest rate is 6 %.

With regard to the different combinations of the hybrid energy system, the optimal sizing of energy components and economic cost are analyzed by HOMER simulation. From the simulation results (Table 1.1), the wind-solar hybrid energy system is the most recommended power solution for the technical shelter.

Table 1.1 Different combinations of the hybrid energy system

No.	PV (kW)	Wind unit (7.5 kW)	Diesel generator (kW)	Batt. no. (360 Ah, 6 V)	Converter (kW)	Initial capital	Operating cost ($/yr)	Total NPC	COE ($/kWh)	Renewable fraction (%)
1	5	1	5	32	3	$66,470	4,934	$123,067	0.808	77
2	0	1	5	32	3	$41,470	8,024	$133,503	0.876	48
3	10	0	5	32	3	$64,600	8,851	$166,121	1.090	47
4	0	0	5	24	3	$12,200	16,983	$206,992	1.358	0

The optimal configuration consists of 5 kWp PV, a 7.5 kW wind turbine unit, and a 5 kW diesel generator, where 77 % of the energy demand can be satisfied by renewable energy generation. For systems with wind turbine and diesel generator back-up, solar PV and diesel generator back-up as well as only diesel generator system, the renewable fraction will be 48, 47 and 0 %, respectively. In the terms of economic cost, although the wind-solar hybrid system has the largest initial cost of $66,470, its lowest operation cost leads to the lowest unit cost of energy (COE) 0.808 $/kWh. On the contrary, the high operation cost of diesel generator system off-sets its lowest initial cost, where the COE is 1.358 $/kWh.

1.5 Conclusion

Both experiments and numerical simulation are carried out in this study to analyze the indoor environment and energy performance of a technical shelter. In addition, a hybrid energy system is designed as an alternative solution to power the technical shelter, in order to achieve a net-zero energy target. According to the findings and discussions above, the main conclusions are as follows:

- The vertical temperature gradient is apparent in the technical shelter. The air temperature difference between floor and ceiling zone can reach more than 10 °C. This phenomenon is good for reducing the cooling demand, if the electric equipments are located in the lower zone. In addition, it will be more energy efficiency, if the exhaust opening is positioned at the top of the shelter, where the warmest air can be extracted to the outside directly.
- Due to the high inner heat load density, the cooling demand is the dominant energy demand during the whole year. As indicated by the simulation results, the annual cooling demand linearly rises while increasing envelope insulation thickness. Although the low insulation thickness increases the heating demand potential, the amount of heating need is much less than the cooling need.
- A ventilative cooling system significantly reduces the cooling demand by utilizing outdoor air as cooling resource. However, after the ventilation rate reaches a certain level, the cooling demand cannot be entirely satisfied by continuous increasing ventilation rate. Thus, an energy efficient combination of ventilative cooling and an air conditioner can be created by appropriate design of the ventilation rate.

- An alternative power solution for a technical shelter is to utilize renewable energy resources. An optimization model for hybrid energy system is developed, which combined a wind turbine, a PV panel and a back-up diesel generator. The total renewable energy fraction of electricity is 77 %, which significantly reduces the need of conventional fossil fuel.

References

1. Glania G, Rolland S, Patel A (2011) Best practises of the alliance for rural electrification. Renewable Energy House, Brussels, pp 1–2
2. Nakao M, Ohshima K, Jitsukawa H (1988) Thermal control wall for telecommunication equipment rooms. In: Proceedings of the 10th international telecommunications energy conference, San Diego, Canada, pp 280–284
3. Zhang Y, Chen Y, Wu J, Meng Q (2008) Study on energy efficient envelope design for telecommunication base station in Guangzhou. Energy Build 40:1895–1900
4. Hayama H, Nakao M (1989) Air flow systems for telecommunications equipment rooms. In: Proceedings of the 11th international telecommunications energy conference, Florence, Italy, pp 1–7
5. Chen Y, Zhang YF, Meng QL (2009) Study of ventilation cooling technology for telecommunication TBS in Guangzhou. Energy Build 41:738–744
6. Katti K, Khedkar MK (2007) Alternative energy facilities based on site matching and generation unit sizing for remote area power supply. Sci Direct Renew Energy 32:1346–1366
7. White paper, Alternatives for powering telecommunications base stations. http://www.motorola.com
8. Ashok S (2007) Optimised model for community-based hybrid energy system. Renew Energy 32:1155–1164
9. Trechsel HR (1994) Moisture control in buildings. ASTM Manual Series: MNL 18. American Society for Testing and Materials, Philadelphia, pp 225–227
10. BSim—Building simulation. http://sbi.dk/en/publications/programs_models/bsim/bsim-building-simulation
11. Energy modeling software for hybrid renewable energy systems. http://www.homerenergy.com/
12. http://eosweb.larc.nasa.gov/sse/RETScreen/
13. http://www.windustry.org/resources/how-much-do-wind-turbines-cost
14. Nema P, Nema RK, Rangnekar S (2010) PV-solar/wind hybrid energy system for GSM/CDMA type mobile telephony base station. Energy Environ 1(2):359–366
15. http://www.fuel-prices-europe.info/

Chapter 2
The Study on Paraffin-Water Emulsion PCM with Low Supercooling Degree

Xiyao Zhang, Jianlei Niu, Jianyong Wu and Shuo Zhang

Abstract This study aims to develop paraffin waxes based phase change material emulsion with low supercooling degree, which can be applied in a Thermal Energy Storage (TES) systems to maximize the use of natural heating and cooling sources via solar thermal collectors or evaporative coolers, and to raise the energy efficiency of the chillers operating at off-peak period. In this study, a kind of hexadecane-water emulsion with small droplet size was prepared and analyzed. The modified Multi-Wall Carbon Nano-Tube (MWCNT) particles were dispersed in emulsion as the nucleating agent to reduce supercooling degree. The MWCNT particles were modified with strong acids H_2SO_4 and HNO_3 to increase the compatibility with the organic liquid. Thermal analysis of the hexadecane-water emulsions with well-dispersed MWCNT particles by Differential Scanning Calorimeter (DSC) indicated that the supercooling degree of emulsion was significantly decreased. The effective ranges of nucleating agent concentration were summarized which provided a promising way of improving the performance of system energy efficiency in TES systems.

Keywords TES · Supercooling · PCM · Emulsion · MWCNT · Nucleating agent

X. Zhang · J. Niu (✉) · S. Zhang
Department of Building Service Engineering, The Hong Kong Polytechnic University, Kowloon, Hong Kong, China
e-mail: jian-lei.niu@polyu.edu.hk

J. Wu
Department of Applied Biology and Chemical Technology, The Hong Kong Polytechnic University, Kowloon, Hong Kong, China

A. Li et al. (eds.), *Proceedings of the 8th International Symposium on Heating, Ventilation and Air Conditioning*, Lecture Notes in Electrical Engineering 262,
DOI: 10.1007/978-3-642-39581-9_2,

2.1 Introduction

Thermal Energy Storage (TES), as it deals with energy saving and the optimum use of renewable energy, have obtained considerable attention in the past 20 years. In particular, the energy storage materials applied in TES system is a key factor to maximize the use of the energy sources. Generally, the energy storage materials have a high energy storage density which can store or release a large amount of latent heat during their phase transformation processes, so they are also named Phase Change Materials (PCM).

However, as the thermal conductivity of most PCM is comparatively low, they generally have a low heat transfer rate which is unacceptable in the heat exchange processes. For solving this problem, PCM emulsions and microencapsulated PCM are often used to improve the heat transfer between the PCM and the ambient by increasing the surface to volume ratio of the PCM [1, 2].

Besides, the PCM liquid usually can be cooled below its melting point without occurring in crystallization. This phenomenon is called supercooling which is unexpected in the latent heat storage as it leads to a shift of the controlling temperature range of the systems and even an increase of the energy consumption of the chiller resulted from a low COP. Furthermore, from the nucleation theory, supercooling of PCM in small volumes is expected to be more severe than in large volumes, which indicates that the supercooling in emulsion will be more serious than that in bulk PCM as their small droplet size. Günther et al. studied in detail the supercooling in hexadecane emulsions with droplet size in the range of about 0.1–20 μm. An increased supercooling of at least 10 K for small droplets was observed [3]. For decreasing the supercooling, an effective approach is the addition of liquid or solid nucleating agents to the PCM liquids as the seeds and catalysts for nucleation and crystal growth [4], such as 1-Tetradecanol for microencapsulated *n*-Tetradecane [5], paraffin wax for tetradecane and hexadecane paraffin-in-water emulsion [6], and TiO_2 [7] or α-Al_2O_3 [8] for the pure water.

Our previous study [9] has investigated the effects of Multi-Wall Carbon Nano-Tube (MWCNT) particles as nucleating agent to inhibit supercooling in the PCM liquid, which showed a good performance at low concentration. This study is to evaluate the effectiveness of the MWCNT nano-particles as nucleating agent in emulsions. Hence, in this study, a kind of *n*-hexadecane emulsion was designed and prepared and the MWCNT particles were well dispersed in emulsions at various concentrations. The effectiveness of the nucleating agent for emulsion was evaluated by comparing the DSC results of emulsions.

2.2 Experiment

2.2.1 Materials

In this study, *n*-hexadecane $C_{16}H_{34}$ (99 %) was chosen as the PCM liquid (purchased from International Laboratory USA), and the multi-walled carbon nano-tube (MWCNT) used as raw material of the nucleating agent, which had an outer diameter 10–20 nm, length 0.5–2 μm, and 95 % purity (purchased from Chengdu Organic Chemicals Co. Ltd., Chinese Academy of Sciences, China). The nitric acid (70 %) and sulfuric acid (98 %) were obtained from Aldrich. 1-decanol (decan-1-ol) and Tween-20 (polysorbate 20) were chosen as surfactants for dispersing the MWCNT particles in hexadecane and the emulsion preparing respectively, which were all of analytical grade.

2.2.2 Modification of MWCNT Particles

The original MWCNT particles were oxidized by the concentrated H_2SO_4 (98 %) and HNO_3 (70 %) at 3:1 volume ratio in a flask with reflux at 65 °C for 4 h. After cooling down to room temperature, the resulting diluted nanotube-acid mixture was then filtered using a 0.2 μm nylon membrane filter (Millipore), and leaving a MWNT filter cake. The nanotubes were then rinsed with water until a pH above 5 was obtained. Final rinsing was done using ethanol and the resulting solid particles were dried at 80 °C in an oven for about one day.

2.2.3 Preparation of PCM Slurry and PCM-Water Emulsion

After furbished, the surface-modified MWCNT particles were re-dispersed in hexadecane with the 1-decanol as the surfactant. In this step, an ultrasound probe (Sonics Vibra-Cell, model VCX130) was used to help the well dispersion with 30 % amplitude of power for 20 min. By repeating the above steps, the PCM slurry with the nucleating agent at various concentrations from 0.05 to 0.5 wt% was yielded for the following studies.

The above different PCM slurries were then mixed with water at 1:2 mass ratio and the Tween 20 (5 wt%) as the surfactant was added into the mixture. A disperser (type ULTRA-TURRAX T25 by IKA-Labor-Technik) was used for the formation of emulsion with a rotate speed at 8,000 rotations per minute for 10 min. The emulsions with different concentration of nanoparticles were prepared by the method above.

2.2.4 Characterization and Analysis of Emulsion Droplets and the Nanoparticles

The size distributions of emulsion droplets and the nanoparticles were determined by using a laser diffraction particle size analyzer of type Malven Zetasizer. This analyzer has a broad measuring range from 0.02 to 5,000 μm. 100 measurements were performed for 20 min at a scattering angle of 90° at 25 °C. The average particle size (in nm) and the polydispersity index were analyzed out by the Zetasizer 3000HSA-Advanced Software.

The morphology of the PCM-water emulsion droplets were examined with an optical microscope type Leica DM4000 under 400x. The images were processed by Leica LAS AF software.

2.2.5 Thermal Analysis

To determine the melting and nucleation temperatures, a DSC type METTLER TOLEDO DSC-822e with aluminum crucibles was used. The temperature and sensitivity calibration were carried out by using the standard materials. The temperature program for each material was created in such a way: The heating/cooling rate was 5 °C/min. The samples were first cooled to the initial temperature of −5 °C for at least 15 min for stabilization, and then heated to 30 °C, held for 5 min at 30 °C, and finally cooled to −5 °C.

2.3 Results and Discussion

2.3.1 The Particle Size Distribution of Modified MWCNT Particles

The average hydrodynamic diameter of MWCNT-1-decanol in hexadecane shown in Fig. 2.1 was 1,762 nm or 1.76 μm by the dynamic light scattering analysis with the count rate at 248 ± 5.2 kilo count per second (kcps) at 25 °C. The range difference within the repeated measurements was ±94.8 nm, therefore the MWCNT particles were well dispersed. The polydispersity index was 1, which means the range of particle size distribution was wide. Besides, it can be seen that the particle size of the MWCNT was obviously increased after the modification. The main reason was the aggregation occurring in the modification process, especially in the drying step. Moreover, in the dispersion procedure, the MWCNT particles were coated by the 1-decanol to enhance the compatibility in liquid [9], which eventually enlarged the average hydrodynamic diameter. However, from our observation, the growing of the particle size did not show an obvious negative affection on the nucleation.

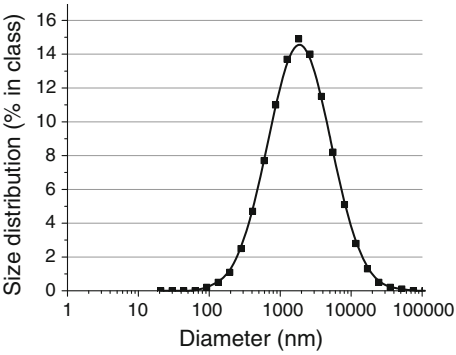

Fig. 2.1 The particle size distribution of the modified MWCNT particles

2.3.2 The Droplet Size Distribution of the PCM-Water Emulsion

After a high-speed stirring of the disperser, the emulsion with small droplets of PCM was obtained. For scaling the droplet size of the emulsion, the nucleating agent was not added in. And also measured by the dynamic light scattering analysis at 25 °C, the average diameter of hexadecane droplets was 2,082 nm with a wide distribution (PDI = 1) shown in Fig. 2.2. The count rate was at 231.2 ± 31.9 kcps.

2.3.3 The Morphology of PCM-Water Emulsion Droplets

Optical photomicrographs of the PCM-water emulsion droplets under 400x are presented in Fig. 2.3. The size and shape of droplets can be observed clearly and are consistent with the results from the DLS, with a centralized outer diameter of 0.1–10 μm. The modified MWCNT particles are hardly observed as their small diameter and low concentration.

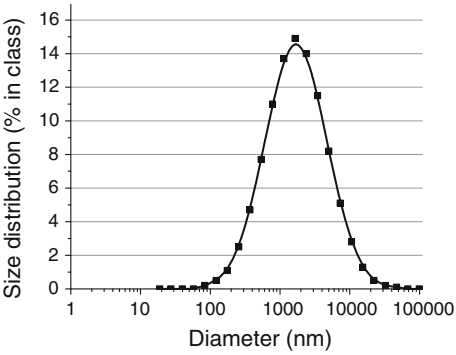

Fig. 2.2 The particle size distribution of PCM-water emulsion

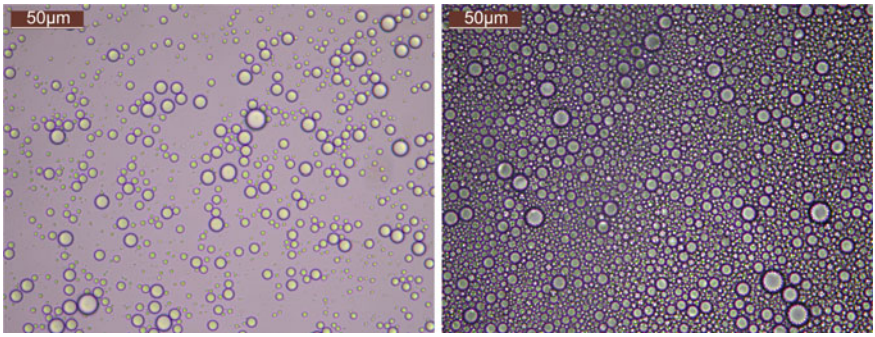

Fig. 2.3 The morphology of the PCM-water emulsion droplets (*left* diluted, *right* undiluted)

2.3.4 The Supercooling in PCM-Water Emulsion

We have observed the capacity of the modified MWCNT as the nucleating agent (NA) to reduce the supercooling of PCM crystallization in previous work [9], especially in relatively light concentrations. The optimal concentration of NA was around 0.1–0.2 wt% versus the *n*-hexadecane. In this section, a detailed investigation in emulsions was conducted to find out an optimum concentration of nucleating agent. The differential scanning calorimetry was used to analyze the thermal property of the *n*-hexadecane-water emulsion. The melting peak point was defined as the melting temperature $T_{\text{m.peak}}$ and the freezing peak point as the nucleation temperature $T_{\text{f.peak}}$. The difference between the melting and nucleation temperature was considered as the supercooling degree.

According to the nucleation theory, the supercooling is expected to increase along with the droplets decline [3]. From the DSC heating/cooling curves of the PCM-Water emulsion shown in Fig. 2.4, when the nucleating agent was absent

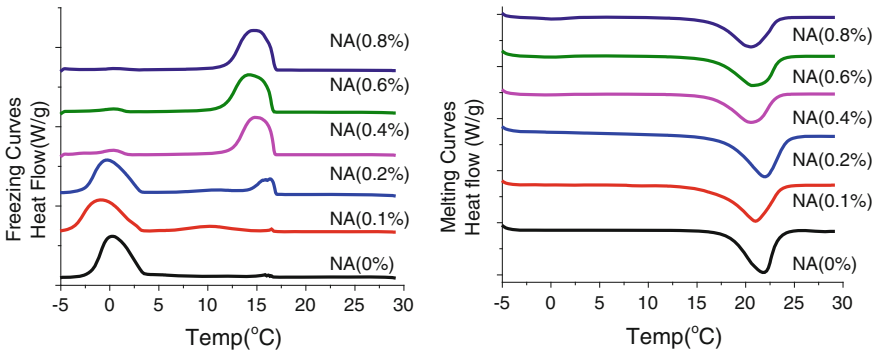

Fig. 2.4 The DSC freezing/melting curves of different emulsion samples with MWCNT as NA (weight concentration vs. the *n*-hexadecane)

Table 2.1 Melting and crystallization properties of PCM-water emulsion with MWCNT as NA

Sample	ΔH_m (J/g)	ΔH_f (J/g)	$T_{m.peak}$ (°C)	$T_{f.peak}$ (°C)	ΔT (°C)
NA (0 wt%)	−73.86	73.61	19.44	1.37	18.07
NA (0.1 wt%)	−98.51	73.71	19.69	0.48	19.21
NA (0.2 wt%)	−82.94	1st: 11.12	20.34	1st: 16.92	3.42
		2nd: 51.82		2nd: 0.76	19.58
NA (0.4 wt%)	−72.53	66.76	19.49	16.00	3.49
NA (0.6 wt%)	−80.56	75.21	19.69	15.49	4.20
NA (0.8 wt%)	−80.51	77.39	19.37	15.97	3.40

(MWCNT at 0 wt%), the PCM droplets hardly occurred crystallization until near the ice point, in despite of tiny energy fluctuations occurring in freezing circle at approximate 15 °C, thus a dramatically large extent of supercooling of 18.07 °C was observed. Associated with the increasing concentrations of the nucleating agent, there are two obvious peaks can be observed on the freezing curves and the extent of the releasing energy at zones above 10 °C enhanced gradually with the other peak going down until the mass ratio of MWCNT and PCM reached to 0.6 wt%. After that, the nucleation effect was also significant but similar to that at 0.6 wt%. And it should also be noticed that the supercooling was controlled to below 4 °C by the effect of modified MWCNT. The detailed melting and crystallization properties calculated from the DSC data are presented in Table 2.1.

Considered that the mass ratio of PCM and water was 1:2, the 'macroscopical' concentration of the nucleating agent should be approximate 1/3 of that in PCM, thus the results coincide with the performance of MWCNT in PCM liquid in our previous work. Moreover, in the microcosmic view, as the PCM was separated into many small volumes, nucleation had to occur in every volume individually [3]. Especially when the nucleating agent particles in a low concentration only existed in some droplets, the heterogeneous nucleation was limited to this part of PCM droplets and the rest PCM volumes could only solidify after homogeneous nucleation, which contribute to the two freezing peaks in some curves. Therefore, there existed an optimal or a least effective concentration of the nucleating agent and it was 0.6 wt% versus the *n*-hexadecane for the emulsion investigated in this work.

2.4 Conclusion

In this study, the experimental results show that, as the nucleating agent, a low concentration of modified MWCNT nano-particles were effective to reduce the supercooling degree in the PCM-Water emulsions. Besides, it is clear that there existed an optimal or a least effective concentration of the nucleating agent for the emulsion and it was 0.6 wt% (weight concentration vs. the *n*-hexadecane) for the emulsion investigated in this work. Eventually, a kind of emulsion which has heat capacity at approximate 80 J/g and freezes around 16 °C was obtained.

Acknowledgments The authors are grateful to the Research Grant Council of the Hong Kong SAR government for providing support to this research through GRF PolyU 5241/11E.

References

1. Kasza KE, Chen MM (1985) Improvement of the performance of solar energy or waste heat utilization systems by using phase-change slurry as an enhanced heat-transfer storage fluid. J Sol Energy Eng 107:229–236
2. Regin AF, Solanki SC, Saini JS (2008) Heat transfer characteristics of thermal energy storage system using PCM capsules: a review. Renew Sustain Energy Rev 12(9):2438–2458
3. Günther E, Schmid T, Mehling H, Hiebler S, Huang L (2010) Subcooling in hexadecane emulsions. Int J Refrig 33:1605–1611
4. Sangwal K (2007) Additives and crystallization processes: from fundamentals to applications. Wiley, New York
5. Yamagishi Y, Sugeno T, Ishige T, Takeuchi H, Pyatenko AT (1996) An evaluation of microencapsulated PCM for use in cold energy transportation medium. In: Proceedings of the 31st intersociety energy conversion engineering conference, IECEC 96, Washington, DC, USA, pp 2077–2083
6. Huang L, Gunther E, Doetsch C, Mehling H (2010) Subcooling in PCM emulsions—part 1: Experimental. Thermochim Acta 509:93–99
7. He Q, Tong W, Liu Y (2007) Experimental study on super-cooling degree of nanofluids for cryogenic cool storage. J Refrig 28:33–36
8. Zhang XJ, Wu P, Qiu LM, Zhang XB, Tian XJ (2010) Analysis of the nucleation of nanofluids in the ice formation process. Energy Convers Manage 51:130–134
9. Zhang S, Wu J-Y, Tse C-T, Niu J (2012) Effective dispersion of multi-wall carbon nano-tubes in hexadecane through physiochemical modification and decrease of supercooling. Sol Energy Mater Sol Cells 96:124–130

Chapter 3
Analysis of Energy Utilization on Digestion Biogas Tri-Generation in Sewage Treatment Works

Zhiyi Wang, Hongxing Yang, Jinqing Peng and Lin Lu

Abstract This paper presents a combined heating, cooling, and power generation (tri-generation)system using sewage treatment digestion biogas according to the principle of energy gradient utilization technology. The tri-generation scheme adopts Lithium Bromide (LiBr) absorption cooling technology for office air conditioning, a biogas power generator, a heating system for digestion tanks. The performance analysis demonstrates that the scheme is practical in Hong Kong. Surplus cooling of the chiller is used to cool the inlet air of the generator for increasing the biogas power generator output. The electricity generation capacity can be increased by around 7 % annually owing to the inlet air cooler. For a case study of a local sewage water treatment work, the cooling capacity is equal to 422.72 MWh. The hot water meets the digester heating load at the same time. It is estimated that the economic payback period will be about 2 years.

Keywords: Sewage treatment plant · Biogas generator · Absorption chiller · Inlet air cooling

3.1 Introduction

Nowadays, the world is facing potential energy crisis due to the rising demand of primary energy and shrinking storage of fossil fuels. Renewable energy, such as biomass, solar, and wind power, is regarded as the main way to overcome this

Z. Wang (✉)
School of Civil Engineering and Architecture, Zhejiang University of Science and Technology, Hangzhou, China
e-mail: zywang-wf@163.com

Z. Wang · H. Yang · J. Peng · L. Lu
Renewable Energy Research Group (RERG), Department of Building Services Engineering, The Hong Kong Polytechnic University, Hong Kong, China

A. Li et al. (eds.), *Proceedings of the 8th International Symposium on Heating, Ventilation and Air Conditioning*, Lecture Notes in Electrical Engineering 262,
DOI: 10.1007/978-3-642-39581-9_3,

challenge [1]. Biomass is organic-rich biological material, which can be either used directly or converted into another kind of fuels such as biogas or biofuel. Sewage treatment works are now popular in large cities, which have two functions: one is to treat sewage into harmless water and the other is to convert the dissolved organic matter in the sewage into biogas [2, 3]. During the digestion process of sewage treatment works, some biodegradable organic materials contained in the sludge are decomposed under anaerobic condition. At the same time, a flammable and harmful gaseous mixture, which is mainly constituted by methane (CH_4) and carbon dioxide (CO_2), is released together with trace amounts of volatile organic compounds (VOC) [4, 5].

Gas turbines are usually used to generate electricity [6, 7]. Enhancement of the gas turbine engines' energy performance by adding an inlet air cooler has been studied [8, 9]. The proposed tri-generation system in this paper adopts this inlet air cooling technology and generates electricity, chilled water, and hot water jointly. Biogas generators are used to generate electricity and their exhaust heat can be used by a lithium bromide (LiBr) absorption chiller for producing chilled water, which can not only be used for space air conditioning, but also for cooling the inlet air of the gas turbine so that the power generation efficiency of the generators is improved in turn. Hot water is the byproduct of the tri-generation system which can be used to heat the digestion tanks or supply hot water to other users.

3.2 Present Situation of the STW

The sewage released by residences and industries consists of 99.94 % water and only 0.06 % dissolved and/or suspended solid material. A sewage treatment work can treat about 80,000–93,000 m^3 of wastewater every day, and the digester is a continuous reactor stirred using an injection of part of the generated biogas. Electricity is used to recycle the sludge and inject the biogas. Biogas is produced in the digester by mesophilic (30–35 °C) microorganisms. The production capacity of biogas is almost constant (about 11,000–13,000 Nm^3/d) at 35 °C.

For energy analysis reported below, the average methane content in the biogas is assumed to be 64 %. Typical composition of the biogas produced in a local sewage treatment works is given in Fig. 3.1.

3.2.1 Heating Load of Digester

Digesters have to be operated at a design temperature. The heating load of the anaerobic reaction in it can be calculated by steady state heat transfer.

$$\mathrm{HL} = \sum \left(\mathrm{HL}_{\mathrm{wall}}, \mathrm{i} + \mathrm{HL}_{\mathrm{soil}}, \mathrm{i}\right) + \mathrm{HL}_{\mathrm{soil}} \tag{3.1}$$

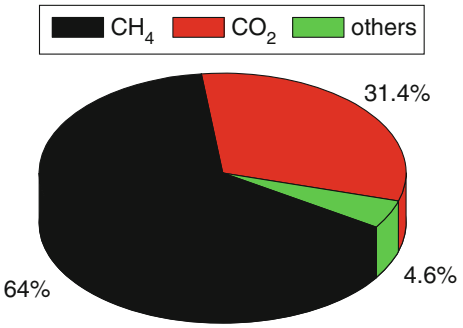

Fig. 3.1 Biogas composition in sewage treatment works

Table 3.1 Average heating load of anaerobic digester typical months in Hong Kong

Months	Ambient temperature (°C)	Soil temperature (°C)	Sludge temperature (°C)	Digester heating load (kW)
January	16.3	18.9	14	849.8
February	16.8	18.8	14	843.8
March	19.1	20.4	16	761.3
April	22.6	23.1	16	714.0
November	21.8	24.4	14	773.3
December	17.9	20.6	14	827.3

$$H_{\text{sludge}} = m_{\text{sludge}} \cdot C_p \Delta T_x \tag{3.2}$$

$$\text{HL}_i = F_{\text{digester}} \cdot K_i \Delta T_i \tag{3.3}$$

The monthly average temperatures were used to calculate the heating load of a digester. Table 3.1 presents the digester heating load in typical months in Hong Kong.

3.2.2 Disadvantages of the Present Biogas Utilization Scheme

The digestion biogas can be utilized in more efficient ways. One of the efficient ways to utilize the digestion biogas is to burn biogas in a gas turbine for generating electricity and then the waste heat produced in the gas turbine can be used to heat the sludge digestion tank, i.e., a combined heating and power generation by using biogas as fuel for gas turbine. In this utilization mode, the high-grade thermal energy produced by burning biogas is used for generating high-quality electricity power and the low-grade thermal energy from the gas turbine is used for heating the sludge digestion tank. Therefore, the combined heating and power is a more reasonable utilization way for using biogas from the viewpoint of thermodynamics.

For a combined heating and power system, however, the inconsistency problem still exists between the thermal energy generation capacity and demand. In the months from April to November, the required thermal energy in sludge digestion tanks is reduced and a large amount of thermal energy produced by the combined heating and power system has to be uselessly released to surrounding atmosphere through radiators.

3.3 Proposed Digestion Biogas Combined Cooling, Heating, and Power System

To improve the energy utilization efficiency of biogas from sewage treatment plants, an innovative scheme is proposed in this paper, i.e., a tri-generation system to combine cooling, heating, and power. A schematic diagram of this tri-generation system is shown in Fig. 3.2, which provides multiservices by using a single energy source, including electricity supply, space air conditioning, and heating of sludge digestion tank or hot water supply to other users.

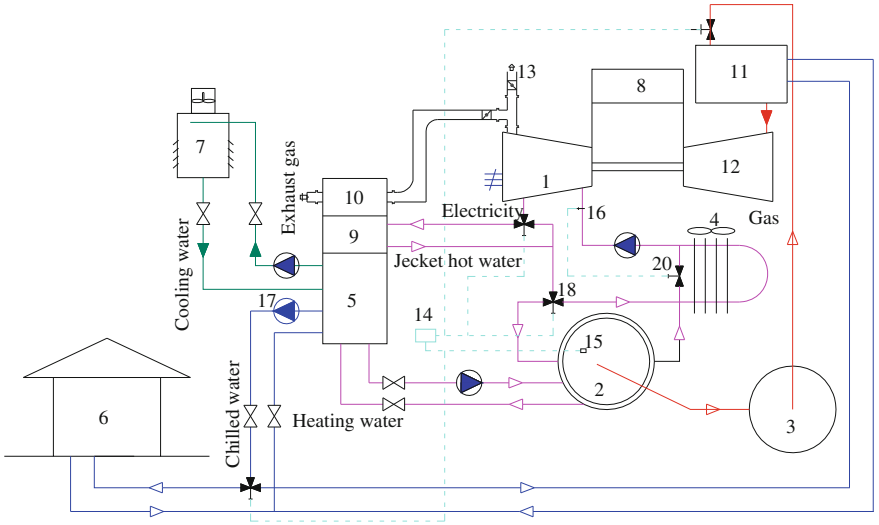

Fig. 3.2 Schematic diagram of the proposed tri-generation system *1* Biogas generator, *2* Sludge digestion tank, *3* Gas holder, *4* Radiator, *5* Lithium Bromide absorption chiller, *6* Office building, *7* Cooling tower, *8* Combustor, *9* Hot water generator, *10* Flue gas generator, *11* Inner air cooler, *12* Compressor, *13* Chimney damper, *14* Controller, *15* Temperature sensor, *16* Thermometer, *17* Pump, *18* Three-port regulation valve, *19* Valve, *20* Two-port regulation valve

3.3.1 Biogas Generator

A biogas generator consists of an air compressor, a biogas combustor, and a turbine with permanent magnet alternator rotor. According to the biogas production capacity, two biogas generators are selected. The parameters are shown in Table 3.2.

3.3.2 Lithium Bromide Absorption Chiller

Absorption chillers often use water and lithium bromide or aqua ammonia as absorbent-refrigerant working fluid pairs among 40 refrigerant and 200 absorbent compounds [6]. Water lithium bromide is selected in the combined cooling, heating, and power system on the basis of the nontoxicity of lithium bromide and water, low volatility of lithium bromide, absence of requirement for an extra component (i.e., dephlegmator), as well as lower installation, maintenance, and operating costs relative to aqua ammonia systems.

The cooling capacity of the lithium bromide absorption chiller has to satisfy the maximum cooling load of nearby office building in summer. The chiller capacity is determined by the hottest day's hourly peak load of the office building (1,556.46 kW), which is shown in Fig. 3.3. Based on the manufacturer catalogue, two lithium bromide absorption chillers with a rated cooling capacity of 780 kW are employed here.

It is worth noted that the chillers' standard working conditions are: environmental pressure of 101.3 kPa, environmental temperature of 15 °C and relative humidity of 60 %. There are two generators in the Lithium Bromide absorption chiller, i.e., a flue gas generator and a hot water generator. The design parameters of the chiller are shown in Table 3.3.

Table 3.2 Design parameters of the biogas generator

Unit type	500GF-NK
Rated power (kW)	500
Rated speed (r/min)	1000
Nominal voltage (V)	400
Rated current (A)	902
Rated frequency (Hz)	50
Power factor (COSΦ)	0.8 (lag)
Specific heat consumption of biogas (MJ/kWh)	$\leq$10
Generator thermal efficiency (%)	$\geq$36
Discharge temperature (°C)	$\leq$550
Dimensions (m)	5120 × 2040 × 2780
Unit weight (kg)	12500

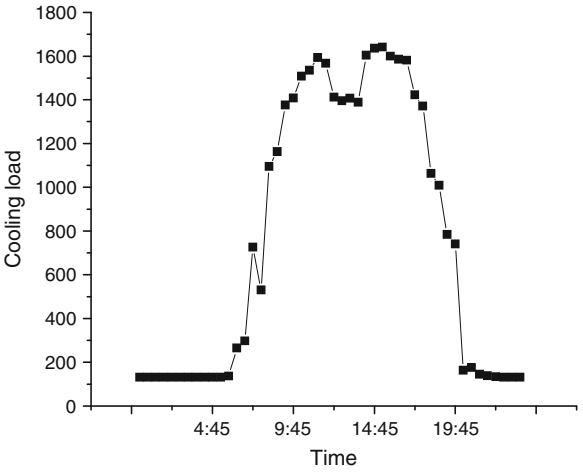

Fig. 3.3 The hourly cooling load of an office building in the hottest day

Table 3.3 Key parameters of the Lithium Bromide absorption chiller

Cooling capacity (kW)	780
Inlet and outlet temperature of chilled water (°C)	12/7
Flow rate of chilled water (m^3/h)	134
Inlet and outlet temperature of cooling water (°C)	32/37
Flow rate of cooling water (m^3/h)	262

The ambient temperature in Hong Kong is higher than the ISO condition of a biogas generator (15 °C) throughout the year. An air to water heat exchanger, which is installed at the inlet duct of compressor, can be installed as an inlet air cooler for increasing the energy output efficiency of the generator.

3.4 Operation of the Tri-Generation System

In a summer season from May to October, hot water from the cylinder jacket of the biogas generator is first pumped into the hot water generator, and heats and regenerates the absorbent, and then flows into the sludge digestion tank to heat the sludge. If the return water temperature from the sludge tank is still higher than the temperature required by the biogas generator, it will pass through a radiator and releases part of heat into surrounding atmosphere before it goes back to the biogas generator. A thermometer can be used to measure the temperature of the return water of the biogas generator and the temperature of the return water can be regulated by a two-port regulation valve.

In the flue gas generator, the high temperature exhaust gas from the biogas generator is also used to regenerate the absorbent to produce chilled water.

Table 3.4 Energy distribution of the biogas generator

No.	Item	Heat recovery (kW)
1	Cylinder jacket	930
2	Exhaust gas	634
3	Electricity	1003
4	Radiation and exhaust gas loss	442

The exhaust gas from the flue gas generator and high temperature generator will be vented into atmosphere.

The office air conditioning cooling load varies hourly and there is no cooling load at night as shown in Fig. 3.3. The ambient temperature is much higher than the ISO condition of biogas generator (15 °C) in summer. A return chilled water temperature sensor is used as the input signal of a controller to control the water flow rate of the office air conditioning system by regulating a three-port valve. Then, the surplus cooling capacity is used to cool the inlet air of the biogas generator so as to increase its power generation efficiency.

In the months from November to April of the next year, no space air conditioning is needed in an office in Hong Kong and part of the thermal energy generated by the biogas generator is used to heat the sludge digestion tank. As shown in Table 3.4, under this operation mode, the jacket hot water is directly pumped into the sludge digestion tank to heat it. The heating capacity of the cylinder jacket hot water is sufficient to meet the heating load in winter season.

The exhaust gas of the biogas generator is used to drive the flue gas generator of the chillers for hot water production, which is also used for heating the digestion tank. If the temperature of the sludge digestion tank cannot be maintained at 35 °C only by the jacket hot water and exhaust gas, part of the biogas can be used to drive the high temperature generator to provide hot water for the digestion tank.

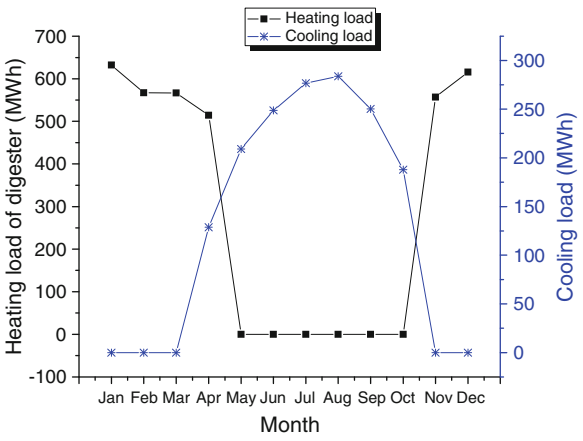

Fig. 3.4 Heating and cooling load of the system

The heating load and cooling load are shown in Fig. 3.4. There is surplus heat of the cylinder jacket hot water. Two three-port regulation valves will be used to regulate the flow rate and the temperature of the hot water supplied to the digestion tank to maintain its temperature at required value. A temperature sensor (15) will be installed in the digestion tank and its temperature signal will be used as the input signal of the controller (14) to control the temperature of the digestion tank through regulating the two three-port valves. The cooling capacity of the surplus cylinder jacket hot water and exhaust air are used to cool the inlet air cooler and increase the biogas power generation efficiency.

3.5 Cost-Benefit Analysis

The net electricity production increase is around 7806 MWh/year. If the COP of an air source heat pump is assumed to be 3 from May to October, about 422.72 MWh electric energy can be saved from the absorption chillers. At the same time, the power consumption is 1340 MWh every year The economic benefit due to the increase of energy generation efficiency is calculated to be HK$5.17 m based on the current electricity price in Hong Kong. The economic payback time is 1.7 years.

3.6 Conclusions

In this paper, an innovative and more efficient utilization way for using the digestion biogas from sewage treatment works was developed. The main findings can be concluded as follows:

(1) After replacing the boiler by Lithium Bromide absorption chillers, the cooling capacity produced by the chillers can be used for space air conditioning as well as for cooling the inlet air of the biogas generator so as to improve its power generation efficiency.
(2) The tri-generation system is cost-effective.
(3) The inconsistence of heating and cooling loads can be solved by the system, and the comprehensive energy efficiency is much higher.

References

1. Cao Y, Pawlowskia A (2012) Sewage sludge-to-energy approaches based on anaerobic digestion and pyrolysis: brief overview and energy efficiency assessment. Renew Sustain Energy Rev 16:1657–1665
2. Hao X, Hongxing Y, Guoqiang Z (2008) Tri-generation: a new way for landfill gas utilization and its feasibility in Hong Kong. Energy Policy 36:3662–3673
3. Popli S, Rodgers P, Eveloy V (2013) Gas turbine efficiency enhancement using waste heat powered absorption chillers in the oil and gas industry. Appl Therm Eng 50:918–931
4. Moya M, Bruno aJC, Eguia P, Torres E, Zamora I, Coronas A (2012) Performance analysis of a combined cooling, heating, and power system based on a micro gas turbine and an air-cooled, indirect fired, ammonia-water absorption chiller. Applied Energy 88:4424-4440
5. Ameri M, Hejazi SH (2004) The study of capacity enhancement of the Chabahar gas turbine installation using an absorption chiller. Appl Therm Eng 24:59–68
6. Ashley DS, Sarim AZ (2011) Gas turbine performance at varying ambient temperature. Appl Therm Eng. 31:2735–2739
7. Srikhirin P, Aphornratana S, Chungpaibulpatana S (2001) A review of absorption refrigeration technologies. Renew Sustain Energy Rev 5:343–372
8. Yousef S, Najjar H (1996) Enhancement of performance of gas turbine engines by inlet air cooling and cogeneration system. Appl Therm Eng 16:163–173
9. Gulkowska A, Leung HW, So MK, Taniyasu S, Yamashit N, Leo WYY, Bruce JR, Leic AP, Giesy JP, Paul KSL (2008) Removal of antibiotics from wastewater by sewage treatment facilities in Hong Kong and Shenzhen. Water Res 42:395–403

Chapter 4
Approach and Practice of District Energy Planning Under Low-Carbon Emission Background

Baoping Xu, Changbin Zhu and Wenlong Xu

Abstract District energy planning is an important approach to achieve a low-carbon target. However, district energy planning has not yet been incorporated in the official planning system, and there are still no clear standards and specifications defining the content and depth of low-carbon emissions reform. In this paper, low-carbon energy planning practices of several new districts are summarized and a general theoretical and practical framework for district energy planning is proposed. In addition, six key points of concern in the planning process are identified. These include low-carbon estimation and index control, overall planning of infrastructure, linkage between city planning and other special low-carbon eco-planning, investment and financing and operation modes, planning management mechanisms, and the construction of a growing energy system which is combined with a project schedule. Finally, it is suggested that energy planning should be standardized as soon as possible and planned comprehensively from the aspects of technology, commerce, and management, in order to realize the low-carbon target.

Keywords Regional energy planning · Low-carbon · Standardization · Infrastructure · Index

B. Xu (✉) · C. Zhu
School of Energy Power and Mechanical Engineering, North China Electric Power University, 102206 Beijing, China
e-mail: xubaoping@gmail.com

W. Xu
China Architecture Design and Research Group, 100120 Beijing, China

A. Li et al. (eds.), *Proceedings of the 8th International Symposium on Heating, Ventilation and Air Conditioning*, Lecture Notes in Electrical Engineering 262,
DOI: 10.1007/978-3-642-39581-9_4,

4.1 Introduction

Before the Copenhagen conference, the China state council conference announced that the CO_2 emissions per GDP (Gross Domestic Product) in the period leading to 2020 will be decreased by 40–45 % compared to the ratio in 2005. China is, however, still a developing country, and in an accelerated development stage of industrialization and urbanization, energy demand continues to grow, resulting in an increased need for greenhouse gas emissions mitigation.

An energy infrastructure is developed as a natural byproduct of extensive urban construction, and usually one location develops its whole infrastructure during a period of rapid growth. Thus, good energy planning is very important, especially for a new district. Inspiration from successful energy systems in domestic and foreign low-carbon eco-cities [1] is not a simple application of technology, but is the balance and integration of the technology, sharing, and quantitative management and localization.

Fu and Zheng [2, 3] proposed an urban energy planning method that incorporated space distribution and time dynamic simulation, and developed a simulation tool to assist with energy planning for urban expansion. Besides, the macro energy planning method has been applied to several fields, such as regional integrated energy plans [4], urban energy supply and security [5], community energy planning [6], and energy consumption simulation for the building sector [7–10]. However, macro energy planning methods are more appropriate at the state or national levels. At the urban or local level, it is necessary to consider more engineering application factors.

District energy planning has not yet been incorporated into the official planning system, and its content and depth remain undefined. In this paper, the low-carbon energy planning practices of several new districts are summarized and a general theoretical and practical framework for district energy planning is proposed. Analysis of the data reveals six key points of concern in the planning process.

4.2 General Methodology

4.2.1 Low-Carbon Strategies

After reviewing domestic and international examples of low-carbon districts, and engineering practices such as the low-carbon planning of the Future Technology City, our planning team has proposed the CLEAR (capturing looping efficient additional renewable) system for district low-carbon planning.

The CLEAR system utilizes five pathways to address the troubling trend of high carbon emissions, by implementing green, sustainable, and healthy development strategies with low energy consumption to limit pollution and carbon emission. Emissions can be effectively reduced through a variety of methods based on five

principles: efficiency, renewability, looping, capture and storage, and additional districts. These methods begin with reducing energy demand and improving energy efficiency (efficiency). Using alternative and renewable energy sources (renewability), recycling already existing energy sources (looping), and capturing carbon dioxide (capture and storage) also prove effective. An additional method includes the development of low-carbon industries for outside of the district (additional districts).

Our work demonstrates the use of the CLEAR system for district energy planning and describes how to construct a low-carbon energy system. The approaches include building energy-saving, high-efficiency energy systems and device applications (efficiency), renewable and reasonable energy applications (renewability), as well as waste heat recycling and solid waste energy applications (looping). Additionally, the industrial structure will be adjusted to ensure low-carbon and green, environmentally friendly production (additional) sources will be demonstrated. Finally, a low-carbon energy system that combines conventional and renewable energy resources, integrates distributed and centralized modes, and considers recent and forward reasonable transitions will be built through energy planning.

4.2.2 Integrated Framework

By synthesizing a series of regional energy planning practices, we designed a basic framework for the CLEAR system. The framework includes three major steps. These include determining the target plan, formulating a master plan, and then formulating an indexing and implementation program. The target plan is comprised of the objectives and priorities, which are identified based on policies, standards, and case investigations of field surveys and higher-level planning, integrating the results of an analysis of resource conditions, infrastructure, and energy demand. According to the comprehensive analysis of output and demand, the master and zoning plans are used to optimize the energy system, and achieve a diverse assessment of economic, social, and environmental benefits. The third major component focuses on indexing and implementation. The regional energy system general control indexes are assigned to different zones and the investment, financing and operations modes are clarified before proceeding to the implementation (Fig. 4.1).

4.3 Discussion of Key Points

4.3.1 Assessment of Low-Carbon

Taking carbon emissions and carbon intensity as planning constraints is the foundation of the low-carbon concept in regional energy planning. Based on the information of planning, building capacity, functional layout, building energy

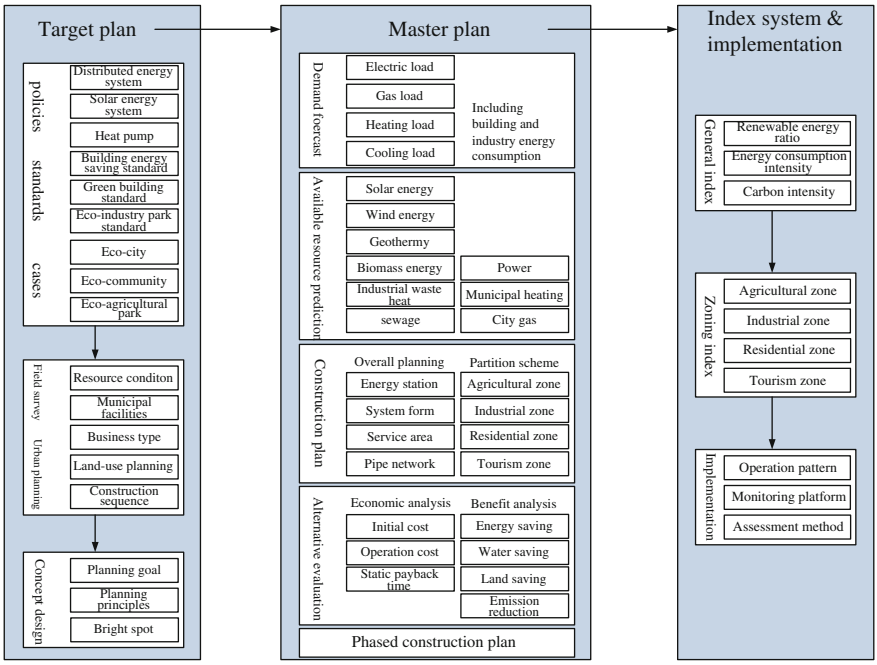

Fig. 4.1 Integrated framework of regional energy planning

efficiency standards, and energy consumption statistics, total energy consumption, energy structure, and carbon emissions are estimated in the baseline scenario. When building an energy planning program, possible energy consumption and carbon emission reduction of each low-carbon technology is analyzed, and technologies according to the local conditions are chosen. Finally, total energy consumption, energy structure, and carbon emissions can be calculated under low-carbon conditions. During the process, the critical steps include setting a reasonable baseline scenario, obtaining the basic data of reliable energy consumption, choosing each energy carbon emission factor, and applying each low-carbon technology scientifically. For specific calculation methods, see Ref. [11]. The quantitative target from low-carbon assessment is included in the control indicators for new district low-carbon construction.

4.3.2 Integrated Planning of Infrastructure

Heating, gas, and electricity generally a re considered separately in conventional special planning even though there is much correlation and interaction between these individual components of the energy infrastructure. For example, the gas heating energy consumption characteristics will affect the gas transmission and

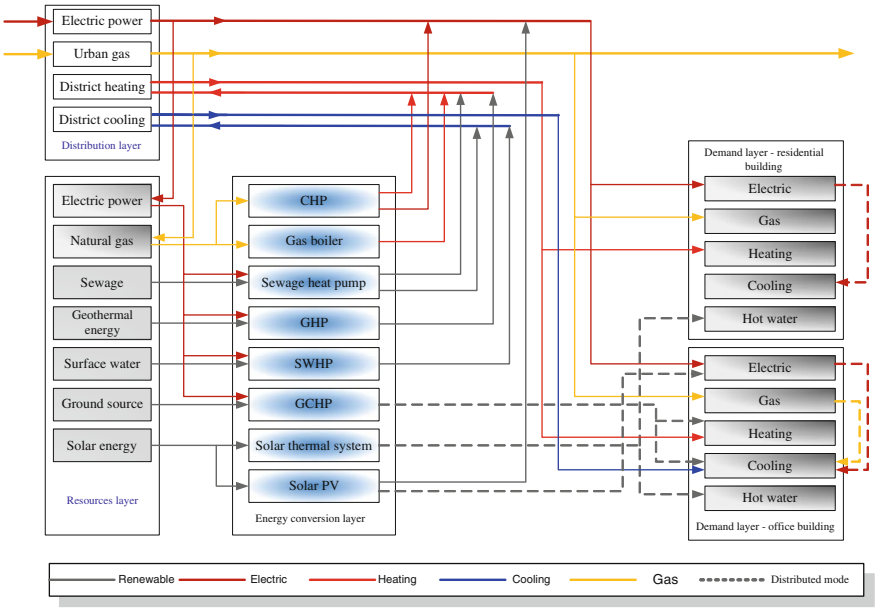

Fig. 4.2 The chart of a regional integrated energy system

distribution system, while the cogeneration heating scale has a certain impact on the grid, and gas-distributed generation, in turn, impacts gas, heating and electricity transmission, and distribution systems.

By applying system engineering methodology to regional energy planning, and coordinating heating, gas, electricity, and other energy uses, the allocation of resources is optimized. When forecasting the load demand and energy consumption, we should determine the demand of heat, electricity, and gas of the area based on the energy planning program rather than take general indicators from traditional planning to estimate this.

Figure 4.2 is a comprehensive energy planning diagram, and intuitively reflects the composition of a regional energy system and the relationship between each part. Components include source, distribution, requirement, and energy conversion layers. Solid lines represent centralized systems while dotted lines indicate decentralized systems. After completing the integrated energy planning, the amount of the energy flowing into and out of each connection is clear.

4.3.3 Planning Interaction

Vertically, regional energy planning is associated with conventional city planning. Combining energy and city planning with general, control, and revision regulations prevents already existing energy planning methods from derailing the broader

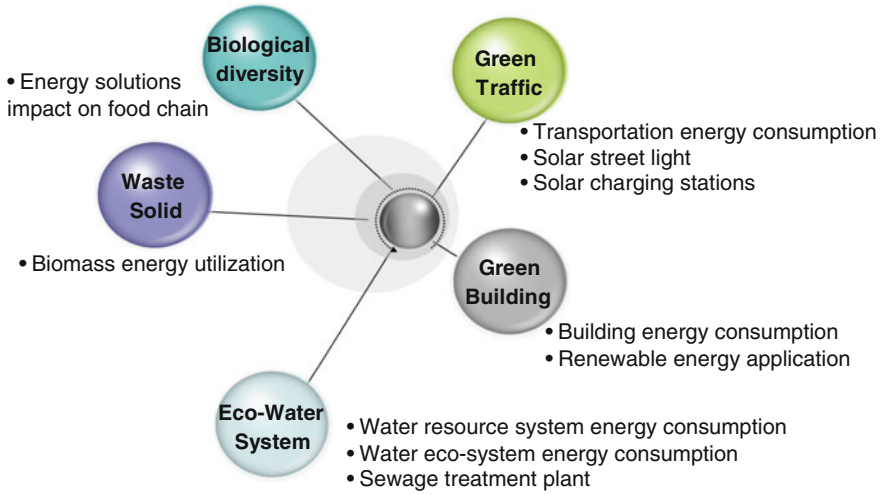

Fig. 4.3 Relevance between low-carbon energy planning and other low-carbon subsystems

planning goals and ensures that related plans, designs, and management will succeed. During the conventional planning stage, strategies and execution methods with the core objective of low-carbon are integrated into the process. At the general regulation stage, we confirm the planning positioning and the concept scheme with the main goal of low-carbon emissions. As part of the control regulation stage, the index system with the main goal of low-carbon, facilities location and floor area, is used to make sure that the low-carbon planning scheme can be executed and assessed. At the revised regulations stage, technical solutions, and design guidelines for realizing the goals of the index system is given.

Laterally, regional energy planning agrees with each special item of low-carbon planning (see Fig. 4.3). As current energy-saving policies proceed, and regional sustainable development is required, energy planning is carried out as a subsystem of the overall systematic low-carbon eco-planning work. It therefore becomes necessary to sort out the relevance of the energy systems and other low-carbon subsystems in order to ensure that each subsystem is unified and coordinated.

4.3.4 Investment and Operation Mode

Thus far, we have discussed technological concerns for decreasing the carbon to GDP ratio, but market analysis is also important to ensure that sources of funding for energy planning are available and well-managed, and to guarantee sufficient funds during the project plan period. Once the mode of construction has been designed, a market-oriented and profitable operation is finally possible. At the same time, national and energy-related policies are considered and their effect

Fig. 4.4 Regional integrated energy system

against the economics of applying energy technology should be analyzed. Figure 4.4 illustrates the sources of funding for energy-related projects, with the main aspects including investment and financing, construction, and operation.

4.3.5 Planning Management Mechanism

A regulatory mechanism is necessary to manage the entire process of energy system construction and operation. The management mechanism must consider indicators for control methods, assessment methods, and information management systems.

An example of the management mechanism can be found in Jiangsu province, where a new district energy plan was formulated based on the research of the energy planning scheme. In this instance, we developed a series of energy systems indexes for government departments. We not only clarified the control values of the indicators, but also defined the primary responsibilities of the organization. To realize these targets, we also analyzed executive departments and specific task type and description. Thus, a protection mechanism was provided for the construction of a low-carbon energy system at the management level.

4.3.6 Combination with the Progress of Construction

The construction of energy systems should be coordinated with the progress of the project. It is necessary to pay attention to the space and time constraints of energy demand and resource supply. With overall planning and progressive implementation, a growing energy system should be built that will achieve a reasonable transition between short-term needs and long-term goals. Ensuring a safe and reliable energy supply requires the elimination of redundant construction and intentionally planning the roles of investment, financing, and construction.

A new district energy planning in Fangshan District in Beijing illustrates this nicely. The existing infrastructure is poor, but power facilities are relatively complete and heating and natural gas infrastructure construction depends on the smooth implementation of Fangshan District's Twelfth Five-Year plan; therefore, short-term plans should first consider the existing resources of the zone to solve energy problems while the energy supplies of long-term planning relies on large municipal facilities. Achieving a reasonable transition from the short-term to the long-term is the key issue during the energy planning process.

4.4 Conclusions

It is necessary to establish standardized regional energy planning as soon as possible. The focus and depth of the standards need to be clarified, to ensure that regional energy planning is practical and effective. Existing energy planning should coordinate a variety of aspects such as technology, the market, and management and consider these factors generally. This paper has proposed a general conceptual and working foundation for district energy planning. Six key points of concern in the planning process are outlined below.

(1) *Low-carbon assessment*. This entails establishing a standard unified algorithm that accounts for intensified carbon emissions and energy consumptions at the district level. It is also necessary to assess and optimize the already existing energy scheme. To do this, the above indicators should be incorporated into new district-wide low-carbon construction controls.
(2) *Integrated planning of infrastructure*. During this stage, electricity, gas, heating, and hot water sources are coordinated and conventional and renewable energy sources are reasonably combined. A combination of distributed and centralized systems are optimized in a way that not only emphasizes low-carbon, ecological, and renewable sources but also focuses on and analyzes conventional energy supply conditions and efficient applications.
(3) *Planning interaction*. The planning should consider the vertical relationships that occur in the interaction between alternative energy planning and conventional city planning. Main points of concern are energy supply and demand, existing facilities, and other indicators. Laterally, the plan should

consider other low-carbon ecological related considerations, taking into account eco-planning for green construction, the ecological footprint, transportation, water resources, and solid waste resources.

(4) *Investment and operation mode*. To ensure the economic feasibility of the energy planning scheme, planning must include consideration of the capital investment and financing channels that energy technology applications require. This step requires combining national and local financial subsidy policies and thus provides the financial guarantee needed for the implementation of energy programs.

(5) *Planning management mechanism*. During this stage, the cooperation and coordination mechanism of the whole process for energy-related sectors are set up and mechanisms protecting the implementation of energy planning programs are provided.

(6) *Coordination with construction activities*. This part of the plan requires an overall plan to achieve a transition from short-term to long-term, resulting in the achievement of a growing energy system.

References

1. Liu X, Ye W, Gao B (2010) Eco-friendly municipal infrastructure planning with the idea of low-carbon—take the case of Sino-Singapore Tianjin eco-city. In: Proceedings of international conference on urban development and planning 2010
2. Zheng ZH, Fu L, Chen J (2008) One simulation tool for urban building energy planning. In: The 1st international conference on building energy and environment (COBEE)
3. Fu L, Zheng ZH, Di HF, Jiang Y (2008) Urban building energy planning with space distribution and time dynamic simulation. In: ASME 2nd international conference on energy sustainability
4. Ramachandra TV (2009) RIEP: regional integrated energy plan. Renew Sustain Energy Rev 13(2):285–317
5. Donald WJ (1991) How urbanization affects energy-use in developing countries. Energy Policy 19(7):621–630
6. Long WD (2008) Important stage of building energy efficiency: community energy planning. HVAC 38(3):31–38
7. Yamaguchi Y, Shimoda Y, Mizuno M (2007) Transition to a sustainable urban energy system from a long-term perspective: case study in a Japanese business district. Energy Build 39(1):1–12
8. Yoshiyuki S, Takuro F, Takao M (2004) Residential end-use energy simulation at city scale. Build Environ 39(8):959–967
9. Shem H, David JS (2008) Using building energy simulation and geospatial modeling techniques to determine high resolution building sector energy consumption profiles. Energy Build 40(8):1426–1436
10. Sadegh Z (2007) An energy efficiency plan for the Iranian building sub-sector. Energy Policy 35:1164–1171
11. Xu BP, Liu P, Li N (2012) Research and practice of carbon emissions assessment for the new district planning. In: Proceedings of the 8th international conference of green building and building energy saving, pp18–27

Chapter 5
Study on the Heat Insulation Performance of EMU Structure

Huasheng Xiong and Xuquan Li

Abstract In recent years, with the improvement of the EMU performance, the EMU structure and material also had a series of changes. These changes can produce certain effect on the train body heat insulation performance. Heat insulation performance is the main factor of structure heat transfer, the motor train unit section heat insulation performance, and the factor for analyzing motor train unit operation energy consumption, which is of great significance on determining its air-conditioning load, avoiding the bad working environment (wall condensation and local high temperature) appear, and maintain the car comfortable thermal environment. This paper studies the practical operation heat insulation performance and studies a new generation of high speed EMU thermal performance design provide theoretical guidance and practical tool, which integrated by means of the theoretical analysis, numerical simulation, and experimental test methods, through the heat insulation performance of the EMU structure calculation and analysis.

Keywords EMU structure · Heat insulation · Experiment

5.1 Introduction

Our country enters the period of high speed air-conditioning train in the twenty-first century, especially in recent years, the state shall pay attention to the railway construction, as well as to the research and development of high speed EMU. With the high speed EMU vehicle running speed and expanding the types of EMU, the train structure and material also have a great change. The structure and the

H. Xiong (✉) · X. Li
School of Environmental and Municipal Engineering,
Qingdao Technological University, Qingdao, China
e-mail: xionghuashengni@163.com

A. Li et al. (eds.), *Proceedings of the 8th International Symposium on Heating, Ventilation and Air Conditioning*, Lecture Notes in Electrical Engineering 262,
DOI: 10.1007/978-3-642-39581-9_5,

material influence train's heat transfer coefficient and insulation performance. The structure section heat insulation performance has a large influence on the body heat load effect. If body heat insulation is bad, it will lead to the increase of air-conditioning load, the influence of indoor air-conditioning, and it can't satisfy the human body thermal comfort requirements.

Therefore, combined with high speed EMU, and the specific design characteristics, study body section and insulating performance and reduce high speed EMU vehicles through the body energy loss, is not only in conformity with the development of the motor train unit needs, but also for accurate calculation provide basis for car interior cold and hot load.

5.2 The Simulation Calculation Method

With finite element method for the car body structure division and the third kind of boundary conditions, we use the simulation software to study the thermal performance of the car body.

The body heat conduction differential equation three dimensional problem on inner heat source for the steady temperature field of isotropic:

$$\nabla^2 T = \frac{\partial^2 T}{\partial x^2} + \frac{\partial^2 T}{\partial y^2} + \frac{\partial^2 T}{\partial z^2} = 0 \tag{5.1}$$

The third kind of boundary condition is to point to objects in contact with fluid temperature and heat transfer coefficient is known.

$$-k\frac{\partial T}{\partial n}|_r = \alpha(T - T_f)|_{\mathrm{r}} \tag{5.2}$$

The static and different speed of the EMU of outside surface heat transfer coefficient are determined by the standard of "air conditioning coach thermal calculation" (TB1957-87), the heating and ventilation design parameters "(TB1955-87) and the EMU-air conditioning design parameters" (TB1951-87). The surface heat transfer coefficient recommended for 8 w/(m^2.k) for the speed of 350 km/h, the outside surface heat transfer coefficient considering influence on speed, according to the railway cooperation organization memos (P-538/3) recommend coefficient of heat transfer calculation formula:

$$\alpha_W = 9 + 3.5\omega^{0.66} \tag{5.3}$$

Through the formula, we can calculate the surface convection heat transfer coefficient at different speed, For example, the appearance of convection heat transfer coefficient was 176.17 at 350 km/h.

5.3 The Heat Transfer Model of EMU Structure and Simulation

According to the typical structure and simulation temperature, this paper uses the simulation of the boundary conditions in the following:

(1) The indoor calculation temperature is 20 °C in winter;
(2) The outdoor calculated temperature is −9 °C in winter;
(3) The outside surface convection heat transfer coefficient is 176.2 w/(m^2.k);
(4) The inner surface convection heat transfer coefficient is 8 w/(m^2.k) (Figs. 5.1, 5.2);

It is shown in Fig. 5.3 that under the condition the aluminum alloy coefficient of thermal conductivity is 227.6 w/(m.k) and stationary air layer coefficient of thermal conductivity is 0.03 w/(m.k) (Fig. 5.4).

From the double aluminum alloy heat transfer model simulation results, to conclusion, aluminum alloy coefficient of thermal conductivity is very large, mainly through the aluminum alloy heat transfer, and the air flow on heat transfer is almost no effect, the temperature difference between inside and outside and double aluminum alloy is not more than 1 °C.

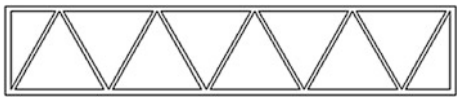

Fig. 5.1 The heat transfer model the EMU structure

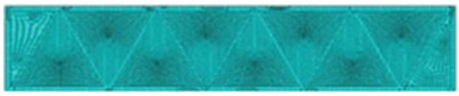

Fig. 5.2 Grid painting points

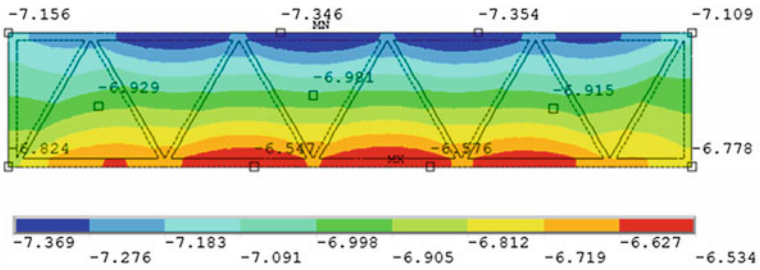

Fig. 5.3 Temperature distribution

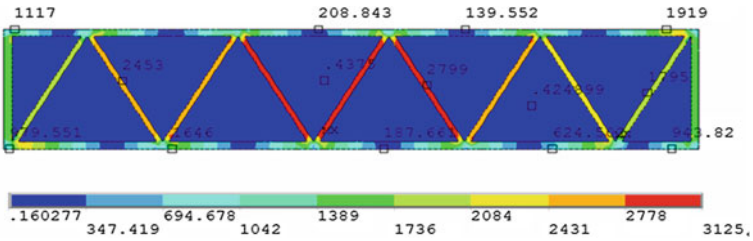

Fig. 5.4 Heat flow density distribution

5.4 By Experimental Verification

5.4.1 Experimental Testing Method

This experiment adopts thermal box method to test specimen in order to improve the reliability of the test data. According to conservation of heat, heat the electric heater of heat generation including through the hot box wall transfer quantity of heat, through the specimen box transfer of heat, and through the specimen wall heat transfer. Through the specimen of the heat flux density and the specimen of heat and specimen area, and the both sides of the specimen surface temperature, the specimen coefficient of thermal conductivity calculation according to the formulas as follows:

$$\lambda = \frac{q\delta}{t_{s1} - t_{s2}} \tag{5.4}$$

We can ignore the effects of radiation because this experiment of temperature thermocouple probe do radiation treatment, namely in the thermocouple probe place with aluminum tape seal.

5.4.2 The Experiment Equipment

5.4.2.1 The Experiment Device

The experiment equipment mainly consists of the cold box, hot box, hot suites, cold suites, electric heater, refrigeration units, specimen box, etc. Experimental installation plan is shown in Fig. 5.5.

The both hot and cold box experiment table size is 1.8 m × 1.5 m × 1.8 m, and are tightness of insulator. Both of the hot and cold box wall thickness are 10 cm and heat conduction coefficient is 0.02 w/(m.k). Specimen box adopts 6-cm thick

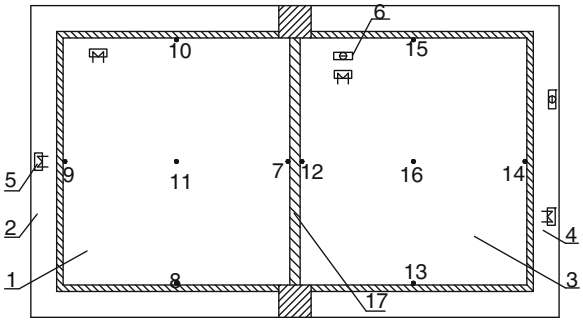

Fig. 5.5 Build things member of the thermal performance test device schematic diagram. *1*-hot box; *2* -heat suite; *3*-cold box; *4*-cold suite; *5*-electric heater; *6*-refrigerating unit; *7*- a hot surface temperature thermocouple thermometer; *8,9,10*- the wall temperature thermocouple thermometer; *11* - thermal air temperature thermocouple thermometer; *12*- The thermocouples of cold surface temperature; *13,14,15*- The thermocouples of the wall temperature t; *16*- The thermocouples of cold air temperature; and *17*- specimen box

Fig. 5.6 Experimental apparatus Local graphics

extruded polystyrene board, the heat conduction coefficient is 0.03 w/(m.k), the test specimen area is 1.8 m^2, and the experiment device local diagram are shown in Fig. 5.6.

Table 5.1 Insulation test instrument parameter list

Instrument name	Instrument image	Correlation parameter
Agilent 34970A temperature acquisition meter		Power supply frequency:45–66 Hz Power consumption:12 W The whole accurac 0–55 °C Storage temperature: −40–70 °C
UJ34D power meter		Measuring range:0–2.111110 V Minimum resolution:1 μV Accuracy level:0.01 %
DC potentiometers		Rated voltage:0–300 V Current rating: 0–5 A Accuracy:0.2
K type thermocouple		Temperature measurement range:−40 ~ +375 °C Tolerance value:±1.5 °C

5.4.2.2 The Experiment Test Instrument

Experimental test instrument basically include Agilent 34970A temperature acquisition meter, UJ34D power meter, DC potentiometers, K type, Main instruments, and dondels were listed in Table 5.1:

Hot box side Cold box side

Fig. 5.7 Arrangement

5.4.2.3 The Arrangement of Test Points

There are two temperature measuring point layout on specimen box and six temperature measuring point specimen surface uniformly arranged in the hot box side and cold box side. At the same time, in hot chamber side, specimen wall uniformly arranged nine heat flow meter SMT, and were carried out, in turn, numbers 1–9, as shown in Fig. 5.7.

5.4.2.4 Test Result Analysis

The experiment test object is a 50-mm train side wall, and its size is 1.5 × 1.2 × 0.05 m. The achieve steady state temperature is fluctuation ±0.2 °C in 3h, and then

Table 5.2 Test results

Order	t_{s1} (°C)	t_{s2} (°C)	Δt_1(°C)	A(m^2)	δ (m)	$\lambda w/(m \cdot k)$
1	−6.32	−7.35	1.03	1.8	0.05	1.84
2	−6.08	−7.11	1.03	1.8	0.05	1.84
3	−6.04	−7.05	1.01	1.8	0.05	1.82
4	−6.36	−7.36	1.0	1.8	0.05	1.81
5	−6.11	−7.16	1.05	1.8	0.05	1.87
6	−6.27	−7.32	1.05	1.8	0.05	1.87

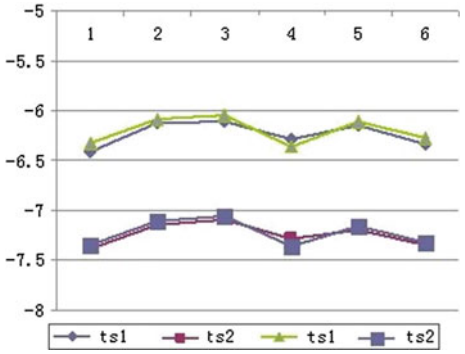

Fig. 5.8 The contrast diagram of simulation and experimental temperature

record data every half an hour, collection of six groups data, test condition for =195 w test data as shown in Table 5.2.

Compared the simulation temperature with experimental temperature, and the result as shown in Fig. 5.8.

Through the above, the simulation has higher accuracy, two surface deviation of simulation temperature and experimental test temperature control in 5 %. At the same time, the average coefficient of thermal conductivity is 1.84 w/(m.k), and simulation coefficient of thermal conductivity is 1.86 w/(m.k). Compared to the test result, the deviation is 1.1 %. The main reasons why the internal and external surfaces of the specimens loaded look thermal coefficient control, in testing the air between produces convection, to enhance the heat transfer, which affect the heat insulation performance. The deviation between simulation and experimental results is very small, meanwhile satisfy the application of scientific research.

Chapter 6
Thermal Matching of Heat Sources for District Heating System Based on Energy Quality

Kan Zhu, Jianjun Xia, Yi Jiang and Hao Fang

Abstract This paper analyzes the structure of district heating system in Sect. 6.2 and indicates that it is a multistage heat transfer process. The energy quality decreases while the energy quantity remains if heat loss is ignored. In Sect. 6.3, heat sources with different temperature levels, which mean the energy quality, are analyzed. In Sect. 6.4, entransy, a physical quantity which represents the heat transfer ability, is used to describe the energy quality of heat in district heating system. The heat sources must meet the need of both energy quantity and entransy. Then the thermal analysis is carried out to prove the entransy dissipation is related to power generation and it must be reduced. Different methods are suggested for different result of calculation. In the last chapter, a case in Chifeng city is studied to test the theory of this paper.

Keywords Heat source · Entransy · District heating · Energy quality · Matching

6.1 Introduction

With the development of urbanization, the demand for energy, especially the building energy, exceeds the supply by a wide margin. In northern China, enormous energy consumption for district heating, which accounts for a large part of building energy shortage, makes it the focal point in solving the problem of building energy shortage. Boilers and CHP (combined heating and power generation) systems are traditional heat sources for district heating. But with the booming of real estate industry and unmatched energy supply, these old systems

K. Zhu (✉) · J. Xia · Y. Jiang · H. Fang
Department of Building Science, Tsinghua University, Beijing, China
e-mail: zhukan11@mails.tsinghua.edu.cn

A. Li et al. (eds.), *Proceedings of the 8th International Symposium on Heating, Ventilation and Air Conditioning*, Lecture Notes in Electrical Engineering 262,
DOI: 10.1007/978-3-642-39581-9_6,

shoulder great burden. New heat sources are in dire need as one of the solutions to the current situation.

CHP system is a good example of using waste heat, but there are more potential heat sources such as industrial waste heat and condensing heat in CHP systems with condensing turbines. If used properly, these can become very large heat sources. However, most of them are not hot enough for district heating. Therefore, the obstacle which stands in the way is the temperature of these heat sources or in other words the energy quality. Given that some of traditional heat sources have such high temperature that far beyond the need of district heating, the surplus can be used to improve the energy quality of these potential heat sources, which may be a solution for the building energy shortage.

The paper analyzes the district heating system based on energy flow and the energy quality of different heat sources for different heating terminals, such as radiators and floor heating system. The author attempts to establish an assessment system and tries to distinguish when the system is matched and when there is still potential for applying low-quality energy.

6.2 Analysis of District Heating System

A typical district heating system in China mainly consists of heat source, primary network, secondary network, and heating terminal. Take the gas boiler system as an example (Fig. 6.1). The heat comes from the burning gas in the boiler. It first goes into the primary network and then secondary network. At last, heat gets in the room through radiators. If the heat loss in transmission is neglected, then the heat amount does not change from source to terminal. However, the temperature decreases through the process and the quality of energy is the only factor which is lost.

6.3 Properties of Heat Sources

Boilers often use fossil fuel such as coal and natural gas which are considered as primary energy. When fossil fuel combusts in boilers, the temperature may reach 1,000 °C [1], enough to generate electricity power.

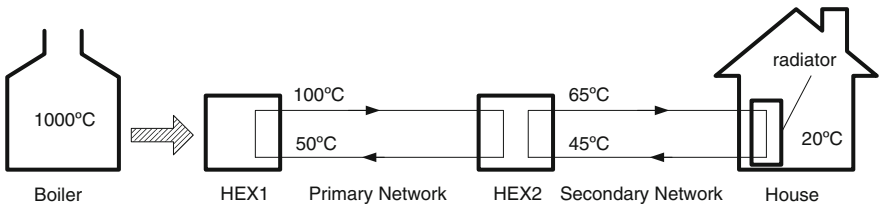

Fig. 6.1 District heating system analysis

Nomenclature					
T	Temperature	K	Q_{store}	Heat stored in a subject	J
c_p	Specific heat at constant pressure	J/kg K	q_{const}	Heat flux from a constant temperature heat reservoir	W
q	Heat flux	W	T_{sup}	Temperature of supply water	K
J	Entransy	JK	T_{ret}	Temperature of return water	K
Q	Heat	J	M	Mass	kg

CHP system is a traditional way of district heating. The exhaust steam or the extracted steam of turbines can be used to heat the water of district heating network. The temperature of exhaust steam is not very high, normally no more than 70 °C while the temperature of extracted steam can reach 200 °C [2].

Condensing heat of condensing turbine is still released into the air by cooling tower. This part of condensing heat, which is at 20–30 °C and not hot enough for district heating, can be a potential large heat source if applied properly.

A large number of industrial processes, covering most industrial sectors, use significant amounts of energy in the form of heat, which is rarely utilized efficiently [3]. The use of waste heat is largely determined by its temperature. Some waste energy, whose temperature varies from 20 to 90 °C, though useless for industry, can be recovered for district heating (Fig. 6.2).

Traditional heat sources such as boilers and CHP systems with condensing turbines are very hot with good quality, which is far beyond the temperature level of district heating. In lack of energy quality, condensing heat of condensing turbines and some industrial waste heat can not be used for heating directly. Its energy quality must be improved to certain level.

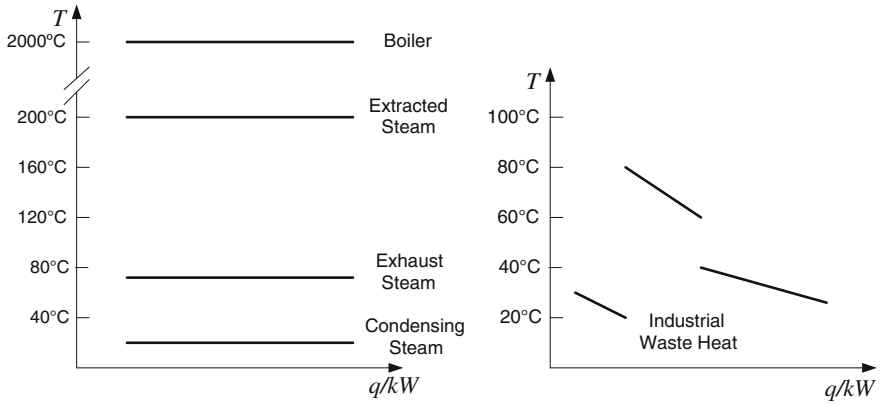

Fig. 6.2 Temperature level of different heat sources

6.4 Thermal Matching Between Heat Sources and Networks

6.4.1 Basic Principles

The heat sources must match the need of space heating terminals thermally to make it possible theoretically. First of all, the quantity of energy that heat sources provide must be enough, or in other words equal to primary network's need if the heat loss is ignored (Eq. (6.1)).

$$\sum q_{\text{source},i} = q_{\text{need}} \tag{6.1}$$

After the balance of energy quantity, energy quality must be satisfied. District heating system is a multilayer heat exchange system essentially. What happens during the process is only heat transfer. Take a simple heat exchange process as an example: based on the second law of thermodynamics, Eq. (6.2) must be satisfied at every infinitesimal heat exchange process. Through simple derivation, Eq. (6.3) can be concluded (Fig. 6.3).

$$\int T_{1m}\delta q \geq \int T_{2m}\delta q \tag{6.2}$$

$$\frac{1}{2}q(T_1' + T_1'') \geq \frac{1}{2}q(T_2' + T_2'') \tag{6.3}$$

A new physical quantity "entransy" describing heat transfer ability is widely used in optimization of heat transfer [4–9]. It can be defined in Eq. (6.4) or (6.5). And a heat transfer process can be considered as a transfer of entransy. Entransy of one side decreases and the other increases, and dissipation of entransy is undoubtedly to occur.

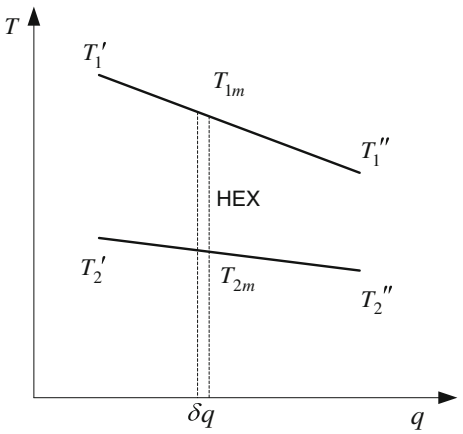

Fig. 6.3 Single heat exchange process

$$J = \frac{1}{2} M c_{\mathrm{p}} T^2 = \frac{1}{2} Q_{\mathrm{store}} T \text{ (constant specific heat subject)} \tag{6.4}$$

$$\text{Or } J = QT \text{ (constant temperature heat reservoir)} \tag{6.5}$$

$$\Delta J_1 = J_1' - J_1'' = \frac{1}{2} M_1 c_{p,1} (T_1' - T_1'')(T_1' + T_1'') = \frac{1}{2} Q (T_1' + T_1'') \tag{6.6}$$

Equation (6.7) can be derivated from the Eqs. (6.3) and (6.6)

$$\Delta J_1 \geq \Delta J_2 \tag{6.7}$$

Therefore, the district heating system can be considered as a process when energy quantity remains unchanged but entransy, which stands for energy quality, goes down.

On this basis, two principles can be concluded:

$$\sum q_{\mathrm{source,i}} = q_{\mathrm{need}} \tag{6.8}$$

$$\sum \Delta J_{\mathrm{source}.i} \geq \Delta J_{\mathrm{need}} \tag{6.9}$$

So, for the first step, the heat sources must be equal in quantity and provide enough entransy for the system.

6.4.2 Importance of Reducing Entransy Dissipation

The entransy dissipation can be indicated by entransy efficiency, which is the quotient between provided by entransy heat sources and needed by the network.

$$EE = \Delta J_{\mathrm{need}} / \Delta J_{\mathrm{source}} \times 100\ \% \tag{6.10}$$

Take the low-temperature floor heating system as an example. The EE of different heat sources is shown in Table 6.1.

Heat source with lower temperature causes more power reduction in CHP system. In other words, district heating system with better entransy efficiency actually save more power. On the premise of reaching a certain point, the smaller

Table 6.1 Entransy efficiency of different heat sources

Heat source	Temperature (°C)	Temperature of supply water (°C)	Temperature of return water (°C)	EE (%)
Boilers	1,000	45	35	25
Extracted steam	200	45	35	66
Exhaust steam	70	45	35	91
Exhaust steam	50	45	35	97

the entransy heat sources provided, the better. The network and terminals cannot be changed at will most times, so it is very important to match the temperature level with the network requirement and reduce the entransy dissipation.

6.4.3 Methods of Matching and Optimization

When heat sources are chosen and combined, these results can be applied. First the energy quantity should be satisfied, and then the heat source with proper quality need be found based on entransy efficiency. Put all factors into Eqs. (6.8) and (6.9), thus heat quantity q_x and temperature T_x required can be calculated.

If q_x is zero, which means no extra heat source is needed. Check the entransy efficiency to see if there is still room for optimization.

For example, extracted steam is around 200 °C, which is much too hot for heating. In this case, we can extract steam with lower temperature or extract steam with different temperature for multistage heating. With this modification, turbines can generate more power without influencing heating capacity.

If T_x is low, then industrial waste heat and condensing heat of CHP system could be useful if their temperature is higher than the required T_x. The methods below could be considered.

1. Use waste heat as preheating;
2. Use heat pump to improve the quality of waste heat.

If T_x is high, which means the existing heat source is not hot enough for district heating, then the methods below may be useful.

1. Change the network or terminals if impossible, so the required temperature can be lower;
2. Add high quality heat source.

6.5 Case Study

The northern residential district in Chifeng city (Inner Mongolia in China) has a heating area of 4.29 million m^2, which is supplied by the thermal power plant A. In this plant, steam at 198 °C, 0.24 MPa is extracted for district heating by 266 t/h. The total heat capacity of extracted steam is 180 MW, and 42 W is consumed for heating per square meter. Because the power plant is far from the residential district, the supply and return water of primary network is at 100 and 50 °C in order to reduce power consumption for water distribution.

For the next heating season, there will be an extra 1.2 million m^2 for district heating, which may require extra 50 MW from heat sources. Some newly developed area is not far from the plant.

The maximum of extracted steam is 450 t/h, which means that there is still a lot of steam condensed. The condensing temperature is 22 °C. Besides that, zinc plant B, which has a lot of industrial waste heat, is not far from power plant A. The temperature of the industrial waste heat is between 40–90 °C.

It can be found that the entransy provided by extracted steam is already large enough for total need including new area (Eq. (6.11)), indicating that the energy quality of extracted steam is too high and the entransy of existing heat source is already enough. What is needed is only extra quantity.

$$180 \times (198 + 273) > (180 + 50) \times \left[\frac{1}{2}(100 + 50) + 273\right] \tag{6.11}$$

On this condition, low-quality heat source such as condensing heat or industrial waste heat should be used. Two plans can be made.

Plan 1:

Keep the extracted steam amount as 266 t/h (180 MW), 118 t/h of which drives an absorption heat pump and recover 71 t/h (50 MW) condensing steam.

Plan 2:

Reduce the extracted steam amount to 243 t/h (164.5 MW), 118 t/h of which drives an absorption heat pump and recover 71 t/h (50 MW) condensing steam. The industrial waste heat system provides 15.5 MW for heating area near the power plant, with an independent system with floor heating terminals and no secondary network.

Traditional Plan for Comparison:

Simply extract 73.6 t/h more steam for district heating.

Compare two plans with traditional plans in Table 6.2

For using condensing steam instead of extracted steam, which still has ability to generate power, Plan 1 and 2 increase power production for power plant A without influencing district heating. With no doubt, the entransy efficiency is higher. On basis of Plan 1, industrial waste heat is used by choosing floor heating as heating terminal in Plan 2, which improved entransy efficiency once more and save more extracted steam.

Table 6.2 Comparison of plans

	Extracted steam (t/h)	Condensing steam (t/h)	Industrial waste heat (MW)	EE (%)	Power generation increased (kWh/d)
Traditional	339.6			73.9	0
Plan1	266	71		80.4	158,485
Plan2	243	71	15.5	81.5	208,012

6.6 Conclusion

District heating system is a multistage heat transfer process. The energy quantity has not change but the energy quality goes down from heat sources to houses. Some traditional heat sources, such as boilers and extracted steam, are very high in quality and able to generate power, while some heat sources like industrial waste heat and condensing steam often lack the quality for district heating.

Entransy can be applied to describe heat transfer ability. The entransy decreases while the heat transfers from heat source to terminal, especially between heat source and primary network. The heat sources should at least provide enough entransy for primary network.

Besides that, using high quality energy as heat source actually influences power generation, which is also low in entransy efficiency. Therefore, the entransy dissipation should be reduced and energy quality of heat source should match the network's need, avoiding waste of quality.

When heat sources are chosen and combined, two principles should be followed. First the energy quantity should be balanced. Second, entransy supply should be enough and entransy dissipation should be controlled. Two equations can help to choose right heat sources and methods of application.

References

1. Xue Z, Liu X et al (2006) One new assessment method for the energy utilization manner. Acta Energiae Solaris Sinic 27(4):349–355
2. Yan Li (2012) Research on the configuration and operation strategy of district heating system with co-generation based on absorption heat exchange (co-ah). Tsinghua University, Beijing
3. Al-Rabghi OM, Beirutty M et al (1993) Recovery and utilization of waste heat. Heat Recovery Syst CHP 13(5):463–470
4. Guo Z, Zhu H et al (2007) Entransy-A physical quantity describing heat transfer ability. Heat Mass Transf 50:2545–2556
5. Chen X, Meng G et al (2005) Potential capacity dissipation minimization and entropy generation minimization in heat conduction optimization. J Eng Thermodyn 26(6):1034–1036
6. Chen X, Li Z et al (2004) Variational principles in heat conduction. J Eng Thermodyn 25(3):457–459
7. Chen X (2004) Entransy and its applications in heat transfer optimization. Tsinghua University, Beijing
8. Zhang T, Liu X et al (2011) Applicability of thermological parameters in thermal-hygro environment building. HVAC 41(3):13–21
9. Liu X, Jiang Y et al (2011) Match properties of heat exchange network in thermal-hygro environment building. HVAC 41(3):29–37

Chapter 7
Performance Analysis of Single Well Groundwater Heat Pump Systems Based on Sand Tank Experiment

Wei Song, Long Ni, Yang Yao and Jeffrey D. Spitler

Abstract As a type of groundwater heat pump, single-well groundwater heat pump systems have received much attention in recent years due to its efficient properties. In this chapter, a sand tank experiment system of single-well systems is designed and set up in Harbin Institute of Technology. The aim of this study is to find the relationship among the temperature of outlet water, the power of the single-well systems, the thermal transfixion, and the distance between pumping screen and injection screen. The data obtained demonstrate that the mean temperature of outlet water and the power are increased, and the coefficient of thermal transfixion is decreased when the distance between pumping screen and injection screen is raised. The distance between pumping screen and injection screen is an important factor in the single-well systems that can affect the power of the system directly. The coefficient of thermal transfixion is an appropriate parameter to evaluate the single-well systems.

Keywords Single-well systems · Pumping screen · Thermal transfixion · Standing column well · Pumping and recharging well · Pumping and recharging well filled with gravel

7.1 Introduction

The groundwater heat pump (GWHP) system is an open-loop system that draws water from a well, passes it through a heat exchanger and discharges the water into an injection well [1]. As one type of GWHP, single-well systems have received

W. Song · L. Ni (✉) · Y. Yao
Institute of Heat Pump and Air Conditioning Technology,
Harbin Institute of Technology, Harbin 150090, China
e-mail: nilonggn@163.com

J. D. Spitler
School of Mechanical and Aerospace Engineering, Oklahoma State University,
Stillwater, OK 74078, USA

A. Li et al. (eds.), *Proceedings of the 8th International Symposium on Heating, Ventilation and Air Conditioning*, Lecture Notes in Electrical Engineering 262,
DOI: 10.1007/978-3-642-39581-9_7,

much attention in recent years due to its efficient properties, which can save initial costs and offer important economic benefits.

Until recently, single-well systems contain three types, as shown in Fig. 7.1, i.e., standing column well (SCW) system, pumping and recharging well (PRW) system, and pumping and recharging well filled with gravel (PRWFG) system. Considerable research efforts have been spent on the SCW system in recent decades, especially on the model development and applications [2–12]. However, thermal breakthrough always occurs [13], which impacts the efficiency of SCW system. So engineers have made well deeper and bleed rate is higher, while a tail pipe is installed in order to segregate the outlet and inlet water. But the effect is not conspicuous, and then two new alternatives come out. There are some intervals in the well to separate the production and injection zone in PRW system and PRWFG system. Related research articles indicate that the research field is useful [14–20]. However, there is little attention has been paid to the experiment of single-well systems. Although such models in the previous research may provide a useful set of parameters to 'fit' data accurately, there is not so much data available.

The purpose of this paper is to provide a framework for discussing the influence on distance between pumping screen and injection screen, the temperature of outlet and inlet water, and thermal transfixion in single-well systems. To our knowledge, this is the first demonstration of sand tank experiment of single-well systems, which focuses on parameters of the three types of single-well systems. Although the experiment system cannot simulate every aspect of real geological condition, it can be assumed to show the characteristics of the single-well systems in some extent. The results show that the distance between pumping screen and injection screen is an important factor in the single-well systems and the coefficient of thermal transfixion is an appropriate parameter to evaluate the single-well systems.

7.2 Experiments

7.2.1 Experiment Description

The experiment system is designed and set up as shown in Figs. 7.2 and 7.3 to study the heat transfer performance and the temperature variation of the system during the process of pumping water from the bottom of the well into the top of the well. The experiment system consists of a sand tank with enough water to approximate an aquifer, two load tanks to simulate the building load, two initial tanks to control the initial aquifer temperature, an isobaric tank to maintain the water level, and an air source heat pump to cool off the water in the load tank. Moreover, all the details of the experiment system can be found in Table 7.1.

There are 32 thermocouples and 20 pressure points located at different positions in the system to measure the distribution of temperature and pressure.

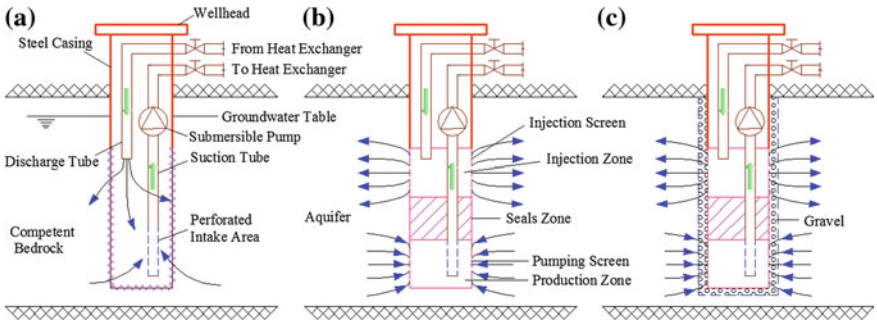

Fig. 7.1 Single-well systems. **a** SCW. **b** PRW. **c** PRWFG

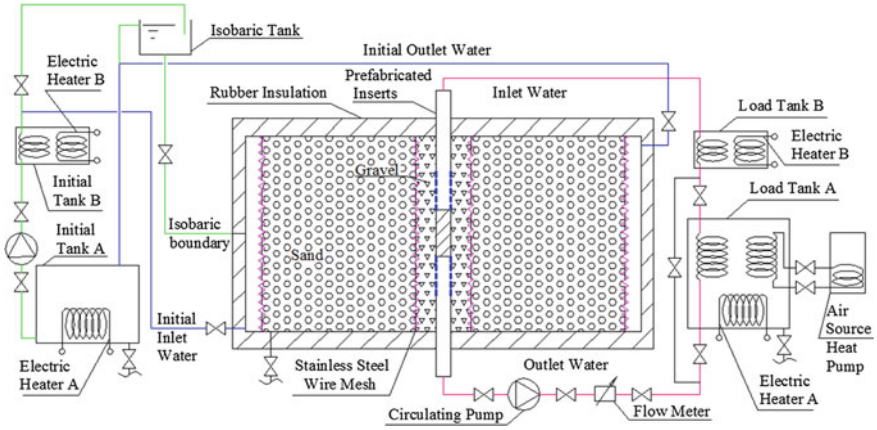

Fig. 7.2 Test system diagram

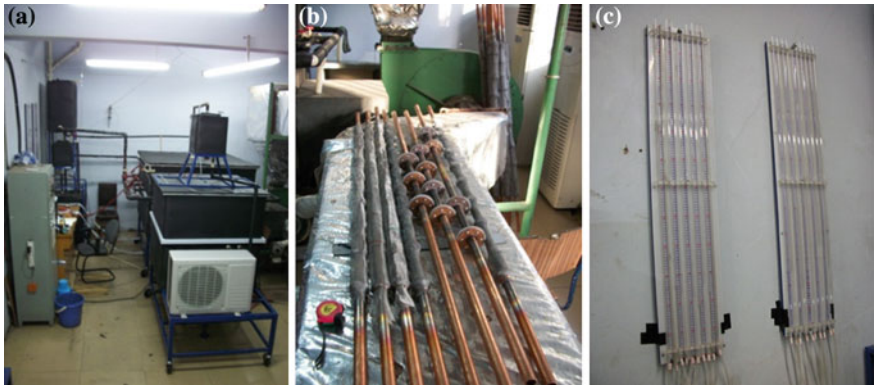

Fig. 7.3 Experiment system. **a** Photo of experiment system. **b** Photo of prefabricated inserts. **c** Photo of capillary pressure tube

Table 7.1 Summary of details of the experimental system

Contents	Units	Values
Sand tank	m	1.5 × 1.5 × 1
Initial tank A	m	0.7 × 0.7 × 0.7
Load tank A	m	1 × 1×1
Isobaric tank	m	0.4 × 0.4 × 0.8
Electric heater A	kW	1
Electric heater B	kW	0.5
Air source heat pump	kW	2.5
Circulating pump	kW	0.28
Diameter of well	mm	73
Diameter of inserts	mm	22
Diameter of sand	mm	1–2
Diameter of gravel	mm	2–4
Length of well	m	0.92
Length of inserts	m	1.5

Arrangement plan of thermocouples and pressure points are shown in Fig. 7.4, and we highlight the thermocouple positions of Nos. 10 and 11 for following analysis. In addition, a flow meter is installed at the outlet water pipe to measure the water flow rate, and the quantity of outlet water is equal to the quantity of inlet water to maintain a closed loop circulation. Moreover, different types of inserts are fabricated to replace the three kinds of single-well systems, i.e., SCW system, PRW system, and PRWFG system, as shown in Fig. 7.5. The distance between pumping screen and injection screen in the prefabricated inserts are four values, i.e. 0, 150, 300, and 450 mm.

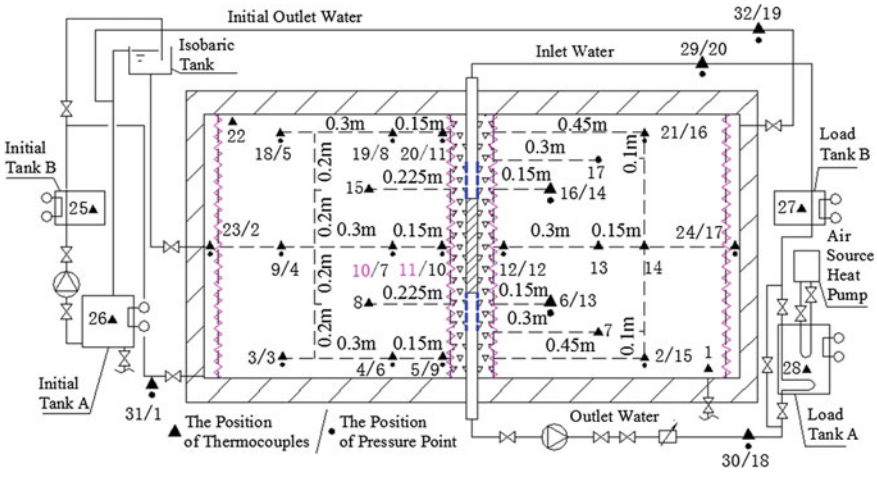

Fig. 7.4 Arrangement plan of thermocouples and pressure points

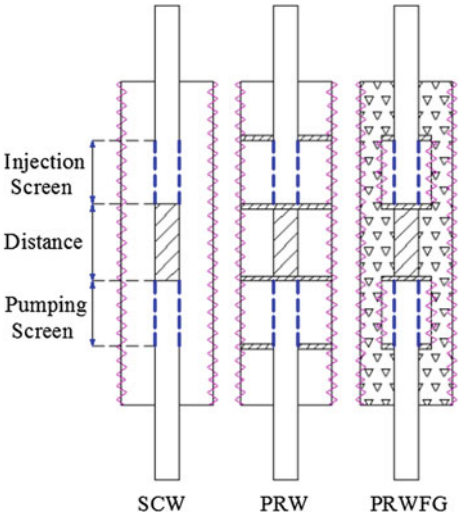

Fig. 7.5 The structure of prefabricated inserts

7.2.2 Test Procedure

Before starting the test system, the aquifer in the sand tank is saturated with water when the valves of initial inlet and outlet water are opened. To avoiding surge, this process spends about 24 h to make the sand tank filled with water, remove all bubbles in the aquifer, and let the initial aquifer temperature be constant. Then the valves of initial inlet and outlet water are closed when the valve of isobaric tank is opened. The test starts when the water level is stable that process spends 15 min generally. Finally, the valves of inlet and outlet water are opened, while circulating pump and test system is working. Considering the factors of boundary stable, each case tests about 20 min. According to the temperature of observation point, it is judged whether the boundaries are affected in order to increase or decrease the test time.

To estimate the distance between pumping and injection screens in the single-well systems, we control the parameters in the experiment system are constant except the prefabricated inserts. For example, initial aquifer temperature is 20 °C, flow rate of inlet water is 0.15 L/s, the temperature of load tank is 5 °C to simulate the cooling load, and the distance between pumping and injection screens are 0, 150, 300, 450 mm in each case individually.

7.3 Results and Discussion

7.3.1 Test Results

In order to find the characteristic of the three types of single-well systems, we test 12 cases that contain four different screen distances in SCW system, PRW system, and PRWFG system. In our study, each test spends 18 min, and the mean

temperature of outlet and inlet water is calculated from the data. As can be seen in Fig. 7.6, the mean temperature of outlet water is increased when the distance between pumping screen and injection screen is raised. However, the mean temperature of outlet water of PRWFG system is the highest one in the three kinds of single-well systems. Although the mean temperature of outlet water of SCW system is increased quickly when the distance is raised, it is still lower than other two types'. It also can be observed that the mean temperature of outlet water in PRW system does not climb when the distance is increased to 300 mm.

Similar trend can be found in Fig. 7.10, which shows the power of three kinds of single-well systems. However, the power of PRWFG system is increased when the distance is increased from 0 to 300 mm, and then decreased sharply when the distance is increased from 300 to 450 mm. In addition, the larger power points are surrounded in Fig. 7.10, which means they are efficient structure of single-well systems. These results suggest that data obtained in the experiment may provide more sensitive information for assessing the SCW system is not a good choice when the single well system needs to be installed.

There are 24 thermocouples in the sand tank, so the diversification of inner temperature can be observed easily. In this research, we find two typical positions in the sand tank to analyze, i.e., Nos. 10 and 11. As can be seen in Fig. 7.8, the temperature of No. 11 in SCW system changes slightly, which is maintaining the initial temperature when the distance between pumping screen and injection screen is different. This phenomenon reflects that the temperature field of No. 11 is not affected by the inlet water temperature. However, the influence on the temperature of No. 11 in PRW system decreases gradually with increasing distance between pumping screen and injection screen, because the intervals in the well separate the production and injection zone. Comparing Figs. 7.7, 7.8, and 7.9 show that final temperature of Nos. 10 and 11 in PRWFG system is close to the mean temperature of inlet water individually. Moreover, the same trend can be found in the temperature of No. 10 in SCW system and PRW system, whose final temperature is also near to the mean temperature of inlet water separately.

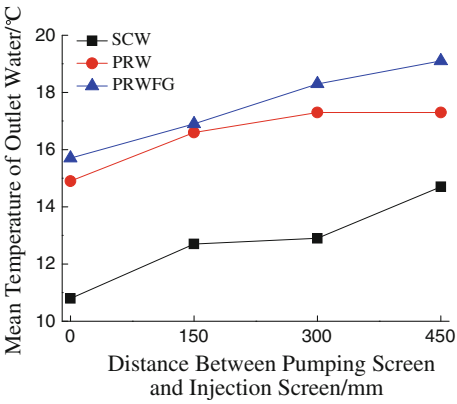

Fig. 7.6 Mean temperature of outlet water

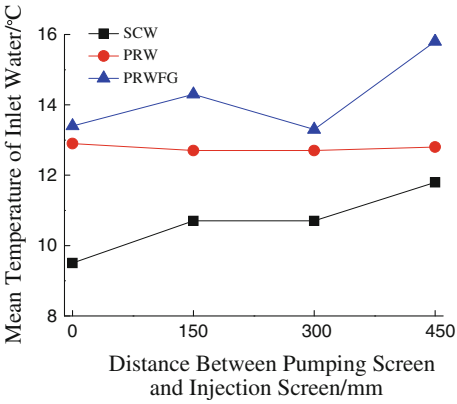

Fig. 7.7 Mean temperature of inlet water

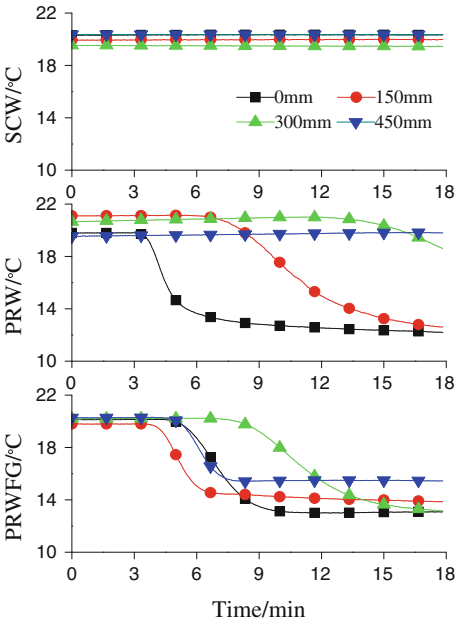

Fig. 7.8 The temperature curve of No. 11

7.3.2 Thermal Transfixion

From the test results, we can see thermal breakthrough impacts the efficiency of single-well systems, especially in SCW system. Thermal transfixion is a phenomenon that the temperature of outlet water is changed when the heat pump system is in motion. In addition, the coefficient of thermal transfixion is defined as [19]:

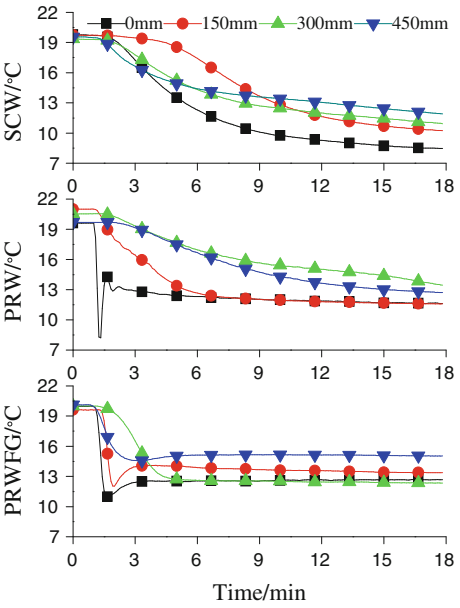

Fig. 7.9 The temperature curve of No. 10

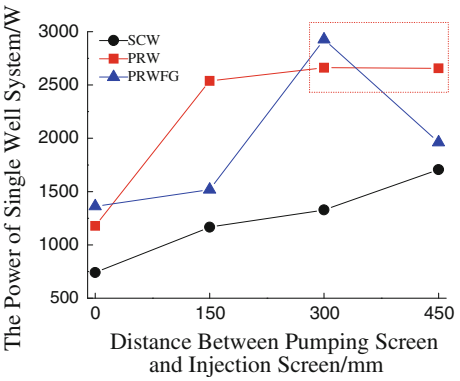

Fig. 7.10 The power of single-well systems

$$\delta = \frac{\Delta T_t}{\Delta T_t + \Delta T_L} \tag{7.1}$$

Here δ is the coefficient of thermal transfixion, dimensionless, proportion of inlet water among outlet water, $\Delta T_t = T_0 - T_{g,m}$ is the mean temperature of thermal transfixion, °C, T_0 is initial aquifer temperature, $T_{g,m}$ is the mean temperature of outlet water in heating, °C, $\Delta T_L = T_{g,m} - T_{r,m}$ is the mean temperature difference in heat absorption, °C, $T_{r,m}$ is mean temperature of inlet water, °C.

As we can see from Fig. 7.11, the coefficient of thermal transfixion in SCW system is decreased as the distance between pumping screen and injection screen is

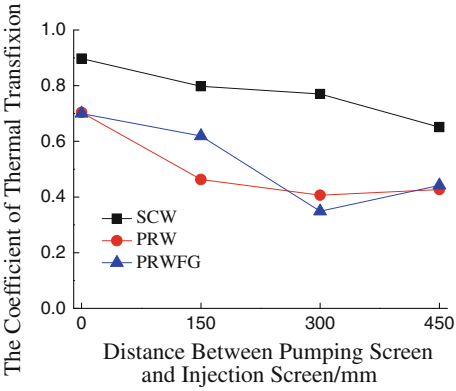

Fig. 7.11 The coefficient of thermal transfixion

increased. However, in PRW system the coefficient of thermal transfixion is little changed when the distance between pumping screen and injection screen is increased from 300 to 450 mm. Moreover, there is a minimum coefficient of thermal transfixion in PRWFG system while the distance between pumping screen and injection screen is 300 mm. Comparing Figs. 7.10 and 7.11 show that the coefficient of thermal transfixion is related to the power of single-well systems. Furthermore, the power of single-well systems, the temperature of outlet water, and the coefficient thermal transfixion all affect by the distance between pumping screen and injection screen that is an important factor in single-well systems.

7.4 Conclusions

In this study, we tested the temperature of outlet and inlet water, the aquifer temperature, and flow rate of outlet water. From the reasonable results obtained in the test, the power of single-well systems and the coefficient of thermal transfixion have been calculated. When the distance between pumping screen and injection screen is raised in the three types of single-well systems, we find that the mean temperature of outlet water and the power are increased, and the coefficient of thermal transfixion is decreased. The distance between pumping screen and injection screen is an important factor in the single-well systems, which can affect the power of the system directly. The coefficient of thermal transfixion is an appropriate parameter to evaluate the single-well systems.

However, there could be some difference in the results between the test system and a real system with complicated geological condition. The trend of the results in this paper could be as same as the results in the real world. In future, we will discuss the changes in the single-well systems that are affected by the initial aquifer temperature, flow rate of outlet water, and building load.

Acknowledgments This work was supported by the National Natural Science Foundation of China (No. 41002085) and the Programs Foundation of Beijing Municipality Key Lab of Heating, Gas Supply, Ventilating and Air Conditioning Engineering (No. KF201011).

References

1. Nam Y, Ooka R (2010) Numerical simulation of ground heat and water transfer for groundwater heat pump system based on real-scale experiment. Energy Build 42:69–75
2. Deng Z, Rees SJ, Spitler JD (2005) A model for annual simulation of standing column well ground heat exchangers. HVAC R Res 11(4):637–655
3. O'Neill ZD, Spitler JD, Rees SJ (2006) Modeling of standing column wells in ground source heat pump systems. In: Proceedings of the tenth international conference on thermal energy storage-ECOSTOCK 2006, Pomona
4. O'Neill ZD, Spitler JD, Rees SJ (2006) Performance analysis of standing column well ground heat exchanger systems. ASHRAE Trans 112(2):633–643
5. Al-Sarkhi A, Abu-Nada E, Nijmeh S, Akash B (2008) Performance evaluation of standing column well for potential application of ground source heat pump in Jordan. Energy Convers Manage 49:863–872
6. Orio CD, Johnson CN, Rees SJ, Chiasson A, Zheng Deng, Spitler JD (2005) A survey of standing column well installations in North America. ASHRAE Trans 111(2):109–121
7. Orio CD, Johnson CN, Poor KD (2006) Geothermal standing column wells: ten years in a New England school. ASHRAE Trans 112:57–64
8. Rees SJ, Spitler JD, Zheng Deng, Orio CD, Johnson CN (2004) A study of geothermal heat pump and standing column well performance. ASHRAE Trans 110(1):3–13
9. Li M, Diao N, Fang Z (2007) Analysis of seepage flow in a confined aquifer with a standing column well. J Hydrodyn Ser B 19(1):84–91
10. Ng BM, Underwood CP, Walker SL (2011) Standing column wells—modeling the potential for applications in geothermal heating and cooling. HVAC R Res 17(6):1089–1100
11. Abu-Nada E, Akash B, Al-Hinti I et al (2008) Modeling of a geothermal standing column well. Int J Energy Res 32:306–317
12. Lee K-S (2011) Modeling on the cyclic operation of standing column wells under regional groundwater flow. J Hydrodyn 23(3):295–301
13. Gao Q, Zhou X-Z, Jiang Y et al (2013) Numerical simulation of the thermal interaction between pumping and injecting well groups. Appl Therm Eng 51:10–19
14. Yuill GK, Mikler V (1995) Analysis of the effect of induced groundwater flow on heat transfer from a vertical open-hole concentric-tube thermal well. ASHRAE Trans 101(1):173–185
15. Mikler V (1993) A theoretical and experimental study of the 'energy well' performance. Master thesis, Pennsylvania State University
16. Xu S, Rybach L (2003) Utilization of shallow resources performance of direct use system in Beijing. Geotherm Resour Council Trans 27:115–118
17. Yang Z, Qu M (2006) Applications and development of single-well technology in China. HVAC 36:208–210
18. Ni L, Li H, Jiang Y et al (2011) A model of groundwater seepage and heat transfer for single-well ground source heat pump systems. Appl Therm Eng 31:2622–2630
19. Ni L (2007) Operation performance research on heat source/sink well of groundwater heat pump with pumping and recharging in the same well [D]. Harbin Institute of Technology
20. Ni L, Jiang Y, Yao Y, Ma Z (2006) Groundwater heat pump with pumping and recharging in the same well in China. In: Liu M, Zhang J (eds) Sixth international conference for enhanced building operations, vol 3. Allied Kingsway Publishing International, Shenzhen, pp 8–14

Chapter 8
Investigating the Thermal Performance of Horizontal Slinky Ground Heat Exchangers for Geothermal Heat Pump

Ping Cui, Jie Yang, Yun Lin and Zhaohong Fang

Abstract The horizontal ground heat exchanger (HGHE) with slinky-coiled pipes recently has been used as a heat source/sink for geothermal heat pump systems because of the significant lower initial cost. A simplified heat transfer model suitable for engineering design of the slinky HGHEs is developed. The model is based on the one-dimensional transient heat transfer in an infinite medium, considering the influence of the tube length per area and the different effects of long-term mean load and short-term intermittent load. A case study is carried out to design the HGHE size by using the proposed model. Some key factors which influence the performance of the HGHE are also discussed such as the thermal properties of the ground and the pipe length per area.

Keywords Ground-coupled heat pump · Slinky-coil horizontal ground heat exchanger · Heat transfer model

8.1 Introduction

Ground couped heat pump (GCHP) systems are now widely used in commercial and residential heating, cooling, and water heating applications because they offer significant reductions in electrical energy use and demand, have low maintenance

P. Cui (✉)
Key Laboratory of Renewable Energy Utilization Technologies in Buildings, Ministry of Education, Jinan, China
e-mail: nature_cui@126.com

P. Cui
Shandong Key Laboratory of Building Energy-saving Technique, Shandong Jianzhu University, Jinan, China

P. Cui · J. Yang · Y. Lin · Z. Fang
School of Thermal Energy Engineering, Shandong Jianzhu University, Jinan, China

A. Li et al. (eds.), *Proceedings of the 8th International Symposium on Heating, Ventilation and Air Conditioning*, Lecture Notes in Electrical Engineering 262,
DOI: 10.1007/978-3-642-39581-9_8,

requirements, and are environmentally attractive [1]. In a GCHP system, heat is extracted from or rejected to the ground via a closed loop through which pure water or an antifreeze solution circulates. The ground heat exchangers (GHEs) used in the closed loop systems typically consist of pipes installed in vertical boreholes or horizontal trenches, which are called vertical or horizontal GHE systems, respectively. The horizontal GHE (HGHE) usually consists of straight or spiral coiled pipes which are buried in a trench at a depth of approximately 1.2–2 m [2]. A disadvantage of the horizontal systems is that they are more affected by weather and air temperature fluctuations because of their proximity to the surface. However, the excavation cost for the shallow trenches is significantly lower than the drilling cost for the vertical boreholes. Therefore, the HGHE offers a cost-effective alternative for GCHP system in some circumstances where the land area is sufficient for the tube installation, such as the small-sized buildings or the buildings near large playground or golf course. Recently, the HGHE with slinky-coil tubes have attracted the great interest in practical engineering and research field owing to its advantages of less land area requirement and higher installation density of tubes compared to conventional straight HGHEs. Figure 8.1 shows one typical HGHE configuration with slinky-coil tubes.

Mei first proposed a numerical model suitable for HGHEs with straight pipes in 1986 [3]. In recent years, research into the HGHE systems with different configurations has been carried out on thermal performance, thermal impact, and energy behavior for different operation conditions and loop arrangements [4–8]. However, the majority of the studies were conducted either experimentally or numerically, which are inconvenient to be employed directly in HGHE design. A review of the literature shows that few studies have been conducted on the development of scientific design procedures for slinky HGHE and the thermal influences of both the long-term and short-term intermittent loads. The deficiency of an accurate

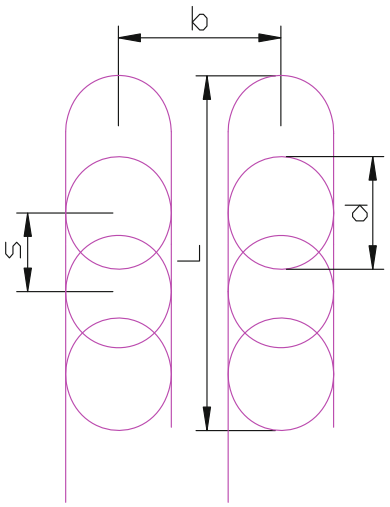

Fig. 8.1 Typical slinky-coil HGHE configuration

design procedure can be attributed to the inherent difficulty of the thermal analysis of the slinky HGHE since the temperature fluctuations around a year in the shallow ground as well as on the boundary (the ground surface) cannot be neglected as in the cases of the vertical borehole GHEs.

This paper proposes a simplified one-dimensional transient model suitable for slinky HGHE design. The temperature rises of the circulating fluid in the tubes can be derived by means of the time-dependent thermal resistances and the superposition principle.

8.2 Heat Transfer Model

The main objective of the thermal analysis of a HGHE is to determine the temperature of the heat carrier fluid based on certain operating conditions. The design goal is then to control the temperature of the circulating fluid within minimum and maximum limits over the lifespan of the system.

In view of the complication of this problem and its long time scale, the heat transfer process can be analyzed in two separated regions. One is the ground outside the pipes, where the heat conduction must be treated as a transient process. With the knowledge of the temperature response in the ground, the temperature on the pipe wall can then be determined for any instant on specified operational conditions. The second sector segregated for analysis is the region including the circulating fluid inside the pipe, the pipe wall and the adjacent pipes which can cause additional thermal resistance between pipes.

8.2.1 Ground Temperature Distribution

The thermal effect of the temperature fluctuations of the ground surface on the HGHE cannot be negligible because of the shallow buried depth. In this thermal analysis, the ground surface temperature is assumed to be an annual temperature wave oscillating around the annual mean temperature. Therefore, the ground temperature wave at a certain distance from the surface behaves amplitude attenuation and a time delay compared to the surface temperature wave. In other words, the peak temperatures of the underground occur at different time from the peak loads of buildings, which are beneficial for the thermal process of the HGHE in the ground. To simplify the thermal phenomena, the time delay of the temperature wave is neglected, which is also a conservative assumption.

The temperature deviation on the point z from the mean surface temperature (also the constant temperature in the deep ground t_{∞}) can be approximated by the following exponential function of depth z:

$$\theta_0 = \pm A_w \exp\left(-\sqrt{\frac{\pi}{aT}}z\right) \tag{8.1}$$

where: T is the annual temperature wave period, z is the buried depth of the horizontal pipes, A_w is the annual temperature wave amplitude of ground surface, a is the ground thermal diffusivity. It is noticed that the temperature deviation takes positive during cooling season and negative during heating season.

8.2.2 The Plane Heat Source Model Outside the Pipes

The heat transfer phenomena in the ground are very complex and difficult to model in all their details. Therefore, it is necessary to make the following simplifying assumptions in order to develop a HGHE model for engineering applications.

- The ground is regarded as an infinite medium with an initial uniform temperature;
- The heat dissipation in the direction of the two lateral surfaces of the horizontal pipes is neglected;
- The dimension of the pipe is neglected, and its heat source is assumed to be uniformly distributed along the plane of $x = 0$ where the horizontal pipes are buried. So it is regarded as a plane heat source.

The first assumption of initial uniform temperature is reasonable since the influence of the temperature fluctuation in the ground is taken into account through a temperature deviation from the ground surface temperature. Based on the foregoing assumptions, the heat conduction process in the ground is, therefore, simplified as a one-dimensional transient problem. The plane heat source model, which is simple and effective for most engineering applications, can be used for prediction of the temperature response in the ground. According to the plane heat source theory, the temperature response in the ground caused by a constant heat rate can be calculated directly using the Green's function solution:

$$\theta_1 = t - t_\infty = \frac{q}{\lambda_s}\sqrt{a\tau}\,\mathrm{ierfc}\left(\frac{x}{2\sqrt{a\tau}}\right) \tag{8.2}$$

where, x is the distance from the plane source and τ is the time since the start of the operation; t is the temperature of the ground at distance x and time τ; t_∞ is the initial temperature of the ground; q is the heating rate per area of the plane source, W/m^2; λ_s and a are the ground thermal conductivity and diffusivity.

The temperature rise on the plane source, where $x = 0$, is of interest as the representative temperature in the design of HGHE and is obtained by substituting $x = 0$ into Eq. (8.2).

$$\theta_1 = \frac{q}{\lambda_s}\sqrt{\frac{a\tau}{\pi}} = q\sqrt{\frac{\tau}{\pi\rho c\lambda_s}} \tag{8.3}$$

where, ρ and c are the ground density and specific heat capacity.

Consequently, the thermal resistance on the plane source can be derived from Eq. (8.3):

$$R_1 = \sqrt{\frac{\tau}{\pi\rho c\lambda_s}}\ \left(\mathrm{Km}^2/\mathrm{W}\right) \tag{8.4}$$

It is noteworthy that the thermal resistance of the transient heat transfer process is closely related to the operating time of the heating load. The thermal resistance increases with the operating time and reaches the maximum value at the end of the operation period. Accordingly, the heat transfer efficiency of the HGHE decreases to the lowest value after a heating/cooling season.

8.2.3 Heat Transfer Process from the Fluid Inside the Pipe to the Plane Source

In order to derive the fluid temperatures to/from the HGHE, it is necessary to calculate the thermal resistances inside and outside of the pipe wall, as well as the thermal resistance between the adjacent pipes. In this region, the one-dimensional steady-state heat transfer analysis can usually approximate the heat transfer process since the pipe diameter is relatively small compared to the heat transfer region outside the pipes. Introducing the parameter β to denote the length of the slinky coils per area ($\mathrm{m/m}^2$); thus, the heating rate per unit length of pipe can be expressed by $q_l = q/\beta$ (W/m).

Based on the forced convective mechanism inside the pipe and the heat conduction of the pipe wall, the thermal resistance R_p inside the pipe can be approximately evaluated by the following equation:

$$R_\mathrm{p} = \frac{1}{2\pi\lambda_p}\ln\frac{d_\mathrm{o}}{d_i} + \frac{1}{\pi d_i h} \tag{8.5}$$

where, d_0 and d_i are the outer and inner diameters of the pipe; λ_p is the thermal conductivity of the pipe; h is the convection heat transfer coefficient inside the pipe.

The heat transfer between the adjacent pipes is quite complex and difficult to calculate since it is affected by many factors. Among these factors, the length of the buried pipes per area plays a dominant role in determining the thermal resistance. To simplify the heat transfer process, the slinky coils are supposed to be evenly spaced straight pipes in parallel. Then, the space between the straight pipes is $1/\beta$ (m). The one-dimensional heat conduction can be approximately employed to calculate the thermal resistance R_g between the adjacent pipes,

$$R_g = \frac{1}{2\pi\lambda_s}\ln\left(\frac{1}{\beta d_0}\right) \tag{8.6}$$

Thus, the total thermal resistance per pipe length can be expressed by $R_l = R_p + R_g$, and the thermal resistance per unit area is $R_2 = R_l/\beta$. The temperature rise caused by the total thermal resistance is given as follows:

$$\theta_2 = \frac{q}{\beta}\left(\frac{1}{\pi d_i h} + \frac{1}{2\pi\lambda_p}\ln\frac{d_0}{d_i} + \frac{1}{2\pi\lambda_s}\ln\frac{1}{\beta d_0}\right) = \frac{q}{\beta}R_l \tag{8.7}$$

8.2.4 *Simplified Model for the Various Heating/Cooling Loads*

The temperature responses from Eqs. (8.3) to (8.7) are obtained with the assumption of a constant heat pulse. Actually, the heat extracted from or rejected to the ground varies with time because of the various building loads. The variable heat flow can be approximated by a series of continuous rectangular of heating or cooling pulses [9]. Furthermore, the discontinuous operation of the GCHP system is assumed to be a simple periodic on–off operation. For rectangular heating pulses the temperature rises can be easily obtained by superposition. Similar to any other GHEs, the maximum/minimum temperature rise of the fluid in HGHE after a operation period is of interest since it determines the operating efficiency of the GCHP system. The peak value can be found through calculating all the temperature responses for heat pulses, which is quite time-consuming, especially for long-term operation. The authors have proposed a simplified method to solve the peak values. The maximum pipe wall temperature rise due to the periodic on–off load can be approximated by the superposition of a continuous mean load and a single heating pulse as shown in Fig. 8.2. Thus, the maximum temperature rise caused by the plane source can be rewritten as the following formula,

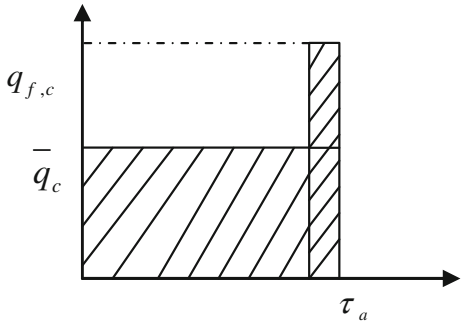

Fig. 8.2 Periodic pulse load and simplified load

$$\theta_1 = \frac{\sqrt{a}}{\sqrt{\pi}\lambda}\left[\overline{q}_c\sqrt{\tau_a} + (q_{f.c} - \overline{q}_c)\sqrt{\tau_d}\right] \tag{8.8}$$

where: $\overline{q}_c$ is the mean heat flux per unit area during the whole cooling season W/m^2; $q_{f,c}$ is the peak heat flux per unit area during the cooling season W/m^2. τ_a is the operating time of the cooling season, s; τ_d is the duration of the peak load, s.

As for a practical engineering, the maximum/minimum fluid temperature is mainly determined by the peak load for a short period. Therefore, it is reasonable to employ the peak loads (i.e., the design loads) to calculate the temperature rises of the fluid. Equation (8.7) for the cooling mode can be revised as,

$$\theta_2 = \frac{q_{f,c}}{\beta} \cdot R_l \tag{8.9}$$

For winter heating mode, the temperature drop caused by the peak load can be also obtained:

$$\theta_2 = \frac{q_{f,h}}{\beta} \cdot R_l \tag{8.10}$$

where, $q_{f,c}$ and $q_{f,textith}$ are the peak cooling load and peak heating load per unit area.

8.2.5 The Peak Fluid Temperatures

The main objective of the heat analysis for the HGHE is to determine the entering and leaving temperatures of the circulating fluid in the HGHE according to the pipe wall temperature and its heat flow. The average fluid temperature in the HGHE can be expressed as a superposition of the three separate temperature responses, i.e., the initial ground temperature rise, the temperature rise on the plane source, and temperature rise of the pipe caused by the heat fluxes per unit area:

$$\overline{t}_f = t_\infty + \theta_0 + \theta_1 + \theta_2 \tag{8.11}$$

The peak (maximum and minimum) entering fluid temperatures to the HGHE can be calculated using the principle of energy balance:

$$t_{\max} = \overline{t}_f + \frac{q_{f,c}A}{2Mc} \tag{8.12}$$

$$t_{\min} = \overline{t}_f - \frac{q_{f,h}A}{2Mc} \tag{8.13}$$

where A is the trench area of each loop, M is flow rate of each loop, c is the fluid specific heat capacity.

8.3 Case Study

8.3.1 Project Description and Building Loads

The example project is a golf clubhouse with a floor space of 5,000 m^2 that is located in the south of a golf course in Chengdu, China. The horizontal slinky-coil pipes will be buried at a depth of 2 m below the ground surface of the golf course. The designed dry bulb temperature of the outside air for winter heating is 2 °C, and the summer design temperature is 31.6 °C. The annual mean ground temperature in the location is 16 °C and the annual temperature amplitude is $A_w = 13.7$ °C. According to the in situ thermal response test, the predicted mean thermal conductivity and thermal diffusivity of the ground around the example building are 1.5 W/m °C and 0.6×10^{-6} m^2/s, respectively. The volumetric specific heat capacity is 2,500 kJ/m^3K.

Figure 8.3 presents the hourly cooling and heating loads of the example building. The peak heating and cooling loads are 215 and 483 kW, respectively. The mean heating and cooling loads are 54 and 164 kW. The duration time for the peak heating load is defined as 8 h and the peak cooling hour is 12 h.

The designed maximum and minimum fluid temperatures to the pipe when all factors have been taken into consideration, including the initial ground temperature, are defined as 35 and 3 °C.

8.3.2 Results and Discussion

Substituting the ground thermal properties and the loads into the foregoing simplified models, the required pipe length and the land area can be conveniently obtained under the conditions of the peak limitation of the fluid temperatures to the ground. The results are listed in Table 8.1.

The HGHE configuration for the example project is given as:

A total of 310 loops are arranged in parallel with a loop spacing of 2.4 m. The buried pipe length is 342.7 m in each loop. The coil diameter and pitch are

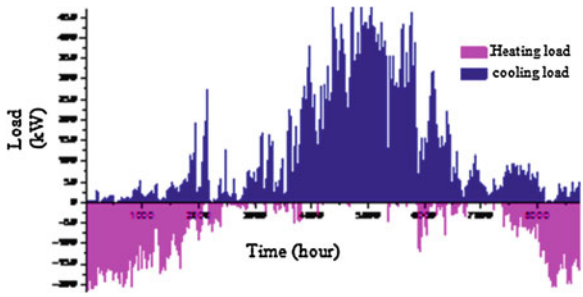

Fig. 8.3 Building annual hourly loads

Table 8.1 HGHE design results

Required land area (m^2)	Required pipe length (m)	t_{max} (°C)	t_{min} (°C)	Cooling load per unit area (W/m^2)	Heating load per unit area (W/m^2)
22,320	106,250	35.09	3.69	25.9	7.2

d = 1.2 m and s = 0.4 m, the pipe diameter is 32 mm. The pipe length per unit area is $\beta = 4.76$ m/m^2.

It can be observed that the predicted maximum fluid temperature to the HGHE exceeded the limit of the maximum temperature, whereas the predicted minimum temperature was still higher than the designed lowest value. This demonstrates that the HGHE size is primarily determined by the cooling loads because the example project is dominated by cooling loads.

A set of parameters, such as the ground thermal properties, pipe installation density per unit area β, trench geometry, the operation of the heat pump, and the characteristics of the slinky pipes, affect the size of the HGHE to some extent, but the ground thermal properties and the pipe installation density are the most important factors. The following section discusses the influences of these parameters on the HGHE size and performance based on the design case.

8.3.2.1 Effect of the Ground Thermal Properties on HGHE Size

In this section, the remaining parameters are the same as those that are used in the design case. Figure 8.4 shows the total pipe length against the ground specific heat capacity for different values of ground thermal conductivity. As expected, a larger heat capacity results in a shorter total pipe length, and a greater thermal conductivity absolutely decreases the HGHE length.

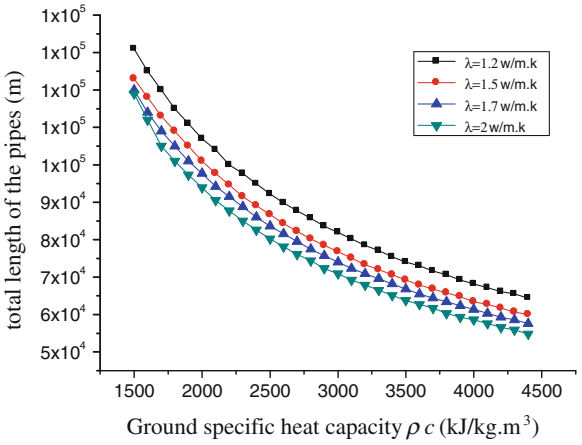

Fig. 8.4 Effect of ground thermal properties on HGHE length

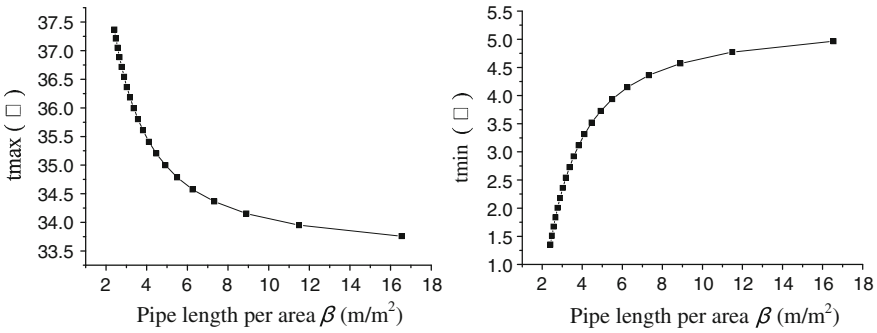

Fig. 8.5 Effects of pipe length per area on peak temperatures of fluid to HGHE

8.3.2.2 Effect of the Pipe Installation Density on the Performance of HGHE

Figure 8.5 illustrates the sensitivity of the peak fluid temperatures to the pipe length per unit area β ranging from 2 to 17 m/m^2 for the cooling and heating modes. As Fig. 8.5 shows, a higher pipe installation density allows a lower fluid temperature in cooling mode and a higher temperature in heating mode. A 6 % reduction in the fluid temperature in cooling mode is obtained if β is increased from 2.4 to 4.76 m/m^2. However, the pipe installation density is unimportant to the HGHE performance when the value exceeds about 6 m/m^2. It should be noticed that more buried pipes causes more initial cost. Therefore, it is strongly recommended that the HGHE size should be optimally designed in the economical view of point.

8.4 Conclusions

In this paper, the heat transfer process of the HGHE with slinky coils is simplified as a one-dimensional transient problem which employs the plane source model and the superposition principle for calculating the thermal resistances of different parts. A simplified method is also proposed to analyze the discontinuous heating/cooling loads for a long-term operation. The simplified model that can be used to determine the optimum size of HGHEs with slinky coils provides a useful design/simulation tool for engineering applications.

A case study has been carried out based on the simplified model. A set of parameters that strongly affect the HGHE performance is discussed in detail. The specific heat capacity of the ground is the most critical factor in determining the appropriate HGHE size. It is necessary for designers and engineers to obtain dependable on-site data of the thermal properties of the ground as a basis for designing an optimum HGHE system. The influence of pipe installation density on HGHE performance is also considerable, especially for lower buried density.

Acknowledgments The research is supported jointly by a grant from National Natural Science Foundation (Project No. 51208286) and a grant from Shandong Provincial Natural Science Foundation (Project No. ZR2010EQ006) and a grant from 12th Five-Year National Science and Technology Support Program (2012BAJ06B03-01).

References

1. Spitler JD (2005) Ground-source heat pump system research—Past, present, and future. HVAC & R Research 11(2):165–167
2. Philippe M, Bernier M, Marchio D, Lopez S (2011) A semi-analytical model for serpentine horizontal ground heat exchangers. HVAC & R Res 17(6):1044–1058
3. Mei VC (1986) Horizontal ground-coil heat exchanger: theoretical and experimental analysis, ORNL/CON-193. Oak Ridge National Laboratory, Oak Ridge
4. Demir H, Koyun A, Temir G (2009) Heat transfer of horizontal parallel pipe ground heat exchanger and experimental verification. Appl Therm Eng 29:224–233
5. Gonzalez RG, Verhoef A, Vidale PL, Main B, Gan G, Wu Y (2012) Interactions between the physical soil environment and a horizontal ground coupled heat pump, for a domestic site in the UK. Renew Energy 44:141–153
6. Wu Y, Gan G, Verhoef A, Vidale PL, Gonzalez RG (2010) Experimental measurement and numerical simulation of horizontal-coupled slinky ground source heat exchangers. Appl Therm Eng 30:2574–2583
7. Congedo PM, Colangelo G, Starace G (2012) CFD simulations of horizontal ground heat exchangers: a comparison among different configurations. Appl Therm Eng 33(34):24–32
8. Benazza A, Blanco E, Aichouba M, Río JL, Laouedj S (2011) Numerical investigation of horizontal ground coupled heat exchanger. Energy Procedia 6:29–35
9. Fang ZH, Diao NR, Cui P (2002) Discontinuous operation of geothermal heat exchangers. Tsinghua Sci Technol 7(2):194–197

Chapter 9
The Secondary Ring-Shaped Pipe Network Optimization Design of a District Cooling Project in Chongqing

Xiaodan Min, Xiangyang Rong, Pengfei Si, Hai Liu and Lijun Shi

Abstract In the paper, through a District cooling project in Chongqing, optimized design and evaluation methods of secondary loop network system are concluded, by optimizing the design of the secondary ring-shaped pipe network, analyzing hydraulic conditions in the case of part load rate (100, 75, 50, and 25 %) and the most unfavorable accident conditions of various options, evaluating various schemes in terms of energy efficiency, economy, and reliability.

Keywords The secondary ring-shaped pipe network · Optimization design · Energy efficiency · Economy · Reliability

9.1 Introduction

District cooling system secondary pipe network refers to the chilled water line between the regional cold source station and users. Because of the large amount of cooling, long distance for cooling supply, large investment in secondary network and large cost for energy consumption of secondary pump operation, the quality of design for the network have a significant impact on system investment and operation economy. The application of loop system in district cooling secondary network has unique advantages in improving the system reliability, economy, and mobility, relative to branch system. In the paper, through a District cooling projects in Chongqing, optimized design and evaluation methods of secondary loop network system are concluded. It will provide a meaningful reference for this type engineering.

X. Min (✉) · X. Rong · P. Si · H. Liu · L. Shi
China Southwest Architectural Design and Research Institute Corp.Limited, Chengdu 610042, China
e-mail: 469536835@qq.com

A. Li et al. (eds.), *Proceedings of the 8th International Symposium on Heating, Ventilation and Air Conditioning*, Lecture Notes in Electrical Engineering 262,
DOI: 10.1007/978-3-642-39581-9_9,

9.2 Project Overview

The project services buildings of 800,000 square meters construction area, consisting of 15 buildings, including office, hotel, apartment, exhibition, commerce, repast, finance functions, a total of 12 plots. The project uses a district cooling system. The chilled water supply from the regional cold source station to users through regional pipeline network.

Secondary pump variable flow system is used in the chilled water system. The water flow varies with the load changes by the variable frequency pump. Heat exchanger stations are set in buildings or plots, by which the regional pipeline network and water system in the buildings are insulated. In order to ensure the reliability of the system, the ring-shaped pipe network is used, laid along the roads. Chilled water supply and return temperature is 5.5/13.5 °C.

9.3 Secondary Ring-Shaped Pipe Network Optimization Design

9.3.1 Ring-Shaped Pipe Network Hydraulic Calculation

The difference between ring-shaped pipe network hydraulic calculation and branched network hydraulic calculation is that the pipe flow direction has two possibilities, when a pipe resistance change, not only itself and other pipe flow will change, but also some pipe flow direction will convert. So ring-shaped pipe network hydraulic calculation is more complex than branched network.

The software *Ring-shaped pipe network hydraulic calculation and hydraulic conditions analysis* is used to check the hydraulic parameters of each pipe sections, adjust pipe diameter, ultimately determine the various parameters of the main ring-shaped pipes. Ring-shaped pipe network is shown as Fig. 9.1. The design of the main ring-shaped pipes is considered three options: Option 1 the main ring-shaped pipe sections diameter are not equal, Option 2 the main ring-shaped pipe sections diameter are equal (800 mm diameter), Option 3 the main ring-shaped pipe sections diameter are equal (700 mm diameter). The calculation results are shown in Table 9.1.

The pump pressure calculation results are shown in Table 9.2.

According to the above calculation results, parameters of the selected pumps are as follows Table 9.3

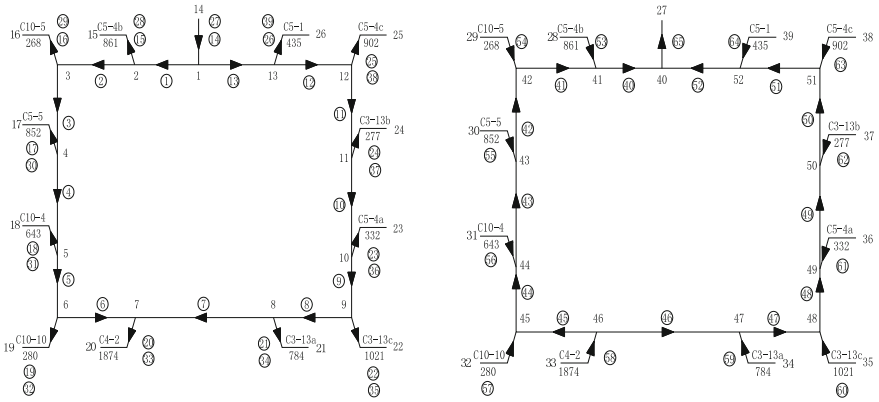

Fig. 9.1 Ring-shaped pipe network (supply water/return water)

Table 9.1 The main ring-shaped pipes calculation results

Section numbers	Option 1		Option 2		Option 3	
	Flow m^3/h	Diameter m	Flow m^3/h	Diameter m	Flow m^3/h	Diameter m
1	3372	0.8	4295	0.8	4270	0.7
2	2511	0.7	3434	0.8	3409	0.7
3	2243	0.6	3166	0.8	3141	0.7
4	1391	0.5	2314	0.8	2289	0.7
5	748	0.4	1671	0.8	1646	0.7
6	468	0.4	1391	0.8	1366	0.7
7	1406	0.6	483	0.8	508	0.7
8	2190	0.7	1267	0.8	1292	0.7
9	3211	0.8	2288	0.8	2313	0.7
10	3543	0.8	2620	0.8	2645	0.7
11	3820	0.8	2897	0.8	2922	0.7
12	4722	0.9	3799	0.8	3824	0.7
13	5157	0.9	4234	0.8	4259	0.7

Table 9.2 The calculation results of Pump head

	Option 1	Option 2	Option 3
Pump head (m H_2O)	28.32	28.48	35.48

Table 9.3 Parameters of pumps

	Flow (m^3/h)	Head (m H_2O)	Efficiency (%)	Power (kW)	Rated speed (rpm)	Numbers
Option 1/Option 2	800	33	74	97	1450	8
	1000	30	84	97		
	1400	22	84	100		
Option 3	750	41	67	125	980	8
	1000	38	82	126		
	2100	24	75	183		

9.3.2 Ring-Shaped Pipe Network Operation Conditions Analysis

9.3.2.1 Typical Conditions Analysis

Four conditions of 100, 75, 50, and 25 % load rate are defined as the typical conditions. After selecting pumps, operation condition of 100 % load is simulation to calculate the actual operation condition of pumps under full load. The calculation results are shown in Table 9.4.

After he actual operation condition of 100 % load is determined, analyze other typical operation conditions of the system. The flow of the typical operation condition is determined by the system full load flow and the corresponding typical load rate. The head of the typical operation condition is determined by the pipe network hydraulic characteristic curves corresponding to different control modes. Secondary pump control mode of the project is as follows: Based on the pressure difference of the main supply and return pipes, when the pressure difference is greater than the set value, reduce the frequency of the secondary pump; when the pressure difference is less than the set value, improve the frequency of the secondary pump; when the pressure difference is above 110 % of the corresponding single pump flow, reduce or increase a pump operation. System control curve graph is shown in Fig. 9.2. A, B, C, and D stand for the typical conditions of 100, 75, 50, and 25 %.

9.3.2.2 Accident Conditions Analysis

The main advantage of the ring-shaped pipe network is the reliability under accident conditions. So first consider the guaranteed rate of accident conditions

Table 9.4 The actual operation condition of pumps under full load

	Design flow (m^3/h)	Actual flow (m^3/h)	Single pump flow (m^3/h)	Pump head (m H_2O)	Pump efficiency (%)
Option 1	8529	8594	1074	28	84
Option 2	8529	8575	1072	28	84
Option 3	8529	8706	1088	36	82

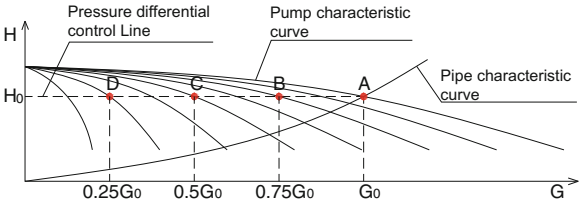

Fig. 9.2 System control curve graph

Table 9.5 The guaranteed rate of individual users under accident condition

User number	Option 1 The guaranteed rate (%)	Option 2 The guaranteed rate (%)	Option 3 The guaranteed rate (%)
C5-4b	109.65	95.44	93.40
C10-5	109.43	94.93	92.68
C5-5	106.44	91.54	87.94
C10-4	104.38	90.74	86.70
C10-10	90.60	88.59	83.54
C4-2	42.95	82.70	74.59
C3-13a	41.59	81.70	73.01
C3-13c	41.27	81.07	72.01
C5-4a	41.25	80.92	71.77
C3-13b	41.22	80.76	71.51
C5-4c	41.20	80.64	71.34
C5-1	40.74	77.52	67.32

when comparing the three options. The most unfavorable accident condition occurs in the case that the pipe adjacent cold source node can not normally work by accident, outflow on both sides of the node is replaced by outflow on one side, resulting in non-incident side flow increases, resistance of pipe network raises, transport distance becomes longer [1]. The most unfavorable accident condition of the project appears in the pipe segment 13 off. The guaranteed rate of individual users under accident condition are shown in Table 9.5.

9.3.3 Ring-Shaped Pipe Network Comprehensive Evaluation

9.3.3.1 Energy Efficiency Evaluation

The total pump energy consumption is equal to the sum of the product of the pump power under operation point and operation time [2]

$$N = \int P_i(G_i)T_i(G_i)dG \tag{9.1}$$

Table 9.6 The pump operation time under various typical conditions

Load range	100–75 %	75–50 %	50–25 %	Less than 25 %
operation time (h)	220	390	933	2129

Table 9.7 The pump annual energy consumptions and operation costs

	Option 1	Option 2	Option 3
The pump annual energy consumptions ($\times 10^4$ kWh)	82.07	81.96	109.43
The pump annual operation costs ($\times 10^4$ yuan)	49.32	49.26	65.77

where N is the total pump energy consumption, kWh; P_i is the pump energy consumption by G_i flow, kW; T_i is the pump operation time by G_i flow, h. Time-consuming energy analysis software must be used for the formula calculation, so in this paper, the time period of the pump operation typical conditions can be simplified to the total energy consumption calculation. (1) Based on the flow, head and pump efficiency under typical conditions, calculate the pump energy consumption P_i of 100, 75, 50, and 25 % load rate. (2) Add up the pump operation time respectively under load rate from 100 to 75 %, from 75 to 50 %, from 50 to 25 %, and less than 25 %. (3) Calculate the total pump energy consumption by a weighted sum of various typical conditions. The simplified formula is as follows:

$$N = \frac{1}{2}(P_A + P_B)T_{AB} + \frac{1}{2}(P_B + P_C)T_{BC} + \frac{1}{2}(P_C + P_D)T_{CD} + \frac{1}{2}P_D T_D \qquad (9.2)$$

where P_A, P_B, P_C, P_D is the pump energy consumption under 100, 75, 50, and 25 % load rate, kW; T_{AB}, T_{BC}, T_{CD}, T_D is the pump operation time, respectively, under load rate from 100 to 75 %, from 75 to 50 %, from 50 to 25 %, and less than 25 %, h.

In this paper, DOE-2 software is used for all year hourly load simulation analysis of the district cooling system, the pump operation time under various typical conditions is summarized as shown in Table 9.6. The cooling period is from May 1 to September 30. Because of the different buildings function, the system operates 24 h a day, the total operation time of 3672 h.

Based on the energy prices, the pump annual operation costs are calculated as Table 9.7 in accordance with 0.601 yuan/kWh.

It can be seen that from the operation energy consumptions, Options 1 and 2 are little difference. Option 3 is more than 33 % compared to others.

9.3.3.2 Economic Evaluation

Estimate the investment of the pipe network. Buried water secondary pipe network investment mainly consists of three parts: the price of the buried pipes, buried pipes construction costs, investment of chilled water secondary pumps (pumps and the corresponding frequency control devices). Fitting fees and charges in accordance with the sales price and the project cost of manufacturers are as the following formula [3]:

Table 9.8 The initial investments of the three options

	Option 1	Option 2	Option 3
Water pumps costs ($\times 10^4$ yuan)	148.55	148.55	192.77
Frequency control devices costs ($\times 10^4$ yuan)	39.38	39.38	52.19
The buried pipes costs ($\times 10^4$ yuan)	466.29	507.74	424.74
Buried pipes construction costs ($\times 10^4$ yuan)	122.72	134.77	107.62
Total costs ($\times 10^4$ yuan)	776.93	830.44	777.33

Table 9.9 The users' guaranteed rate under the most unfavorable accident condition

	Option 1 (%)	Option 2 (%)	Option 3 (%)
Minimum guarantee rate	40.74	77.52	67.32
Maximum guaranteed rate	109.65	95.44	93.40
Average guaranteed rate	67.56	85.55	78.82

The price of water pumps: $C_{pu} = 1700.8P + 19861$, yuan; The price of frequency control devices $C_{VFD} = 492.97P + 1157.4$, yuan; Where P is the pump rated power, kW. The price of the unit length buried pipe $C_{pipe} = 10.863 + 1917.3d + 1339.2d^2$, yuan/m; Unit length buried pipe construction costs $C_{ps} = 11.459 + 208.89d + 717.12d^2$, yuan/m; Where d is diameter, m.

Because of the same tree-shaped pipes of three options, in comparison, only calculate the main ring-shaped pipes investment. The initial investments of the three options are as Table 9.8.

It can be seen that from the investments, Options 1 and 3 are little difference. Option 2 is more than 7 % compared to others.

9.3.3.3 Reliability Evaluation

Reliability evaluation of pipe network is the users' guaranteed rate under the accident condition, as described in Sect. 9.3.2.2. The users' guaranteed rate of three options under the most unfavorable accident condition is shown in Table 9.9.

It can be seen that under the most unfavorable accident condition, Option 2 is the highest, Option 3 is relatively lower, and Option 1 is the lowest.

9.4 Conclusion

In the paper, through the secondary ring-shaped pipe network optimization design of a District cooling projects in Chongqing, evaluation in terms of energy efficiency, economy, and reliability of secondary loop network system is concluded as follows:

(1) Due to the smaller diameter of some pipe sections of Option 1, under accident conditions, there will be "throat" phenomenon, which is not conducive to the smooth passage of the chilled water, so the users have a lower guaranteed rate. Due to the same main ring-shaped pipes of Options 2 and 3 , there will be not this phenomenon and the users have a higher guaranteed rate. Through the comparison of Option 2 and Option 3, it can be seen that the larger diameter, the higher users' guarantee rate.
(2) Larger diameter pipe network, the greater initial investment, but the lower pump head and operation energy consumption. There should be a reasonable judgment. Compared to Options 2 and 3 , the former has larger diameter pipe network and initial investment, but also has lower pump operation energy consumption, the static payback period is calculated as 3.2 years, which can be accepted.
(3) The evaluation of the pipe network should not be a single evaluation index, all aspects factors should be considered. In the project, Option 1 has advantages in energy-saving and economy, but it is poor in reliability; economy; and reliability of Option 3 is excellent, but the pump energy consumption is higher; Advantages in terms of reliability of Option 2 is obvious. Although the initial investment is higher, due to the low pump energy consumption and short static payback period, Option 2 is the final scheme.

Acknowledgments This study was financially supported by the China science and technology support project (2011BAJ03B12-3). The co-authors of this paper would like to thank the managers for their contribution and hard work.

References

1. Xiaohong H., Pinghua Z., Guangming C. (2004) Hydraulic calculation and emergency regime analysis of multi-heat source ring-shaped heat supply network. J Gas Heat 6(6):307–311
2. Xiaoting W., Yan L. (2006) Example analysis on variable frequency drive operation of circulating pumps. J HVAC 36(8):25–32
3. Jinping L., Zhiqing C. (2006) Optimal design for tree-shaped chilled water pipe network in district cooling systems. J HVAC 36(7):18–22

Chapter 10
Factor Analysis for Evaluating Energy-Saving Potential of Electric-Driven Seawater Source Heat Pump District Heating System Over Boiler House District Heating System

Haiwen Shu, Hongbin Wang, Lin Duanmu and Xiangli Li

Abstract Although the seawater source heat pump district heating system is often regarded as a renewable energy utilization system, it cannot be guaranteed to obtain the energy-saving effect. The authors provided an energy-saving judgement method for the electric-driven seawater source heat pump district heating system over the conventional boiler house district heating system in former research. However, many factors will influence the energy efficiency of the system. In order to enhance its energy efficiency and make the best use of the system, detail analysis of those factors is conducted in the paper. First, an energy-saving potential evaluation model is derived for the system with part-time operation mode. Then all the factors influencing the energy efficiency of the system are ascertained and analyzed. These factors include the electricity generation efficiency, energy performance of seawater source heat pump units, the seawater temperature, the energy consumption of the seawater pump, the local outdoor air temperature, and the heating district radius. The research results are expected to provide clear directions for the seawater source heat pump system to raise its energy efficiency.

Keywords District heating system · Energy-saving · Factor analysis · Seawater source heat pump · Boiler house

10.1 Introduction

As a renewable energy utilization system, the seawater source heat pump system attracts interests of many researchers [1–11]. The authors have pointed out in literature [11] that the seawater source heat pump district heating system is not

H. Shu (✉) · H. Wang · L. Duanmu · X. Li
Faculty of Infrastructure Engineering, Dalian University of Technology,
Dalian 116023, China
e-mail: shwshw313@sina.comshuhaiwen@dlut.edu.cn

A. Li et al. (eds.), *Proceedings of the 8th International Symposium on Heating, Ventilation and Air Conditioning*, Lecture Notes in Electrical Engineering 262,
DOI: 10.1007/978-3-642-39581-9_10,

always be more energy efficient than the conventional boiler house district heating system. Further the authors put forward a quasi-dynamic energy-saving judgement method for the seawater source heat pump district heating system in literature [12]. However, there are cases that the seawater temperature is too low to run the heat pump unit under severe cold climate in northern areas. Assistant heat source is necessary in such cases, but how to evaluate the energy-saving potential during the normal operation period of seawater source heat pump system? Apart from the seawater temperature, what other factors affect the energy-saving potential of the system? On the basis of former research, the authors will establish energy-saving evaluation model for the seawater source heat pump district heating system during its normal operation period, and further summarize the factors that affect the energy efficiency of the system and also examine the extent of impact those factors have on the energy efficiency of the system. The results will give clear directions to raise the energy efficiency of the seawater source heat pump district heating system.

10.2 Energy-Saving Evaluation Model of the Seawater Source Heat Pump District Heating System During Its Operation Period

As put forward in literature [11, 12], the energy-saving effect of the seawater source heat pump district heating system is achieved under the comparison with the conventional boiler house district heating system. The typical schematic diagrams of the two types of systems are shown in Figs. 10.1 and 10.2, in which the supply and return hot water temperature differences are 10 and 25 °C, respectively. The same end users and pipeline topology of the two systems are the prerequisites of energy efficiency comparison.

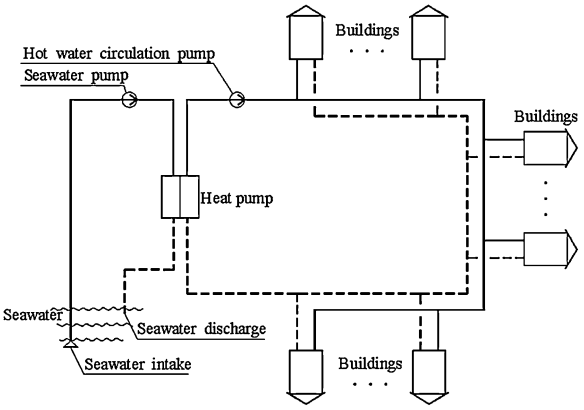

Fig. 10.1 Schematic diagram of the electric-driven seawater source heat pump district heating system

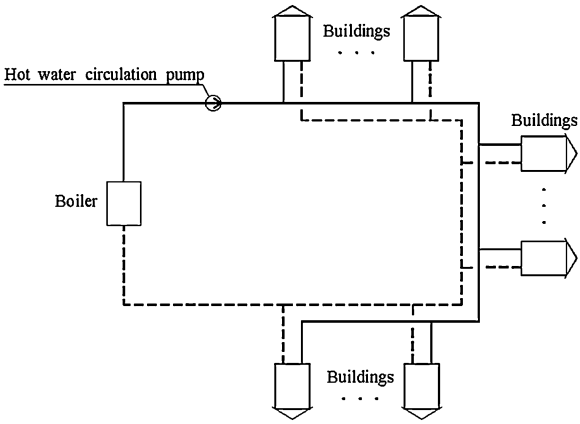

Fig. 10.2 Schematic diagram of the boiler house district heating system

Equation (10.1) expresses the definition of the energy efficiency of the two systems.

$$\text{Energy efficiency} = \frac{\text{Total heat transported by pipeline}}{\text{Total energy input from heat source + Energy consumption of pumps}} \tag{10.1}$$

When the energy efficiencies of the two systems are assumed to be equal, the expression of the critical average COP of the heat pump unit (i.e., $\text{COP}_{h,\text{mc}}$) is derived as Eq. (10.2). (Refer to literature [12] for more information.)

$$\text{COP}_{h,\text{mc}} = \frac{1}{1/\text{COP}_{1,\text{mc}} - W_{\text{pu,sw}}/Q_t} \tag{10.2}$$

in which,

$$\text{COP}_{1,\text{mc}} = \frac{1}{0.297/\eta_m - (W_{\text{pu,cw1}}/Q_t - W_{\text{pu,cw2}}/Q_t)} \tag{10.3}$$

$\text{COP}_{1,\text{mc}}$ is the critical value of $\text{COP}_{1,m}$, and $\text{COP}_{1,m}$ is the average comprehensive COP of the heat pump unit and the seawater pump during the system operation period; $W_{\text{pu,sw}}$ is the total electricity consumption of the seawater pump during the system operation period (kWh); Q_t is the accumulative heat load of the heat users during the system operation period (kWh); η_m is the average heating efficiency of the coal-fired boiler house, %; $W_{\text{pu,cw1}}$ is the total electricity consumption of the hot water circulation pump in the heat pump district heating system (kWh); $W_{\text{pu,cw2}}$is the total electricity consumption of the hot water circulation pump in the boiler house district heating system during the same period of the seawater source heat pump system in its normal operation (kWh).

According to Eqs. (10.2) and (10.3), the following four parameters should be calculated out before he critical average COP of the heat pump unit ($\text{COP}_{h,\text{mc}}$) can

be obtained: Q_t, $W_{\text{pu,cw1}}$, $W_{\text{pu,cw2}}$ and $W_{\text{pu,sw}}$. The users' heat load (Q_a) under certain outdoor air temperature t_a is calculated by Eq. (10.4) according to literature [13].

$$Q_a = Q_d \frac{t_i - t_a}{t_i - t_{o,d}} \tag{10.4}$$

in which, Q_d is the total design heat load of users (kW); t_i is the design indoor air temperature of the heating season, it is 18 °C according to the Chinese National Design Standard [14]; t_a is the outdoor air temperature (°C); $t_{o,d}$ is the design outdoor air temperature for heating (°C).

Then the accumulation heat load of users during a certain period (e.g., from 1st to Nth day) can be calculated by Eq. (10.5).

$$Q_t = 24 Q_d \sum_{j=1}^{N} \frac{t_i - t_{a,j}}{t_i - t_{o,d}} \tag{10.5}$$

in which, $t_{a,j}$ is the mean outdoor air temperature of the jth day of the heating season (°C).

Please refer to literature [12] for the calculation method of the other three factors ($W_{\text{pu,cw1}}$, $W_{\text{pu,cw2}}$ and $W_{\text{pu,sw}}$). Then the following three equations can be obtained.

$$\frac{W_{\text{pu,cw1}}}{Q_t} = \frac{T_B(14 + \alpha \sum L)}{2933A} \tag{10.6}$$

$$\frac{W_{\text{pu,cw2}}}{Q_t} = \frac{T_B(14 + \alpha \sum L)}{7332.5A} \tag{10.7}$$

$$\frac{W_{\text{pu,sw}}}{Q_t} = \frac{(\text{COP}_{h,d} - 1)[T_B + A(n-1)]H_{sw}}{2933 n \text{COP}_{h,d} \Delta t_{sw} A} \tag{10.8}$$

in which,

$$A = 24 \sum_{j=1}^{N} \frac{18 - t_{w,j}}{18 - t_{o,d}} \tag{10.9}$$

T_B is the operation hours of the circulation pumps during the seawater source heat pump system operation period (h); $\sum L$is the total length of the main hot water pipeline including both supply and return hot water pipes (m); α is the coefficient whose value is set as following: $\sum L \leq 500$ m, $\alpha = 0.0115$; 500 m $< \sum L < 1,000$ m, $\alpha = 0.0092$; $\sum L \geq 1,000$ m, $\alpha = 0.0069$; $\text{COP}_{h,d}$ is the heating coefficient of performance of the heat pump unit under the unfavorable design conditions; n is the number of seawater pumps; H_{sw} is the design water head of the seawater pump (kPa); Δt_{sw} is the seawater temperature difference flowing in and out of the evaporator of the seawater source heat pump unit (°C).

Finally, the expression of the critical average COP of the heat pump unit (i.e., $\mathrm{COP}_{h,\mathrm{mc}}$) is derived as shown in Eq. (10.10).

$$\mathrm{COP}_{h,\mathrm{mc}} = \left\{ \frac{0.297}{\eta_m} + \frac{T_B(14+\alpha\sum L)}{7332.5A} - \frac{T_B(14+\alpha\sum L)}{2933A} - \frac{(\mathrm{COP}_{h,d}-1)[T_B+A(n-1)]H_{\mathrm{sw}}}{2933n\mathrm{COP}_{h,d}\Delta t_{\mathrm{sw}}A} \right\}^{-1} \tag{10.10}$$

So, after the actual average COP value of seawater source heat pump units ($\mathrm{COP}_{h,\mathrm{ma}}$) is obtained according to the capacities of equipment designed for a given project, the amount of electricity that can be saved during the operation period of the seawater source heat pump system (ΔQ) can be calculated by Eq. (10.11)

$$\Delta Q = Q_t/\mathrm{COP}_{h,\mathrm{mc}} - Q_t/\mathrm{COP}_{m,a} \tag{10.11}$$

10.3 Influencing Factors Analysis on the Energy-Saving Potential of the Electric-Driven Seawater Source Heat Pump District Heating System

In order to ascertain the factors that influence the energy-saving potential of the seawater source heat pump district heating system and further analyze their influencing extent quantitatively, an assumed case project is adopted here.

10.3.1 Case Project

The case project is located in the northern seaside city of Dalian, China whose heating season is from November 15th to March 15th next year. And the outdoor air temperature for heating design is −11 °C. All the users are residential buildings with the total design heat load of 5,200 kW. The seawater source heat pump district heating system is supposed to be adopted in the project. The total length of the main hot water pipeline (including both supply and return hot water pipes) of the district heating system is 2.6 km, that is R_H = 1.3 km, and the seawater temperature profile is shown in Fig. 10.3.

According to the requirement of the heat pump unit, the seawater temperature should be higher than 2.5 °C during the heat pump operation period. So there are totally 25 days (accounting for 20.7 % of the heating season) that the heat pump system could not be operated. An assistant boiler is used here to satisfy the heating demand of users during this period. The heat pump system is thus designed under the seawater temperature of 2 °C (2.5/0.5 °C) on the basis of seawater temperature conditions here. As a result, three pumps are designed to be operated in parallel at the maximum heating load with the water head of each pump being 40 $\mathrm{mH_2O}$.

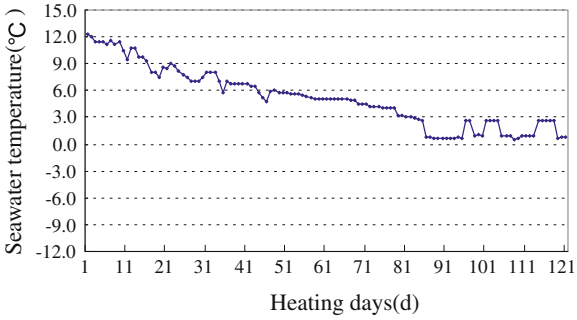

Fig. 10.3 Seawater temperature during heating season

Then the total electricity that will be saved during the operation period of the seawater source heat pump system can be calculated by the model provided in Sect. 10.2. Here the result is $\Delta Q = 3.40 \times 10^5$kWh. That is, if the electric-driven seawater source heat pump district heating system is to be adopted in the case project, a total amount of 3.40×10^5 kWh electricity will be saved in a heating season.

10.3.2 Influencing Factors Analysis

From above analysis and calculation, the factors that influence the energy efficiency of the seawater source heat pump district heating system can be summarized as follows:

1. Electricity generation efficiency of the primary energy

In the case project, the coal-fired electricity generation efficiency is set as 33 % [12]. If this electricity generation efficiency is raised by 10, 20, and 30 % (i.e., 36.3, 39.6, and 42.9 %) respectively without changing other conditions, then the corresponding electricity-saving potential are increased by 65.3, 122.1, and 178.9 %, respectively. Or with every 10 % of electricity generation efficiency enhancement, an average of 59.7 % electricity-saving rate can be achieved.

2. The performance of seawater source heat pump unit

If the actual average COP of the heat pump unit during the heating season (i.e. $COP_{h,ma}$) is raised by 10, 20, and 30 % (i.e. 3.73, 4.07, and 4.40) respectively without changing other conditions, then the corresponding electricity-saving potential are increased by 34.9, 64.0, and 88.6 %, respectively. Or with every 10 % enhancement of the actual average COP of the heat pump unit during the heating season, an average of 29.5 % electricity-saving rate can be achieved.

3. The seawater temperature

If the seawater temperature is raised by 1, 3, and 5 °C without changing other conditions, then the corresponding electricity-saving potential are increased by 8.7, 47.8, and 71.0 %, respectively. Or with every 1 °C increase of seawater temperature, an average of 14.2 % electricity-saving rate can be achieved.

4. Electricity consumption of seawater pump

If the electricity consumption of seawater pump is lowered by 10, 20, and 30 % without changing other conditions, then the corresponding electricity-saving potential are increased by 7.1, 14.2, and 21.3 %, respectively. Or with every 10 % decrease of electricity consumption of seawater pump, an average of 7.1 % electricity-saving rate can be achieved.

5. The outdoor air temperature during heating season

If the average outdoor air temperature is lowered by 1, 3, and 5 °C without changing other conditions, then the corresponding electricity-saving potential are increased by 3.6, 9.9, and 10.9 % respectively. Or with every 1 °C outdoor air temperature lowered, an average of 2.2 % electricity-saving rate can be achieved.

6. The district heating radius

If the district heating radius is decreased by 10, 20, and 30 % without changing other conditions, then the corresponding electricity-saving potential are increased by 0.8, 1.5, and 2.3 %, respectively. Or with every 10 % decrease of district heating radius, an average of 0.8 % electricity-saving rate can be achieved.

10.4 Conclusions

In the paper, an energy-saving evaluation model for the seawater source heat pump district heating system over the conventional boiler house district heating system is established. The model is especially presented for the cases that the severe cold seawater temperature prevents the seawater source heat pump unit being operated during the heating season. Then six factors that influence the energy-saving rate of the seawater source heat pump district heating system are ascertained after the analysis of the energy-saving evaluation model. These factors are the electricity generation efficiency, energy performance of seawater source heat pump units, the seawater temperature, the energy consumption of the seawater pump, the local outdoor air temperature and the heating district radius. Then how these factors will influence the energy-saving rate of the seawater source heat pump district heating system are carefully studied through more calculations. The research results are expected to give clear directions to evaluate the energy efficiency of the seawater source heat pump system and help to design the system with higher energy efficiency.

References

1. Nagota T, Shimoda Y, Mizuno M (2008) Verification of the energy-saving effect of the district heating and cooling system—Simulation of an electric-driven heat pump system. Energy Build 40:732–741
2. Chow TT, Fong KF, Chan ALS, Yau R, Au WH, Cheng V (2004) Energy modelling of district cooling system for new urban development. Energy Build 36:1153–1162
3. Chow TT, Au WH, Yau R, Cheng V, Chan A, Fong KF (2004) Applying district-cooling technology in Hong Kong. Appl Energy 79:275–289
4. Shimoda Y, Nagota T, Isayama N et al (2008) Verification of energy efficiency of district heating and cooling system by simulation considering design and operation parameters. Build Environ 43:569–577
5. Okamoto S (2006) A heat pump system with a latent heat storage utilizing seawater installed in an aquarium. Energy Build 38:121–128
6. Song Y, Akashi Y, Yee JJ (2007) Effects of utilizing seawater as a cooling source system in a commercial complex. Energy Build 39:1080–1087
7. Zhen L, Lin DM, Haiwen S, Jiang S, Yingxin Z (2007) District cooling and heating with seawater as heat source and sink in Dalian, China. Renew Energy 32:2603–2616
8. Li Z, Songtao H (2006) Research on the heat pump system using seawater as heat source or sink. Build Energy Environ 25(3): 34–38 (in Chinese)
9. Zhen L, Lin DM, Haiwen S et al (2005) Development of seawater air conditioning systems and application perspective of the technology in China. HV AC 35(11):20–26 (in Chinese)
10. Xiuru Z, Jihong X, Dong C, Haijiao Y, Lijuan S (2007) Analysis of characteristics of seawater heat pumps in winter. Energy Eng 2:58–61 (in Chinese)
11. Haiwen S, Lin DM, Xiangli L, Yingxin Z (2010) Energy-saving judgment of electric-driven seawater source heat pump district heating system over boiler house district heating system. Energy Build 42(6):889–895
12. Haiwen S, Lin DM, Xiangli L, Yingxin Z (2010) Quasi-dynamic energy-saving judgment of electric-driven seawater source heat pump district heating system over boiler house district heating system. Energy Build 42(12):2424–2430
13. Deying L (2004) Heat supply engineering. China Construction Industry Press, Beijing (in Chinese)
14. China Building Science & Research Institute (2010) Design standard for energy efficiency of residential buildings in severe cold and cold zones (JGJ26–2010). China Construction Industry Press, Beijing (in Chinese)

Chapter 11
A Review on Radiant Cooling System in Buildings of China

Hongbin Wang, Haiwen Shu and Lin Duanmu

Abstract The authors systematically summarized the research on the radiant cooling system in recent years. On the basis of a brief introduction of the radiant cooling system and its working principles, the advantages and disadvantages of the system were concluded compared with the conventional air conditioning system. The reasons for the slow development of radiant cooling system in China and its future trend were then discussed. It was suggested the solution to the condensation problem be focused on collecting and discharging the condensation water. This measure will not only improve the capacity of the radiant cooling system but also expand the application scope of the radiant cooling system.

Keywords Radiant cooling system · Energy-saving · Condensation

11.1 Introduction

Radiant heating system has been widely applied nowadays in mainland China [1] because of its thermal comfort and energy efficiency. At the same time, the radiant cooling system is attracting more and more researchers' attention.

Radiant cooling system is well recognized and widely adopted in Europe for its advantages of high thermal comfort and energy-saving characteristics. The advantages of the radiant cooling system also include more choices for the cooling source and more building space spared. But in China, radiant cooling system is still in the stage of theoretical and experimental studies and is rarely used in actual

H. Wang · H. Shu (✉) · L. Duanmu
Faculty of infrastructure engineering, Dalian University of Technology,
116023 Dalian, China
e-mail: shwshw313@sina.com; whbalzx@qq.com

A. Li et al. (eds.), *Proceedings of the 8th International Symposium on Heating, Ventilation and Air Conditioning*, Lecture Notes in Electrical Engineering 262,
DOI: 10.1007/978-3-642-39581-9_11,

projects mainly because of the condensation problem as well as the lack of reliable automatic control system. So the research on the solution of condensation problem was summarized in the paper.

11.2 Characteristics of Radiant Cooling System

11.2.1 Advantages of Radiant Cooling System

(1) Compared with conventional central air conditioning system, radiant cooling system can increase the chilled water temperature that resulted in improvement of chillers' efficiency. Also the increase of chilled water temperature makes more natural cooling sources (e.g., groundwater) available for space cooling purpose.
(2) When occupants reach their thermal comfort, the percentages of the three ways of heat transfer between human body and its environment are convective 30 %, radiant 45 %, and evaporation 25 % [2]. Radiant cooling system increases the proportion of radiant heat transfer, thus improves the human thermal comfort.
(3) The design indoor air temperature for radiant cooling system can be increased by 1 $\sim$ 2 °C compared with the conventional air conditioning system under the same thermal comfort level, which leads to a reduction of the cooling load.
(4) Radiant cooling system has the characteristics of self-regulation [3]. When the indoor cooling load increases, the temperature of the surface of building envelop increases as well, and this raises the radiant heat transfer between cooling surface and building envelop in turn.
(5) The radiant cooling system of buried-pipes type has the ability of peak-load shifting through cooling storage, which reduces the operation cost.

11.2.2 Disadvantages of Radiant Cooling System

(1) When the cooling surface temperature is below the dew point temperature of the surrounding air, there will be condensation phenomenon. Condensate is adversary to the indoor air quality and interior decoration. So the condensation phenomenon limits the application of radiant cooling system especially in hot and humid regions.
(2) The radiant cooling system should be combined with a fresh air distribution system, and displacement ventilation system is often recommended. If natural ventilation system is to be adopted, the condensate water should be under effective control.

(3) In order to avoid the condensation on the cooling surface, the chilled water temperature should not be lower than the dew point temperature of indoor air, which limits the cooling capacity of the radiant cooling system.

11.3 Comparison of Different Types of Radiant Cooling System

According to the position of the radiating surface, radiant cooling system can be divided into three types: roof type, floor type, and wall type. The roof type and floor type are more commonly utilized.

Most of researchers prefer the radiant roof cooling system, because the heavy cooled air strengthens the natural convection heat exchange. And the radiant roof cooling system also reduces the gradient of the indoor air temperature, which improves the human thermal comfort by reducing the draft sensation. But as hot air rises, it increases the risk of condensation. Compared to the radiant roof cooling system, radiant floor cooling system has advantages of easy construction, lower cost, sharing the same terminal system throughout summer and winter.

Simulation results show that the thermal comfort of radiant roof and wall cooling system is better than that of radiant floor cooling system [4]. Tables 11.1 and 11.2 show the vertical temperature difference at different level and the temperature efficiency of different radiant cooling systems.

Table 11.1 Comparison of vertical temperature difference in workspace

Type	$t_{0.1}$(°C)	$t_{1.1}$(°C)	$t_{1.1-0.1}$(°C)
Roof type	23.5	25	1.5
Floor type	21	24.8	3.8
Wall type	22.4	24.6	2.2

$t_{0.1}$, $t_{1.1}$ represent the air temperature at 0.1 and 1.1 m high from the ground, respectively

Table 11.2 Comparison of temperature efficiency

Type	t(°C)	t_e(°C)	t_s(°C)	E_T
Roof type	25	26	20	1.2
Floor type	24.6	27.3	20	1.59
Wall type	24.5	26.5	20	1.44

t,t_e,t_s represent air temperature of workspace, exhaust and supply respectively; E_T represents temperature efficiency

11.4 Condensation Problems

Many researchers suggest to avoid the condensation by dew point temperature control, and by combining with displacement ventilation or other form of fresh air system to achieve the temperature and humidity independent control [5–8].

Xia Xueying compared radiant cooling system and radiant cooling combined with displacement ventilation system [9]. The experimental results showed that the ventilation system enhanced the convective heat exchange between the air and the building envelope. The average surface temperature of building envelope dropped about 3 °C than only using radiant cooling system, and the indoor air temperature gradient of radiant floor cooling combined with displacement ventilation system is about 1.5 °C which is lower than the value of 3 °C suggested by ASHRAE.

He Jing concluded that radiant cooling system cannot be used in such places as beauty salon, swimming pool, sauna room, etc. due to their heavy moisture load or rapid moisture load changes. And the system should not used in operating rooms or clean rooms either as special requirement of ventilation rate is necessary. The author further put forward a new concept of dehumidification capacity per unit fresh air mass to judge whether a radiant cooling system can be adopted [10].

Also, some researchers put forward new types of terminal devices for radiant cooling system trying to solve the condensation problem. Zhang Bin et al. claimed that condensation problem can be solved by covering the cooling surface with a special film that only long wave radiation is allowed to pass through [11]. Kong Xianglei put forward a kind of "leading condensation" radiant panel, which gathered the condensation water at the edge of the radiant panel by the tiny channel on the surface of the panel. The author also designed the radiant panel and analyzed the relationship between the size of the channel and the condensate flow [12, 13].

11.5 Research Progress

11.5.1 Application of Radiant Cooling System in Engineering

In actual projects, radiant cooling system is either adopted in combination with some forms of air system or just as an auxiliary system. In the Hamburg House of Shanghai World Expo and Tianjin Railway Station, the radiant roof cooling system combined with independent dehumidification air system were adopted [14, 16]. And in the Audience lounge of Beijing Wukesong Stadium, the radiant floor cooling system only served as an auxiliary system to help the traditional air conditioning maintain the indoor air quality [15]. Also the radiant cooling system has been adopted in some hotels and office buildings in Beijing, Tianjin, and Weifang.

11.5.2 Domestic Research Progress

In China, the studies of the radiant cooling system are mainly about numerical simulation and experimental analysis of different terminal devices in recent years.

Lu Shikui and Lv Yan used a CFD software to simulate the radiant cooling system combined with the displacement ventilation system. The results showed obvious temperature drop of interior wall temperature, improved cooling capacity of the system and a reduced vertical temperature gradient of test room [17]. Xuan Yongmei used EnergyPlus software to simulate the same type of radiant cooling system, and made a comparison with the experimental data with the maximum error was less than ±7 %. He found if the supply air temperature of the displacement ventilation system increases 1 °C, the radiation heat transfer of the floor will increase 1.9 % [18]. Yan Zhenhua analyzed the performance of a new type of the terminal devices for radiant cooling system—the capillary tube. He indicated that the capillary tube can be combined with evaporative cooling technique in northwest China [19].

Gao Zhihong studied the independent temperature and humidity control system combined with the capillary tube. The results showed that the cooling capacity of exposed capillary tube was twice greater than the capillary tube combined with metal plate. The capacity of this combination system would be increased by 20 ~ 30 % if the indoor air temperature changed from 26 °C into 28 °C [20]. Gao Zhihong et al. analyzed the existing calculation method of radiant heat transfer, and indicated to use the equivalent indoor air radiation temperature as the calculating parameter [21]. Zhang Lun et al. put forward a simplified method to calculate the radiation heat transfer of a floor and the temperature distribution of a building envelope surface [22].

K. F. Fong et al. put forward a solar hybrid system that can be used in hot and humid climate. This hybrid system used solar energy as the driving force of the absorption chiller and the desiccant wheel. The author concluded that the annual primary energy consumption of this solar hybrid cooling system was lower up to 36.5 % than that of the conventional vapor compression refrigeration system [23].

11.5.3 Foreign Research Progress

Michele De Carli concluded that the solar radiation influenced the efficiency of radiant cooling system. By simulation, a simplified model that considered solar radiation as uniformly distributed in a room cannot be used for a detailed comfort analysis. And the author concluded that the most important parameter to affect the cooling capacity was the thermal conductivity of the covering layer [24].

Doosam Song and Taeyeon Kim pointed out that the condensation problem did exist where only radiant cooling system was adopted. So they control the condensation by integrating with the dehumidified ventilation. They used both

physical experiment and TRNSYS software simulation for an apartment in Korea. The results showed that this combination system not only solved the condensation problem well but also control the indoor thermal environment in a comfortable range [25].

Corina Stetiu described their study developed to estimate the energy and peak power savings potential of the radiant cooling systems in commercial buildings in the US. The results showed that a building with radiant cooling system can be operated with low risk of condensation in any US climate. A radiant cooling system can save on average 30 % of the energy consumption and 27 % of the peak power demand due to space conditioning. The savings potential depends on the climate, which is larger in retrofitted buildings than in new construction [26].

Suya Wang et al. investigated the impact of various air conditioning parameters on the exergies of chilled water used to radiant panels and a cooling coil. They used CFD to analyze the indoor airflow and thermal environments, and added models for the calculation of thermal transfer to radiant panels and a cooling coil. The result showed the impact of various air conditioning parameters on the exergies of chilled water quantitatively [27]. For example, by reducing the cooling load rate from 100 to 57 and 27 %, the exergy of chilled water reduced by 47 and 67 %, respectively.

Prapapong Vangtook and Surapong Chirarattananon reported the results of a series of whole-year simulations by using TRNSYS software on applications of radiant cooling to a room model, this room represented an actual experimental room. The author admitted the inability of radiant cooling to accept latent load. In daytime, the 10.1 °C chilled water was supplied to the cooling coil to precool the ventilation air, and the water cooled by cooling tower was used for radiant cooling; in the night, the cooling water supplied by cooling tower can be sufficient to achieve thermal comfort [28].

Simos Oxizidisa and Agis M. Papadopoulos compared the radiant and convection systems with respect to final energy consumption and thermal comfort in a test cell representing an office room. The results showed it is important that proper control of radiant cooling system to take full advantage of their features and of the appropriate evaluation of thermal comfort conditions provided by these systems [29].

11.6 Discussions

The essence of the solutions to condensation problem of radiant cooling system is to keep the temperature of the radiation surface higher than the indoor air dew point temperature, which limits the cooling capacity of the system. In turn, the limited cooling capacity limits the application of the radiant cooling system in actual projects. The higher temperature of the radiant cooling surface also reduces the radiation heat transfer per unit surface area. In practical application, whether the area of building envelops meets the area required for the radiant panel becomes an important factor to choose the radiant cooling system. The actual applications

of the radiant cooling system as an auxiliary system also indicate the limited cooling capacity. Therefore, this chapter considers that the temperature of the radiation surface does not need to be higher than the indoor air dew point temperature in order to improve the cooling capacity of the radiant cooling system. The solution to the condensation problem can be turned to focus on collecting and discharging the condensation water. This measure will not only improve the capacity of the radiant cooling system by lowering the cooling surface temperature, but also can expand the application scope of the radiant cooling system. Then the radiant cooling system will be no longer limited to the building types, building function, or climatic conditions.

11.7 Conclusions

(1) The radiant cooling system has distinct advantages compared with the conventional air conditioning system including higher thermal comfort, more choices for the cooling source, increased chiller's COP (coefficient of performance) value, increased indoor air temperature (or lowered design cooling load), and more building space spared.
(2) The studies about radiant cooling system in China are mostly still in the stage of theoretical research and numerical simulation, the amount of applications in actual projects is relatively small.
(3) In existing examples of the applications, the radiant cooling system is often adopted as an auxiliary system.
(4) It is demonstrated to be a good practise to use independent temperature and humidity control system to solve the condensation problem of the radiant cooling system.

References

1. Hu R, Niu J (2012) A review of the application of radiant cooling & heating systems in Mainland China. Energy Build 52:11–19
2. Wang Z (2004) Radiant heating and raiant cooling. Chian Machine Press, Beijing
3. Han G, Qu X (2011) An analysis of radiant cooling with displacement ventilation composite system. ChengShi Jianshe LiLun Yan Jiu 22
4. Chen L, Liao S (2010) Three approaches to the comparative study of indoor thermal environment for radiant cooling system. Build Energy Environ 29(3):53–56
5. Lu S, Zhang S (2011) Theory study on condensation problem of floor radiant cooling system. J Jiangsu Univ Sci Technol (Nat Sci Ed) 25(6):565–571
6. Shi Y, Chen Y et al (2011) Air quality of radiant cooling combined with wall-attached-jet system. HV&AC 41(2):60–63
7. Zhou G, Shi Y et al (2011) Studies of anti-condensation of the radiant cooling system with wall-attached-jet. Build Energy Environ 30(5):20–22

8. Xiao Y, Fu X (2002) Dehumidifying capability of outdoor air in cooling ceiling system application. HV&AC 32(3):15–17
9. Xia X, Zhang X et al (2008) Technology analysis and experimental research on radiant floor cooling combined with dedicated outdoor air system. J Refrig 29(4):18–23
10. He J, Shen J et al (2008) Discussion on condensation of radiant cooling system combined with DOAS. HV&AC 38(6):159–162
11. Zhang B, Song L, Wang J (2009) Experimental study on cooling ceiling air-conditioning system covered and airproofed with the film whose long wave transmittance (LWT) is high. CC&AC 3:23–26
12. Kong X, Zhang X, Lu S (2008) Research status of condensation of radiant cooling and its countermeasures. Build Energy Environ 27(1):20–23
13. Kong X, Zhang D, Zhang X (2011) Design and analysis of leading condensation radiant panel. J Jiangsu Univ Sci Technol (Nat Sci Ed) 25(5):440–446
14. Liu J, Wu Z et al (2010) Radiant ceiling system design and research for EXPO Hamburg Haus. Refrig Air-conditioning 10(3):94–97
15. Fan L, He K, Wan S (2005) Study and application of floor panel heating/cooling system in lobbies of Wukesong Gymnasium. HV&AV 35(6):87–90
16. Zou Z, Li G, Zhu J (2010) Design of air conditioning system for tianjin railway station. HV&AC 40(5):32–35
17. Lu S, Lv Y et al (2010) Numerical simulation and experiment research for radiant cooling-displacement ventilation system. Build Energy Environ 29(2):25–29
18. Xuan Y, Wang H, Huang X (2012) Simulation analysis of radiation floor with displacement ventilation air conditioning system by energyplus. Fluid Mach 40(8):65–68
19. Yan Z (2010) Discussion on combined air- conditioning system based on radiant heating and cooling with evaporative cooling. Refrigeration 114:18–23
20. Gao Z, Liu X, Jiang Y (2011) Experiment study on cooling capacity of capillary-tube radiation air-conditioner. Acta Energiae Solaris Sinica 32(2):101–106
21. Gao Z, Liu X et al (2011) Influence factors and calculation method of radiant panel cooling capacity. HV&AC 41(1):33–37
22. Zhang L, Liu X et al (2012) Simplified calculation method for the cooling capacity and surface temperature distribution of floor panel. HV&AV 42(5):41–46
23. Fong KF, Chow TT et al (2011) Solar hybrid cooling system for high-tech offices in subtropical climate—Radiant cooling by absorption refrigeration and desiccant dehumidification. Energy Convers Manage 52:2883–2894
24. De Carli M, Massimo T (2011) Effect of modelling solar radiation on the cooling performance of radiant floors. ScienceDirect 85:689–712
25. Doosam S, Taeyeon K et al (2008) Performance evaluation of a radiant floor cooling system integrated with dehumidified ventilation. ScienceDirect 28:1299–1311
26. Corina S (1999) Energy and peak power savings potential of radiant cooling systems in US commercial buildings. Energy Build 30:127–138
27. Suya W, Megumi M (2008) Evaluating the low exergy of chilled water in a radiant cooling system. Energy Build 40:1856–1865
28. Prapapong V, Surapong C (2007) Application of radiant cooling as a passive cooling option in hot humid climate. ScienceDirect 42:543–556
29. Simos O, Agis MP (2013) Performance of radiant cooling surfaces with respect to energy consumption and thermal comfort. Energy Build 57:199–209

Chapter 12
Performance Analysis on Energy-Storage Heat Transfer Process

Zhen Tong, Xiaohua Liu, Lun Zhang and Yi Jiang

Abstract This paper analyses the heat storage processes in HVAC system and uses the entransy method to calculate the equivalent thermal resistance of energy-storage heat exchangers. Analogous to normal heat exchangers, unmatching coefficient has been introduced to the analysis of energy-storage heat exchanger. It also illustrates the unmatching extent's influence on thermal resistance for convection in heat absorption process and heat release process under constant temperature boundary condition and constant heat flux boundary condition, respectively. Taking the daytime-heat-absorption and nighttime-heat-release of floor as an example, the unmatching coefficients and proportions of the three parts resistance are analyzed, and the main factors restricting thermal storage performance could be obtained. The results are helpful for the design and optimization of the energy-storage heat exchange system.

Keywords Periodic heat transfer · Energy-storage heat exchanger · Heat resistance · Unmatching coefficient

12.1 Introduction

Nowadays, great importance has been attached to building energy efficiency and more and more attention has been paid to dynamic heat transfer processes. For an example, energy consumption of HVAC system can be reduced due to the effect of the heat charge and discharge characteristic of building envelope. In winter, the heat discharge reduces the heating load during night and in summer the heat charge reduces the cooling load during daytime. As another example, for the heat

Z. Tong (✉) · X. Liu · L. Zhang · Y. Jiang
Department of Building Science, Tsinghua University,
Beijing 100084, China
e-mail: tong-tong@foxmail.com

A. Li et al. (eds.), *Proceedings of the 8th International Symposium on Heating, Ventilation and Air Conditioning*, Lecture Notes in Electrical Engineering 262,
DOI: 10.1007/978-3-642-39581-9_12,

transfer process between buried pipe and soil of the ground source heat pump, heat is absorbed by the soil in summer and released to the fluid in pipe in winter. To make better use of the heat storage processes in HVAC system to reduce energy consumption, further analysis and studies on energy-storage heat transfer process are needed.

Yin et al. [1] proposed the nonlinear coupling model for night ventilation and building heat storage, and prove the reliability of the model combined with experiment. Zhang et al. [2] conducted a field test for a U-type vertical buried pipe heat exchanger and analyzed its heat transfer performance. Wang et al. [3] studied the impact of internal thermal mass on maximum indoor temperature, available start-up time and time of ventilation for passive cooling ventilation building with the ideal model. Qiu et al. [4] conducted numerical simulation of the energy-storage process in building structure with PCM, and investigated the effects of PCM modules arrangement in building structure on temperature distribution, heating conduction, energy storage, and discharge time and PCM efficiency. Zhang et al. [5] proposed analysis method of the heat resistance for periodic heat transfer process, and analyzed the restriction factors of heat storage performance according to the proportion of the three parts resistance in the whole heat transfer process. At present, related work focusing on the heat storage performance and its influencing factors is mainly by means of experiment, software simulation, numerical simulation, and heat transfer theory model. Many conclusions are derived from phenomena and using effects. In this paper, entransy method is utilized to further analyze the energy-storage heat transfer processes, and major factors restricting heat storage performance are discussed.

12.2 Energy-Storage Heat Exchanger

Lots of periodic heat charge and discharge processes in HVAC system, including those in the floor or building envelope with phase change materials, night ventilation, and buried pipe ground source heat pump, can be taken as nonsimultaneous heat transfer process between equivalent heat source and cold source. And the media such as floor, building envelope, and soil play the role of heat storage and indirect heat transfer. The period can be 1 day or 1 year.

Figure 12.1 shows the heat transfer process in one period. P_1 is the heat charge period of time, when the temperature of fluid is higher than that of medium surface. The temperature of medium increased because of heat absorption. P_2 is the heat discharge period of time, when the temperature of fluid is lower than that of medium surface. The temperature of medium decreased because of heat release. Due to the thermal inertia of medium, the curve of medium surface temperature has the same period and delayed phase compared with that of fluid temperature.

For further analysis, the heat transfer process in one period is divided into three sub-processes, i.e., the heat absorption process from hot fluid to media surface, the heat release process from media surface to cold fluid, and heat conduction process

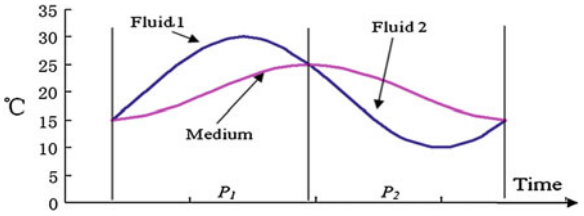

Fig. 12.1 Heat convection between fluid and medium

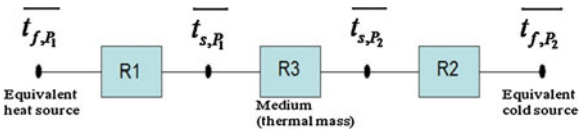

Fig. 12.2 Equivalent channel for heat transfer between the fluid and medium

within the medium. Each process corresponds to the certain temperature difference and thermal resistance, which is illustrated by Fig. 12.2.

$\overline{t_{f,P_1}}$, $\overline{t_{s,P_1}}$, $\overline{t_{f,P_2}}$ and $\overline{t_{s,P_2}}$ are the mean temperatures of fluid and medium surface in P_1 and P_2 period, respectively. And R_1, R_2, R_3 are the thermal resistances for heat absorption process from hot fluid to medium surface, heat conduction process within the medium, and heat release process from medium surface to cold fluid, respectively. The total resistance for the whole process is as follows:

$$R_{ex} = R_1 + R_2 + R_3 \tag{12.2.1}$$

According to the proportion of the thermal resistance for each process, it can be known that which part of resistance is the main influencing factor for the heat transfer process, the resistance for convection between the fluid and medium or the resistance for conduction within the medium.

The essence of the periodic heat transfer process mentioned above is energy-storage heat exchanger, that is, a nonsimultaneous heat transfer process between equivalent heat source $\overline{t_{f,P_1}}$ and cold source $\overline{t_{f,P_2}}$, and the medium plays the role of heat storage and indirect heat transfer. The heat transfer amount depends on the temperature difference between equivalent heat source and cold source and the thermal resistance for each sub-process.

12.3 Performance of Heat Exchanger

12.3.1 Normal Heat Exchanger

Taking a counterflow water–water sensible heat exchanger for an example, the heat transfer process is described by a T-Q diagram, see Fig. 12.3. The shading area in the diagram represents the entransy dissipation ΔJ [6] of the heat transfer process. Averaged according to the heat flux, the mean temperature difference for the heat transfer process can be obtained as follows:

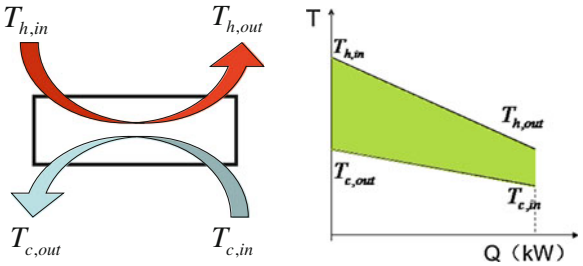

Fig. 12.3 Schematic diagram for heat transfer process of normal heat exchanger

$$\Delta T_s = \frac{\int \Delta T \cdot dQ}{Q} = \frac{\Delta J}{Q} \tag{12.3.1}$$

Hence, the equivalent thermal resistance can be defined as the ratio of the entransy dissipation to the square of the heat flux:

$$R = \frac{\Delta T_s}{Q} = \frac{\Delta J}{Q^2} \tag{12.3.2}$$

Entransy describes the heat transfer ability. Therefore, the smaller the equivalent thermal resistance R of heat exchanger, the less the loss of heat transfer ability between hot and cold fluid per unit quantity of heat transfer, and the better the performance.

When the heat capacity of the two fluids are the same ($cm_h = cm_c$), the thermal resistance is expressed as $R_0 = 1/KF$, where K and F represent the heat transfer coefficient and area of the heat exchanger, respectively. When the heat capacity of the two fluids are different, unmatching coefficient ξ is introduced, which can be expressed as $\xi = R/R_0$. The value of ξ means the equivalent thermal resistance will enlarge to ξ times at the same heat transfer ability. ξ is a number greater than 1. If and only if the heat capacities are the same, the two flows are matched and the unmatching coefficient ξ is minimum, equals to 1. The larger ξ, the bigger the unmatching extent. So the equivalent thermal resistance for the heat transfer process can be expressed as:

$$R = \frac{\xi}{KF} \tag{12.3.3}$$

Figure 12.4 helps to make a better understanding of the unmatching coefficient ξ. It can be seen that worse matching situation of heat capacity makes higher unmatching coefficient, and under larger area the effect of unmatching coefficient will be more apparent.

For normal heat exchanger, the thermal resistance is related to the heat transfer coefficient KF and the unmatching extent of the two fluids. Prior approach of optimization for the heat exchanger can be found out from the perspective of unmatching coefficient. If $\xi \to 1$, which means that the heat capacity of the two fluids are the same and the area of heat exchanger is of uniform distribution, the

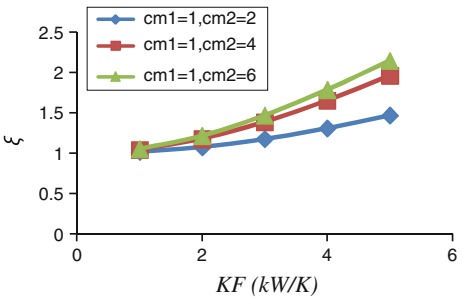

Fig. 12.4 Unmatching coefficient ξ as a function of KF

performance of heat exchanger is mainly restricted by the area, so the resistance of heat exchanger should be reduced by enlarging the area of heat exchanger. While if ξ is very large, which means that the area of heat exchanger is of nonuniform distribution, the resistance of heat exchanger should be reduced by improving the matching situation.

12.3.2 Constant Temperature Boundary

It would be better if the unmatching coefficient can also be used to analyze the performance of energy-storage heat exchanger. First of all, periodic heat transfer process for a one-dimensional plate under constant temperature boundary condition (Fig. 12.5) is investigated. The air temperatures in heat charge and discharge stage are both constant.

Analogous to normal heat exchangers, the heat transfer process for energy-storage heat exchanger can also be described by a T-Q diagram, see Fig. 12.6.

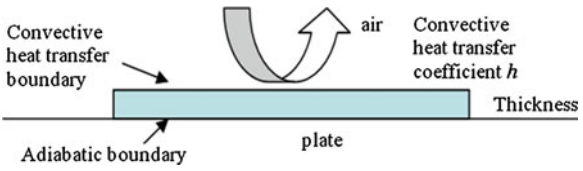

Fig. 12.5 One-dimensional heat transfer model

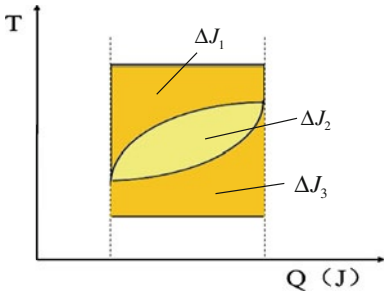

Fig. 12.6 T-Q diagram for heat transfer process under constant temperature boundary

The periodic heat transfer process is equivalent to a heat transfer process between two constant temperature sources and varied-temperature fluid. The entransy dissipation for heat absorption process from hot fluid to medium surface, heat conduction process within the medium, and heat release process from medium surface to cold fluid can be seen from the shading area in the diagram, and they are $\Delta J_1 \Delta J_2$ and ΔJ_3, respectively.

For normal plate (or nonhomogeneous temperature plate), due to the internal thermal resistance for conduction, the heat flux and temperature vary along the thickness direction. Therefore, the whole thermal resistance includes the resistance for convection in heat charge and discharge processes and also the resistance for heat conduction within the plate. With the unmatching coefficient ξ introduced, the whole resistance can be expressed as follows:

$$R = \frac{\xi_1}{K_1 A P_1} + \frac{\xi_2}{K_2 A P_2} + R_3 \tag{12.3.4}$$

where K_1 and K_2 are the heat transfer coefficients in heat charge and discharge processes and A is the surface area of plate. The former two items on the right side of the equation are thermal resistance for convection in heat charge and discharge processes, respectively, which are equal. (The convective heat transfer coefficients and heat transfer areas in these two processes are presumed to be same.) For nonhomogeneous temperature plate, ξ is relevant to thermal conductivity λ, heat capacity cm and the convective heat transfer coefficient h.

When the thermal conductivity of heat storage plate is so large that $Bi = h\delta/\lambda < 0.1$, the internal resistance for conduction can be ignored. The plate can be taken as the homogeneous temperature plate, for which the internal resistance for conduction is zero ($R_3 = 0$) and the resistance for convection in heat charge and discharge processes are $R_1 = R_2 = \frac{\xi}{KA}$. The unmatching coefficient of homogeneous temperature plate is only relevant to cm and h.

The temperatures of the air during heat charge and discharge processes are constant, which means that the heat capacity of air is infinite. So, when the thermal mass is PCM, the heat capacities of air and medium are the same ($cm_{\text{air}} = cm_{\text{plate}} \to \infty$). For phase change plate, $R_3 = 0$, $\xi = 1$ and $R_1 = R_2 = \frac{1}{KA}$.

Taking the heat capacity matching situation into consideration, phase change plate is superior, and this is why research on adding PCM into thermal mass is prevalent. However, if the unmatching coefficient is already very low, there is probably no much space for improvement when adding PCM.

12.3.3 Constant Heat Flux Boundary

For thermal mass with fixed physical property parameters and surface area, the variation trend of fluid temperature will affect the equivalent thermal resistance of the heat transfer process. For example, the equivalent resistances are different

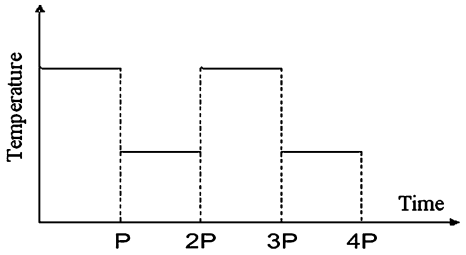

Fig. 12.7 Square wave

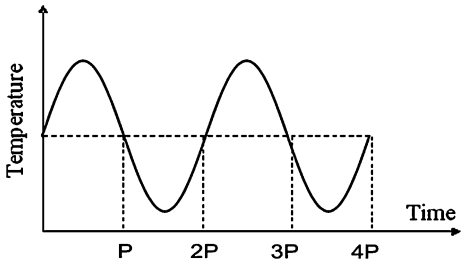

Fig. 12.8 Sine wave

under square wave (Fig. 12.7) and sine wave (Fig. 12.8) air temperature conditions, and the fundamental cause of which is the different matching extents of the heat capacities.

As is mentioned above, under constant temperature boundary condition, the heat capacities are the same when the thermal mass is PCM. Besides, if the plate is nonhomogeneous temperature plate, the heat capacities can be same under constant heat flux boundary condition, and now the temperature difference between fluid and plate surface is constant (Fig. 12.9). Compared to the constant temperature boundary, because of the same heat capacities the thermal resistances for convection in heat charge and discharge processes decrease from $\frac{\xi}{KA}$ to $\frac{1}{KA}$. Consequently the total resistance is reduced, which means that same heat transfer amount can be realized on smaller temperature difference $(\overline{t_{f,P_1}} - \overline{t_{f,P_2}})$.

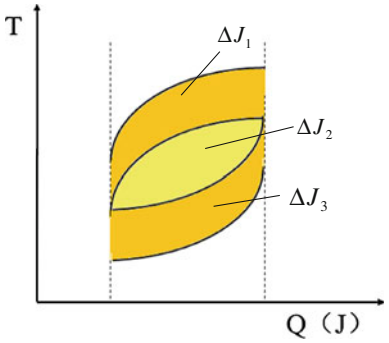

Fig. 12.9 T-Q diagram for heat transfer process under constant heat flux boundary

Table 12.1 Basic parameters and boundary conditions

Period 2P (h)	Heat transfer amount (kJ)	λ (W/m °C)	ρ (kg/m^3)	h (W/m^2/ °C)	c_p (J/kg/ °C)	δ (m)
24	864	1	1000	8	1000	0.2

The one-dimensional plate periodic heat transfer model is still considered, and its parameters are set in Table 12.1. Under the same 864 kJ heat transfer amount, 8.2 and 7.1 °C temperature difference is required for constant temperature boundary and constant heat flux boundary, respectively. Thus, it can be seen that the performance of energy-storage heat exchangers will be better if the matching situation of heat capacities in heat charge and discharge processes is improved.

There are many parameters that influence the thermal resistance of energy-storage heat exchangers. For nonhomogeneous temperature plate, all the three parts of resistance are relevant to h, λ, c_p and ρ [7], and the parameters have different extent of impact on the performance of heat transfer. Here, introducing the unmatching coefficient based on the concept of entransy help to better analyze each parameter that influence the performance of energy-storage heat exchangers. Combining with the proportion of each part of resistance, effective measures can be taken specifically to improve the performance.

12.4 Case Study

Energy-storage floor's heat charge during daytime and discharge during night can be taken as a daily periodic heat transfer process. According to the physical property parameters of some common materials, total resistance per unit area and proportion of each part of resistance are calculated (Table 12.2). Where, h is 8 W/(m^2 °C); time for heat charge and discharge are both 12 h; the thickness of plate is 0.2 m; and the temperatures of hot air and cold air are 28 and 18 °C, respectively (under constant temperature boundary), that is the temperature difference is 10 °C.

In the same conditions, granite has the lowest resistance and wood has the highest resistance of these materials. From the proportion of each part of resistance, it can be seen that for marble and granite the resistance for convection in heat charge and discharge processes is the main component and the resistance for conduction is very little, while for wood the resistance for conduction is very considerable.

The unmatching coefficients are also given in the table. ξ is the unmatching coefficient of the real materials with nonhomogeneous temperature. ξ_0 is the unmatching coefficient eliminating the effect of λ, when $\lambda \to \infty$and other parameters are remain the same.

When h and A is fixed, the unmatching coefficient ξ_0 of homogeneous temperature plate is just relevant to c_p and ρ. The larger ξ_0 is, the worse the matching situation is, and the greater effect the heat capacity has on heat charge

Table 12.2 Physical property parameters and analysis result

	Physical property parameters			Total resistance	Proportion of each part of resistance %			Unmatching coefficient	
	$\rho/(kg/m^3)$	$\lambda/(W/(m\cdot^\circ C))$	$c_p/(J/(kg\cdot^\circ C))$	$R/(10^{-6}\ ^\circ C/J)$	Heat charge	Heat conduction	Heat discharge	ξ	ξ_0
Marble	2500	2.7	924	7.02	43.1	13.8	43.1	1.046	1.047
Granite	820	3.1	2800	6.9	43.8	12.4	43.8	1.044	1.046
Reinforced concrete	2400	1.54	840	7.75	39.8	20.4	39.8	1.066	1.060
Cement mortar	1800	0.93	840	8.99	35.9	28.2	35.9	1.115	1.107
Wood	746	0.14	2431	14.26	28.9	42.2	28.9	1.424	1.075

and discharge performance. For example, ξ_0 of cement mortar is relatively large, so for the floor made of cement mortar adding PCM into the floor and increasing the heat capacity is effective to improve the matching situation and increase the heat transfer amount. As the result of calculation, increasing the heat capacity to 2000 J/(kg· °C) by adding PCM into the cement mortar can enlarge the heat transfer amount by 14 %. While for marble with low ξ_0, when the heat capacity is increased to 2500 J/(kg· °C) by adding PCM into it, the heat transfer amount is only enlarged by 6 %, which means that adding PCM into marble cannot improve the performance of marble floor dramatically. In this sense, not all of the materials can benefit from the PCM adding. Especially, because of the low thermal conductivity of PCM, if adding PCM blindly without analyzing the heat transfer process of energy-storage floor, the loss will outweighs the gain.

From Table 12.2 it can also be seen that ξ of wood reach up to 1.424, and ξ_0 is much lower than ξ for the effect of thermal conductivity is eliminated. By comparing ξ with ξ_0, the thermal conductivity is found the leading influencing factor among all the factors. The low thermal conductivity heavily restricts the heat storage performance of the wood floor by affecting the matching situation. Besides, among the three parts of resistance, the resistance for conduction is very considerable, which means that the thermal conductivity's great effect on performance is also embodied in heat conduction process.

12.5 Conclusion

Analogous to normal heat exchangers, unmatching coefficient has been introduced to the analysis of energy-storage heat exchanger. Entransy method has been used to investigate the heat transfer process of energy-storage system and analyze the influencing factors. Conclusions obtained are as follows:

(1) The concept of unmatching coefficient in normal heat exchangers can also be used in energy-storage heat exchangers. The resistances for convection in heat charge and discharge processes are relevant to the matching extent of heat capacity. So, improving the matching situation can reduce the equivalent thermal resistance and improving the performance.
(2) For nonhomogeneous temperature plate, the matching extents of heat capacities are different under constant temperature and constant heat flux boundaries. Under constant heat flux boundary, the temperature difference required is smaller and the performance is better for fixed heat transfer amount due to the same heat capacities.
(3) In the daily periodic heat transfer process of floors made of different materials, the unmatching coefficient ξ_0 of cement mortar is the largest of all, which means that adding PCM and increasing the heat capacity is of the greatest effect for cement mortar to reduce the resistance for convection. While for the materials with low ξ_0, such as marble, there is no obvious effect when adding

PCM. In the three parts of resistance of wood, the resistance for conduction is considerable, and at the same time the difference between ξ_0 and ξ of wood is large, which means that the thermal conductivity is the main factor restricting the performance of wood having great effect on the resistance both for conduction and convection.

References

1. Yin W, Qin X, Peng J et al (2006) Nonlinear coupling between night ventilation and thermal mass [J]. Building Energy Environ 25(3):81–82
2. Zhang Y, Li B, Chen J et al (2007) Test and analysis on heat exchanging performance for vertical U-shaped ground heat exchangers [J]. HV&AC 37(7):72–78
3. Wang Z, Zhang G, Wang M et al (2008) Impact of internal thermal mass on maximum indoor temperature and energy consumption [J]. Refrig Air-Conditioning 8(5):86–91
4. Qiu L, Liu X (2009) Research on energy storage of building structure with phase change material [J]. J Building Mater 12(5):621–624
5. Zhang H, Liu X, Jiang Y (2011) Performance analysis of periodic heat transfer process of energy-storage heat exchangers [J]. HV&AC 41(3):44–50
6. Guo Z, Zhu H, Liang X (2007) Entransy—A physical quantity describing heat transfer ability[J]. Int J Heat Mass Transf 50:2545–2556
7. Zhang H (2011). Optimization analysis for heat exchange network in the building heat environment control [D]. Beijing, 2011:1–131

Chapter 13
Analysis and Optimization on Solar Energy Chemical Heat Storage Material

Qiuhui Yan, Xuedong Zhang and Li Zhang

Abstract Conditions and screening criteria of chemical heat storage material are introduced in the paper. Hydroxide is chosen as the research object. The thermodynamic parameters of the material have been calculated using HSC chemistry software. The main parameters are steering temperature and equilibrium constant. The results show that steering temperature of calcium hydroxide is 798 K, and its enthalpy difference is 100 kJ/mol. In the vicinity of this temperature, Gibbs free energy changes from the positive to the negative, indicating that above this temperature, the reaction can be spontaneous. Calcium hydroxide is a kind of ideal heat storage material as a large-scale storage of solar energy.

Keywords Chemical heat storage · Material · Solar energy · HSC chemistry

13.1 Introduction

Heat storage technology is of vital importance in improving the efficiency of energy and protecting environment, which can help to balance the supply and demand of heat energy. It is expected that the heat storage technology can be used in shifting load of electricity, utilization of solar energy, recollection of unused heat, saving energy for heating and air-conditioning for industrial and residential buildings [1]. With heat storage technology, we store extra heat with certain method and use it later when it is needed. As the key factor in developing and applying of the heat storage technology, materials used for heat storage have become the hot topic in the research. The chemical reaction heat storage material is one of the materials which have a promising future. Heat storage materials are

Q. Yan (✉) · X. Zhang · L. Zhang
School of Environmental and Municipal Engineering, Xi'an University of Architecture & Technology, Xi'an, China
e-mail: yanqiuhui@xauat.edu.com

A. Li et al. (eds.), *Proceedings of the 8th International Symposium on Heating, Ventilation and Air Conditioning*, Lecture Notes in Electrical Engineering 262,
DOI: 10.1007/978-3-642-39581-9_13,

Table 13.1 Comparison of three thermal storage materials

Characteristics	Sensible heat	Latent heat	Chemical heat
Storage heat capacity	Less	Little	Large
Recovery characteristics	Variable temperature	Fixed temperature	Variable temperature
Heat insulation measures	Yes	Yes	No
Energy loss	Large (long-term storage)	Considerable (long-term storage)	Little
Working temperature	Low	Low	High
Traffic condition	Short-distance	Short-distance	Long-distance

the core of heat storage technology [2]. There are three kinds of heat storage materials, sensible heat regenerative materials, latent heat storage materials, and chemical reaction heat storage materials, as the graph shown in Table 13.1.

13.2 Chemical Reaction Heat Storage Material

Chemical reaction heat storage is an efficiency method with high energy density. It stores heat through transformation between heat and chemical heat in reversible chemical reactions. According to the principle of chemical reaction heat storage, this kind of materials can store much higher density energy than other kinds of materials, because of the higher reaction heat. This advantage makes chemical reaction heat storage low cost. The main point does not only refer to the large heat storage, but also heat can be stored for a long period if the reaction process can be controlled by catalyst or the reactants. Nowadays, four reactants such as crystalline hydrate, hydroxide, metal hydride, and amide have already been arisen people's attention.

13.2.1 Crystalline Hydrate

When the temperature of material is lower than its melting point, crystalline hydrate will wholly or partially strip its water of crystallization. Hydration heat will be absorbed and stored during the dewatering process. While we need to recover heat, it could come into contact with the water and dehydrated salt. For example:

$$Na_2S \cdot nH_2O(s) + \Delta H \leftrightarrow Na_2S(s) + nH_2O(g) \qquad (13.2.1)$$

When forward reaction occurs, heat is absorbed and $Na_2S{\cdot}nH_2O(s)$ is converted into $Na_2S(s)$ and vapors, as a result, heat is stored. During the process, the heat is reserved. When the temperature decreases, $Na_2S(s)$ adsorbs vapors and transforms

into $Na_2S{\cdot}nH_2O(s)$. Then, reverse reaction occurs and the reserved heat is released. Under many circumstances, such hydration heat could be much higher than dissolution heat.

13.2.2 Inorganic Hydroxides

Inorganic hydroxide stores and releases the heat by hydration/dehydration reactions [3]. Dehydration enthalpy and dehydration heat capacity of inorganic hydroxide are displayed in Table 13.2.

13.2.3 Metal Hydride

Heat storage principle of metal hydride is to make some of the metal or alloy have the ability to absorb hydrogen. Metal or alloy would react with hydrogen under appropriate temperature and pressure. The metal hydrides can be obtained through this process. At the same time, reaction could release a large amount of heat. Conversely, metal hydride may lead endothermic reaction and release storage hydrogen in the case of being heated and reducing pressure.

$$MH_n + \Delta H \leftrightarrow M + \frac{1}{2}H_2 \tag{13.2.2}$$

Due to the advantages of high energy density, clean and pollution-free, hydrogen storage materials has great application prospects in chemical heat pumps, thermal storage, refrigeration, and solar energy utilization [4].

13.2.4 Amide

Reversible decomposition combination reaction of amide,

$$2NH_3 + \Delta H \leftrightarrow 3H_2 + N_2 \tag{13.2.3}$$

Table 13.2 Dehydration enthalpy and dehydration temperature of hydroxide

Inorganic hydroxides	Dehydration enthalpy $\Delta H/(\mathrm{kJ \cdot mol^{-1}})$	Dehydration temperature $Cp/(\mathrm{kg \cdot K^{-1}})$
LiOH	132.8	2760
$Be(OH)_2$	54.3	3567
$Mg(OH)_2$	116.2	1400
$Ca(OH)_2$	108.1	1459
$Sr(OH)_2$	135.2	1111
$Ba(OH)_2$	154.2	899

The thermal reaction has a high speed when there is catalyst, the temperature is high and it is far away from equilibrium [5]. Now, some countries have used the reaction as experimental study of solar thermal storage power generation. The ammonia system has many advantages as follows. First, ammonia industry has developed perfectly. Second, the catalyst is cheap and easily available. Finally systems are relatively simple and with high energy storage density. However, during the reversible reaction of ammonia used to produce gas, which must be considered is that the leak proofness of the storage containers and systems and some problems such as corrosion.

13.3 Screening Criteria

According to the characteristics and the applicable conditions of the chemical reaction storage, this paper summarizes and formulates screening criteria of heat storage material of chemical reaction as below. (1) Inversion temperature of chemical heat storage is suitable, (2) reaction heat is large, (3) high energy storage density, (4) appropriate reversible reaction rate, (5) nontoxic, noncorrosive, nonflammable, nonexplosive, (6) a small change in the volume of the material in the reaction, and (7) economic.

13.3.1 Inversion Temperature

While changing the reaction temperature in the same sign of ΔH and ΔS, the reaction changes from spontaneous to non-spontaneous (or from nonspontaneous to spontaneous). The inversion temperature will be defined. The inversion temperature is the most important screening criteria in the thermodynamic analysis of the chemical heat storage. Reaction conditions cannot be realized if the reaction temperature is too high or too low. Thermal decomposition reaction equilibrium which is applicable to the chemical heat storage is based on the generic reaction.

$$\mathrm{AB(l)} \leftrightarrow \mathrm{A(l)} + \mathrm{B(g)} \tag{13.3.1}$$

According to the second law of thermodynamics, the variation of standard free energy of a reaction is shown below,

$$\Delta G = \Delta H - T\Delta S \tag{13.3.2}$$

the relationship between the equilibrium constants with ΔG,

$$\Delta G = RT \ln K \tag{13.3.3}$$

unite Eqs. (13.3.2) and (13.3.3),

$$T = \Delta H / (\Delta S - R \ln K) \tag{13.3.4}$$

in which $\Delta Cp = 0$. and $K = 1$

$$T = \Delta H/\Delta S \ (\Delta Cp = 0, K = 1) \tag{13.3.5}$$

The temperature is referred as ‘‘inversion temperature”, which is the boundary temperature of the positive and adverse reaction. Temperature higher than inversion temperature promotes the reaction, and vice versa. Inversion temperature is an important criterion to screen chemical heat storage system. For the rational utilization of solar energy, heat storage of endothermic reaction occurs in the temperature of 1273 K or higher. It is easy to achieve the temperature for focused collector and solar tower center receiving apparatus, $773 < T < 1273$ K is ideal.

13.3.2 Reaction Heat

A chemical reaction occurs under the condition of constant pressure as well as nonexpansion work, when the product's temperature goes back to the starting temperature of the reactants [6]. Then the system emits or absorbs the heat which is defined as the heat of reaction. Chemical reaction heat is an important thermodynamics data. Calculation formula for reaction heat is:

$$Q_p = \Delta U + p\Delta V = \Delta U + RT\Sigma vB(g) \tag{13.3.6}$$

In the equation, $\Delta U \equiv U_{\text{Final}} - U_{\text{Initial}} \equiv U_{\text{Product}} - U_{\text{Reagent}}$ and $\Sigma vB(g) = \Delta n(g)/\text{mol}$, which equals the difference between the total amounts of gas molecules of the reagent and the product when 1 mol reaction happens. Whether the isobaric heating effect is equal to the isometric heating effect depends on whether the total amount of gas molecules changes, see Eq. (13.3.6).

13.4 Calculation and Analysis of the Thermodynamic Parameters

13.4.1 Theoretical Basis of the Thermodynamic Parameters

If there are differences between the heat capacity of products and reactants in a chemical reaction, ΔH and ΔG is related to the temperature. While Cp is expressed as $Cp = a + bT + C'T^{-2}$, ΔH_T can be expressed as

$$\Delta H_T = \Delta H_{T_s} + \Delta aT + \frac{\Delta b}{2}T^2 - \Delta C'T^{-1} \tag{13.4.1}$$

The Gibbs–Helmholtz formula is,

$$\left[\frac{\partial}{\partial T}\left(\frac{\Delta G}{T}\right)_p\right] = -\frac{\Delta H}{T^2} \tag{13.4.2}$$

we take (13.4.1) into (13.4.2), the relationship between ΔG_T and temperature can be obtained after the transformation.

$$\Delta G_T = \Delta H_{T_0} + CT + \Delta aT \ln T - \frac{1}{2}\Delta BT^2 - \frac{1}{2}C'T^{-1} \tag{13.4.3}$$

$$\Delta S_T = (\Delta H_{T_0} - \Delta G_T)/T \tag{13.4.4}$$

$$T^* = \Delta H_{298}/\Delta S_{298} \tag{13.4.5}$$

$$K = e^{-\Delta G_T/RT} \tag{13.4.6}$$

The thermodynamic parameters of the thermal decomposition reaction can be calculated by using above relationships.

13.4.2 Use HSC Chemistry to Calculate Thermodynamic Parameters

According to the above screening indicators, it can be calculated and analyzed for hydroxide. The main heat storage reaction equation is given by Eqs. (13.4.7)–(13.4.10)

$$Mg(OH)_2(s) \leftrightarrow MgO(s) + H_2O(g) \tag{13.4.7}$$

$$Ca(OH)_2(s) \leftrightarrow CaO(s) + H_2O(g) \tag{13.4.8}$$

$$Sr(OH)_2(s) \leftrightarrow SrO(s) + H_2O(g) \tag{13.4.9}$$

$$Ba(OH)_2(s) \leftrightarrow BaO(s) + H_2O(g) \tag{13.4.10}$$

The thermodynamic parameters with different temperature calculated by HSC chemistry software, and the results are shown in Tables 13.3, 13.4, 13.5, 13.6.

While the temperature is over the inversing temperature, the Gibbs free energy of the heat storage reaction changes from positive to negative. Thermal decomposition reaction can be carried out spontaneously. So the higher the temperature is, the more complete the reaction is. It can be approximately calculated by $T = \Delta H/\Delta S$, and the calculated results are 760 K($Ca(OH)_2$), 982 K($Ba(OH)_2$), 1009 K($Sr(OH)_2$), and 532 K($Mg(OH)_2$), respectively. There is a good agreement between the above results and the results calculated by the software, therefore this formula can be used as standard. The inversion temperature increases according to

Table 13.3 $Mg(OH)_2$ decomposition reaction thermodynamic parameters changes with temperature

Temperature (K)	ΔH (kcal/mol)	ΔS (cal/Ka)	ΔG (kcal)	K
298	19.417	36.484	8.544	5.409E − 007
373	19.238	35.955	5.826	3.854E − 004
473	18.868	35.082	2.274	8.894E − 002
573	18.419	24.222	−1.191	2.845E + 000
673	17.925	22.428	−4.572	3.055E + 001
773	17.402	32.704	−7.878	1.689E + 002
873	16.860	32.045	−11.115	6.066E + 002
973	16.303	31.441	−14.289	1.621E + 003
1073	15.736	30.887	−17.405	3.511E + 003
1173	15.160	30.374	−20.468	6.514E + 003
1273	14.577	29.896	−23.481	1.075E + 004

Table 13.4 $Ca(OH)_2$ decomposition reaction thermodynamic parameters changes with temperature

Temperature (K)	ΔH (kcal/mol)	ΔS (cal/Ka)	ΔG (kcal)	K
298	26.089	34.306	15.866	2.309E − 012
373	25.858	33.617	13.319	1.569E − 008
473	25.492	32.752	10.001	2.392E − 005
573	25.064	31.932	6.767	2.623E − 003
673	24.576	31.148	3.613	6.708E − 002
773	24.030	30.394	0.536	7.053E − 001
873	23.431	29.665	−2.467	4.145E + 000
973	22.780	28.960	−5.398	1.631E + 001
1073	14.791	21.158	−7.912	4.089E + 001
1173	13.291	19.911	−9.964	7.188E + 001
1273	12.030	18.797	−11.898	1.104E + 002

the order $Mg(OH)_2 \rightarrow Ca(OH)_2 \rightarrow Ba(OH)_2 \rightarrow Sr(OH)_2$. Inversion temperature of magnesium hydroxide is too low, according to one of the screening index. It cannot take advantage of the medium temperature heat offered by the reversible exothermic reaction. Inversion temperatures of the other three metal hydroxides are within a standard temperature range. That would cause difficulties for the solar collector and the thermal decomposition reactor, because inversion temperature of barium hydroxide is too high. The strontium is so expensive that can't be widely used. Among these materials, only calcium hydroxide has the best inversion temperature, for its low price and rich source. It is appropriate for a large number of applications. Decomposition products can be long-term storage in the form of solid or liquid at ordinary temperature. Therefore, calcium hydroxide is a kind of ideal heat storage material as a large-scale storage of solar energy.

Table 13.5 $Sr(OH)_2$ decomposition reaction thermodynamic parameters changes with temperature

Temperature (K)	ΔH (kcal/mol)	ΔS (cal/Ka)	ΔG (kcal)	K
298	32.520	32.215	22.025	7.005E − 017
373	32.526	35.242	19.381	4.399E − 012
473	32.322	34.770	15.876	4.611E − 008
573	31.861	33.893	12.440	1.798E − 005
673	31.133	32.728	9.107	1.102E − 003
773	30.133	31.347	5.902	2.144E − 002
873	23.565	23.057	3.437	1.379E − 001
973	22.013	21.372	1.217	5.328E − 001
1073	20.495	19.887	−0.844	1.486E + 000
1173	19.009	18.563	−2.765	3.276E + 000
1273	17.555	17.373	−4.561	6.069E + 000

Table 13.6 $Ba(OH)_2$ decomposition reaction thermodynamic parameters changes with temperature

Temperature (K)	ΔH (kcal/mol)	ΔS (cal/Ka)	ΔG (kcal)	K
298	36.036	36.701	25.099	3.899E − 019
373	35.805	36.020	24.956	7.792E − 014
473	35.226	34.659	17.557	1.985E − 009
573	33.505	31.355	14.300	1.183E − 006
673	32.637	29.958	11.187	8.880E − 005
773	27.672	22.764	8.076	1.416E − 003
873	26.540	21.386	5.870	1.071E − 002
973	25.443	20.197	2.408	4.999E − 002
1073	24.385	19.161	−0.252	1.662E − 001
1173	23.366	18.253	−2.755	4.321E − 001
1273	22.387	17.452	−5.699	9.345E − 001

13.5 Conclusions

Based on the previous research about chemical reaction heat storage, this paper puts forward the optimization in chemical reaction heat storage, according to the characteristics and working conditions of heat storage chemical reaction. In the results of calculation, four hydroxides, $Mg(OH)_2$, $Ca(OH)_2$, $Ba(OH)_2$, $Sr(OH)_2$ are displayed in the increasing order of temperature for transformation. According to the available temperature of concentrating collectors or tower solar energy central receivers ($773 < T < 1273$ K), $Ca(OH)_2$ is the most suitable heat storage materials for high temperature solar energy. This research provides reference for research of solar energy heat storage system home and abroad and also provides more choices for application of solar energy heat storage materials.

Acknowledgments This work was financially supported by the State Key Development Program for Basic Research of China through contract No.2009CB220000 and open fund of State Key Laboratory of Multiphase Flow in Power Engineering and Department of Education project of Shaanxi Province through contract NO. 12JK0788.

References

1. He Y, Zhang H, Shuchun Yan J (1994) Research progress of thermal energy storage material. Mod Chem Ind 8:8–12
2. Guy Ervin J (1977) Solar heat storage using chemical reactions. J Solid State Chem 22:51–61
3. Schaube F, Koch L, Worner AJ, (2012 Article in press) A thermodynamic and kinetic study of the de- and rehydration of $Ca(OH)_2$ at high H_2O partial pressures for thermo-chemical heat storage. Thermochimica Acta 20:9–20
4. Li A, Zhang R, Xiaoxia Zhou J (2002) Development and application of chemical energy storage materials. J Guangdong Univ Technol 3:81–84
5. Lovegrove K, Luzzi AJ (1996) Endothermic reactors for an ammonia based thermochemical solar energy storage and transport system. Sol Energy 56:361–371
6. Wang M, Zhao XM (2008) Physical chemistry. Chemical Industry Press, Beijing

Chapter 14
CO_2 Heat Pump Water Heater: System Design and Experimental Study

Yefeng Liu, Zhiyang Zhuo, Feng Zhang and Tuanwei Bao

Abstract A performance testing experiment platform of heat pump water heater of CO_2 trans-critical cycle whose evaporator and gas cooler are both sleeve type heat exchanger has been designed and then constructed. CO_2 refrigerant charge amount of the system is 1.23 kg. System performance has been researched by adjusting the degree of opening of the expansion valve and controlling the flow of water of the gas cooler. The results show that: The system can provide hot water of 65 degrees when its cop is 3.2. And hot water of above 80 degrees can be obtained when system's cop is above 2.0. The water flow of the gas cooler has the greatest impact on the cop of the system, the temperature of water out of the gas cooler, and the exhaust pressure of the system. With highly efficient heat exchanger, the temperature of water out of the gas cooler could be increased while compressor discharge temperature is remained the same. So when the system provides high temperature water, it could run in higher cop.

Keywords Carbon dioxide · Heat pump water heater · Trans-critical cycle · Experimental study

14.1 Introduction

CO_2 has been already used as a refrigerant for a hundred of years. It belongs to the first batch of the refrigerants. Most of those refrigerants are flammable or toxic. Because of its excellent properties, Freon refrigerant quickly occupied the refrigerant market and became a milestone in the commercial refrigeration. Until

Y. Liu · Z. Zhuo (✉) · F. Zhang
University of Shanghai for Science and Technology, Shanghai 200093, China

T. Bao
Shanghai Delphi Automotive Air Conditioning Systems Ltd, Shanghai 201204, China

A. Li et al. (eds.), *Proceedings of the 8th International Symposium on Heating, Ventilation and Air Conditioning*, Lecture Notes in Electrical Engineering 262,
DOI: 10.1007/978-3-642-39581-9_14,

the American environmental scientist Molina and Rowland found that chlorine atoms which is contained in the Freon could destroy atmospheric ozone layer, people are once again looking for a new environmentally friendly refrigerant. The natural refrigerant once again attracts people's attention. Among them, the most representative is CO_2.

Currently, Japan and some countries in Europe have conducted research on CO_2 as a refrigerant. And outstanding achievements about the research have been made. In foreign countries, Petter NeksÜa and the others established the prototype in NTNU-SINTEF heat Laboratory in 1997 and issued a series of theoretical and experimental results on CO_2 heat pump water heater. Zakeri who was studying in the Norwegian University of Science and Technology established the first industrial CO_2 heat pump water heater in the Norway Larvik in 2000 [1]. In 2002, three-stage counter flow gas cooler is designed by Stene [2] who belonged to department of refrigeration and air conditioning in Norwegian University of Science and Technology. The gas cooler has a better match with temperature slip. Stene and the other also established the 615 kw CO_2 heat pump system which has run in August 2002. Wang and Hihara [3] have studied the performance of CO_2 and R22 heat pump water heater system, and established model of each components and the whole system in 2002. The first domestic CO_2 water–water heat pump system was developed in Tianjin University [4], in 1999. On this basis, the system's performance has been improved by using expander to replace compressor and using different types of heat exchanger. Zhu [5], who studied in University of Shanghai for Science and Technology, researched CO_2 heat pump system with capillary as throttling device and DC inverter compressor and analyzed the feasibility of CO_2 heat pump system with capillary as throttling device and the influence on the system's performance by changing the frequency of the compressor [6].

Because of the unique tradition of the bathtubs, Japanese need more hot water. So they also do a lot of research in this area. Japanese standard requires the temperature of water out of heat pump water heater cannot below 65 °C [7]. It's important to people's health because water with temperature above 65 °C can eliminate pathogenic bacteria widely present in the soil and water, such as Legionella. The water temperature of the heat pump water heater is difficult to elevate due to thermodynamic limit of regular working fluids. With unique thermodynamic properties, CO_2 as working fluids can provide hot water of 65 °C in higher efficiency.

14.2 Characteristics and Application Prospects of CO_2 Heat Pump

Former president of the International Institute of Refrigeration Lorentzen believes that carbon dioxide is irreplaceable refrigeration working fluid [8]. He proposed the carbon dioxide transcritical cycle theory and pointed out that it is expected to play an important role in the field of automotive air conditioning and heat pump.

Most of the CO_2 refrigeration system used in the present study adopt transcritical cycle. Many scholars have done a lot of researches on CO_2 used in fields of refrigeration, air conditioning, and heat pump. As a refrigerant, CO_2 has many advantages. It is safe, nontoxic, and nonflammable. With good thermodynamic properties, ease of transportation and low price, CO_2 is also easily available from a lot of industrial appendages. Because of its Ozone Depression Potential (ODP) is 0 and Global Warming Potential (GWP) is 1, CO_2 does not need to recycle. In CO_2 transcritical cycle, the exothermal process with larger temperature slip is a variable temperature process. The process was precisely matched with the hot water temperature rise. It can effectively reduce the energy loss in the heat transfer process and make the system with higher coefficient of performance.

14.3 Experimental Device Design and the Test

As shown in Fig. 14.1, it's the T-S figure of CO_2 transcritical cycle. At supercritical pressure, without state of saturation, temperature and pressure of CO_2 are independent of each other. So the system using CO_2 as refrigerant can meet a variety of actual needs.

Based on the principles of Fig. 14.1 and testing standards developed by Japan Refrigeration Association (JAR): JAR4050-2005 [9], the system of CO_2 heat pump water heater whose evaporator and gas cooler are both coaxial tubes and whose cooling medium is water has been designed and constructed. And operating performance of the system has been researched.

Flow diagram of the experimental device and major temperature, pressure, and flow measurement points are shown in Fig. 14.2. The system mainly consists of compressor, gas cooler, evaporator, coaxial tubes recuperator, manual throttle valve, safety valve, and other components.

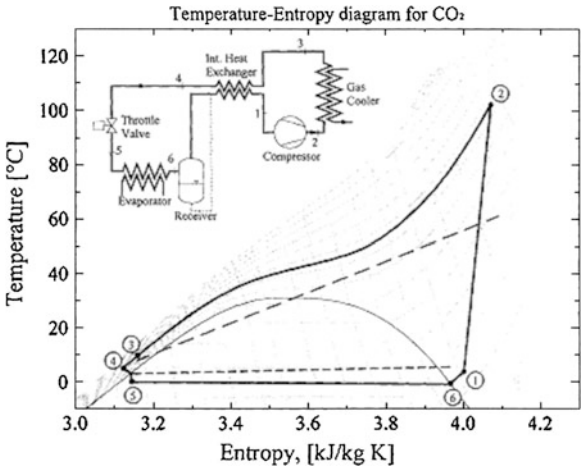

Fig. 14.1 Temperature-entropy diagram for CO_2

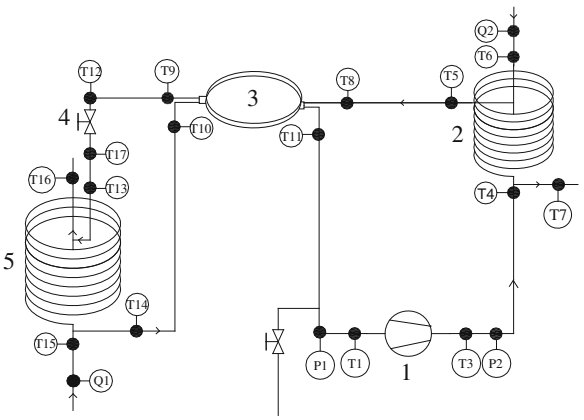

Fig. 14.2 Schematic diagram of experimental device processes and measuring points distribution. 1: compressor; 2: coaxial tubes gas cooler; 3: coaxial tubes recuperator; 4: manual throttle; 5: coaxial tubes evaporator; *T*: thermocouple; *P*: pressure sensors; *Q*: water side flow measurement equipment

The CO_2 transcritical dedicated compressor whose model is CD180H is developed by Italy Dorin Company Limited. The compressor's theoretical displacement is 1.12 m^3/h. In order to ensure the safety of experimenter and the system, a D505/18D high-pressure protection switch is installed in the high-pressure side of the system. The compressor shut down pressure is set to 12 MPa. The other major components of the system are self-designed. Electronic expansion valve on the market does not meet the requirements, so we choose a manually adjustable throttle valve for the Throttling device of the system. The sizes of heat exchangers are shown in Table 14.1.

Due to higher working pressure of the CO_2 transcritical cycle, the high pressure can reach up to 10 MPa. It's approximately 6–8 times to system pressure using traditional working fluids. So it should be carried out as safety analysis on the system's tubes. The pressure security was checked according to JB/T4750-2003 refrigeration apparatus pressure vessel standards [10]: The theoretical requirement of the copper tube thickness is 0.51 mm, so 1 mm thickness of the copper tube fully meets the requirements.

The location of the temperature, pressure, and flow rate measurement points are shown in Fig. 14.2. The system's temperature and pressure data acquisition is achieved by using 34970A data acquisition instrument manufactured by the

Table 14.1 Size table of heat exchangers of the system

Name	Gas cooler	Evaporator	Intermediate heat exchanger
Form	Sleeve: a large pipe sleeves two small tubes	Sleeve: a large pipe sleeves two small tubes	Sleeve: large pipe sleeves small tube
Size (mm)	Outer tube diameter: 19	Outer tube diameter: 22	Outer tube diameter: 12
	Wall thickness: 1.5	Wall thickness: 1.5	Wall thickness: 1
	Inner tubes diameter: 5	Inner tubes diameter: 6	Inner tube diameter: 6
	Wall thickness: 1	Wall thickness: 1	Wall thickness: 1
Length (m)	8.5	8.0	3.0

Agilent Company in USA. Temperature measuring device is copper-constantan thermocouple wire (also known as T-type thermocouple) with measurement accuracy is ± 0.5 °C and measurement temperature range is −40–350 °C. Pressure measurement device is NS-I1 pressure sensor with measurement accuracy is ± 0.1 %. High-pressure gauges are, respectively, equipped in the system to measure static high and low pressure of the system. So pressure changes of the system can conveniently obtained when CO_2 is charged into the system. AN7931A three-phase electrical parameter measurement instrument is used to measure the power of the compressor.

14.4 Experimental Results and Analysis

14.4.1 The Impact of Expansion Valve

When the water flow in gas cooler and evaporator is constant, test the change of pressure and temperature by changing the opening of expansion valve, every 0.5 MPa is a measuring point. Figure 14.3 shows the relationship between gas cooler inlet temperature (i.e., the outlet temperature of compressor) and outlet water temperature.

Decreasing the opening of the expansion valve and increasing compressor outlet pressure. When the pressure increase 2.5 MPa, the temperature of procreant water increases only 7 °C. Therefore, only changing the opening of expansion valve can make the outlet pressure of compressor increase quickly, but the effect of procreant hot water is not as good as expected.

Consequently, at the condition of water flow from gas cooler and evaporator is constant, only change the expansion valve opening cannot get expected temperature of water, makes the exhaust pressure too high, influence the system operation and cost more energy, at the same time, the high pressure will threaten to the security of the system.

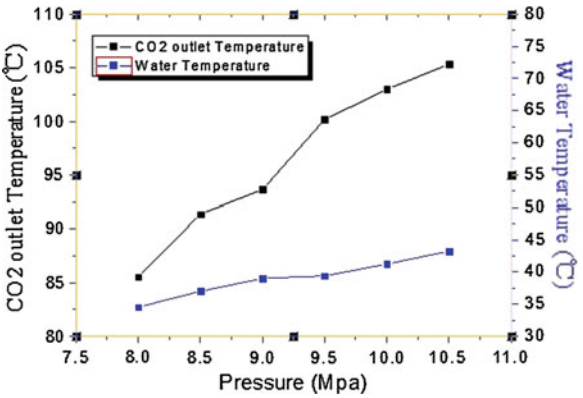

Fig. 14.3 Compressor outlet temperature versus exhaust pressure

14.4.2 *Effects of Heat Exchanger on the System Performance*

14.4.2.1 Effect of Water Flow Rate on the System Performance

At the conditions of throttle valve and gas cooler inlet water temperature remains unchanged, by changing the flow of produced hot water to get the information of the system. Figure 14.4 is the changes of outlet pressure and water temperature regard to water flow. The exhaust pressure as well as the water temperature decreases with the water flow increase. From the trend of the two curves, the pressure increases faster. From Fig. 14.5 can get that the energy consume of the system increases with the water flow deeply increase, and the rising rate also increase. At the conditions of producing 81 °C water, the energy cost of the compressor is 1301 W.

The decrease of water flow can significantly increase the water temperature, simultaneously, substantially increase the exhaust pressure, consume more energy, and caused system COP dropt. Figure 14.6 is system COP versus water flow, when

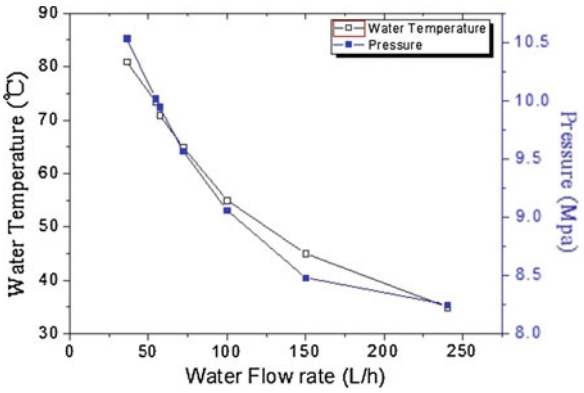

Fig. 14.4 The changes of outlet pressure and water temperature regard to water flow

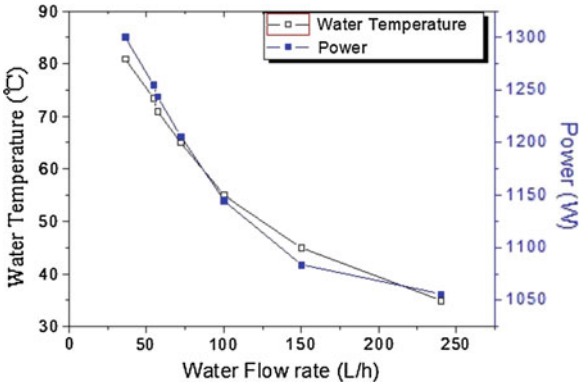

Fig. 14.5 Power versus water flow

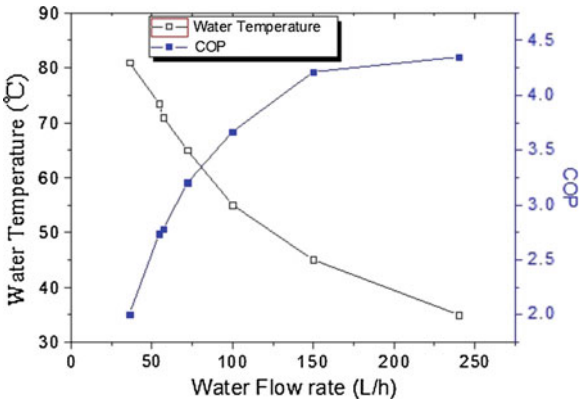

Fig. 14.6 System COP versus water flow

the water flow is 36 L/h, the system can produce hot water which temperature is 81 °C, while the COP can only reach 2.0. Therefore, the reasonable water flow can balance the produced water temperature and the system performance.

14.4.2.2 The Performance of Evaporator

Can get the relationship of evaporator and the produced water temperature at the conditions of expansion valve and water through evaporator are unchanged. Figure 14.7 is evaporation pressure versus hot water temperature, the pressure out evaporator changes little with the water temperature increase. The temperature increases 50 °C, while the pressure only decreases 0.5 MPa. Figure 14.8 is water temperature at the inlet and outlet of the evaporator versus hot water temperature, when the inlet water temperature invariant, temperature of the water that out from evaporator change little, only increases 2 °C. Figure 14.9 is hot water flow versus carbon dioxide temperatures at the inlet and outlet of the evaporator, the

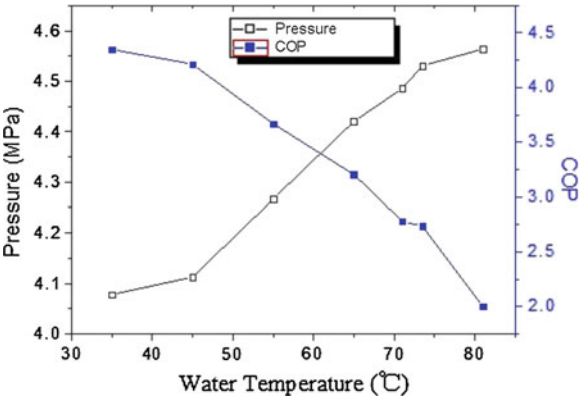

Fig. 14.7 Evaporation pressure versus hot water temperature

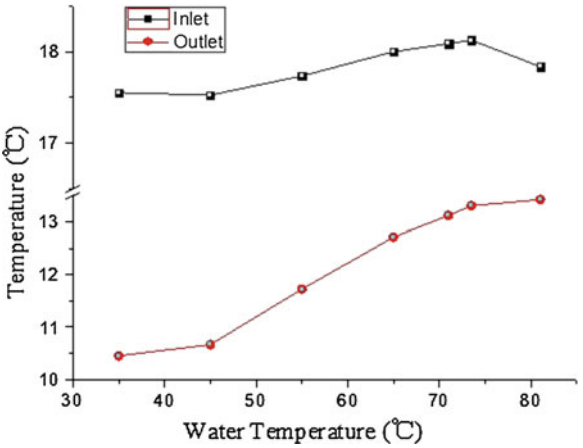

Fig. 14.8 Water temperature at the inlet and outlet of the evaporator versus hot water temperature

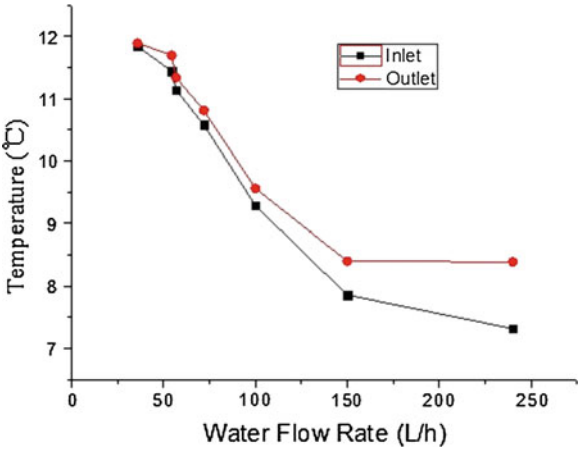

Fig. 14.9 Hot water flow versus carbon dioxide temperatures at the inlet and outlet of the evaporator

temperature of refrigeration changes little when it through the evaporator, especially in the low water flow, this shows that there is also some refrigerate in the evaporator not evaporation, so, the evaporator is not suitable.

From Figs. 14.7, 14.8, and 14.9 can get that, the evaporator design is too small and need to improve its heat exchange capacity.

14.4.2.3 The Intermediate Heat Exchanger Performance

Figure 14.10 is temperature in the intermediate heat exchanger versus water flow, from the curves can get that the temperature of high-pressure side dropped obvious, but the low-pressure side not. The phenomenon shows that the refrigeration from the evaporator does not completely evaporate; it is also the mixture of

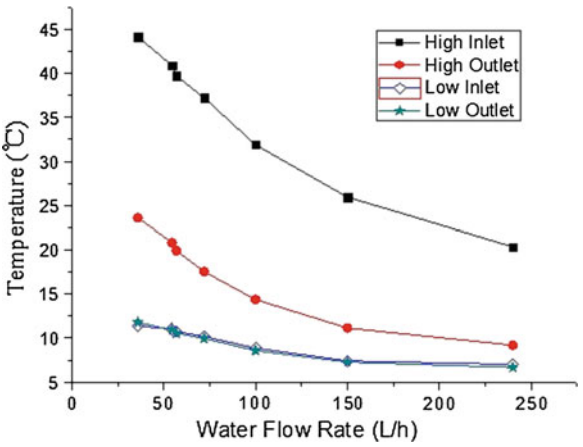

Fig. 14.10 Temperature in the intermediate heat exchanger versus water flow

liquid and gas. The heat from the high pressure was absorbed by refrigerant in the form of latent heat, so, the refrigerant which through the low pressure of the intermediate heat exchanger temperature changed little.

14.4.3 Theoretical and Measurement COP

The operational efficiency is an important index to evaluate a system, when the temperature of hot water reached the requirements, the system should have the highest operating efficiency. In 2000 years, Liao et al. analyze the relationship of CO_2 system COP and high side pressure by establishing a simulation, and summarize the formula of optimal exhaust pressure [11].

$$P_{\text{otp}} = \frac{2.7572 + 0.2304t_{\varepsilon} - 3.072K/C}{1 + 0.0538t_{\varepsilon} + 0.1606K/C}t_{\text{c}} - \frac{8.7946 + 0.02605t_{\varepsilon} - 105.48K/C}{1 + 0.05136t_{\varepsilon} + 0.2212K/C} \tag{14.1}$$

In the formula, K and C are constants related to the compressor, $K = 0.121$, $C = 1.003$, applicable scope is $-10\ ^{\circ}\text{C} < t_{\text{e}} < 20\ ^{\circ}\text{C}$, $30\ ^{\circ}\text{C} < t_{\text{c}} < 60\ ^{\circ}\text{C}$, $0 < K/C < 0.3$.

From the formula 1 can get that affecting of compressor efficiency is not obvious, and the CO_2 compressor isentropic efficiency is relatively high, so, the impact of the compressor efficiency can be ignored. The formula can be simplified as:

$$P_{\text{otp}} = (2.778 - 0.0157t_{\text{e}})t_{\text{c}} + (0.38t_{\text{e}} - 9.34) \tag{14.2}$$

In the formula, the unit of P_{otp} is bar, the unit of t_{e} and t_{c} is °C.

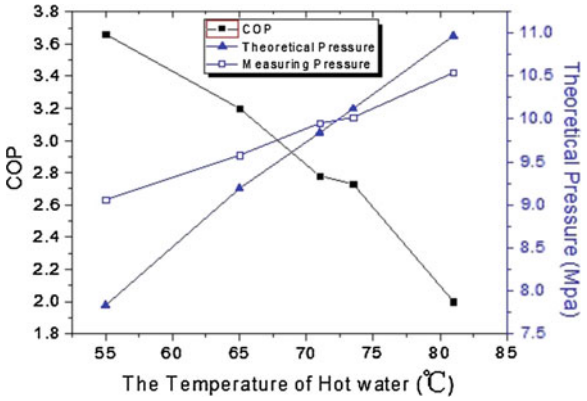

Fig. 14.11 Theoretical optimal pressure and actual measurement pressure of the system versus hot water temperature

Figure 14.11 is theoretical optimal pressure and actual measurement pressure of the system versus hot water temperature, from the curves can get that, the measured exhaust pressure at design water temperature 65 °C is higher than theory pressure, and the system COP is 3.2. When the operating pressure equal to optimal operation pressure, the hot water temperature is 73 °C, the COP is 2.7, operating pressure is 10.03 MPa. When the produced water temperature is 81 °C, the system COP can reach 2.0, but, the quantity of hot water is very small as shown in Fig. 14.12.

From Fig. 14.11 can get that, the system COP is increased with the water flow increase, and decreased with the water temperature increase. Suggest to decreasing the water temperature to increase the system COP upon the conditions that can satisfy the requirements.

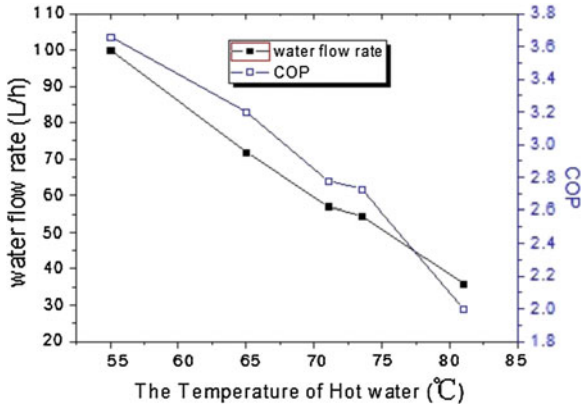

Fig. 14.12 Hot water flow versus water temperature

14.5 Conclusion

On CO_2 heat pump water heater system experimental platform, the impact of each heat exchanger on the system's performance has been researched and the trends of series of parameters have been analyzed. Conclusions are as follows:

1. The system can provide 65 °C hot water when the COP can reach 3.2. And above 80 °C hot water that meets industrial requirements can be obtained.
2. When the system is running, compressor discharge temperature is relatively modest. When temperature of hot water is 65 °C, the high pressure of the system is 9.7 MPa. The pressure is higher than the optimal design pressure. When running in the optimal design pressure, the system can produce 73 °C hot water, then COP is 2.7.
3. The heat exchanger efficiency of gas cooler has great impacts on performance of the system. It decides whether the system with high COP can run in safe and efficient working condition. The COP of the system is increased with the increase of the water flow of the gas cooler and decreased with the decrease of the temperature of water generated by the system.
4. The COP of the system is increased with the increase of the water flow of the gas cooler and decreased with the decrease of the temperature of water generated by the system. So the right water temperature and the water flow is the key to maintaining high efficiency of the system.
5. The evaporator and the intermediate heat exchanger do not have so much impact on the temperature of hot water produced by the system, but have greater impact on the COP of the system. The size of evaporator should be optimally designed.

References

1. Zakeri GR, Neks P (2000) Results and experiences with the first commercial pilot plant CO_2 heat pump water heater. In: 4th IIR Gustav Lorentzen conference on natural working fluids. Purdue University, USA, pp 59–65
2. Stene J (2002) Investigation of a residential brine-to-water CO_2 heat pump for combined low-temperature space heating and hot water preparation. In: 5th IIR Gustav Lorentzen conference on natural working fluids, Guangzhou, China, pp 268–275
3. Wang Jf, Hihara E (2002) Performance comparison of heat pump water heaters using carbon dioxide and R22 as refrigerants. In: Preliminary proceedings of the 5th IIR-Gustav Lorentzen conference on natural working fluids, Guangzhou, China, pp 260–267
4. Gu HQ, Ma YT, Yang J et al (2003) Design and analysis of shell-and-tube heat exchanger with integrated tube-box. Press Vessel 20(9):17–20
5. Zhu LX, Zhang H, Wang YT et al (2012) Performance study of DC inverted frequency air-source heat pump water heater with trans-critical CO_2 cycle. Fluid Mach 40(4):73–76
6. Bao TW, Liu YF, Cai CP (2011) Experimental study on CO_2 heat pump water heater with capillary tube as throttling device. Refrig Technol 2:23–26

7. Paul RP et al (1995) Why evaporative coolers have not caused legionnaires' disease. ASHRAE J 1:29–33
8. Lorentzen G (1995) The use of natural refrigerants: a complete solution to the CFC/HCFC predicament. Int J Refrig 18(3):190–197
9. JRA4050-2005, "Heat pump water heater (natural refrigerant carbon dioxide)" standard. Japan Refrigeration Industry Association
10. JB/T4750-2003, Pressure vessel refrigeration device
11. Liao SM, Zhao TS, Jakobsen A (2000) A correlation of optimal heat rejection pressures in trans-critical carbon dioxide cycles. Appl Therm Eng 20:831–841

Chapter 15
Design and Analysis on a Kind of Compound Renewable Energy System for Heating

Guohui Feng, Mingzhi Jiang, Kailiang Huang, Jialin Sun and Cheng Cheng

Abstract This paper aims to optimizing the conjunctive use of sewage source heat pump technology and solar hot water heating technology and improving the drawbacks when they are, respectively, applied. By adopting key technologies such as cooperation technology of sewage source heat pump technology and solar hot water heating technology, efficient phase change technology, scientific operation strategies, continuous automatic control of each equipment and others, the system realizes the efficient operation of sewage source heat pump units and solar hot water heating system, storage and delay of energy, full utilization of peak and valley time price policy which enables the system to gain the best heating effect and efficient operation of each equipment. We conduct a test and statistical analysis on the indoor comfort parameter, electricity, and water consumption of major equipments and the performance change of equipments at operation time for the system, and continuously optimize design conception for providing significant reference and guidance to the future field of renewable energy, finally completing the transition from nonrenewable energy to renewable energy.

Keywords Sewage source heat pump · Solar collector · Simulation · Optimization

15.1 Introduction

The phenomenon of the heating network cannot meet the demand of district heating exists generally, but solar energy resources in these areas is very rich and the use of solar energy to meet the heating demand is quite promising [1–3]. Therefore, based on the status quo of the cold northern climate characteristics,

G. Feng (✉) · M. Jiang · K. Huang · J. Sun · C. Cheng
School of Municipal and Environment Engineering, Shenyang Jianzhu University, Shenyang 110168, China
e-mail: fengguohui888@163.com

A. Li et al. (eds.), *Proceedings of the 8th International Symposium on Heating, Ventilation and Air Conditioning*, Lecture Notes in Electrical Engineering 262,
DOI: 10.1007/978-3-642-39581-9_15,

we propose a kind of compound renewable energy system for heating, characterized by solar-water source heat pump systems with phase change energy storage.

By testing the conjunctive operation system of solar energy hot water heating system and sewage source heat pump system, this paper aims to analyzing and studying the operation effect, equipments performance parameter and energy consumption under different operational mode and conditions, proposing a best conjunctive operation to achieve its best heat supply effect and efficient operation of equipments, and finally realizing the best economical and environmental effect.

15.2 System Illustration

15.2.1 System Design Objective and Key Technology

To fully utilize the solar energy and sewage energy by technology integration to fundamentally achieve the comprehensive utilization of composite green energy, method such as Fully utilizing solar energy heating; Utilizing sewage source heat pump to boost temperature and energy; Adopting the technology of phase change for heat storage to realize the conversion and storage of energy; Utilizing the policy of peak-valley electricity price [2] has been adapted.

The system project is designed for the conjunctive heating of solar energy and sewage source heat pump, while the system was running the solar energy hot water heating system is connected to the evaporation end of heat pump unit through the cold tank, and the water source temperature is 15 °C. The sewage heat pump unit [1] can absorb the heat from the cold tank while the system is running, and the heat of cold tank absolutely comes from solar energy hot water heating system during the day, after absorbing the low-grade heat energy of cold tank [3]; the sewage heat pump unit can release the high-grade heat energy through its heating cycle to store the heat in the hot tank, whose water temperature can keep the level of 48 °C while the system is running; with the help of phase change materials, the thermal storage capacity and heat lag capacity of hot tank are both improved, meanwhile its size and cost can be reduced. The terminational equipment is fan coil,the supply water temperature is 45 °C, and the return water temperature is 38 °C, so its temperature difference is 7 °C.

The sewage heat pump unit is running during the valley electricity, it can supply heating for indoor heat and heat storage of hot tank; The sewage heat pump is shut off during the peak electricity [2], the hot tank releases its heat which is stored during the valley electricity and provided for the fan coil to satisfy the demand of indoor heating; meanwhile, solar energy hot water heating system starts work to heat the sewage of cold tank as well as store its heat in the water for heat pump unit. Therefore, the system can take full use of the peak and valley electricity policy to make the heat pump achieve the best operation economics, so as to lower the running cost.

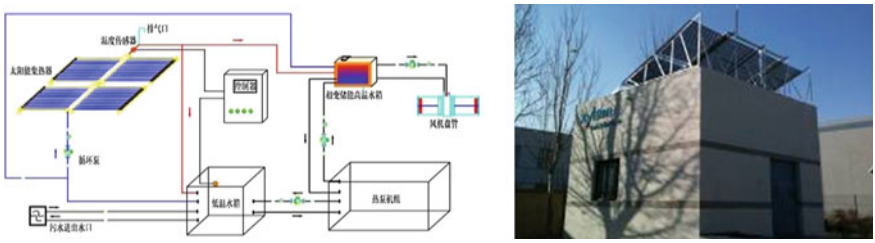

Fig. 15.1 System flow chart and the project appearance

The energy conservation system can save 802 kg of standard coal compared with traditional central heating system every year. The system is helpful to lower 3307 kg of discharged dust and PM2.5 [4] from the air; lower 2303 kg of carbon dioxide emission to weaken the greenhouse effect; lower 8 kg of sulfur dioxide emission to weaken the acid rain; lower 7 kg of nitrogen oxides discharge to reduce the formation of acid rain and photochemical pollution (Fig. 15.1).

15.3 Test and Data Reduction

15.3.1 Test Items and its Instruments

Integrated Part-Load Value (IPLV) Test of Sewage Heat Pump Unit Instruments: Ultrasonic flow meter, Paperless recorder, and Power indicators analyzer; The Test of Heat-collecting Efficiency and Heat Loss Factor for Solar Energy Hot Water Heating System.

Instruments: Ultrasonic flow meter and Paperless recorder; Start Time and Power Consumption of Electric Heaters Instruments: Power index analyzer (Fig. 15.2).

15.3.2 Test Design and Data Reduction

15.3.2.1 Heating Supply Condition of Sewage Heat Pump Running Individually

The temperature test of supply and return water of sewage heat pump condensation end: Surfaces of supply and return pipe of sewage heat pump condensation end were, respectively, fixed with Temperature sensor (KZWP).

Ultrasonic flow meter was placed on the return pipe condensation end (Figs. 15.3, 15.4, 15.5).

Fig. 15.2 Test instruments

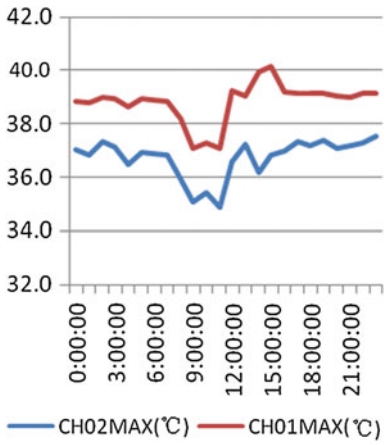

Fig. 15.3 Temperature of supply and return water of condensation end

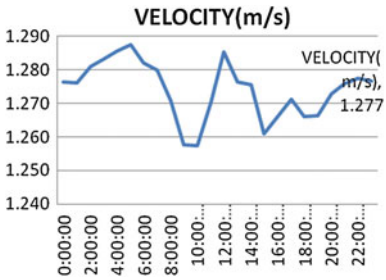

Fig. 15.4 Velocity of condensation end

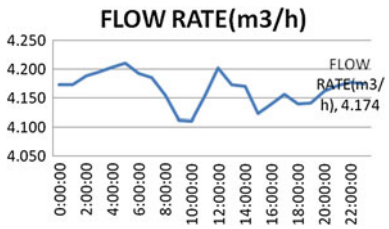

Fig. 15.5 Flow rate of condensation end

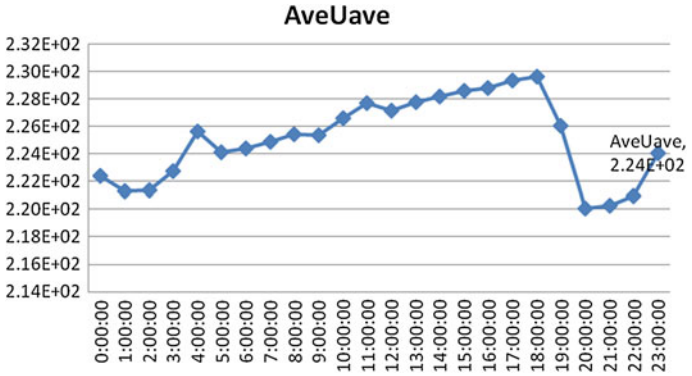

Fig. 15.6 Average voltage of heat pump

The current, voltage, power, start time, and power consumption test of sewage heat pump: Voltage clamps of power index analyzer are, respectively, connected in parallel to three front lines and a zero lines under the air switch of sewage heat pump unit, and three front lines are, respectively, clamped by current clamps (Figs. 15.6, 15.7, 15.8).

The current, voltage, power, start time, and power consumption test of electric heater: Voltage clamps of power index analyzer [5] are, respectively, connected in parallel to three front lines and a zero lines under the air switch of electric heater, and three front lines are, respectively, clamped by current clamps (Figs. 15.9, 15.10, 15.11).

(i) Heat pump unit:

$$\text{IPLV} = \frac{Q}{P} = \frac{cm\,\Delta t}{P} = \frac{4.20\,(\text{kj/kg}\cdot^{\circ}\text{C}) * 4.15\,(\text{t}/h) * 6.20\,(^{\circ}\text{C})}{1.03 * 10^2\,(\text{kw})} = 7.20$$

(ii) Power consumption of heat pump unit is $1.03 * 10^2$ (kw.h)
(iii) Power consumption of electric heater is $6.08 * 10^{-1}$ (kw.h)
(iv) Total consumption of system equipments is $1.11 * 10^2$ (kw.h).

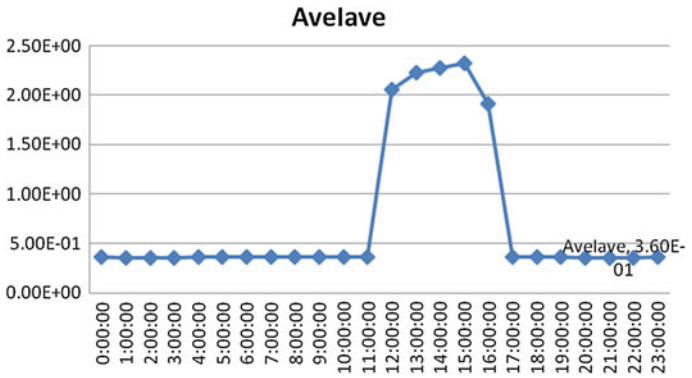

Fig. 15.7 Average current of heat pump

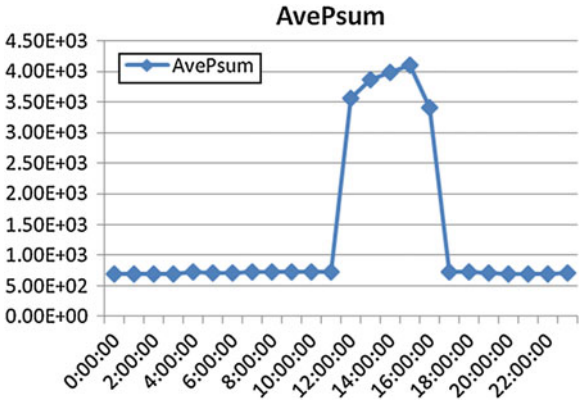

Fig. 15.8 Average power of heat pump

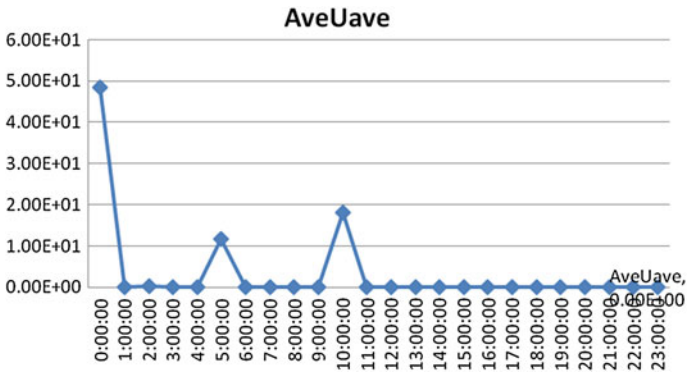

Fig. 15.9 Average voltage of electric heater

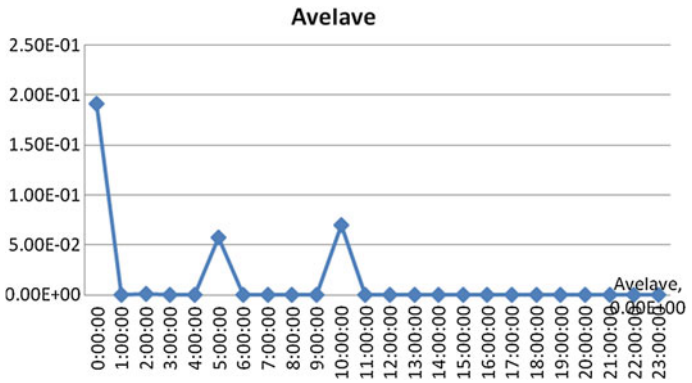

Fig. 15.10 Average current of electric heater

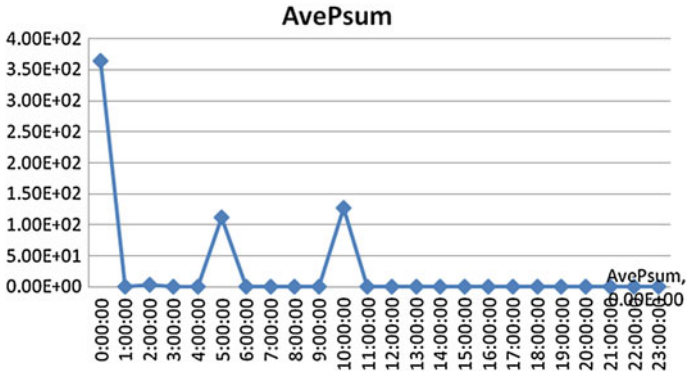

Fig. 15.11 Average power of electric heater

15.3.2.2 Heating Supply Condition of Solar Energy Hot Water Heating System Running Individually

1. The temperature test of supply and return water of solar energy hot water heating system:

Surfaces of supply and return pipe of solar energy hot water heating system were, respectively, fixed with KZWP.

2. The flow test of solar energy hot water heating system:

Ultrasonic flow meter was placed on the return pipe of solar energy hot water heating system (Figs. 15.12, 15.13, 15.14).

3. The current, voltage, power, start time, and power consumption test of electric heater:Voltage clamps of power index analyzer are, respectively, connected in

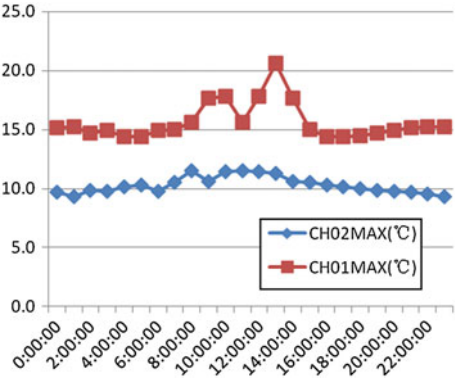

Fig. 15.12 The temperature of supply and return water

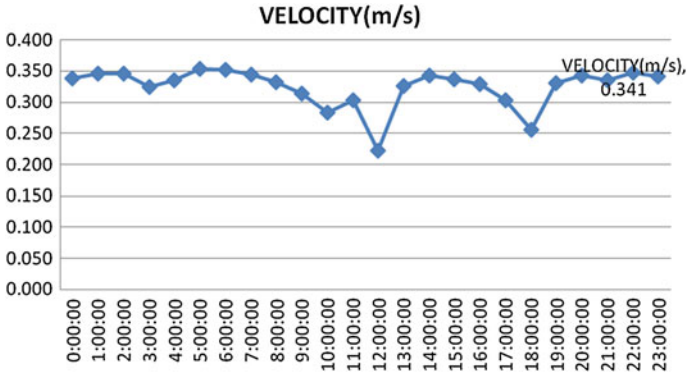

Fig. 15.13 Velocity of solar energy system

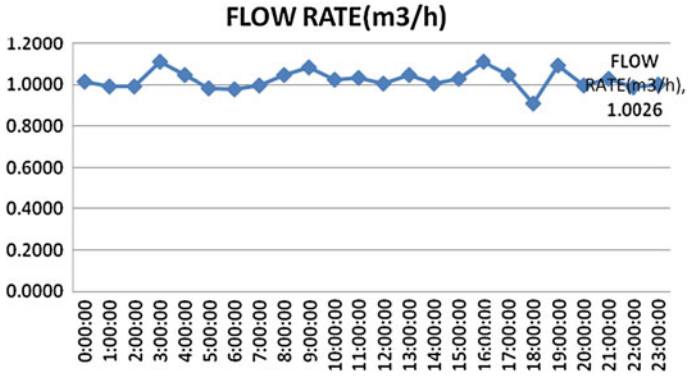

Fig. 15.14 Flow rate of solar energy system

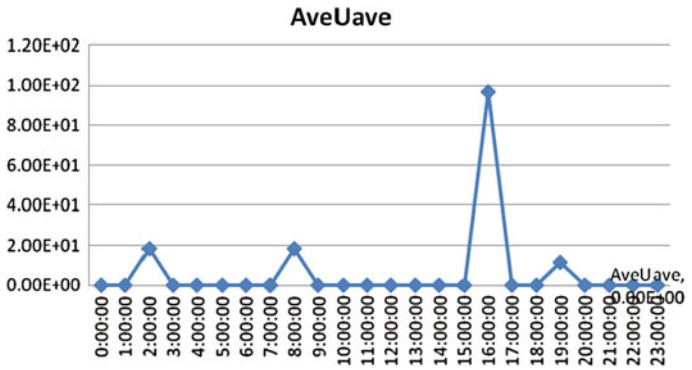

Fig. 15.15 Average voltage of electric heater

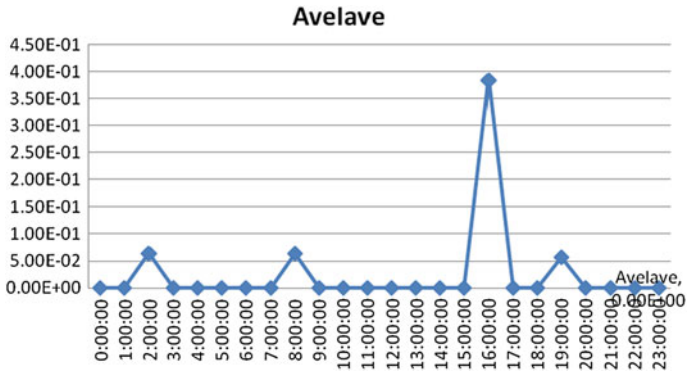

Fig. 15.16 Average current of electric heater

parallel to three front lines and a zero lines under the air switch of electric heater, and three front lines are, respectively, clamped by current clamps (Figs. 15.15, 15.16, 15.17).

(i) $A = \dfrac{\alpha_1 Q_1}{J_1 \eta_1 (1 - \eta_2)}$

A: Collector area (m^2) Q1: Building load (kj/d) a1: Solar fraction (a1 = Q2/Q1, Q2: The daily heat provided by solar energy hot water system) J1: Annual average daily solar radiation (kj/m^2.d); $\eta 1$: Annual average collector efficiency; $\eta 2$: Loss rate

$$\eta_2 = 1 - \frac{Q_2}{AJ_1\eta_1} = 1 - \frac{4.2\,(\text{kj/kg}\cdot^\circ\text{C}) * 1.09\,(t/h) * 6\,(^\circ\text{C})}{30\,(m^2) * 3600 * 6\,(\text{kj/m}^2 \cdot \text{d}) * 60\ \%} = 0.435$$

The power consumption of electric heater is 0.722 (kw.h). Total consumption of system equipments is 0.853 (kw.h).

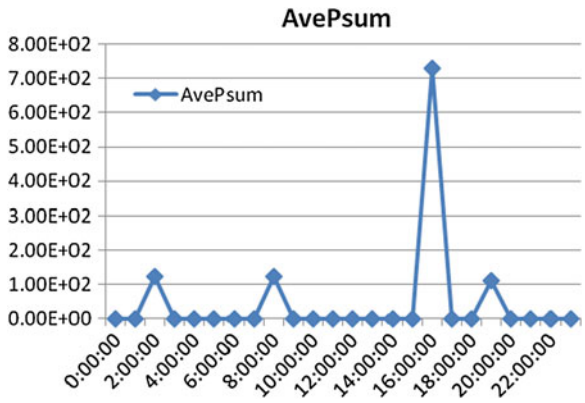

Fig. 15.17 Average power of electric heater

15.3.2.3 Conjunctive Operation Condition of Solar Energy Hot Water Heating System Heating the Cold Tank that Supplying Heat for the Evaporation End of Sewage Heat Pump Unit Meanwhile its Condensation End Starting to Supply Heat for Hot Phase Change Tank

The temperature test of supply and return water of sewage heat pump condensation end: Surfaces of supply and return pipe of sewage heat pump condensation end were, respectively, fixed with KZWP. The flow test of sewage heat pump condensation end: Ultrasonic flow meter was placed on the return pipe of sewage heat pump condensation end (Figs. 15.18, 15.19, 15.20).

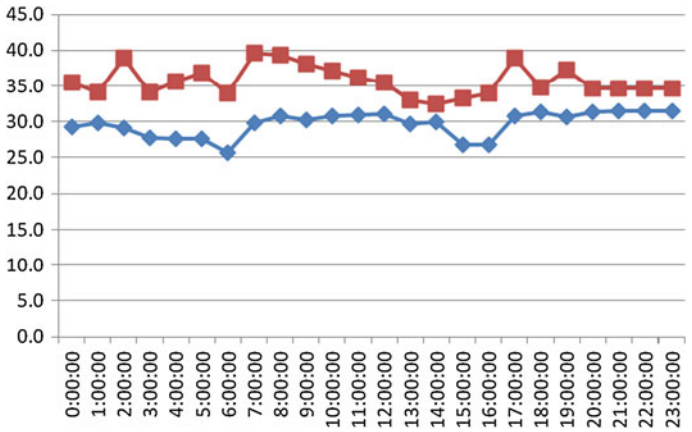

Fig. 15.18 The temperature of supply and return water of condensation end

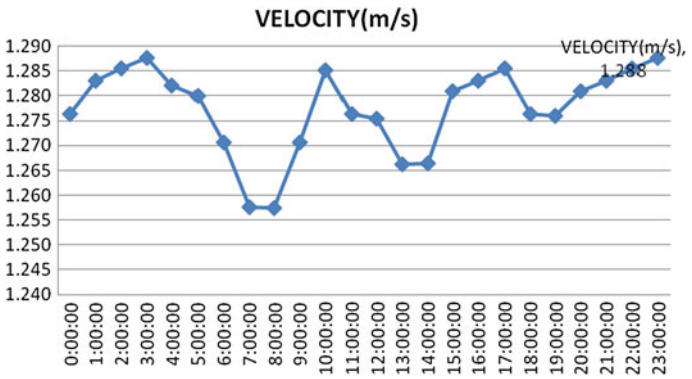

Fig. 15.19 Velocity of condensation end

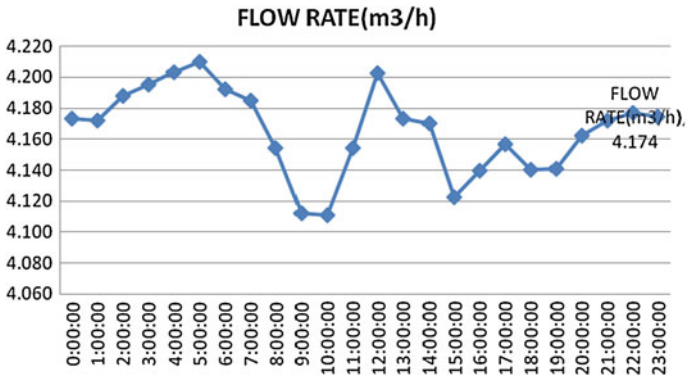

Fig. 15.20 Flow rate of condensation end

The current, voltage, power, start time, and power consumption test of sewage heat pump: Voltage clamps of power index analyzer are, respectively, connected in parallel to three front lines and a zero lines under the air switch of sewage heat pump unit, and three front lines are, respectively, clamped by current clamps (Figs. 15.21, 15.22, 15.23).

The temperature test of supply and return water of solar energy hot water heating system: Surfaces of supply and return pipe of solar energy hot water heating system were, respectively, fixed with KZWP. The flow test of solar energy hot water heating system: Ultrasonic flow meter was placed on the return pipe of solar energy hot water heating system (Figs. 15.24, 15.25, 15.26).

The current, voltage, power, start time, and power consumption test of electric heater: Voltage clamps of power index analyzer are, respectively, connected in parallel to three front lines and a zero lines under the air switch of electric heater, and three front lines are, respectively, clamped by current clamps (Figs. 15.27, 15.28, 15.29).

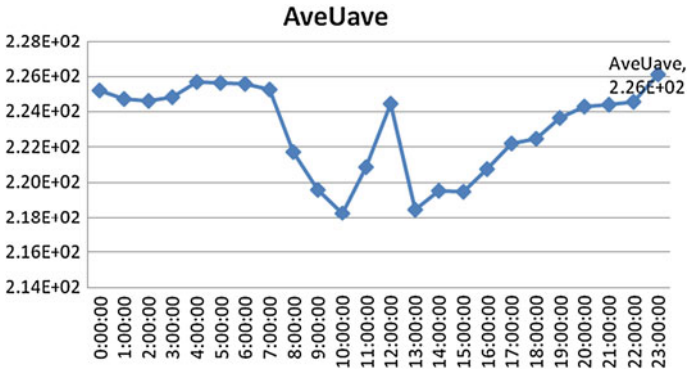

Fig. 15.21 Average voltage of heat pump

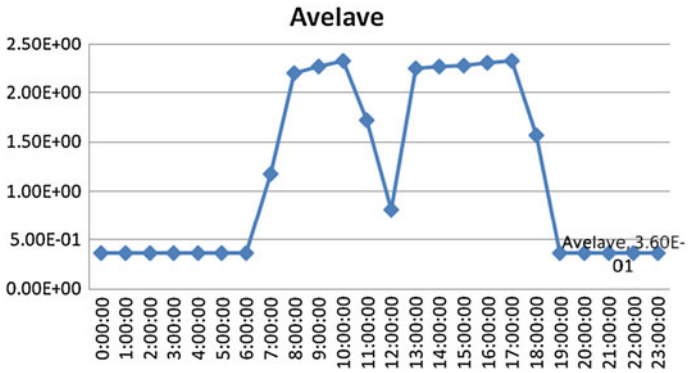

Fig. 15.22 Average current of heat pump

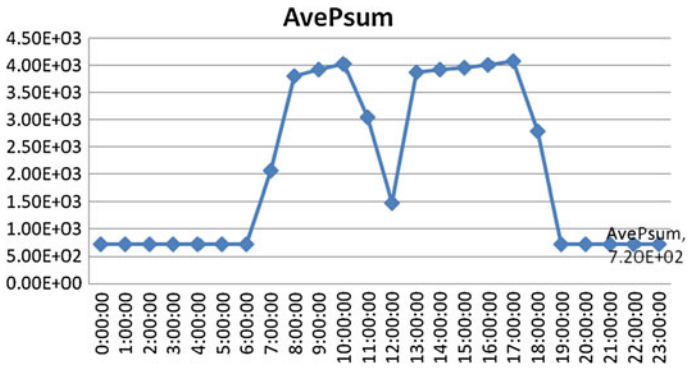

Fig. 15.23 Average power of heat pump

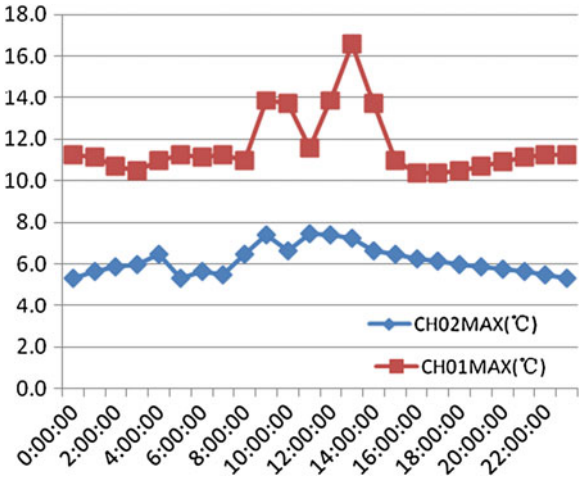

Fig. 15.24 The temperature of supply and return water

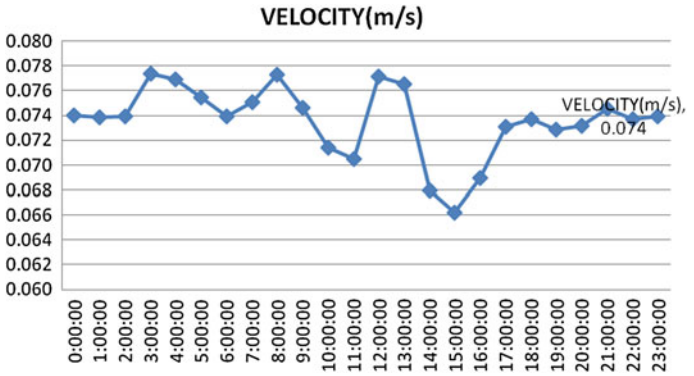

Fig. 15.25 Velocity of solar energy system

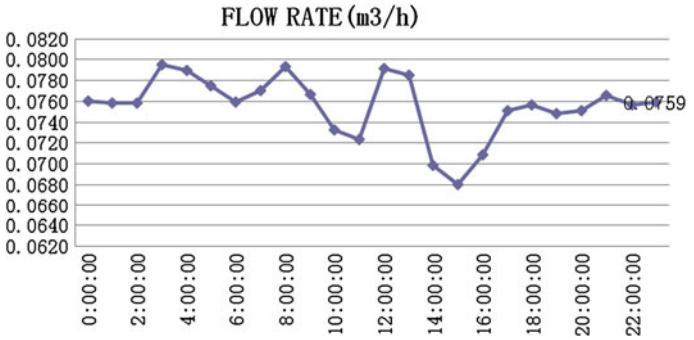

Fig. 15.26 Flow rate of solar energy system

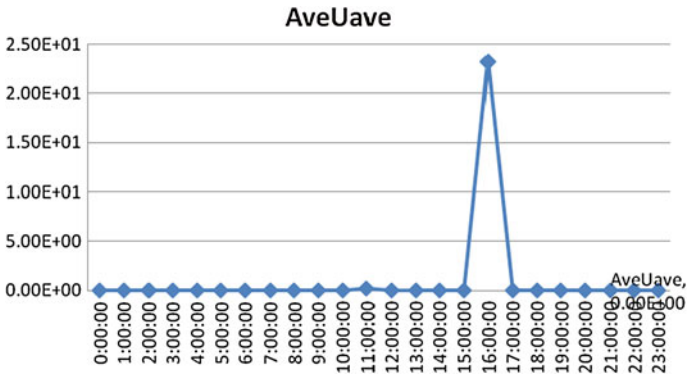

Fig. 15.27 Average voltage of electric heater

Fig.15.28 Average current of electric heater

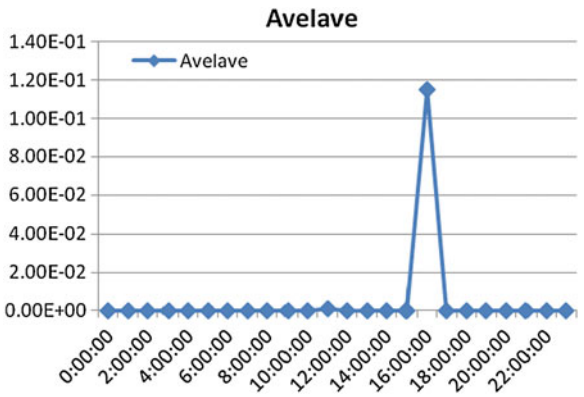

Fig. 15.29 Average power of electric heater

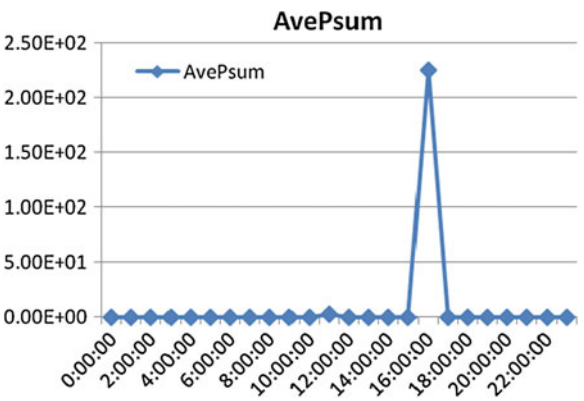

(i) Heat pump unit:

$$\text{IPLV} = \frac{Q}{P} = \frac{cm\,\Delta t}{P} = \frac{4.20\,(\text{kj/kg}\cdot^{\circ}\text{C}) * 4.16(\text{t}/h) * 6.80\,(^{\circ}\text{C})}{0.94 * 10^2\,(\text{kw})} = 9.54$$

(ii) Power consumption of heat pump unit is 0.83 * 10^2 (kw.h) (iii) Power consumption of electric heater is 1.15 * 10^{-1} (kw.h) (iv) Total consumption of system equipments is 0.92 * 10^2 (kw.h)

(v) $\eta_2 = 1 - \frac{Q_2}{AJ_1\eta_1} = 1 - \frac{4.2\,(\text{kj/kg}\cdot^{\circ}\text{C}) * 0.78(t/h) * 8.80\,(^{\circ}\text{C})}{30\,(\text{m}^2) * 3600 * 6\,(\text{kj/m}^2 \cdot \text{d}) * 60\,\%} = 0.378$

15.3.2.4 Conjunctive Operation Condition of Solar Energy Hot Water Heating System Heating the Hot Phase Change Tank that Supplying Heat for the Condensation End of Sewage Heat Pump Unit Meanwhile its Condensation End Starting to Supply Heat for Hot Phase Change Tank

The temperature test of supply and return water of sewage heat pump condensation end: Surfaces of supply and return pipe of sewage heat pump condensation end were, respectively, fixed with KZWP. The flow test of sewage heat pump condensation end: Ultrasonic flow meter was placed on the return pipe of sewage heat pump condensation end (Figs. 15.30, 15.31, 15.32).

The current, voltage, power, start time, and power consumption test of sewage heat pump: Voltage clamps of power index analyzer are, respectively, connected in parallel to three front lines and a zero lines under the air switch of sewage heat pump unit, and three front lines are, respectively, clamped by current clamps (Figs. 15.33, 15.34, 15.35).

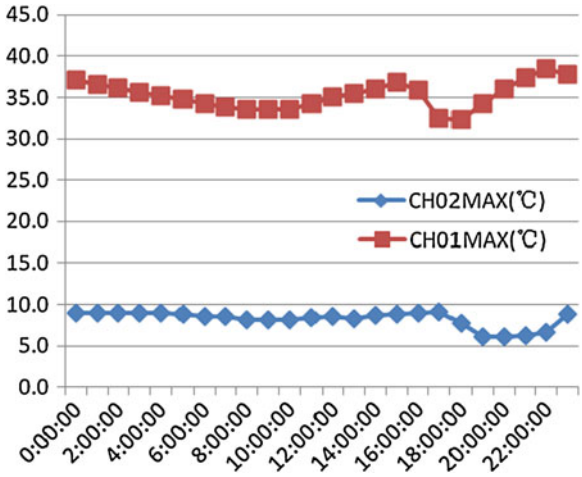

Fig. 15.30 The temperature of supply and return water of condensation end

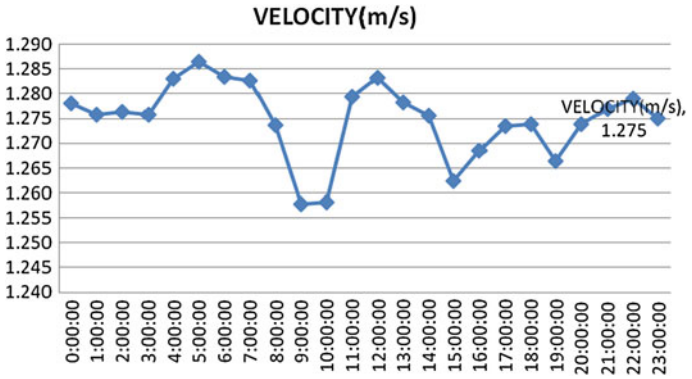

Fig. 15.31 Velocity of condensation end

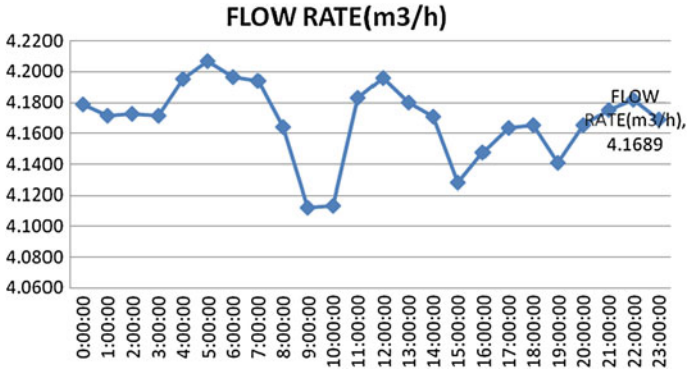

Fig. 15.32 Flow rate of condensation end

Fig. 15.33 Average voltage of heat pump

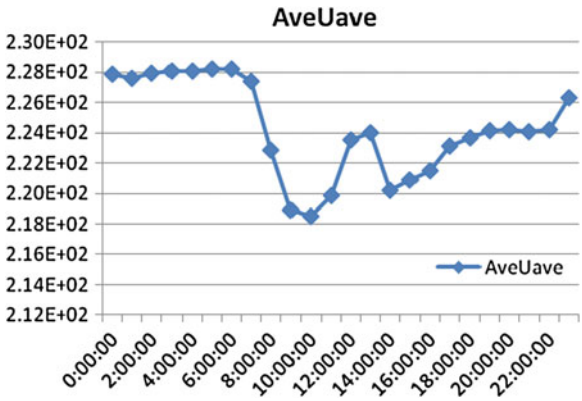

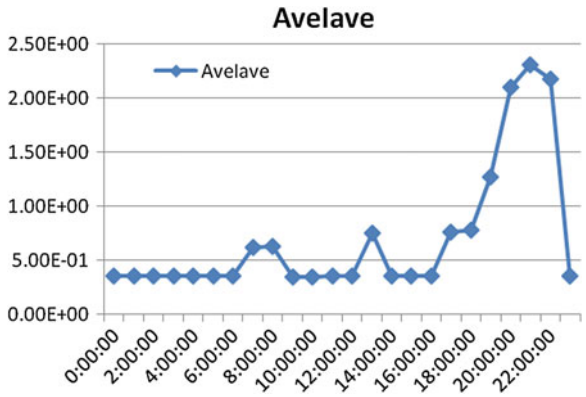

Fig. 15.34 Average current of heat pump

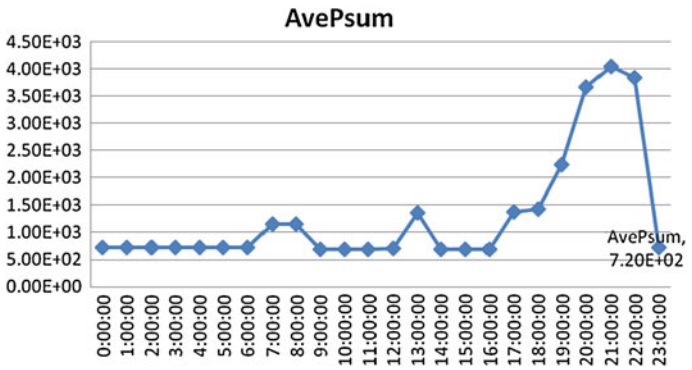

Fig. 15.35 Average power of heat pump

The temperature test of supply and return water of solar energy hot water heating system: Surfaces of supply and return pipe of solar energy hot water heating system were, respectively, fixed with KZWP. The flow test of solar energy hot water heating system: Ultrasonic flow meter was placed on the return pipe of solar energy hot water heating system (Figs. 15.36, 15.37, 15.38).

The current, voltage, power, start time, and power consumption test of electric heater: Voltage clamps of power index analyzer are, respectively, connected in parallel to three front lines and a zero lines under the air switch of electric heater and three front lines are, respectively, clamped by current clamps (Figs. 15.39, 15.40, 15.41).

(i) Heat pump unit:

$$\mathrm{IPLV} = \frac{Q}{P} = \frac{cm\,\Delta t}{P} = \frac{4.20\,(\mathrm{kj/kg{\cdot}^{\circ}C}) * 4.16\,(\mathrm{t}/h) * 7.80\,(^{\circ}\mathrm{C})}{0.80 * 10^2\,(\mathrm{kw})} = 10.14$$

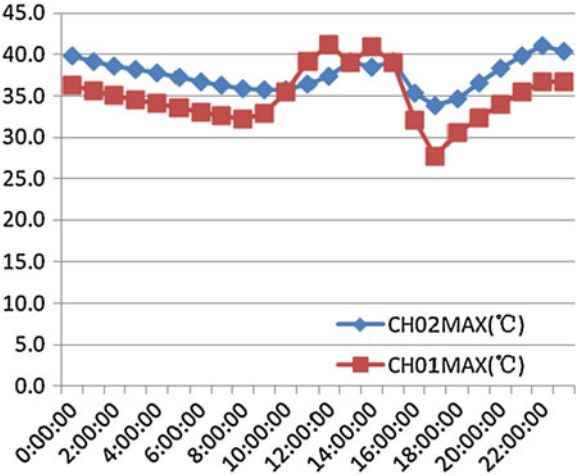

Fig. 15.36 The temperature of supply and return water

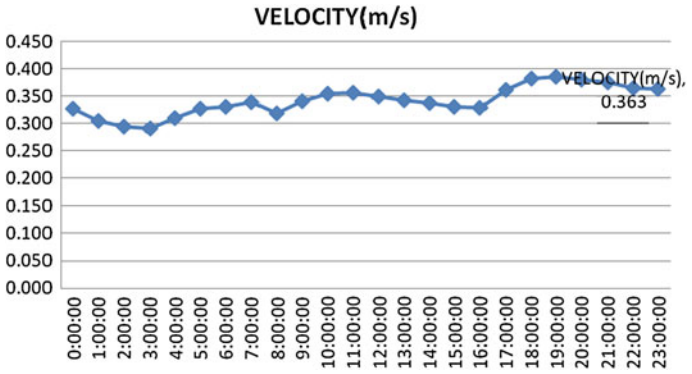

Fig. 15.37 Velocity of solar energy system

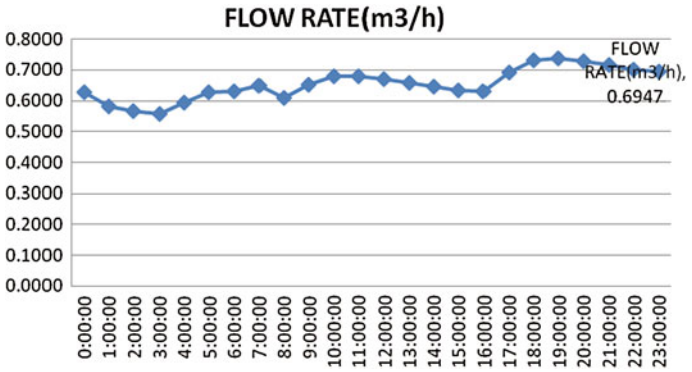

Fig. 15.38 Flow rate of solar energy system

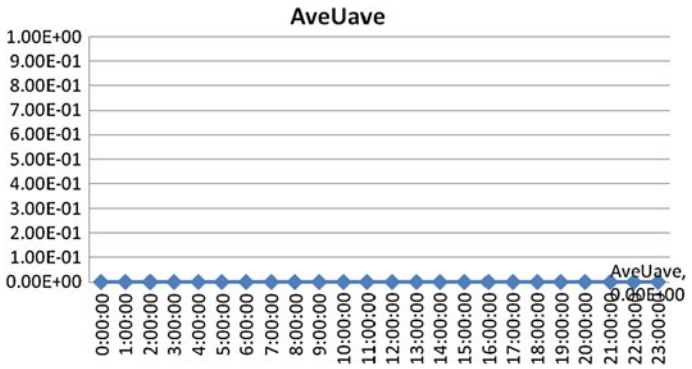

Fig. 15.39 Average voltage of electric heater

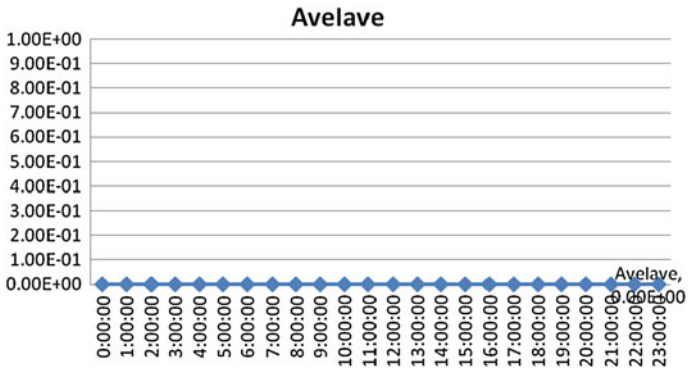

Fig. 15.40 Average current of electric heater

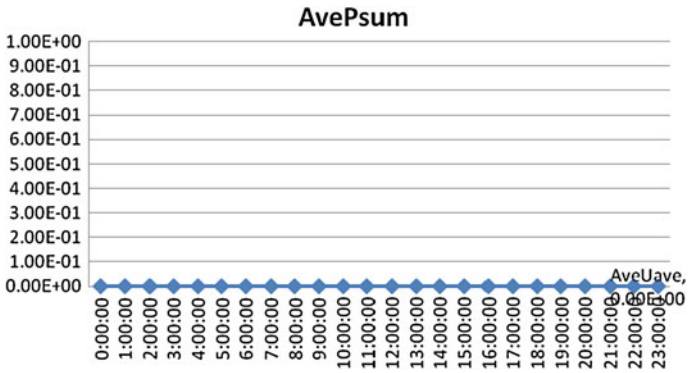

Fig. 15.41 Average power of electric heater

(ii) Power consumption of heat pump unit is 0.80 * 10^2 (kw.h) (iii) Power consumption of electric heater is 0 (kw.h) (iv) Total consumption of system equipments is 0.85 (kw.h)

(v) $\eta_2 = 1 - \frac{Q_2}{AJ_1\eta_1} = 1 - \frac{4.2\,(\mathrm{kj/kg}\cdot{}^\circ\mathrm{C})*0.65\,(\mathrm{t}/h)*5.70\,({}^\circ\mathrm{C})}{30\,(\mathrm{m}^2)*3600*6\,(\mathrm{kj/m}^2\cdot\mathrm{d})*60\,\%} = 0.612$

15.4 Results and Discussion

Under the operation of condition "3", as the evaporation end of solar energy hot water heating system is connected with sewage heat pump unit through the cold tank, the evaporation temperature of heat pump unit increased, leading higher IPLV and less power consumption of heat pump unit compared with condition "1". Compared with condition "2", the loss rate of solar energy hot water heating system under the operation of condition "3" is lower as soon as the temperature of supply and return water of the system is lower. Under the operation of condition "2", indoor heat load is jointly provided by the solar energy hot water heating system and the electric heater, while indoor heat load is jointly provided by the heat pump unit and electric heater under the operation of condition "3", and solar energy is just used as the cold heat source of the heat pump unit, so with the same collector area, the power consumption of condition "2" is more than the power consumption of condition "3". In the case of same power consumption, the collector area of condition "3" is smaller compared with condition "2", which can reduce the investment of solar energy hot water heating system. Under the operation of condition "4", the solar energy hot water heating system can increase its condensing temperature as hot heat source of its condensation end, so the IPLV of heat pump will increase compared with condition "1". Compared with condition "3", the supply and return water of solar energy hot water heating system under condition "4" is higher, which leading a higher loss rate.

As the solar energy hot water heating system can provide partial indoor heat load, under the operation of condition "4" whose power consumption is less than the power consumption of condition "1" and of condition "3" while keeping the power of heat pump unit the same, and in the case of same power consumption of electric heater, the output power is less than the power of condition "1" and of condition "3", which can reduce the investment and running costs of heat pump unit. According to data reduction above, the IPLV of condition "4" is a bit higher than it of condition "3", the total power consumption of condition "2" is less than the power consumption of condition "1", meanwhile the total power consumption of condition "4" is less than the power consumption of condition "3".

15.5 Conclusions

The total power consumption produced during the individual running of the solar energy hot water heating system for heating is lower than the power consumption produced when the heat pump heating being used alone, leading to a better economical efficiency and energy saving ability of system operation. The conjunctive operation of sewage source heat pump unit and solar energy hot water heating system can efficiently improve the IPLV of both systems, as well as reduce the investment and operation costs of the system. When they are connected at the evaporation end, the conjunctive operation of sewage heat pump unit and solar energy hot water heating system can obviously improve the IPLV of the heat pump unit, reducing its operation costs, collector area, and loss rate of solar energy hot water heating system, so as to reduce the operation costs of the solar energy hot water heating system. When they are connected at the condensation end, the conjunctive operation of sewage heat pump unit and solar energy hot water heating system can obviously improve the IPLV of the heat pump unit, reducing its output power, so as to reduce its investment and running costs.

Compared with sewage heat pump unit and solar energy hot water heating system being connected at the evaporation end, the total consumption power of the conjunctive use at the condensation end is lower, leading to a better economical efficiency and energy saving ability of system operation.

Acknowledgments This study is supported by National Science & Technology Pillar Program during the 12th Five-Year Plan Period (2012BAJ26B02).

References

1. Chang MJ, Chow LC, Chang WS (1991) Improved alternating-direction implicit method for solving transient three-dimensional heat diffusion problems (B). pp. 69–84. Taylor & Francis, New york
2. Omer AM (2008) Renewable building energy systems and passive human comfort solutions. Renew Sustain Energy Rev12(6):1562–1587
3. Ochoa CE, Capeluto IG (2008) Strategic decision-making for intelligent buildings: comparative impact of passive design strategies and active features in a hot climate. Build Environ 43(11):1829–1839
4. Li DHV, Wong SL (2007) Daylighting and energy implications due to shading effects from nearby buildings. Appl Energy 84(12):722–729
5. Ghisi E, Tinker JA (2005) An ideal window area concept for energy efficient integration of daylight and artificial light in buildings. Build Environ 40(1):51–60

Chapter 16
Operation Regulation of Combined District Heating Systems with Multiple Large-Scale Peak-Shaving Heat Sources

Haichao Wang, Wenling Jiao, Chengzhao Jiang, Risto Lahdelma and Pinghua Zou

Abstract Combined district heating is one of the development trends of central heating in China, mainly due to its high flexibility, reliability, and energy saving potential. In this paper, we analyzed the applicable operation regulation ways for a combined district heating system with combined heat and power (CHP) plant as the basic heat source and two large-scale coal- and gas-fired boilers in primary heating network as the peak-shaving heat sources. Four operation regulation ways were studied in the paper, including quality regulation in different phases (alternative 1), quality–quantity regulation (alternative 2), quality regulation before combined heating and quality–quantity regulation after combined heating (alternative 3), quality regulation before combined heating and quantity regulation after combined heating (alternative 4). The results indicate that alternative 1 is constrained by the design supply water temperature of CHP plant. Alternative 2 has a relative high possibility to lead to hydraulic maladjustments. Alternative 4 requires high management capabilities and sound automatic control devices, therefore alternative 3 is recommended as the most applicable operation regulation way.

Keywords Combiend district heating system · Primary network · Operation regulation · Peak-shaving heat sources · Combined heat and power (CHP)

H. Wang (✉) · R. Lahdelma
Department of Energy Technology, Aalto University School of Engineering, 14100 FI 00076 Espoo, Finland
e-mail: haichao.wang@aalto.fi

H. Wang · W. Jiao · P. Zou
School of Municipal and Environmental Engineering, Harbin Institute of Technology, Harbin 150090, China

C. Jiang
District Heating Co., Ltd of Dalian Development Zone, Dalian 116600, China

A. Li et al. (eds.), *Proceedings of the 8th International Symposium on Heating, Ventilation and Air Conditioning*, Lecture Notes in Electrical Engineering 262,
DOI: 10.1007/978-3-642-39581-9_16,

16.1 Introduction

The district heating (DH) in China is coal-based, e.g., coal-fired combined heat and power (CHP) plants and district boilers. In the near future, coal will still dominate the fuel market of DH in China with projection share still more than 50 % even by the year of 2050 [1]. The traditional DH systems in China face some severe problems, including low energy efficiency, high energy consumption, and ambient air pollution, etc. In order to alleviate these problems, combined district heating system should be used due to due to its high flexibility, reliability, and energy saving potential according to the experiences from some developed countries with advanced DH sectors [2]. For such combined district heating systems, we should highlight an important parameter named basic heat load ratio (β), which indicates the share of basic heat load supplied by basic heat source(s) in relation to the design heat load.

In this paper, we introduce a combined district heating system with multiple large-scale peak-shaving heat sources in primary heating network. The basic heat source is CHP plant and there are two peak-shaving heat sources, a coal-fired boiler, and a gas-fired boiler (see Fig. 16.1). The reason that we adopt a gas-fired boiler in the study is that the ultimate way to improve the atmospheric environment is to change the energy structure [3, 4], and under the background of energy structure reformation and promotion in natural gas industry in China, we believe natural gas can penetrate into the DH market in China. Finally, in order to make full use of the advantages of combined district heating systems, operation regulation ways should be taken into account seriously.

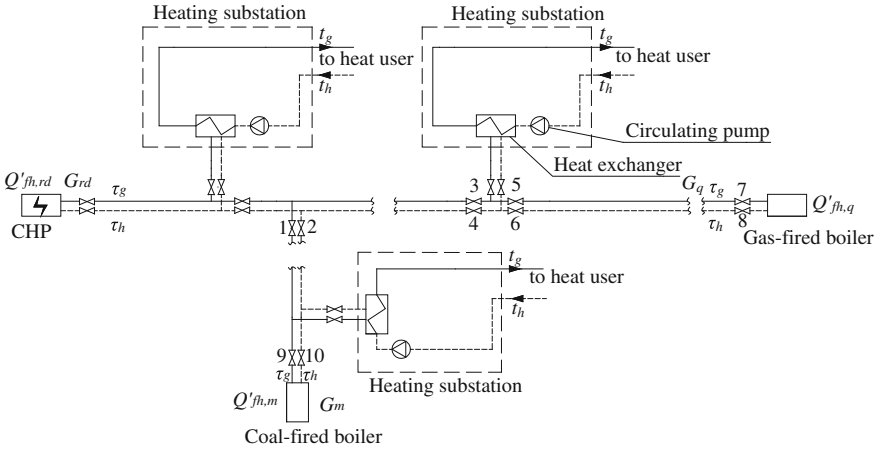

Fig. 16.1 Sketch of the combined district heating system with primary peak heating

16.2 Objective Combined District Heating System

The sketch of the objective combined district heating system with CHP plant as basic heat source and two large coal- and gas-fired boilers as peak-shaving heat sources is demonstrated in Fig. 16.1.

The design heat load of this combined district heating system is:

$$Q' = Q'_{fh,jb} + Q'_{fh,tf} = Q'_{fh,rd} + Q'_{fh,m} + Q'_{fh,q} \tag{16.1}$$

where Q' is the design heat load of the combined district heating system; $Q'_{fh,jb}$ and $Q'_{fh,tf}$ are the design basic heat load and design peak-shaving heat load; $Q'_{fh,rd}$, $Q'_{fh,m}$ and $Q'_{fh,q}$ are the design heat loads of CHP plant, coal-fired boiler, and gas-fired boiler. All the design heat loads are in megawatts (MW).

The design flowrate of the combined district heating system is:

$$G' = \frac{3600 \times Q'}{c_s(\tau'_g - \tau'_h)} \tag{16.2}$$

where G' is the design flowrate of the combined district heating system, *t/h*; c_s is the heating capacity of water, $c_s = 4.1868$ kJ/(kg·K); τ'_g and τ'_h are design supply and return water temperatures in the primary network, °C.

The basic heat load ratio of CHP plant (β_1) is:

$$\beta_1 = \frac{Q'_{fh,rd}}{Q'} \tag{16.3}$$

The basic heat load ratio of CHP plant and coal-fired boiler (β_2) takes form:

$$\beta_2 = \frac{Q'_{fh,rd} + Q'_{fh,m}}{Q'} \tag{16.4}$$

In the study, we assume $\beta_1 = 0.6$, $\beta_2 = 0.8$. The design supply and water temperatures of primary and secondary network are 130/70 °C and 85/60 °C; the exponent of heat transfer coefficient of radiators $b = 0.3$. In addition, quality regulation is used in secondary network to enhance the hydraulic stability of the system; and the applicable regulation ways used in primary network are shown in Table 16.1.

Table 16.1 The regulation alternatives of objective combined district heating system

Alternative	Regulation ways in primary network
1	Quality regulation in different phases
2	Quality–quantity regulation
3	Quality regulation before combined heating and quality–quantity regulation after combined heating
4	Quality regulation before combined heating and quantity regulation after combined heating

16.3 Analyses of Operation Regulation Alternatives

16.3.1 Regulation Alternative 1

This alternative divides the heating season into several stages according to the outdoor temperature t_w; quality regulation is used in all stages but with different flowrates. In this study, heating season is divided into three stages: (1) $\bar{G}_{yi} = \beta_1$, when $t_{w1} \le t_w < 5\ ^\circ\mathrm{C}(\bar{Q}_k < \bar{Q} \le \beta_1$, $\bar{Q}_k$ is the start relative heat load at $t_w = 5\ ^\circ\mathrm{C}$); (2) $\bar{G}_{yi} = \beta_2$, when $t_{w2} \le t_w < t_{w1}(\beta_1 < \bar{Q} \le \beta_2)$; and (3) $\bar{G}_{yi} = 1$, when $t'_w \le t_w < t_{w2}(\beta_2 < \bar{Q} \le 1)$.

The supply and return water temperatures in primary network can be calculated according to the regulation equations of this alternative and shown in Fig. 16.2a, the flowrates in the 3 stages are illustrated in Fig. 16.2b.

It can be concluded from Fig. 16.2 that, quality regulation in different phases (alternative 1) can reduce the electricity consumption for water circulation, and maintain relative stable hydraulic condition in each regulation stage. But its application is apparently constrained by the design supply water temperature of CHP plant, because the supply water temperature should not exceed the design value.

16.3.2 Regulation Alternative 2

In the whole heating season, the primary network are operated using quality–quantity regulation (alternative 2). When $t_{w1} \le t_w < 5\ ^\circ\mathrm{C}(\bar{Q}_k < \bar{Q} \le \beta_1)$, the flowrate of CHP plant increases along with the increasing value of $\bar{Q}$; when $t_{w2} \le t_w < t_{w1}(\beta_1 < \bar{Q} \le \beta_2)$, CHP plant operates under the design heat load, and coal-fired boiler starts operation; during the stage of $t'_w \le t_w < t_{w2}(\beta_2 < \bar{Q} \le 1)$, CHP and coal-fired boiler all reach the design heat loads, while gas-fired boiler is put into service.

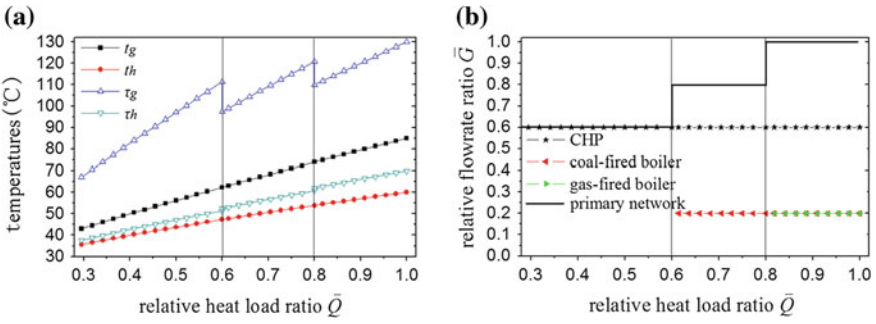

Fig. 16.2 Temperature and flowrate regulation curves for alternative 1. **a** temperature regulation curve. **b** flowrate regulation curve

The temperature regulation curve can be obtained according to the regulation equations of this kind of regulation way, and shown in Fig. 16.3a. The flowrate regulation curve is determined as following,

1.

$$t_{w1} \le t_w < 5\,^{\circ}\mathrm{C} (\bar{Q}_k < \bar{Q} \le \beta_1)$$

the flowrate of CHP plant is:

$$G_{rd} = \bar{Q} G' \tag{16.5}$$

2.

$$t_{w2} \le t_w < t_{w1} (\beta_1 < \bar{Q} \le \beta_2)$$

the flowrates of CHP plant and coal-fired boiler are:

$$G_{rd} = \beta_1 G' \tag{16.6}$$

$$G_m = (\bar{Q} - \beta_1) G' \tag{16.7}$$

3.

$$t'_w \le t_w < t_{w2} (\beta_2 < \bar{Q} \le 1)$$

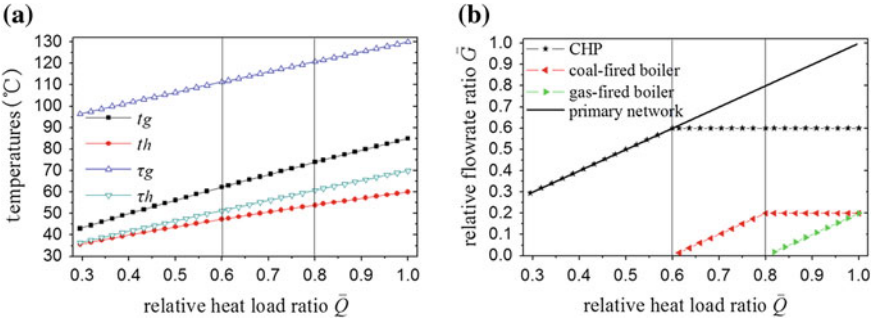

Fig. 16.3 Temperature and flowrate regulation curves for alternative 2. **a** temperature regulation curve. **b** flowrate regulation curve

in this period, the flowrate of CHP plant maintains stable as shown in Eq. (16.6), and the flowrates of coal- and gas-fired boilers are:

$$G_m = (\beta_2 - \beta_1)G' \tag{16.8}$$

$$G_q = (\bar{Q} - \beta_2)G' \tag{16.9}$$

The flowrate regulation curve of regulation alternative 2 is shown in Fig. 16.3b.

Figure 16.3 indicates that the start relative flowrate is only 0.3, which may lead to severe hydraulic maladjustment. Although, the electricity consumption for water circulation is small but the supply water temperatures maintains relative high compared to other alternatives in the whole heating season, which reduce the thermal efficiency of CHP plant and electricity generation from CHP.

16.3.3 Regulation Alternative 3

Regulation alternative 3 originates from alternative 2, it just changes the regulation from quality–quantity to quality regulation before combined heating in order to reduce the hydraulic maladjustment when $\bar{Q}$ is small. The temperature regulation curve under this regulation alternative is indicated in Fig. 16.4a.

The flowrate regulation curve is determined as following,

1.

$$t_{w1} \le t_w < 5\,^{\circ}\mathrm{C}(\bar{Q}_k < \bar{Q} \le \beta_1)$$

the flowrate of CHP plant is the same as Eq. (16.6).

2.

$$t_{w2} \le t_w < t_{w1}(\beta_1 < \bar{Q} \le \beta_2)$$

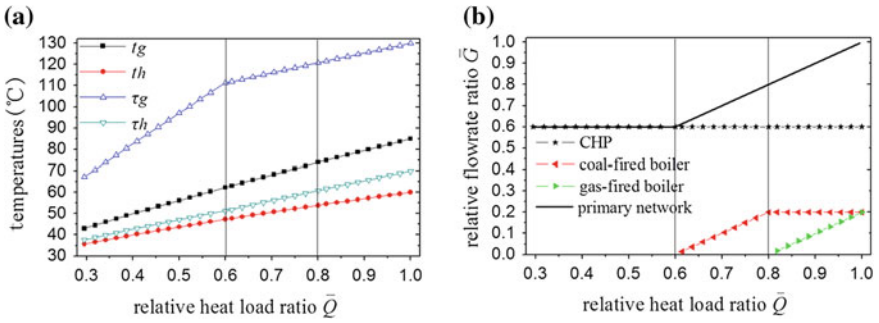

Fig. 16.4 Temperature and flowrate regulation curves for alternative 3. **a** temperature regulation curve. **b** flowrate regulation curve

the flowrate of CHP plant does not change, and the flowrate of coal-fired boiler is the same as Eq. (16.7).

3.

$$t'_w \le t_w < t_{w2} (\beta_2 < \bar{Q} \le 1)$$

the flowrate of CHP plant still maintains stable in this period, and the flowrates of coal- and gas-fired boilers are expressed as in Eqs. (16.8) and (16.9).

The flowrate regulation curve of regulation alternative 3 is shown in Fig. 16.4b.

It can be concluded from Fig. 16.4 that the regulation alternative 3 reduce the supply water temperatures of CHP at $\bar{Q} \le \beta_1$, thus increase the thermal efficiency compared to regulation alternative 2. Besides, this regulation way also reduces the possibility of hydraulic maladjustment.

16.3.4 Regulation Alternative 4

As to regulation alternative 4, quality regulation is adopted before combined heating and quantity regulation is used after combined heating. The temperature regulation curve under this regulation alternative is shown in Fig. 16.5a.

The flowrate regulation curve is determined as following,

1.

$$t_{w1} \le t_w < 5\,^{\circ}\mathrm{C} (\bar{Q}_k < \bar{Q} \le \beta_1)$$

CHP plant reaches the design heat load at $t_w = t_{w1}$, and then the flowrate is:

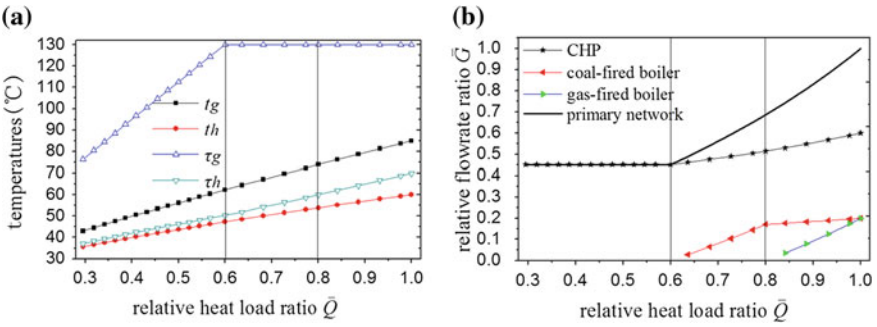

Fig. 16.5 Temperature and flowrate regulation curves for alternative 4. **a** temperature regulation curve. **b** flowrate regulation curve

$$G_{rd} = \frac{\beta_1 \times 3600 \times Q'}{c_s(\tau'_g - \tau_h^{tw1})} \tag{16.10}$$

where τ_h^{tw1} is the return water temperature at $t_w = t_{w1}$.

2.

$$t_{w2} \le t_w < t_{w1} (\beta_1 < \bar{Q} \le \beta_2)$$

$$G_{rd} = \frac{\beta_1 \times 3600 \times Q'}{c_s(\tau'_g - \tau_h)} \tag{16.11}$$

$$G_m = \frac{(\bar{Q} - \beta_1) \times 3600 \times Q'}{c_s(\tau'_g - \tau_h)} \tag{16.12}$$

3.

$$t'_w \le t_w < t_{w2} (\beta_2 < \bar{Q} \le 1)$$

the flowrate of CHP plant maintains stable as Eq. (16.15), and the flowrates of coal- and gas-fired boilers are:

$$G_m = \frac{(\beta_2 - \beta_1) \times 3600 \times Q'}{c_s(\tau'_g - \tau_h)} \tag{16.13}$$

$$G_q = \frac{(1 - \beta_2) \times 3600 \times Q'}{c_s(\tau'_g - \tau_h)} \tag{16.14}$$

The flowrate regulation curve of regulation alternative 4 is shown in Fig. 16.5b.

Figure 16.5 shows that the flowrate of CHP plant is small which can save electricity consumption for water circulation to some extent; however, the thermal efficiency of CHP is reduced due to the high supply water temperature. The application of this regulation alternative need water pumps equipped with variable frequency units and very sound automatic control devices, because the flowrate changes constantly by quantity regulation after combined heating.

16.4 Conclusions

In this paper, we studied the operation regulation ways for the combined district heating system with CHP plant as basic heat source and two coal- and gas-fired boilers as peak-shaving heat sources. Four operation regulation ways were studied,

including quality regulation in different phases (alternative 1), quality–quantity regulation (alternative 2), quality regulation before combined heating and quality–quantity regulation after combined heating (alternative 3), quality regulation before combined heating and quantity regulation after combined heating (alternative 4). We found that pure quality regulation does not satisfy such kind of combined district heating systems, because peak-shaving boilers are put into service only when outdoor temperature is too low. Namely, the applicable operation regulation ways in primary network should be of variable flowrate control. And the regulation stages for each regulation alternative should be divided into several stages according to the value of β. The results indicate that alternative 1 is constrained by the design supply water temperature of CHP plant. Alternative 2 can save the electricity consumption of circulation water pumps, but it also has a relative high possibility to lead to hydraulic maladjustments. Alternative 3 overcomes the shortcomings of alternative 2. Alternative 4 is more energy-efficient than alternative 3, but during the quantity regulation stage, the flowrate varies constantly by quantity regulation, which requires high management capabilities and sound automatic control devices. It is not easy to be realized compared to alternative 3, therefore alternative 3 is recommended as the most applicable operation regulation way for the combined district heating systems with peak heating in primary network.

References

1. Zhang M, Mu HL, Ning YD (2009) Accounting for energy-related CO2 emission in China, 1991–2006. Energy Policy 37(3):767–773
2. Wang HC, Jiao WL, Lahdelma R, Zou PH (2011) Techno-economic analysis of a coal-fired CHP based combined heating system with gas-fired boilers for peak load compensation. Energy Policy 39(12):7950–7962
3. Marbe Â, Harbvery S, Berntsson T (2006) Technical, environmental and economic analysis of co-firing of gasified biofuel in a natural gas combined cycle combined heat and power plant. Energy 31(10):1614–1619
4. Tromborg E, Bolkesjo TF, Solberg B (2007) Impacts of policy means for increased use of forest-based bio-energy in Norway. Energy Policy 35(12):5980–5991

Chapter 17
Study on the Energy System of Ice Storage Air Conditioning of China World Trade Center Phase 3 by the Method of 'Local-Global Optimization'

Zonggen Si, Hongqi Li and Yongpeng Shen

Abstract This article adopts the method of 'Local-Global optimization' to analyze the energy system of ice storage air conditioning of China World Trade Center Phase 3 by the tool of eQuest energy consumption simulation software. We found the influential factors of the air conditioning system through the actual measurement and simulation analysis results of energy consumption of air conditioning system. Then we adopt the method of 'Local-Global optimization' from the Angle of energy system and combine with the actual condition of the ice storage air conditioning, we make three optimization scheme, which are reducing cooling water temperature difference, adopting variable flow rate chilled water pumps, and improving the fan delivery ratio. And then we analyze energy consumption change of three schemes and find out the interactive effect of the local system. Finally, we sort the energy saving effect and find out the optimal overall optimization scheme.

Keywords Ice storage cold · Energy system · 'Local-global optimization'

Recently, Most of energy saving of the air conditioning was focused on a part energy saving research, although the research component was energy efficient, but other components were increased energy consumption; so the overall system energy-saving effect was discounted, even more energy-consuming, the COP of unit was improved, but it did not save money. Based on this problem, this article uses a new energy-saving concept. From the point of view of the entire energy system, not only analyzes ice storage energy system refrigeration unit, pump systems, cooling tower systems, fan systems, but also analyzes the local system optimization contribution to the overall system energy saving, as well as analyzes the impact on other system. Then sort the energy-saving measures and their effects, and analysis of the global energy-saving effect, in order to identify the most energy-efficient, and most effective energy-saving measures.

Z. Si · H. Li (✉) · Y. Shen
College of Environmental and Energy Engineering, Beijing University of Technology, Beijing 100022, China
e-mail: hongqili@sina.com

A. Li et al. (eds.), *Proceedings of the 8th International Symposium on Heating, Ventilation and Air Conditioning*, Lecture Notes in Electrical Engineering 262,
DOI: 10.1007/978-3-642-39581-9_17,

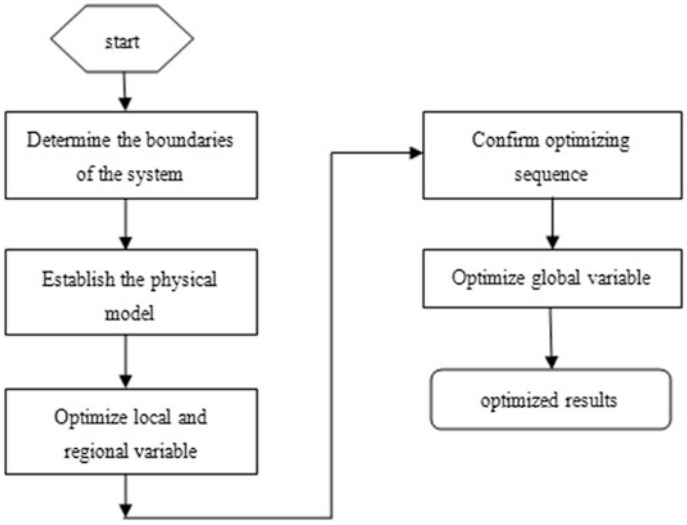

Fig. 17.1 The 'local-global optimization method'

'Local-global optimization method' is under the guidance of this idea. The method makes various subsystems cooperate with each other to achieve the overall system optimization in the overall goal of the system. The local optimization means that a large system decomposed into a number of simple subsystem, in order to achieve the local optimization of subsystem. Global optimization is that local subsystem information feedback to large systems, and the large systems weigh the system's overall mission and overall goal, then send the instructions to the various subsystems, exchange of information between large system and subsystem repeated by this way, the entire system are optimize.

Figure 17.1 is the main step of the 'local-global optimization method'.

17.1 Ice Storage Energy System

Now Ice storage is widely used in the storage air conditioning system, the study of ice storage energy system performance analysis and evaluation is constantly being improved, The traditional studies based on the first law of thermodynamics, and analyze energy balance of the system, Then some scholars use exergy analysis to ice storage systems based on the second law of thermodynamics, they established the exergy loss model of each components in the system, and presented the exergy efficiency as the evaluation of the thermal performance of the system. However, it should be pointed out that only from the angle of exergy to analysis and evaluation system still has limitations. Exergy in the system always equivalent, it does not mean the price of exergy equivalent everywhere. From the thermodynamic point

of view, the different forms of energy has exergy can be transformed into each other, but from the economic point of view, exergy value of different forms of energy are not equivalent. Consider the actual process exergy is not equivalent and economic factors, Tribus, and Evans defined as thermoeconomic.

This article analyzes China World Trade Center Phase 3 ice storage air conditioning system base on the energy systems analysis model of thermo economic: 'local-global optimization method' analysis model.

17.1.1 Input Model of Ice Storage Energy System

Beijing International Trade Center three uses ice storage air conditioning cooling. The ice storage air conditioning energy system consists mainly of four energy subsystems: refrigeration units, pumps, fans, cooling towers. The input model parameters of energy system as shown in Table 17.1

17.1.2 Actual Energy Consumption of Ice Storage Energy Systems Compare with Simulation Results

The building simulation calculation is 8760 h throughout the year by hourly energy simulation software EQUEST, the computing core of the software is DOE-2.2 which is the advanced version of DOE-2, and have many optimization.

After completion of the modeling process, we use the BIN format typical meteorological year data of Beijing to simulated calculation, and compare the simulation results with the actual annual energy consumption of 2012 to verify the accuracy of the model.

Table 17.1 The input model parameters of energy system

Equipment	Parameter	Quantity
Double condition host	Air conditioning condition:3268.5 kW Ice conditions:refrigerating capacity 2614.8 kW input power 653.7 kW	7
Glycol water pump	Flow (158 l/s), input power 55 kW efficiency 75 %	6
Primary frozen water pump	Flow (206 l/s), input power 75 kW efficiency 75 %	12
Secondary frozen water pump	Flow (231 l/s), input power 80 kW efficiency 75 %	15
Cooling water pump	Flow (370 l/s), input power 100 kWefficiency 75 %	9
Cooling tower	Heat dissipating capacity (1978 kW) Fan Motor Power:7.5 kW	22
Fan	VAV BOX Fan delivery ratio 0.00088 kW/m^3 h	

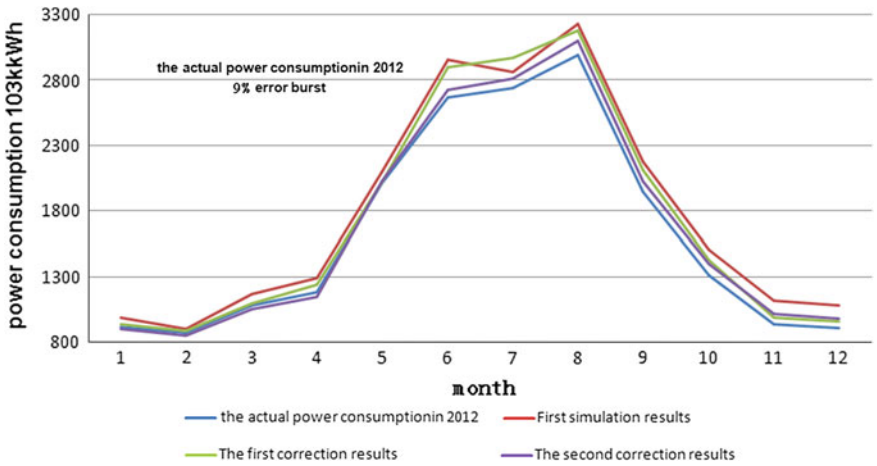

Fig. 17.2 Simulation results compared with the actual results

Compared the initial calculation of the simulation results with the actual data, we make two amendments to the model, in order to make the model more in line with the actual working of construction.

- Using actual meteorological data of 2012 instead of typical meteorological year meteorological data in Beijing
- Replace the model assumes value with the actual lighting load: hall instead 15 W/m^2, office instead 10 W/m^2, garage instead 3.2 W/m^2, corridor instead 5 W/m^2.

Simulation results compared with the actual results as shown (Fig. 17.2).

Although the simulation results and the actual results still have a certain deviation, but the deviation within the allowable range, which is mainly due to the daily usage of the actual construction.

17.2 Energy System Optimization Program

17.2.1 Analysis Models

For such a large ice storage system, to achieve an overall optimization is quite difficult. Because of the complex structure of the energy system, many factors like functional integration, a lot of evaluation, and so on, it is difficult to determine the systems if they are optimal for all indicators. In general, it only using a local optimization method cannot make the overall system, even a partial improvement but the overall performance deterioration.

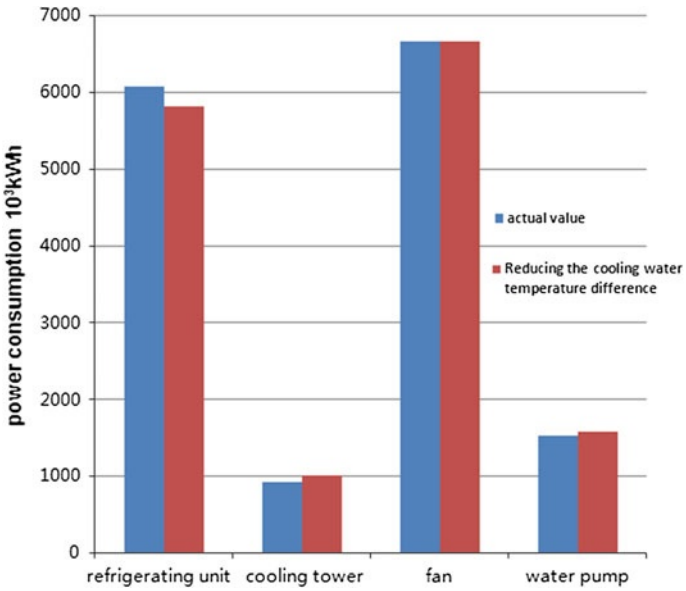

Fig. 17.3 Reducing the cooling water temperature difference

Therefore, from the point of view of the energy system and based on "local-overall optimization method" energy system, it also combined with the actual situation of the building, We propose three local optimization of energy-saving programs: (1) reduce the cooling water temperature difference from Δ6 °C to Δ4 °C, to improve the COP of the refrigeration unit; (2) pump variable flow; (3) improve the delivery of the fan ratio increased from 0.00088 kW/m^3 h. to 0.000647 kW/m^3 h.

Figures 17.3, 17.4, 17.5 are a simulation results of the three energy-saving schemes. Through the analysis of simulation results, we will find out the mutual influence between the various local energy conservation measures as well as the contribution to the overall energy efficiency, then sort the effect of energy saving and identify the overall optimal solution.

17.2.2 Analysis of Results

(1) It can be seen from Fig. 17.3, when the temperature difference of cooling water between inlet and outlet becomes smaller, the COP of the refrigeration unit is improvement, but the energy consumption of pumps and cooling tow is increased. The energy consumption of refrigeration units reduces by 272,000 kWh, the energy consumption of the cooling tower increases by 50,000 kWh. Although reducing the temperature difference of cooling water between inlet

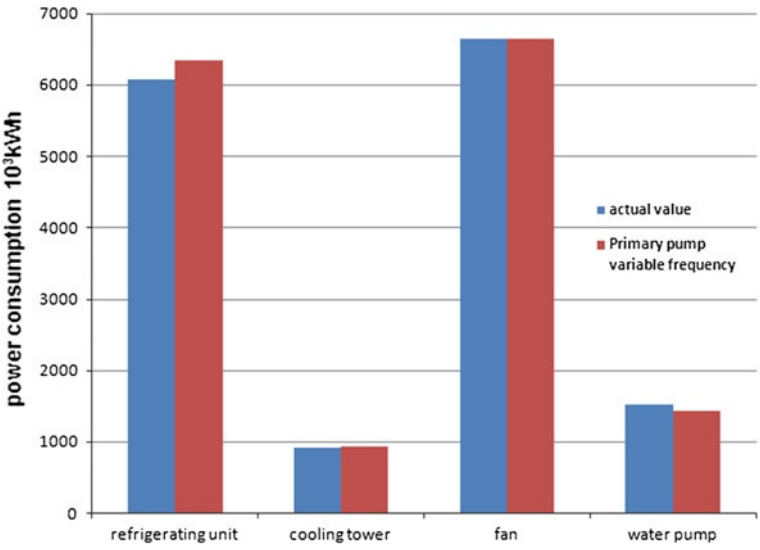

Fig. 17.4 Primary pump variable frequency

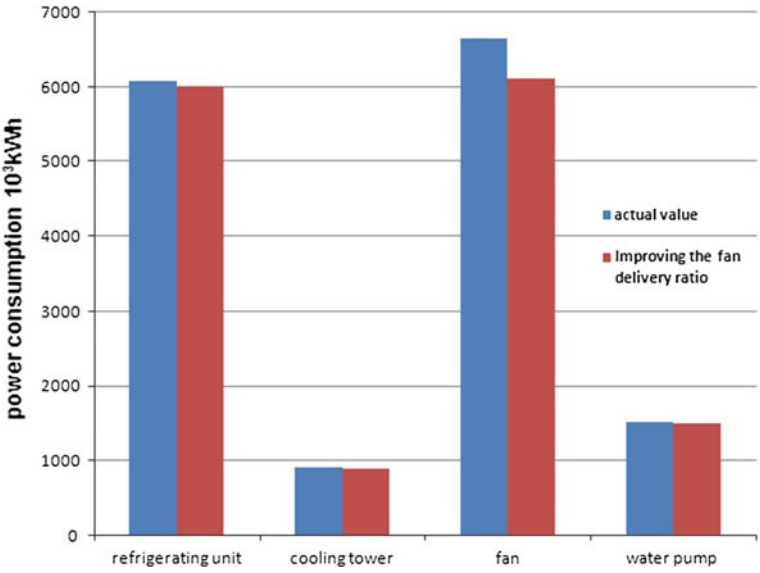

Fig. 17.5 Improving the fan delivery ratio

and outlet can increase the refrigeration efficiency of the refrigeration unit, but the energy consumption of pump is increased. So analysis the energy system as a whole, the overall energy saving, but the energy-saving effect has been discounted.

(2) It can be seen from Fig. 17.4, when chilled water pump variable flow, the refrigeration efficiency of the refrigeration unit COP decreased and the energy consumption of pump is decreased. The energy consumption of refrigeration unit increases by 259,000 kWh, and the energy consumption of pump reduces by 90,000 kWh. According to pump, variable flow operation is good for energy saving, but it has some influence on refrigeration unit and make COP decreased. So analyze the energy system as a whole, measure whether once chilled water pump variable flow operation is saving energy, consider both the energy saving of pump and energy consumption of the refrigeration unit.
(3) It can be seen from Fig. 17.5. by Improving the delivery ratio of fan, COP of the refrigeration unit, pumps, cooling tower, energy consumption of fan has been reduced. Energy consumption of refrigeration unit reduces by 61,000 kW, energy consumption of pump reduces by 16,000 kWh, energy consumption of cooling tower reduces by 10,000 kWh, and energy consumption of fan reduces by 524,000 kWh.

17.2.3 Global Optimization

From the point of view of the energy system, we sort the effect of the local optimization solution, finally gave up 2 program and takes 1 and 3 programs into account, The energy-saving rate of overall optimization is 4.5 %. Meanwhile, the total initial investment of overall optimization model is 2.49 million yuan, it can save 541,600 yuan per year, If not considering interest rates and other factors, the initial investment can be recovered in 4.6 years.

17.3 Conclusion

(1) We use eQuest [1] energy simulation software to build the calculation model of China World Trade Center Phase 3 ice storage air conditioning system, then the model is done twice correction, the error of the simulation results and the actual energy consumption data is within an allowable range, The maximum error 1 month is 8.52 % and the maximum error 1 year is 2.39 %. Calibrated model can basically reflect the actual energy use of the building, it can help property managers make better energy management of the buildings, and make up the lack of data cased by lack of field testing conditions.
(2) In the local optimization program 2, although the energy consumption of pump is decreased, but the COP of refrigeration unit is decreased too. Therefore, from the point of view of the energy system, measurement of the energy efficiency standards should be consider the overall energy conservation

rather than only considering a separate local energy saving. The local energy conservation does not means the overall energy conservation, it may consume more energy.

Reference

1. eQuest V3.64 manual[CP] (2006) The US Department of Energy

Chapter 18
Experimental Study on Heat Transfer of Pool Boiling and In-tube Condensation

Ming Wang and Yajun Guo

Abstract An experimental study was conducted on pool boiling heat transfer and in-tube condensing heat transfer in different working conditions. Analysis the total heat transfer, so as to verity weather tank can meet remove the heat amount produced by electric heating equipment in steam generator. Also the influence of each experimental parameters was analyzed on heat transfer coefficient, as well as the pool boiling heat transfer of boiling scene. The result shows that, steam in tube was condensed into saturate water after 3 min 2 MPa and 2.4 m in 5 MPa. This paper analyzes the relations among pool boiling heat transfer coefficient, in-tube condensing heat transfer coefficient, and total heat transfer coefficient. It concluded that, for 2 MPa, pool boiling heat transfer coefficient was the highest. The contrast of system total heat transfer capacity and pool boiling heat transfer capacity shows that their error was in the range of rationale, which meant the heat transfer capacity of cooling tank can remove system residual heat.

Keywords Pool boiling heat transfer · In-tube condensing heat transfer · Heat transfer coefficient · Mass flow · Heat flux

18.1 Introduction

Pool boiling and in-tube condensation heat transfer were important parts of thermal hydraulics and were applied in many nuclear reactor systems, such as passive residual heat removal system [1]. Compared with active system, passive residual heat removal system was not only needs less facilities but also eliminates the dependence on external power supplying operation, therefore, it had a higher

M. Wang (✉) · Y. Guo
School of Environmental and Municipal Engineering, Xi'an University of Architecture and Technology, Xi'an 710055, China
e-mail: andyroddickming@yahoo.com.cn

A. Li et al. (eds.), *Proceedings of the 8th International Symposium on Heating, Ventilation and Air Conditioning*, Lecture Notes in Electrical Engineering 262,
DOI: 10.1007/978-3-642-39581-9_18,

security and reliability [2]. Presently however, the research on low-pressure pool boiling and in-tube condensation heat transfer in the passive system as the secondary side of nuclear reactor is inadequate, so the optimized design of the passive residual heat removal system is significant to improve the safety of nuclear power system.

18.2 Experimental Device and Research Method

18.2.1 Experimental System

The experimental system was the secondary side of passive residual heat removal system, and its working medium was water. The system consists of two circuits: the heating circulation and the condensation circulation. In the heating circulation, the water in steam generator was heated to be steam with high temperature and pressure by low voltage transformer below the generator, and then was conducted to the water tank to finish heat exchange with cooling water. After heat exchange, the steam would change back into water to be heated for another circulation. Condenser was designed to be inclined for the readiness of circulation. In the condensate circuit, cooling water was condensed by condenser and then returned into the water tank over the high-pressure for the next exchange. When this system was used to simulate actual accident conditions, the water pump was closed and passive residual heat removal system relied only on natural cycle to complete the operation of the entire system (Fig. 18.1).

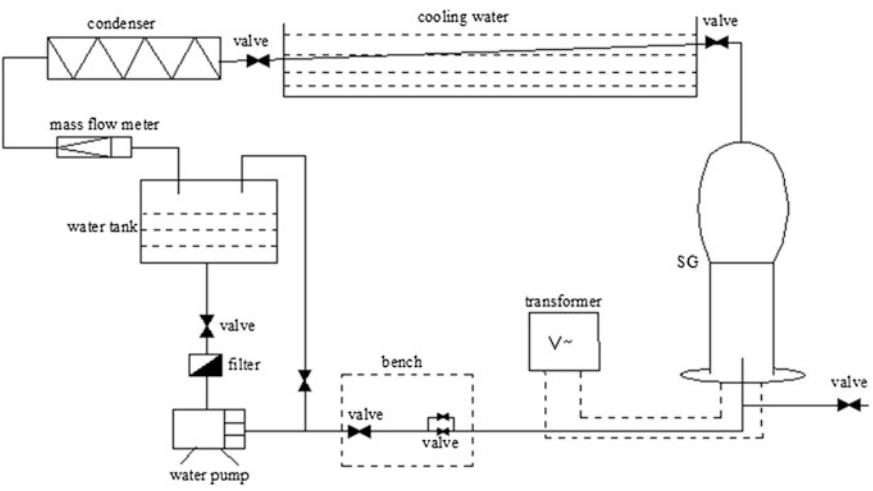

Fig. 18.1 Schematic of experimental system

18.2.2 Experimental Method

Parameters needed to be measured directly in the experiment are as follows: inlet and outlet pressure and flow rate in steam generator; three pressure drops at three different heights; inlet and outlet pressure and flow rate of cooling pipe; outer wall temperature; water temperature in tank; electrical power for heating. In order to analyse the cooling effect of cooling pipe and heat transfer coefficient, five positions were selected for setting thermocouples along the pipe. What's more, in order to obtain inner wall temperature distribution of cooling pipe, along the longitudinal direction of pipe, several thermocouples was set to measured outer wall temperature so as to calculate inner wall temperature.

The experiment was conducted to acquire that whether the passive residual heat removal system can meet the demand of residual heat removing by steady state condensation heat transfer and boiling heat transfer, and thus can be an actual reference for experiments afterward.

18.2.3 Heat Transfer Mechanism

Rohsenow boiling heat transfer correlation (method 1) was based on the bubble perturbation model theory, and it is a pool boiling heat transfer correlation which was taken pipe wall material impact into consideration [3].

$$q = \mu_f r \left[\frac{g(\rho_\mathrm{f} - \rho_\mathrm{g})}{\sigma}\right]^{1/2} \left[\frac{c_\mathrm{pf}(t_\mathrm{w} - t_\mathrm{s})}{C_\mathrm{wf} r \mathrm{Pr}_\mathrm{f}^s}\right]^3 \tag{18.1}$$

μ_f Liquid dynamic viscosity, N·s/m^2
r Latent heat of vaporization, kJ/kg
σ Vapor–liquid surface tension, N/m
c_pf Saturate liquid specific heat, J/(kg·K)
C_wf Experimental constant, combination with pipe wall material and liquid
Pr_f Saturate liquid Prandtl number
s Experience index, for water: $s = 1$, for other liquid: $s = 1.7$

Mihai Aliyev boiling heat transfer correlation (method 2) set up a determine relationship between boiling surface heat transfer coefficient and boiling temperature difference [4]. This pool boiling heat transfer correlation applied to with the pressure from (1-40) $\times$ 10^5Pa.

$$h = C_1 \Delta t^{C2} p^{C3} \tag{18.2}$$

h Boiling surface heat transfer coefficient, W/(m^2·K)
p Boiling adiabatic pressure, MPa
Δt Wall superheat, °C

Chaddoek and Chato based on Nusselt's laminar flow vertical wall theory analytical solution estimated the average surface heat transfer coefficient formula of condensation heat transfer [5](Re < 35000):

$$h = 0.555\left[\frac{g\rho(\rho-\rho_g)\lambda^3 r'}{\mu d(t_s - t_w)}\right]^{1/4} \tag{18.3}$$

t_s Saturate temperature, °C
t_w Inner wall temperature, °C
λ Condensate thermal conductivity, W/(m·K)
ρ Condensate density, kg/m^3
ρ_g Vapor density, kg/m^3
μ Condensate viscosity coefficient, N·s/m^2
r' Correction value of latent heat

18.3 Experimental Results and Discussion

18.3.1 Effects of Mass Flux on Pool Boiling Heat Transfer Coefficient

From Fig. 18.2, the average surface heat transfer coefficient increased as mass flux increased, and the two curves calculated by methods 1 and 2 had nearly the same trends. Heat transfer coefficient of method 1 was a little more than that of method 2, and heat transfer coefficient had a larger increase as mass flux changed in 5 MPa than in 2 MPa. In the same mass flux, the average pool boiling heat transfer coefficient value in 5 MPa was much higher than that in 2 MPa (Fig. 18.3).

18.3.2 Effects of Mass Flux on Pool Boiling Heat Transfer Coefficient

This figure showed the changes in the relationship between condensation heat transfer coefficient and mass flux in 2 and 5 MPa. In both two pressures, the condensation heat transfer coefficient increased with mass flux changed. Comparing with their values of condensation heat transfer coefficient showed the value in 5 MPa was higher than that in 2 MPa (Fig. 18.4).

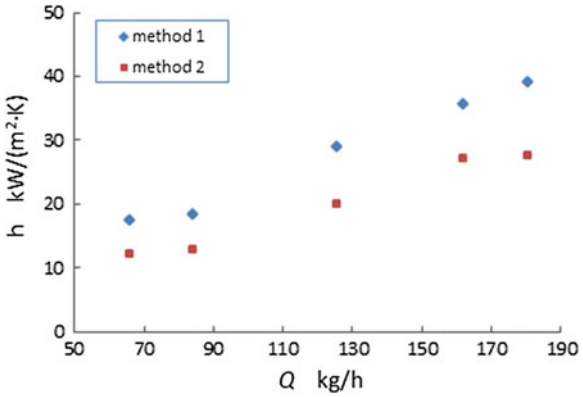

Fig. 18.2 Average heat transfer coefficient in 2 MPa

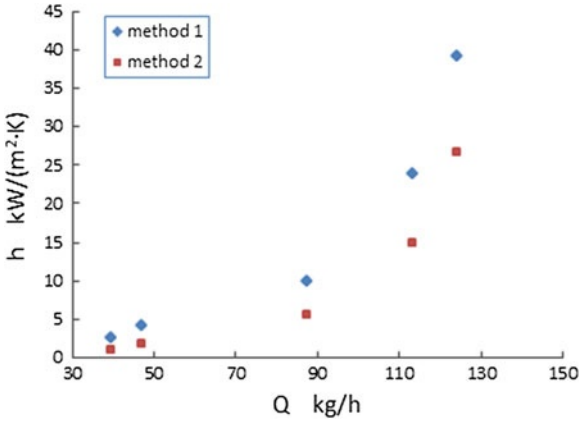

Fig. 18.3 Average heat transfer coefficient in 5 MPa

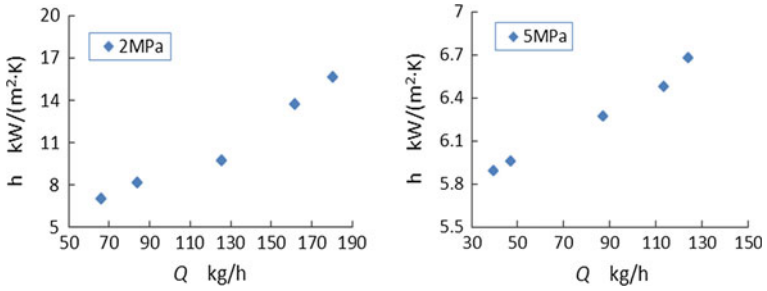

Fig. 18.4 Condensation heat transfer coefficient changed with mass flux

18.3.3 Inner Wall of Condenser Pipe Temperature Distribution

This figure showed that the temperature distribution of inner wall of condenser pipe in 2 MPa. Along the working medium flow direction selected 17 sections on the outside of condenser pipe and calculated their temperature values. From the figure can be seen, the greater the electric heating power, the higher the inner wall temperature of condenser pipe, and the temperature drop existed in the import of condenser pipe, but with the increase of pipe length, the inner wall temperature mainly maintained the same value. The working medium was gas–liquid two phase state in condenser pipe, so the condensate constantly precipitation and went through the export of condenser pipe along the pipe length direction. It concluded that experiment design of condenser pipe can guarantee the idea of experiment expected and meet the requirement of removing residual heat (Fig. 18.5).

Figure 18.6 showed that the inner wall temperature distribution of condenser pipe in 5 MPa. The inner wall temperature increased with electric power increased, and there was significant temperature drop apparent in the entrance of condenser pipe, because outside pipe was belong in pool boiling heat transfer unstable regions. With the increase of pipe length, the inner wall temperature mainly maintained the same value, but the temperature distribution had some slight fluctuations in high heating power. Because of these values fluctuated in a very small extent, which can meet condensation heat transfer of condenser pipe.

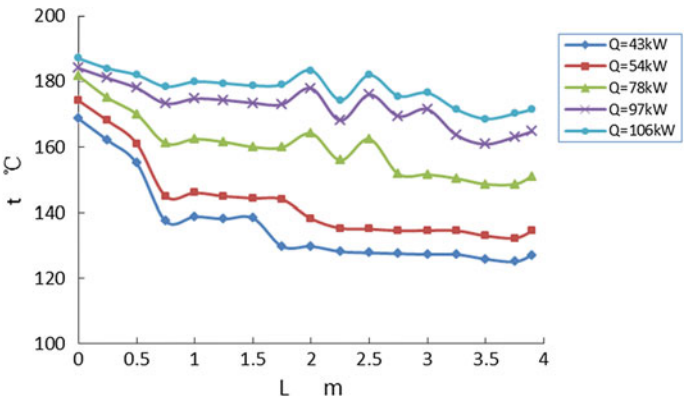

Fig. 18.5 Inner wall temperature distribution of condenser pipe along the pipe length in 2 MPa

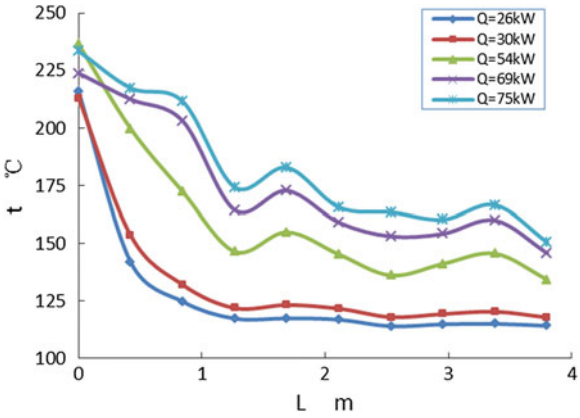

Fig. 18.6 Inner wall temperature distribution of condenser pipe along the pipe length in 5 MPa

18.3.4 Comparison of Two Kinds of Heat Transfer Amount

As shown, pool boiling heat transfer amount and total heat transfer amount changed with mass flux increased. All the heat transfer amount curves increased with mass flux increase. Theoretically total heat transfer amount was equal to pool boiling heat transfer amount, but in fact, they existed some deviation. It can be explained that the pool boiling heat transfer coefficient was calculated by Rohsenow and Mihai Aliyev correlations, and each correlation had some limitation for practical problem, also each physical parameter and operation conditions were diffident, therefore the two pool boiling heat transfer amounts calculated by two methods existed some errors. But the error was in the range of rationale, it meant the heat transfer capacity of cooling tank can remove system residual heat within the experiment pressure (Figs. 18.7, 18.8).

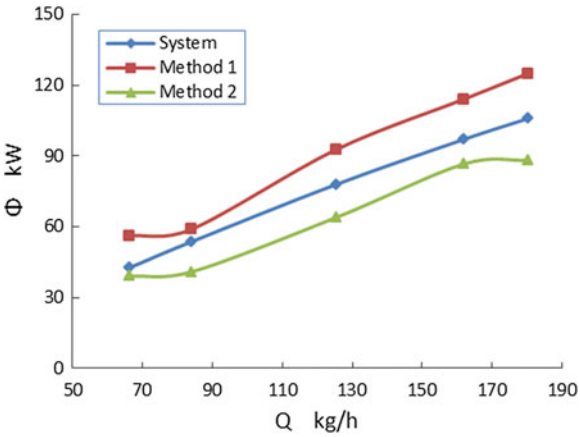

Fig. 18.7 Comparison of pool boiling and total heat transfer amount in 2 MPa

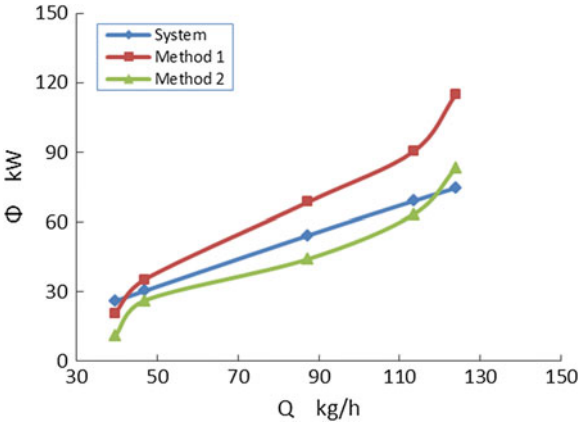

Fig. 18.8 Comparison of pool boiling and total heat transfer amount in 2 MPa

18.4 Conclusion

An experimental study is conducted on pool boiling heat transfer and in-tube condensing heat transfer in different working conditions (including mass flow, heating power, heat flux and pressures of 2 and 5 MPa). The experiment conclusions as follows:

(1) The average surface pool boiling heat transfer coefficient increased with mass flux increased, and in the same mass flux, the average pool boiling heat transfer coefficient value in 5 MPa was much higher than that in 2 MPa.
(2) The average surface condensation heat transfer coefficient increased with mass flux increased, and in the same mass flux, the average condensation heat transfer coefficient value in 2 MPa was higher than that in 5 MPa.
(3) The greater the electric heating power, the higher the inner wall temperature of condenser pipe, but with the increase of pipe length, the inner wall temperature mainly maintained the same value. It concluded that experiment design of condenser pipe can guarantee the requirement of removing residual heat.
(4) Pool boiling heat transfer amount and total heat transfer amount did not coincide, but their values were in the range of allowable error, that means the heat transfer capacity of cooling tank can remove system residual heat within the experiment pressure.

References

1. Li Yong (2009) Harbin engineering university. Experimental study on boiling heat transfer enhancement of passive residual removal heat exchanger. 1–3. China
2. He Weidong (1989) Unclear power engineering. Comment on advanced pressurized water reactor AP600. 10(3):63–70. China

3. Ralph L, Webb, Nac-hyun Kim (2006) Taylor and Francis group. Principles of enhanced heat transfer. 246–248
4. Mikic BB , Rohaenow WM (1969) Heat transfer. New correlation of pool boiling data including the effect of heat surface characteristis. 91, 245
5. Dhir VK, Liendard JH (1971) ASME J Heat transfer. Laminar film condensation on plane and axisymmetric Bodies in nonuniform gravity. 93(1):97–100

Chapter 19
Optimum Design of a Solar-Driven Ejector Cooling System

Wei Zhang, Saffa B. Riffat, Xiaoli Ma and Siddig A. Omer

Abstract A novel solar-powered ejector air-conditioning system with a nominal capacity of 5 kW cooling is described in this chapter. The system comprised an evacuated tube solar collector system, an ejector cooling system, and an MEPCM cooling storage system. The full size system has been laboratory tested, and the results are in good agreement with CFD simulation. A COP of up to 0.32 is obtained for the ejector cooling system during the test at the boiler temperature around 90 °C. Coefficient of performance of is up to 0.16 is predicted for the integrated system in operation. Guidelines for the design of system components based on the results of computer modeling and laboratory testing is given. Related correlations between these parameters will be obtained and presented in an easy step-by-step manner, in order to facilitate design and integration of system components for various applications. These will include analytical equations to match climate conditions and building air-conditioning load.

Keywords Solar energy · Air conditioning · Ejector cooling

19.1 Introduction

Deployment of the solar powered ejector air conditioning systems would be particularly beneficial during peak consumption hours when both air-conditioning load and solar energy resources are at their maximum. It would reduce the load on the generating sector significantly; it would also improve the sustainability of the

W. Zhang (✉)
College of Architecture and Environment, Sichuan University, Chengdu 610065, China
e-mail: xskin821@163.com

S. B. Riffat · X. Ma · S. A. Omer
Department of Architecture and Built Environment, Institute of Sustainable Energy Technology University of Nottingham, Nottingham NG7 2RD, UK

A. Li et al. (eds.), *Proceedings of the 8th International Symposium on Heating, Ventilation and Air Conditioning*, Lecture Notes in Electrical Engineering 262,
DOI: 10.1007/978-3-642-39581-9_19,

built environment, as well as the global environment by reducing CO_2 emission associated with generation of electricity from fossil fuels. Solar-powered ejector air-conditioning system has the potential to provide cooling and air conditioning for a range of public buildings using renewable resources [1].

Many ejector systems have been developed to use water as the refrigerants (called steam ejector). In these steam ejector systems, the generator temperature is designed to within 120–140 °C [2–4]. These systems would not be efficient when used with solar collectors for vapor generation. This is because the efficiency of the solar collectors reduces with the increase of its temperature. Therefore, systems using solar energy require relatively low generator temperatures. Reviewing the literature over the last few years, there is only limited information available on comparing model results to experimental data, especially when concerning real working fluids in a wide range of operating conditions [5–7].

In this study, a novel steam ejector cooling system was evaluated. The steam ejector used water as refrigerant and was designed to operate at suitable temperature range. The temperature range would be suitable for air-conditioning application using vacuum tube solar collectors. The generator temperature was set at 90 °C. In addition, a spindle was added as a new feature. A spindle is used to provide fine tuning and flexibility for ejector operation as heat input changes with solar radiation.

19.2 Modeling Solar-Driven Ejector System

As shown in Fig. 19.1, solar collectors absorb solar energy, and heat the transfer fluid. According to the vapor generator, the fluid is vapor as steam, known as primary or motive fluid, is evolved. This enters the primary nozzle of the ejector, where it expands to produce a supersonic flow within a low-pressure region. The partial vacuum created by the supersonic primary flow is fed by a secondary (suction) flow consisting of entrained refrigerant vapour coming from the evaporator. The primary (motive) and secondary (suction) fluids combine in the mixing chamber of the ejector and discharge through a diffuser to the condenser, where the refrigerant vapour is liquefied. The rest of the cooled fluid in the evaporator will transfer the cold energy to MEPCM in the cold storage tank. The MEPCM will exchange cold energy with the air handing unit. Finally, the typical air conditioning cycle will cool down the indoor air temperature. These three subsystems of a solar powered air conditioning system and the corresponding system components should be designed for carefully selected operating conditions.

A 1-D model of a solar-driven ejector system modeling was developed in order to analyze the system performance. The simulation of the system is under steady conditions, and the thermal losses during fluid transport are negligible. The working fluid is water. The cooling load corresponds to the maximum power, which can be produced by the ejector.

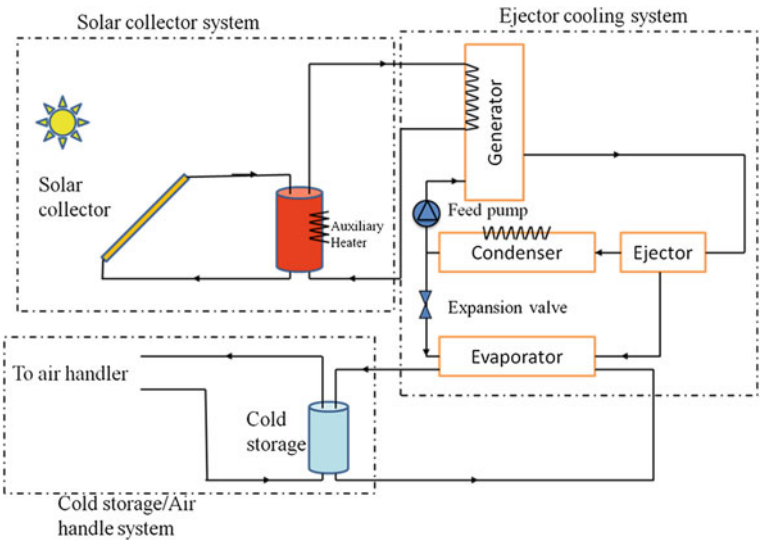

Fig. 19.1 A preliminary design of solar-driven ejector air-conditioning system

19.2.1 Solar Collector System

The energy output from the collector is [8]:

$$Q_{\text{out}} = F_R(\propto \tau)AG - F_R U_L A(T_{\text{in}} - T_{\text{amb}}) \tag{19.1}$$

Solar collector efficiency η_{col} is defined as a proportion of energy incident on the collector.

$$\eta_{\text{col}} = F_R(\propto \tau) - F_R U_L\left(\frac{T_{\text{in}} - T_{\text{amb}}}{G}\right) \tag{19.2}$$

Typical values of $F_R(\propto \tau)$, 0.80 and $F_R U_L$, 1.5 for an evacuated tube solar collector were chosen [8].

19.2.2 Ejector System

As shown in Fig. 19.2, a typical ejector for the entire ejector is made up of the primary nozzle, secondary inlet, constant area section and diffuser. The overall energy balance r is given [9]:

$$m_g h_g + m_e h_e = \left(m_g + m_e\right) h_e \tag{19.3}$$

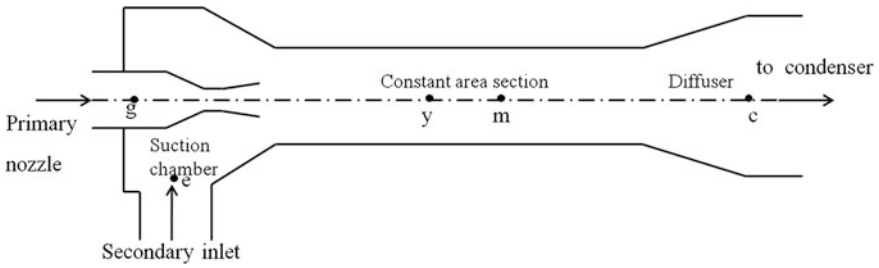

Fig. 19.2 Ejector cross-section

In Eq. (19.3), the enthalpy of the vapour from the generator (h_g) and the evaporator (h_e) can be evaluated assuming saturation.

Input of heat from the generator and rejected heat from the condenser required to operate the cooling cycle can be estimated from the following equations:

$$Q_g = m_g\left(h_g - h_{c,\mathrm{liq}}\right) \tag{19.4}$$

$$Q = \left(m_g + m_e\right)\left(h_c - h_{c,\mathrm{liq}}\right) \tag{19.5}$$

It is assumed that the fluid leaving the condenser is at saturated liquid state, therefore it enthalpy ($h_{c,\mathrm{liq}}$) can be determined from T_c.

Considering that the secondary fluid undergoes an adiabatic expansion before entering the evaporator, the secondary mass flow rate required to supply the required cooling capacity at T_e can be derived:

$$m_e = \frac{Q_e}{\left(h_c - h_{c,\mathrm{liq}}\right)} \tag{19.6}$$

Ejector performance is often measured by the entrainment ratio (λ) defined as:

$$\lambda = \frac{m_e}{m_g} \tag{19.7}$$

The coefficient of performance (COP) of the cooling cycle between the cooling capacity at the evaporator and the generator can be obtained from the following expression:

$$\mathrm{COP} = \frac{Q_e}{Q_g} = \lambda \times \frac{\Delta h_e}{\Delta h_g} \tag{19.8}$$

In Eq. (19.8) Δh_e and Δh_g are the enthalpy changes in the evaporator and generator respectively.

19.2.3 Solar-Driven Ejector Cooling System Performance

The system efficiency can be defined as

$$\eta_{\text{sys}} = \eta_{\text{coll}} \times cop \tag{19.9}$$

Solar fraction is defined as the ratio of the useful solar power to the power necessary in the generator to run the system

$$F_{\text{sol}} = \frac{Q_{\text{coll}}}{Q_g} \tag{19.10}$$

According to the supplied climate data, the solar radiation is set as 700 W/m^2, and the ambient temperature is 28 °C. And the indoor cooling load is assumed 5 kW based on the typical building cooling load building.

According to Eqs. (19.1)–(19.10), a typical solar-driven ejector cooling system for Mediterranean climate data is simulated using a numerical procedure in the EES program (F-Chart Software, USA). Design variables, T_g, T_e, T_c, Q_e and the physical properties of the working fluid must be inputs. Inlet and outlet pressures can be determined from saturation conditions [10].

The simulation result is summarized in Table 19.1. The evaporator cooling load was 5 kW. Evacuated tube type solar collectors generator temperature is normally in the range of 90–110 °C. Evaporator temperature is determined by phase change temperature range of the MEPCM used as cooling storage. Very low evaporator temperatures (depending on the working fluid) would result in a low COP of the ejector cooling cycle. A high T_e would improve COP, however would worsen heat transfer rate in the air handling unit. Typical evaporator temperatures for air-conditioning should be in the range of 8–15 °C. In order to achieve the acceptable system performance, the outlet temperature of solar collector needs 100 °C at least. It is confirmed evacuated tube collectors are more suitable to drive an ejector cooling system. When the evaporator temperature is below 10 °C, or condenser temperature is over 35 °C, they were also resulted in very poor system performance (<0.1). The large collector area will increase the system cost.

Table 19.1 Summary of solar-driven ejector system

T_g (°C)	T_e (°C)	T_c (°C)	COP	η_{col}	η_{sys}
90	10	35	0.13	0.67	0.08
100	10	35	0.18	0.64	0.12
110	10	35	0.24	0.63	0.15
90	10	30	0.30	0.66	0.20
100	10	40	0.05	0.66	0.03
110	10	40	0.10	0.64	0.06
90	5	35	0.02	0.67	0.01
100	15	35	0.35	0.64	0.22
110	15	35	0.41	0.63	0.26

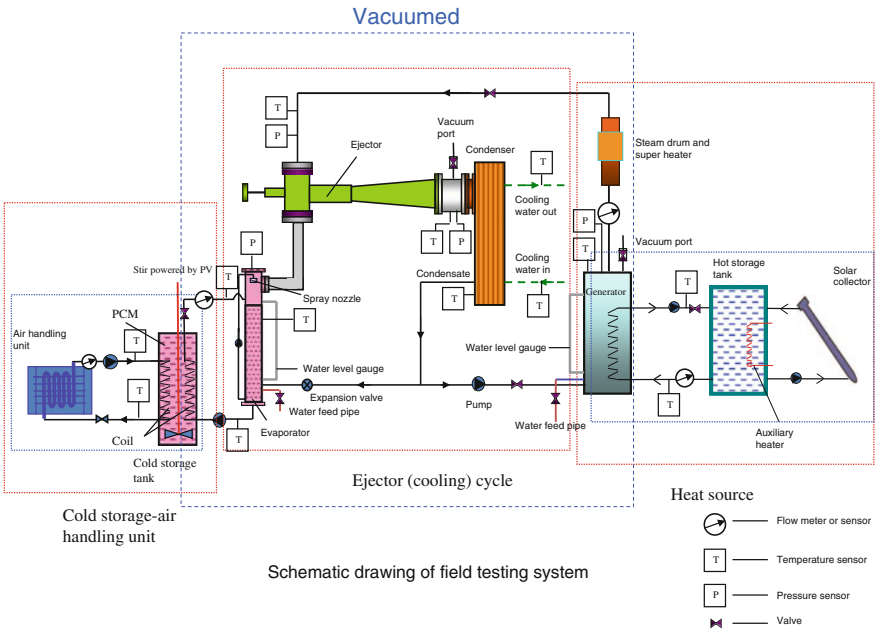

Fig. 19.3 Solar-driven ejector air conditioning system

19.3 5 kW Solar-Driven Ejector Cooling System Design

Figure 19.3 shows the schematic drawing of the field test system. The system includes three parts, i.e., cold storage-air handling unit, ejector cycle, and heat source part. The control and measurement system, i.e., sensors and valves are also shown in this drawing. Solar collectors absorb solar energy, and heat the transfer fluid. A hot storage tank is used to maintain the steady temperature. According to a flat plate exchanger used as vapor generator, the fluid is vaporized as steam, known as primary or motive fluid evolves. This enters the primary nozzle of the ejector, where it expands to produce a supersonic flow within a low-pressure region. The partial vacuum created by the supersonic primary flow is fed by a secondary (suction) flow consisting of entrained refrigerant vapour coming from the evaporator. The primary (motive) and secondary (suction) fluids combine in the mixing chamber of the ejector are discharge through a diffuser to the condenser, where the refrigerant vapour can be liquefied. The remainder liquid water is returned to the boiler via a feed-pump while the rest is expanded through the throttling to the evaporator to complete the cycle. The cooled fluid in the evaporator will transfer the cold energy to MEPCM in the cold storage tank. MEPCM will exchange cold energy with water–air handing unit. At last, the typical air conditioning cycle will be cooling down the indoor air temperature. In the following sections, each subsystem for field test is separately indicating the most important parameters.

19.3.1 Solar Collector System

The solar subsystem is made by 20 TZ58-1800 solar evacuated tube collectors system from SUNRAIN with 2.41 m^2 absorber area and 30 tubes each. Total area is 48.2 m^2. Collectors are installed in the flat roof just near the test area of the university, at a tilt angle of 20° and facing South.Water glycol mixture is used in the circuit to avoid freezing risks (only at 15 % glycol). The solar collector field is mounted on the roof using metallic basements and profiles so as to respect the existing water proof structure. The size of the storage tank does not considerably influence the system performance. The collector field is linked to hot buffer storage of 3 m^3 in order to increase the stability and performance of the system where an electric heater on the upper part is added. By using a larger storage tank, less auxiliary heat is required; therefore solar fraction is somewhat higher. A three-way valve is used as a bypass to preheat the solar collector field in the morning or during the day while the backup can feed the ejector separately. The secondary pump is used to connect the buffer storage with the ejector (still with water/glycol to avoid the temperature pitch of an exchanger). The solar system is designed to work on outlet temperature 100 °C so the nominal temperature of the generator inlet to the ejector is fixed at 90 °C. This choice has been made to be able to work with water/glycol at a reasonable pressure level (to avoid leakages) and with standard pumps. A controller is in charge of controlling the two pumps, the three-way valve and the electric heater as well as for monitoring the different energy loops (two loops) of the subsystem. Solar irradiation is measured and the controller will be connected to the main ejector and distribution controller.

19.3.2 Ejector Cooling System

The ejector cooling system was installed in Tunis as show in Fig. 19.4, including the tested ejector, generator, condenser, and evaporator.

19.3.3 Cold Storage-Air Handle System

The cold storage tank has a capacity of approximately 700 L of DPNT08-0042 PCM. It includes two heat transfer coils, one from the evaporator of the ejector cycle and another one from the air handler. One stirrer powered by PV is used to stir the MEPCM in order to increase heat transfer speed. The storage tank was designed to provide 5 kW heating/cooling power using water as heat transfer media. The cold storage tank is produced as design specification by HAVEL THERM, Ltd. 10 kW air handling unit was installed in the office.

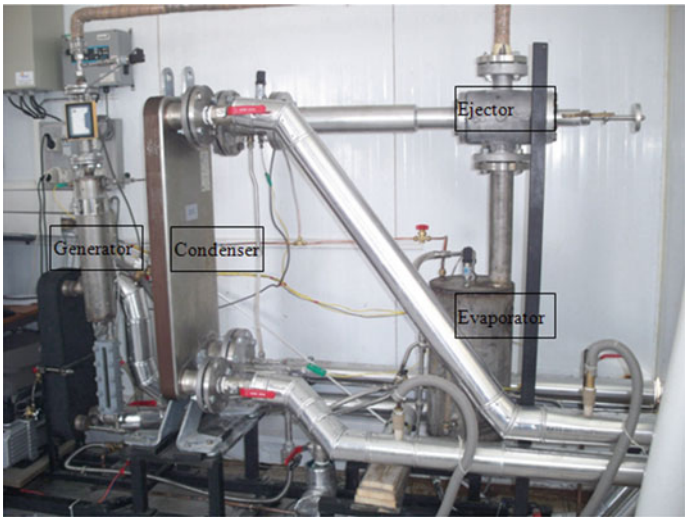

Fig. 19.4 Ejector cooling system for field test

19.4 System Performance Predictions and Conclusions

The energy performance of the system is defined as the system thermal ratio:

$$\eta_{\text{sys}} = \frac{Q_e}{A \cdot G} = \frac{Q_e}{Q_g} x \frac{Q_g}{A \cdot G} = \text{COP} x \eta_{\text{col}} \tag{19.11}$$

The ejector system and collector system simulation have been described in previous work [11, 12].

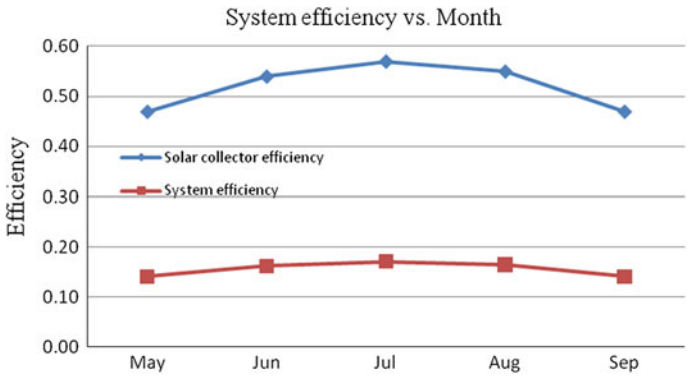

Fig. 19.5 Solar-driven ejector cooling system efficiency during summer

The above analysis is based on steady conditions. The heat loss has not been considered. The inlet and outlet temperature of the solar collector set as 90 °C/100 °C. Ejector efficiency is 0.3 when the generator temperature is 90 °C, condenser temperature is 35 °C and the evaporator temperature is 10 °C. From Fig. 19.5, it can be seen that the solar-driven ejector cooling system can reach 17 % on the hottest month of July. The lowest system efficiency is 14 % in September because of the lower solar radiation. The average system efficiency is 16 % during the summer. Thus during the summer, the solar-driven ejector cooling system can provide 5 kW cooling.

References

1. Keukeleire S (2000) The Foreign Policy of Europe Union. http://ec.europa.eu
2. Aphornratana S, Eames IW (1997) A small capacity steam-ejector refrigerator: experimental investigation of a system using ejector with movable primary nozzle. Int J Refrig 20(5):352–358
3. Chunnanond K, Aphornratana S (2004) An experimental investigation of a steam ejector refrigerator: the analysis of the pressure profile along the ejector. Appl Therm Eng 24:311–322
4. Eames I, Aphornratana A, Haider H (1995) A theoretical and experimental study of a small-scale steam jet refrigerator. Int J Refrig 18(6):378–386
5. Zhu Y, Cai W, Wen C et al (2009) Numerical investigation of geometry parameters for design of high performance ejector. Appl Therm Eng 29:898–905
6. Ablwaifa A, Eames I, Petrenko V (2009) Experimental validation of CFD model used to design jet-pumps. International Seminar on Ejector/Jetpump Technology and Application., Louvain-la-Neuve, p 19
7. Rusly E, Aye L, Charters W et al (2005) CFD analysis of ejector in a combined ejector cooling system. Int J Refrig 28:1092–1101
8. Pridasawas W (2006) Solar-driven refrigeration systems with focus on the ejector cycle (PhD thesis). Royal Institute of Technology, Stockholm, pp. 54–123
9. Huang B, Chang J, Wang C et al (1999) A 1-D analysis of ejector performance. Int J Refrig 22:354–364
10. IDEMC (2008) Project report submited to EU-an advanced solar-driven air conditioning system for the mediterranean climate(IDEMC part). Institute of Mechanical Engineering, University of Porto, Portugal
11. Zhang W, Ma X , Omer SA, Riffat SB (2012) Optimum selection of solar collectors for a solar-driven ejector air conditioning system by experimental and simulation study. Energy Convers Manage 63c:106–111
12. Ma X, Zhang W, Omer SA, Riffat SB (2010) Experimental investigation of a novel steam ejector refrigerator suitable for solar energy applications. Appl Therm Eng 30(11–12): 1320–1325

Chapter 20
Influence of Intermittent Operation on Soil Temperature and Energy Storage Duration of Ground-Source Heat Pump System for Residential Building

Tao Yu, Zhimei Liu, Guangming Chu and Yunxia Qu

Abstract A residential building of 11-story was chosen as the objective buildings. Load characteristics under continuous and intermittent operating condition were analyzed by DeST software. Soil temperature variation of single ground-source heat pump under different operating condition was simulated by GeoStar software. Thermal energy storage duration of the solar-assisted ground-source heat pump system was further discussed on the basis of geothermal temperature balance. Results show that the intermittent operation has great influence on load characteristics, soil temperature, and energy storage period. Building function and system operating mode should be paid much attention during the engineering practice.

Keywords Energy storage · Ground source heat pump · Intermittent operation · Load characteristics · Residential building

20.1 Introduction

Solar-assisted GSHP (Ground-Source Heat Pump) system utilizes solar energy and underground energy synthetically. The underground heat load imbalance restricting the application of GSHP in cold region is solved by solar energy recharging during non-heating periods. Efficiency of solar collector and heat pump are both improved. Solar-assisted GSHP features for high-efficiency, energy-saving, and environmental protection, is widely used in China [1, 2].

T. Yu (✉) · G. Chu · Y. Qu
Key Laboratory of Renewable Energy Utilization Technology in Building of the National Education Ministry, Shan Dong Jian Zhu University, Jinan, Shandong, 250101, China
e-mail: hgdyutao@sina.com

Z. Liu
Coal Industry Jinan Design & Research Co.Ltd, Jinan, Shandong, 250000, China

A. Li et al. (eds.), *Proceedings of the 8th International Symposium on Heating, Ventilation and Air Conditioning*, Lecture Notes in Electrical Engineering 262,
DOI: 10.1007/978-3-642-39581-9_20,

Intermittent operation is the outstanding characteristic of the air conditioning system for residential building. Influence of intermittent operation on soil temperature variation and performance of buried tube heat exchanger have been researched [3–5]. Continuous and intermittent operation was compared [6]. Methods to optimize the operation of ground heat exchanger system were suggested [7]. We have reached an agreement that the intermittent operation helps to improve the heat transfer effect between buried U-tube and soil, reduce the extreme temperature around the ground heat exchangers, and then decrease the energy consumption and initial investment [8, 9]. But research about the load characteristics and energy storage duration of the solar-assisted GSHP is few. Furthermore, some designers design the GSHP for residential building on the basis of continuous mode, while leave the actual condition of intermittent operation out of account. Deviation between working and designing condition of the GSHP is therefore aggravated. And the operational efficiency of the system cannot be ensured.

In this paper, Beijing, Jinan, and Xi'an were chosen as the typical cities representing the northeast, middle-east, and west of the cold region in China, respectively. One 11-story residential building with a total construction area of 7229 m^2 was selected as the target building. Hourly load and annual load under continues and intermittent operating conditions were computed by DeST. Load characteristics were further analyzed and compared. Soil temperature variation during 10-year operation of single GSHP was simulated and calculated by 'GeoStar'. Based on the equilibrium soil temperature, the reasonable energy-storage period of the solar-assisted ground-source heat pump was discussed.

20.2 Load Characteristic of the Building

20.2.1 Building Summary and Designing Parameters

The 11-story residential building has three units and 66 households, with the total construction area of 7229 m^2 and air conditioning area of 2864.4 m^2. Domestic hot water of 60 °C is provided by the central hot water system. Shape factor of the building is 0.27. Area ratio of window to wall is 0.2. Heat transfer coefficient of the exterior wall and window is 0.55 and 2.8 W/m^2K, respectively. The simultaneous utilization factor of the air conditioning system is 0.6.

Designing parameters of the main rooms are shown in Table 20.1. The intermittent operation time in summer is given in Table 20.2. Continuous operation is 24 h operation in summer and winter. The heating time in winter is from November 15th to March 15th, and the air conditioning time in summer is from June 1st to September 30th.

Table 20.1 Designing parameters of main rooms

Rooms	Summer			Winter		
	Indoor temperature	Indoor relative humidity	Indoor air velocity	Indoor temperature	Indoor relative humidity	Indoor air velocity
Living room, bedroom	26 °C	60 %	0.3 m/s	18 °C	50 %	0.2 m/s

Table 20.2 Operation time of air-conditioning system in summer

Items	Bedroom	Living room
Workday	From 21:00 to 7:00 on the next day	From 18:00 to 22:00
Weekend	From 13:00 to14:00	From 10:00 to 22:00
	From 22:00 to 8:00 on the next day	

20.2.2 Load Characteristics

The yearly dynamic load under continuous and intermittent operating condition is calculated by DeST, with the location of the building is Beijing, Jinan, and xi'an, respectively. Load indexes and annually loads are listed below in Table 20.3.

It can be seen from Table 20.3 that annual heat load is greater than or close to cooling load in cold region. If air conditioning system operates intermittently in summer, the accumulated cooling load will decrease, and the ratio of annual heat load to cooling load will increase more or less.

Table 20.3 Load indexes and annually accumulative load under different operation mode

Items		Beijing	Jinan	Xi'an
	Cooling load index (W/ m^2)	40.4	48.6	39.8
	Heat load index (W/m^2)	31.3	30.6	27.3
Continuous operation	Annually accumulated heat load (kW)	249815.1	207088.4	238904.2
	Annually accumulated cooling load (kW)	104020.7	208315.6	222658.5
	Ratio of annual heat load to cooling load	2.40	0.99	1.07
Intermittent operation	Annually accumulated heat load (kW)	249815.1	207088.4	238904.2
	Annually accumulated cooling load (kW)	68423.1	129117.0	154203.8
	Ratio of annual heat load to cooling load	3.65	1.60	1.55
	Energy absorbed from underground yearly (kW)	199852.1	165670.7	191123.4
	Energy released to underground yearly (kW)	124824.8	154940.4	185044.6
	Thermal imbalance ratio (%)	23.1	3.34	1.62

20.3 System Schematic and Designing

As Fig. 20.1 shows, geothermal heat exchangers are divided into air-conditioning borehole (geothermal heat exchanger 1) and heat storage borehole (geothermal heat exchanger 2). The operation modes change with seasons. In winter, geothermal heat exchanger and solar collector work in a combined mode. They share heat load together, and the former undertakes the main load. Domestic hot water is provided by GSHP in the case that solar collector cannot meet the demand. In summer, GSHP and solar system operate separately. Building heat gain is transferred to the geothermal heat exchanger 1, and surplus solar energy is stored underground by geothermal heat exchanger 2. In this way, soil temperature can be recovered in some degree. In transition seasons, GSHP system stops running. Redundant solar energy except for domestic hot water consumption is stored underground. Soil temperature is increased further. Length of geothermal heat exchanger 1 is determined by building heat load, while length of geothermal heat exchanger 2 is determined by the extra solar energy. Solar collector area and drill depth are designed according to T. Yu et al. [10].

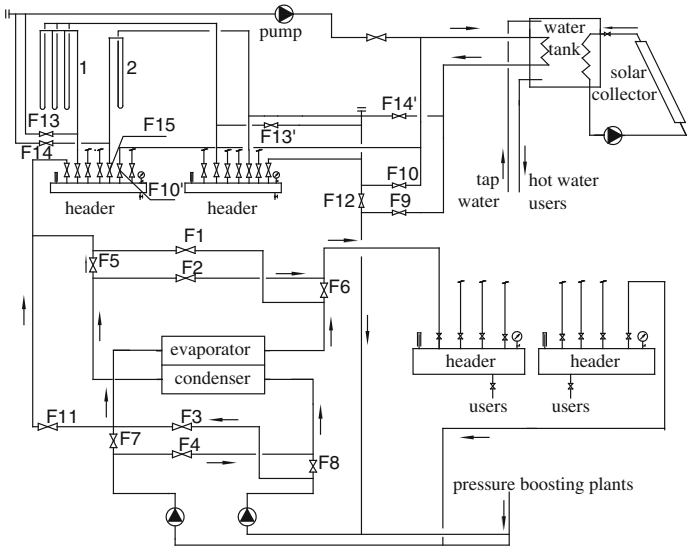

Fig. 20.1 Solar-assisted ground-source heat pump system schematic

20.4 Soil Temperature Variation of Single GSHP

20.4.1 The Building in Beijing

In Beijing, the required geothermal heat exchanger length is 4851 m, and the corresponding solar collector area is 592.2 m^2. Soil temperature of single GSHP system under 10-year continuous and intermittent operation is as Figs. 20.2 and 20.3, where Tb is the monthly average wall temperature of the borehole, EWT, and OWT denote the inlet and outlet temperature of heat pump, respectively.

It can be seen from Figs. 20.2 and 20.3 that the soil temperature decreases about 3 °C after 10-year continuous operation, and decreases about 4.5 °C after a 10-year intermittent operation. Intermittent operating mode intensified the load imbalance. To avoid efficiency reducing and even system failure, thermal energy underground must be replenished in time.

20.4.2 The Building in Jinan

Drill depth of 5842 m and solar collector area of 635.6 m^2 are needed in Jinan city. Ten-year temperature variation curves under continuous and intermittent operation are shown in Figs. 20.4 and 20.5, respectively.

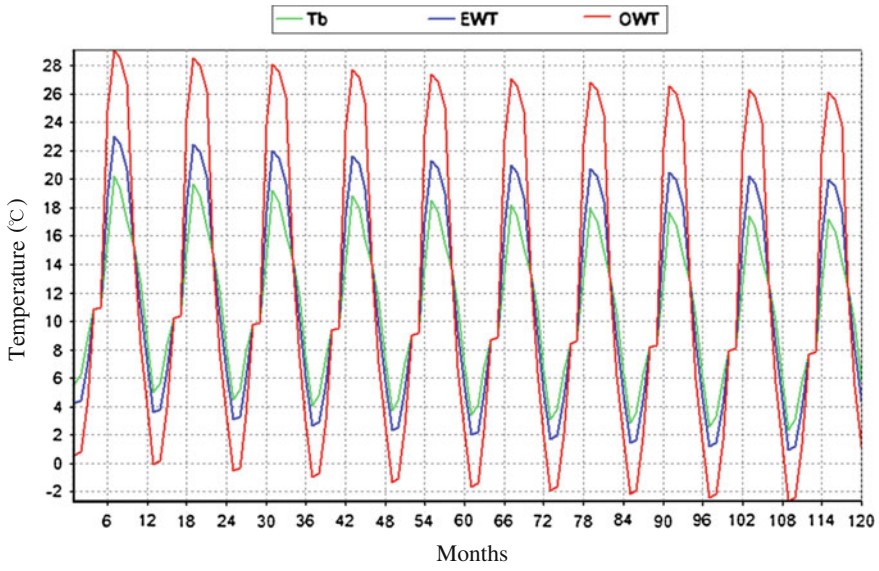

Fig. 20.2 Soil temperature of single GSHP during 10-year continuous operation (in Beijing)

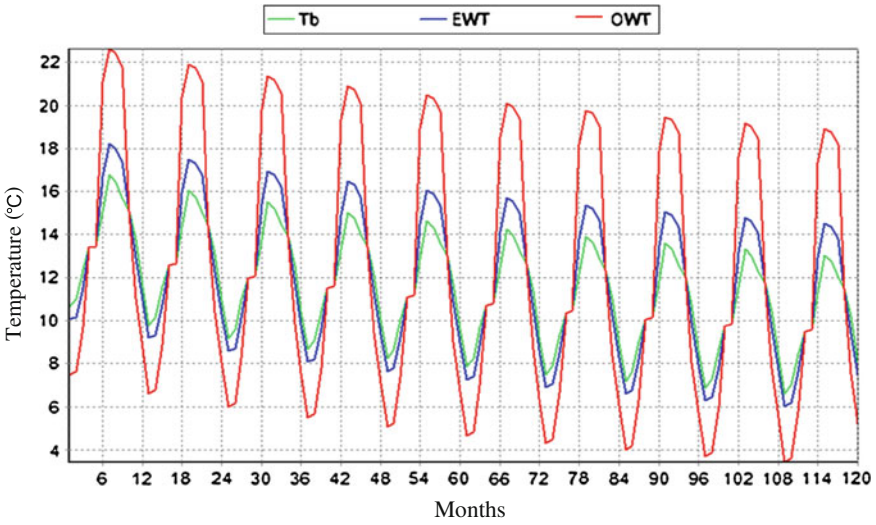

Fig. 20.3 Soil temperature of single GSHP during 10-year intermittent operation (in Beijing)

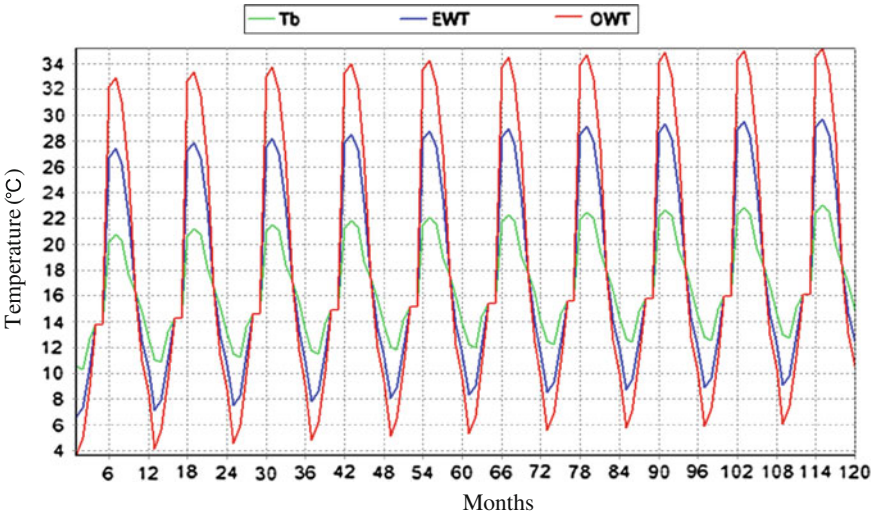

Fig. 20.4 Soil temperature of single GSHP during 10-year continuous operation (in Jinan)

In Jinan, the annual heat load is slightly larger than the cooling load, but electricity consumed by heat pump unit converts to thermal energy and is stored underground. So the soil temperature raises about 1.5 °C after 10-year continuous operation (Fig. 20.4). While under intermittent operating condition, the difference between heat and cooling load increase, and soil temperature drops about 1 °C after 10 years (Fig. 20.5). Intermittent operating mode changed the variation trend of soil temperature.

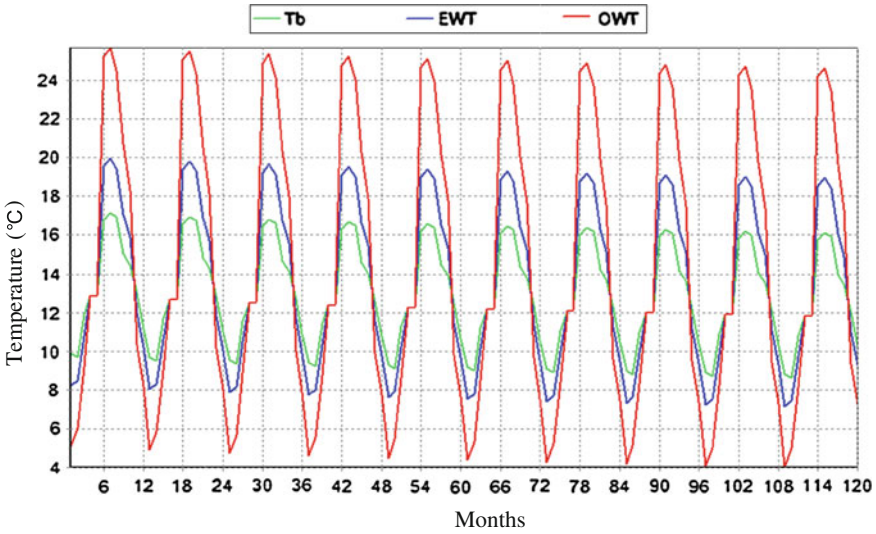

Fig. 20.5 Soil temperature of single GSHP during 10-year intermittent operation (in Jinan)

20.4.3 The Building in Xi'an

The same building in Xi'an needs a solar collector area of 475.4 m^2 and a drill depth of 4775 m. Soil temperature of single GSHP system under 10-year continuous and intermittent operation is as Figs. 20.6 and 20.7.

As shown in Fig. 20.6, although the annual heat load is greater than cooling load, soil temperature raises about 6 °C after 10 years continuous operation because of the heat released from the heat pump unit. Energy accumulation underground in Xi'an is more serious than that in Jinan. The accessorial radiating facility is necessary to keep the underground temperature. If the GSHP system works in intermittent mode, soil temperature will raise just 0.1 °C after 10 years (Fig. 20.7). Single GSHP system is enough for this residential building. Neither solar collector nor cooling tower is required.

20.5 Energy Storage Duration of Solar-Assisted GSHP

20.5.1 The Building in Beijing

In Fig. 20.8, solar energy is collected and stored underground by vertical boreholes during all the transition seasons. Soil temperature keeps constant basically during 10-year intermittent operation. It means that the energy absorbed from the soil is equal to that released to the soil. The seasonal storage of solar energy is effective for recovering the soil temperature.

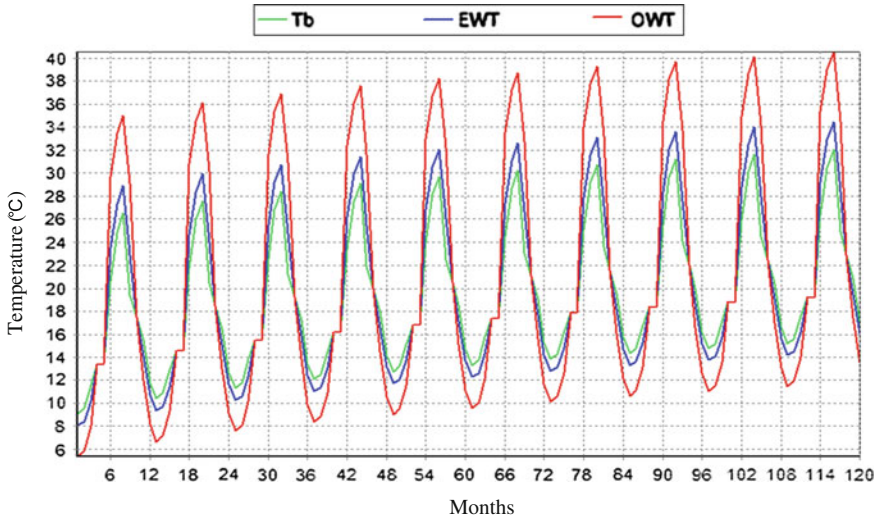

Fig. 20.6 Soil temperature of single GSHP during 10-year continuous operation (in Xi'an)

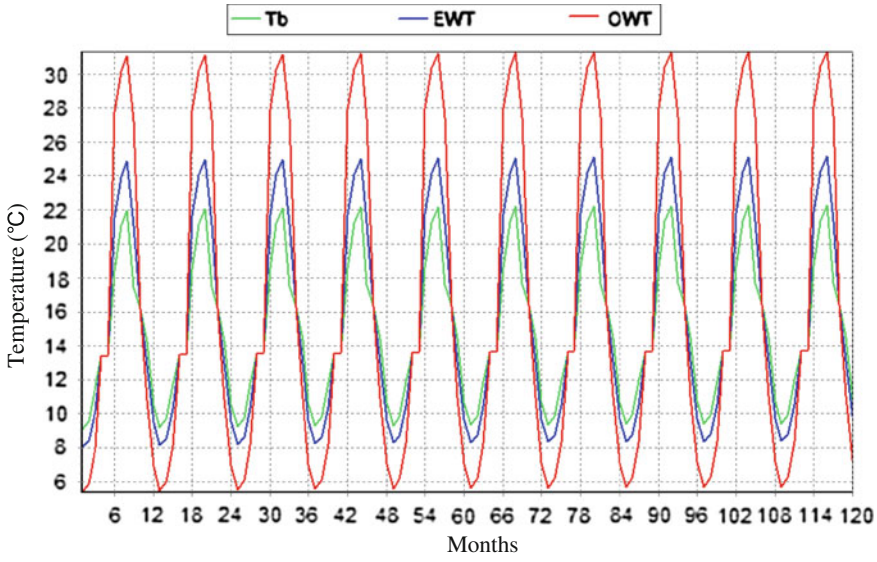

Fig. 20.7 Soil temperature of single GSHP during 10-year intermittent operation (in Xi'an)

20.5.2 The Building in Jinan

In Jinan, if solar energy is stored underground during all the transition seasons, the geothermal temperature will raise about 4 °C after 10 years (Fig. 20.9). It indicates that the thermal energy stored is overabundant. Another excellent approach is

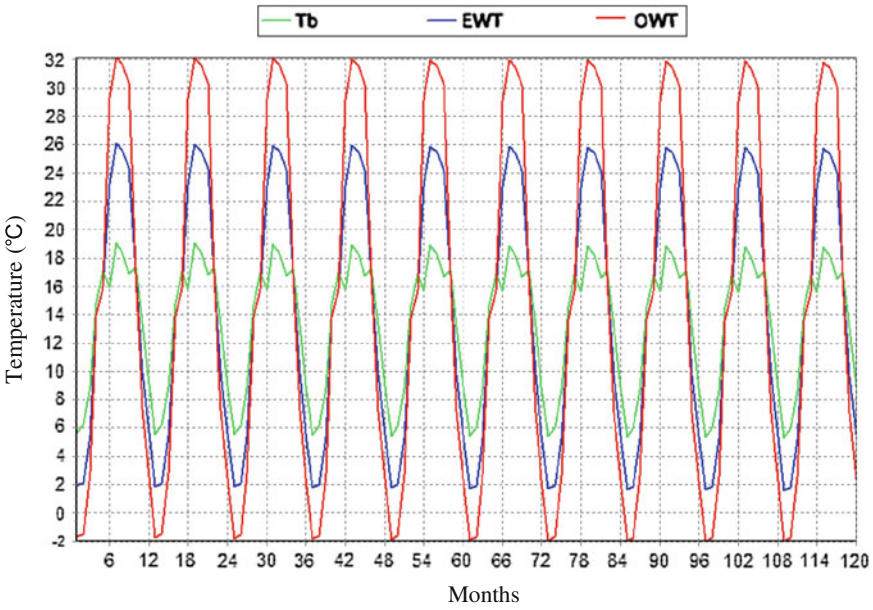

Fig. 20.8 Soil temperature of solar-assisted GSHP during 10-year intermittent operation (in Beijing, solar energy is stored during all the transition seasons)

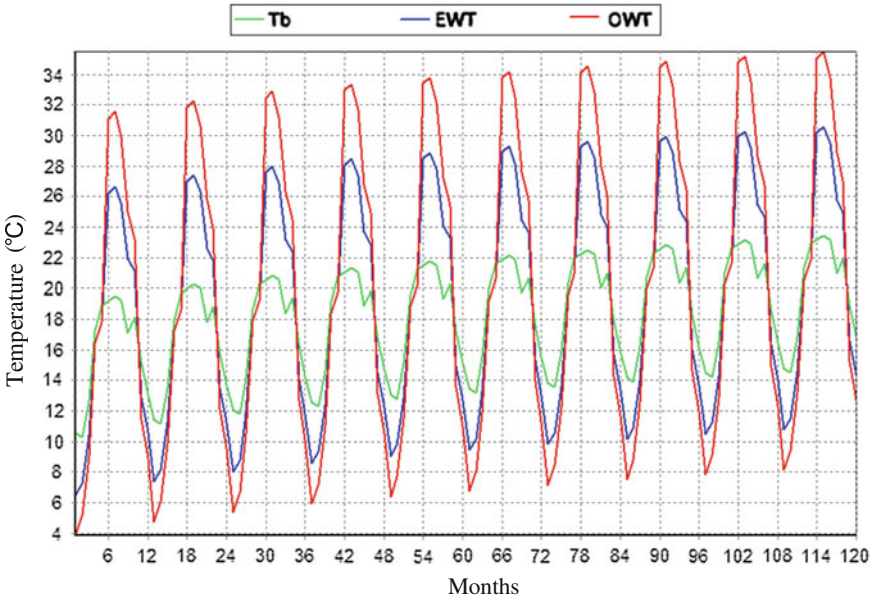

Fig. 20.9 Soil temperature of solar-assisted GSHP during 10-year intermittent operation (in Jinan, solar energy is stored during all the transition seasons)

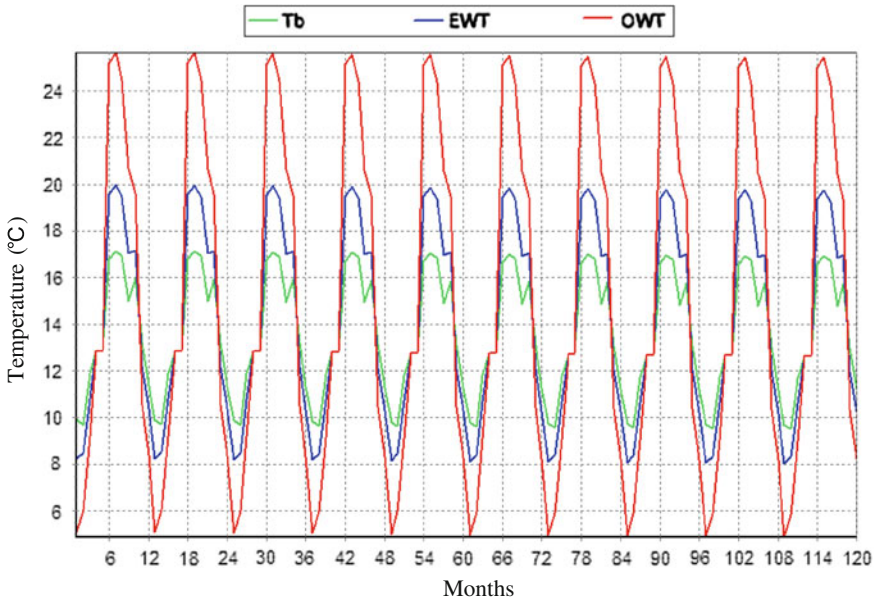

Fig. 20.10 Soil temperature of solar-assisted GSHP during 10-year intermittent operation (in Jinan, solar energy is stored only in October)

to store thermal energy only in October. In this way, soil temperature keeps steady as shown in Fig. 20.10, which means thermal energy collected can just make up the heat loss underground. System efficiency is guaranteed and operating cost is saved at the same time.

20.6 Conclusions

(1) To residential buildings lying in northeast cold region of China (e.g., Beijing), great difference exists between the annual heat load and cooling load. Soil temperature tends to decrease during the long-term operation of single GSHP, and the intermittent operation aggravates this trend. Thermal energy storage in transition seasons by solar collecting system is effective for recovering soil temperature and ensuring high efficiency of GSHP system.

(2) To residential buildings lying in middle-east cold region of China (e.g., Jinan), soil temperature rises under continuous condition and decreases under intermittent condition. Solar-assisted GSHP system should be adopted. Thermal energy storage during October can just make up the heat loss underground, but energy storage during the whole transition seasons is superfluous.

(3) To residential buildings lying in west cold region of China (e.g., Xi'an), annual heat load differs little from cooling load. Soil temperature rises under continuous condition and keeps constant under intermittent condition. Single GSHP system is suitable in this region.
(4) Intermittent operating condition is an important factor influencing the building load characteristics and soil temperature, and finally determining the energy storage duration of the solar-assisted GSHP. Building function and system operating condition should be considered adequately during the engineering practice.

Acknowledgments The authors acknowledge the financial supports from the research and development projects of ministry of housing and urban–rural development of the People's Republic China (2012-K1-33) and (2013-K1-39).

References

1. Zhao L, Zhou Y, Zhang X et al (2010) Simulation on soil temperature recovery for ground source heat pump. Build Energ Effi 38(10):34–38
2. Zhou D, Shi C, Yuan W (2011) Research on the applicability of solar energy-ground source heat pump in different regions of China. Paper presented at the second international conference on digital manufacturing and automation (ICDMA), pp 1026–1029
3. Shang Y, Li S, Dai L (2012) Study of characteristics of soil temperature variation and recovery under intermittent operation of ground-source heat pump. J Dalian Univ Technol 52(3):26–32
4. Liu D, Qu Y, Pan X (2012) Simulation of ground source heat pump system under intermittent operation condition. Eng Constr 44(1):5–9
5. Chu G, Yu Y, Cai Z (2008) Experimental research and simulation on inlet and outlet water temperatures of borehole for ground source heat pump with different operation modes. J Nanjing Normal Univ (Eng Technol Ed) 8(3):30–34
6. Maki I, Emiko S, Hirokazu M et al (2010) Appropriate operation and its advantages of geothermal heat pump system in a high geothermal gradient and high thermal conductivity area. In: Yokohama P (ed) Proceedings of Renewable Energy pp 70–73
7. Wang D, Yan L, Wang P (2010) Study on the operation characteristics of ground heat exchanger with different run-stop rations. Build Sci 8(8):17–20
8. Gao Q, Li M, Yu M, (2010) Experiment and simulation of temperature characteristics of intermittently-controlled ground heat exchanges. Renew Energ 35(6):1169–1174
9. Soldo V, Ruševljan M, Grozdek M et al (2011) Impact of the ground-source heat pump running time duration on the system efficiency. In: Proceedings of the 23rd IIR international congress of refrigeration 2011, international institute of refrigeration press, Prague, Czech Republic, 2011 pp 21–26
10. Yu T, L Peng, Chu G et al (2012) Seasonal underground storage of SGSHP system design based on equilibrium soil temperature. Adv Mater Res 512–515:864–868

Chapter 21
China's Low-Carbon Economy and Regional Energy Efficiency Index Analysis

Huifen Zou, Hao Tang, Ying Zhang, Fuhua Yang and Yingchao Fei

Abstract Energy is an important material basis for the survival and development of human society, China's rapid economic growth accompanied by low efficiency of energy utilization, the pressure of the rapid rise in carbon emissions, reasonable measure, and a comprehensive analysis of energy efficiency, which is a clear understanding of an important part of China's current economic development, energy use and carbon dioxide emissions overall efficiency of the situation. Economic development is the most important determinant of the increase in carbon dioxide emissions in China, but we cannot mitigate carbon dioxide emissions by slowing down economic growth, we should focus on reducing energy intensity, increasing the consumption of low-carbon energy. Therefore, from the point of view of regional differences, through the analysis of the regional characteristics of the energy consumption and carbon emissions, measuring 2005 to 2011, China's 30 provinces and municipalities energy efficiency, building energy efficiency index of different dimensions, compare the energy efficiency differences, fluctuations, balance of China's eastern, central and western regions and provinces, and do the energy efficiency forecasting at the same time. Found that there is an obvious persistent regularity in the evolution of the energy efficiency of other regions. The energy efficiency of the various regions will continue to maintain growth. It has a very important practical significance to achieve corresponding to different regions of the improvement of energy intensity and energy structure of the low-carbon target.

Keywords Carbon emissions · Regional energy efficiency · Regional energy utilization

H. Zou · H. Tang (✉) · Y. Zhang · F. Yang · Y. Fei
School of Municipal and Environment Engineering, Shenyang Jianzhu University, Shenyang, China
e-mail: tanghaotc@126.com

A. Li et al. (eds.), *Proceedings of the 8th International Symposium on Heating, Ventilation and Air Conditioning*, Lecture Notes in Electrical Engineering 262,
DOI: 10.1007/978-3-642-39581-9_21,

21.1 Current Situation of China's carbon Emissions

The essence of a low-carbon economy is to improve energy efficiency and optimize the energy structure. From the point of total carbon emissions, China is ranking second in the world, and is placed after the United States, but the high growth of economic and rapid energy consumption makes the entire international community identified in the next 20 years; China will become the world's largest emitter of carbon [1]. From the growth rate of carbon emissions, according to the World Resources Organization (WRI) calculation, the amount of carbon emissions grow up 108.3 % from the year 1990 to 2004, far exceeding the growth rate of 19.8 % in the United States [2]. This shows that the trend of China's carbon emissions growth is obvious.

Cities are the main source of carbon emissions. China has more than 600 cities, statistics 287 prefecture-level cities, the city's energy consumption accounted for 55.48 % of the country's total energy consumption, and CO_2 emissions accounted for 58.84 % of the country's total emissions. If the rest of the cities or towns add to the mix, energy consumption will account for more than 80 % of the total social energy consumption [3].

Overall, economic development is the most important determinants of the increase in carbon dioxide emissions, China's energy consumption and economic growth changes positively correlated. Here we will introduce a concept: energy consumption elasticity coefficient, it reflects the indicators of proportional relationship between the growth rate of energy consumption and economic growth, energy consumption elasticity coefficient is less than 1, indicating that the energy consumption growth rate is less than the rate of economic growth.

Due to China's rapid economic development, the demand for energy has increased dramatically. As can be seen from Table 21.1, there's a significant rise on the domestic energy consumption growth in 2003 and 2004, which is much

Table 21.1 Energy consumption elasticity coefficient

Years	Energy consumption than the previous year (%)	Power consumption than the previous year (%)	(GDP) growth than the previous year (%)	Energy consumption elasticity coefficient
2000	3.5	9.5	8.4	0.42
2001	3.3	9.3	8.3	0.40
2002	6.0	11.8	9.1	0.66
2003	15.3	15.6	10.0	1.53
2004	16.1	15.4	10.1	1.60
2005	10.6	13.5	11.3	0.93
2006	9.6	14.6	12.7	0.76
2007	8.4	14.4	14.2	0.59
2008	3.9	5.6	9.6	0.41
2009	5.2	7.2	9.2	0.57
2010	6.0	13.2	10.4	0.58
2011	7.1	12.1	9.3	0.76

Table 21.2 Total energy consumption and constitute

Years	Total energy consumption (million tons of standard coal)	The proportion of the total energy consumption (%)			
		Coal	Petroleum	Gas	Hydropower, nuclear power, wind power
2000	145531	69.2	22.2	2.2	6.4
2001	150406	68.3	21.8	2.4	7.5
2002	159431	68.0	22.3	2.4	7.3
2003	183792	69.8	21.2	2.5	6.5
2004	213456	69.5	21.3	2.5	6.7
2005	235997	70.8	19.8	2.6	6.8
2006	258676	71.1	19.3	2.9	6.7
2007	280508	71.1	18.8	3.3	6.8
2008	291448	70.3	18.3	3.7	7.7
2009	306647	70.4	17.9	3.9	7.8
2010	324939	68.0	19.0	4.4	8.6
2011	348002	68.4	18.6	5.0	8.0

larger than the GDP growth rate of the same period, energy consumption growth rate is 15.3 and 16.1 %, respectively, while the GDP growth rate is 10 and 10.1 %, and makes energy consumption elasticity coefficient more than 1.

There is a strong correlation among economic development, energy consumption, and carbon emissions. Since the year of 1751 initial industrialization to 1998, the growth of global carbon emissions has increased by more than 2,200 times, in the coal-dominated former 210 years, global carbon emissions is the fastest growing [4]. In China's energy consumption structure, the proportion of coal has always played a very large share. As can be seen from Table 21.2, the proportion of coal in China is about 70 %, much greater than the proportion of oil, natural gas and other energy. This is mainly due to China's rich coal resources. In energy consumption coal is dominant. Total coal resources of China is 5.6 trillion tons, in which there has been proved is 1 trillion tons, the proved reserves accounted for 94 % of the fossil energy. Coal-based Resources also decided coal in the dominant position of China's energy consumption will continue for quite a long period of time [5].

According to the forecasts, at the end of the Twelfth Five-Year Plan, China's primary energy consumption will reach about 4.3 billion tons of standard coal, carbon dioxide emissions caused by the fossil fuel combustion is about 9.18 billion tons [6]. In order to achieve the Twelfth Five-Year Plan energy-saving target, should increase efforts to optimize energy efficiency.

21.2 Building Regional Energy Planning

China's urban existing buildings area is about 40 billion m^2, and has increased by 2 billion m^2 per year [7]. Most cities are in a stage of rapid development, the dramatic increase in energy consumption in various cities, to the year of 2050,

China's urbanization level will reach 70–75 %, the value created by the unit energy consumption and resource consumption in the Chinese cities will increase 15–20 times on the basis of 2000 [8]. Due to the lack of rational planning and the blind expansion of urban development, leading to the building density of city center is too large, resulting in shortage of land. Water, electricity, natural gas and other departments of the city did not collaborate in the planning and construction stage, caused infrastructure redundant construction and significant energy waste. So, there is a very important significance for regional energy planning in cities (Table 21.3).

At present, China's building of regional energy planning has problems of two aspects:

(1) There is no special plan of building energy in urban planning system;
(2) Departments lack of mutual coordination in urban planning caused infrastructure repeat

Building regional energy system is a pluralistic, complex systematic project, affected by factors such as urban development stage, economic level, and people spending habits. Now there is no specific provision for the urban energy planning in China, but we can base on the principle of maximizing the functionality of the infrastructure, improve energy efficiency and economic benefits and summarize four focus of regional energy planning:

1. Energy selection should be adapted to local conditions;
2. Combination of energy planning and municipal facilities planning;
3. Achieve energy cascade utilization;
4. Optimized matching between energy systems and building energy systems.

In the energy selection, planning building regional energy supply system, we can consider the following two characteristics of the energy for a rational allocation. Different energy substitutes for one another and diversity of energy supply.

The same type of energy can replace each other by the way of cascade utilization and mutual conversion. Such as heating, cooling, and other living energy can supply by industrial high-temperature waste heat, city gas and other energies; the same energy systems using various forms of energy constitution and renewable

Table 21.3 China's urbanization strategy objectives

	Years				
	2006	2020	2030	2040	2050
Urbanization rate %	43.9	55–60	60–65	65–70	70–75
The urban economic contribution rate %	63.2	75	80	85	90
City energy consumption (standard coal) million tons	13.67	16.15	16.74	15.94	13.90
Carbon emissions	291607.7	372434.8	399673.3	387500.9	362067.1

energy sources such as solar combined with coal, natural gas and other primary energy. Meanwhile, energy utilization should also take into account the factors of carbon emission and achieve the low carbonization target of energy consumption.

21.3 The Regions Energy Efficiency Analysis in China

21.3.1 Regions Energy Efficiency Statistics

According to the statistics of the GDP and the total energy consumption of the country between 2005 and 2010, calculating the value of energy efficiency, the greater the efficiency values the higher energy efficiency is.

As can be seen from Table 21.4, during this period, China's overall regional energy mean value in a steady upward trend, especially in 2008, the efficiency increase is 12.5 % higher than last year. Considered from the perspective of technical developments, the improvement of world-wide attention to the energy field, this environment promote the intensity of introduction research and development technology in China, this is the main reason for the improvement of the energy efficiency of this period. At the same time, government policy also played a key role.

However, while energy efficiency is growing, the problem that the efficiency value of the different parts has a huge difference is very obvious. As can be seen, the average energy efficiency value of the eastern part such as Shanghai, Jiangsu has been in the forefront of the country. The average energy efficiency value of southwest and northwest regions are always lower than the national average, Xinjiang in 2009 efficiency value even fell slightly.

According to the energy efficiency mean value of the various regions from 2005 to 2010, 30 regions across the country can be sorted by the size of the efficiency values; the ranking is shown in Fig. 21.1.

From the distribution of China's 30 regional energy efficiency mean value ranking, there is some imbalance among the energy efficiency of the various regions. In this period, the energy efficiency of the northern part has been lower than the national mean value, Inner Mongolia and Shanxi Energy efficiency value listed only 26 and 28, while Beijing as the capital city, whether economic conditions or technical conditions have an absolute advantage, energy efficiency value has been in a leading position in the country. In addition to Beijing, all the rest of regions with the high efficiency value distributed in the southeast coastal areas without exception. Western region only Chongqing efficiency value is in the middle position of the ranking, most of the rest areas in almost all in the behind, efficiency value is significantly lower than the eastern region, the last ranked Ningxia efficiency value is only about one-fifth of Beijing.

Table 21.4 The regional efficiency value statistics

Region	Regional efficiency values					
	2005	2006	2007	2008	2009	2010
Beijing	1.26	1.37	1.57	1.76	1.85	2.03
Tianjin	0.96	0.99	1.06	1.25	1.28	1.35
Hebei	0.50	0.53	0.58	0.66	0.68	0.74
Shanxi	0.33	0.35	0.39	0.47	0.47	0.55
Inner Mongolia	0.40	0.44	0.50	0.60	0.63	0.69
Northern region	0.69	0.74	0.82	0.95	0.98	1.07
Liaoning	0.59	0.62	0.67	0.77	0.80	0.88
Jilin	0.68	0.72	0.81	0.89	0.95	1.04
Heilongjiang	0.68	0.71	0.76	0.83	0.82	0.92
Northeastern region	0.65	0.69	0.75	0.83	0.85	0.95
Shanghai	1.12	1.19	1.29	1.38	1.45	1.53
Jiangsu	1.08	1.14	1.24	1.39	1.45	1.61
Zhejiang	1.12	1.19	1.29	1.42	1.48	1.64
Anhui	0.82	0.86	0.95	1.06	1.13	1.27
Fujian	1.07	1.11	1.22	1.31	1.37	1.50
Jiangxi	0.95	1.03	1.15	1.30	1.32	1.49
Shandong	0.76	0.82	0.88	1.01	1.05	1.13
Eastern region	0.99	1.05	1.15	1.27	1.32	1.45
Henan	0.72	0.76	0.84	0.95	0.99	1.08
Hubei	0.65	0.69	0.77	0.88	0.95	1.05
Hunan	0.68	0.73	0.81	0.94	0.98	1.08
Guangdong	1.26	1.33	1.43	1.57	1.60	1.71
Guangxi	0.82	0.88	0.97	1.08	1.10	1.21
Hainan	1.09	1.14	1.19	1.32	1.34	1.52
Southern region	0.87	0.92	1.00	1.12	1.16	1.27
Chongqing	0.70	0.73	0.79	0.90	0.93	1.01
Sichuan	0.63	0.67	0.74	0.83	0.87	0.96
Guizhou	0.36	0.38	0.42	0.50	0.52	0.56
Yunnan	0.57	0.60	0.67	0.76	0.77	0.83
Southwestern region	0.56	0.59	0.66	0.75	0.77	0.84
Shanxi	0.71	0.77	0.85	0.99	1.02	1.14
Gansu	0.44	0.48	0.53	0.59	0.62	0.70
Qinghai	0.33	0.34	0.38	0.45	0.46	0.53
Ningxia	0.24	0.26	0.30	0.37	0.40	0.46
Xinjiang	0.47	0.50	0.54	0.59	0.57	0.66
Northwestern region	0.44	0.47	0.52	0.60	0.61	0.70
National region	0.76	0.80	0.88	0.99	1.02	1.12

21.3.2 Differences Factors of Energy Efficiency Value

In terms of China's economic restructuring, institutional transition, industrialization boost phase, main factors which causing the differences in the energy efficiency of various regions are the following four points:

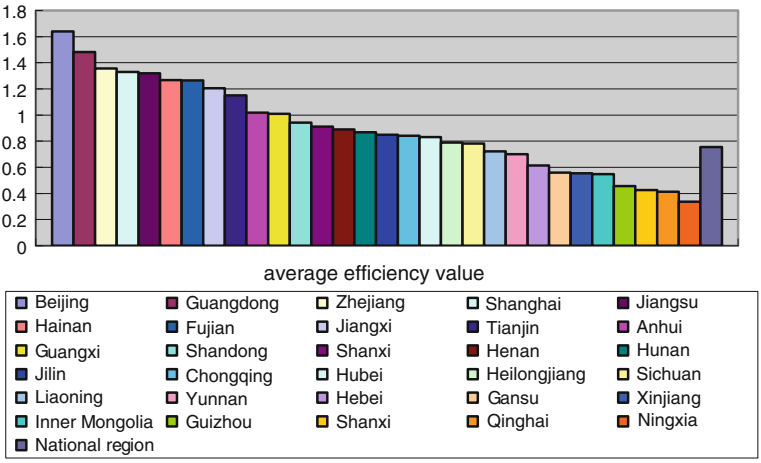

Fig. 21.1 Regional average efficiency value rankings

(1) The economic structure;
(2) The degree of marketization and opening up to the outside world;
(3) Technical conditions;
(4) Related policies and systems.

The eastern region economic aggregate, energy consumption, and carbon emissions occupy most proportion of the country. The rapid economic growth is often driven by the higher speed of industrial growth, industrial growth means that demand for energy is larger, which also stimulates the development of the energy field technology. On the other hand, the economic development will provide strong support to research development and introduction of technology. Technological progress can improve the efficiency of the equipment, thereby reducing energy consumption per unit of product, reducing intermediate energy loss; can improve the efficiency of resource allocation.

From geographical perspective analysis, particularly in coastal areas of the eastern region people and capital flows more freely and frequently, more convenient to attract foreign investment, and more adequately to the introduction digestion and absorption of technology to enhance the energy efficiency. In addition, the technological advances of the eastern region have played a leading role in the enhancement of the energy efficiency. From the southeast coast to the central and northwestern parts, the economic and technical development has gradually weakened, the central and western regions due to its relatively closed geographical location, level of economic development is relatively backward, relatively difficult to obtain more advanced technical and personnel support from

the trade and investment, and their technical level is relatively backward. In addition, due to the impact of past China's eastern, central, and western regional economic development strategy, the development of the central and western long term be at a disadvantage.

21.4 Conclusions

Economic development is the most important determinants of the increase in carbon dioxide emissions in China, but we cannot mitigating carbon dioxide emissions by slowing down the economic growth, the focus should be on reducing energy intensity, reducing the proportion of high-carbon energy in energy consumption structure, and increased consumption of low-carbon energy.

For the overall planning of the country, we should increase investment in the field of energy technology development and introduction, regard improving the energy efficiency of resource utilization and reducing pollution as an important criterion for the adjustment of economic structure. From the angle of market degree and opening up, improve the opening degree of the eastern region, strengthen the central and western regions and the eastern part of the contact, promote exchanges and cooperation between the regions, accelerate the western region of the capital flows, and even will give more financial support and technical support to the backward areas of the western regions, narrow the gap between eastern and western regions.

For the urban local planning, building regional energy planning, we should change the traditional planning method of "fighting each other by professions," unified and coordinated the planning of urban water supply, heat supply, power supply, gas supply, and other energy-related, increase the input into the development of energy-saving technologies and new energy, accelerate the technological transformation and equipment renewal. Selection of building regional energy considering energy diversity, substitutability, achieves energy gradient, utilizes, maximizes, and optimizes the infrastructure functions, improves energy efficiency, and maximizes economic benefits.

References

1. Zhuang G (2007) Low-carbon economy- Choice of China J China Petrochem (13):32–35
2. Tang X (2008) "After the Kyoto Protocol" China Directions [N]. Twenty first century Business Herald
3. Qiu B (2010) The general idea of low-carbon ecological city development in China. J Constr Sci Technol (15):12–17

4. Zhang L (2003) Economic Development and Its Bearing on CO_2 Emissions. J Acta Geogr Sinica (1):61–70
5. Zhuang G (2006) The decline in energy intensity energy demand and policy measures of our 20 % objective constraints during "the eleventh five-year plan". J Rev Econ Res (77):92–96
6. Liao H, Wei Y (2011) "12th Five-Year Plan" Forecast and prospect of China's energy and carbon emissions. Bull Chin Acad Sci 26(2):150–153
7. Wang D (2011) Low carbon city construction and building energy planning. J HV&AC (4):17–19
8. China's Low Carbon Eco-City Development Strategy. China City Press, Beijing, 2009

Part II
HVAC&R Component and System

Chapter 22
A Flexibility Chilled Beam System in Hot and Humid Climate

Risto Kosonen

Abstract The latest studies indicate that an investment in a better indoor environment is a profitable one, even with very minor productivity changes. In addition to the indoor environment, the functionality of the workspace significantly affects the productivity of employees. Often a compromise must be made among the needs of the employee, team, and organization when arranging workspaces. Organizational changes in most companies are continuous and require flexible changes in work methods and workspaces. Layout changes in workplaces are a rule, not an exception. Due to management reorganization, changes in business models, and technological innovations, companies may already change their workplace interior layout once a year. Churn cost is often one of the highest operating costs in modern offices being 330 to 2000 € per moved person a year.

Keywords Chilled beams · Hot and humid climate · Flexibility

22.1 Introduction

Recent studies have clearly proven the correlation between indoor air quality and the work performance of employees [1]. Similarly, it has been demonstrated that the thermal conditions of the room have a significant impact on the productivity of work. Employee salaries and the potential change in productivity amount to many times the cost of a building technology system. The studies indicate that an

R. Kosonen (✉)
Aalto University, School of Engineering, Department of Energy Technology, 14400FI, Aalto 00076, Finland
e-mail: risto.kosonen@aalto.fi

R. Kosonen
Halton Oy, Esterinportti 2, Helsinki 00240, Finland

A. Li et al. (eds.), *Proceedings of the 8th International Symposium on Heating, Ventilation and Air Conditioning*, Lecture Notes in Electrical Engineering 262,
DOI: 10.1007/978-3-642-39581-9_22,

investment in a better indoor environment is a profitable one, even with very minor productivity changes.

In addition to the indoor environment, the functionality of the workspace significantly affects the productivity of employees. Often a compromise must be made among the needs of the employee, team, and organization when arranging workspaces. Addressing the interaction and privacy needs of employees both of which are important considerations in organizations, it is particularly challenging. In general, it can be stated that, from the perspective of dispersing silent information (views, experiences, intuitions), fully autonomous workspaces do not support the business models of most companies. On the other hand, reducing the autonomy afforded by individual workspaces reduces acoustic privacy, which disturbs concentration.

Organizational changes in most companies are continuous and require flexible changes in work methods and workspaces [2]. The traditional one-person office areas, or cells, and open offices, or hives, seen in traditional offices are today changing into spaces that are more suited to team work, referred to as dens or clubs (Table 22.1). In addition to this, information technology contributes to independence of time and location, transforming offices more into meeting places for sharing information. The office space must be utilized efficiently, and therefore a dedicated workstation is no longer deemed necessary for a worker who spends only a few hours a day at the office. Working at several workstations and at customer sites is becoming more common.

Layout changes in workplaces are a rule, not an exception. Due to management reorganization, changes in business models, and technological innovations, companies may already change their workplace interior layout once a year. Churn cost is often one of the highest operating costs in modern offices being 330 to 2000 € per moved person a year [3]. Building services are the major cost generator and a slowing, or even preventing factor in layout changes.

In the Tropical climate, it is important to control relative humidity concurrently with temperature. The majority of air-conditioning systems installed in the Tropics are designed based on all-air systems. Ceiling mounted ventilated chilled beam system could be other attractive approaches for improving energy and ventilation efficiency. These systems minimize the quantity of airflow rate handled and have ability to provide a high quality indoor environment. This means that the space requirement of ductworks and air-handling units are much smaller than with traditional mixing systems. This means savings in the structural and building services costs.

Table 22.1 Adapting space types and business processes in office buildings

Space	Interaction	Autonomy	Operation	Example
Hive	Low	Low	Customer service	Call center
Cell	Low	High	Support tasks	Financial administration
Den	High	Low	Team work	Media
Club	High	High	Expert work	Consultancy

This paper discusses the flexibility requirements imposed by changing office processes for a beam system and covers certain solution models that help to improve the adaptability and flexibility of the system as well as the indoor conditions in the room. Also, the feasibility of a ventilated beam system is studied using a case-study approach. The results of a field measurement in the Tropics, served by a ventilated beam system, were discussed.

22.2 Flexibility

In order to be able to manage indoor environment efficiently through the lifetime of building, it requires performance-based changes in room units and ductwork. Traditional chilled beams cannot be easily used with variable air flow rates. The ventilation ductwork should be designed for constant pressure, which enables demand-based air flow control. Flexibility requires possibility to control both throw pattern and airflow rate in changing conditions. For maintaining a constant supply air flow (2 l/s per m^2), an adjustment range of 15–30 l/s is required of the room device. This range increases to 15–40 l/s if it must be possible to convert a one-person office room into a meeting room. Together with airflow rate, air velocity conditions should be controlled to maintain draft-free conditions.

Ready adaptability of air flow and space arrangements also increases the need to manage air distribution such that it reflects the various space solutions. It must be possible to reduce the total air flow from a beam in situations where, for example, the room device is close to a partition wall and the distance of the workstation from the wall is short. It should also be noted that, owing to individual differences between people, some people perceive even low air velocities as a draft. This means an increased need to manage the individual room conditions.

An efficient way of managing room space air velocities is to reduce the induction ratio of the room device to an appropriate level. Figure 22.1 presents the principle of operation for the induction ratio adjustment in a ventilation beam.

Case-studies carried out in laboratories examined the significance of induction adjustment in a situation where beams installed in a suspended ceiling were

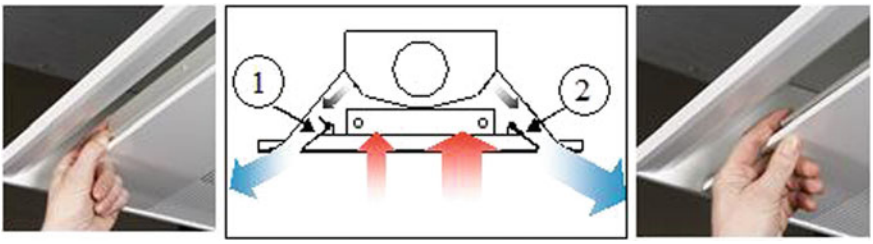

Fig. 22.1 Principle behind induction ratio adjustment: (1) induction ratio adjustment on and (2) induction ratio adjustment off

perpendicular to the window. According to the measurements made [4], induction adjustment could significantly reduce air velocities in the proximity of the employees (Fig. 22.2).

The primary airflow rate of each beam could be adjusted using an air quality control unit. Thus, there is no need to change or plug nozzles of the chilled beam. Air quality controller also allows increasing the airflow rate of a chilled beam—e.g., to meet the ventilation requirements of meeting rooms (up to 4–6 l/s per m^2).

Abstract Traditional chilled beams cannot be easily used with variable air flow rates. The ventilation ductwork should be designed for constant pressure, which enables demand-based air flow control. Flexibility requires possibility to control both throw pattern and airflow rate in changing conditions. An efficient way of managing room space air velocities is to reduce the induction ratio of the room device to an appropriate level. Case-studies carried out in laboratories examined the significance of induction adjustment in a situation where beams installed in a

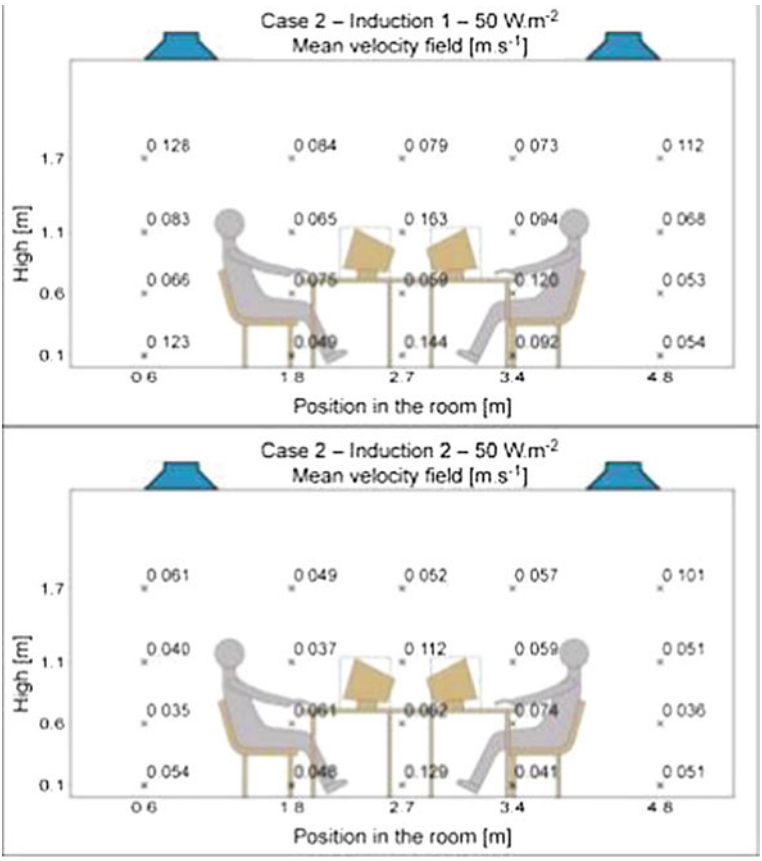

Fig. 22.2 Impact of induction ratio adjustment on air velocity in laboratory tests. *Upper Image* Induction ratio adjustment off. *Underneath image* Induction ratio adjustment on

suspended ceiling were perpendicular to the window. According to the measurements made, induction adjustment could significantly reduce air velocities in the proximity of the employees.

22.3 Beam System in Hot and Humid Climate

The feasibility of a ventilated beam system is evaluated using field measurement in an office building [5]. The condensation risk during the morning start-up period and operation hours is studied by monitoring room conditions. In the office, two rooms were installed with a ventilated beam system. The rest of office rooms are served by the all-air system. An office of 20 m^2 is located in the perimeter zone where possible air infiltration increase humidity level. The other room is a conference room of 56 m^2, which is located in the central area. This internal room is not affected by infiltration and the main humidity source is from the people.

In the measurement arrangement, the room temperature and humidity is measured with portable data logger. The same system is used to measure the supply air and outdoor conditions. The supply air flow rate to the room spaces is measured using a pressure measurement tap of the ventilated beam. The water inlet and outlet temperatures were measured with the thermocouples installed on the water pipe. The good contact of the thermocouples is secured using glue and covered the thermocouples with the insulation. In Fig. 22.3, it is shown the measurement results of the system during one typical working day.

The room temperatures are 21–23 °C in the conference room and about 23 °C in the office room. The dewpoint of the conference room is about 17 °C and 14.5–16.5 °C in the office. The dewpoint of the conference and office rooms are

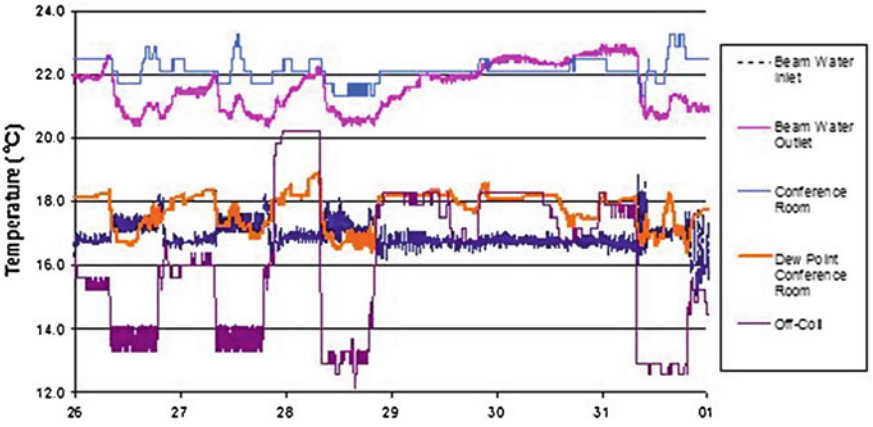

Fig. 22.3 The operation conditions in the ventilated beam system during one working day

quite close the water inlet temperature. However even the surface temperature was short time slightly below the dewpoint in reality condensation was not happening.

In the Topical climate where the humidity is always high, it is important to maintain the dewpoint of the room space lower than the water inlet to prevent condensation. The most challenging time periods are Monday mornings. In the Tropics, the inlet temperature should be higher to prevent condensation in the ventilated beams. The target temperature and humidity level are the starting point for the system design.

Typically, the target for the room temperature is 23–24 °C and 60–65 % for the relative humidity. Nowadays, there is trend to rise up the room temperature up to 26 °C that reduces the required cooling capacity significantly. It should be that thermal comfort is not restricted to humidity limit in the indoor air. The humidity can be as high as 75 % if the air temperature is within the acceptable level. It should be noted that mold growing should be taken account. The mold growing could be possible if the relative humidity is over 78 % at the room temperature [6].

The conducted measurements indicate that the infiltration could be quite small if the windows frames and doors are airtight. Thus, the night-time generated humidity is possible to ventilate by starting the operation of air-handling unit about 30–60 min earlier than water-based cooling. Anyhow, the dehumidified period must be longer and the supply air flow rate should be higher if the building is less airtight.

In the mornings, the air-based cooling should start earlier and after certain time when the humidity level will be at the design level water-based cooling should start. This means that control strategy should be designed taken into account the characteristic of the building. Also, the commissioning and the tuning of the automation system have to conduct probably. In the Tropical conditions, faults in the automation system are much more critical than in the temperate climate.

Abstract In the Topical climate where the humidity is always high, it is important to maintain the dewpoint of the room space lower than the water inlet to prevent condensation. In the Tropics, the inlet temperature should be higher to prevent condensation in the ventilated beams. The target temperature and humidity level are the starting point for the system design In the Tropics, the inlet temperature should be higher to prevent condensation in the ventilated beams. The target temperature and humidity level are the starting point for the system design. The commissioning and the tuning of the automation system have to conduct probably. In the Tropical conditions, faults in the automation system are much more critical than in the temperate climate.

22.4 Conclusion

Organizational changes in most companies are continuous and require flexible changes in work methods and workspaces. The traditional one person office areas, or cells, and open offices, or hives, seen in traditional offices are today changing

into spaces that are more suited to team work, referred to as dens or clubs. This means that building system should be easily to be adaptable for the needs for continuously changing users. Specially, throw pattern and air flow rate should be easily to be adjustable.

In hot and humid climate, the room design conditions of 23 °C and 65 % is attainable with the water inlet and the supply temperatures 17 and 14 °C when the specific supply air flow rate is 10 l/s per person. Together with the previous design parameter and with dehumidified the indoor air properly prior the operation of the water-based cooling, it is possible to maintain dry cooling without any condensation in the ventilated beam system.

Acknowledgments The study is supported by Technology Agency of Finland (TEKES) in RYM-SHOK research program.

References

1. Wargocki P, Seppänen O, Andersson J, Clements-Croome D, Fitzner K, Hanssen SO (2006) Indoor climate and productivity in offices. REHVA guidebook NO.6
2. Kosonen R, Virta M (2007)Taking flexibility into account in designing beam systems. WellBeing Indoors Clima 10–14 June 2007. Helsinki Finland. Proceedings of Clima
3. CIBSE TM27: Flexible Building Services for Office-Based Environments, Principles for Designers, Dec 2000. The Chartered Institution of Building Services Engineers, London
4. Zhoril V, Melikov A, Kosonen R (2006) Air flow distribution in rooms with chilled beams. 17th Air–conditioning and ventilation conference 17–19 May 2006 in Prague
5. Kosonen R (2005) Tan Freddie: A feasibility study of a ventilated beam system in the hot and humid climate: a case-study approach. Build Environ 40:1164–1173
6. Viitanen H (1997) Modelling the time factor in the development of mould fungi in wood—the effect of critical humidity and temperature conditions. Holzforschung 51(1):6–14

Chapter 23
Experimental Evaluation of a Total Heat Recovery Unit with Polymer Membrane Foils

Lei Fang, Shu Yuan and Jinzhe Nie

Abstract A laboratory experimental study was conducted to investigate the energy performance of a total heat recovery unit using a polymer membranes heat exchanger. The study was conducted in twin climate chambers. One of the chambers simulated outdoor climate conditions and the other simulated the climate condition indoors. The airflows taken from the two chambers were connected into the total heat recovery unit and exchange heat in a polymer membrane foil heat exchanger installed inside the unit. The temperature and humidity of the air upstream and downstream of the heat exchanger were measured. Based on the measured temperature and humidity values, the temperature, humidity, and enthalpy efficiencies of the total heat recovery unit were calculated. The experiment was conducted in different combinations of outdoor climate conditions simulating warm and humid outdoor climates and air-conditioned indoor climate. The test was also conducted in isothermal conditions to observe the moisture transfer performance of the polymer membrane heat exchanger. The results of the experiment shows that total heat recovery equipment tested can recover up to 60 % of the total heat from the ventilation air. Around 87 % of the recovered total heat is latent heat that comes from the moisture transfer.

Keywords Total heat recovery · Energy recovery · Enthalpy · Moisture transfer · Ventilation

L. Fang (✉) · S. Yuan · J. Nie
International Centre for Indoor Environment and Energy, Department of Civil Engineering, Technical University of Denmark, Lyngby 2800, Denmark
e-mail: fl@byg.dtu.dk

A. Li et al. (eds.), *Proceedings of the 8th International Symposium on Heating, Ventilation and Air Conditioning*, Lecture Notes in Electrical Engineering 262,
DOI: 10.1007/978-3-642-39581-9_23,

23.1 Introduction

Ventilation consumes around 30 % of total energy used in buildings. With the improvement of thermal insulation in modern buildings, the proportion of energy consumption for ventilation will further increase. Energy recovery for ventilation is becoming an urgent issue for energy saving in buildings. Total heat recovery technology is used for recovering both sensible and latent heat from the exhaust air of the ventilated buildings. It is a very effective energy saving technology in ventilation system where latent load is the major part of the thermal load. Traditionally, rotary desiccant wheel (often known as rotary enthalpy exchanger) is used for total heat recovery. The desiccant wheel transfers both sensible heat and moisture (latent heat) between the supplied fresh air and the exhausted indoor air. The total heat transfer efficiency of a desiccant wheel is usually in a range between 55 to 85 % [1]. Such a performance seems quite satisfied from energy point of view. However, rotary enthalpy exchanger often transfers air contaminants in the process of heat and moisture transfer [2, 3]. Such contaminants transfer may be due to leakage, carryover and/or adsorption/desorption of the contaminants when an enthalpy wheel is in operation, and it is very difficult to avoid this contaminants transfer when using enthalpy wheel for energy recovery. For ventilation purpose, such a contaminants transfer is not acceptable since it reduces the effectiveness of ventilation and makes the energy recovery meaningless.

The plate heat exchangers (cross flow or counter flow heat exchanger) using aluminium foils to separate the two air streams of supply and exhaust can avoid the contaminants transfer problem encountered when using the enthalpy wheel for heat recovery. However, the aluminium foil allows only for sensible heat transfer but not for the moisture transfer. The plate heat exchanger that is made of polymer membranes instead of aluminium foils is a new technology that allows for not only sensible heat but also very efficient moisture transfer in the plate heat exchanger. It makes the plate heat exchanger a total heat exchanger (enthalpy exchanger). The polymer membranes allow moisture to penetrate but not other gas phase chemicals [4], particles and microorganisms. Therefore, the plate heat exchanger made of polymer membranes is a total heat exchanger without contaminants transfer between supply and exhaust air streams.

This paper presents a laboratory experimental study that investigated the sensible heat, moisture, and enthalpy transfer performance of a plate heat exchanger made of polymer membranes.

23.2 Method

The experiment was conducted in climate chambers with climatic environments simulated both indoor and outdoor climates. The detailed method of the experiment is described below.

23.2.1 The Heat Recovery Unit Tested

The total heat recovery unit tested has a counter flow enthalpy exchanger (Zehnder comfoAir 160). The rated airflow rate is 160 m^3/h. The enthalpy exchanger in the heat recovery unit tested is made of porous polymer membranes that allow water vapor to be transferred between the supply and exhaust air flow without transferring odors, gases, and contaminants, e.g., microorganisms that are larger compared with water molecules. The humidity is transferred as water vapor by diffusion from the high to the low vapor pressure side so that the enthalpy exchanger can be perfectly used in cold as well as warm humid regions the whole year around.

23.2.2 Experimental Setup

The experiment was conducted in twin climate chambers. One chamber simulated outdoor climate and the other simulated indoor climate. A hole that was made on the door between the twin chambers allows connecting a duct to transport air from one chamber to the other. The total heat recovery unit to be tested was installed in the chamber that simulated indoor climate (Fig. 23.1). The inlet of the unit for outdoor air input was connected directly to the duct come from the chamber simulating the outdoor climate conditions. The duct connecting the total heat recovery unit to the chamber simulating outdoor climate was thermally insulated to avoid condensation inside. The inlet of the unit for indoor air input took the air directly from the chamber simulating indoor climate conditions. The outlets of both outdoor and indoor air were connected directly to the exhaust of the chamber and the air was exhausted without mixing with the air in the chamber.

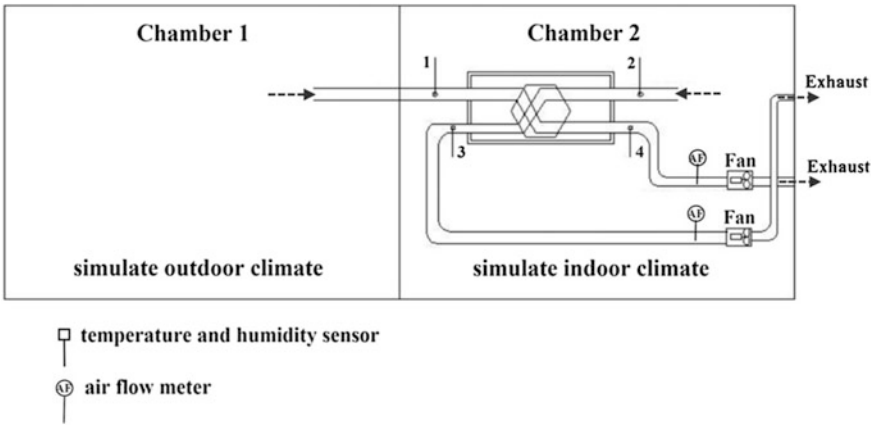

Fig. 23.1 Experimental setup for testing the total heat recovery unit in twin climate chambers

Temperature and humidity of the air at all inlets and outlets of the total heat recovery unit were measured to calculate the temperature, humidity, and enthalpy efficiencies of the total heat recovery unit. The temperature and relative humidity were measured using Vaisala sensors (HMT130 three-wire transmitter). The sensors were all calibrated before the experiment with an accuracy of ±0.2 °C and ±2 % RH. Airflow rate on both supply and exhaust sides of the unit were measured and controlled at the same level 120 m^3/h which was 80 % of the rated airflow rate of the test unit.

The temperature, humidity, and enthalpy efficiencies were calculated using the following formulas.

$$\text{Temperature efficiency}: \ \eta_{t,c} = \frac{t_{c,\text{out}} - t_{c,\text{in}}}{t_{w,\text{in}} - t_{c,\text{in}}}$$

$$\text{Humidityefficiency}: \ \eta_{x,c} = \frac{X_{c,\text{out}} - X_{c,\text{in}}}{X_{w,\text{in}} - X_{c,\text{in}}}$$

$$\text{Enthalpy efficiency}: \ \eta_{I,c} = \frac{I_{c,\text{out}} - I_{c,\text{in}}}{I_{w,\text{in}} - I_{c,\text{in}}}$$

where:

$\eta_{t,c}$	is the temperature efficiency;
$t_{c,\text{out}}$; $t_{c,\text{in}}$; $t_{w,\text{in}}$	are temperatures of the exhaust, indoor and outdoor air
$\eta_{x,c}$	is the humidity efficiency;
$x_{c,\text{out}}$; $x_{c,\text{in}}$; $x_{w,\text{in}}$	are humidity ratios of the exhaust, indoor and outdoor air
$\eta_{l,c}$	is the enthalpy efficiency;
$I_{c,\text{out}}$; $I_{c,\text{in}}$; $I_{w,\text{in}}$	are enthalpies of exhaust, indoor and outdoor air.

The enthalpies of air were calculated from the measured air temperature and humidity using the following formula.

$$E = 1.006t + 0.622(2501 + 1.84t) \times \frac{0.01\emptyset e^{\left(23.58 - \frac{4043}{t+273.15-37.58}\right)}}{P_0 - 0.01\emptyset e^{\left(23.58 - \frac{4043}{t+273.15-37.58}\right)}}$$

where

E	is enthalpy of the air, kJ/kg;
t	is temperature of the air, °C;
$\emptyset$	is relative humidity of the air, %;
P_0	is barometric pressure of the air, pa

23.2.3 Experimental Design and Procedure

The experiment was designed to exam the temperature, humidity, and enthalpy efficiencies of the total heat recovery unit at different levels of air temperature and humidity of summer outdoor conditions. Table 23.1 shows the design of the

Table 23.1 Different combination of indoor and outdoor climate conditions

Indoor climate condition	Outdoor climate conditions			
25 °C/50 %RH	40 °C/65 %RH	35 °C/65 %RH	25 °C/65 %RH	25 °C/85RH

experimental conditions. This design allows to exam the heat recovery efficiency at both isothermal and nonisothermal conditions, i.e., to exam the impact of air temperature on humidity recovery efficiency.

Each pair of the designed experimental conditions simulating different outdoor climates and a constant indoor climate were established in the twin climate chambers sequentially. Temperature, humidity at inlet and outlet of both sides of the heat recovery unit were measured continuously at an interval of about 1 s. Each condition was established and stabilized before the data collection started. After the test climate conditions reached steady state, temperature, humidity at inlet and outlet of both sides of the heat recovery unit were recorded at an interval of about 8 s for at least 30 min.

23.3 Results

The temperature, humidity, and enthalpy efficiencies of the heat recovery unit measured at the three levels of outdoor air temperature with the relative humidity of 65 % and indoor condition of 25°C/50 %RH are shown in Figs. 23.2 and 23.3. The figures show that the temperature efficiencies of the heat recovery unit were slightly over 70 %. This efficiency is not influenced by the temperature difference between indoor and outdoor conditions. Humidity efficiencies were slightly lower than 60 % also regardless of temperature difference between indoor and outdoor. Enthalpy efficiencies were 60 % at two nonisothermal conditions, while 8 % lower

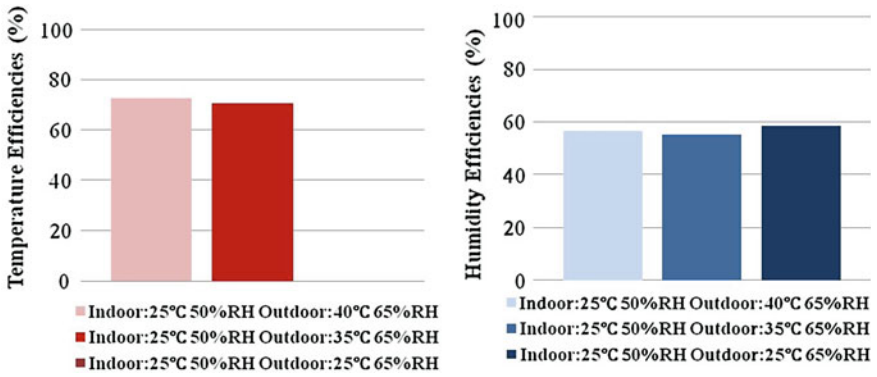

Fig. 23.2 Temperature and humidity efficiencies measured at three different outdoor air temperature conditions with the same relative humidity of 65 %

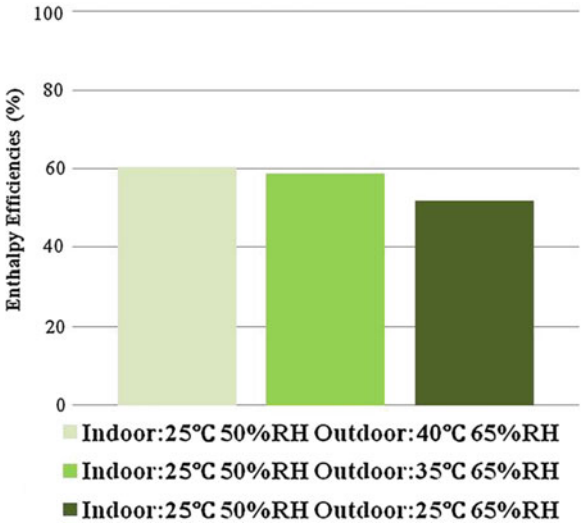

Fig. 23.3 Enthalpy efficiencies measured at three different outdoor air temperature conditions with the same relative humidity of 65 %

at the isothermal condition. The 8 % higher enthalpy efficiency measured at the nonisothermal conditions should be the contribution from the heat recovery due to temperature difference, which means that 87 % of the recovered total heat is the latent heat that come from the moisture transfer.

The humidity and enthalpy efficiency were also studied at two isothermal conditions at 25 °C. The differences of relative humidity between indoor and outdoor were 15 and 35 %, respectively. The experimental results were demonstrated in Fig. 23.4. These results showed that the humidity efficiency was at a level of 60 % and was not influenced by the humidity difference between indoor and outdoor air. The enthalpy efficiencies of the heat recovery unit at the isothermal condition were at the level 55 %. Since the results were obtained at isothermal condition, the driving force was the difference of the moisture content indicating that the polymer film used in the heat exchanger has high moisture penetrability.

Comparing the enthalpy efficiencies between nonisothermal and isothermal conditions shown in Figs. 23.3 and 23.4, it is found that the enthalpy efficiency at the nonisothermal conditions was only few percentages higher than that of isothermal conditions which means that temperature difference had very small contribution on the total heat recovery on these test conditions.

23.4 Discussion

The results of this experiment show that enthalpy efficiency of the heat recovery unit tested is 60 % when used at warm and humid summer climate. This means that 60 % of the energy used for conditioning the ventilation can be saved by using the

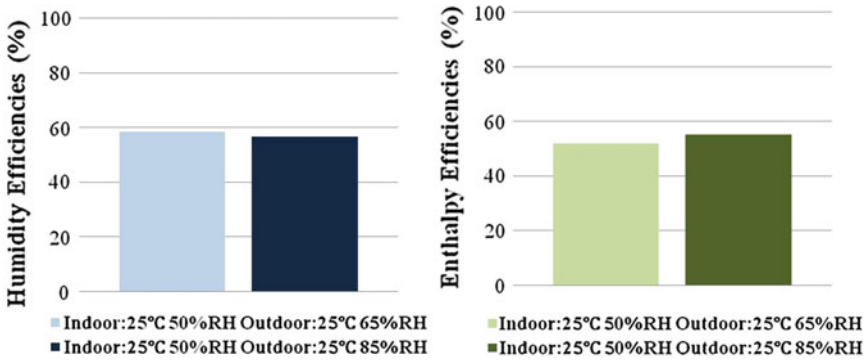

Fig. 23.4 Humidity and enthalpy efficiencies measured at the two isothermal conditions

polymer film total heat exchange technology. Compared to a counter flow sensible heat exchange technology, the polymer film total heat exchange technology increases the energy recovery by 40–50 % which is very significant for energy conservation in air conditioned buildings in warm and humid climate zones.

The enthalpy efficiency of the polymer film total heat exchange technology is comparable to the rotary desiccant total heat recovery technology. Although the enthalpy efficiency of a desiccant wheel can reach a higher level than 60 %, it is usually achieved by increasing the rotation speed which will result in higher carryover of the air contaminants. This is known to transfer some air pollutants from the exhaust air back to the supplied fresh air. Apart from the carryover, the desiccant wheel also transfers contaminants from the exhaust air to supply air due to the adsorption and desorption process, which greatly reduced the effectiveness of a ventilation system. Studies have shown that the polymer film has a selective penetration performance that allows only moisture to penetrate but obstructs other molecules in ai,r e.g., VOCs to penetrate [4]. Such a performance was not studied in this experiment and is remained to be verified. If it is proved by further experiments, the polymer film heat exchange technology will become one of the ideal total heat recovery technologies for ventilation.

23.5 Conclusions

In the warm and humid climates, a total heat recovery equipment using polymer film counter flow heat exchange technology can recover 60 % of the total heat from the ventilation air. Around 87 % of the recovered total heat is the latent heat that comes from the moisture transfer.

Acknowledgments This work is sponsored by the research project "Development of new total heat recovery ventilation technology for energy conservation in buildings" funded by Bjarne Saxhofs Fond, Denmark.

References

1. Rabbia M, Dowse G (2000) Understanding energy wheels and energy recovery ventilation technology, Energy Recovery Ventilation, Carrier Corporation, New York
2. Anderson B, Anderson K, Sundell J, Zingmark P-A (1993) Mass transfer of contaminants in rotary heat enthalpy exchangers. Indoor Air 3:143–148
3. J Pejterson H (1996) Sensory air pollution caused by rotary heat exchangers. Proc of Indoor Air 3:459–464
4. Zhang L-Z, Zhang X-R, Miao Q-Z, Pei L-X (2012) Selective permeation of moisture and VOCs through polymer membranes used in total heat exchangers for indoor air ventilation. Indoor Air 22:143–148

Chapter 24
Radiant Floor Behavior in Removing Cooling Loads from Large Glassed Buildings

Stefano P. Corgnati and Matteo Jarre

Abstract When radiant systems are installed in highly glazed rooms large amounts of solar radiation directly hit the cooled surface; this specific behavior of radiant systems in this situation should be studied in order to modify the procedure that is traditionally applied to design radiant cooling systems. Furthermore, radiant systems behave in different ways depending on their thermal mass. Based on previous researches, a model is proposed in this work to determine the conversion of heat gains into cooling loads; the model is specifically adapted to highly glazed buildings, and is differentiated for low and high thermal masses radiant systems. A numerical model is developed to provide a calculation example that confirms the proposed procedure.

Keywords Radiant cooling floors · Glassed buildings · Direct water load

24.1 Introduction

Radiant floors are more and more adopted for both heating and cooling purposes. At the same time, large buildings projects (such as airports, large halls…) involve more and more often the use of entirely or almost entirely glassed envelopes [1]. The combination of these two factors causes a large amount of solar radiation to directly hit the floor surface, which is cooled; the way in which heat gains are transformed into cooling loads for the system gets therefore different and should be studied by dedicated models. The modeling and the analysis of the different types of thermal exchange through which this transformation occurs are the object of this

S. P. Corgnati (✉) · M. Jarre
TEBE Research Group, Department of Energetics, Politecnico di Torino,
Corso Duca degli Abruzzi 24, 10129 Torino, Italy
e-mail: stefano.corgnati@polito.it

A. Li et al. (eds.), *Proceedings of the 8th International Symposium on Heating, Ventilation and Air Conditioning*, Lecture Notes in Electrical Engineering 262,
DOI: 10.1007/978-3-642-39581-9_24,

study. The main aim is to provide new guidelines for the design and dimensioning of radiant floors under the conditions of large amounts of solar radiation.

As a starting point researches in the literature concerning the behavior of radiant ceilings were reviewed [2–4, 8]. Both the theoretical approach and the developed numerical models have been modified in order to be applied to the radiant floor case. The main modification required is due to the necessity to take into account the thermal inertia of the radiant floors and its fundamental role in delaying the external load transfer to the cooling system. The theoretical procedure that leads to the assessment of the radiant floor model is presented in detail: starting from the trivial case of an all-air system, the model is adapted step-by-step to the radiant systems, both low (ceilings and walls) and high (floors) thermal mass. The additional hypothesis of highly percentage of glassed envelopes, and consequent high amount of solar heat gains, is introduced as a final step.

Finally a numerical model that takes into account the opportunity to modify the dimensioning procedure for the radiant floors in large glassed buildings in order to get an optimized functioning of the cooling system has been developed. The model allows indeed a more accurate comparison of the studied cooling system with the ones that are more commonly and normally adopted.

24.2 Heat Gains and Cooling Loads

The object of this work is to assess a new procedure to take into account the way in which Heat Gains (HG) that affect a certain environment are converted into Cooling Loads (CL) when radiant systems are installed. Therefore, a preliminary definition of these concepts and a brief summary of the way they are calculated are required. From [5] the following definitions apply:

- Heat Gains constitute the total amount of heat generated or introduced into the room at a certain time.
- Cooling Loads constitute the total amount of heat that must be removed from the room at the same time in order to maintain the design conditions of temperature and relative humidity.

Note that HG and CL calculated at a given time θ have different values because of the role of thermal masses of building. This role is different depending on the considered type of load, that can be a convective one or a radiant one: while the convective gain acts directly on the air present in the room, and is therefore not influenced in anyway by the thermal mass of the building, the radiant gain gets absorbed into the building mass and is re-irradiated into the room just in a further moment. This fraction influences the room air temperature just after a certain time delay and depends on building thermal mass [2, 3].

It is useful to introduce the Room Load (RL) as the sum of all the heat gains that are converted into cooling loads at a given time θ; this is the load that has to be removed in order to keep the design temperature and relative humidity in the room.

Since dynamic models are required for cooling calculations in which thermal mass must be taken into account, if we consider in particular the Radiant Time Series method (see [5] for more details) the following formula applies for the determination of RL at a given time θ for a generic system.

$$RL_{\theta,\text{conv}} = HG_{\theta,\text{conv}} \tag{24.1}$$

$$RL_{\theta,\text{rad}} = \sum_{n=0}^{23} r_n \cdot HG_{\theta-n,\text{rad}} \tag{24.2}$$

In the next paragraphs it is highlighted that the radiant fraction of room load is strongly influenced by the adopted cooling system while the convective one is not.

24.2.1 All-Air Systems

The definitions given in the previous paragraph allow to straight-forward assess the procedure to calculate cooling loads for a room cooled by an all-air system; in this kind of system the total cooling load simply corresponds to Room Load at every time and the RTS model can be applied without any modification. In Fig. 24.1 the conceptual scheme summarizes this model. The total cooling load is here called Cooling Air Load (CAL) because it is absorbed by the air system.

24.2.2 Radiant Systems: Traditional Model

If a traditional model is used to calculate the cooling loads in a room served by a radiant ceiling, wall, or floor there will be no substantial difference with the just presented procedure concerning all-air systems cooled environments: RL at a

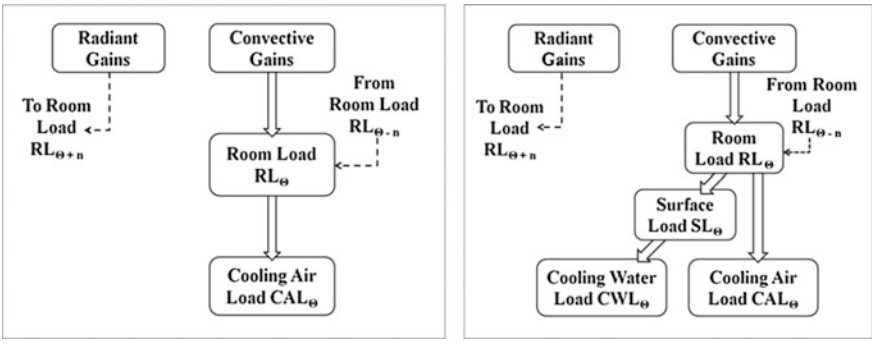

Fig. 24.1 All-air and traditional radiant system

certain time are calculated through (24.1) and (24.2) and must be removed instant by instant. This is made by the radiant system through the so-called Surface Load (SL), that is due to the energy exchanged between the air and the cold surface of the radiant system [2, 3]. This load is therefore calculated simply as:

$$SL = h_{\text{tot}} * \left(T_{\text{sup}} - T_{\text{op}}\right) \tag{24.3}$$

where T_{sup} is the surface temperature of the floor, T_{op} is the operative temperature, and h_{tot} is the total heat exchange coefficient. The SL represents in this model the whole cooling capability of the radiant system, that can be defined as Cooling Water Load (CWL) analogously to the definition of the Cooling Air Load.

It is well known by manufacturers and it is shown in (24.3) that the surface load that can be removed by a radiant system has an upper limit value [2, 6, 7]. This limitation and the opportunity to control not just thermal conditions but also the hygrometric ones inside an environment makes much common the adoption of an air-water system, i.e., the combination of a radiant and a ventilation system. It must be underlined that the common control strategies to follow the room load variations during the day for air-water systems involve the regulation of supply air flow rate rather than regulation of water temperature or water flow rate. Because of that the CAL of an air-water system is calculated simply as

$$CAL_{\theta} = RL_{\theta} - CWL_{\theta} = RL_{\theta} - SL \tag{24.4}$$

The latent load, due for example to occupancy, must be always assigned to CAL because radiant system cannot effect hygrometric conditions inside the room. The previous formula shows clearly that, since maximum Surface Load is constant, the variations of the Cooling Air Load depend solely on the variations of the Room Load, that are again depending primarily on outdoor climate conditions.

24.2.3 Radiant Systems: Up-dated Model

As previously stated, when radiant systems are used for cooling in rooms where a large amount of solar radiation directly hits the radiant surface the model should be changed. The main modification that applies to every type of radiant system is due to the fact that the fraction of radiant energy that directly hits the cooled surface gets now consistent; this fraction should be considered separately from all the other heat gains because it is removed directly by the action of the radiant cooling system before becoming part of the Room Load, without changing therefore in anyway the thermal conditions of the room, as discussed in [2, 4, 8].

The Direct Water Load (DWL) is introduced as the fraction "F" of all the radiant heat gains generated or introduced into the room that are directly removed by the radiant cooling system. In principle, the DWL is generated by all the radiant gains that characterize the studied environment, not just by the solar one. On the other hand, in highly glazed buildings the contribution to radiant gains given by

solar energy is much greater than the contribution given by internal gains. For this reason, the following simplified formula can be used in all those cases in which internal gains are low compared to solar ones:

$$DWL_\theta = F_{sol,\theta} * HG_{\mathrm{rad,sol},\theta} \tag{24.5}$$

The origin of the DWL is different if a low or a high thermal mass cooling system is considered: for radiant ceilings or walls, whose thermal mass is typically neglected, the radiant heat gains that hit the cooled surface are instantly removed; therefore the DWL at a certain time θ can be calculated simply through (24.5).

On the other hand, radiant floors have a thermal mass that depends on materials properties and thicknesses but is very often not negligible [4, 12]. It will have therefore the effect to delay in time the removal of radiant heat gains by the cooled floor; it is useful to define an additional quantity called Floor Load (FL) that represents the ratio "F" of radiant heat gains that hits the floor at the given time θ and causes the DWL in a future moment $\theta + n$; the DWL at a certain time θ will therefore be caused by Floor Load generated in a past moment $\theta - n$:

$$\mathrm{DWL}_\theta = \mathrm{FL}_{\theta-n} = \mathrm{F{*}HG}_{\mathrm{rad},\theta-\mathrm{n}} \tag{24.6}$$

Even if DWL is instantly removed from the room by the radiant cooling system the $(1 - \mathrm{F})$ fraction of radiant heat gains and all the convective heat gains that generate the RL at a certain time are still present in the room and must be removed instant-by-instant by the combined action of the radiant system (through the Surface Load) and the ventilation system (through the Cooling Air Load).

From what stated in the previous paragraphs it is clarified the importance of the theoretical approach here followed, that aimed to the definition and identification of the Direct Water Load; this load represents now a "new potential" of the radiant systems that is additional to the Surface Load. For the radiant ceilings and walls this new potential is removed instantly as it hits the cooled surface, and contributes directly to the CWL at the given time θ together with the SL:

$$\mathrm{CWL}_\theta = \mathrm{SL} + \mathrm{DWL}_\theta = SL + \mathrm{F{*}HG}_{\mathrm{rad},\theta} \tag{24.7}$$

Since the role of the thermal mass cannot be neglected for the radiant floors, the DWL at a given time θ is caused by the FL referred to a past time, as previously explained; the CWL of a radiant floor can be therefore expressed as

$$\mathrm{CWL}_\theta = \mathrm{SL} + \mathrm{DWL}_\theta = \mathrm{SL} + \mathrm{FL}_{\theta-n} = SL + \mathrm{F{*}HG}_{\mathrm{rad},\theta-n} \tag{24.8}$$

No formal difference applies to the calculation of the CAL at the given time θ; the important substantial difference with respect to (24.4) is of course that the CWL is improved by the presence of DWL, and the consequent load on the air system is therefore much lower for given boundary conditions. The CAL for radiant systems is then calculated by the following formula, keeping in mind the different temporal origin of DWL for low and high thermal mass radiant systems.

$$CAL_\theta = RL_\theta - CWL_\theta = RL_\theta - (SL + DWL_\theta) \tag{24.9}$$

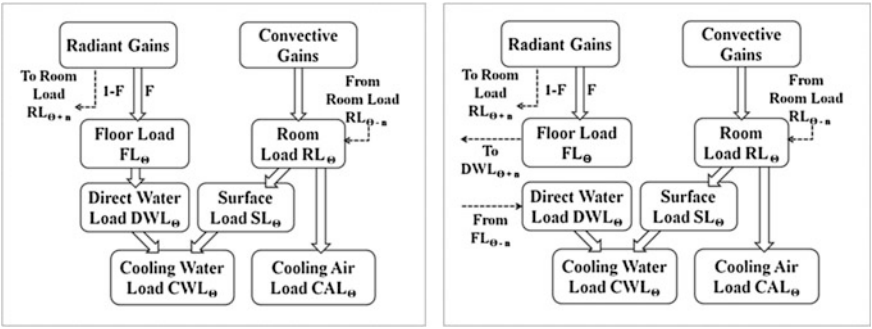

Fig. 24.2 Updated model for radiant systems: low and high thermal mass cases

The conceptual schemes in Fig. 24.2 summarize the load distribution in a room cooled by a low/heavy thermal mass radiant system and a ventilation system.

24.3 Numerical Model

The RTS procedure reported in [5] has been modified accordingly to the described procedure for radiant floors. The model was applied to a case-study office room whose main characteristics are reported in Table 24.1 [4]. The obtained results can be easily compared in order to understand the importance of separately considering the fraction of radiant heat gains that is directly removed by the cooled floor.

The present analysis is focused on the "room side", meaning that no consideration has been made about the "water side" and the optimal plant solutions providing the chilled water. The aim of this work is to show the specific behavior of radiant systems and to underline that radiant floors have an higher potential under large amounts of solar heat gains conditions with respect to the value resulting from traditional calculation models. From this perspective only the FL is evaluated and not the DWL, since for radiant floors the former is in fact the component that must not be added to the RL at every time in the updated model.

Table 24.1 Case-study office room main characteristics

Climatic data	Italy Turin	Floor reflectance to solar radiation (-)	0,5	# People (-)	20
	Lat: 45,03° N	Wall glassed fraction (-)	100 %	Metabolic activity (met)	1,2
	Long: 7,73° E	Windows characteristics	N–W orientation	Lighting gains (W/m^2)	15
Dimensions (m)	9 × 9 × 3		No shading devices	Electric devices gains (W/m^2)	40
Mass structure (-)	Average	Internal design temperature (°C)	26	Building usage profile (-)	8–20

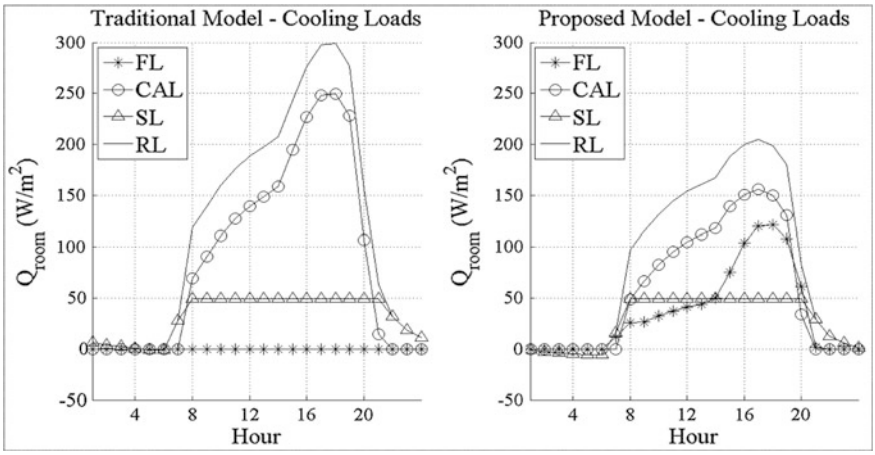

Fig. 24.3 Cooling loads determination for the given case-study

The evaluation of the fraction "F" of radiant heat gains that directly hit a specific surface (in our case the floor) is definitely not trivial. Many critical aspects characterize this problem and the simplifying hypothesis that sustain every model have a strong influence on the final results. Different models are proposed in the literature to study the paths of solar radiation inside a room [9–11]; some of these are simplified models that use very strict hypothesis that are not always applicable while others are much more precise but more difficult to be used for every-day commercial design. Since the aim of this work is not to evaluate the solar radiation that enters a room but to study the behavior of radiant floors under given assumptions, the used "F" factor is the one that has been determined in [8] (Fig. 24.3).

The obtained results show the importance of separating FL from RL when considering radiant floors; the reported graph correctly shows that with traditional model the CAL is very high, due to the fact that SL is limited and RL is high because of the high amount of solar radiation; FL is set to zero for this model and, as previously explained, CAL is different from zero just when RL is higher than the maximum SL. By the introduction of the FL in the updated model the CAL gets consistently reduced because the RL itself is reduced. This, as previously explained, happens because FL is not even accounted as part of the RL, being instantly removed by the action of radiant floor. Globally, instant by instant, the cooling floor removes both the SL and the FL. It can be clearly seen that this reduction effect is much more evident in the 12–18 period, when solar gains are higher.

24.4 Conclusions

A model for the design of radiant systems is proposed, aimed at evaluating the Cooling Load in a room served by a radiant floor and a ventilation system. This model has been obtained by the successive modifications of theoretical models that have been developed in previous literature works.

The developed model suggests the opportunity to consider separately from others a fraction "F" of radiant heat gains that enter in the studied environment; this fraction, called Direct Water Load, is directly removed by the radiant cooling system without becoming Room Load. The effect of this modification is that the calculated Room Load is obviously lower and the total Cooling Water Load of radiant floor is increased, being not anymore constituted by the Surface Load only.

The RTS method has then been modified accordingly to the developed model and applied to a case-study room in order to provide a calculation example.

Further work is required to deeply analyze the connection between the Floor Load and the Direct Water Load, i.e., the time-delay effect that is due to floor thermal mass; in addition, parametric studies are required that analyze floor behavior changes with variations of thermal properties and building characteristics.

References

1. Gaw W, Holst S, Reuss S, Simmonds P (2000) Using radiant cooled floors to condition large spaces and maintain comfort conditions. ASHRAE Transactions 106(1):695–701
2. Causone F, Corgnati SP, Filippi M, Olesen BW (2009) Solar radiation and cooling load calculation for radiant systems: definition and evaluation of the Direct Solar Load. Energy Build. doi:10.1016/j.enbuild.2009.09.008
3. Causone F, Corgnati SP, Filippi M (2007) Calculation method for summer cooling with radiant panels. In: CLIMA 2007 WellBeing Indoors, Helsinki
4. Corgnati SP, Fracastoro GV, Perino M (2000) Un metodo di calcolo per il dimensionamento dei soffitti radianti per il raffrescamento estivo. CDA 7:731–741
5. ASHRAE Handbook Fundamentals (2009)—SI Edition
6. Causone F, Corgnati SP, FIlippi M, Olesen BW (2009) Experimental evaluation of heat transfer coefficients between radiant ceiling and room. Energy Build 41:622–628
7. Causone F, Baldin F, Olesen BW, Corgnati SP (2010) Floor heating and cooling combined with displacement ventilation: possibilities, limitations. Energy Build 42:2338–2352
8. Corgnati SP, Fracastoro GV, Perino M (2000) Sistemi radianti per il raffrescamento estivo: dinamiche di asportazione dei carichi termici. In: Congressi ATI-55, Matera
9. De Carli M, Tonon M (2011) Effect of modeling solar radiation on the cooling performance of radiant floors. Sol Energy 85:689–712
10. Chatziangelidis K, Bouris D (2008) Calculation of the distribution of incoming solar radiation in enclosures. Appl Therm Eng 29:1096–1105
11. Bouchair A (2004) Infinite reflections method for calculation of radiation exchange between Grey-Diffuse surfaces : Up to four surface interactions (Part 1). Rev Energ Ren 7:53–71
12. Koschenz M, Dorer V (1996) Interaction of an air system with concrete core conditioning. Energy Build 30:139–145

Chapter 25
Influence of Different Temperature Control Patterns Through TRV on District Heating Loads

Valentina Monetti, Enrico Fabrizio and Marco Filippi

Abstract This paper describes the application of dynamic energy simulation in order to analyze the application of thermostatic radiator valves (TRVs) on four existing multi-family buildings that are served by a district heating network. A complex and detailed energy model of each case study was defined by means of the energy simulation code EnergyPlus, in order to predict the effect of the employment of TRVs on the heating energy consumptions. The building geometry and envelope characteristics were extracted from the building energy performance certificates; each room equipped with a radiator was defined as a single thermal zone in order to simulate the effect of the TRVs. Measured energy rates and water flow rates of the district heating were used to calibrate the numerical model. In the calibrated model, the impact of TRV control as well as the consequent heat transfer between neighboring rooms were taken into account. Each case study was simulated with and without TRVs. The simulation results show that the use of TRVs can bring a reduction on total heating energy consumption ranging from a minimum of 5 % to a maximum of 20 %.

Keywords District heating · Building simulation · Thermostatic radiators valves (TRVs) · Calibrated simulation

25.1 Introduction

The building sector is responsible for 40 % of Europe's energy needs [1], which represents almost 10 % more than the energy required in the transport sector [2]. For this reason, the European Directive EPBD recast on the energy efficiency of

V. Monetti · M. Filippi
Dipartimento di Energia (DENERG), Politecnico di Torino, Corso Duca degli Abruzzi 24
10129 Turin, Italy

E. Fabrizio (✉)
DEIAFA, University of Torino, Grugliasco, Italy
e-mail: enrico.fabrizio@unito.it

A. Li et al. (eds.), *Proceedings of the 8th International Symposium on Heating, Ventilation and Air Conditioning*, Lecture Notes in Electrical Engineering 262,
DOI: 10.1007/978-3-642-39581-9_25,

buildings [1] requires Member States to improve building energy performance aiming for the nearly zero energy target by 2020. The Directive addresses both new and existing buildings but, due to the low efficiency rate of the existing dwellings and the low replacement rate of old dwellings by new buildings (around 1–3 % per year) [3], refurbishment of the existing stock has become a crucial objective. In Italy residential building are often seen as long-term assets, and the 2008 census survey confirmed a lack of renovation in residential buildings and recorded an increase of 9 % in energy consumptions [2]. The age of the building and its heating installations have therefore a great impact on the building's energy consumptions. For instance, a great amount of residential buildings were built before 1950 [4] and the most common system is the central heating system with columns [5], which, considered together with the decayed building envelope, has a quite low efficiency in terms of losses related to heating needs. The potential energy savings that can be obtained by retrofitting the existing dwellings are clearly high. In this regard, district heating can represent a valuable step to be taken into consideration in the overall urban refurbishments for its role in the transition from fossil to renewable energy in Europe, and for its high potential in achieving the EU 20-20-20 targets [6, 7]. In Italy, especially in the North, the use of district heating showed an upward trend, from 1997 to 2003, reaching 57 %. These results are however far lower than the European average [8]. Turin represents an example of excellence, serving 17,000 houses (150,000 families), covering 40 % of urban building stock with a reduction of 1 million tons of CO_2 emissions.

TRVs represent quite a common refurbishment measure which is to be reinforced by law by 2014 in the city of Turin. Past studies have demonstrated that the effect of TRVs bring an average energy saving from 10 % [9] to 50 % if considered together with the strengthening of the envelope thermal insulation [10]. This paper aims to analyze the application of heating control devices such as thermostatic radiator valves (TRVs) on existing multi-family buildings of a typical Northern Italian city (Turin). The case studies were modeled by means of dynamic simulation. Their application brought back positive results in terms of occupants' thermal comfort and significant energy saving, from 5 to 20 %.

25.2 Case Studies

The case studies, that were selected, are Example Reference Buildings [11], representative of typical apartment buildings located in Turin. They have been selected between a small set of buildings in which energy consumptions were recorded and available in the heating season 2011–2012. The building geometry and envelope characteristics were extracted from the building energy performance certificates and implemented with on-spot-investigations. Table 25.1 lists the main geometric characteristics. The typical floor, with a rectangular plan, has a gross mean area of 100 m^2 and consists of two apartments composed of five main rooms:

Table 25.1 Main geometric data of the case studies

	Construction age	Story	Total gross area (m^2)	Flats	Refurbishments
Case study A	1957	8	1300	13	Partial windows replacement
Case study B	1933	5	1000	12	Partial windows replacement
Case study C	1958	7	1550	21	Not noted
Case study D	1900	4	2114	12	Not noted

Table 25.2 Thermal characterization of case studies envelope main components

	U-value (W/m^2 K)			
	Case study A	Case study B	Case study C	Case study D
Walls	1.9	1.3	1.2	1.5
Roof	2.17	2.17	2.17	2.17
Ground slab	2.1	1.9	1.9	1.9
Windows	4.9	4.9	4.10	4.10
Replaced windows	2.2	2.2	–	–

a kitchen, a living room, one double and one single bedroom, and a bathroom. With regard to the envelope characteristics, the most prevailing construction is the bearing brick walls with no thermal insulation and a pitched roof. The transparent envelope components have been replaced only in a few apartments, and are therefore, in almost all cases, single glazing windows with wood frame and internal blinds. None case study fulfills national energy performance requirements in terms of thermal insulation. Table 25.2 lists the *U*-values of the main envelope components. All buildings have recently been connected to the urban district heating network and have their proper on-site substation with a heating capacity ranging from 100 to 250 kW. The building supply systems are composed of vertical columns and of cast-iron radiator units.

25.3 Monitored Data Analysis

The measured data, concerning each case study individually, were analyzed and revised in order to use them for the calibration.

Available in a mean time step of 6 min, they regarded the total water flow rate (m^3/h), the delivered heating rate (W), the primary loop inlet temperature (°C), the primary loop outlet temperature (°C), and the outdoor dry-bulb temperature (°C). In Fig. 25.1 heating rate during February 2012 is illustrated together with the outdoor dry-bulb temperature. Usually the heating system operates from 6 a.m. to 10 p.m., with a turning off from 10 to 12 a.m. but due to quite cold temperatures up to −7 °C, in the second week of the month, it was operated continually. The average inlet temperature of the primary loop ranged from a minimum value of 85 °C and a maximum of 125 °C.

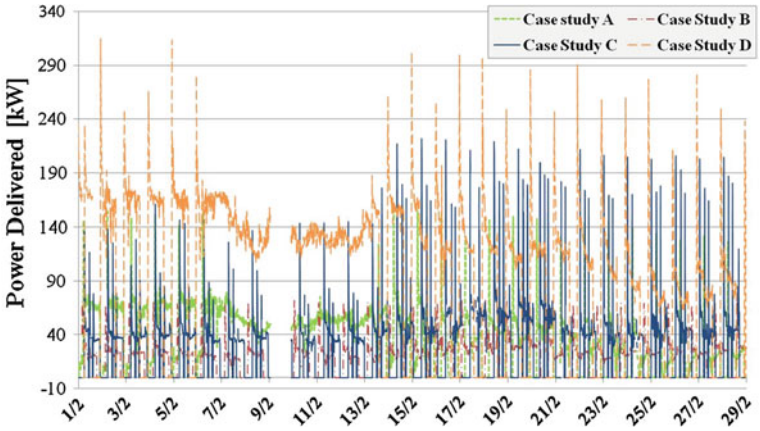

Fig. 25.1 District heating rate of each case study for the February 2012 month

25.4 Methodology

The analysis and verification of the case studies were performed on the basis of a tailored energy rating [12], by means of dynamic simulation through a data-driven approach. Standard boundary conditions were set in order to create a first model. Second, in order to compare the simulate building energy performance with measured data, a calibration methodology was adopted for tuning the models and for making the simulated heating demand match with monitored data. The adjustment was made on the ventilation flow rate and on the thermal conductance of opaque components. At a later stage, in order to simulate the TRVs, an hydraulic model of the TRVs was not modeled while different temperature set point strategies were determined, depending of different TRVs opening, as defined by the occupants.

Since no data about the occupants' controls were noted, the operation modes were distinguished for living area and sleeping area, and for the level of story (e.g., intermediate story tend thus to be affected by the lower and upper neighboring story). The models were thus tested under nine different conditions summarized into three strategies. Validation strategies #1 (VS1) assumed the TRVs were kept open and constant in all rooms and flats with an imposed temperature set point of 20.5, 21, and 21.5 °C, respectively for VS1a, VS1b, VS1c, selected as considered the most frequent used by the occupants. Validation strategies #2 (VS2) were based on different temperature set points depending on the story (ground floors, intermediate floors, and upper floors), with an increasing gradient difference of 0.5 °C (Fig. 25.2). It was assumed that intermediate floors had the same set point temperatures due to similar boundary conditions. Validation strategies #3 (VS3) distinguished the temperature set point for three zones (living area, sleeping rooms and entry for the intermediate story). The ground floor and the upper floor temperature were indeed kept constant, maintaining thus the same temperature set point as in VS2.

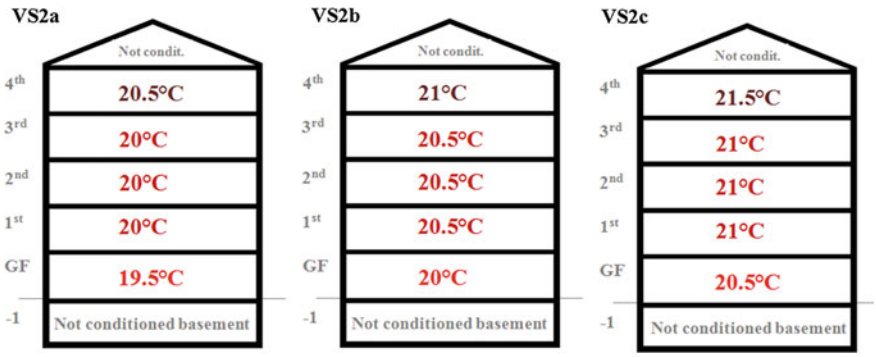

Fig. 25.2 Heating set point temperature of validation strategy #2

25.5 Energy Modeling

The energy simulation code used within this study was EnergyPlus v.7.0 [13] together with the plug-in for the Google sketch-up program, OpenStudio [14], for the geometric modeling. Each conditioned room that was equipped with a radiator, was modeled as a single thermal zone. In order to carry on accurate dynamic simulations, the influence of the surrounding urban context was taken into account. The main neighboring and facing buildings were modeled as shading surfaces with their own reflectance properties (Fig. 25.3).

For the envelope characterization, the Italian Technical Standard UNI TS 11300-1 [15] and the sub-typology construction elements of TABULA project [16] were used. Due to the lack of information about the real building usage, the schedules regarding the internal gains were defined on the basis of rule of thumbs, distinguishing the zones (living area and sleeping area). Lighting and appliances power densities were set to 3.88 and 5.38 W/m^2. The occupancy, lighting and

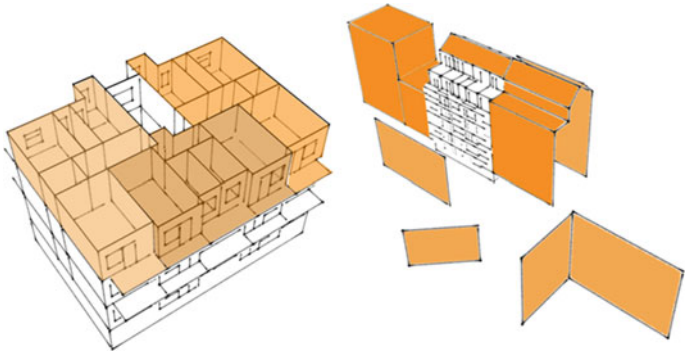

Fig. 25.3 Axonometric cross section of a building energy model on the *left* and energy model together with the neighboring buildings

equipment schedules, and the power densities, were extracted from the benchmark building models database of the US Department of Energy [17]. According to National Standard UNI 10339 [18], people per zone floor area were fixed to 0.04 pers/m^2. The air flow rate for natural ventilation and infiltration was set to 0.3 ACH for dimensioning the radiator units. The radiators water flow rates were refined on the basis of the on-spot-investigations, of the measured data and of the simplified procedure of Appendix A in the National Standard UNI 10200 [19].

25.6 Calibration

In order to tune the energy models on the basis of the measured data of the district heating rates, some input data were revised. A real weather data for the considered heating season was created for running the calibrated models. The air flow rate for natural ventilation and infiltration was adjusted approximately to 0.5–0.6 ACH, depending on the case study, due to the decay of the building envelope and in particular of the transparent envelope components. On this regard, the *U*-values of the building envelope components were also adjusted to better reflect the building envelope decay. Heating temperature set points were set through schedules defined on experts' assumption since no monitored data were available. Ground floors, intermediate and upper floors were respectively set with a heating temperature set point of 20.5 °C, 21.5–22 °C, and 21 °C.

25.7 Results

Simulations results confirmed the effectiveness of TRVs. All validation strategies assumed similar energy saving trends with light variations, depending on the case study characteristics, as reported in Fig. 25.4. In particular, VS1 brought to a minimum reductions threshold when the TRVs opening is set on a temperature set point of 21.5 °C (VS1c) with a absolute reduction of 4 %. In VS1 the maximum threshold is represented VS1a. VS2 is the more realistic as it is fairly acceptable to have different temperature set points in different flats. It is not unlikely to have the same temperature set point in a whole building (VS1), especially when having central heating systems, but it is more uncertain to have different TRVs openings in different rooms of the same apartment (VS3). In fact occupants are still conscious of the big potentialities of TRVs and especially do not know properly how to control them. Even if the results trends were similar, VS3 revealed to bring more suitable results, with a mean reduction on energy consumptions of 15.6 %, compared to 12.4 % in VS1 and 14.9 % in VS2. In absolute terms, VS2a of case study B reached minimum energy consumption with a value of 62.6 kWh/m^2, while the maximum value, was reached with 112.8 kWh/m^2 in VS1c of case study C. The mean energy consumption recorded a value of 82.9 kWh/m^2 with a mean energy savings of −14.3 %.

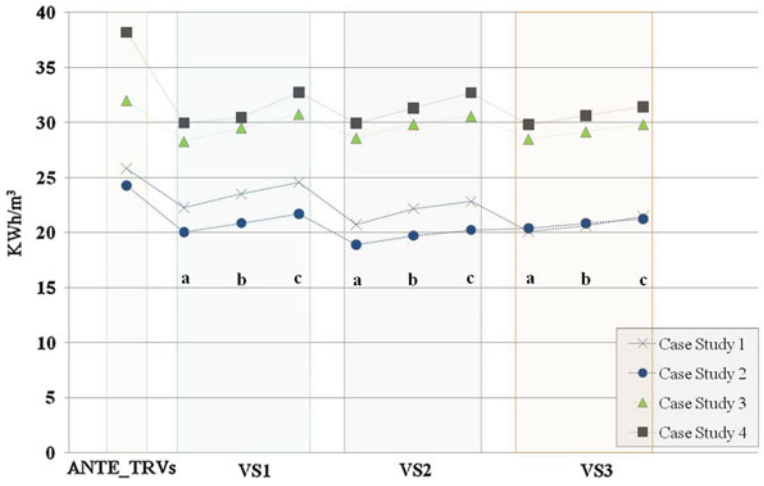

Fig. 25.4 Heating energy consumptions for all validation strategies

25.8 Conclusion

Each case study was simulated with and without TRVs. The results demonstrated that a conscious use of TRVs by occupants can bring a reduction on the total heating energy consumption, during a complete heating season, from a minimum of 5 % to a maximum of 22 %. The lack of a greater number of monitored data made possible to only simulate the use of TRVs simulated on the basis of theoretical assumptions (due to the fact that the indoor temperature distribution was unknown). However the calibration methodology, even if it could be refined, gave back reliable results, also consistent with the general consideration regarding this type of heating control devices [9, 10]. Undoubtedly each flat achieved different level of energy savings depending on its size, on the number of story and mainly on the TRVs openings. Top and ground floor flats require in fact higher heating energy needs than middle floor flats mostly due to the fact that its envelope elements (i.e., walls and floors/ceilings) face unconditioned zone, like the basements and the outdoor. As previously explained the TRVs opening was defined on the basis of experts' assumptions with three calibration validation strategies. The knowledge of occupants' real life use of TRVs, could of course quantify more realistically the amount of achievable energy savings. To this end, a study on the calibration of building models in the presence of measured indoor air temperature and energy requirements, for each apartment, is currently under development. The control of such input data will make it possible to analyze the effect of this type of heating control device on energy consumptions in more details.

References

1. European Parliament, Council (2010) Directive 2010/31/EU of the European Parliament and of the Council of 19 May 2010 on the energy performance of buildings. Off J Eur Union, p 13
2. ENEA, Italian National Agency for New Technologies, Energy and Sustainable Economic Development (2013) RAEE 2011, Energy Efficiency National Report, Executive Summary, ISBN 978-88-8286-279-4. Roma. www.efficienzaenergetica.enea.it
3. Ma Z, Cooper P, Daly D, Ledo L (2012) Existing building retrofits: Methodology and state-of-the-art. Energy Build 55:889–902. doi:10.1016/j.enbuild.2012.08.018
4. ISTAT, Italian National Institute of Statistics (2010) L'abitazione delle famiglie residenti in Italia: Anno 2008. Statistiche in breve: famiglia e società. http://www.istat.it/it/archivio/6489
5. Bo M (2012) Riqualificazione dei vecchi impianti di riscaldamento a radiatori. AICARR J (12)
6. DHC+ Technology Platform (2012) District heating & cooling: a vision towards 2020–2030–2050. http://www.dhcplus.eu/
7. Fabrizio E, Filippi M, Torbino M (2011) Operational optimization of actual energy systems by means of the energy hub theory. Build Simul, Sydney, pp 2793–2798
8. Mazza M, Antinucci M, Brollis M (2004) Vademecum sul teleriscaldamento, Aess (Agency for Energy and Sustainable development of the city of Modena)
9. Xu B, Fu L, Di H (2008) Dynamic simulation of space heating systems with radiators controller by TRVs in buildings. Energy Build 40:1755–1764
10. Tahersima F, Stoustrup J, Rasmussen J (2011) Stability performance dilemma in hydronic radiators with TRV. In: 2011 IEEE International Conference on Control Applications (CCA) Denver, CO, USA, 28–30 Sept 2011, pp 103–106, ISBN 978-1-4577-1063-6
11. Corgnati SP, Fabrizio E, Filippi M, Monetti V (2013) Reference buildings for cost optimal analysis: method of definition and application. Appl Energy 102:983–993
12. UNI EN ISO (2008) Energy performance of buildings—calculation of energy use for space heating and cooling. Standard UNI EN ISO 13790:2008, Italian National Body for Standard (UNI), Milan
13. U.S. Department of Energy, EnergyPlus energy simulation software, 2012. http://apps1.eere.energy.gov/buildings/energyplus/
14. U.S. Department of Energy, National Renewable Energy Laboratory, Openstudio Suite. http://openstudio.nrel.gov/
15. UNI TS (2008) Energy performance of buildings—Part 1: Evaluation of energy need for space heating and cooling. Standard UNI/TS 11300-1:2008
16. Ballarini I, Corgnati SP, Corrado V, Talà N (2011) Building typology brochure—Italy, Italian TABULA Report, Oct 2011. www.building-typology.eu
17. NREL, PNNL, LBNL, U.S, Department of Energy (2011) Commercial Reference building models of the National Building Stock, Technical Report NREL/TP-5500-46861, Feb
18. UNI (1995) Air-conditioning systems for thermal comfort in buildings. General, classification and requirements. Offer, order and supply specifications. Standard UNI 10339:1995
19. UNI (2005) Centralized heating systems—heating costs sharing. Standard 10200:2005. Italian National Body for Standard (UNI), Milan

Chapter 26
Window Operation and Its Impacts on Thermal Comfort and Energy Use

Liping Wang

Abstract Operable windows provide occupants' ability to control over local environment and satisfy human's expectation to access to outdoor environment. Operation strategies for operable windows can have significant impacts on indoor thermal comfort and energy consumption of building performance. It is not uncommon that building facility managers complain that operable windows were left open in buildings with a conventional HVAC system. However, optimum control strategies of window operation can improve thermal comfort and reduce energy consumption for building using natural ventilation or mixed mode ventilation. The study focuses on the investigation of the impacts of window operations on building performance for different types of building systems including natural ventilation, mixed mode ventilation, and conventional HVAC systems in a medium-size reference office building. Building performance simulation tool EnergyPlus is used to simulate window operations for each system in three different climates. Various control strategies of window operations for building operation systems, implemented using (EMS) in EnergyPlus, are evaluated based on the criteria of thermal comfort and energy consumption. The results highlight the impacts of window operations on thermal comfort and energy use and identify that hybrid ventilation for perimeter zones has 12–20 % saving potentials of annual HVAC site energy consumption.

Keywords Natural ventilation · Mixed mode · Window operation · Energy · Thermal comfort

L. Wang (✉)
Lawrence Berkeley National Laboratory, One Cyclotron Road, Building 90, MS90-3145, Berkeley, CA 94706, USA
e-mail: lwang@lbl.gov

A. Li et al. (eds.), *Proceedings of the 8th International Symposium on Heating, Ventilation and Air Conditioning*, Lecture Notes in Electrical Engineering 262,
DOI: 10.1007/978-3-642-39581-9_26,

26.1 Introduction

Operable windows enable physical connection with outdoor environment and provide occupants' ability to control over local environment by natural ventilation to improve thermal comfort and reduce cooling loads, if properly designed and operated. On one hand, as the benefits of natural ventilation, including reducing operation costs, improving indoor air quality, providing satisfactory thermal comfort in certain climates, are well-recognized, natural ventilation through operable windows has become an attractive alternative to alleviate the issues associated with air-conditioned buildings. On the other hand, it is not uncommon that building facility managers complain that operable windows were left open in buildings with a conventional HVAC system and triggered the central system running heavily. Based on occupant survey in office buildings [1], 66 % of occupants open their office's windows very often and another 19 % do so sometimes.

Through proper control strategies of operable windows, hybrid ventilation integrates natural ventilation and conventional mechanical heating and cooling systems to minimize HVAC energy consumption and satisfy indoor thermal comfort. Karava et al. [2] investigated mixed-mode cooling strategies using an institutional building with motorized façade openings integrated with an atrium and high levels of exposed thermal mass. Menassa [3] studied different hybrid ventilation strategies for a laboratory building located in Madison, Wisconsin, and the best strategy could result in 20 % savings in mechanical cooling over the summer. Although natural ventilation is difficult to design and control, we are facing more challenges for contemporary building design with operable windows for hybrid ventilation as operable windows would require integration with mechanical systems, and they create dynamic variability in the thermal environment.

The objective of this study is to quantify the impacts of window operations on building performance for different types of building systems including natural ventilation, mixed mode ventilation, and conventional HVAC systems for an existing medium-size office building.

26.2 Technical Approach

EnergyPlus [4] is used as the simulation tool in the study for modeling various scenarios on window operation. EnergyPlus, developed by U.S. Department of Energy, is an open-source whole-building energy simulation program built upon subhourly zone heat balance and integrated solutions of building loads, HVAC systems, and central plant equipment. In the study, a commercial building reference model [5] in compliance with ASHRAE 90.1-2010 [6] for a medium-size office building is used as the baseline for the study to investigate the impacts of window operations on energy use and thermal environment of various types of HVAC systems. There are three stories and 15 thermal zones in the medium-size

office reference model. There are four perimeter zones and one core zone for each floor (Fig. 26.1). The window to wall ratio (WWR) is 0.48 for all four orientations. The lighting-power density and electric plug-load density are 8.87 and 8.07 W/m^2, respectively. A multi-zone variable air volume (VAV) system, with a two-speed direct-expansion (DX) cooling coil and a gas burner, is used to provide the conditioned environment for each floor. There are three multi-zone VAV systems in total. An electric reheating coil is available for each thermal zone.

Occupant controls of window vary with personal styles, indoor and outdoor environment. Four scenarios with different control strategies for HVAC and window operation were studied.

Scenario 1—Open window (OW)

An operable window in one of the perimeter zones on the middle floor is kept 12 % open throughout the year.

Scenario 2—Natural ventilation (NV)

Natural ventilation is only applied to cool the perimeter zones. Mechanical cooling serves as the core zones. Mechanical heating is provided for all thermal zones to meet heating setpoints. Temperature-based control strategy is used to control the fraction of window opening. Operable window is available to be modulated all the time. If zone air temperature is greater than outdoor air temperature and cooling setpoints, operable windows are modulated based on indoor–outdoor temperature difference to avoid large temperature swings.

Scenario 3—Hybrid ventilation type 1 (HV1)

Whenever the window in a particular zone is open, the heating and cooling air supply to that zone is turned off. The interlock between operable windows and mechanical systems can be as basic as a switch that automatically turns off local HVAC components when windows are open. Temperature-based control strategy is used to control the fraction of window opening. Windows are operable only when outdoor air temperature is less than cooling setpoints.

Scenario 4—Hybrid ventilation type 2 (HV2)

Natural ventilation is taken as the first priority to provide cooling for perimeter zones and mechanical cooling is available when natural ventilation alone is not

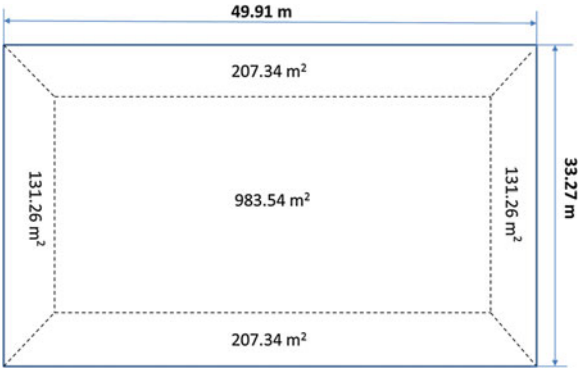

Fig. 26.1 Layout of five thermal zones per floor

enough to meet cooling setpoints. If natural ventilation meets the cooling load for a thermal zone, VAV damper at zone level will move to turn down to minimum damper position. Mechanical heating is provided for all thermal zones to meet heating setpoints. Temperature-based control strategy is used to control the fraction of window opening. Temperature-based control strategy is used to control the fraction of window opening. Windows are operable only when outdoor air temperature is less than cooling setpoints.

Airflow network model is used to simulate airflow movement for perimeter zones. Energy management system (EMS) in EnergyPlus is used to implement different control strategies for operable windows. EMS is an advanced feature of EnergyPlus and designed for users to develop customized high-level, supervisory control routines to override specified aspects of EnergyPlus modeling in the EMS program. The thermal zone layout is kept the same for all the scenarios in this study. Three core zones are served by central HVAC systems for the four scenarios to meet the same cooling and heating setpoints as baselines. For natural ventilation and hybrid ventilation, cooling setpoint is defined based on mean monthly outdoor air temperature according to 90 % acceptability for naturally conditioned spaces in ASHRAE 55-2010 [7]. Three cities—Chicago, Houston, and San Francisco— are chosen to represent typical climates in the United States.

26.3 Results and Discussion

26.3.1 Analysis for a Typical Hot Day

To better understand the impacts of window operation on building performance, key system performance parameters such as zone air temperature and mechanical ventilation rate were analyzed for different operations. Figure 26.2 illustrates the hourly outdoor air temperature, cooling setpoints for a perimeter zone on the middle floor of baseline, and the other four scenarios on a typical hot day in September, San Francisco. Mechanical cooling setpoint is 24 °C during occupied hours and setback by 2.7 °C during unoccupied hours. The cooling setpoint for naturally ventilated spaces is determined by mean monthly outdoor air temperature based on ASHRAE 55-2010. For natural ventilation (NV) scenario, cooling setpoint can be met during early morning and night for the hot day. With the increase of outdoor air temperature during late morning and afternoon, natural ventilation alone is not sufficient to meet cooling loads. The highest indoor air temperature reaches 31 °C for natural ventilation scenario during the hot day. Hourly zone air temperature of the two hybrid ventilation scenarios (HV1 and HV2) are also shown in Fig. 26.2. Since either natural ventilation or mechanical cooling can be applied to local zones for HV1, natural ventilation may not be sufficient to meet cooling loads for some periods, depending on climate and design. As can be seen from Fig. 26.2, zone air temperatures during 11:00−14:00 and 17:00−18:00 for

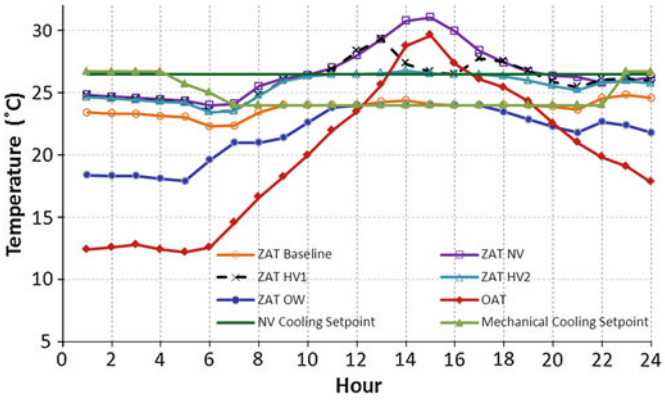

Fig. 26.2 Comparisons of hourly zone air temperature among various scenarios on a hot day, San Francisco

HV1 are above the cooling setpoint. Since both natural ventilation and mechanical cooling can be applied concurrently to local zones for HV2, mechanical cooling can be provided to meet the cooling setpoint whenever natural ventilation alone is not sufficient to meet cooling loads. As can be seen from Fig. 26.2, zone air temperature can always meet the cooling setpoint.

Figure 26.3 shows the hourly mechanical ventilation rate for the perimeter zone. This parameter reflects system cooling energy and fan energy consumptions. The scenario with a window left open in the conditioned zone is the one with highest mechanical ventilation rate for most of the day except 10:00 AM−1:00 PM. As shown in Fig. 26.3, in early morning, through the window opening, too

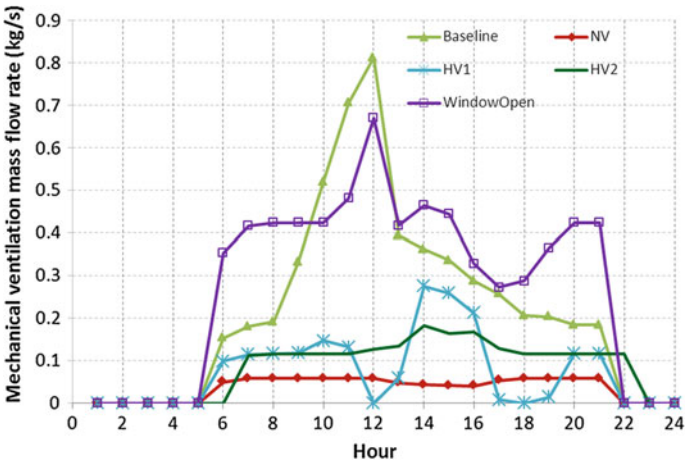

Fig. 26.3 Comparison of hourly mechanical ventilation mass flow rates among various scenarios on a hot day, San Francisco

much cold outdoor air flowed into the perimeter zone. This set the zone in heating mode, called the reheating coil at zone level and increased mechanical ventilation rates. With the increase of outdoor air temperature in the afternoon, the extra ventilation through window opening increased cooling load and then increased mechanical ventilation load. Mechanical ventilation flow rates for both HV1 and HV2 are less than those for baseline.

26.3.2 Annual Analysis

Figure 26.4 shows the percentage of annual HVAC site energy consumption for the three scenarios in comparison to baselines of three climates. Based on the simulation results, the scenario "OW" with an open operable window throughout the year for one perimeter zone introduces 14–48 % HVAC site energy penalty; the hybrid ventilation 1 scenario ("HV1") can provide 12–20 % savings for HVAC site energy; the hybrid ventilation 2 scenario ("HV2") can provide 9−18 % savings for HVAC site energy; the natural ventilation scenario ("NV") can provide 11−22 % savings for HVAC site energy. Leaving an operable window open for one perimeter zone has the most negative energy impacts on Chicago climate.

Figure 26.5 shows the percentage of annual cooling energy consumption for the four scenarios compared with baselines for the three different climates. Based on the simulation results, the scenario "OW" with an open operable window throughout the year for one perimeter zone introduces 0.4−6.5 % cooling energy penalty; the hybrid ventilation 1 scenario ("HV1") can provide 18−21 % savings

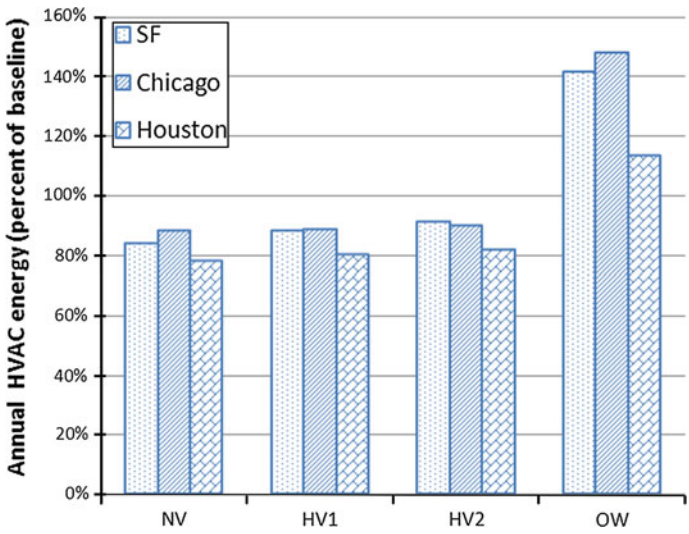

Fig. 26.4 Comparison of annual HVAC energy consumption

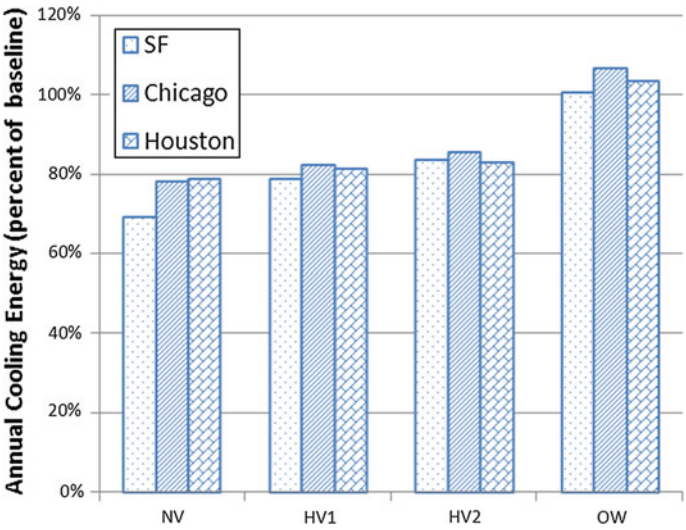

Fig. 26.5 Comparison of annual cooling energy consumption

for cooling energy; the hybrid ventilation 2 scenario ("HV2") can provide 15−17 % savings for cooling energy; and the natural ventilation scenario ("NV") can provide 22−32 % savings for cooling energy. However, natural ventilation alone cannot meet indoor thermal comfort for cooling throughout the year. The number of unmet hours, in which zone mean air temperature is higher than cooling setpoints for naturally ventilated spaces are 1,259, 1,839, and 2,452 h for San Francisco, Chicago and Houston, respectively. Hybrid ventilation provides the most benefits for Houston climate in terms of HVAC annual energy use.

26.4 Conclusion

Without changing existing layout of medium-size office building, window operation strategies play an important role to ensure energy efficiency and thermal comfort. While keeping the core zones served by mechanical HVAC systems, hybrid ventilation for perimeter zones can provide substantial HVAC energy savings. Two control strategies for hybrid ventilation are compared in this study. Although the energy saving by "HV1" (12−20 % of HVAC site energy) is higher than that by "HV2" (9−18 % of HVAC site energy), there is risk that cooling setpoints are not met when natural ventilation alone is not sufficient for "HV1". When a window is left open at a perimeter zone, it costs 14−48 % extra HVAC site energy and 0.4−6.5 % extra cooling energy. Although natural ventilation provides the most savings among all the scenarios (11−22 % HVAC site energy), it also brings substantial number of unmet hours based on existing building design

and layout in the study. The following opportunities were identified for further research and development:

- Reconfigure façade design and internal layout to reach maximum utilization of natural ventilation and minimize the number of unmet hours. The percentage of time in a year when natural ventilation is feasible is pre-determined by climate conditions. The realization of natural ventilation for thermal comfort and energy efficiency are based on design or retrofits of façade elements and internal layouts for commercial buildings.
- Use coupled CFD and airflow network model approach to improve the accuracy of natural ventilation prediction. The limitation of airflow network model for natural ventilation study is that it is assumed that air inside each thermal zone is well-mixed. However, indoor air in naturally ventilated spaces, especially for large spaces, is normally non-uniformly distributed. Coupling CFD and airflow network model can provide detailed indoor thermal environment and improve model prediction.
- Implement control strategies of operable windows in existing building and examine the impacts of various types of controls and degrees of sophistication and difficulties in terms of implementation in existing building systems.

References

1. Nisiforou OA, Poullis S, Charalambides AG (2012) Behaviour, attitudes and opinion of large enterprise employees with regard to their energy usage habits and adoption of energy saving measures. Energy Build 55:299–311
2. Karava P et al (2012) Experimental study of the thermal performance of a large institutional building with mixed-mode cooling and hybrid ventilation. Build Environ 57:313–326
3. Menassa CC, Taylor N, Nelson J (2013) Optimizing hybrid ventilation in public spaces of complex buildings—a case study of the wisconsin institutes for discovery. Build Environ 61:57–68
4. EnergyPlus (2012) http://www.energyplus.gov/
5. Commercial Prototype Building Models (2013) http://www.energycodes.gov/development/commercial/90.1_models
6. ASHRAE (2010) ANSI/ASHRAE/IES standard 90.1-2010, in energy standard for buildings except low-rise residential buildings. Atlanta, GA
7. ASHRAE (2010) ANSI/ASHRAE standard 55-2010, in thermal environmental conditions for human occupancy. Atlanta, GA

Chapter 27
An Evaluation of Filtration and Air Cleaning Equipment Performance in Existing Installations with Regard to Acceptable IAQ Attainment

H. E. Burroughs, Chris Muller, Wenlei Yao and Qingli Yu

Abstract A number of trends are stimulating interest in the usage of filtration and air cleaning as an adjunct to the environmental conditioning of buildings. These include escalation of energy costs, heightened awareness about acceptable IAQ, aging of the commercial building inventory, numerous revisions and addenda to ventilation standards and building codes, and green building/sustainability initiatives and energy tax credits. A field study was performed on established installations of particulate and gas-phase filtration in and around Atlanta, Georgia (USA), and included a variety of building types and usage and evaluated environmental conditions and airborne contaminants. The study was undertaken in two parts with Phase I being to establish and finalize test and measurement protocols and a Phase II for field investigation. This paper provides a summary of both Phases, including characteristics of untreated outdoor air, and air cleaning with particulate filters and gas-phase air filtration. Overall, there was a TVOC reduction of 38−74 %, 0.5 μm particulate removal efficiency of 28−95 %, and an ozone removal efficiency of 100 %. Each building had annual operational cost savings ranging between US$10,000 and US$800,000. The field study is intended to establish the parameters of dilution air compared with similar characteristics of air treated with particulate and gas-phase filtration. The field study demonstrated that filtered air can meet or exceed the IAQ level from simple dilution with outdoor air. The study also documents the comparable energy savings as a result of a reduction in outdoor air ventilation rates and significant control of specific contaminants of concern regarding occupant safety and building security.

Keywords Air cleaning · Contamination control · Indoor air quality · Gas-phase air filtration

C. Muller (✉)
Purafil, Inc, 2654 Weaver Way, Doraville, GA 30340, USA
e-mail: cmuller@purafil.com

H. E. Burroughs · W. Yao · Q. Yu
Building Wellness Consultancy, Inc, 225 Mt. Ranier Way, Alpharetta, GA 30022, USA

A. Li et al. (eds.), *Proceedings of the 8th International Symposium on Heating, Ventilation and Air Conditioning*, Lecture Notes in Electrical Engineering 262,
DOI: 10.1007/978-3-642-39581-9_27,

27.1 Introduction

The usage of enhanced particulate filtration and gas-phase air cleaning for contaminant control as an adjunct or as a substitution for excessive ventilation has been an accepted practice since the energy concerns of the early 1970s. It has been an acceptable alternate method for attaining acceptable indoor air quality within established ventilation standards since the publication of ASHRAE Standard 62-1981 [1]. However, eventhough the technique provides compelling savings in equipment capacity and operating costs, the widespread usage of the practice has been limited because of more rigorous engineering and commissioning requirements and the lack of documented energy usage results. The interest in filtration and gaseous air cleaning applications has been revitalized for a number of concurrent reasons, such as the following converging stressors.

- *The Aging Building Population*. In North America, the construction peak of the last quarter of the twentieth century involved a large number of high-rise office complexes, institutional buildings, and other large public buildings. As these buildings mature beyond 15−20 years, their mechanical systems deteriorate and must be replaced, upgraded, modernized, and brought up to current code and energy requirements.
- *Energy Management and Conservation*. The confluence of Middle-East conflict(s), natural disasters with related domestic production restrictions, and the exponential growth of emerging nations have brought the price of energy in all forms to new daily heights. Thus, the energy concerns of the 1970s have returned, which is motivating both regulators and users to seek effective conservation approaches.
- *Heightened Awareness of IAQ Concerns by Occupants*. The rash of notorious and well-publicized incidents of problem buildings in both the public and the private sector has raised the issue of acceptable IAQ to the "top of the list" of important issues to building tenants.
- *Re-issuance of Standard 62.1 and Related Addenda*. ASHRAE[1] Standard 62.1-2010 [2] requirements have been modified dramatically with recent republications and a large number of addenda that pertain to the outdoor ventilation requirements; classification of air; treatment of outdoor air; and the application of the IAQ Procedure.
- *Emergence of New Standards of Care*. The role of standards and code writing bodies is shifting toward simplicity and single accountability. This is creating a "new set of rules" for dealing with code bodies, both local and national. In response to these issues, ASHRAE with the sponsorship of the U.S. Environmental Protection Agency has published Advanced Indoor Air Quality Design Guide documents [3].

[1] American Society of Heating, Refrigerating, and Air-Conditioning Engineers, Inc.

- *Green Building and Sustainability Initiatives*. The growing concern for green building and sustainability priorities have given rise to a series of incentive programs including LEED, Energy Star, and even Federal income tax credits. ASHRAE has announced a significant and dominant initiative toward sustainability in their current strategic plan. Under ASHRAE leadership, a multidiscipline and intersociety task force prepared the code-language Standard 189.1 [4] to address the subject of sustainability building design. Such programs provide substantial momentum to IAQ, occupant health effects, and energy usage accountability.
- *The Threat of Potential or Real Vulnerability of the Building Stock to Airborne Weapons of Mass Destruction (WMD)*. Although to date, the Federal Homeland Security agency has not focused upon the building stock, other authorities view filtration, and air cleaning as a significant potential contributor to survivability in an incident of airborne WMDs. This federal level attention, added to the fact that ambient outdoor air is a significant risk factor, triggers an entirely new motivation for both the reduction and pre-treatment of outdoor air.

Studies have reported that higher ventilation rates, some as high as 45 cfm (77 m^3/h) per person, improve workers' and students' health, productivity, and learning; however, using these higher ventilation rates come with a significant energy penalty. This opposes the current trend for more sustainable, greener buildings, which require higher energy efficiency levels to meet sustainability guidelines, and higher ventilation rates are becoming too costly as energy costs continue to rise. Also, in many areas the outdoor air has elevated pollution levels such that using high outdoor air ventilation rates are undesirable, which has become an issue at many U.S. schools. Using the ASHRAE 62.1 IAQ Procedure and employing gas-phase filtration combined with particulate filtration is a solution to optimizing the indoor air quality without raising ventilation rates. The IAQ Procedure has been shown to receive wide acceptance for several reasons such as: (1) the need to specify and design for the Contaminants of Concern (COCs) for both indoor and outdoor pollutants and a lack of understanding of how to do this; (2) the lack of field performance data demonstrating the efficacy and cost-effectiveness of this approach; and (3) concerns about determining filter lifetimes [5].

27.2 Project Scope

Phase I of this project consisted of the following elements:

- *Acquisition of field performance data* on existing filtration and air cleaning systems; monitored and verified by a third-party research entity.
- *Determination of the COCs* in the urban outdoor air and indoor environments of commercial buildings to establish the resulting profile of "acceptable" IAQ or Class I air as listed by Standard 62.1 [4].

- *Comparison of identified acceptable IAQ profile* (Class I air) with air treated using enhanced air filtration in existing participant sites to verify delivery of air quality comparable to that achieved by dilution alone.
- *Quantification of energy savings* through the use of enhanced air filtration based on site-specific operating circumstances and documentation.

In order to help provide answers to these concerns, a field research study consisting of an on-site evaluation and analysis of seven commercial buildings providing 15 discreet study sites in and around Atlanta, Georgia (USA) was performed. These sites were selected from varied building styles and usage to represent a cross section of commercial facilities using air cleaning technology to attain acceptable IAQ while reducing energy usage from HVAC operation and all had enhanced air filtration systems consisting of gas-phase and higher efficiency particulate filters and each of the selected sites was thoroughly characterized as to the nature of the ambient outdoor air, the performance of the air cleaning system, and the cleanliness and contaminant control levels attained within the occupied space. The evaluation included testing and analysis of particulate matter, viable airborne microbial constituents, and chemical content of the air—both organic and inorganic [6].

In Phase II of this study, the effectiveness of the enhanced air filtration systems to remove airborne contaminants at all 15 sites and the operational cost savings and paybacks over time were measured at the 11 of the 15 sites evaluated in Phase I.[2] The results of the data are intended to provide scientific documentation and a more thorough understanding of the performance of air cleaning equipment as an adjunct and/or potential alternative to the use of outdoor air for dilution and control of IAQ. The results from the Phase II research are detailed below.

27.3 Methodology

Seven commercial buildings in the greater Atlanta metropolitan area were identified for inclusion in the study. These are described in Table 27.1. Specific building names are not provided due to owner confidentiality agreements.

On-site measurements were made of total and individual volatile organic compounds (TVOCs/IVOCs, thermal desorption/gas chromatographic/mass spectrometric analysis); acid gases (sulfur dioxide, nitrogen oxides, hydrogen sulfide), ozone, carbon dioxide, and particles (both viable and total). Measurements were taken upstream and downstream of the filtration systems and in the outdoor air. A financial analysis was performed of the energy cost savings for use of the IAQ Procedure (reduced outdoor air ventilation rates) versus use of the more commonly used Ventilation Rate Procedure (outdoor air for dilution of contaminants).

[2] The enhanced air filtration systems in the archival storage facility and specialty museum did not filter outdoor air. These systems operated in 100 % recirculation mode and were installed for the protection and preservation of the archival materials and artifacts stored at these locations.

Table 27.1 Description of buildings used in Phase II

Building type	Site description
Archival storage facility (sites 1 and 2)	Four-storey building adjacent to active urban thoroughfare, in primary approach pathway for Atlanta Hartsfield-Jackson airport; storage site for historical paper documents; outdoor air treated with high efficiency solid bed gas-phase filtration using blended granular media (activated carbon (GAC) + permanganate-impregnated activated alumina (PIA)); MERV 6 pre-filters; MERV 17 post-filters; air is dehumidified
High occupancy sports arena (sites 3 and 4)	Occupancy of 80,000; adjacent to major interstate highways, rail and subway lines, and parking garages; original ventilation system design (built in 1991) based on IAQ Procedure of ASHRAE Standard 62-1989; MERV 13 pre-filters of an electronic air treatment device with medium efficiency gas-phase filters; outdoor air reduced to 5 cfm (7.5 m^3/h)/occupant (total outdoor air reduction of 720,000 cfm [1,224,000 m^3/h])
University hotel and conference center (site 5)	Ten-storey hotel and conference center; located in high traffic urban area near major interstate highways; deep-bed high capacity gas-phase filtration (blended GAC+PIA media) installed to reduce odors from re-entrained bathroom exhaust; MERV 12 mini-pleat filters
High-rise atrium hotel (sites 6–9)	Aging hotel in high traffic urban area near interstate highway system; retrofitted with four gas-phase/particulate filter systems; deep-bed gas-phase filter modules filled with dual media; MERV 13 cartridge particulate filters; MERV 6 pre- and post-filters; reduced ventilation air supply with 80,000 cfm (136,000 m^3/h) recirculation air
Low-rise atrium hotel (sites 10 and 11)	Urban location in high traffic area; retrofitted two gas-phase/particulate filter systems to treat exhaust from lobby, conference center, and toilet exhaust; deep-bed high efficiency gas-phase filter modules filled granular filter media; MERV 6 pre-filters; MERV 14 particulate final filters
Specialty museum (sites 12 and 13)	Specialty museum storage and restoration facility; suburban location; deep-bed gas-phase filter modules filled granular filter media; MERV 6 pre-filters; MERV 14 particulate final filters
Office building (sites 14 and 15)	Aging office tower facing tenant demands for current code application; aging mechanical equipment with poor access for service or replacement; upgrade to current version of standard 62.1 using medium efficiency combination particulate + gas-phase air filter; blended GAC/PIA media

27.4 Results and Discussion

27.4.1 Particulate Contaminant Control

Table 27.2 summarizes the performance of the installed particulate filters against a single size particle for presentation simplicity and clarity of comparison. A size of 0.5 μm was selected because it is the lower size of most viable particles; thus, it is a challenging particle size to control. It is also representative of typical fungal colony forming units. It is also used by the cleanroom industry as the critical particle size for their filtration system quality assurance testing. The table reports removal efficiency comparing the air cleanliness upstream and downstream of the filter bank; and provides system efficiency comparing the indoor supply air and the outdoor air.

The comparative data indicate a significant reduction in this size, ranging from 86 to 94 % total reduction in supply air particulate over the measured outdoor air content. The actual single pass efficiencies ranged from 27 to 70 dependent upon the MERV rating of the filters. The overall particle counts are somewhat depressed in the outdoor air as these measurements were taken in springtime when frequent rains generally lower the particulate matter in the submicron sizes. Normally, the MERV 17 cartridges at the archive sites would also be expected to produce higher removal efficiencies; however, they were installed in conventional slide tracks that allowed some visible by-pass.

27.4.2 Gaseous Contaminant Control

Reductions in VOC concentrations and particulate counts were observed at all sampled sites. The overall TVOC reductions representing the gas-phase air filter efficiency when comparing upstream versus downstream concentrations ranged from 42 to 71 (Table 27.3).

There were significant reductions in the majority of total identified and quantified specific VOCs (IVOCs) at all sites in all buildings when comparing the

Table 27.2 Particle removal efficiency @0.5 μ through air filtration systems (site avg.)

Study building	Filter efficiency (%)	Range (%)	System efficiency (%)	Range (%)
Archival storage facility	78	77–79	99	99
Sports arena	52	24–80	92	90–95
Hotel and conference center	55	–	55	–
High-rise hotel	30	12–43	62	42–79
Low-rise hotel	86	74–97	–	–
Specialty museum	66	54–78	95	–
Office building	–	–	89	87–91

Table 27.3 TVOC reduction through gas-phase filtration systems (site avg.)

Study building	Reduction (%)
Archival storage facility	71
Sports arena	71
Hotel and conference center	42
High-rise hotel	50
Low-rise hotel	50
Specialty museum	52
Office building	59

upstream versus downstream concentrations. The source of many of IVOCs (Table 27.4), such as benzaldehyde, α-pinene, eucalyptol, limonene, and camphor were assumed to be from cleaning products.

Ozone was removed completely (100 %) by the gas-phase filters at each site in each building. Acid gases (e.g., sulfur dioxide, SO_2; nitrogen dioxide, NO_2; hydrogen sulfide, H_2S) were not detected in the outdoor or indoor air at any sampling site. The reduction in total particle counts for 0.5 μm and larger particles ranged from 28 to 95 %.

27.4.3 HVAC Operational Cost (Energy) Savings

An analysis was performed of the energy cost savings comparing the use of lower outdoor air ventilation rates with enhanced air filtration with the IAQ Procedure versus simple dilution using the Ventilation Rate Procedure. The sports arena had the most dramatic savings of any of the buildings due to the size of the facility as well as the amount of ventilation air required. When completed in 1991, this facility had been able to reduce its chiller capacity by 2,350 tons and saved US$2.5 million in construction costs. Heating requirements were reduced by 40 million BTU which resulted in a US$800,000/year energy costs savings. Accounting for inflation and the increases in energy costs, this facility continues to realize a net energy saving of more than US$1,300,000/year. In fact, the accumulated savings are greater than original building cost!

Table 27.4 Selected, identified, and quantified VOCs

Acetic acid	Benzoic acid	2-Ethyl-1-hexanol	Limonene	α-Pinene	Toluene
Acetone	2-Butoxyethanol	2-Ethyl-1-hexene	Methyl ethyl ketone	Styrene	Undecane
Acetophenone	Butyraldehyde	2-Ethylhexanal	Nonane	Tetrachloroethylene	Vinyl acetate
Benzaldehyde	Decane	Ethyl acetate	Naphthalene	Tetradecane	
Benzene	Diethyl phthalate	Isopropanol	Phenol	Texanol	

Table 27.5 Annual energy cost savings (avg. in 2013 dollars)

Study building	Net energy cost savings, US$/year
Archival storage facility	N.A.
Sports arena	1,347,001.00
Hotel and conference center	49,000.00
High-rise hotel	249,000.00
Medium-rise atrium hotel	10,500.00
Specialty museum	N.A.
Office building	41,000.00

The annual net energy cost savings for the other study buildings ranged from US$9,662 to $105,101/year over and above the cost for the filter replacement and maintenance at the time these buildings were first occupied. These savings are adjusted for inflation and summarized in Table 27.5.

These results clearly demonstrate the energy cost savings and reduced energy usage from using the IAQ Procedure over the Ventilation Rate Procedure by being able to reduce that amount of outdoor ventilation air required. Additional savings are obtained from the ability to use smaller heating and cooling systems if the IAQ Procedure is applied in the original design.

27.5 Summary and Conclusions

Previous field research has established the useful role of particulate filtration in keeping HVAC systems clean. Although the successful usage of enhanced air filtration that combines proven technologies for gas-phase air cleaning and particulate filtration for energy conservation has occurred over the past few decades, details of these installations and the related performance and energy data has been deficient. This project documents the effectiveness of enhanced air filtration to control both internally and externally generated contaminants as well as documenting the resulting energy utilization economics through reductions in the amounts of outdoor air required for ventilation and IAQ.

All of the buildings studied were retrofitted with enhanced filtration systems and in each there was an overall measurable and significant reduction in particulates >0.5 μm, TVOCs, and ozone. Further, each building realized a considerable annualized operational cost savings ranging from US$10,000 to US$1,300,000 over and above the cost of filters and maintenance. Additionally, these results provide valuable data on selection of the contaminants of concern, thus providing guidance to designers and other users of the IAQ Procedure.

In areas where the outdoor air is contaminated such as in the case of the “toxic air” around many of our schools [7], focusing on fine particulates, ozone, and those VOCs most commonly encountered from cleaning compounds may be useful as the focus for the target indoor used in the building and HVAC system design

process. Another study on the use of the IAQ Procedure in schools reported the additional benefit of a 50 % reduction in the use of emergency medical inhalers by asthmatic students [8].

This study clearly demonstrates that the IAQ Procedure from ASHRAE Standard 62.1 can be effectively applied to buildings and improve the indoor air quality and reduce operating costs, particularly as a retrofit option to existing buildings. The indoor air pollutants were clearly reduced over those in the outdoor air showing the applicability of the IAQ Procedure.

Acknowledgments This project was sponsored by a consortium of local and national firms that made the effort possible with financial support and in-kind contribution of equipment and services. We gratefully acknowledge funding for this research from Kimberly-Clark Company, Purafil, Inc., the Alfred P. Sloan Foundation, the Indoor Air Quality Association, and Building Wellness Consultancy, Inc. In-kind contributions were furnished by The Filtration Group, McKenney's, Inc., AirEnergy, Inc., and Purafil Inc.

Copies of the final reports for Phase I and Phase II of this project including full descriptions of the study sites, air filtration systems, and test data may be obtained through a written request to the authors.

References

1. ASHRAE (1981) Standard 62-1981—ventilation for acceptable indoor air quality. The American Society of Heating, Refrigerating, and Air-Conditioning Engineers, Inc., Atlanta
2. ASHRAE (2010) Standard 62.1-2010—ventilation for acceptable indoor air quality. The American Society of Heating, Refrigerating, and Air-Conditioning Engineers, Inc., Atlanta
3. ASHRAE (2009) Indoor air quality guide: best practices for design, construction and commissioning. The American Society of Heating, Refrigerating, and Air-Conditioning Engineers, Inc., Atlanta
4. ASHRAE (2011) Standard 189.1-2011—standard for the design of high-performance, green buildings (except low-rise residential buildings). The American Society of Heating, Refrigerating, and Air-Conditioning Engineers, Inc. Atlanta
5. Bayer C, Burroughs HE, Muller C (2009) Demonstration of ASHRAE IAQ procedure effectiveness for improved IAQ and greater energy efficiency. In: Proceedings of healthy buildings 2009, Paper #538, 13–17 Sept. Stockholm, Sweden
6. Burroughs HE (2008) Role of filtration and air cleaning in sustaining acceptable indoor environmental quality through ventilation air replacement. Building Wellness Consultancy, Alpharetta
7. Morrison B, Heath B (2008, 2009) The smokestack effect: toxic air and America's Schools, USA Today, 2008, 2009
8. Lamping GA, Muller CO (2009) Air cleaning in practice—school sustainability and commercial building field study results. In: Proceedings of indoor air quality association—12th annual meeting and indoor air expo, 24−26 Feb, 2009, Fort Worth, Texas

Chapter 28
Variation Law of Aqua Ammonia Falling Film Absorption Vertically Outside of Transversally Grooved Tube

Xiaozhuan Chen, Wei Sheng, Xiufang Liu, Junjie Chen and Jianhua Liu

Abstract Aqua ammonia absorption refrigeration system involves design of condenser, evaporator, absorber, heat exchange equipment. Absorber is very important equipment in refrigeration system. Aiming at different sizes transversally grooved tube (TGT), a series of experiments are carried out to find approach which can enhance absorption efficiency and to choose an optimal tube type. The experiment results show that ammonia solution can absorb the more ammonia gas following increase of pressure difference and velocity of cooling water inside tube, therefore mass transfer coefficient becomes larger. When spray density of ammonia solution outside tube alters from small to large, mass transfer coefficient increases firstly and then decreases, so that gets a optimum. The group experiment results indicate that transversally grooved tube have better mass transfer ability than smooth tube. For example, when spray density of solution is 472.1 kg m^{-1} h^{-1}, mass transfer coefficient of transversally grooved tube rise by 109.6 % compared to smooth tube. A common law is discovered during three groups of experiment. Different sizes of TGT have different ability to absorb ammonia gas, and Number 2 tube is the best tube considering absorption efficiency. Flow patterns of blend and vortex flow are compared among three transversally grooved tubes with solutions flowing through grooves. The reason why series of TGT of different sizes have different absorption efficiency is obtained by means of analysis on flow model ammonia solution flowing through TGT.

X. Chen (✉)
College of Mechanical, Henan Polytechnic University, Jiaozuo 454003, China
e-mail: chenxiaoz@qq.com

W. Sheng · X. Liu · J. Chen
School of Mechanical and Power Engineering, Henan Polytechnic University, Jiaozuo 454003, China

J. Liu
School of Energy and Power Engineering, University of Shanghai for Science and Technology, Shanghai 200093, China

A. Li et al. (eds.), *Proceedings of the 8th International Symposium on Heating, Ventilation and Air Conditioning*, Lecture Notes in Electrical Engineering 262,
DOI: 10.1007/978-3-642-39581-9_28,

Keywords Aqua ammonia · Falling film · Absorption · Transversally grooved tube · Mass transfer coefficient

28.1 Introduction

With the world's attention to environmental protection, refrigeration, and air conditioning industry have new understanding of green refrigerants and concern. Ammonia is regarded as a kind of refrigerant friendly to environment, for its ozone depleting potential (ODP) and global warming potential (GWP) are both zero. Ammonia water absorption refrigerator (AWSR) is an example of cooling or heating using ammonia. Because AWSR can produce cooling capacity less than 0 °C, ammonia water absorption refrigeration will be applied to more fields. The absorber is key equipment in ammonia water absorption refrigerator system, so its steady operation is directly related to the normal work of the whole system. The absorber with high absorption efficiency can save a lot of metal materials. Absorber in the absorption refrigeration system metal consumption accounted for about 40 % [1–3]. As a result, to strengthen the absorber heat and mass transfer efficiency is a worth researching direction. The current research on absorber is mainly centered on lithium bromide absorption chiller system, and the research on AWSR is relatively absent [4–6]. On account of ammonia's strong irritation and danger, the research using experiment methods is very scarce [7]. This paper did a series of research on absorber from the experiment and theoretical aspects.

In recent years at home and abroad many studies on absorber had to be carried out, and these studies had achieved positive results. Early YANG Siwen systematically discussed the type of absorber and thermodynamic calculation, and pointed out that absorber was a heat and mass transfer coupling complex process. Therefore interrelationship and influence mechanism should be studied in detail. Du et al. [8] intensively studied experimental law on ammonia water falling film absorption in external magnetic fields. Yong Tae Kang carried out an experimental analysis for ammonia water falling film absorption process in a plate heat exchanger with enhanced surfaces, and examined the effects of liquid and vapor flow characteristics, inlet subcooling of the liquid flow, and inlet concentration difference on heat and mass transfer performance [9]. They found that lower inlet liquid temperature and higher inlet vapor temperature led to the higher Nusselt and Sherwood numbers. They also found that the performance of an absorber could be seriously influenced by inlet subcooling of the solution. Kyongmin Kwon measured heat and mass transfer performance for ammonia water in both parallel and countercurrent flow [10], and did many experiments for three different solution concentrations (3, 14, and 30 %). Sheng conducted a lot of experimental study on enhancement of ammonia bubble absorption process by adding nanoparticles, altering the ammonia vapor flow flux and concentration ratio of bulk ammonia solution [11]. A good many scholars realized that ammonia water absorption

efficiency was related mainly to performance of heat transfer process, and obtained some valuable achievement. Huang planned the experimental scheme of shape optimization of transversely ridged tube by orthogonal test, and brought forward the optimum configuration by analyzing the results of test [12]. Li and Liu discovered the heat transfer coefficient of LiBr aqueous solution absorption water vapor enhanced by grooved tube was 2.1–3.25 times that of smooth tube, and the mass transfer coefficient was 1.25–1.93 times that of smooth tube [13]. From the geometry of the structure transversally grooved tube (TGT) not only increases the contact area of gas and liquid, but also enhances flow disturbance of falling film solution. Marangoni effect generates disturbance in the liquid film for the absorption of ammonia water mixture, and these disturbances and eddy cause heat transfer coefficient to increase, and ammonia absorption rate will rise spontaneously. It is necessary to adopt this kind of tube when designing absorber of ammonia water absorption refrigeration system. In order to research efficiency and mechanism of TGT falling film absorption, a set of experimental system should be established. These research results will be helpful to design absorber of high efficiency and compact size.

28.2 Experimental System

As shown in Fig. 28.1 is system diagram of ammonia water absorption experimental system. Certain concentration ammonia solution before falling film was inhaled by metering pump, and flowed through flow meter, finally entered into

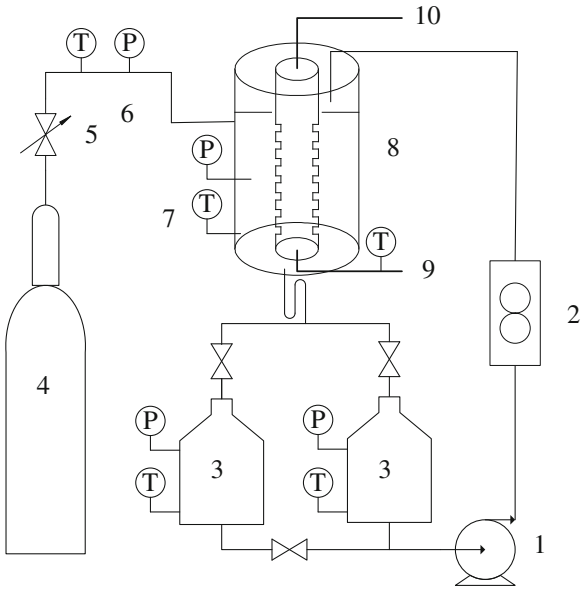

Fig. 28.1 Experimental system diagram of ammonia water falling film absorption, *1* ammonia pump, *2* flow meter, *3* ammonia solution container, *4* ammonia container, *5* valve, *6* pressure gage, *7* thermometer, *8* absorber, *9* entrance of cooling water, *10* cooling water outlet

liquor distributor of absorption experimental section. Liquor distributor was designed with superior performance, so ammonia solution can form stable liquid membrane outside of tubes, and ensured that falling film absorbed was kept in functional order. Ammonia solution flowed through absorption experimental section, and absorbed ammonia outside of tubes. In the last, these solution entered into solution storage container, thus the solution can be analyzed and investigated, for example, measuring temperature and density, and so on. Ammonia absorbed came from liquid ammonia container. Ammonia evaporated from liquid into gas, and flowed through pressure maintaining valve made from stainless steel. The valve's function was to maintain ammonia of pipeline pump import certain pressure. Cooling water's flowing direction was opposite exactly to that of ammonia solution, therefore heat transfer between ammonia solution and cooling water will be best level. Ammonia solution pump used JMW type mechanical diaphragm metering pump to experiment system which was produced by Shanghai Shangcheng Pump and Valve Manufacturing Co. Ltd. This kind of pump's quantity of flow can be adjusted precisely, in order to meet different solution flow of experiment. The whole experiment system used stainless steel materials according to requirement of chemical and physical properties of ammonia water. The PID controller precisely maintained the specified temperature in the solution container. Experiment system was equipped temperature and pressure measuring element. Stainless steel thermocouples were installed in the two ammonia solution container, and the thermocouples can be used to measure temperature of solution before and after absorption experiments. In addition, thermocouples were also installed at the inlet and outlet position of ammonia solution and cooling water. Pressure gages were equipped at the room of outside of tube and two solution containers. The *U*-tube at the bottom of the heat exchanger prevented the vapor in solution container from flowing into the heat exchanger. After the experiment, these experimental data was outputted to computer using the data acquisition instrument from Agilent Company. Finally these experiment data was analyzed and studied with the purpose of revealing variation law of falling film performance and function relation between heat and mass transfer.

Falling film tubes had mainly four types, and these tubes were made from stainless steel. Among these tubes, one was smooth tube with size Φ27 mm $\times$ 3 mm, the other three tubes were transversally grooved tube (TGT) which was processed based on the same smooth tube. Photo of transversally grooved tube and smooth tube are shown in Fig. 28.2, and structure chart are shown in Fig. 28.3. The effective absorption height of these falling film tubes is 850 mm. Three transversally grooved tubes number tube1, 2, 3. Its specific dimensions are listed in Table 28.1. As shown in Fig. 28.4 is liquor distributor, whose production method is that blind plate was welded with a stainless steel cylinder. During the course of manufacture, Center round hole among top and bottom blind plate and liquor distributor must be kept concentric, which is ensured that TGT is installed exactly. Different size membranes should be placed at center of liquor distributor, which are used to adjust interval between liquor distributor and falling film tube with purpose of maintaining ammonia solution uniform distribution.

Fig. 28.2 Photograph of transversally grooved tube and smooth tube

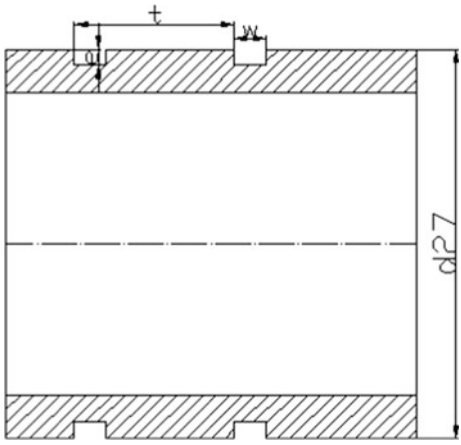

Fig. 28.3 Structure chart of TGT

Table 28.1 Dimension parameters of TGT

Tube number	*t*/mm	*e*/mm	*w*/mm	*w/d*	*t/d*	e^2/td
1	9.6	0.8	1.6	0.0592	0.356	0.00247
2	13.2	1.1	2.2	0.0814	0.489	0.0034
3	16.8	1.4	2.8	0.1038	0.622	0.00432

Fig. 28.4 Photograph of liquor distributor

28.3 Experimental Data Processing Method

28.3.1 Calculating Method on Spray Density of Falling Film Solution

According to the definition of the spray density, it can be obtained as follows.

$$\Gamma = \frac{q_V \rho_l}{\pi d} \tag{28.1}$$

In the formula, Γ is ammonia solution spray density, whose unit is kg m^{-1} h^{-1}. q_v is solution's volume flow, whose unit is m^3 h^{-1}. ρ_l is density of falling film solution, whose unit is kg m^{-3}. As a result, falling film Reynolds number of ammonia water can be obtained from the following formula.

$$\mathrm{Re} = \frac{4\Gamma}{\mu} \tag{28.2}$$

28.3.2 Ammonia Gas Absorption Rate

An important parameter is ammonia gas absorption rate which indicates how quick absorption rate, and according to the physical meaning its formula is shown as follows:

$$m_a = q_V M(c_o - c_i)/3600 \tag{28.3}$$

In the formula, m_a is ammonia gas absorption rate whose unit is kg s^{-1}. M is molecular weight. c_i and c_o is ammonia solution's molar concentration before absorption and after absorption respectively, and its unit is mol L^{-1}. Ammonia solution's density before and after absorption can be measured by precise densimeter, such as ρ_i and ρ_o. Then corresponding molar concentration will be calculated using related formula from literature [14].

28.3.3 Gas-side Mass Transfer Coefficient

Mass transfer driving force of absorption is difference value between ammonia gas pressure outside of tube and partial pressure of saturated ammonia gas at the solution surface according to definition. The formula can be given as follows:

$$k_m = \frac{m_a}{S\Delta p} \tag{28.4}$$

In the formula, k_m is gas-side mass transfer coefficient, and its unit is kg s^{-1} m^{-2} kPa^{-1}. Where S is mass transfer area, and it is considered that heat and mass transfer are equal falling film outside of tube.

Ammonia gas pressure can be measured by highly precise pressure gage. Partial pressure of saturated ammonia at the solution surface can be calculated according absorption Henry's law.

28.4 Experimental Results and Analysis

28.4.1 Effect of Pressure Difference on TGT Absorption Performance

Spray density of falling film solution was assumed 479.6 kg m^{-1} h^{-1} during the series experiments, and cooling water's flow velocity inside tube was 1.5 m s^{-1}. Heat and mass transfer coefficient of falling film solution outside of tube was calculated changing the mass transfer driving force. This series of experiments mainly investigated the absorption of law of pressure difference to falling film. Here pressure difference was difference value between ammonia gas pressure outside of tube and partial pressure of saturated ammonia gas at the solution surface. These experiments chose four different kinds of pressure difference, which was 70, 90, 110, 130 kPa, respectively. Specific adjustment method was shown as follows: Opening sizes of pressure valve at ammonia solution container outlet was changed in order to alter outlet pressure. The experimental results were shown in Fig. 28.5. Mass transfer coefficient of falling film solution increased with the increase of the pressure difference. Taking number 2 tube for example, when pressure difference increased from 70 to 110 kPa, mass transfer coefficient rose by

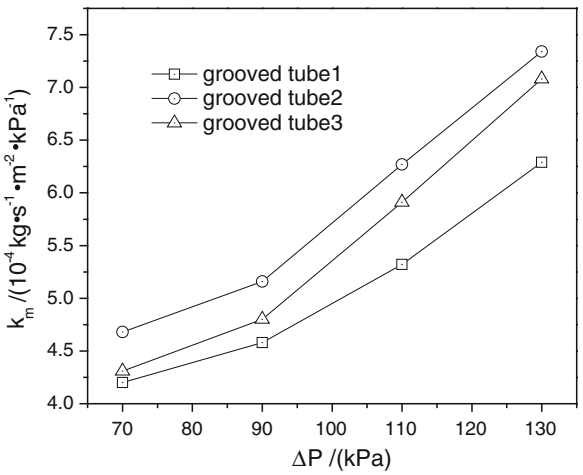

Fig. 28.5 Mass transfer coefficients versus pressure difference

34.0 %. With the increase of the ammonia gas pressure outside of tube, ammonia was easy to dissolve in the solution, therefore the heat and quality transfer ability can be enhanced. But the pressure difference also has certain limits. During the ammonia water absorption refrigerate system, outlet pressure of ammonia flowing out from evaporator was directly related to size of evaporating temperature [15]. The most appropriate pressure difference should be selected according to a specific environment in practical application.

28.4.2 *Effect of Velocity of Cooling Water on TGT Absorption Performance*

This series of experiments mainly investigated the absorption law of cooling water velocity to falling film. Spray density of falling film solution was assumed 479.6 kg m^{-1} h^{-1} during the series experiments, and pressure difference was 90 kPa. Cooling water inlet temperature was 12 °C. The experimental results were shown in Fig. 28.6. Mass transfer coefficient of falling film solution increased with the increase of velocity of cooling water. Velocity of cooling water was set at 0.9, 1.2, 1.5, 2.0 m s^{-1}, respectively. Taking Number 2 tube for example, when velocity of cooling water increased from 0.9 to 2.0 m s^{-1}, mass transfer coefficient rose by 39.5 %. This demonstrated that heat transfer performance between ammonia solution and cooling water has very big effect on mass transfer performance. Ammonia gas absorption process is a heat and mass transfer process of mutual coupling. Heat transfer restricts the effect of mass transfer process. Ammonia water absorption process will give off a lot of heat. Only the quantity of heat is taken away quickly by cooling water, thus temperature of falling film solution can be maintained in an appropriate level. Only in this way ammonia gas absorption process can perform well continuously.

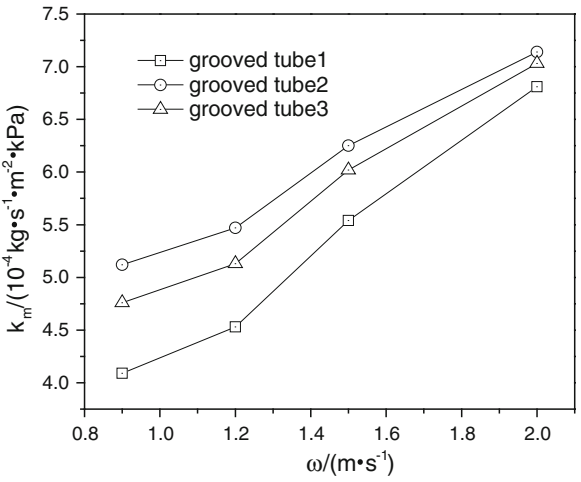

Fig. 28.6 Mass transfer coefficients versus velocity of cooling water

28.4.3 Effect of Spray Density of Falling Film Solution on Absorption Performance

This series of experiments mainly investigated effect of spray density of falling film solution on absorption performance. These experiments were carried out making use of TGT of different pitch and smooth tube. Spray density of falling film solution increased from 229.3 to 571.9 kg m^{-1} h^{-1}, correspondingly falling film Reynolds number increased from 150.5 to 451.6. The experimental results shown in Fig. 28.7, from which it can be seen that transversally grooved tube, have better mass transfer ability than smooth tube. For example, when spray density of solution is 472.1 kg m^{-1} h^{-1}, mass transfer coefficient of transversally grooved tube rise by 109.6 % compared to smooth tube. Groove outside of tube can increase heat exchange area and gas–liquid contact area. It is significant that groove disturbs flowing form of falling film solution. Eddy and mixing become more intense, so mass transfer ability improves more quickly [16]. It is worth noting that TGT and smooth tube have similar falling film absorption law. When spray density of aqua ammonia outside tube alters from small to large, mass transfer coefficient increases firstly and then decreases, so that gets a optimum. In the beginning,with the increase of spray density falling film Reynolds number will also increase consequently. The turbulent flow of falling film solution is more intense; therefore heat and mass transfer performance will become larger. Subsequently mass transfer performance will reaches maximum when spray density increases to a certain degree. However when spray density of falling film solution continues to increase, thickness of the film will become thicker. At this time the resistance of heat and mass transfer will increase, so heat and mass transfer performance of falling film solution will become smaller.

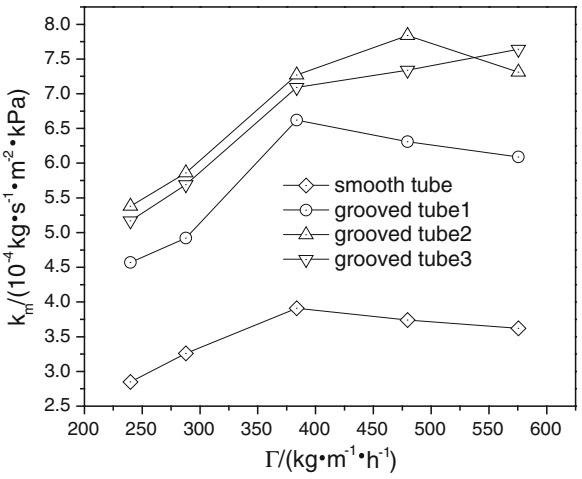

Fig. 28.7 Mass transfer coefficients versus spray density of aqua ammonia

28.5 Conclusions

The following conclusions are drawn from the present experimental study.

(1) Mass transfer coefficient of falling film solution increased with the increase of the pressure difference. When pressure difference increased from 70 to 110 kPa, mass transfer coefficient of Number 2 tube rose by 34.0 %.
(2) Mass transfer coefficient of falling film solution increased with the increase of velocity of cooling water. When velocity of cooling water increased from 0.9 to 2.0 m s^{-1}, mass transfer coefficient of Number 2 tube rose by 39.5 %.
(3) When spray density of ammonia solution outside tube altered from small to large, mass transfer coefficient increased first and then decreases, so that got a optimum. The experiments results indicated that transversally grooved tube had better mass transfer ability than smooth tube.
(4) Different sizes of TGT had different ability to absorb ammonia gas, and Number 2 tube was the best tube considering absorption efficiency. The reason why series of TGT of different sizes have different absorption efficiency is obtained by means of analysis on flow model ammonia solution flowing through TGT.

Acknowledgments This study is funded by Campus Youth Fund of Henan Polytechnic University (No. Q2012-03).

References

1. Killion JD, Garimella S (2001) A critical review of models of coupled heat and mass transfer in falling-film absorption. Int J Refrig 24:755–797
2. Goel N, Goswami DY (2005) Analysis of a counter-current vapor flow absorber. Int J Heat Mass Transfer 48:1283–1292
3. Taboas F, Valles M, Bourouis M et al (2012) Flow boiling heat transfer of ammonia water mixture in a plate heat exchanger. Int J Refrig 33:695–705
4. Garimella S, Determan MD, Meacham JM et al (2011) Microchannel component technology for system-wide application in ammonia/water absorption heat pumps. Int J Refrig 34:1184–1196
5. Cardenas R, Narayanan V (2010) A numerical model for ammonia-water absorption into a constrained microscale film. Int J Therm Sci 49:1787–1798
6. Park CW, Cho HC, Kang YT (2004) The effect of heat transfer additive and surface roughness of micro-scale hatched tubes on absorption performance. Int J Refrig 27:264–270
7. Lee JK, Koo J, Hong H et al (2010) The effects of nanoparticles on absorption heat and mass transfer performance in NH_3/H_2O binary nanofluids. Int J Refrig 33:269–275
8. Niu XF, Du K, Xiao F (2010) Experimental study on ammonia-water falling film absorption in external magnetic fields. Int J Refrig 33:686–694
9. Kang YT, Akisawa A, Kashiwagi T (1999) Experimental correlation of combined heat and mass transfer for NH_3-H_2O falling film absorption. Int J Refrig 22:250–262

10. Kwon K, Jeong S (2004) Effect of vapor flow on the falling-film heat and mass transfer of the ammonia/water absorber. Int J Refrig 27:955–964
11. Sheng W, Wu W, Zhang H et al (2010) Experimental study on enhancement of ammonia bubble absorption process by adding nanoparticles. J Refrig 31:31–34 (in Chinese)
12. Huang W, Deng X, Huang D (2005) Shape optimization of transversely ridged tube by orthogonal numerical simulation test. J Chem Ind Eng 56:1445–1450 (in Chinese)
13. Li H, Liu K (2011) Experimental study on heat and mass transfer enhancement by grooved tube of absorber. Chem Eng 39:14–18 (in Chinese)
14. Niu X, Du K, Hu Z et al (2008) Experimental analysis on the effect of magnetic field on ammonia water falling film absorption. J Eng Thermophy 29:919–922 (in Chinese)
15. Woo Park C, Soo Kim S, Churl Cho H et al (2003) Experimental correlation of falling film absorption heat transfer on micro-scale hatched tubes. Int J Refrig 26:758–763
16. Yang S, Tao W (1998) Heat transfer, 3rd edn. Higher Education Press, Beijing (in Chinese)

Chapter 29
Experimental Research on Resistance Characteristics of Filtering Materials of Biofilter Process of Sludge Composting Plants

Gaoju Song, Henggen Shen, Wenjuan Ren, Yonggang Song and Jiaping Zhang

Abstract A lot of hazardous gases will be produced during sludge composting, if treated improperly, pollution may be caused to the environment. Biofilter process is an effective deodorizing method. But the resistance of biofilter materials that in turn have critical effects on whether the ventilation system of the workshop can operate normally. The research group conducts researches on resistance characteristics of four commonly used filter materials in a view to helping similar sludge composting plants in designing ventilation system, choosing fans, and managing operation. The results of the researches show that biofilter material is of the law of high-speed non-Darcy flow, their resistance characteristics are related with the characters, superficial velocity, bed thickness, etc., of the filter material, about which the empirical computation formulas are given.

Keywords Biosolid sludge composting · Superficial velocity · Biofilter media · Resistance characteristics

Sponsor by National Twelfth Five-Year Technology Support Program (2012BAJ10B02).

G. Song (✉) · H. Shen
College of Environmental Science and Engineering, Donghua University, Shanghai 201620, China
e-mail: songgaoju@sina.com

G. Song · W. Ren · Y. Song · J. Zhang
No. 6 Institute of Project Planning and Research of Machinery Industry Co., Ltd, Zhengzhou 450007, China

A. Li et al. (eds.), *Proceedings of the 8th International Symposium on Heating, Ventilation and Air Conditioning*, Lecture Notes in Electrical Engineering 262,
DOI: 10.1007/978-3-642-39581-9_29,

29.1 Introduction

According to statistics, there are 2,881 urban sewage treatment plants in China, which process 72.9 % of the urban sewage [1]. The sludge precipitated at sewage treating becomes another severe pollution source. Sludge composting is effective in decreasing urban sludge, administering biosafety treatment to the sludge, and making the sludge useful. As of now, sludge composting has become one universal technology in treating urban solid garbage over the world.

However, a lot of harmful gases may form during sludge composting, which include ammonia, hydrogen sulfide, sulfur alcohol, amine substances, etc. [2–4]. These gases are harmful to human body, even carcinogenic, if treated improperly, they might wreak severe potential hazards to workers who are exposed to these gases in the sludge composting plant and bring about occupational health problems [4]. Meanwhile, if discharged into the atmosphere without proper treatment, these gases might cause secondary pollution to the environment [3, 4]. Therefore, these gases must be sent to deodorizing equipments for treatment in an organized way before being discharged, during which the organized ventilation and deodorizing equipment will play important roles. The deodorizing methods commonly used in sludge composting plants include biofilter process, soil method, etc. [5, 6]. The biofilter process is used for most projects, which uses the microorganisms in the process to treat harmful gases [7, 8].

Biofilter process plays an important role in deodorizing. During his research, Song Gaoju [9] finds that the ventilation system of a sludge composting plant is an typical variable resistance system, wherein, the changes of resistance is mainly induced by resistance changes of biofilter materials that in turn have critical effects on whether the ventilation system of the workshop can operate normally. The research group conducts researches on resistance characteristics of four commonly used filter materials in a view to help similar sludge composting plants in designing ventilation system, choosing fans, and managing operation.

29.2 Research Situation at Home and Abroad

Because of its low cost and high efficiency, researchers both at home and abroad carry out researches on biofilter process from different perspectives. As early as in 1923, Bach [5] used soil to treat odorant gases like H_2S, etc., discharged by the sewage treatment plant. Biofilter materials in the biofilter process include screened compost, coke-compost mixture, root wood with bark, coconut fiber, bit of wood, ceramist, etc. Researchers both at home and abroad mainly focus on the filter efficiency while the filter resistance is rarely touched upon.

Biofilter material is a typical porous medium. And researches on the flowing characteristics of polluted air in the filter material are conducted on simulation model of the porous medium. Problems faced in researches and engineering in porous medium include petroleum exploitation and movement of underground

water, etc. Darcy's Law is a basic law about permeable flow. It is an important law in describing the resistance characteristics of porous media. It is widely acknowledged that Darcy's Law can only be used when Reynolds number of the laminar flow is between 1 and 10. However, there are more researches focusing on non-Darcy flow with Reynolds number above 10 and relevant empirical computation formulas are correspondingly worked out [10]. People like Li Qitao et al. [11] have conducted experiments to study the ventilation resistance of piles of three different kinds of grain and come up with the empirical formula after improving on Darcy's relationship expression. People like Li Zhenpeng et al. [12] studied the resistance characteristics of microspheric porous media and worked out empirical computation formulas with different Reynolds numbers. During the literature survey, it can be found that most of the researches focus on porous heat-conducting media; researches on biofilter materials are rare.

29.3 Experiment on Resistance Characteristics of Filter Materials of Biofilter

According to the literature [5], the experimental superficial velocity should be between 0.02 and 0.04 m/s. Therefore, in some project of Song Yong-gang et al. [8, 13], the designed superficial velocities are, respectively, 0.03 and 0.06 m/s.

The following Eq. (29.1) can be used to identify the flowing regime when the fluid going through the biofilter materials and compute the Reynolds number:

$$\mathrm{Re} = \frac{\rho v d}{\mu} = \frac{v d}{\upsilon} \tag{29.1}$$

In Eq. (29.1), "d" stands for the average diameter of solid particles in the porous medium. "v" stands for permeability velocity of the fluid whose unit is m/s, at this experiment it is actually the superficial velocity. "μ" stands for dynamic viscosity coefficient of the fluid. "υ" stands for kinematic viscosity coefficient of the fluid, whose unit is m^2/s.

The computed Reynolds number under experimental conditions of different biofilter materials are between 70 and 200. The fluid state is of non-Darcy flow [8]. The total energy loss in the porous media equals the viscous energy loss and dynamic energy loss. The dynamic energy loss dominates at high flowing speed while the viscous energy loss dominates at low flowing speed. When the inertia force dominates, Darcy's Law does not apply because inertia force is proportional to the square of speed. The high-speed non-Darcy flow can be described by the following nonlinear laminar law [13], namely,

$$v = KJ^m \left(\frac{1}{2} \le m < 1\right) \quad \text{or} \quad \Delta P = Av^n \quad (1 \le n < 2) \tag{29.2}$$

In the above Eq. (29.2), "K", "A", "m", "n" are experimental constants.

29.3.1 Experimental Methods

The experiment workbench arrangement is as what is shown in Fig. 29.1. The superficial velocity can be computed with the tested systematic air quantity at the straight section of the air pipe. The static pressure measured in the plenum chamber is the resistance of the filter material. The filter materials are surveyed by group. Each filter material will be tested at 2 or 3 thickness values. At each thickness value, the air valve will be adjusted to see what will happen at five air quantities. The specific measuring methods can be found in *Code of acceptance for construction quality of ventilation and air conditioning works* [14] and *Industrial fans-performance testing* in situ [15].

29.3.2 Experimental Plan and Apparatus

Experimental plan: in accordance with the methods described in the literature [14, 15], the testing ports will be arranged and parameters will be measured. The Table 29.1 will be referred to for experimental apparatus and main parameters.

29.3.3 Experimental Apparatus

The experiment workbench will be set up as directed by literature [14, 15]. Different superficial velocity will be made by adjusting the valve installed at the discharge outlet of the ventilator to give different air quantity. The air quantity will be measured through the anemometer at ventilating pipe. The hot wire anemometer will be used to verify and adjust the precision of the air flow gauge. Resistance of the filter material will be measured by using the pilot tube and electronic differential pressure gauge. The difference between pressure in the plenum chamber and the atmospheric pressure is the resistance of the filter material.

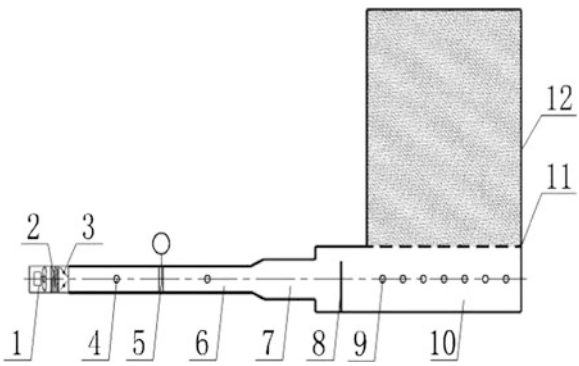

Fig. 29.1 Sketch for installation of test-bed for biofilter: *1* fanner, *2* soft coupling, *3* air valve, *4* measuring port, *5* anemometer, *6* DN100 air hose, *7* DN300 air hose, *8* fender, *9* measuring port, *10* plenum chamber, *11* air distribution plate, *12* biofilter material

Table 29.1 Instruments of the testing and the parameters

Title	Model	Resolution ratio/range	Precision
Hot wire anemometer	KANOMAX A531	0.01 m s^{-1}	±(reading × 2 % + 0.01) m s^{-1}
Differential pressure gauge	Testo 512	0.01 hPa	reading × 0.5 %
Pilot tube	L shaped		$K = 1$
Air flow gauge	TY-LUGB-2310	125–1247 m^3/h	reading × 1.0 %

29.3.4 Selection of Experiment Materials

After analysis of factors affecting the resistance of the filter material, it can be seen that there are mainly the following factors such as superficial velocity, thickness of the biofilter media, impurities, porosity and the kind of material, etc. In the experiment, we will choose four commonly used materials in China namely, mixture of peanut shell and bark, bits of wood, ceramsite, and mixture of ceramsite and bits of wood in different proportion. During the experiment, each filter material will be tested at two or three different thickness values and at each thickness value the filter resistance will be measured under five difference superficial velocities. Fresh air will be sent into the workbench through a ventilator. About the four filter materials used in the experiment, the mixture of peanut shell and bark has been used for 2 years before the experiment, bits of wood for 6 months; ceramsites are purely new ones; mixture of wood bits; and ceramsites are made in different proportion.

29.4 Experimental Data, Analysis, and Results

29.4.1 Experimental Results

The experimental results are shown as in Figs. 29.2, 29.3, 29.4, 29.5, 29.6, 29.7, and 29.8.

29.4.2 Analysis of the Experimental Results

29.4.2.1 Analysis of Change Pattern of Superficial Velocity

As shown in Figs. 29.2, 29.3, 29.4, 29.5, and 29.6, filtering resistance and superficial velocity of the biofilter material have an exponential relationship and a better degree of fitting, which suits the description of Eq. (29.2). Because it is the

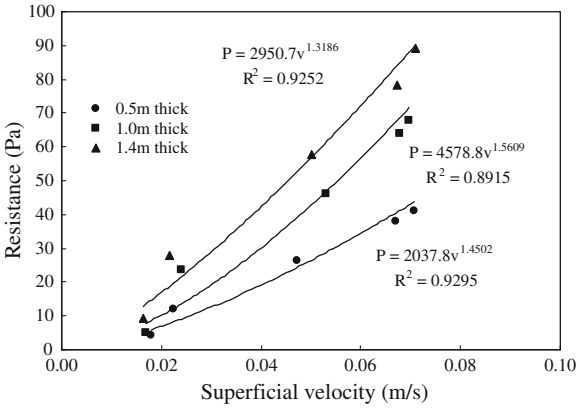

Fig. 29.2 Relationship between the filtration resistance and superficial velocity of wood bits

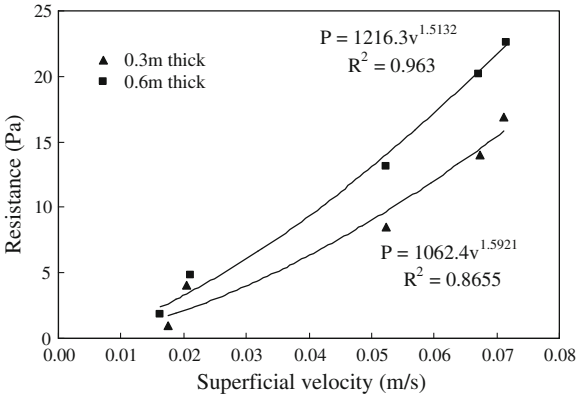

Fig. 29.3 Relationship between the filtration resistance of ceramsite and superficial velocity of ceramsite

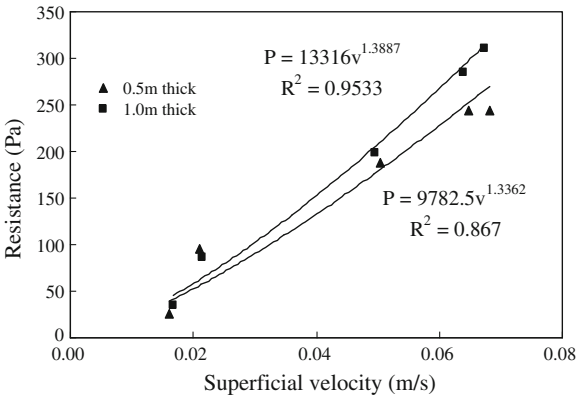

Fig. 29.4 Relationship between the filtration resistance and superficial velocity of ceramsites and wood bits mixed at 3:7

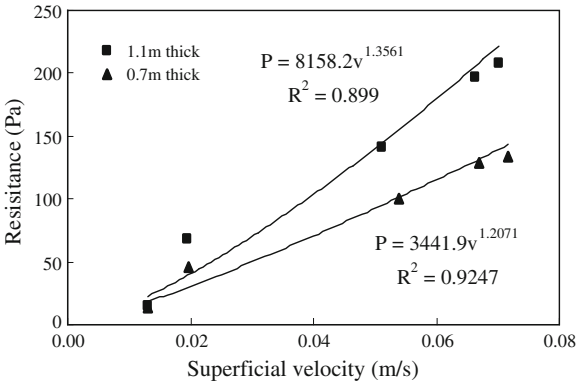

Fig. 29.5 Relationship between the filtration resistance and superficial velocity of ceramsites and wood bits mixed at 1:1

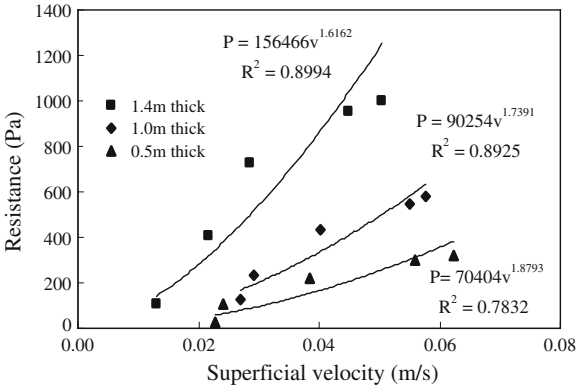

Fig. 29.6 Relationship between the filtration resistance and superficial velocity of mixture of peanut shell and bark

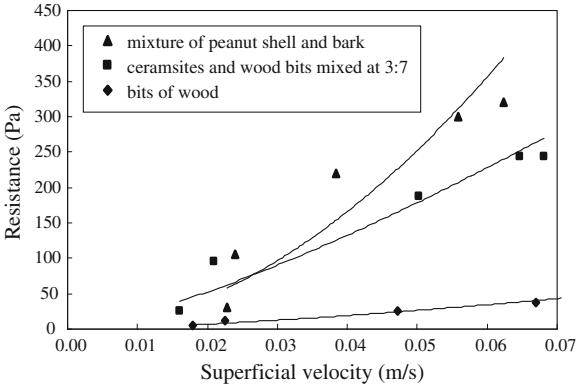

Fig. 29.7 Relationship between the filtration resistance and superficial velocity at the thickness of 1 m

high-speed non-Darcy flow used in the experiment and there are different Reynolds numbers, viscous energy loss, and dynamic energy loss account for different part of it and different empirical coefficients are come up with. In actual

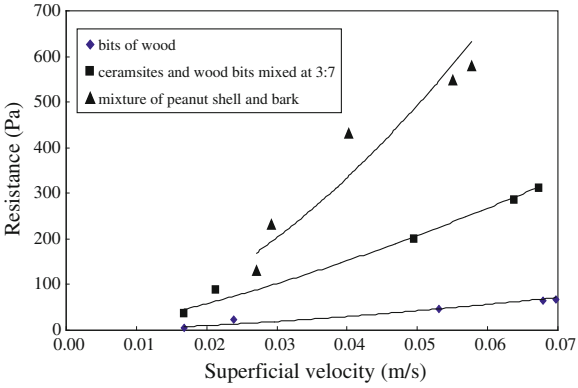

Fig. 29.8 Relationship between the filtration resistance and superficial velocity at the thickness of 0.5 m

project conditions, thickness and superficial velocity of filter material are all set inside the required range. To facilitate its use in actual projects, the filtering resistance and superficial velocity are fitted into an empirical computation formula on the experimental basis and marked in Figs. 29.2, 29.3, 29.4, 29.5, and 29.6. On application in real projects, the resistance can be worked out by using the experimental empirical formula.

29.4.2.2 Analysis of Effects of Kinds and Thickness of Filter Materials

As shown in the experiment, the changes of filtering resistance with superficial velocity relates to the kind of filter material. Filter materials differ in change patterns of filtering resistance. Moreover, the experimental results (as shown in Figs. 29.2, 29.3, 29.4, 29.5, and 29.6) show that different thickness of the filter materials will bring about different empirical coefficient (coefficient and exponent) in their change pattern. With thickness of the filter material increasing, change rate of the resistance differs as the superficial velocity grows. As shown in Figs. 29.7 and 29.8, when at the same thickness, the filtering resistances of experimental filter materials change with the superficial velocity. When the superficial velocity does not change, the filtering resistance of wood bits is the smallest while that of peanut shell and bark mixture is the biggest.

29.4.2.3 Analysis of Added Earth and Sand's Effects on Filtering Resistance

As known from actual project experiences, earth and sand are often brought into the biofilter process at filling. To show the earth and sand's effects on filtering resistance, a comparative study has been conducted between a pure filter material and the same filter material with earth and sand blended into it, about which the experimental result are 125.2 and 250.9 Pa, respectively. From the results we

know that when earth and sand are blended into the filter material the filtering resistance increases. This is because that earth and sand have smaller particle size which will reduce porosity of the filter material. Therefore, earth and sand should be avoided when filling the biofilter material so as to prevent the filtering resistance from increasing.

29.5 Conclusion

1. Sludge composting is a major measure to reduce urban sludge, to administer biosafety treatment to the sludge and turn the sludge a useful resource. Biofilter is important in treating waste gases forming during sludge composting. To guarantee better performance of biosafety treatment of these waste gases will help sludge composting plants run better and exert greater environmental benefits.
2. The filtering resistance expresses an exponential relationship with the superficial velocity. The filtering flow fits the law of high-speed non-Darcy flow. Results of this experiment will help compute the filtering resistance of relevant filter materials.
3. Factors influencing the resistance characteristics include the biofilter material's character (like particle size, porosity, etc.), its bed thickness and service time, etc.
4. The blended impurities will have some bearing on resistance characteristics of the filter material, therefore, impurities like earth and sand etc., should be avoided when filling the filter material.
5. Resistance characteristics of the filter material change with its service time because the material may change in quality and undergo natural compaction; however, the change pattern requires further study.

References

1. Environmental Protection Administration of the People's Republic of China (2011) Annual statistic report on environment in china, 2010. China Environmental Science Press, pp 4–10 (in Chinese)
2. Liu L, Chen T et al (2010) Odor production and treatment technologies in sewage sludge composting plant. China Water & Wastewater 26(13):120–124 (in Chinese)
3. Komilis DP, Ham RK et al (2004) Emission of volatile organic compounds during composting of municipal solid wastes. Water Res 38(7):1707–1714
4. Domingo JL, Nadal M (2009) Domestic waste composting facilities: a review of human health risks. Environ Int 35(2):382–389
5. Schlegelmilch M, Streese J et al (2005) Odour control at biowaste composting facilities. Waste Manage (Oxford) 25(9):917–927

6. Pagans E, Font X et al (2006) Emission of volatile organic compounds from composting of different solid wastes: abatement by biofiltration. J Hazard Mater 131(1–3):179–186
7. Chung Y (2007) Evaluation of gas removal and bacterial community diversity in a biofilter developed to treat composting exhaust gases. J Hazard Mater 144(1–2):377–385
8. Song Y, Chen H et al (2009) Design of sludge composting treatment project in Zhengzhou city. China Water & Wastewater 25(6):41–43 (in Chinese)
9. Song G, Ren W, Luo Z et al (2013) Field test and analysis of the ventilation system in the biosolid sludge composting plant. Ind Saf Environ Protect 39(3):35–37
10. Jamialahmadi M, Müller-Steinhagen H et al (2005) Pressure drop, gas hold-up and heat transfer during single and two-phase flow through porous media. 26(1):156–172
11. Lee J, Hu T et al (1996) Experimental study of fluid drag in granary ventilation. Chin J Hydrodyn Ser A 21(4):473–478 (in Chinese)
12. Li ZP, Sun ZN et al (2009) The research on the resistance characteristics of microsphere packed bed porous media in non-Darcy regime. Appl Sci Technol 4:61–64 (in Chinese)
13. Wang H (2008) Dynamics of fluid flow and contaminant transport in porous media. Higher Education Press, pp 9–13 (in Chinese)
14. Standards Press of China (2002) GB 50243-2002. Code of acceptance for construction quality of ventilation and air conditioning works. Standards Press of China, Beijing (in Chinese)
15. Standards Press of China (2006) GB/T10178-2006. Industrial fans-performance testing in situ. Standards Press of China, Beijing (in Chinese)

Chapter 30
Research of Data Center Fresh Air Ventilation Cooling System

Yin Liu, Renbo Guan, Jing Ma and Ke Zhang

Abstract A variety of data centers have come into being as required by the continuous development of social network and information technology; meanwhile, wide concern has been aroused about the issue on data center's high energy consumption in which the air conditioning energy consumption accounts for more than 40 %. Thus, it is of great importance to achieve the energy conservation of air conditioning system in data center. According to the new requirement for IT equipment performance and new design range of temperature in data center, this paper presents a full fresh air ventilation and cooling scheme for ambient temperature control of data center, which, without mechanical refrigeration equipment and under the premise of meeting the design requirements for ambient temperature, has greatly reduced the energy consumption and provided a new idea for the design of next-generation data center.

Keywords Data center · Fresh air · Ventilation · Cooling

30.1 Introduction

With the continuous progress of network and information technology of all walks of life, an increasing number of data centers emerge with the rapid growth of service volume, followed by gradually prominent issues on power consumption

Y. Liu (✉) · R. Guan
Zhongyuan University of technology, 41 Zhongyuan Middle Road, Zhengzhou 450007, China
e-mail: hvacr@126.com

J. Ma
Henan University of Technology, Zhengzhou, China

K. Zhang
Jiangsu Hanyun Information Technology Co., Ltd, Yangzhou, China

A. Li et al. (eds.), *Proceedings of the 8th International Symposium on Heating, Ventilation and Air Conditioning*, Lecture Notes in Electrical Engineering 262,
DOI: 10.1007/978-3-642-39581-9_30,

and costs: expense for energy consumption has reached 25 % of the hardware purchase cost, and constantly growing at a compound annual growth rate of 52 %. Energy conservation of data center is not only required by enterprises for cost reduction but also is a key aspect of energy-saving and emission reduction work launched by the state. At present, the energy consumption of global data centers is equivalent to 1.5 % of the sum of the world's energy, namely, a year's total power generation capacity of 50 large power plants. At the same time, up to 2.1 billion tons of carbon dioxide is produced every year, which is equivalent to the carbon emissions of 41 million vehicles. What's more is , along with the rapid growth of data center market, by 2014, the energy consumption of global data centers and resulting influence on environment will be doubled compared with current status. It is an urgent mission for data communication equipment manufacturers, data center designers, and operating managers to establish a new type of data center which shall be provided with advantages of "high efficiency, energy conservation and convenient management" to reduce the users' direct costs, resolve management issues, and make contribution to the building of a conservation-oriented society.

30.2 Analyses on Energy Consumption of Data Center

The energy consumption of data center refers to the sum of energy consumed by various electric equipments in the facility including IT equipment like server and switch as well as the auxiliary system like air conditioning and power distribution. Based on the current energy efficiency level of data center, the composition of energy consumption is generally as shown in Fig. 30.1. The energy consumption of IT equipment accounts for the largest proportion, approximately 50 % of the total energy consumption of data center, in which the energy consumption of server accounts for about 40 %, storage device and network communication device, respectively, accounting for 5 %. The energy consumption of air

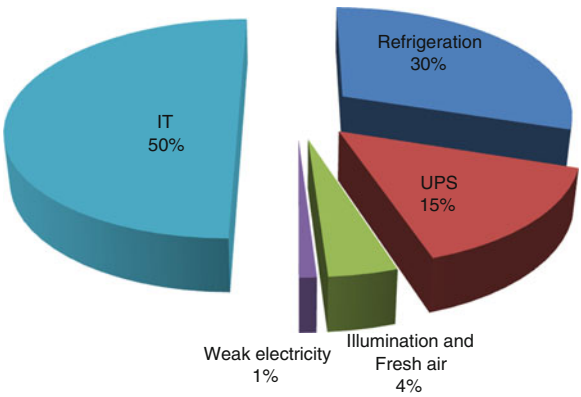

Fig. 30.1 Composition of energy consumption of data center

conditioning system ranks the second place, accounting for about 40 %; while the energy consumption of power distribution system accounts for around 10 % of the total energy consumption of data center [1].

PUE (Power Usage Effectiveness) is usually adopted to make an assessment of the energy efficiency of data center.

$$\begin{aligned}\mathrm{PUE} &= \frac{\text{Total Facility Power}}{\text{IT Equipment Power}} \\ &= \frac{\text{IT Equipment Power} + \text{Air conditioning systems Power} + \text{Electricity distribution system Power} + \text{Other Power}}{\text{IT Equipment Power}} \\ &= 1 + \frac{\text{Air conditioning systems Power} + \text{Electricity distribution system Power} + \text{Other Power}}{\text{IT Equipment Power}}\end{aligned} \tag{30.1}$$

Up to now, the PUE of domestic data centers basically remains between 2 and 3.0, while the average energy efficiency of data centers in the United States is about 2.0. For all the operating data centers around the world, the best PUE has reached 1.046. Energy conservation of the air conditioning system is the key to actually realize the energy conservation of data center.

30.3 Measures for Energy Conservation of Air Conditioning in Data Center

30.3.1 Application of Special High-Efficiency Unit

Due to a large amount of heat release and the requirement for basically continuous operation at constant temperature and humidity, the data center can only apply the suitable air conditioning system with high reliability, large cooling capacity, small difference in temperature, and large air volume. Compared to the comfort air conditioning with the same cooling capacity, the special air conditioning for computer room has about doubled circulating air volume with only half of the enthalpy difference, which does not need dehumidification during the operation as the large circulating air volume would enable the unit in motion above the air dew point, unlike the comfort air conditioning that has to cool the air under the dew point for coping with the moisture load. Therefore, the unit is able to increase the thermal efficiency of operation by raising the evaporating temperature of the refrigerant, thereby improving the operational economic effect.

30.3.2 Division of Hot and Cold Partition

The following deficiencies exist in air distribution of the traditional data room: absence of hot/cold aisle containment and uneven distribution of temperature in the room: in some parts, the temperature is particularly low with excessive

refrigeration status while for the other areas the temperature is much higher than the design temperature of air conditioning, because of that, the temperature inside the data equipment is a little high and abundant cool air circulates in short circuit. More reasonable air distribution would send the cold air from air conditioning directly to the cabinet, avoiding the situation of first cooling the environment and then the equipment, which can significantly enhance the refrigeration efficiency of air conditioning. At the same time, it is more practical for the data center with high power density in part but low power density on the whole. Both sides of the server have been divided into the suction passage and exhaust passage, which enables the air conditioning unit to save 20–25 % of energy.

30.3.3 Enhance the Computer Room Design Temperature

On the premise of ensuring the stably normal operation, increase the ambient temperature in data center, and thus reduce the cooling cost and improve the energy efficiency of data center. It is estimated that an increase in temperature of 1 degree will save 4 % of cooling energy consumption. In accordance with GB50174-2008 [2], the temperature in host computer rooms of Class A and Class B is required to be 22–24 °C and the temperature in cold aisle shall be 20–25 °C as specified in ANSI/TIA-942-2005 [3]. The new standard temperature in computer room defined by ASHRAE (American Society of Heating, Refrigerating and Air Conditioning Engineers) in 2008 had been raised to 18–27 °C from 20–25 °C in 2004.

30.4 Full Fresh Air Ventilation and Cooling Design

30.4.1 Design Temperature

Modern server and network equipment are not so delicate as regarded in traditional (10 or 20 years ago) concepts: most of servers can be in normal operation at a temperature of 10–35 °C and a relative humidity of 20–80 %. The above-mentioned design requirement for air conditioning in data center is set for traditional data centers. With the continuous development of IT technology, IT equipment performance has been greatly enhanced; specific to the performance of latest IT equipments, ASHRAE, in the 2011 White Paper on Air-Conditioning Technology of Data Center [4], has made amendments to the design parameters of air conditioning in data center, greatly raising the limit of design temperature of data center with the maximum temperature adjusted to 45 °C. Companies including Intel, Dell, etc. have successively released the high-temperature resistant and stable data server, providing new opportunities for the air conditioning energy-saving design of data center. The design parameters of ASHRAE 2011 IDC White Paper are as given in Table 30.1.

Table 30.1 Design parameters of ASHRAE 2011 IDC white paper

Classes	Equipment environmental specifications							
	Product operations					Product power off		
	Dry-bulb temperature (°C)	Humidity range, noncondensing	Maximum dew point (°C)	Maximum elevation (m)	Maximum rate of change (°C/h)	Dry-bulb temperature (°C)	Relative humidity (%)	Maximum dew point (°C)
Recommended (Applies to all A classes; individual data centers can choose to expand this range based upon the analysis described in this document)								
A1–A4	18–27	5.5 °C DP–60 % RH and 15 °C DP						
Allowable								
A1	15–32	20–80 % RH	17	3,050	5/20	5–45	8–80	27
A2	10–35	20–80 % RH	21	3,050	5/20	5–45	8–80	27
A3	5–40	−12 °C DP and 8–85 % RH	24	3,050	5/20	5–45	8–85	27
A4	5–45	−12 °C DP and 8–90 % RH	24	3,050	5/20	5–45	8–90	27
B	5–35	8–80 % RH	28	3,050	NA	5–45	8–80	29
C	5–40	8–80 % RH	28	3,050	NA	5–45	8–s80	29

30.4.2 Design Program

Even thoush the energy consumption level of data center has been reduced and PUE has declined on its original base after the application of different air conditioning energy-saving technologies, the energy consumption of air conditioning system is still high. Following the constant upgrade of the temperature-resistance performance of IT equipment, the higher temperature in data center is set as "external air introduction" to make good preparations for achieving new energy-saving methods.

Full fresh air cooling adopts the external air with temperature lower than that in data center as cold source, just blowing the external air into data center to accomplish the cooling process; the hot air from server can be discharged to outdoor through passages, realizing 40 % of the air conditioning energy conservation and the PUE dropping to under 1.4. So far, the data center of Yahoo located in Lockport of New York, data center of Facebook, data center of Google in Belgium, data center of HP in Wynyard of UK and data center of Microsoft in Dublin all apply the method of external air introduction.

The green IDC without air conditioning of Hanyun Technology applies the cooling capacity of external air and heat generated from IT equipment all through the year to achieve the temperature regulation of data center. Specific to the requirement for temperature control of data center, DACS (Distributed Airflow Cooling System) and BDVCS (Blowing and Drawing Ventilation Cooling System) based on external air introduction are designed to realize the temperature control of the data center without air conditioning equipment throughout the year.

(1) Load calculation

The cooling load of the cooling system in traditional data center includes the cooling loads from computer equipment, conductive heat of building envelope, human body, lighting equipment and outdoor air, etc. Full fresh air cooling data center applies the outdoor fresh air as cold source to eliminate all the hot loads of data center; the outdoor fresh air load need not to be taken into consideration during the design.

(2) Design of air volume

DACS and BDVCS based on external air introduction apply the outdoor fresh air as cold source to eliminate all the hot loads of data center. In accordance with design parameters in the 2011 IDC White Paper of ASHRAE, the temperature in data center shall be controlled within the range of not exceeding the outdoor temperature by 8 °C, with the maximum air volume of:

$$G = \frac{Q}{h_2 - h_1} \tag{30.2}$$

where G is the maximum volume of the air introduced from outdoor to indoor; Q is the cooling load of data center; h_1 is the enthalpy content in outdoor air; h_2 is the enthalpy content in exhaust air from indoor.

(3) Air distribution

The air distribution of data center is designed to orderly organize the hot and cold air, taking efficient use of the cold air cooled by air conditioning equipment or introduced from outside to keep the IT equipment cool and driving the heated hot air back to air conditioning or out to outdoor, which is realized based on the integration of IT equipment layout and air conditioning equipment layout. As IT equipment is characterized by high heating flux, reasonable air distribution is the guarantee for the efficient and reliable operation of IT equipment and data center.

By absorbing characteristics of the traditional data center air distribution and integrating features of external air introduction for cooling with consideration of the demands of some IT equipments and data center for capacity expansion, the full fresh air data center applies the DACS and BDVCS based on external air introduction with container-type modular design.

The container-type modular design structure solves the demands of some IT equipments and data center for capacity expansion and meanwhile provides basis for DACS and BDVCS. For the internal container-type module, the comprehensive division of hot and cold partition is achieved by the base frame densely covered by data servers, adopting the blowing and drawing ventilation technology to introduce the outdoor cool air into modular cold area and after modular cooling lead it into modular hot area through data server so as to realize the efficient utilization of outdoor cool air and efficient cooling of data server. In addition, the temperature regulation in the low-temperature season is achieved by the DACS in data room and inside the module. The data center with container-type modular design of Hanyun Company is as shown in Fig. 30.2.

Fig. 30.2 Data center with container-type modular design of Hanyun Company

30.4.3 Implementation Effect

Since the first operation of the data center with container-type modular design of Hanyun Company on Aug. 1, 2011, the temperature in data center and internal module has been controlled under 40 °C, which complies with the design standard of ASHRAE.

30.5 Conclusions

Following the constant upgrade of the IT equipment performance, the design range of the temperature in data center has been gradually expanded, which provides new approaches to the energy-saving design of air conditioning system in data center. Full fresh air ventilation and cooling system applies the outdoor air to keep the data center cool, which not only ensures the IT equipment in normal operation but also greatly reduces the energy consumption of temperature control unit by eliminating the need for mechanical refrigeration plant, achieving the goals of environment protection and energy conservation and providing a new promising program for the development of next-generation data center.

References

1. Zhong J (2010) The planning and design of the new generation green data center. Electronic Industry Press, Beijing
2. Electronic information system room design specification. GB 50174-2008
3. Telecommunications Infrastructure Standard for Data Centers. ANSI/TIA-942-2005
4. ASHRAE (2011) Thermal guidelines for data processing environments—expanded data center classes and usage guidance

Chapter 31
Design Principle of Air Curtain Ventilation

Haiguo Yin and Angui Li

Abstract The air distribution characteristics formed by an "air curtain" ventilation approach are presented. The design principle of this novel air distribution pattern is investigated. A design example is introduced; meanwhile, the design programs and effectiveness evaluation were carried out. The current results show the air curtain ventilation (ACV) is a particular air distribution to combine the mixing ventilation and displacement ventilation together. In additional, the air lake phenomena of occupied zones resembles displaced air movement in some extent. The design process of the air distribution formed by ACV is demonstrated.

Keywords Ventilation · Air distribution · Air curtain ventilation · Design procedures

31.1 Introduction

Air diffusion within spaces play an important and direct role in ventilation and air-conditioning effect, and therefore affects the indoor air quality (IAQ), occupied zone contaminant distribution, and even the human health [1, 2]. Traditionally, two distinct airflow patterns are commonly used to characterize air movement in rooms: mixing ventilation and displacement ventilation [3]. Comprehensive utilization of the advantages of both airflow patterns, a new method of air distribution known as the air curtain ventilation (ACV) has been developed [4]. The supply air system of ACV is easy to install, and do not take up the space of occupied zone. Meanwhile, ACV seems to be a promising airflow concept due to its better IAQ

H. Yin (✉) · A. Li
School of Environmental and Municipal Engineering, Xi'an University of Architecture and Technology, Xi'an, 710055 Shaanxi, China
e-mail: yinhaiguo@xauat.edu.cn; haiguo_yin@163.com

A. Li et al. (eds.), *Proceedings of the 8th International Symposium on Heating, Ventilation and Air Conditioning*, Lecture Notes in Electrical Engineering 262,
DOI: 10.1007/978-3-642-39581-9_31,

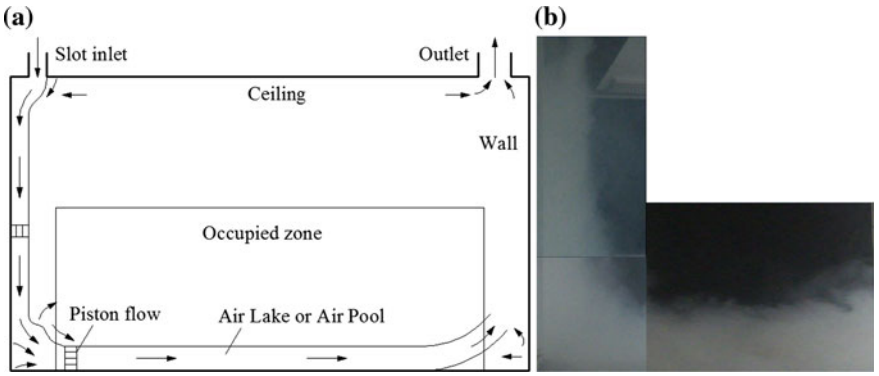

Fig. 31.1 Air distribution of ACV: **a** Probable airflow patterns with using ceiling mounted slot inlet; **b** Visualization experimental observation

and higher energy efficient, which is similar to the displacement ventilation system in certain extent [5, 6].

The principle of ACV is shown in Fig. 31.1. The air diffuser of ACV model located on the upper space of the room, and is close to a vertical sidewall. When the supply air moves downward through the slot, it can be attached to the vertical wall using the Coanda effect [7, 8]. As the air jet with high momentum downwards onto the wall-floor corner, it impinges the ground, then separates from the attached wall and reattaches to the floor surface. The resulting flow from the ACV forms the "Air Lake" or "Air Pool" phenomena over the floor, which is beneficial to create good IAQ and improve ventilation efficiency.

The airflow characteristics of ACV with a linear slot diffuser have been studied by experiment testing, and the expressions for each characteristic parameter were obtained [4–6]. The main aim of this work is to present the design principle and process of ACV model, and evaluate whether this air distribution can be used in room ventilation and air-conditioning system.

31.2 Design Principle

31.2.1 Air Curtain Ventilation Modeling

In air curtain ventilation modeling, some theoretical and semi-empirical models were found and validated in the earlier studies, see Table 31.1. Using these formulas, the velocity and temperature field in the occupied zone can be designed to meet the requirements.

As shown in Table 31.1, there are two attached modes. In full-attached mode, the distance between the slot location and the attached wall is very small ($s/b \leq 2$).

Table 31.1 Semi-empirical formulas that define the airflow characters of ACV in occupied zone

Airflow characters	Full-attached mode ($s/b = 2$)	Partial-attached mode ($s/b = 5$)
Maximum jet velocity	$\frac{u_m(x)}{u_0} = 2.45\left(\frac{x}{b}\right)^{-0.55}$	
Non-dimensional jet temperature	$\theta_m(x) = \frac{t_n - t_m}{t_n - t_0} = 0.587e^{-0.015\left(\frac{x}{b}\right)}$	
Air temperature in room height direction	$\left(t_y - t_0\right) = \frac{12.28}{u_0}\left(1 - e^{-0.036\frac{y}{b}}\right)^{0.14}$	$\left(t_y - t_0\right) = \frac{11.67}{u_0}\left(1 - e^{-0.036\frac{y}{b}}\right)^{0.14}$

Where, s is distance between the slot location and attached wall, b is width of slot diffuser $u_m(x)$ is maximum jet velocity in the flow direction, u_0 is the supply air velocity of diffuser $\theta_m(x)$ is non-dimensional jet temperature in the airflow direction (x direction), t_n is the design temperature in occupied zone, t_m is axis temperature of the supply jet, t_0 is the supply air temperature of diffuser, t_y is the air temperature in room height direction (y direction)

When the supply air jet moves from the slot diffuser, it can attach to the sidewall immediately. Correspondingly, in partial-attached mode, the distance is larger ($2 \leq s/b \leq 6$). Before the supply jet attached to the sidewall, it had moved a certain distance from the diffuser. By contrast, in partial-attached mode, before the supply jet enters into the occupied zone, it had certain entrainment with the ambient air, and then the energy coefficient of this mode is lower. However, the temperature gradient in y direction is less than full-attached mode, and this is helpful for avoiding discomfort that caused by larger vertical air temperature difference between head and ankles.

31.2.2 Design Requirements

A reasonable air distribution should meet the design requirements firstly, the existing standards [9–11] provided by different associations are summarized in Table 31.2. Based on these standards, the design requirements for ACV mode is chosen and presented in the last column of Table 31.2. For u_n, as the design air temperature in occupied zone increase, the allowable value of u_n could increase [12].

31.2.3 Design Principle Analysis

As shown in Table 31.2, the air distribution design of ACV should meet the requirements of u_n, $t_{0.1,\min}$, and $t_{0.1\text{–}1.1/1.8}$ first, and then meet the requirements of *PMV* and *PPD* for thermal comfort.

For u_n, if the maximum jet velocity in axis position is lower than u_n, and then the whole velocity in occupied zone can meet this requirement. As shown in Table 31.1, u_m is decreases as the airflow moves along the x direction, and the maximum velocity located on the left boundary of occupied zone (x = 1.0 m).

Table 31.2 Different standards of air distribution design in occupied zone

Standard			ISO 7730-2005	ASHRAE 55-2004	CIBSE 1990	ACV
Index	Allowable velocity in occupied zone, u_n	Winter	≤ 0.15 m/s	≤ 0.20 m/s	–	≤ 0.20 m/s
		Summer	≤ 0.25 m/s	≤ 0.20 m/s		≤ 0.30 m/s
	Allowable minimum air temperature in 0.1 m height, $t_{0.1,min}$		19–26 °C	18–29 °C	Winter: 20 °C Summer: 22 °C	Winter: 19 °C Summer: 21 °C
	$t_{0.1-1.1} = t_{1.1} - t_{0.1}$ (Sitting posture)		≤ 3 °C	–	≤ 3 °C	≤ 3 °C
	$t_{0.1-1.8} = t_{1.8} - t_{0.1}$ (Standing posture)		–	≤ 3 °C	–	≤ 3 °C
	PMV/PPD		−0.5–0.5/ ≤ 10 %	−0.5–0.5/ ≤ 10 %	–	−0.5–0.5/ ≤ 10 %

Meanwhile, u_m is defined by supply air velocity u_0 and the width of slot diffuser b. To avoid draft risk, the value of u_0 and b should be choosen properly.

For $t_{0.1,min}$, the expression of non-dimensional jet temperature $\theta_m(x)$ shows this parameter is directly affected by the supply air temperature t_0, choose a proper value for t_0, and this need is being met.

For $t_{0.1-1.1/1.8}$, this parameter is indirect calculated by the air temperature in room height direction t_y, while t_y is in inverse proportion to u_0, and in proportion to b, to meet the requirements of $t_{0.1-1.1/1.8}$, a larger value of u_0, and a smaller value of b is required. If the change of u_0 and b cannot meet the design requirements of $t_{0.1-1.1/1.8}$, changing the full-attached mode into the partial-attached mode.

When the above three parameters meet the design requirements, the air distribution of ACV can be design, and then the value of *PMV* and *PPD* can be calculated to evaluate the thermal comfort. This part will present in next section.

31.3 Design Process

31.3.1 Design Procedures

Based on above analysis, the air distribution by using ACV mode can be designed as the steps shown in Fig. 31.2.

31.3.2 Design Example

To better understand the design procedures as shown in Fig. 31.2, a design example is introduced. Figure 31.3 is the air distribution design pattern, while Table 31.3 is the computing process. The design example is described as follows.

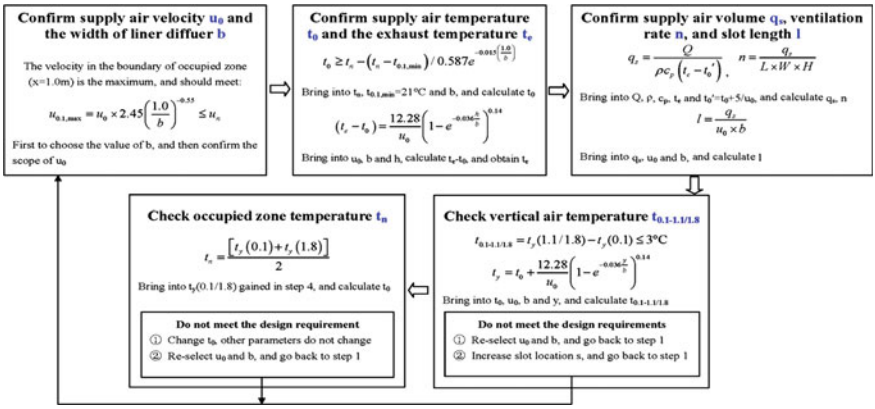

Fig. 31.2 Design procedures of air distribution by using ACV method

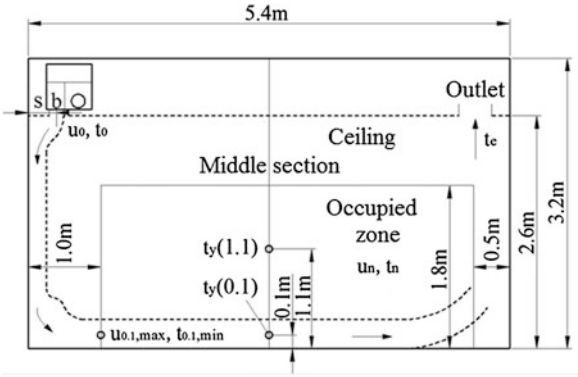

Fig. 31.3 Design pattern of air distribution for ACV by using a ceiling mounted slot inlet

An air-conditioning room, with the dimension of $5.4 \times 7.0 \times 3.2$ m^3 (Length × Width × Height), the cooling load Q is 6,800 kJ/h in summer, the design temperature t_n is 27 ± 0.5 °C. The staffs in occupied zone always in sitting posture. There is not enough space to arrangement air diffuser in the bottom of the room, and then ACV mode is chosen for room air-conditioning.

31.3.3 Design Evaluation

Based on the design example, and the corresponding experimental measurement, the effectiveness of this design is verified by the following evaluation indexes.

Table 31.3 Design calculation of air distribution by using ACV method

Design step		Computational procedure	Parameter select
1	Choose attached wall	★ The vertical wall with a dimension of 7.0 × 2.6 m^2 is chosen	
2	Confirm u_0 and b	★ $u_{0.1,\max} = 2.45 \times u_0 \times (1.0/b)^{-0.55} \leq 0.5$, and then $u_0 \times b^{0.55} \leq 0.204$	$b = 0.05$ m $u_0 = 1.0$ m/s
3	Confirm t_0 and t_e	★ Design requirement: $t_m(1.0) \geq t_{0.1,\min}(1.0) = 21$ °C, $t_0 \geq t_n - (t_n - t_m)/0.587e^{-0.015(x/b)} = 13.2$ °C, When $t_n = 27$ °C, $\Phi = 50$ %, t_{dew} is 15.5 °C, and then $t_0 \geq 15.5$ °C ★ $t_e - t_0 = 12.28 \times (1 - e^{-0.036 \times h/b})^{0.14}/u_0 = 12$ °C	$t_0 = 17$ °C $t_e = 29$ °C
4	Confirm q_s and n	★ $t_0' = t_0 + 5/u_0 = 17 + 5/0.64 = 22$ °C, $q_s = Q_0/[\rho \times c_p \times (t_e - t_0)] = 802.2$ m^3/h ★ $n = q_s/(L \times W \times h) = 8.16 > 5$ l/h	
5	Confirm l	★ $l = q_s/3600/(u_0 \times b) = 802.2/3600/(1.0 \times 0.05) = 4.46$ m, ★ $l{:}b = 4.5{:}0.05 = 90{:}1$, the attached wall meet the requirement	$l = 4.5$ m
6	Check $t_{0.1-1.1}$	★ $t_y(0.1) = t_0 + 12.28 \times (1 - e^{-0.036 \times y/b})^{0.14}/u_0 = 25.5$ °C, $t_y(1.1) = 28.3$ ★ $t_{0.1-1.1} = t_y(1.1) - t_y(0.1) = 2.8$ °C ≤ 3 °C, meeting design requirement	
7	Check t_n	★ $t_n = [t_y(0.1) + t_y(1.1)]/2 = 27.1$ °C, meeting requirement $t_n = 27 \pm 0.5$ °C	
8	Define design parameters	$u_0 = 1.0$ m/s, $t_0 = 17$ °C, dimension of slot: $l \times b = 4.5 \times 0.05$ m^2	

31.3.3.1 Ventilation Efficiency

$$E = \frac{t_e - t_0}{t_n - t_0} \tag{31.1}$$

The ventilation efficiency of ACV model is $E_{\mathrm{ACV}} = (t_e - t_0)/(t_n - t_0) = (29-17)/(27-17) = 1.2$. Under the same design conditions, the ventilation efficiency for mixing ventilation (MV) and displacement ventilation (DV) is $E_{\mathrm{MV}} = (27-22)/(27-22) = 1.0$, $E_{\mathrm{DV}} = (29.5-18.5)/(27-18.5) = 1.3$, respectively. The ventilation efficiency of ACV is higher 20 % than MV system, but lower 7.7 % than DV system.

31.3.3.2 Non-uniform Coefficient

$$K_v = \frac{\sqrt{\frac{1}{n}\sum_{i=1}^{n}(u_i - \overline{u_i})^2}}{\overline{u_i}} \text{ and } K_t = \frac{\sqrt{\frac{1}{n}\sum_{i=1}^{n}(t_i - \overline{t_i})^2}}{\overline{t_i}} \tag{31.2}$$

where, n is the number of measured points, u_i and t_i is the local air speed and temperature, $\overline{u_i}$ and $\overline{t_i}$ is the local mean air speed and temperature, respectively.

As shown in Table 31.4, the mean value of K_v and K_t in the occupied zone is 0.22 and 0.014, respectively, which can meet the design requirement and create a comfort environment in occupied zone.

31.3.3.3 Draft Rate (DR)

$$DR = \left[(34 - t_i) \times (\overline{u_i} - 0.05)^{0.62}\right] \times (0.37 \times \overline{u_i} \times I_i + 3.14) \tag{31.3}$$

where I_{i} is the local turbulence intensity, $I_i = \sqrt{\frac{1}{n}\sum_{i=1}^{n}(u_i - \overline{u})^2}/\overline{u} \times 100\,\%$

As shown in Table 31.4, the design procedures of ACV system can meet the requirement of DR $\leq$ 20 % [10]. When the value of DR is equal to 20 %, recalculating the design example, and then the allowable velocity in occupied zone u_n can achieve 0.55 m/s.

Table 31.4 Calculated non-uniform coefficient and draft rate along the airflow direction

Non-dimensional distance from the impinging corner, x/L	0.17	0.21	0.26	0.35	0.44	0.54	0.63	0.72	0.81
K_v	0.10	0.11	0.08	0.09	0.26	0.42	0.19	0.20	0.54
K_t	0.018	0.017	0.016	0.014	0.013	0.012	0.011	0.011	0.011
DR (%)	16.70	16.02	14.90	13.42	10.65	7.98	2.62	1.13	2.14

31.3.3.4 PMV and PPD

PMV is the predicted mean vote and PPD is the predicted percentage of dissatisfied, the expressions and specific meanings of these two parameter can be find in Ref. [9] or [10].

According to the design example, the measured mean air velocity in occupied zone is 0.24 m/s, both the air temperature and mean radiant temperature is 27.1 °C, the suggested metabolic rates, relative humidity, and clothing insulation is 1.2met, 50 %, and 0.5clo, respectively. Based on these parameter values, the calculated PMV is 0.469, and the PPD is 9.60 %, which can meet the design requirements. When increases the mean air velocity to 0.3 m/s, the PMV is 0.396, and PPD is 8.27 %. If the air velocity is further increased to 0.5 m/s, the PMV and PPD is 0.215 and 5.96 %, respectively. Therefore, when the design air temperature in occupied zone is higher (27 °C in current study), increasing the air velocity in certain extent is helpful to improve the environmental comfort.

31.4 Conclusion

This paper shows a new air distribution pattern—air curtain ventilation. The current study and its results are helpful for designers and engineers using ACV mode in room air distribution design.

The air distribution of ACV is between that of mixing ventilation and displacement ventilation. It can create comfort environment in occupied zone, and has higher ventilation efficiency. When the arrangement of side air supply at occupant zone is not suitable, using ACV model can reach the effect of displacement ventilation, and is better than mixing ventilation.

The design principle and procedures of ACV model was introduced. The air distribution of ACV is mainly affected by supply air velocity u_0 and the width of slot diffuser b. In order to design effectively, a larger u_0 and smaller b is recommended. Meanwhile, in the partial-attached mode, the ventilation effectiveness is lower than full-attached mode, but the distribution of air temperature in the occupied zone is more uniform, which can avoid local comfort in certain extent.

The index evaluations show the design process provided in this paper is reasonable and effective. The allowable velocity in occupied zone u_n is associated with the design temperature t_n. When temperature t_n is higher, the value of u_n can be larger than the specified value shown in the existed standards. In addition, a larger u_n is helpful to reduce the mean air temperature in occupied zone, and this is benefited to improve personnel comfort.

Acknowledgments This research was supported by National Natural Science Foundation of China (50778145, 50278025), and Shaanxi Province "13115" Science and Technology Innovation Key Project (2009ZDKG-47).

References

1. Awbi HB (2003) Ventilation of buildings. Taylor & Francis, New York
2. Seppänen O (2008) Ventilation strategies for good indoor air quality and energy efficiency. Int J Vent 6(4):297–306
3. ASHRAE (2001) ASHRAE handbook: fundamentals. American Society of Heating, Refrigeration and Air-Conditioning Engineers Inc, Atlanta, pp F26.2–26.3
4. Li AG, Yin HG, Zhang WD (2012) A novel air distribution method—principles of air curtain ventilation. Int J Vent 10(4):383–390
5. Yin HG, Li AG (2012) Airflow characteristics by air curtain jets in full-scale room. J Cent South Univ T 19(3):675–681
6. Li AG, Yin HG, Wang GD (2012) Experimental investigation of air distribution in the occupied zones of air curtain ventilated enclosure. Int J Vent 11(2):171–182
7. Coanda H (1936) Device for deflecting a stream of elastic fluid projected into an elastic fluid. US patent, 2052869, 1 Sept 1936
8. Reba I (1966) Applications of the Coanda effect. Sci Am 214(6):84–92
9. ISO Standard 7730 (2005) Ergonomics of the thermal environment—analytical determination and interpretation of thermal comfort using calculation of the PMV and PPD indices and local thermal. International Organization for Standardization, Geneva
10. ANSI/ASHRAE Standard 55 (2004) Thermal environmental conditions for human occupancy. American Society of Heating, Refrigeration and Air-Conditioning Engineers, Inc., Atlanta
11. CIBSE Standard 1990 (2006) Environmental design-CIBSE guide A, 7th edn. CIBSE Publications, Norwich
12. GB 50019 (2004) Code for design of heating ventilation and air conditioning (in Chinese). China Planning Press, Beijing

Chapter 32
The Comparison of Cooling Performance Between New-type Capillary Radiant Panel and Traditional Radiant Panel

Jianbo Chen, Haizhao Yu and Gang Liu

Abstract New-type cooling ceiling capillary radiant panels are more convenient in installing and much easier in ensuring the quality of produce than the traditional capillary radiant panels. The present study compared the cooling performance between the new-type cooling ceiling capillary radiant panels and overseas traditional capillary radiant panels by numerical simulation and experimental test. The results indicated that new-type cooling ceiling capillary radiant panels are more energy-saving and convenient in use than traditional capillary radiant panels. It provides some scientific references for the application and popularization of the new-type cooling ceiling capillary radiant panels.

Keywords Numerical simulation · Experimental test · Comparison · Radiant panel

32.1 Introduction

Due to radiant heating and cooling is comfortable, energy-saving, and can sufficiently use low-quality energy within different styles, it is relatively advanced and being concerned more and more [1]. In addition, through a lot of literature research found that at home and abroad have been the in-depth study on radiation technology [2–7]. The traditional ceiling capillary radiant panels (hereafter referred to as panel2) have been extensively applied because of their comfortable and energy-saving [8]. But they are hard in installing on-site and ensuring the quality, their development is limited.

J. Chen · H. Yu (✉) · G. Liu
School of Environment and Architecture, University of Shanghai for Science and Technology, Shanghai 200093, China
e-mail: haizhao_yu@163.com

A. Li et al. (eds.), *Proceedings of the 8th International Symposium on Heating, Ventilation and Air Conditioning*, Lecture Notes in Electrical Engineering 262,
DOI: 10.1007/978-3-642-39581-9_32,

However, the new-type cooling ceiling capillary radiant panels (hereafter referred to as panel1) can be processed in the factory and assembled on-site. They are convenient in using and easy in controlling the quality. Thus panel1 would be used more extensive in the future. This study compared the cooling performance between panel1 and panel2 by using numerical simulation and experimental test.

32.2 Numerical Simulation by Fluent

32.2.1 Physical Model

A set of supply and return water pipe in these two radiant panels is taken as object of study. The actual thermal transfer process is simplified to a two-dimension thermal transfer construction unit model. The mean temperature of fluid in whole pipe t_f is selected as the qualitative temperature. The temperature of inside pipe wall is t_w. The qualitative size is the inside diameter d. d_1 and d_2 is the outside diameter and inside diameter of the model for panel1, while d_1' and d_2' is the outside diameter and inside diameter of the model for panel2 respectively. The model for panel1 is showed in Fig. 32.1. The model for panel2 is showed in Fig. 32.2.

32.2.2 Mathematical Model

1. According to Energy conservation rule and Fourier rule, the equation for the interior temperature pattern t of the radiant panel is [9] :

$$\rho c \frac{\partial t}{\partial \tau} = \lambda \left(\frac{\partial^2 t}{\partial x^2} + \frac{\partial^2 t}{\partial y^2} \right) \tag{32.1}$$

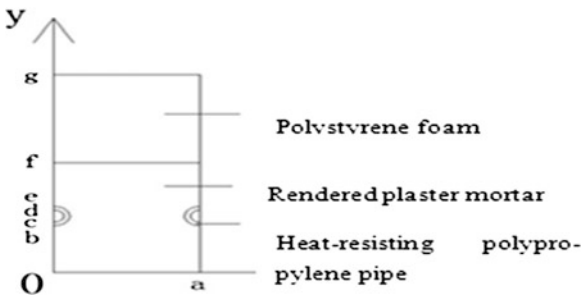

Fig. 32.1 The model for panel1

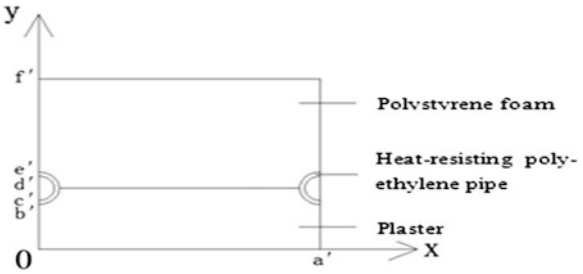

Fig. 32.2 The model for panel2

- The Boundary Conditions for the thermal transfer of panel1.

The convection heat exchange between the hot or cold water in pipe and interior wall of the pipe is the third kind Boundary Conditions:

$$-\lambda\frac{\partial t}{\partial x}=h\left(t_w-t_f\right)\left(x=\sqrt{\left(\frac{d_1}{2}\right)^2-\left(y-\frac{c+d}{2}\right)^2},c<y<d\right) \tag{32.2}$$

$$-\lambda\frac{\partial t}{\partial x}=h\left(t_w-t_f\right)\left(x=\sqrt{\left(\frac{d_1}{2}\right)^2-\left(y-\frac{c+d}{2}\right)^2}+a,c<y<d\right) \tag{32.3}$$

Herein the equation of convention heat transfer factor is

$$h=\frac{\lambda_w Nu}{d} \tag{32.4}$$

The supine surface of the radiant panel is adiabatic surface:

$$\frac{\partial t}{\partial y}=0 \tag{32.5}$$

The lateral surfaces expect for the interior and exterior surface of the pipe are adiabatic surface:

$$\frac{\partial t}{\partial x}=0(0<y<b,x=0;e<y<f,x=0) \tag{32.6}$$

$$\frac{\partial t}{\partial x}=0(0<y<b,x=a;e<y<f,x=a) \tag{32.7}$$

- The Boundary Conditions for the thermal transfer of panel2 is the same as panel1.

2. The total quantity of thermal transfer in the surface of the radiant panel [10]:

$$q = q_r + q_c \tag{32.8}$$

- The equation for the radiant heat exchange q_r is [11] :

$$q_r = 5 \times 10^{-8}\left[\left(t_p + 273.15\right)^4 - (\mathrm{AUST} + 273.15)^4\right] \tag{32.9}$$

Herein t_p is the effective surface temperature, °C; AUST is weighted mean temperature of other indoor surface expect the surface of radiant panel.

- The equation for the convection heat exchange q_c in summer is:

$$q_c = h_c A_p\left(t_a - t_p\right)(t_a = \mathrm{AUST}) \tag{32.10}$$

32.2.3 Results in Numerical Simulation

We have substituted the related parameters in the numerical model and acquired following the distribution of temperature, the curves of performance in cooling for the radiant panels within different supply water temperature or room temperature, the distribution of temperature for the surface of the radiant panels are as follows [12].

32.2.3.1 Distribution of Temperature

The distribution of temperature of the thermal transfer unit model for the radiant panel is regular in different cases of cooling. Thus this study compared the distribution of temperature when the supply water temperature is 18 °C and room temperature is 25 °C. The results are shown in Figs. 32.3 and 32.4.

Fig. 32.3 The distribution of temperature of panel1

Fig. 32.4 The distribution of temperature of panel2

Obviously, these figures indicated that the distribution of temperature of panel1 is more uniform than panel2.

32.2.3.2 The Cooling Performance with Different Supply Water Temperature

The outputs of heat exchange (Q) in different cases are calculated, and the outputs of heat exchange per unit area is q = Q/A. When the room temperature is 25 °C, and the flow rate of supply water is 0.0617 m^3/h, Fig. 32.5 shows that the cooling capacity per unit area of panel1 and panel2 vary with the supply water temperature change [13].

When the cooling load is equal, the supply water temperature of panel1 is much higher than the panel2. Namely, panel1 is more energy-saving because panel2 would consume more energy to acquire lower supply water temperature.

32.2.3.3 The Cooling Performances with Different Room Temperature

Figure 32.6 shows that the cooling capacity per unit area of panel1 and panel2 vary with the room temperature changed when the supply water temperature is 18 °C.

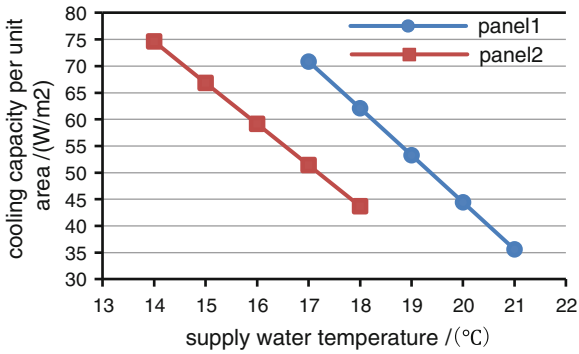

Fig. 32.5 The curve of different radiant panels in different supply water temperature

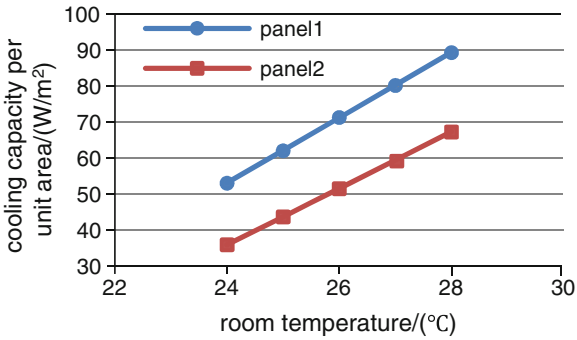

Fig. 32.6 The curve of different radiant panels in different room temperature

The figure indicates that panel1 is more sensitive when the room temperature changed and can compensate the change of indoor temperature. Thus it has better performance in thermal transfer than panel2.

32.3 Experimental Test

32.3.1 Experimental Introduction

To validate the results in the numerical simulation by FLUENT, the cooling performances of these radiant panels were tested in our lab. According to the European test standard of cooling radiant ceiling EN 14240:2004[E] [14], the experimental cell, which is abbreviated cell in this study, is assembled in the enthalpy difference environmental lab in University of Shanghai for Science and Technology.

32.3.2 Experimental Results

32.3.2.1 The Cooling Performance with Different Supply Water Temperature

Figure 32.7 shows that the cooling capacity per unit area of the radiant panels vary with the supply water temperature changed in the experiment, when the room temperature is 25 °C, and the flow rate of supply water is 0.0617 m^3/h.

When the cooling load is equal, the supply water temperature of panel1 is 5 °C higher than panel2. Namely, panel1 is more energy-saving. The results are similar with numerical simulation. Thus the theoretical model is correct. But there are deviations between experimental results and theoretical results. The main reasons include: (1) the simplified two-dimension constant heat transfer model has deviation with the actual heat transfer process; (2) the selection of the physical

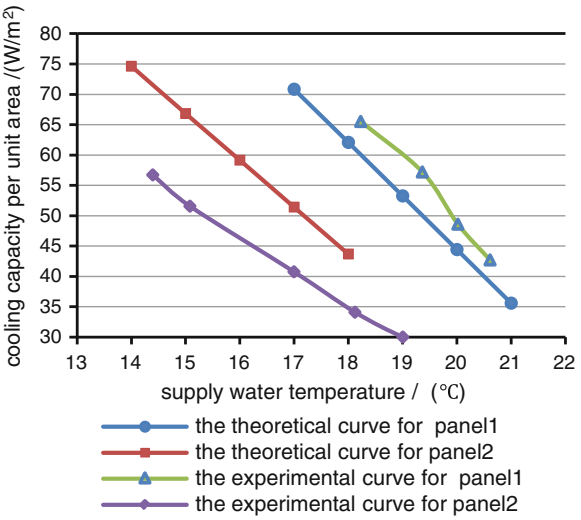

Fig. 32.7 The curve of the radiant panels in different supply water temperature

parameters for materials in numerical simulation may has disparity with the actual materials in the experiment, especially the conductivity factors of plaster in these radiant panels; (3) the convectional circulation in the cell and heat-insulating performance of the cell also has influence in the experimental results. Compared to the experimental results, the theoretical results in the numerical simulation are relatively larger.

32.3.2.2 The Cooling Performance with Different Room Temperature

Figure 32.8 shows that the cooling capacity per unit area of the radiant panels varies with the supply water temperature changed in the experiment, when the supply water temperature is 18 °C.

The curves indicate the tendency of variation between experimental results and theoretical results are consistent. But the experimental results are not equal to the theoretical results. The potential reasons are the same as above.

32.3.2.3 The Distribution of Temperature for the Radiant Panel Surface

The temperature for ambient air, supply water in panel1, and supply water in panel2 is set in 25, 18, and 14 °C, respectively. Figures 32.9 and 32.10 show the distribution of temperature for these radiant panel surfaces in summer with using infrared temperature test instrument.

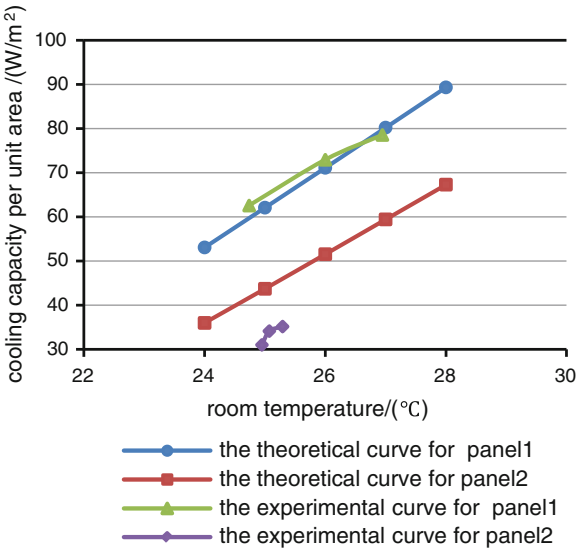

Fig. 32.8 The curve of the radiant panels in different room temperature

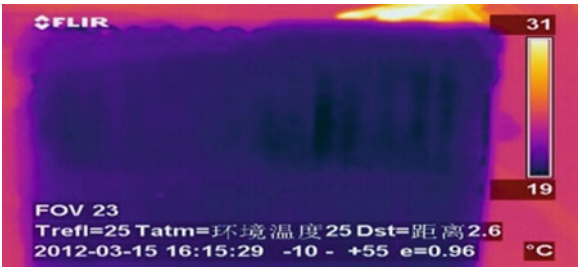

Fig. 32.9 The distribution of temperature for panel1 in summer

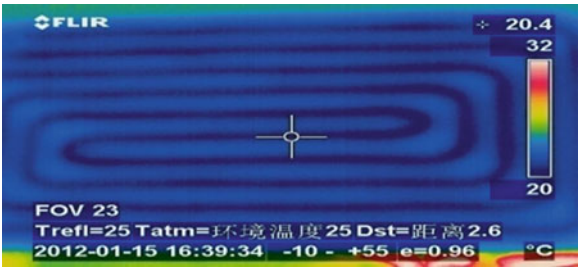

Fig. 32.10 The distribution of temperature for panel2 in summer

The variation of the distribution of temperature in panel2 surface is larger than in panel1 surface. Moreover, temperature in panel2 surface is higher. Thus panel1 has better cooling performance.

32.4 Conclusion

This study compared the cooling performance between two different radiant panels by numerical simulation and experimental test. The results were uniform. When the cooling load is equal, the supply water temperature of panel1 is 5 °C higher than panel2. The panel1 was more sensitive when the room temperature changed, and the temperature distribution for the surface of panel1 was more uniform. Thus panel1 has better cooling performance than panel1.

References

1. Xinghong Zhou (2007) Numerical calculation & preheat time studying of radiant floor heating system. Refrig Air Cond 21(4):90–93
2. Hongfa Di, Yi Jiang et al (2000) Experiment of radiant ceiling. HV AC 30(4):5–8
3. Cho SH, Zaheer-uddin M (2003) Predictive control of intermittently operated radiant floor heating systems. Energy Convers Manage 44(8):1333–1342
4. MacCluer CR (1990) Analysis and simulation of outdoor reset control of radiant slab heating systems. ASHRAE Trans 96(1):1283–1287
5. Tingyao Chen (2002) Application of adaptive predictive control to a floor heating system with a large thermal lag. Energy Build 34(1):45–51
6. Songtao H, Li Z, Gang W (2005) Combined operating of a solar-ground source heat pump and floor radiant system. HV AC 35(3):41–44
7. Lihua Zong (2000) Thermal performance analysis of concrete embedded plastic radiant floor heating. HV AC 30(1):6–8
8. Defu Shi, Wufeng Jin, Hua Chen (2012) Performance study on cold ceiling radiant panel with new capillary tube. Build Sci 28(10):55–58
9. Ximing Z (2001) Heat transfer. China Architecture & Building Press, Beijing, pp 45–56
10. ASHRAE (2008) ASHRAE handbook—HVAC systems and equipment, Atlanta
11. Yaoqing L (2008) Design handbook of practical heating ventilation. China Building Industry Press, Biijing, pp 334–341
12. Lihong Zheng (2011) Numerical simulation and analysis of new metal cold ceiling radiant panel. Refrig Air-Conditioning 11(1):22–25
13. Jianxing C (2009) Numerical simulation and experimental study of temperature field of Cooling system/radiant floor heating. Tianjin University of Commerce, Tianjin
14. EN 14240 (2004) Ventilation for buildings chilled ceilings testing and rating

Chapter 33
Analysis on Influence Factors of Lewis Number in a Crossflow Reversibly Used Cooling Tower by Experimental Investigation

Jiasheng Wu, Yanshun Yu, Lin Cao and Guoqiang Zhang

Abstract Reversibly used cooling towers (RUCT) are used to extract heat from atmospheric to water. In this study, the factors influencing the value of Lewis number in a RUCT are analyzed by experimental investigation. The results show that Lewis number increases with the increase of water−air flow rate ratio. When the water−air flow rate ratio is constant, the Lewis number decreases with the increase of inlet water temperature and inlet air wet-bulb temperature, increases with the increase of inlet air dry-bulb temperature and water sprinkle density. This research offers a fundamental basis for studying heat and mass transfer characteristics in a cross flow reversibly used cooling tower and practical application.

Keywords Reversibly used cooling tower · Heat and mass transfer · Experimental investigation · Lewis number

33.1 Introduction

Cooling tower often acting for heat dissipation harbors unique advantages and application prospects when reversibly used to absorb heat as low-temperature heat source for heat pump [1]. Therefore, a year-round hot water supply in buildings can be made possible without requiring any other backup electric heating equipment [2]. Under winter operating conditions, although the COP was lower than that under summer operating conditions, the system is more economical than

J. Wu (✉) · Y. Yu · L. Cao
School of Energy and Power Engineering, Nanjing University of Science and Technology, Nanjing 210094, China
e-mail: jswu@188.com

G. Zhang
College of Civil Engineering, Hunan University, Changsha 410082, China

A. Li et al. (eds.), *Proceedings of the 8th International Symposium on Heating, Ventilation and Air Conditioning*, Lecture Notes in Electrical Engineering 262,
DOI: 10.1007/978-3-642-39581-9_33,

electric water heating. Another advantage of this system is that only a single system is required to supply hot water and chilled water. This heat pump system coupled with RUCT is most suitable to buildings in tropical or subtropical areas [3].

The theoretical analysis of cooling tower has a long history, which has led to an excessively large number of publications [4–10]. Since there does not exist enough research on this aspect, there are differences in heat and mass transfer between standard cooling tower and reversibly used cooling tower [11–14]. The value assumption of Lewis number equaled to 1 in the analysis of thermal performance of the reversibly used cooling tower is not realistic [15]. The objective of this paper is to consider the effects of inlet air wet and dry-bulb temperature, inlet water temperature, water sprinkle density, and water–air flow rate ratio on the value of Lewis number changes. Considering the lack of research on reversibly used cooling tower under crossflow condition, the performance experiment of heat and mass transfer was conducted for reversibly used cooling tower stuffed with PVC film packing under crossflow condition.

33.2 Method for Evaluation of Lewis Number

33.2.1 Experimental Method

Extensive field experimental work on the heat and mass transfer characteristics of a crossflow RUCT has been carried out. The experimental setup for the study essentially consists of a reversibly used cooling tower, a heat pump, recirculated water pump, and a piping system. A set of instruments were installed to measure parameters required to evaluate the performance characteristics of the RUCT. The tested RUCT was an induced draft crossflow type with the cross-sectional area of 9.9 m^2, filled with 144 pieces of packing with each surface area of 6 m^2. There are many nozzles at the top inside the RUCT to ensure uniform distribution of water and total wetting of the packing. An axial fan was fixed on the top of the tower to extract the air from the tower (Fig. 33.1).

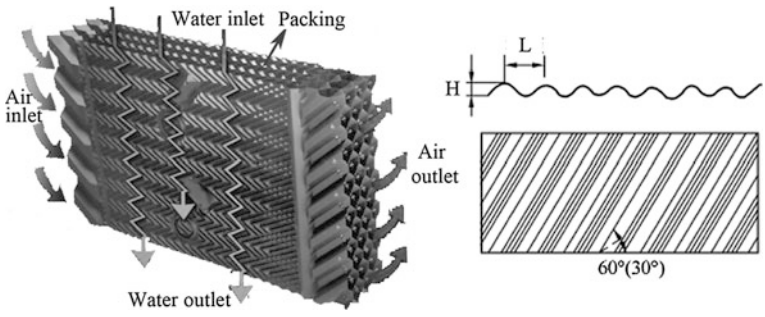

Fig. 33.1 Oblique wave wet packing of the crossflow RUCT

33.2.2 Regression Analysis

In order to get a better regression fit, several different forms of regression equations were tested by adding the parameter one by one. Then multiple regression analysis is utilized to deal with the experimental data, revealing the function equation relating Lewis number with inlet air wet and dry bulb temperature ($T_{a,i}$ and $T_{wb,i}$), inlet water temperature ($T_{w,i}$), water sprinkle density (q), and water−air flow rate ratio (λ).

The general form of the Le equation can be expressed as follows:

$$\mathrm{Le} = \varsigma_1 \cdot T_{a,i}^{\varsigma_2} \cdot T_{wb,i}^{\varsigma_3} \cdot T_{w,i}^{\varsigma_4} \cdot q^{\varsigma_5} \cdot \lambda^{\varsigma_6} \tag{33.1}$$

The Le equation incorporating the 5 parameters developed from the regression analysis are as follows:

$$\mathrm{Le} = 0.6901 \cdot T_{a,i}^{0.7761} \cdot T_{wb,i}^{-0.6545} \cdot T_{w,i}^{-0.0532} \cdot q^{0.2993} \cdot \lambda^{0.0186} \tag{33.2}$$

The final regression equation of Le (33.2) was selected in terms of simplicity and accuracy (Table 33.1).

33.3 Results and Discussion

Figure 33.2 shows the effect of the air inlet dry-bulb temperature at different water−air flow rate ratios. Figure 33.3 is a plot between Le and air inlet wet-bulb temperature, for different values of the mass flow ratio (m_w/m_a). Figure 33.4 shows the effect of the water inlet temperature on Le at different water−air flow rate ratios. Figure 33.5 is a plot between Le and sprinkle density, for different values of mass flow ratio.

Figures 33.2 and 33.3 are generated based on the following input data: P_{atm} = 101.325 kPa, q = 3.3 kg/(m^2·s), $T_{w,i}$ = 7 °C. As shown in Fig. 33.3, when the air inlet wet-bulb temperature is 7 °C, water inlet temperature is 5 °C, and the sprinkle density was 3.3 kg/(m^2 s). It is obvious that Le increases as the air inlet dry-bulb temperature increases at different water−air flow rate ratios. Furthermore, Fig. 33.2 implies that the changes in water−air flow ratio has relatively more effect on Le, which increases as the water−air flow rate ratios at different air

Table 33.1 Five weight linear regression analysis of variance table

	Degree of freedom	Quadratic sum	Mean square	F	p
Regression	5.0000	44.8159	8.9632	887.1399	0.0000
Residual	1298.0000	13.1143	0.0101		
Total	1303.0000	55.9301			

Root MSE = 0.1005, R^2 = 0.7736, Dependent mean = −0.1068, Adjusted R^2 = 0.7727

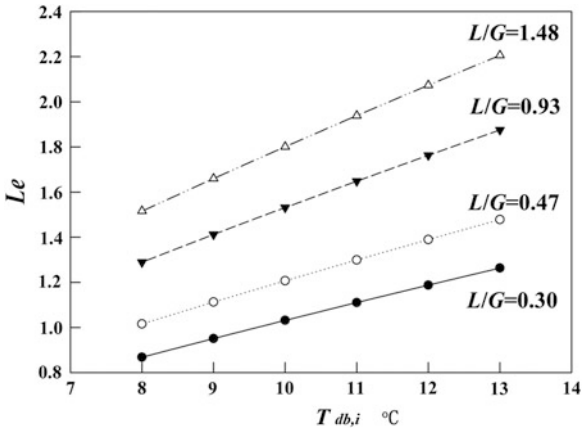

Fig. 33.2 Effect of air inlet dry-bulb temperature on Le at different water–air flow rate ratios

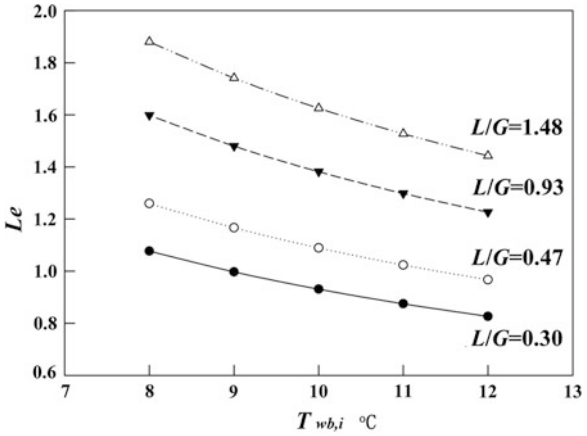

Fig. 33.3 Effect of air inlet wet-bulb temperature on Le at different water–air flow rate ratios

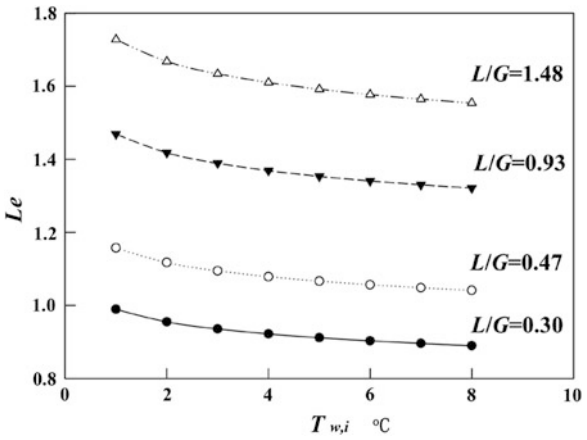

Fig. 33.4 Effect of water inlet temperature on Le at different water–air flow rate ratios

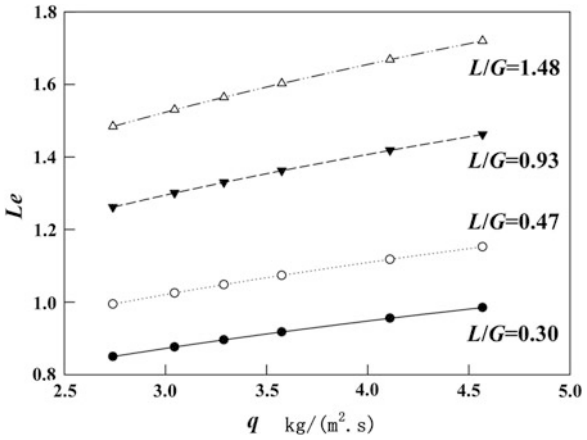

Fig. 33.5 Effect of sprinkle density on Le at different water–air flow rate ratios

inlet dry-bulb temperatures. The variation of air inlet wet-bulb temperature of RUCT is shown in Fig. 33.3 for the above input simulation data. This figure shows that when the air inlet wet-bulb temperature increases from 8 to 12 °C, the Le of RUCT reduces obviously. However, when the air inlet wet-bulb temperature remains unchanged, the Le reduces as the water−air flow ratios.

Figures 33.4 and 33.5 are generated based on the following input data: P_{atm} = 101.325 kPa, $T_{\text{db},i}$ = 12.1 °C, $T_{wb,i}$ = 10.6 °C. As shown in Fig. 33.4, when the water−air flow rate ratio reduces from 1.48 to 0.30, the Le of RUCT also reduces from 1.55−1.73 to 0.88−0.99. However, when the water−air flow rate ratio remains unchanged, the variations of the water inlet temperature have little influence on the Le. On the other hand, in contrast to air inlet dry-bulb and wet-bulb temperatures in Figs. 33.2 and 33.3, the changes in air temperature have relatively more effect on Le compared to changes in the water inlet temperature for the same RUCT. Figure 33.5 offers the opportunity to understand the change of sprinkle density which effects the Le of RUCT. It can be seen that when the RUCT has a low sprinkle density and low water−air flow rate ratio, the Le decreases rapidly.

33.4 Conclusions

In this paper, the multiple regression analysis is used to deal with the experimental data, revealing the function equation relating Lewis number with air inlet dry and wet-bulb temperature, water inlet temperature, water sprinkle density, and water−air flow rate ratio. Besides, the factors influencing the value of Lewis number are analyzed. Based on the existing heat and mass exchange model for RUCT, the calculation deviation due to the assumption that Lewis number is 1 under low temperature condition is dismissed, a further step will be used to improve the model of the crossflow RUCT.

Acknowledgements The research reported herein has been carried out with the help of the National Natural Science Foundation of China (No. 50806034)

References

1. Deng S, Song Z, Tan K (1998) Air-cooled heat pump with desuperheater: retrofit for year-round service hot water supply. Build Serv Eng Res Technol 19(3):129–133
2. Tan KX, Song ZY, Deng SM (1998) Service hot water supply using central air conditioning systems for buildings in subtropics. In: International conference on energy and environment. China Machine Press, Beijing, pp 16−21
3. Tan KX (2000) A study of a desuperheater heat recovery system complete with a reversibly used water cooling tower (RUWCT) for hot water supply, dissertation for the doctoral degree. The Hong Kong polytechnic university department of building services engineering, Hong Kong
4. Milosavljevic N, Heikkilä P (2001) A comprehensive approach to cooling tower design. Appl Therm Eng 21(9):899–915
5. Khan JUR, Yaqub M, Zubair SM (2003) Performance characteristics of counter flow wet cooling towers. Energy Convers Manage 44(13):2073–2091
6. Stabat P, Marchio D (2004) Simplified model for indirect-contact evaporative cooling-tower behaviour. Appl Energy 78(4):433–451
7. Heidarinejad G, Karami M, Delfani S (2009) Numerical simulation of counter-flow wet-cooling towers. Int J Refrig 32(5):996–1002
8. Klimanek A, Bialecki RA (2009) Solution of heat and mass transfer in counterflow wet-cooling tower fills. Int Commun Heat Mass Trans 36(6):547–553
9. Hajidavalloo E, Shakeri R, Mehrabian MA (2010) Thermal performance of cross flow cooling towers in variable wet bulb temperature. Energy Convers Manage 51(6):1298–1303
10. Lemouari M, Boumaza M (2010) Experimental investigation of the performance characteristics of a counterflow wet cooling tower. Int J Therm Sci 49(10):2049–2056
11. Li Y, Chen G, Tang L et al (2011) Analysis on performance of a novel frost-free air-source heat pump system. Build Environ 46(10):2052–2059
12. Tan KX, Deng SM (2002) A method for evaluating the heat and mass transfer characteristics in a reversibly used water cooling tower (RUWCT) for heat recovery. Int J Refrig 25(5):552–561
13. Tan KX, Deng SM (2003) A numerical analysis of heat and mass transfer inside a reversibly used water cooling tower. Build Environ 38(1):91–97
14. Wen X, Liang C, Zhang X (2012) Experimental study on heat transfer coefficient between air and liquid in the cross-flow heat-source tower. Build Environ 57:205–213
15. Zhang Q, Wu J, Zhang G et al (2012) Calculations on performance characteristics of counterflow reversibly used cooling towers. Int J Refrig 35:424–433

Chapter 34
Study on Energy Efficiency Evaluation Method of Cooling Water System of Surface Water Source Heat Pump

Jibo Long and Siyi Huang

Abstract Water source heat pump system is a green air-conditioning system which has high efficiency, energy saving, and environmental protection, but inappropriate design of the system type of water intake will impact on energy efficiency ratio of the system. In order to evaluate the efficiency of heating and cooling source use of water source heat pump system, the impacts of temperature, flow and static head of cooling water on the energy efficiency ratio of water source heat pump system are analyzed in this paper. The cooling load of air condition and parameters of cold water are set as control objectives, and the analytical model of energy efficiency ratio including the energy consumption of cooling water system and cooling water unit is proposed. The running energy efficiency ratios of two types of water source heat pump system are analyzed by using this model (direct heat transfer that surface water flowing into condenser directly, indirect heat transfer through plate heat exchanger). The results show that the impact of change of cooling water temperature on energy efficiency ratio is bigger than the change of static head of cooling water system.

Keywords Surface water · Water source heat pump · Water intake system · Energy efficiency ratio (EER) · Energy-saving evaluation

J. Long (✉) · S. Huang
College of Civil Engineering and Mechanics, Xiangtan University, 411105 Xiangtan, China
e-mail: longjibo2010@126.com

S. Huang
e-mail: 1970904645@qq.com

A. Li et al. (eds.), *Proceedings of the 8th International Symposium on Heating, Ventilation and Air Conditioning*, Lecture Notes in Electrical Engineering 262,
DOI: 10.1007/978-3-642-39581-9_34,

34.1 Introduction

Surface water source heat pump system (SWHPs) is a device for surface water such as river, lake and sea water utilization, which converts those low level heat source into high level with a spot of electrical energy consumed. Surface water has merits of large water volume, large heat capacity, high heat transfer coefficient, high unit efficiency, without recirculation, low investment, and small environment damage when compared with air, soil, underground water, and other heating and cooling source [1, 2]. Currently, water source heat pump system as a technology of sustainable and high efficiency energy use has been used with more and more attention. Heat pump system used river as low level heat source has first successfully applied in Switzerland in the 1930s, and it has been widely used in the United States, Eastern Europe, Japan, and other regions [3–7]. In China, the energy-saving technology of water source heat pump system has made great progress, three main surface water transportation forms such as open system, closed system, and indirect system are developed [8], some energy-saving design and evaluation methods for water source heat pump system are proposed [9, 10]. But, due to the difference of sites and surface water forms, when the same energy-saving technology is applied to different heat pump system, different effect of energy saving will be obtained. Even, the situation that using energy-saving technology to design high energy consumption heat pump system may appear. In this paper, energy consume analysis model for cooling water system that considers the type of water intake, water temperature and heat transfer type is established. And the energy-saving efficiency of each type of water intake system is analyzed. The results can give reference for the design of water source heat pump system.

34.2 Energy Consumption Analysis Model of Cooling Water System

The energy efficiency ratio of the water source heat pump system is closely related to the energy consumption of chilled water system, cooling water systems, refrigeration system, and so on. Therefore, in order to simplify the analysis, in the establishment of the energy consumption model, assuming the chilled water parameters and the energy consumption of building chilled water system are unchanged, and based on this assumption, the analysis is given on the energy consumption of the water system which includes the chiller's cooling water system and the chiller. The main factors that affect the energy efficiency ratio are the two parts energy consumption of refrigeration system and cooling system. The factors that affect the refrigeration system energy consumption are chilled water temperature, cooling water temperature, temperature difference of evaporator heat exchanger, temperature difference of condenser heat exchanger, mechanical efficiency of refrigeration system, and so on. The factors that affect the cooling water

system's energy consumption are cooling water flow, cooling water head, and other equipments energy consumption such as cooling towers.

The energy consumption of cooling water transportation of water source heat pump system is the important factor that affects the economy and energy efficiency ratio. And the cooling water flow and pump head have great impact on the energy consumption. In order to simplify analysis, water loss in the operation phase is not considered. Thus, the cooling water flow G_c (m^3/h), pump head H_c (m), and power W_c (KW), respectively, can be expressed by

$$G_c = 3600 \cdot \frac{Q_e + W_e}{\rho c \cdot \Delta t} \tag{34.1}$$

$$H_c = H_0 + S\left(\frac{G_c}{3600}\right)^2 \tag{34.2}$$

$$W_c = \frac{gG_cH_c}{3600} = \frac{(Q_e + W_e)gH_c}{\rho c \Delta t} \tag{34.3}$$

The energy consumption of the cooling water system is

$$\sum W_c = \sum \frac{(Q_e + W_e)gH_c}{\rho c \Delta t} + W' \tag{34.4}$$

where Q_e is the cooling capacity (KW), W_e is the power of cooling water unit (KW), W_c is the power consumption of cooling water pump (KW), W' is the other energy consumption of the cooling water system, Δt is the temperature difference between supply water and return water of cooling water (°C), η is pump efficiency, G_c is the cooling water flow (m^3/h), H_c is the cooling water static head (m), H_0 is the static pump head of cooling water (m), S is the resistance coefficient (S/m^5).

The resistance coefficient of pipeline can be expressed by

$$S = \frac{8\rho\left(\lambda \frac{l}{d} + \sum \zeta\right)}{\pi^2 d^4} \tag{34.5}$$

For reverse Carnot cycle refrigeration, the theoretical refrigeration coefficient and the actual cooling coefficient were

$$\mathrm{COP}_{l,e} = \frac{T_e}{T_c - T_e} \tag{34.6}$$

$$\mathrm{COP} = \frac{Q_e}{W_e} \tag{34.7}$$

where $\mathrm{COP}_{l,e}$ is the theory refrigeration coefficient of refrigerator, COP is the actual refrigeration coefficient of refrigerator, T_e is the chilled water temperature (°C), T_c is the cooling water temperature (°C).

Actually, the actual refrigeration efficiency is less than the theoretical value of refrigerator. Set there is a function $f(\Delta t)$ which is associated with the factors such

as the difference in temperature of the evaporator heat exchanger, the difference in temperature of the condenser heat exchanger, the mechanical efficiency of the refrigeration system, and so on. Then, according to Eqs. (34.6) and (34.7), the following formula can be obtained

$$Q_e = f(\Delta t) \cdot \frac{T_e}{T_c - T_e} \cdot W_e \tag{34.8}$$

According to the definition of energy efficiency ratio of the air-conditioning system, it can be obtained that the energy efficiency ratio of chiller and the cooling water system of air conditioning system is the ratio of the system cooling capacity and the power consumption of chillers and cooling water system, it can be expressed as

$$\mathrm{EER}_L = \frac{Q_e}{W_e + \sum W_c} \tag{34.9}$$

The Eqs. (34.4) and (34.5) substituted into the above equation and can be rearranged into

$$\mathrm{EER}_L = \frac{f(\Delta t) \cdot \frac{T_e}{T_c - T_e} \cdot W_e}{W_e + \sum \frac{\left(f(\Delta t) \cdot \frac{T_e}{T_c - T_e} + 1\right) g H_c}{\rho c \Delta t} W_e + W'} \tag{34.10}$$

About water source heat pump system, the pumps energy consumption is the major energy consumption of cooling water system, if the other energy consumption W' is not considered, the above formula can be changed to

$$\mathrm{EER}_L = \frac{f(\Delta t, \eta) \cdot \rho c \Delta t \cdot T_e}{\rho c \Delta t \cdot (T_c - T_e) + \sum (f(\Delta t, \eta) \cdot T_e + (T_c - T_e)) g H_c} \tag{34.11}$$

According to the same method, it can be obtained that the energy efficiency ratio of chiller and cooling water system of air conditioning system under heating conditions is

$$\mathrm{EER}_R = \frac{f(\Delta t, \eta) \cdot \rho c \Delta t \cdot T_c}{\rho c \cdot (T_c - T_e) + \sum (f(\Delta t, \eta) \cdot T_c + (T_c - T_e)) g H_c} \tag{34.12}$$

As shown in Eqs. (34.11) and (34.12), when the parameters of cooling capacity and chilled water is invariant, the energy efficiency ratio of chiller and cooling water system of air-conditioning system is related with the COP of water chilling unit, cooling capacity, chilled water temperature, cooling water temperature, temperature difference between supply and return water of the cooling water, cooling water flow rate, pump static head of cooling water, the resistance coefficient of pipeline, and the other power of water chilling unit.

34.3 Calculation and Analysis

Taking Xiangtan, located in the east of Hunan province, China, as an example. The water temperature of Xiangjiang River in Xiangtan region changes between 6.8 and 32.5 °C in a year. In an air-conditioning system, screw chiller is selected; the cooling capacity is 420 KW and the power is 84 KW. The supply and return water temperature of chiller water are 7/12 °C, the average is 9.5 °C. The temperature difference between supply and return water of cooling water is 5 °C. And option 1 (cooling tower), option 2 (surface water directly into chiller water unit), and option 3 (surface water with plate heat exchanger) are considered in the paper. The parameters of water resistance in the condition of design velocity are shown in Table 34.1.

According to Eq. (34.10), the EER_L of option 1 is 4.73 in the design condition. If cooling water temperature is invariant in the three options, the relationships of EER_L and static head are shown in Fig. 34.1.

As shown in Fig. 34.1, when cooling water of the three options has the same temperature and the project is in the design conditions, the EER_L of option 1 is 4.73. The EER_L of option 2 decreases from 4.78 to 4.61 when the static head increases from 0 to 14 m, the EER_L is reduced by 3.6 %. The EER_L of option 3 decreases from 4.58 to 4.42, the EER_L is reduced by 3.5 %. And when the static head equal to 4 m, the EER_L of option 2 is equal to option 1. If static head is less than 4 m, the EER_L of option 2 is greater than option 1. If static head is more than 4 m, the EER_L of option 2 is less than option 1. While, no matter the static head how to change, the EER_L of option 3 is less than option 1. And the EER_L of option 2 is larger 4.4 % than option 3 in the condition of static head is the same.

It can be seen from Figs. 34.2 and 34.3, the EER_L of cooling water system is increased resulting from cooling water temperature decreases. When cooling water temperature decreases from 32.5 to 18.5°C, the EER_L of option 2 is increased by 31 %, 31 %, 30 %, 30 %, and the EER_L of option 3 is increased by 29 %, 29 %, 28 %, 28 %, in the four kinds of static head conditions, respectively.

In the study, it is indicated that the pump head of cooling water system is mainly influenced by cooling water flow rate, static head, and resistance coefficient of pipe line. And the COP of water chiller is impacted by cooling water

Table 34.1 The water resistance and other parameters of cooling water system

	Option 1	Option 2	Option 3	
Cooling water unit (m)	8	8	8	–
Filter of surface water (m)	–	2	–	2
Pipe line and accessories (m)	4	8	4	4
Static head of cooling water (m)	5	h	–	h
Cooling tower water pressure (m)	3	–	–	–
Plate heat exchanger (m)	–	–	10	10
Cooling water temperature (°C)	30/35	5	5	5
Cooling water flow rate (m^3/h)	87	87	87	87

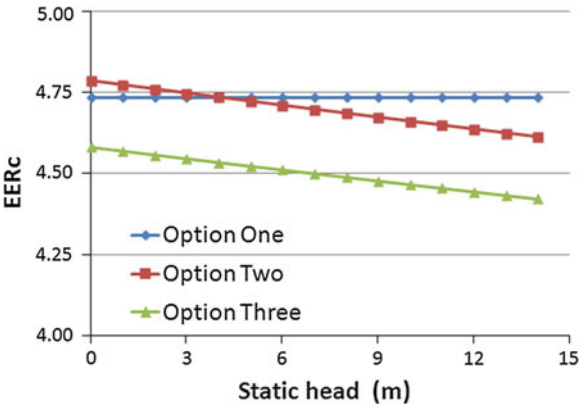

Fig. 34.1 The EER_L of three options in the condition of cooling water temperature is invariant

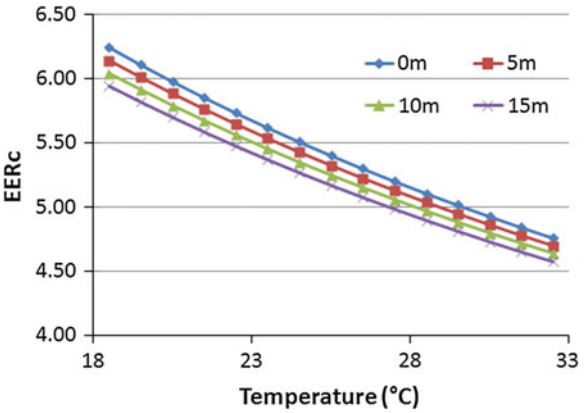

Fig. 34.2 The EER_L of option 2 when cooling water temperature is variable

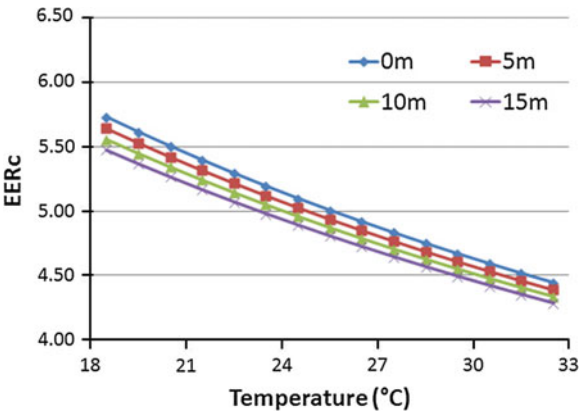

Fig. 34.3 The EER_L of option 3 when cooling water temperature is variable

temperature. From the analysis results, it can be seen that the change of cooling water temperature has a great influence on energy efficiency ratio. When surface water temperature and cooling water temperature of cooling tower without big difference, water source heat pump system has no advantage compared with cooling water system used cooling tower, even the energy consumption of surface water system is higher. Only when the surface water temperature is relatively low, water source heat pump system has advantages of energy saving. And, because of the influence of local resistance of plate heat exchanger, the EER_L of cooling water system used plate heat exchanger is less than the system that surface water directly into chiller water unit. When the static head of cooling water system is higher, the system used plate heat exchanger can eliminate the influence of static head.

34.4 Conclusion

Water source heat pump system is applied to reduce air-conditioning energy consumption and enhance energy efficiency ratio in operation. In the paper, the impact of cooling water temperature, flow rate, static head, and resistance coefficient of pipeline on energy consumption of cooling water system is analyzed. And the energy efficiency model of cooling water system including water chiller unit is established. The main conclusions may be listed as follows:

(1) The change of cooling water temperature has a great influence on energy efficiency ratio, it is a important factor for water source heat pump system energy saving.
(2) The EER_L of cooling water system used cooling tower is greater than cooling water system used surface water, when cooling water temperature is the same.
(3) If the static head is the same, the EER_L of cooling water system used plate heat exchanger is less than the system that surface water directly into chiller water unit. For the higher static head system, the cooling water system used plate heat exchanger can eliminate the influence of static head on energy efficiency ratio.

Acknowledgments This study is supported by the Science and Technology Department of Hunan Province, China (2012SK3164).

References

1. Zhang PF (2003) Overview of the development of the water source heat pump at home and abroad (in Chinese). Gen Mach 2(5):13–16
2. Liu GY, Chen XH (2001) Brief introduction of russian heat pump technology (in Chinese). Energy Res Utilization 13(3):17–19
3. Nam YJ, Ooka R (2010) Numerical simulation of ground heat and water transfer for groundwater heat pump system based on real-scale experiment. Energy Build 42:69–75

4. Lohani SP, Schmidt D (2010) Comparison of energy and exergy analysis of fossil plant, ground and air source heat pump building heating system. Renew Energy 35:1275–1282
5. Nuntaphan A, Chansena C, Kiatsiriroat T (2009) Performance analysis of solar water heater combined with heat pump using refrigerant mixture. Appl Energy 86:748–756
6. Aristov YI, Dawoud B, Glaznev IS et al (2008) A new methodology of studying the dynamics of water sorption/desorption under real operating conditions of adsorption heat pumps: Experiment. Int J Heat Mass Transf 51:4966–4972
7. Urchueguía JF, Zacarés M, Corberán JM et al (2008) Comparison between the energy performance of a ground coupled water to water heat pump system and an air to water heat pump system for heating and cooling in typical conditions of the European Mediterranean coast. Energy Convers Manage 49:2917–2923
8. Qian JF, Sun DX, Zhang CH et al. (2007) Analysis of new surface water heat pump and correlative technology. J Harbin Univ Commer (Nat Sci Ed) (in Chinese) 23(2):231–234
9. Hu PF, Li FR, Sun QM et al. (2009) Thermodynamic analysis of the economy of GSHP systems. J Huazhong Univ Sci Tech (Nat Sci Ed) 37(4):97–100
10. Bai XL, Zhang YJ, Wang HH (2010) Energy efficiency of water transportation system for surface water source heat pump. J Civ Architect Environ Eng 32(6):86–91

Chapter 35
Experimental Measurement of Airflow Turbulence Characteristics in a Full-Size Aircraft Cabin

Chen Shen, Junjie Liu, Wei Wang and Nan Jiang

Abstract This study applied experimental methods to gather airflow turbulence information by different anemometers in a full-size MD-82 aircraft cabin, including turbulence energy spectrum densities (TESD) at the sidewall diffusers and time-average flow fields. The results indicated that the large range of TESD of airflow must be measured by high-frequency equipments, such as hot-wire anemometers (HWA), at 50 kHz, and for flow fields, three-dimensional ultrasonic anemometers (UA) were needed to obtain accurate velocity magnitudes and turbulence intensities (TI) at the cross section of one row in the cabin. This investigation verified that TI had a reciprocal relationship with mean velocity and calculated the regression equations.

Keywords Aircraft cabin · Airflow field · Turbulence energy spectrum density (TESD) · Turbulence intensity (TI) · Inertial subrange

35.1 Introduction

Nowadays, a healthier and safer cabin environment has become, more than ever before, a prominent demand of the passengers. Experiments and computational fluid dynamics (CFD) were widely used to investigate cabin air distributions [1].

C. Shen · J. Liu (✉)
School of Environmental Science and Engineering, Tianjin University, 300072 Tianjin, China
e-mail: jjliu@tju.edu.cn

W. Wang · N. Jiang
School of Mechanical Engineering, Tianjin University, 300072 Tianjin, China

W. Wang · N. Jiang
Tianjin Key Laboratory of Modern Engineering Mechanics, 300072 Tianjin, China

A. Li et al. (eds.), *Proceedings of the 8th International Symposium on Heating, Ventilation and Air Conditioning*, Lecture Notes in Electrical Engineering 262,
DOI: 10.1007/978-3-642-39581-9_35,

Turbulence energy spectrum density (TESD) curves have to be measured by high-frequency equipments which can obtain the dissipation of airflow energy within eddies of different scales in an airliner cabin [2]. Large eddy simulation (LES) model needs to confirm the levels of grid resolutions and time steps, however, both of them also have to be determined by turbulence energy spectrum. So it is crucial to obtain the accurate TESD by applicable instruments for studying cabin air turbulence characters.

Liu et al. [1] reviewed the previous experimental studies and summarized three available instrumentations which include hot-wire anemometer (HWA) and hot-sphere anemometer (HSA) [3], ultrasonic anemometer (UA) [3], and optical anemometer (OA) [4]. HWA and HSA cannot measure the airflow direction normally. Despite the deficiencies, HWA is still the most widely used instrument in measuring the velocity fluctuations for its higher measuring frequency compared with other anemometers. Liu et al. [3] proved that UAs can give accurate time average information on velocity and direction at the point-by-point measurement. Because the laser beam will be reflected by the occupancy and seats, OAs cannot give the whole field information.

This investigation carried out experiments on velocity measurement of the sidewall diffusers and flow field which includes the case of empty cabin (EC) and in the case of cabin occupied with heated manikins (COHM) in the economy-class cabin of a full-size MD-82 aircraft. The objective of this study was to analyze the relationship between mean velocity and TI and give the law of TESD of cabin airflow.

35.2 Experimental Setup

The MD-82 airplane is placed in outdoor environment. The geometry model is shown in Fig. 35.1 [5]. The dimensions of the economy class cabin at the floor level are 27.79 m (L) × 2.91 m (W) × 2.04 m (H). The cabin contains 32 rows of seats. Row 11 was set as the measuring area.

Figure 35.2 shows the diffuser on each sidewall as the velocity inlet. The outlets were also located on the sidewalls near the floor. Each diffuser has 280 slots (22 mm (L) × 3 mm (W)) being arranged into two rows equally. The airflow of the cabin was supplied by a ground air-conditioning cart (GAC). The flow rates

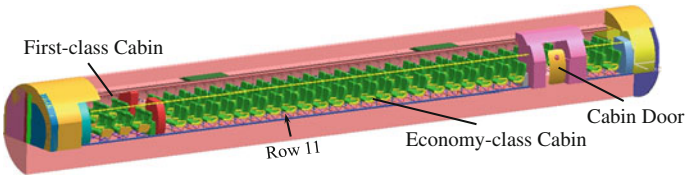

Fig. 35.1 Profile of the inner cabin of the MD-82 aircraft [5]

Fig. 35.2 One sidewall diffuser

were 3160 ± 53 m^3/h which equal to 26 air changes per hour (ACH) in the economy-class cabin. The supply air temperature was controlled at 19.5 ± 0.4 °C for EC and 18.3 ± 0.2 °C for COHM. The airplane was covered with the insulation which has a thermal resistance of 0.857 (m^2 K)/W to avoid the effect of solar radiation. The temperature difference between two test days was controlled in ±1 °C. For COHM, 35 manikins were placed in the seats from row 7 to row 13. Figure 35.3a is the profile of heated manikin and b shows the temperature distributions of manikins which was shot by an infrared camera. The surface of manikin was covered with resistance wires heated by 380 V AC power supply. The sensible heat production from one manikin is 75 W. Note that this manikin cannot simulate human latent heat.

This study utilized an IFA 300 HWA to measure the velocity inlet to investigate TESD (Fig. 35.4a). Figure 35.4b shows the setup of HWA [2]. The sampling frequency of this equipment was set at 50 kHz and its measuring range is 0–300 m/s. Seven sets of DA-650 UA were to collect time-average airflow magnitude, direction, and TI in the cabin. The measurement range of UA is 0–10 m/s with a measuring resolution of 0.005 m/s. The measuring frequency is 20 Hz.

During the experimental period, the GAC supplied airflow for 3 h in advance to ensure thermal boundary conditions were stable. The monofilament wire probe of HWA was fixed in the flow field. Before the experiment, the wire probe was calibrated in a wind tunnel. One slot of the right sidewall diffuser was measured and Fig. 35.5 shows the locations of measuring points. The wire probe was placed perpendicular to the sidewall and aimed at the center of slot. There were four points set along the perpendicular direction of diffusers and located respectively at the distance of 3, 8, 13, and 20 mm from a diffuser. Other two points were set along the diffuser. The distance between point A and diffuser are 3 mm in Fig. 35.5, as well as point B and C. The measurement took nearly 84 s and the amount of data was 41,94304.

Figure 35.6 shows the setup of the three-dimensional UAs. On the basis of the research by Liu et al. [3], our study set the stabilizing and measurement time as 8 and 4 min, respectively. As shown in Fig. 35.7a and b, the location of measuring

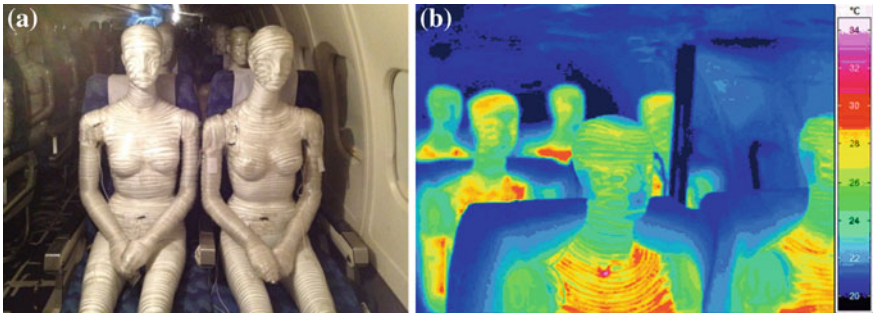

Fig. 35.3 **a** Profile of heated manikin and **b** Infrared photo of heated manikin

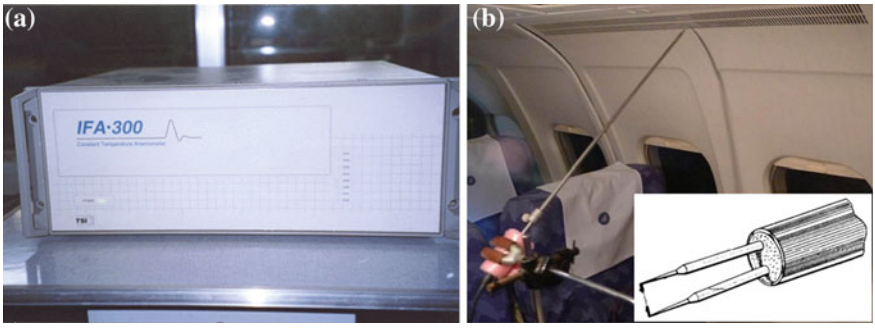

Fig. 35.4 **a** IFA300 hot wire anemometer and **b** Monofilament wire probe and setup of the probe in the cabin[2]

Fig. 35.5 Location of measuring points near the diffuser

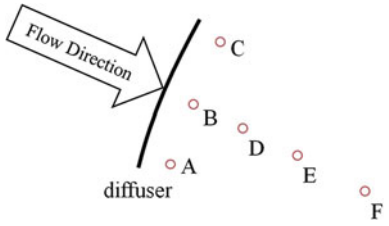

points were represented by the intersections of red lines and its measuring resolution was 0.1 m × 0.1 m. There were 341 points for EC case and 223 points for COHM case. Seven UAs were fixed on two support sticks to measure the cross section of row 11 (CS11) and then moved manually to cover all the measuring points.

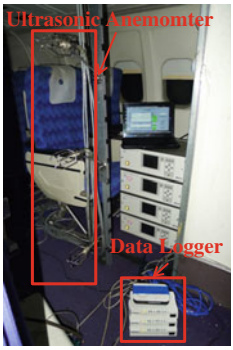

Fig. 35.6 Setup of the UAs

35.3 Results

35.3.1 Air Velocity from the Diffusers

The measuring data of HWA indicated that the average velocity had the linear attenuation and TI had an exponential growth along the direction of the jet flow, as shown respectively in Fig. 35.8a and b. The measured results show that the mean velocities of point A, B, and C labeled in Fig. 35.5 were almost the same, so Fig. 35.8 only shows the result of point B.

Compared with point B, air velocity magnitude of point F was attenuated merely to 32 % as shown in Fig. 35.8a. Figure 35.8a also shows the increase of TI along the flow direction which indicated that an increasing momentum was transferred from jet flow to ambient quasi-stationary turbulence airflow. The integral of frequency f and TESD represents $E(f)$ equal the average value of the square of fluctuation velocity (v'). The function can be derived as Eq. 35.1:

$$\int_0^\infty E(f)df = \overline{v'^2} \tag{35.1}$$

where

$$f = \frac{n}{N \cdot \Delta t} \tag{35.2}$$

Δt is the interval time of discrete sampling of HWA and its value is 0.00002 s

Analyzing $E(f)$ of point D, E, and F which are labeled in Fig. 35.8b, it revealed clearly that $E(f)$ had reduced obviously with an increased distance between the diffuser and the measuring points. Simultaneously, different measuring points had similar trend of TESD distribution and the fully-developed turbulence existed in very small scale eddies (i.e., turbulence energy dissipated completely at the frequency of 1,000 Hz or more). Note that Fig. 35.8b has dual-logarithmic coordinates.

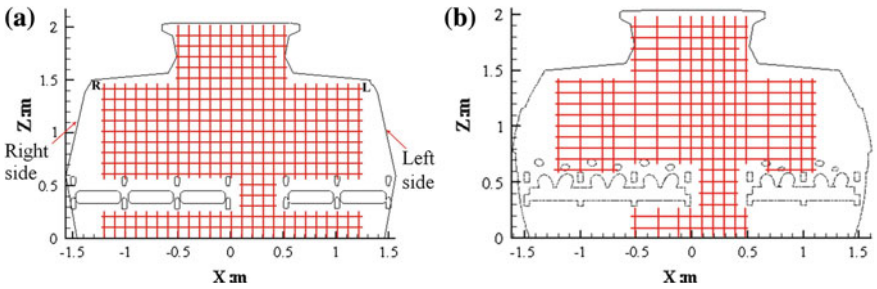

Fig. 35.7 Measuring resolutions of cases: **a** EC and **b** COHM of row 11 in the cabin

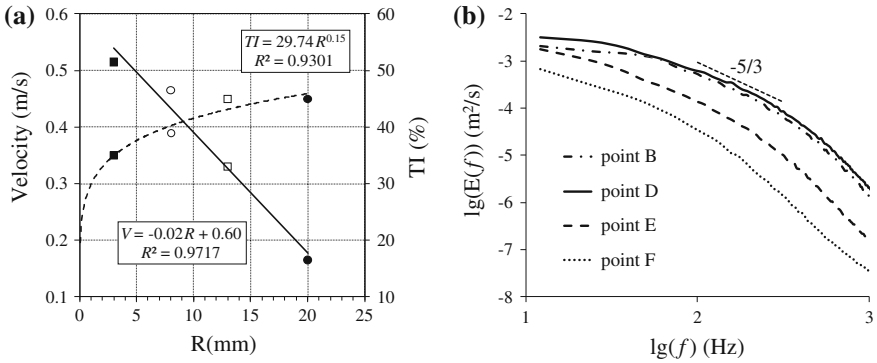

Fig. 35.8 Measured air characters along the flow direction of the diffuser: **a** Mean velocity and TI (solid square, hollow circle, hollow square, and solid circle stands for point B, D, E, and F, respectively) and **b** TESD

The inertial subrange focused at a frequency larger than 100 Hz which means β representing the slope of TESD curves was close to –5/3 (i.e., Kolmogorov hypothesis of local isotropic turbulence).

The frequency of inertial subrange implies that the time step of LES should be confined to less than 0.01 s (1/100 Hz) at this diffuser. But it should also be found that, with *E(f)* decaying, the inertial subrange moved to a smaller frequency region. This trend indicated that with TI growing, air turbulence energy dissipated faster and β value decreased more.

35.3.2 Airflow Field

Figure 35.9a and b illustrate that nearly 100 % of the measuring points were located at the upper area of seats where the velocities were lower than 0.2 m/s and 91 % of the points had a TI lower than 70 %. In fact, the air with medium TI

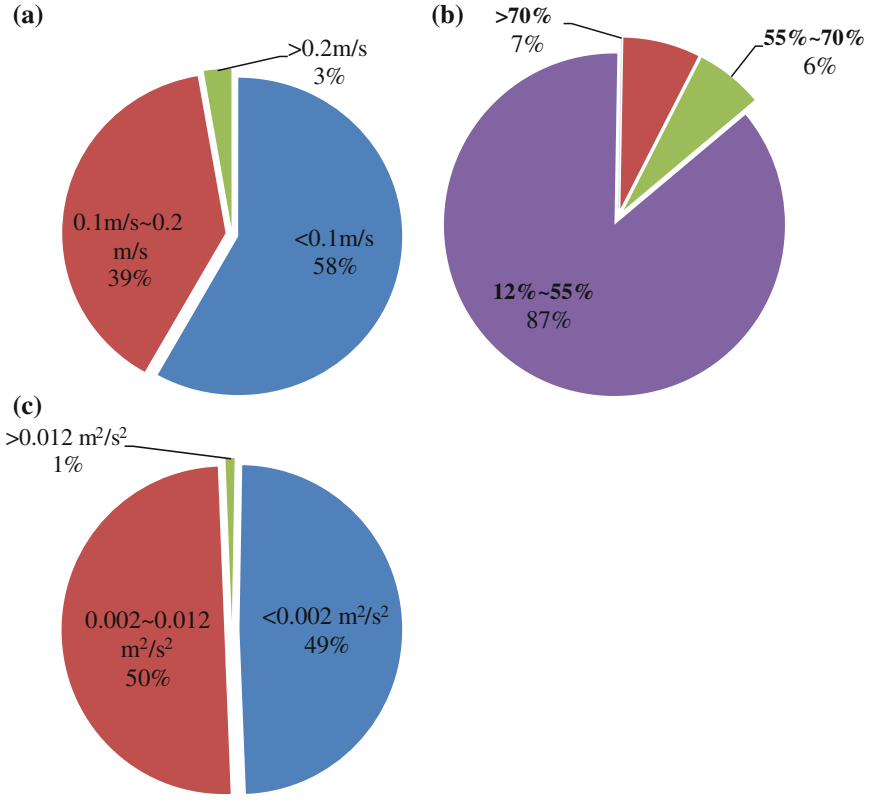

Fig. 35.9 Measured turbulence characters at the upper part of seats in CS11 (above the floor within 0.6–1.5 m) of cases of COHM: **a** Velocity magnitude distribution, **b** TI distribution, and **c** TKE distribution

(12–55 %, i.e., Fanger et al. [6]) accounted for 83 %. This consequence was different from that of the first-class cabin [3] which has only 57 % at three cross sections. Figure 35.9c indicates that the level of TKE is focused on 0–0.002 m^2. ASHRAE standard [7] requires the air velocity around the bare surface of human body encounters to be lower than 0.3 m/s. Besides, Griefahn et al. [8] discovered that, even when the ambient air velocity was lower than 0.1 m/s, if the air TI was higher than 70 %, 1/4 of the passengers would feel discomfort. Obviously, the cabin airflow satisfies these requirements.

Figure 35.10 displays the relation between mean air velocity and TI for corresponding measuring points. Statistical results show that TI has a significant reciprocal relationship with mean velocity. According to the law summarized by Fanger et al. [6], this investigation summarized the regression equations as follows:

$$TI = 0.018/\overline{v} + 0.136;\ R^2 = 0.775 \tag{35.3}$$

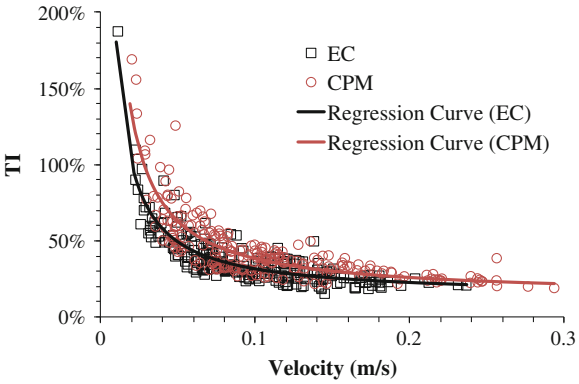

Fig. 35.10 Relationship between TI and velocities of measuring points in CS11

$$TI = 0.025/\bar{v} + 0.134;\ R^2 = 0.87 \tag{35.4}$$

Formulas 35.3 and 35.4 represented, respectively, the regression equations of the case of EC and COHM, and the correlation coefficients were listed after the formulas. The factors in the formulas were different from that of Fanger et al. [6]. It can be seen from the formulas that on one hand, heated manikins made the slope of the regression line larger than that of EC; on the other hand, in the case of EC, there was a higher TI in the field of low speed compared with other fields.

35.4 Conclusion

The measurement results showed that the inertial subrange of inlet air was focused in the frequency larger than 100 Hz. The accurate and high-resolution time-average turbulence information including velocity magnitude and TI were obtained by UAs. In the case of COHM, almost all the air velocities at the upper part of seats were lower than 0.2 m/s and 87 % of the measuring points had a medium TI in the range of 12–55 %. Experiments validated that TI had a reciprocal relationship with mean velocity and the regression equations were summarized.

Acknowledgments The research presented in this paper was financially supported by the National basic research program of China (The 973 Program) through grant No. 2012CB720100.

References

1. Liu W, Mazumdar S, Zhang Z, Poussou SB, Liu J, Lin C-H, Chen Q (2012) State-of-the-art methods for studying air distributions in commercial airliner cabins. Build Environ 47:5–12
2. Wang W, Jiang N, Cao X et al (2012) HWA measurement and analysis of MD82 aircraft cabin environment flow field. J Tianjin University (Sci and Technol) 41:89–91

3. Liu W, Wen J, Chao J et al (2012) Accurate and high-resolution boundary conditions and flow fields in the first-class cabin of an MD-82 commercial airliner. Atmos Environ 56:33–44
4. Lin C-H, Wu T, Horstman R et al (2006) Comparison of large eddy simulation predictions with particle image velocimetry data for the airflow in a generic cabin model. HVAC&R Res 12:935–951
5. Chao J, Mu X, Liu W et al (2011) Rapid construction of a three-dimensional digital geometric model of an airliner cabin for CFD simulations. In: Proceedings of the 12th international conference on air distribution in rooms, ROOMVENT 2011, Trondheim, Norway
6. Fanger P, Melikov A, Hanzawa H (1988) Air turbulence and sensation of draught. Energy and Buildings 12:21–39
7. American Society of Heating, Refrigerating and Air-Conditioning Engineers (2007) ASHRAE Standard 161–2007. Air Quality within Commercial Aircraft
8. Griefahn B, Künemund C, Gehring U (2000) The significance of air velocity and turbulence intensity for responses to horizontal drafts in a constant air temperature of 23 °C. Int J Ind Ergon 26:639–649

Chapter 36
Measurement and Control System of HVAC&R Integration Testing Platform

Kai Zhang, Xiaosong Zhang, Shuhong Li and Geng Wang

Abstract To control the products quality and ensure the benign development of HVAC&R industry, it is of great importance to test and measure the quality of HVAC&R products. Due to the reality of diversification of HVAC&R products, unifunctional platform cannot meet the needs of test. In this paper, a multifunctional testing platform was founded, which can complete various performance tests of different kinds of HVAC&R products. Based on this multifunctional testing platform, a measurement and control system were designed. The software of this system was developed with VB, and different kinds of communication protocol were used to achieve the connection between the computer and instruments of data acquisition and control. Several key points such as data acquisition, data storage, and real-time curve were described in this paper. A period of use shows that, the multifunctional testing platform can achieve the various performance tests of various different kinds of HVAC&R products with good reliability, stability, and precision. Also, it indicates that the structure and functions of this system were suitable.

Keywords HVAC&R · Testing platform · Measurement and control system

36.1 Introduction

With the increasing use of refrigerators and air-conditioning products, quantities as well as categories of products, and the number of producers rise greatly [1, 2]. To control the products quality, energy consumption and ensure the benign

K. Zhang (✉) · X. Zhang · S. Li · G. Wang
School of Energy and Environment, Southeast University, 2# Sipailou, Nanjing 210096, China
e-mail: kai.zhang.ch@gmail.com

A. Li et al. (eds.), *Proceedings of the 8th International Symposium on Heating, Ventilation and Air Conditioning*, Lecture Notes in Electrical Engineering 262,
DOI: 10.1007/978-3-642-39581-9_36,

development of HVAC&R industry, it is of great importance to test and measure the quality of HVAC&R products.

Testing platform provides testing condition for products that can be of different types and categories [3–7]. However, present unifunctional platform that only allow single kind of test cannot meet the needs of diversified products, a multifunctional performance testing platform, which can accomplish various performance tests at wider working conditioning range of refrigerators and air-conditioning products, can be an economic and advisable choice.

Besides offering specific operating condition for a HVAC&R product, the functions for control system to realize real time monitoring, measure the process parameters, record, chart, and analyze the performance parameters are required [8, 9]. The complexity of control system increases with the testing platform functions. Basically, more instruments of control and acquisition are employed in the measurement and control system. Moreover, these instruments always work under different conditions and in the different communication protocol. Therefore, solutions of communication in this system are absolutely critical.

In this paper, through sharing hardware resources, a multifunctional testing platform, which can complete various performance tests of different kinds of HVAC&R products, such as room air-conditioners, fan-coil units, central-station air handing units, water chilling/heating pump units, are found. Based on this multifunctional testing platform, a measurement and control system is designed. This system cannot only conduct real time monitoring of testing parameters, automatic recording, charting and analysis functions, but also carry out many other operations, including starting and stopping the equipments, alarming and fault diagnosis, etc. In this system, different kinds of communication protocol were used to achieve the connection between the computer and instruments of data acquisition and control. The software system of this measurement and control system was developed with Visual Basic. Several key points, such as data acquisition, data storage, real-time curve, report forms printing, were achieved in this system.

36.2 Design of the Multifunction Testing Platform

The testing platform was constructed based on the methods of enthalpy and flow temperature difference. Most of performances required in national standards both of air chilling and water chilling packages, such as cooling/heating capacity, cooling/heating power input, indoor discharge airflow, energy efficiency ratio, etc., can be tested with this testing platform. The testing range was shown in Table 36.1.

Indoor and outdoor temperatures, listed in Table 36.1, were provided by the indoor and outdoor AHU. Two test bodies were set to ensure the precision and save initial investment for the wide testing range of this testing platform. The small and the big test bodies shared a room, and which of them used for the test was determined by the airflow rate. The airflow rate of small test body was

Table 36.1 The testing range of this testing platform

Cooling/heating capacity (kW)	Airflow rate (m^3/h)	Water flow rate (m^3/h)	Indoor air temperature[a] (°C)	Outdoor air temperature[a] (°C)
2–80	250–12000	0.5–17	Dry bulb: 2–35 wet bulb: 2–32	Dry bulb: −15–52 wet bulb: −16–34

[a] The design temperature of the indoor and outdoor simulation environment

250–2200 m^3/h, and that of the big one was 2000–12000 m^3/h. The top view of the schematic diagram was shown in Fig. 36.1.

The water system in Fig. 36.1 is shown in detail in Fig. 36.2, mainly composed of condensing unit, cooling water system, and chilled water system. The condensing unit ensures the cooling environment in both indoor side and outdoor side. The cooling water of condensing unit, chilled packages and using for testing are supplied by cooling system. The chilled water is supplied by a chilled package.

A surface cooler and a plate exchanger are used in the water system for heat/cold recovery. The surface cooler is set in the outdoor side. By switching the valves, the flowrate of chilled water in the coil of surface cooler can be changed. Due to the difference in temperature between the water in the coil and outdoor side, heat/cold recovery can be achieved. And with the changes of flow, the performance of the chilled package in the testing platform is improved. Similar to the surface cooler, heat/cold recovery performing in the plate exchanger can also improve the performance of chilled package. But what is different was the plate exchanger was not in the outdoor side, and the heat/cold exchange occurred between water.

The two methods of heat/cold recovery used in this system save the investment and energy but also enhance system stability.

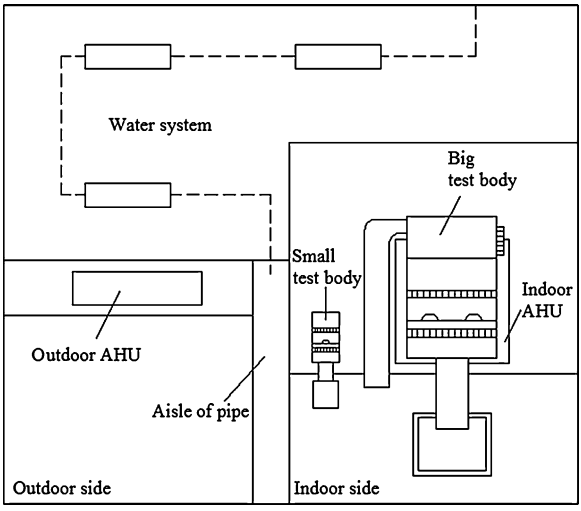

Fig. 36.1 The top view of the schematic diagram of testing platform

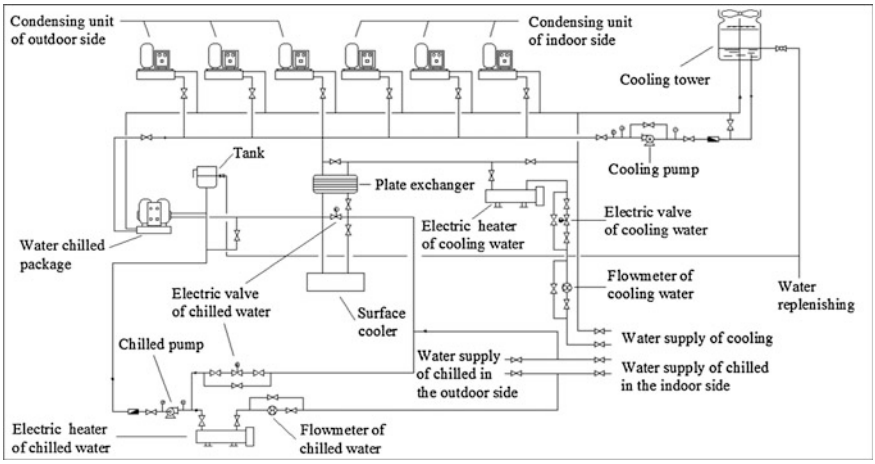

Fig. 36.2 The schematic diagram of water system in testing platform

36.3 Structure of the Measurement and Control System

36.3.1 Hardware Structure

The hardware structure of this measurement and control system is shown in Fig. 36.3.

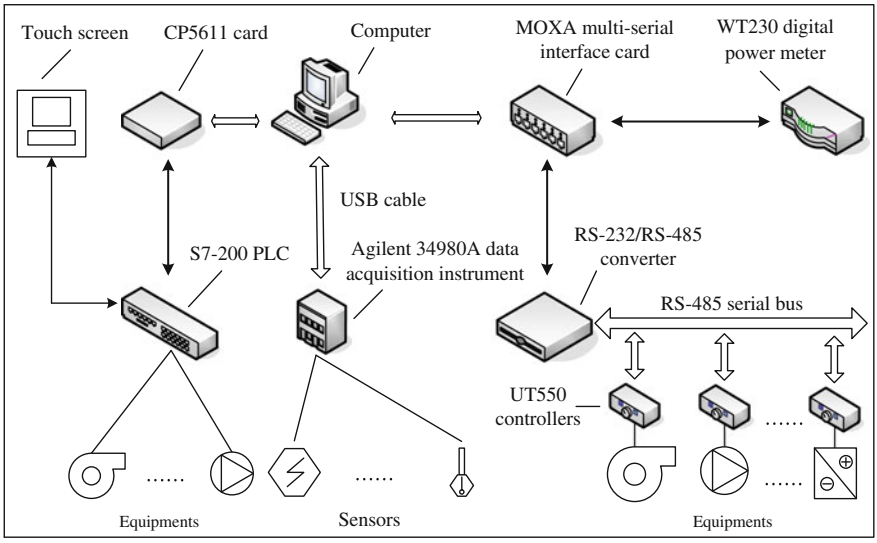

Fig. 36.3 The structure of hardware system

This structure consists of five parts. The methods of connection between instruments and computer as well as the functions are as follow.

The touch screen which is connected to the PLC via RS-232, utilizes the PLC to control the start and stop to the equipments.

A CP5611 card is installed in the computer, and connected to the PLC via MPI cable so that functions of start and stop can be achieved on computer.

The data acquisition instrument is connected to the computer via USB cable, by which the testing data collected by data acquisition instrument can be sent to the computer.

For more serial ports, a multi-serial interface card is installed in the computer.

Controllers and power meter can be connected to the computer by using the multi-serial interface card. Controllers are employed to control the airflow rate, temperature, humidity, and the switch proportion of valves so that indoor air parameters achieve the requirement of national standards. Power meter is used to measure the power parameters of the HVAC&R products.

36.3.2 Software System

Visual Basic is an advanced programming language running in Windows platform, which is fit for exploiting visual window application program. The software of this system is developed with Visual Basic 6.0. The software system is composed of five modules, and the structure of the software system is shown in Fig. 36.4.

The system control module includes three functions. The remote control function is used to start and stop the equipments on computer. The parameters setting function is used to set the requirement parameters of a certain testing, such as temperature, flowrate, and pressure. After the completion of setting, the test is

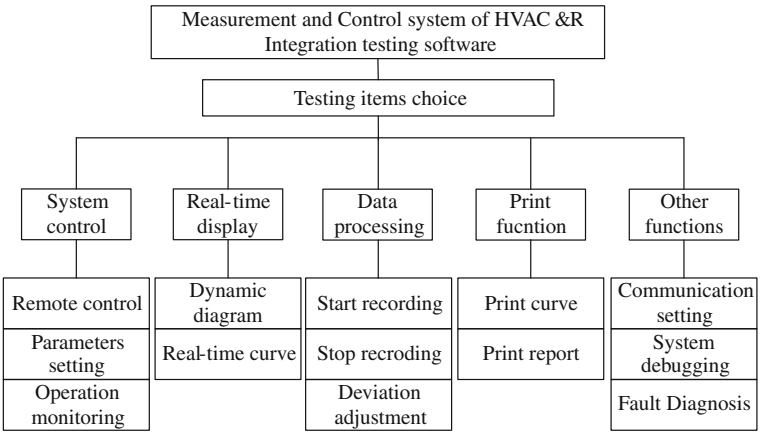

Fig. 36.4 The structure of the software system

start, and then all of the real-time data will be saved in real-time database. The operation monitoring function is used to monitoring the operating of the equipments.

The real-time display module includes two functions. Parameters of the test can be dynamic displayed in corresponding textbox of diagram on the screen, and the real-time curve of a parameter can be charted.

By using the functions of start recording and stop recording the data processing module, data are saved in report database between the time points of start and stop. If the testing parameters of sensors deviate from the calibration certificate, the deviation can be compensated with the deviation function of the data processing module.

The chart and report can be printed with the function of the print function module for the data stored in the report database.

There are three functions in the module of the other functions. The parameters of communication between instruments and computer can be set and tested with the function of communication setting. System debugging function is used to test the equipments of the testing platform. If anything wrong happened in the measurement and testing system, it will be shown in the fault diagnosis function and solutions will be given.

36.4 Key Technology and Solution

36.4.1 Data Acquisition

As is shown in hardware structure in Fig. 36.3, various control and acquisition instruments with different kinds of connection methods are used in the measurement and control system. It also means several varied kinds of communication protocol are adopted in this system. Therefore, how to resolve the communication between instruments and computer is critical. Solutions are given in Fig. 36.5.

The commands of communication of data acquisition and power meter are described in the respective user guide of them. The communication protocol of controller complies with Modbus protocol. A software package named PRODAVE (Process Data Traffic) supplies mass DLL (Dynamic Link Library), by using which the communication between PLC and computer is achieved.

36.4.2 Data Storage and Report Print

During the test, in order to ensure the integrity of data, all the data are written to the real-time database. After a certain period of steady data for testing, software system reminds the user to record the data for testing report. At this time, data are

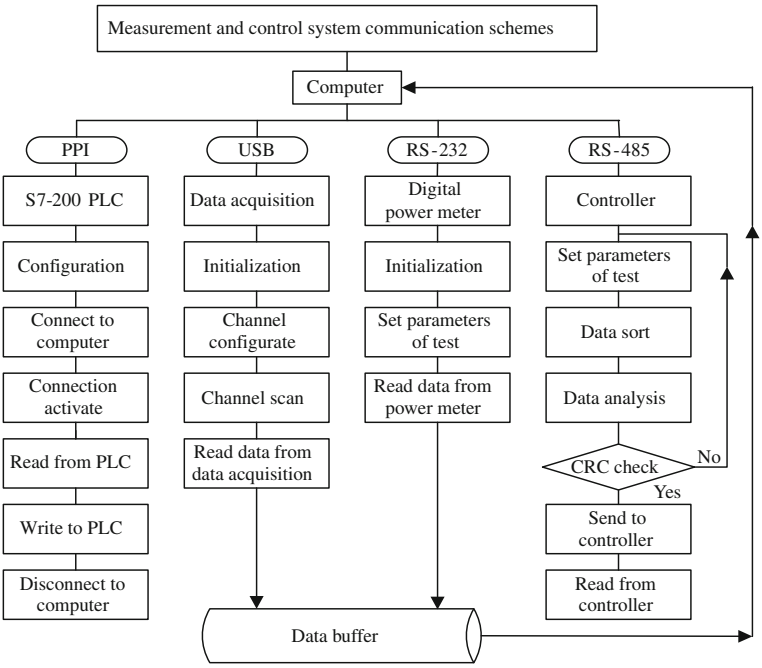

Fig. 36.5 Solutions to the communication

written to both real-time database and report database as soon as the user chooses to record. When data recording continues for the time span required without any deviation, the testing report is ready for print. The date process flow of measurement and control system is shown in Fig. 36.6.

36.4.3 Chart and Print of Curve

Curve drawing is also a focus and difficulty of this system. The process and data of the test can be inspected directly from the real-time curve. The fluctuation of the curve indicates the tendency of collected parameter so that test can be stabilized by the user as soon as possible. The deviation, testing process and time of recording are also shown in the interface of curve drawing. The data of curve derived form the real-time database. Therefore, it can be printed at any time according to the selected time period.

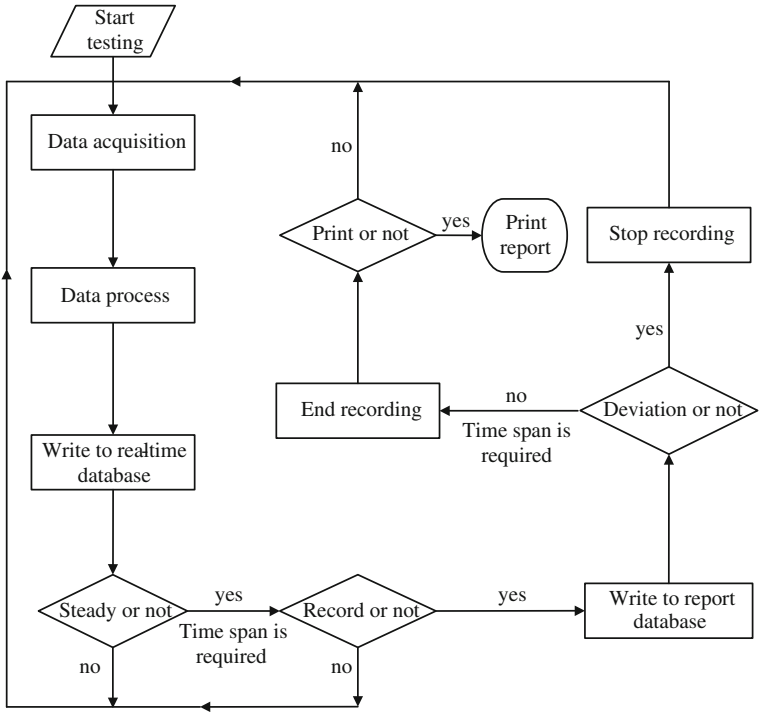

Fig. 36.6 Data process flow

36.5 Conclusions

A surface cooler and a plate exchanger are used in the testing platform for heat/cold recovery. By switching the valves, the amount of heat/cold exchange happened as well as the flowrate can be changed. With the changes of flow, the performance of the chilled package in the testing platform is improved. The two methods of heat/cold recovery used in this system save the investment and energy but also enhance system stability.

The structure and functions are suitable for this measurement and control system. The problems of communication between varied kinds of instruments and computer are solved. The functions of real time monitoring of testing parameters, recording, charting, controlling, alarming and fault diagnosis, etc., are included.

A period of use shows that the multifunctional testing platform can achieve the various performance tests of various different kinds of HVAC&R products with good reliability, stability, and precision successfully.

Acknowledgments This study was funded by the 12th Five Year National Science and Technology Support Key Project of China (NO.2011BAJ03B05).

References

1. Ji J, Chow T-t, Pei G et al (2003) Domestic air-conditioner and integrated water heater for subtropical climate. Appl Therm Eng 23(5):581–592
2. Liu X, Wu L, Zhang F et al (2012) 2011 market analysis of refrigeration and air-conditioning industry at home and abroad. Refrig air Cond 12(3):1-8
3. International Standards Organization (1994) Non-ducted air conditioners and heat pumps testing and rating for performance. ISO 5151:1994, ISO, Geneva
4. General Administration of Quality Supervision, Inspection and Quarantine of the People's Republic of China (2004) Room air Conditioner. GB/T 7725-2004, National Bureau of Standards, Beijing
5. General Administration of Quality Supervision, Inspection and Quarantine of the People's Republic of China (2007) Water chilling (heat pump) packages using the vapor compression cycle–Part 1: water chilling (heat pump) packages for industrial and commercial and similar application. GB/T 18430.1-2007, National Bureau of Standards, Beijing
6. General Administration of Quality Supervision, Inspection and Quarantine of the People's Republic of China (2008) Water chilling (heat pump) packages using the vapor compression cycle–Part 2: water chilling (heat pump) packages for household and similar application. GB/T 18430.2-2008, National Bureau of Standards, Beijing
7. General Administration of Quality Supervision, Inspection and Quarantine of the People's Republic of China (2003) Fan-coil unit. GB/T 19232-2003, National Bureau of Standards. Beijing
8. Anderson M, Buehner M, Young P et al (2006) An experimental system for advanced heating, ventilating and air conditioning (HVAC) control. Energy Build 39(2):136–147
9. Li H, Qi X (2010) Design of compressor displacement testing system for air-conditioner of air-conditioned passenger train. In: Proceedings of the 2009 third international symposium on intelligent information technology application workshops, Nanchang, China, pp 424–426

Chapter 37
Discussion on Testing Method of Ventilation System Air Leakage Rate

Jing Ma, Yin Liu and Renbo Guan

Abstract The air leakage of duct is an important indicator to inspect the quality of ventilation and air-conditioning system project. The strength and tightness of air duct in the ventilation and air-conditioning system is one of the important indicators to measure the processing and production quality of duct. According to the relevant provisions of the specification, the duct should be tested for its tightness according to the system category after the production and installation. In the construction, the tightness test of duct system is more cumbersome, and there is some difficulty in operation to really do well in the air leakage test of the duct system, as the testing task needs not only special testing equipment, instruments and, meters, but also certain technicians. This paper introduces a simplified air leakage testing method in accordance with the specification. The application and inspection in practical projects prove that the method is a correct and simple test method with strong operability.

Keywords Testing method · Ventilation system · Air leakage rate

37.1 Introduction

The strength and tightness of air duct in the ventilation and air-conditioning system is one of the important indicators to measure the processing and production quality of duct. According to the relevant provisions of the specification [1], the

J. Ma (✉)
Henan University of Technology, Lianhua street, Zhengzhou 450001, China
e-mail: mjja@163.com

Y. Liu · R. Guan
Zhongyuan University of Technology, Zhongyuan Middle Road.41, Zhengzhou 450007, China

Y. Liu
e-mail: hvacr@126.com

A. Li et al. (eds.), *Proceedings of the 8th International Symposium on Heating, Ventilation and Air Conditioning*, Lecture Notes in Electrical Engineering 262,
DOI: 10.1007/978-3-642-39581-9_37,

duct should be tested for its tightness according to the system category after the production and installation. In the construction, the tightness test of duct system is more cumbersome, and there is some difficulty in operation to really do well in the air leakage test of the duct system, as the testing task needs not only special testing equipment, instruments, and meters, but also certain technicians [2]. In combination with project examples, this paper introduces a simplified air leakage testing method in accordance with the relevant provisions of the specification [1].

37.2 An Air Leakage Testing Requirements

37.2.1 System Types

According to the specification [1], the air duct system is divided into three categories in accordance with its system working pressure, i.e., static pressure of duct, as shown in Table 37.1. According to the different work pressure level, the maximum allowable air leakage volume is stipulated, as the formula (37.1) to (37.3).

The allowable air leakage of duct system:

$$Q_{\mathrm{L}} \leq 0.1056P^{0.65} \tag{37.1}$$

$$Q_{\mathrm{M}} \leq 0.0352P^{0.65} \tag{37.2}$$

$$Q_{\mathrm{H}} \leq 0.0117P^{0.65} \tag{37.3}$$

where, Q_{L}, Q_{M}, Q_{H} is the allowable air leakage volume in the unit area per unit time, respectively under the corresponding pressure of low pressure system, medium pressure system and high pressure system, $m^3/(h.m^2)$. P is the working pressure of duct system, Pa.

37.2.2 The Test Method for Air Leakage

After installation of air duct and components, leakproofness test should be conducted according to pressure rating of the system and air leakage volume shall be

Table 37.1 Classification of duct system level

System type	System working pressure (Pa)
Low pressure system	$P \leq 500$
Middle pressure system	$500<P \leq 1500$
High pressure system	$P > 1500$

in accordance with the specification and requirements of design. Air duct sampling of low-pressure system is 5 %. Please adopt light leakage detection method under the premise of ensuring processing technology and installation operation quality; as to leakproofness test of air duct in intermediate pressure system, you should carry out a spot check on duct system test, sampling rate is 20 % and there shall be at least one system; air leakage volume test shall be carried out on all air ducts in high-pressure system. Please refer to the testing device and test method for the device in Appendix A of "Ventilation and Air Conditioning Construction Quality Acceptance Specification" (GB50235-2002). However, in the strict sense, the method provided by the specification is a kind of laboratory method. If it is applied to the construction site, there shall be some limitations; ①Settings of gate valve: the device is mainly used to adjust flow rate of the fan, it has a high market price and installation process is complex; ②Settings of damping screen: damping screen has flow equalizing function and the air can have parallel linear flow after going through the screen to ensure the accuracy of flow measurement and stability of wind pressure of the system. But there are no specific provisions concerning thickness, material and eyelet size of damping screen in the specification, different types of damping screen have different resistances, and it is quite difficult to buy a suitable damping screen on the market; ③Standard orifice plate: standard orifice plate is not a universal measuring instrument for different air systems, it shall be custom-made and its coefficients shall be marked and revised according to different air-conditioning test systems. The cycle is long and the price is quite high.

During application in practical projects, the writer correspondingly simplifies the test system and test method in the specification under the premise of meeting the requirements of the specification, thus they can complete the leakproofness test of air duct system more conveniently with high efficiency and accuracy.

37.3 Test Methods and Application of Simplified

37.3.1 Project Overview

The project has a total area of air conditioning of 100 m^2. The duct is quite thin with many branches. Total area of air duct is about 180 m^2 and temperature accuracy is ± 0.5 °C. The air will be sent into the room after centralized processing by the unit and the residual pressure of unit outlet is 650 Pa. According to the specification [1], we can know that the system is intermediate pressure air supply system and test pressure is about 800 Pa.

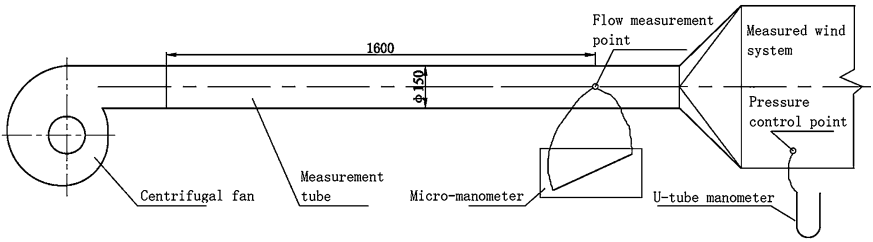

Fig. 37.1 Duct air leakage rate testing program

37.3.2 Test Scheme

In order to ensure the required accuracy and principle of simplifying test device and method in the specification, we formulate the test scheme as shown in Fig. 37.1. The scheme simplifies the damping screen, flow orifice plate and other required parts in the specification and enlarges the length of straight duct in front of the measuring point to ensure that the air at the measuring point inside the tested duct is uniform laminar flow. At the same time, lay out measuring points on measuring point section according to the area equivalent principle [3] as shown in Fig. 37.2 to further ensure the accuracy of test results.

37.3.3 Air Leakage Testing

(1) Strictly seal the opening (air inlet) of the system to ensure that there is no air leakage, and connecting part of key parts of test device must be hermetic without air leakage.
(2) Put the test section as shown in Fig. 37.1 in the test system, insert the two pitot tubes which measure the flow and system pressure into the test orifice and respectively connect them to the micro manometer and U-tube manometer.
(3) Start the centrifugal fan to inject air into the system and adjust supply air rate of the fan until readings of U-tube manometer are stable in 800 Pa.
(4) Use the pitot tube probe to measure different measuring points on measured section according to area equivalent principle, and please see Table 37.2 for test results.

37.3.4 Calculation of Air Leakage

According to the local atmospheric pressure, measure air pressure and calculate the density of the air thermometer:

Fig. 37.2 Measuring points

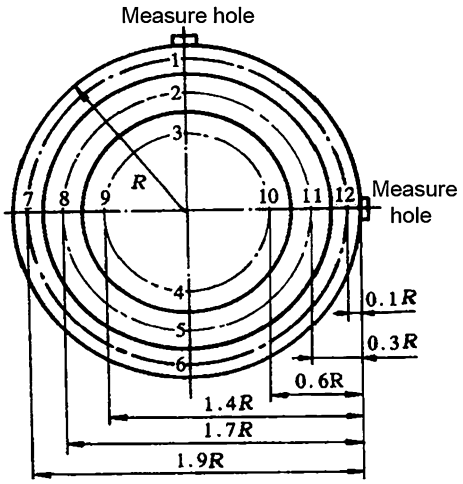

Table 37.2 Duct system flow test results

Location of the dynamic pressure	P_d (mm H_2O)					
	(1 mm $H_2O \approx$ 10 Pa, t_{air} = 37.4 °C)					
Measuring point	1	2	3	4	5	6
Vertical	6.1	6.2	6.4	6.4	6.2	6.1
Horizontal	6.2	6.4	6.6	6.6	6.4	6.2

$$\rho = \frac{P_0 + P_{\text{test}}}{287 \cdot (273.15 + t_{\text{air}})} \tag{37.4}$$

where: p_0 is the measured atmospheric pressure region, Pa; P_{test} is test section static pressure, 800 Pa; t_{air} is the measured air temperature, °C.

Air velocity of each measuring point:

$$v_i = \sqrt{2K \cdot P_d/\rho} \tag{37.5}$$

where: v_i is speed of measuring point; K is coefficient of micromanometer, 0.30; P_d is dynamic pressure value of measuring point; ρ is air supply density of test section.

Average velocity of air on test section:

$$\bar{v} = \frac{1}{n}\sum_{i=1}^{n} v_i \tag{37.6}$$

where: $\bar{v}$ is the average air velocity of the test section.

Air leakage volume of air duct system:

$$Q = \bar{v} \cdot \frac{\pi d^2}{4} \cdot 3600 \tag{37.7}$$

where: Q is air leakage volume of air duct system, m^3/h; d is air duct diameter of test section, 150 mm.

According to test data and the above equation, air leakage volume of the air-conditioning's air system is calculated as 366 m^3/h. According to Eq. (37.2), the allowable maximum air leakage volume in the specification is calculated as 488 m^3/h, thus, we know that air leakage volume of the system is in accordance with requirements of specification.

37.3.5 Verification and Analysis

In the simplified test method of air leakage volume of air duct system, the tested system pressure control and pressure measurement are in accordance with those in the specification, so the correctness is beyond all doubt. The area equivalent principle used in air volume measurement is the air volume measurement method through scientific calculation and engineering verification. In order to further verify the simplified test system, we adopt the specified measurement method in the specification to measure the air system's air leakage volume and the result is 358 m^3/h. The measurement results show that the difference between test results of the simplified test method and the specified test method in the specification is just about 2 %, and the measured air leakage volume of the simplified method is slightly larger than that of the specified test method in the specification. If the results of the simplified test method are in accordance with requirements of the specification, the measured system's air leakage volume is sure to meet requirements of the specification. By contrast to the specified test method in the specification, we confirm the feasibility and correctness of using the simplified test method of air leakage volume in the text to measure the air leakage volume of air duct system.

37.4 Conclusion

The air leakage of duct is an important indicator to inspect the quality of duct manufacturing and installation. After completion of manufacturing and installation of air duct, construction units shall adopt the test method meeting the requirements of specification [1] to conduct leakproofness test on air duct according to the specified three categories of pressure level in the specification [1]. The application and inspection in practical projects prove the simplified test method of air duct system's air leakage volume which is presented in the text and which meets the requirements of the specification is a correct and simple test method with strong operability.

References

1. GB50235-2002 (2002) Ventilation and air conditioning construction quality acceptance
2. Sun B, Li F, Zhu T et al (2006) Ventilation and air conditioning engineering application of air leakage testing. Constr Technol 2006 (08):87–89
3. Chen W (ed) (2001) Air-conditioning engineering and equipment operation principles structure maintenance. Shanghai Jiaotong University Press, Beijing

Chapter 38
Dynamics Characteristics of an Indirect District Heating System and Operational Optimization

Lei Zhao, Jia Wang, Lidong Zhu and Lianzhong Li

Abstract Based on energy conservation principle and heat transfer mechanisms, a set of dynamic model was established for an indirect district heating system. Dynamic start-up process under ideal condition was simulated and the influence of heat loss from piping network, make-up water and intermediate heat exchange station, and radiator area surplus on the dynamic characteristics of the system was discussed. Dynamic process without control was simulated under the hourly outdoor temperature measured in the days from February 13 to 19, 2012. To overcome the obvious indoor temperature variation with outdoor temperature, four PI control strategies were proposed. The dynamic characteristic and energy consumption of the system operated under these four control strategies were discussed. It is found that the control strategy 3, controlling the fuel flow rate, and water flow rate in the first loop not only produce stable working performance but also obtain considerable energy saving potentials. These results are very helpful to realize the dynamic characteristics of the indirect district heating system and to select suitable control strategy and optimal performance.

Keywords District heating system · Dynamic modeling · Control strategy · Operational performance

L. Zhao (✉) · J. Wang · L. Zhu
Xi'an University of Architecture and Technology, 13 Yanta Road, Xi'an, 710055, Shaanxi, China
e-mail: leizhao0308@hotmail.com

L. Li
Danfoss Automatic Controls Management (Shanghai) Co. Ltd, Shangai, China

A. Li et al. (eds.), *Proceedings of the 8th International Symposium on Heating, Ventilation and Air Conditioning*, Lecture Notes in Electrical Engineering 262,
DOI: 10.1007/978-3-642-39581-9_38,

38.1 Introduction

District heating systems have been widely developed in China and the scales become larger and larger in the past decades. Some provinces and cities in southern China are also active in developing this kind of systems now. In northern China, the energy consumptions of heating systems have amount to 40 % of the total building energy consumed in towns [1]. And the overheating rate of heating systems ranges from 15 to 30 %. Therefore, how to reduce the energy consumption of district heating system arouses many attentions. It is significant to study on how to improve the continuous operational efficiency of central heating systems.

To this end, an indirect district heating system (IDHS) in Dalian was chosen as the prototype for this research. Hot water from the boiler house was utilized to heat two residential zones through three heat exchange stations. A set of dynamic model was developed for the overall system and its dynamic characteristics were studied [2]. And the dynamic operational states and energy consumptions of the system under different control strategies were obtained. This is useful information for choosing good control strategy and optimization of district heating system.

38.2 Dynamic Modeling

38.2.1 System Description

The schematic diagram of the IDHS is illustrated in Fig. 38.1. It consists of a boiler, three intermediate heat exchangers (IHE), connecting pipe network in the primary and the secondary systems, mixing valves and radiators in terminals [3]. There are two primary loops connecting the boiler with one intermediate heat exchanger station for YX community and the other for SGL community, including 2 sub-communities (SGL1 and SGL2). The communities are denoted as $1^{\#}$, $2^{\#}$, and $3^{\#}$ zones. The length of the connecting pipelines in the primary loops to the two communities is 3.0 and 3.8 km, respectively. The heating areas are 74, 48, and 65 thousand square meters for three zones and corresponding design heating indexes are 55.7, 60.4, and 60.4 W/m^2, respectively. Radiant floor heating coil is applied in $1^{\#}$ zone, while column radiators with convective heat transfer are used in $2^{\#}$ and $3^{\#}$ zones. The design parameters of the heating system are shown in Table 38.1 [4].

38.2.2 Dynamic Modeling of the System

Based on the mass and energy conservation principles, the models were developed for all the components involved in the system [5].

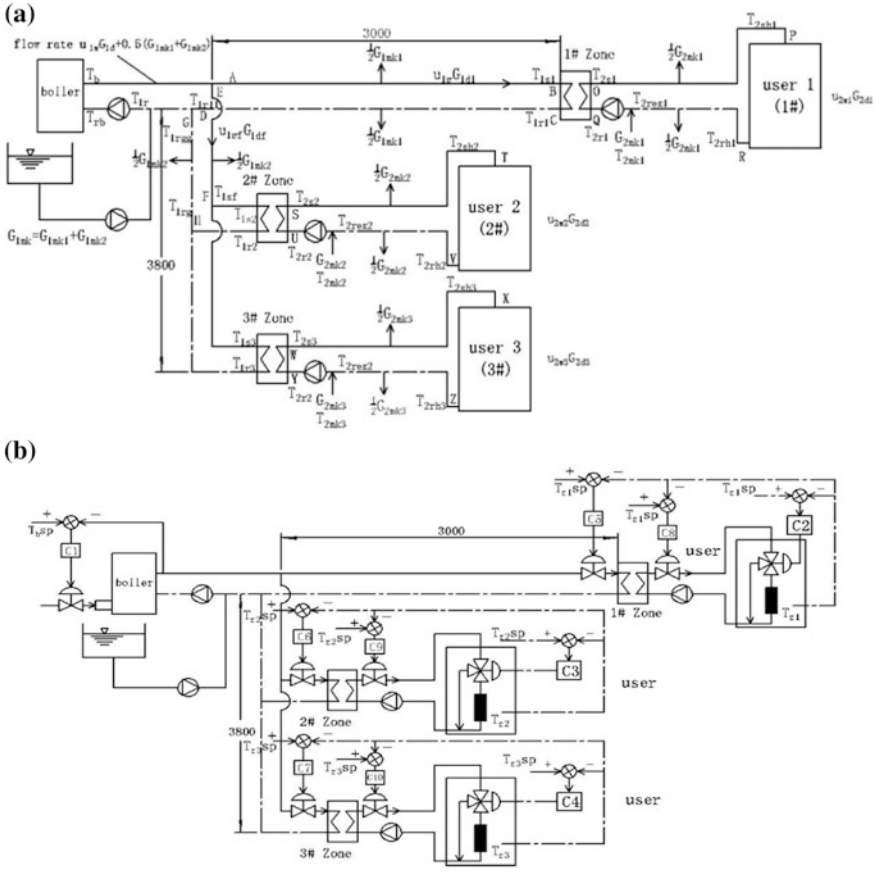

Fig. 38.1 The schematic diagram of the IDHS connecting with three zones and its control system. **a** Physical system. **b** Control system

Table 38.1 Design parameters of the central heating system

Items	Value
Supply/return water temperature of the primary system/ °C	110/70
Supply/return water temperature of the secondary system to 1# zone/ °C	60/50
Supply/return water temperature of the secondary system to 2# and 3# zones/ °C	75/55
Indoor and outdoor heating design air temperature/ °C	18/−11
Make-up water temperature in the primary system/ °C	50
Make-up water temperature in the secondary system/ °C	5
Rated boiler heating capacity/MW	14
Rated fuel consumption rate/$Nm^3 \cdot h^{-1}$	1466
The highest boiler supply water temperature allowed/ °C	115
Heating value of fuel/$kJ \cdot (Nm^3)^{-1}$	3.7×10^4

Boiler:

$$C_b \frac{\mathrm{d}T_b}{\mathrm{d}\tau} = u_f G_{\mathrm{fmax}} H_v \left[1 - (1 - \eta_{\mathrm{bmax}}) \left(\frac{T_{\mathrm{bmax}}}{T_b}\right)^a\right] - c_w [u_{1w} G_{1d} + 0.5(G_{1\mathrm{mk1}} + G_{1\mathrm{mk2}})](T_b - T_{rb}) \tag{38.1}$$

$$u_{1w} G_{1d} = u_{1w1} G_{1d1} + u_{1wf} G_{1df} \tag{38.2}$$

$$u_{1wf} G_{1df} = u_{1w2} G_{1d2} + u_{1w3} G_{1d3} \tag{38.3}$$

in which, C_b is the boiler heat capacity and its value is $1.21 \times 10^5 / \mathrm{kJ}\,^{\circ}\mathrm{C}^{-1}$.

$$IHE: \; C_{1\mathrm{ex},i} \frac{\mathrm{d}T_{1r,i}}{\mathrm{d}\tau} = c_w u_{1w,i} G_{1d,i} \left(T_{1s,i} - T_{1r,i}\right) - f_{\mathrm{ex},i} U_{\mathrm{ex},i} \frac{\left(T_{1s,i} - T_{2s,i}\right) - \left(T_{1r,i} - T_{2r,i}\right)}{\ln\left[\frac{\left(T_{1s,i} - T_{2s,i}\right)}{\left(T_{1r,i} - T_{2r,i}\right)}\right]} \tag{38.4}$$

$$C_{2\mathrm{ex},i} \frac{\mathrm{d}T_{2s,i}}{\mathrm{d}\tau} = c_w u_{1w,i} G_{1d,i} \left(T_{1s,i} - T_{1r,i}\right) - c_w \left(u_{2w,i} G_{2d,i} + 0.5 G_{2\mathrm{mk},i}\right) \left(T_{2s,i} - T_{2r,i}\right) \tag{38.5}$$

when maintaining the boiler supply and the return water temperature from the secondary system constant. And the heat capacities $C_{1ex,i}$ are $1.97 \times 10^3, 1.41 \times 10^3$ and $1.88 \times 10^3\,\mathrm{kJ} \cdot^{\circ} \mathrm{C}^{-1}$ and $C_{2\mathrm{ex},i}$ are $3.93 \times 10^3, 2.81 \times 10^3$ and $3.74 \times 10^3\,\mathrm{kJ} \cdot^{\circ} \mathrm{C}^{-1}$.

Pipe segments:

$$C_{1p,i} \frac{\mathrm{d}T_{1s,i}}{\mathrm{d}\tau} = c_w (u_{1w,i} G_{1d1} + 0.5 G_{1\mathrm{mk},i}) T_b - c_w u_{1w,i} G_{1d,i} T_{1s,i} - 0.5 c_w G_{1\mathrm{mk},i} \left(\frac{T_b + T_{1s,i}}{2}\right) - U_{1p,i} \left(\frac{T_b + T_{1s,i}}{2} - T_0\right) \tag{38.6}$$

$$C_{1p,i} \frac{\mathrm{d}T_{1r,i}}{\mathrm{d}\tau} = c_w u_{1w,i} G_{1d,i} T_{1r,i} - c_w \left(u_{1w,i} G_{1d,i} - 0.5\, G_{1mk,i}\right) T_{1r,i} - 0.5 c_w G_{1mk,i} \left(\frac{T_{1r,i} + T_{1r,i}}{2}\right) - U_{1p,i} \left(\frac{T_{1r,i} + T_{1r,i}}{2} - T_0\right) \tag{38.7}$$

The heat capacities of the pipe segments in the primary system to YX and SGL communities are 6.16×10^3 and $7.81 \times 10^3\,\mathrm{kJ} \cdot^{\circ} \mathrm{C}^{-1}$.

$$C_{2p,i} \frac{\mathrm{d}T_{2\mathrm{sh},i}}{\mathrm{d}\tau} = c_w (u_{2w,i} G_{2d,i} + 0.5 G_{2\mathrm{mk1}}) T_{2s,i} - c_w u_{2w,i} G_{2d,i} T_{2\mathrm{sh},i} - 0.5 c_w G_{2\mathrm{mk},i} \left(\frac{T_{2s,i} + T_{2\mathrm{sh},i}}{2}\right) - U_{2p,i} \left(\frac{T_{2s,i} + T_{2\mathrm{sh},i}}{2} - T_0\right) \tag{38.8}$$

$$C_{2p,i}\frac{\mathrm{d}T_{2\mathrm{rex},i}}{\mathrm{d}\tau} = c_w u_{2w,i} G_{2d,i} T_{2\mathrm{rh},i} - c_w\left(u_{2w,i}G_{2d,i} - 0.5G_{2\mathrm{mk},i}\right)T_{2\mathrm{rex},i} - 0.5c_w G_{2\mathrm{mk},i}\left(\frac{T_{2\mathrm{rh},i}+T_{2\mathrm{rex},i}}{2}\right) - U_{2p1}\left(\frac{T_{2\mathrm{rh},i}+T_{2\mathrm{rex},i}}{2} - T_0\right) \tag{38.9}$$

The heat capacities of the pipe segments in the secondary loops of 1#, 2# and 3# zones are all $2.05 \times 10^3\,\mathrm{kJ}\cdot{}^\circ\mathrm{C}^{-1}$.

$$Joints: T_{\mathrm{rb}} = \frac{T_{1r}}{u_{1w1}G_{1d1} + u_{1wf}G_{1df} + 0.5\left(G_{1\mathrm{mk1}} + G_{1\mathrm{mk2}}\right)} \tag{38.10}$$

$$T_{1r} = \frac{(u_{1w1}G_{1d1} - 0.5G_{1\mathrm{mk1}})T_{1r11} + (u_{1wf}G_{1df} - 0.5G_{1\mathrm{mk2}})T_{1\mathrm{rgg}}}{u_{1w1}G_{1d1} + u_{1wf}G_{1df} - 0.5(G_{1\mathrm{mk1}} + G_{1\mathrm{mk2}})} \tag{38.11}$$

$$T_{1\mathrm{rg}} = \frac{u_{1w2}G_{1d2}T_{1r2} + u_{1w3}G_{1d3}T_{1r3}}{u_{1w2}G_{1d2} + u_{1w3}G_{1d3}} \tag{38.12}$$

$$T_{2\mathrm{rh},i} = u_{h,i}T_{h,i} + \left(1 - U_{h,i}\right)T_{2\mathrm{sh},i} \tag{38.13}$$

$$T_{2r,i} = \frac{G_{2\mathrm{mk},i}T_{2\mathrm{mk},i} + (u_{2w,i}G_{2d,i} - 0.5G_{2\mathrm{mk},i})T_{2\mathrm{rex},i}}{u_{2w,i}G_{2d,i} + 0.5G_{2\mathrm{mk},i}} \tag{38.14}$$

Exterior wall model:

Heat transfer through exterior walls is deemed as 1-D [6]. Then,

$$C_{\mathrm{wl},i}\frac{\mathrm{d}T_{\mathrm{wl},i}}{\mathrm{d}\tau} = U_{\mathrm{wlin},i}\left(T_{z,i} - T_{\mathrm{wl},i}\right) + U_{\mathrm{wlout},i}(T_0 - T_{\mathrm{wl},i}) \tag{38.15}$$

$$C_{z,i}\frac{\mathrm{d}T_{z,i}}{\mathrm{d}\tau} = c_w u_{h,i}u_{2w,i}G_{2d,i}\left(T_{2\mathrm{sh},i} - T_{h,i}\right) + Q_{\mathrm{sol},i} + Q_{\mathrm{int},i} + U_{z,i}\left(T_0 - T_{z,i}\right) \tag{38.16}$$

Radiant floor coil and radiator model:

For simplification, heat transfer from floor radiator and column radiator are both expressed by heat transfer coefficient multiplying temperature difference, only coefficients are different [7]. Their dynamic model are expressed as,

$$C_{h,i}\frac{\mathrm{d}T_{h,i}}{\mathrm{d}\tau} = c_w u_{h,i}u_{2w,i}G_{2d,i}\left(T_{2\mathrm{sh},i} - T_{h,i}\right) - f_{h,i}U_{h,i}\left[0.5\left(T_{2\mathrm{sh},i} + T_{h,i}\right) - T_{z,i}\right]^{(1+b_i)} \tag{38.17}$$

The heat capacities of the heating device of terminals in 1#, 2#, and 3# zones are 3.5×10^5, 2.49×10^5 and $3.33 \times 10^5\,\mathrm{kJ}\cdot{}^\circ\mathrm{C}^{-1}$, respectively.

As stated above, the mathematical model of the IDHS consists of 37 equations in the whole. It can be used to study the transient characteristics, optimize control strategies, and analyze energy consumption of the overall system.

38.3 Dynamic Characteristics of the System

38.3.1 Start-up Characteristics at Design Outdoor Temperature

The mathematic models are programmed by using software Matlab. Assuming the pipelines were well insulated, no water leakage, and heat transfer area surplus in the system, the ideal start-up process of the whole system with 0.778 opening of the fuel valve were simulated at first. In practice, heat loss through pipelines and make-up water is inevitable and radiator or IHE area surplus ratios always exist. The dynamic operational processes under the real condition with make-up water, heat loss, and heat transfer area surplus ratios being 1, 12.5, and 20 % are simulated as well. From Fig. 38.2a and b, it can be found that the steady state supply and return water temperatures of both the boiler and the second loop under real condition are lower than those under ideal one. This is mainly caused by the heat transfer area surplus of heating device of terminals and IHEs. The heat loss and water leakage through the pipelines bring about the necessity of enlarging the fuel valve. It must be adjusted to 0.919 to achieve the design indoor air temperature under real situation when outdoor air temperature remains −11 °C.

38.3.2 Dynamic Characteristics of the System

The continuous operational states from February 13 to 19, 2012 were simulated with the outdoor temperature measured and the solar and internal heat gains of 1#, 2#, and 3# zones ranging from 0.16 to 1.65 MW, 0.11 to 0.92 MW, and 0.14 to 1.24 MW, respectively. With heat loss, make-up water and heat transfer area surplus ratio stated above and the fuel control valve opening remains at 0.919, the operational states of the heating system are shown in Fig. 38.3a. It can be seen that

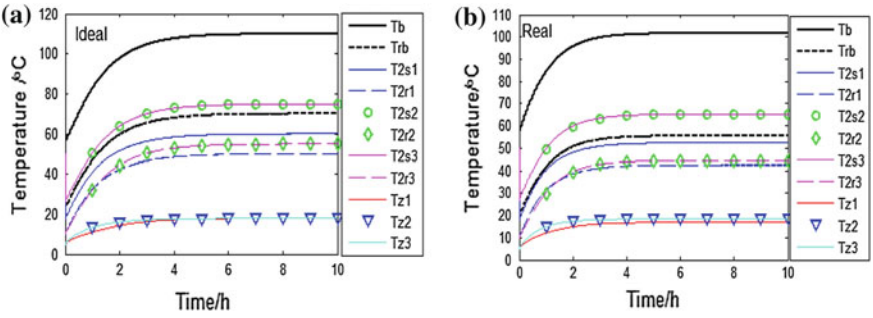

Fig. 38.2 Dynamic characteristic of starting up at −11 °C outdoor temperature. **a** Ideal condition. **b** Real condition

the indoor temperatures are higher than the design value since the outdoor temperature is higher than −11 °C, ranging from 15.6 to 38.2 °C. The indoor temperature, the supply and return water temperatures in the primary and secondary systems fluctuate severely. This means if the fuel valve opening is not adjusted, it cannot meet the design requirement to achieve a comfortable indoor temperature, and also results in the waste of energy.

38.4 Operational Performance Under Different Control Strategies

38.4.1 The Variation of the Boiler Supply Water Resetting Temperature Value with Outdoor Temperature

From the discussion mentioned above, it can be found that control strategies must be applied to offset the indoor temperature deviation from its design value incurred by outdoor air temperature variation [8, 9]. This situation can be achieved by adjusting the heating amount supplied from the system. Neglecting the solar and internal heat gains, to maintain the indoor temperature and circulating water flow rate at design values, the fuel valve opening must trace the change of outdoor air temperature [10]. And the boiler supply water temperature will follow it to change. By simulation with different outdoor air temperature, the relationship between the boiler supply water temperature and the outdoor temperature is almost linear, as shown in Fig. 38.3b. Fitting the curve, it yields,

$$T_{\mathrm{bsp}} = -2.62T_{\mathrm{o}} + 73.39 \tag{38.18}$$

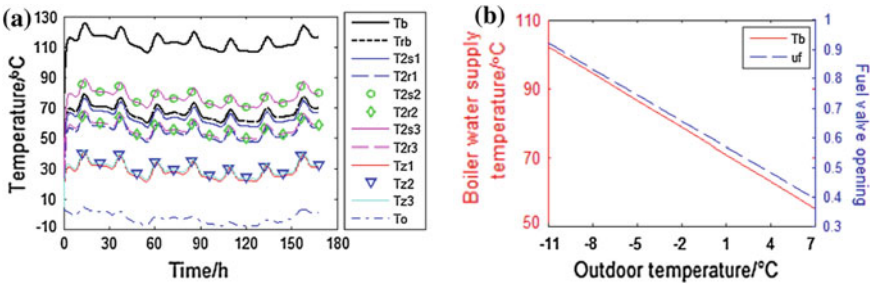

Fig. 38.3 Relationships among fuel valve opening, boiler supply water temperature, and outdoor temperature

38.4.2 Operational State Under Different Control Strategies

Typical PI control algorithm can be formulated as $u = k_p e + k_i \int_0^\tau e d\tau$, and different operational states are obtained when the following control strategies are applied.

Control strategy 1: The fuel flow rate is controlled by adjusting the fuel valve opening according to the deviations between the resetting and real values of the boiler supply water temperature

Controlling the fuel flow rate by adjusting the fuel valve opening through resetting the boiler supply water temperature according to Eq. (38.18) when the outdoor temperature varies, the operational states of the system are illustrated in Fig. 38.4. It can be seen that though the change aroused by outdoor temperature change can be offset to some extent, the indoor temperature of 1#, 2#, and 3# still periodically changes between 17.8–23.5 °C and 19.7–24.9 °C. This is resulted from solar and internal heat gains.

Control strategy 2: The fuel flow rate control plus water mass flow rate control of heating device in terminals

In addition to the fuel flow rate adjusting, controllers C2, C3, and C4 can be installed to control the water flow rates of the heating device. Taking the indoor design temperature as the temperature set point, PI algorithm is applied to determine the Tee valve openings to control the circulating water flow rate through the terminals. Under this control strategy, the total water flow rate of the primary and the secondary systems remain unchanged and the operational states are shown in Fig. 38.4.

Comparing Fig. 38.4 with Fig. 38.5, it can be found that the boiler water supply temperature are almost identical, however, the boiler return temperatures improve slightly. In addition, the indoor temperatures fluctuate about the set point only by

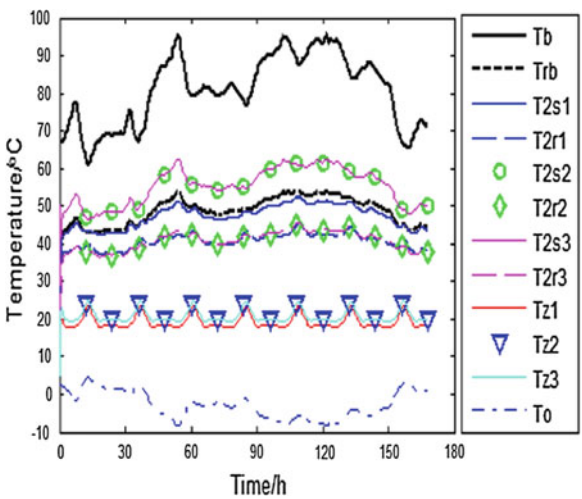

Fig. 38.4 Operational state under control strategy 1

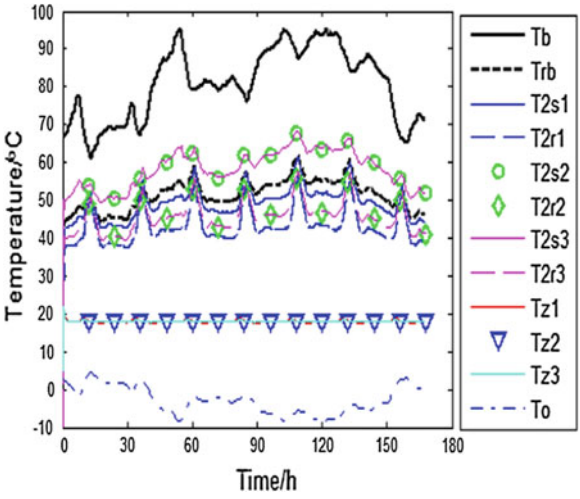

Fig. 38.5 Operational state under control strategy 2

0.4 °C. This is for reason that the water flow rates through the radiators are also adjusted to offset the influence of solar and internal heat gains. Meanwhile, the supply and return temperatures of the secondary system fluctuate obviously.

Control strategy 3: Control the fuel flow rate plus control water flow rate in the primary system

In addition to adjusting the fuel flow rate as previously as the outdoor temperature changes, controllers C5, C6, and C7 are installed to adjust the water flow rate in the primary system to offset the influence of solar and internal heat gains. It can be found in Fig. 38.6 that the indoor temperatures vary about the design value. The peak fluctuations reach 2.1 and 1.8 °C in $1^{\#}$ zone and in $2^{\#}$ and $3^{\#}$ zones, respectively.

Control strategy 4: Control the fuel flow rate plus control water flow rate in the secondary system

In addition to adjusting the fuel flow rate, controllers C8, C9, and C10 can be installed to adjust the water flow rate in the secondary system to offset the influence of solar and internal heat gains. Figure 38.7 shows the operational states under control strategy 4. It can be seen that the water temperature fluctuation in the second system turns stronger, but the indoor temperatures fluctuation becomes weaker. Nevertheless, unstable operation will be created if the sensitivity of the control is improved. This reveals that based on the fuel flow rate control, the control of the water flow rate in the second loop will affect the operational stabilities of the whole system.

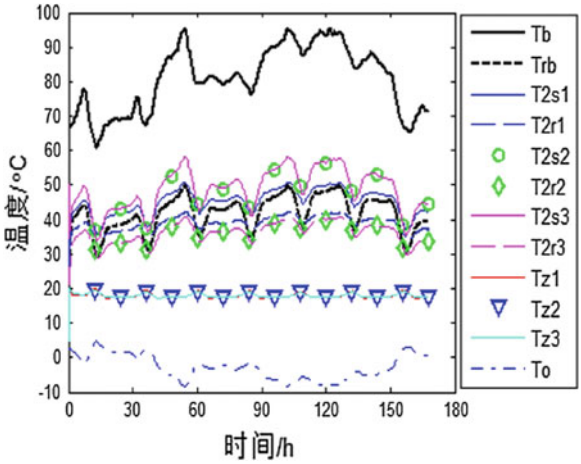

Fig. 38.6 Operational state under control strategy 3

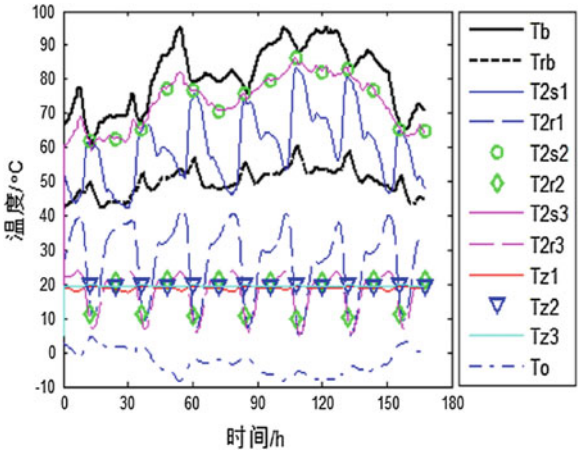

Fig. 38.7 Operational state under control strategy 4

38.4.3 Energy Consumption Under Different Control Strategies

Adopting different control strategies leads to different amount of fuel consumption. The fuel consumption can be reduced by 9.2 % if the control strategy 2 is applied instead of control strategy 1. While it can be reduced by 1.5 % if control strategy 3 is used instead of control strategy 2 though the fluctuations of the indoor air temperature become slightly obvious. It should be mentioned that the energy saving by pumps has not been accounted. If variable flow water circulating pumps are implemented, the energy saving potential under control strategy 3 can be explored further.

38.5 Conclusions

An overall dynamic simulation model was developed for an indirect district heating systems. Based on the dynamic model, the start-up process under constant outdoor temperature and variable temperature wave was simulated. Its dynamic characteristics are discussed. Then, dynamic simulation was conducted based on the outdoor temperature measured from February 13 to 19, 2012 without any control strategy was taken. It is found that the indoor temperatures fluctuate severely and energy waste is considerable. And then, to achieve better operational performance, four PI control strategies were proposed for this IDHS and the dynamic operational states were carried out and given in figures. Simulation results are shown that it is more effective to control the fuel flow rate as well as control water flow rate in the first loop. All the parameters in the system stably vary as the outdoor temperature changes and the indoor temperature approximate the design value. At the same time, the energy used is also efficient by applying this kind of control strategy.

A.1 Appendix

Symbols			
c	Specific heat based on mass/kJ $\cdot$ (kg $\cdot^{\circ}$ C)$^{-1}$	u	Valve opening, 0–1
C	Heat capacity/kJ $\cdot^{\circ}$ C^{-1}	$f_{ex,i}$	Surplus heat transfer area coefficient of IHE
G	Mass flow rate/kg/s	a	Coefficient related to boiler efficiency
H_v	Combustion heat value per unit volume under standard state/kJ $\cdot$ (Nm^3)$^{-1}$	G_f	Volumetric flow rate/Nm^3 $\cdot$ s^{-1}
k_p	Proportional coefficient in PI control algorithm	η	Boiler efficiency
k_i	Integral coefficient in PI control algorithm	α_1, α_2	Fitting coefficients
U	Heat transfer rate driving by 1 °C per unit area of IHE/W $\cdot$ K^{-1}	b_i	The index related to heat transfer coefficient. $b_1 = 1$, accounting for the effect of radiation heat transfer, b_2 and $b_3 = 0.28$ with only convective heat transfer
T	Temperature/°C	e	Temperature deviation
τ	Time/s		
subscripts			
z	Zone	b	Boiler
d	Design	rb	Return water into boiler

(continued)

(continued)

Symbols			
ex	Heat exchanger	*w*	Circulating water
f	Fuel of boiler	*s*	Supply water
htr	radiator	*r*	Return water
sh	user inlet	sp	Set point
1, 2, 3	$1^{\#}$, $2^{\#}$ or $3^{\#}$ zone	*p*	Parameters related to pipelines
o	Outdoor parameters	rex	inlet of make-up water pump in the secondary system
max	Maximum	int	Internal heat gain
mk	Make-up water	sol	Solar gain
1rgg	Joints on the return water pipe in the primary system to $2^{\#}$, $3^{\#}$ zones	1r11	Joint on the return water pipe in the primary system to $1^{\#}$, zones $1^{\#}$

References

1. Yu CR, Xia YX, Zhang ZM, Huang GF (2008) Energy saving and emission reduction of city central heat supply system. Building Energy Effic 36(7):10–12
2. Felgner F, Cldera R, Merz R, Litz L (2003) Modeling thermal building dynamics with Modelica. In: Proceedings of the 4th MATHMOD Conference, Vienna, 2003
3. Li LZ (2008) Simulations on system properties and control strategies for an indirect hot water district heating system. Energy Conserv 27(9):8–15
4. Lu YQ (1993) Practical heating and air conditioning design manual. China Architecture & Building Press, Beijing
5. Choi SY, Yoo KY, Lee JB, Shin CB, Park MJ (2010) Mathematical modeling and control of thermal plant in the district heating system of Korea. Appl Therm Eng 30:2067–2072
6. Liao Z, Dexter AL (2004) A simplified physical model for estimating the average air temperature in multi-zone heating systems. Build Environ 39(9):1013–1022
7. Liu CL, Yang CZ (2002) Energy analysis of low-temperature floor radiant heating system based on computer simulation. Energy Conserv Technol 20(06):20–25
8. Li SC, Li LZ (2011) Simulations of control strategies for heating system of buildings with different types of outer-wall. HV&AC 41(12):74–78
9. Wang J (2005) Dynamic supervise control network and saving energy strategy in central heating system based on heat meter. Shanghai Jiaotong University, Shanghai
10. Li LZ, Zaheeruddin M (2004) A control strategy for energy optimal operation of a direct district heating system. Int J Energy Res 28(7):597–612

Chapter 39
Simulation on a Two-Stage Compression Heat Pump with Focus on Optimum Control

Shuang Jiang, Shugang Wang, Xu Jin and Tengfei Zhang

Abstract An appropriate control logic is very important to optimize the performance of a two-stage compression heat pump system. In this paper, a numerical simulation model of two-stage compression heat pump system with intercooler was first presented and then validated by comparing simulation results with measured data. In addition, the model was used to analyze the performance characteristics of the heat pump, according to the superheat at suction line of the high-stage compressor and injection point, with frequency of low-stage compressor varying from 30 to 80 Hz. The simulation results showed that the heating capacity increased linearly with an increase of frequency of low-stage compressor, and the optimum heating capacity and COP were determined when the quality of the injection point was very close to unity. It was suggested that the superheat at the injection point was kept at 2 °C by controlling the 2nd EEV's opening, and the frequency of low-stage compressor was adjusted to meet the heating command of the user during space heating.

Keywords Two-stage compression · Heat pump · Optimum control · Simulation

Nomenclature

a_1, a_2	Coefficients in volumetric efficiency formula
$b_1 - b_5$	Coefficients in electrical efficiency formula
Bo	Boiling number
$c_1 - c_3$	Coefficients in volumetric efficiency correction formula
COP	Coefficient of heating performance
$d_1 - d_3$	Coefficients in electrical efficiency correction formula
f	Frequency of compressor [Hz]
h	Specific enthalpy [kJ kg^{-1}]
M	Refrigerant flow rate [kg s^{-1}]

S. Jiang (✉) · S. Wang · X. Jin · T. Zhang
Faculty of Infrastructure Engineering, Dalian University of Technology, Dalian 116024, China
e-mail: sgwang@dlut.edu.cn

A. Li et al. (eds.), *Proceedings of the 8th International Symposium on Heating, Ventilation and Air Conditioning*, Lecture Notes in Electrical Engineering 262,
DOI: 10.1007/978-3-642-39581-9_39,

n	Ploytropic index
P	Pressure [kPa]
P_r	Pressure ratio [kPa]
N	Power input [kW]
Q	Heating performance [kW]
q	Heat flux [W/m^2]
Re	Reynolds number
s	Slip ratio of the compressor motor
SH	Superheat [°C]
V	Refrigerant volume flow rate [m^3 s^{-1}]
X	Vapor mass fraction

Greek symbols

β	Chevron angle [radian]
λ	Volumetric efficiency
η	Electrical efficiency
μ	Viscosity [Ns/m^2]
v	Specific volume [m^3 kg^{-1}]

Subscripts

1–9	Point of the cycle
cy	Compressor cylinder
dis	Compressor discharge
EG	Ethylene glycol–water
f	Liquid phase
g	Vapor phase
H	High-stage compressor
inter	Intercooler
L	Low-stage compressor
Suc	Compressor suction
w	Wall/water

Superscripts

*	Parameters at base frequency

39.1 Introduction

Two-stage compression refrigeration systems, first developed in the 19th century, have been proved to be a more efficient and readily available solution than those single-stage compression systems [1]. When energy and environment become

more and more important, researchers begin to take interest on heat pump and the two-stage compression technology for heating that is used for domestic hot water production or space heating in cold climate areas, or for some specific situation that needs hydronic heating distribution with temperatures up to 65 °C or more [2]. Zehnder [2] in his doctoral dissertation performed system tests on some experimentally realized concepts, which are one-stage compression cycle with intermediate injection of saturated vapor, two-stage economizer cycle and booster concept, and liquid subcooling through an auxiliary cycle. The tested result of COP revealed that, the most important improvements, compared to the standard setup, were obtained by the two-stage cycle (at A-2/W50) and by the auxiliary cycle for subcooling (at B-2/W50). An increase of 20–35 % in heat output was obtained on all concepts. Bertsch and Groll [3] simulated, designed, constructed, and tested a two-stage air source heat pump for water and air heating using R410a as refrigerant. The system was able to operate at ambient temperatures between –30 and 10 °C with supply water temperatures of up to 50 °C. The system could run in single-stage and in two-stage operating mode, and at the same ambient temperature, two-stage mode operation approximately doubles the heating capacity compared to single-stage mode operation. The discharge temperatures of the compressors in two-stage mode stayed below 105 °C at all times. References [4, 5] performed experimental investigation and numerical simulation of an air source heat pump for cold climates. The unit studied was a two-stage compression cycle with two-stage throttling, and R22 as the refrigerant, and a flash tank was used. Jin et al. [6] established a dynamic compressor coupling model for a two-stage compression system with variable capacity, which was experimentally verified. His system was a typical economizer or intercooler cycle with R410a as refrigerant [7], as show in Fig. 39.1. It was pointed that among all factors related to the intermediate pressure, the effect of the ratio of the theoretical displacement of the low-stage compressor to that of the high-stage compressor on the intermediate pressure was the most vital determinant, and the intermediate pressure was sensitive to the variation of heating capacity, but passivated to heating COP.

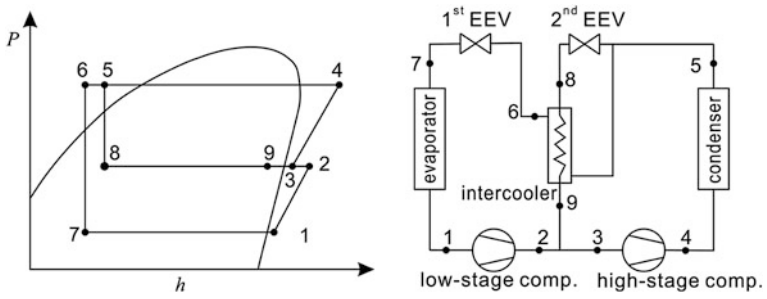

Fig. 39.1 Pressure-enthalpy and schematic diagram of a two-stage heat pump system with intercooler

Unlike a two-stage heat pump system with vapor-injected compressor [8–12], which is called quasi two-stage compression heat pump system [13], or one-stage compression with intermediate injection ports [2], the system studied in this paper refers to two-stage compression cycle that consists of two compressors: the low- and high-stage compressor. Two-stage compression systems with one compressor have been quickly commercialized for its relatively simpler structures and lower manufacturing cost than two-stage compression systems with two compressors. However, the latter has its advantages. First of all, the volume ratio of the low- and high-stage can be optimally designed for a specific application. What's more, when one compressor of the system, low-stage or high-stage, uses inverter compressor, the displacement ratio of the two compressors can be changed at various conditions to reach optimal system performance.

However,the control of the system is more difficult because of the flexibility of two-stage compression heat pump systems. Bertsch and Groll [3] pointed that the main challenges in the implementation of the two-stage compression heat pump system were the appropriate logic to control the system. When running under various working conditions, volume ratio of the two compressors and their coupled characters will change, so an appropriate control logic to maximize heating capacity and COP will be necessary. What's more, for some commercial used units, compressor failure of motor burnout can be found sometimes [14].

Optimum cycle control of two-stage heat pump systems with vapor-injected compressor has been reported by several researchers. Wang et al. [15] proposed a set of general principles for the design and operation of heat pump system with gas-injected scroll compressor based on the identified evaporator characteristics and thermodynamic analysis. The optimal control of the injection system was focused on controlling the injection pressure and specific enthalpy. It was concluded that the heating capacity might be kept constant or slightly increased when the injection pressure was larger than the optimal injection pressure (OIP_{CC}), and the maximum COP would be reached when the injection pressure was less than the optimal injection pressure and sometimes equaled to it. Heo et al. [16] proposed an optimum cycle control method for a refrigerant injection heat pump with a double expansion subcooler based on the intermediate pressure and the injection ratio. Based on experimental results, the optimum subcooler pressure ratio was proposed from 0.4 to 0.7 in view of the heating capacity, and from 0.7 to 0.8 in view of the COP. Wang et al. [10] experimentally investigated the performance of a 11 kW R410a heat pump system with vapor injection compressor and intercooler. They showed that the cooling capacity decreased with an increase in the superheat at the injection port and the heating capacity increased with an increase in the injection ratio (R_{inj}).

However, the optimum cycle control approaches mentioned above were all about two-stage heat pump systems with vapor-injected compressor. What's more for a small commercial heat pump unit and for reasons of cost consideration, it is impractical to control the unit based on refrigerant mass flow or injection pressure monitoring. For cycle showed in Fig. 39.1, there are two EEVs (Electronic

Expansion Valve) in the system, and the 1st EEV can adopt the conventional control method, which employs the evaporator outlet superheat as the control parameter. The superheat control method is the simplest and cheapest control method that employs only several temperature sensors. For the 2nd EEV, superheat at two points can be used to control its opening: superheat at the suction line of the high-stage compressor and superheat at the injection point. Wang et al. [10] experimentally studied the effect of injected vapor superheat on the cooling performance. Experimental results showed that the cooling capacity decreased with an increase of superheat but the cooling COP increased with that. But their research couldn't show the cooling performance under liquid refrigerant injection, which couldn't be measured by superheat. For a two-stage heat pump system, the injection mass is very important to the performance of the system. But the injection mass can't be arbitrary in view of the safe operation of high-stage compressor. To avoid wet compression, the superheat at the high-stage compressor suction line must be ensured. It is just because the injection mass flow rate decreases with an increase of the superheat at high-stage compressor suction line, which was discussed in later part of this paper, so we think that the superheat at the high-stage compressor suction line, which can be changed at a relatively wide range, will lead to more comprehensive research on the performance with vapor or liquid injection.

The objective of this paper has been to investigate the optimal control logic for the frequency of low-stage compressor and 2nd EEV of a two-stage compression heat pump system with intercooler by system modeling. Superheat at the high-stage compressor suction line and injection point (point 9) as shown in Fig. 39.1 under different working conditions were employed to study the influence of different injection mass on system performance.

39.2 Simulation Model

39.2.1 Modeling of Compressor with Variable-Speed

Refrigerant mass flow rate was expressed as

$$M^* = \lambda^* f^* (1 - s^*) V_{\mathrm{cy}} / v_{\mathrm{suc}} \tag{39.1}$$

$$M = \lambda f (1 - s) V_{cy} / v_{\mathrm{suc}} \tag{39.2}$$

Refrigerant mass flow rate ratio:

$$\frac{M}{M^*} = \frac{\lambda (1 - s) f}{\lambda^* (1 - s^*) f^*} \tag{39.3}$$

Then relation between refrigerant mass flow ratio and compressor frequency could be expressed as the second-order function of compressor frequencies [17]:

$$\frac{M}{M^*} = c_1(f - f^*)^2 + c_2(f - f^*) + c_3 \tag{39.4}$$

If different slip ratio of the compressor motor was not considered here, volumetric efficiency was expressed as follows from Eqs. (39.3) to (39.4):

$$\lambda = \frac{\lambda^* f^*}{f}\left\{c_1(f - f^*)^2 + c_2(f - f^*) + c_3\right\} \tag{39.5}$$

A semi-empirical formula [18] was employed to get the volumetric efficiency at base frequency:

$$\lambda^* = a_1 + a_2\left(\frac{P_{\text{dis}}}{P_{\text{suc}}}\right)^{1/n} \tag{39.6}$$

The values of n, a_1, a_2 could be get from experimental data at base frequency working conditions. So Refrigerant mass flow rate at arbitrary frequency was calculated via Eqs. (39.2), (39.5), and (39.6):

$$M = \left\{a_1 - a_2\left(\frac{P_{\text{dis}}}{P_{\text{suc}}}\right)^{1/n}\right\}\left\{c_1(f - f^*)^2 + c_2(f - f^*) + c_3\right\} f^* V_{\text{cy}}/v_{\text{suc}} \tag{39.7}$$

It could be seen form Eq. (39.7) that when $f = f^*$, $c_1(f - f^*)^2 + c_2(f - f^*) + c_3$ is equal to unity constantly, which means that $c_3 \equiv 1$. Shao et al. [17] couldn't point it out in their paper, but simulation results of c_3 in all the three models in their paper were very close to unity.

Compressor theoretical power of the polytropic process was defined as:

$$N_{\text{th}} = P_{\text{suc}} f(1 - s) V_{\text{cy}} \frac{n}{n - 1}\left[\left(\frac{P_{\text{dis}}}{P_{\text{suc}}}\right)^{(n-1)/n} - 1\right] \tag{39.8}$$

$$N^*_{\text{th}} = P_{\text{suc}} f^*(1 - s^*) V_{\text{cy}} \frac{n}{n - 1}\left[\left(\frac{P_{dis}}{P_{\text{suc}}}\right)^{(n-1)/n} - 1\right] \tag{39.9}$$

Power input of the compressor:

$$N = N_{\text{th}}/\eta,\ N^* = N^*_{\text{th}}/\eta^* \tag{39.10}$$

$$\frac{N}{N^*} = \frac{\lambda f(1 - s)}{\lambda^* f^*(1 - s^*)}\frac{\eta^*}{\eta} \tag{39.11}$$

Similarly, the relation between power input ratio and compressor frequency could be expressed as the second-order function of compressor frequencies [17]:

$$\frac{N}{N^*} = d_1(f - f^*)^2 + d_2(f - f^*) + d_3 \tag{39.12}$$

Ding and Zhang [18] showed that Eq. (39.13) could be employed to establish the correlation of electrical efficiency of compressors, which was a compromise between simplicity and good regression precision:

$$\eta^* = b_1 + b_2\left(\frac{p_{\text{dis}}}{p_{\text{suc}}}\right)^{1/n} \tag{39.13}$$

However, it was found that the electrical efficiency dropped very fast when discharged pressure was close to suction pressure. So a piecewise function was employed in this paper such that electrical efficiency function fitted well with the experimental data.

$$\eta^* = \begin{cases} b_1 + b_2\left(\frac{p_{\text{dis}}}{p_{\text{suc}}}\right)^{1/n} & \text{when } \frac{p_{\text{dis}}}{p_{\text{suc}}} \geq 1.5 \\ b_3 + b_4\left(\frac{p_{\text{dis}}}{p_{\text{suc}}}\right) + b_5\left(\frac{p_{\text{dis}}}{p_{\text{suc}}}\right)^2 & \text{when } \frac{p_{\text{dis}}}{p_{\text{suc}}} < 1.5 \end{cases} \tag{39.14}$$

Electrical efficiency at arbitrary frequency was determined via Eqs. (39.5), (39.11), and (39.12):

$$\eta = \frac{c_1(f - f^*)^2 + c_2(f - f^*) + c_3}{d_1(f - f^*)^2 + d_2(f - f^*) + d_3}\eta^* \tag{39.15}$$

It was evident that d_3 is unity in Eq. (39.15).

Discharge temperature was calculated as follows:

$$T_{\text{d}} = T_{\text{s}}\left(\frac{p_{\text{dis}}}{p_{\text{suc}}}\right)^{\frac{n-1}{n}} \tag{39.16}$$

39.2.2 Heat Exchanger Model

Convection heat transfer coefficient of single phase refrigerant and water in vertical plate heat exchanger (PHE) was determined with the Eq. (39.17) [19], and that of Ethylene Glycol–Water was determined with Eq. (39.18) [20].

$$Nu = \text{Re}^{0.78}\text{Pr}^{1/3}(\mu/\mu_{\text{w}})^{0.14} \tag{39.17}$$

$$Nu = 1.6774(\beta/30)^{0.38}(D/L)^{1/3}\text{Re}^{0.5}\text{Pr}^{1/3}(\mu/\mu_{\text{w}})0.14 \tag{39.18}$$

For two-phase refrigerant condensation process, Eq. (39.19) was selected to determine convection heat transfer coefficient [21].

$$Nu = 4.118\mathrm{Re}_{\mathrm{eq}}^{0.4}\,\mathrm{Pr}_{\mathrm{f}}^{1/3} = 4.118\left\{\frac{\dot{m}D\left[(1-X)+X\left(\rho_{\mathrm{f}}/\rho_{\mathrm{g}}\right)^{0.5}\right]}{\mu_{\mathrm{f}}}\right\}^{0.4}\mathrm{Pr}_{\mathrm{f}}^{1/3} \quad (39.19)$$

As for two-phase refrigerant evaporation process, which happens in both evaporator and intercooler, Eq. (39.20) [22] was chosen for the calculation of convection heat transfer coefficient. Because equivalent Reynolds number in intercooler might be very small when injection mass was little, linear correction was performed when equivalent Reynolds number in intercooler was not within the scope of this equation.

$$Nu = C\mathrm{Re}_{\mathrm{eq}}^{m}\mathrm{Bo}_{\mathrm{eq}}^{0.3}\,\mathrm{Pr}_{\mathrm{f}}^{1/3} \quad (39.20)$$

$\mathrm{Re}_{\mathrm{eq}}$ and $\mathrm{Bo}_{\mathrm{eq}}$,respectively, represented the equivalent Reynolds number and equivalent boiling number, which were defined as follows:

$$\mathrm{Re}_{\mathrm{eq}} = \dot{m}D\left[(1-X)+X\left(\rho_{\mathrm{f}}/\rho_{\mathrm{g}}\right)^{0.5}\right]\Big/\mu_{\mathrm{f}} \quad (39.21)$$

$$\mathrm{Bo}_{\mathrm{eq}} = q\Big/\left\{\dot{m}\left[(1-X)+X\left(\rho_{\mathrm{f}}/\rho_{\mathrm{g}}\right)^{0.5}\right]\gamma_{\mathrm{fg}}\right\} \quad (39.22)$$

where γ_{fg} was the latent heat of evaporation in kJkg^{-1}. Besides, the expressions for correction parameters C and were defined as follows:

$$C = \begin{cases} 2.81\left(\mathrm{Re}_{\mathrm{eq}}/100\right)^{1.38}(p_{\mathrm{co}}/D)^{-0.041}(\pi\beta/180)^{-2.83} & \mathrm{Re}_{\mathrm{eq}} \le 100 \\ 2.81(p_{\mathrm{co}}/D)^{-0.041}(\pi\beta/180)^{-2.83} & \mathrm{Re}_{\mathrm{eq}} > 100 \end{cases} \quad (39.23)$$

$$m = 0.746(p_{\mathrm{co}}/D)^{-0.082}(\pi\beta/180)^{0.61} \quad (39.24)$$

where p_{co} was corrugation pitch of PHE in m.

39.2.3 System Simulation Model

The system simulation model consisted of models of low- and high-stage compressors, condenser, intercooler, and evaporator. Mass balance and energy balance were considered, which satisfied:

$$M_{\mathrm{L}} + M_{\mathrm{inj}} = M_{\mathrm{H}} \quad (39.25)$$

$$M_{\mathrm{L}}h_2 + M_{\mathrm{inj}}h_9 = M_{\mathrm{H}}h_3 \quad (39.26)$$

Mass balance was implicit in calculation. As in Fig. 39.2, only P_3 and P_7 were iterated for convergence in the system simulation model. Input data contained parameters of secondary refrigerant (inlet temperature, flow rate, etc.), the superheat of high-stage compressor suction line ($SH_{\mathrm{suc,H}}$), the superheat of low-

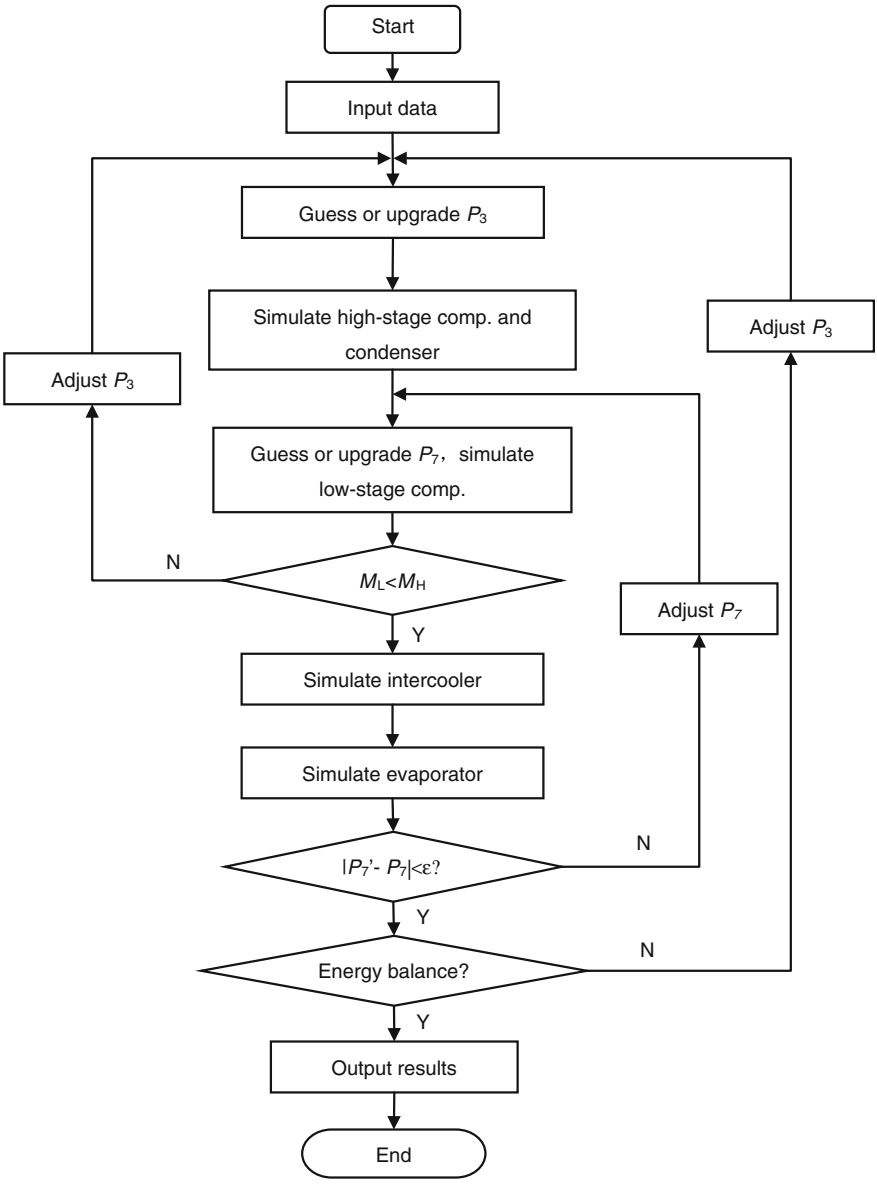

Fig. 39.2 Flow chart of simulation

stage compressor suction line ($SH_{suc,L}$), and frequency of the compressor. Calculation of high-stage compressor and condenser were performed together such that M_H and condenser pressure were worked out in one iteration process.

39.3 Model Validation

Figure 39.3 and Table 39.1 show the schematic diagram and specifications of the two-stage compression heat pump with an intercooler. Detailed explanations of the experimental device can be found form a previous paper by Jin et al. [6]. The simulation program was validated by conditions with injection that were conducted with evaporation temperature −20 °C, condenser inlet water temperature 35 and 45 °C, compressor frequency changed from 30 to 70 Hz, and high-stage compressor frequency fixed at 50 Hz.

Figure 39.4 shows the comparison of simulated results with the measured data at different low-stage compressor frequencies. The simulated pressures at high-stage compressor suction line (P_3) were consistent with the measured data within +11 and −2 %. The simulated heating capacity (Q) were consistent with the measured data within +5 and −10 %. The simulated power input of low-stage compressor (N_L) were consistent with the measured data within +5 and −7 %, and that of high-stage compressor (N_H) were consistent with the measured data within +10 and −2 %. The average deviations of P_3, Q, N_L, N_H were 3.2, 3.1, 1.0, and 4.4 %, respectively.

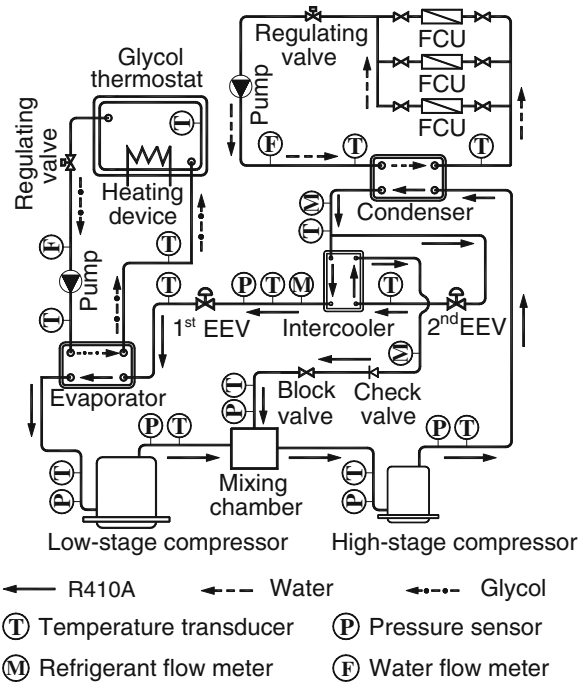

Fig. 39.3 Schematic diagram of experimental device

Table 39.1 Specifications of the experimental heat pump

Components	Specifications
High-stage compressor	Type: constant frequency
	Cylinder volume: 8.3 $cm^3 rev^{-1}$
	Power: 1Ph 220 V 50 Hz
Low-stage compressor	Type: Inverter-driven twin rotary
	Cylinder volume: 23.3 $cm^3 rev^{-1}$
	Power: 3 Ph 148 V 60 Hz
1st and 2nd EEVs	Motor: 4 phase stepping
	Pulse rate: 2000 steps
	Orifice diameter 1.3 mm
Condenser	Type: brazed plate heat exchanger
	Fluid flow plate length: 304.0 mm
	Plate width: 124.0 mm
	Area of the plate: 0.03 m^2
	Enlargement factor: 1.1836
	Angle of the corrugation: 0.9599 rad
	Corrugation amplitude: 2.0 mm
	Number of plates: 50
Evaporator	Type: brazed plate heat exchanger
	Fluid flow plate length: 304.0 mm
	Plate width: 124.0 mm
	Area of the plate: 0.03 m^2
	Enlargement factor: 1.1836
	Angle of the corrugation: 0.9599 rad
	Corrugation amplitude: 2.0 mm
	Number of plates: 40
Intercooler	Type: brazed plate heat exchanger
	Fluid flow plate length: 306.0 mm
	Plate width: 106.0 mm
	Area of the plate: 0.0255 m^2
	Enlargement factor: 1.1836
	Angle of the corrugation: 0.9599 rad
	Corrugation amplitude: 2.0 mm
	Number of plates: 10

39.4 Simulation Results and Discussion

The superheat at the high-stage compressor suction line ($SH_{suc,H}$) is defined as the temperature of point 3 (T_3) in Fig. 39.1 minus the saturation temperature of point 3. The superheat at the injection point (SH_{inter}) is defined as the temperature of point 9 (T_9) in Fig. 39.1 minus the saturation temperature of that. Table 39.2 shows the simulation conditions with variation of $SH_{suc,H}$ and f_L. $SH_{suc,H}$ starts from 2 °C to the superheat at which the simulation program cannot converge in the maximum set steps. It is noted that when f_L is set 80 Hz at condition 1, the intermediate pressure (P_9) is very close to condenser pressure, which is meaningless for a two-stage compression system. So frequency of 80 Hz is neglect at condition 1.

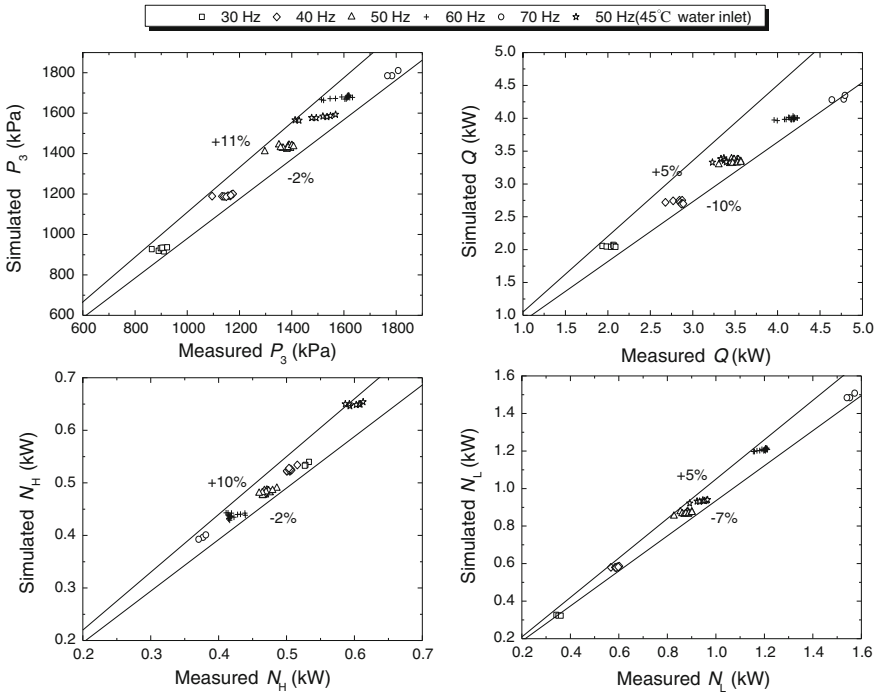

Fig. 39.4 Pressure-enthalpy and schematic diagram of a two-stage heat pump system with intercooler

Table 39.2 Simulation conditions

Simulation condition	$T_{EG,inlet}$ (°C)	$T_{W,inlet}$ (°C)	$SH_{suc,H}$ (°C)	$SH_{suc,L}$ (°C)	f_L (Hz)
Condition 1	−15	35	Start at 2 with steps of 2 or 0.2	2	30, 40, 50, 60, 70
Condition 2	−20	45	Start at 2 with steps of 2 or 0.2	2	30, 40, 50, 60, 70, 80

Figure 39.5 shows the variations of injection mass flow rate with $SH_{suc,H}$. The injection mass flow rate decreases with an increase of the superheat at high-stage compressor suction line ($SH_{suc,H}$). When $SH_{suc,H}$ increases to a certain degree, the injection mass flow rate drops very fast to near zero. So it is evident that the range of $SH_{suc,H}$ in our simulation can comprehensively show the feasible injection mass flow rate, just as mentioned above. In addition, when the $SH_{suc,H}$ keeps constant, the higher the f_L is, the more injection mass flow rate can reach. In addition, the maximum $SH_{suc,H}$ that can reach in the simulation increases with an increase of f_L. As shown in Fig. 39.5(b), the maximum $SH_{suc,H}$ at 30 Hz is about 20 °C, and that is about 42 °C at 80 Hz.

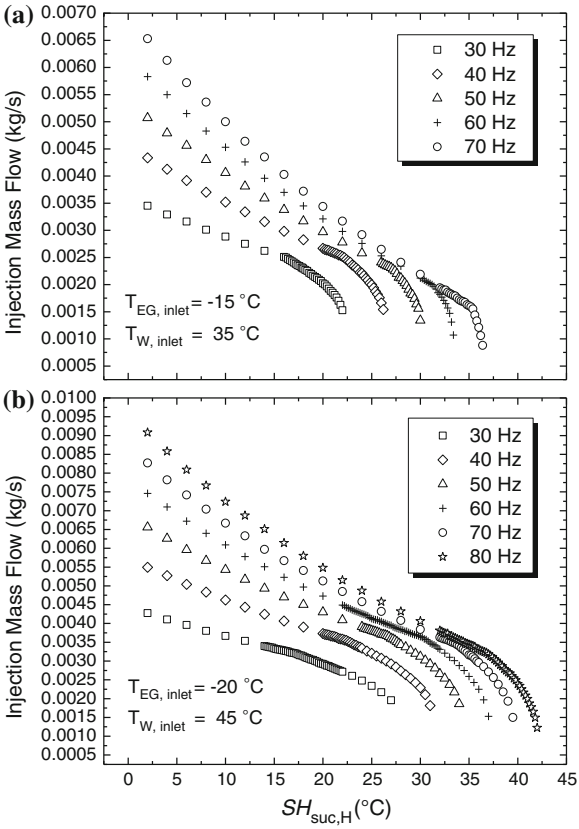

Fig. 39.5 **a, b** Variations of injection mass flow rate with $SH_{suc,H}$

Figure 39.6a shows variations of heating capacity (Q) and heating COP with $SH_{suc,H}$ at condition 1. With an increase of $SH_{suc,H}$, both Q and COP increase to maximum and then fast drops. The maximum Q and COP appear at the same $SH_{suc,H}$ for the same frequency of low-stage compressor (f_L), but the value of $SH_{suc,H}$ changes with f_L when both Q and COP reach the maximum. For example, $SH_{suc,H}$ is 16.2 °C at frequency of 30 Hz and that is 35 °C at frequency of 70 Hz, when Q and COP are maximum. Figure 39.6b shows variations of heating capacity (Q) and heating COP with $SH_{suc,H}$ at condition 2. The regularity showed in Fig. 39.6b is similar with that in Fig. 39.6a, except that $SH_{suc,H}$ is a little different when Q and COP are maximum.

Figure 39.7 shows variations of Q and COP with f_L. The value of $SH_{suc,H}$ almost lineally increases with f_L when maximum Q appears, but the value of $SH_{suc,H}$ is approximately a third order polynomial of f_L when maximum COP reaches, as shown in both Fig. 39.7a, b. The maximum COP appears when f_L is about 45 Hz at condition 1 (as shown in Fig. 39.7a), and that is about 50 Hz at condition 2 (as shown in Fig. 39.7b). The value of f_L when maximum COP reaches is very useful for the case that the heat pump unit is used for domestic hot water. This is because that, in most cases, the system can produce hot water with

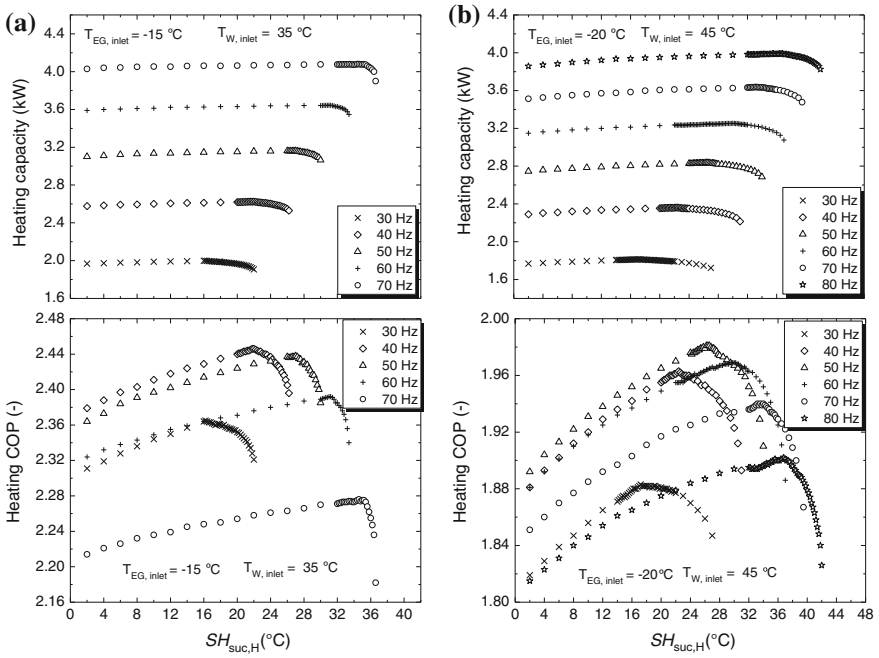

Fig. 39.6 **a, b** Variations of Q and COP with $SH_{\mathrm{suc,H}}$

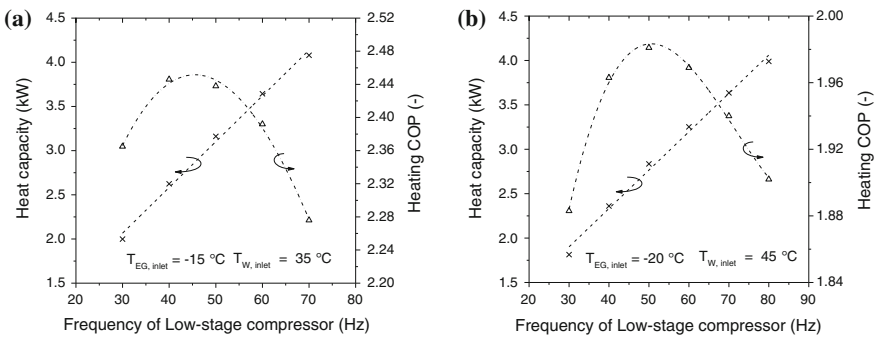

Fig. 39.7 **a, b** Variations of Q and COP with f_{L}

longer time to get over a decline in heat capacity. So a higher heating COP means less quantity of electricity needed. In other cases, when the heating demand comes first such as space heating, f_{L} can be adjusted to increase or decrease the heating capacity such that the heating demand is met.

However, differences of $SH_{\mathrm{suc,H}}$ with different f_{L} when maximum Q and COP appear, and the rapidly declining trend of COP, as shown in Fig. 39.6, make it a little troublesome to employ the $SH_{\mathrm{suc,H}}$ to control the 2nd EEV's opening.

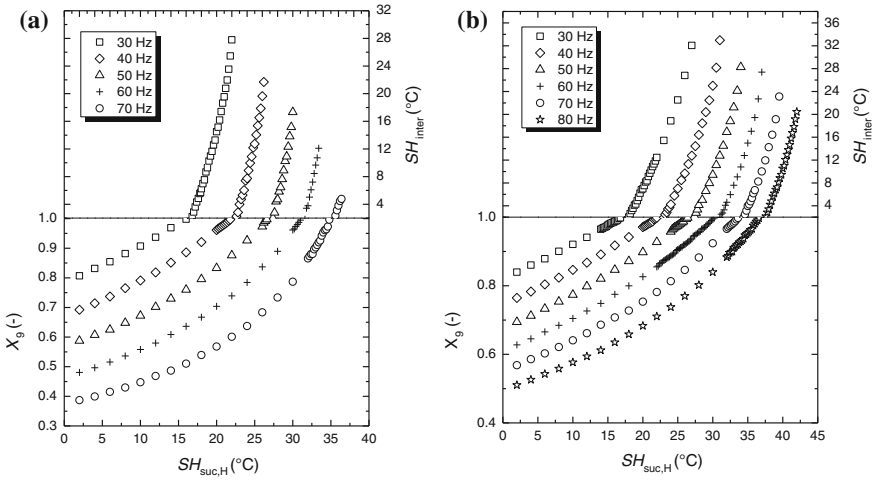

Fig. 39.8 **a, b** Variations of X_9 and SH_{inter} with $SH_{suc,H}$

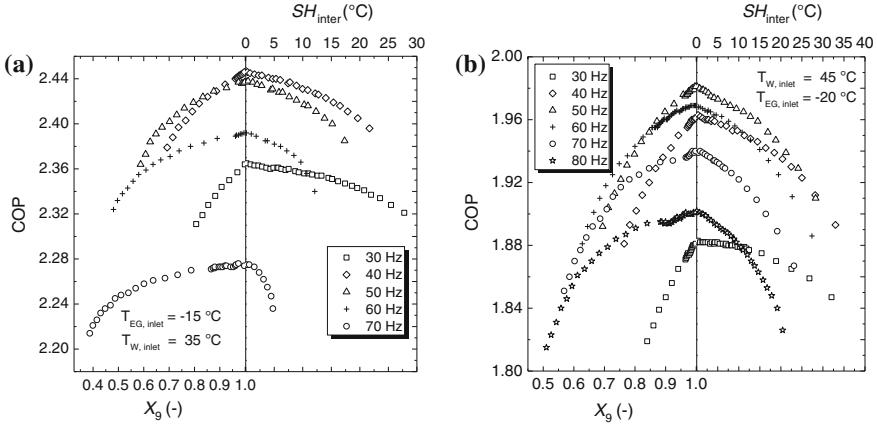

Fig. 39.9 **a, b** Variations of COP with vapor mass fraction of point 9 and SH_{inter}

Figure 39.8 shows variations of the vapor quality of point 9 (X_9) and SH_{inter} with $SH_{suc,H}$. When point 9 is in two-phase area, X_9 is used, and when it is in superheated area, the SH_{inter} is used. With an increase of $SH_{suc,H}$, X_9 increases to unity, and then SH_{inter} starts to increase rapidly from 0. It is evident that there is a one-to-one correspondence between $SH_{suc,H}$ and X_9 and SH_{inter}. Figure 39.9 shows variations of COP with X_9 and SH_{inter}. It is because when f_L keeps constant, both maximum Q and COP appears at the same value of $SH_{suc,H}$, or the same value of X_9 or SH_{inter}, as analyzed above, only COP data is used for analysis in the following. It should be noted that Fig. 39.9 employs the same COP data sets as

Table 39.3 Maximum COP and COP at SH_{inter}=2

	Condition 1					Condition 2					
f_L (Hz)	30	40	50	60	70	30	40	50	60	70	80
Maximum COP	2.365	2.446	2.438	2.392	2.276	1.883	1.963	1.981	1.969	1.940	1.902
COP at SH_{inter}=2	2.363	2.443	2.435	2.389	2.268	1.882	1.960	1.978	1.966	1.938	1.899

Fig. 39.6 employed. Figure 39.9 uses the state of point 9 for horizontal axis instead of $SH_{suc,H}$. It can be seen from both Fig. 39.9a, b that, COP increases with an increase of X_9. The maximum COP appears when X_9 is close to unity. Then COP decreases with an increase of SH_{inter}. As shown in Table 39.3, COP at SH_{inter}=2 is very close to maximum COP. In view of temperature control of 2nd EEV, a superheat of about 2 °C will be suitable.

39.5 Conclusion

A numerical simulation model of two-stage compression heat pump systems with intercooler was presented and validated by comparing simulation results with measured data. The model was then employed to analyze the performance characteristics of the heat pump according to different superheats. With an increase of $SH_{suc,H}$, both Q and COP increase to maximum at almost the same $SH_{suc,H}$ and then fast drop. Corresponding to $SH_{suc,H}$, X_9 and SH_{inter} are employed to analyze variation of COP. It is found that the maximum COP appears when X_9 is close to unity. Because COP at SH_{inter}=2 is very close to maximum COP, a superheat of about 2 °C would be suitable for controlling the 2nd EEV's opening. In addition, for control of the frequency of low-stage compressor, when the unit is used for domestic hot water, it will be suitable to adjust the value of f_L to reach maximum COP in most cases. And when the unit is used for space heating, to adjust f_L to meet the heating demand will be necessary.

Acknowledgments This research was supported by the Research Fund for the Doctoral Program of Higher Education of China (No.20120041110006).

References

1. Torrella E, Llopis R, Cabello R et al (2009) Experimental energetic analysis of the subcooler system in a two-stage refrigeration facility driven by a compound compressor. Hvac&R Res 15(3):583–596
2. Zehnder M (2005) Efficient air-water heat pumps for high temperature lift residential heating, including oil migration aspects. Dissertation for the Doctoral Degree. Lausanne: EPFL
3. Bertsch SS, Groll EA (2008) Two-stage air-source heat pump for residential heating and cooling applications in northern U.S. climates. Int J Refrig 31(7):1282–1292

4. Jin X, Wang SG, Huo M (2008) Experimental investigation of a novel air source heat pump for cold climate. In: 1st international conference on building energy and environment (COBEE 2008), Dalain. Dalian: Dalian University Technology Press, pp 1437–1443
5. Huo M, Wang S G, Jin X, Wu Q R (2009) Numerical simulation of an air source heat pump for low temperature climates. Vent Air Cond (ISHVAC 2009), Nanjing. Southeast Univ Press, Nanjing, pp 518–524
6. Jin X, Wang SG, Zhang TF et al (2012) Intermediate pressure of two-stage compression system under different conditions based on compressor coupling model. Int J Refrig 35(4):827–840
7. Torrella E, Larumbe JA, Cabello R et al (2011) A general methodology for energy comparison of intermediate configurations in two-stage vapour compression refrigeration systems. Energy 36(7):4119–4124
8. Agrawal N, Bhattacharyya S, Sarkar J (2007) Optimization of two-stage transcritical carbon dioxide heat pump cycles. Int J Therm Sci 46(2):180–187
9. Kim Y (2008) Effects of gas injection on the heating performance of a two-stage heat pump using a twin rotary compressor with refrigerant charge amount. Int J Air-Cond Refrig 16(3):77–82
10. Wang XD, Hwang Y, Radermacher R (2009) Two-stage heat pump system with vapor-injected scroll compressor using R410A as a refrigerant. Int J Refrig 32(6):1442–1451
11. Xu X, Hwang Y, Radermacher R (2011) Refrigerant injection for heat pumping/air conditioning systems: literature review and challenges discussions. Int J Refrig 34(2):402–415
12. Xu X, Hwang Y, Radermacher R (2013) Performance comparison of R410A and R32 in vapor injection cycles. Int J Refrig 36(3):892–903
13. Xu SX, Ma GY (2011) Exergy analysis for quasi two-stage compression heat pump system coupled with ejector. Exp Therm Fluid Sci 35(4):700–705
14. Roth K, Dieckmann J, Brodrick J (2009) Heat pumps for cold climates. ASHRAE J 21:69-72
15. Wang BL, Shi WX, Han L et al (2009) Optimization of refrigeration system with gas-injected scroll compressor. Int J Refrig 32(7):1544–1554
16. Heo J, Kang H, Kim Y (2012) Optimum cycle control of a two-stage injection heat pump with a double expansion sub-cooler. Int J Refrig 35(1):58–67
17. Shao SQ, Shi WX, Li XT et al (2004) Performance representation of variable-speed compressor for inverter air conditioners based on experimental data. Int J Refrig 27(8):805–815
18. Ding GL, Zhang CL (2001) Simulation and optimization of refrigeration and air-conditioning system. Science Press, Beijing (in Chinese)
19. Ge YT, Cropper R (2005) Performance evaluations of air-cooled condensers using pure and mixture refrigerants by four-section lumped modelling methods. Appl Therm Eng 25(1):1549–1564
20. Muley A, Manglik RM, Metwally HM (1999) Enhanced heat transfer characteristics of viscous liquid flows in a chevron plate heat exchanger. J Heat Transf 121(4):1011–1017
21. Yan YY, Lin TF (1999) Evaporation heat transfer and pressure drop of refrigerant R-134a in a plate heat exchanger. J Heat Transf 121(1):118–127
22. Han DH, Lee KJ, Kim YH (2003) Experiments on the characteristics of evaporation of R410A in brazed plate heat exchangers with different geometric configurations. Appl Therm Eng 23(10):1209–1225

Chapter 40
Experimental Analysis of Direct Evaporative Cooling in Special Temperature Range and Extended Application Study

Yao Chen, Yonggao Yin and Xiaosong Zhang

Abstract The experiments of one counter-flow direct evaporative cooling (DEC) system have been carried out to investigate the characteristics of heat and mass transfer between air and water in temperature range of 20 to −7 °C. Three kinds of driving forces in DEC are defined and adopted in this paper, while novel evaluation indices are proposed to evaluate the performance of the process. Experimental data under different parameters of air and water are compared and analyzed. The results show that DEC in unconventional-temperature range is more sensitive to driving forces than in normal temperature range. Consequently, energy performance of DEC would be highly influenced driving forces. Furthermore, to making full use of cooling potential of DEC in lower temperature range, a novel evaporative cooling and heat pump-driven liquid desiccant hybrid system is proposed and its performance has been preliminarily studied.

Keywords Low temperature evaporative cooling · Heat and mass transfer · Hybrid refrigeration system · Experimental analysis

40.1 Introduction

Direct evaporative cooling (DEC) is a refrigeration technology that has been widely used in HVAC and other industrial fields with environmental friendly and energy-efficient properties [1, 2]. In most of the previous studies [3, 4], it was often assumed that the air handling process in DEC is adiabatic, and always just concerned the temperature changes of water, moreover the temperatures were fixed in normal range. Actually, in DEC both temperature of air and water are changing.

Y. Chen (✉) · Y. Yin · X. Zhang
School of Energy and Environment, Southeast University, Nanjing, 210096 Jiangsu, China
e-mail: cykeeper@gmail.com

A. Li et al. (eds.), *Proceedings of the 8th International Symposium on Heating, Ventilation and Air Conditioning*, Lecture Notes in Electrical Engineering 262,
DOI: 10.1007/978-3-642-39581-9_40,

When the heat and mass transfer process between water and air with different inlet temperature is happening in a limited contact area. As the air temperature decreases, its enthalpy and wet-bulb temperature are varying, and the air's final state cannot reach completely saturated while the water temperature will continue to reduce until near the wet-bulb temperature of the air. Moreover, compared to normal temperature condition (20–35 °C), the characteristics of heat and mass transfer of DEC in the temperature range of 0–20 °C or even lower interval are changed.

The cooling capacity of DEC is produced by the direct contacts of process air and water, thus the change characteristics of heat and mass transfer between water and air have a great impact on the energy efficiency of DEC. Besides the technique not only can be used for the preparation of cold air, but also can be simultaneously used for the preparation of chilled-water. In addition, for many technology fields like ice production, there is still great value of DEC in very low temperature range [5]. Therefore, the purpose of this study is to obtain the characteristics of DEC that in low temperature range by focus on the influence of different driving forces and to explore its extended application.

Based on the analysis above, in this paper, experiments of one counter-flow DEC system are carried out in a psychrometric chamber to test its different reactions to the variety of driving forces with temperature range of 20 to −7 °C. Experimental results under different parameters are compared and analyzed. Combined with experimental data, the enhancement of the system performance and potential of water temperature drop are investigated. Furthermore, a novel liquid desiccant evaporative cooling water chiller is constructed, and its performance is preliminarily studied.

40.2 Characteristics of Unconventional-Temperature DEC

40.2.1 Experimental System and Procedure

The counter-flow DEC apparatus is shown in Fig. 40.1, which primarily consists of three parts: water circulation system, air system, and evaporative cooler. On the upper portion of the evaporative cooler is a water distribution groove, to guarantee the circulating water can flow down uniformly. In order to reduce its heat exchange outside effectively, the outer wall of evaporative coolers covers with insulation material. For the two thermostatic water tanks, they can both be used as feed/recovery tank and switching between each other. The porous filler placed in the middle of the evaporative cooler, as one core component where air is cooled and humidified. The filler is made of the alumina (Al_2O_3) ceramic foam block of 30 PPI, and its bottom size is 0.3 × 0.3 m with 0.275 × 0.275 m top surface dimensions, 0.1 m high, and the porosity comes to 85 %.

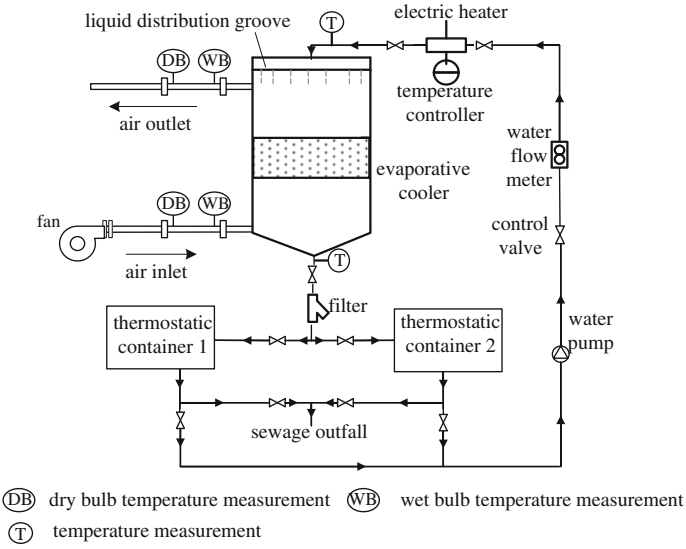

Fig. 40.1 The schematic diagram of the test system

Experimental monitoring systems: The imported HMT330 temperature and humidity-sensing instrument is utilized to measure the instantaneous value of the dry and wet-bulb temperature. The air flow rates through the evaporative cooler is calculated by the nozzle differential pressure across and in the front of the main-induced draft fan placed in the environmental chamber. Meanwhile the accuracy of the differential pressure transmitter of the measuring nozzle is ±0.3 %. Water flow is measured by the meter (accuracy of ± 1 $L{\cdot}h^{-1}$) while its temperature is adjusted by the thermostat and heater, besides it is measured by Pt-100 platinum resistance. Pt-100 platinum resistance measurement range is 0–100 °C with an accuracy of 0.1 °C. All measured data are collected by the 34970A data acquisition instrument and put into computer for analysis.

The experiments aimed at investigating the principle and characteristics of DEC under unconventional-temperature range. Therefore, the experiments process was divided into two parts: the evaporative cooling stage (20–0 °C) and the evaporative freezing stage (0 to −7 °C). By changing the states of inlet air and water, different sets of driving forces were reflected. The entire experimental apparatus sited in an environmental chamber, for ensuring the stability of the parameters of the test. While the enthalpy difference method was used to control and adjust the temperature of inlet air, its flow rates can be controlled by changing the frequency of draft fan. For the inlet water, its temperature and flow rates were controlled through the thermostat tank and the water pipeline valve connected with the water flow meter, respectively. Finally, the inlet and outlet air's dry bulb temperature and wet-bulb temperature, flow rates, as well as the inlet and outlet water's temperature and flow rates were all measured.

40.2.2 Experiment Test and Discussion

The conditions of the reference cases are selected as listed in Table 40.1, which are marked out by dots on each figure in the following graphs. During the experiment, we changed the state of the inlet air, and reduced its temperature slowly, correspondingly controlled the temperature of the imported water, and make sure it was always slightly higher than the wet-bulb temperature of the air and substantially consistent with the decrease of the air temperature during the evaporative cooling stage. However, the subcooled state of water is hard to maintain, so for the evaporative freezing stage the temperature of the imported water was kept at 3.46 °C. Besides, the mass flow rate of the air and water were maintained at 0.09 and 0.02 $kg{\cdot}s^{-1}$ as constants, respectively.

40.2.2.1 Definition of Driving Forces and Evaluation Indices

There are many difference driving forces during the heat and mass transfer process between air and water. Three driving forces in DEC are adopted in this paper, which can mainly describe the characteristics of the process. The heat transfer driving force is temperature difference between air and water $(\Delta T = |T_a - T_w|)$, and the mass transfer driving force is the water vapor partial pressure difference between saturated air which is in equilibrium with water and process air $\left(\Delta p = p_{\mathrm{Tw,equ}} - p_a\right)$ while the total heat and mass transfer driving force is their enthalpy difference $\left(\Delta h = h_{\mathrm{Tw,equ}} - h_a\right)$.

Energy performance of the DEC is a major concern, while in various temperature ranges its evaluation index should be different. For evaporative cooling stage, evaporative cooling efficiency ($\eta_{a,\mathrm{DEC}}$) is a widely used index for evaluating the actual heat transfer performance of DEC, and it is defined by Eq.(40.1). However, this index is only suitable when the temperature of air drops and ignoring the temperature change of water. As for evaporative freezing stage, the temperature of air is increasing and the focus of this stage ought to be the temperature decrease of water. Therefore, a new evaporative cooling efficiency ($\eta_{w,\mathrm{DEC}}$), as defined by

Table 40.1 Experiment parameters for reference cases

	Evaporative cooling stage					Evaporative freezing stage				
Temp.range(°C)	20 to 0					0 to −7				
Typical data sets(No.)	1	2	3	4	5	1	2	3	4	5
Inlet air conditions										
Dry bulb temp.(°C)	14.4	8.2	4.8	2.9	1.4	−0.5	−1.1	−2.5	−3.5	−4.0
Wet-bulb temp.(°C)	11.7	6.4	2.5	−0.04	−0.8	−2.7	−3.2	−3.9	−4.5	−5.1
Inlet water conditions										
Temp.(°C)	13.6	7.6	3.8	2.0	1.3			3.46		

Eq.(40.2), is created to analysis the energy efficiency of evaporative freezing stage from water side.

$$\eta_{a,\mathrm{DEC}} = \frac{T_{a,\mathrm{in}} - T_{a,\mathrm{out}}}{T_{a,\mathrm{in}} - T_{a,s}} \times 100\ \% \tag{40.1}$$

$$\eta_{w,\mathrm{DEC}} = \frac{T_{w,\mathrm{in}} - T_{w,\mathrm{out}}}{T_{w,\mathrm{in}} - T_{a,s}} \times 100\ \% \tag{40.2}$$

where $T_{a,\mathrm{in}}$ and $T_{a,\mathrm{out}}$ stand for inlet and outlet air dry bulb temperature, respectively; $T_{a,s}$ is the air wet-bulb temperature; $T_{w,\mathrm{in}}$ and $T_{w,\mathrm{out}}$ symbolize the inlet and outlet water temperature, respectively.

In DEC, from evaporative cooling stage to evaporative freezing stage the total heat and mass transfer driving force is the same. It can be described as the enthalpy difference between process air and saturated air that is in equilibrium with water. Therefore, the enthalpy efficiency of evaporative cooling (η_h) can indicate validity of heat and mass transfer, and the η_h has a comprehensive reaction of the temperature efficiency and mass transfer efficiency of DEC. The definition of the enthalpy efficiency in DEC is shown as Eq.(40.3):

$$\eta_h = \frac{h_{a,\mathrm{in}} - h_{a,\mathrm{out}}}{h_{a,\mathrm{in}} - h_{T_{w,\mathrm{equ}}}} \times 100\ \% \tag{40.3}$$

where $h_{a,\mathrm{in}}$ and $h_{a,\mathrm{out}}$ stand for inlet and outlet air enthalpy, respectively; $h_{Tw,\mathrm{equ}}$ is the enthalpy of saturated air which is in equilibrium with water.

40.2.2.2 Results and Discussion

Based on the above principle, the typical experimental results of the evaporative cooling stage and evaporative freezing stage are summarized below. By using the evaluation indices defined the influence of driving forces on DEC in unconventional-temperature ranges are analyzed and the characteristics of DEC are discussed.

Figure 40.2 shows the effects of temperature difference between inlet air and water on evaporative cooling efficiency. As can be seen from the curve of Fig. 40.2a, in evaporative cooling stage, with the increase of the temperature difference between air and water, the $\eta_{a,\mathrm{DEC}}$ increases significantly. Consequently, the improvement of the efficiency of evaporative cooling can be simply realized by appropriately increasing the temperature difference between inlet air and water. Comparatively, as shown in Fig. 40.2b, in evaporative cooling stage, as the heat transfer driving force strengthen the $\eta_{w,\mathrm{DEC}}$ is also markedly increased, hence, the water temperature would fall more closely to the air wet-bulb temperature. To sum up, the cooling and freezing efficiency of DEC is very sensitive to changes of the heat transfer driving force.

The relationship between the increment of the mass transfer driving force and air humidity ratio (Δd) are shown in Fig. 40.3. Obviously, the two ones are visible

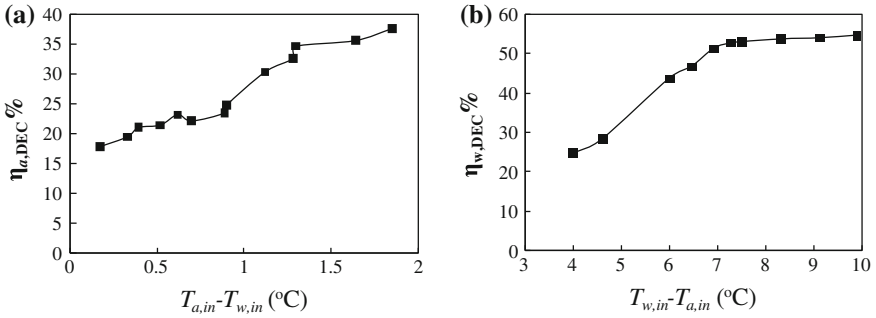

Fig. 40.2 Influence of $\triangle T$ on the cooling efficiency

corresponding to each other, the air humidification has a significant increase with the mass transfer driving force enhance. Although in evaporative cooling and freezing stage the tendencies of the curves are the same, the air humidity ratio of the latter is much lower. This is because at the same relative humidity (RH), the absolute humidity of air in evaporative cooling stage is much higher than in evaporative freezing stage. Taking RH at 95 % for example, the absolute humidity of air in 10 °C is 4.1 g·kg^{-1} higher than in −2 °C. For all this, DEC has a close connection with variations of the mass transfer driving force.

Figure 40.4 demonstrates that the influence of enthalpy difference driving force on enthalpy efficiency and water temperature drop. The data curve of η_h in evaporative cooling stage shows that the enthalpy efficiency had a significant increase when the driving forces become larger. However, in evaporative freezing stage, the numerical values of η_h are fluctuant, and the reason for these changes is complicated. First, when the enthalpy difference increased from 5.83 to 13.47 kJ·kg^{-1}, the cooling effect cannot go so far as to make water temperature below 0 °C, and the enthalpy efficiency increases smoothly. Then, as the enthalpy

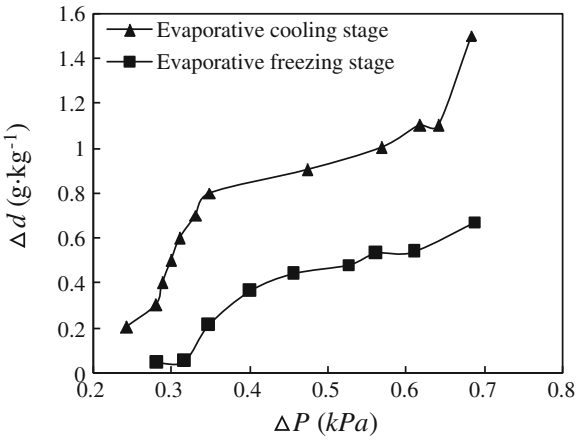

Fig. 40.3 Influence of $\triangle p$ on the air humidity

difference continues to rise, the inlet water temperature become too low (below −3.4 °C), as a result, the water are cooled to subcooled state (0 to −3.4 °C). Moreover, in the experimental apparatus, the flow disturbance is unstable, the subcooled state of water will release and then water freezes in the filler. Thus, the water–ice crystals retard the heat and mass transfer process, at the same time the enthalpy efficiency decline. This is why in evaporative freezing stage the enthalpy efficiency is fluctuated as the enthalpy difference driving force growing. In general, in the lower temperature range, the overall enthalpy efficiency of DEC is not high, which means that the heat and mass transfer between air and water is not completely. Even so, from Fig. 40.4, it can still learn that with the increase of driving force of enthalpy difference, the decrease of the water temperature in the lower temperature range are still apparent and continuous.

The changes of enthalpy efficiency across the entire process from the normal temperature range to the lower temperature interval are shown in Fig. 40.5. The experiment data of 20–35 °C are introduced from the work of Wang [6] and Chen [7]. When the driving force of enthalpy difference is 9.5 and 14.8 kJ·kg^{-1}, in normal temperature range of 20.0–35.0 °C, enthalpy efficiency has tiny fluctuations between 16.11–18.04 kJ·kg^{-1} and 19.75–19.58 kJ·kg^{-1}, respectively. Comparatively, while in lower temperature interval of 20.0 to −5.0 °C, the enthalpy efficiency significantly elevate from 5.38 to 16.11 kJ·kg^{-1} and reduce from 26.48 to 19.75 kJ·kg^{-1}, respectively. Therefore, Fig. 40.5 intuitively shows that in DEC the change of enthalpy efficiency caused by the driving force of enthalpy difference in lower temperature range is much larger than that in normal temperature range. In addition, it can be seen from the two curves, while the driving force of enthalpy difference remains constant, with the temperature increase, the enthalpy efficiency changes with nondeterminacy. That is, it may increase or reduce. This is because there is complex correlation between the enthalpy difference of the import and export of air $\left(\left|h_{a,\text{in}} - h_{a,\text{out}}\right|\right)$ and the overall experimental parameters. However, it

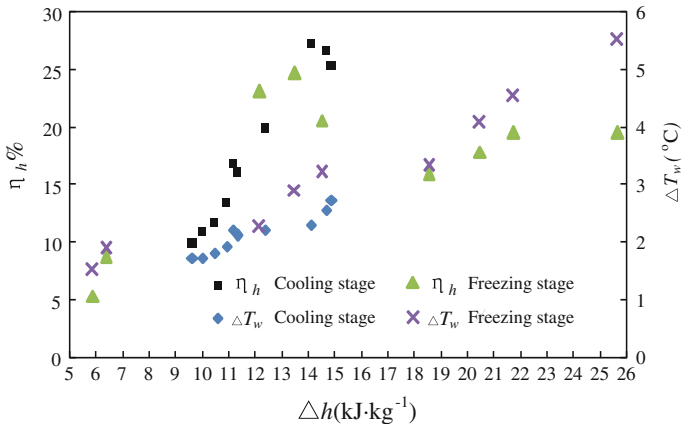

Fig. 40.4 Influence of $\triangle h$ on the enthalpy efficiency and water temperature drop

can be sure that with the same increment of the enthalpy difference (5.3 kJ·kg^{-1}), the average variation value of enthalpy efficiency (the vertical distance between the two curves) in lower temperature range is much greater than that in normal temperature range.

Although efficiencies of DEC in lower temperature range are much lower than that in normal temperature range, the purposes of them are not the same, so the evaluation indices should be different, too. The main use of the latter one is to cool the air with water evaporative effect, so it focuses on the level of efficiency of the evaporative cooling. While the former one is mainly aims at continually making use of the potential of heat and mass transfer of both air and water, in order to achieve sustained decrease of water temperature. Characteristics of unconventional-temperature DEC is that it is more sensitive to driving forces than that of in normal temperature range. Therefore, it is very beneficial to the study of heat and mass transfer processes. Subtle changes in experimental conditions will lead to large changes of parameters and experimental results, which is very favorable to analyze heat and mass transfer characteristics and development of their potential.

40.3 Application Prospects of Performance in Lower Temperature Conditions

40.3.1 The Potential of Temperature Drop

The purpose of evaporative cooling under lower temperature condition is making use of heat and mass transfer potential of the air and water, thereby continually to reduce the temperature of the air and water at the same time, even up to icing condition. Table 40.1 and experiment results above show that when the inlet water temperature is controlled lower than the inlet air dry bulb temperature and higher than the wet-bulb temperature, the outlet temperature of the air steadily reduce in each segment of the temperature. In theory, the temperatures of air would finally in

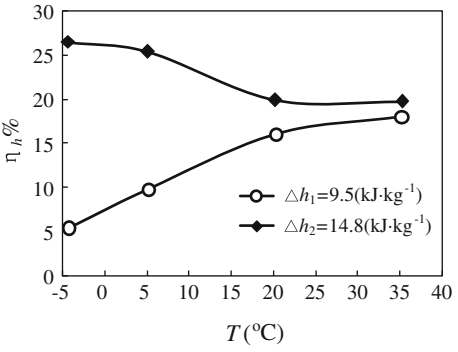

Fig. 40.5 Influence of Δh on the enthalpy efficiency in all temperature range

equilibrium with water if the process continues all the time. Besides, there are many studies related to the temperature drop of air in DEC [8, 9].

Table 40.2 complements the data in Table 40.1 while in line with the typical data sets number, and based on that to analyze changes of the water temperature. In working condition 1, the water temperature could be reduced closely to 11.7 °C theoretically, but the experimental result is 13.2 °C, this is mainly due to the high inlet air relative humidity. In working condition 2 and 3, the relative humidity of air has been reduced that making the temperature drop of outlet water is more evident than that in working condition 1, and the outlet water temperature is 6.7 and 2.8 °C, respectively. In working condition 4 and 5, the relative humidity of the air is already so low and the wet-bulb temperature is corresponding low enough, even below 0 °C. However, this make the water temperature still be able to reduce even when it is already seemed low enough. At the same time, the relative humidity of the air determines the water vapor partial pressure of the air. Table 40.2 shows that with higher relative humidity, the water vapor partial pressure of the air is much closer to the water vapor partial pressure of saturated air that is in equilibrium with water. This means that the driving force of mass transfer between air and water will reduce, and it is disadvantageous for the mass transfer process between air and water.

The above analysis indicates that appropriately reducing the relative humidity of the inlet air is useful for the performance upgrade of evaporative cooling in lower temperature range. Therefore, it can make use of the dehumidification cycle to reduce the humidity ratio of the air, in order to provide ideal conditions for the evaporative cooling. In addition, the potential of temperature drop of DEC can be fully tapped by combining it with a dehumidification thermodynamic cycle.

40.3.2 Evaporative Cooling and Heat Pump Driven Liquid Desiccant Hybrid System

40.3.2.1 Advanced System Introduction

Evaporative cooling process in lower temperature range not only can make cold air but also chilled-water. Moreover, the whole refrigeration process has no refrigerant and low energy consumption. These characteristics make it useful in a variety of refrigeration systems and air conditioning systems, and in particular, it

Table 40.2 Inlet parameters of lower temperature range

No.	1	2	3	4	5
RH	73.3 %	67.4 %	66.1 %	53.9 %	62.6 %
$T_{a,s}$/°C	11.7	6.4	2.5	−0.04	−0.8
$P_{a,\text{in}}$/kPa	1.203	0.733	0.569	0.406	0.423
$P_{\text{Tw,equ}}$/kPa	1.558	1.044	0.802	0.706	0.671

can play a huge role in the chilled-water producing systems. In order to utilize the refrigerating capacity of DEC in lower temperature range, one system of evaporative cooling and heat pump driven liquid desiccant water chiller is designed and shown in Fig. 40.6.

The principle of the system is as follows: First, the liquid desiccant dehumidification cycle is used to reduce the humidity ratio of the air. After that, the dry air and water complete the heat and mass transfer process in evaporative cooler, then temperature of air and water reduced simultaneously. As the circulation continues, the air with lower temperature and higher humidity ratio is delivered to dehumidifier to remove moisture again, and then fed back to the evaporation cooler, and contact with the cooling water. In the evaporative cooler, due to the continuous cycle of the cooling water and the dry air, the temperature would all decrease unceasingly. Consequently, the purpose of producing chilled-water is achieved. In this system, the cooling capacity of the vapor compression refrigeration cycle is used to cooling liquid desiccant, and its condenser heat is used for liquid desiccant regeneration. Therefore, the dehumidification and regeneration ability of the entire cycle also has been strengthened.

40.3.2.2 Preliminary Experiment

According to the system designed above, preliminary experiment of the evaporative cooling and heat pump driven liquid desiccant hybrid system has been done, some judgment about the performance of entire apparatus is made, and the results are shown in Fig. 40.7. It can be seen that the temperature of inlet and outlet air has a fluctuated decline tendency. The reason for this is that, there is temperature drop when the air went through the evaporator, then the air carry though the liquid desiccant dehumidification process and this process lead to certain temperature

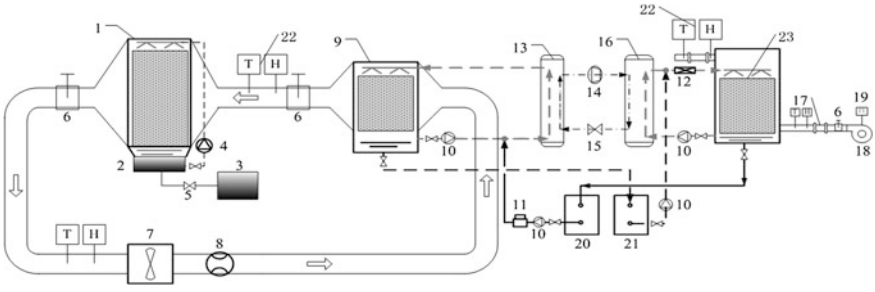

Fig. 40.6 Schematic diagram of evaporative cooling and heat pump driven liquid desiccant hybrid system 1. Evaporative cooler 2. water tank 3. frozen water tank 4. circulating pump 5. cut-off valve 6. wind valve 7. fan 8. air flow meter 9. dehumidifier 10. solution pump 11. micro flow meter 12. electric heater 13. evaporator 14. compressor 15. expansion valve 16. condenser 17. gas turbine flowmeter 18. centrifugal fan 19. inverter 20. concentrated solution of barrel 21. dilute solution bucket 22. *T*, *H* temperature and humidity sensors 23. regenerator

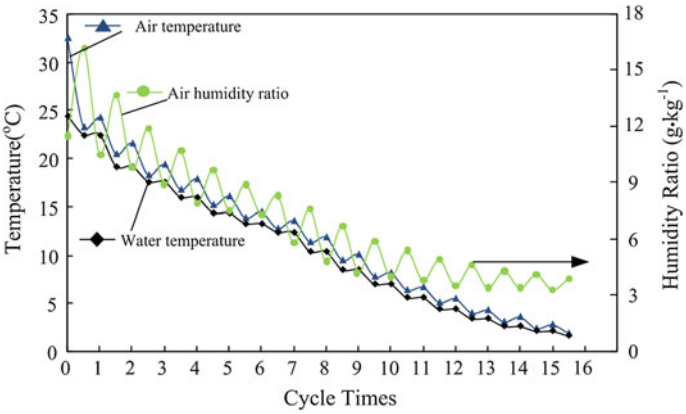

Fig. 40.7 Preliminary experiment result

recovery of the air. The comprehensive variation of air humidity ratio between the evaporator and dehumidifier shows that when the air goes through the evaporator and absorbs water, accordingly the humidity ratio would increase significantly. Therefore, in order to ensure that the evaporative cooling cycle proceed, the air has to be sent to the liquid desiccant dehumidifier, these its humidity ratio is reduced to original level or even lower. In evaporator, due to the continuous cycle of the dry air, the temperature of water decreases reposefully. Preliminary experimental results show that evaporative cooling and liquid desiccant hybrid cycle can successfully meet the purpose of producing low temperature air and chilled-water.

40.4 Conclusion

In this paper, experiments of DEC in unconventional-temperature range were carried out to investigate its principle and characteristics. Furthermore, the potential of temperature drop of these special processes were analyzed. Finally, a novel liquid desiccant evaporative cooling water chiller was proposed and its performance had been preliminarily studied, and the following conclusions can be obtained:

1. Characteristic of DEC in unconventional-temperature range (20 to −7 °C) is that it is more sensitive to driving forces than in normal temperature range. Consequently, energy performance of DEC will be highly influenced by changes of heat transfer, mass transfer, and enthalpy difference driving force.
2. The novel liquid desiccant evaporative cooling water chiller can take full advantage of the cooling potential of DEC. The preliminary study of its operating characteristics showed that this hybrid system is capable of producing chilled-water and cold air simultaneously and efficiently.

Acknowledgments This work is supported by the 12th Five Year Science and Technology Support Key Project of China (No.2011BAJ03B14) and Natural Science Foundation of China (key project No.51036001).

References

1. Khandelwal A, Talukdar P, Jain S (2011) Energy savings in a building using regenerative evaporative cooling. Energy Build 43:581–591
2. Maerefat M, Haghighi AP (2010) Natural cooling of stand-alone houses using solar chimney and evaporative cooling cavity. Renew Energy 35:2040–2052
3. Wu JM, Huang X, Zhang H (2009) Theoretical analysis on heat and mass transfer in a direct evaporative cooler. Appl Therm Eng 29:980–984
4. Chenguang Sheng AG, Nnanna A (2012) Empirical correlation of cooling efficiency and transport phenomena of direct evaporative cooler. Appl Therm Eng 40:48–55
5. Li X-W, Zhang X-S, Cao R-Q, Fu X-Z (2009) A novel ice slurry producing system: producing ice by utilizing inner waste heat. Energy Convers Manage 50:2893–2904
6. Wang G, Zhang X, Chen Y, Xu G (2012) Experimental study on heat and mass transfer characteristics in evaporative cooler with ceramic foam packings. J Southeast Univ (Natural Science Edition) 42:457–462 (in Chinese)
7. Chen Y, Yin Y, Zhang X, Wang G (2013) Characteristics of heat and mass transfer in direct evaporative cooling process with different temperature range. CIESC J 64:1532–1540 (in Chinese)
8. Heidarinejad G, Farahani MF, Delfani S (2010) Investigation of a hybrid system of nocturnal radiative cooling and direct evaporative cooling. Build Environ 45:1521–1528
9. Camargo JR, Ebinuma CD, Silveira JL (2005) Experimental performance of a direct evaporative cooler operating during summer in a Brazilian city. Int J Refrig 28:1124–1132

Chapter 41
Hydraulic and Thermodynamic Condition Analysis of Unidirectional Loop Hot Water Heating System

Shanshan Cao, Yang Yao, Hua Zhao and Huanhuan Li

Abstract A novel unidirectional loop hot water heating system has been proposed in order to improve the adaptability of the district heating system heat load growth and improve system hydraulic stability. There are four parts in this paper. The composition of the new system was introduced in this paper firstly. The hydraulic design and condition were discussed secondly. Then the thermal condition including node temperature calculation and local regulation mode were studied. In the end, a case study was done to analyze the hydraulic and thermodynamic condition during the operation. The results showed that the new system had straightforward hydraulic and thermal condition. Through this research, some reference could be provided for the practical application of the unidirectional loop hot water heating system.

Keywords Hydraulic condition · Thermodynamic condition · Unidirectional loop hot water heating system

41.1 Introduction

District heating has been developed a lot in China; however, there are still some questions in application. It takes large square to lay the supply and return pipelines of heating network which hinders the application of district heating in some crowd old cities. Complicated hydraulic condition of multi-source heating systems and distributed pump systems limit the utilization of modern technology. And there are still many other similar questions. Under this circumstance, unidirectional loop hot water heating system has been proposed by researchers [1–4].

S. Cao (✉) · Y. Yao · H. Zhao · H. Li
Scool of Municipal and Environmental Enginneering, Harbin Institute of Technology, Harbin 150090, China
e-mail: css_2005@126.com

A. Li et al. (eds.), *Proceedings of the 8th International Symposium on Heating, Ventilation and Air Conditioning*, Lecture Notes in Electrical Engineering 262,
DOI: 10.1007/978-3-642-39581-9_41,

It is significant to study the hydraulic condition and thermodynamic condition in application of the unidirectional loop hot water heating system.

41.2 System Description

In traditional heating systems, heat medium is sent to the heat user by the supply pipe, then return to the heat source by the return pipe after exchange heat with the heat users' heat transfer equipment. In the new system, the heat users are series connection. There is only one direction of the heat medium flow in the new district heating system which is the reason why it is called unidirectional ring hot water heating system. Unidirectional loop hot water heating system is network which transports the heat from the heat source to the heat users and return heat source, the main pipeline is not only supply pipe but also return pipe. Both single heat source and multi-heat source can be applied in the system. System schematic is shown in Figs. 41.1 and 41.2.

41.3 Hydraulic Condition Analysis

Hydraulic condition is relatively stable compared with traditional dual pipe system. In unidirectional loop hot water heating system, the main pipeline flow is constant when users' local condition changes.

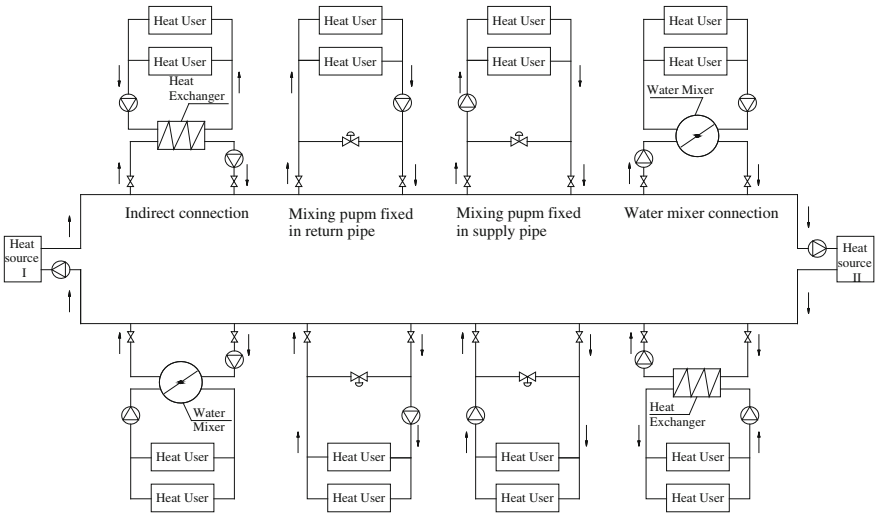

Fig. 41.1 System diagram of single loop dual heat source unidirectional loop hot water heating system

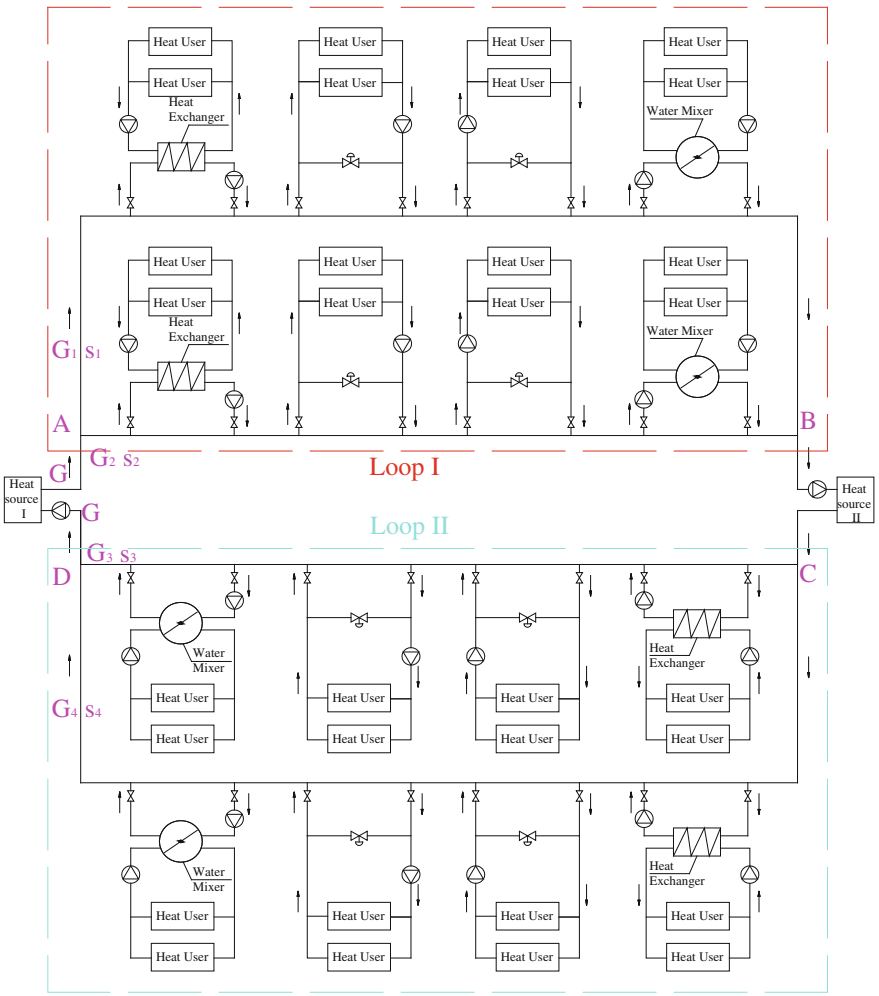

Fig. 41.2 System diagram of double loop dual heat source unidirectional loop hot water heating system

41.3.1 Hydraulic Condition of Main Pipeline

Assuming that the parallel pipe lines have the same temperature drop, and the start and end temperatures are, respectively, same at the beginning. Take system shown in Fig. 41.2 for example. Assume that design temperature of point A and C is 130 °C, design temperature of point B and D is 70 °C. Given that design load of each pipeline is known, the design flow of each pipeline can be can be calculated by (41.1).

$$G = \frac{Q}{\Delta t} \tag{41.1}$$

where G (t/h) is design flow of each parallel pipeline, Q (kW) is design heat load of each parallel pipeline, Δt is design temperature difference of heat source.

Pressure drop of main pipeline can be calculated by equations as follows:

$$\Delta P = R(l + l_d) = sG^2 \tag{41.2}$$

$$s = 6.88 \times 10^{-3} \frac{K^{0.25}}{(\rho d)^{5.25}} (l + l_d) \tag{41.3}$$

$$R = 6.88 \times 10^{-3} K^{0.25} \frac{G^2}{\rho d^{5.25}} \tag{41.4}$$

where ΔP (Pa) is pressure reduce of calculated pipe, R (Pa/m) is specific frictional resistance of calculated pipe, l (m) is length of calculated pipe, l_d (m) is equivalent length of local resistance, s (Pa/(m^3/h)^2) is resistant value of calculated pipe, G (m^3/h)^2 is flow of calculated pipe, K (m) is equivalent absolute roughness, d (m) is inside diameter of calculated pipe, ρ (kg/m^3) is density of hot water.

Different from dual pipeline systems, there is only one main pipeline, so pressure drop is smaller. The pressure level of total system can be reduced.

For double loop systems, flow adjustment should be done by the principle that node flow is constant and loop pressure drop is zero. Take Fig. 41.2 for example. For loop I,

$$\begin{cases} G_1 + G_2 = G \\ s_1 G_1^2 - s_2 G_2^2 = 0 \end{cases} \tag{41.5}$$

For loop II,

$$\begin{cases} G_3 + G_4 = G \\ s_3 G_3^2 - s_4 G_4^2 = 0 \end{cases} \tag{41.6}$$

41.3.2 Hydraulic Condition of Thermal Stations

As shown in Figs. 41.1 and 41.2, the connection mode in unidirectional loop hot water heating system may be indirect connection and mixing connection. The application of each mode is analyzed below.

41.3.2.1 Indirect Connection Mode

Indirect connection can be applied to the users near the heat source. Initial invest of the connection mode is higher, the thermal stations need more space, there are large heat loss and high maintenance costs. For heating system with high-rise buildings or complex terrain, it is necessary to apply indirect connection in order to guarantee the system safety (Fig. 41.3).

41.3.2.2 Mixing Connection Mode

In unidirectional loop hot water heating system, mixing pump can be fixed in supply pipe and return pipe, system and pressure diagrams are shown in Figs. 41.4, and 41.5. As pressure difference between point 1 and 8 is very small, it can be ignored during calculation.

41.4 Thermodynamic Condition Analysis

In unidirectional loop hot water heating system, heat medium goes through the users successively, so node temperature reduces along the main pipe in turn (see Fig. 41.6). Node temperature calculation formulas are as follows:

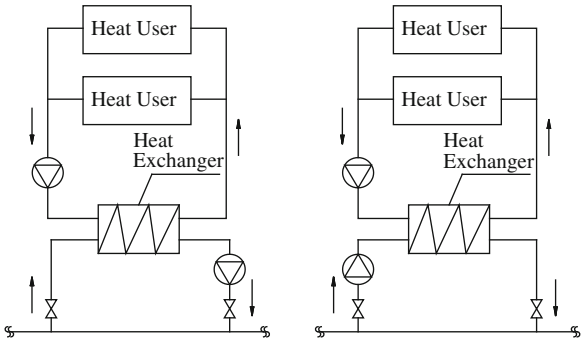

Fig. 41.3 Indirect connection

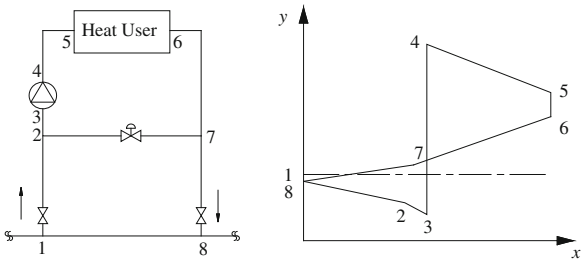

Fig. 41.4 System and pressure diagram when mixing pump fixed in supply pipe

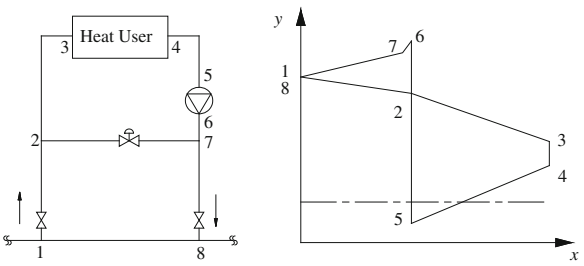

Fig. 41.5 System and pressure diagram when mixing pump fixed in return pipe

$$G = \frac{0.86Q_i}{\tau_{i+1} - \tau_i} \tag{41.7}$$

$$\tau_{i+1} = \tau_i - \frac{0.86Q_i}{G} \tag{41.8}$$

where τ_i (°C) is the ith heat users' supply node temperature (when i=1, the temperature is heat source supply temperature), τ_{i+1} (°C) is $(i + 1)$th heat users' supply node temperature, G (t/h) is heating system's total flow, Q_i (kW) is ith heat users load which changes with outdoor temperature.

It can be seen from (41.8), τ_i is always related to Q_i. When Q_i increases or decreases, τ_{i+1} reduces or increases separately.

For mixing system, calculation formula of mixing ratio is shown in (41.9).

$$u_i = \frac{G_{\mathrm{hi}}}{G_{0i}} \tag{41.9}$$

According to Fig. 41.6, thermal balance equation can be obtained as follows:

$$cG_{0i}\tau_i + cG_{\mathrm{hi}}t_{\mathrm{hi}} = cG_{\mathrm{gi}}t_{\mathrm{gi}} \tag{41.10}$$

So

$$u_i = \frac{\tau_i - t_{\mathrm{gi}}}{t_{\mathrm{gi}} - t_{\mathrm{hi}}} \tag{41.11}$$

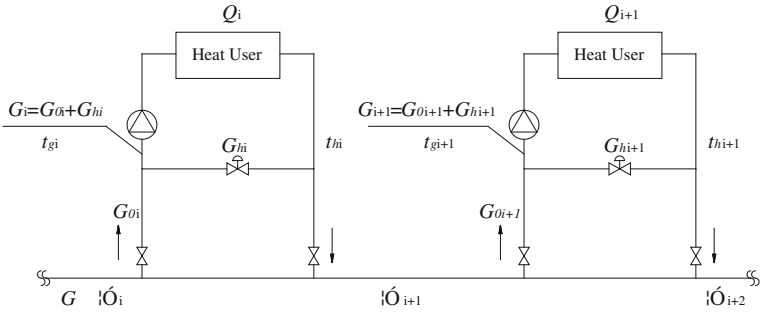

Fig. 41.6 Mixing connection mode in unidirectional loop hot water system

where u_i is the ith heat users' mixing ratio, G_{hi} (t/h) and G_{0i} (t/h) separately represents secondary side return water flow and primary side supply water flow of the ith heat user, t_{gi} (°C) and t_{hi} (°C) separately represent secondary side supply and return water temperature of the ith heat user.

41.5 Case Study

Take system shown in Fig. 41.7 for example. The system is located in Harbin. The total area is 16000000 m^2, each users' area is 200000 m^2. Heat source I and II separately carry half of the total heat load. Primary supply and return temperature is 130/70 °C, secondary supply and return temperature are 60/50 °C.

The thermal parameters under design condition can be calculated by (41.7), (41.8), and (41.11). The results are shown in Table 41.1.

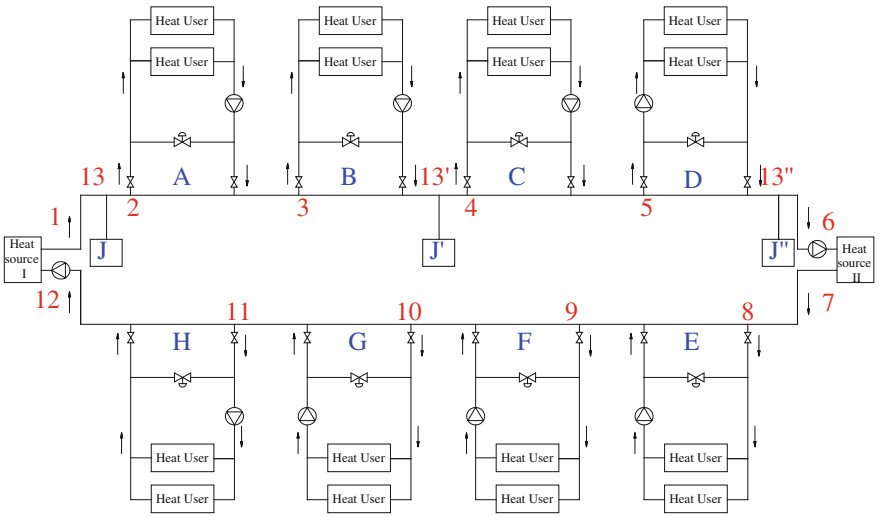

Fig. 41.7 A unidirectional loop hot water heating system with 8 users and dual heat source

Table 41.1 Thermal parameters under design condition

Node	Node temperature (°C)	Mixing ratio	Node	Node temperature (°C)	Mixing ratio
1	130	–	7	130	–
2	130	7	8	130	7
3	115	5.5	9	115	5.5
4	100	4	10	100	4
5	85	2.5	11	85	2.5
6	70	–	12	70	–

41.5.1 Adding Users Condition

If add user J whose area is 200000 m^2 wherever in the system, the total flow keeps constant so that the hydraulic condition of main pipeline is nearly stable. However, the thermodynamic condition should be analyzed renewedly.

Calculate the thermal parameters under the three circumstances that user J is located between heat source I and user A, between A and C, and between D and heat source II. The results are shown in Table 41.2.

It can be seen from Table 41.2 that when adding new user, the operation condition of users before the new one keep constant, the node temperature and mixing ratio of users after the new one reduce. Especially, when the new users became the last user, the node temperature may not meet the users supply temperature need. At this time, it needs to improve the supply temperature or flow of heating system.

41.5.2 Cutting Users Condition

If some users have to be turn off for operation failure or other reasons, the total flow keeps constant so that the hydraulic condition of main pipeline is nearly stable. Now, the thermodynamic condition should be analyzed too.

Table 41.2 Thermal parameters after adding user J

Node	Design condition		Adding J		Adding J′		Adding J″	
	Node temperature (°C)	Mixing ratio	Node temperature (°C)	Mixing ratio	Node temperature (°C)	Mixing ratio	Node temperature (°C)	Mixing ratio
1	130	–	130		130		130	
13			130	7				
2	130	7	115	5.5	130	7	130	7
3	115	5.5	100	4	115	5.5	115	5.5
13′					100	4	100	4
4	100	4	85	2.5	85	2.5	85	2.5
5	85	2.5	70	1	70	1	70	1
13″							55	
6	70	–	55	–	55			
7	130	–	130	–	130	–	130	–
8	130	7	130	7	130	7	130	7
9	115	5.5	115	5.5	115	5.5	115	5.5
10	100	4	100	4	100	4	100	4
11	85	2.5	85	2.5	85	2.5	85	2.5
12	70	–	70	–	70	–	70	–

Table 41.3 Thermal parameters after adding user J

Node	Design condition		Cutting A		Cutting B		Cutting D	
	Node temperature (°C)	Mixing ratio	Node temperature (°C)	Mixing ratio	Node temperature (°C)	Mixing ratio	Node temperature (°C)	Mixing ratio
1	130	–	130		130		130	
2	130	7	130		130	7	130	7
3	115	5.5	130	7	115		115	5.5
4	100	4	115	5.5	115	5.5	100	4
5	85	2.5	100	4	100	4	85	
6	70	–	85	–	85		85	
7	130	–	130	–	130	–	130	–
8	130	7	130	7	130	7	130	7
9	115	5.5	115	5.5	115	5.5	115	5.5
10	100	4	100	4	100	4	100	4
11	85	2.5	85	2.5	85	2.5	85	2.5
12	70	–	70	–	70	–	70	–

Calculate the thermal parameters under the three circumstances that cutting user A or B or D. The results are shown in Table 41.3.

It can be seen from Table 41.3 that when cutting some user, the operation condition of users before the new one keep constant, the node temperature and mixing ratio of users after the new one increase.

41.6 Conclusion

Hydraulic and thermodynamic condition of unidirectional loop hot water heating system were analyzed in this paper and some conclusions were obtained.

Equal temperature drop method was introduced to solve the hydraulic calculation. Thermodynamic calculation equations were established by energy conservation equation.

Through the case study, it can be seen that hydraulic condition of unidirectional loop hot water heating system was relatively constant. When users' local conditions changed, the main pipeline's flow kept unchanged. Therefore, users in the new system are independent in hydraulic condition which makes local regulation become easy.

As for thermodynamic conditions, if one user changed, the rest users after the user changed consequently. It may happen that heat load increased so much that the node temperature of end users dropped even lower than their design temperature. Therefore, further study on thermodynamic condition should be done to make sure the system meet the users' temperature need.

Through this research, some reference could be provided for the practical application of the unidirectional loop hot water heating system.

Acknowledgments This study is supported by the '125 Project' of China (No. 2012BAJ04B01) and (No. 2011BAJ05B04).

References

1. Wang Y (2008) The one-pipe centralized heating system and comparison analysis. Dissertation for the Master Degree in Engineering of Taiyuan University of Technology
2. Zhang Z (2010). Study on the design method of the single-pipe water mixing directly connecting heating. Dissertation for the Master Degree in Engineering of Taiyuan University of Technology
3. Luo L (2012) The single-pipe heating system and applied research. Dissertation for the Master Degree in Engineering of Taiyuan University of Technology
4. Ji M (2012). Research on cascade mixing water heating system. Dissertation for the Master Degree in Engineering of Harbin Institute of Technology

Chapter 42
Experimental Study on Measuring the Amount of Jet Entrainment by the Tracer Gas Concentration Method

Xin Wang, Youqin Liu and Yuntian Dai

Abstract The jet entrainment from motional air to the ambient stationary air is one of the important characteristics for jet airstream. Entrainment can change its internal distribution of temperature, velocity, jet flow, and energy distribution, which are closely related with the engineering design of ventilation and air conditioning. Thereby, it is significant to quantify the amount of jet entrainment which is caused by nozzle jet from the ambient air in an air-conditioning room. Basing on the basic theory of fluid mechanics, we had proposed a measurement method of jet entrainment by the tracer gas. In this paper, we have made an experimental study in a constant temperature and humidity laboratory to measure and calculate the entrainment for the air conditioning jet motion, compared the results to the traditional method of velocity measurement, and predicted the related factors of the jet entrainment.

Keywords Jet entrainment · Experimental study · Gas concentration method

42.1 Introduction

Large space buildings often adopt stratified air-conditioning system and the nozzle side airflow organization. Because the jet airstream can entrain the heat in upper non air-conditioned area into the lower air conditioning area, extra heat load would be caused. The amount of entrainment is an important factor in affecting the transfer amount of heat. Presently, many studies for jet entrainment focused on the empirical and semi-empirical formulas. Using the experimental method to determine the jet entrainment of ambient air is limited. Ellison and Turner studied the

X. Wang (✉) · Y. Liu · Y. Dai
School of Environment and Architecture, University of Shanghai for Science and Technology, Shanghai 200093, China
e-mail: wangxinshiyun@126.com

A. Li et al. (eds.), *Proceedings of the 8th International Symposium on Heating, Ventilation and Air Conditioning*, Lecture Notes in Electrical Engineering 262,
DOI: 10.1007/978-3-642-39581-9_42,

surface jet and the inclined plume with a small size saline experiment table, analyzed the relationship between the amount of entrainment and Ri [1]. Fernando made a full size air jet experimental study, and the results were compared with Ellison and Turner' study [2]. D. Yang monitored tracer gas concentration to determine the entrainment in stratified flows [3]. Based on the basic theory of fluid mechanics, we had proposed a tracer gas concentration method to measure the amount of jet entrainment [4].

For the study of jet entrainment, we had used the sectional multipoint velocity measurement method, meshed the section perpendicular to the direction of the jet in the jet flow field by using velocimeter recording measuring point velocity value, determined the selected section sizes and average wind velocity, and then gotten the flow across the section. The difference between two adjacent sections is the entrainment among these sections in jet. However, this method needs many works. Those sites in large amounts had disturbance on the flow, and the reading error was also inevitable in the process. This paper presents a method by measuring the concentration of tracer gas mixed in the jet, according to the change of concentration to determine the jet entrainment. Thereby we can reduce the workload, improve the accuracy, and compare the experimental results with velocity measurement method results and the theoretical results which base on the fluid mechanics.

42.2 Tracer Gas Concentration Method

42.2.1 Basic Principles

We have used SF_6 as the tracer gas. The tracer gas existed inflow field when it is injected into the hose in front of the air jet tube. Along with the increase of jet range, tracer gas concentration value decreased due to entrainment of ambient air into the main jet. We selected one of the jet range segment as a control volume, as shown in Fig. 42.1. The concentration of tracer gas in the jet tube is denoted as Y_0, the concentration in the inflow section is denoted as Y_{in}, the concentration in the outflow section is denoted as Y_{out}.

M_{in}, M_{out} and M_e represented the mass flow rate of jet in the inflow section, outflow section, and the entrainment mass flow rate into the gas control body, respectively. Based on the law of mass conservation, we got:

$$M_{\text{in}} + M_e = M_{\text{out}} \tag{42.1}$$

From the components of conservation law, we got:

$$M_{\text{in}}.Y_{\text{in}} = M_{\text{out}}.Y_{\text{out}} \tag{42.2}$$

Simultaneous Eqs. (42.1) and (42.2) had:

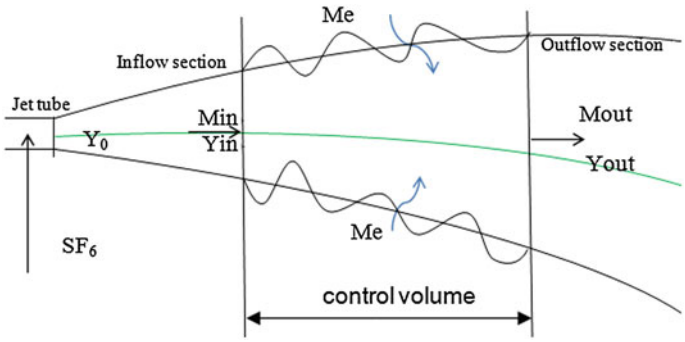

Fig. 42.1 Basic principles picture

$$M_{\text{in}} \cdot (Y_{\text{in}} - Y_{\text{out}}) = M_e \cdot Y_{\text{out}} \tag{42.3}$$

Use volume flow and density to express the mass flow, to:

$$Q_{\text{in}} \cdot \rho_{\text{in}} (Y_{\text{in}} - Y_{\text{out}}) = Q_e \cdot \rho_e \cdot Y_{\text{out}} \tag{42.4}$$

where, the unit of Y_O, Y_{in}, and Y_{out} is mg/g; the unit of M_{in}, M_{out} and M_e is mg/s. Q_{in}, which equal to the algebra of previous control flow in inflow section and its entrainment, is the jet flow in outflow section of the previous control volume. By the Eq. (42.4), we got under certain ambient temperature and certain temperature of the jet in the laboratory. Moreover, we measured the tracer gas concentration in inflow and outflow section of the control volume to obtain the corresponding control volume entrainment.

42.2.2 Working Conditions Set

Furthermore, we predicted the factors which can influence the entrainment. In the present study, only the jet flow velocity was considered. When nozzle diameter was in certain circumstances, the jet Reynolds number was changed by changing the air speed. Therefore, we keep the jet temperature and indoor temperature constant, and set the different wind speeds as the off-design conditions. The selected conditions are showed in Table 42.1.

The jet region was divided into five control bodies with 0.5 m interval, in each section of the jet axis, a concentration measuring point was arranged. Totally, there are six measuring points, as shown in Fig. 42.2. In the laboratory, in order to avoiding the influence on the jet flow filed, the measuring poles only are arranged in 1.5 and 3 m, the remaining points were draped over the cords between these poles.

Table 42.1 Experimental conditions

Conditions	Air speed (m/s)	Re	Air output (m^3/s)	Jet temperature (°C)	Indoor temperature (°C)	Initial concentration (mg/m^3)
1	1	5.57E + 03	0.002826	12.7	8.4	2502.25
2	1.5	8.04E + 03	0.004239	18.4	14.4	2351.482
3	2	1.10E + 04	0.005652	15.0	11.0	2365.967
4	2.5	1.35E + 04	0.007065	17.3	13.2	1931.233
5	3	1.60E + 04	0.008478	18.9	15.0	2153.95
6	3.5	1.86E + 04	0.009891	19.6	15.6	1505.16

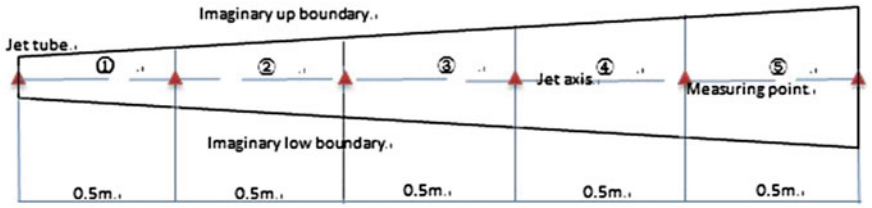

Fig. 42.2 Measuring point and control bodies

42.2.3 The Experimental Instrument

The experimental instruments are listed in Table 42.2. The instrument which was used to measure the tracer gas concentration value is INNOVA multi gas monitoring instrument. It was divided into gas gathering and gas analysis. The measuring points are connected by the hose. We adopted the descent method in this experiment. When the tracer gas concentration in each measuring point remained constant after the jet stability, the data were read. The mean of all the concentration values which measured during 30 min was set as its concentration value.

42.3 Results and Discussion

The Table 42.3 showed the experiment results with Sectional Multi-point velocity measurement method results and fluid mechanics theory results of experimental

Table 42.2 The experimental instruments

Number	Instrument name	Precision	Instrument effect
1	INNOVA-multi gas monitoring instrument	0.01	Measuring air concentration
2	Hot wire anemometer	0.1	Measuring air speed and temperature
3	Hygrometer	0.1	Measuring indoor temperature
4	Venturi nozzle		Supply air into jet

Table 42.3 The results comparison of condition 3 and 5

Control body	Entrainment m^3/h					
	Air output 20 m^3/h			Air output 30 m^3/h		
	C method	V method	Theory	C method	V method	Theory
①	168.372	126.036	82.341	224.676	214.884	123.511
②	184.392	173.268	89.527	231.336	214.020	134.291
③	164.808	128.232	89.527	195.804	172.440	134.291
④	48.312	45.072	89.527	55.476	53.928	134.291
⑤	5.796	3.816	89.527	6.192	9.468	134.291

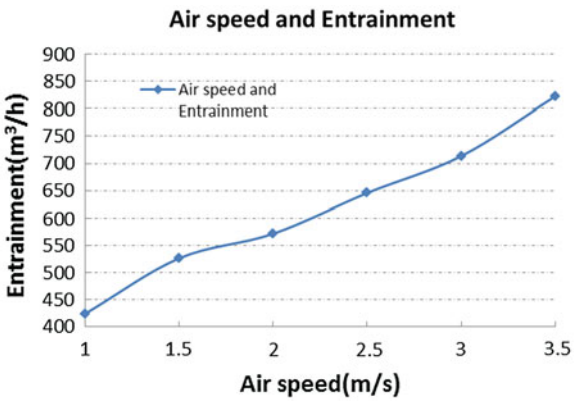

Fig. 42.3 Air speed and entrainment

condition 3 and 5. Then the four figures explained the variation tendency of entrainment with air speed, air output, jet axis speed, Re number changing.

From Table 42.3, we found that the results in every control body have little difference. This experimental method is feasible. The total entrainment added from 400 to 900 m^3/h along with the air speed increasing from 1 to 3.5 m/s (Fig. 42.3). The scaling of the entrainment in air output decreased from 45 to 20 along with the air output increasing from 10 to 40 m^3/h (Fig. 42.4). The control body entrainment reduced with the Jet axis speed falling, and also increased with condition's air speed rising (Fig. 42.5). The total entrainment also increased with Re adding from 5,000 to 20,000 (Fig. 42.6).

42.4 Conclusions and Prospect

According to the experimental results, it is feasibility to using the tracer gas concentration method in measuring the amount of jet entrainment. By determining of entrainment, jet range has a certain extent. When the jet reached a certain

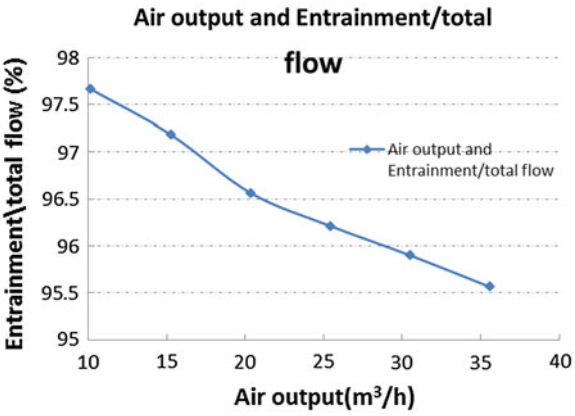

Fig. 42.4 Air output and entrainment

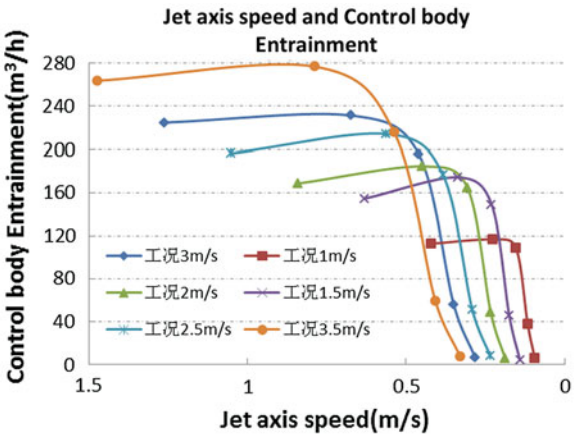

Fig. 42.5 Jet axis speed and entrainment

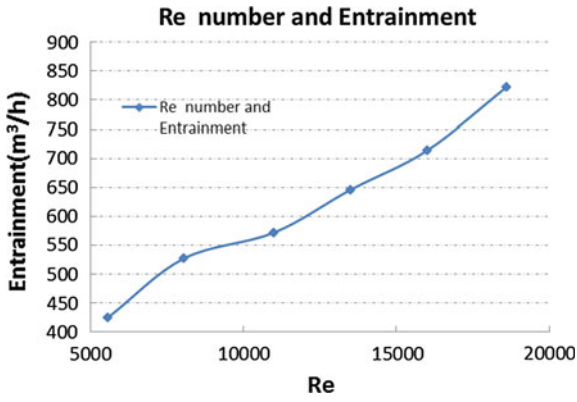

Fig. 42.6 Re number and entrainment

distance, it has been completely mixed with indoor air, the tracer gas concentration in the air remained basically constant, and the velocity values were close to zero.

Through measured the jet entrainment in different air velocity conditions, we found the jet Reynolds number that can influence the entrainment. In the future research, other factors should be considered, such as different temperature between jet and indoor air, the Archimedes number and Richardson number, as well as the nozzle position, distance and position from the air interface.

Acknowledgments This work is financially supported by the National Natural Science Foundation of China (51108263; 51278302).

References

1. Ellison TH, Turner JS (1959) Turbulent entrainment in stratified flows. University of Manchester, Department of the Mechanics of Fluids
2. Strang EJ, Fernando HJS (2001) Entrainment and mixing in stratified shear flows. J Fluid Mech 428:349–386
3. Yang D (2010) Studies on characteristics of stratification and entrainment of smoke layers in channel fires, PhD thesis, University of Science and Technology of China
4. Dai Y (2013) Research of the horizontal jet motion model in multiple plumes of large space, Ph.D thesis, University of Shanghai for Science and Technology

Chapter 43
Experimental Investigation of Airflow Pattern of Fabric Air Dispersion System

Xiaoli Wang and Angui Li

Abstract The air distribution characteristics formed by fabric air dispersion system (FADS) are investigated by visualization experiment in a full-scale room. The airflow structure of FADS was presented and verified by this experiment, and compared with the traditional airflow patterns. The jet supply velocity and the outlet orientation are choosing as major factors influent on airflow field of FADS. A semi-empirical expression was given to calculate the jet deflection angle causing by different jet supply velocities. Meanwhile, the induction and flow junction phenomena are analyzed under different combination of outlet orientation, and the experimental results show that this induction is beneficial in design and application of FADS in practical engineering. The current experimental study and its results are helpful for using fabric air dispersion method in HVAC system.

Keywords Ventilation · Air distribution · Fabric air dispersion system · Visualization

43.1 Introduction

Fabric air dispersion system (FADS) is effective terminal equipment in ventilation and air-conditioning system. It can be used both in air transmission and air diffusion process. FADS is made of special high-tech polyester material, and installed under the roof of the building by lifting accessories (see Fig. 43.1). Compared to the conventional air distribution system, the dispersed airflow through fabric permeation and designed multi-row orifices or linear vents to form a tridimensional airflow pattern. The resulting flow from the FADS can create a clean, quiet,

X. Wang (✉) · A. Li
School of Environmental and Municipal Engineering, Xi'an University of Architecture and Technology, Xi'an 710055 Shaanxi, China
e-mail: wxl@xauat.edu.cn

A. Li et al. (eds.), *Proceedings of the 8th International Symposium on Heating, Ventilation and Air Conditioning*, Lecture Notes in Electrical Engineering 262,
DOI: 10.1007/978-3-642-39581-9_43,

and comfortable environment [1]. The system can also prevent condensation on surfaces in the cool environment and the microorganisms can be easily removed by the routine washing [2]. It is more and more widely used in the HVAC system of large space buildings [3, 4].

The FADS has been earlier studied and applied by some manufacturers and engineering staffs as a ventilation terminal. Notably, Gebke et al. [4] provided an overview of the mechanical codes that apply to DuctSox products, including the most recent developments, in a technical research report named "A summary of air dispersion systems (Fabric)." Brown et al. [5] proved the theory that permeable fabrics yield the lowest possibility for condensation by an experimental test and give an evaluation of condensation of permeable and impermeable materials for air distribution. Kaufmann's [6] technical research report showed that the jet form of orifices making by laser technology is cleaner, quieter, and more accurate, and it is the superior choice in fabric air distribution. Brown et al. [7] calculated the inlet static pressure (ISP), static pressure regain (PR), and friction losses (FL) along the entire length of duct. The calculation is important for understanding the variance in pressure from inlet to the end cap. Meanwhile, some scholars also researched the comfort and indoor air quality using FADS. Nielsen et al. [8] experimentally studied the air distribution in a room generated by a textile terminal, and compared the results with other air diffusers. They concluded that the system was able to generate comfortable velocity and temperature conditions. They also numerically and experimentally studied the feasibility of FADS in personalized ventilation to improve protection of people in a contaminated room [9]. They concluded that the personalized ventilation improves the protection of occupants by increasing the personal exposure index. Chen et al. [2, 11] predicted the characteristics of airflow through FADS with the porous media model. The simulation results well matched with the corresponding experimental value, and showed that the airflow is radials discharged out in the direction perpendicular to the spatial cambered porous fiber

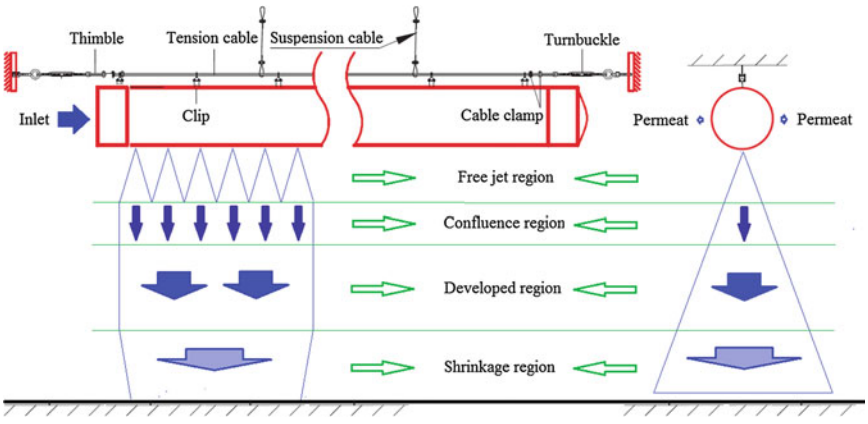

Fig. 43.1 Probable airflow pattern and installed method of FADS

in lower velocity, and evenly distributed along its length direction. The FADS is evenly distributed along the flow direction with a very low velocity. The indoor velocity is very low, and the vertical air temperature difference is small (less than 2 K). Meanwhile, the Draught Rating (DR) around the ankle and neck is immune to supply air flow rate and location. It is also concluded that the change regulation of total pressure (TP) and dynamic pressure (DP) and static pressure (ISP) along the flow direction of the FADS. However, the air distribution characteristic of FADS still not entirely clear, especially through multi-row orifices to form air diffusion, a lot of work can be done to develop the theory of FADS and improve its database of design process.

The main aim of this work is to obtain knowledge of the flow field of FADS in a full-scale room by visualization experiment. The specific objectives are investigating airflow structure of FADS, and studying the effect of outlet orientation and velocity on jet deflection and shrink phenomenon. The previous work can provide theoretical basis and experimental observation data for further study the airflow characteristic of FADS.

43.2 Experimental Setup

The air distribution characteristics formed by fabric air dispersion system (FADS) are investigated by visualization experiment in a full-scale room. The Test chamber and facilities and Measurement conditions are discussed in this section.

43.2.1 Test Chamber and Facilities

Visualization experiment was carried out in a full-scale room (4.0 × 7.0 × 3.14 m). The test chamber consists of a well-insulated wall and the jet supply device, which a type of SPICE^{TM} -TS-LHT. The length and diameter of the fabric air dispersion are 4.0 m and 0.3 m, respectively. Nine row orifices located in the duct, with the outlet orientation of 3, 4, 4.5, 5, 6, 7, 7.5, 8, and 9 o' clock, see Fig. 43.2a. The diameter of these orifices is 0.08 m, with a uniform interval of 0.1 m, see Fig. 43.2b. During the measurement, the supply air for the jet was generated by a centrifugal fan with the airflow rated of 1500 m^3/h, and the supply air volume was controlled by a throttle valve.

The distribution of the measurement sections was also shown in Fig. 43.3. They were distributed throughout two regions: The front view zone (Section A), and the side view zone (Section B). The shooting areas were 3.2 × 3.14 m^2 and 3.0 × 3.14 m^2 (Width × Height), respectively.

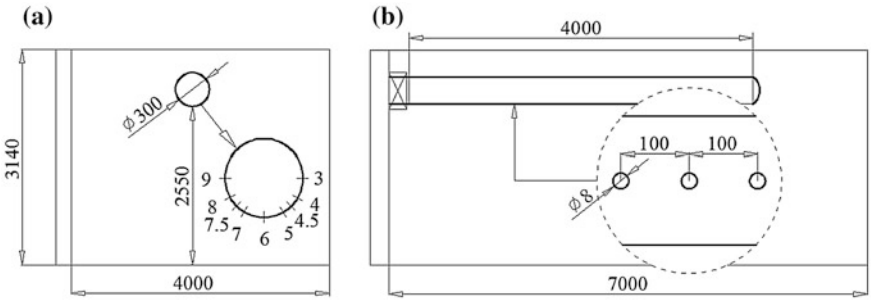

Fig. 43.2 Layout of test room and fabric air dispersion device

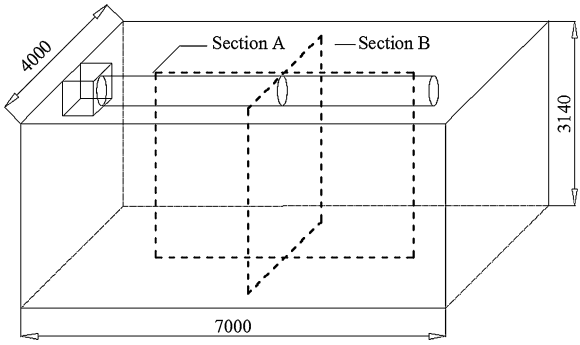

Fig. 43.3 Locations of the visualization sections

43.2.2 Measurement Conditions

According to the supply air speed recommended by the manufacturer [11] for FADS design, three orifice jet velocities, 6.5, 10, and 14 m/s were used. Meanwhile, to study the effect of outlet orientation on airflow pattern, nine combined forms of different orifice outlet orientation were chosen. Three different cases were performed under isothermal and undisturbed conditions as presented in Table 43.1.

43.2.3 Measuring Instruments and Accuracy

The airflow patterns were measured using smoke generator Rosco 1700 and the CCD camera. The field visualization was achieved by injecting glycol into the air supply pipe with a smoke generator. The observed flow field information was then recorded by a high-speed digital camera. The stabilized flow field screenshots for different cases were extracted and presented.

Table 43.1 Experimental conditions in three measured cases for isothermal airflow

Case	Experiment content	Orientation (o'clock)	Jet supply velocity (m/s)	Temperature (°C)
1	Airflow pattern	6	6.5, 10, 14	25 ± 0.3
2	Jet deflection	6	14	
		5, 7		
		5, 6, 7		
		4, 5, 6, 7, 8		
3	Induction and flow junction	5, 7	6.5	
		4, 8		
		4.5, 7.5		
		5, 6, 7		
		4, 6, 8		
		4.5, 6, 7.5		
		4, 5, 7, 8		
		4, 5, 6, 7, 8		

The supply air velocity was measured using a Swema 3000 with a draught probe of type SWA 10. The probe has a measurement range of 0.10–30.0 m/s with an accuracy of ±0.04 m/s at 0.10–1.33 m/s and ±3 % read value at 1.33–30.0 m/s. Pressure was measured in the supply duct using a Swema 3000 md with a probe of type SWA 10. The probe has a measurement range of −300 to 1500 Pa with an accuracy of ±1 % read value and minimum of 0.3 Pa. Before the measurements were made, all these probes had just been calibrated by the manufacturer.

The acquiring period for each measurement was 180 s to ensure accurate time-averaged results for turbulent airflow. The average value over time, at a point, was used for analysis and presentation.

43.3 Result and Discussion

43.3.1 Airflow Pattern

As shown in Fig. 43.1, the airflow field can be divided into four regions: (I) a free jet region, (II) the confluence region, (III) the developed region, and (IV) the shrinkage region. There are also transitional zones between these regions.

This airflow structure is effectively verified by the corresponding experimental observation, as shown in Fig. 43.4. In region I, the supply air from an orifice did not "feel" the presence of others, the air jet is somewhat similar to a free jet. In region II, include the confluence region and the probable transition region. The supply air joins to each other, the interspace among the orifices in region I is disappearing. In region III, which represents the self similarity of the jet, the air jet behaves as a traditional plane jet. In region IV, the supply air affects by the ground,

the main body of the jet in front view begin to shrink. Afterwards, the air jet impinges the ground, and then spreads over the floor.

The jet supply velocity has less influence on the flow field of FADS, the airflow pattern in Fig. 43.4a, b, and c is similar to each other. However, as the supply velocity increases, the free jet region is shortening, and the shrinkage phenomenon in region IV is clearer.

Figure 43.5 shows the airflow field causing by three traditional air diffusers. In the front view, the airflow pattern of linear slot is similar to FADSs, and has a tendency to inward contracting. By contrast, the main body of other airflow structures spread to the surrounding environment. In the side view, the airflow pattern of circular nozzle has the better agreement with FADSs. The supply jet can moves downward and impinging the ground, and then takes more cooling capacity to the occupied zone. However, the other two supply jets have certain mixing with the ambient air before them enters into the working area. Therefore, the FADS model has larger controlling area than circular nozzles, but has similar movement power to flow into the occupied zone and create a good environment.

43.3.2 Jet Deflection

FADS is different from the general pipeline ventilation device, when the airflow moves in the fabric duct, the static pressure will act to the pipe wall perpendicularly. Because the differential pressure exists between the inside and outside of orifices and duct wall, the supply air will flow out of the pipe wall obliquely, as shown in Fig. 43.6. The deflection angle can be calculated by Eq. (43.1) [12].

$$\sin\beta = \frac{U_d}{U} \tag{43.1}$$

where β is the deflection angle, U_d is the air velocity in the fabric duct, U is the jet supply velocity from the orifices.

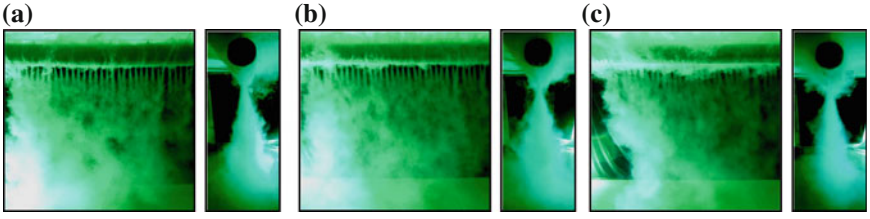

Fig. 43.4 Airflow pattern of FADS at the different velocity for outlet orientation of 6 o'clock: **a** 6.5 m/s; **b** 10 m/s; **c** 14 m/s

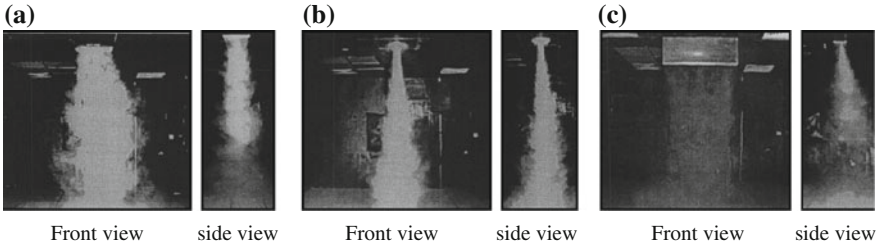

Fig. 43.5 Airflow pattern of different ventilation terminals: **a** rectangular diffusers; **b** circular nozzle; **c** linear slot

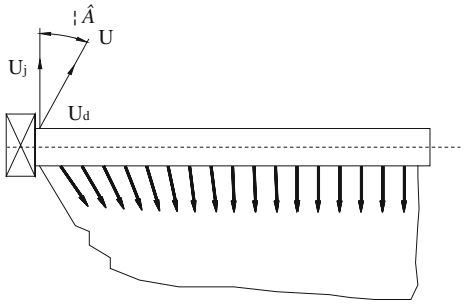

Fig. 43.6 Schematic diagram of jet deflection and synthesis velocity

Figure 43.7 is the visualization experimental results in the front view, the jet deflection phenomenon is clearly in these images. The outlet orientation has important influence on deflection angle, but the essential reason is the changing of air velocity in the fabric duct. With the corresponding of four combination of outlet orientations (1 row, 2 rows, 3 rows and 5 rows) in Fig. 43.7, U_d is 2.85, 3.69, 4.24, and 4.83 m/s, respectively. The jet supply velocity is 14 m/s, and then the deflection angle β is 11.7, 15.3, 17.6, and 20.2°. However, the calculated values by Eq. (43.1) did not match the actual angle obtained in Fig. 43.6b–d, where the opening orifices distribution in two or more rows, and the observed angle is 26, 30, and 34°, respectively. Compared the computational and experimental results, a revised equation used for deflection angle of multi-row orifices obtained as follow.

$$\sin\beta = K\frac{U_d}{U},\ K = 1.7 \tag{43.2}$$

43.3.3 Induction and Flow Junction

The effect of outlet orientation on airflow pattern in the side view also was studied. As shown in Fig. 43.8, the induction phenomenon is existed. Comparing

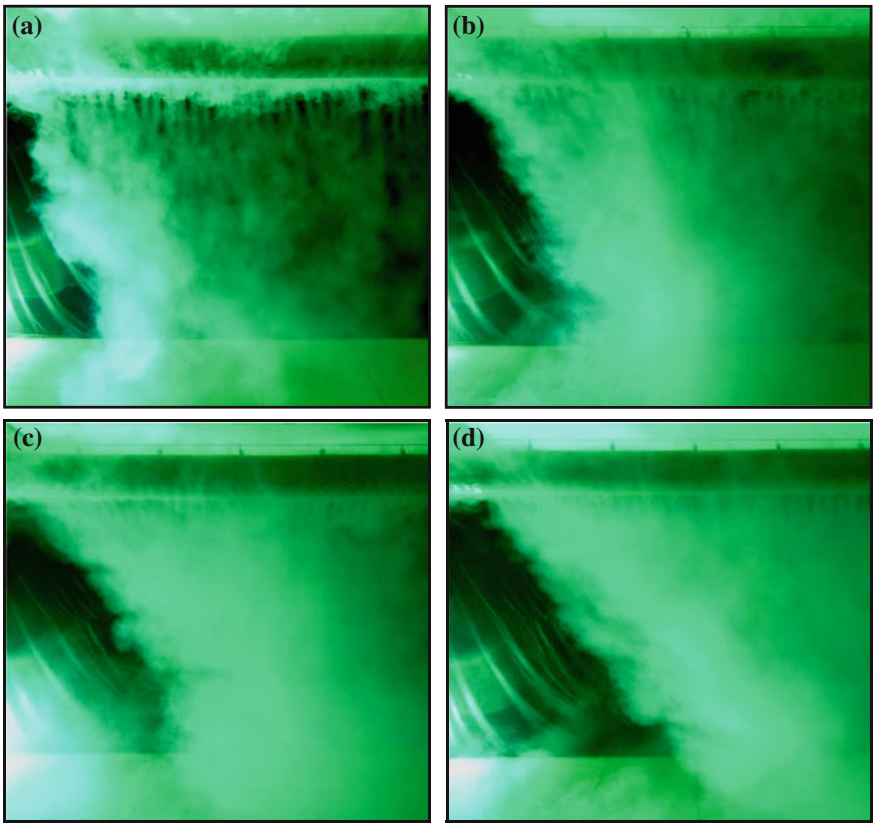

Fig. 43.7 Jet deflection at different outlet orientation (o'clock) for jet velocity 14 m/s: **a** 6 (o'clock); **b** 5, 7 (o'clock); (c) 4, 6, 8 (o'clock); **d** 4, 5, 6, 7, 8 (o'clock)

Fig. 43.8a,e, when chose 5 and 7 orifices as outlet, the air jet will move along these two orientations, but added another row of 6 o'clock, it will induced the air jet from 5 and 7 orifices, and then the main body of supply jet shrank intermediately. This phenomenon also happened in Fig. 43.8b, f. However, the induction of 6 o'clock orifices became not obvious in Fig. 43.8c, g, when the angle between the inducing and the induced jet is 45°. But in this instance, if it continues to add two row of 5 and 7 o'clock orifices, the air jet from 4 and 8 will induced by them, and further induced by the jet from 6 o'clock orifices, this transfer inducing also can form the flow junction phenomenon, and this is helpful for improve the ventilation efficiency.

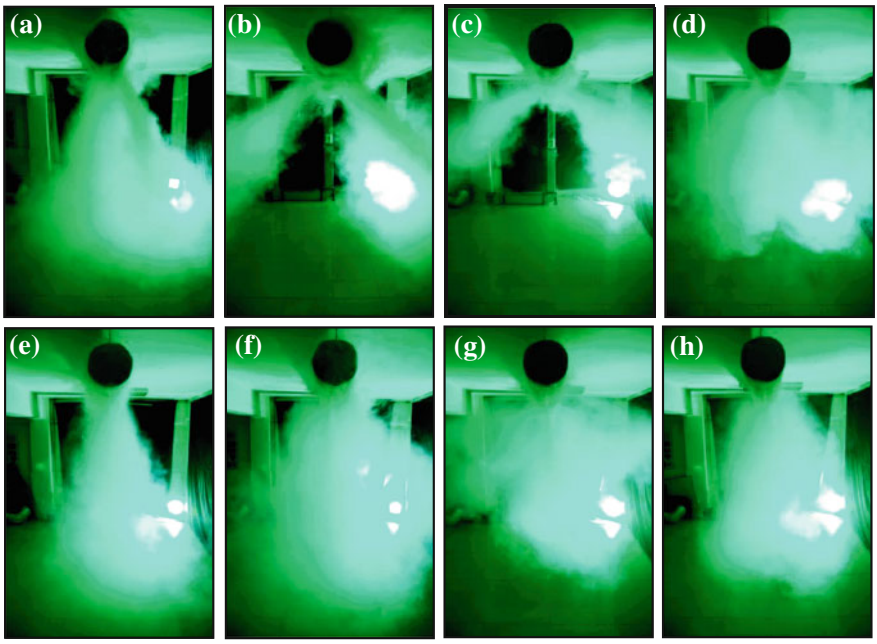

Fig. 43.8 Induction and flow junction phenomenon at different outlet orientation (o'clock) for jet velocity 6.5 m/s: **a** 5, 7 (o'clock); **b** 4.5, 7.5 (o'clock); **c** 4, 8 (o'clock); **d** 4, 5, 7, 8 (o'clock); **e** 5, 6, 7 (o'clock); **f** 4.5, 6, 7.5 (o'clock); **g** 4, 6, 8 (o'clock); **h** 4, 5, 6, 7, 8 (o'clock)

43.4 Conclusion

The air distribution characteristic of FADS was studied by experiment in a full-scale room, based on the previous theory and the visualization images shown in this paper, the airflow structure of FADS was presented and verified. Compared with the jet supply velocity, the outlet orientation of air jet has more important influence on airflow pattern of FADS. Meanwhile, the FADS model can create a more uniform and comfort environment in the occupied zone. In the front view, the supply jet from the left side orifices has obviously deflect to the right direction, and a revised semi-empirical model was given to calculate the deflection angle. In the side view, the influence of outlet orientation on jet shrink phenomenon is existed. The air jet from side outlet orientation will be direct or transfer inducted by the air jet moves vertically, which is the jet from 6 o'clock orifices. In order to improve the ventilation efficiency, these inductions are recommended for actual application. Future research will be directed at the quantitative and optimization design of FADS.

Acknowledgments This study is supported by National Science Foundation of China (No.51178374), Specialized Research Fund for the Doctoral Program of Higher Education (No. 20106120110008).

References

1. Li WG, Shen GM (2007) Fabric air distribution system and its application (in Chinese). Refrig Air Cond 3:99–104
2. Chen FJ, Chen HX, Xie JL et al (2003) Characterizing airflow through fabric air dispersion system using a porous media model. Energ Build 43:665–670
3. DuctSox (2012) Benefits of fabric HVAC ductwork system. http://ductsox.com/why-fabric
4. Pinkalla C (2003) Fabric duct air dispersion for HVAC systems. Constr Specif 56:57–58
5. Gebke K, Paschke N (2011) A summary of air dispersion systems (Fabric). Technical research report of DuctSox Corp. No. DSWPBC1111A
6. Brown R, Gebke K, Paschke N (2005) Condensation evaluation of permeable and impermeable materials for air distribution. Technical research report of DuctSox Corp. No. DSWP01A_1005A
7. Kaufmann N, Gebke K (2009) Why are laser vents superior to mesh vents? Technical research report of DuctSox Corp. No. 2009 DSWPLV0609A
8. Brown R, Paschke N (2006) Design methods for fabric duct systems. Technical research report of DuctSox Corp. No. DSWP02A_0806B
9. Nielsen PV, Topp C, Sonnichsen M et al (2005) Air distribution in rooms generated by a textile terminal-comparison with mixing and displacement ventilation. ASHRAE Trans 8:733–739
10. Chen FJ, Chen HX, Xie JL et al (2011) Air distribution in room ventilated by fabric air dispersion system. Build Environ 46:2121–2129
11. DuctSox (2009) Engineering design manual. DuctSox Corp. No. DSD0909J
12. Ji ZL, Jiang J (2009) Study on the terminal of cold air distribution systems (in Chinese). J Xi'an Univ Architect Technol 41:100–105

Chapter 44
Dynamic Soil Temperature of Ground-Coupled Heat Pump System in Cold Region

Tian You, Wei Wu, Baolong Wang, Wenxing Shi and Xianting Li

Abstract Ground-coupled heat pump (GCHP) has been widely used as an energy-saving and environment-friendly heating and cooling system. But for the buildings in cold regions, because the heat extracted from ground is much larger than the heat rejected into it, the ground cannot keep thermal balance and consequently the soil temperature will decrease year by year. With the decrease of the soil temperature, the ground-coupled heat pump system declines in performance or even stops running after a longtime operation. This paper aims at specifically revealing the phenomenon of soil temperature decrease in cold regions by an integrated dynamic simulation. 10 year's dynamic soil temperatures of GCHP used for just heating and for both heating and cooling in four typical cities are simulated and compared. The results show that the office building using GCHP just for heating has a severer soil temperature decrease: the temperature drop is respectively 11.7 °C in Harbin, 9.6 °C in Shenyang, 9.0 °C in Beijing, 5.8 °C in Zhengzhou. For the system with both heating and cooling, the soil temperature drop is 8.2 °C and 3.4 °C in Harbin and Shenyang, while the soil temperature rise is 0.02 °C and 5.5 °C in Beijing and Zhengzhou. The results of simulation are valuable for the design and operation of GCHP system applied in cold region.

Keywords Ground-coupled heat pump · Dynamic soil temperature · Thermal imbalance · Simulation

T. You · W. Wu · B. Wang (✉) · W. Shi · X. Li
Department of Building Science, Tsinghua University, Beijing 100084, China
e-mail: wangbl@tsinghua.edu.cn

A. Li et al. (eds.), *Proceedings of the 8th International Symposium on Heating, Ventilation and Air Conditioning*, Lecture Notes in Electrical Engineering 262,
DOI: 10.1007/978-3-642-39581-9_44,

44.1 Introduction

The energy consumption increases rapidly in the world with the development of economy, which results in lots of problems, such as energy crisis, large amount emission of CO_2 and SO_2, and PM2.5. All of these have forced human to search for new energy resources, and that is why heat pumps have become a popular choice for space conditioning in new residences [1–3]. And the ground is a thermally stable heat exchange medium, essentially unlimited, and always available. The ground-coupled heat pump (GCHP) system exchanges heat with the ground, and maintains a high level of performance even in colder climates [4]. As the GCHP is environment-friendly and energy-saving, it becomes a widely applied heating and cooling way in the worldwide nowadays [5, 6]. During the past two decades, a number of countries have encouraged individual house owners to install GCHPs to heat their houses in winter and (as needed) cool them in summer. Financial incentive schemes have been set up, commonly funded by the governments and electric utilities, as the heat pumps reduce the need for peak power and thus replace new electric generating capacity.

As most GCHPs are installed in cold region where the heating load of building is dominant [2, 7–9], the heat extracted from the ground is larger than the heat rejected into the ground. So, the soil temperature decreases yearly, which will lead to the yearly decrease of soil temperature and heating performance of GCHP system, even the failure of GCHP system. This paper aims at specifically revealing the phenomenon of soil temperature decrease in cold regions by an integrated dynamic simulation. The results of simulation are valuable for the design, operation, and research of GCHP system applied in cold region. If the temperature decrease is not so large, even though the performance declines, the GCHP system can still operate. Otherwise, some methods should be taken to keep the ground thermal balance.

44.2 Methodology

44.2.1 Building Model

To analyze the soil temperature variation of GCHP system for office building, a typical 16,000 m^2 office building with 10 floors is selected. This office building model is built in the software DeST and the corresponding parameters are set. Two typical cities (Beijing and Zhengzhou) in the cold region of China and two typical cities (Harbin and Shenyang) in the serve cold region of China are selected to reflect the soil temperature variation in cold region. As shown in Table 44.1, the heating seasons of different cities are given by practical heating period, but as the cooling seasons are flexible for different buildings, they are unified for different cities.

Table 44.1 Heating and cooling season of different cities

	Zhengzhou	Beijing	Shenyang	Harbin
Heating season	12.01–03.01	11.15–03.15	11.01–04.01	10.15–4.15
Cooling season	06.01–08.31	06.01–08.31	06.01–08.31	06.01–08.31

Table 44.2 Parameters of heating and cooling system in the building

Type	Season	Indoor temperature (°C)	RH (%)	Fresh air rate (m^3/(h·person))	Operating time
Office building	Winter	20–22	35–40	30	7:00–20:00
	Summer	24–26	50–65		

Besides, building envelope parameters are based on the public building energy efficiency design standards as Table 44.2 shows.

44.2.2 GCHP Model

In this simulation, the supplied hot water temperature for heating is 40 °C, the supplied chilled water temperature for cooling is 7 °C. The performance of GCHP under variable working conditions is fitted from the heat pump sample provided by manufacturer. The heating COP is fitted as:

$$P_H = 0.34t_{\mathrm{ei}} + 33.32,\ R^2 = 0.9871 \tag{44.1}$$

$$Q_H = 5.82t_{\mathrm{ei}} + 115.43,\ R^2 = 0.9899 \tag{44.2}$$

The cooling COP is fitted as:

$$P_C = -1.64t_{\mathrm{ci}} + 201.21, R^2 = 0.9956 \tag{44.3}$$

$$Q_C = 0.65t_{\mathrm{ci}} + 22.40, R^2 = 0.9973 \tag{44.4}$$

where, COP is coefficient of performance of GCHP, t_{ei} is inlet water temperature of evaporator, t_{ci} is inlet water temperature of condenser.

44.2.3 Ground Borehole Model

The dynamic simulation is conducted in software TRNSYS [10], which is developed specially to simulate the transient system and widely applied in the GCHP simulation. The models of GCHP and HCUT unit are simulated based on the above correlations and the ground heat exchanger is simulated by Module Type 557 whose parameters are listed in Table 44.3. The ground heat exchanger with

Table 44.3 Parameters of ground heat exchanger in GCHP system simulated in TRNSYS

Parameters	GCHP system
Borehole depth (m)	100
Header depth (m)	1.0
Borehole radius (m)	0.1
Soil thermal conductivity (W/mK)	1.4
Soil heat capacity (kJ/m^3 K)	2016
Outer radius of U-tube pipe (mm)	16
Inner radius of U-tube pipe (mm)	13
Center to center half distance (mm)	25
Fill thermal conductivity (W/mK)	1.8
Pipe thermal conductivity (W/mK)	0.5
Borehole flow rate (m/s)	0.8
Fluid	Ethylene glycol

single-U tubes is applied and its number is calculated by heat exchange rate per unit length for simplification which is 25 W/m in winter and 50 W/m in summer [11, 12].

The simulation period is 10 years with a time step of 1 h. Dynamic ground thermal imbalance ratio, average soil temperature can be achieved after the simulation is completed.

44.3 Results

44.3.1 Building Load

The heating and cooling loads of the typical office buildings in different cities are shown in Fig. 44.1. The maximum value in winter and summer can be taken as the design heating and cooling load. So the design heating load in the typical cities is 1,117 kW in Harbin, 1,019 kW in Shenyang, 798 kW in Beijing, and 726 kW in Zhengzhou, respectively. And the design cooling load is 784 kW in Harbin, 1,021 kW in Shenyang, 1,639 kW in Beijing, and 1,256 kW in Zhengzhou, respectively.

44.3.2 Dynamic Soil Temperature

The GCHP systems providing heating only and providing both heating and cooling used in different cities are dynamically simulated in TRNSYS. The designed ground borehole numbers of different cities are listed in Table 44.4. The dynamic

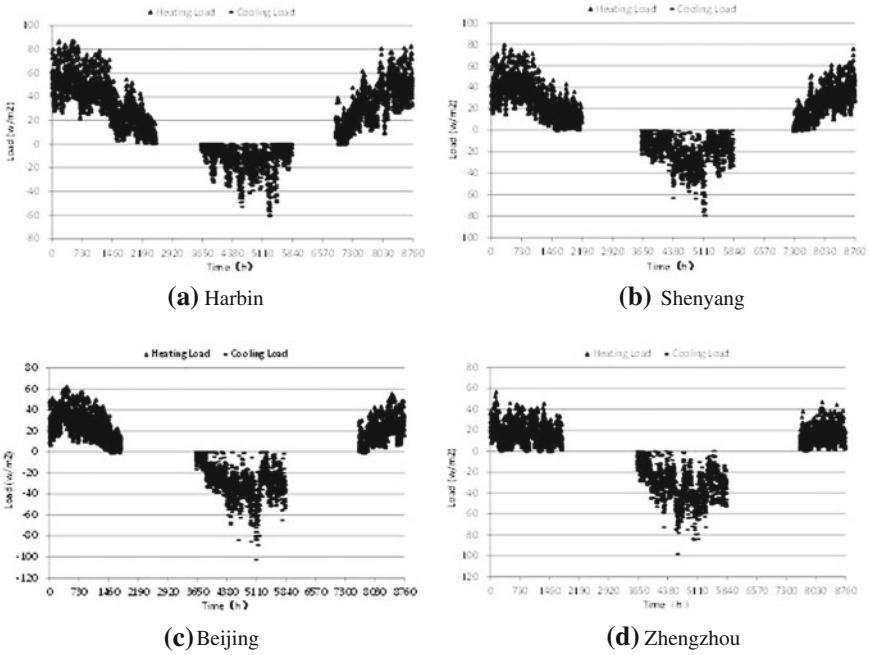

(a) Harbin **(b)** Shenyang

(c) Beijing **(d)** Zhengzhou

Fig. 44.1 Heating and cooling load of the typical office building

soil temperature during 10 years of operation can be obtained to evaluate the influence of thermal imbalance.

Figure 44.2 illustrates the variation of dynamic soil temperature of GCHP system applied in Harbin. For the building with heating only, the soil temperature decreases from 6.1 to −5.6 °C, with a reduction of 11.7 °C during 9 years. The GCHP may stop working under such a low soil temperature. This is because the heating load in Harbin is very high, as shown in Fig. 44.1a, the heat extraction in winter is also very high and there is no heat rejection to the soil in summer. Therefore, the thermal imbalance underground is very serious and the drop of soil temperature is very great, which will finally lead to obvious deterioration of the heat pump performance after long-term operation.

For the building with both heating and cooling, the soil temperature decreases from 6.1 to −2.1 °C, with a reduction of 8.2 °C during 10 years. Compared with the situation with heating only, the reduction is 3.5 °C less. This is because the heat rejection to the soil in summer can effectively reduce the thermal imbalance and slow down the decrease of soil temperature. However, the cooling load in Harbin is usually very low compared to its heating load. So the drop of soil temperature is still serious even for the building with both heating and cooling.

Figure 44.3 shows the variation of dynamic soil temperature of GCHP system applied in Shenyang. For the building with heating, the soil temperature decreases

Table 44.4 Borehole numbers of GCHP system in different cities

	Zhengzhou		Beijing		Shenyang		Harbin	
	Heating and cooling	Just heating	Heating and cooling	Just heating	Heating and cooling	Just heating	Heating and cooling	Just heating
Borehole numbers	308	232	397	252	299		328	

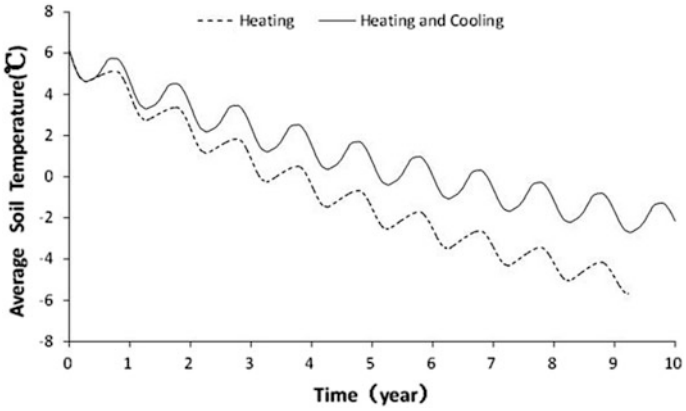

Fig. 44.2 The dynamic soil temperature of GCHP system in Harbin

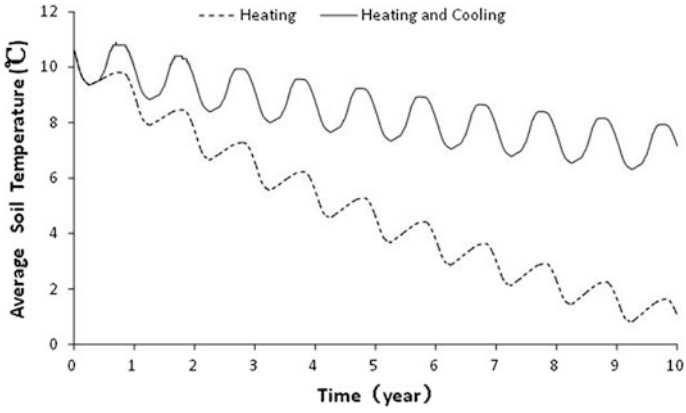

Fig. 44.3 The dynamic soil temperature of GCHP system in Shenyang

from 10.6 to 1.0 °C, with a reduction of 9.6 °C during 10 years, which is slightly less than that of Harbin.

For the building with both heating and cooling, the soil temperature decreases from 10.6 to 7.2 °C, with a reduction of 3.4 °C during 10 years. Compared with the situation with heating only, the reduction is 6.2 °C less. So the improvement caused by cooling in Shenyang is much more obvious than that in Harbin. This can be explained by the lower heating load and higher cooling load in Shenyang, as shown in Fig. 44.1b. In spite of this, the cooling load in Shenyang is still much lower than the heating load, which means the thermal imbalance of GCHP will still have a great influence on the soil temperature.

Figure 44.4 demonstrates the variation of dynamic soil temperature of GCHP system applied in Beijing. For the building with heating only, the soil temperature

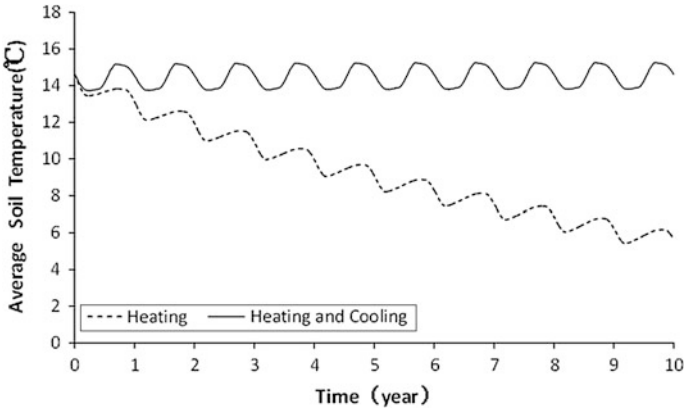

Fig. 44.4 The dynamic soil temperature of GCHP system in Beijing

decreases from 14.6 to 5.6 °C, with a reduction of 9 °C during 10 years, which is slightly less than that of Shenyang.

However, for the building with both heating and cooling, the soil temperature is not decreasing anymore with a small rise of 0.02 °C during 10 years. Compared with the situation in Harbin and Shenyang, the variation is relatively stable and can be ignored. So the improvement caused by cooling in Beijing is pretty good. This mainly owes to the balance between heating load and cooling load in Beijing, as shown in Fig. 44.1c. So it can be concluded that GCHP with both heating and cooling is suitable in the regions like Beijing, where the soil temperature can keep relative stable and the heat pump performance can stay highly efficient for long-term running.

At last, Fig. 44.5 shows the variation of hourly soil temperature of GCHP system applied in Zhengzhou. For the building with heating only, the soil temperature decreases from 16.7 to 10.9 °C, with a reduction of 5.8 °C during 10 years, which is smallest reduction during all the typical cities. And this is because of the relative lower heating load in Zhengzhou.

However, for the building with both heating and cooling, the soil temperature increases from 16.7 to 22.2 °C, with a rise of 5.5 °C during 10 years. So the thermal imbalance in Zhengzhou is not reduced by cooling, but is changed from an imbalance to another imbalance. The rise of soil temperature mainly owes to the lowest heating load and highest cooling in Zhengzhou, as shown in Fig. 44.1d. So the heat extraction from soil in winter is the least and the heat rejection in summer is the most.

Through the analysis, all GCHP systems with just heating only applied in these four typical cities will face the problems of underground thermal imbalance in a long-term run. If the heating load is higher, the temperature drops more seriously. For Harbin, the low soil temperature may lead to the failure of system in the 10th year. For the GCHP system with both heating and cooling, the heat rejected into soil in summer contributes a lot to preventing soil temperature decreasing. For Harbin and Shenyang, the soil temperature decreases 3.5 and 6.2 °C less

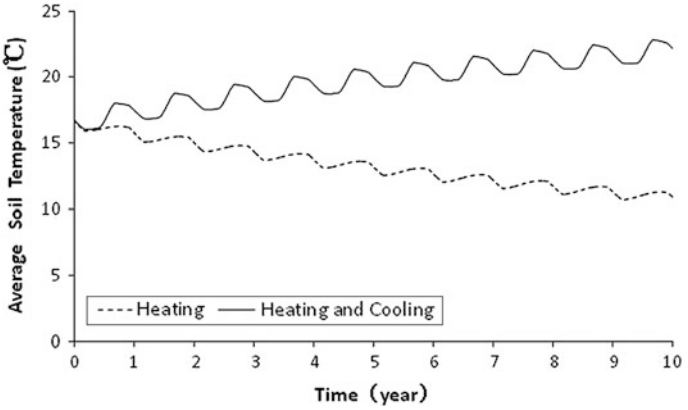

Fig. 44.5 The dynamic soil temperature of GCHP system in Zhengzhou

respectively and the underground thermal imbalance is relieved. This system is suitable for Beijing as the soil temperature keeps steady in 10 years. For Zhengzhou, the underground thermal imbalance still exists, as the rejected heat is larger than the extracted heat.

44.4 Conclusion

In order to specifically reveal the phenomenon of soil temperature decrease of GCHP in cold regions, systems with heating only and with both heating and cooling during long-term operation in typical cities are dynamically simulated. Conclusions can be draw as follows:

(1) For the building with heating only, the soil temperature decreases from 6.1 to −5.6 °C in Harbin, decreases from 10.6 to 1.0 °C in Shenyang, from 14.6 to 5.6 °C in Beijing, and decreases from 16.7 to 10.9 °C in Zhengzhou;
(2) For the building with both heating and cooling, the soil temperature decreases from 6.1 to −2.1 °C in Harbin, decreases from 10.6 to 7.2 °C in Shenyang, increases from 14.60 to 14.62 °C in Beijing, and increases from 16.7 to 22.2 °C in Zhengzhou;
(3) GCHP with both heating and cooling is suitable in the regions like Beijing, where the soil temperature can keep relative stable and the heat pump performance can stay high-efficient for long-term running.

The results of simulation are valuable for the design, operation, and research of GCHP system applied in cold region. If the temperature decrease is not so large, even though the performance declines, the GCHP system can still operate. Otherwise, some measures should be taken to keep the ground thermal balance.

Acknowledgments The authors gratefully acknowledge the support from the Natural Science Foundation of China (grant No.51176084) and the National last five-year science and technology support project of China (grant No. 2011BAJ03B09).

References

1. İnallı M, Esen E (2004) Experimental thermal performance evaluation of a horizontal ground-source heat pump system. Appl Therm Eng 24(14–15):2219–2232
2. John WL, Derek HF, Tonya LB (2011) Direct utilization of geothermal energy 2010 worldwide review. Geothermics 40(3):159–180
3. Pawel O (2004) The Possibility of Using the Ground as a Seasonal Heat Storage: The Numerical Study. ASME Conference Proceedings 2(Parts A and B): Computational Fluid Dynamics and Heat Transfer
4. Ozgener O, Hepbasli A (2007) Modeling and performance evaluation of ground source (geothermal) heat pump systems. Energ Build 39(1):66–75
5. Sannera B, Karytsasb C, Mendrinosb D et al (2003) Current status of ground source heat pumps and underground thermal energy storage in Europe. Geothermics 32(4–6):579–588
6. Zhai XQ, Qu M, Yu X et al (2011) A review for the applications and integrated approaches of ground-coupled heat pump systems. Renew Sust Energ Rev 15(6):3133–3140
7. Yang W, Zhou J, Xu W et al (2010) Current status of ground-source heat pumps in China. Energ Policy 38(1):323–333
8. Lund J, Sanner B, Rybach L et al (2004) Geothermal(ground-source) heat pumps: A world overview. GHC Bull 9:1–10
9. Hepbasli A, Akdemir O, Hancioglu E (2003) Experimental study of a closed loop vertical ground source heat pump system. Energ Convers Manage 44(4):527–548
10. Klein SA et al (1994) TRNSYS: a Transient Simulation Program. University of Wisconsin, Solar Energy Laboratory
11. Qu YX, Fang ZH, Zhang LH et al (2003) The economic analysis of ground-coupled heat pump by using the solar energy as an assisted source. Renew Energ 1:8–10 (in Chinese)
12. Li SH, Yang WH, Zhang XS (2009) Soil temperature distribution around a U-tube heat exchanger in a multi-function ground source heat pump system. Appl Therm Eng 29:3679–3686

Chapter 45
Study on Heat Transfer of Soil Thermal Recovery of Ground Source Heat Pump System

Ping Zhou, Chao Chen, Jinshun Wu, Guixia Hu, Yang Guo and Kang Li

Abstract The imbalance of heat extracted from the soil by the ground heat exchangers (GHEs) in winter, and rejected into it in summer is expected to affect the long-term performance of ground source heat pump (GSHP) in areas of southern China. This chapter presents a new operation mode to resolve this problem that in summer night the intermittent operation of GHEs with the cooling tower as the supplemental heat rejecter of GSHP system and in transition seasons the coupling operation of cooling tower combined with the GHEs. The practical analytical model of GHEs based on the line-source theory is established. The computer program based on established model is developed to do the feasibility analysis under the proposed operating mode for a GSHP system in Nanjing of southern China. The results indicate that the imbalance problem of the rejected/extracted heat for the GSHP system in Nanjing of southern China is effectively resolved. In addition, under the proposed operating mode the COP of heat pump unit can be improved, design capacity of cooling tower can be reduced and utilization rate of cooling tower throughout the year can also be increased. The results can improve the energy efficiency of GSHP system.

Keywords GSHP · Soil heat imbalance · Line-source model · Intermittent operation · Coupling operation of cooling tower combined with GHEs

45.1 Introduction

The imbalance of heat extracted from the soil by the ground heat exchangers (GHEs) in winter, and rejected into it in summer is expected to affect the long-term performance of ground source heat pump (GSHP) in areas of southern China.

P. Zhou · C. Chen (✉) · J. Wu · G. Hu · Y. Guo · K. Li
Beijing University of Technology, 100124 Beijing, China
e-mail: chenchao@bjut.edu.cn

A. Li et al. (eds.), *Proceedings of the 8th International Symposium on Heating, Ventilation and Air Conditioning*, Lecture Notes in Electrical Engineering 262,
DOI: 10.1007/978-3-642-39581-9_45,

About this issue, the ASHRAE manual [1] first discussed the advantages of the hybrid ground source heat pump (HGSHP) system which uses the cooling tower as supplemental heat rejecter. Gilbreath [2] conducted a more detailed study based on a HGSHP system installed in an office building and presented some design suggestions. Kavanaugh [3] modified the existing design procedures recommended by the ASHRAE manual and a method to balance the heat transfer in the ground on an annual basis was proposed. Phetteplace and Sullivan [4] described the operating performance of a HGSHP system using the measured data over a 22-month period. Singh and Foster [5] investigated the initial cost savings of the HGSHP system designed for two sample buildings. Hongxing Yang [6] used the line-source model of GHEs to study the HGSHP system designed for a hypothetic private residential building located in Hong Kong.

Accordingly, this paper presents a new operation mode to resolve the imbalance problem that in summer night the intermittent operation of GHEs with the cooling tower as supplemental heat rejecter of GSHP system and in transition seasons the coupling operation of cooling tower combined with the GHEs. The computer program based on practical analytical model of GHEs is developed to do the feasibility analysis under the proposed operating mode for a GSHP system in Nanjing of southern China. The analysis results demonstrate the scientific nature of the proposed operating mode.

45.2 Heat Transfer in the GHE

The physical model in the GHE is illustrated in Fig. 45.1. Heat transfer between a GHE and its surrounding soil/rock is difficult to model for the purpose of sizing the exchanger or energy analysis of the system. Because of all the complications of this problem and its long time scale, the heat transfer process may usually be analyzed in two separated regions. One is the solid soil/rock outside the borehole; another sector isolated for analysis is the region inside the borehole, including the grout, the U-tubes and the circulating fluid inside the pipes [7].

45.2.1 Heat Transfer Inside Boreholes

A quasi-three-dimensional model was proposed by Zeng et al. [8]. Take into account the fluid axial convective heat transfer and thermal "short-circuiting" among U-tube legs. Being minor in order, the conductive heat flow in the grout and ground in the axial direction, however, is still neglected to keep the model concise and analytically manageable. The energy balance equations for downward and upward of the circulating fluid can be written as

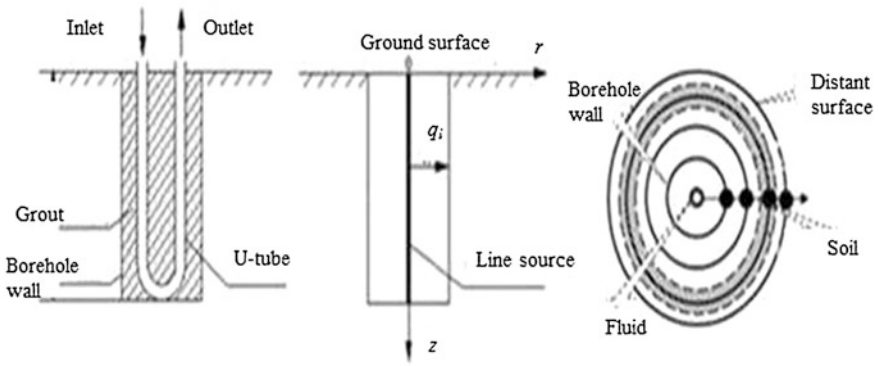

Fig. 45.1 The physical model in the GHE

$$\begin{cases} -Mc_p \dfrac{\mathrm{d}T_{f1}}{\mathrm{d}z} = \dfrac{T_{f1} - T_b}{R_a} + \dfrac{T_{f1} - T_{f2}}{R_0} \\ Mc_p \dfrac{\mathrm{d}T_{f2}}{\mathrm{d}z} = \dfrac{T_{f2} - T_b}{R_a} + \dfrac{T_{f2} - T_{f1}}{R_0} \end{cases} (0 \le z \le H) \tag{45.2.1}$$

where, M, C_p, T_{f1}, T_{f2}, T_b ,R_a, and R_0 are the mass flow rate of circulating fluid, fluid specific heat, temperature of inlet circulating fluid, temperature of outlet circulating fluid, temperature of borehole wall, thermal resistance between the inlet/outlet circulating fluid, and the borehole wall and thermal resistance between the inlet and outlet pipes (Fig. 45.2), respectively. The temperature profiles of the fluids running in the U-pipes in the boreholes:

$$\Theta_d(Z) = \mathrm{ch}(\beta z) - \frac{1}{\beta S_{12}} \left[\left(\frac{S_{12}}{S_1} + 1 \right) - \frac{\beta S_1 \cdot \mathrm{ch}(\beta) - \mathrm{sh}(\beta)}{\beta S_1 \cdot \mathrm{ch}(\beta) + \mathrm{sh}(\beta)} \right] \mathrm{sh}(\beta Z) \tag{45.2.2}$$

$$\begin{aligned} \Theta_u(Z) = {} & \frac{\beta S_1 \cdot \mathrm{ch}(\beta) - \mathrm{sh}(\beta)}{\beta S_1 \cdot \mathrm{ch}(\beta) + \mathrm{sh}(\beta)} \mathrm{ch}(\beta Z) \\ & - \frac{1}{\beta S_{12}} \left[1 - \left(\frac{S_{12}}{S_1} + 1 \right) \frac{\beta S_1 \cdot \mathrm{ch}(\beta) - \mathrm{sh}(\beta)}{\beta S_1 \cdot \mathrm{ch}(\beta) + \mathrm{sh}(\beta)} \right] \mathrm{sh}(\beta Z) \end{aligned} \tag{45.2.3}$$

Fig. 45.2 Heat transfer inside boreholes

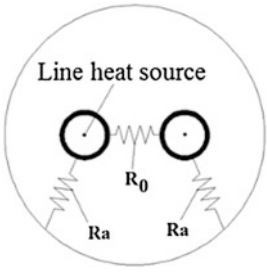

where Θ_d/Θ_u denote the temperature of non-dimensional temperature of inlet/outlet circulating fluid in the GHE, S_1, S_{12}, β, R_a, and R_0 were presented in the paper [9].

45.2.2 Heat Transfer Outside Boreholes

The theoretical model for a single borehole in a geothermal heat exchanger is illustrated in Fig. 45.3. Set a virtual line sink with the same length H but a negative heating rate $-q_l$ on symmetry to the boundary. If the temperature excess is defined as $\theta = t - t_0$, the boundary condition $\theta = 0$, is compiled due to the symmetry of the line source and the virtual line sink. The real solution of the temperature excess $M(r, z)$ can be obtained by integrating contributions of all the increments of the line source and sink. That is [10],

$$\theta = \frac{q_l}{4\pi\lambda}\int_0^H \left\{ \frac{\operatorname{erfc}\left[\frac{\sqrt{r^2+(z-h)^2}}{2\sqrt{\alpha\tau}}\right]}{\sqrt{r^2+(z-h)^2}} - \frac{\operatorname{erfc}\left[\frac{\sqrt{r^2+(z+h)^2}}{2\sqrt{\alpha\tau}}\right]}{\sqrt{r^2+(z+h)^2}} \right\} \mathrm{d}h \tag{45.2.4}$$

where and denote the thermal conductivity and thermal diffusivity of the medium, respectively. In view of heat balance for the single U-tube also has

$$Mc_p(T_{f2} - T_{f1}) = q_l H \tag{45.2.5}$$

Combined M, C_p, T_{f1}, R_a, R_0, and T_b with Eq. (45.2.1)–(45.2.5), the hourly temperature distribution and variation trend of soil temperature field around GHEs can be simulated, including the response of borehole wall temperature T_b which varies from time to time.

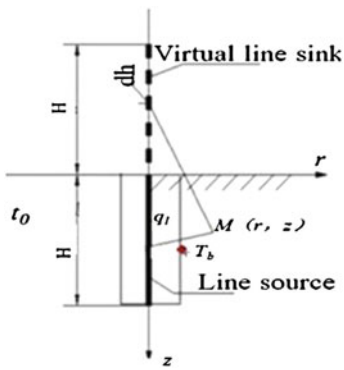

Fig. 45.3 The geometry of a finite line-source system

45.3 Verification of the Line-Source Model

To verify the line-source model, comparison of the calculated results with measured results of an actual GSHP project in Nanjing of China is made. This indicates that the line-source method is completely acceptable for the practicable engineering.

45.3.1 Project Description

A high-rise residential building with 7,000 m^2 area located in Nanjing of China is used as the sample building. The cooling season is from May to September, and the heating season is from November to April. Correspondingly, the GHE has 1,111 boreholes arranged in liner configuration, and each borehole with a depth of 35 and 5 m apart is designed. The initial temperature of soil is 18 °C. Typical geometrical and thermal characteristics inside and outside the borehole are given in Table 45.1.

45.3.2 Annual Hourly Heat Extracted/Rejected to Soil

According to the analysis of the measured data on GSHP system in 2009, the heat rejected to soil in summer accounts for 61 % of the annual accumulated heat, and the heat extracted from soil in winter accounts for 39 % of the annual accumulated heat. The imbalance rate of the heat rejected to soil in summer and that extracted from soil in winter has reached up to 55.6 % (Fig. 45.4).

45.3.3 Annual Hourly Inlet/Outlet Water Temperature

As shown in Fig. 45.5, due to the heavy heat imbalance in the soil, the inlet and outlet water temperature of GHEs increase significantly during 3 years

Table 45.1 Parameters of the reference borehole

1. Inside the borehole (pipe and grout region)		
Borehole diameter (mm)	Pipe thermal conductivity (W/(m K))	Grout thermal conductivity (W/(m K))
150	0.35	1.6
2. Outside the borehole (soil region)		
Soil thermal conductivity (W/(m K))	Soil specific heat (J/(kg K))	Soil density (kg/m^3)
1.5	1,800	1,500

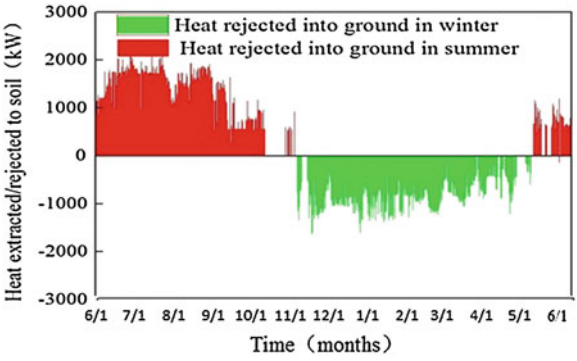

Fig. 45.4 Annual hourly heat extracted/rejected to soil

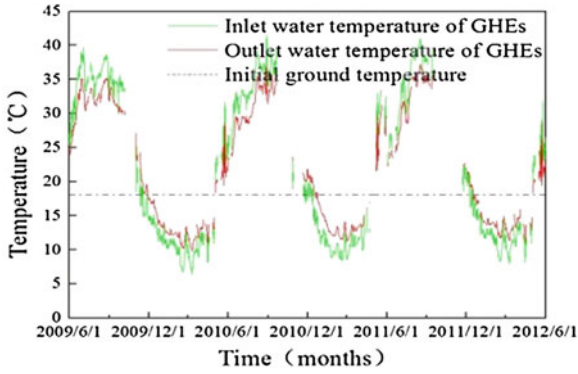

Fig. 45.5 Inlet and outlet water temperature of GHEs in 2009–2012

(2009–2012) operation of the GSHP system for this residential sample building. Especially, during the period of peak load in summer, the average inlet/outlet water temperature can be up to 36–38 °C/32–35 °C which results in performance degradation of heat pump. On the contrary, the heating efficiency is much better in winter.

The comparisons between the calculated and measured outlet water temperatures of GHEs in summer and winter are presented in Fig. 45.6. The comparisons show, on the whole, a great agreement during the operating time. The relative errors between the calculated and measured temperatures in summer and winter are 2.6 and 3.7 %, indicating the effectiveness of the calculation method.

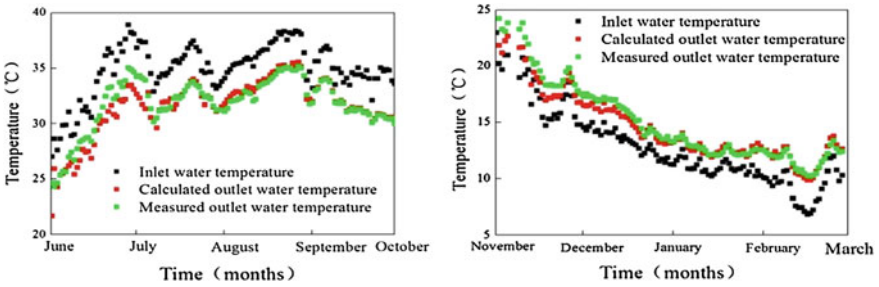

Fig. 45.6 Comparison of the calculated and measured outlet water temperatures of GHEs

45.4 The Feasibility Analysis on the Method of Solving the Heat Imbalance Problem

45.4.1 Soil Thermal Recovery Under Intermittent Operation

Based on the line-source model in Sect. 45.2.1 and residential sample building in Sect. 45.3, the soil thermal recovery under intermittent operation is analyzed.

45.4.1.1 Calculation Condition

Figure 45.7 shows the hourly measured variation of heat rejected into soil through GHEs in a typical summer day. The heat quantity rejected into ground in night time only accounts for 67 % of that in daytime (from 8:00 a.m. to 18:00 p.m.). As a consequence, the intermittent operation of GHEs with the cooling tower as the supplemental heat rejecter of GSHP system in summer night is selected. In order to

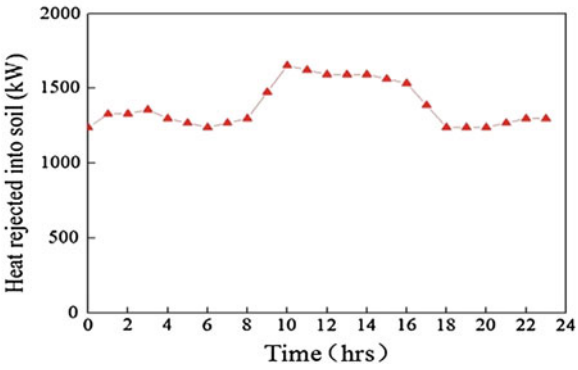

Fig. 45.7 Heat quantity rejected into soil in a typical summer day

Table 45.2 Intermittent operation periods

Case	Case 1	Case 2	Case 3	Case 4	Case 5
Intermittent period	Continuous operation	4:00–8:00	0:00–8:00	20:00–8:00	16:00–8:00

select a suitable intermittent operation period of GHEs, the intermittent operation periods of GHEs for 4, 8, 12, and 16 h a day are, respectively, taken into account (Table 45.2).

45.4.1.2 Result and Discussion

The borehole wall temperature responses under different intermittent operation periods a day (Table 45.2) are provided in Fig. 45.8. With the GSHP system rejecting heat to the soil continuously (Case 1), the increment of borehole wall temperature is 5.3 °C. As the intermittent operation periods of 4 h (Case 2), 8 h (Case 3), 12 h (Case 4), and 16 h (Case 5), the increment of borehole wall temperature are 3.4, 2.1, 1.4, and 0.9 °C, and soil temperature recovery rate (divide temperature difference during intermittent operation period by the recovery time) are 0.44, 0.34, 0.26, and 0.21 °C/h, respectively. Combined the increment of borehole wall temperature with soil temperature recovery rate, the intermittent operation period of 8 h (Case 3) is a better intermittent operation period.

Figure 45.9 shows the borehole wall temperature responses of the GSHP system during 2009 summer running under Case 1 and Case 3. The average borehole wall temperature of the GSHP system during the summer running under Case 1 and Case 3 is 28.2, 25.9 °C, respectively. Obviously, the intermittent operation mode of GHEs with the cooling tower as the supplemental heat rejecter of GSHP system for 8 h in summer night is helpful for soil thermal recovery and the resolution of the imbalance problem of the rejected/extracted heat. For the heavy heat imbalance in the soil, the design capacity of cooling tower should be much larger

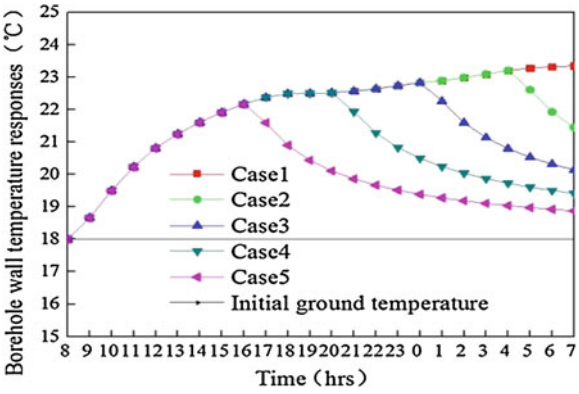

Fig. 45.8 The borehole wall temperature responses under different intermittent operation period a day

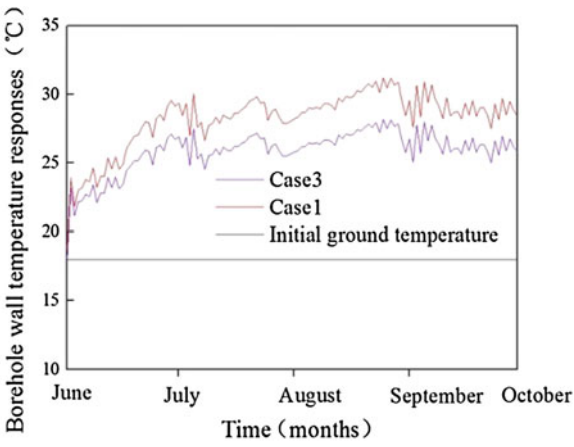

Fig. 45.9 The borehole wall temperature responses under Case 1 and Case 3 in 2009 summer

or the duration of intermittent operation should be much longer, the technological economy level of intermittent operation is low.

45.4.2 Soil Thermal Recovery Under Coupling Operation of Cooling Tower Combined with GHEs

45.4.2.1 Basic Operation Strategy

Considering the results in Sect. 45.4.1, a new operation mode is proposed to resolve the heat imbalance problem. That is, the excess heat in summer than winter is divided into two parts: one part rejected into the air through cooling tower in summer night; another part removed by the coupling operation of cooling tower combined with the GHEs in transition seasons. This operation strategy can effectively solve the imbalance problem of the rejected/extracted heat. In addition, the COP of heat pump unit can be improved, design capacity of cooling tower can be reduced and utilization rate of cooling tower throughout the year can also be increased (Fig. 45.10).

According to calculation, the heat rejected into the air through cooling tower in summer night for 8 h should account for 44 % of total condensing heat of heat pump in summer for the sample building. The transition seasons of the coupling operation of cooling tower combined with the GHEs should be March, October 15th–30th, and November in Nanjing that is presented in our previous paper [11].

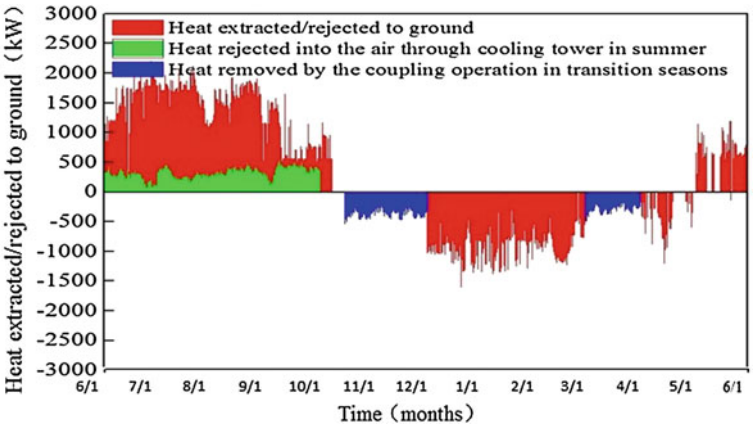

Fig. 45.10 Schematic diagram of the proposed operation mode

45.4.2.2 Feasibility Analysis

The borehole wall temperature responses and inlet and outlet water temperature of GHEs in 2009–2015 are compared and plotted in Figs. 45.11 and 45.12. From June 2012 on, based on the operation mode mentioned in Sect. 45.4.2.1, the borehole wall temperature is decreased from 33 °C (peak-load period in 2011 summer) to 28 °C, correspondingly, the outlet water temperature of GHEs is decreased from 35 °C (peak-load period in 2011 summer) to 29 °C. It shows that, the outlet water temperature of GHEs decreases with the decrease of borehole wall temperature, the heat pump in the GSHP system can achieve beneficial heat sink, and operate with higher efficiency.

Obviously, the new method that in summer night the intermittent operation of GHEs with the cooling tower as the supplemental heat rejecter of GSHP system and

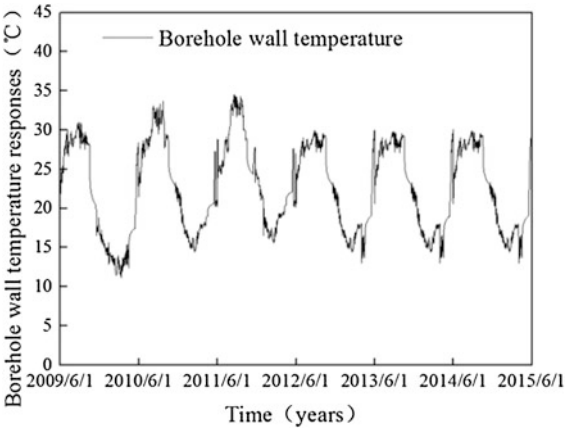

Fig. 45.11 Borehole wall temperature in 2009–2015

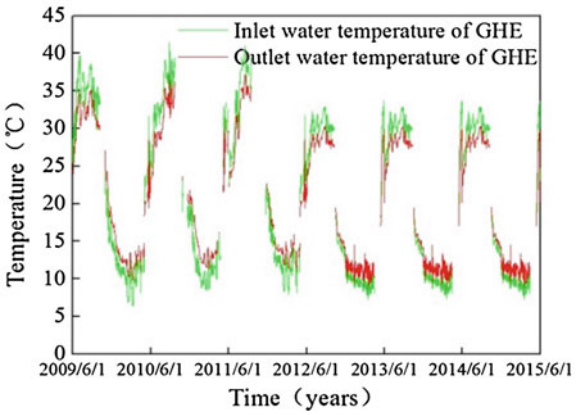

Fig. 45.12 Inlet and outlet water temperature of GHEs in 2009–2015

in transition seasons the coupling operation of cooling tower combined with the GHEs can effectively solve the imbalance problem of the rejected/extracted heat.

45.5 Conclusions

1. To resolve the imbalance problem of the rejected/extracted heat of ground source heat pump (GSHP) in areas of southern China, this paper presents a new operation mode that in summer night the intermittent operation of GHEs with the cooling tower as the supplemental heat rejecter of GSHP system and in transition seasons the coupling operation of cooling tower combined with the GHEs.
2. The practical analytical model of GHE based on the line-source theory is established. The relative errors between the calculated and measured temperatures in summer and winter are 2.6 and 3.7 %, indicating the effectiveness of the calculation method.
3. The analysis under the proposed operating mode for a GSHP system in Nanjing indicates it is feasible to use the proposed operation mode, and the borehole wall temperature is decreased from 33 °C (peak-load period in 2011 summer) to 28 °C, correspondingly, the outlet water temperature of GHEs is decreased from 35 °C (peak-load period in 2011 summer) to 29 °C. The imbalance problem of the rejected/extracted heat is effectively resolved.

Acknowledgments This study is funded by Beijing Nature Science Foundation (3102006), Xinjiang Science and Technology Foundation (201091115) and Xinjiang Youth Science Foundation (2010211B03).

References

1. ASHRAE(1995) Commercial/institutional ground-source heat pump engineering manual. American society of heating, refrigerating and Air-conditioning engineerings Inc, Atlanta
2. Gilbreath CS (1996) Hybrid ground-source heat pump systems for commercial applications. Master's thesis, University of Alabama, Tuscaloosa
3. Kavanaugh (1998) S.P.A design method for hybrid ground-source heat pumps. ASHRAE Trans 104(2):691–698
4. Phetteplace G, Sullivan W(1998) Performance of a hybrid ground-coupled heat pump system. ASHRAE Trans 104(1b):763–770
5. Singh JB, Foster G(1998) Advantages of using the hybrid geothermal options. The second Stockton College of New Jersey, New Jersey
6. Man Y, Yang HX, Wang JG (2010) Study on hybrid ground-coupled heat pump system for air-conditioning in hot-weather areas like Hong Kong. Appl Energy 87:2826–2833
7. Lee CK, Lam HN (2008) Computer simulation of borehole ground heat exchangers for geothermal heat pump systems. Renew Energy 33:1286–1296
8. Zeng HY, Diao NR, Fang ZH (2003) Heat transfer analysis of boreholes in vertical ground heat exchangers. Int Heat Mass Transf 46(23):4467–4481
9. Chen C, Wang YF, Ren Y et al (2009) Comparison of vertical U-tube ground heat exchanger thermal resistance calculation methods. J Hunan Univ 36(12):58–62
10. Zeng HY, Diao NR, Fang ZH (2002) A finite line-source model for boreholes in geothermal heat exchangers. Heat transf Asian Res 31(7):558–567
11. Chen C, Zhou P, Wu JS, et al (2012) Feasibility analysis on seasonal soil thermal recovery technology of cooling towers. 18th China HVAC annual conference, p 222

Chapter 46
Optimized Configuration of Cooling Source in Districted CCHP System: A Case Study in Guangxi

Chundie Li, Jun Lu, Chuck Yu, Xinhui Zhang and Wenzhuo Wang

Abstract This study has the objective to study the optimized configuration of cooling source of a districted natural gas Combined Cooling Heating and Power (CCHP) system, and as a result, models of cooling source, distribution and system energy efficiency were established. Through a C# program, hourly simulation of operation quantity, power consumption, and equivalent thermal coefficient (ETC) of the cooling system during May to October was conducted under three configuration strategy schemes. The results revealed that when the waste heat of CCHP system was properly utilized, increasing the number of electric chiller could increase primary energy utilization rate. Scheme One with the most electric chiller units (15 units) consumed the most power, but had the highest ETC of 1.031 (mean),which was, respectively, 0.268 and 0.346 higher than that of Scheme Two with 11 electric chiller units and Scheme Three with most steam BrLi absorption chiller units (nine units). Scheme Three needed the most steam which led to the least electricity generated. Although in this scheme, the electric chillers consumed the least power, the average remaining electricity of the CCHP system was the lowest (64,992.4 kWh), which was 21,441.9 and 6,233.8 kWh less than that of Scheme One and Scheme Two. ETC of the three schemes (1.031, 0.763, and 0.685, respectively) were much less than that of electric chiller (2.630), which meant that the main reason for the decrease of primary energy utilization rate of the cooling system was due to low primary energy utilization rate of the distribution system.

C. Li (✉) · J. Lu · X. Zhang
Key Laboratory of the Three Gorges Reservoir Region's Eco-Environment, Ministry of Education, Chongqing University, Chongqing 400045, China
e-mail: lcdshiwo@126.com

C. Yu
International Society of the Built Environment (ISBE), Milton Keynes MK7 8HQ, UK

W. Wang
Archtecture College, Changan University, Xi'an 710061, China

A. Li et al. (eds.), *Proceedings of the 8th International Symposium on Heating, Ventilation and Air Conditioning*, Lecture Notes in Electrical Engineering 262,
DOI: 10.1007/978-3-642-39581-9_46,

Keywords Districted cooling CCHP · Cooling source · Optimized configuration · Equivalent thermal coefficient

46.1 Introduction

This study was based on a building project in Guangxi. The CCHP (Combined Cooling Heating and Power) system uses natural gas as fuel, and it is an energy conversion and supply system which supplies power, heating, and cooling simultaneously. The system has an obvious energy conservation potential, and because of its economic efficiency and low impact on environment, it is widely utilized in various public buildings or building complex [1].

Because of the complex energy supply methods, there are many configurations of CCHP system for the same cooling, heating, and electric load demands. In order to insure the system's economical and effective operation, reasonable configuration of CCHP system is needed based on the cooling, heating, and electric load characteristics. Satoshi et al. [2] analyzed the optimal configuration and operation of Fuel cell-CCHP system under different load distribution through a case study. Satoshi et al. used linear programming and mixed integer linear programming to optimize the micro gas turbine CCHP system, and confirmed the system's optimal unit number by analyzing the relationship between the optimal gas turbine's number and maximum energy demand under variable working conditions [3]. Zhang [4] used mathematical software to fit the main performance parameters of a micro gas turbine and BrLi absorption unit into analytical function. Through a case study, optimal analysis of CCHP system's configuration and operation was achieved [4].

However, the researches above mostly concentrate on optimal configuration of ideal steady load, which could lead to differences between analysis results and actual operation. Configurations based on actual case's annual dynamical load are rare, and there are almost no research on the integrative system of cooling source and distributed system of districted CCHP system. This study is based on a building project in Guangxi, and undertook energy consumption analyses by annual load prediction. The objective was to establish an integrative model of the cooling source and distribution system. Based on certain system operation strategy and the choosing principle cooling source units' configuration, the study has proposed an optimal cooling source units' configuration scheme, which would provide the basis for CCHP system's design and whole energy utilization rate advancement to achieve energy and operation efficiency.

46.2 General Description of the System

The studied districted CCHP system supplies cooling and power for a building complex of an area of 259×10^4 m^2, the cooling period is during May 1st–October 20th. The buildings' hourly cooling load characteristic simulated by DeST software is shown in Fig. 46.1, the max cooling load is 163.42 MW which occurs at 15:00 on August 6th typical year; The hourly electric load characteristic based on hourly and monthly share ratio [5] is shown in Fig. 46.2, the max electric load is 1,36,852.3 KW which occurs at 14:00 during every July of typical year.

Based on the results of cooling and electric load simulation, the electricity generating part of the CCHP system used three gas-steam turbine combined cycle units, which has a rated generating output of nearly 43 MW and a generating efficiency of 42 % per unit set of gas turbine. The extraction condensing steam turbine has a rated generating output of 12 MW, a generating efficiency of 11 % under straight condensing condition and 5 % under extraction condensing condition. In this case study, the gas turbine was assumed to be steadily operated, the exhaust rate was adjusted by regulating the steam turbine's straight/extraction condensing conditions. The cooling source used hot water BrLi absorption chiller unit with refrigerating capacity of 4,536 kW, steam BrLi absorption chiller unit with refrigerating capacity of 9,100 kW and electric chiller unit with refrigerating capacity of 8,800 kW. The steam of the steam BrLi absorption chiller units would come from the steam turbine's exhaust, the best exhaust per unit set was 32 t/h. The hot water of the hot water BrLi absorption chiller units would come from heat recovery boiler's waste heat. The electricity needed by the electric chiller units and other electric equipments of the cooling system was defined as onsite electrical system, which comes from the gas-steam turbine combined cycle system's electric generation.

The districted CCHP system operated following the cooling load strategy is connected to grid but not internet electric. The cooling source operate strategy is open hot water and steam BrLi units preferentially.

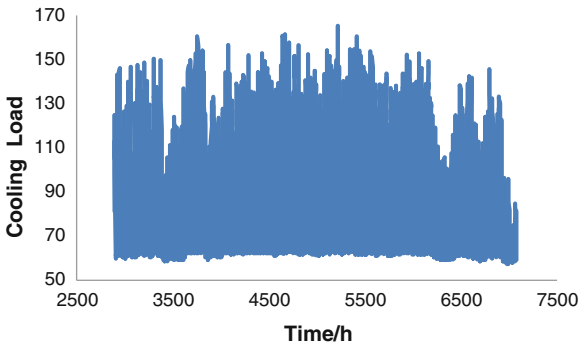

Fig. 46.1 Hourly cooling load characteristic during annual cooling season

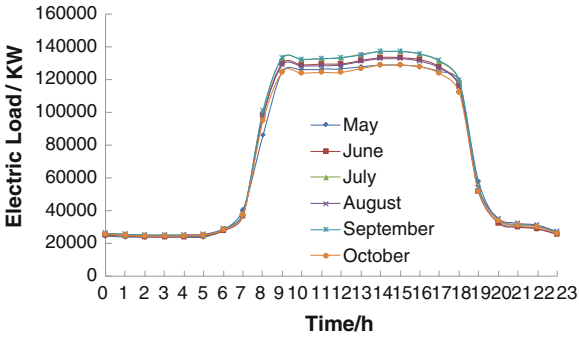

Fig. 46.2 Electric load during a cooling season

The electric chiller units was used at peak level, and controlling the units' open-stop number was the priority method for regulating cooling capacity of the CCHP system, in order to make sure that the units were maintained at efficient operation region. The chilled water system used variable flow system by secondarily pump with 7 °C temperature difference control, temperature of supply/return water was 6/13 °C, primary pump system's operation strategy was "one unit to one pump" mode, in order to keep constant flow in units; the secondary pump system was divided into four circuits, among them there were two circuits, each with four pumps and has an assumed 25 % rated load. The other two circuits, each with three pumps has an assumed 35 % rated load. The cooling water system used "not one unit to one tower" mode and operated in constant flow. The cooling water pump used "one unit to one pump" mode.

46.3 System's Energy Consumption Model

46.3.1 Cold Source Model

Utilizing the data of 8,800 kW electric chiller units under different working condition provided by manufacturer, using the origin 8.0 software to matching its performance characteristics, the relationship of units' EER, cooling water inflow temperature and units' load rate was determined based on the definition shown in Eq. (46.3.1). This model applies to cooling water constant flow operation condition.

$$\begin{aligned} \mathrm{EER} &= \frac{Q_c}{W} \\ &= \frac{-1.47917 + 10271.86174\varepsilon - 0.10417t_{c,i} - 1.60985\varepsilon^2 - 0.00208t_{c,i}^2 - 0.01515\varepsilon t_{c,i}}{578.71637 + 727.94359\varepsilon - 36.43155t_{c,i} + 206.86553\varepsilon^2 + 0.70387t_{c,i}^2 + 23.12987\varepsilon t_{c,i}} \end{aligned} \tag{46.3.1}$$

In Eq. 46.3.1,

Q_c unit refrigerating output, kW

W unit power, kW

ε unit load rate, $0.1 < \varepsilon < 1$

$t_{c,i}$ unit cooling water inflow temperature, 20 °C $< t_{c,i} <$ 38 °C.

Through matching, the models of hot water and steam BrLi absorption chiller are shown in Eqs. (46.3.2) and (46.3.3) (Fig. 46.3).

$$\xi_{rs} = -0.0032t_{c,i} + 0.85976 \tag{46.3.2}$$

$$\xi_{zq} = -0.00207t_{c,i} + 1.46017 \tag{46.3.3}$$

In the equations,

ξ unit heat ratio

$t_{c,i}$ unit cooling water inflow temperature, 20 °C $< t_{c,i} <$ 38 °C

46.3.2 *Distribution Model of Secondary Chilled Water Variable Flow*

After frequency conversion, which was based on hourly flow assumed by the water pump, combining with the pump's frequency conversion regular pattern, the single water pump power was calculated using Eq. (46.3.4):

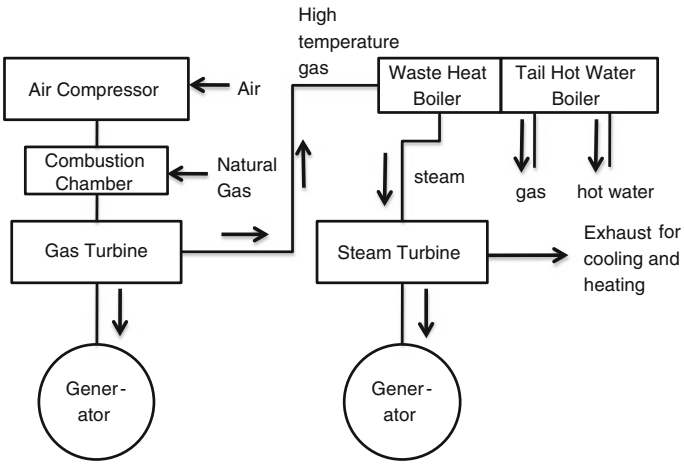

Fig. 46.3 Schematic diagram of the distributed energy system of this project

$$P_{E,\tau} = \left(\frac{Q_\tau}{Q_E}\right)^3 P_E \tag{46.3.4}$$

In Eq. (46.3.4):

$P_{E,\tau}$ at τ moment, after frequency conversion, the single water pump's power, kW;
Q_τ at τ moment, the flow of water pump, m^3/h;
Q_E water pump's rated flow, m^3/h;
P_E water pump rated power, kW

The Circuit j, secondary pump's power consumption was calculated using Eq. (46.3.5):

$$P_{E,\tau,j} = \sum_i P_{i,E,\tau} N_{i,E,\tau} \tag{46.3.5}$$

In the equation:

$P_{E,\tau,j}$ at τ moment, secondary pump's power of j circuit, kW;
$P_{i,E,\tau}$ at τ moment, i tyle water pump's power after frequency conversion of j circuit, kW;
$N_{i,E,\tau}$ at τ moment, i type water pump's open number of j circuit

The secondary system's total energy consumption was calculated using Eq. (46.3.6):

$$P_{s2,\mathrm{var}} = \sum_j P_{E,\tau,j} \tag{46.3.6}$$

In the equation: $P_{s2,\mathrm{var}}$—the total power after secondary pump's frequency conversion, kW.

46.3.3 Heat Engineering Calculation Model of Cooling Tower

Merkel enthalpy method was used to simulate hourly passing in and out water temperature of the cooling tower. The main theory of this method is to find the best outflow water temperature of the cooling tower, in order to make the cooling tower's characteristic number N', which is only related to the cooling tower's structure and the cooling number N, which is equal or very close to the integration of the changing temperature

$$N' = \frac{K_{dv} V}{G_w} \tag{46.3.7}$$

$$N = \frac{1}{K} \int_{T_{w2}}^{T_{w1}} \frac{\mathrm{d}T_w}{(h_w - h)} \tag{46.3.8}$$

In the equations:

K_{dv} the cooling tower's volumetric mass transfer coefficient, kg/(m^3 s);
V padding volume, m^3;
G_w cooling water flow, m^3/s;
K the coefficient considering water evaporation taking away heat;
T_{w1} the inflow water temperature, °C;
T_{w2} the outflow water temperature, °C;
h_w saturated air enthalpy under corresponding water temperature, J/kg. Assumed only related to water temperature.

Based on the heat transfer characteristic of the cooling tower, the relationship of air flow enthalpy and cooling water's temperature difference was conducted:

$$\Delta h = \frac{\Delta T_w c_w \mu}{K} \tag{46.3.9}$$

In the equation:

Δh Increment of air enthalpy value caused by absorption of cooling water heat when air flow through an infinitesimal segment of the cooling tower fill, J/kg;
ΔT_w The temperature difference caused by cooling of cooling water when air flow through an infinitesimal segment of the cooling tower fill, °C;
c_w Specific heat of water, J/(kg °C);
μ Water–gas ratio.

When the cooling tower's air quantity, water flow, cooling tower's cross sectional area, padding volume mass transfer coefficient, etc., are known, the outflow water temperature could be calculated by using Eq. (46.3.9) combining with the above equations.

46.3.4 Evaluation Model of Energy Conservation

Cooling system's ETC was utilized to conduct energy conservation evaluation for the cooling source part of CCHP system. The cooling system's ETC indicates that the system's output cooling (kJ) by consuming 1 kJ of primary fuel's heat. The cooling system's energy consumption includes two parts:

- The system's heat consumption Q_{hc}, which includes that of hot water BrLi absorption chiller and steam BrLi absorption chiller;

- The system's power consumption W_a, which includes that of electric chiller units, solution pump, cooling water pump, chilled water pump cooling tower, etc.

The cooling system's ETC (ξ_{ca}) was calculated using Eq. (46.3.10):

$$\xi_{ca} = \frac{Q_c}{Q_{hc}/(\mu\eta_{hs}) + W_a/(\eta_e\eta_n)} \tag{46.3.10}$$

In the equation:

ξ_{ca} Cooling source system's ETC
Q_c System's cooling output, kW
Q_{hc} Heat energy needed by absorption refrigeration unit, kW
W_a System's power consumption, kW
μ High grade heat energy by unit fuel burning amount to low grade heat energy by cogeneration turbine extraction or at back pressure steam mouth, literature [6] study this coefficient as key point, specific to this project's system layout of equipment, the suggested value is 2.65/KJ^{-1}
η_{hs} heat supply efficiency, specific to this project's system layout of equipment, the suggested value by [6] is 0.215
η_e combined cycle generating efficiency, under extraction condensing condition of this distributed energy supply system, the generation efficiency is 0.48
η_n grid efficiency, utilize grid electricity, the value is 0.9 [6].

46.4 Simulation Method

C# program was utilized to develop a cooling system energy consumption simulation software. Based on the CCHP system's cooling system of the building project in Guangxi, the case study's annual dynamic load was input, the system's energy consumption characteristics were analyzed with the cooling source model and distribution model (see in Fig. 46.4).

46.5 Contrast of Cooling Source Configuration Scheme

46.5.1 Configuration Principle of Unit Number

1. The configuration of unit number needs to satisfy the demand of the max cooling load in a day and part load ratio adjustment.

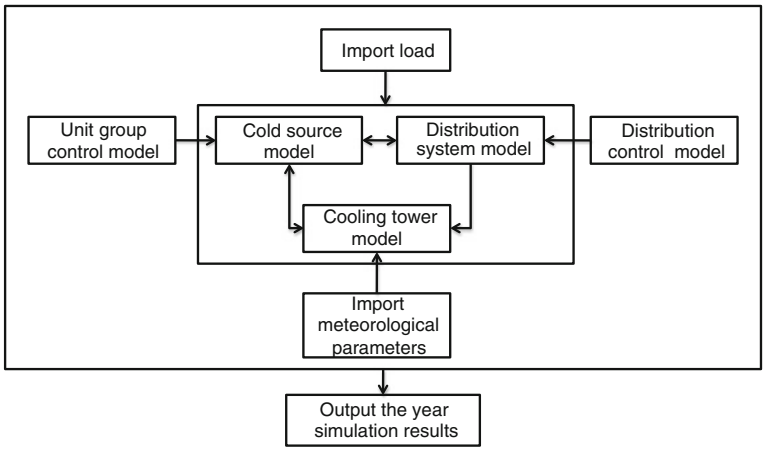

Fig. 46.4 Simulation process

2. Steam BrLi absorption chiller unit's number needs to satisfy the best exhaust rate of the steam turbine, which means the steam that the steam BrLi absorption chiller unit needed cannot exceed the sum of three steam turbines' best exhaust rate of 96 t/h. Therefore, the number of steam BrLi absorption chiller unit X_{BrLi} : $0 < X_{\mathrm{BrLi}} \leq 9$.

46.5.2 Configuration Scheme of Unit Number

Because the hot water needed in the hot water BrLi absorption chiller come from heat recovery boiler's waste heat, this needs to be maximized for utilization, the number of hot water BrLi absorption chiller would not change in this case. Nevertheless, steam BrLi absorption chiller's heat source come from steam turbine's medium pressure suction, which would influence the gas-steam turbine combined cycle system's power generation. The electric chiller's power come from the gas–steam turbine combined cycle system, and its number could influence the quantity of electricity sent to users. Consequently, discussion of cooling system's energy conservation is conducted by changing numbers of these two kinds of units, and the specific scheme is shown in Table 46.1.

Table 46.1 indicates that, Scheme One is a configuration with maximum number of electric chiller units, Scheme Three is a configuration with maximum number of steam BrLi absorption chiller units, the ratio of three kinds of units in these three schemes were respectively: 0.83:1.11:8.06; 0.83:3.31:5.86; 0.83:4.93:4.24.

Table 46.1 The total installed capacity of district cooling station

	Type of cooling source unit/ unit set refrigerating output (kW)	Hot water BrLi absorption chiller unit/4536	Steam BrLi absorption chiller unit/9100	Electric chiller unit/ 8800
Scheme one	Capacity (MW)/number	13.608/3	18.2/2	132/15
Scheme two	Capacity (MW)/number	13.608/3	54.6/6	96.8/11
Scheme three	Capacity (MW)/number	13.608/3	81.9/9	70.4/8

46.5.3 Results of Comparative Analysis

From Figs. 46.5, 46.6, and 46.7, the three hot water BrLi absorption chiller units were kept open during the whole cooling period in Scheme One and Scheme Two. In Scheme Three, the number of steam BrLi absorption chiller units kept open was nine during daytime and six at night. Electric cooling units were used to operate at peak level, so they were opened and stopped frequently. In all three schemes, more than four units were kept opened during most of the operation period.

Figure 46.8 shows that the system power consumption was the highest with Scheme One, with a hourly mean value of 14,766.78 kWh and annual total power consumption of 6,20,50,025 kWh. The system power consumption of Scheme Two was between Scheme One and Scheme Three, with hourly mean value of 9,637.89 kWh and annual total power consumption of 4,04,98,403 kWh. The cooling system power consumption of Scheme Three was the lowest, with hourly mean value of 7,315.69 kWh and annual total power consumption of 3,07,40,527 kWh.

Figure 46.9 shows the cooling system ETC: Scheme Three < Scheme Two < Scheme One. Based on the simulating data, the mean value of the system

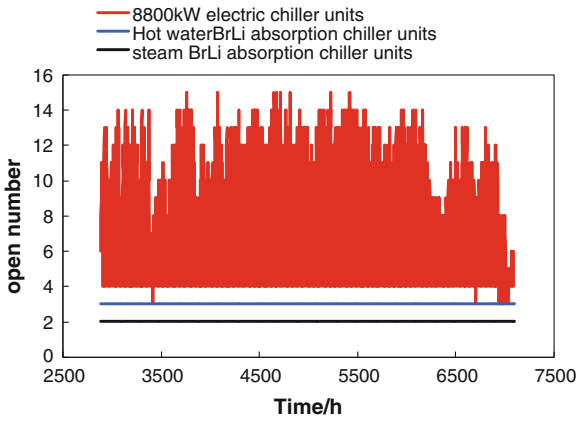

Fig. 46.5 Annual units combination and operation way (scheme one)

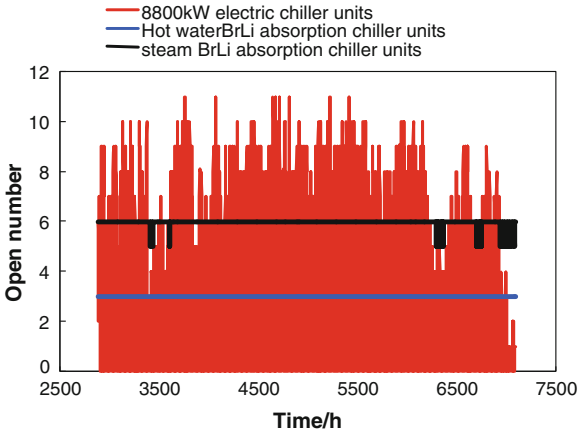

Fig. 46.6 Annual units combination and operation way (scheme two)

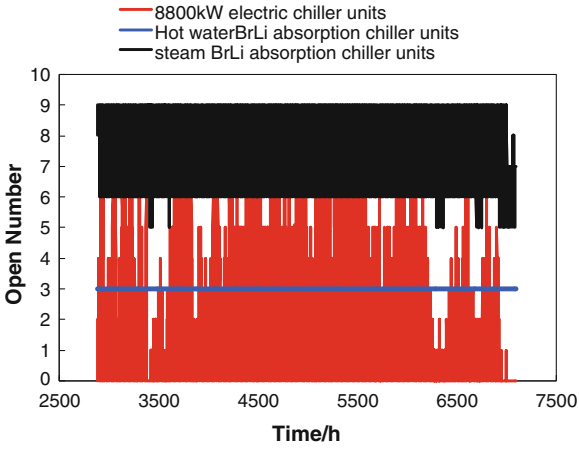

Fig. 46.7 Annual units combination and operation way (scheme three)

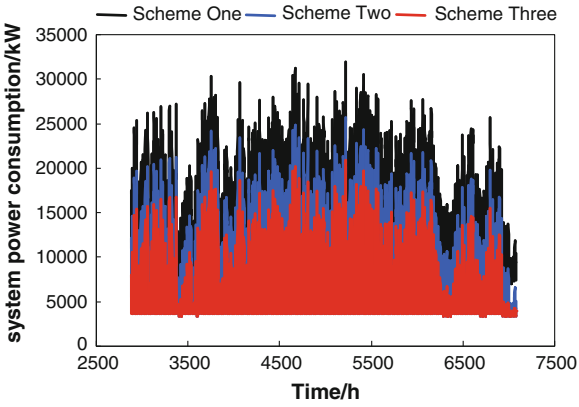

Fig. 46.8 Hourly cooling system power consumption of three schemes

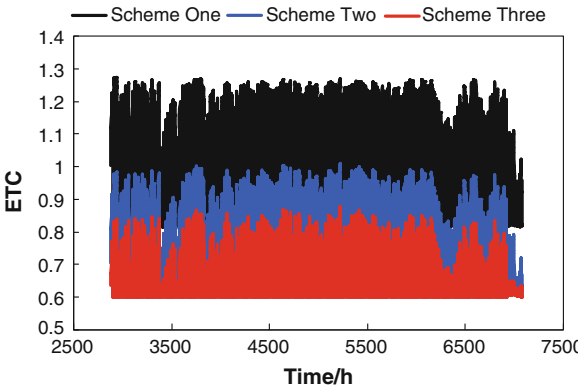

Fig. 46.9 Hourly cooling system ETC of three schemes

ETC for the three schemes is obtained: the ETC of Scheme One was 1.031, the ETC of Scheme Two was 0.763, and the ETC of Scheme Three was 0.685.

The situation of refrigerating unit's primary energy utilization was evaluated using Eq. (46.3.10). When evaluating electric chiller units' ETC alone, set $Q_{\mathrm{hc}} = 0$; When evaluating BrLi absorption chiller unit alone, W_a should be the power consumption of BrLi absorption chiller unit, which is the power consumption of solution pump far less than heat consumption, so W_a approximately equal to 0.

When translating the energy efficiency of electric chiller unit into ETC, which means when $Q_{\mathrm{hc}} = 0$, there is:

$$\xi_{8800} = 6.088 \times 0.48 \times 0.9 = 2.630$$

When translate the energy efficiency of BrLi absorption chiller unit into ETC, which means when $W_a = 0$, there is:

$$\xi'_{rs} = 0.777 \times 2.65 \times 0.215 = 0.443$$

$$\xi'_{zq} = 1.408 \times 2.65 \times 0.215 = 0.802$$

By contrasting the cooling system and unit ETC of Scheme One, Scheme Two, and Scheme Three. The cooling system ETC were, respectively, 1.031, 0.763, 0.685, which were all close to the ETC of steam BrLi absorption chiller unit (0.802), but far less than the ETC of electric chiller units (2.630), and in these three schemes, electric chiller units' capacity occupied at least 42.43 % of the total capacity (in Scheme One), indicating that the primary energy utilization rate of this project's distribution system was low, and lead to the low primary energy utilization rate of the whole system.

Table 46.2 shows the electric quantity of each scheme after deducting building complex electricity load and cooling system power. The number of electric chiller units in Scheme One was the most, and the power remained was also the most too, with a mean value of 86,434.3 kWh, so there is no need to buy power from the

Table 46.2 The power of each scheme after generating electricity

	Maximum remaining power (kWh)	Mean remaining power (kWh)	The hour demand to buy power from the grid (h)	Mean value of power purchase (kWh)
Scheme one	144340.9	86434.3	0	0
Scheme two	127933.4	71226.2	81	1593.9
Scheme three	127933.4	64992.4	750	4463.6

grid. Scheme Three has the least number of electric chiller units, but has the most number of steam BrLi absorption chiller units, and the consumption of steam was lower than the generating efficiency of the steam turbine, so has the least power remained with a mean value of 64,992.4 kWh; requiring to buy 750 h of demand of power from the grid, the mean value of power purchase would reach 4,463.6 kWh. If take the steam turbines' remained power as the main consideration, Scheme One would be the best.

46.6 Conclusions

This paper has considered the ETC of cooling system as energy conservation evaluation index, and conducted hourly simulation of cooling system power consumption and ETC of three different configuration schemes by establishing models of their cooling source, distribution system, and energy efficiency, in order to find the optimal configuration for the cooling source. The conclusions are as follows:

(1) Scheme One has the most electricity consumption, with a mean value reaching 14,766.78 kWh; the ETC of the cooling system was the highest of the three schemes, with an annual mean value of 1.031. Scheme Three has the most number of steam BrLi absorption chillers, with the least the power consumption of 7,315.69 kWh; but the ETC of cooling system was the lowest by comparison to the other schemes, with an annual mean value of 0.685. Therefore, when the waste heat of CCHP system was fully utilized, the increased number of electric chiller units would increase the energy efficiency effectively, in order to maximize the benefits of CCHP system.
(2) Although Scheme Three has the least power consumption of the electric chiller units, the number of steam BrLi absorption chiller units in Scheme Three was the most with the largest need of steam quantity, So the time to keep steam turbine on extraction condensing condition would be longer than that of the other two schemes; therefore, leading to less power generated. The mean remained power of the whole system was 64,992.4 kWh, so would require

purchasing power to meet the 750 h of energy demand from the grid. The mean value of power purchased reached 4,463.6 kWh, which in contrast to the situation in Scheme One that had more power remained, therefore, if taking the remained power of the steam turbine as the main consideration, Scheme One would be the best.

(3) The ETC of the cooling system were: 1.031, 0.763, 0.685, these were far less than the ETC of the electric cooling unit which was 2.630. This indicates that the primary energy utilization rate of CCHP system in district distributed energy system was low, which was the main reason for the low primary energy utilization rate of the whole system. Hence, lower the distribution energy consumption should be the emphasis in engineering design and management.

References

1. Fu L, Li H (2007) The technology and application of natural gas combined cooling heating and power system. China Building Industry Press, Beijing (in Chinese)
2. Satoshi G, Ryohei Y, Koiehi I (2002) Optional Unit sizing of cogeneration systems in consideration of uncertain energy demands as continuous random variables. Energy Convers Manage 9(43):1349–1361
3. Satoshi G, Ryohei Y, Koichi I (2005) Parametrc study on economic feasibility of mieroturbine cogeneration systems by an optimizaion approach. J Eng Gas Turbine Power 2(127):389–396
4. Zhang WK (2003) The BCHP cogeneration system's configuration and its optimal application analysis. Dissertation for the Master Degree, Shanghai Jiao Tong University, Shanghai (in Chinese)
5. Jin HG, Xu JZ, Zheng XD (2009) Distributed heating and power cogeneration system devices and application. Power Industry Press, Beijing (in Chinese)
6. Hu SC (2009) Energy saving research of combined cooling, heating and power system based on absorption refrigeration. Dissertation for the Master Degree, Lanzhou University of Technology, Lanzhou

Chapter 47
Experimental Study on Performance Comparison Between Heavy and Lightweight Radiant Floor Cooling Combined with Underfloor Ventilation Air Conditioning System

Dongliang Zhang, Ning Cai, Yingxiang Rui, Hu Tang and Minghui Liu

Abstract Indoor air temperature, floor temperature, and wall surface temperature were measured when lightweight radiant floor cooling combined with underfloor ventilation (LRFCUV) air conditioning system and heavy radiant floor cooling combined with underfloor ventilation (HRFCUV) air conditioning system operated. And indoor air temperature field, heat-transfer capability, and thermal comfort were analyzed. Experimental results show that LRFCUV air conditioning system started up faster than HRFCUV air conditioning system. When the system reached stable condition, net radiant floor heat quantity of HRFCUV air conditioning system was larger than that of LRFCUV air conditioning system, and thermal comfort of HRFCUV air conditioning system was better than that of LRFCUV air conditioning system.

Keywords Lightweight radiant floor cooling · Heavy radiant floor cooling · Underfloor ventilation · Experimental study

47.1 Introduction

The use of radiant floor heating (RFH) systems to achieve occupant thermal comfort in buildings with low-energy demands has been greatly increased in China and other countries. To reduce air conditioning equipment investment, radiant floor heating system can also be used for radiant floor cooling. And due to thermal comfort and dew condensation, radiant floor cooling system usually combines with

D. Zhang (✉) · N. Cai · Y. Rui · H. Tang · M. Liu
Nanjing Institute of Technology, 1 Hongjing Road, Nanjing 211167, China
e-mail: zhangdongliang@njit.edu.cn

A. Li et al. (eds.), *Proceedings of the 8th International Symposium on Heating, Ventilation and Air Conditioning*, Lecture Notes in Electrical Engineering 262,
DOI: 10.1007/978-3-642-39581-9_47,

underfloor ventilation system. Because of the advantages of independent temperature and humidity control, radiant floor cooling combined with underfloor ventilation air conditioning system will effectively reduce the energy consumption for the environment control. At present, two main types of radiant floor systems exist: heavy and lightweight radiant floor systems. In heavy radiant floor system, the pipes applied to the floor heating or cooling systems are usually laid out in the concrete layer of the floor construction. While in lightweight radiant floor system, the pipes are placed in aluminum foil.

There have been several studies dealing with radiant floor cooling (RFC) systems in literature. Zhen [1] analyzed thermal comfort of 82 subjects in radiant cooling system, and found that thermal comfort model in radiant cooling system is consistent with PMV model. Meanwhile, discomfort caused by vertical temperature gradient and blowing can be effectively improved. Leigh [2] compared energy consumption of conventional air conditioning system to that of radiant floor cooling combined with dehumidifying ventilation system during cooling period, and found that the latter accounts for only 1/3 of the former. Corina [3] found that radiant cooling system can be operated in the USA with low possibility of dew condensation, and found that the energy consumption of radiant cooling system can be saved by 30 % compared to that of all air conditioning system. Eusébio [4] compared thermal comfort of radiant floor cooling system and radiant ceiling cooling system under the same condition by numerical simulation, and found the former thermal comfort is better. Laouadi [5] developed a model for analyzing radiant heating and cooling systems which can be used in building energy simulation software. Strand [6] summarized a radiant system model within building energy simulation program. Jin [7] proposed a calculation method for the floor surface temperature in radiant floor heating/cooling system. Tye-Gingras [8] investigated on heat-transfer modeling assumptions for radiant panels with serpentine layout. The construction method of LRF system was first introduced by Qi [9] in China. And Qiu [10] presented a new design in combination of prestressed concrete hollow floor units with a new dry floor structure without the filling layer of concrete, and proposed heat-transfer theory and analyzed effect of the factors on radiant floor cooling capability by field test [11]. Weitzmann et al. [12] developed a method for calculating thermal properties of LRF panels based on an experimental setup.

Up to now, seldom researches have been conducted on performance comparison between HRFCUV air conditioning system and LRFCUV air conditioning system. In this paper, indoor air temperature field, heat-transfer capability, and thermal comfort of the above two systems are compared under the same operating conditions. This kind of work is aimed to provide experimental basis for the design of operation, construction, and commissioning of radiant floor cooling system.

47.2 Radiant Floor Cooling Combined with Underfloor Ventilation Air Conditioning System Characteristic

Indoor heat and humidity are eliminated by convective heat transfer in traditional air conditioning system. While they are eliminated by both thermal radiation and convection heat transfer in radiant floor cooling combined with underfloor ventilation air conditioning system. Indoor velocity field and humidity field are determined by underfloor ventilation system operating parameters. And indoor temperature field is affected by both underfloor ventilation system operating parameters and inner surface temperature parameters which are mainly affected by radiant floor cooling system parameters.

Indoor air humidity is not able to be eliminated by radiant floor cooling system, so people will feel stuffy when indoor air humidity is large. Meanwhile, floor surface will appear dew condensation if floor surface temperature is lower than dew point temperature of the air near floor. Therefore, underfloor ventilation system is introduced. Its role is reflected in the following aspects: (1) fresh air is introduced to meet indoor health requirements; (2) indoor air humidity is able to be eliminated by underfloor ventilation system; (3) underfloor ventilation system can also bear part of sensible heat load in order to make up for the defects of radiant floor cooling system insufficient cooling capability; (4) air lake will be formed around floor surface to prevent direct contact between high humidity air and low temperature floor, so as to avoid dew condensation; and (5) attached flow will increase convective heat transfer between indoor air and floor surface, and research [13] shows that, convective heat-transfer coefficient between floor and indoor air of radiant floor cooling combined with underfloor ventilation system is 45 % lager than that of single radiant floor cooling system, and total heat-transfer capability will be increased by 30 %.

47.3 Experimental System and Procedure

47.3.1 Test Room Layout

Two same test rooms are equipped with heavy and lightweight floor cooling system. Figure 47.1 shows the lab sketch. The height of the room is 2.8 m. Outside the test room is a compensate room. The units in the compensate room is used to support the environment that the experiments demands. The thickness of the wall is 240 mm. The heat-transfer coefficient of the wall is 1.97 W/(m^2·K). The distance between pipes next each other is 100 mm and the diameter of the pipe is 16 mm.

Chilled water is produced by ground source heat pump and then distributed to air handling unit of underfloor ventilation system and every water loop by manifold to produce space cooling. Water supply temperature is controlled by changing the

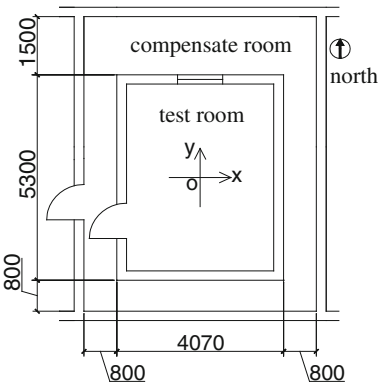

Fig. 47.1 Lab sketch

mixing ratio of primary water supply and backwater. Fresh air and primary return air are mixed and handled by air handling unit and then transferred by concealed wind pipe to skirting outlet which is 0.3 m high from floor.

47.3.2 Measuring Instruments and Test Points

In this experiment, temperature of water supply, backwater, outdoor air, indoor air, upper floor surface, interior surface of each wall, ceiling, window, water supply, and backwater are measured. Three classic test points of indoor air temperature are selected in the middle of the test room as follows: 0.1 m high from floor which represent human ankle position, 1.1 m high from floor which represent human respiratory position when sitting, and 1.7 m high from floor which represent human respiratory position when standing. Temperature variation is not obvious in short time due to large thermal inertia of radiation system, so the above parameters are measured in every half hour. Velocity of fresh air, primary air, and supply air, and water flow are measured as well. Table 47.1 shows testing parameters, measuring instruments and the parameters of measuring instruments. Both heavy and lightweight radiant floor cooling combined with underfloor ventilation air conditioning system operate from 9:00 to 12:00.

Table 47.1 Testing instruments and parameters

Testing parameters	Surface temperature (°C)	Air temperature and humidity		Water flow	Water temperature
Testing instruments	Infrared thermometer	Psychrometer		Ultrasonic flowmeter	Thermometer
Measuring range	−32–535 °C	−20–60 °C	10–95 %	0–±32 m/s	0–100 °C
Measuring precision	±1 °C	±0.8 °C	±3 %	±1 %	–

47.4 Experimental Results and Analysis

47.4.1 Temperature Field Distribution Analysis

The variation of indoor air temperatures of three classic test points during operation are shown in Fig. 47.3. Indoor air temperature of LRFCUV system decreases quickly in the first hour and then decreases slowly. While indoor air temperature of HRFCUV system decreases quickly in the second hour and then decreases slowly. LRFCUV system starts up quicker than HRFCUV system. When the above two systems reaches stable operating condition, indoor air temperature of LRFCUV system is 26.2 °C, while that of HRFCUV system is 25.6 °C. Performance of HRFCUV system is better than that of LRFCUV system. Indoor air temperature gradient in vertical direction of both LRFCUV system and HRFCUV system are less than 0.2 °C per meter. And indoor air temperature increases with the increase of height because of small hot air density (Fig. 47.2).

47.4.2 Heat-Transfer Capability Analysis

Total heat-transfer capability equals to refrigerating capacity supplied by both underfloor ventilation system and radiant floor cooling system. Refrigerating capacity supplied by underfloor ventilation system is calculated by Eq. (47.1).

$$q_c = G_n(h_2 - h_1) \tag{47.1}$$

where, G_n is air supply volume; h_2 is return air enthalpy; h_1 is supply air enthalpy.

The underfloor ventilation parameters measured value are presented in Table 47.2.

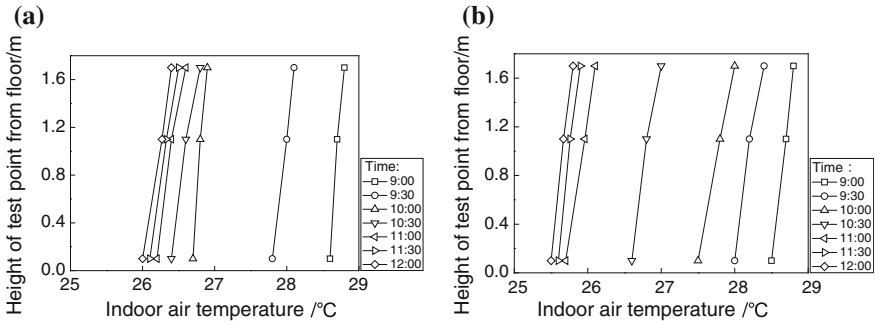

Fig. 47.2 Variation of indoor air temperature. **a** LRFCUV air conditioning system, **b** HRFCUV air conditioning system

Table 47.2 underfloor ventilation parameters

Parameters	Air outlet	Air velocity (m/s)	Air temperature (°C)	Relative humidity (%)
LRFCUV system	Air inlet 1	1.3	20.2	74.4
	Air inlet 2	1.0	21.6	66.2
	Return air outlet	1.9	26.8	60.0
HRFCUV system	Air inlet 1	1.3	20.2	74.4
	Air inlet 2	1.0	21.6	66.2
	Return air outlet	1.9	26.1	60.4

Heat-transfer capability of floor by radiation is calculated with Gebhart Method [14]. In a closed system, heat-transfer capability by radiation of surface j is calculated by Eq. (47.2).

$$Q_j = E_j F_j - \sum_{i=1}^{n} B_{i,j} E_i F_i \tag{47.2}$$

where, E_i and E_j are radiant heat-transfer power of surface i and surface j, respectively, $E_i = \sigma_b \varepsilon_i T_i^4$; F_i and F_j are the area of surface i and surface j, respectively; $B_{i,j}$ is the absorption factor of surface i to surface j, which represents quotient of energy absorbed by surface j from surface i. $B_{i,j}$ is calculated by Eq. (47.3).

$$\begin{bmatrix} \phi_{1,1}\rho_1 - 1 & \phi_{1,2}\rho_2 & \cdots & \phi_{1,n}\rho_n \\ \phi_{2,1}\rho_1 & \phi_{2,2}\rho_2 - 1 & \cdots & \phi_{2,n}\rho_n \\ \cdots & \cdots & \cdots & \cdots \\ \phi_{n,1}\rho_1 & \phi_{n,2}\rho_2 & \cdots & \phi_{n,n}\rho_n - 1 \end{bmatrix} \begin{bmatrix} B_{1,j} \\ B_{2,j} \\ \vdots \\ B_{n,j} \end{bmatrix} = \begin{bmatrix} -\varepsilon_j \phi_{1,j} \\ -\varepsilon_j \phi_{2,j} \\ \vdots \\ -\varepsilon_j \phi_{n,j} \end{bmatrix} \tag{47.3}$$

where, $\phi_{i,j}$ is angle factor for surface i on surface j; ρ_i is reflectivity of surface i; ε_i is emissivity of surface i.

Calculated results are shown in Fig. 47.3. Net radiant heat-transfer quality of LRFCUV air conditioning system increases quickly in one and a half hour and

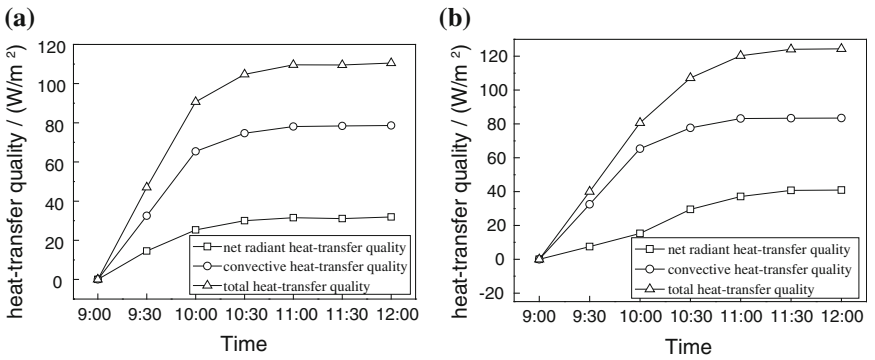

Fig. 47.3 Variation of floor heat-transfer capability. **a** LRFCUV air conditioning system, **b** HRFCUV air conditioning system

then tends to be stable. Its net radiant heat-transfer quality is 32 W/m^2 when the system reaches stable operating condition, which occupies 29 % of the total. While radiant heat-transfer quality of HRFCUV air conditioning system increases quickly in two and a half hour and then tends to be stable. Its net radiant heat-transfer quality is 41 W/m^2 when the system reaches stable operating condition, which occupies 32 % of the total. LRFCUV system starts up quicker than HRFCUV system. However, heat-transfer quality of HRFCUV air conditioning system is more than that of LRFCUV air conditioning system.

47.4.3 Thermal Comfort Analysis

According to the analysis of thermal comfort of 82 subjects in radiation cooling system conducted by Zhen [1], thermal comfort model in radiant cooling system is consistent with Predicted Mean Vote (PMV) model. So PMV and Predicted Percent Dissatisfied (PPD) index are adopted to evaluate thermal comfort of radiant floor cooling system. The above two indexes are obtained by Fanger [15] who gathered 1,396 American and Denmark examinees' reflection on cold and hot feeling. Regression formula makes thermal comfort measurable. The recommended range of PMV and PPD in ISO7730 are as follows: $-0.5 \leq \text{PMV} \leq +0.5$, PPD ≤ 10 %.

In radiant floor cooling system, thermal comfort is greatly affected by thermal radiant between interior room surface and humane body. So mean radiant temperature (MRT) and operating temperature (OT) are proposed to evaluate thermal comfort in addition.

Thermal comfort indexes calculated results are shown in Fig. 47.4. MRT, OT, PMV, and PPD value of LRFCUV air conditioning system decreases more quickly than that of HRFCUV air conditioning system in the first hour. Because of its excellent heat storage performance of floor structure, HRFCUV air conditioning system starts up slower than LRFCUV air conditioning system. When system reaches stable operating condition, thermal comfort of LRFCUV air conditioning

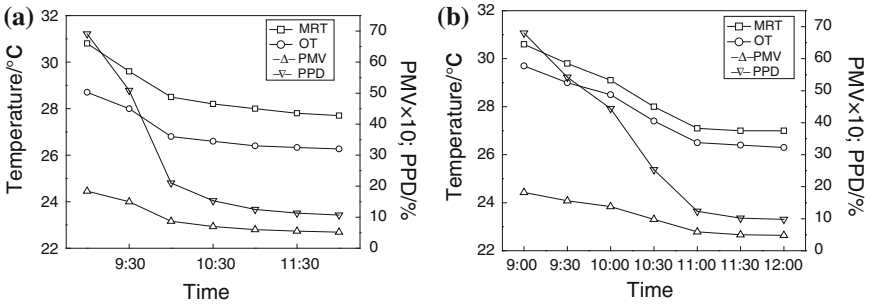

Fig. 47.4 Thermal comfort indexes calculated results. **a** LRFCUV air conditioning system, **b** HRFCUV air conditioning system

system is better than that of HRFCUV air conditioning system. Thermal comfort of LRFCUV air conditioning system can be improved by increasing radiant floor heat-transfer capability or refrigerating capability of underfloor air conditioning system.

47.5 Conclusion

In this paper, indoor air temperature field, heat-transfer capability, and thermal comfort of both LRFCUV air conditioning system and HRFCUV air conditioning system were compared by experiments.

In summary:

(1) LRFCUV air conditioning system starts up faster than HRFCUV air conditioning system.
(2) Indoor air temperature gradient in vertical direction of both LRFCUV system and HRFCUV system is less than 0.2 °C per meter. And indoor air temperature increases with the increase of height because of small hot air density.
(3) When the system reaches stable condition, net radiant floor heat-transfer quantity of HRFCUV air conditioning system is larger than that of LRFCUV air conditioning system.
(4) Thermal comfort of HRFCUV air conditioning system is better than that of LRFCUV air conditioning system.

Acknowledgments This research was supported by Scientific research fund of Nanjing Institute of Technology under Grant No. YKJ201213, YKJ201212, and College students practice and innovation training project of Jiangsu province under Grant No. 2012JSSPITP1988.

References

1. Zhen T, Love JA (2008) A field study of occupant thermal comfort and thermal environments with radiant slab cooling. Build Environ 43(10):1658–1670
2. Leigh SB, Archd, Song DS et al (2005) A study for evaluating performance of radiant floor cooling integrated with controlled ventilation. ASHRAE Transaction ,111(1):71–82
3. Corina S (1999) Energy and peak power saving potential of radiant cooling systems in US commercial buildings. Energy build 30(11):127–138
4. Eusébio ZE, Conceio D, Manuel M, Lúcio JR (2011) Evaluation of thermal comfort conditions in a classroom equipped with radiant cooling systems and subjected to uniform convective environment. Appl Math Model 35(6): 1292–1305
5. Laouadi A (2004) Development of a radiant heating and cooling model for building energy simulation software. Build Environ 39:421–431
6. Strand RK, Baumgartner KT (2005) Modeling radiant heating and cooling systems: integration with a whole-building simulation program. Energy Build 37:389–397

7. Jin X, Zhang XS, Luo YJ (2010) A calculation method for the floor surface temperature in radiant floor system. Energy Build 42:1753–1758
8. Tye-Gingras M, Gosselin L (2011) Investigation on heat transfer modeling assumptions for radiant panels with serpentine layout. Energy Build 43:1598–1608
9. Qi ZX, Lu YJ (2002) Dry modus of water heating system. Build Energy Environ 1:32–34 in Chinese
10. Qiu L, Liu. et al ZS (2005) Feasibility study on floor heating by application of prestressed concrete hollow floor and dry floor structure. Build Sci 21:44–47 in Chinese
11. Qiu L, Wang WH, Zheng SH (2005) Experimental research on radiant cooling of a dry structure floor system, fluid. Machinery 33:68–71 in Chinese
12. Weitzmann P, Svendsen S (2005) Method for calculating thermal properties of lightweight floor heating panels based on an experimental setup. Int J Low Energy Sustain Build 3:1–15
13. Wang ZJ (2004) Low temperature radiant heating and cooling, 1st edn. China Machine Press, Beijing in Chinese
14. Yu QZ (1990) Radiant heat-transfer foundation, 1st edn. Higher Education Press, Beijing Chinese
15. Fanger PO (1982) Thermal comfort. Krieger Publishing Company, Malabar

Chapter 48
Optimization and Energy Efficiency Research of a Large Reclaimed Water Source Heat Pump System

Ziping Zhang and Fanghui Du

Abstract This work describes a large reclaimed water source heat pump system, and elaborate on the composition of the system and its design principles. We make an energy planning for its service area and in accordance with the progress of the project's investment and construction, the system is divided into two stages: the phase I with the energy bus system; the project of phase II uses centralized indirect district heating system, it uses a two-stage heat pump unit in order to reduce the temperature lift of the main heat pump. The whole system adopts the distributed circulating pump power system. The work also analyzes the heating capacity of the system, when the phase II project is completed, the system can provide hydronic heating water with the supply and return water temperature of 55/15 °C, and meet the hydronic heating demand of 8 million square meters of residential buildings. Calculated the coal consumption indicators per unit area in a heating period and compared with the regional boiler room heating system, 8 million square meters of district heating in a heating season can save 53,161 tons of standard coal. The coal saving rate reaches 39.32 %.

Keywords Reclaimed water source heat pump · Distributed heat pump · Two-stage series heat pump · Units distributed power system · Energy saving

48.1 Introduction

Nowadays, the energy input for building operation is mainly constituted by fossil energy carriers and; therefore, building operation is responsible for a large share in global greenhouse gas emissions [1]. As the accelerate development of urban

Z. Zhang · F. Du (✉)
Department of Air Conditioning and Refrigeration Engineering, Hebei University of Engineering, Handan, China
e-mail: dfh1009@163.com

A. Li et al. (eds.), *Proceedings of the 8th International Symposium on Heating, Ventilation and Air Conditioning*, Lecture Notes in Electrical Engineering 262,
DOI: 10.1007/978-3-642-39581-9_48,

construction, heating gap exists in many cities in china. With the energy shortage and the requirement of having a better environment and in order to decrease the energy demand and the related emission, it is necessary for us to develop and use renewable energy source in the urban heating.

Reclaimed water, which is the sewage plant secondary or tertiary effluent in this paper, has the advantages of the concentrated water flow, high temperature (compared to surface water) and relatively clean, etc., so it is the ideal heat source for heat pump units. The wastewater treatment plant is generally located in the edge of the city and in recent years, the reality is that urban construction has been extended to within closer range from the wastewater treatment plant, and the high cost of laying in the water distribution network will no longer be the main problem of no large-scale application in water source heat pump works. Taking the reclaimed water as the heat source of the urban hydronic heating can achieve efficient recycling of urban sewage heat energy, turning waste into treasure, which fully embodies the concept of the development of recycling economy, greatly improves the energy efficiency of the city and reduces the city's dependence on the fossil fuel. It is very significant for us to control air pollution, protect environment, and to construct energy-efficient city.

48.2 Project Overview

The project uses the city's reclaimed water, which is the sewage plant secondary or tertiary effluent and contains a large number of renewable energy, to develop the new energy technologies, and to complement the traditional district heating gap, strengthen the pace of new energy development and use. It can meet 8 million square meters of space heating, and provide cooling of 3 million square meters. Through the reclaimed water heat pump technology, it can realize to provide heating and cooling for the area of around the sewage treatment plant, such as public building, campus, and residents and achieve the goal of energy conservation and emissions reduction.

The sewage plant covers an area of 540 acres with the designed treatment capacity of 700,000 tons and nowadays the daily output reaches 500,000 tons of reclaimed water, it is currently one of the largest sewage treatment plant in china. The wastewater generally comes from urban sewage and industrial wastewater in the east of Beijing-Guangzhou line. The temperature of the effluent is 22–27 °C in summer and 14–19 °C in winter.

The average effluent available flow is 20,833 t/h, and the available temperature lift or drop is about 10 °C. The hot and cold medium for heating and cooling are the effluent of the wastewater treatment plant, it will be delivered to each consumer through the distribution network laying in project of phase I. Intake point of water catchment is located on the tertiary treatment outlet pipe which will extend to the Minxin river, so the water supply has high quality, no secondary pollution.

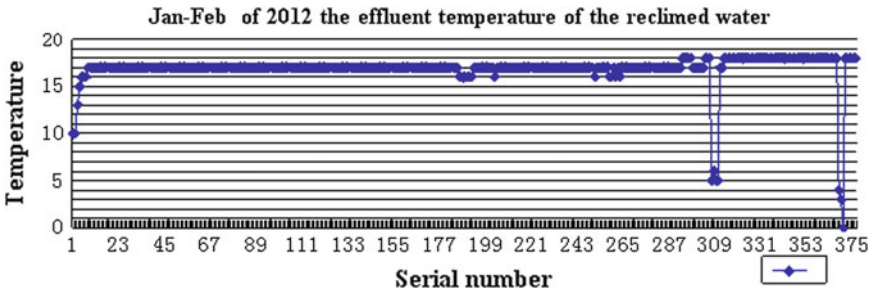

Fig. 48.1 Water outlet temperature in the winter of 2012, January 17–February 17

48.3 System Design Options

48.3.1 Determination of the Water Temperature

As shown in Fig. 48.1, the average water temperature of the water effluent of the coldest month in the winter to 17 °C, using Hong Chang HC2102R, paperless recorder with pt100 thermal resistance probe continuous data collection, thermal resistance probe is suspended on the end of the ultraviolet disinfection drainage where the water velocity is relatively stable, about 20 m from the water catchment point, the thermal resistance probe is 1 m in length, the probe is located 0.5 m below the water surface when water flow under normal circumstances. It will record a data per min that it is difficult for mapping, so taking a data from all the 45,000 per interval 2 h. A total of 375, horizontal axis is the sequence number, and the vertical axis is the measured temperature. Some individual points of lower temperature are the ambient temperature because of the low amount of water caused due to the maintenance of the sewage plant.

48.3.2 Project Phase I Using the Energy Bus System

According to the New User's heating demand, the heating area is 1.59 million square meters, subdivided into six blocks, each block has a heat pump equipment room. According to the actual situation of the communities construction, heating demand is not consistent, even if in the same community, the end user's load rate also varied, taking into account the projects initial investment and rational use of water resources, the project phase I takes the form of the energy bus system with main circulation pump, all adopt the screw heat pump units, its exergy loss coefficient decreases with decreasing loading rate [2], it is suitable for variable load state. In the project phase I, the 17 °C reclaimed water directly provided by the competent network is sent to the user heat pump equipment room as the heat source of the heat pump, and then providing users hot water of 45/35 °C. The system diagram is shown in Fig. 48.2.

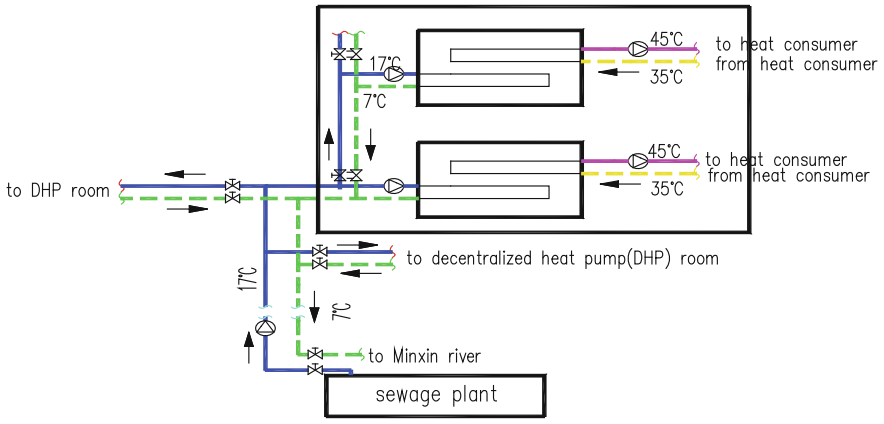

Fig. 48.2 Schematic diagram of phase I project of heat pump system

The energy bus system [3] will deliver the water which comes from renewable energy and unused energy heat source heat sink water to the heat consumer through the pipe network infrastructure. The heat source/heat sink water emit or absorb heat through the heat exchanger and then back to the source or emissions to surface water or re-use. Only a circulating pump or heat exchanger equipment is installed in the places of heat source and heat consumers individually configured heat pump units to heat the water coming from centralized pipe network and then get hot (cold) water needed.

Energy bus system not only has the advantage of large-scale application of district heating/cooling, and also has the flexibility of the dispersion. The large-scale use of natural cooling source (heat), not only improves the efficiency in the use of new energy sources, but also complement the local heat supply gap. Using water source heat pump units can realize cooling, space heating, and water heating at the same time. Centralized return water can be used for irrigation of communities and urban greening, which will save water resources and create profits for their owners, it will promote the renewable water recycling on a large scale.

48.3.3 The Second Phase of the Project Adopt Two-stage Series Heat Pump Units

Currently, the conventional single-stage heat pump [4] can only provide hot water of about 50 °C, but also is limited by the temperature of heat-source water, when the heat source water temperature is reduced, the pressure ratio of the compressor is increased, the gas transmission coefficient is reduced, so that the degree of which compression cycle process deviated from the isentropic process increases, the heat of cycle decline, the power consumption is increased, and the performance of the

system decreases rapidly. Based on the theory of heat pump, some experts and scholars concluded a double stage coupling heat pump heating system which is suitable with characteristics of cold regions [5] (*Double-stage Coupled Heat Pumps Heating System*, referred to as DSCHP), Two sets of single-stage heat pump system were integrated in the system by water circulation line and coupled together to form a suitable heat pump heating system for cold regions.

As shown in Fig. 48.3, due to the community's construction scheduling in the second phase project, the 10 °C temperature difference between supply water and return water mentioned before already cannot meet the heating requirements, so we will build the main heat pump plant in the second phase of the project, and it still using the renovated water pipe network which are constructed in the first phase project. The second phase of the main heat pump plant is located 200 m to the north of the wastewater treatment plant and takes the form of concentration and indirect system. The sewage plant effluent will be leaded into large centrifugal pump units through 4 DN1200 steel pipe, the biggest water inflow is the biggest effluent of the wastewater treatment plant, about 20,833 t/h. The main electric heat pump plant will be built in the Qiao dong sewage treatment plant on the north side,

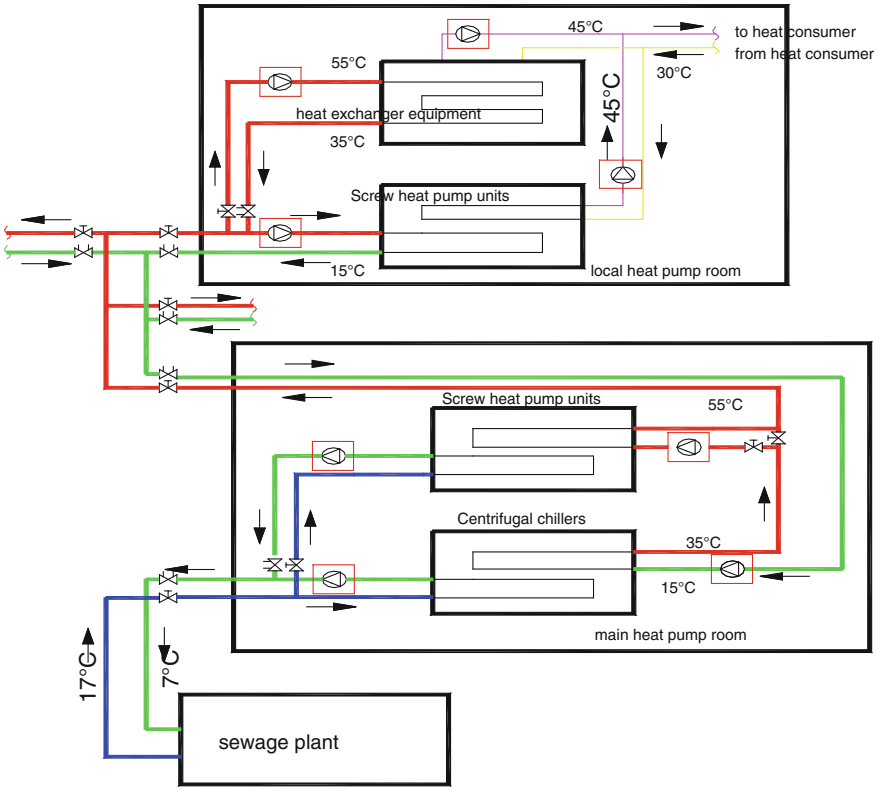

Fig. 48.3 Schematic diagram of phase II project of heat pump system

using the tertiary effluent of the sewage treatment plant for cooling in summer and heating in winter.

Under the condition of heating, the main heat pump plant adopts the mode of two-stage heating. In the first stage, with the heat absorbed from the reclaimed water, the centrifugal pump units heat the return water in middle loop from 15 to 35 °C and then the water of 35 °C goes into the second stage of screw heat pump units in series connection, exchanging heat with another branch of the reclaimed water and the latter will be heated from 35 to 55 °C. The main heat pump station can achieve total temperature rise of 40 °C. We only run the first stage centrifugal heat pump units at part load heating season.

In order to make full use of the large temperature difference of heat source which the main supply network provides, the decentralized local heat pump room also take the form of two-stage exchanging heat, the 55 °C hot water flow into the plate heat exchanger first and release heat quantity to the hot water of the user side. It will provide users with 45 °C hot water. About 35 °C backwater of the plate heat exchanger series goes into the evaporator of the heat pump units and releases heat quantity for the second time, the temperature of medium water reduces from 35 to 15 °C. The temperature of water supply in the side of heat consumer is 45 °C, return 30 °C.

48.3.4 Distributed Power System

Generally, there will be the main circulating pump (the first-stage pump) in the heat source to overcome the loss of heat source internal resistance, and local hydraulic pump (the second-stage pump) in the local heat pump room in a distributed power system. The second-stage pump will overcome the resistance of pipe network and the local heat pump station [6]. The lift head of the second-stage circulation pump is equal with [7] the loss of the pipeline network plus the lift head of the heat pump station of the heat consumer. Figure 48.4. shows a schematic diagram of a distributed secondary circulation pump system

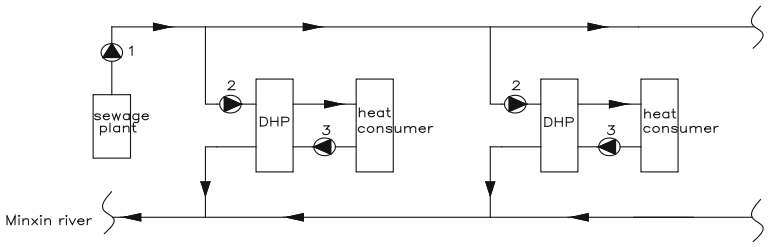

Fig. 48.4 Distributed circulation pump system diagram, *1*-main circulation pump, *2*-distributed pump (DP), *3*-local hydraulic pump (LHP)

Using a distributed power system in the heating pipe network is conductive to the regulation of the system and can save the investment and operating costs. Distributed power systems are based on the water pump in place of the valve in the operation. The distributed power system changes the traditional power centralized heating network into power decentralized pipeline network and reduces the level of the pipe network pressure and eliminates meaningless energy consumption in valve, so as to achieve the purpose of saving energy.

48.4 Heating Capacity Analysis

The sewage flow of the Qiao dong sewage treatment plant is about 500,000 tons per day, namely the effluent can reach 20,833 t/h. The effluent temperature is at an average of 17 °C in winter, and it can reduce to 7 °C after release heat. The diameter of the main supply and return water pipe in the phase I of the project is DN1000, and designing flow rate is 3 m/s, the heat pump units of the heating coefficient of COP_h take 4.0 provisionally and return water temperature according to 17/7 °C.

48.4.1 The Heating Capacity of Project Phase 1

By the heat of the water in the formula [8]:

$$Q_1 = cM\Delta t \tag{48.1}$$

$$M = \pi R^2 \times \upsilon \times 3,600 \tag{48.2}$$

$$\mathrm{COP}_h = \frac{Q_2}{P},\ Q_2 = Q_1 + P \tag{48.3}$$

c water specific heat capacity, take 4.187 kJ/(kg °C);
M Mass flow, project phase I the main transport capacity, kg/s;
Δt Temperature difference between supply and return water;
Q_1 The heat quantity extracted from the tertiary treatment effluent, kW;
Q_2 The total heat quantity to heat consumer, kW;
P Input power of heat pump unit, kW.

Substitute the data to the Formulas (48.1, 48.2, 48.3) and calculate, the heating capacity of project phase I can achieve heating area:

$$S = \frac{131,539 \times 1,000}{40} = 32,88,476\ (\mathrm{m}^2) \tag{48.4}$$

(heating design index by 40 W/m^2).

Therefore, it can be concluded that directly using the effluent water to extract 10 °C temperature difference can meet heating of 3.2 million square meters, and it can cover the heating needs of project phase I of 1.59 million square meters.

48.4.2 Heating Capacity of the Phase II Project

The phase II project adopts the joint system which consists of the centralized centrifugal chillers, district heat transfer station and distributed heat pump station. When the water flows into the main heat pump plant and reaches to the maximum, i.e., 20,833 t/h, by the Formula (48.1), the heat quantity (Q) extracted from the water is:

$$Q = 4.187 \times 20,833 \times 10 \div 3.6 = 242.299 \text{ (MW)} \tag{48.5}$$

When the heating coefficient of performance COP_h of the double stage coupling heat pump units is assumed as 4.0 :

$$Q_2^{'} = \left(1 + \frac{1}{\text{COP}_h - 1}\right) Q = \frac{4}{3} \times 242.3 = 323 \text{ (MW)} \tag{48.6}$$

It basically can meet the heating needs of 8 million square meters building area. Taking into account that the temperature may be not enough and the loss of the pipeline, heat pump units can be used as auxiliary heating on some of the engine rooms to meet the needs of heating better.

Supply and return water pipe are still the one that has been laid in the project phase I using centrifugal heat pump units, the supply and return water temperature reach 55/15 °C, respectively, the temperature difference is 40 °C, when the heating capacity is 320 MW by the Formulas (48.1, 48.2, 48.3), and combined with the known parameters, we can get the pipe network flow M′:

$$M' = \frac{Q_2^{'}}{c \times \Delta T} \times 3.6 = 6,878 \text{(t/h)} \tag{48.7}$$

It is in the range of the pipe network transport capacity.

48.5 Energy Saving Analysis

Taking land A, which is one part of the project phase I, for example. With an area of 310,000 square meters and all for residential using, it is divided into high, medium, and low zones. The thermic load value is 10,979 kw and the electricity load is as follows:

48.5.1 According to the Index of Heat Loss of Building to Calculate the Fuel Consumption Index q_p

New buildings must be designed in accordance with the Energy Conservation Code requirements. At first, we need calculate the index of heat loss of building which is based on the mean outdoor temperature during heating period. The weather conditions of the project place are known in [9, 10]:

Heating design heat load index: $q = 35$ W/m^2);
Heating indoor design temperature: $t_N = 18$ °C;
Heating outdoor design temperature: $t_W = -4.8$ °C;
The average outdoor temperature of the heating period: $t_e = 0.9$ °C;
Heating period for calculation: $Z = 97$ days;
The actual heating period: $Z_S = 120$ days;
Coal-fired boiler thermal efficiency: $\eta_2 = 0.68$;
Efficiency of network: $\eta_1 = 0.90$;
Standard coal calorific value: $H_C = 8.14$ (kW·h/kg) = 29,306 (kJ/kg);

Calculating the index of heat loss of building [11]:

$$q_H = q\frac{t_N - t_e}{t_N - t_W} = 35 \times \frac{18 - 0.9}{18 + 4.8} = 26.25\left(\mathrm{W/m^2}\right) \tag{48.8}$$

In one heating period, the heat consumption Q is:

$$\begin{aligned} Q &= 24 \times q_H \times Z_S \times 3,600 \div 1,000 = 24 \times 26.25 \times 120 \times 1,000 \\ &= 75.6\left(\mathrm{kW \cdot h/m^2}\right) \end{aligned} \tag{48.9}$$

When using the Regional boiler room heating:

1. Fuel consumption index q_C:

$$q_C = \frac{Q}{\eta_1 \eta_2 H_C} = \frac{75.6}{0.90 \times 0.68 \times 8.14} = 15.18\left(\mathrm{kg/m^2}\right) \tag{48.10}$$

2. Boiler heating system power consumption (including auxiliary boiler and the pumps of main network and pumps of the secondary network) in one heating period:

$$E_B = 0.05Q = 0.05 \times 75.6 = 3.78\left(\mathrm{kW \cdot h/m^2}\right) \tag{48.11}$$

Converted into standard coal:

$$g' = \frac{E_B}{\eta_D \eta_{\mathrm{DW}} Q_b} = \frac{3.78}{0.3 \times 0.9 \times 8.14} = 1.72\left(\mathrm{kg/m^2}\right) \tag{48.12}$$

3. The amount of consumption of standard coal in a heating period for land A is :

$$G = 310,000 \times (15.18 + 1.72) \times 1,000 = 5239.0 \text{ t} \tag{48.13}$$

48.5.2 Calculating the Coal Consumption of Heat Pump Station

The calculation formula of converting the power consumption into coal consumption is [10]:

$$G_{\text{HPZ}} = \frac{24 \times 0.8N_H \times 120}{1000\eta_D\eta_{\text{DW}}H_C} \tag{48.14}$$

0.8 N_H–set the actual power consumption is 80 % of the rated power. The heat pump units cannot always operate at full load throughout the heating period and the capacity of the units is chosen according to the heat load index of 35 w/m^2 (including the electric consumption of both the low level heat pump and the water pump of the users' side);

η_D–generation efficiency,

η_D = 0.25–0.35; η_{DW}–transmission and distribution efficiency,

η_{DW} = 0.9; From Table 48.1. It can be Seen that the total power consumption is 3032.5 kw, and substituted into the formula (48.14) :

Table 48.1 Land A heat pump room equipment

No	Equipment name	Model number	Heating capacity (kW)	Power (kW)	Quantity	Total (kW)
1	HP units R-1, R-2	610 CC	2,037	477	2	954
2	HP units R-3, R-4	610 CC	2,037	477	2	954
3	HP units R-5, R-6	480 CC	1,701	385	2	770
4	DP YCB-1, 2, 3			45	3	90
5	DP YCB-4, 5, 6			45	3	90
6	DP YCB-7, 8, 9			45	3	90
7	LHP FZB-1, 2, 3			11	3	22
8	LHP FZB-4, 5, 6			11	3	22
9	LHP FZB-7, 8, 9			11	3	22
10	Constant pressure device (low)			5.5	1	5.5
11	Constant pressure device (medium)			4	1	4
12	Constant pressure device (high)			3	1	3
13	Water treatment device			3	1	3
14	Water treatment device			3	1	3
					Total	3032.5

$$G_{\mathrm{HPZ}} = \frac{24 \times 120 \times 0.8 \times 3032.5}{0.3 \times 0.9 \times 8.14 \times 1,000} = 3,179 \text{ t} \tag{48.15}$$

Therefore, in a heating period for land A. Using reclaimed water source heat pump system will save standard coal ΔG:

$$\Delta G = G - G_{\mathrm{HPZ}} = 2,026 \text{ t} \tag{48.16}$$

For a 800 million square meters of heating area, in a heating period, it can save standard coal 53,161 t. Economizer rate:

$$\eta = \frac{\Delta G}{G} \times 100\ \% \ = \frac{2,060}{5,239} \times 100\ \% \ = 39.32\ \% \tag{48.17}$$

48.6 Conclusion

In order to ease the energy crisis, and at the same time to make full use of the renewable water which contains a large number of low quality energy, this article describes a large reclaimed water source heat pump system. We elaborate the energy planning and design philosophy for a large district heating system. The project construction is divided into two stages based on the actual situation of the financial strength and the heating needs of local user. The project phase I takes the form of the energy bus system with main circulation pump. In the Project phase I, the 17 °C reclaimed water provided by the competent network is directly sent to the local heat pump equipment room as the heat source of the heat pump, and then providing users hot water of 45/35 °C. Energy bus system not only has the advantage of large-scale application of district heating/cooling, but also has the flexibility of the dispersion.

We will build the main heat pump plant in the second phase of the project. The main heat pump station can achieve total temperature rise of 40 °C. We only run the first stage centrifugal heat pump units at part load heating season. In order to make full use of the large temperature difference of heat source which the main supply network provides, the decentralized local heat pump room also take the form of two-stage exchanging heat, it will eventually meet the demand of 8 million square meters of heating.

The power consumption of the water source heat pump system in a heating season is converted into coal consumption, compared with coal-fired boiler room for heating area of 8 million square meters. The calculation shows that in a heating period the water source heating system will save 53,161 tons of standard coal, and the coal saving rate is 39.32 %, which indicates the advantages of using the new energy and a new heating system. Since the project is still in progress, it is necessary to do further research in many aspects, such as the actual COP of the double-stage series heat pump units, the matching problem of the unit with pipe

network, the control method of local heat pump units running with variable flow, to achieve better energy-saving.

This article will provide a reference for the future use of the large urban reclaimed water heating system.

References

1. Matthias M, Hansjürg L (2012) Introduction and analysis of a concept for decentralized heat pumping in hydronic networks. Energ Build vol 54 p 461–469
2. Jian-qiang W, Wen-hong W (2008) Exergy analysis of the vapor compression refrigeration. J Hebei Univ Eng (Nat Sci Ed) No.8101:71–73 + 80
3. Pei-pei W, Wei-ding L (2009) Study on energy bus system—semi-central DHC. J Hunan Univ (Nat Sci) 12(36):137–141
4. Bao-lian N, Zong-he Z (2004) Design of a new type water-source heat pump system. J Fluid Mach 5(32):39–41, 64
5. Zui-liang M, Yang Y (2010) Theoretical basis and practice of the heat pump technology applications. China Building Industry, Henan (in Press)
6. Xiao-bo G, Feng-long H (2007) The application of two-stage hydraulic pump in heating boiler room heating. J Dist Heat 3:37–39
7. Zhi-gang Z (2008) Application of heat-supply system with distributed secondary circulation pump. J Gas Heat 10(28):19–20
8. Zhang C (2008) Heat pump technology and applications. Mechanical industry, Guangzhou (in press)
9. Civil building energy-saving design standard JGJ26-95 (1995) China building industry, Tianjin (in press)
10. Urban heating network design specification CJJ34-2002 (2012) China building industry, Beijing (in press)
11. Zui-liang M, Yong-hong L (1995) Economic evaluation of motor-driven heat pump station used in China (I) —the result of energy conservation in heat pump station. J Harbin Univ civ Eng Archit 3(28):71–76

Chapter 49
Study on Thermal Storage Performance of Phase Change Heat Storage Type Air Conditioning Cooling Reservoir in Civil Air Defense Engineering

Guozhu Li, Guohui Feng, Xiaolong Xu, Na He, Huixing Li and Qizhen Chen

Abstract The heat storage capacity of the existing air conditioning cooling reservoir is not enough due to the increase in equipment and personnel. The problem of insufficient heat storage capacity can be solved by using phase change energy storage technology. In this paper, the model experiment of air conditioning cooling water reservoir is established. Different number of phase change heat storage modules (PCHSMs) of 0, 104, 208, 312, 412, 512, and 614 are separately put into the reservoir, and then the heat storage capacity of the reservoir is tested. The test results indicate that it takes 17.37 h for the outlet water temperature of the reservoir to rise from 19° to 37° with 0 PCHSM, then the heat storage capacity of the reservoir increases as the number of PCHSMs increases. Comparing with the 0 PCHSM, the heat storage capacity of the reservoir increased 42.25 % with 614 PCHSMs. The heat storage capacity of reservoir can be obviously improved by using of PCHSMs. Therefore, the phase change heat storage type air conditioning cooling reservoir (PCACCR) is a meaningful way to guide reconstruction of existing reservoirs and construction of new reservoirs.

Keywords Phase change heat storage · Phase change material · Civil air defence engineering · Air conditioning reservoir · Phase change heat storage module

G. Li · G. Feng (✉) · X. Xu · N. He · H. Li · Q. Chen
School of Municipal and Environment Engineering, Shenyang Jianzhu University, 110168 Shenyang, China
e-mail: fengguohui888@163.com

A. Li et al. (eds.), *Proceedings of the 8th International Symposium on Heating, Ventilation and Air Conditioning,* Lecture Notes in Electrical Engineering, 262,
DOI: 10.1007/978-3-642-39581-9_49,

49.1 Introduction

The civil air defense engineering is built to protect people's air defense command, communications, masking protection building. The normal operation of the air conditioning system is an important guarantee for the civil air defense engineering with good thermal environment [1]. In order to avoid the exposure of civil air defense engineering due to the application of the cooling tower, the air conditioning cooling water is provided by air conditioning cooling reservoir that constructed in the underground or mountain. However, with the increasing in heating equipment and people, as a result a significant increase in internal condensation heat of the civil air defense projects. Because of limited initial design capacity of the existing air conditioning cooling reservoir, it is definitely difficult to continue to run the air conditioning system. For existing air conditioning cooling reservoir, it is hard to add the cooling tower and unrealistic to expand air conditioning cooling reservoir to increase the water capacity of the air conditioning cooling reservoir [2]. In order to ensure the normal operation of the air conditioning system of the civil air defense projects, it is necessary to find out effective ways to enhance the heat storage capacity of the air conditioning cooling reservoir. The solution that using phase change energy storage technology [3–5] is proposed in this paper to solve the problem of the inadequate heat storage of air conditioning cooling reservoir. The specific measure of the solution is that phase change heat storage modules (PCHSMs) are placed in the air conditioning cooling reservoir that formed a new type air conditioning cooling reservoir, it is defined as phase change heat storage type air conditioning cooling reservoir (PCACCR).

49.2 Model Experiment of PCACCR

In this section, we first establish the PCACCR model experiment and introduce the apparatus, and then discuss the encapsulation of phase change material, at last design the connection and placement of PCHSMs.

49.2.1 Establishment of PCACCR Model Experiment

The apparatus of PCACCR model experiment consisted of one reservoir used as air conditioning cooling reservoir, one heating water tank, one circulating pump, several PP-R hot water pipes, copper ball valves, and heat preservation material.

The reservoir is produced by polypropylene plastic plate with a thickness of 15 mm, its length, width, and height (L×W×H) are 2000, 1200, and 1300 mm respectively and the rated water volume during the testing is 2.5 m^3. The specification and pipe interface of the reservoir are shown in Fig. 49.1.

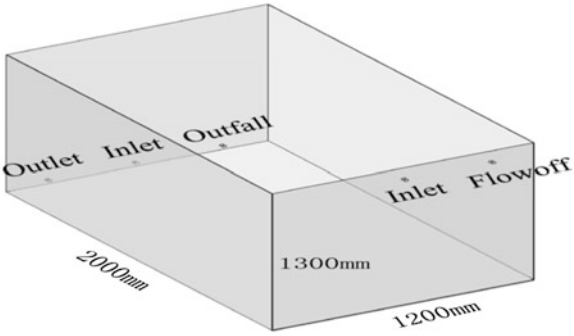

Fig. 49.1 Structural representation of reservoir

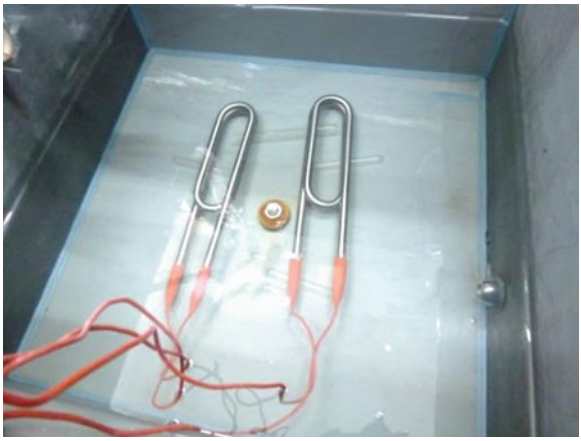

Fig. 49.2 Heating water tank

Heating water tank that is used to simulate the condensation heat generated by air conditioning system is shown in Fig. 49.2. The electric heater has a power of 3 kW and "one-work and one-standby". The circulating pump has three gears to control the flow; the parameters of circulating pump are listed in Table 49.1. Inner diameter of PP-R hot water pipe is 20 mm. Water flow is regulated by three gears of circulating pump and copper ball valves. The heat preservation material with the thickness of 15 mm used in model experiment in order to reduce heat loss. The insulated PCACCR model experiment is shown in Fig. 49.3.

49.2.2 The Encapsulation of Phase Change Material

Homemade $Na_2SO_4.10H_2O$ composite phase change material with which the phase change temperature of 26–28 °Cand the latent heat of 150 J/g is used as phase change material (PCM) in PCACCR model experiment.

Cylindrical polyethylene terephthalate (PET) plastic bottles are chosen as the encapsulation container of the PCM, the parameters of the PET bottle are listed in

Fig. 49.3 Thermal insulation of PCACCR model experiment

Table 49.1 Parameters of circulating pump

Power (W)			Maximum flow (L/min)	Maximum delivery lift (m)	Rated voltage (V)
High	Medium	Low			
280	250	120	95	9	220

Table 49.2 Size and style of encapsulation bottle

Bottle body			Bottle mouth		Average wall thickness (mm)	Net volume (m^3)
Structure	Height (mm)	Diameter (mm)	Sealed form	Diameter (mm)		
Columnar convex surface	225	65	Screw cap	30	0.23	5.5×10^{-4}

Table 49.2. The PCM is encapsulated into a PET bottle; we call it a phase change heat storage module (PCHSM).

49.2.3 Connection and Placement of PCHSMs

PCHSMs are placed in the reservoir and should give full consideration to the heat exchange performance between PCHSMs and water. PCHSMs are equidistantly strung by rope Fig. 49.4 and evenly placed in the reservoir with staggered form Fig. 49.5.

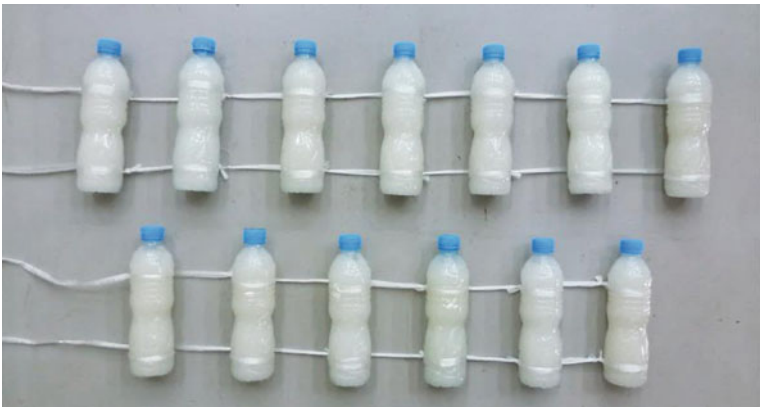

Fig. 49.4 Connecting form of phase change heat storage module

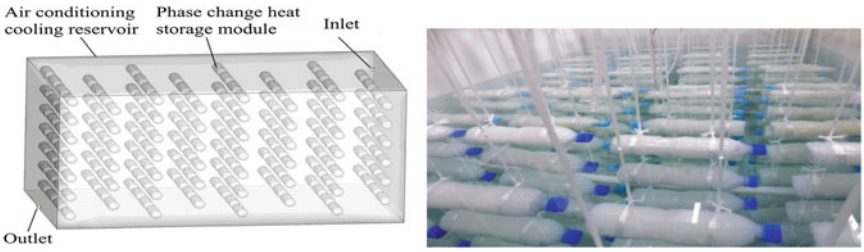

Fig. 49.5 PCHSMs in reservoir with staggered form. The left is a schematic diagram of staggered form; the right is the actual placement state

49.3 Running Process and Measuring Points of PCACCR Model Experiment

In this section, we first present the running process of PCACCR model experiment. Second, introduce the test modes in order to do contrastive experiment to analyze the heat storage capacity of PCACCR, and then describe the data collection instruments used in the test. Finally, illustrate the location of the measuring points.

49.3.1 Running Process

The running of PCACCR model experiment is in accordance with the actual air conditioning cooling water system. Condensing heat of the air conditioning system is simulated by the heat that generated by electric heater in the heating water tank.

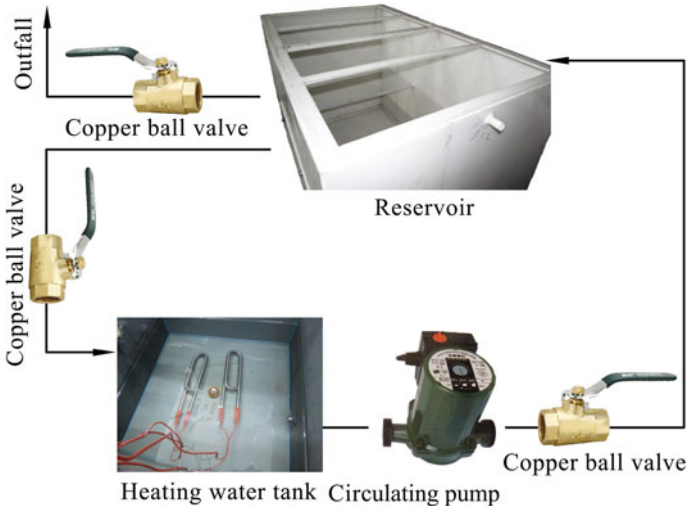

Fig. 49.6 Running process of PCACCR model experiment

Circulating pump provides the water cycle power; the water flow is controlled by three gears of circulating pump and copper ball valves in pipeline.

The running process of PCACCR model experiment Fig. 49.6: turn on circulating pump and electric heater, the circulating pump as a power source, hot water in the heating water tank is pumped into the reservoir, then the heat exchange will be occurred between the hot and cold water in the reservoir. Water in the reservoir that relies on their own water pressure is transported to the heating water tank via the outlet in the middle position of the reservoir bottom. The heated water in the heating water tank is pumped into the reservoir again. This process will be not stopped until outlet water temperature of the reservoir reaches at 37 , then the electric heater and circulating pump should be turned off. The flow and rate of the circulating water are set to 1.13 m^3/h and 1 m/s respectively.

49.3.2 Test Modes

The test modes of PCACCR model experiment are divided into two cases. The first test mode is no added PCHSMs (0 PCHSMs), merely relying on sensible heat of water to store heat. The second test mode is that the different number of PCHSMs (104, 208, 312, 412, 512, and 614 PCHSMs) are separately placed into the reservoir, relying on the latent heat (primary) and sensible heat (secondary) of PCM and sensible heat of the rest water that excludes the total volume of PCHSMs from the rated water volume of reservoir (2.5 m^3) to store heat. The purpose of these two

test modes is to obtain the relationship between different number of PCHSMs and heat storage capacity of PCACCR.

49.3.3 Data Collection Instruments

The paperless recorder is used for collecting the testing data, setting the data save time interval of 1 s, temperature accuracy is 0.1 . Platinum resistance thermometers (PT 100) which the temperature range of −50–450 are used as temperature probe. The testing instruments are calibrated before the test.

49.3.4 Measuring Points

Heat storage capacity of PCACCR is reflected in the time when the outlet water temperature of the reservoir reaches at 37 (This temperature is usually a upper limit temperature of air conditioning cooling water system). As it is inconvenient to put the resistance thermometers in the inlet and outlet of the reservoir, also the PCACCR model experiment has been insulated, the measuring points of inlet and outlet of the reservoir are arranged in the heating water tank, and respectively marked as $1^{\#}$ and $2^{\#}$. In order to investigate the relationship between the change of PCHSMs internal temperature and the heat storage capacity of PCACCR, a measuring point is put into one PCHSM which is in the central position of the reservoir, and marked this measuring point as $3^{\#}$.

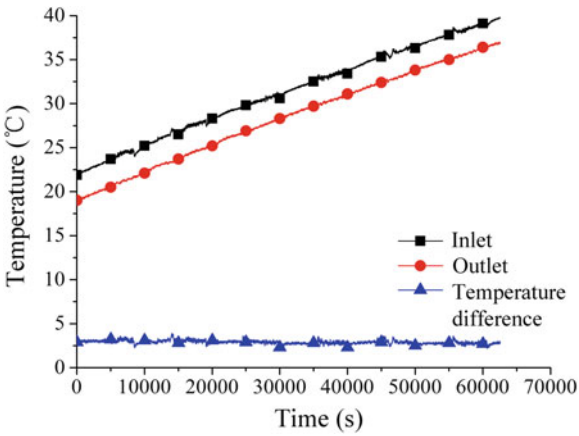

Fig. 49.7 Temperature trends of inlet and outlet when 0 PCHSM in the reservoir

49.4 Analysis of Testing Results of PCACCR Model Experiment

In this section, the test results of PCACCR model experiment are analyzed. In the PCACCR model experiment, different number of PCHSMs that 0, 104, 208, 312, 412, 512, and 614 PCHSMs are separately put into the reservoir. The testing results, including the temperature increasing trends of inlet, outlet as well as PCHSM center, and the temperature difference between inlet and outlet are similar, the only different is the time they are taken. Therefore, just taking 0 and 104 PCHSMs in the reservoir as examples to analyze the process and effect of PCHSMs in enhancing the heat storage capacity of the reservoir. Then the results that addition of different number of PCHSMs are summarized and analyzed. To ensure the test data of each experimental group has a better contrast, the test data are all in a temperature interval which limits the reservoir outlet water temperature rise from 19 to 37 . The analysis and research of the testing results will be in this temperature interval.

49.4.1 Test Results of 0 PCHSM in Reservoir

When 0 PCHSM (no PCHSM) is added into the reservoir, the heat is stored totally dependent on the sensible heat of water. The temperature trends of inlet and outlet of the reservoir are shown in Fig. 49.7 and it shows the temperature of inlet and outlet rise linearly. The average temperature difference between inlet and outlet is 2.9 . It takes 17.37 h to rise the temperature of outlet water from 19 to 37 .

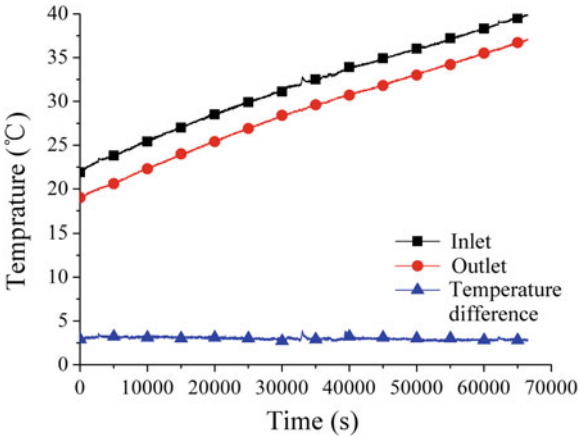

Fig. 49.8 Temperature trends with 104 PCHSMs in reservoir

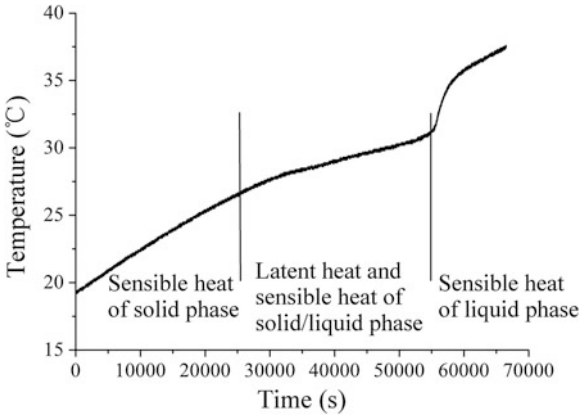

Fig. 49.9 Temperature trend of PCHSM center

49.4.2 Test Results of 104 PCHSMS in Reservoir

Taking 104 PCHSMs in the reservoir as an example to analyze the process and effect of PCHSMs in enhancing the heat storage capacity of the reservoir.

The temperature trends of inlet and outlet of PCACCR model experiment are shown in Fig. 49.8. The results indicate that the temperature of inlet and outlet rise stable, the mean temperature difference between inlet and outlet is 3 . It takes 18.47 h for temperature of outlet water to go up from 19 to 37 . Compared with the results of which 0 PCHSM is added into the reservoir, we can see that inlet and outlet temperature rises linearly in former 25000 s, then the heating rate gets slower during 25000–55000 s, and then the temperature of inlet and outlet linearly rise again from 55000 s. These three stages of outlet temperature increase become more evident when more PCHSMs are added in the reservoir Fig. 49.10.

Because of the addition of PCHSMs in the reservoir, the heating rate slows down in the second stage of temperature rising process. Taking the addition of 104 PCHSMs in reservoir for example, these three stages of outlet temperature increase are analyzed: the first temperature rising stage is before 25000 s. The temperature of reservoir water is below 26 °C which is lower than the phase change temperature of PCM. So PCM is solid and heat is stored in this stage by sensible heat of water and solid-phase PCM. The second temperature rising stage is between 25000 s and 55000 s. The water temperature of the reservoir increases from 26 to 33 . When the water temperature reaches 26–28 , PCM begins to melt and uses latent heat to store heat. The more water temperature rising, the more PCM melting, and a solid–liquid coexisting state is appeared. When the water temperature goes up to 33 , PCM is completely melted. As a result of the heat storage capacity of latent heat is much larger than sensible heat, the temperature of inlet and outlet becomes slower rising. The third temperature rising stage is after 55000 s, water temperature of reservoir is higher than 33 . PCM is completely melted to liquid; heat is stored by sensible heat of water and liquid PCM. The temperature, in the central of PCHSM, changes over time which recorded by $3^{\#}$

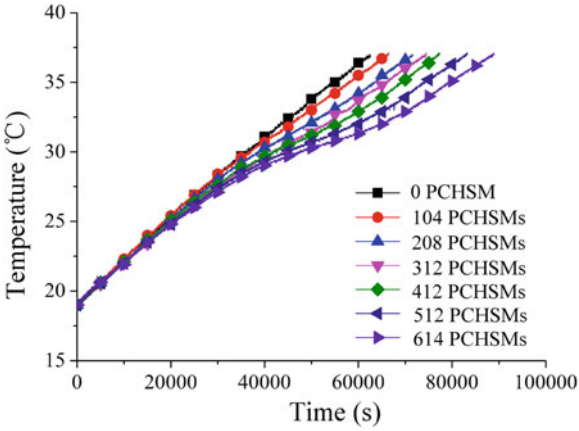

Fig. 49.10 Outlet water temperature trends

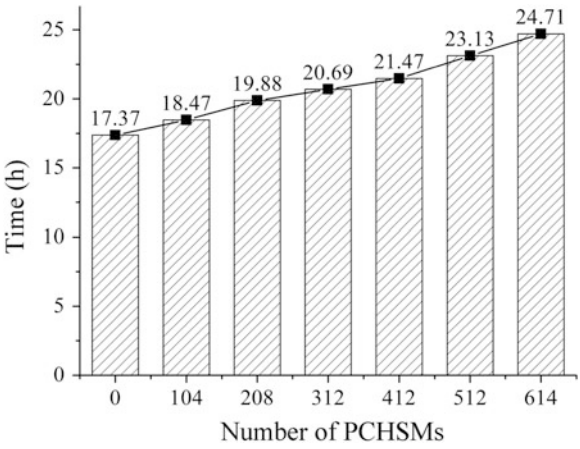

Fig. 49.11 Time of outlet water rise

measuring point is shown in Fig. 49.9. It is more clearly to investigate the relationship between changing of PCHSM center temperature and these three temperature rising stage.

49.4.3 Analysis of Addition of Different Number of PCHSMs

Testing results trends of that separately placing 208, 312, 412, 512, and 614 PCHSMs into reservoir are similar to that of 104 PCHSMs. The mean temperature difference between inlet and outlet is 3 . Therefore, it is not essential to do more analysis. The key point to study the relationship between heat storage capacity of

PCACCR and number of PCHSMs, which reflected in the change of outlet water temperature over time after addition of different number of PCHSMs.

Outlet water temperatures which changing with time are obtained by analyzing test data from addition of different numbers PCHSMs in the reservoir. The results are shown in Fig. 49.10. Time when outlet water temperature rises from 19 to 37 gets longer with the increase in number of PCHSMs. It indicates heat storage capacity of reservoir has a significant strengthening after the addition of PCHSMs.

Relationship between running time and number of PCHSMs is shown in Fig. 49.11. From Fig. 49.11, it shows that as the more number of PCHSMs put into the reservoir, the longer time it takes when outlet water temperature rising from 19 to 37 , the larger heat storage capacity the reservoir has. Volume of 614 PCHSMs accounting for 13.51 % of the rated water volume of reservoir, and comparing with the addition of 0 PCHSMs, the heat storage capacity of reservoir is enhanced to 42.25 %. Consequently, PCACCR by addition of PCHSMs can significantly improve the heat storage capacity of air conditioning cooling reservoir.

49.5 Conclusion

The normal operation of air conditioning system is an important guarantee for civil air defense engineering. However, heat storage capacity of existing air conditioning cooling reservoir is not enough due to the increase in equipment and personnel. By establishing the PCACCR model experiment, the heat storage capacity of PCACCR with different number of PCHSMs is tested. The PCACCR model experiment results indicate that the heat storage capacity of reservoir increases as number of PCHSM increases. It takes 17.37 h for the temperature of outlet water rise from 19 to 37 with 0 PCHSM. Comparing with the 0 PCHSM, the heat storage capacity of reservoir enhanced 42.25 % with 614 PCHSMs. Therefore, PCACCR is a meaningful way to guide reconstruction of existing reservoirs and construction of new reservoirs.

Acknowledgments This study is supported by National Science and Technology Pillar Program during the 12th Five-Year Plan Period (2012BAJ26B02).

References

1. Jinfeng M, Yong L, Shibin G et al (2012) Research progress of thermal environment inside protection works. Heat Ventilating Air Conditioning 42(9):6–12
2. Jinsheng W, Wenjie L, Hao C et al (2008) Underground thermal storage defensive cooling tower. Refrig Air Conditioning 24(5):1–3
3. Zhou D, Zhao CY, Tian Y (2012) Review on thermal energy storage with phase change materials (PCMs) in building applications. Appl Energy 92:593–605

4. Zhang Y, Rao Z, Wang S et al (2012) Experimental evaluation on natural convection heat transfer of microencapsulated phase change materials slurry in a rectangular heat storage tank. Energy Convers Manage 59:33–39
5. Guohui F, Kailiang H, Qizhen C et al (2011) Experimental research on phase change energy storage floor heating system. J Chongqing Univ 34:52–57

Chapter 50
Study on Components Match of Solar-Ground Source Heat Pump and Heating Network Complementary Heating System in Severe Cold Region

Hong Hao, Xiujuan Zhao, Guohui Feng and Xiangyuan Xue

Abstract The typical building in severe cold region was selected. The form of the complementary heating system on solar-ground source heat pump and heating network was proposed in this paper. The simulation model of the complementary system was established by TRNSYS which is transient simulation software as design platform. The various components were designed. The matching relationship among the components which including the solar collector and the ground heat exchanger and the storage tank and the heating network were researched. The results of the simulation demonstrate that the average COP of the heat pump unit is 4.04, and monthly average COP is 4.0 or more. The heat taken from the soil is reduced by 30 % in the auxiliary role of solar. Under the same of supplying heat, when the area of solar collector is increased by every 1 m^2, and the length of ground heat exchanger can be approximately decreased by 5.6 m. When the matching relationship of the volume of the storage tank and the solar collector area is 60–80 L/m^2, and the efficiency of the water tank is highest in the solar short-term heat storage system.

Keywords Solar-ground source heat pump · Heating network · Complementary heating · Match relationship · TRNSYS

H. Hao · X. Zhao · G. Feng (✉) · X. Xue
School of Municipal and Environment Engineering, Shenyang Jianzhu University, 110168 Shenyang, China
e-mail: fengguohui888@163.com

A. Li et al. (eds.), *Proceedings of the 8th International Symposium on Heating, Ventilation and Air Conditioning,* Lecture Notes in Electrical Engineering, 262,
DOI: 10.1007/978-3-642-39581-9_50,

50.1 Introduction

With the shortage of energy and the further be deteriorated of the environment. People gradually save conventional energy source, and improve energy utilization and the development and utilization of renewable energy, which as an important means to solve energy and environmental problems [1]. The way of solar and ground source heat pump combined heating obtained more attention [2–4], and the experiments and simulations were carried out by many achievements. However, the research on solar energy and ground source heat pump complementary heating with the conventional energy is few. Therefore, I propose to combine solar and ground source heat pump with urban heating network complementary heating. Which make up for the shortcomings of the northeast cold regions thermal network cannot meet the requirements of district heating, and combine with energy-saving reform of the existing building. Give solar and ground source heat pump full are played to the advantages, and energy consumption is reduced. The purpose of energy saving and emission reduction will be achieved, Combine with energy saving of existing building, which more conducive to the promotion and application of renewable energy [5]. Therefore, the study of the complementary heating system on solar-ground source heat pump and heating network that is a new energy-saving heating system is very meaningful, and the future prospects for the use is broad. Complementary use of renewable energy and conventional energy will be the main way of heating and cooling in the next century.

50.2 Complementary Heating System Simulations

50.2.1 System Introduction

A single residential building in a district of Shenyang is selected as a benchmark building, which consists of eleven floors, and since the first floor to the eleventh floor is a ladder of three householders. Building area is 7,730.91 m^2 and height is 33.2 m. Heat transfer coefficients of the building envelope are shown in Table 50.1. The total annual heat load of the building is 6,4430 kWh. As the TRNSYS transient simulation software for the platform [6], a system simulation model was established as shown in Fig. 50.1. The complementary heating system is composed of four parts that are the solar collector system, the ground source heat pump system, the heating network system, and the end system, in which the solar

Table 50.1 Coefficient of heat transfer of palisade structure

The name of the building envelope	Roofing	Facade	Outside the window	Door	Wall and floor
Heat transfer coefficient ($W/m^2 \cdot K$)	0.36	0.42	2.00	1.5	0.79

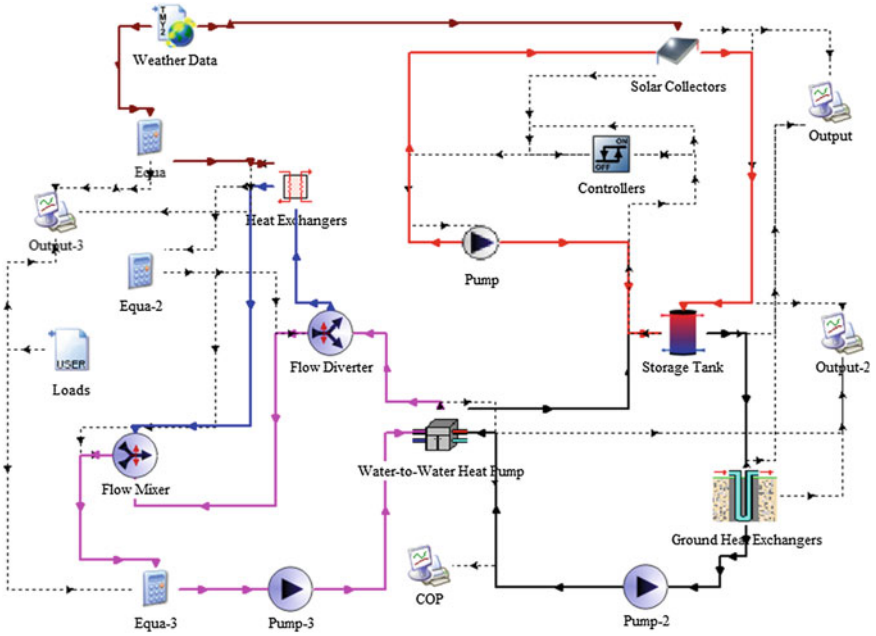

Fig. 50.1 Schematic of the simulation system in TRNSYS

collector area of 180 m^2 and the storage tank volume of 10 m^3, and the power of water source heat pump unit is 31.5 kW, and single U-pipes heat exchanger consisting of tube linking in parallel [7]. The underground heat exchanger is composed by 20 drillings with the depth of 80 m.

50.2.2 Complementary System Workflow

The solar collector system save for the heat to the heat storage tank, the fluid circulation first passes through the heat exchanger of the heat storage tank, and then into the borehole heat exchanger (when the inlet temperature of the heat exchanger lower than the outlet temperature, a endothermic process is carried out, on the contrary, an exothermic process is carried out), the exit fluid of the exchanger finally into the evaporator of the heat pump units, after a exothermic process, the cryogenic fluid back to the storage tank and carried next cycle. Outlet fluid into the heat exchanger of the heating network takes heat to meet demand of the end when the outlet temperature of the heat pump condenser is lower than the design temperature.

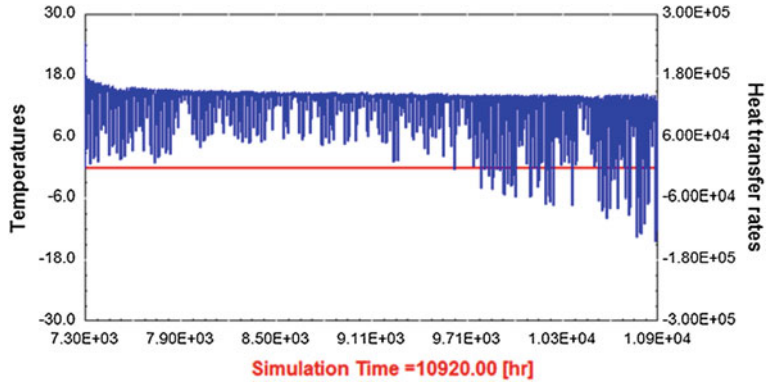

Fig. 50.2 Underground heat transfer in the heating period

50.2.3 Complementary System Performance Analysis

Figure 50.2 shows heat transfer of borehole heat exchanger, above the zero line, on behalf of the heat absorbed from the soil and below the zero line is heat release from the soil.

As can be seen, the amount of solar radiation is small in the interim of heating; basically the heat is only extracted from the soil, ground source heat pump system to undertake most of the heat load. In the initial and final of the heating, solar radiation gradually improves, which increase the release of soil heat so that the soil heat down. It is considered that heat from the soil decreased in the supporting role of solar. In the period of heating, the total heat transfer of ground heat exchanger is 98,571 kWh and the total heat release of soil is 39,120 kWh. The supporting role of solar to reduce by 30 % of heat soil.

Figure 50.3 shows the heating network for heat in complementary system. Can be seen from the figure, heat of heating network for almost nothing in the initial and final of the heating, the heating network for heat is mainly concentrated from

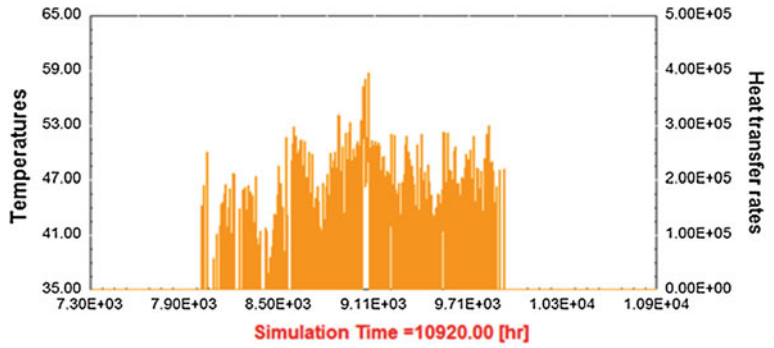

Fig. 50.3 Heating network for heat

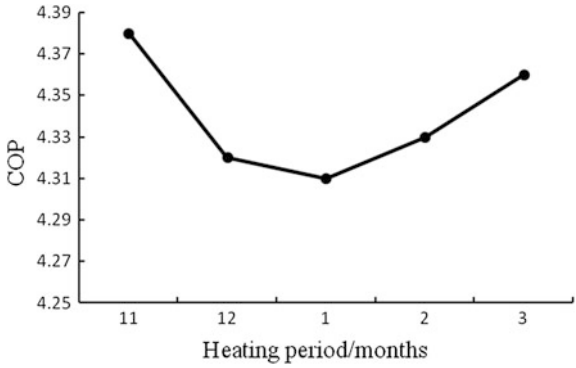

Fig. 50.4 Monthly average COP of the heat pump unit

December to February. Heating network can be considered to use in around the middle of the heating in the actual project.

Figure 50.4 shows the trend of monthly average COP of the heat pump unit in the period of heating. As can be seen from the figure, the monthly average COP of the heat pump units is highest in November, up to 4.08, followed by March. The lowest in January month with an average COP of 4.01. In the period of heating, the monthly average COP of the heat pump units is 4.0 or more.

Table 50.2 shows the value of the average value of the part of the temperature parameters of the simulation system and the average COP of the heat pump units in the period of heating.

50.3 The Match of Components in the Complementary System

There are many components in the system, the capacity parameter of each component change has different degrees of impact on the system, and therefore it is particularly important to explore the match relationship between the various components.

50.3.1 The Match of Solar Collector and Ground Heat Exchanger

The size of collector area direct impact on the initial investment and operating costs of the system, which is an important parameter in the system. In order to analyze the changes in the number of solar collector area and the borehole impact on the system, and Table 50.3 shows that the variation of thermal parameters in the

Table 50.2 Operation parameters of system

Parameters	Value ( )
Average COP of heat pump unit	4.04
Inlet temperature of average evaporator	6.5
Outlet average temperature of heat pump condenser	49.8
Inlet the average temperature of pipe	3.1
Outlet to the average temperature of pipe	5.6
Average temperature of water supply	52.9

Table 50.3 Operation parameters under different solar collector area

The name of parameters	Solar collector area/m^2		
	160	180	200
Water tank heat storage capacity/kWh	30,509	34,858	38,582
Borehole heat transfer/kWh	102,320	98,571	95,147
Evaporator heat absorption/kWh	133,257	134,163	135,137

Table 50.4 Operation parameters under different number of boreholes

The name of parameters	Number of boreholes		
	19	20	21
Water tank heat storage capacity/kWh	31,498	31,369	31,171
Borehole heat transfer/kWh	95,152	96,755	98,254
Evaporator heat absorption/kWh	126,850	128,324	129,625

system under different collector area, and the parameters under different borehole in Table 50.4.

The results of simulation shows that the storage of tank is increased with the increasing of the area of the collector under different collector area, when the area of solar collector is every increased by 10 m^2, and the heat storage amount of tank average increase by 2,241 kWh. Borehole heat transfer decreases with the increasing of collector area, due to the heat extraction from the ground decrease with the increase of collector area, so that the soil temperature recover faster. By analyzing heat absorption of the evaporator, the impact of the increase of collector area to the evaporator heat absorption is relatively small, when the area of solar collector is every increased by 10 m^2, and the average increase of only 491 kWh. We can therefore conclude that changing the collector area within a certain range, the less impact of the system for heat.

As can be seen from Table 50.4, Water tank heat storage capacity reduction with the increase of the number of borehole, while Borehole heat transfer gradually increases, the heat absorption of the heat pump evaporator also increases, in Table 50.3, when the area of solar collector is every increased by 1 m^2, and the evaporator heat absorption can be average increased by 49 kWh; The borehole each additional, and the evaporator heat absorption can be average increased by

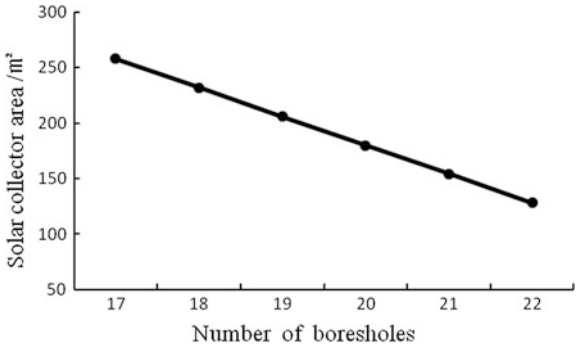

Fig. 50.5 The number of boreholes variation with solar collector area under equivalent heating

1399 kWh. In order to ensure the same heat absorption of the evaporator, solar collector area approximately is 28.5 m^2. We can conclude that when the number of borehole is every increased by one, and solar collector area is reduced approximately 28.5 m^2, the relationship between the borehole and collector area shown via the once function in Fig. 50.5, the fitting equation as the first equation.

$$A = 750 - 28.5N \tag{50.1}$$

The depth of boreholes is 80 m in the system, when the boreholes depth changes, the first fitting equation does not have universal significance, it is possible to define using the length of exchanger, when the area of solar collector is every increased by 1 m^2, and the length of ground heat exchanger can be approximately decreased by 5.6 m. the fitting equation as the second equation.

$$A = 4208 - 5.6L \tag{50.2}$$

50.3.2 The Match of Collector Area and Storage Tank Volume

The matching relationship of the volume of the storage tank and the solar collector area is 50–100 L/m^2 in the solar short-term heat storage system. Table 50.5 shows the change of system parameter under different storage tank volume.

As can be seen from the table, the amount of stored heat of the water tank is also gradually increased with the volume of the storage tank increases, while the

Table 50.5 Operation parameters under different volume of heat storage tank

The name of parameters	Volume of heat storage tank/m					
	5	10	15	20	25	30
Water tank heat storage capacity/kWh	34,562	34,858	35,320	35,739	35,981	36,171
Borehole heat transfer/kWh	98,792	98,571	98,194	97,860	97,702	97,589

borehole heat transfer reduces, the tank volume for each additional 5 m^3, and the heat storage capacity of tank averagely increases 321 kWh.

In order to study the relationship between the increased rate of heat storage amount of the water tank and the tank volume increase, the increased rate of tank stored heat is shown in Fig. 50.6.

As can be seen from the figure, the increasing rate of the stored heat of the water tank and the tank volume is not linearly changing, but it is a change process that first raised and then reduced. The increase rate has a maximum value in the range of 10–15 m^3; the increase rate of the maximum that can be obtained when the solar collector area of 180 m^2 with 10–15 m^3 water tank. Water tank heat storage capacity is fastest when the tank volume is greater than 15 m^3, then the heat storage capacity continues to increase, but the rate of increase is slow. Therefore, it can be concluded that when the matching relationship of the volume of the storage tank and the solar collector area is 60–80 L/m^2, the efficiency of the water tank is highest in the solar short-term heat storage system.

50.3.3 The match of Heating Network and Ground Heat Exchanger

The design of the heating network system circulating water flow directly affects the heat transfer of the heat network, The overall heat transfer coefficient of the heat exchanger is 5,400 W/m^2· °C. In order to study the impact that the change of the heating network circulating water flow and the number of boreholes to heating network, Simulate heating network heat transfer under different circulating water flow, and the results are shown in Table 50.6. Statistics results of condenser heat release and heating network heat transfer under different quantity of boreholes are shown in Table 50.7.

As can be seen from Table 50.6, the heating network heat transfer increases with the increasing of heating network system circulating water flow, when the circulating water flow increases from 10 to 20 m^3/h, and the heating network heat transfer increases by 6,508 kWh. Therefore, the heating network circulating water

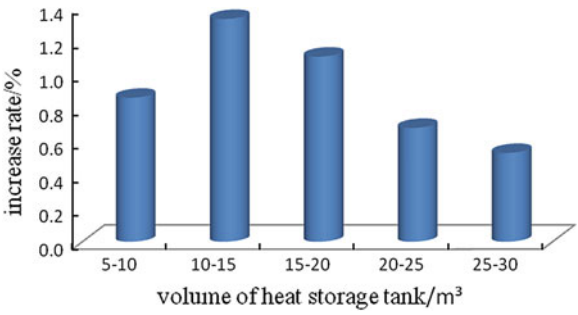

Fig. 50.6 The increase rate of the heat reservoir under different volume of tank range

Table 50.6 The heating network for heat under different circulating water flow

The name of parameters	Circulating water flow of the heating network/m·h^{-1}		
	10	14.5	20
Heating network heat transfer/kWh	106,270	109,309	112,778

Table 50.7 Operation parameters under different number of boreholes

The name of parameters	Number of boreholes		
	22	20	18
Condenser heat release/kWh	172,116	169,221	165,880
Heating network heat transfer/kWh	105,444	109,309	113,780

for each additional 1 m^3/h, and the total heat of the heating network averagely increases by 650 kWh.

As can be seen from Table 50.7, the condenser heat release gradually reduced, and heating network heat transfer gradually increasing with the reduction in the number of boreholes. Mainly due to the reduction in the number of boreholes leads to lower water temperature of the heat pump condenser side, and increases the heat exchange time of the heat pump condenser and heating network, the heat transfer of the heat network gradually increasing. The number of boreholes decreased from 22 to 18, and the heating network for heat total increases to 8,336 kWh. We can conclude that the heating network circulating water for each additional 1 m^3/h, and the total heat of the heating network averagely increase by 650 kWh. To ensure the same for the heat, when the amount of borehole is every reduced by one, and the circulating water flow of the heating network system can be increased to about 3.2 m^3/h. When the circulating water flow of the heating network system is every increased by 1 m^3, and the length of ground heat exchanger can be approximately decreased by 50 m.

50.4 Conclusions

1. The typical building in severe cold region was selected as the research object. The complementary heating system on solar-ground source heat pump and heating network was designed by TRNSYS software to achieve the complementary use of conventional energy and renewable energy.
2. The system simulation results showed that the heat taken from the soil is reduced by 30 % in the auxiliary role of solar. The heat transfer time of the heating network focused on the middle of the heating period, and monthly average COP of the heat pump units is 4.0 or more in the period of heating.
3. Under the same supply of heat, when the amount of borehole is increased by one, and the area of solar collector can be approximately decreased by 28.5 m^2.

When the area of solar collector is increased by every 1 m^2, and the length of ground heat exchanger can be approximately decreased by 5.6 m.

4. When the matching relationship between the volume of the storage tank and the solar collector area is 60–80 L/m^2, and the efficiency of the water tank is highest in the solar short-term heat storage system.
5. To ensure the same for the heat, when the amount of borehole is reduced by one, and the circulating water flow of the heating network system can be increased to about 3.2 m^3/h. When the circulating water flow of the heating network system is every increased by 1 m^3, and the length of ground heat exchanger can be approximately decreased by 50 m.

Acknowledgments This study is supported by National Science and Technology Pillar Program during the 12th Five-Year Plan Period (2011BAJ05B02).

References

1. Kadir B (2010) Evaluation of the performance of a ground-source heat-pump system with series GHE (ground heat exchanger) in the cold climate region. Energy 35:3088–3096
2. Augustine NA, Anish CP (2007) Integrated conceptual design of a robust and reliable waste-heat district heating system. Appl Therm Eng 27:1158–1164
3. Papadopoulos AM, Oxizidis S, Papandritsas G (2008) Energy, economic and environmental performance of heating systems in Greek buildings. Energy and Buildings 40:224–230
4. Stojanovic B, Akander J (2010) Build-up and long-term performance test of a full-scale solar-assisted heat pump system for residential heating in Nordic climatic conditions. Appl Therm Eng 30:188–195
5. Bauer D, Marx R (2010) German central solar heating plants with seasonal heat storage. Sol Energy 84:612–623
6. Feng X, Xin Zhang Y (2011) Composite of solar and ground source heat pump system optimization configuration operating mode. HVAC 41(12):79–83
7. Ni L, Tang Q (2010) The analysis of ground source heat pumps with auxiliary heat source design load ratio. J Refrig 31(5):18–23

Chapter 51
Experimental Study on Running Spacing of Buried Pipe and System Heating Performance in GSHP System

Songtao Hu, Bo Lin, Zhigang Shi and Hengjie Yu

Abstract The bigger buried pipe spacing will increase buried pipe surface area, go against to save land and initial investment; the smaller buried pipe spacing will cause obvious thermal interference phenomenon between adjacent buried pipes, go against to heat transfer of the buried pipe heat exchanger and stable operation of the system. In the actual operation process of heat pump system, the actual heat load is often less than the design load, so we can try to open different buried pipes, adjust the actual operation spacing, to reduce the heat interference phenomenon between adjacent buried pipes, make for the operation of the heat pump system. The experiment was done in a villa Ground source heat pump system, in which kind of buried pipe spacing system running more energy saving was analyzed. Conclusions as follow: the bigger buried pipe spacing the higher unit and system COP, Spacing for the 3.6 m, System COP is 3.4, unit COP is 5.1; Spacing for the 5.4 m, System COP is 3.5, unit COP is 5.3; Spacing for the 7.2 m, System COP is 3.6, unit COP is 5.5; Spacing for 5.4 m system COP is 2.9 % higher than spacing 3.6 m, unit COP is 3.9 % higher; Spacing for 7.2 m, System COP is 2.8 % higher than spacing 5.4 m, unit COP is 3.77 % higher; So, at the same load, we can adjust running spacing by opening different buried pipe wells to improve COP of system and unit, to save energy.

Keywords GSHP · Buried pipe different operation spacing · COP

S. Hu (✉) · B. Lin · Z. Shi · H. Yu
Qingdao Technological University, No.11 Fushun Road, Qingdao, China
e-mail: h-lab@163.com

A. Li et al. (eds.), *Proceedings of the 8th International Symposium on Heating, Ventilation and Air Conditioning*, Lecture Notes in Electrical Engineering 262,
DOI: 10.1007/978-3-642-39581-9_51,

51.1 Introduction

During the Ground source water-cooled multi-line system operation, many factors can affect pipe heat exchanger efficient, two of them are very important, one is the heat transfer capability of the soil, the greater it is, the more easily the heat transfer to the remote soil around the heat exchanger, the stronger heat recovery capability of the soil; Another is heat interaction between the heat exchanger, the smaller the thermal interference between adjacent two heat exchanger, the better the effect of heat transfer, the system run more stable, and vice versa is not conducive to the heat transfer [1–3].

Underground pipe spacing is an important parameter of the vertical ground source heat pump system design process. Our Specification provides that drilling spacing should satisfy the heat exchanger, spacing should be 3−6 m [4]. ASHRAE requires drilling spacing is generally 15 ∼ 25 ft (about 4.57−7.62 m) [5]. Buried spacing is too small to make the tube group produce significant thermal interference between the ground heat exchanger; pipe spacing is too large, buried surface area will be increased [6].

This experiment studied the influence of pipe spacing to the return water temperature of the unit and the influence on the unit and the system COP, analyzed in which buried spacing the system run more energy-efficient, to provide some reference to the actual project.

51.2 The Survey of the Experiments

51.2.1 The Tested Building

This experiment was conducted in a townhouse in Wenquan Town, Jimo, which had the basement, ground floor, second floor, with a total construction area of 430 m^2. Exterior wall heat transfer coefficient of 0.438 W/(m^2· K), interior wall heat transfer coefficient to 1.364 W/(m^2· K), the roof heat transfer coefficient of 1.90 W/(m^2· K). The basement storey 3.45 m, was divided into four rooms. The ground floor storey 3 m, a total of four rooms; storey varies second floor, four rooms. The building floor plan, buried Figure, see in Fig. 51.1.

The digital scroll water-cooled air conditioning system was adopted in this building; the system rated cooling capacity of 56 kW, 16 indoor units connected to a single host. There were six buried pipe wells (respectively numbered as A, B, C, D, E, F), as shown in Fig. 51.2. Layout of heat pump units shown in Fig. 51.3 and Join of inside buried pipe system is shown in Fig. 51.4.

Fig. 51.1 Plan of building floor

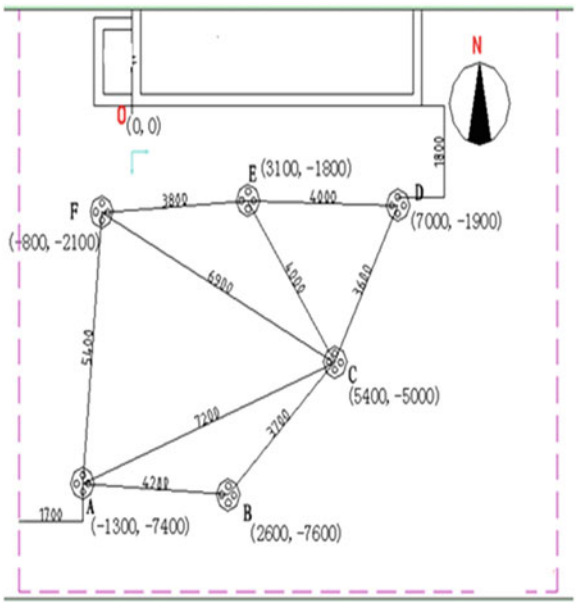

Fig. 51.2 Layout of buried pipe figure

51.2.2 The Experiment Methods

In the experiment, following parameters were measured:

(1) Outdoor air temperature and air relative humidity.

Fig. 51.3 Layouts of heat pump units

Fig. 51.4 Join of inside buried pipe system

(2) Indoor hump units operating parameters: heating capacity of unit, condensing temperature and pressure, supply and return air temperature of unit.
(3) Indoor air temperature and air relative humidity.
(4) Unit supply and return water temperature and flow of buried pipe side in the closed-loop water system.
(5) Power consumption of every device.

51.2.3 Experimental Conditions

In this study, the experiments were carried out from February 24 to 26, 2011. The running spacing was adjusted through operating different buried pipe wells, and

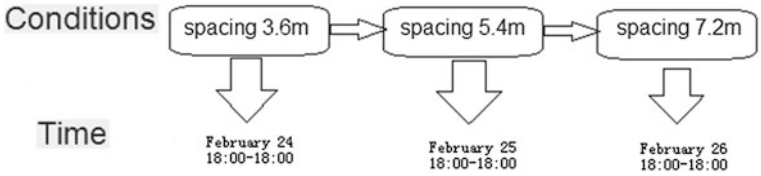

Fig. 51.5 The flowchart of different operating spacing experimental conditions

the spacing was respectively 3.6, 5.4, 7.2 m. During the periods, the outdoor average air temperature was 2.5 °C, 2.8 °C, 3.2 °C respectively, as much as possible to reduce the outdoor temperature fluctuations on the experimental results.

Each experimental condition lasted 24 h, from today 18 o'clock to the next day 18 o'clock, while the indoor air temperature was set at 18 °C, water flow rate of system retained 4.7 m^3/h, each station conditions continuously. Sequentially switched the C and the D well, the A and the F well, the B and the D well, the experimental process as shown in Fig. 51.5.

51.3 The Experimental Results and Discussion

51.3.1 The Supply and Return Water Temperature of Unit Cooling Side at Different Operating Spacing Conditions

The return water temperature at different operating spacing conditions was shown in Fig. 51.6.

Figure. 51.6 shown the return water temperature of units increased with buried pipe spacing. In the experiment only two-buried pipe wells were opened, heating load of building was too large, the soil temperature around underground heat exchanger was lower. Therefore, supply and return water temperature is also lower. While buried pipe spacing was 3.6 m, the lowest backwater temperature of unit up to 4.9 °C, was not conducive to the unit heat transfer.

The heating loads of building varied with outdoor temperature, the unit supply and return water temperature decreased gradually, since 9:00, the unit for the return water temperature was gradually and then began to decline. After 15:00, Fig. 51.7 was supply and return water temperature difference trends.

The supply and return temperature difference of the unit was about 1.5 °C, the value approximately fixed, 1.68 °C at spacing of 3.6 m, 1.62 °C at spacing of 5.4 m, 1.57 °C at spacing of 7.2 m. But at about 14:00, there was a clear downward trend, it was because heat load of building dropped.

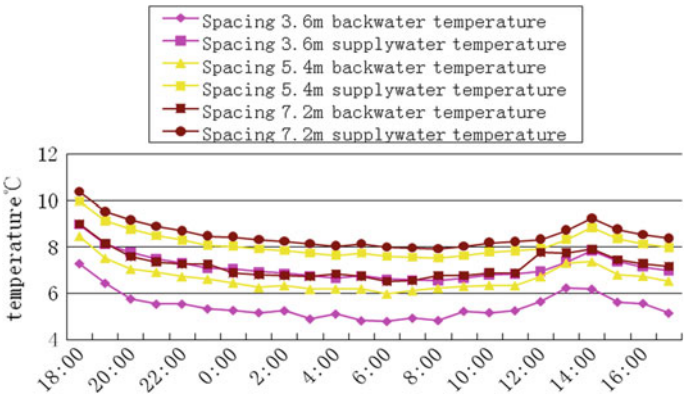

Fig. 51.6 The supply and return water temperature trend

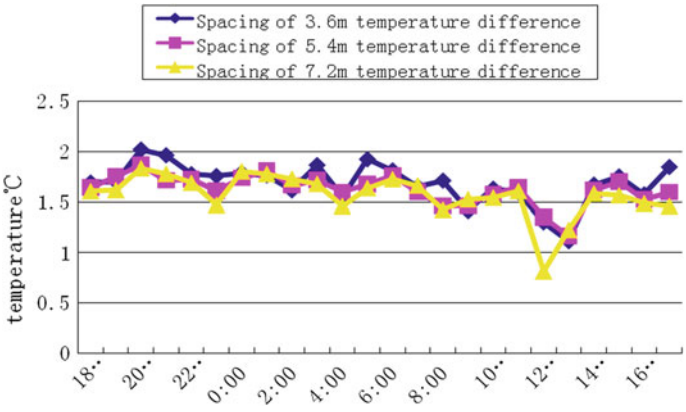

Fig. 51.7 Temperature difference versus spacing

51.3.2 The Unit and the System COP of Different Spacing Conditions

From Fig. 51.8, the system load all the day maintained 230 kWh around, basically fixed. The building heat load could be considered constant during the experimental period.

From Fig. 51.9, the power consumption of the pump was essentially the same, the power consumption of the unit drooped lightly with increase of spacing. This was because that two different buried pipe wells were opened in every experiment condition, then water flow of system was substantially constant, so the power consumption of the pump was substantially constant. On the other hand, the power consumption of the unit was subject to the building heat load and unit backwater

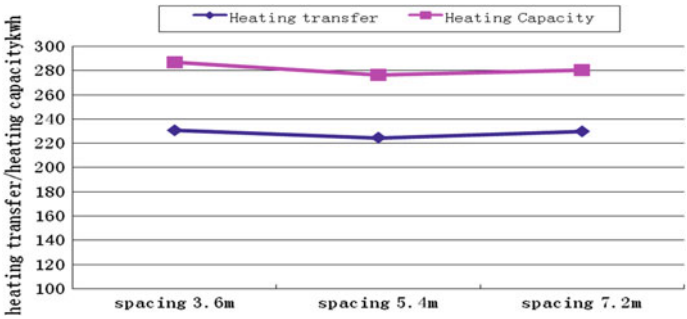

Fig. 51.8 Heating transfer and Heating capacity of different spacing conditions

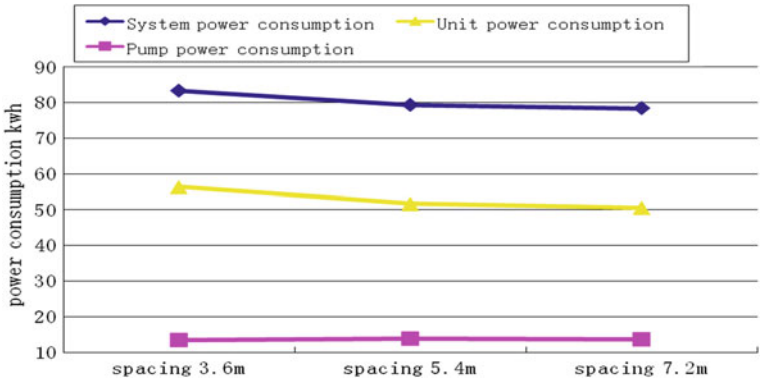

Fig. 51.9 Power consumption at different spacing conditions

temperature. At the same load, larger buried spacing, smaller thermal interference between the buried pipes, and easier the heat released to soil spread to the remote, so that the soil temperature near the buried pipe was not too low. These were helpful to improve the return water temperature of the unit the efficiency of the unit heat exchanger, finally to reduce the energy consumption of the unit. All of those energy consumption of the unit decreased with the pipe spacing increase.

Be seen from Fig. 51.10, the bigger buried pipe spacing, the higher unit and system COP, Spacing for the 3.6 m, System COP is 3.4, unit COP is 5.1; Spacing for the 5.4 m, System COP is 3.5, unit COP is 5.3; Spacing for the 7.2 m, System COP is 3.6, unit COP is 5.5; Spacing for 5.4 m system COP is 2.9 % higher than spacing 3.6 m, unit COP is 3.9 % higher; Spacing for 7.2 m system COP is 2.8 % higher than spacing 5.4 m, unit COP is 3.77 % higher.

So, at the same load, we can adjust running spacing by opening different buried pipe wells to improve COP of system and unit, to save energy.

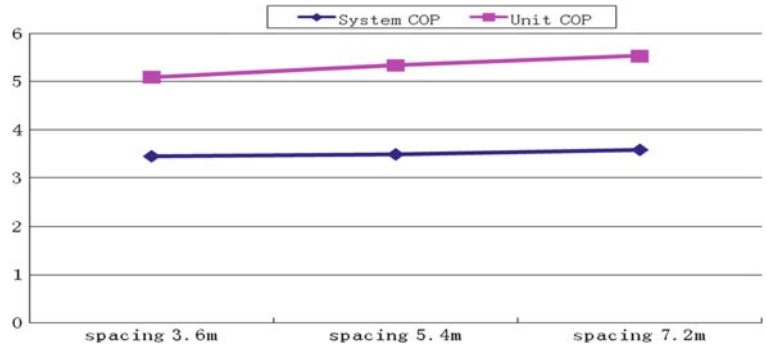

Fig. 51.10 The unit and the system COP of different spacing conditions

51.4 Conclusion

Big pipe spacing can increase underground heat exchanger area, make connection piping too long, the cost higher, appropriate buried pipe spacing should be considered in the scheme. Moreover, the building actual loads vary timely and often are lower than the designed value. So, we can open different wells to increase running spacing to save energy. In our experiment, the bigger buried pipe spacing, the higher unit and system COP. Spacing for the 3.6 m, System COP is 3.4, unit COP is 5.1; Spacing for the 5.4 m, System COP is 3.5, unit COP is 5.3; Spacing for the 7.2 m, System COP is 3.6, unit COP is 5.5; Spacing for 5.4 m system COP is 2.9 % higher than spacing 3.6 m, unit COP is 3.9 % higher; Spacing for 7.2 m system COP is 2.8 % higher than spacing 5.4 m, unit COP is 3.77 % higher.

So, at the same load, we can adjust running spacing by opening different buried pipe wells to improve COP of system and unit, to save energy.

References

1. Hao W (2007) Heat transfer characteristics research of ground heat exchanger. Master Thesis, Shandong University
2. Jun Z, Huajun W (2006) Numerical simulation on heat transfer characteristics of soil around compact pile-buried underground heat exchangers. HV&AC 36(2):11–14
3. He K (2011) Research on Soil Temperature Field around Ground Heat Exchanger System in Differen Boreholes' Arrangements. Master Thesis, Donghua University
4. GB50366 2005, Ground source heat pump systems engineering and technical specifications [S]
5. ASHRAE. Handbook of HVAC Applications. American Society of Heating [J].Refrigerating and Air conditioning Engineers, Inc, 2003,Atlanta, USA
6. Qian B, Xu Z (2010) The study of buried tube spacing ground source heat pump systems in shanghai station. Rail hvac academic annual conference in 2010

Chapter 52
Electricity Consumption of Pumps in Heat Exchanging Stations of DH Systems in China

Lei Dong, JianJun Xia and Yi Jiang

Abstract This study analyzed the current electricity consumption of heating exchanging stations in China. By testing the pressure drop of each opponent and the operating condition of pumps, the conclusion was that the largest amount of potential energy saving was inside of stations. The improper selection of pumps, heat exchangers, and pipes was the important reason to cause extra energy loss.

Keywords DH system · Heat exchanging station · Pressure drop

52.1 Introduction

DH system, consisting of heat source, primary network, substation, secondary network, and users, is the major way of heating in North China. In European countries, secondary heating network just includes pipes inside of the building, and the heat exchanger is always so small that can be located in the basement of the building. But in China, the secondary network is always lager, including the pipes inside the building and pipes that connect buildings. Figure 52.1 shows the difference of network in China and European countries [1].

Figures 52.2 and 52.3 show two kinds of substations: heat exchanging stations and water mixing stations. Water mixing stations are always used in place near the heat source where the available head of the primary network is high enough to overcome the fluid resistance of secondary network. To achieve the needed supply water temperature of secondary network (40–45 °C), pumps in parallel are needed to mix the secondary return water whose temperature is lower (30–35 °C) with the primary supply water (70–90 °C). The amount of electricity consumption of water

L. Dong (✉) · J. Xia · Y. Jiang
Building Energy Research Center, 203A, 10084 Beijing, China
e-mail: leistone5@yahoo.com.cn

A. Li et al. (eds.), *Proceedings of the 8th International Symposium on Heating, Ventilation and Air Conditioning*, Lecture Notes in Electrical Engineering 262,
DOI: 10.1007/978-3-642-39581-9_52,

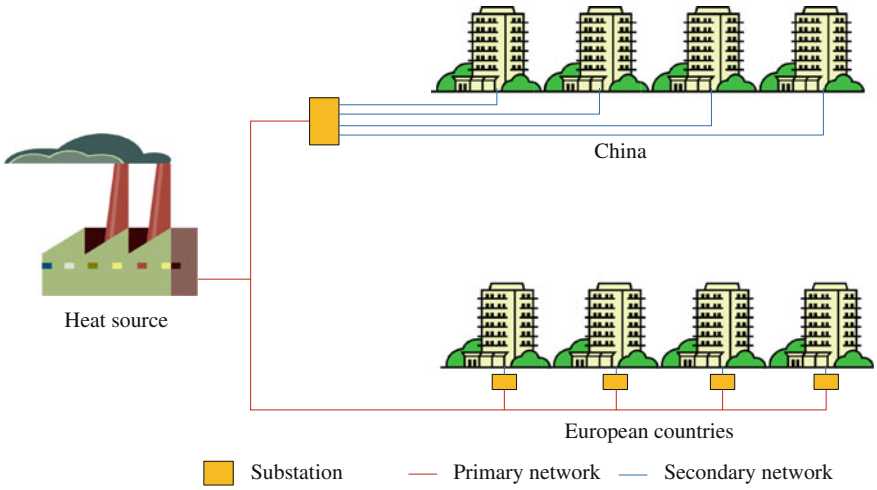

Fig. 52.1 DH system in China and European countries

Fig. 52.2 Water mixing station

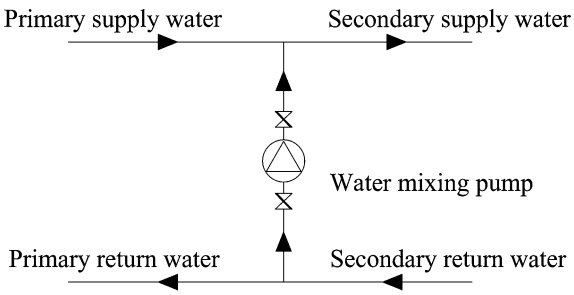

mixing pumps is small, because there are no heat exchangers in the system. The other kind of substations is the heat exchanging station. General components in a heat exchange station are showed in Fig. 52.3. Rather than charging pumps, cycling pumps working continuously take the greatest percentage of the total electricity consumption [2].

In order to save the total energy consumption of DH systems and lower the operating cost of heating companies, it is important to evaluate the electricity consumption of pumps of the secondary side [3]. Based on the field testing data, this thesis focuses on the distribution of pressure drop on each opponent of the secondary system and the efficiency of cycling pumps. Furthermore, the proper way to select and control them has been discussed.

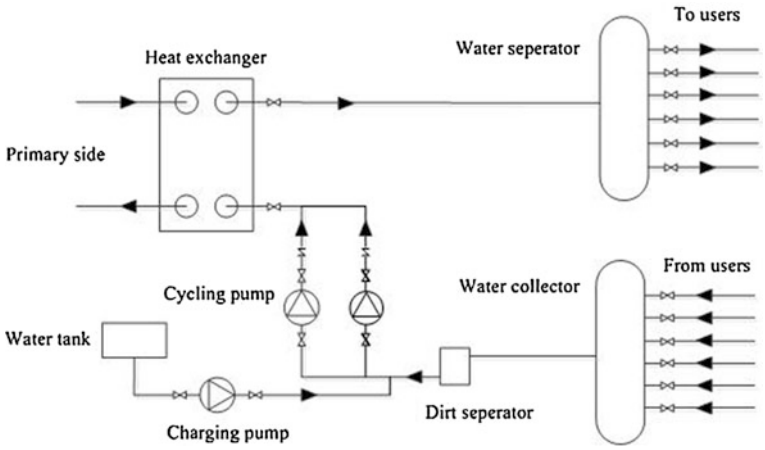

Fig. 52.3 Heat exchanging station

52.2 Method

52.2.1 Data Source

ChiFeng is a city of more than 8,00,000 people and 2×10^7 m^2 heating area (2010) in Northern China. The DH system of ChiFeng has a history of more than 30 years (since 1980). In this thesis, ChiFeng has been chosen as the typical city.

Data from the heating company of ChiFeng, including parameters of primary/secondary system, electricity consumption statistics, and heating area of substations, supported the basic research of the total electricity consumption.

For further study, several typical substations were chosen, and system parameters of them were tested, including the pressure drop of each opponent, flow of primary/secondary side, supply/return water temperature, and the power of pump.

52.2.2 Instrument and Accuracy

Table 52.1

Table 52.1 Instrument and accuracy of each testing item

Testing item	Instrument	Range	Accuracy
Pressure	HongQi high accuracy pressure gate YB-200	0–1.6 MPa	0.4 %
Flow	XianChao ultrasonic flowmeter XCT-2000	Flow velocity: ± 32 m/s Pipe diameter DN50–1000	1 %
Temperature	TianJianHuaYi WZY-1A	−20–80 °C	±0.3 °C
Electricity	HIOKI clamp on power tester 3169-20	75.000 W–900.0 kW	0.5 %

52.3 Result and Discussion

52.3.1 Electricity Consumption of Pumps of Secondary Side

The electricity consumption per area of each heat exchanging station in 2011 is shown in Fig. 52.4. The average value is 1.57 kWh/(m^2a), when the difference of values is obviously large. The total electricity consumption of all the heat exchanging stations in 2011 is 1.38×10^8 kWh.

The temperature difference of each station is almost the same, 10 °C, so the difference of electricity consumption per area can be caused by the efficiency of the distribution system. The heating area of stations, whose electricity consumption is higher than the average value, is 3.97×10^6 m^2. If the electricity consumption of them can be reduced to the average value, about 2.3×10^6 kWh electricity would be saved per year. In a word, the potential amount of energy saving is obviously large, accounting for 16.7 % of the total electricity consumption of heat exchanging stations.

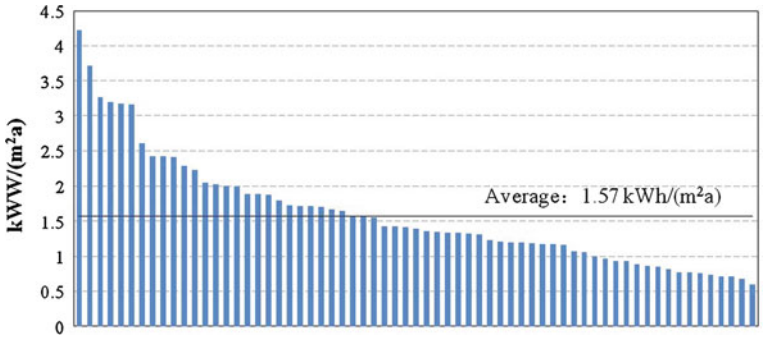

Fig. 52.4 Electricity consumption per area of heat exchanging stations

52.3.2 Pressure Drop of Each Opponent

52.3.2.1 Distribution of Pressure Drop

The testing data are organized in the Table 52.2 and Fig. 52.5.

As can be seen in Fig. 52.6, the pressure drop of users, only takes 17 % of the total pumping head, much less than that of heat exchangers (32 %) and pipes connecting pump (38 %). Opponents inside of substations have the largest amount of potential energy saving of the secondary network.

52.3.2.2 Heat Exchangers

As shown in the third column of Table 52.2, the pressure drop of heat exchangers varies from 3.6 to 12.3 mH_2O, and the mean is 6.7 mH_2O.

The pressure drop of a heat exchanger consists of two parts, the pressure drop of runner between sheets and that of corner cores. The formulas to calculate them are followed.

The pressure drop of runner between sheets:

$$\Delta P' = 2f\frac{L}{d_c}\rho w^2 m\left(\frac{\mu}{\mu_0}\right)^{-0.17} \tag{52.1}$$

The pressure drop of corner cores:

$$\Delta P''=mf\left(\frac{\rho w^2}{2}\right)\left(1+\frac{n}{100}\right) \tag{52.2}$$

Table 52.2 Pressure drop of heat exchanging stations

Substation	Pumping head	Pressure drop (mH_2O)				
		Heat exchanger	Dirt separator	Users	Pipes connecting pumps	other
BJC	24.0	3.6	2.0	4.1	9.7	4.6
ZF	31.7		7.7		8.2	
MX		6.1	2.0	6.1		
LH	17.3	4.1	1.5	3.1	5.6	3.1
YHHY	20.9	5.6	2.0	3.1	10.2	
TX	20.3	6.6	1.0	3.6	9.0	
SZY	22.2	12.3	1.0	3.1	5.8	
HG	24.4	4.1	2.0	6.1	12.1	
BJL	22.1	11.2	3.1	2.0	5.7	

Note 1. The pressure drop of "users" means the pressure drop between water separator and water collector

2. 'Pipes connecting pumps' means the 2 pipes directly connect the pump, generally involving 2 5 m-long pipes, 2 butterfly valves and 1 check valve

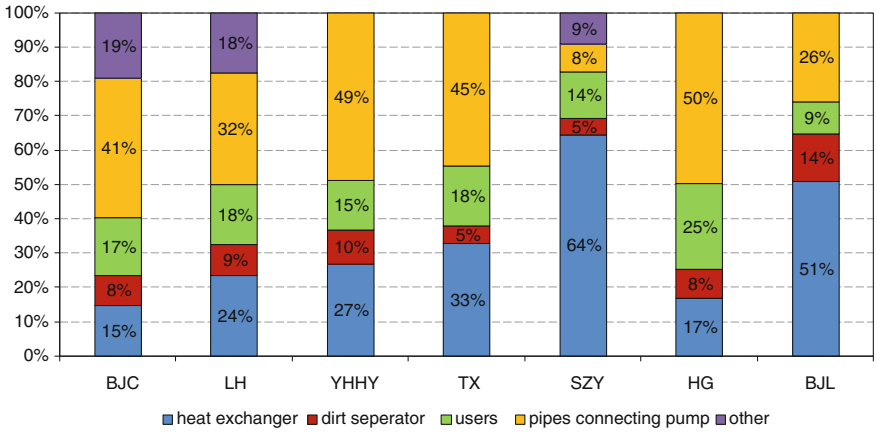

Fig. 52.5 Pressure drop of heat exchanging stations

Fig. 52.6 Pressure drop proportion

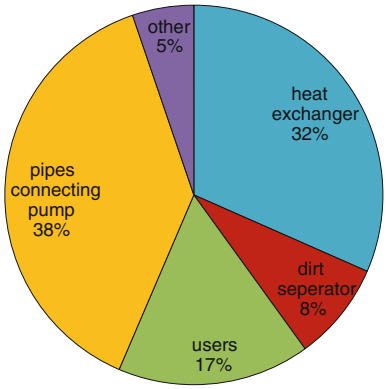

f, L, d_c, m, n in the formulas are parameters of the structure of heat exchangers, μ, μ_0, ρ are parameters of water characteristic. When the style and the number of unit remain unchanged, the pressure drop of a heat exchanger is just depended by the square of flow velocity.

Table 52.3 shows the style, number, and pressure drop of heat exchangers in substations. Heat exchangers of different style have different 'flow-pressure drop curve.' Substations TX, MX, BJL, and SZY have the same style of heat exchangers (LanZhouShiHua). The single flow and pressure drop of each substation are shown in Fig. 52.7. It is obvious that the pressure drop and single flow have a positive correlation. The overlarge single flow is caused by the expanding of heating area of each substation, which means the current heating area is always more than planned. Taking 'SZY' for example, if its pressure drop meets the average level by adding the number of heat exchangers from 2 to 4, 3.5×10^4 kWh electricity would be saved per year.

Table 52.3 Style, number, flow and pressure drop

Substation	Style	Number	Total flow m^3/h	Single flow m^3/h	Pressure drop mH_2O
BJC	SiPingBeiFang BR0.8-1.6-100-E	9	627	69.7	3.6
TX	LanZhouShiHua BR0.6-1.6-100-E	7	565	80.7	6.6
MX	LanZhouShiHua BR0.6-1.6-100-E	9	700	77.8	6.1
LH	Accessen AC70/97/ PN16/304	3	404	134.7	4.1
BJL	LanZhouShiHua BR0.6-1.6-100-E	4	629	137.5	11.2
HG	SiPin Vicarb V60	3	425	141.7	4.1
SZY	LanZhouShiHua BR0.6-1.6-100-E	2	275	157.3	12.3

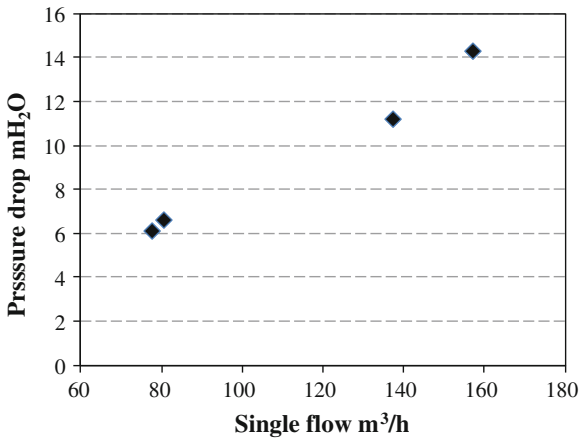

Fig. 52.7 Single flow and pressure drop of four substations

Additionally, the water scaling can add the pressure drop, too. According to the past research of Russia, the pressure drop of the secondary side may increase by 5–10 % after a 7-month heating season. So it is important to clean the heating exchangers before the beginning of heating season.

52.3.2.3 Pipes Connecting Pumps

As can be seen from the sixth column of Table 52.2, the pressure drop of pipes connecting pumps varies from 5.6 to 12.1 mH_2O, and the mean is 8.3 mH_2O.

Pipes connecting pumps generally involve two 5 m-long pipes, two butterfly valves, and one check valve. According to the research, the pump worked singly

now was designed to work in parallel, leading to the overlarge flow velocity in the pipes connecting the pump. The formula to calculate the specific frictional head loss of a pipe is followed.

$$R = 6.88 \times 10^{-3} K^{0.25} \frac{G^2}{\rho d^{5.25}} \tag{52.3}$$

The theoretical pressure drop of each pipe has been calculated in Table 52.4. Because of the small diameters of pipes, the specific frictional head losses are all far more than rated. The reason for the difference of the theoretical value and real value is the difference of the resistance coefficients of valves caused by the ageing of valves.

52.3.3 Operating Conditions of Pumps

52.3.3.1 Overlarge Selection of Pumps

The good operating condition of pumps depends on the match of the pump and the net. The overlarge selection of pump always causes the low efficiency and high electricity consumption. In order to investigate the efficiency of pumps, heat exchanging station 'ZF' was chosen. The overlarge pump of it was replaced, and the power and efficiency of pumps were tested.

As can be seen in Table 52.5, the overlarge pump before reform causes the lower efficiency and the higher power [4]. The reason is shown in Figs. 52.8 and 52.9.

In Fig. 52.8, curve a and curve b are the character curves of net, curve A-B is the character curve of pump, and curve η_A–η_B is the efficiency curve of pump. If the head of pump is higher than really needed, which means the real character curve of net is b rather than a, the real working point will be B, which corresponded a higher efficiency than point A. At the same time, as shown in Fig. 52.9,

Table 52.4 Calculation of pressure drop of pipes connecting pumps

Substation	Diameter DN	Velocity m/s	Specific frictional head loss Pa/m	Theoretical pressure drop mH_2O	Real pressure drop mH_2O
BJC	200	5.5	1890.0	4.2	9.7
ZF	200	5.7	2024.9	4.5	8.2
LH	150	6.4	3556.7	5.6	5.6
YHHY	150	4.9	2092.1	3.3	10.2
TX	200	5.0	1534.7	3.4	9.0
SZY	200	5.6	1902.1	4.3	5.6
HG	150	6.7	3932.1	6.2	12.1
BJL	150	4.3	1646.3	2.6	5.7

Table 52.5 The parameters of pumps in substation ZF

Type	Before Two pumps in parallel	After Single pump
Choice of pumps	Head: 45 m Flow: 374 m3/h × 2 Power: 75 kW × 2	Head: 33.5 m Flow: 630 m3/h Power: 75 kW
Tested flow m^3/h	610	649
Tested head mH_2O	39.0	31.7
Tested power kW	110.7	66.4
Efficiency	59 %	84 %

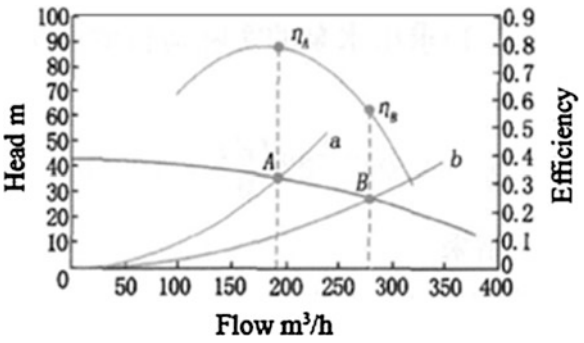

Fig. 52.8 Low efficiency of the overlarge pump

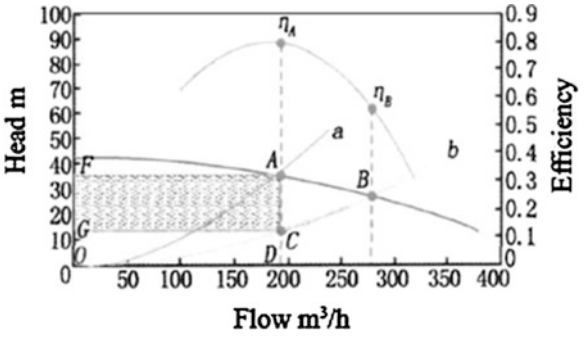

Fig. 52.9 Great electricity loss of the overlarge pump

in order to prevent the overlarge flow, the opening of valves in the network may be smaller, causing the extra energy loss as the square ACGF.

52.3.3.2 Proper way to Control Pumps in Parallel

When two pumps work in parallel, 'one pump fixed frequency and the other variable frequency' is a kind of controlling strategy now being used in China.

Table 52.6 Operating condition of two pumps of different frequency

Frequency of pumps	*f* HZ	Flow m^3/h	Head mH_2O	Power kW	Efficiency (%)
Fixed	50.0	580	27.0	51.8	82
Variable	40.0	114	20.5	20.2	32

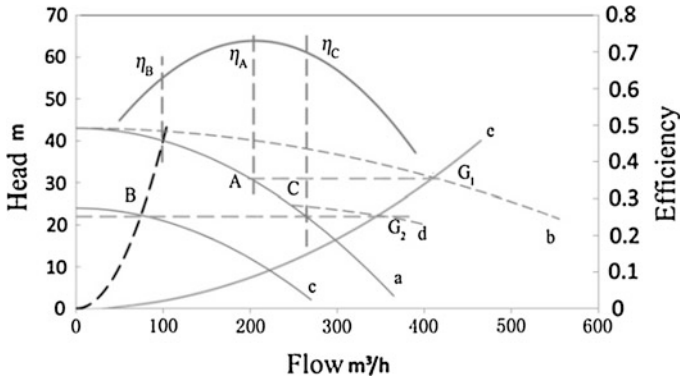

Fig. 52.10 Wrong control strategy of pumps in parallel

Substation 'ZF' is using this strategy, and the operating condition of two pumps in it has been tested and shown in Table 52.6.

The efficiency of the variable frequency pump is just 32 %, much lower than the fixed one. The reason is shown in Fig. 52.10. Assuming that the fixed frequency pump and the variable frequency pump have the same pump character curve a. Curve b is the character curve when they work in parallel. η_A–η_B–η_c is the efficiency curve of single pump. η_A is the efficiency when they work in fixed frequency. G_1 is the total flow. If the frequency of one pump is variable (curve c)

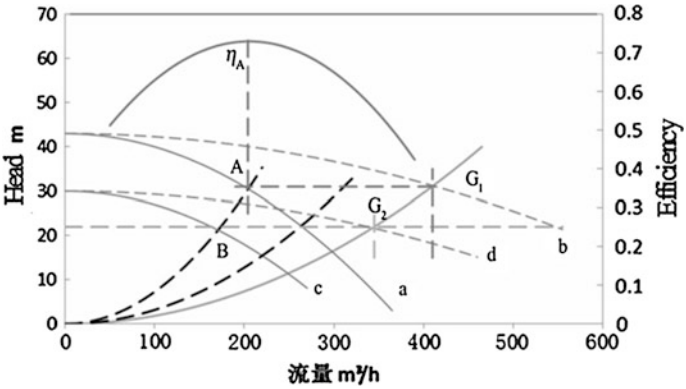

Fig. 52.11 Right control strategy of pumps in parallel

and the other fixed (still curve a), the whole curve of them will be d, and the total flow will become G_2. OB is the equal-efficiency curve of the variable frequency pump. Then the efficiency of the variable frequency one becomes η_B. The efficiency of the other becomes η_C. Both are lower than η_A.

The proper way of controlling is shown in Fig. 52.11. Two pumps converted their frequency synchronously. When getting the same flow G_2, the efficiency is still η_A.

52.4 Conclusion

From the result of test, we can come to following conclusions:

52.4.1 The Potential Amount of Energy Saving in Heat Exchanging Stations is Large

As can be seen in Fig. 52.4, if all the heat exchanging stations meet the average level, the potential amount of energy saving will be 2.3×10^6 kWh, accounting for 16.7 % of the current total electricity consumption of heat exchanging stations.

The pressure drop of users takes 17 % (maximum 25 %) of the working head of pump, less than that of opponents in the substation. For the flow velocity of opponents in substation is high, the improper selection or damage of opponents will lead to great amount of energy loss. As a result, the key point of saving electricity consumption of secondary side is inside of heat exchanging station.

52.4.2 Flow of a Single Heat Exchanger Should not be too Large

The pressure drop of heat exchangers takes a large proportion (33 %) of the total head of pump. On one hand, the heat exchangers should be properly selected, to prevent the overlarge flow which would cause the extra pressure drop. On the other hand, they should be cleaned before the beginning of heating season, to prevent the pressure drop caused by scaling.

52.4.3 Diameter of Pipes Connecting Pumps Should be Properly Selected

The pressure drop of pipes connecting pumps takes the largest proportion (38 %) of the total head of pump, because of the small diameter that lead to the overlarge water velocity and specific frictional head loss. When designing the system, the diameter of pipes should be bigger than currently needed, to prepare for the expanding of heating area of the substation in the future.

52.4.4 Pumps should be Properly Selected and Operated

As showed in Table 52.5, the smaller selection of pumps would significantly reduce the electricity consumption [5], because of the higher efficiency of pump and less pressure drop of valves and pipes caused by overlarge flow. Otherwise, a fixed-frequency pump should not work in parallel with a variable-frequency one. Pumps working in parallel should convert their frequency synchronously.

References

1. Poulsen H (1992) Improvement of existing district heating substations. Report: NEI-DK-961; ISBN 87-88038-26-2 1992. 9
2. Dalla Rosa A (2012) District heating (DH) network design and operation toward a system-wide methodology for optimizing renewable energy solutions (SMORES) in Canada: a case study. Energy 45(1):960–974
3. Zsebik A, Sitku G Jr (2001) Heat exchanger connection in substations-a tool of decreasing return temperature in district heating networks. Energy Eng: J Assoc Energy Eng 98(5):20–28 + 31
4. Liu L (2001) Electrical power consumption analysis of circulating pumps in central heating systems for residential quarters, Heating Ventilating and Air Conditioning 1
5. 2011 Annual Report on China Building Energy Efficiency, China Architecture and Building Press

Chapter 53
The Study on Thermal Property of the Rural Traditional Kang Surface Within 24 Hours

Qi Feng, Yongan Ao, Lin Duanmu, Zongshan Wang and Feng Qiu

Abstract The research, based on the rural traditional Kang which is a kind of heated fixed bed, studied the thermal property of the Kang surface through the combination ways of experiment and computer simulations. The main research focused on the Kang surface temperature within 24 h, the percentage of heat amount transferred into the indoor from the Kang, the temperature drop delay of the Kang surface because of the Kang's thermal storage capacity, and the temperature fluctuation of Kang surface due to different inlet size of smoke entering the Kang, the purpose is to provide reference for integrated heating system within the rural indoor room. The research is based on the theoretical mathematical models and experimental data fitting models, using VB programming language to develop software to simulate the Kang surface temperature within 24 h under different conditions, at the same time using the Fluent software to simulate and revise the mathematical models based on VB programming language. The simulative results were compared with the experimental measured ones. The results show that the temperature distribution of the Kang surface is not uniform. Existing phenomenon is that the temperature of Kang surface closed to the smoke inlet (smoke entering from cooker to the Kang) is too high, but the temperature of Kang surface far from the smoke inlet is too low. When the fire is off, the Kang surface temperature will not drop immediately, it will slow down to a certain temperature instead because of the Kang thermal storage. Under certain conditions, the Kang surface temperature and the percentage of heat amount transferred to the room from the Kang will gradually changed with the size of the smoke inlet, and the Kang surface temperature will drop much more slowly after the fire ceased, which will improve the thermal comfort of a Kang.

Z. Wang
School of Municipal and Environmental Engineering, Shenyang Jianzhu University, No. 9, Hunnan East Road, Hunnan New District, Shenyang, China

Q. Feng · Y. Ao · L. Duanmu (✉) · F. Qiu
Faculty of Infrastructure Engineering, Dalian University of Technology, Dalian 116024, China
e-mail: duanmulin@sina.com; xiaoqi880229@163.com

A. Li et al. (eds.), *Proceedings of the 8th International Symposium on Heating, Ventilation and Air Conditioning*, Lecture Notes in Electrical Engineering 262,
DOI: 10.1007/978-3-642-39581-9_53,

Keywords Rural heated Kang · Kang surface temperature · Thermal storage · Visual basic · Fluent

53.1 Introduction

In recent years, numerous villagers pay more attention to the improvement of the living environment with the improvement of people's living standard. The heated Kang is widely used in rural areas in north China, it is a necessary and important heating facility for people, and it can effectively solve the problem of north rural buildings heating and improve the indoor thermal environment and thermal comfort. The heated Kang's form and thermal property are very different, for simple structure of the heated Kang, the heating process is very complicated, involving heat storage and heat conduction, convection and radiation and so on [1]. For the traditional heated Kang in northern countryside, many researchers have studied it. Zhi Zhuang adopted experiment combined with numerical simulation method to study the smoke flow regularity in the heated Kang, the conduction process of heated Kang, and pointed out that only by kitchen waste heat cannot satisfy the demand of indoor heating, other auxiliary heating equipment need to be adopted [2]. Peihong Zhang and others adopted numerical simulation method, analyzed the factors that influence the result of heated Kang heating and pointed out that the increase of Kang height can enhance indoor temperature [3]. Yang Zhao and others used experimental method, analyzed the thermal performance of heated Kang from the fluid mechanics and heat transfer and put forward some new evaluation indexes, such as the Kang surface temperature standard deviation, the heat storage capacity of heated Kang [4, 5]. Xiangxiang Gao and others researched the traditional rural heating mode and the indoor thermal environment a lot and put forward measures that can improve indoor thermal environment of traditional rural house [6]. Junliang Zhu and others used experimental method to analyze the heated Kang structure improvement on whether it can influence the thermal performance of heated Kang [7]. Dan Wang and others adopted numerical simulation method to simulate the distribution trend of Kang surface temperature, and pointed out the Kang surface temperature non-uniformity [8]. The previous researches focus most on the heated Kang itself, only some people study the rural building integrated heating system, and few people study the question of Kang surface hourly temperature through the numerical simulation technology for the subsequent integrated heating system, in addition, the study about the heat storage capacity of heated Kang board and the uneven distribution of Kang surface temperature is not common. For the current heated Kang, although some people have studied it by numerical simulation method, the research through experimental method still holds most.

Smoke flow into the internal Kang from the entrance of the heated Kang, on one side it flows forward and diffuses, on the other side passes the heat on the Kang

board and surrounding wall, on the contrary its temperature decreases continually, the range of temperature with the Kang board and surrounding wall will get smaller, the heat conduction through the range of temperature will also be less and less, so when the smoke flow into the internal Kang, it often leads to uneven flue gas distribution, resulting in uneven distribution of Kang surface temperature, and at the same time also can affect heat transfer to the indoor room [8]. The size of the flue gas inlet will inevitably influences the smoke temperature in the heated Kang, with the increase of the flue gas inlet size, the flux flowed into the Kang will increase, the Kang surface temperature will gradually raised, the percentage of heat amount transferred to the room from the Kang will gradually grow, the Kang thermal storage will increase, so the Kang surface temperature will drop much more slowly after the fire ceased, which will improve the thermal comfort of a Kang [11]. This paper will use the theoretical mathematical models and experimental data fitting models, at the same time using VB programming language and Fluent numerical simulation software to study the above mentioned problems, put forward measures that improve uneven distribution of Kang surface temperature, improve the comfort of Kang surface, the purpose is to provide reference for integrated heating system within the rural indoor room.

53.2 The Establishment of the Models

53.2.1 The Physical Model of the Heated Kang

This research chose the heated Kang in a rural traditional building in Wafangdian city, Liaoning province as the research object. The length, width, and height of the heated Kang are 3, 1.8, 0.67 m; the thickness of plaster layer of Kang board is 0.03 m, the thickness of concrete plate is 0.04 m, the thickness of heated Kang wall is 0.06 m; and the thickness of the soil ash layer at the bottom of the heated Kang is 0.15 m. The length, width, and height of the six columns in the heated Kang are 0.12 m, 0.12 m, 0.06 m; the length, width, and height of internal smoke plate are 0.72 m, 0.06 m, 0.06 m; the width and height of smoke entrance are 0.2, 0.16 m and the width and height of smoke outlet are 0.2, 0.2 m (Fig 53.1).

53.2.2 The Mathematical Models of the Internal Smoke and Kang Surface Temperature

The Kang will be divided into nine uniform parts and numbered the nine parts from 1 to 9 (see Fig. 53.2), the mathematical model of each part is established, at present, we assume that the flue gas temperature of each part and the Kang surface temperature of each part (or one unit) are uniform.

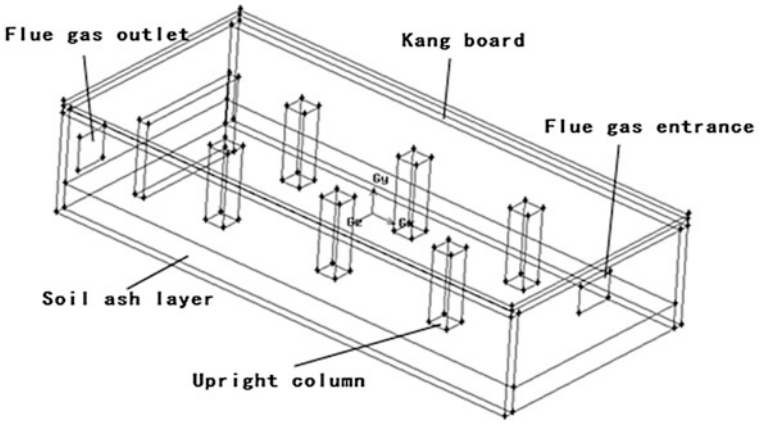

Fig. 53.1 The structure of heated Kang

Fig. 53.2 The partition of Kang surface

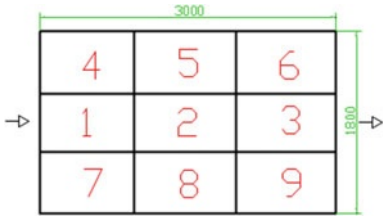

Firstly, the establishment of the mathematical model of the internal smoke dynamic temperature: according to the finished experiment data, and the basic heat and mass transfer formula of thermal fluid combined heat transfer, the ideal hypothesis of energy consumption, etc., we established the dynamic mathematical models of the internal smoke temperature and heat transfer; based on energy conservation and numerical method, simulated the dynamic average smoke temperature of nine parts.

Secondly, establishing the mathematical model of the Kang surface dynamic temperature: according to the basic heat and mass transfer formula of thermal fluid combined heat transfer and solid heat conduction, the ideal hypothesis of energy consumption, etc., based on the above mathematical model of the internal smoke dynamic temperature, we established the nine mathematical model of the Kang surface dynamic temperature, and simulated the dynamic average Kang surface temperature of nine parts.

The mathematical model of the internal flue gas temperature of the heated Kang is [11, 13]:

$$C_p \cdot \nu_\lambda \cdot S_\lambda \cdot \rho \cdot t_1 = C_p \cdot \rho \cdot V \cdot t_2 \tag{53.1}$$

where, Q_1 is the heat in the hearth, J; Q_2 is the flue gas heat of first piece of the Kang, J; C_p is the specific heat of flue gas, J/(kg·k); ν_λ is the average velocity of flue gas entering to the Kang, m/s; S_λ is the entrance area of flue gas from hearth into the Kang, m^2; ρ is the density of smoke, K_g/m^3; t_1 is the hourly temperature of the entrance of flue gas, K; V is the volume of each Kang, m^3; t_2 is the hourly average temperature of each internal Kang, K.

The dynamic mathematical model of the Kang surface temperature is [11, 12]:

$$Q_s = \frac{1}{\frac{1}{\alpha_1} + \frac{\xi_1}{\lambda_1} + \frac{\xi_2}{\lambda_2} + \frac{1}{\alpha_2}} \cdot A \cdot (t_2 - t_s) \cdots Q_s = \frac{\lambda_b}{\xi_b} \cdot (t_2 - t_b) \cdot A \tag{53.2}$$

where, Q_s is the sporadic heat of the smoke, J; α_1 is the compound heat transfer coefficient of flue gas to Kang board, $w/m^2 \cdot k$; α_2 is the convection and radiation heat transfer coefficient of Kang board to indoor air, $w/m^2 \cdot k$; ξ_1, ξ_2 are the thickness of the Kang board, m; λ_1, λ_2 are the thermal conductivity coefficient of Kang board, w/(m·k); A is the area of each Kang board, m^2; t_s is the hourly temperature of indoor air, K; t_b is the Kang surface temperature, K.

53.2.3 The Mathematical Models of the Kang's Thermal Storage and Heat Release

As above assumption, the Kang will be divided into nine uniform parts, at same time we established the thermal storage and heat release mathematical models of each part.

Firstly, established the mathematical model of the Kang thermal storage based on the mathematical models of the internal smoke dynamic temperature and the Kang surface dynamic temperature. It is assumed that the Kang surface temperature of each part is uniform and the initial temperature of each part is a constant value, according to the basic heat and mass transfer formula of thermal fluid combined heat transfer and solid heat conduction, established the mathematical model of the Kang thermal storage and simulated heat storage amount of each part.

Secondly, established the dynamic mathematical model of heat release after the fire ceased. According to the basic heat and mass transfer formula of combined heat transfer of the Kang board with interior fluid and interior wall, accomplished mathematical model of the Kang thermal storage; to the assumed that the Kang surface temperature of each part is uniform, simulated the Kang surface temperature after the fire ceased.

The mathematical model of the Kang thermal storage is [13]:

$$Q_x = C_p \cdot \rho \cdot V \cdot (t_h - t_c) \tag{53.3}$$

where, Q_x is the amount of Kang board's thermal storage, J; C_p is the specific heat of Kang board, J/(kg·k); ρ is the density of Kang board, K_g/m^3; V is the volume of

Kang board, m^3; t_h is the temperature of Kang board after heating, K; t_c is the initial temperature of Kang board, K.

The dynamic mathematical model of heat release is [13]:

$$Q_x - Q_s = C_p \cdot \rho \cdot V \cdot (t_h - t_c) \tag{53.4}$$

where, Q_x is the amount of Kang board's thermal storage, J; Q_s is the hourly dissipating heat of Kang board to indoor air, J; C_p is the specific heat of Kang board, J/(kg·k); ρ is the density of Kang board, K_g/m^3 ; V is the volume of Kang board, m^3; t_h is the temperature of Kang board after heating, K; t_c is the initial temperature of Kang board, K.

53.3 The Simulation Results and Analysis

53.3.1 The Kang Surface Temperature

The Kang surface hourly temperature by VB:

In simulating the Kang surface temperature of each part, we selected three typical Kang surfaces, namely the center of Kang head, the center of Kang middle, and the center of Kang tail, corresponding numbers 1, 2, 3.

The simulation conditions: fuel is corn stalk, flue gas inlet area is 0.16 square meter, flue gas inlet velocity is 1 m/s, the Kang board is divided into two layers, the upper material is cement mortar, the low material is reinforced concrete, their physical property parameters in Table 53.1, the simulative time is cooking in the morning from 7 a.m. to 9 point, and cooking lasts 80 min, to simulate a set of temperature every 2 min, the following figure is the Kang surface temperature corresponded numbers for 1–3 through VB programming language.

The right figure is the Kang surface average temperature corresponded numbers for 1 to 9 through VB programming language.

Figure 53.3 shows that during cooking in the morning, the no. 1 temperature raises from 30 to 60 °C, the no. 2 raises from 15 to 28 °C, and the no. 3 raises from 9 to 14 °C. Figure 53.4 shows the Kang surface average temperature. By the above two figures we can see, the Kang surface temperature distribution is not uniform, the Kang surface temperature distribution emerges downward trend from the Kang head to Kang tail. The study finds that the basic temperature range of

Table 53.1 The physical property parameters of heated Kang

Component	Material	δ(mm)	ρ(kg/m^3)	λ(w/(m·k))	Cp(J/(kg·k))
Kang board	Plaster layer	30	1800	0.698	837
	Reinforced concrete	40	2400	1.547	837
Soil ash layer	Clay	200	1800	0.698	837
Wall	Red brick	60	1668	0.430	754

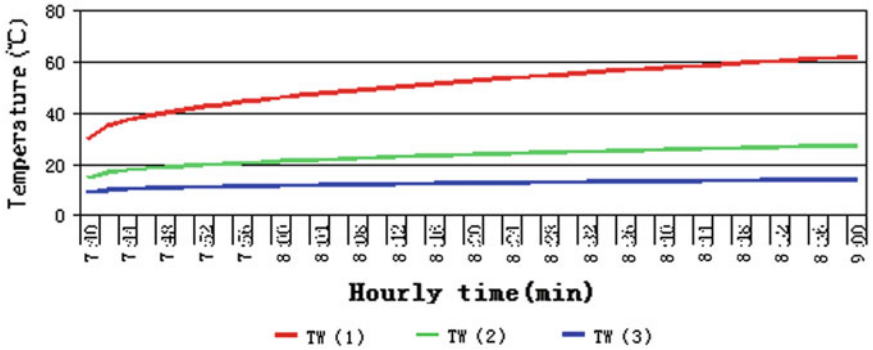

Fig. 53.3 The Kang surface temperature during cooking time TW(1): The temperature of no.1 TW(2): The temperature of no.2 TW(3): The temperature of no.3

comfortable feeling is 30-35 °C. The Kang surface mean temperature from 24 to 35 °C is appropriate [5], so the Kang surface temperature is too high in some places at some time, we should take measures to improve the condition of the Kang surface high temperature.

The simulative results by Fluent:

The boundary condition by Fluent is speed inlet boundary condition, speed is 0.5 m/s, the direction is perpendicular to the plane of entrance, entrance flue gas temperature is 523 k, the flue gas outlet boundary conditions set as free flow. The simulation uses the discrete coordinates radiation model (DO) for radiation heat transfer process [15], the lower right corner is the Kang surface temperature cloud based on the above conditions:

Figure 53.5 shows that when the inlet temperature is 523 k, the center-weighted average temperature of Kang head is 52 °C, the center-weighted average temperature of Kang middle is 30 °C, and the center-weighted average temperature of Kang tail is 14 °C.

The simulative results contrast by Fluent and VB:

The simulative results by VB show that, when the flue gas inlet temperature is 523 k, the center average temperature of Kang head is 43.28 °C, the center average temperature of Kang middle is 21.31 °C, the center average temperature of Kang tail is 11.58 °C, the simulative results by VB are a little different compared to the results through Fluent, because the results through Fluent are in a steady state, but the results through VB are in a instantaneous state, and there are

Fig. 53.4 The Kang surface average temperature (°C)

20.77	11.37	8.68
51.31	23.10	12.26
20.77	11.37	8.68

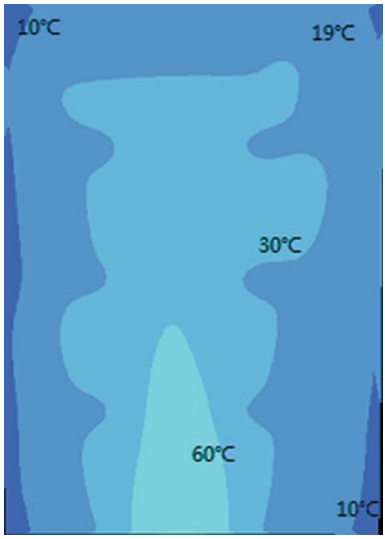

Fig. 53.5 The Kang surface temperature cloud

many factors we will consider in Fluent, but we simplified many factors in VB simulation, so we think the error is in an acceptable range, we believe that the results are comparable.

53.3.2 The Capacity of the Kang Board's Thermal Storage

The heated Kang is divided into nine average pieces, here we choose the center of Kang head, namely the Kang surface of no.1 as the research object, the conditions of simulating are same as the above descriptions, the following figure is the Kang surface hourly temperature of the center of Kang head after the fire ceased.

Figure 53.6 shows that the Kang surface temperature does not immediately fall after the fire ceased, but lasts for a period of time then slow down, and the general sustaining time is 6-10 h, it will be stable when the Kang surface temperature falls a certain temperature, so it also ensures that the thermal comfort of rural buildings.

53.3.3 The Influence of the Flue Gas Inlet Area for the Kang Surface Temperature

The premise conditions are as the same as the above descriptions, here we choose the center of Kang head as the research object, the following figure is the Kang surface temperature of the center of Kang head corresponded the flue gas inlet area are 0.1, 0.13, and 0.16 m^2.

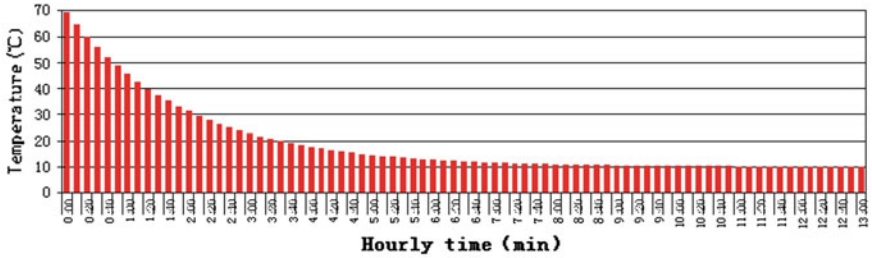

Fig. 53.6 The Kang surface hourly temperature of the center of Kang head after the fire ceased

$$\text{TW11}: \ S = 0.1\,\text{m}^2 \ \text{TW12}: \ S = 0.13\text{m}^2 \ \text{TW13}: S = 0.16\,\text{m}^2$$

Figure 53.7 shows that when the size of the flue gas inlet area changes, the Kang surface temperature also will change at the same time, and the Kang surface temperature gradually raises with the increase of the inlet area, this is because the smoke flux into the heated Kang increases, which enhances heat transfer between the smoke and the Kang board, so the Kang surface temperature raises.

53.3.4 The Influence of the Flue Gas Inlet Area for the Percentage of Heat Amount Transferred to the Room from the Kang

The premise conditions: flue gas inlet velocity is 1.3 m/s, flue gas inlet area are 0.16, 0.20, and 0.25 m^2, the surplus of the conditions are as the same as the above descriptions, the following form is the percentage of heat amount transferred to the room from the Kang under different flue gas inlet area.

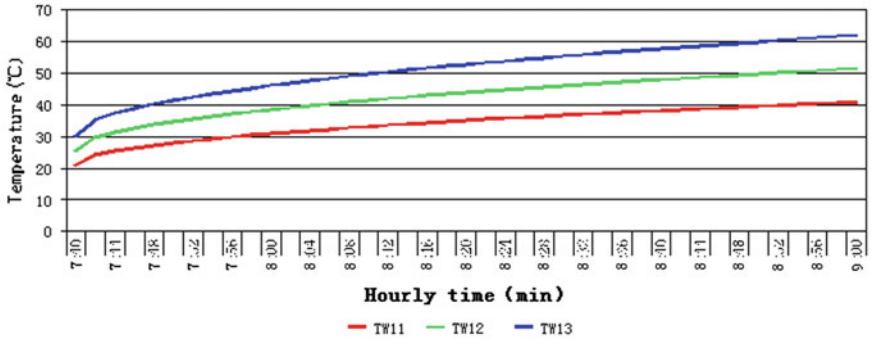

Fig. 53.7 The Kang surface temperature of the center of Kang head under different smoke inlet area

Table 53.2 The percentage of heat amount transferred to the room from the Kang under different flue gas inlet area

Flue gas inlet area (m^2)	The percentage of heat amount transferred to the room from Kang (%)
0.16	22
0.20	34
0.25	54

Table 53.2 shows that when the size of the flue gas inlet area changes, the percentage of heat amount transferred to the room from the Kang will change, and the percentage increases gradually with the increase of the inlet area.

53.4 Conclusions

In this study we can see that the heated Kang surface temperature is not uniform through the simulative results of Kang surface hourly temperature, existing phenomenon is that the temperature of Kang surface closed to the smoke inlet (smoke entering from cooker to the Kang) is too high, so we should take measures to solve the problem of heterogeneous Kang surface temperature. The Kang surface temperature is too high, in order to ensure the comfort of the heated Kang, we need to install the heat exchanger under the Kang head. Because of the capacity of Kang board's thermal storage, the Kang surface temperature will maintain at a certain range during some time after the fire ceased, but the general sustaining time is 6–10 h, so the Kang surface temperature will be very low in the rest of the night, so we need to consider installing auxiliary heat source to improve thermal comfort of rural buildings.

The Kang surface temperature relates to the structure of heated Kang, increasing the smoke inlet area and the input of the flue gas can effectively improve the Kang surface temperature. The percentage of heat amount transferred to the room from the Kang relates to the structure of heated Kang, increasing the smoke inlet area can effectively improve the heat into the indoor, as the same time improve the indoor thermal comfort.

References

1. Yuguo Li, Yang Xu (2006) The scientific questions of northeast rural heated Kang and the present and future of heated Kang. Southeast University Press, Nanjing
2. Zhuang Zhi (2009) The gas flow and heat transfer performance study of Chinese Kang. Faculty of Infrastructure Engineering, Dalian University of Technology Dalian, Dalian
3. Peihong Zhang, Fulong Xia, Jingyu Fu etc. The numerical simulation and analysis aim at the influential factors of heated Kang heating. Journal of Shenyang Jianzhu University (Social Science). 2009, (2): 342-346

4. Zhao Yang, Duan Mulin (2010) Zongshan Wang etc. The experimental study of hot-wall Kang about the heat transfer characteristics and internal flue gas flow characteristic. Building Science 26(4):17–26
5. Yang Zhao, Mulin Duan, Zongshan Wang etc. The experimental study of hot-wall Kang thermal performance. Building Science, 2010, 26 (the): 29-36
6. Xiangxiang Gao. The study of north rural traditional heating way and the indoor thermal environment. Xi'an: Department of architecture of Xi'an University of Architecture and Technology, 2010
7. Junliang Zhu, Zongshan Wang, Mulin Duan etc. The experimental study of hot-wall Kang structure improvement. Building Science, 2011, 2
8. Dan Wang, Zhi Xucong, Guiwen Li, Hongbin Cai. The simulation technology of improving the heated Kang surface temperature distribution. Journal of Harbin Industrial University, 2012, 44 (4)
9. Zhi Zhuang, Yuguo Li, Bin Chen. Thermal storage performance analysis on Chinese Kang. Building and Environment. In Press, Corrected Proof, Available online 18 November 2008
10. Hong Jin, Hua Zhao, Xiuping Wang. The winter indoor thermal comfort environment study of cold region rural house. Journal of Harbin Institute of Technology, 2006, (12)
11. Zhang Ximin, Ren Zepei (2001) Heat Transfer. China Architecture & Building Press, Beijing
12. Feng Junkai, Shen Youting, Yang Ruichang (2003) Principles of Boiler and Calculation. Science Press, Beijing
13. Wang Buxuan (1998) Engineering Heat and Mass Transfer. Science Press, Beijing
14. Bingwen Liu. Visual Basic Programming Tutorial (third edition) Beijing: Tsinghua University Press, 2006
15. Han Zhanzhong, Wang Jing, Lan Xiaoping (2005) Fluent Fluid Engineering Simulation Instance and Application. Beijing Institute Of Press, Beijing

Chapter 54
Comparison of the Distribution and Concentration of Dust Particles by Different Ventilated Systems

Yang Lv, Bailin Fu, Genta Kurihara and Hiroshi Yoshino

Abstract Dust particles include mold spores or excrement and corpses of the mite and so on. There is a high possibility of allergic reactions in child whose breathing zone is near the floor. Ventilation is one of the best ways to remove dust particles. It is important to know the removal efficiency of dust particles in different ventilation strategies room. In this study, two kinds of ventilation strategies were considered, namely ceiling exhaust and slit exhaust. In the experiments, comparison of the number of particle shows that the ceiling exhaust was a little higher than the slit exhaust. Computational fluid dynamics (CFD) simulations concerning diffusion fields completed. In the simulations, the removal efficiencies of ceiling exhaust and slit exhaust were found 81.5 and 85.8 %, respectively. From the data we concluded that slit exhaust ventilation strategy will produce less dust particles comparing with ceiling exhaust ventilation strategy in room.

Keywords Dust particles · Ventilation strategy · Measurement · CFD

54.1 Introduction

In recent years, the levels of air tightness and insulation of residential houses are becoming better for energy saving, and hence living comfort has been improved. However, the problem of dust particles, due to the lack of ventilation rate, has become increasingly serious. Dust particles include mold spores or excrement and

Y. Lv (✉) · B. Fu
Lab of Building Evironment and New Energy Resource, School of Civil Engineering, Dalian University of Technology, Dalian, China
e-mail: lvyang20022002@yahoo.com.cn

G. Kurihara · H. Yoshino
Department of Architecture and Building Science, Tohoku University, Sendai 9808579, Japan

A. Li et al. (eds.), *Proceedings of the 8th International Symposium on Heating, Ventilation and Air Conditioning*, Lecture Notes in Electrical Engineering 262,
DOI: 10.1007/978-3-642-39581-9_54,

corpses of the mite and so on, which are the cause of allergy, asthma, and unspecific hypersensitivities [1, 2]. Ventilation is one of the best ways to remove dust particles, it is important to know the removal efficiency of dust particles in different ventilation strategies room. In recent years, a number of numerical simulation studies using computational fluid dynamics (CFD) predicted dust particles distribution and deposition. Murakami et al. [3] found that numerical simulation seems to be very useful method for predicting air velocity and contaminant distribution in clean rooms. Bouilly et al. [4] carried out both numerical simulations and measurements to study the particle decay rates with three different ventilation modes using the Lagrangian formulation. Zhao et al. [5] compared the spatial distribution of particles with four different ventilation modes. A 3D drift-flux model for particle movements in turbulent indoor airflows combining with the Eulerian approaches was developed by Gao and Niu [6]. However, research studies that focus on the removal efficiency of dust particles by ventilation strategies which is still lacking.

The purpose of this study is to clarify the removal effect of the dust particles for the various ventilation strategies by experiments and CFD-based simulations.

54.2 Experiment

The different ventilation strategies room (L × W × H = 5.37 m × 2.74 m × 2.25 m) is on the second floor of experimental house which is located at Tohoku University, Japan. The window is sheltered to prevent solar radiation, and the walls are insulated by expanded polystyrene board, room volume is 27.0 m^3. Two mechanical ventilation strategies were considered in this construction. As shown in Fig. 54.1, for case 1, inlet and outlet are located at the ceiling (ceiling exhaust). It can be considered as a representative ventilation strategy in Japan currently.

For case 2, inlet is located at the center of ceiling as case 1, but considering the dust particles are usually falling on the floor, exhaust slit is set at the corner between wall and floor (slit exhaust). Figure 54.2 shows slit exhaust ventilation strategy structure, dust particles were exhausted out of room through exhaust slit over in-wall ventilation.

Table 54.1 shows the experimental conditions. In this study, riboflavin particles were used as dust particles. Figure 54.3 shows dispersal devices and measurement points for riboflavin particles. 3D ultrasonic anemometer (CLIMATEC, CYG-81000) was used for measuring airflow directions and velocities. The riboflavin particles were put in a measuring flask, N_2 was blown into the measuring flask to disperse the riboflavin particles. The positions of the monitoring points were set in the center of a quarter of the room and set at 1.0 m height. Additionally, for case 2, the airflow velocity of exhaust slit was measured at 6 points using a thermistor anemometer (F6204E, SHIBAFU electron).

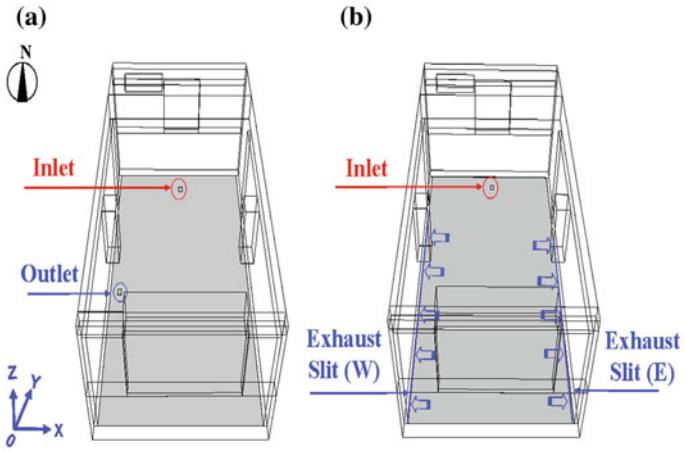

Fig. 54.1 Different ventilation strategies room, **a** Case 1 (ceiling exhaust) **b** Case 2 (slit exhaust)

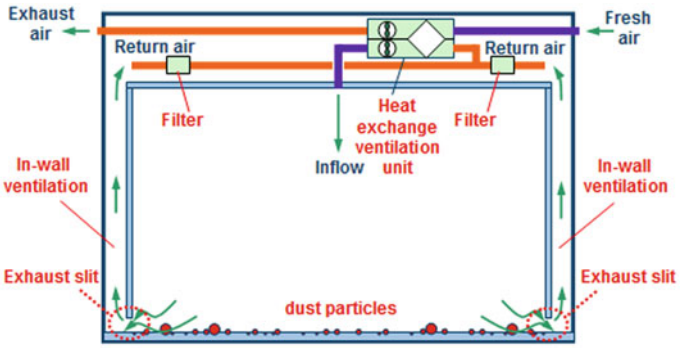

Fig. 54.2 The slit exhaust ventilation strategy structure

Table 54.1 Experimental condition

Case	Air change rate (ach)	Inlet velocity (m/s)	Outlet velocity (m/s)	Temperature (°C)			Height of slits (m)
				Indoor	Outdoor	Supply	
Case 1	2.5	3.34	3.8	19.69	3.84	21.59	–
Case 2			0.5	18.95	2.55	22.37	0.005

The experimental procedure was determined as Fig. 54.4: in the first 1 h, the riboflavin particle was dispersed, and during the following 8 h the particle fell on the ground freely, and for the last 15 h, ventilation system was started.

The above-mentioned different ventilation strategies room was modeled by CFD. Commercial CFD software Flow Designer was used (http://www.akl.co.jp/). The calculation period was about 1 h, and the time-step was 1 s. For indoor and

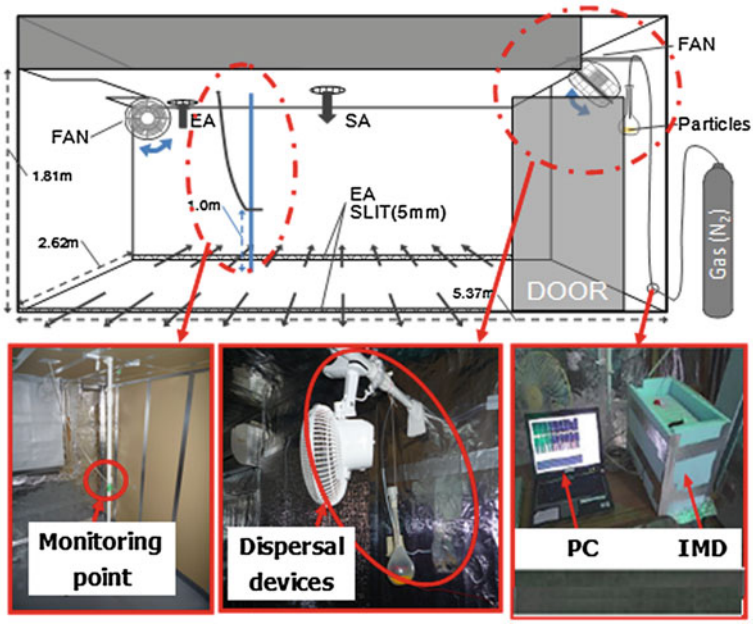

Fig. 54.3 Dispersal devices and measurement points

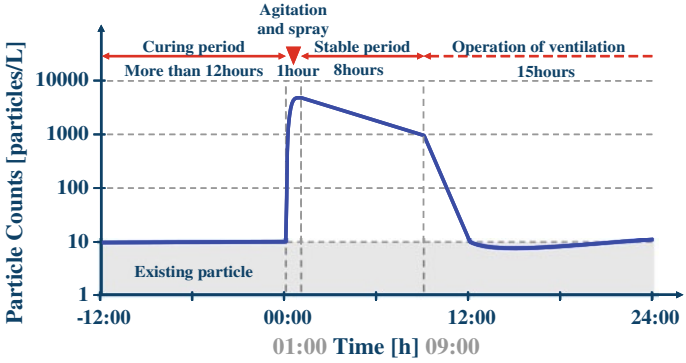

Fig. 54.4 The schedule of particles experiment

outdoor air temperatures and velocities, measured values were used. For case 2, the measured averaged velocities in slit were 0.5 m/s, and there was no significant difference among the 6 points. Table 54.2 gives the calculation conditions.

Table 54.2 Calculation conditions

CFD software	Flow Designer	
Turbulence model	The standard k–ε model	
Amount of meshes	About 200,000	
Solution	Improved SIMPLE method	
Boundary conditions	Generalized logarithmic law	
	Floor and east wall: heat-insulated	
	Ceiling and other walls:	
	heat fluxes measured in experiment	
Inflow and outflow	Inflow	Velocity and temperature based on experiment (constant)
		$k_{in} = 3/2(I \cdot U_{in})^2$
		I: Turbulence intensity (=0.05), U_{in}: Inflow velocity (m/s)
		$\varepsilon_{in} = C_\mu k_{in}^{3/4}/l_{in}$ $C_\mu = 0.09$ l_{in}: Turbulent length scale (m)
	Outflow	Velocity (constant)

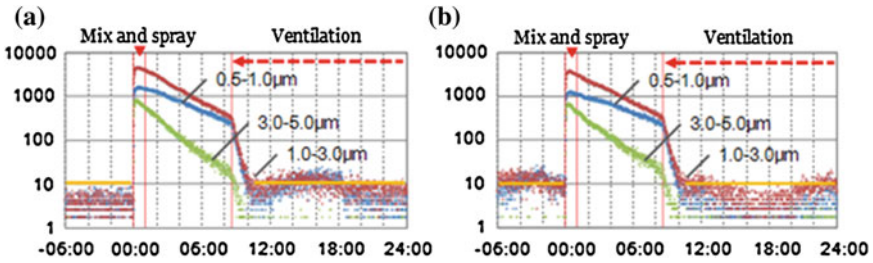

Fig. 54.5 Experiment results of particles, **a** Case 1 (ceiling exhaust) **b** Case 2 (slit exhaust)

54.3 Results

The experiment results of case 1 and case 2 were shown in Fig. 54.5. For the two cases, different sizes of indoor particles showed smooth decay curve due to the influence of gravity before ventilation system operating. After ventilation system is operated, the decay rate of the particles becomes faster than that before the ventilation system is on. After ventilation system is operated, the decay rate of the particles becomes faster than that before the ventilation system is on. After 15 h of ventilation system operation, the number of particles for all sizes decreased to the same level as background. The number of particles in the case 1 (ceiling exhaust) was a little higher than that in the case 2 (slit exhaust) after particle decreased to the same level as background.

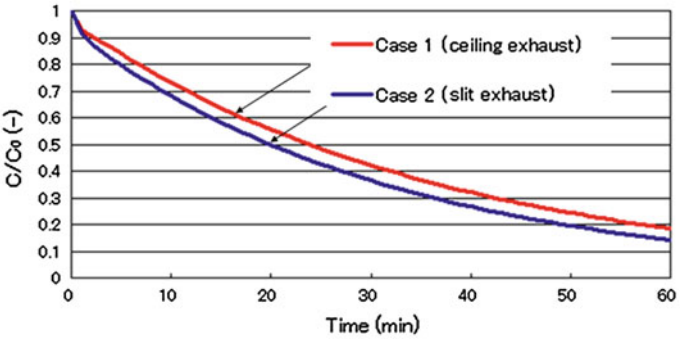

Fig. 54.6 Comparison of the concentration of dust particles within the whole room

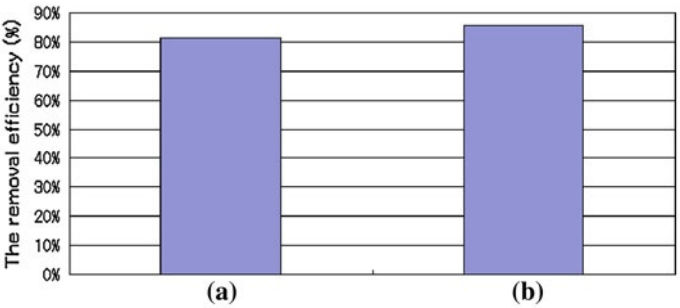

Fig. 54.7 The removal efficiency of dust particles, **a** Case 1 (ceiling exhaust) **b** Case 2 (slit exhaust)

54.4 Discussion

Figure 54.6 compares the time variation of the volume-average concentrations within the whole room. It is seen that the volume-average concentrations of dust particles within the whole room decrease gradually. Based on these results, a conclusion is drawn that, the volume-average concentration of dust particles within the whole room is lower in case 2 (slit exhaust) than that of case 1 (ceiling exhaust). Figure 54.7 compares the removal efficiencies after 1 h. The removal efficiency is defined as Eq. 54.1. The removal efficiencies of case 1 (ceiling exhaust) and case 2 (slit exhaust) are 81.5 and 85.8 %, respectively. From the data, we concluded that slit exhaust ventilation strategy will produce less dust particles comparing with ceiling exhaust ventilation strategy. But, the impact of an ACH 2.5 with larger wind combined with the size of particle on the distribution of house dust is not obvious.

$$\eta = \frac{C_0 - C_{60}}{C_0} \times 100\ \% \tag{54.1}$$

where

η: Removal efficiency (%),

C_0: Initial volume-average concentration of dust particles in the room (kg/m^3),

C_{60}: The volume-average concentration of dust particles in the room after 1 h (kg/m^3)

54.5 Conclusions

This paper clarifies the removal efficiencies of dust particles by different ventilation strategies (ceiling exhaust and slit exhaust) in room. The following conclusions have been drawn from the present study:

Two kinds of ventilation strategies in room were considered, namely ceiling exhaust and slit exhaust. In the experiments, comparison of the number of particle shows that the ceiling exhaust was a little higher than the slit exhaust ventilation strategy.

CFD simulations concerning diffusion fields have been completed. The removal efficiencies of ceiling exhaust and slit exhaust were found 81.5 and 85.8 %, respectively. From the data we concluded that slit exhaust ventilation strategy will produce less dust particles comparing with ceiling exhaust ventilation strategy in room.

Acknowledgments This research is supported by Ministry of Land, Infrastructure, Transport and Tourism of Japan, the 12th 5-Year National Technology Key Project (2012BAJ02B05) ,the National Nature Science Foundation of China (51308088), the SRFDP (20120041120003), the Liaoning Provincial Scientific Research Foundation (20111027), the Liaoning Provincial Science and Technology Fund projects, the Dalian Science and Technology Fund projects.

References

1. Zureik M, Neukirch C, Leynaert B, Liard R (2002) Sensitisation to airborne moulds and severity of asthma: cross sectional study from European Community respiratory health survey. BMJ 325:411
2. Elliott L, Arbes SJ, Harvey ES, Lee RC, Salo PM, Cohn RD, London SJ, Zeldin DC (2007) Dust weight and asthma prevalence in the national survey of lead and allergens in housing (NSLAH). Environ Health Perspect 115:215–220
3. Murakami S, Kato S, Nagano S, Tanaka Y (1992) Diffusion characteristics of airborne particles with gravitational settling in a convection-dominant indoor flow field. ASHRAE Trans 98:82–97

4. Bouilly J, Limam K, Beghein C, Allard F (2005) Effect of ventilation strategies on particle decay rates indoors: an experimental and modeling study. Atmos Environ 39:4885–4892
5. Zhao B, Wu J (2009) Effect of particle spatial distribution on particle deposition in ventilation rooms. J Hazard Mater 170:449–456
6. Gao N, Niu JL (2007) Modeling particle dispersion and deposition in indoor environments. Atmos Environ 41:3862–3876

Chapter 55
Research and Apply on DCS Based Water-Source Heat Pump System

Pengfei Si, Xiangyang Rong, Angui Li, Xiaodan Min and Zhengwu Yang

Abstract District cooling technology is advantageous in warm and hot climatic regions, in that chilled water from a central refrigeration plant is delivered through a distribution network to groups of buildings in an urban district. At a central refrigeration plant, chilled water is generated and supplied to a district to support the air-conditioning systems in buildings. Because of the large scale production, the chiller plant is higher in efficiency than those in individual buildings. Therefore, district-cooling system (DCS) has been applied in a number of countries. In the paper, the technical requirements and the cooling scheme options in the context of the urban environment are discussed. A government-commissioned feasibility study of a proposed district cooling site in Chong Qing is then described. The Results indicate that, firstly the technology is most suitable for new urban developments where system design and construction receive much freedom; secondly the areas, which near a river, are ideal sites for the application of water-source heat pump technology (WHP) to provide district cooling and heating; lastly a large number of benefits, such as economic benefit and environment economic, will be obtained in this project.

Keywords District cooling system · Water-source heat pump · HVAC

P. Si (✉) · X. Rong · X. Min · Z. Yang
China Southwest Architectural Design and Research Institute Corporation Limited, Chengdu, 610041 Sichuan, China
e-mail: 175987342@163.com

P. Si · A. Li
School of Environmental and Municipal Engineering, Xi'an University of Architecture and Technology, Xi'an, 710055 Shaanxi, China

A. Li et al. (eds.), *Proceedings of the 8th International Symposium on Heating, Ventilation and Air Conditioning*, Lecture Notes in Electrical Engineering 262,
DOI: 10.1007/978-3-642-39581-9_55,

55.1 Introduction

District cooling technology is advantageous in warm and hot climatic regions, in that chilled water from a central refrigeration plant is delivered through a distribution network to groups of buildings in an urban district. At a central refrigeration plant, chilled water is generated and supplied to a district to support the air-conditioning systems in buildings. Because of the large scale production, the chiller plant is higher in efficiency than those in individual buildings. Therefore, district-cooling system (DCS) has been applied in a number of countries.

However, because of the expected considerable investment and lengthy payback period, well-planned and optimized system design and operation are crucial areas leading to the success of the implementation. In the paper, the technical requirements and the cooling scheme options in the context of the urban environment are discussed.

55.2 DCS Based Water-Source Heat Pump System Technology

55.2.1 Basic Operation Principle

A district-cooling system (DCS) is a sustainable means of cooling energy distribution through mass production [1]. A cooling medium like chilled water is generated at a central refrigeration plant and supplied to a site area comprising multiple buildings, through a closed-loop piping network. From each connection point of the distribution mains, a controlled flow of the coolant is delivered to the air-conditioning equipment of the user buildings to handle their space-cooling demands. The DCS chiller plant is higher in efficiency than the conventional chiller plants at individual buildings. The tri-generation air conditioning process schematic in winter and summer are shown in Fig. 55.1.

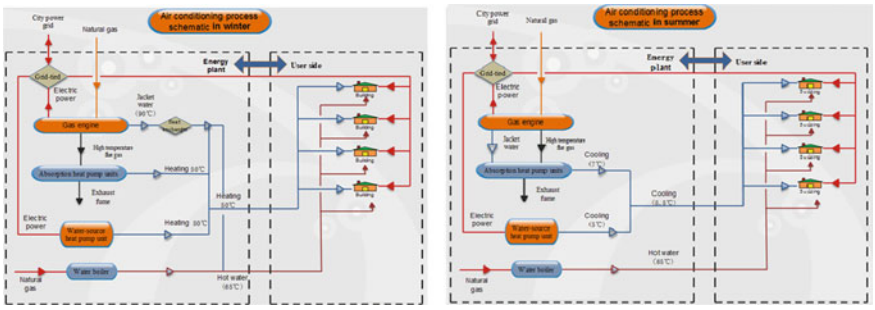

Fig. 55.1 The tri-generation air conditioning process schematic in winter and summer

55.2.2 System Configurations and Design Considerations

Many aspects of main components are similar to air conditioning, such as distribution piping system. However, DCS technology based water-source heat pump system has some special details which are different from traditional air conditioning [2].

1. Heat pump capacity selection: DCS technology based water-source heat pump system is generally higher in initial investment and lower in operation costs than conventional system based on the experience of operated projects. So, it is important to utilize the heat pump as many hours as possible to have a better return on the investment cost. Heat pumps are therefore considered typical base load production units. In general, supplemental boilers or chillers are needed. In order to maximize its benefits to a new urban development, an optimized scheme for selecting the capacity of heat pumps and auxiliary equipments should be adopted.
2. Distribution network design: Different from district heating, district cooling in summer and district heating in winter use the same distribution network in China. For the difference of supply/return temperature in summer and winter and the difference of heating and cooling demand, pipeline diameter and thermal insulation should be carefully considered to find an optimal design.

55.3 Feasibility Study

55.3.1 The DAN-ZISHI Project

The DAN-ZISHI project will provide 14 land development, through several phases of development. The total gross floor-area (GFA) will amount to approximately 1.3 million m^2. This study, started from 2008, was led by Chong Qing Urban and Rural Construction Committee. The study was to assess the feasible using of DCS system for the project. In order to estimate the required DCS plant size, comprehensive information on the site layout was gathered and surveys were taken.

55.3.2 The Hydrological Characteristics

55.3.2.1 River Water Temperature Characteristics

River water temperature characteristics of different hydrometric stations (ChunTan hydrometric station and BeiBei hydrometric station) between 2008 and 2009 were shown in Fig. 55.2. The two hydrometric station are near the project. From the

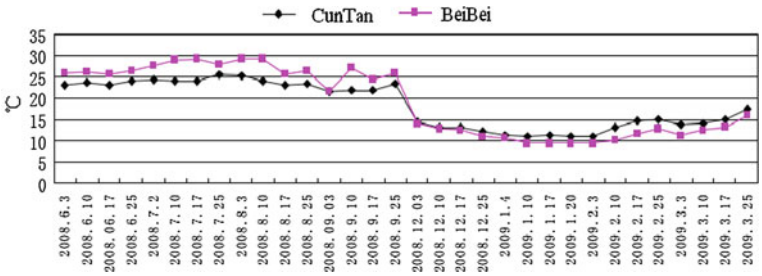

Fig. 55.2 The tri-generation air conditioning process schematic in winter and summer

Fig. 55.2, we can see that no matter in summer or winter temperature is appropriate. Therefore, good energy saving benefit will be obtained by the use of river water source heat pump system.

55.3.2.2 River Water Level and Flow

Detailed water level and water flow material were research in the feasibility study period. The result indicated that: firstly water flow is about 44,100 m^3/s in most of the time; secondly more than 97 % of the time, low water level is about 158 m. Water is abundant, and the water level appropriate.

55.3.3 Load Estimation

A total load of eight categories of building types based on functions were established, as in Table 55.1. It can be seen that the peak cooling-load and heating-load demand of the entire district were found to be 64.2 and 18.2 MW respectively.

Table 55.1 A total load of eight categories of building types

Function	Cold load		Heating load	
	(kW)	ratio (%)	(kW)	ratio (%)
Office	33,020	36	15,850	38
Finance	7,068	8	3,625	9
Hotel	5,702	6	3,283	8
Apartment	4,490	5	2,872	7
Exhibition	5,068	6	2,432	6
Business	18,430	20	7,781	19
Entertainment	8,533	9	2,713	7
Repast	4,071	4	1,550	4
Others	5,423	6	1,550	4
Coincidence factor	0.7		0.8	33,325
Total	64,263	100	1,817	100

55.3.4 Scheme Design

55.3.4.1 Energy Plant Design

The following problems should be pay attention to when choice the position of energy station and heat transfer station. (i) As far as possible close to the load center; reduce the cold and hot water pipeline network length; reduce air conditioning circulating water and living hot water transport energy consumption. (ii) Give attention to river water source heat pump system application; reduce energy consumption; considering the condition of water inlet. (iii) Meet the needs of the construction of the regional stage.

55.3.4.2 Cold and Hot Medium Parameters

In summer, the supply water temperature of Water source heat pump system is 5 °C, the supply water temperature of Absorption heat pump system is 7 °C, the supply water temperature of mixed water is 5.5 °C; the return water temperature is 13 °C, and the temperature difference between supply water and return water is 7.5 °C. In winter, the supply water temperature of Waste heat system is 60 °C, the supply water temperature of Water source heat pump system is 45 °C, the supply water temperature of mixed water is 47 °C; the return water temperature is 39 °C, and the temperature difference between supply water and return water is 8 °C.

55.3.5 The Analysis of Economic

55.3.5.1 Initial Investment

At present, the most common form of central air conditioning in ChongQin is the buildings independently install air conditioning system which uses water chilling units as its cold source that based on open cooling tower use for cooling device. It also use gas of atmospheric pressure hot water unit as its hot source of air conditioning system and heating water. So in this paper, we use the most common form air conditioning system (Referred to as scheme 1) as the comparison scheme. The cold and hot source scheme initial investment cost is shown in Table 55.2.

From the result of calculation, we can find that the initial investment of composite system which includes Combined Cooling Heat and Power system and River water source heat pump system far more than the common air conditioning system. The increased cost mainly includes gas diesel generator investment and water supply projects investment, the two parts of the whole tri-generation system about 28 % of the investment.

Table 55.2 The cold and hot source scheme initial investment cost summary

Cost (10,000 yuan)	Scheme 1	Scheme 2
Cost of main device	6,902	10,402
Cost of enlarge energy scale	1,420	2,658
Control system	1,000	1,500
Others	6,700	11,833
Total	16,022	26,393

55.3.5.2 Operation Cost

The scheme 2 in operation cost far less than scheme 1, this paper analyzes the two scheme's cost structure, find that the reasons as follow: the first one is energy station power consumption than scheme 1 reduced greatly, this is due to use the district cooling heating and the energy station focus Settings, it results to air conditioning cold/heat source install capacity is reduced, and it also can adjust the total installed capacity according to the whole area of the load case, a single host can use can effect comparing high large capacity equipment, together with the river water unit, cooling season most of the time condenser side of the inlet water temperature at 25–27 °C range, and cooling tower as the heat source of the conventional system of water cooling water temperature is usually is 33–35 °C, so host can greatly higher than conventional system; Moreover the flue gas hot water complex absorption unit, make full use of the generator of the waste heat, further improve the energy efficiency. The second is to use natural gas power generation, power generation efficiency is high according to the current chongqing gas prices, each hair kilowatt-hour cost about 0.54 yuan, and mains sales price is 0.828 yuan/kWh, reduce the cost of the power of the area. But those who need a specification is, because the cause of the phased implementation, thermal balance is not necessarily can achieve the ideal state. But to give consideration to the phased implementation, comprehensive consideration of the construction cost, the investment in equipment usually slightly large, so the project income will be lower than the 8,00,000 m^2 after completion of the income. At the same time in installment construction process, the progress of the late engineering degree will also affect the use of early, so in the later unfinished project before the operation of the system efficiency is not necessarily can achieve this report of the results of the study (Table 55.3).

Table 55.3 The cost of each scheme (10,000 yuan/a)

	Scheme 1	Scheme 2
Cost of operation	10,482	7,837
Cost of investment	1,600	2,557
Cost of maintenance	260	395
One year's total cost	12,342	10,789
Cost increasing rate	-	−12.6 %

55.4 Conclusions

The results indicate that first the technology is most suitable for new urban developments, where system design and construction receive much freedom; second the areas, which near a river, are ideal sites for the application of water-source heat pump technology (WHP) to provide district cooling and heating; lastly a large number of benefits, such as economic benefit and environment economic, will be obtained in this project.

References

1. Chow TT, Au WH, Yau R (2004) Applying district-cooling technology in Hong Kong. Appl Energy 79:275–289
2. Zhen Li, Lin DM, Shu HW (2007) District cooling and heating with seawater as heat source and sink in Dalian, China. Renewable Energy 32:2603–2626

Chapter 56
Waste Heat Recovery System Using Coal-Fired Boiler Flue Gas to Heat Heating Network Return Water

Hua Zhao, Pengfei Dai, Shanshan Cao and Qing Hao

Abstract At present, exhaust flue gas temperature of coal-fired boiler is generally above 120 °C, while the temperature of boiler burning high sulfur coal may be higher in China. Meanwhile, the boiler burns large amount of fuel to heat the heating network return water to the supply temperature. A specially designed waste heat recovery system, which can reduce exhaust flue gas temperature to 60–70 °C and recycle large amount of sheat and latent heat in the flue gas to heat the return water, is designed. This paper included three parts. In the first part, the return water temperature duration in the heating season of 99, 64, 29 MW boilers which are three typically used in Harbin are calculated. The feasibility of the system is verified with the results that the return water temperature kept lower than 55 °C for a long period of time. In the second part, the system implementation plan including the material of heat transfer equipment and the choice of heat pump concerned are discussed. The titanium alloy plate heat exchanger and first absorption heat pump are selected. Then thermodynamic and hydraulic calculations of the system are done to determine the amount of flue gas heat recovery, structure of water spray chamber, plate heat exchangers, and absorption heat pump design. In the third part, the dynamic payback periods of waste heat recovery system used in these three boilers are calculated and the results are less than the life cycle of the heat recovery system.

H. Zhao · S. Cao (✉) · Q. Hao
School of Municipal and Environmental Engineering, Harbin Institute of Technology, 150090 Harbin, China
e-mail: css_2005@126.com

H. Zhao
e-mail: zhaohua_hit@sina.com

P. Dai
China Aviation Planning and Construction Development Co. Ltd, Beijing 100120, China

A. Li et al. (eds.), *Proceedings of the 8th International Symposium on Heating, Ventilation and Air Conditioning*, Lecture Notes in Electrical Engineering 262,
DOI: 10.1007/978-3-642-39581-9_56,

Keywords Exhaust gas temperature · Coal-fired boilers · Waste heat recovery · Heating network return water · Water spray chambers · Plate heat exchanger · Absorption heat pump

56.1 Introduction

Because of coal-fired boiler flue gas heat recovery equipment has low temperature dew point corrosion problem, exhaust flue gas temperature of coal-fired boiler is generally above 120 °C [1] while the temperature of boiler burning high sulfur coal may be higher in China. Researchers did much work to reduce flue gas temperature. Yang et al. (2012) designed low-temperature gas waste heat recovery system by heat pipe technology and did economic analysis [2]. Li et al. (2009) designed associated heating system of solar energy and boiler afterheat [3]. Hu and Yue (2012) found that low pressure economizer was able to reduce exhaust flue gas temperature and coal consumption [4].

Exhaust flue gas temperature is so high that there is still large quantity of sensible latent heat left unused. Under this circumstance, author designed a heat recovery system which used the flue gas to heat heating system return water.

56.2 Feasibility Analysis of Coal-Fired Boilers' Flue Gas Heat Heating System Backwater

Quality regulation is most commonly used in China. According to the statistics of Xi'an in recent years, return water temperature lasts lower than 55 °C for about half time of each heating season in district heating systems with the supply and return water temperature of 95/70 °C [2].

When heating systems use quality regulation, the calculation formulas of supply and return water temperature are (56.1) and (56.2).

$$\tau_g = t_g = t_n + 0.5(t'_g + t'_h - 2t_n)\overline{Q}^{1/(1+b)} + 0.5(t'_g - t'_h)\overline{Q} \tag{56.1}$$

$$\tau_h = t_h = t_n + 0.5(t'_g + t'_h - 2t_n)\overline{Q}^{1/(1+b)} - 0.5(t'_g - t'_h)\overline{Q} \tag{56.2}$$

$$\overline{Q} = \frac{t_n - t_w}{t_n - t'_w} \tag{56.3}$$

where t_g and t_h separately represent supply and return water temperature when outdoor temperature is t_w, t'_g, and t'_h separately represent supply and return water temperature when outdoor temperature is t'_w, $\overline{Q}$ is relatively heat load ratio, b is

radiator coefficient, t_n is design indoor temperature, t_w is outdoor temperature, t'_w is outdoor calculated temperature of heating.

The return water temperature and their duration with quality adjustment are analyzed.

t'_w in Harbin is known as −26 °C, t_n is known as 18 °C, and the three boilers t'_g and t'_h are all 150/90 °C. Then according to (56.1, 56.2), the supply and return water temperature in corresponding to different outdoor temperature can be calculated. According to weather datas of Harbin and (56.3), duration corresponding to different Relative heat load ratios can be obtained. The results are shown in Table 56.1.

$\overline{Q}$ is 0.48 when heating system return water temperature is about 61 °C and duration is about 130 days. Total days of heating season are 179 days in Harbin. So the last time of heating system return water temperature below 60 °C is 49 days.

According to the analysis, it is feasible to design a certain system which uses boiler exhaust flue gas to heat heating network backwater. In the case of low return water temperature, the system can take full advantage of the exhaust flue gas waste heat to raise the return water temperature in order to reduce the amount of coal and save energy.

Table 56.1 Supply and return water temperature corresponding to different outdoor temperature of 150/90 °C heating system with quality regulation

t_w(°C)	t_g (°C)	t_h(°C)	$\bar{Q}$	N(d)
5	66.8	49.1	0.3	179
3	72.8	52.4	0.34	164
0	81.6	57	0.41	145.1
−2	87.3	60	0.45	133.3
−4	92.9	62.9	0.5	123.3
−6	98.4	65.6	0.55	113.6
−8	103.8	68.3	0.59	104.5
−10	109.1	71	0.64	94.5
−12	114.4	73.5	0.68	83.2
−14	119.7	76	0.73	70.4
−16	124.8	78.5	0.77	55.5
−18	130	80.9	0.82	41.6
−20	135	83.2	0.86	28.4
−22	140.1	85.5	0.91	16.2
−24	145.1	87.8	0.95	8.3
−26	150	90	1	3.4

56.3 Introduction and Heat Gain of Coal Burned Boilers' Gas Flue Heat Recovery System

56.3.1 System Introduction

The system using coal-buren boiler exhaust flue gas to heat heating system return water designed in this paper is shown in Fig. 56.1. In this system, the flue gas passes through 1, 2, a short duct, 3, 5 successively and then releases into the atmosphere.

Heat recovery process is divided into two parts. In the first part, water is pumped by 9, through 6 and 11, get to 3 to exchange heat with the flue gas. There is not much spray water deposit in the spray chamber. As a certain slope existed in the first spraying chamber, water flow by gravity to 7 where impurities are removed. The first water spray chamber at the same time acts as the role of dust removal and desulfurization. The backwater is heated by 6 and then fed back to the boiler. In the second part, water is pumped by 10, through 8 and 11, get to 3. As gas temperature is reduced after the first spray heat exchanger, the water temperature in 3 will not be very high. The circulating water temperature of the second paragraph is below the dew point of water vapor in the flue gas, a large number of latent heat can be obtained. Heating network backwater is heated by 8 whose low-temperature heat source is the water gained in the second paragraph and then fed back to the boiler. The quantity of heating system backwater into the plate heat exchanger or heat pump system control should be controlled by the valve based on actual situation.

Where 1 is dust collector, 2 is the first spray chamber, 3 is the second spray chamber, 4 is exhaust pipe, 5 is eliminator, 6 is plate heat exchangers, 7 is

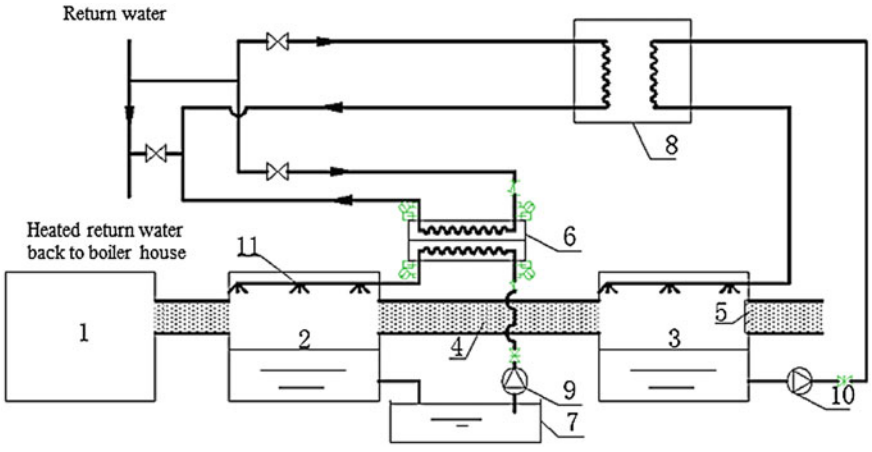

Fig. 56.1 Schematic of coal-fired boiler's flue gas heat recovery system

Table 56.2 Operation parameters of the three different boilers under the worst condition

Project		SHW99-1.6/150/90-H	SHW64-1.6/150/90-H	SHW29-1.25/130/70-H
Coal type		Lignite	Lignite	Lignite
Exhaust gas temperature		156 °C	165 °C	158 °C
Total amount of smoke (under exhaust gas temperature)		301526 m^3/h	227586 m^3/h	107273 m^3/h
Dust content		-	-	-
Amount of coal		$M_1 = 30\ 431.5$ kg/h	$M_2 = 19\ 818.8$ kg/h	$M_3 = 9\ 034$ kg/h
Flue gas composition	Actual flue gas volume	6.8536 Nm^3/kg	6.8536 Nm^3/kg	8.1311 Nm^3/kg
	RO_2 Volume fraction	0.0982	0.0982	0.0993
	H_2O Volume fraction	0.1204	0.1204	0.1089

sedimentation pool, 8 is heat pump system, 9 and 10 are both circulating pump, 11 is stainless steel nozzles, 12 is evaporator, 13 is absorber, 14 is generation, 15 is condenser, 16 is throttle valve, 17 is solution valve, 18 is working fluid pump, 19 is solution pump, and 20 is solution heat exchanger.

56.3.2 Heat Gain of Heat Recovery System

In the flue gas heat recovery system, flue gas contacts with water directly and force spray heat exchange happened which is complex heat and mass transfer process. In this article, the recovery heat quantity of spray chamber is obtained by calculating the difference between the enthalpy of the flue gas at different temperatures.

In this paper, three typical boilers fed by brown coal are chosen for example in Harbin, which are 99, 64, and 29 MW boiler. The three boilers operation parameters are shown in Table 56.2.

The process of heat exchange in the heat recovery system is divided into two sections. The gas flue temperature is expected to reduce from 130 to 100°C in the first spray chamber and then to 60–70 °C in the second one. In this paper, it is assumed that the flue gas temperature is reduced to 100 °C in the first paragraph, to 60 °C in the second one when the heat gain calculation is done. Excess air ratio is assumed as 1.6. The results of heat gain calculation are shown in Table 56.3.

Table 56.3 Heat gain of spray chamber

Boiler type (MW)	Heat gain (kW)	
	First paragraph	Second paragraph
99	4216	2971
64	3188	1953
29	1448	984

56.4 Equipment Selection Analysis and Calculations of Heat Exchange System

56.4.1 Design of Plate Heat Exchangers

Plate heat exchangers and evaporator of heat pump system in this paper both contact with the recycled water which exchanged heat with the gas flue directly. As there are still little impurities and sulfide left after the flue gas go through the dust collector and the sulfide would react with water to generate sulfate, acid corrosion should be taken into account. Given that titanium and titanium alloy are highly corrosion resistant and have long service life, titanium alloy are chosen as materials of heat exchangers in this article.

Take design of 99 MW boiler's plate heat exchanger for example. Known conditions are that heat exchanging quantity without considering heat loss. Inlet and outlet temperature of high temperature water obtained by the water exchanging heat with the flue gas side (which is called hot side of plate heat exchanger below) are 80, 70 °C. Inlet temperature of return water side (which is called cool side below) is 55 °C. Outlet temperature of cool side can be calculated according to energy conservation law.

$$Q_1 = cM_c(t_{co} - t_{ci}) \tag{56.4}$$

where c (kJ/(kg·K)) is specific heat of water, M_c (t/h) is water flow into plate heat exchangers equals to 1/3 of boiler circulating water, t_{ci} (°C) and t_{co} (°C) separately represent in and out water temperature of plate heat exchangers' cool side.

So

$$t_{co} = \frac{Q_1}{cM_c} + t_{ci} = \frac{4216 \times 10^3 \times 3600}{4.2 \times 473 \times 10^6} + 55 = 63\,^{\circ}\mathrm{C}$$

Water flow of plate heat exchangers' hot side can be calculated.

$$M_h = \frac{Q_1}{c_h(t_{hi} - t_{ho})} = \frac{4216 \times 3600}{4.2 \times (75 - 65)} = 361.4 \text{ t/h}$$

where M_h(t/h) is water flow of plate heat exchangers' hot side, t_{hi} (°C) and t_{ho} (°C) separately represent in and out water temperature of plate heat exchangers' hot side.

Plate heat exchangers' calculation of 64 and 29 MW boilers is same as 99 MW boiler. The results are shown in Table 56.4.

56.4.2 Selection Analysis and Calculations of Heat Pump System

The second paragraph of the heat exchange system is combined of the second spray chamber and a heat pump system. Given that the boiler can supply high temperature water as driving heat source, absorption heat pump can be used here.

Working fluid of heat pump is HBr-H_2O. Heat load of each heat exchanging equipment is shown in Table 56.5.

56.4.3 Design of Spray Chamber

Structure sizes would be obtained by controlling flue gas flow rate, the results were shown in Table 56.6. Model number of stainless steel nozzles should be decided by flue gas flow. 99 MW boiler needs 16 nozzles, 64 MW boiler needs 12 nozzles, 29 MW boiler needs 8 nozzles.

Under the premise to meet heat exchange requirements, spray chambers' structure sizes, nozzles' number and arrangement form can be serialized for different boilers' heat recovery system.

56.5 Economic Analysis of the Heat Recovery System

Dynamic investment return period is the time that takes present value of project annual net income to recover present value of all investment.

$$\sum_{i=0}^{\mathrm{PBP}} (\mathrm{CI} - \mathrm{CO})_i (1+j)^{-i} = 0 \tag{56.5}$$

Table 56.4 Design calculation parameters of plate heat exchangers

Boiler type (MW)	Heat exchange amount (KW)	Heat side			Cool side	
		Inlet temperature (°C)	Outlet temperature (°C)	Flow (t/h)	Inlet temperature (°C)	Outlet temperature (°C)
99	4216	80	70	361	55	63
64	3188	75	65	273	55	64
29	1448	80	70	124	55	64

Table 56.5 Each heat exchange equipment's load of absorption heat pump

Equipment	Q_e(kW)	Q_g(kW)	Q_a(kW)	Q_c(kW)
99 MW boilers	2971	3941.9	3784.1	2907.5
64 MW boilers	1935	2567.3	2464.6	1893.6
29 MW boilers	984	1305.6	1253.3	963

COP of absorption pump is 1.698

Table 56.6 Structure sizes of spray chamber corresponding to different boilers

Structure sizes boiler type (MW)	Length (m)	Width (m)	Height(m)	Length of inlet and outlet (m)	Width of inlet and outlet (m)
99	4	4.5	3	1.75	4
64	4	4	3	1.5	3.5
29	4	3	3	1.5	2.5

where *PBP* (year) is dynamic investment return period, *j* is annual interest rate which is 10 % in this paper, *CI* is income in year *i*, *CO* is expenditure in year *i*.

Obviously, a project is not feasible when its *PBP* is longer than its project life cycle. When a project is feasible, the *PBP* is shorter, the project is more economic.

PBP of 99 MW boiler heat recovery system is 4.7 year, *PBP* of 64 MW boiler heat recovery system is 3.74 year, *PBP* of 29 MW boiler heat recovery system is 5.65 year. It can be seen from economic analysis that *PBP* for different boilers is shorter than heat recovery system's life cycle which means that the project is feasible.

56.6 Conclusion

In this paper, a heat recovery system which used the flue gas to heat heating system return water is designed and studied. The return water temperature duration in the heating season in Harbin is calculated. The feasibility of the system is verified with the results that the return water temperature kept lower than 55 °C for a long period of time.

The system implementation plan of 99, 64, 29 MW boilers which are three typically used in Harbin including the material of heat transfer equipment and the choice of heat pump concerned are discussed. The titanium alloy plate heat exchanger and first absorption heat pump are selected. Then thermodynamic and hydraulic calculations of the system are done to determine the amount of flue gas heat recovery, structure of water spray chamber, plate heat exchangers and absorption heat pump design.

The dynamic payback periods of waste heat recovery system used in these three boilers are calculated and the results are less than the life cycle of the heat recovery system.

Acknowledgments This study is supported by the '125 Project' of China (No. 2012BAJ04B01) and (No. 2011BAJ05B04).

References

1. Ren S (2000) Dew point corrosion and prevention of waste heat boiler. Corrosion and prevention in petrochemical, 17(1)
2. Yang W, Zhao D, Wang X, Jiang L (2012) Economic analysis and calculations of low-temperature gas waste heat recovery by heat pipe technology. Industrial furnace, 2012(1): 46–49
3. Li J, Li D, Chang J, Qiao M (2009) Associated heating system and its economic of solar energy and boiler after heat. Energy conservation, 2009(4): 29–30
4. Hu G, Yue Y (2012) Research and practice on recover boiler waste heat by reduce the exhaust gas temperature. Energy conservation technology, 2012(4): 295–298

Chapter 57
District Heating System Adjustment Theoretical Based on Heat Users' Real Load

Shanshan Cao, Hua Zhao, Xin Xie and Xiaolin Liu

Abstract With the passage of time and enhanced insulation in buildings, nonnegligible change may occur in the existing buildings' thermal performance. Under this circumstance, the original heating system will not guarantee the heat users' demand. Therefore, it is necessary to re-calibrate the thermal characteristics of the building, based on which the users' supply and return water temperature should be determined. In this paper, a model to solve the heat users' real heat load was established based on energy balance equation, considering that the building's heat load was uncertain. A correction coefficient β was introduced to illustrate the relationship between the design heat load and the real heat load. A demonstration project in Harbin was tested during the period from January 27, 2011 to February 25, 2011 with the application of this adjustment method to verify the validity of this model. The results showed that the users' actual room temperature deviated from the design room temperature seriously before the adjustment method used and this deviation was reduced after this method used.

Keywords District heating system · Real heat load · Adjustment theoretical

S. Cao (✉) · H. Zhao
School of Municipal and Environmental Engineering, Harbin Institute of Technology, Harbin 150090, China
e-mail: css_2005@126.com

H. Zhao
e-mail: zhaohua_hit@sina.com

X. Xie · X. Liu
State Nuclear Electric Power Planning Design and Research Institute, Beijing 100095, China

A. Li et al. (eds.), *Proceedings of the 8th International Symposium on Heating, Ventilation and Air Conditioning*, Lecture Notes in Electrical Engineering 262,
DOI: 10.1007/978-3-642-39581-9_57,

57.1 Introduction

Along with the development of district heating business in our country, energy conservation is more and more valued and the operational regulation of heating system is one of main factors to affect energy consumption. Gong, etc. (2012) analyzed the advantages and disadvantages and application condition of several adjustment ways of district heating system and studied the ways to meet the demand of heat users [1]. Li, etc. (2001) discussed the applicability of the existing flow adjustment formula for heating systems and offered a modified formula through analysis of the computational temperature difference of radiator which was preferable to be adopted in design of metering heating system [2]. Wu, etc. (2012) divided the heating season into two stages according to magnitude of the heating load, in which respectively regulating the supply water temperature under the minimum flow rate condition and adjusting the supply water flow at settled supply temperature and their case calculation showed that the method had a better energy efficient effect [3]. Zhang Hongyan, etc. (2007) discussed the principle of operation parameter optimization of supply heat system and the operation regulation of supply heat system and the method of equipment reconstruction after the operation parameter optimization [4].

With the passage of time and enhanced insulation in buildings, nonnegligible change may occur in the existing buildings' thermal performance. Under this circumstance, the original heating system will not guarantee the heat users' demand. Therefore, it is necessary to re-calibrate the thermal characteristics of the building, based on which the user's supply and return water temperature should be determined.

57.2 Building Real Heat Load Model

In order to obtain building real heat load, a simplified single room with radiator was introduced as shown in Fig. 57.1. According to the following figure, the basic thermal balance equations were written as follows.

$$\beta Q' = Gc(t'_g - t'_h) \tag{57.1}$$

$$\beta Q' = aF(t'_{pj} - t'_n)^{1+b} = aF\left(\frac{t'_g + t'_h}{2} - t'_n\right)^{1+b} \tag{57.2}$$

$$\beta Q\prime = (qV)(t'_n - t'_w) \tag{57.3}$$

where $\beta Q'$ is building design heat load, Q' is building operation heat load, β is correction coefficient, $t_n{}'$ is design indoor temperature, G is design flow, c is specific heat capacity of water, $t_g{}'$ and $t_h{}'$ separately present design supply and return water temperature, qV is building thermal parameters, a and b are radiator thermal parameters, F is radiator area, and $t_w{}'$ is design outdoor temperature.

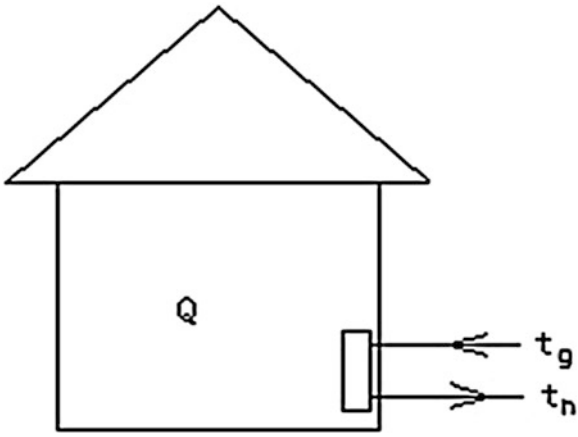

Fig. 57.1 Simple single room with radiator

According to the three equations above, computational formulas of theoretical design supply and return water temperature can be obtained as Eqs. (57.4), (57.5), and (57.6).

$$t_g = t'_n + 0.5(t'_g + t'_h - 2t_n)\overline{Q}^{\frac{1}{1+b}} + 0.5(t'_g - t'_h)\overline{Q} \tag{57.4}$$

$$t_h = t'_n + 0.5(t'_g + t'_h - 2t_n)\overline{Q}^{\frac{1}{1+b}} - 0.5(t'_g - t'_h)\overline{Q} \tag{57.5}$$

$$\overline{Q} = \frac{t'_n - t_w}{t'_n - t'_w} \tag{57.6}$$

Indoor temperature should be measured to verify that the calculated supply water temperature meet heat users' demand. If indoor temperature does not meet the requirement, calculation error of Q' is thought to be the reason here. Due to all kinds of parameters of the radiator are available, we can assume that given data are correct, then take specific discussion on the building thermal load correction.

As mentioned, building design heat load is $\beta Q'$, design flow is G, supply water temperature is t_{g0} (corresponding to any outdoor temperature t_{w0}). After the system is stable, measure indoor temperature t_{n0} and return water temperature t_{h0}. If $t_{n0} \neq t_n{}'$ and $t_{h0} \neq t_h{}'$, it means that hot water which we supply users does not reach their requirement. Therefore, solution of the model problem is to solve β.

57.2.1 The Solution to β

If real building heat load is assumed to be $\beta Q'$, Eqs. (57.1), (57.2), and (57.3) hold. We can give the reason which the heat load is wrong can be summed up in building thermal parameters (qV) is not accurate.

When water flow is G, supply water temperature is t_{g0}, indoor temperature is t_{n0}, return water temperature is t_{h0}, assume that such hot water supply to the user actual heat Q''. So it is easy to get the following formulas.

$$Q'' = Gc(t_{g0} - t_{h0}) \tag{57.7}$$

$$Q'' = aF(t''_{pj} - t_{n0})^{1+b} = aF\left(\frac{t_{g0} + t_{h0}}{2} - t_{n0}\right)^{1+b} \tag{57.8}$$

$$Q'' = (qV)_{\text{true}}(t_{n0} - t_{w0}) \tag{57.9}$$

Where t_{w0} is outdoor temperature of trial operation, $(qV)_{\text{true}}$ is real building thermal performance parameters.

If $(qV)_{\text{true}}$ can be resolved, real building design heat load can be gained by Eq. (57.10).

$$Q' = (qV)_{\text{true}}(t'_n - t'_w) \tag{57.10}$$

$$\beta = \frac{(qV)(t'_n - t'_w)}{(qV)_{\text{true}}(t'_n - t'_w)} = \frac{(qV)}{(qV)_{\text{true}}} = \frac{(qV)}{\frac{Q''}{t_{n0} - t_{w0}}} \tag{57.11}$$

So

$$\beta = \frac{(qV)}{\frac{Q''}{t_{n0} - t_{w0}}} = \frac{\frac{\beta Q'}{(t'_n - t'_w)}}{\frac{Gc(t_{g0} - t_{h0})}{t_{n0} - t_{w0}}} = \frac{\beta Q'}{Gc(t_{g0} - t_{h0})} \cdot \frac{t_{n0} - t_{w0}}{(t'_n - t'_w)} \tag{57.12}$$

Calculation equation of real heat load is shown in (57.13).

$$Q' = \frac{\beta Q'}{\beta} = \frac{Gc(t_{g0} - t_{h0})}{t_{n0} - t_{w0}} \cdot (t'_n - t'_w) \tag{57.13}$$

57.2.2 Solution of Real Supply and Return Water Temperature on the Basis of Real Building Heat Load

$$Q'' = Gc(t''_g - t''_h) \tag{57.14}$$

$$Q' = aF(t''_{pj} - t''_n)^{1+b} = aF\left(\frac{t''_g + t''_h}{2} - t''_n\right)^{1+b} \tag{57.15}$$

$$\overline{Q} = \frac{t_n - t_w}{t'_n - t'_w} = \frac{(t_g + t_h - 2t_n)^{1+b}}{(t''_g + t''_h - 2t'_n)^{1+b}} = \frac{t_g - t_h}{t''_g - t''_h} \tag{57.16}$$

where t_g'' is real design supply water temperature, t_h'' is real design return water temperature.

Supply and return water temperature corresponding to any outdoor temperature can be obtained by Eqs. (57.17) and (57.18).

$$t_g = t_n + 0.5(t_g'' + t_h'' - 2t_n)\overline{Q}^{\frac{1}{1+b}} + 0.5(t_g'' - t_h'')\overline{Q} \tag{57.17}$$

$$t_h = t_n + 0.5(t_g'' + t_h'' - 2t_n)\overline{Q}^{\frac{1}{1+b}} - 0.5(t_g'' - t_h'')\overline{Q} \tag{57.18}$$

This model can be used directly under quality regulation mode, and only in solving cooling temperature difference always make a change a bit when it is in other control mode such as quantity control, but it does not affect the use of the model.

As for quantity regulation, solving method is same to quality regulation mode except that Eqs. (57.14) and (57.15) need to be replaced by (57.19) and (57.20) separately.

$$Q' = Gc(t_g'' - t_h'') \tag{57.19}$$

$$Q\prime = aF\triangle t_d^{1+b} = aF\left(\frac{t_g'' - t_h''}{\ln\frac{t_g'' - t_n'}{t_h'' - t_n'}}\right)^{1+b} \tag{57.20}$$

57.3 Measurement Verification

The demonstrate project is located in Harbin Railway District with four high-rise buildings. There are 2 (No. 20 and No. 21) 15-layers and 2 (No. 22 and No. 23) 12 layers buildings whose total area is 47,500 m^2 with 42,9600 m^2 ground area. Indoor heating system is floor heating while basement is radiator system. Floor heating system is divided into high area and low area which was tested respectively (see Table 57.1) from January 27, 2011 to February 25, 2011.

Table 57.1 Area of each heating system

Building	High area (m^2)	Low area (m^2)	Basement area (m^2)	Total (m^2)
20#	5,929	5,929	2,691	14,549
21#	5,182	4,535	621	10,338
22#	5,842	5,843	632	12,317
23#	5,173	4,527	596	10,296
Total (m^2)	22,126	20,834	4,540	47,500

Design supply and return water temperature was 60 and 50 °C. The supply and return water temperature of heat supply network side and user side and indoor temperature were measured during the test process. The model established was used to modify the real supply and return water temperature in order to make the heat users' indoor temperature meet requirements.

57.3.1 Engineering Correction Parameters

Actual operation and design conditions were vary considerably before the test. Average indoor temperature was measured after the system operated for a period. The results showed that users' actual indoor temperature had deviated from the design value seriously. Then the operation parameters were corrected according to the established real load model.

Operation parameters without correction under −12 °C are shown in Table 57.2. Take the measured value into Eqs. (57.12), (57.13), (57.15), and (57.16) so that β and operation supply and return water temperature can be calculated. The results are shown in Table 57.3.

Table 57.2 Heating parameters measured before the real heat model was used

Temperature System	t_w	t_g'	t_h'	t_n
20# high district	−12	34.9	30.4	22.46
20# low district	−12	33.5	30	20.56
21# high district	−12	33.2	29.6	24.35
21# low district	−12	31.8	29.8	23.2
22# high district	−12	32.9	29.2	22.21
22# low district	−12	31.7	29.1	21.69
23# high district	−12	33.3	30.4	22.54
23# low district	−12	29.3	26.6	19.18

Table 57.3 Heating parameters after revised

Parameters System	β	t_g''	t_h''
20# high district	1.467	34.52	27.92
20# low district	1.497	35.33	30.09
21# high district	1.500	29.23	23.83
21# low district	1.500	28.85	25.85
22# high district	1.500	31.96	26.41
22# low district	1.500	30.94	27.04
23# high district	1.500	32.08	27.73
23# low district	1.500	31.10	27.05

57.3.2 Engineering Test Data and Analysis

The supply and return water temperature were measured before and after the model was corrected from February 9 to 24, 2011. System operation temperature curve was shown from Figs. 57.2, 57.3, 57.4, 57.5, 57.6, 57.7, 57.8, and 57.9.

Each system operated according to unrevised temperature control curve in February 9, 2011. And they began to operate according to the revised temperature control curve in February 16, 2011.

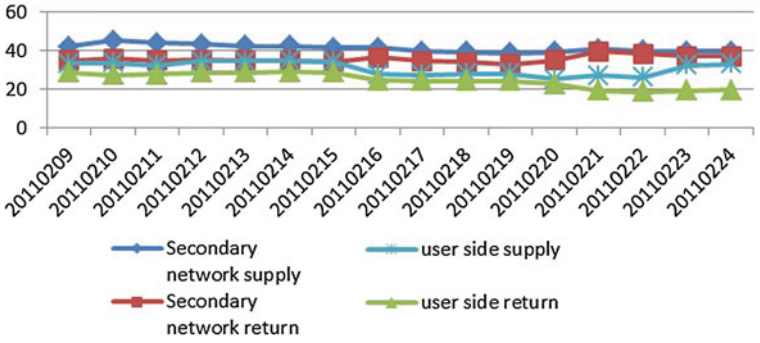

Fig. 57.2 Supply and return water temperature curve of 20# high area

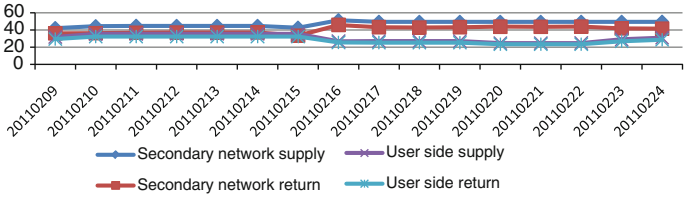

Fig. 57.3 Supply and return water temperature curve of 20# low area

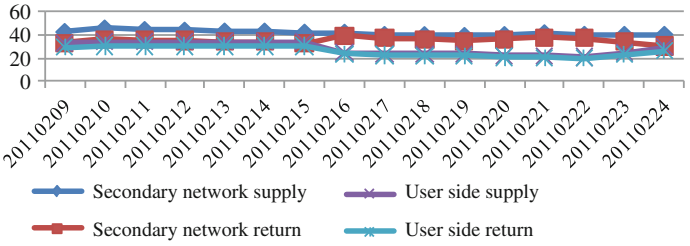

Fig. 57.4 Supply and return water temperature curve of 21# high area

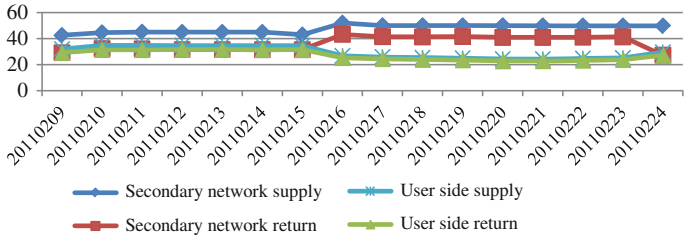

Fig. 57.5 Supply and return water temperature curve of 21# low area

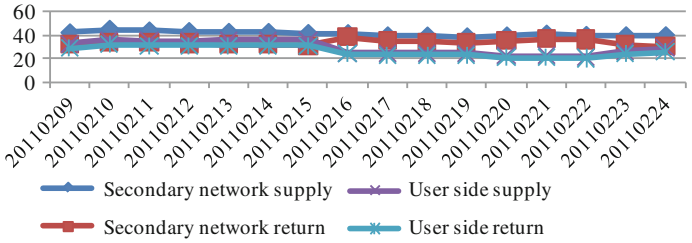

Fig. 57.6 Supply and return water temperature control curve of 22# high area

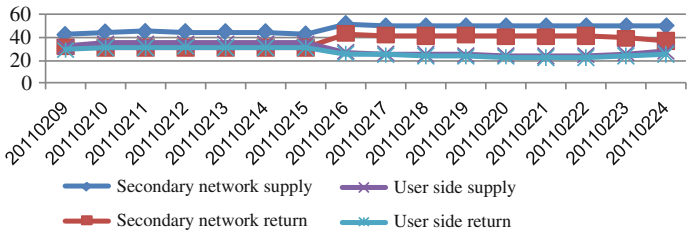

Fig. 57.7 Supply and return water temperature curve of 22# low area

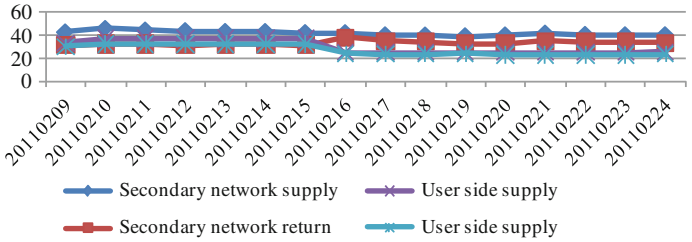

Fig. 57.8 Supply and return water temperature curve of 23# high area

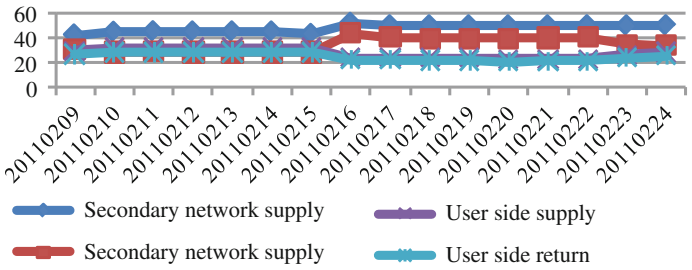

Fig. 57.9 Supply and return water temperature curve of 23# low area

From Figs. 57.1, 57.2, 57.3, 57.4, 57.5, 57.6, 57.7, and 57.8, jump point can be seen in February 16. But supply and return water temperature can be stable in 3 days.

The revised model of each system user side supply and return water temperature was lower than before the amendment of the user side of the supply and return water temperature and the revised supply and return water temperature difference was reduced after the correction.

Average indoor temperature was measured after heating system operated according to unrevised control curve for a period. The data are given in Table 57.4.

Heating system operated according to revised temperature curve for a period since February 16, 2011. The measured average indoor temperature is given in Table 57.5.

Comparison of average indoor temperature before and after correction is shown in Fig. 57.10. It can be seen from the figure that indoor thermal condition improved to a certain extent after correction. Some users' were overheated before correction, such as average indoor temperature of 21# low area was near to 24 °C. Meanwhile, some users' indoor temperature difference was larger than 3 °C. These meant that there had been serious thermal imbalance before the model was introduced. Conversely, average indoor temperature after correction was about 20 °C and users' indoor temperature difference was all less than 1 °C. It meant that the real heat load model helped eliminate overheating problems and make indoor temperature uniform.

Table 57.4 Average indoor temperature of each system before correction

Testing time	System	Average indoor temperature	Number of users
2011.02.09–2011.02.15	20# high area	21.23	54
2011.02.09–2011.02.15	20# low area	20.26	54
2011.02.09–2011.02.15	21# high area	23.4	64
2011.02.09–2011.02.15	21# low area	23.77	40
2011.02.09–2011.02.15	22# high area	22.62	72
2011.02.09–2011.02.15	22# low area	21.46	73
2011.02.09–2011.02.15	23# high area	22.32	74
2011.02.09–2011.02.15	23# low area	20.55	48

Table 57.5 Average indoor temperature of each system after correction

Testing time	System	Average indoor temperature	Number of users
2011.02.16–2011.02.24	20# high district	19.67	54
2011.02.16–2011.02.24	20# low district	19.68	54
2011.02.16–2011.02.24	21# high district	20.64	64
2011.02.16–2011.02.24	21# low district	20.62	40
2011.02.16–2011.02.24	22# high district	20.5	72
2011.02.16–2011.02.24	22# low district	20.45	73
2011.02.16–2011.02.24	23# high district	20.46	74
2011.02.16–2011.02.24	23# low district	19.36	48

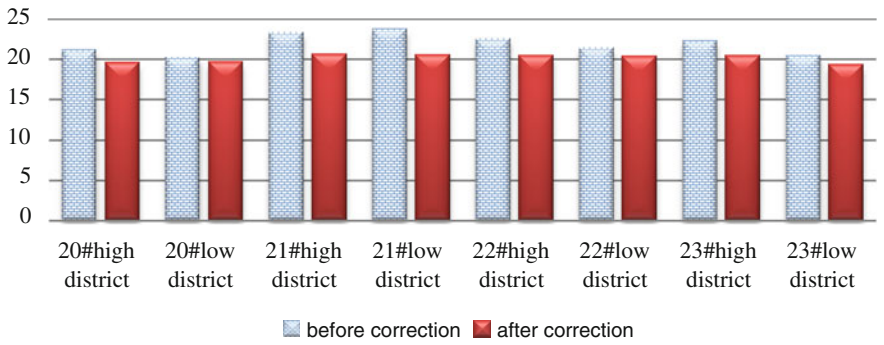

Fig. 57.10 Comparison of average indoor temperature before and after correction

57.4 Conclusions

A model to solve real building heat load was established in this paper and the method of calculating real supply and return water temperature was given. According to the project measurement, it was verified that the real heat load model eliminated overheating problems and made indoor temperature uniform.

This study was done on district heating system adjustment theoretical which provides some key information for the people working in the area for better design, analysis, and operation of the system.

Acknowledgments This study is supported by the '125 Project' of China (No. 2012BAJ04B01) and Science Foundation of Heilongjiang (No. E201036).

References

1. Keqin G, Hongfang J, Shengjie G (2012). The technical analysis of the operational regulation in the system of district heating. Low Temp Archit Technol 7:132–134
2. Jianxing L, Guangbei T, Yi W (2001). Employment of flow adjustment fomulas in heat metering systems. HVAC 31:112–114
3. Jieqing W, Yongcheng J, Gaoyang Z, Xiumu F, Ruiyun Z (2012). Energy efficient analysis of staged constant variable flow regulation for heating systems. HVAC 42:137–140
4. Hongyan Z, Wenqiang T, Hongfu Z (2007). Operation parameter optimization, regulation and reconstruction of heat-supply system. Gas Heat 8:87–89

Chapter 58
Design of Split Evaporative Air Conditioner of Evaporative Cooling and Semiconductor Refrigeration

Zhe Sun, Xiang Huang and Jiali Liu

Abstract This paper firstly discusses two different operation modes of the split evaporative air conditioner combined evaporative cooling with semiconductor refrigeration technology. Then the sizes of water flow which is required by the outdoor unit are deduced and calculated in two modes of operation. The design step and selection calculation of the split evaporative air conditioner are given in Xi'an region under 2,500 W sensible heat load. For purpose, it lays the foundation for future design and development of the split evaporative air conditioner.

Keywords Evaporative cooling · Semiconductor refrigeration · Design of split evaporative air conditioner

List of Symbols

W_c	Outlet water flow of outdoor unit (kg/h)
W_h	Inlet water flow of outdoor unit (kg/h)
W_r	Water flow of heating channel of semiconductor refrigeration device (kg/h)
W_l	Water flow of cooling channel of semiconductor refrigeration device (kg/h)
W_m	Water flow of indoor terminal (kg/h)
t_c	Outlet water temperature of outdoor unit (kg/h)
t_h	Inlet water temperature of outdoor unit (kg/h)
t_r	Outlet water temperature of heating channel of semiconductor refrigeration device (°C)
t_l	Outlet water temperature of cooling channel of semiconductor refrigeration device (°C)

This work is supported by the project plan of science and technology innovation in Shaanxi (Foundation No. 2011KTCQ01-10).

Z. Sun (✉) · X. Huang · J. Liu
College of Environmental and Chemical Engineering, Xi'an Polytechnic University, Xi'an 710048, China
e-mail: sunzhe_hvac@163.com

A. Li et al. (eds.), *Proceedings of the 8th International Symposium on Heating, Ventilation and Air Conditioning*, Lecture Notes in Electrical Engineering 262,
DOI: 10.1007/978-3-642-39581-9_58,

t_m Outlet water temperature of indoor terminal (°C)
Q_n Indoor load (W)
C_m Specific heat at constant pressure of water (J/(kg°C))
Q_a Air mass flow (kg/h)
βv Volumetric mass transfer coefficient $\left(\mathrm{kg/m^3 \times s}\right)$
g_w Mass flow rate of water $\left(\mathrm{kg/m^2 \times s}\right)$
g_a Mass flow rate of air $\left(\mathrm{kg/m^2 \times s}\right)$
λ_0 Water at 0°C of vaporization latent heat (2,500 kJ/kg)
Δt Difference of in-outlet water (°C)
q Sprinkling density $\left(\mathrm{kg/m^2 \times s}\right)$
H Filler height (m)
t_{g_1} Dry bulb temperature of inlet air (°C)
t_{s_2} Wet bulb temperature of inlet air (°C)
v_v Windward air velocity (m/s)
ε Specific surface area of filler ($\mathrm{m^2/m^3}$ (ε= 400–500 ($\mathrm{m^2/m^3}$))
η_{DEC} Efficiency of filler

58.1 Introduction

The "*Twelfth Five-Year*" *energy-saving environmental protection industry development planning* issued by State Council of China clearly pointed out the need to research and development of air conditioning energy-saving products in one of the areas of the energy-saving industry, as well as the capture of air conditioning refrigerant alternative technologies. Evaporative cooling air conditioning technology as a use of natural cold source alternative to artificial energy source is gotten more and more attention. Evaporative cooling air conditioning technology in accordance with the output of media can be divided into evaporative air cooling and evaporative water cooling.

Evaporative water cooling air conditioning technology is based on the principle of evaporative cooling, using direct evaporative cooling (DEC) or indirect evaporative cooling (IEC) or with mechanical refrigeration assisted to product cold water [1]. Currently, using evaporative water cooling air conditioning technology, the indirect-direct evaporative cooling (IDEC) chillers or evaporative cooling and mechanical refrigeration combined operation chiller is to achieve a certain effect in the actual project. However, the temperature of IDEC chiller water is instability, and the evaporative cooling-mechanical refrigeration chiller system is too complexity. They are not suitable as a small-decentralized air conditioning. We try to design a split evaporative air conditioner combined evaporative cooling with semiconductor refrigeration technology. It can achieve temperature stability of

evaporative water cooling, the higher energy efficiency of semiconductor refrigeration and simpler system [2, 3]. This article gives a brief analysis of the split evaporative air conditioner, and it shows the specific design steps. The main parameters of the split evaporative air conditioner are ascertained. The completely design selection is done for your reference.

58.2 Operational Modes of the Unit Under Different Conditions

The split evaporative air conditioner of combination of evaporative cooling and semiconductor refrigeration mainly divided into three parts, including outdoor unit, semiconductor refrigeration device, and air conditioning terminal. In order to meet the air conditioning terminal needs, outdoor unit adopts indirect-direct evaporative cooling technology to take cold water [4, 5]. So as to meet the needs of indoor plumbing, indirect evaporative cooling technology cools fresh air into the interior. Water systems operate have two modes, respectively, for only run the evaporative cooling outdoor unit and evaporative cooling and semiconductor cooling device running at the same time.

58.2.1 Only Run the Evaporative Cooling Outdoor Unit

When the water temperature meets the requirements (water temperature usually is 16–18 °C), it does not need to open the semiconductor refrigeration device. Through indirect-direct evaporative cooling, the product water of outdoor unit is directly access to indoor terminal. The process is shown in Fig. 58.1. Just running the evaporative cooling outdoor unit, the mass flow of circulating water as required:

$$W_c = \frac{Q_n}{c_m(t_h - t_c)} \tag{58.1}$$

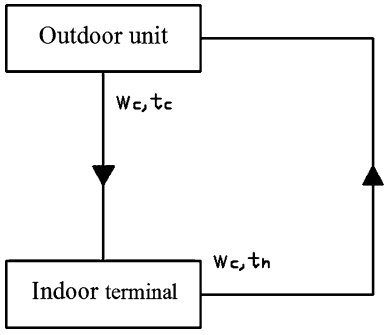

Fig. 58.1 Only run the evaporative cooling outdoor unit

58.2.2 Evaporative Cooling and Semiconductor Cooling Device Running at the Same Time

When the water temperature does not meet the requirements of water temperature or air needs dehumidification, the process is shown in Fig. 58.2. Among them, the semiconductor refrigeration means for the modular apparatus of the upper and lower heating channel, the intermediate cooling passage. At this time, two kinds of operation are shown in Fig. 58.2a, b.

58.2.2.1 When the Outlet Water Temperature of Indoor Terminal is Higher than the Outlet Water Temperature of the Outdoor Unit

The outdoor unit, semiconductor refrigeration device and indoor terminal need series connection. The product water of IDEC divided into two parts. One part passes into the heating channel to absorb heat, the other part passes into the cooling channel to cool. Water in cooling channel then passes into the terminal. Finally, two parts of water get together and return into the outdoor unit. Mass flow in indoor terminal:

$$W_l = \frac{Q_n}{c_m(t_h - t_l)} \tag{58.2}$$

In and out of the water mass flow in outdoor unit: $W_c = W_r + W_l$

The semiconductor refrigeration device design and the experimental study shows that usually the mass flow of water in heating and cooling channel of this semiconductor refrigeration device is set to 1:1, $W_r = W_l$.

So the mass flow of water that outdoor unit processing for:

$$W_c = \frac{2Q_n}{c_m(t_h - t_l)} \tag{58.3}$$

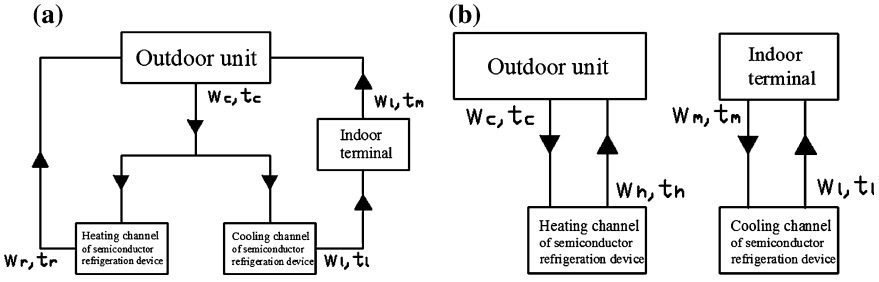

Fig. 58.2 Evaporative cooling and semiconductor cooling device running at the same time

58.2.2.2 When the Outlet Water Temperature of Indoor Terminal is Lower than the Outlet Water Temperature of the Outdoor Unit

Outdoor unit and heating channel of semiconductor refrigeration device are connection in series. Also, the indoor terminal and cooling channel of semiconductor refrigeration device are connected in series. The product water of IDEC in outdoor unit all pass into the heating channel of semiconductor refrigeration device with endothermic process. Then it is back into outdoor unit. The cold water of lower temperature taken by the semiconductor refrigeration device leads to the indoor terminal with endothermic process, and then it comes back to cooling channel of the semiconductor refrigeration device. The terminal water mass flow as:

$$W_l = \frac{Q_n}{c_m(t_m - t_l)} \tag{58.4}$$

Also, water mass flow of the heating and cooling channel of the semiconductor refrigeration device is provided in the 1:1, so the water mass flow of outdoor unit processing for:

$$W_c = \frac{Q_n}{c_m(t_m - t_l)} \tag{58.5}$$

58.3 The Design for Split Evaporative Air Conditioner

58.3.1 The Process of Design

As is shown in Fig. 58.3, the process of design is divided into the following six steps. First, unlike air conditioning design of traditional mechanical refrigeration, this split evaporative air conditioner designs are in strict accordance with the outdoor meteorological parameters. The meteorological parameters in different areas directly determine water temperature. Therefore, it leads to select the number and power size of semiconductor refrigeration device that are not the same. Hence, the first design process is to determine the outdoor meteorological parameters and indoor cooling load. Indoor cooling load in accordance with Section I formula calculates the total water flow. This is the second step of the process of design. The third step of the process of design based on water flow and gas–water ratio determine the amount of air, fresh air, and working air flow. The fourth step is an indirect heat exchanger size calculated according to the air flow. The fifth step is the most important, selecting the size of the filler, which directly determines the efficiency level of the output cold water. The sixth step is to select accessories equipment according to the above parameters. The paper as a sensible heat load of 2,500 W small area in Xi'an area as an example, in accordance with the steps of the design, try to calculate this split evaporative air conditioner.

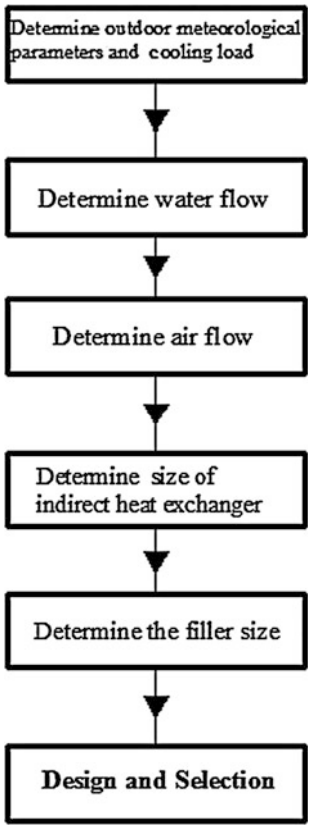

Fig. 58.3 Steps of design of split evaporative air conditioner

58.3.2 Determine Outdoor Meteorological Parameters and the Cooling Load

Assumed that the Xi'an area as design areas where meteorological parameters for the dry bulb temperature of 35.1 °C, wet bulb temperature of 25.8 °C. Assumed that the small area of the sensible heat load to 2,500 W.

58.3.3 Determine Water Flow

The water system uses two modes of operation. The outdoor unit in accordance with the evaporative cooling and semiconductor refrigeration device should run at the same time to determine the water flow. According to the formula $W_c = \frac{2Q_n}{c_m(t_h - t_l)}$, in condition that the indoor terminal of the inlet and outlet water temperature difference of 5 °C, the mass flow of the water is approximately 860 kg/h.

58.3.4 Determine Air Flow

According to the gas–water ratio, air flow can be determined with the water for the exchange of heat and moisture. Gas–water ratio (λ) is the ratio of the air mass flow (Q_a) and spray water mass flow (W) into the filler $\left(\lambda = \frac{Q_a}{W}\right)$. The gas–water ratio is an important factor to affect the evaporative cooling system to take cold water. We must consider the evaporative water cooling of the top air–water ratio for the efficiency highest of heat and moisture exchanging. The gas–water ratio generally choice of 1.0–2.0. This design uses a gas–water ratio of 1.4 [6]. It is calculated that the air flow is 1,003 m^3/h for the air exchange with water in heat and moisture.

The minimum fresh air is provided in *practical heating and air conditioning design manual.* According to it, the fresh air is designed to be 100 m^3/h. Therefore, the air flow of primary air is 1,103 m^3/h through indirect heat exchanger. According to the test of a plurality of the actual construction site, the secondary air than the primary air ratio is usually 1:1 in the middle-humidity areas. Then the secondary air flow is 1,103 m^3/h through the indirect heat exchanger.

58.3.5 Determine the Size of Indirect Heat Exchanger

The plate-fin heat exchanger of sensible heat is used in indirect segment of the outdoor unit. Derived through theoretical and experimental demonstration, the secondary passage width of the staggered flow plate indirect evaporative cooler is about 5 mm, and the secondary passage width is slightly larger than the width of the primary passage [7]. According to the samples provided by the manufacturer, we determine the windward air velocity and calculate frontal area. Plate-fin heat exchanger size (420 × 450 × 450 mm) is finalized with flow passage spacing of 5 mm.

58.3.6 Determine the Filler Size

The windward air velocity of filler is generally 2.0–3.0 m/s. Considered the unit overall size, processing technology, and other factors, the frontal area of filler is designed for 300 × 420 mm, and windward air velocity to 2.2 m/s.

From the Merkel Equation and its correction [8–13] obtain:

$$\frac{\beta v}{q} H = \frac{C_m}{K} \int_{t2}^{t1} \frac{\mathrm{d}t}{h'' - h} \tag{58.6}$$

1. Volumetric mass transfer coefficients of equation reflecting the cooling capacity of the watering device, according to the formula drawn: $\beta_v = 3.926\, g_w^{0.1607} g_a^{1.290}$
2. Biemans corrected Merkel equations. The introduction of the considerations takes heat away due to evaporation of water and, it can be calculated in accordance with the formula: $K = 1 - (C_m t_2)/\lambda_0$
3. Solving the exchange number: $N = \frac{1}{K}\int_{t2}^{t1} \frac{\mathrm{d}t}{h''-h}$

From Simpson approximate integral method for solving:

$$N = \frac{\mathrm{d}t}{3\mathrm{K}}\left(\frac{1}{\Delta h_0} + \frac{4}{\Delta h_1} + \frac{2}{\Delta h_2} + \frac{4}{\Delta h_3} + \frac{2}{\Delta h_4} + \ldots\ldots + \frac{2}{\Delta h_{\mathrm{n}-2}} + \frac{4}{\Delta h_{\mathrm{n}-1}} + \frac{1}{\Delta h_{\mathrm{n}}}\right) \tag{58.7}$$

where in Δh_0, $\Delta h_1 \ldots\ldots \Delta h_n$ refers to the corresponding enthalpy when water temperature respectively is t_2, $t_2 + dt \ldots\ldots t_2 + (n-1)dt$, $t + ndt$.

When the calculation accuracy is not required, $\Delta t < 15$ °C, it can be calculated by the following simplified:

$$N = \frac{\Delta t}{6K}\left(\frac{1}{h'' - h_2} + \frac{4}{h''_m - h_m} + \frac{2}{h''_2 - h_1}\right) \tag{58.8}$$

where: $h'' - h_2$ is difference between saturated air enthalpy under inlet water temperature and exhaust air enthalpy. $h''_m - h_m$ is difference between saturated air enthalpy under in-outlet water average temperature and in-outlet air average enthalpy. $h''_2 - h_1$is difference between saturated air enthalpy under outlet water temperature and inlet air enthalpy.

The material we use for is the plant fiber filler. Rounding up after a series of calculations, taking into account economic factors such as filler resistance, we eventually come packing height H is 300 mm. The whole specifications are 300 × 420 × 300 mm.

When filler height H has been calculated, efficiency can be authenticated from equation:

$$\eta_{\mathrm{DEC}} = 1 - \exp\left(-0.029 t_{g1}^{1.678} t_{s1}^{-1.855} v_y^{-0.97} \varepsilon H\right) \tag{58.9}$$

58.3.7 Design and Selection

58.3.7.1 Choice of Sprinkler Way

Watering spray way is to take the spray manifold punched a hole because of smaller watering spray area. Every other 4 cm spacing is punched on tube. Holes on every tube are staggered arrangement. Meanwhile, the 150 mm filler is

increased between the plate-fin heat exchanger and the spray manifold, in order to achieve the purpose of further water cooling with uniform water distribution.

58.3.7.2 Water Tank Selection

The volume of the tank should not be less than 1.2 % of hour-cycle water in the filler segment. Computational design is derived that indirectly collecting tank size is 450 × 420 × 100 mm, and directly collecting tank size is 300 × 420 × 150 mm.

58.3.7.3 Selection of Pumps and Fans

Fan options: by viewing the heat exchanger and the filler sample, we calculate the pressure loss of the individual segments. Air pressure which fan required is derived by adding. The fan selected is based on the amount of air and the air pressure.

Pump selection: From equipped with the semiconductor refrigeration unit number and the indoor terminal, in accordance with series of the semiconductor refrigeration device and the indoor terminal, resistance is calculated by adding. The pump selected based on the amount of water and resistance.

58.3.8 Selection of Semiconductor Refrigeration Device

Semiconductor refrigeration device has been designed and tested. It is stereotypes modular device. Each of the semiconductor refrigeration devices has two thermopiles and three water channels. There are two layers of semiconductor thermopile folder in the middle of the water channel. The number of six cooling pieces is chained together in thermopile layer. Two thermopile layers in parallel are connected to the DC power. There are fin in water channel to enhance heat transfer. According to the moderate humidity climatic characteristics of the region, we select four groups of semiconductor refrigeration device as auxiliary adjust to the water temperature.

58.3.9 Calculation Results of Each Parameter

In accordance with designed Steps, the calculation results of the main parameters about this split evaporative air conditioner are finished as shown in Table 58.1.

Table 58.1 Parameter calculation results

Name	Parameter
Outdoor design parameters	Dry bulb temperature: 35.1 °C
	Wet bulb temperature: 25.8 °C
Cooling load	2,500 W
Water flow	Maximum 860 L/h
Fresh air flow	100 m^3/h
Total inlet air flow	1,103 m^3/h
Secondary air flow	1,003 m^3/h
Size of the heat exchanger	420×450×450 mm
Filler size	300×420×300 mm
Size of indirectly water tank	450×420×100 mm
Size of directly water tank	300×420×150 mm
Semiconductor refrigeration device	Four groups

58.4 Conclusion

Evaporative cooling equipment of small air-conditioning area is more than the main unit evaporative air cooler. Their output medium is cold air. Affected by building storey and noise factors, it is difficult to promote air conditioning in the field of home and office. The evaporative water cooling could resolve storey and noise limited, but water temperature is instability. The temperature of cold water made by jointed operation of evaporative cooling and mechanical refrigeration system is stable, but the system is too complex and is not advisable to apply small air-conditioning units. Therefore, this paper presents a split evaporative air conditioner combined evaporative cooling with semiconductor refrigeration technology. We show how to determine, the water and air flow, the size of indirect heat exchanger, the filler size, and other designs and selections. But we have not yet carried out the experimental study. There may be unreasonable design parameters. So we hope to show our results to you to explore together. This paper is to lay the foundation for future theoretical and experimental analysis, unit design, and development.

Acknowledgments This study is supported by the project plan of science and technology innovation in Shaanxi (Foundation No. 2011KTCQ01-10).

References

1. Huang X, Sun T-z, W Chao (2012) Explanation of evaporative air-conditioning technology (1). Refrig Air Cond 12:1–6
2. Zhe S, Xiang H, Chao W et al (2012) The preliminary exploration for air-conditioning system of combination of evaporative cooling and semiconductor refrigeration. CIESC J S2:156–160
3. Sun Z, Huang X, Fan K, Wang C, Sun T-z (2013) The discus of the performance of semiconductor refrigeration along with evaporative cooling. J Xi'an Polytech Univ 27:88–92

4. Huang X (2010) Theory and applications of evaporative cooling air conditioning. China Architecture & Building Press, Beijing
5. Sun T-z (2012) Study on evaporative cooling and mechanical refrigeration compound high-temperature chiller. Xi'an Polytechnic University, Xi'an
6. Bai Y-b, Huang X, Sun T-z, Wen L (2011) Research of how the air water ratio affect the outlet temperature of the evaporative cooling high temperature Chiller. Fluid Mach 39:83–86
7. Zhang D (2005) Theoretical and experimental research of evaporative cooling air conditioning simplified thermal calculation and system design methodology. Xi'an Polytechnic University, Xi'an
8. Ren Z-p, Cai R-x (2002) Thermal manual. China Machine Press, Beijing
9. Zhao R-yi, Fan C-y, Xue D-h (2000) Air conditioning. China Architecture &Building Press, Beijing
10. Zhao Z-g (1997) Cooling tower. China WaterPower Press, Beijing
11. Zhu Y-h (2008) Circulating cooling water. China Architecture & Building Press, Beijing
12. Xie X-y, Jiang Y, Liu S-q (2007) Design and development of an indirect evaporative water chiller. HV&AC 37:66–71
13. Sun T-z, Huang X, W Li (2011) Discussion of design of evaporative cooling and mechanical refrigeration compound high-temperature chiller. J Xi'an Polytech Univer 25:679–683

Chapter 59
Energy-Efficient Heating and Domestic Hot Water Systems Suitable for Different Regions

Wei Wu, Baolong Wang, Wenxing Shi and Xianting Li

Abstract Heating and domestic hot water consume a large amount of energy. The heat supply systems based on fossil fuel burning are of low energy efficiency as well as high air pollution. Air source electricity heat pump (ASAHP) was analyzed to be energy-saving for heating in cold regions. In order to select suitable system for different areas, the primary energy efficiency of electricity heating, coal boiler, gas boiler, electrical heat pump, and ASAHP-driven by various heat sources are compared. Combing the weather characteristics in different areas, the applicability of different systems in China are investigated in the energy efficiency point of view. Results show that the primary energy efficiency of ASAHP is generally higher than that of ASEHP except when the air temperature is very high. Both ASEHP and ASAHP are efficient in the hot summer and warm winter area for domestic hot water. And direct gas-fired ASAHP is the best choice in hot summer and cold winter area, temperate area, cold area as well as severe cold area. Additionally, hot water-driven ASAHP using gas boiler is the second choice for heating in hot summer/cold winter area and temperate area, and for both heating and domestic hot water in cold and severe cold areas. This work is to explore the most suitable heat supply systems for different regions, and is expected to make contributions to building energy saving and emission reduction.

Keywords Heating · Domestic hot water · Absorption heat pump · Air source · Energy saving

W. Wu · B. Wang · W. Shi · X. Li (✉)
Department of Building Science, Tsinghua University, Beijing 100084, China
e-mail: xtingli@tsinghua.edu.cn

A. Li et al. (eds.), *Proceedings of the 8th International Symposium on Heating, Ventilation and Air Conditioning*, Lecture Notes in Electrical Engineering 262,
DOI: 10.1007/978-3-642-39581-9_59,

59.1 Introduction

Heating and domestic hot water consume a large amount of energy, and will keep increasing due to the development of urbanization and improvement of living standards. Figure 59.1 shows the energy consumption of heating and domestic hot water in China in the recent years, including heating in the northern towns, heating in the towns in hot summer and cold winter area, heating in the rural area and domestic hot water in all the towns [1].

At present, the energy systems for heat supply are mainly based on the fossil fuel burning, such as boiler and heat network, which are of low energy efficiency as well as high air pollution [2]. Though the heat pump systems are widely used recently [3, 4], they are limited in lots of occasions, especially in the cold regions [5, 6]. Additionally, the power grid pressure will increase sharply if the electrical heat pump systems are applied in large scale for heat supply. In order to solve the above problems, novel heating and domestic hot water systems based on Air source electricity heat pump (ASAHP) were proposed in the previous work [7]. The energy saving potential of single-stage ASAHP used in different areas was analyzed and compared with the traditional boiler system [8], and the applicability of single-stage and double-stage ASAHP used in cold and severe cold regions

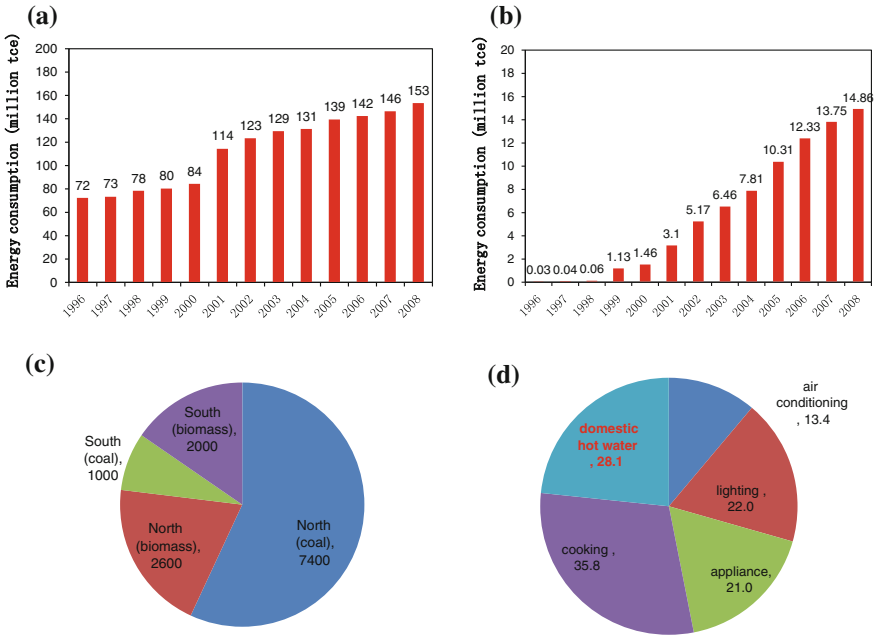

Fig. 59.1 Energy consumption of heating and domestic hot water in China (million tce). **a** Heating in the northern towns, **b** Heating in the hot summer and cold winter towns, **c** Heating in the rural area, **d** Domestic hot water in towns

were summarized [9]. However, the coverage of analyzed applications and systems was limited. For example, in hot summer and cold winter region or South China, ASEHP is also widely used. Is the ASAHP still has its advantage when compared with ASEHP?

This work is to give a comprehensive analysis and comparison of different heating and domestic hot water systems in different regions, including North China (cold and severe cold region), temperate region, hot summer and cold winter region and South China (hot summer and warm winter).

59.2 Heating and Domestic Hot Water System Based on ASAHP

The schematic of the proposed system based on ASAHP is shown in Fig. 59.2. The ASAHP can either be driven by a boiler or heat network (Fig. 59.2a) or fired by the gas directly (Fig. 59.2b).

In Fig. 59.2a, the high temperature hot water or steam from boiler (or district heating network) is used to drive the ASAHP instead of being supplied to users directly, so the heat amount can be increased since the evaporator can extract low-grade heat from the ambient air. The traditional plate heat exchanger is installed in parallel with the ASAHP to ensure heating security when the air temperature is too low or the devices are under maintenance. For this system, as the temperature of driving source are usually not so high, the ASAHP can be single-effect in cold regions and be double-stage, double-stage coupling, or compression-assisted in severe cold regions [10].

In Fig. 59.2b, the ASAHP is fired by gas directly, so the generation temperature can be much higher. Therefore, double-effect ASAHP can be adopted to obtain higher COP. If the ambient temperature is too low and the double-effect cycle

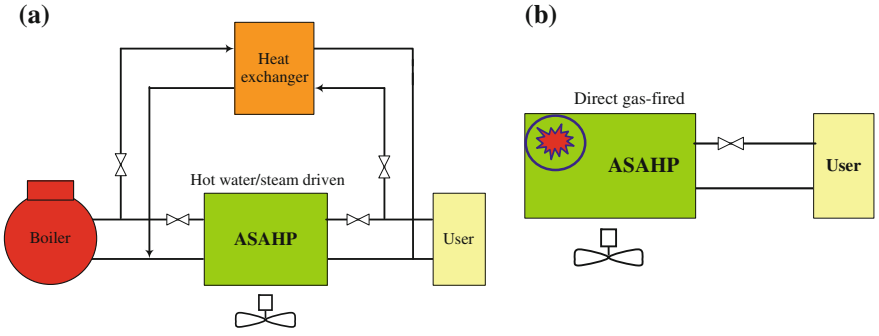

Fig. 59.2 Heating and domestic hot water system based on ASAHP. **a** Hot water/steam driven, **b** Direct gas-fired

Table 59.1 Characteristics of different absorption cycles

Absorption cycle	Heat source	COP	Remark
Double-stage Double-stage coupling Compression-assisted absorption	Boiler	1.2–1.3	Double-stage ASAHP is used in severe cold regions in this work
Single-effect	Boiler gas	1.3–1.5	For gas-fired ASAHP, double-effect is not advantageous under very low ambient temperature
Double-effect	Gas	1.5–2.1	Double-effect is very efficient in warm areas. The generation temperature is limited by corrosion

cannot operate under this condition, the single-stage has to be applied even for directly gas-fired ASAHP.

The ammonia-based working fluids are used considering that H_2O-LiBr cannot operate under low evaporation temperature and is easy to crystallize in heat pump mode [11]. Different absorption cycles are suitable for different heat sources and weather conditions. The main characteristics of different absorption cycles are listed in Table 59.1.

59.3 Comparison of Primary Energy Efficiency

In order to select suitable heating and domestic hot water system for different areas, the primary energy efficiency of electricity heating, coal boiler, gas boiler, electrical heat pump, and absorption heat pump driven by various energy source are calculated with the ambient temperature ranging from −30 to 40 °C. The performance of ASEHP is fitted from the data provided by manufacturers, and the performance of different ASAHP is simulated using the fluid properties of ammonia-based solutions [12]. For simplification, the temperature differences of main heat exchangers of ASAHP are taken as 10 °C for evaporator, 10 °C for generator, 5 °C for absorber, and 5 °C for condenser. The heat efficiency of coal boiler is average 70 % and the value of gas boiler is taken as 90 %. As electricity power based on coal generation is the most widely used in China, so the generation efficiency 33 % is used to convert the electricity to primary energy [1]. The results are illustrated in Fig. 59.3.

It can be found in Fig. 59.3 that ASEHP has the highest primary energy efficiency when the ambient temperature is above 28 °C, while the direct gas-fired ASAHP always performs the best when the ambient temperature is below 28 °C. And the hot water-driven ASAHP starts to perform better than ASEHP when the ambient temperature gets lower than 21 °C. Besides, the primary energy efficiency of ASEHP even turns worse than that of gas boiler when the ambient temperature is below −6 °C.

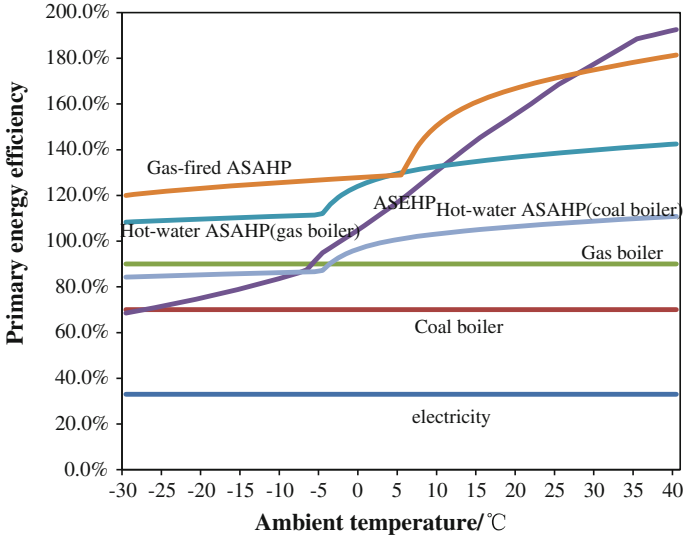

Fig. 59.3 Primary energy efficiency of different heating and domestic hot water systems

In a word, the primary energy efficiency of ASAHP is generally higher than that of ASEHP except when the air temperature is very high, at which domestic hot water is demanded in summer.

59.4 Applicability of Different Systems in Different Areas

Five typical cities in different kind of areas are chosen to investigate the applicability of different heating and domestic hot systems in China, i.e. Guangzhou (hot summer and warm winter), Guiyang (temperate), Wuhan (hot summer and cold winter), Beijing (cold) and Harbin (severe cold). The dry-bulb temperature throughout the year is divided into different ranges with a step of 5 °C to describe the weather characteristics of the typical cities, as shown in Fig. 59.4.

Based on the primary energy efficiency in Fig. 59.3 and the weather characteristics in Fig. 59.4, the most suitable system can be selected to supply heating and domestic hot water for different regions, on the point of view of energy conversion.

It can be summarized that both ASEHP and ASAHP are efficient in the hot summer and warm winter area to provide whole-year domestic hot water. But if the hours when air temperature is above 28 °C is relatively less than the remaining hours, which may happen in most cities in south China, the ASAHP is a better choice. In hot summer and cold winter area, as well as temperate area, direct gas-fired ASAHP is the best choice for both heating and domestic hot water, while hot water-driven ASAHP using gas boiler is the second choice for heating in winter and ASEHP is the second choice for domestic hot water in the whole year.

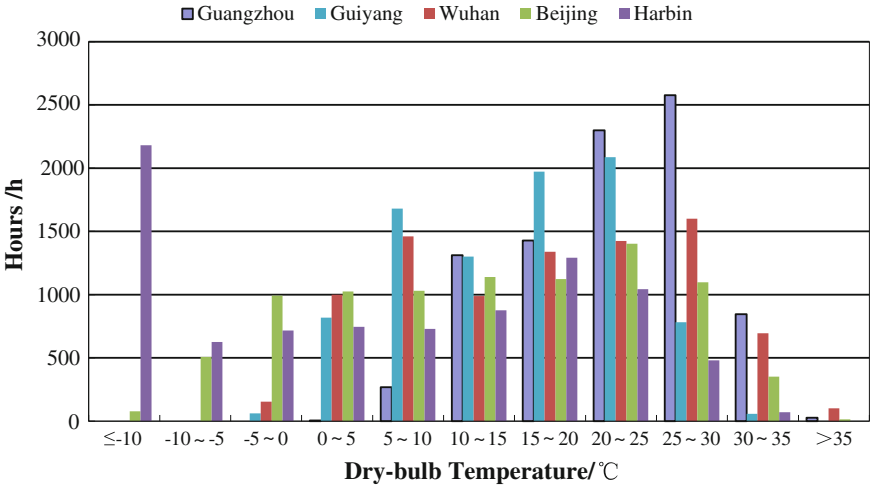

Fig. 59.4 The weather characteristics of the typical cities

As for North China (cold and severe cold region), direct gas-fired ASAHP and hot water-driven ASAHP using gas boiler are the first and second choice for both heating and domestic hot water.

59.5 Conclusion

Heating and domestic hot water system based on ASAHP with different absorption cycles and driving sources are analyzed on the potential of improving the energy efficiency of traditional systems. It can be concluded as follows:

(1) The primary energy efficiency of ASAHP is generally higher than that of ASEHP except when the air temperature is very high;
(2) Both ASEHP and ASAHP are efficient in the hot summer and warm winter area for domestic hot water. Direct gas-fired ASAHP is the best choice for both heating and domestic hot water in hot summer and cold winter area, temperate area, cold area as well as severe cold area;
(3) Hot water-driven ASAHP using gas boiler is the second choice for heating in hot summer and cold winter area as well as temperate area, and for both heating and domestic hot water in cold and severe cold areas. ASEHP is the second choice for domestic hot water in hot summer and cold winter area.

Acknowledgments The authors gratefully acknowledge the support from the Natural Science Foundation for Distinguished Young Scholars of China (Grant No. 51125030) and the National Basic Research Program of China (Grant No. 2010CB227305).

References

1. Tsinghua University Building Energy Saving Research Center (2011) 2011 annual report on China building energy efficiency. China Architecture and Building Press, Beijing (in Chinese)
2. Wang L, Chen X, Wang L et al (2011) Contribution from urban heating to China's 2020 goal of emission reduction. Environ Sci Technol 45:4676–4681
3. Liang CH, Zhang XS, Li XW et al (2011) Study on the performance of a solar assisted air source heat pump system for building heating. Energ Buildings 43(9):2188–2196
4. Cabrol L, Rowley P (2012) Towards low carbon homes—a simulation analysis of building-integrated air-source heat pump systems. Energ Buildings 48:127–136
5. Ma GY, Chai QH, Jiang Y (2003) Experimental investigation of air-source heat pump for cold regions. Int J Refrig 26(1):12–18
6. Ma GY, Chai QH (2004) Characteristics of an improved heat-pump cycle for cold regions. Appl Energy 77(3):235–247
7. Li XT, Shi WX, Dong LY et al (2010) Heat multiple heat exchanger unit: Chinese patent ZL201019114015.X
8. Li XT, Wu W, Zhang XL et al (2012) Energy saving potential of low temperature hot water system based on air source absorption heat pump. Appl Therm Eng 48(1):317–324
9. Wu W, Zhang XL, Li XT et al (2012) Comparisons of different working pairs and cycles on the performance of absorption heat pump for heating and domestic hot water in cold regions. Appl Therm Eng 48(1):349–358
10. Du S, Wang RZ, Lin P et al (2012) Experimental studies on an air-cooled two-stage NH_3–H_2O solar absorption air-conditioning prototype. Energy 45(1):581–587
11. Karamangil MI, Coskun S, Kaynakli O et al (2010) A simulation study of performance evaluation of single-stage absorption refrigeration system using conventional working fluids and alternatives. Renew Sust Energ Rev 14(7):1969–1978
12. Sun DW (1998) Comparison of the performances of NH_3–H_2O, NH_3–$LiNO_3$ and NH_3–NaSCN absorption refrigeration systems. Energ Convers Manage 39(5–6):357–368

Chapter 60
Match Properties of Heat and Mass Transfer Processes in the Internally-Cooled Liquid Desiccant System

Jingjing Jiang, Xiaohua Liu and Yi Jiang

Abstract Liquid desiccant system is more and more popular in the air-conditioning system. This paper focuses on the match property analyses of the internally-cooled liquid desiccant system. The unmatched coefficients both of the sensible heat transfer process between the desiccant and the cooling medium and the coupled heat and mass transfer process between the desiccant and the air were defined for the internally-cooled device. Numerical model of the dehumidifier was established for calculating the unmatched coefficients. Match properties of different kinds of liquid desiccant systems under various boundary conditions were then compared. The results show that the internally-cooled device has much smaller unmatched coefficients compared to the two-flow devices (adiabatic dehumidifier and sensible heat exchanger). The unmatched coefficients are good indicators for system improvement with identical heat and mass transfer area.

Keywords Unmatched coefficient · Internally-cooled · Liquid desiccant · Heat resistance · Closed wet cooling tower

60.1 Introduction

Liquid desiccant air-conditioning system is drawing increasing attention nowadays due to its high efficiency of dealing with latent load and the possibility of utilizing low-grade thermal energy (solar, waste heat, etc.) [1–3]. Dehumidifier is one of the key components in the system, which can be classified into adiabatic type and internally-cooled type [4]. The internally-cooled dehumidifier with extra cooling medium, such as cooling water, cooling air, refrigerant, etc. combines heat transfer

J. Jiang (✉) · X. Liu · Y. Jiang
Department of Building Science, Tsinghua University,
Beijing 100084, China
e-mail: cindy_19890201@sina.com

A. Li et al. (eds.), *Proceedings of the 8th International Symposium on Heating, Ventilation and Air Conditioning*, Lecture Notes in Electrical Engineering 262,
DOI: 10.1007/978-3-642-39581-9_60,

process between the cooling medium and the desiccant and coupled heat and mass transfer process between the humid air and the desiccant into one device, which is believed to be one of the most promising development directions of the liquid desiccant air-conditioning systems.

Researches concerning internally-cooled liquid desiccant system have been conducted by carrying out experiments [1, 6–8] and solving numerical or theoretical models [4, 9–12]. A lot of efforts have been put into optimizing the operation of the system. Liu et al. [4] analysed the effect of the flow pattern on the dehumidification performance. Bansal et al. [8] optimized the flow rate ratio of the desiccant to the air. Khan [10] analysed the influence of the inlet parameters on the dehumidification performance. The evaluation indices of these researches are usually dehumidification rate and thermal efficiency, which could not accurately diagnose the performance restriction point of the design or give directional guidance for the modification of the system, although they are effective when comparing different operation conditions.

Zhang et al. [13] specifically proposed the concept of match properties and introduced unmatched coefficients based on entransy analyses [14, 15] to quantificationally evaluate the match properties and help to point out the performance restrictions caused by improper flow pattern, flow rate ratio, or inlet parameters. This research method has been proved to be useful when studying the adiabatic liquid desiccant system and sensible heat exchanger.

Since the match property analyses of the internally-cooled liquid desiccant system has not been involved yet, this paper is aiming at understanding and describing the match properties of the internally-cooled system. Two kinds of unmatched coefficients derived from the entransy loss method are defined and calculated under different boundary conditions. The comparison between the internally-cooled and the pre-cooled adiabatic dehumidifiers from the view of match properties is launched. The research method and the conclusions in this paper are also applicable in other complicated heat and mass transfer systems with three-fluids functioning in the same device, like the closed wet cooling tower, etc.

60.2 Heat and Mass Transfer Model

Figure 60.1 shows the schematic of a typical internally-cooled cross-flow dehumidifier, which is the most popular flow pattern in literatures [4–7]. Define the cooling medium flow direction as z axis and the desiccant flow direction as x axis. The height and thickness of the dehumidifier is H and L, respectively. Cooling water is selected as the cooling medium here. The energy balance equation for the three fluids is:

$$c_{p,w}\frac{\dot{m}_w}{H}\frac{\partial t_w}{\partial z}-\frac{\dot{m}_a}{L}\frac{\partial h_a}{\partial x}+\frac{1}{L}\frac{\partial(\dot{m}_s h_s)}{\partial x}=0 \tag{60.1}$$

where $\dot{m}$ is the mass flow rate, t is the temperature, h is the enthalpy, $c_{p,w}$ is the specific heat of the cooling medium. The subscripts a, s and w represent air, liquid desiccant and cooling water, respectively.

The mass conservation equation of the desiccant and the air, and the solute conservation equation of the liquid desiccant are given by:

$$-\dot{m}_a \frac{\partial \omega_a}{\partial x} + \frac{\partial \dot{m}_s}{\partial x} = 0 \tag{60.2}$$

$$d(\dot{m}_s X_s) = 0 \tag{1.3}$$

where ω is the humidity ratio of the air and X_s is the desiccant concentration.

The sensible heat transfer process between the desiccant and the cooling water is expressed as:

$$\frac{\partial t_w}{\partial x} = \frac{\mathrm{NTU}_h}{H}(t_s - t_w) \tag{60.4}$$

The total heat exchange and the moisture exchange between the air and the desiccant are given as Eqs. (60.5) and (60.6). The subscript of e means the state of the air in equilibrium with the desiccant.

$$\frac{\partial h_a}{\partial x} = -\frac{\mathrm{NTU}_m \cdot Le}{H}\left[(h_e - h_a) + r\left(\frac{1}{Le} - 1\right)(\omega_e - \omega_a)\right] \tag{60.5}$$

$$\frac{\partial \omega_a}{\partial x} = -\frac{\mathrm{NTU}_m}{H}(\omega_e - \omega_a) \tag{60.6}$$

The dimensionless numbers in Eqs. (60.4)–(60.6) are defined as:

$$\mathrm{NTU}_h = \frac{\alpha_w A}{c_{p,w}\dot{m}_w},\ \mathrm{NTU}_m = \frac{\alpha_m A}{\dot{m}_a},\ \mathrm{Le} = \frac{\alpha}{\alpha_m c_{p,m}} \tag{60.7}$$

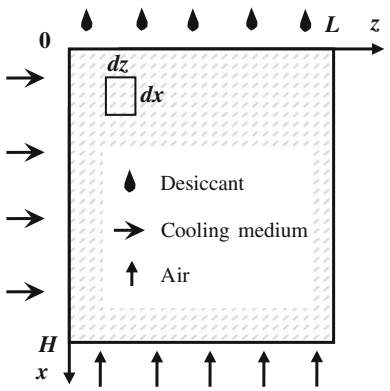

Fig. 60.1 The schematic of the internally-cooled dehumidifier

where α_w is the heat transfer coefficient between the cooling water and the desiccant, α_m and α are the mass transfer and sensible heat transfer coefficients between the air and the desiccant, A is the heat and mass transfer area of the dehumidifier. $c_{p,m}$ is the specific heat of the moist air.

60.3 Unmatched Coefficients

Two kinds of unmatched coefficients are introduced to describe the match properties of the internally-cooled liquid desiccant system. ξ_h is defined for the sensible heat transfer process between the desiccant and the cooling medium, while ξ_m is for the mass transfer process between the air and the desiccant.

60.3.1 Definition

The definitions of the unmatched coefficients are based on the entransy loss theory [14]. Since analytical solution of the entransy loss is not available for the three-flow internally-cooled dehumidifier, the transfer loss is numerically calculated in present paper. For the two-dimensional cross-flow dehumidifier, the total entransy loss is the integration of that in each control volume. For any control volume, shown in Fig. 60.2a, the desiccant state is influenced by the air and the cooling water simultaneously. As indicated in Fig. 60.2b, the entransy dissipation of the heat transfer process ($\Delta J_{\text{loss},\ h}$) between the desiccant and the cooling medium is the area of the shaded part [14]. The entransy dissipation of the mass transfer ($\Delta J_{\text{loss},m}$) process between the air and the desiccant is the shaded area in Fig. 60.2c. The entransy loss for each control volume and the whole device could be calculated from Eqs. (60.8) and (60.9).

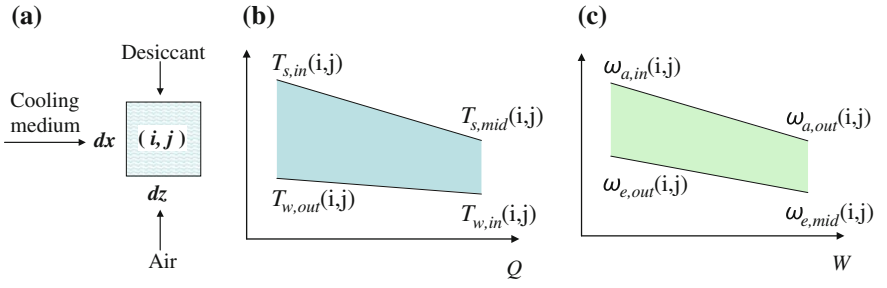

Fig. 60.2 Schematics of the entransy loss in any control volume, **a** control volume location, **b** heat transfer T–Q diagram, **c** mass transfer ω–W diagram

$$\Delta J_{\text{loss},h}(i,j) = \frac{1}{2} Q(i,j)\left[T_{s,in}(i,j) + T_{s,\text{mid}}(i,j) - T_{w,in}(i,j) - T_{w,\text{out}}(i,j)\right] \quad (60.8)$$

$$\Delta J_{\text{loss},m}(i,j) = \frac{1}{2} W(i,j)\left[\omega_{a,in}(i,j) + \omega_{a,\text{out}}(i,j) - \omega_{e,\text{mid}}(i,j) - \omega_{e,\text{out}}(i,j)\right] \quad (60.9)$$

where Q is the sensible heat exchange between the cooling medium and the desiccant, W is the moisture exchange during the dehumidification process.

As a consequence, the heat and mass transfer resistances (R_h and R_m) and unmatched coefficients are [13, 14]:

$$R_h = \frac{\Delta J_{\text{loss},h}}{Q^2},\ R_m = \frac{\Delta J_{\text{loss},m}}{W^2} \quad (60.10)$$

$$R_h = \frac{\xi_h}{\alpha_w A},\ R_m = \frac{\xi_m}{\alpha_m A} \quad (60.11)$$

The unmatched coefficient (ξ_h or ξ_m) is equal to or higher than 1. Only when perfect match property is achieved [14], ξ_h and ξ_m equal to 1. Equation (60.11) implies that the heat and mass transfer resistances are caused by limited contacting area and improper match properties. As increasing heat and mass transfer area is accompanied by remarkable rise of the initial investment, trying to improve match properties is sometimes a more economical and effective way. As indicated by Eq. (60.11), the larger unmatched coefficient (ξ_h or ξ_m), the smaller of the increased heat or mass transfer area contributes to the system performance improvement.

60.3.2 Typical Value in the Internally-Cooled System

Unmatched coefficients of two typical internally-cooled dehumidifiers are calculated in this section. The cooling media are refrigerant and cooling water, respectively. The calculation conditions are listed in Table 60.1. NTU_h is changed from 0 to 5, while NTU_m is from 0 to 2.5. LiBr solution is utilized as the desiccant.

60.3.2.1 Refrigerant as the Cooling Medium

Figure 60.3 represents the numerical results of the refrigerant-cooling dehumidifier. The results of $\text{NTU}_h = 0$ imply the adiabatic dehumidifier condition, while

Table 60.1 Calculation conditions

	T_{in}/°C	ω (kg/kg)/X (%)	$\dot{m}$ (kg/s)
Air	35	0.018	1
Desiccant	30	45	0.1 (solute flow rate)
Cooling medium	10	–	1

those of $NTU_m = 0$ belong to the sensible heat exchanger condition. As shown in Fig. 60.3a, ξ_m of the adiabatic dehumidifier monotonously grows with the increase of NTU_m, which demonstrates the impact of unmatched coefficients on the system performance is protruded when enough heat and mass transfer area is inputted. The same principle applies to ξ_h.

When it comes to the refrigerant-cooling dehumidifier, the unmatched coefficients ξ_m and ξ_h have a significant decrease compared to those of the two-flow devices, shown in Fig. 60.3a and b. Even a little heat transfer area input, e.g. $NTU_h = 0.3$, will make a difference to the mass transfer ξ_m, from 1.62 to 1.09 when $NTU_m = 1$. So is the sensible heat transfer condition. It is believed that the three-flow internally-cooled device has the self-adjust ability in terms of the match property, which is rather good for the system performance. From another perspective, since the unmatched coefficients of the internally-cooled dehumidifier under the condition of abundant NTU inputs are varied in a narrow band, the contribution of the match property improvement inside the three-flow device would not be so distinct in contrast with the two-flow heat and mass transfer processes.

Figure 60.3c displays the variation of the air outlet humidity ratio with different NTU_m and NTU_h. $\omega_{a,\text{out}}$ decreases monotonously both with the rise of NTU_m and NTU_h, which corroborates that more area input, better heat and mass transfer performance. Although the input area increases proportionally with the growth of

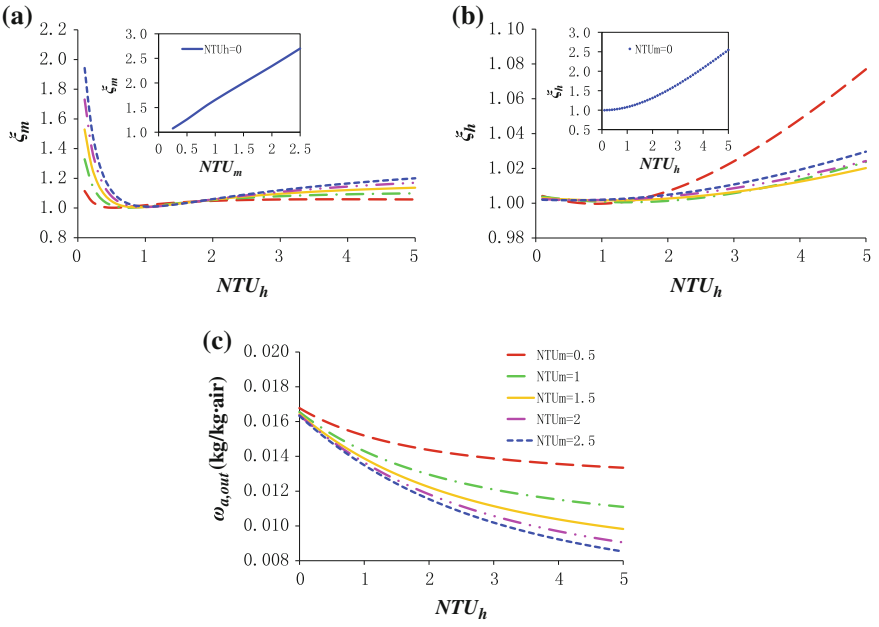

Fig. 60.3 Numerical results of the refrigerant-cooling dehumidifier, **a** mass transfer unmatched coefficient ξ_m, **b** heat transfer unmatched coefficient ξ_h, **c** air outlet humidity ratio $\omega_{a,\text{out}}$

the NTU, the improvement of the dehumidification performance has a lower trend when NTU is larger. When NTU_h is 4, ξ_m rises from 1.06 to 1.17 when NTU_m changes from 0.5 to 2.5, which indicates that the disadvantage caused by improper match properties is strengthened, i.e. the contribution of the added input area is weakened according to Eq. (60.11). As a consequence, the moisture removal rate increases by 3.18 g/s when NTU_m varies from 0.5 to 1.5, while the increase rate slows down to 1.15 g/s when NTU_m varies from 1.5 to 2.5.

60.3.2.2 Cooling Water as the Cooling Medium

Figure 60.4 shows the match property and the dehumidification performance of the water-cooling dehumidifier. Since the heat capacity $\dot{m}c_p$ difference between the water and the desiccant is much smaller than that between the refrigerant and the desiccant, the flow matching property is meliorated in the water-cooling system [13]. As a result, the unmatched coefficients ξ_h and ξ_m are decreased when introducing cooling water as the cooling medium, shown in Fig. 60.4b.

Although the water-cooling dehumidifier has better match property, the dehumidification performance seems worse compared to the refrigerant-cooling device, shown in Fig. 60.4c. The reason is that the average temperature of the cooling water is higher than that of the refrigerant with the same inlet temperature, shown

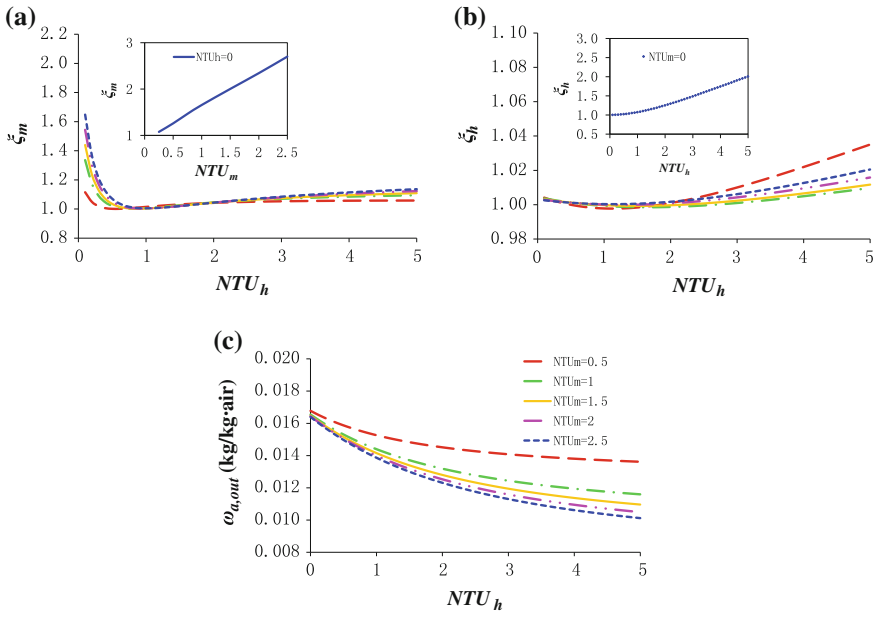

Fig. 60.4 Numerical results of the water-cooling dehumidifier. **a** mass transfer unmatched coefficient ξ_m, **b** heat transfer unmatched coefficient ξ_h, **c** air outlet humidity ratio $\omega_{a,\text{out}}$

in Table 60.1. There is reason to believe that the performance of the water-cooling dehumidifier could be better when the average temperature of the cooling medium is identical.

60.4 Application of the Unmatched Coefficients

The conventional pre-cooled adiabatic liquid desiccant air-conditioning system is displayed in Fig. 60.5b, in which there are an adiabatic dehumidifier and a counter flow sensible heat exchanger. The desiccant is cooled by the refrigerant before going to the dehumidifier. Figure 60.5a describes the internally-cooling dehumidifier, where desiccant is cooled when dehumidifying air. The dehumidification performance is analyzed from the view of match property.

The boundary conditions are listed in Table 60.1, and the typical parameters are shown in Fig. 60.5. The results show that with the same inlet fluid parameters and the same NTU_m and NTU_h, the internally-cooled dehumidifier has smaller ξ_m and ξ_h, due to the self-adjust characteristic stated in the earlier part. Moreover, the air outlet humidity ratio is also lower in the internally-cooled device, which supports that the internally-cooled dehumidifier has better dehumidification behavior than the adiabatic one. The gap of the dehumidification performance between the two dehumidifiers is bigger when NTU_m and NTU_h is larger, which illustrates that the match property is a good indicator for performance assessment and improvement (Fig. 60.6).

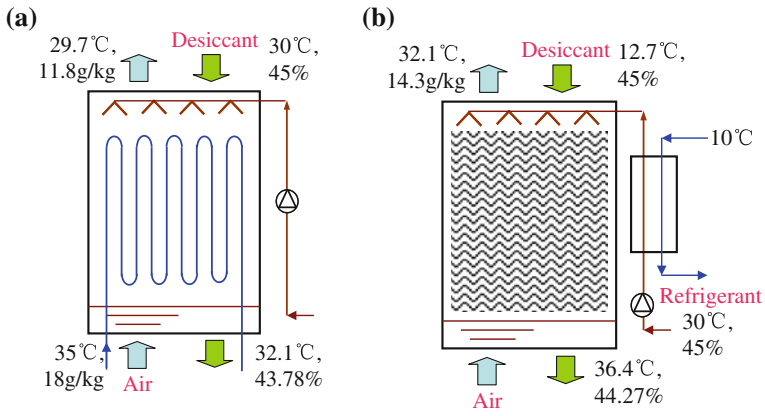

Fig. 60.5 Schematics of **a** internally-cooled dehumidifier and **b** adiabatic dehumidifier + heat exchanger (typical parameters for $NTU_m = 2$ and $NTU_h = 2$)

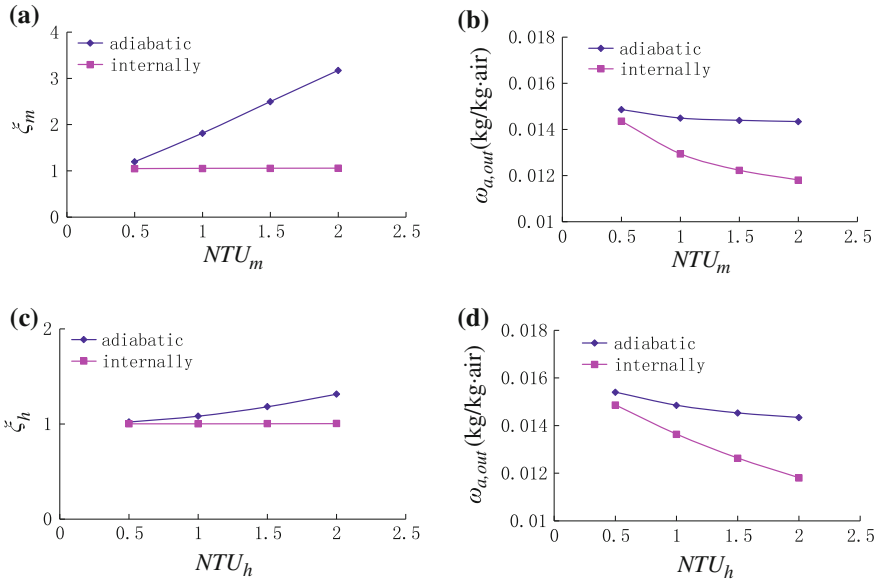

Fig. 60.6 Match properties and dehumidification performance of two kinds of liquid desiccant system. **a** ξ_m, **b** $\omega_{a,\text{out}}$ with different NTU_m, **c** ξ_h, **d** $\omega_{a,\text{out}}$ with different NTU_h

60.5 Conclusion

Numerical model of the internally-cooled dehumidifier was established in this paper to calculate and analyze the match properties of the liquid desiccant system. The definition and calculation method of the unmatched coefficients in the three-flow internally-cooled device was also developed. The typical unmatched coefficients in the refrigerant-cooling and water-cooling dehumidifiers were calculated and compared. The match properties and dehumidification performance of two kinds of liquid desiccant systems were compared. The main conclusions can be summarized as follows:

(1) The unmatched coefficients are direct indicators of whether or not the limited heat and mass transfer area is fully utilized. The larger the unmatched coefficient, the smaller the increased heat or mass transfer area contributes to the system performance improvement.
(2) The match properties of the three-flow internally-cooled device are better than the two-flow heat and mass transfer devices, which indicates that the internally-cooled device has the ability of self-adjust in terms of match properties;
(3) The internally-cooled dehumidifier has better performance than the pre-cooled adiabatic liquid desiccant system due to better match properties.

Acknowledgments The authors appreciate the support from the National Natural Science Foundation of China (No. 51138005) and the foundation for the author of National Excellent Doctoral Dissertation of China (No. 201049).

References

1. Jain S, Dhar PL, Kaushik SC (2000) Experimental studies on the dehumidifier and regenerator of a liquid desiccant cooling system. Appl Therm Eng 20(3):253–267
2. Peng CSP, Howell JR (1981) Analysis and design of efficient absorbers for low-temperature desiccant air conditioners. J Sol Energy 103:67–74
3. Xiong ZQ, Dai YJ, Wang RZ (2010) Development of a novel two-stage liquid desiccant dehumidification system assisted by $CaCl_2$ solution using exergy analysis method. Appl Energy 87(5):1495–1504
4. Liu XH, Chang XM, Xia JJ, Jiang Y (2009) Performance analysis on the internally cooled dehumidifier using liquid desiccant. Build Environ 44(2):299–308
5. Kessling W, Laevemann E, Kapfhammer C (1998) Energy storage for desiccant cooling systems component development. Sol Energy 64(4–6):209–221
6. Zhang XS, Yin YG, Gao YR (2004) Experimental study of dehumidification performance of liquid desiccant cooling system with energy storage. J Therm Sci Tech 3(1):60–64 (in Chinese)
7. Saman WY, Alizadeh S (2002) An experimental study of a cross-flow type plate heat exchanger for dehumidification/cooling. Sol Energy 73(1):59–71
8. Bansal P, Jain S, Moon C (2011) Performance comparison of an adiabatic and an internally cooled structured packed-bed dehumidifier. Appl Therm Eng 31(1):14–19
9. Khan AY (1998) Cooling and dehumidification performance analysis of internally-cooled liquid desiccant absorbers. Appl Therm Eng 18(5):265–281
10. Khan AY, Sulsona FJ (1998) Modeling and parametric analysis of heat and mass transfer performance of refrigerant cooled liquid desiccant absorbers. Int J Energy Res 22(9):813–832
11. Yin YG, Zhang XS (2010) Comparative study on internally heated and adiabatic regenerators in liquid desiccant air conditioning system. Build Environ 45(8):1799–1807
12. Ren CQ, Tu M, Wang HH (2007) An analytical model for heat and mass transfer processes in internally cooled or heated liquid desiccant-air contact units. Int J Heat Mass Tran 50(17):3545–3555
13. Zhang T, Liu XH, Zhang L, Jiang Y (2012) Match properties of heat transfer and coupled heat and mass transfer processes in air-conditioning system. Energy Convers Manage 59:103–113
14. Guo ZY, Zhu HY, Liang XG (2007) Entransy—A physical quantity describing heat transfer ability. Int J Heat Mass Tran 50(13–14):2545–2556
15. Chen Q, Ren JX (2008) Generalized thermal resistance for convective heat transfer and its relation to entransy dissipation. Chinese Sci Bull 53(23):3753–3761

Chapter 61
Frosting Characteristics of Fin-Tube Heat Exchanger at Temperature Range of −18 to 6 °C of a Cascade Heat Pump

Xing Han, Wei Fan, Jianbo Chen and Qiuhuo Chen

Abstract The frost on the heat exchanger of the air-source heat pump has a great influence of the operating performance. The frosting experiment based on a cascade type air-source heat pump water heater is carried out in the enthalpy-difference in this paper, and the outdoor evaporator of the unit is a finned-tube heat exchanger. In addition, the outdoor environmental conditions include that the outdoor temperature is from −18 to 6 °C and outdoor relative humidity is from 70 to 90 % in this experiment. Experimental results are described below. First of all, the amount of frosting almost changes linearly with the frosting time which is of maximum in this outdoor temperature range of −3 to 3 °C, and the lower outdoor temperature, the more frosting amount; Second, the outdoor relative humidity has a great influence of the quantity, and the more humidity, the more frosting quantity. Finally, the frosting factor is from 6.51 to 10.31 kg/(m^2·°C·min) and the average value is 8.58×10^{-4} kg/(m^2·°C·min), based on the relationships of the area and form of evaporator coil, the time of frosting, the difference of the dew point temperature, and the temperature on the evaporator coil and the frosting quantity.

Keywords Air-source heat pump · Finned-tube heat exchanger · Outdoor temperature · Outdoor humidity · The frosting amount

X. Han (✉) · W. Fan · J. Chen · Q. Chen
School of Environment and Architecture, University of Shanghai for Science and Technology, Jun Gong Road 516, Shanghai, China
e-mail: hanxing@usst.edu.cn

A. Li et al. (eds.), *Proceedings of the 8th International Symposium on Heating, Ventilation and Air Conditioning*, Lecture Notes in Electrical Engineering 262,
DOI: 10.1007/978-3-642-39581-9_61,

61.1 Introduction

The frosting and defrosting are one of important factors which restrict the development of air-source heat pump, and the defrosting is based on the frosting researches. Therefore, before the defrost study, the frost layer performances including frost amount are obtained by frost experiment in this paper.

The former academics [1, 2] found the amount of frosting almost changes linearly with the frosting time which is of maximum in this outdoor temperature (about 0 °C), and the more outdoor relative humidity, the more frost amount. To the amount of frosting, some measurement methods were performed by researchers, including weighing method and indirect calculation method. The former is as follows: Senshu T [3] got the amount of frosting by measuring the difference between the quality of the finned-tube heat exchanger before and after frost, and the finned-tube of the heat exchanger could be removed freely. Xia Y [4] saw the quality of defrost water as the amount of frost, and the water amount was measured by the electric balance in a defrost cycle (it is from frost to defrost end). Shinhyuk Yoo [5] placed a removable aluminum tape on the surface of the heat exchanger and measured the difference between the quality of the aluminum tape before and after frost. The amount difference was the frost amount. Another one was found by 0'Neal [6] that it was calculated by measuring the air flow and import and export humidity ratio through the evaporator. In summary, the later method is implemented easily and used widely by lots of domestic and foreign researchers [7, 8].

Currently, the frost study is mainly in the easy frosting area (outdoor temperature is from −7 to 5 °C) [8, 9, 10] and seldom in the lower outdoor temperature. Guo Xianmin [2] researched the frost problem in a lager outdoor temperature area (−7 to 5 °C), but pointing out a serious frost area merely. And Luo Chao [11] discussed only the performance of the evaporator under frosting conditions in an outdoor temperature (−18 °C). At the same time, Liu Feng zhen [12] believed that the performance of the evaporator was made a great influence by the outdoor relative humidity and the study should focus on inhibition frost. Because the experimental study of frosting and defrosting features based on the cascade type air-source heat pump water heater which can operate in the lower outdoor temperature (< −10 °C) in some situations, the frost performance should be discussed not only in the easy frosting area (outdoor temperature is from −6 to 6 °C), but also in the lower outdoor temperature (from −18 to −6 °C) in this paper.

61.2 Experimental Apparatus and Methods

61.2.1 Experimental Apparatus

The cascade type air-source heat pump water heater can achieve the goal of the production of 80 °C hot water under the ultralow temperature environment (−25 °C). The system consists of a low temperature level cycle and a high temperature level cycle. In the low temperature level cycle, R410A is used as the refrigerant, while in the high temperature level cycle R134A is used as the refrigerant. The schematic and physical pictures are shown in Figs. 61.1 and 61.2.

The parameters of the outdoor fin-tube heat exchanger are shown in Table 61.1.

In addition, the experiment was carried out in the enthalpy-difference lab, and the low temperature level cycle lies in the outdoor side of the lab, while the high temperature level cycle lies in the indoor of the one. The performance of this unit including coefficient of performance (COP), suction and discharge pressure, and temperature and heating capacity, etc., can be read out by the data acquisition system of the lab.

To the frost amount, the air flow and import and export air temperature and relative humidity through the evaporator need to be measured by nine Italian Delta

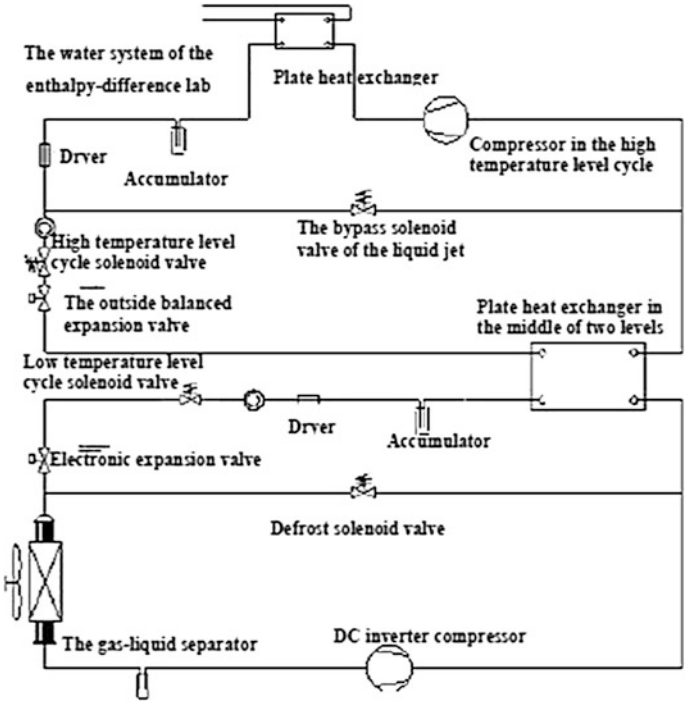

Fig. 61.1 The cascade type system diagram

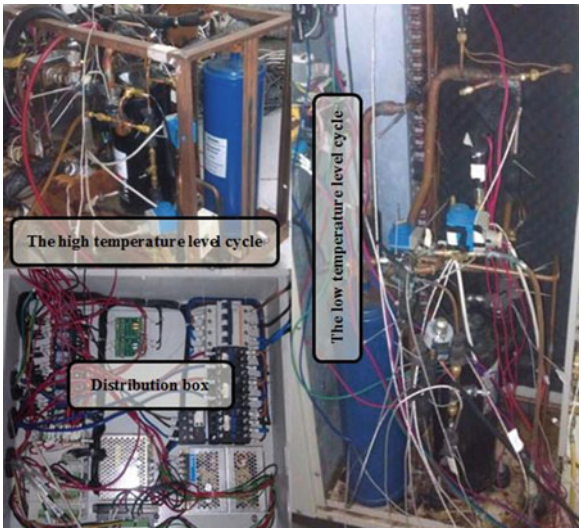

Fig. 61.2 The cascade type system picture

Table 61.1 Outdoor fin-tube heat exchanger parameters

Row spacing (S_2)	18.19 mm	Tube diameter	7.35 mm
Tube spacing (S_1)	21 mm	Tube thickness	0.25 mm
Fin thickness ()	0.115 mm	Total heating exchanging area	23.145 m^2
Fin spacing (S_f)	2 mm		

OHE universal anemometers and 14 temperature and humidity sensors known as E + E21. The formula is as follows:

$$\Delta M = m_a \Delta\tau (d_{in} - d_{out}) \tag{61.1}$$

where ΔM is the amount of frosting in the low temperature level cycle of the unit in same time, g; d_{in} and d_{out} are respectively import and export humidity ratio through the evaporator, g/kg; *ma* is the air flow through the evaporator, kg/s; $\Delta\tau$ is the frost time, s.

61.2.2 Experimental Methods

61.2.2.1 Measuring Points

a) The export temperature and humidity sensors arrangements

The export consists of two 52 mm diameter fan ports in the low temperature cycle. To the accurate temperature and humidity, the distribution measurement points are shown as Fig. 61.3

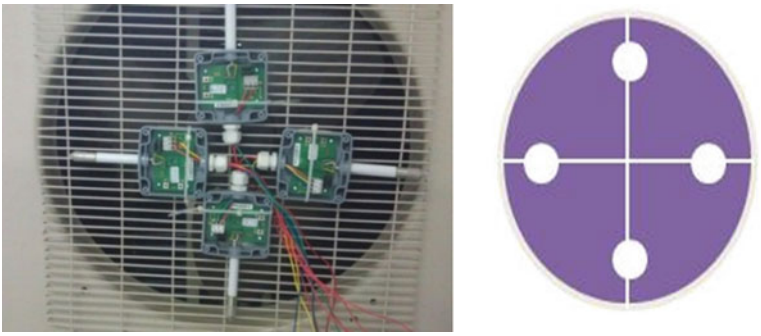

Fig. 61.3 Temperature and humidity sensors arrangements in the export of the evaporator

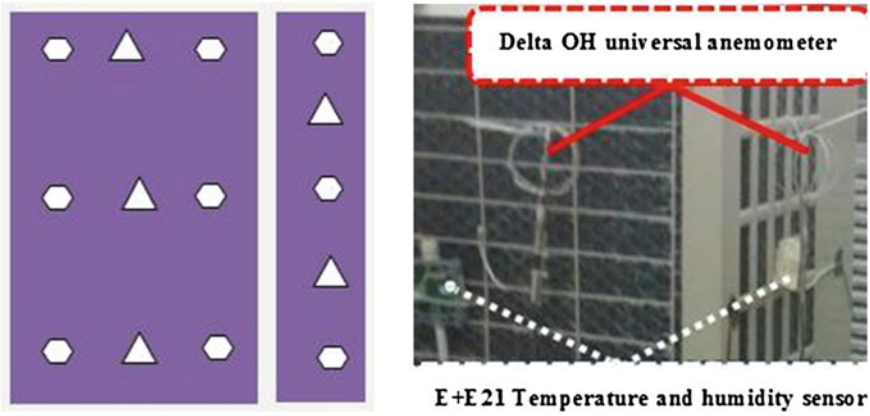

Fig. 61.4 Temperature and humidity sensors and velocity arrangements in the import of the evaporator

b) The import temperature and humidity sensors and velocity arrangements

The import of the low temperature cycle is a L-shaped finned-tube heat exchanger. To the average temperature and humidity, five measuring points shown as Fig. 61.4 (triangles in Fig. 61.4) are arranged in this import. To the average air velocity, six measuring points shown as Fig. 61.4 (rounds in Fig. 61.4) are arranged in this import.

c) the important parameters of this unit measuring points

Besides of temperature and humidity, some performance parameters of the air-source heat pump systems are also measured in the frost experiment. These parameters shown in Fig. 61.5 include the evaporator coil temperature in the low temperature level cycle and the intake and exhaust gas temperature and pressure in the high or low temperature level cycle, etc.

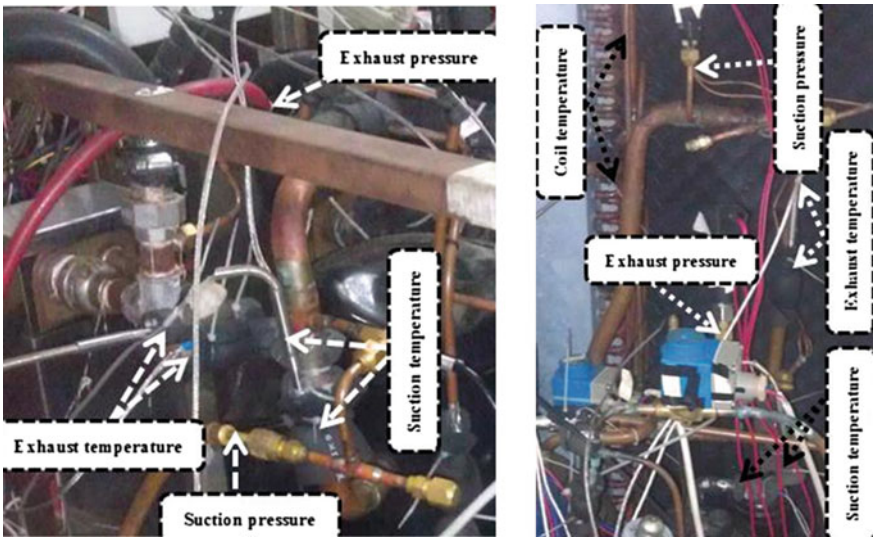

Fig. 61.5 The performance parameters of this unit (the *left* picture is high temperature level cycle and the *right* picture is low temperature level cycle)

Table 61.2 Experiment conditions (delegates the actual experiment conditions)

T (°C) RH (%)	6	3	0	−3	−6	−9	−12	−15	−18
70									
80									
90									

61.2.2.2 Experiment Conditions

Because this heat pump water heater operates in the larger outdoor temperature area, the frost experiments are not only in the easy frosting area (outdoor temperature is from −6 to 6 °C), but also in the lower outdoor temperature (from −18 to −6 °C) in this paper. In additions, outdoor relative humidity (70–90 % in the experiment) is also discussed. Based on the actual operational conditions in which the evaporator is not frost or the frosting is a long time or the higher humidity is not achieved in the enthalpy-difference lab, the outdoor conditions of temperature and humidity are in Table 61.2.

61.3 The Amount of Frosting

The frost experiment is in 20 outdoor conditions and the frost amount is obtained by Eq. 61.1.1. And the experiment pictures are shown in Figs. 61.6, 61.7 and 61.8 and got by shooting every 20 min.

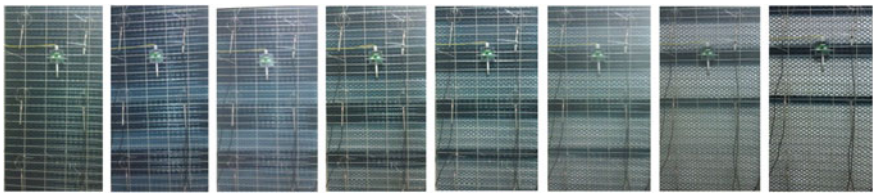

Fig. 61.6 The frost picture in the outdoor 0 °C temperature and 80 % relative humidity

Fig. 61.7 The frost picture in the outdoor −6 °C temperature and 80 % relative humidity

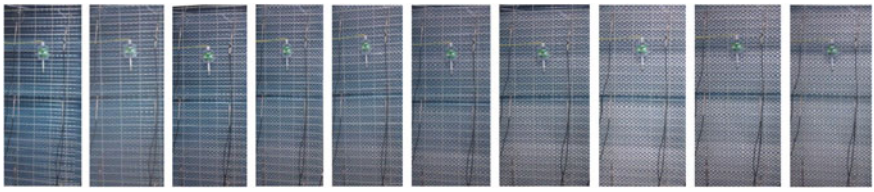

Fig. 61.8 The frost picture in the outdoor −12 °C temperature and 80 % relative humidity

61.3.1 The Frost Experiment in Different Outdoor Temperature

In 70 % outdoor relative humidity and different outdoor temperature, the relationship of frost amount and time is shown in Fig. 61.9. From Fig. 61.9, lower outdoor temperature, lower change rate of frost amount with time. But the rate of decrease is not large.

In 80 and 90 % outdoor relative humidity and different outdoor temperature, the relationships of frost amount and time are shown in Figs. 61.10 and 61.11. Figure 61.10 shows in this temperature area (−6 to 3 °C), the change rate of frost amount with time is almost of same (about 0.05 kg/min); but in another outdoor temperature area (−1 to −9 °C), the distribution of the amount with temperature is very obvious (when the frost time is 80 min, the proportions of the amount in −18 to −9 °C and in −9 °C are respectively 75.3, 63.6, 53.4, and 35.4 %), and lower outdoor temperature, lower change rate of frost amount with time. In summary, lower outdoor temperature, more difficult frosting.

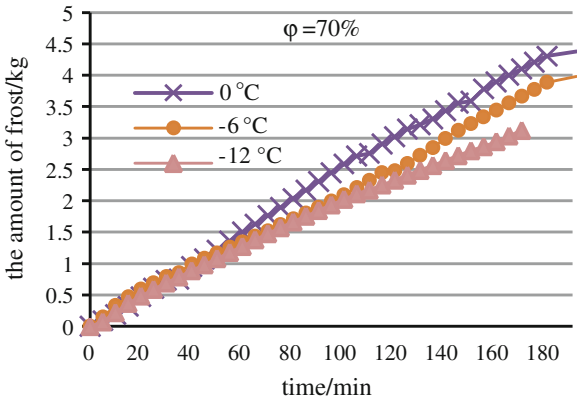

Fig. 61.9 The frost amount in different outdoor temperature and 70 % relative humidity

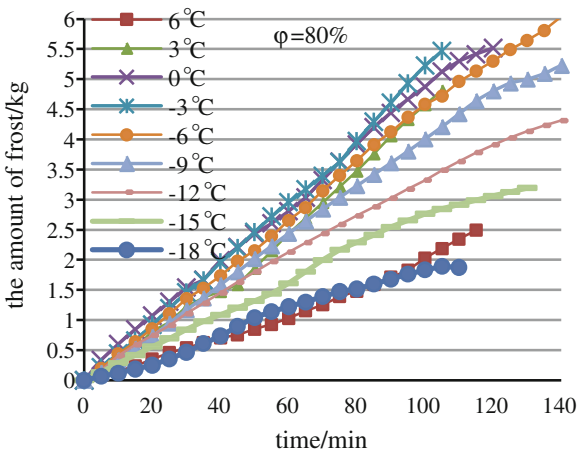

Fig. 61.10 The frost amount in different outdoor temperature and 80 % relative humidity

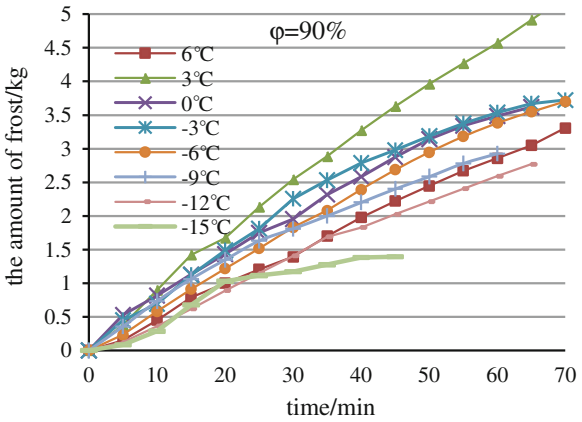

Fig. 61.11 The frost amount in different outdoor temperature and 90 % relative humidity

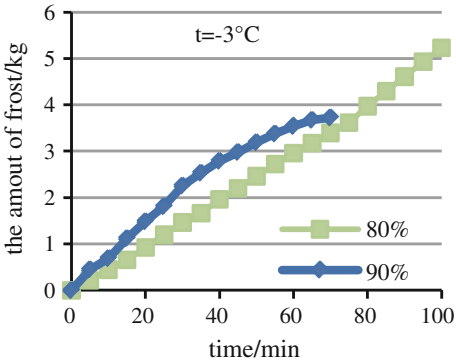

Fig. 61.12 The frost amount in different outdoor relative humidity and −3 °C temperature

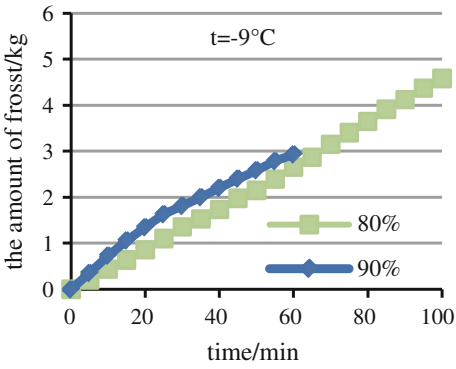

Fig. 61.13 The frost amount in different outdoor relative humidity and −9 °C temperature

The results of Fig. 61.11 are of same with one of Fig. 61.10. But the conditions of the most change rate of frost amount with time are different.

61.3.2 The Frost Experiment in Different Outdoor Humidity

Frosting amount under different outdoor air temperature and humidity are shown in Figs. 61.12, 61.13 and 61.14. The reason of above is that larger the humidity, the more moisture content of air, and easier frost. In addition, because the condition of 90 % RH is not achieved in −18 °C in the enthalpy-difference lab, the frost experiment is only in −18 °C or more outdoor temperature.

61.3.3 The Frost Amount in Different Outdoor Conditions and the Same Time

In the previous two sections, the result shows the change of the frost amount with time is almost liner. In order to compare the change rate of frost amount with time,

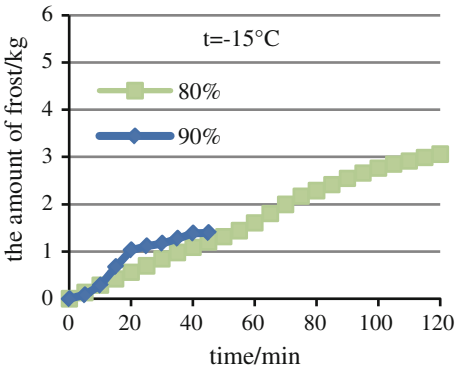

Fig. 61.14 The frost amount in different outdoor relative humidity and −15 °C temperature

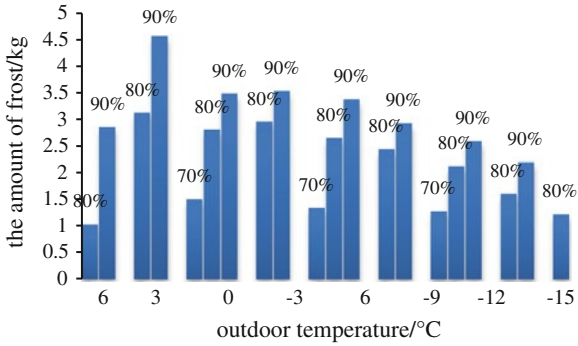

Fig. 61.15 The frost amount in different outdoor conditions in 60 min

the amount of frosting in 60 min is shown in Fig. 61.15 in different outdoor conditions.

From Fig. 61.15, the change rate of frost amount with time is almost equal in 70 % RH and most in this temperature area (−3 to 3 °C) in 80 and 90 % RH. And when temperature is −3 °C or less, lower outdoor temperature, lower change rate of frost amount with time.

61.4 Frost Factor

61.4.1 The Relationship of the Difference of the Dew Point Temperature and the Temperature on the Evaporator Coil and the Frosting Quantity

The relationship of the difference of the dew point temperature and the temperature on the evaporator coil (Δt_1) and the frosting quantity is shown in Figs. 61.16, 61.17 and 61.18 in 80 % outdoor relative humidity and this temperature area (−15

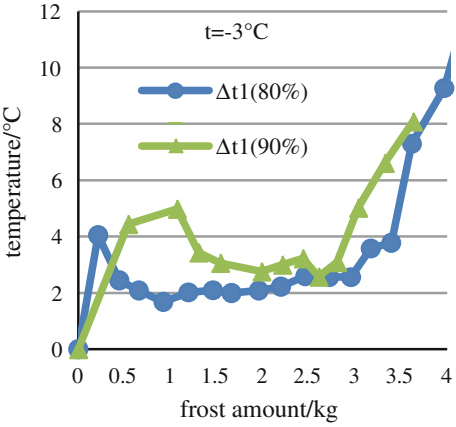

Fig. 61.16 The relationship of Δt_1 and frost quantity in −3 °C outdoor temperature

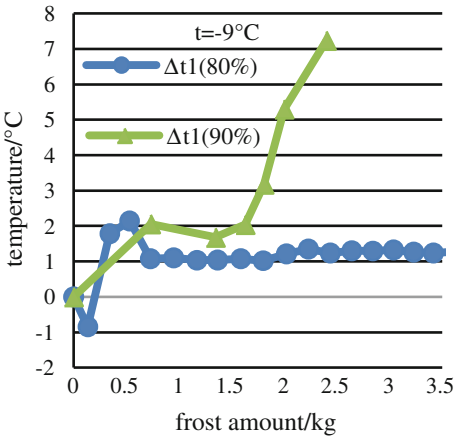

Fig. 61.17 The relationship of Δt_1 and frost quantity in −9 °C outdoor temperature

to 6 °C). Because of no dew point thermometer, the dew point temperature is calculated by the moister content formula. From Figs. 61.16, 61.17 and 61.18, Δt_1 is continuously rising with frosting. And as similar to the difference of outdoor temperature and the temperature on the evaporator coil (that is used in Time–temperature difference defrost control method [13]), Δt_1 can also be the determining conditions of defrost starting. Besides, frosting is caused by the difference of the partial pressure of water vapor in the air and on the finned-tube coil, while the dew point temperature and the temperature on the evaporator coil can be on behalf of the partial pressure of water vapor in the air and on the finned-tube coil respectively. In summary, the relationships of (Δt_1) and frost amount are studied in this paper.

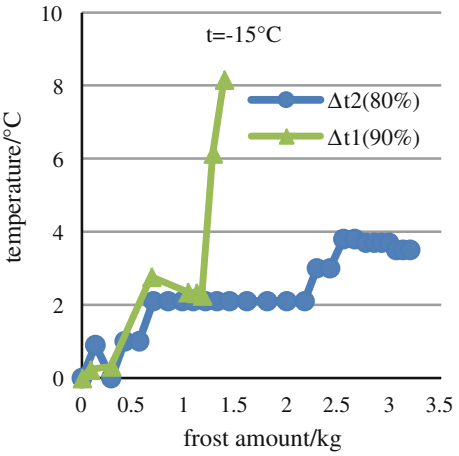

Fig. 61.18 The relationship of Δt_1 and frost quantity in −15 °C outdoor temperature

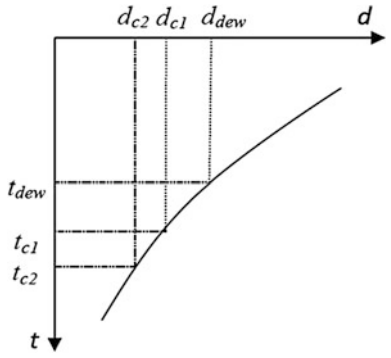

Fig. 61.19 The relationship of Δt_1 and Δd

61.4.2 Theoretical Base of Frost Factor Proposed

The reason of frost on the finned-tube coil is that the coil temperature is less than the dew point temperature in the air. So based on the difference of the air moisture content on the coil surface and in the outdoor dew point temperature (Δd), Δt_1 can also be frost amount and the determine conditions of defrost starting. And the relationship of Δt_1 and Δd is almost linear:

$$\frac{\Delta d}{\Delta d'} \approx \frac{\Delta t_1}{\Delta t_1'} \tag{61.2}$$

where Δd and $\Delta d'$ are respectively the difference of the air moisture content on the coil surface and the outdoor dew point temperature, that is $d_{\text{dew}}-d_c$ and $d_{\text{dew}}-d'_c$;Δt_1 and $\Delta t_1'$ the difference of the temperature on the coil surface and the outdoor dew point temperature, that is $t_{\text{dew}}-t_c$ and $t_{\text{dew}}-t'_c$; and the relationship of Δt_1 and Δd is shown in Fig. 61.19.

Table 61.3 The relationship of Δt_1 and Δd

Outdoor temperature (°C)	Outdoor relative humidity (%)	$t_{dew}d_{dew}$		t_cd_c		$t'_cd'_c$		$\frac{\Delta d}{\Delta d'}$	$\frac{\Delta t_1}{\Delta t'_1}$
		t_{dew} (°C)	d_{dew} (g/kg)	t_c (°C)	d_c (g/kg)	t'_c (°C)	d'_c (g/kg)		
−12	80	−14.7	0.91	−17.7	0.70	−20.7	0.54	1.79	2
0	80	−3.0	2.32	−6	1.84	−9	1.45	1.81	2

In order to prove the formula (61.2) reasonable in the actual case, Δd and $\Delta d'$ are calculated in the actual outdoor conditions (−12 and 0 °C outdoor temperature, 80 % outdoor relative humidity) and the result is shown in Table 61.3.

From Table 61.2, the differences of $\Delta d/\Delta d'$ and $\Delta t/\Delta t_1'$are almost 10 % in the different outdoor conditions. So Δt_1 can also be frost amount and the determining conditions of defrost start.

61.4.3 Frost Factor Calculated

Analysis shows that the frost amount is related with the area and form of evaporator coil, the time of frosting, the difference of the dew point temperature, and the temperature on the evaporator coil. Besides, from the relationship of the difference of the dew point temperature and the temperature on the evaporator coil and the frosting quantity in Sect. 61.4.1, when the frost quantity is less than 3 kg, the temperature difference of the dew point and the coil almost does not change. So the ratio of frost amount and these factors are proposed and the formula is as follows:

$$k = G/(F\Delta\tau\Delta t_1) \tag{61.3}$$

where the ratio of frost amount and time and the temperature difference of the dew point and the coil is kg/(m^2·°C·min); G is the amount of frosting, kg; F is the area of heat exchanger in the low temperature cycle, that is 1.176 m^2; $\Delta\tau$ is frost time, min; Δt_1 is the difference of the dew point temperature, and the temperature on the evaporator coil, °C;

When the frost quantity is less than 3 kgs, k is shown in Fig. 61.20 in this outdoor temperature area (−15 to 6 °C) and 80 and 90 % relative humidity. From Fig. 61.20, when outdoor temperature is from −15 to 0 °C, k is about 9×10^{-4} kg/(m^2·°C·min) in every outdoor condition, while the ratio difference of several conditions (outdoor temperature is more than 0 °C) is great. Therefore, the average ratio of these outdoor conditions (outdoor temperature is from −15 to 0 °C) is known as frost factor in this paper.

And the frost factor is 8.58×10^{-4} kg/(m^2·°C·min) by calculation and as to the conditions of perfecting frost amount and defrost starting in control method.

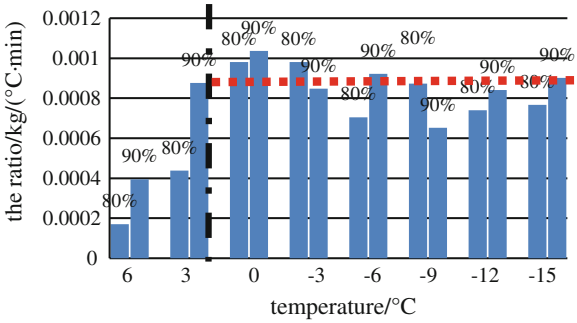

Fig. 61.20 The ratio of frost amount and time and the temperature difference of dew point and the coil in outdoor conditions

Besides, the factor does not apply to all heat exchangers but the finned-tube coil of the air-source heat pump.

61.5 Conclusion

1. The amount of frosting almost changes linearly with the frosting time which is of maximum in this outdoor temperature range of −3 to 3 °C, and the lower outdoor temperature, the more frosting amount.
2. Outdoor relative humidity has a great influence of the quantity, and the more humidity, the more frosting quantity.
3. The frost factor is found to be 8.58×10^{-4} kg/(m^2·°C·min) which is the average ratio of frost amount and time and the temperature difference of the dew point and the coil in some outdoor conditions in this paper.

Acknowledgments This work is supported by the National Natural Science Foundation of China (No. 51208298), the Science Innovation Project of Shanghai Municipal Education Commission (No. 13YZ070), and Leading Academic Discipline Project of Shanghai Municipal Education Commission (No. J50502)

References

1. Yang Y, Yiqiang J, Zuiliang M (2002) Frosting for airside heat exchanger of the water chiller/heater of air source heat pump[J]. J Haerbin Inst Technol 34(5):660–662
2. Xianmin G, Yiguang C, Weihua W, Chunzheng C (2006) Effects of outdoor air parameters on frosting characteristics of fin-tube evaporator for air source heat pump unit. J Refrigeation. 27 (6):29–33
3. Senshu T, Yasuda H, Oguni K (1990) Heat pump performance under frosting conditions:Part I:heat and mass transfer on cross finned tube heat exchangers under frosting conditions[J]. ASHRAE Trans 96(1):324–329 (SHRAE)

4. Xia Y, Zhong Y, Hrnjak PS (2006) Frost, defrost, and defrost and its impact on the air side thermal-hydraulic performance of louvered-fin,flat tube heat Exchangers. Int J Refrigeration 29(6):1066–1079
5. Shinhyuk Y, Hayase G, Cho K (2011) Measurements of frost thickness and frost mass on a flat plate under heat pump condition. Heat Transfer Eng 31(12):965–972
6. Kondepudi SN, 0'Neal DL (1990) The effects of different fin configurations on the performance of finned tube heat exchangers under frosting condition.ASHRAE Trans 96 (2):439–444
7. Yang Y, Yiqiang J, Zuiliang M (2003) Change of frost density and thickness for finned-tube heat exchanger under frosting. J Eng Thermophys 24(6):1040–1042
8. Xianmin G, Chengsheng W, Weihua W, Chunzheng C (2006) Numerical simulation and experimental verification dynamic performance of air source heat pump under frosting conditions. J Xi'an jiaotong univ 40(5):544–548
9. Huang H, Pengcheng S, Zhihao L (1998) Experimental study on operation characteristics of air-cooled heat pump under frosting condition. Fluid Mach 26(12):43–47
10. Changfa JI, Dong H, Xiuling Y (2005) Dynamic characteristics of air-to-water heat pump under frosting/defrosting conditions. J xi'an jiaotong univ 39(5):480–484
11. Chao L, Xinghua H, Jiangping C (2008) Experimental investigation on the dynamic performance of finned-tube evaporator in the frosting process. Fluid Mach. 36(2):5–9
12. Fengzhen L (2002) Effect on the performance of finned-tube evaporator of frost with low temperature conditions. Refrig Aircond 2(6):12–14
13. Hu H, Zhihao L, Pengcheng S (1999) Analysis on defrost control methods of air-cooled heat pump. Build Energy Environ 3:38–40

Chapter 62
Research on the Character of Discharge Temperature of Air Conditioning System with R32

Deyin Zhao, Wenhong Ju, Zhangquan Chen and Xu Zhang

Abstract Many papers have already done performance study in different types of AC systems on R32 and got a series of conclusions. But research papers on the discharge temperature are scarce. Discharge temperature is one of the important indicators of system security. High discharge temperature will cause the compressor lubricant carbonation, wire protection layer aging and has a severe impact on system security after long running. This paper first does comparison of discharge temperature difference between R32 and R410a in commonly used evaporation and condensation temperature range, then predicts the discharge temperature of air conditioning system with R32 through simulation with lumped models. The results show that the discharge temperature of R32 is higher than R410a's and the lower–upper limit value range is about 0 $\sim$ 35.4 °C under the same evaporation and condensation temperature. It is found that the model predictions for the discharge temperature showed about deviations of ± 10 % compared with actual test data.

Keywords R32 · Discharge temperature · Air conditioning system · Simulation · Lumped models

D. Zhao · X. Zhang (✉)
Institute of HVAC&GAS Engineering, Tongji University, Shanghai 200092, China
e-mail: zhangxu-hvac@tongji.edu.cn

W. Ju · Z. Chen
Green Electric Appliance Co. Ltd, Zhuhai 519070, China

A. Li et al. (eds.), *Proceedings of the 8th International Symposium on Heating, Ventilation and Air Conditioning*, Lecture Notes in Electrical Engineering 262,
DOI: 10.1007/978-3-642-39581-9_62,

62.1 Introduction

R32 as one kind of environment friendly refrigerants, with no ozone depletion, low GWP potential, has been more and more widely used in residential air conditioning system, and has appeared the trend to replace R410a.

Several papers [1–10] had already done performance study in different types of air conditioning systems on R32 and got a series of conclusions. But research papers focus on the character of discharge temperature are scarce. Discharge temperature is one of important indicators of system security. High discharge temperature will cause the compressor lubricant carbonation, wire protection layer aging and have a severe impact on system security after long running. Paper [1] analyzed theoretically the change of refrigerant system after replacement of R410a with R32 and pointed up that such replacement led to the increase of discharge temperature of the system. That paper proposed one method of gas refrigerant injection to reduce the discharge temperature and was validated by experiment. But it is difficult for many air conditioning systems to take this method to reduce the discharge temperature for the complexity or cost or even envelope restriction. Actually many optional methods, such as heat exchanger modification or refrigerant charge adjustment or throttling device replacement can also get the same target only if we get full understanding of the discharge temperature character of R32. This paper focuses on the character of discharge temperature of refrigerant R32 while no discussion of its thermodynamic performance. The discharge temperature difference between R32 and R410a and the prediction of discharge temperature of R32 through simulation are presented. Results may give contribution to the design process and improve the reliability of air conditioning system.

62.2 Theoretical Analysis

Temperature and entropy can be described as the function of h and P from engineering thermodynamics as below,

$$t = f(h, P) \tag{62.1}$$

$$S = f(h, P) \tag{62.2}$$

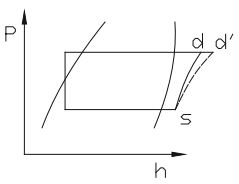

Fig. 62.1 Diagram of vapor compression cycle

The discharge temperature can be obtained if discharge enthalpy h_d and discharge pressure P_d known, P_d and h_d are connected with suction pressure P_s and suction enthalpy h_s through vapor compression cycle, as Fig. 62.1 shows,

In the cycle, process s → d is isentropic process and s → d′ is actual process. η is used to describe the extent of deviation from process sd to sd′.

According to paper [11], η can be described as,

$$\eta = \frac{m(h_d - h_s)}{W} \tag{62.3}$$

where m and W are flow rate and compressor power input, respectively.

Combined with Eqs. (62.1) and (62.2), discharge temperature can be obtained through the following equations with the help of REFPROP7 software [12],

$$h_s = f(t_s, P_s) \tag{62.4}$$

$$t_d = f(h_d, P_d) \tag{62.5}$$

$$S = f(h_d, P_d) \tag{62.6}$$

$$S = f(h_s, P_s) \tag{62.7}$$

$$\eta = \frac{h_d - h_s}{h_{d'} - h_s} \tag{62.8}$$

62.3 Isentropic Efficiency η

Isentropic efficiency varies with the operating conditions of compressor, but the efficiency can be treated as constant value in order to affiliate calculation process, i.e, paper [1] takes the value 0.7 while papers [4, 13] take the value 0.75. In this paper, two R32 rotary compressors A and B are tested under different evaporating and condensing temperature conditions to get the actual isentropic efficiency values and the mean of test data is taken as the constant isentropic efficiency value to do calculations. Compressor specification and test conditions and output parameters are shown in Tables 62.1 and 62.2.

Table 62.1 Compressor specification

Compressor	Refrigerant	Displacement volume [CC]	Rated power input [W]	Power supply [~V/Hz]
A	R32	9.2	690	220/50
B	R32	21	1500	220/50

Note: rated test conditions: evaporating temperature 7.2 °C, condensing temperature 45 °C, liquid temperature 36.7 °C, suction temperature 18.3 °C. Test standard: GB/T 5773-2004

Table 62.2 Test input conditions and output parameters

Input conditions			Output parameters		
Evaporating temperature [°C]	Condensing temperature [°C]	Suction temperature [°C]	Rated power input [W]	Flow rate [m^3/h]	Discharge temperature [°C]
5	35	17	–	–	–
15	35	27	–	–	–
5	40	17	–	–	–
15	40	27	–	–	–
5	45	17	–	–	–
15	45	27	–	–	–
5	50	17	–	–	–
15	50	27	–	–	–
5	55	17	–	–	–
15	55	27	–	–	–

As described before, actual isentropic efficiency η in different conditions can be calculated by Eq. (62.3) with the output parameters. All the calculated values are shown in Fig. 62.2.

Mean value of all the test data is 0.65 which is used in the following calculations.

62.4 Discharge Temperature Difference Between R32 and R410a

Different couples of evaporating temperature and condensing temperature within commonly used range are used to calculate the discharge temperature and do comparison between two refrigerants of R32 and R410a. In order to get the upper

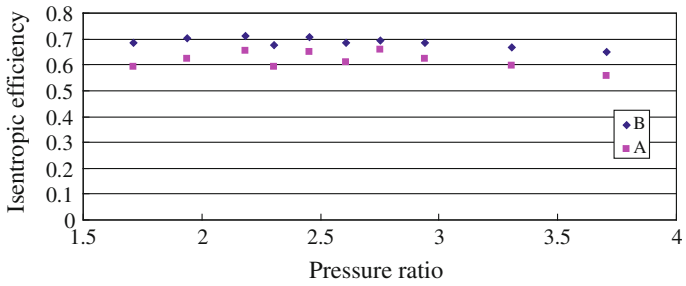

Fig. 62.2 Actual test values of isentropic efficiency

and lower limit values, maximum suction superheat 12 °C and minimum suction superheat 1 °C are used.

Tables 62.3 and 62.4 show that the lower limit value of discharge temperature difference is 0 °C and the upper limit value is 35.4 °C during the evaporating and condensing temperature range listed in table.

It can also be seen from the two tables that temperature difference becomes small along with evaporating temperature increasing while condensing temperature decreasing.

The comparison process also finds that the discharge temperature difference ranges from 12 to 23 °C with same suction superheat while keeping same evaporating temperature and condensing temperature.

62.5 Discharge Temperature Prediction of Refrigerant R32

Discharge temperature is one of the important parameters in air conditioning system and varies with different compressors, heat exchangers, and indoor (outdoor) air volumes. It can be predicted precisely only if some parameters such as suction pressure, discharge pressure, suction temperature, etc., are known. All these parameters can be procured through simulation.

62.5.1 Simulation of Air Conditioning System

Progress of simulation was presented in papers [14, 15] and kinds of models were established to do simulation. Although have been validated by test results, these models need many system structural parameters to do calculation with complex process [16, 17]. Bearing in mind that the best simulation model is the one which provides the desired results with a minimum computational effort, this paper gives

Table 62.3 Minimum temperature difference between R32 and R410a

	Condensing temperature [°C]					
Evaporating temperature [°C]	39	42	45	48	51	54
8.5	1.1	2.4	3.6	4.9	6.1	7.3
9.0	0.8	2.1	3.3	4.6	5.8	7.0
9.5	0.5	1.8	3.0	4.3	5.5	6.7
10.0	0.2	1.5	2.7	4.0	5.2	6.4
10.5	0	1.2	2.4	3.7	4.9	6.1
11.0	0	0.9	2.2	3.4	4.6	5.8

Note: Suction superheat 1 °C of R32 while 12 °C of R410a are used to calculate the temperature difference

Table 62.4 Maximum temperature difference between R32 and R410a

	Condensing temperature [°C]					
Evaporating temperature [°C]	39	42	45	48	51	54
8.5	27.9	29.4	31.0	32.5	34.0	35.4
9.0	27.5	29.1	30.6	32.1	33.6	35.1
9.5	27.2	28.7	30.2	31.8	33.2	34.7
10.0	26.8	28.4	29.9	31.4	32.9	34.3
10.5	26.5	28.0	29.5	31.0	32.5	34.0
11.0	26.1	27.7	29.2	30.7	32.2	33.6

Note: Suction superheat 12 °C of R32 while 1 °C of R410a are used to calculate the temperature difference

lumped models with little structural parameters to do air conditioning system simulation. Similar to paper [18], only one set of test data is needed (commonly the data under rating conditions), most of other performance data can be obtained through simulation.

62.5.1.1 Compressor Model

Vapor compression is a complicated polytropic process and difficult to be described precisely. Usually polynomial function of evaporating temperature t_e and condensing temperature t_c are used to calculate cooling capacity Q and power input W of compressor. Functions were shown as follows [19],

$$Q = a_0 + a_1 t_e + a_2 t_e^2 + a_3 t_e^3 + a_4 t_e t_c + a_5 t_e t_c^2 + a_6 t_e^2 t_c + a_7 t_c + a_8 t_c^2 + a_9 t_c^3 \tag{62.9}$$

$$W = b_0 + b_1 t_e + b_2 t_e^2 + b_3 t_e^3 + b_4 t_e t_c + b_5 t_e t_c^2 + b_6 t_e^2 t_c + b_7 t_c + b_8 t_c^2 + b_9 t_c^3 \tag{62.10}$$

The constants a_0 to a_9 and b_0 to b_9 applicable to Eqs. (62.9) and (62.10) can be obtained through data fitting supplied by compressor manufacture.

62.5.1.2 Heat Exchanger Model

Internal flow states and pressure drop of refrigerant are out of consideration. The entire heat exchanger are regarded as one point and take the saturated temperature of corresponding suction (discharge) pressure as refrigerant temperature. In this regard, the heat exchange process can be described as

$$Q = KA \frac{t_o - t_i}{\ln \frac{t_r - t_i}{t_r - t_i}} \tag{62.11}$$

$$Q = cm\zeta(t_i - t_o) \tag{62.12}$$

$$Q_c = Q_e + W \tag{62.13}$$

where coefficient KA, t_o, t_i, t_r, c, m, ζ, Q, Q_e, Q_c are thermal conductance (W K^{-1}), air out temperature (°C), air in temperature (°C), saturated refrigerant temperature (°C), air flow volume, moisture separation coefficient, heating capacity, evaporator capacity, and condenser capacity, respectively.

62.5.1.3 Flow Rate of Throttling Device

Expansion valve model is used to do simulation, equations were described as [20]

$$m = C_D A\sqrt{2\rho(P_i - P_O)} \tag{62.14}$$

$$C_D = 0.02005\sqrt{\rho} + 0.643\upsilon \tag{62.15}$$

where m, C_D, A, ρ, υ, P_i, P_o are refrigerant flow rate, constant coefficient, flow channel area, before throttling density, after throttling specific volume, inlet pressure, and outlet pressure, respectively.

62.5.2 *Discharge Temperature Difference due to Location Difference*

The discharge temperature is different with different location although in the same refrigeration system due to conductance, convection, and radiation effect. Usually, the test point is located in the end of discharge tube of compressor and temperature difference must be considered. Paper [21] pointed out that temperature difference was function of discharge pressure P_d and suction pressure P_s. Still the compressor A and B mentioned above are used to evaluate the difference. Test results and fitting curve are shown in Fig. 62.3.

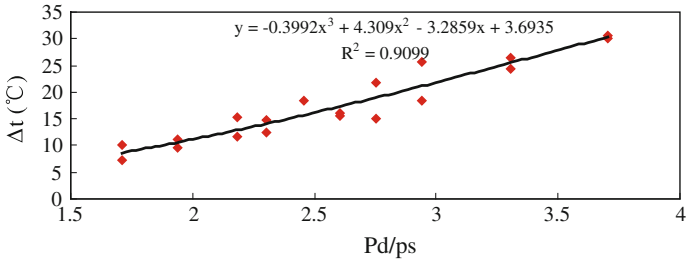

Fig. 62.3 Temperature difference of location difference with pressure ratio

62.5.3 Procedure of System Simulation

Model needed for simulation are set up in the above and system simulation can be done with some reasonable assumptions,

Saturated air layer exists on the surface of water film condensed on copper tube,

No considerations of pressure drop of heat exchangers and connecting pipes,

No changes of air thermal properties,

No changes of thermal conductance of heat exchanger,

The flow chart representing the method of solving is shown in Fig. 62.4 as following,

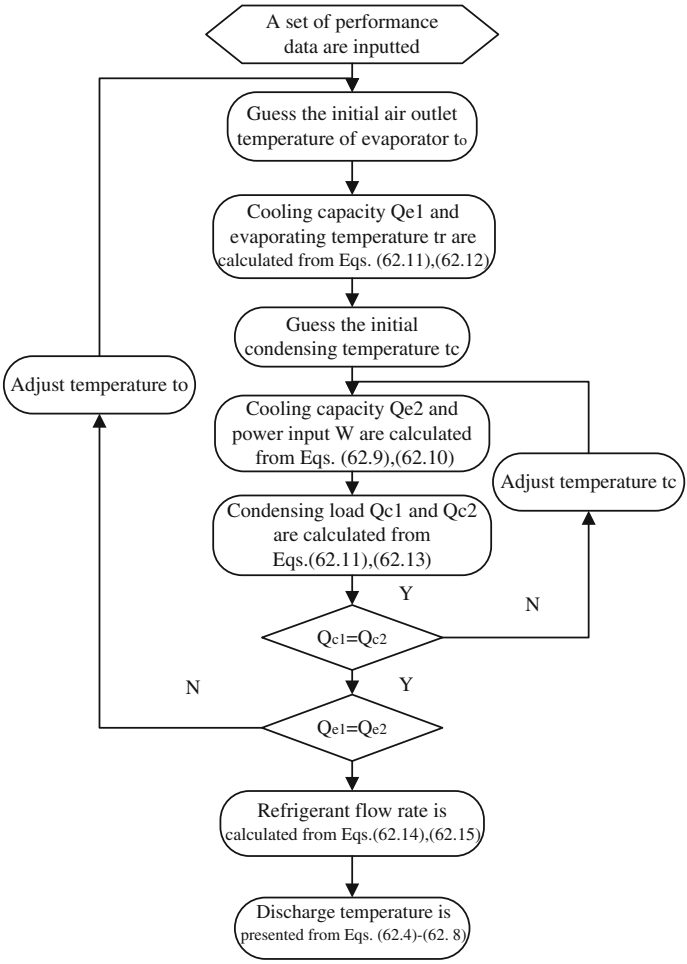

Fig. 62.4 A flow chart for air conditioning system simulation

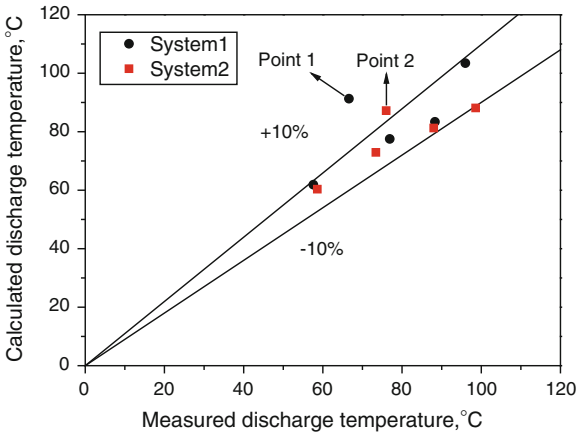

Fig. 62.5 Comparison between calculated and measured values

62.6 Simulation Results Compared with Actual Test

Air conditioning system1 with R32 compressor A and system2 with R32 compressor B are tested in enthalpy difference lab (complied with GB/T 7725-2004). Different indoor and outdoor air temperature conditions are used to do test to verify the simulation models. Fig. 62.5 compares the measured discharge temperatures and calculated discharge temperatures. It can be seen that the model predictions are close to the experimental data with deviation of about ±10 % except point1 and point2. Different fan speed is used to test in the two cases which violate the assumption of no change of thermal conductance in heat exchanger.

62.7 Conclusions

The character of discharge temperature of refrigerant R32 is presented in this paper. Compared to R410a, discharge temperature of R32 is higher, the lower–upper limit range of discharge temperature is 0 ∼ 35.4 °C under the conditions of same evaporating temperature and condensing temperature which are commonly used in air conditioning systems. Besides that the limit range of temperature difference is 12 ∼ 23 °C which varies with changes of evaporating temperature and condensing temperature, if same superheat also considered.

Prediction of discharge temperature of R32 also is presented which shows the deviation with actual test data of about ±10 % and may be helpful to system design and the improving of reliability of system.

References

1. Qin Y, Zhang J (2012) Study on the method of reducing discharge temperature of refrigerant system with R32. J Refrig 33(1):14–17
2. Wang C, Zhu X, Gong Y (2011) Experiment research on R32 substituting for R410a in household air conditioning. Fluid Mach 39(7):65–67
3. Mei K, Li M, Liang L (2011) Comparative research on the cycle performance of R32 & R410a. Refrig Air Conditioning 11(2):56–59
4. Shi M, Jia L, Zhong Y et al (2011) Performance test onR32 unitary air conditioner. Refrig Air Conditioning 11(2):78–80
5. Zhou Y, Liu Z (2011) Application experimental study of R32 refrigeration compressor. Refrig Air Conditioning 11(2):53–55
6. Xiong J, Tang D, Zhou H (2011) Experimental study on air cooled water chiller & heater unit using R32 instead of R410a. Refrigeration Air Conditioning Electr Power Mach 32(3):13–15
7. Shi L, Zhu M (2010) Re-analysis on using R32 to substitute for R22 in household/commercial air-conditioning. J Refrig 31(1):1–5
8. Lin C (2011) Performance of R32 and its applicable studies on air conditioner. Refrigeration 30(3):1–5
9. Han X, Xu Y, Qin Y et al (2010) Experimental study on the cycle performance of refrigerant R32. Refrig Air Conditioning 10(2):68–70
10. Zhang L, Liu Y (2010) Theory analysis about application of refrigerant R32 on air-conditiong. Refrig Air Conditioning 10(3):76–78
11. Waltrich M, Hermes CJL, Melo C (2011) Simulation-based design and optimization of refrigeration cassettes. Appl Energy 88:4756–4765
12. Lemmon EW, McLinden MO, Huber ML (2002) NIST reference fluids thermodynamic and transport properties – REFPROP 7.0. standard reference database 23. Gaithersburg, NIST
13. Zhu M, Shi L (2009) Exploration of using R32 to substitute for R22 in household/commercial air conditioning. Refrig Air Conditioning 9(6):31–34
14. Anand S, GGupta A, Tyagi SK (2013) Simulation studies of refrigeration cycles: a review. Renew Sustain Energy Rev 17:260–277
15. Ding G (2007) Recent developments in simulation techniques for vapor-compression refrigeration systems. Int J Refrig 30:1119–1133
16. Han H, Xiao R, He S et al (2008) Dynamics simulation of the air-conditioning system with inverted based on the moving-boundary model. Fluid Mach 36(6):71–75, 85
17. Wang W, Zhao J (2005) Dynamic simulation of condenser. J Eng Thermophys 26(4):631–634
18. Zhou Y, Zhang X, Chen P (2002) Experimental study on heating operation of GSHP. J Dong Hua Univ 28(1):5–9, 25
19. Xi D, Gu B (2006) Performance fitted equations establishment of scroll compressor under variable conditions. Refrig Air Conditioning 6(4):14–18
20. Wang T, Chen H, Zhao W et al (2007) Steady simulation of mini-refrigerating system. Eng Sci 9(3):97–102
21. Cuevas C, Lebrun J (2009) Testing and modeling of a variable speed scroll compressor. Appl Therm Eng 29:469–478

Chapter 63
Experimental Study of Heat Transfer and Resistance on Finned Tube Exchanger

Yajun Guo, Ming Wang and Guangcai Liu

Abstract An experimental study of heat transfer was conducted on rectangular finned heat exchanger with 8-row tubes and wind tunnel system. And compared with four different empirical correlation calculate the heat transfer coefficient of finned tube heat exchanger, Then compared with two different empirical correlation calculate the drag coefficient of finned tube heat exchanger. As can be seen from the result of fitting formula, the total heat transfer coefficient increased as Reynolds number. Finally, the result was fitted into formula of heat transfer coefficient and drag coefficient, which was applicable to a certain velocity range of the same type of tube bundle. Results show that, within the range of wind velocity, both the total heat transfer coefficient and flow resistance were increased as Reynolds number. And it can be concluded the outside tube heat transfer coefficient based on exterior area of bare tube increased obviously as Reynolds number, while that of finned tube increased not obviously as Reynolds number.

Keywords Finned tube exchanger · Heat transfer coefficient · Flow resistance

63.1 Introduction

Finned tube becomes one of the most common measures of heat transfer enhancement and mainly used in gas side in heat exchanger. Finned tube heat exchanger is used in many industrial areas recently, such as chemistry and refrigerant industry [1]. Heat transfer rate and efficiency were influenced by several factors as follows: (1) the geometric parameters of finned tube, (2) production process and material, and (3) operating conditions [2]. In this paper, heat transfer

Y. Guo (✉) · M. Wang · G. Liu
School of Environmental and Municipal Engineering, Xi'an University of Architecture and Technology, Xi'an 710055, China
e-mail: andyroddickming@yahoo.com.cn

A. Li et al. (eds.), *Proceedings of the 8th International Symposium on Heating, Ventilation and Air Conditioning*, Lecture Notes in Electrical Engineering 262,
DOI: 10.1007/978-3-642-39581-9_63,

conditions and resistance of rectangular finned tube was experimentally studied and analysed to deepen the understanding of heat transfer mechanism. Thus, this paper can be a reference for heat transfer formula of finned tube heat exchanger.

63.2 Experimental System and Principle

63.2.1 Experimental Facility

The experiment used water–air system as a research object, and the fluid in finned tube was hot water under atmospheric pressure, while outside is air. This experiment was done on a low speed wind tunnel driven by variable fan and the experimental part was a tube bundle box (500 × 675 mm).

Finned tubes were arranged with eight rows and seven or eight columns crossly; the external and internal diameter of each tube was 25 and 20 mm, respectively. The number of the tubes was 380 in every meter. Under atmospheric pressure, the hot water was produced by electric heating boiler and passed through the tube bundle from bottom to top, while the air produced by induced draft fan entered the wind tunnel to finish the heat transfer with water countercurrently. Cooled water out flowed from the tube bundle at the top of one lateral. An electric boiler was used for reheat water outflowed. The experiment system diagram is given in Fig. 63.1.

63.2.2 Experimental Methods

The amount of heat transfer in water side was calculated by inlet and outlet temperature and mass flow in tube bundle. Thermocouples and electromagnetic flowmeter were used to measure temperature and flow rate, respectively. The amount of heat absorption in air side was calculated by air flow and temperature rise, and the air velocity was adjusted through the inverter of induced draft fan. Temperature rise was measured by 20 thermocouples which were arranged in both inlet and outlet sides of wind tunnel. Pitot tube was equipped for wind velocity measurement. When heat absorption of air side and heat release of steam side was equal, the system reached a thermal equilibrium. The heat transfer coefficient in a certain wind velocity can be obtained according to the ratio of measured heat release and absorption amount. And then the resistant factor was calculated by measuring the pressure drop in the tunnel of experiment section.

The experimental medium was deionized water with a hardness value of 0 and conductivity of 0.5 μs/cm to prevent scaling and corrosion. Inverter was used to ensure the stability of air flow, and thus reduced the error of experiment. The voltage of the electric boiler was adjustable so as to change the heat amount

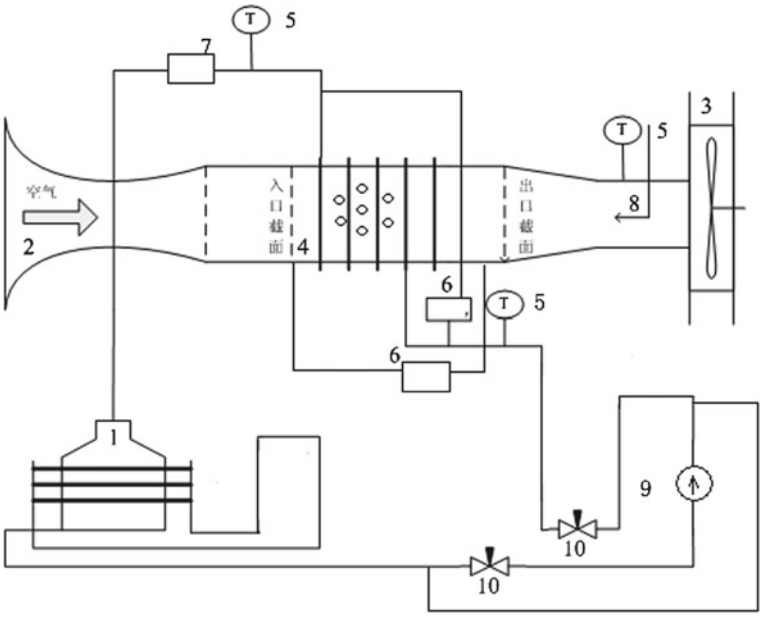

1.electric boiler; 2.wind tunnel; 3.inverter fan; 4.expermental part; 5.sheathed thermocouple; 6.differential pressure gauge; 7.flowmeter; 8.pitot tube; 9.water pump; 10.needle valve.

Fig. 63.1 Experimental system diagram

for experimental balance. The interval of measurement was controlled to be 40–50 min to guarantee the heat transferred fully.

63.2.3 Experimental Principle

The amount of heat transfer is obtained by heat transfer Eq. [3]:

$$Q = K_o F_o \Delta t_m = K_f F_f \Delta t_m \tag{1}$$

F_f, F_o —Actual and optical outside area of finned tube, m^2;
$K_f,\ K_o$ —Total heat transfer coefficient based on actual and optical outside area of finned tube, $W/(m^2 \cdot K)$;
Δt_m —Logarithmic mean temperature difference, °C

If ignoring fouling resistance, the heat transfer equation of finned tube can be written as:

$$\frac{1}{K_o}=\frac{1}{h_i}\frac{F_o}{F_i}+\frac{d_o}{2\lambda}\ln\frac{d_o}{d_i}+\frac{1}{h_f\eta}\frac{F_o}{F_f} \tag{2}$$

h_i, h_f —Inner tube heat transfer coefficient based on optical tube and outside tube heat transfer coefficient based on actual finned tube, W/(m^2·K);
F_i —Inner area of optical tube, m^2;
λ —Thermal conductivity of tube, W/(m·K);
η —Fin efficiency;
d_i, d_o —Inner and outside diameter of optical tube, m;

The flow resistance in tube bundle was important parameter in actual engineering design and application. Usually E_u is characterized as bundle flow resistance and defined as:

$$\mathrm{Eu}=\frac{\Delta p}{\frac{\rho u^2}{2}Z} \tag{3}$$

u —Fluid velocity of the smallest flow cross-section bundle;
Z —Tube rows of experimental tube bundle;
ρ —Air density;
Δp —Pressure drop of experimental tube bundle;

Finned tube heat exchangers had many different types, purposes and structures, so there was no universal formula to calculate heat transfer coefficient and pressure drop in the fin side. This paper listed four common heat transfer coefficient experimental correlations of finned tube and two flow resistance experimental correlations. By fitting the result calculated by experiment with these correlations, heat transfer coefficient and flow resistance formula apply to this experimental device was gotten.

Four common heat transfer coefficient correlations of finned tube were as follows:

(1) Briggs-Young (Method 1): Research on heat transfer of more than 10 annular finned tube [4].
(2) Briggs-Young (Method 2): Briggs and Young gave a comprehensive heat transfer formula when fluid lateral pass finned tube [4].
(3) Стасюлявичюс-Сурвила-Скринска method: This formula apply to literal finned tube the Re number range from 10^2 to 1.4×10^4 and the Pr number range from 0.7 to 5000 [5].
(4) Schmidt method: In this Th.E.Schmidt method, average heat transfer coefficient formula of annular literal finned tube bundle can be seen in Ref. [6].

Two resistance correlations of finned tube heat exchanger were as follows:

(1) Zukauskas-Локшин method: This method carefully study on spiral finned tube bundle with several parameters, then based on experimental data, calculating the experimental formula of spiral finned tube bundle.
(2) Robinson-Briggs method: Specific formula consult Ref. [7].

63.3 Experimental Results and Discussion

63.3.1 The Relationship Between Reynolds Number and Heat Transfer Coefficient

In Fig. 63.2, h_o and h_f represented air side heat transfer coefficient based on outside area of optical tube and finned tube, and K_o was total heat transfer coefficient based on outside area of optical tube. The fluctuation of h_f was not obvious with the increase of Re, whereas h_o was obvious, especially when Re was in the range of 12,500–16,099

In Fig. 63.3, h_o was air side heat transfer coefficient and h_i was water side heat transfer coefficient, K_o was total heat transfer coefficient. As can be seen from the figure, the maximum thermal resistance was in the air side, and h_o was soptically larger than K_o.

In Fig. 63.4, 1, 2, 3, and 4 represented the calculation results of Briggs-Young (Method 1), Briggs-Young (Method 2), Стасюлявичюс-Сурвила-Скринска method and Schmidt method, respectively. But Fig. 63.4 shows that empirical correlation cannot fit with experimental results well, so the fourth empirical correlation was chosen to fit the experimental data (Fig. 63.5).

As can be seen from the result of fitting formula, the total heat transfer coefficient increased following the increase of Reynolds number. (Re ranges from 2,236 to 16,099)

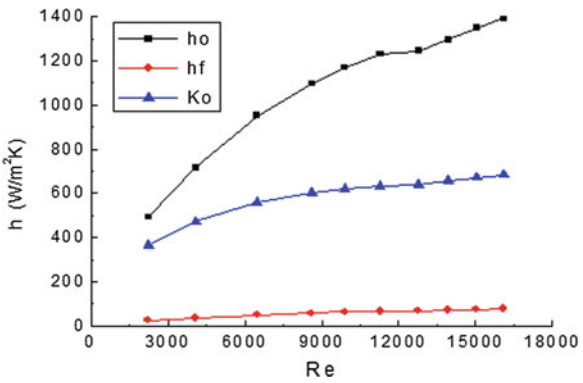

Fig. 63.2 Air side heat transfer coefficient distribution

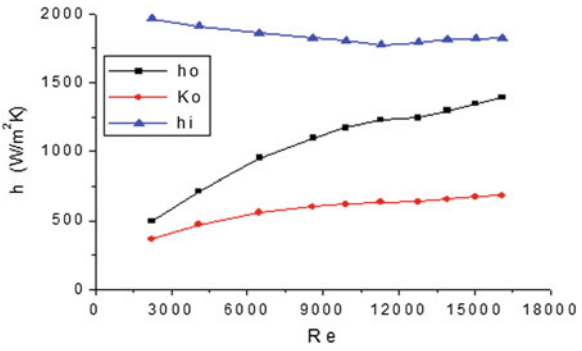

Fig. 63.3 Total heat transfer coefficient and inner and outside tube heat transfer coefficient comparison

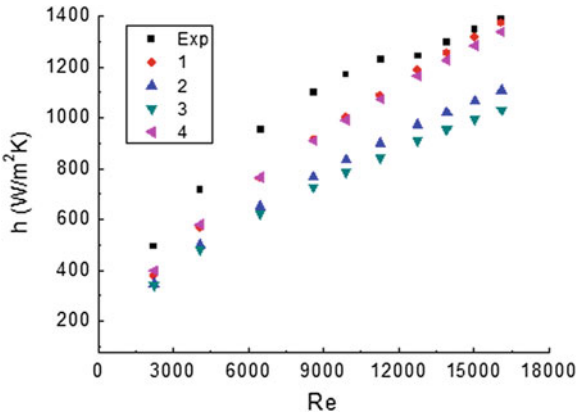

Fig. 63.4 Comparison of calculation results of empirical formula with experiment value

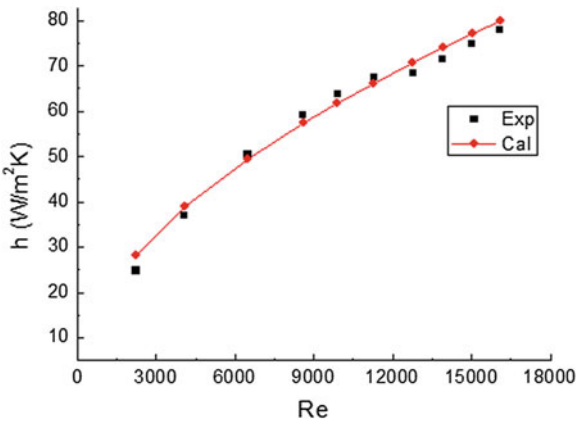

Fig. 63.5 Fitting the total heat transfer coefficient distribution

$$\mathrm{Nu}_f = \frac{d_b h_f}{\lambda} = 0.594(s_f/l_f)^{0.200}(s_f/\delta_f)^{0.1134}\mathrm{Re}_f^{0.537}\mathrm{Pr}_f^{1/3} \tag{4}$$

63.3.2 The Relationship Between Reynolds Number and Flow Resistance

In Fig. 63.6 1 and 2 represents the calculation results of two empirical resistance correlation and the highest curve is experimental data. And then the second empirical correlation was chosen to fit the experimental data. (Re ranges from 2,236 to 17,567)

$$\mathrm{Eu} = 139.515\varepsilon_f \mathrm{Re}^{-0.579} a^{-0.55} b^{-0.5} \tag{5}$$

In this formula: ε_f was fin ratio of finned tube; a and b represents relative transverse and longitudinal pitch of finned tube bundle, respectively (Fig. 63.7).

63.4 Conclusions

In this paper, heat transfer experiment on circular finned tube heat exchanger using wind tunnel device in which inlet wind velocity ranges from 0.81 to 5.60 m/s was experimentally studied. The experiment conclusions are as follows:

(1) For the air side, the fluctuation of heat transfer coefficient based on outside area of finned tube was not obvious as Re increases, whereas heat transfer coefficient based on outside area of optical tube increases obvious, especially when the Re number was in the range of 12,500–16,099.
(2) Based on the comparison of heat transfer coefficient of inner tube, outside tube and total heat transfer coefficient, the biggest thermal resistance was in the air

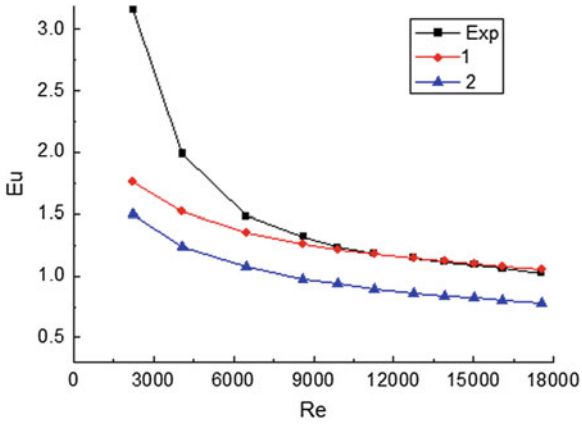

Fig. 63.6 Comparison of the experimental results with two different empirical correlations

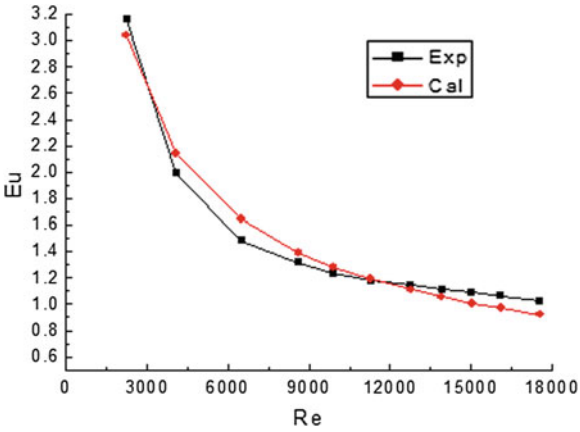

Fig. 63.7 Fitting the drag coefficient distribution

side, and the heat transfer coefficient of air side was soptically larger than total heat transfer coefficient.

(3) Both total heat transfer coefficient and thermal resistance increase as Re number increased within the experimental wind velocity range.

(4) The existing heat transfer coefficient correlation and flow resistance correlation cannot fit with the experimental results very well, so this experiment concluded a new tube bundle heat transfer coefficient correlation and a new flow resistance correlation which applies to a certain flow rate range.

References

1. Yan H, Gan Y (1991) New heat exchanger and heat transfer enhancement. Astronautics press, China
2. Shi M, Wang Z (1996) Heat exchanger principle and design (2).Southeast university press, China
3. Zhang X (2007) Heat transfer (5). China building industry press, China
4. Briggs DE, Young EH (1963) Convective heat transfer and pressure drop of air flowing across triangular pitch banks of finned tubes. Chem Eng Prog Symp Ser 59(41):1–10
5. Cangwen MA (1986) The convective heat transfer within the heat exchanger. Science press, China
6. Hausen H (1983) Heat transfer in counter flow,parallel flow and cross flow. McGraw-hill book company, Blacklic
7. Robinson KK, Briggs DE (1966) Pressure drop of air flowing across triangular pitch banks of finned tubes. Chem Eng Prog Ser 62(64):177–184

Chapter 64
Analytical Thermal Analysis of Novel Foundation Pile Ground Heat Exchanger with Spiral Coils

Man Yi, Hongxing Yang, Zhaohong Fang and Yunxia Qu

Abstract The extensive application of ground-coupled heat pump system (GCHP) is restricted by the installation of conventional borehole ground heat exchangers (GHE). Combining the GHE and building foundation piles as "energy piles" can eliminate the drilling cost and land area requirement of a conventional borehole GHE. In this study, the accurate analytical thermal analysis is carried out for simulating the heat transfer process of the novel pile GHE with spiral coils. The temperature responses of the coil pipe wall and the circulating water entering/effusing the pile GHE to the short time step heat transfer loads are deduced based on the established analytical transient three-dimensional spiral source model. Then the operation performance as well as the heat exchange capacity of novel pile GHE is investigated and compared with conventional borehole GHE. The analytical solutions developed in this study can provide an appropriate and convenient tool for thermal analysis and design of the novel foundation pile GHE with spiral coils. It is believed to be a new contribution in the foundation pile GHE field.

Keywords Ground-coupled heat pump system · Novel foundation pile ground heat exchanger · Vertical spiral coils · Analytical thermal analysis · Transient three-dimensional spiral source model

M. Yi (✉) · Z. Fang · Y. Qu
Shandong Key Laboratory of Building Energy Saving Technique, Ministry of Education Key Laboratory of Building Renewable Energy Utilization Technologies, Department of Thermal Engineering, Shandong Jianzhu University, Jinan 250101 Shandong, China
e-mail: manyilaura@163.com

H. Yang
Department of Building Services Engineering, The Hong Kong Polytechnic University, Kowloon, Hong Kong, China

A. Li et al. (eds.), *Proceedings of the 8th International Symposium on Heating, Ventilation and Air Conditioning*, Lecture Notes in Electrical Engineering 262,
DOI: 10.1007/978-3-642-39581-9_64,

64.1 Introduction

The ground-coupled heat pump (GCHP) system is identified as one of the best sustainable energy technologies for space air-conditioning and has been installed in many countries all over the world [1]. The key component distinguish the GCHP system from other conventional air- conditioning systems is the ground heat exchanger (GHE), which is utilized to reject heat into or extract heat from the ground. The GHE with vertical boreholes has been the mainstream for the GCHP system, and it is also a major obstacle to apply the GCHP technology. Recently, foundation piles of buildings started to be utilized as part of GHE, these so-called "energy pile" combines the GHE with building foundation piles as a progress in the GCHP domain, and its most competitive advantage is it can reduce the initial cost as well as ground requirement for the borehole field installation.

From literature review, most of existing studies [2–5] of pile GHE were based on either experiments or numerical simulations. Besides, pipes are buried in piles in configurations of U-tubes or W-tube in these researches, the heat transfer area in a certain pile is small and the air chocking may occur in tubes. In order to overcome these drawbacks, the author proposes a novel foundation pile GHE with spiral coils [6], which consist of vertical spiral coils pre-intertwined in the building foundation pile. The distinct advantage of this novel GHE is that they can offer higher heat transfer efficiency, reduce pipe connection complexity and decrease the thermal "short-circuit" between the feed and return pipes. The schematic diagrams of a conventional single U-tube vertical borehole GHE and a novel pile GHE with spiral coil are compared in Fig. 64.1.

As shown in Fig. 64.1, the geometry of the pile in novel pile GHE has much thicker diameter and shorter depth compared with the borehole in conventional GHE. Obviously, the classical heat transfer models for boreholes fail for the novel pile GHE. In order to better understand and simulate the heat transfer in novel pile GHE with spiral coils, the author has established the novel heat transfer model referred as "spiral source model" based on classical models [7]. Temperature field of the whole novel pile GHE and its surrounding soil can be

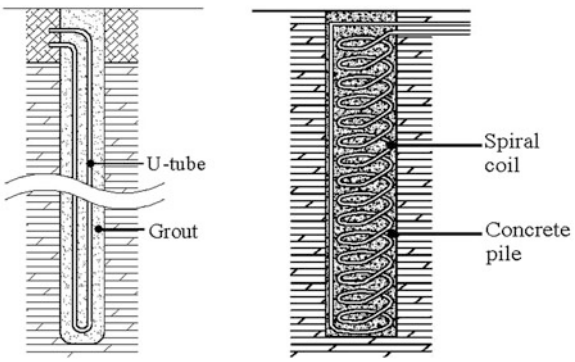

Fig. 64.1 Schematic diagram of a vertical borehole and a novel pile with coils

simulated with the three-dimensional spiral source model. However, the analytical study on the heat transfer performance of novel pile GHE with spiral coils is still highly required.

In this study, the temperature response of the spiral coil pipe wall will be predicted based on the established spiral source model. By analyzing the heat transfer resistance between the coil pipe and the circulating fluid, the temperature response of fluid entering and effusing the pile GHE will be deduced. The temperature response of coil pipe wall and circulating water for a sample novel pile GHE will be simulated as the case study. Outputs of this study provide an efficient analytical method to analyze the thermal features of the novel pile GHE with spiral coils.

64.2 Coil Pipe Wall Temperature Simulations

64.2.1 Temperature Response of Points Located on Spiral Coil Pipe

When taking the dimension of coil pipe into account, the heat source can be approximated as located in the center of coil pipe and the temperature response of coil pipe wall located at r_p away from spiral heat source can be deduced according to the established spiral source model.

The relative position of spiral heat source and coil pipe is shown in Fig. 64.2a, and the cross section of coil pipe is plotted in Fig. 64.2b. Then the dimensionless coordinate values of points located on the coil pipe wall can be represented as:

$$\begin{cases} R = \dfrac{r}{r_0} = \dfrac{r_p}{r_0} \cdot \cos\alpha + 1 = R_p \cdot \cos\alpha + 1 \\ Z = \dfrac{z}{r_0} = \dfrac{r_p}{r_0} \cdot \sin\alpha + Z_0 = R_p \cdot \sin\alpha + Z_0 \qquad 0 < \alpha < 2\pi \end{cases} \tag{64.1}$$

Then the temperature distribution on the coil pipe wall can be deduced according to the spiral source model:

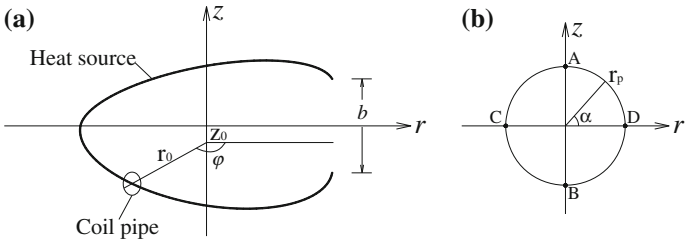

Fig. 64.2 Spiral coil pipe buried in pile GHE

$$\Theta_{f,\,\text{spiral, pipe}}(\alpha,\varphi,Fo)=\frac{B}{16\pi^{5/2}}\int_0^{Fo}\left(\frac{1}{Fo-Fo'}\right)^{3/2}\cdot\exp\left[-\frac{\left(R_p\cdot\cos\alpha+1\right)^2+1}{4(Fo-Fo')}\right]\cdot \int_{2\pi H_1/B}^{2\pi H_2/B}\exp\left[\frac{2\left(R_p\cdot\cos\alpha+1\right)\cos(\varphi-\varphi')}{4(Fo-Fo')}\right]\cdot \left\{\exp\left[-\frac{\left(R_p\cdot\sin\alpha+B/2\pi\cdot(\varphi-\varphi')\right)^2}{4(Fo-Fo')}\right] -\exp\left[-\frac{\left(R_p\cdot\sin\alpha+B/2\pi\cdot(\varphi+\varphi')\right)^2}{4(Fo-Fo')}\right]\right\}d\varphi' dFo' \tag{64.2}$$

64.2.2 Temperature Response of Coil Pipe at Certain Depth

The integral mean value of dimensionless coil pipe wall temperature located at φ can be used to represent the dimensionless coil pipe wall temperature located at φ:

$$\Theta_{f,\,\text{spiral, pipe}}(\varphi,Fo)=\frac{1}{2\pi}\int_0^{2\pi}\frac{B}{16\pi^{5/2}}\int_0^{Fo}\left(\frac{1}{Fo-Fo'}\right)^{3/2}\cdot\exp\left[-\frac{\left(R_p\cdot\cos\alpha+1\right)^2+1}{4(Fo-Fo')}\right]\cdot \int_{2\pi H_1/B}^{2\pi H_2/B}\exp\left[\frac{2\left(R_p\cdot\cos\alpha+1\right)\cos(\varphi-\varphi')}{4(Fo-Fo')}\right]\cdot \left\{\exp\left[-\frac{\left(R_p\cdot\sin\alpha+B/2\pi\cdot(\varphi-\varphi')\right)^2}{4(Fo-Fo')}\right] -\exp\left[-\frac{\left(R_p\cdot\sin\alpha+B/2\pi\cdot(\varphi+\varphi')\right)^2}{4(Fo-Fo')}\right]\right\}d\varphi' dFo' d\alpha \tag{64.3}$$

Take an example of pile GHE with finite spiral coil pipe in $B = 1$, $H_1 = 5.0$, $H_2 = 55.0$, $m = 50$, and $R_p = 0.04$ as the sample pile GHE, the calculated integral mean value of dimensionless coil pipe wall temperature at the dimensionless time of $Fo = 5.0$ and at different depths are described in Fig. 64.3.

The integral mean value is in high accuracy, however, its calculation is time consuming and inconvenient for engineering utilization. Alternatively, the mean value of temperature response at points A, B, C, D located on the pipe wall (as shown in Fig. 64.2b) can be selected to represent the temperature response of the pipe wall at certain position:

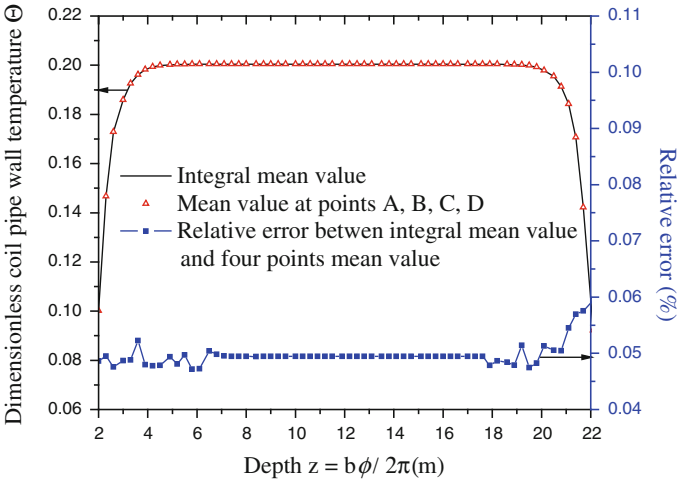

Fig. 64.3 Comparison of pipe wall temperature located at different depth

$$\Theta_{f,\,\text{spiral, pipe}}(\varphi, Fo) = \frac{1}{4}\cdot \sum_{\alpha=0,0.5\pi,1\pi,1.5\pi} \left\{ \frac{B}{16\pi^{5/2}} \int_0^{Fo} \left(\frac{1}{Fo-Fo'}\right)^{3/2} \cdot \exp\left[-\frac{\left(R_p\cdot\cos\alpha+1\right)^2+1}{4(Fo-Fo')}\right]\cdot \right.$$
$$\int_{2\pi H_1/B}^{2\pi H_2/B} \exp\left[\frac{2\left(R_p\cdot\cos\alpha+1\right)\cos(\varphi-\varphi')}{4(Fo-Fo')}\right]\cdot$$
$$\left.\left\{\exp\left[-\frac{\left(R_p\cdot\sin\alpha+B/2\pi\cdot(\varphi-\varphi')\right)^2}{4(Fo-Fo')}\right]-\exp\left[-\frac{\left(R_p\cdot\sin\alpha+B/2\pi\cdot(\varphi+\varphi')\right)^2}{4(Fo-Fo')}\right]\right\} d\varphi' dFo'\right\} \tag{64.4}$$

The mean value of temperature response at points A, B, C, D are plotted side by side with the integral mean value in Fig. 64.3. Comparison denotes that, the relative error is less than 0.06 %. It is reasonable to utilize the mean value of point A, B, C, D to represent the dimensionless temperature response of coil pipe wall located at certain depth for engineering utilization in order to decrease the calculation time.

64.2.3 Temperature Response of the Whole Coil Pipe

In order to make the calculation more suitable for engineering utilization, it needs to use one value to represent the temperature response of whole coil pipe wall. First, integral mean temperature response of coil pipes in z-direction is selected:

$$\Theta_{f,\,\text{spiral, pipe}}(Fo) = \frac{B}{4\pi^2(H_2-H_1)} \cdot \int_{2\pi H_1/B}^{2\pi H_2/B} \int_0^{2\pi} \frac{B}{16\pi^{5/2}} \int_0^{Fo} \left(\frac{1}{Fo-Fo'}\right)^{3/2} \cdot \exp\left[-\frac{(R_p\cdot\cos\alpha+1)^2+1}{4(Fo-Fo')}\right] \cdot \int_{2\pi H_1/B}^{2\pi H_2/B} \exp\left[\frac{2(R_p\cdot\cos\alpha+1)\cos(\varphi-\varphi')}{4(Fo-Fo')}\right] \cdot \left\{\exp\left[-\frac{(R_p\cdot\sin\alpha+B/2\pi\cdot(\varphi-\varphi'))^2}{4(Fo-Fo')}\right] - \exp\left[-\frac{(R_p\cdot\sin\alpha+B/2\pi\cdot(\varphi+\varphi'))^2}{4(Fo-Fo')}\right]\right\} d\varphi'\cdot dFo'\cdot d\alpha\cdot d\varphi \tag{64.5}$$

The integral mean value is in high accuracy, however, its calculation is time consuming and inconvenient for engineering utilization. Alternatively, the mean temperature response value of point A, B, C, and D located at midpoint of spiral coil pipe is selected to represent the temperature response of the whole pipe wall:

$$\Theta_{f,\,\text{spiral, pipe}}(Fo) = \frac{1}{4} \cdot \sum_{\alpha=0,0.5\pi,1\pi,1.5\pi} \left\{\frac{B}{16\pi^{5/2}} \int_0^{Fo} \left(\frac{1}{Fo-Fo'}\right)^{3/2} \cdot \exp\left[-\frac{(R_p\cdot\cos\alpha+1)^2+1}{4(Fo-Fo')}\right] \cdot \int_{2\pi H_1/B}^{2\pi H_2/B} \exp\left[\frac{2(R_p\cdot\cos\alpha+1)\cos(\pi(H_1+H_2)/B-\varphi')}{4(Fo-Fo')}\right] \cdot \left\{\exp\left[-\frac{(R_p\cdot\sin\alpha+B/2\pi\cdot(\pi(H_1+H_2)/B-\varphi'))^2}{4(Fo-Fo')}\right] - \exp\left[-\frac{(R_p\cdot\sin\alpha+B/2\pi\cdot(\pi(H_1+H_2)/B+\varphi'))^2}{4(Fo-Fo')}\right]\right\} d\varphi' dFo'\right\} \tag{64.6}$$

For the sample pile GHE, the temperature responses calculated with Eqs. (64.5) and (64.6) are plotted side by side in Fig. 64.4. Comparison denotes that, the

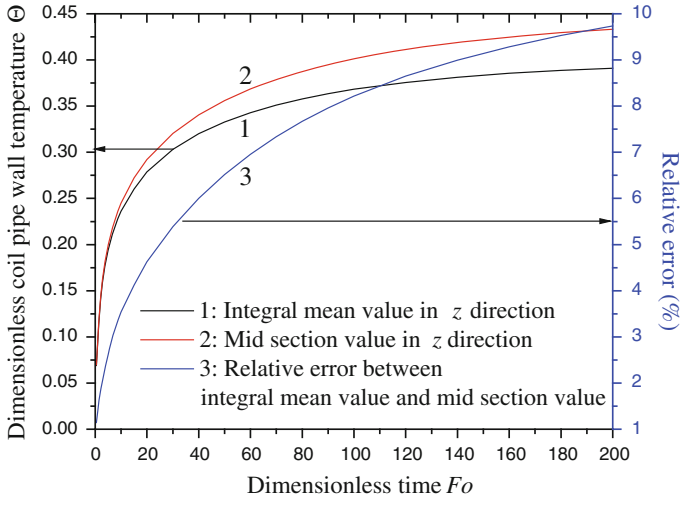

Fig. 64.4 Comparison of temperature response of whole spiral pipe wall

relative error between integral mean value and midpoint value of temperature response increase with the time goes by. It is reasonable to utilize the dimensionless temperature response of coil pipe wall at mid point in z-direction to represent the value of whole pile GHE for engineering utilization to increase the calculation efficiency.

Then the coil pipe wall temperature response to a constant step heat current q_l can be calculated with the mean value for engineering utilization:

$$\theta_{\text{spiral, pipe}}(Fo) = \frac{q_l \cdot B}{64k \cdot \pi^{5/2}} \sum_{\alpha=0,0.5\pi,1\pi,1.5\pi} \left\{ \int_0^{Fo} \left(\frac{1}{Fo - Fo'} \right)^{3/2} \cdot \exp\left[-\frac{(R_p \cdot \cos\alpha + 1)^2 + 1}{4(Fo - Fo')} \right] \cdot \int_{2\pi H_1/B}^{2\pi H_2/B} \exp\left[\frac{2(R_p \cdot \cos\alpha + 1)\cos(\pi(H_1 + H_2)/B - \varphi')}{4(Fo - Fo')} \right] \cdot \left\{ \exp\left[-\frac{(R_p \cdot \sin\alpha + B/2\pi \cdot (\pi(H_1 + H_2)/B - \varphi'))^2}{4(Fo - Fo')} \right] - \exp\left[-\frac{(R_p \cdot \sin\alpha + B/2\pi \cdot (\pi(H_1 + H_2)/B + \varphi'))^2}{4(Fo - Fo')} \right] \right\} d\varphi' dFo' \right\} \tag{64.7}$$

64.3 Coil Pipe Temperature Response to the Practical Heat Current

On basis of research in borehole GHE, the concepts of p-function and q-function represent the non-dimensional temperature responses of pipe wall to the step heat current and the pulse heat current are developed in order to calculate the pipe wall temperature response to practical heat current which varies from time to time:

$$p(\tau) = \frac{k \cdot \theta_{\text{ring, pile}}}{q_l}, \quad q(\tau - \tau_{i-1}) = p(\tau - \tau_{i-1}) - p(\tau - \tau_i) \tag{64.8}$$

The practical mutative heat currents impose on pile GHE during period from 0 to τ can be approximated by the sum of a serious of rectangular pulse heat currents. Further, the single pulse heat current can be approximated by superposition of two step heat currents with the initial one q_{l_0}=0. According to superimposing theory, the temperature response of borehole wall at moment τ can be deduced:

$$\begin{aligned} \theta_{\text{spiral, pile}} &= \frac{1}{k} \sum_{i=1}^{\infty} (q_{l_i} - q_{l_{i-1}}) . p(\tau - \tau_{i-1}) \\ &= \frac{1}{k} \left[\sum_{i=1}^{\infty} q_{l_i} . p(\tau - \tau_{i-1}) - \sum_{i=1}^{\infty} q_{l_{i-1}} . p(\tau - \tau_{i-1}) \right] \\ &= \frac{1}{k} \left[\sum_{i=1}^{\infty} q_{l_i} . p(\tau - \tau_{i-1}) - q_{l_0} . p(\tau - \tau_0) - \sum_{j=1}^{\infty} q_{l_j} . p(\tau - \tau_j) \right] \\ &= \frac{1}{k} \sum_{i=1}^{\infty} q_{l_i} . [p(\tau - \tau_{i-1}) - p(\tau - \tau_i)] = \frac{1}{k} \sum_{i=1}^{\infty} q_{l_i} . q(\tau - \tau_{i-1}) \end{aligned} \tag{64.9}$$

64.4 Temperature of Fluid Circulating in GHE

Compared with the ground outside pile, both the dimensional scale and thermal mass of the coil pipe are much smaller. Moreover, the temperature variation inside coil pipe is usually slow and minor. Thus, the heat transfer of fluid inside pile GHE can be approximated as a steady-state process. The heat transfer resistance between external wall of coil pipe and circulating fluid can be calculated:

$$R_{ip} = \frac{1}{2\pi k_p} \ln\left(\frac{r_e}{r_i}\right) + \frac{1}{2\pi r_i h_f} \tag{64.10}$$

Then the average temperature of fluid circulating inside pile GHE is calculated:

$$T_f = \frac{T_f' + T_f''}{2} = T_p + \frac{q_l \cdot b}{\sqrt{(2\pi \cdot r_0)^2 + b^2}} \cdot R_{ip} \tag{64.11}$$

In view of heat balance for the pile GHE, one also has:

$$\Delta T = T_f' - T_f'' = \frac{q_l b \cdot m}{M \cdot C_p} \tag{64.12}$$

By solving the Eqs. (64.11) and (64.12), the solution of effusing fluid temperature of GHE can be deduced:

$$\begin{cases} T_f' = T_p + \dfrac{q_l \cdot b \cdot R_{ip}}{\sqrt{(2\pi \cdot r_0)^2 + b^2}} + \dfrac{q_l b \cdot m}{2M \cdot C_p} \\ T_f'' = T_p + \dfrac{q_l \cdot b \cdot R_{ip}}{\sqrt{(2\pi \cdot r_0)^2 + b^2}} - \dfrac{q_l b \cdot m}{2M \cdot C_p} \end{cases} \tag{64.13}$$

64.5 Simple Simulation of the Sample Novel Pile GHE

64.5.1 Sample Novel Pile GHE

A novel pile GHE with normal pile configuration for engineering application is selected as the sample in this study. For the sample pile GHE, the length and radius of pile are 20 and 0.4 m respectively, the spiral coil pipe buried inside pile has the exterior diameter in 32 mm and interior diameter in 26 mm, and the coil pipe distribute in z-direction from $h_1 = 2$ to $h_2 = 22$ m with pitches b in 0.4 m.

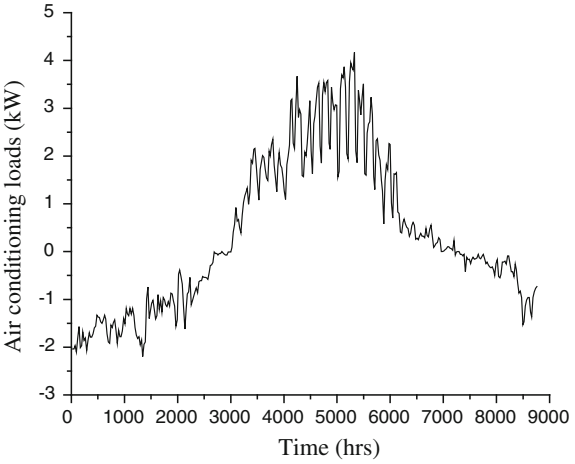

Fig. 64.5 Hourly air conditioning loads afforded by the sample pile GHE

64.5.2 Sample Air Conditioning Loads

The sample pile GHE is buried in the ground with undisturbed temperature in 12.5 °C, and the hourly air conditioning loads need to be afforded by sample pile GHE are shown in Fig. 64.5.

64.5.3 Mass Flow Rate Selection of Sample Pile GHE

The flow velocity of fluid inside coil pipe cannot be too small for ensuring the turbulent flow inside pipe, and cannot be too large for ensuring small energy consumption of circulation pump. By calculation, the mass flow rate of 0.27 kg/s is selected for the sample pile GHE, the flow velocity inside pipe is 0.51 m/s, and the flow Reynolds number is 16222.4, the flow status is the turbulent flow.

64.5.4 Simulative Temperature Response of Sample Pile GHE

The temperature response of coil pipe wall, circulating water temperature entering and effusing the sample pile GHE are simulated and plotted in Fig. 64.6.

According to simulation data plotted in Fig. 64.6, the maximum temperature difference between water entering and effusing pile GHE is 3.77 °C for cooling provision and 1.97 °C for heating provision. The maximum temperature and minimum temperature effusing the pile GHE for cooling provision and heating provision is 28.42 and 3.81 °C, respectively. The heat exchange capacity of the

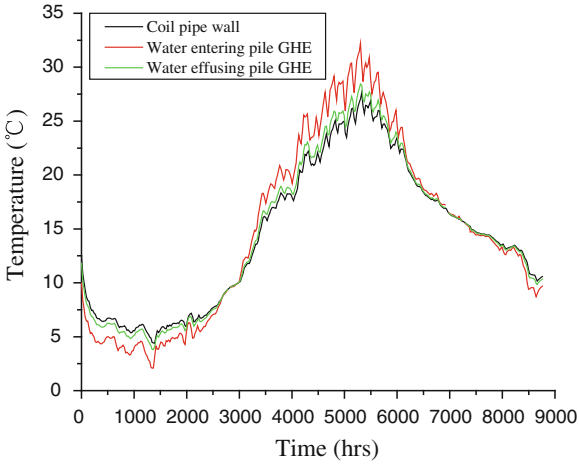

Fig. 64.6 Temperature response of coil pipe wall and circulating water

sample novel pile GHE is about 212 W/m. For the normal building with cooling load quota in 45 W/m^2, and heating load quota in 35 W/m^2, the air-conditioning area can be afforded by the sample novel pile GHE is about 100 m^2.

64.6 Conclusions

The accurate analytical thermal analysis is highly required for simulating the heat transfer process of novel pile GHE with spiral coils, which is vital to its successful application. Based on the established novel three-dimensional analytical spiral source model, the temperature responses of the coil pipe wall and the circulating water entering/effusing the pile GHE to the short time step heat transfer loads are deduced. Then the operation performance as well as the heat exchange capacity of novel pile GHE is investigated. As expected, the heat exchange capacity could be as high as 212 W/m for a novel pile GHE with normal foundation configuration based on simulation results. The analytical solutions developed in this study can provide an appropriate and convenient tool for thermal analysis and design of the novel foundation pile GHE with spiral coils. It is believed to be a new contribution in the foundation pile GHE field.

References

1. Spitler JD (2005) Ground-source heat pump system research past, present and future. HVAC and R Res 11(2):165–167
2. Morino K, Oka T (1994) Study on heat exchanged in soil by circulating water in a steel pile. Energy Build 21(1):65–78

3. Pahud D, Fromentin A, Hubbuch M (1999) Heat exchanger pile system for heating and cooling at Zurich airport. IEA Heat Pump Cent Newsl 17(1):15–16
4. Laloui L, Nuth M, Vulliet L (2006) Experimental and numerical investigations of the behaviour of a heat exchanger pile. Int J Numer Anal Meth Geomech 30(8):763–781
5. Hamada Y, Saitoh H, Nakamura M, Kubota H, Ochifuji K (2007) Field performance of an pile GHE system for space heating. Energy Build 39(5):517–524
6. Man Y, Yang HX, Diao NR, Liu JH, Fang ZH (2010) A new model and analytical solutions for borehole and pile ground heat exchangers. Int J Heat Mass Transf 53:2593–2601
7. Man Y, Yang HX, Diao NR, Cui P, Lu L, Fang ZH (2011) Development of spiral heat source model for novel pile ground heat exchangers. HVAC R Res 17(6):1075–1088

Chapter 65
The Experimental Analysis of GSHP_RF Heating System in Controlled Operation

Weiwei Yin and Qian Zhang

Abstract Two control methods are presented for the ground source heat pump (GSHP) and radiant floor (RF) heating system, one is the set return water temperature control method, and another one is the set indoor air temperature control method. To search for performance differences of the combined system mentioned above, some experimental exploration is carried out mainly in four aspects: the performance of ground heat exchanger, soil temperature distribution at different depths, the load trace damping during shutdown of the system, and the system energy consumption. Experiment results show that the set indoor air temperature control method gives a better performance in heat exchange ability and system energy consumption when compared with the set return water temperature control method. Both of them have an excellent performance in soil temperature distribution and load trace damping.

Keywords GSHP · RF · Combined heating · Controlled operation

65.1 Introduction

GSHP and RF heating are emerging techniques in recent years. GSHP has gained rapid development for its advantages in energy saving, long service life, while RF heating is favored for its comfort, energy saving, and access to natural heat source. For GSHP system, the efficiency will be significantly reduced after continuous

W. Yin (✉)
Faculty of Urban Construction and Environment Engineering, Chongqing University, Chongqing 400045, China
e-mail: yinww20070209@163.com

Q. Zhang
CISDI R&D CO., LTD, Chongqing 401122, China
e-mail: qian.b.zhang@cisdi.com.cn

A. Li et al. (eds.), *Proceedings of the 8th International Symposium on Heating, Ventilation and Air Conditioning*, Lecture Notes in Electrical Engineering 262,
DOI: 10.1007/978-3-642-39581-9_65,

operation due to the large soil thermal inertia. So shutdown of the system for recovery is required. When the RF system stops, the indoor comfort can still be ensured by the heat storage of floor for a period. Taking the complementary characteristics into account, the combined GSHP_RF system appears in projects.

For GSHP_RF system, the exploration of the operating characteristics, indoor comfort, energy efficiency and other aspects is insufficient. On the basis of experiments, this paper analyzed the performance of ground heat exchanger, heating capacity and ground source soil recovery in GSHP_RF systems under different operation control strategies, aimed at promoting the research and market application of GSHP_RF system.

65.2 Operation Control Strategy

RF heating system is characterized by large thermal inertia. When system is in operation, a lot of the heat from RF is absorbed by building envelopes. As a result, the indoor air temperature rises slowly; when RF heating system is off, the heat stored by the building envelope is released to the air and the indoor air temperature drops slowly.

One significant feature of the GSHP system is that the thermal inertia of the soil around the heat exchanger is large. At the start of the operation, the heat extraction ability is outstanding. But along with the operation, the load is accumulated without effectively release. As a result, soil temperature drops. The temperature difference of soil and circulating water decreases, as is with the ability of heat removal.

Based on the analysis of operating characteristics of RF and GSHP system, two different types of operation control methods are promoted: 1. unit return water temperature control; 2. indoor air temperature control.

Method 1: unit return water temperature control.

To adapt to different load requirements and guarantee the heating efficiency of the unit at the same time, in the experiment two compression cycles are operating in parallel. When there is large indoor load, two compressors are operating at the same time, with a low return water temperature at the user side; when the indoor load is small, the supply and return water temperature of the user side will rise compared to large indoor load. When the return water temperature T return-test $>$ unit set return water temperature T return-set, a compressor is shutdown, the remaining compressor keeps running. In the experiment, the set return water temperature of the user side is 40 °C.

Method 2: indoor air temperature control.

Indoor air temperature is set according to indoor thermal comfort needs. Taking the 1 $\sim$ 2 °C higher indoor operative temperature in RF heating system into account, the set point of indoor air temperature is from 16 to 18 °C [1]. Turn off the unit when the indoor air temperature rises to 18 °C and shutdown both sides of the circulating pump. After a period of time, the indoor air temperature drops to 16 °C, then turn on both sides of the circulating pump and the unit [2].

65.3 Experimental Devices and Test Methods

The test platform is located at a villa in Chongqing. It consists of the ground heat exchangers, water–water heat pump unit and floor radiant terminal. The experimental unit is with a rated heating capacity of 28.9 kW and a rated heating input power of 7.7 kW. The nominal loop water flow of GSHP side and user side are 5.4 and 4.1 m3/h.

There are 4 wells at GSHP side, one is single U-shaped, one is double U-shaped, another two in the form of TIOO (i.e., ground heat exchangers with three inlet pipes and one outlet pipe) [3]. In this paper, experimental test of the return water side soil temperature is from TIOO ground heat exchangers.

In the test, the measure points for the soil temperature are arranged at depths of 6.2, 16.2, 36.2, 56.2, and 96.2 m. In order to obtain the system energy consumption, three ammeters are applied to record the power consumption of heat pump unit, ground source side circulating pump and user side circulating pump.

65.4 Results and Analysis of the Experiment

One of the features of the GSHP_RF heating system is that the heat extraction medium of the ground source side is soil. The soil has large thermal inertia and little liquidity, so the heat extracting ability gradually declines as load accumulated.

In different methods of operation, heat extraction and the temperature recovery of underground soil show inconsistence. In this section, differences for the combined system under different operating methods are discussed, mainly in ground heat exchanger capacity, soil temperature changes during operation, the load trace damping during shutdown, and the system energy consumption.

65.4.1 Heat Transfer Ability of Ground Heat Exchanger

Heat transfer capacity of ground heat exchanger in this paper is characterized by the heat extraction per meter q_l, which is calculated as:

$$q_l = Q \times 1000/L \tag{65.1}$$

$$Q = m \cdot c_P \cdot (t_{\text{out}} - t_{\text{in}}) \tag{65.2}$$

.

where, q_l is ground heat exchanger heat extraction per meter, in W/m; Q is ground heat exchanger heat transfer, in kW; m is water flow of ground heat exchanger, in kg/s; c_P is specific heat at constant pressure, in kJ/(kg. °C); in, out

are ground heat exchanger inlet and outlet temperature, in ° C; L is buried depth, in m, $L = 96.2$m.

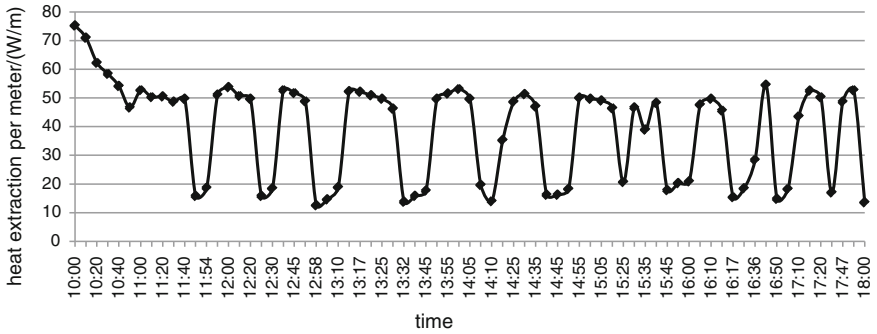

Fig. 65.1 Heat extraction of ground exchanger per meter under return water temperature control operation

Figures 65.1 and 65.2 are, respectively, corresponding to the heat extraction of ground heat exchangers changing under return water temperature control and indoor air temperature control. The figures show that at the initial stage of system operation (10:00 to 11:40), the unit maintains a full load operation (two compressors running at the same time), then diversity appears between the two conditions. As the indoor load demand Qd is between the set load of full load operation Qtwo-c and set load of unit part load operation Qone-c, there are up to 11 switching between the single and double compressor operation in the unit return water temperature control method. While in room air temperature control conditions, the unit keeps running at full capacity. When the requirement of indoor air temperature is ensured (18 °C), the unit is shutdown until the temperature drops to 16 °C. There are only two startup–shutdown cycles during the whole process.

In the condition of Fig. 65.1, when two compressors are in operation, the value of unit meter heat extraction is approximately 50.9 W/m, while for single compressor the value is 17.4 W/m. For the entire operation cycle, the average value is 37.4 W/m. In the condition of Fig. 65.2, the unit meter heat extraction is 47.8 W/m. Thus, the unit meter heat extraction under indoor air temperature control is about

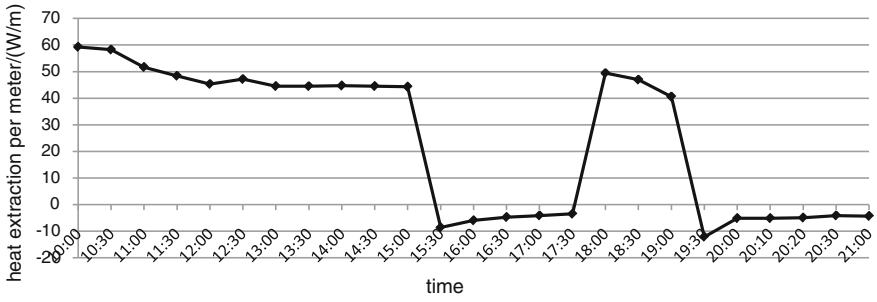

Fig. 65.2 Heat extraction of ground exchanger per meter under indoor air temperature control operation

28 % bigger than that under return water temperature control. The main reason is that the second condition avoids the low efficiency of one single compressor and poor heat extraction capacity. At the same time, the soil has a certain degree of endothermic restoration in the shutdown period, so the heat capacity is improved. When launched again the unit meter heat extraction is 49.43 W/m, which is 11.6 % higher than the value before shutdown.

65.4.2 Soil Temperature Variation

The underground soil initial temperature distribution is studied before the analysis of heat exchanger performance. Soil initial temperatures at various underground depths were tested prior to the operation of the system. The average day temperature during the test is 7.3 °C; the outdoor relative humidity is 85 %. Table 65.1 reveals that the soil initial average temperature is 18.76 °C and the fluctuation is negligible.

Figures 65.3 and 65.4 show the changes of soil temperature at different depths (6.2, 16.2, 36.2, 56.2, 96.2 m) during operation cycle (24 h) under two operating conditions. In order to compare the impact on underground soil, a third condition, continuous operation condition, is carried out. The soil temperature changes of the continuous operation condition are recorded, as shown in Fig. 65.5.

Table 65.1 Soil initial temperature distribution

Parameters	Measure point depths				
Point depth/m	−6.2	−16.2	−36.2	−56.2	−96.2
Soil temperature/°C	18.17	18.79	18.92	18.95	18.96
Mean temperature/°C			18.76		

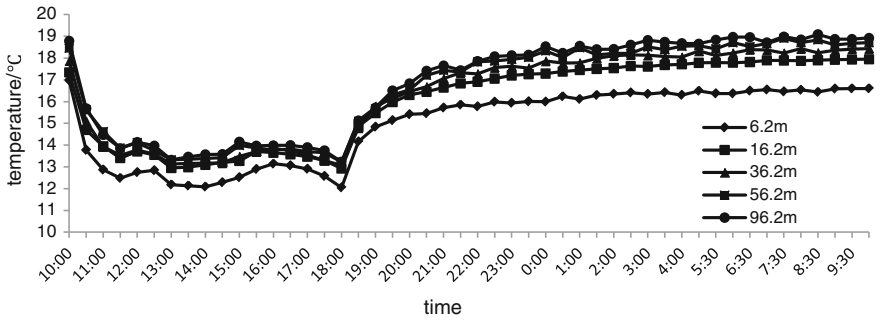

Fig. 65.3 Soil temperature changes of ground exchanger under return water temperature control operation

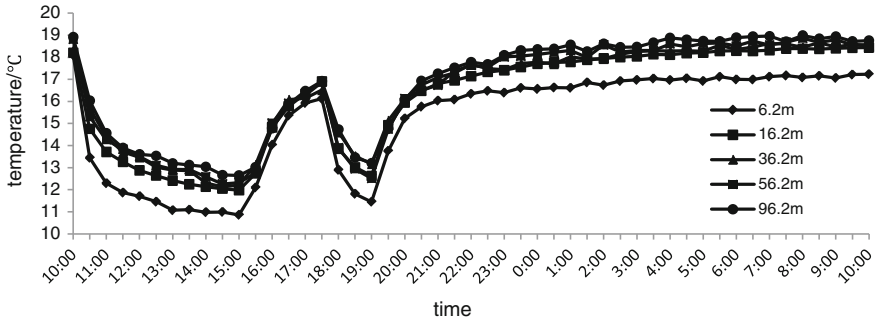

Fig. 65.4 Soil temperature changes of ground exchanger under indoor air temperature control operation

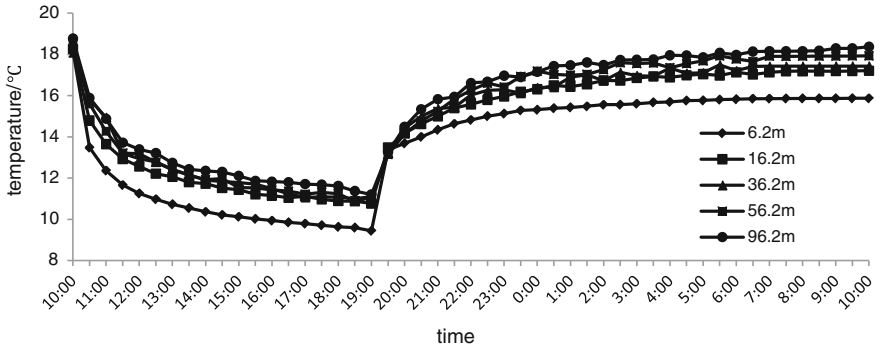

Fig. 65.5 Soil temperature changes of ground exchanger under continuous operation

65.4.2.1 Soil Temperature Changes During Operation

The operation time of three conditions is mainly the same, which is from 10:00 to 19:00. As the initial conditions of the three conditions are the same, temperature difference of the soil temperature is small. In the beginning 1.5 h, in three conditions two compressors are running, and soil temperature drops significantly. For the later 7.5 h, soil temperature changes appear due to different operation methods. Detailed information of soil temperature drop at different depths is in Table 65.2.

Table 65.2 shows that within the first 1.5 h, there are little differences between soil temperature drops under three conditions. The average soil cooling rates are 2.98 °C·h−1, 3.45 °C·h−1, 3.61 °C·h−1, which indicates that the heat exchange efficiency of ground heat exchanger heat transfer efficiency has little difference and the return water temperature control has slightly higher heat transfer efficiency.

During the latter 7.5 h, there are differences in soil cooling rate due to different operation method. The average soil cooling rate is 0.069 °C·h−1, 0.079 °C·h−1,

Table 65.2 Soil temperature drop at different depths

Operation method	$t \leq 1.5$ h					1.5 $h < t \leq 9$ h				
	–6.2 m	–16.2 m	–36.2 m	–56.2 m	–96.2 m	–6.2 m	–16.2 m	–36.2 m	–56.2m	–96.2 m
Return water temperature/ °C·h^{-1}	3.00	2.63	2.90	3.06	3.29	0.058	0.060	0.062	0.085	0.082
Indoor air temperature/ °C·h^{-1}	4.16	3.30	3.10	3.33	3.35	0.055	0.084	0.072	0.096	0.091
Continuous/ °C·h^{-1}	4.36	3.56	3.26	3.53	3.37	0.30	0.29	0.28	0.29	0.33

0.30 °C·h−1 under return water temperature control operation, indoor air temperature control operation, and continuous operation. The cooling rates of the first two are mainly the same, and much smaller than the cooling rate of continuous operation, which shows that heat transfer efficiencies of ground heat exchanger for the first two conditions are both much higher than that of continuous operation. Also the soil cooling rate is less than 0.1 °C·h−1 under return water temperature condition and indoor air temperature control condition, which means soil is recovered effectively to ensure the long time operation and reflects the necessity of operation control for GSHP_RF system.

65.4.2.2 Soil Temperature Changes During the Recovery Stage

When the system is shutdown, the heat exchanger stops extracting heat from soil, so the soil temperature is recovered. The definition of "load traces" is introduced to evaluate the restoration of surrounding soil temperature. The "load trace" is defined as the temperature difference between the initial soil temperature and the soil temperature affected by the GSHP system.

Figures 65.3, 65.4, and 65.5 indicate an upward trend of soil temperature recovery after system shutdown under three conditions. The average load traces are −5.9 °C,−6.0 °C, and −8.0 °C corresponding to return water temperature control operation, indoor air temperature control operation, and continuous operation at the shutdown point. Within 5 h after that, the temperature rises faster. The average load traces under three conditions are −1.4 0°C, −1.2 °C, −2.3 °C, respectively, which means the soil average temperatures can be restored to 93, 94, and 88 % of the initial temperature. Within 15 h after shutdown, the average load traces of the three conditions are −0.63 °C, −0.45 °C, −1.37 °C, which means the soil average temperatures restored to 97, 97, and 93 % of the initial temperature. Heat exchange conditions of the soil in three conditions have been recovered well, especially for indoor air temperature control condition and unit return water control condition, where the soil temperatures have basically reached the initial ones. At the same time, at least 5 h's recovery time should be guaranteed between two operation conditions for a good ability of heat extraction when running again.

65.4.3 Analysis of System Energy Consumption

Power consuming equipments include the unit, ground source side circulating pump, and user side circulating pump. When the unit is running, there are two different conditions: two compressors operation and single compressor operation, which means different power consumption. Specific equipment current consumptions are: 5.5 kW · h for two compressors, 3.0 kW · h for single compressor, 1.88 kW · h for ground source side water pump and 1.47 kW · h for user side water pump.

For unit return water temperature control method, the unit is shutdown after 8-h operation. In the 8 h, operation time of two compressors situation accounts for 286 min, and that of single compressor situation accounts for 194 min. Total power consumption is 62.7 kW · h.

For indoor air temperature control, two compressors keep running. After running for 5.5 h, indoor air temperature achieves the requirement, the unit and pumps of two sides are shutdown. The running lasts 6 h in the operation period, with a cumulative power consumption of 53.1 kW.

The comparison shows that energy consumption of indoor air temperature control condition is reduced by 15.3 % compared to the return water temperature control operation. Two reasons contribute to the energy saving of indoor air temperature control condition: (1) the use of the indoor air temperature as a control parameter eliminates the considerable energy consumption of circulating pump; (2) two compressors are running at the same time, which contribute to large output and the indoor air temperature can meet the requirements faster when compared to single-dual compressors switch working conditions.

65.5 Conclusions

Based on experimental study of the GSHP & RF system, following conclusions are summarized:

1) The average heat extraction of return water temperature control method is 37.4 W/m, and that under indoor air temperature control method is 47.8 W/m. The latter is 28 % larger than the former.
2) Within the first 1.5 h, soil temperature changes quickly. During the subsequent 7.5 h, the average soil cooling rate is 0.069 °C·h-1, 0.079 °C·h-1, 0.30 °C·h-1 under return water temperature control operation, indoor air temperature control operation and continuous operation. The heat transfer efficiencies of ground heat exchanger for the first two conditions have little difference, and are much higher than in continuous operation.
3) Within 5 h after shutdown, the soil temperature recovers fast. The average load traces under three conditions are -1.4 °C, −1.2 °C, −2.3 °C, respectively. The speed of recovery slows down within 15 h after shutdown, the average load

traces of the three conditions are −0.63°C, −0.45 °C, −1.37 °C, with the soil average temperatures restored to 97, 97, and 93 % of the initial temperature. Heat exchange conditions of the soil in three conditions have been recovered well. At least 5 h recovery time should be ensured between two operations for a good ability of heat extraction when the system is running again.

4) The power consumption of the return water temperature control operation and indoor air temperature control operation in one operation cycle are 62.7 kW · h and 53.1 kW ·h. The latter saves 15.3 % of the energy compared with the former.

References

1. Huating Zhang (2010) Performance of rock heat exchanger with three inlet pipes and one outlet pipe. Chongqing University, Chongqing, Dissertation for the Master's Degree
2. Zijie Wang (2004) In: Low temperature radiant heating and radiant cooling. China Industrial Press, Beijing
3. L Yanfeng (2004) Study on discontinuous running for radiant heating with low temperature hot water. Energy Saving Technol:5–6
4. Ying Chen, Guangcheng Ding, Min Yang (2011) Experimental investigation on thermal responsive characteristics and shift operation of heat pump. Acta energiae solaris sinica 2(2):257–260
5. Yan Fan (2009) GSHP design methods of dynamic load. Chongqing University, Chongqing, Dissertation for the Master's Degree

Chapter 66
Feasibility Analysis of Utilizing the Concrete Pavement as a Seasonal Heat Storage Device for the Ground-Coupled Heat Pump System

Yunxia Qu, Houxing Cao and Beiping Jia

Abstract For the buildings located in northern areas of china, which belong to the cold climate, their heating loads always larger than the cooling loads in 1 year. When the ground-coupled heat pump (GCHP) systems are utilized in these so-called "heating load dominated" buildings, the unbalance between the heat released into ground in summer and the heat extracted from ground in winter will result in the performance degradation of the GCHP systems year-by-year. In order to ensure the high heating efficiency of the GCHP system used in heating load dominated buildings, it is important to storage the heat into ground to achieve its heat balance. This paper proposes a new type of concrete pavement heat storage system combined with the GCHP system for buildings located in cold climate areas. The operating principle as well as heat transfer mechanism of pavement heat storage system is introduced, the heating capacity of pavement heat storage system is calculated and compared with residential building's heating load. Based on simulation results, the feasibility of utilizing the concrete pavement as a seasonal heat storage device for the GCHP system is analyzed.

Keywords Concrete pavement · Ground-coupled heat pump · Seasonal heat storage · Released and extracted heat · Heat balance

Y. Qu (✉) · H. Cao · B. Jia
Shandong Jianzhu University, Jinan 250101, China
e-mail: quyx@sdjzu.edu.cn

Y. Qu
Laboratory of Building Energy Conservation Technique of Shandong Province, Shandong Jianzhu University, Jinan 250101, China

A. Li et al. (eds.), *Proceedings of the 8th International Symposium on Heating, Ventilation and Air Conditioning*, Lecture Notes in Electrical Engineering 262,
DOI: 10.1007/978-3-642-39581-9_66,

66.1 Introduction

Ground-coupled heat pump (GCHP) system is a high energy efficient air-conditioning system utilizing the shallow underground geothermal energy (which including thermal energy stored in groundwater, soil, or surface water) to provide space heating in winter and cooling in summer. The GCHP system can raise the temperature of thermal energy into higher level by consuming a small amount of high-grade energy (e.g. electricity).

Northern China belongs to cold climate. The buildings located in northern area require heating in the lengthy winter, while require little cooling or even does not require cooling in the short summer. When utilized in these heating load-dominated buildings, GCHP system always operated in the single heating mode and just extracts geothermal heat from the soil in winter. The heat exchange unbalance of soil will result in the temperature decrease of soil around ground heat exchanger and the operation performance degradation of the whole GCHP system gradually. After long term running (about 3–6 years), the GCHP system even cannot meet the heating requirements in winter. In order to maintain the high energy efficient and stable operation performance of GCHP system utilized in heating load dominated buildings, it is very important to achieve the heat exchange balance of the soil around the ground heat exchanger. One of the available options is to save heat in the underground reservoir in summer. By investigation, the solar energy resource of concerned northern China region is usually abundant. Transferring the solar energy absorbed in concrete pavement in summer into soil around the ground heat exchanger cannot only improve the heating performance of the GCHP system in winter, but also achieve the shift quarter utilizing of solar energy [1].

Penrod first proposed the idea of combining the solar collectors and the buried coils in 1956, and then he presented the work principle schematic and design process of the so called "solar energy-GCHP" system [2, 3]. Zheng et al. [4, 5] of Harbin Institute of Technology have been engaged in the experimental as well as the theoretical studies of the solar energy-GCHP-coupled system, and they have got some useful conclusions in solar seasonal thermal storage and phase change thermal storage. Based on these previous studies, we propose a new type of concrete pavement heat storage system to achieve underground soil heat storage. This heat storage system can be combined with the GCHP system for buildings located in cold climate areas to ensure the high heating performance of the GCHP system.

66.2 The Principle of Concrete Pavement Heat Storage System

The principle of concrete pavement heat storage system is to absorb solar radiation with concrete pavement in summer [11], the solar energy absorbed by concrete pavement will increase the temperature of circulating medium circulated in the

pipes buried under the pavement. When the surface of concrete road reaches a certain temperature, start the road system circulating pump will be activated, and the medium absorbs heat within the pipes buried under the pavement will be circulated into storage tanks. When the temperature of media inside tank reaches the thermal storage start-up temperature, the underground loop circulating pump will be turned on, and the media with high temperature in storage tanks will be circulated through the ground heat exchanger to store the heat in the soil for the purpose of the soil accumulator. If the return media temperature of ground heat exchanger is below the set value, the underground loop circulating pump will be turned off and just the road system circulating pump to save the system operating costs. In winter, this system can also be used as an energy supplement of the GCHP system, its operation strategy is determined by the temperature of return media circulated inside ground heat exchanger. The schematic diagram of concrete pavement heat storage system is shown in Fig. 66.1.

The concrete pavement is selected as the heat storage device is due to: (1) Most of the residential areas are around by the concrete pavement; (2) concrete pavement possesses higher heat absorbability and thermal conductivity property; (3) compared with conventional solar collector, concrete pavement collectors requires lower initial investment, ease for installation, and do not need additional effective installation space.

The horizontal uniformly spaced coiled pipe buried under surface of concrete pavement is designed as the structure of heat storage device in this study. Taking both the pressure bearing capacity of pipe and the flow rate of media inside pipes can not be too low into account, the High-density polyethylene pipe (HDPE) with outer diameter of 25 mm and average thickness of 2.8 mm is selected. In order to eliminate the edge thermal effect, the polystyrene insulation board with thickness of 15 mm is pasted close to the edge of the external.

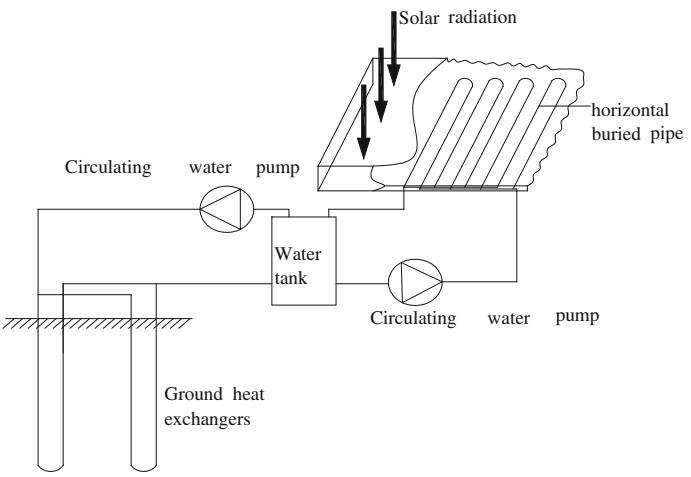

Fig. 66.1 Schematic diagram of concrete pavement thermal energy storage system

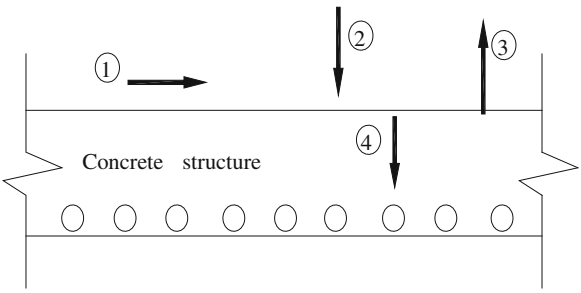

Fig. 66.2 Various concrete structure surface quantity of heat under solar radiation. ①, Concrete pavement's solar radiation heat gain. ②, Convection heat transfer between concrete pavement and the surrounding air. ③, Thermal radiation between concrete road surface and the atmosphere. ④, Heat transfer from concrete pavement

66.3 Heat Transfer Model of Concrete Pavement

The structure of concrete pavement designed in this study is shown in Fig. 66.2. Its heat transfer condition is analyzed as follows: the code ① expresses the solar radiation absorbed by concrete pavement; the code ② presents the convection heat transfer between concrete pavement and the surrounding air; the code ③ is the thermal radiation between concrete road surface and the atmosphere, and the code ④ is the heat transfer from concrete pavement to the soil. The heat transfer directions of ①–④ are denoted in Fig. 66.2.

As shown in Fig. 66.2, the amount of solar radiation absorbed by concrete pavement is Q_α, convection heat transfer between concrete pavement and the surrounding air is Q_h, the thermal radiation between concrete road surface and the atmosphere is Q_r, and the heat transfer from concrete pavement to the soil is Q_c.Then the concrete pavement's energy balance equation can be deduced based on the conservation of energy:

$$Q_\alpha = Q_h + Q_c + Q_r \tag{66.1}$$

66.3.1 Concrete Surface Solar Total Radiation

Since the surface temperature is affected by the direct solar radiation conditions, system working days are setted from May 20 to September 20, in order to ensure the system operated with high efficiency. A working day of the typical design year with high radiation is randomly selected (July 7 for this study) for analyzing, and the curves of solar radiation and atmospheric temperature changes with time are plotted in Fig. 66.3.

As shown in Fig. 66.3, the solar radiation starts from 5 o'clock in the morning and end to 17 o'clock in the afternoon, the sun radiation time interval is 12 h. On July 7, the daily average total solar radiation intensity of sample road located in

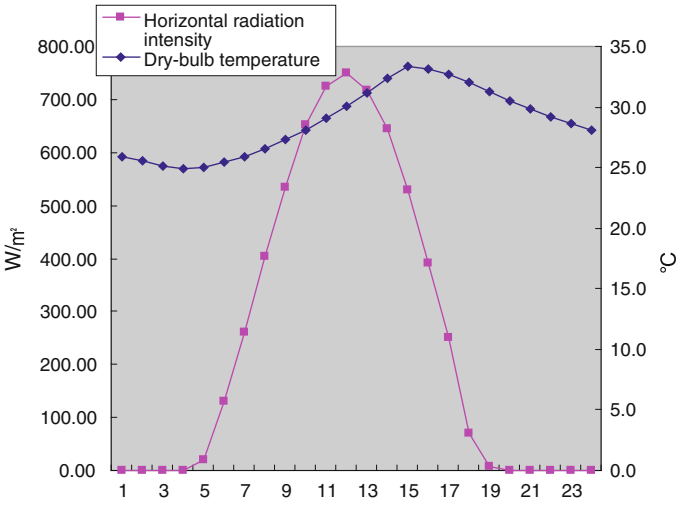

Fig. 66.3 Intensity of solar radiation and outdoor dry-bulb temperature changes over time curves on July 7

Jinan is measured to be 499.06 W/m^2. The total solar radiation absorbed by concrete pavement can be calculated as:

$$Q_\alpha = I\alpha A \tag{66.2}$$

where I—Concrete pavement's mean solar total radiation intensity, W/m^2;

α—The absorptivity of concrete pavement, dimensionless;

A—The road area, m^2.

Due to the concrete belonging to opaque objects, the thermal radiation through the concrete pavement is 0. On the other hand, solar radiation absorptivity of concrete surface nearly keeps constant with change of surface temperature or solar radiation intensity, and its value can be selected from 0.5 to 0.7 in order to calculate the concrete pavement's temperature field. For the new concrete surface, the small value should be selected; for the concrete surface used for a long time, the big value should be selected. In this study, the sample road has been used for a long time, and the concrete solar radiation absorptivity$^{\alpha}$is selected as 0.7 [6].

Calculated with the Eq. (66.2), the average solar radiation absorbed by the unit concrete road surface equals to 349.34 W/m^2.

66.3.2 The Convection Heat Transfer Between Concrete Pavement and the Surrounding Air

Based on the Clarke calculation relationship [7, 10], the convection heat transfer coefficient (h) of concrete pavement can be deduced:

$$h = 5.678\left[a + b\left(\frac{v}{0.304}\right)^n\right] \tag{66.3}$$

where v is wind velocity on the road surface. It can be seen that, the convection heat transfer coefficient goes up with the increase of wind velocity. For rough surface, coefficients in Eq. (66.3) can be selected as follows: $a = 0.775$, $b = 0.35$, $n = 1.0$ ($v < 4.88$ m/s) or $n = 0.78$ ($v > 4.88$ m/s). For summer, the temperature is high and wind velocity is low. The difference of wind velocity between the data from the China building thermal environment analysis special meteorological data collection and the data on-site measured above pavement are quite large. Combining the test data and the consulted data, wind velocity on the road surface is assumed to be 2 m/s in this study. Then, the convection heat transfer coefficient on the road surface (h) is calculated to be 17.47 W/(m^2 k).

According to Newton's Cooling Law, the convection heat transfer between concrete pavement and the surrounding air can be calculated as:

$$Q_h = h(t_s - t_a)A \tag{66.4}$$

where h—Surface convection heat transfer coefficient of concrete pavement, (W/m$^2\cdot$ k.),

t_s—Surface temperature of the concrete pavement, °C,

t_a—Temperature of the surrounding air, °C.

It is indicated by Eq. (66.4) that, the quantity of the heat convection at any given time depends on the temperature difference between the concrete pavement and its surrounding air. Based on the hourly temperatures of concrete pavement and its surrounding air in the typical day, the amount of corresponding heat convection can be calculated.

The on-site-tested temperatures of concrete pavement and its surrounding air are listed in Table 66.1. Calculated based on these data, the average convection heat transfer of concrete pavement equals to 173 W/m^2.

Table 66.1 Concrete pavement and the surrounding air hourly temperature from 5 am to 17 pm

Time	5:00	6:00	7:00	8:00	9:00	10:00	11:00	12:00	13:00	14:00	15:00	16:00	17:00
t_a	25.40	25.94	26.60	27.33	28.14	29.04	30.04	31.15	32.40	33.30	33.13	32.66	32.01
t_s	23.16	24.81	27.70	31.95	37.03	42.25	46.90	50.28	51.70	50.68	47.68	43.38	38.44

66.3.3 The Thermal Radiation Between Concrete Road Surface and the Atmosphere

By absorbing solar radiation, concrete pavement obtains energy and its temperature goes up. Then the concrete pavement can be thought as a heat source, and the radiation heat transfer from pavement to the entire semicircular sky can be calculated by Stefan-Boltzmann's law:

$$Q_r = \varepsilon\sigma_b(T_s^4 - T_{sky}^4)A \tag{66.5}$$

where T_s—Surface temperature of concrete pavement, K,

T_{sky}—The sky effective temperature, K,

σ_b—Stefan–Boltzmann's constant, $\sigma_b = 5.67 \times 10^{-8}$ W/m^2 · K^4),

ε—Emission rate of concrete pavement.

The sky effective temperature is a function of atmospheric water vapor content, cloud cover condition (or sunshine percentage), air temperature, and earth surface temperature. These meteorological parameters have quite obvious characteristics of regional variation and time variation. In China, the temperature difference between the sky effective temperature and the air temperature varies from −15 to 27 °C in winter and varies from −12 to 16 °C in summer [8]. By consulting the difference distribution map of the sky effective temperature and the air temperature, the mean temperature difference between the sky effective temperature and the air temperature is selected as −12 °C in this paper. Consequently, the sky effective temperature can be decided as: $T_{sky} = 290.78$ °K. Besides temperature, the emissivity of concrete pavement is another important parameter to calculate the radiation heat transfer. Since emissivity of concrete surface takes as 0.88–0.92 in the buildings thermal design standard, emissivity of concrete pavement surface is selected as 0.88 in this paper. Then the average heat radiation of concrete pavement can be calculated as 120.29 W/m^2.

66.3.4 Heat Transfer from Concrete Pavement to the Underground Soil

Besides convective heat transfer and radiation heat transfer, most of solar radiation energy obtained by concrete pavement is transferred into the underground soil, which includes: the heat transferred into the horizontal buried pipe under the pavement, and the conductive heat loss from the bottom as well as edge of the soil around the buried pipe. If the collector area of the concrete solid structure is large enough, the conductive heat loss from the bottom and edge of the soil can be ignored. That is to say, the heat transfer from concrete pavement to the underground soil equals to the heat obtained by horizontal buried pipe, which is used in the GCHP system for underground heat storage. By calculation, average heat transfer of concrete pavement in summer equals to 55.9 W/m^2.

66.4 Case Study

An energy saving residential building located in Jinan with construction area of 5000 m^2, and heating load of 30 W/m^2 is selected as the sample in this study. The 24 h heating provision is required from November 15 to March 15 of the following year. The GCHP system is utilized in this sample building for heating, and the total heat consumption of the sample building in the whole heating period is calculated as 311 MJ/m^2.

For the GCHP system with single heating operation, assuming the average heating coefficient of GCHP system in winter equals to 3.0, then the heat absorbed from the soil during the heating period is 207.3 MJ/m^2. In order to achieve the annual heat balance of the soil around the ground heat exchanger, the heat storage capacity should be not less than this value. According to previous calculation, average heat transfer of concrete pavement in summer equals to 55.9 W/m^2. Therefore, the heat transfer from road surface to the soil within 12 h a day is 2.41 MJ/m^2, and the operating time of the summer pavement heat storage system is calculated to be 86 days. If the heat loss rate of the underground heat storage of 20 % [9] is taken into account, the actual running time of the concrete pavement heat storage system should be 107 days.

On the other hand, the surface area of concrete pavement required to bury the horizontal pipes can be calculated based on the heating load of the sample building. According to previous calculation, average heat transfer of concrete pavement in summer equals to 55.9 W/m^2. For the sample building with heating load of 30 W/m^2, the required surface area of concrete pavement to bury the horizontal pipes should be twice of construction area need to be heated after taking the heat loss of storage system into account, and the concrete pavement surface area to bury the horizontal pipes required by the sample building is approximately 2500 m^2.

66.5 Conclusions

Through previous detailed analysis, some useful conclusions can be deduced as follows:

(1) It is feasible to utilize the concrete pavement seasonal heat storage system to maintain the thermal balance of the underground soil around ground heat exchanger for the GCHP system.
(2) Take a conventional concrete pavement located in Jinan as an example, the average heat transfer of concrete pavement in summer can be as high as 55.9 W/m^2.
(3) Select an energy conservation residential buildings located in Jinan as a sample, if the GCHP system operates in the single heating mode combined with the concrete pavement heat storage system, designed to provide heating

for the sample building, the ratio of the concrete pavement surface area to the building construction area is about 1:2.

(4) Running time of the pavement heat storage system in summer need to be calculated based on the heat consumption of building in winter.

(5) The concrete pavement storage system not only can collect the solar energy to realize the accumulation in summer and consumption in winter of the solar energy; but also can effectively reduce the temperature and thermal erosion damage of the concrete pavement to improve the life time and bearing capacity of the concrete pavement.

References

1. Han Z-W, Zheng M-Y, Kong F-H (2008) Cold-seasonal solar simulation study on soil thermal storage and heat pump heating systems. J Solar Energy 29(5):574–580
2. von kubbe HL, Sitaimulai F (1986) Heat pumps: theory and practice (Translation Wang Z). China architecture and building press. pp 28–39
3. Penrod EB, Prasanna KV (1962) Design of a flat-plate collector for a solar Earth heat pump. Sol Energy 6(1):9–22
4. Wang F, Zheng M-Y, Li Z-J et al (2006) Phase change materials in the application of solar-ground source heat pump system. J Solar Energy 27(12):1231–1234
5. Han Z-W, Zheng M-Y, Liu W et al (2006) Phase-change heat storage of solar-ground source heat pump heating system in cold area. J Solar Energy 27(12):1214–1218
6. Liu W-Y, Geng Y-M (2004) Experimental study on concrete surface solar radiation absorption rate. Concr Cem Prod 4(8):8–11
7. Chiasson A, Spitler JD (2000) A modeling approach to design of a ground-source heat pump bridge deck heating system. In: Proceeding of the 5th international symposium on snow removal and ice control technology, Roanoke, 2000, pp 176–192
8. Liu S-Y, Huang Y-F (1983) Discussion on the effective temperature of the sky. J Solar Energy 4(1):63–68
9. Cui J-K, Zhao J, Li X-G. Ground source heat pump system simulation analysis of seasonal soil thermal properties. The Chinese science paper online
10. Chen M-Y (2010) Study on solar collector performance of asphalt pavement, vol 5. Wuhan University of Technology, Wuhan, pp 14–29
11. Huang Y (2010) Road snow melting of ice and heat of solar radiation studies. Jilin University, Jilin, 12:53–59

Chapter 67
Retrofit of Air-Conditioning System in Data Center Using Separate Heat Pipe System

Yuwei Zheng, Zhen Li, Xiaohua Liu, Zhen Tong and Rang Tu

Abstract Data center is developing quickly in China, which consumes much operating energy due to the 24 h operating annually. The energy consumption of air-conditioning (AC) system accounts for 40–50 % of the entire energy consumption in data center. There is large energy saving potential since the AC system operate annually even the outdoor environment is cold enough. The indoor thermal environment and energy utilization of a data center in Shanxi Province before and after retrofitting are tested during the July of 2012. The area of data center is 550 m^2 and there are 145 cabinets. In the original design, eight typical air-cooled CRACs (computer room air conditioner) with total cooling capacity of 600 kW provide the required indoor climate. The original AC systems cannot meet the heat dissipation demand of all the cabinets, due to the reason that 14 cabinets with rather higher heat production of 3–8 kW. The total heat production of the 14 cabinets were accounting for 1/5 total heat production of the data center. The measured outlet temperatures of the 14 cabinets were over 30 °C. The retrofitting is focus on the aforementioned 14 cabinets, using separate heat pipe systems in the back-plane of cabinets which are accompanied by water chiller outdoor as cold source. The on-site measurements show that the retrofit separate heat pipe air-conditioning systems can meet the temperature requirement of safety operation of the high-density cabinet. The COP of AC system can reach 2.7. The entire energy consumption of AC systems after the retrofitting can reduce 18 % energy consumption in summer.

Keywords Data center · Air-conditioning · Retrofit · Heat pipe system · Energy saving

Y. Zheng (✉) · X. Liu · Z. Tong · R. Tu
Department of Building Science, Tsinghua University, Beijing 100084, China
e-mail: cadascq@163.com

Z. Li
School of Aerospace, Tsinghua University, Beijing 100084, China

A. Li et al. (eds.), *Proceedings of the 8th International Symposium on Heating, Ventilation and Air Conditioning*, Lecture Notes in Electrical Engineering 262,
DOI: 10.1007/978-3-642-39581-9_67,

67.1 Introduction

Data center is developing quickly in China, which consumes much operating energy due to the 24 h operating annually. Power consumption of data center mainly includes communication equipment power, air conditioner, batteries, and so on. The appropriate design and optimization of air conditioner are very important to keep beneficial environment and normal operating of data center. Typical air conditioner used in data centers is air-cooled CRACs (computer room air conditioners) which consumes 40–50 % energy of the entire energy consumption [1, 2] and has a lot of energy saving potential since the AC system operates annually even the outdoor environment is cold enough.

There are many common energy saving measures used in data center at present. Firstly, reducing energy consumption using outdoor cold source is an effectively measurement. When outdoor air temperature is relatively low, supplying outdoor air into indoor environment directive can satisfy the indoor thermal environment [1], but it may influence indoor air quality. Then heat pipe technology is a developing technology which can save energy effectively [3]. That is because energy consumption of components in heat pipe system is low and the system can be cooperated by outdoor natural cold source and assisted by mechanical refrigeration. Retrofit fixed frequency air conditioner controlled by on–off to frequency conversion. Moreover, raised-floor air supply can save 20 % energy consumption comparing with upper air supply, and using a ceiling return strategy for the return of hot exhaust air to the CRACs gives a better thermal performance of the data centers [4].

In recent years, heat pipe technology develops impressively and is applied as effective heat transfer component in heat recovery system, preheater system, and heat dissipation parts [5, 6]. And for data centers, heat pipe system is always accompanied by cold energy storage system to produce cooling capacity as outdoor units, and it can help to downsize the chiller and decrease its runtime that will save electricity related cost and decrease greenhouse gas emissions from the electricity generation [7, 8]. In the present work, heat pipe system is applied in cabinets indoor and accompanied with nature cold source and mechanical chiller. Then take a data center in Shanxi Province retrofitted by separate heat pipe system as an example to test energy saving effect of heat pipe technology.

67.2 Data Center Introduction and Retrofit Scheme

The area of the data center is 550 m^2 and there are 145 cabinets arranged in nine rows. The heat production of cabinet equipment in data center is about 350 kW and the heat density is 0.64 kW/m^2. In the original design, eight typical air-cooled CRACs (computer room air conditioners) with total cooling capacity of 600 kW provide the required indoor thermal environment. The air conditioners with double

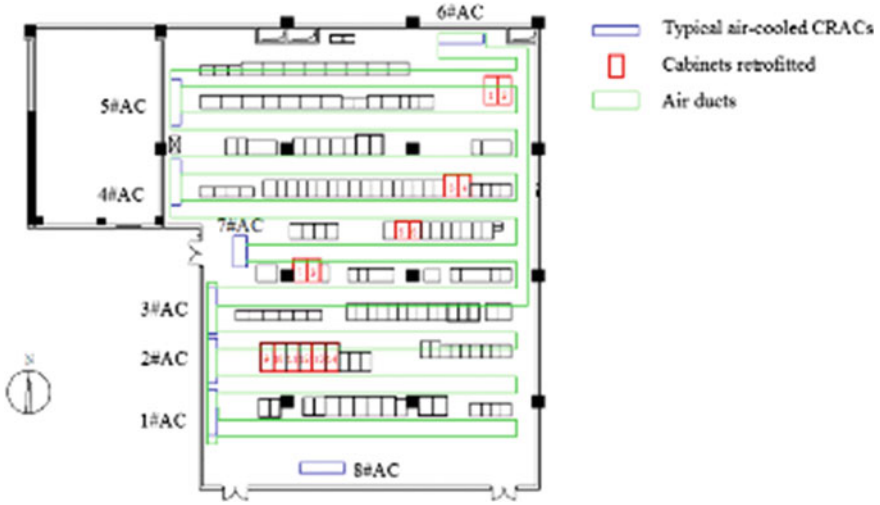

Fig. 67.1 The arrangement in the data center

compressors are on–off controlled by returned air temperature. The inlet of returned air is downside the air conditioner tanks. The cold air is supplied by a set of air duct in the ceiling of the data center, as shown in Fig. 67.1.

There are storage batteries, severs, charging computers, etc., in the data center and heat density of every cabinets are different so that the space heating production is not uniform. The unified air duct in original AC (air-conditioner) scheme can just supply cold air relatively uniformly, which means that air volume cannot meet local area with concentrated heat and the heat cannot be dissipated in time resulting in local overheating phenomenon. Choose 14 cabinets with rather higher heat production of 3–8 kW as retrofit objects through observation and measurement of local overheating points. The total heat production of the 14 cabinets were about 72 kW accounting for 1/5 total heat production of the data center. The measured outlet temperatures of the 14 cabinets were over 30 °C. And the typical air-cooled CRACs consume more energy due to low efficiency.

Therefore, the retrofit aims at reducing energy consumption and solving local overheating. The retrofitting uses separate heat pipe systems in the back-plane of cabinets which are accompanied by water chiller outdoor as cold source. One side of the separate heat pipe is installed inside the cabinet as evaporator, the indoor air is pushed by server fans and back-plane fans to take away heat produced by servers firstly and then cooled by cold side of heat pipe in back-plane. And the other side of the separate heat pipe as condenser will be cooled in outdoor multiplied three heat exchangers by cooling water which is produced by mechanical chiller or outdoor air when the outdoor temperature is low enough. The mechanical chiller is with three on–off compressors and the rated total cooling capacity is 120 kW and rated cop is 2.86. The system diagram is shown in Fig. 67.2. And the photographs of data center and kinds of equipment are shown in Fig. 67.3.

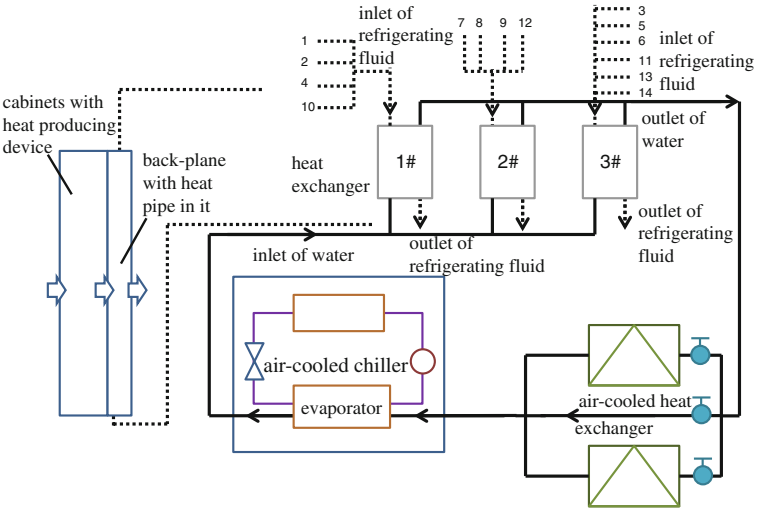

Fig. 67.2 Separate heat pipe system diagram

Fig. 67.3 Photographs of data center and kinds of equipment

67.3 Retrofit Results Analysis

The testing and analysis include outdoor mechanical chiller's performance, indoor thermal environment, and energy consumption comparison before and after retrofitting.

67.3.1 System Performance Testing

The testing is conducted in the mid-month of July. Because outdoor temperature is high, the efficiency of air-cooled heat exchangers is low. Therefore, at that time the mechanical chiller undertook the cooling capacity required. The water flow is 16 m^3/h from water meter on main pipe. The water outlet temperature set point of air-cooled chiller is 12 °C. The measure points are arranged in inlet and outlet of chiller, inlet and outlet of three heat exchangers refrigerating fluid side and outlet of water side with thermocouples measuring and recording temperature.

Testing results in a certain period of time are shown in Fig. 67.4. It indicates that because one compressor in chiller cannot meet the cooling capacity required and two compressors supply more than required, so the first compressor is always on and the second compressor is periodic start-stop. The water outlet temperature can be controlled in range of 12 ± 2 °C. Take 2# heat exchanger for example, the refrigerating fluid outlet temperature fluctuate within 14 ± 1.5 °C, preventing indoor air condensation. Figure 67.5 and Table 67.1 show average system operating condition, including that temperature difference between supplied and return

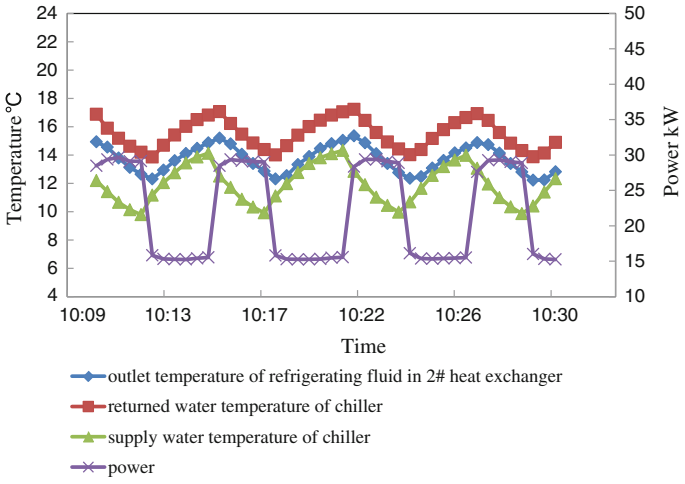

Fig. 67.4 Operating record of outdoor chiller in separate heat pipe system

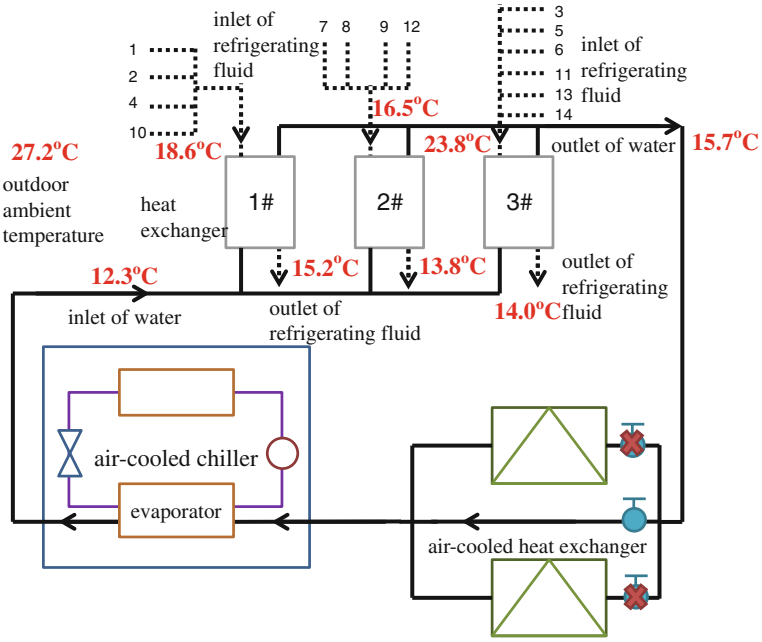

Fig. 67.5 Average operating data of outdoor chiller in separate heat pipe system

Table 67.1 Average operating data of outdoor chiller in separate heat pipe system

Parameters	Values
Testing date	16th July 2012
Testing time	10:00-16:00
Temperature set point of supplied chilled water (°C)	12
Water flow rate in main pipe (m^3/h)	16
Ambient temperature (°C)	27.2
Temperature difference of supplied and return chiller water (°C)	3.4
Total cooling capacity (kW)	63.8
Power input (kW)	22.9
COP of chiller	2.78

chiller water is 3.4 °C, and average outlet temperatures of refrigerating fluid in three heat exchangers are above 13 °C.

Meanwhile, cooling capacity received by indoor air through back-plane was measured to validate the energy conservation. The cooling capacities of 14 back-planes supplied by the separate heat pipe system were obtained by measuring inlet and outlet temperatures of air through back-planes and air flow rates. Heat took away by heat pipe is closely related with heat dissipation of cabinets. Figure 67.6 shows that heat dissipation of 14 cabinets through heat pipe are different and ranges from 3 to 8 kW. Total cooling capacity received is 72.0 kW, and unbalance

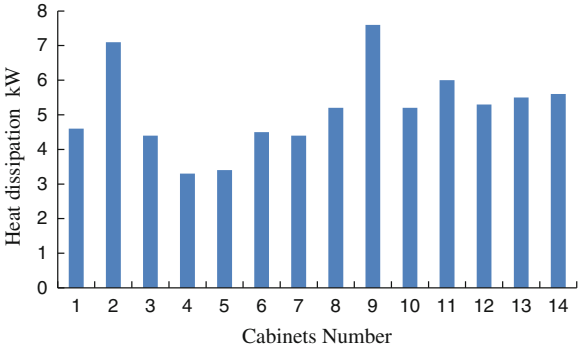

Fig. 67.6 Heat dissipations of 14 cabinets retrofitted

Table 67.2 Outdoor heat exchangers comparison

Supply water temperature of chiller (°C)	12.2		
Heat exchanger number	1#	2#	3#
Outlet temperature of water in heat exchanger (°C)	15.1	16.4	16.1
Temperature difference of water (°C)	2.9	4.3	4.0
Heat exchange amount (kW)	21.4	22.4	29.3
Water flow (m^3/h)	6.2	4.5	6.3
Total water flow in main pipe (m^3/h)	17.0		

rate is 11 % comparing with total cooling capacity of outdoor chiller, indicating that the testing results are acceptable.

Because the air outlet temperature is close with indoor ambient temperature, the total heat dissipation quantity is equal with the cabinets' heat production. Therefore, these 14 cabinets account for 1/10 cabinets of all but their total heat production accounts for 1/5 of all heat production in data center.

Three outdoor heat exchangers undertake heat dissipation of 4–6 cabinets individually, and heat exchange amount of three heat exchangers can be obtained by previous testing data. Computed results are shown in Table 67.2, and heat exchange rate of each heat exchanger accounts for 30–40 % of total amount. Water flow of each can be calculated with temperature difference of water between inlet and outlet in heat exchanger, and total flow is 17 m^3/h. The unbalance rate is 6 % compared with water meter display. According to flow distribution, water flow of 2# heat exchanger is relatively less resulting in bigger temperature difference.

67.3.2 Indoor Environment

One target of the retrofitting is to solve local overheating phenomenon by reducing outlet temperature of air from back-planes. Compare air outlet temperature of 14 cabinets before and after retrofitting is shown in Fig. 67.7. Before retrofitting, the

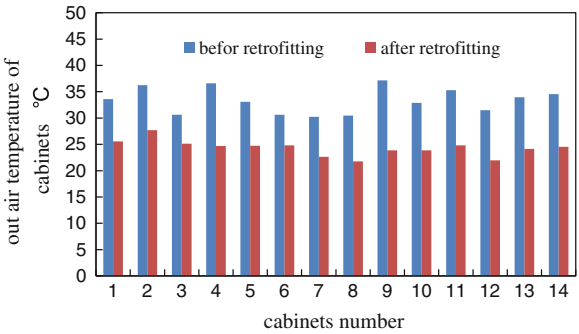

Fig. 67.7 Air outlet temperatures of 14 cabinets before and after retrofitting

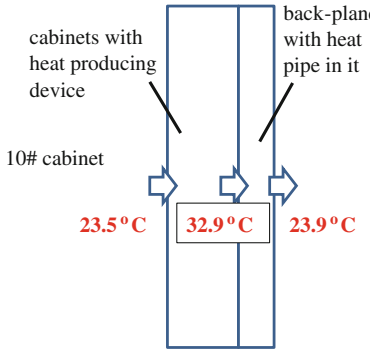

Fig. 67.8 Air temperatures before cabinet, before and after back-plane of 10# cabinet

outlet temperatures of the 14 mentioned cabinets are in the range of 30–37 °C. After retrofitting, the outlet temperatures are reduced to about 23–26 °C, improving indoor thermal environment and safety for the operation of the cabinets. Take 10# cabinet retrofitted as an example as shown in Fig. 67.8. The outlet temperature of air from back-planes is 23.9 °C, close with inlet temperature.

67.3.3 Energy Saving Analysis

From March 2012, the operation of cabinets is similar, and cabinets' power of the center data is always about 260 MWh. The retrofit of separate heat pipe system was accomplished in late May and it was been into use in early June.

The monthly total energy consumption of all air-conditioners from May to July 2012 is shown in Table 67.3. Ignoring outdoor air temperature's influence, energy consumption of ACs in June was 26.1 MWh less than that in May, saving 17.3 % electricity, and energy consumption of ACs in July was 28.1 MWh less than that in May, saving 18.6 % electricity, which indicated much energy saving potential.

Table 67.3 Energy saving data

Month	May 2012	June 2012	July 2012
Monthly average outdoor temperature (°C)	18.4	22.2	23.9
Monthly total energy consumption of all ACs (MWh)	151.3	125.2	123.2
Energy saving comparing with May (MWh)	/	26.1	28.1
Energy saving rate	/	17.3 %	18.6 %

67.4 Conclusion

The indoor thermal environment and energy utilization of a data center in Shanxi Province before and after retrofitting are measured. The original AC systems cannot meet the heat dissipation demand of all the cabinets, due to the reason that 14 cabinets with rather higher heat production of 3–8 kW. The retrofitting is focus on the 14 aforementioned cabinets. The main conclusions are:

1. The retrofitting with separate heat pipe system is processed on the 14 cabinets whose heat production accounts for 20 % of total heat production. The outlet temperatures of the 14 mentioned cabinets reduced to 23–26 °C, improving indoor thermal environment and safety for the operation of the cabinets.
2. The cooling capacity provided by the separate heat pipe system is more than 60 kW with COP of 2.78. Energy consumption of the entire air conditioning system is reduced about 18 % after retrofitting in summer. Much energy could be saved by using natural cold source from cooling tower, when outdoor environment is cold enough.
3. The retrofitting project indicates that separate heat pipe system can realize temperature environment control in data center, solve local hot spots phenomenon, saving energy by utilizing natural cold source.

References

1. Chen X (2009) The feasibility analysis of air-conditioning energy saving project. South China University of Technology, Guangzhou
2. Cabusao G, Mochizuki M, Mashiko K et al (2010). Data center energy conservation utilizing a heat pipe based ice storage system. In: IEEE CPMT symposium japan (Formerly VLSI Packaging Workshop of Japan)
3. Qian XD, Li Z, Li ZX (2012) Experimental study on data center heat pipe air conditioning system. J Eng Thermophysics 33(7):1217–1220
4. Srinarayana N, Fakhim B, Behnia M et al (2012). A comparative study of raised-floor and hard-floor configurations in an air-cooled data centre. In: 13th IEEE interSociety conference on thermal and thermomechanical phenomena in electronic systems (ITherm), 2012, pp 43−50
5. Zhang H, Zhuang J (2003) Research, development and industrial application of heat pipe technology in China. Appl Therm Eng 2003(23):1067–1083

6. Lin S, Broadbent J, McGlen R (2005) Numerical study of heat pipe application in heat recovery systems. Appl Therm Eng 25(1):127–133
7. Wu XP, Mochizuki M, Mashiko K et al (2010) Energy conservation approach for data center cooling using heat pipe based cold energy storage system. In: 26th IEEE SEMI-THERM symposium
8. Fang G, Liu X, Wu S (2009) Experimental investigation on performance of ice storage air-conditioning system with separate heat pipe. Exp Thermal Fluid Sci 33:1149–1155

Chapter 68
The Model for the Separation Efficiency of the Electrostatic Cyclone Dust Collector

Jiajun Luo, Hao Zhang, Dong Yang, Jiguang Zhang and Huajun Tang

Abstract The electrostatic cyclone dust collector is a new combination of mechanism and advantages of both electrostatic and cyclone dust collectors, with several advantages of simple structure, low operating cost and high separation efficiency. The article embarks on the basic theory of electrostatics and cyclone dust collector. The charge process on particle is described. Then this paper elaborates upon the research on dust removal mechanism and particle movement regularity in the electrostatic cyclone dust collector based on predecessors' studies. Finally, the new model for the separation efficiency of electrostatic cyclone dust collector is deduced. The new gas–solid separation theory of cyclone with impulse excitation can provide a theoretical basis for developing a new separator and improving the quality of the separator equipment.

Keywords Solid–gas separation · Separation efficiency · Electrostatic cyclone dust collector · Impulse excitation · Centrifugal force

J. Luo · H. Zhang · D. Yang · H. Tang
Shandong Jianzhu University, Jinan 250101, China

H. Zhang (✉) · D. Yang
Key Laboratory of Renewable Energy Utilization Technologies in Buildings, Ministry of Education, Shandong Jianzhu University, Jinan 250101, China
e-mail: qdzhanghao@126.com

H. Zhang · D. Yang
Shandong Key Laboratory of Building Energy-saving Technique, Shandong Jianzhu University, Jinan 250101, China

J. Zhang
School of Environmental and Municipal Engineering, Qingdao Technological University, Qingdao 266033, China

A. Li et al. (eds.), *Proceedings of the 8th International Symposium on Heating, Ventilation and Air Conditioning*, Lecture Notes in Electrical Engineering 262,
DOI: 10.1007/978-3-642-39581-9_68,

68.1 Introduction

Electrostatic cyclone dust collector is a new dust removal device which is a mixture of the mechanism of whirlwind dust and electrostatic dust removal.

Its features are as follows: simple structure, low price, high dust removal efficiency and good adaptability to load fluctuation, etc. It is very valuable practically under the current economic situation in our country and is an advanced type of dust removal equipment with a bright future. However, as a result of the complexity of the separation mechanism of the electrostatic cyclone dust collector and its internal flow field, it is still applied blindly without satisfying model of its separation efficiency at present. Conclusively, it has vital significance to make a further research on the electrostatic cyclone dust collector. The preliminary theory on the separation efficiency of the electrostatic cyclone dust collector is deduced in the paper, based on the predecessors' experiment and theoretical research results of the separation efficiency of the electrostatic cyclone dust collector [1–5].

68.2 The Calculation of the Electric Field Intensity and Particles' Charging Capacity

68.2.1 The Calculation of the Electric Current and Electric Field Intensity

The structure of the electrostatic cyclone dust collector is shown in Fig. 68.1. The circular corona wires between its outer cylinder and the exhaust pipe are set in the dust collector, and these wires are parallel to the wall surface and are equidistantly distributed on the circumference concentric with the surface. Corona wires and the outside wall connected to the ground are regarded as cathode and the dust collecting pole, respectively, which composes high voltage electrostatic field. Due to large radius of concentric circles and its small curvature, the electric field is approximate to the board-line structure. According to perturbation theory, the electric current equation can be simplified as [4, 5]:

$$i = \frac{4\pi\varepsilon_0 k}{B^2 \ln\left(d/r_d\right)} U(U - U_0) \tag{68.1}$$

U—the voltage produced by cathode and anode of the electrostatic cyclone dust collector, V; U_0—Initial voltage of the corona, according to the data from experiments [4, 5], the initial corona voltage of Φ4 mmburr electrode is 20 kV; E_0—the initial intensity of the corona electric field, V/m; k—the mobility of ions inside the mixed gas, $m^2/(s \cdot V)$; r_d—the radius of the corona wire, m; ξ_0—the dielectric coefficient of the vacuum, $\xi_0 = 8.85 \times 10^{-12} c/(V \cdot m^2)$; B—the distance

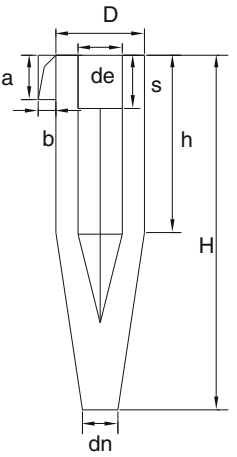

Fig. 68.1 Model of electrostatic cyclone dust collector

from the corona pole to the dust collection pole, m; A—the distance from one corona wire to another, $A = \frac{\pi \cdot (D-2 \cdot B)}{n}$; n—the number of corona poles; d—the parameter depending on the ratio of B and A. In the literature [6], when $B/A \geq 1$, $d = \frac{A}{2\pi \cdot \exp\left(-\pi \cdot B/A\right)}$. In the design of the engineering, the following formula is usually used to calculate the intensity of the electric field near the dust collecting pole:

$$E_c = \sqrt{i \cdot B/(\pi \varepsilon_0 \cdot Ak)} = 2 \cdot \sqrt{\frac{U(U-20000)}{AB \cdot \ln\left(d/r_d\right)}} = \frac{2}{\sqrt{\pi}} \cdot \sqrt{\frac{U(U-U_0)}{\frac{(D-2B)B}{n} \cdot \ln\left(\frac{D-2B}{2n \cdot r_d}\right) + B^2}} \tag{66.2}$$

68.2.2 The Calculation of Particles' Charging Capacity

Charging the dust is the most important step in the process of collecting dusts by electricity. Dusts' charging capacity is related with the radius of particles, the intensity of the electric field, stay time and many other factors. Generally speaking, charging the dust is due to two main mechanisms: charging the dust in the electric field and charging the dust in the process of its diffusion. The two mechanisms are effective throughout the process of charging the dust, however, within the scope of the different radius of dust particles, the role of each mechanism is different: for those whose radiuses are longer than 0.5 μm, charging the dust in the electric field is dominant; while for those whose radiuses are shorter than 0.2 μm, charging the dust in the process of its diffusion plays an important role. For the particles whose radiuses are between 0.2 μm and 0.5 μm, the two mechanisms make a big difference.

68.2.2.1 Charging the Dust in the Electric Field

As is shown in Fig. 68.2, charging the dust in the electric field is that ions, under the action of electric field, collide with dust particles and attach them along the power line, transferring charges to dust particles. In order to simplify the calculation, the following assumptions are usually made: (1) dust particles are spherical; (2) the electric field of one dust particle does not interfere with the one near another dust particle; (3) the diameter of dust particles is far greater than the mean free path of ions; (4) apart from the area around the dust particles, the intensity of the electric field in the whole space is uniform; (5) dust particles and ions are evenly suspended in the fixed electric field.

In the uniform electric field, the electric field near the sphere includes two parts: the additional electric field E_1 and the electric field E_2 caused by charges on the sphere. Due to ions' deposition on the sphere constantly, the electric field E_2 formed by charges on the sphere is continuously strengthened. As the direction of E_2 and that of E_1 are opposite, further deposition of ions repelling each other makes charging dust particles on the sphere speed down so as to stop completely, namely, reaching to the saturated situation. The intensity of the electric field of any point on the sphere is $E = E_1 + E_2$. For conductive spheres with the radius of r_p:

$$E = 3E_0 \cos\theta - \frac{q}{4\pi\varepsilon_0 r_p^2} \tag{68.3}$$

In the formula, θ—the angle formed by the intersection of the direction of charges towards dust particles and the direction of the undisturbed electric field;

q—the capacity of charging the dust particles in the electric field (C); E_0—the intensity of the undisturbed electric field (v/m), to simplify the calculation, set $E_0 = E_c$ [6].

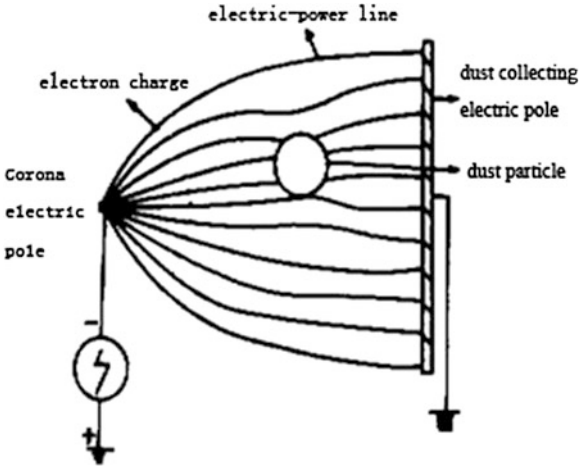

Fig. 68.2 The charge of the dust particle

The rate of the charge with time changing is the integral of the result in which the effective differential area of charging is multiplied by the current density:

$$\frac{dq}{dt} = \int_0^{\theta_0} j\,dA = \int_0^{\theta_0} (N_0 \cdot ekE)\,dA = N_0 \cdot ek \int_0^{\theta_0} \left(3Ec \cdot \cos\theta - \frac{q}{4\pi\varepsilon_0 \cdot r_p^2}\right) dA \tag{68.4}$$

In the equation, j—the current density $j = N_0 ekE\ (A/m^2)$; e—the charge of the electron (c) $e = 1.6 \times 10^{-19}$; N_0—the density of the ion; θ_0—the angle limited by the direction of charges towards dust particles; r_p—the radius of the dust particle; dA—the area unit.

When $E_1 = E_2$, charging the dust particles reaches to the situation of saturation. Charging the dust stops and θ is close to zero, so we set $\cos\theta = 1$. The saturated electric capacity of ions can be gotten by formula (68.3):

$$q_b = 12\pi r^2 \varepsilon_0 Ec \tag{68.5}$$

For any charged state, the limit angle formed by charges flowing towards the sphere can be worked out by setting $E = 0$ in the formula (68.3):

$$\cos\theta = \frac{q}{12\pi r^2 \cdot \varepsilon_0 \cdot E_c} = \frac{q}{q_b} \tag{68.6}$$

The capacity of charging dust particles with time changing can be obtained by Eq. (68.4):

$$\frac{dq}{dt} = 3\pi r_p^2 \cdot E_c \cdot N_0 \cdot ek\left(1 - \frac{q}{q_b}\right)^2 \tag{68.7}$$

At any time, the capacity of charging dust particles can be obtained by integral of Eq. (68.7):

$$q(t) = 12\pi\varepsilon_0 \cdot r_p^2 \cdot E_c\left(\frac{t}{t + t_0}\right) = q_b\left(\frac{1}{1 + t_0/t}\right) \tag{68.8}$$

In the equation, t_0—Time constant of charging the dust $t_0 = 4\varepsilon_0/N_0 ek$; K—Ions' migration rate, $m^2/(s \cdot V)$.

For non-conductive dusts, they are considered by introducing dielectric constant. At this time, formula (68.8) can be written as:

$$q(t) = \left(\frac{3K}{K+2}\right) 4\pi\varepsilon_0 r_p^2 E_c\left(\frac{t}{t + t_0}\right) \tag{68.9}$$

In the formula, K—the relative dielectric coefficient of dust particles, $K = \varepsilon/\varepsilon_0$; ξ_0—Vacuum dielectric coefficient, $\xi_0 = 8.85 \times 10^{-12}$ c/V $\cdot$ m^2.

When the dust is a good conductor, relative dielectric coefficient is $K \to \infty$, and then $3K/(K+2) = 3$. For insulators, $K = 1$ and $3K/(K+2) = 1$. For common dusts, we know $3K/(K+2) = 1.5 \sim 2.0$ and use (68.5) in this paper.

For the actual electric dust collector, the time constant of charging the dust t_0 is commonly within 10^{-3}–10^{-2} s [5], while the stay time of dusts in cyclone dust collector is generally 0.2 s [6]. Dusts getting 99 % of limit charges could be thought that dusts get limit charges (the saturation of charging dusts), namely:

$$q_b = \lim_{t\to\infty}\left(\frac{3K}{K+2}\right)4\pi\varepsilon_0 \cdot r_p^2 \cdot Ec\left(\frac{1}{1+\frac{t_0}{t}}\right) = \left(\frac{12K}{K+2}\right)\pi\varepsilon_0 \cdot r_p^2 \cdot E_0 = 6\pi\varepsilon_0 \cdot r_p^2 \cdot E_0 \tag{68.10}$$

68.2.2.2 Charging the Dust in the Process of Its Diffusion

Charging the dust in the process of its diffusion is due to the random thermal movement of ions. Thermal movement of ions is subject to the theory of gas molecular motion. This movement makes the ions diffuse through the gas so that the ions collide with dust particles contained in the gas, and then stick on them, making the dust charged. Charging the dust in the process of its diffusion mainly relies on the heat, the size of the dust and stay time. In 1951, the formula of charging the dust in the process of its diffusion was deduced by White. In this paper, the simplified formula [5, 6] Heinrich advised is adopted:

$$q_d = ne = 2 \times 10^8 \cdot r_p \cdot e = 3.2 \times 10^{-11} \cdot r_p \tag{68.11}$$

68.2.2.3 Dust Particles' Charging Capacity

The total capacity of charging the dust is approximately the following:

$$q_q = 6\pi \cdot \varepsilon_0 \cdot r_p^2 \cdot E_c + 3.2 \times 10^{-11} \cdot r_p \tag{68.12}$$

Noticeably, to simplify the calculation, only charging the dust in the electric field [6] is usually considered in practice. Therefore,

$$q_q = 6\pi \cdot \varepsilon_0 \cdot r_p^2 \cdot Ec \tag{68.13}$$

68.3 The Derivation of the Driven Velocity

Charged dust particles in the electrostatic cyclone dust collector are mainly affected by centrifugal force, electric field force, viscous resistance of the gas and inertial force. The influence all kinds of forces make is summarized in the following equation:

$$F_e + F_c - F_d - F_i = 0 \tag{68.14}$$

In the equation, F_e—Electric field force, $F_e = q_b E_c$, N; F_c—Centrifugal force, $F_c = m\frac{V_t^2}{R}$, N; F_d—Viscous resistance, $F_d = 6\pi r_p \mu w$, N; F_i—Inertial force, $F_i = m\frac{d\omega}{dt}$, N; q_b—the load capacity when dust particles reach to the state of saturation, C; v_w—Dust particles' tangential velocity near the wall, m/s; R_w^*—Dust particles' rotating radius, m; μ—the viscosity coefficient of the gas, N · s/m^2; ω—the speed caused by dust particles' displacement towards the wall, m/s; t—the time of dust particles staying in the separation space, s.

The expressions of all parameters above are applied to the Eq. (68.14), the following formula can be elicited:

$$m\frac{d\omega}{dt} + 6\pi r_p \mu\omega/m = \frac{q_b E_p}{m} + \frac{V_t^2}{R} \tag{68.15}$$

The equation above is integrated:

$$\omega = \frac{1}{6\pi r_p \mu}(q_b E_p + m\frac{V_t^2}{R})[1 - \exp(-\frac{6\pi r_p \mu t}{m})] \tag{68.16}$$

In this formula, $\frac{m}{6\pi r_p \mu}$ is known as the movement time constant. When the time is more than $5\tau_m$, the velocity expressed by ω is actually the speed of dust particles stopping their movement. And then the required time to make dust particles with all kinds of radius reach their end speed can be determined. It takes about 0.2 s to make dust particles stay in the electrostatic cyclone dust collector. However, for dust particles with radius under 50 μm, the movement time constant expressed by $\tau_m = \frac{m}{6\pi r_p \mu} = \frac{4/3\pi r_p^3 \rho_p}{6\pi r_p \mu} = \frac{2r_p^2 \rho_p}{9\mu}$. In the formula, when $\rho_p = 2750$ kg/m^3, the radius of the dust particle expressed by r_p is 4 μm and $\mu = 18.20 \times 10^{-6}$ N · s/m^2, so $\tau_m = 0.0084$ s and $5\tau_m = 0.042$ s. Therefore, compared with the stay time, the acceleration time of the dust is very little. Finally, the index entry of formula (68.16) can be ignored, namely:

$$\omega = \frac{1}{6\pi r_p \mu}(q_q E_c + m\frac{v_w^2}{R_w^*}) \tag{68.17}$$

The equivalent radius expressed by R_w^* of the cyclone dust collector is pointed out in the literature:

$$R_w^* = \left\{\frac{1}{H}\left[\frac{H-h}{3}\left(R^2 + R_n^2 + R \cdot R_n\right) + R^2 \cdot H\right]\right\}^{\frac{1}{2}} \tag{68.18}$$

The relationship between the tangential velocity near the outer wall of the cyclone dust collector and the entrance velocity expressed by v_1 can be showed by the Alexander empirical formula, namely $v_w = 2.15 \cdot \left(\frac{a \cdot b}{d_e \cdot D}\right)^{0.5} \cdot v_1$. In the formula, a, b—the height and width of the entrance of the dust collector, m; d_e, D—the

diameter of the cylinder and the one of the exhaust pipe, m. Through the above analysis, the driven velocity of the dust can be drawn, namely:

$$\omega = \frac{4\varepsilon_0 \cdot r_p}{\pi\mu} \cdot \frac{U(U-20000)n}{(D-2B)B \cdot \ln\frac{D-2B}{2nr_d} + n \cdot B^2} + \frac{1.08 r_p^2 \cdot \rho_p \cdot ab \cdot v_1^2}{\mu D \cdot d_e \left\{\frac{1}{H} \cdot \left[\frac{H-h}{3}\left(R^2 + R \cdot R_n + R_n^2\right) + R^2 \cdot h\right]\right\}^{1/2}} \tag{68.19}$$

68.4 Establish the Model for the Dust Collector's Efficiency

As is known, the formula of calculating the efficiency of the electrostatic precipitator:

$$\eta = 1 - \exp(-\frac{a_c}{Q}\omega) \tag{68.22}$$

In the formula, Q—the flow volume of the air handled, m^3/h, $Q = V \cdot a \cdot b$ (V is the velocity of entrance, m/s and a, b are the width and height of the entrance respectively, m); a_c—the total area of the dust collecting pole, m^2. As is known:

$$a_c = 2\pi R \cdot h + \pi(R + R_n)\{(H-h)^2 + (R-R_n)^2\}^{1/2} \tag{68.23}$$

68.5 Conclusion

In this paper, the intensity of the electric field and the dust particles' charging capacity of the electrostatic cyclone dust collector are analyzed in theory and deduced respectively. Based on the forces imposed on dust particles, the dust particle's displacement speed is worked out and the model for the separation efficiency of the electrostatic cyclone dust collector is summarized eventually.

Acknowledgments This study is supported by the Key Project of Chinese Ministry of Education (No. 211096), the key project of Shandong province science and technology Program (No. 2008GG2TC01011-14) and the National Natural Science Foundation of China (No. 11272188).

References

1. Zhang J, Shen H, Li H (2002) Analysis of flow field of the electrostatic cyclone separator. Thermal Energy Power Eng 5:500–502
2. Zhang J, Li H, Wang D (2002) The research for the experiment about the flow field of the electrostatic cyclone separator. Fluid Mach 10: 4–7
3. Qian F (2003) Optimizing the structure of the electrostatic cyclone separator. Master's degree thesis. Qingdao Technological University, Qingdao

4. Feng B (1989) Chemical engineering handbook, vol 5. Chemical industry press, Beijing
5. Tan T, Liang F (1984) Ventilation in industry and dust removal technology. China Architecture and Building Press, Beijing
6. Zhang J et al (1990) The new method of calculating dust particles' average stay time in the cyclone dust collector. J Qingdao Constr Eng Coll 3:22–27

Chapter 69
The Exploration on Heat Transfer Models for Borehole Heat Exchanger in the Soil with Groundwater Advection

Lei Zhao, Linlin Zhang and Songtao Hu

Abstract In order to estimate the impact of groundwater advection and axial heat conduction on the performance of borehole heat exchangers in ground source heat pump systems, results obtained from different heat transfer models of a vertical borehole heat exchanger based on line source theory were compared. It is found that the analytical solution from the moving finite line source (MFLS) model reveals the fact that soil temperature field around the borehole migrates along the ground-water advection direction and more obvious variation of the vertical temperature change occurring near the ground surface and the borehole bottom. It means the MFLS model can be used when groundwater advection presents. The results are also validated by 3-D numerical simulation. In addition, the influence of groundwater advection on the soil temperature responses is also analyzed. A larger advection velocity causes the soil temperature to change faster and to achieve a lower stable temperature change as time elapses.

Keywords Ground source heat pump · Groundwater advection · Line heat source model · Temperature response

69.1 Introduction

Energy-saving and environmental friendly ground source heat pump systems (GSHPs) have been widely used for space heating and air-conditioning in residential and commercial buildings. And vertical borehole heat exchangers (BHEs)

L. Zhao (✉) · L. Zhang · S. Hu
School of Environmental and Municipal Engineering, Xi'an University of Architecture and Technology, No.13 Xi'an Yanta Road, Xi'an 710055 Shaanxi, China
e-mail: leizhao0308@hotmail.com

S. Hu
School of Environmental and Municipal Engineering, Qingdao Technological University, Qingdao, China

A. Li et al. (eds.), *Proceedings of the 8th International Symposium on Heating, Ventilation and Air Conditioning*, Lecture Notes in Electrical Engineering 262,
DOI: 10.1007/978-3-642-39581-9_69,

with U-tubes have been widely adopted in practice for its advantage of occupying less land and good performance. However, the BHEs heat transfer performances are determined by the soil thermal physical properties and affected by the groundwater advection if it is in presence. Results have indicated that the groundwater advection may bring about positive and negative influence on the operational performance of heat pump systems [1]. Thus, it is necessary to take the influence of groundwater advection into consideration to improve the BHE design accuracy. Up to now, the reliable models can be referred are still very limited. To this end, the solutions to dynamic temperature responses from the existing models based on the line source theory presented by Ingersoll and Plass [2] are further compared and discussed. Line source theory assumes that the processes are conduction dominated and the borehole can be approximated as an infinite line source (ILS) or finite line source (FLS) with constant heat rejection rate in porous soil [3]. ILS model is too simple and seldom used for design calculation. Since FLS model has taken the influence of ground surface heat convection and axial heat conduction into account, it is widely used in practice [4, 5]. To take the influence of groundwater convection on BHE performance into account, moving infinite line source model (MILS) and moving finite line source model (MFLS) have been developed. The solutions of soil temperature responses from different models will be compared and analysed. Some suggestions are proposed to help designers to choose a more feasible heat transfer model for BHE performance analysis under different conditions to consider the influence of groundwater advection.

69.2 Comparison of Solutions from Different Models

The solutions of the temperature response of the soil to the BHE heat rejection from different models are compared. In the case illustrated, the borehole is 60 m in depth buried in the soil with thermal conductivity of 0.98 W m^{-1} K^{-1}, the volumetric specific heat of 1.4×10^6 J m^{-3} K^{-1} and the thermal diffusivity of 0.7×10^{-6} m s^{-2}. The total heat rejection rate is 3 kW, that is, 50 W/m borehole depth. The soil porosity is 0.31.

69.2.1 Solutions from FLS Model

Figure 69.1 shows the temperature changes obtained from the FLS model for the case without groundwater advection. Figure 69.1a illustrates the temperature change isotherms on the horizontal $Z = 30$ m, which are symmetrically distributed around the borehole in the soil. Figure 69.1b shows the dynamic temperature responses at the positions of (2, 0, 30), (4, 0, 30) and (6, 0, 30) and it tells that it takes a very long time for the temperature to reach stable in the soil without groundwater advection. And it can also be found that the thermal effect distance is

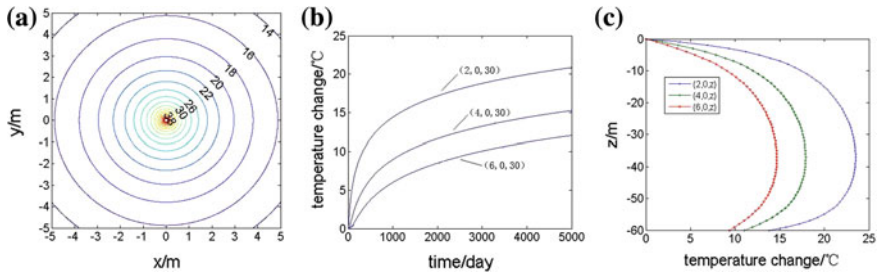

Fig. 69.1 The temperature responses obtained by FLS model. **a** Stable temperature change isotherms on horizontal $Z = 30$ m, **b** dynamic temperature responses at different positions, and **c** temperature changes along the depth at different positions

just about 2 m from the borehole axis on the horizontal $Z = 30$ m and the temperature change is only about 0.4 °C at this position after 10 h continuous heat rejection of the borehole. Figure 69.1c shows the stable vertical temperature change along the depth at the positions of 2, 4 and 6 m from the borehole axis. The temperature change is zero on the ground surface since it is at a fixed temperature. And the temperature change increases along the borehole depth and reaches the maximum around the middle horizontal through the borehole. Then it obviously drops to a certain value as it approaches the horizontal through the borehole bottom. It can be seen that the effect of axial heat conduction is significant.

69.2.2 Solutions from MFLS Model

Figure 69.2a, b shows the soil temperatures change isotherms on the horizontal $Z = 30$ m obtained by MFLS model after 1 month and 1-year continuous heat injection into the soil without groundwater advection, respectively, which circle around the borehole. They are both different from the stable ones illustrated in Fig. 69.2c. However, the temperature change isotherms in Figs. 69.2c and 69.1a are almost in coincident with each other. This means the stable solutions obtained by FLS model are as accurate as those by MFLS when there is no groundwater advection. Figure 69.2d indicates that the undisturbed soil is just about 5 m from the borehole axis after 1-month heat absorption, while the temperature change of the same position reaches 4 °C after 1-year operation, which is lower than the stable value, 16 °C. This reveals that the thermal effect radius increases as time elapses.

Figure 69.3a–d illustrate the soil temperature change isotherms on the horizontal $Z = 30$ m after 1-month and 1 year continuous heat absorption as well as the temperature changes along the x-axis under different uniform Darcy advection velocity of groundwater, $U = 5\times10^{-6}$, 9×10^{-7}, 9×10^{-8} and 5×10^{-9}m s^{-1}, respectively, in which $U = u_x\rho_w c_w/\rho c$ and u_x is the advection velocity. It can be seen that the temperature change isotherms are not symmetrically distributed any more, but migrating along the advection direction obviously as time elapses.

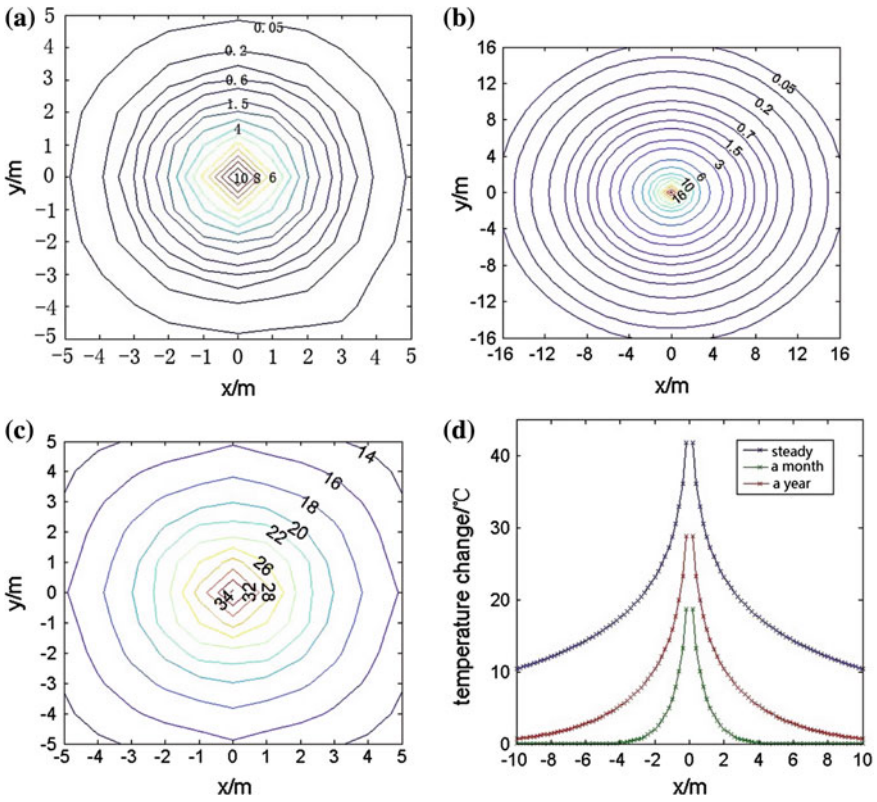

Fig. 69.2 The temperature change isotherms on the horizontal $Z = 30$ m without advection obtained by MFLS model

Furthermore, a larger advection velocity causes a more obvious migration. That is, the function scope becomes larger in the advection direction, while it becomes smaller in the opposite direction. This means the advection may enhance the heat transfer in the soil in the advection direction, but restrain the borehole heat rejection in the opposite direction. In addition, comparing Fig. 69.3a–d with Fig. 69.2a, b reveals that if the groundwater advection velocity is less than 10^{-7}m s^{-1}, the temperatures of the soil closed to the borehole increase more obviously during the initial short period than those do in the case without groundwater advection. But with time elapses, the temperature change reduces if there is ground advection. In the case with groundwater advection velocity larger than 10^{-7} m s^{-1}, the soil temperature changes are obviously less than those in the case without advection. That is, groundwater advection can mitigate thermal accumulation in the soil.

Figure 69.4 shows how the thermal effect distances in and opposite the groundwater advection direction change along x-axis on the horizontal $Z = 30$ m as time elapses. It is clear that the thermal effect distances in both directions are

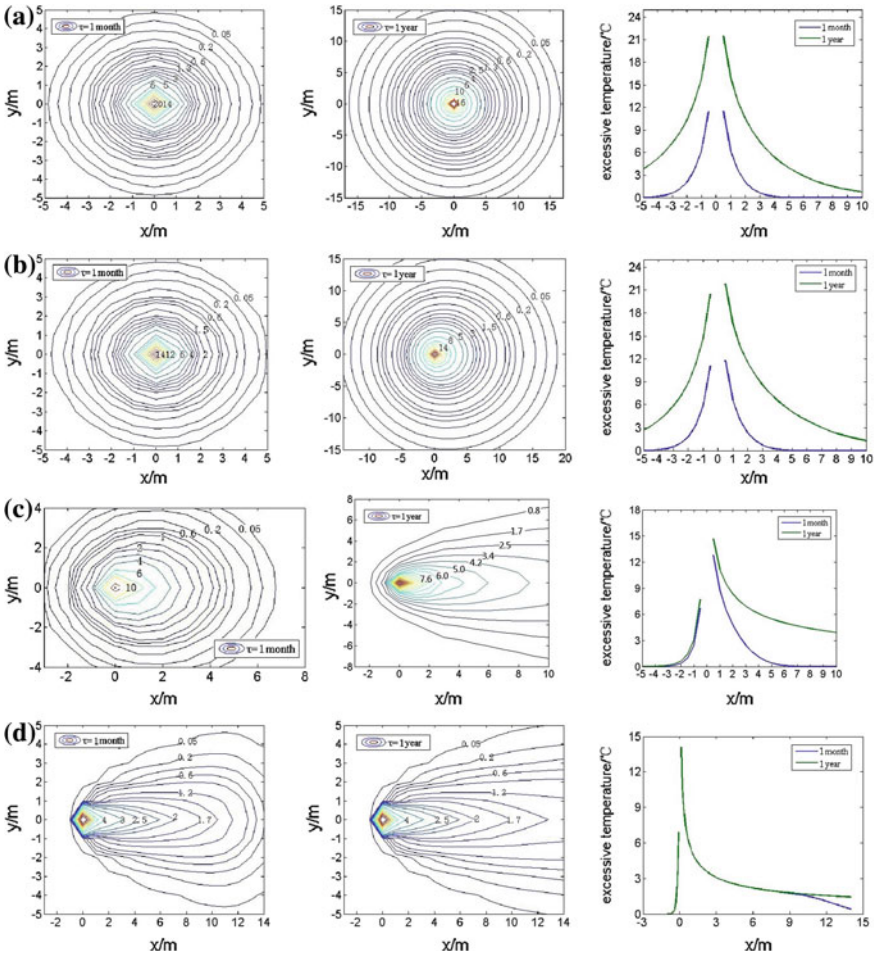

Fig. 69.3 The influence of advection velocity on temperature change isotherms on horizontal $Z = 30$ m

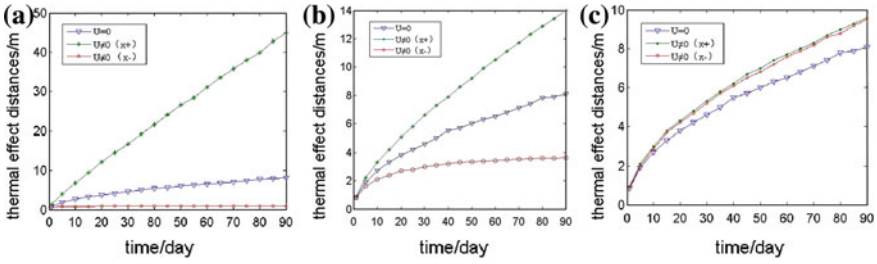

Fig. 69.4 The variation of thermal effect distances upstream and downstream with time on horizontal $Z = 30$ under different advection velocity

almost equal as the U is less than 0.9×10^{-8} m s^{-1}. The upstream and downstream thermal effect distances are just about 2 m after 5 days continuous heat rejection of the borehole in this case. And they are a little larger than the thermal effect radius in the case without advection. As the advection velocity increases, the difference between the downstream thermal effect distance and the upstream one becomes larger. And the one downstream becomes larger than that without advection, but the upstream one reduces to shorter than that without advection. In the case of $U = 0.5 \times 10^{-6}$ m s^{-1}, the thermal effect distance is about 5 m downstream after 5 days continuous heat rejection of the borehole and it may even reach 40 m after 90 days, while the thermal effect distance upstream is just about 1 m.

69.2.3 Comparison of Solutions from MILS and MFLS Model

It can be found that in Fig. 69.5a, b that the stable temperature change obtained by MILS model remains the same along the depth in the soil. However, the value obtained by MFLS model gradually decrease to zero when it approaches the ground surface and the bottom of the borehole. The temperature changes maintain at a relatively constant value and it approaches to the maximum around the horizontal through the borehole center. Furthermore, there are clear differences between the temperature changes at the same position obtained by two models. The temperature change at a certain position downstream obtained by MILS model is larger than that by MFLS model, while the value at a certain position upstream obtained by MILS model is slightly smaller than that by MFLS model. This tells us that though the MILS model accounts for the effect of advection, but can not reveal the influence of ground surface heat convection and axial heat conduction. A relative higher advection velocity may restrain the effect of ground surface heat

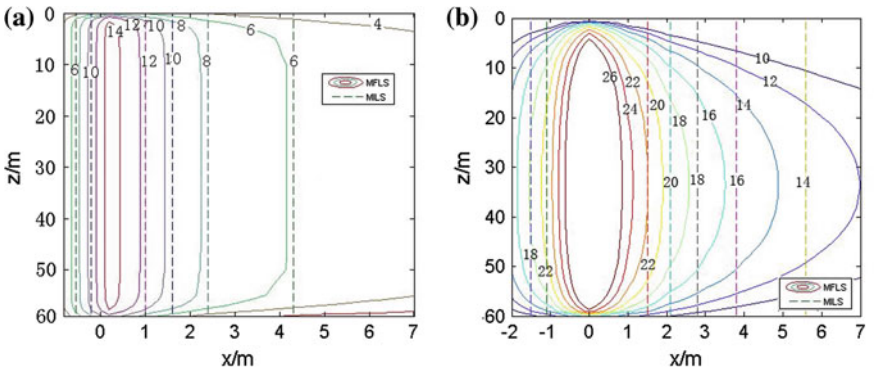

Fig. 69.5 Stable temperature changes along the borehole depth obtained by MFLS and MILS model

convection and axial heat conduction. And the difference between temperature changes obtained by MILS and MFLS model become less along the borehole depth. If the advection velocity is greater than 10^{-7} m s^{-1},neglecting the effect of heat convection and axial heat conduction may cause very less differences between soil temperature changes obtained by two models. But the MILS model is not accurate to be used to design BHE when the advection velocity is less than 10^{-7} m s^{-1}. MFLS model can take not only the effect of ground surface heat convection and axial heat conduction into account, but also accounts for the influence of groundwater advection. It will lead to a more accurate BHE design when there is groundwater in presence in the soil and the advection velocity is less than 10^{-7} m s^{-1}.

69.3 Validation of the MFLS Model by Numerical Simulation

To validate the analytical solution to temperature change obtained by MFLS, a 3-D numerical simulation was conducted for an aquifer domain in size of 20 m × 30 m × 80 m containing a BHE of 60 m in depth represented by a line source with an average heat rejection rate of 50 W/m. Thermal parameters of the aquifer is as above. Fixed-head boundary conditions are applied to the left and the right boundaries of the model. Uniform groundwater flow of 3×10^{-7} m s^{-1} is assigned throughout the aquifer, which is equivalent to Darcy advection velocity of 9×10^{-7} m s^{-1}. In order to ensure the results independence of grid, several unstructured meshes made of hex/wedge elements have been tested to reach a compromise between accuracy and computational effort, the intermediate mesh has been adopted for the final simulation. Figure 69.6a shows the isotherms around the heat source after 1 month heat rejection are in good agreement with those in Fig. 69.3c. And the curve of the soil temperature varying along x-axis obtained by

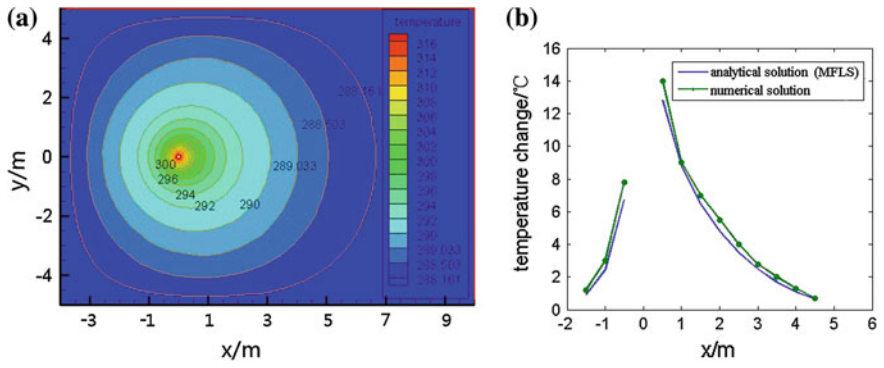

Fig. 69.6 Comparison of solutions obtained by numerical simulation and MFLS model

simulation is coincident with that obtained by analytical solutions of MFLS model as shown in Fig. 69.6b. This means the analytical results is correct.

69.4 Conclusion

Solutions to the soil temperature change obtained by different models based on line source theory, including FLS, MILS and MFLS models, are compared and analyzed. FLS model can reveal the effect of axial heat conduction on vertical temperature distribution in the soil, which is very important for shallow buried BHE design. The temperature change obtained by MFLS and FLS models are coincidence with each other when there is no groundwater advection and the soil temperature field is in central symmetry around the borehole axis. However, the soil temperature field migrates along the advection direction. The thermal effect scope enlarges in the advection direction but the temperature field may reach stable faster as the advection velocity increases. The Darcy advection velocity between 9×10^{-8} and 10^{-7} m s^{-1} brings about a larger temperature change downstream the borehole in the soil at the initial period, but the temperature change becomes less as time elapses. The thermal effect scope vertical to the advection direction becomes narrower than that in the case without advection. It is found that the differences between temperature change obtained by MILS and MFLS model are less if the groundwater advection velocity is greater than 10^{-7} m s^{-1}. Otherwise, MFLS model is recommended for BHE design when there is groundwater advection and the borehole is not very deep. The accuracy of MFLS model solution is also verified by numerical simulation result.

References

1. Diao NR, Li QY, Fang ZH (2003) An analytical solution of temperature response in geothermal heat exchangers with groundwater advection. J Shandong Inst Architect Eng 18(3):1–5
2. Ingersoll LR, Plass HJ (1984) Theory of the ground pipe heat source for the heat pump. ASHVE Trans 47:339–348
3. Zeng HY, Diao NR, Fang ZH (2004) Analysis of the heat transfer inside a borehole of vertical of vertical ground heat exchangers. Acta Energiae Solaris Sinica 25(3):399–405
4. Carslaw HS, Jeager JC (1959) Conduction of heat in solids. Oxford Press, Oxford
5. Nelson MG, Philipp B, Zhu Ke (2011) A moving finite line source model to simulate borehole heat exchangers with groundwater advection. Intl J Therm Sci 50:2506–2513

Chapter 70
Numerical Calculation and Analysis of Apply for the Heat Transfer Performance of Porous Brick

Xiaolu Wang, Fuqin Ma and Huifan Zheng

Abstract Introduces some principles and calculating method used for the problem of porous brick wall in new energy-saving area. Finite volume method is adopted to complete the numerical analysis of building blocks model. The SIMPLE algorithm is used to solve the equation of speed and pressure. Convection–diffusion subject uses second-order upwind format. Calculation mesh adopts the unstructured hexahedral style. A few examples calculated are given. The date comparisons between calculation and experiment are given up. Rectangular hole brick is affected more stronger than circle hole brick. The wall heat flux and wall temperature have been calculated. Thermal performance can be obtained through numerical calculation in the steady heat transfer, being very approximate from the experimental result. According to the calculation of temperature distribution in the brick, thermal performance can be successfully analyzed.

Keywords Heat transfer of porous brick wall · Numerical calculation · Harmonic performance

X. Wang
Jinling Institute of Technology, Mechanical Electrical Engineering Institute, Nanjing, 211169 Jangsu, China

F. Ma · H. Zheng (✉)
Zhongyuan University of Technology, Zhengzhou 450007 Henan, China
e-mail: zhenghuifan@163.com

A. Li et al. (eds.), *Proceedings of the 8th International Symposium on Heating, Ventilation and Air Conditioning,* Lecture Notes in Electrical Engineering 262,
DOI: 10.1007/978-3-642-39581-9_70,

70.1 Introduction

There are a series of advantages about porous brick, such as reliable strength, light weight, a good thermal insulation property, and being convenient to construct. Porous brick is made of sludge of the riverway, gangue, shale, fly ash, and industry off scum, which could be more possible to protect the plow and environment including save energy. So thermal insulation porous brick wall has been already regarded as the major form of energy-saving wall by national standard and design standard of energy-saving building of each city and widely used in the civil architecture [1–2].

However, there are also some problems in the applications. A series of holes distributed in the energy saving porous brick makes the theoretic calculation of the wall thermal performance very difficult, the more expensive cost of experimental method, longer time, less measuring parameters, especially more difficult for the measurement of thermal performance parameters under the periodic, unsteady heat transfer condition. So the damping factor of porous brick acting on the temperature amplitude and the detention period etc., and important thermal parameters, which are closely related to building wall, have not given in the already issued codes for design of air conditioning or manuals for design of heating and air conditioning [3–4]. Numerical calculation has been successful and widely used in architectural mechanics, can also perform well in the calculation of the thermal performance wall both in the steady- and unsteady-state heat transfer with the many advantages such as strong adaptability, widespread application, low cost of the calculation, its rapidity, and accuracy.

70.2 Calculation Model and Theory

70.2.1 Calculation Model

Porous brick has a wide application and variety, including the types of KP1 and DM, which are applied widespread [5]. The KP1 brick with 20 holes sintered by the sludge of the Yellow River is widely applied in Henan province, which measures 230 mm × 110 mm × 90 mm. The diagrammatic sketch of KP1 brick structure is as shown in Fig. 70.1. The DM sintered brick made from coal gangue used for wall with 190 mm × 190 mm × 90 mm is sintered by China University of Mining and Technology and Xuzhou mining bureau with the raw material of gangue of Taiyuan, Xuzhou. The diagrammatic sketch of brick structure is as shown in Fig. 70.2. When calculated, the actual wall bricks status should be taken into consideration, including vertical and horizontal ash seam in the unit of every brick, with the thickness of 10 mm. The two types of brick wall are both laid by sequential structure with single brick.

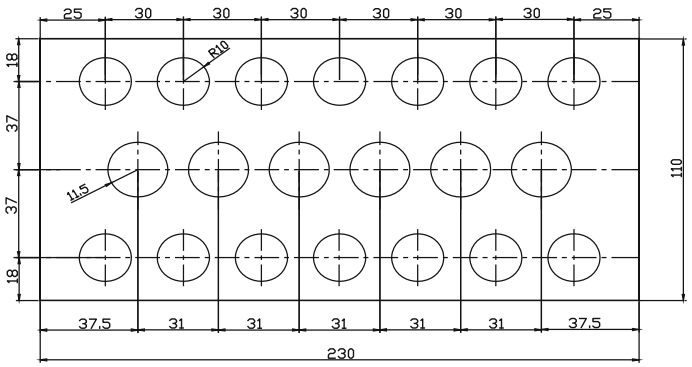

Fig. 70.1 Diagrammatic sketch of KP1 brick structure with 20 holes

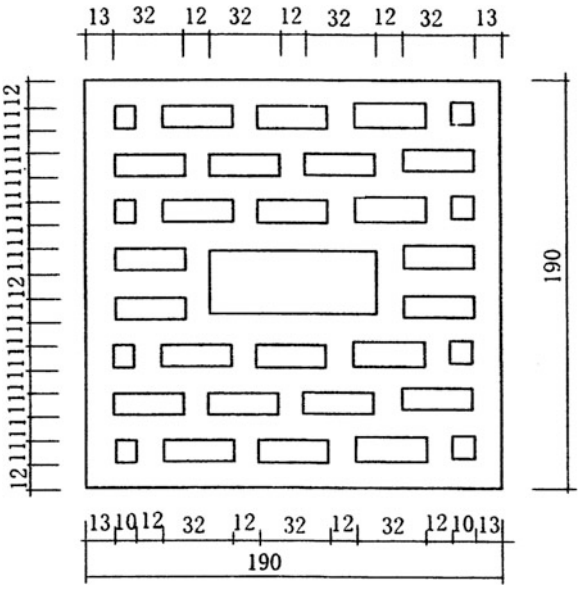

Fig. 70.2 Diagrammatic sketch of sintered modulus brick made from coal gangue

70.2.2 Calculation Formula of and Process

The heat transfer process of the porous brick is a 3-D complex heat transfer process, which is coupled by natural convection heat transfer and thermal conductive, and meets the conservations of mass, momentum, and energy. The equation is as follows [6].

$$\frac{\partial u}{\partial x}+\frac{\partial v}{\partial y}+\frac{\partial w}{\partial y}=0 \tag{70.1}$$

$$\rho\left(\frac{\partial u}{\partial \tau}+u\frac{\partial u}{\partial x}+v\frac{\partial u}{\partial y}+w\frac{\partial u}{\partial z}\right)=-\frac{\partial p}{\partial x}+\mu\left(\frac{\partial^2 u}{\partial x^2}+\frac{\partial^2 u}{\partial y^2}+\frac{\partial^2 u}{\partial z^2}\right) \tag{70.2}$$

$$\rho\left(\frac{\partial v}{\partial \tau}+u\frac{\partial v}{\partial x}+v\frac{\partial v}{\partial y}+w\frac{\partial v}{\partial y}\right)=-\frac{\partial p}{\partial y}+\mu\left(\frac{\partial^2 v}{\partial x^2}+\frac{\partial^2 v}{\partial y^2}+\frac{\partial^2 v}{\partial z^2}\right) \tag{70.3}$$

$$\rho\left(\frac{\partial w}{\partial \tau}+u\frac{\partial w}{\partial x}+v\frac{\partial w}{\partial y}+w\frac{\partial w}{\partial z}\right)=-\frac{\partial p}{\partial z}+\mu\left(\frac{\partial^2 w}{\partial x^2}+\frac{\partial^2 w}{\partial y^2}+\frac{\partial^2 w}{\partial z^2}\right)-\rho g \tag{70.4}$$

$$\rho c\left(\frac{\partial T}{\partial \tau}+u\frac{\partial T}{\partial x}+v\frac{\partial T}{\partial y}+w\frac{\partial T}{\partial z}\right)=\lambda\left(\frac{\partial^2 T}{\partial x^2}+\frac{\partial^2 T}{\partial y^2}+\frac{\partial^2 T}{\partial z^2}\right) \tag{70.5}$$

Energy equation of solid heat conduction:

$$\rho c\frac{\partial T}{\partial \tau}=\lambda\left(\frac{\partial^2 T}{\partial x^2}+\frac{\partial^2 T}{\partial y^2}+\frac{\partial^2 T}{\partial z^2}\right) \tag{70.6}$$

Boundary conditions of each side of brick:

$$x=0,\quad u=v=w=0,\quad h_0(T_{f_0}-T_{w_0})=-\lambda\frac{\partial T_{\mathrm{w}_0}}{\partial x} \tag{70.7}$$

$$x=L,\quad u=v=w=0,\quad h_i(T_{f_i}-T_{w_i})=-\lambda\frac{\partial T_{w_i}}{\partial x} \tag{70.8}$$

$$y=0,\quad y=W:\quad u=v=w=0,\quad \frac{\partial T}{\partial y}=0 \tag{70.9}$$

$$z=0,\quad z=H:\quad u=v=w=0,\quad \frac{\partial T}{\partial z}=0 \tag{70.10}$$

Based on 《Code for design of Heating ventilation and air-conditioning》 (GB 50019-2003), the heat transfer coefficient on left boundary is set as $h_0 = 23$ W/(m^2 K), while the right side is $h_i = 8.7$ W/(m^2 K). According to the 《Construction component heat transfer properties of the steady-state determination calibration and protective heat box method, the air temperatures of two surfaces of brick made from the sludge of the Yellow river are respectively −19 and 19 °C, while the indoor and outdoor design conditions of sintered modulus brick made from coal gangue are −5 and 35 °C. According to the existing research, coefficient of thermal conductivity of solid clay brick materials is 0.754 W/(m^2 K). When added in the coal gangue, coal ash, industrial materials such as slag, the coefficient of thermal conductivity declines slightly, but changes a little [7]. So the coefficient of thermal conductivity of both bricks made from sludge of Yellow river and sintered modulus brick made from coal gangue is set as $\lambda = 0.754$ W/(m^2 K).

Finite volume method is used to make the numerical analysis of building blocks model. The SIMPLE algorithm is used to solve the equation of speed and pressure.

Convection–diffusion subject uses second-order upwind format. Calculation mesh adopts the unstructured hexahedral.

70.3 Calculated Result and Inspection

The distribution of temperature and the quantity of heat transfer of the brick in the experimental conditions are received on 3-D calculation model. The illustrations of distribution of brick temperature are respectively as shown as Figs. 70.3 and 70.4. As shown in the figure, the temperatures of two types of bricks have little change in the vertical direction Z, so heat transfer in the brick can be simplified to 2-D process, and then error will be allowed in the engineering. As seen in Figs. 70.3 and 70.4, the air in the holes is a poor conductor of heat, so the holes have a concentrated temperature lines and large temperature gradient. Holes of each row effect by superimposition and effetely weaken the quantity of heat transfer of brick. Holes interlaced, leading to the fact that it increases the distance between the temperature lines in the rib area of the brick and makes the temperature gradient small, significantly decreases the quantity of thermal conductivity of solid material. As seen from Fig. 70.4, rectangular hole brick effects more stronger than circle hole brick. It is also one of the reasons why the thermal resistance of the rectangular holes is greater than the circle ones.

Along the brick on the cold air side, the central and main area (owing holes) of the brick has a lower temperature and reduces the difference from the cold air. The area close to top surface has a higher temperature and increases the difference from

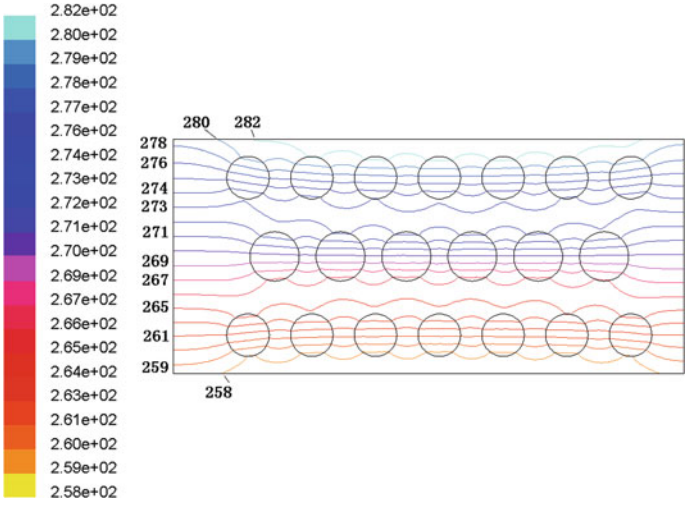

Fig. 70.3 Illustration of xoy cross-sectional temperature of KP1 brick with 20 holes

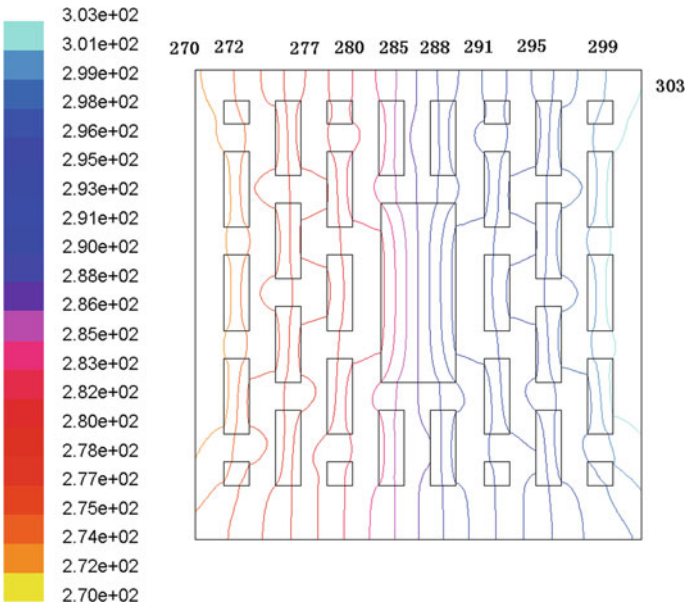

Fig. 70.4 Illustration of xoy cross-sectional temperature of sintered modulus brick made from coal gangue

the cold air. Along the brick on the hot air side, there appears similar phenomenon. What above makes the temperature of surface of the wall not even.

The total heat transfer of the 3-D model calculation result of KP1 with 20 holes is from each side of the article brick (including ash seam):

$$\Phi = 2.409 \text{ W}$$

The heat-flow rate of the brick:

$$q = \frac{2.409}{0.24 \times 0.1} = 100.38 \text{ W}/(\text{m}^2 \text{ K})$$

The overall thermal resistance of the brick:

$$r = \frac{19 - (-19)}{100.38} = 0.379 \ (\text{m}^2 \text{ K})/\text{W}$$

The thermal conductivity resistance of the brick:

$$r_{\text{砖}} \quad 0.378 - \frac{1}{23} - \frac{1}{8.7} = 0.221 \ \ (\text{m}^2 . \text{K})/\text{W}$$

The equivalent coefficient of heat conductivity:

$$\lambda_e = \frac{0.11}{0.221} = 0.498 \text{ W/(m K)}$$

In April 2008, constructional engineering quantity test center adopts guarded hot box method to test the performance of heat transfer of the KP1 brick made from the Yellow river sludge. The specimen is single brick build by laying bricks or stones along the porous brick masonry, with the laying area of 1.2 m × 1.2 m, the test result for equivalent coefficient of thermal conductivity of the KP1 brick made from the Yellow river sludge is $\lambda_e = 0.47$ W/(mk) [8–10]. Numerical calculation and experimental results vary $\frac{0.498-0.47}{0.47} = 5.96$ %.

The coefficient of thermal storage of wall according to the calculation is $s = \sqrt{\frac{2\pi\lambda_e \rho c}{T}} = \sqrt{\frac{2\pi \times 0.498 \times 1800 \times 880}{24 \times 3600}} = 7.572$ W/(m^2 K). Numerical calculation and experimental results vary $\frac{7.572-7.92}{7.92} = 4.39$ %. The index of thermal inertia of the two types of bricks with the laying thickness 240 mm is $Di = 2RS = 2 \times 0.221 \times 7.572 = 3.347$ m^2 K/W. Numerical calculation and the data from the literature vary $\frac{3.347-3.25}{3.25} = 2.98$ %.

The total heat transfer of the 3-D model calculation result of sintered modulus brick made from coal gangue is from each side of the article brick (including ash seam):

$$\Phi = 1.166 \text{ W}$$

The heat-flow rate of the brick:

$$q = \frac{1.166}{0.2 \times 0.1} = 58.284 \text{ W/(m}^2 \text{ K)}$$

The overall thermal resistance of the brick:

$$r = \frac{35 - (-5)}{58.284} = 0.686 \text{ (m}^2 \text{ K)/W}$$

The thermal conductivity resistance of the brick:

$$r_{砖} \quad 0.686 - \frac{1}{23} - \frac{1}{8.7} = 0.528 \quad (\text{m}^2 . \text{K}) / \text{W}$$

The total heat transfer coefficient of the brick: $K = \frac{1}{0.6863} = 1.457$ W/(m^2 K)

Building engineering quality testing center station in Xuzhou adopts the heat-flow meter method to test the thermal parameter of sintered modulus brick made from coal gangue and experiment with the detector for thermal insulation property of the JTRG-1 building envelope. The controlled temperature in the hot test room is 35 ± 0.5 °C, while in the cold test room is −5 ± 0.5 °C. The specimen is single brick build by laying bricks or stones along the porous brick masonry, with the laying area of 1 m × 1 m. Testing result is the total coefficient of heat transfer of the article brick: $K = 1.592$ W/(m^2 K), and the thermal resistance of the article

brick is $R = 0.478\ \mathrm{m}^2$ K/W. Numerical calculations and experimental results respectively vary $\frac{1.592-1.457}{1.592} = 8.47\ \%$ and $\frac{0.528-0.478}{0.478} = 10.46\ \%$.

70.4 Conclusion

(1) The combination of numerical calculation and experiment is an effective method to study the heat transfer of the wall. Thermal performance can be obtained through numerical calculation in the steady heat transfer, being a little different from the experimental result. According to the calculation of temperature distribution in the brick, thermal performance can be easily analyzed.
(2) When heat transfer in the brick can be regarded as 2-D process, errors will be allowed in the engineering.
(3) The numerical calculation method can well simulate the heat transfer performance of the porous brick in the unsteady conditions, so the existing meteorological data in our country can be used to predict the energy consumption and energy saving effect of the new product all over.
(4) When numerical calculation method is applied in researching the thermal performance of all kinds of energy-saving porous bricks, importance should be attached to the research about coefficient of the complex thermal parameters on the attenuation multiples of the harmonic temperature wave amplitude and delayed time of the harmonic temperature wave and coefficient of the thermal storage to supply the basic thermal data badly in need for engineering. At the same time, it can save huge cost of the determination and shorten the cycle of the determination, and then the calculation precision can satisfy the engineering requirement.

References

1. Henan research institutes of building science, Henan design standard for energy efficiency of Residential buildings in cold zones (2005) China Radio and Television publishing house (DBJ41/062-2005), Bejing
2. Bureaux of Wall Materials Innovation and Energy Saving in Buildings in Shandong (2006) Shandong design standard for energy efficiency of Residential buildings(DBJ 14-037-2006), Jinan
3. Department of Construction Engineering Quality and Safety Supervision Ministry of Housing and Urban-Rural Development of the P. R. china and China institute of building standard design and research (2009) National Technical Measures for Design of Civil Construction—Heating, Ventilation and Air Conditioning; China Planning press, Beijing
4. Lu Y (2008) Practical manual for design of heating and air conditioning. China architecture and building press

5. China institute of building standard design and research (2003) Design atlas for national building standard 04J101, Brick building construction. China Planning press, Bejing
6. Tao W (2002) Numerical heat transfer, 2nd edn. Xi'an Jiaotong University Press, Xi'an
7. Ji GQ (2003) Study of influencing factor of thermal conductivity in Hollow brick. Block-Brick-Tile 2:5–8
8. Building engineering quality testing center station of Henan (2008) Test report, 09 class of 2008 No. 559
9. Xu S, Li F, Lv H, Xia D, Wang S (2006) Design on module fired coal shale perforated brick and test on thermal performance of brick wall. Brick-tile 5:13–16
10. Yan Q (1995) Architectural thermal process. China architecture and building press, Beijing

Chapter 71
Optimized Design of Ground-Source Heat Pump System Heat Exchanger

Zhigang Shi, Shangping Song and Songtao Hu

Abstract The research of heat pump mainly focus on experimental research which emphasizes the determination of heat transfer per unit depth, system COP, reasonable buried pipe spacing, soil thermal physical property and so on, but there has been no breakthrough in the aspect of how to ensure the reliability of the system during a long runtime. This paper first heat exchanger, heat pump, the mathematical pump and buildings was modeled and integrated by the mean of connection condition. The optimized method of the heat exchanger was puts forward. The drill hole depth and drilling hole number are taken as optimization variables, the inlet temperature as objective function. Through a case study, the tradition calculation and optimized drill length was compared. The result shows the optimized design method can decreased drill length and number.

Keywords Ground-source heat pump · Heat exchanger · Optimized design

71.1 Introduction

The natural environments contain unlimited resources of energy at low exergy levels. This energy is very cheap or even free. Hence the interest in its utilization increases with the increasing costs or inconvenience of obtaining the highly exergetic energy. One way to exploit this energy resource is using a heat pump. Most heat pumps are used for the heating or cooling of residential buildings. In these cases, air and soil are usually the only available resources and utilization of underground or surface water is usually impossible. The temperature of ground, as the thermal source or sink, is approximately constant and closer to the room

Z. Shi (✉) · S. Song · S. Hu
School of Environmental and Municipal Engineering, Qingdao Technological University, Qingdao, China
e-mail: shi_zhi_gang@163.com

A. Li et al. (eds.), *Proceedings of the 8th International Symposium on Heating, Ventilation and Air Conditioning*, Lecture Notes in Electrical Engineering 262,
DOI: 10.1007/978-3-642-39581-9_71,

temperature than the air temperature during a year. So The GSHP system is used more often than air types. The advantages of GSHP systems are as follows [1]:

(1) Less energy consumption for its operation.
(2) Using a big energy resource with relatively constant temperature during the year.
(3) The system works properly even at very low atmospheric temperatures.
(4) Using lower amount of refrigerants.
(5) Simple design and lower maintenance costs.

With the above advantages, GSHP require more initial investment (about 30–50 %) than the air source heat pumps [2]. Horizontally GSHP are not commonly used in houses because these systems need more space for installation than the vertical GSHP and temperature variations have greater effects on them [3]. Considering the geological specifications of most regions of China, vertical GSHP systems are usually the best option and due to limitations in available surface area in our case study.

During the last decade, many studies have been conducted by various researches in design, simulation and testing of GSHP systems. Hepbasly [4] presented the thermodynamic analysis of GSHP systems with U-tube ground heat exchanger for district heating application using the mass, energy, entropy and exergy balance relations. He evaluated the performance characteristics of the system and its components by both energetic and exergetic approaches using an illustrative example. Nagano et al. [5] applied a developed code to predict the length of the ground heat exchanger using infinite cylindrical heat source theory, specifications of the recirculating pumps, the pressure drop, as well as the COP of GCHP. The optimal design of GSHP system was not among the targets in [4–6] modelled and optimized an open (well) loop ground source heat pump by defining total annual cost as an objective function. Due to the fact that the studied GSHP was an open loop type, there was no need to consider the ground heat exchanger design parameters such as number and depth of boreholes in problem.

In this paper, in order to optimal design of heat exchanger in vertical GSHP system, the mathematical heat pump and buildings was modeled and integrated by the mean of connection condition. The optimized method of the heat exchanger was puts forward. The inlet temperature to establish objective function. The drill hole depth and drilling hole quantity for optimization variables, for the given heating/cooling loads, the optimum values of heat exchanger design parameters were predicted.

71.2 Thermal Modeling of GSHP

In order to calculate the temperature of soil outside the drillings, this paper adopts "step" heat flux method to deal with variable heat flux problem which came up with by Ingersoll [10]. Based on the superposition principle, the temperature

difference between soil far boundary and hole wall at moment can be expressed as follow:

$$\Delta T_{g,n} = \sum_{j=1}^{n} \frac{q_j - q_{j-1}}{\lambda H} G\left[F_{0t_n - t_{j-1}}\right] \tag{71.1}$$

To calculate the thermal resistance inside the hole and the fluid temperature in double U-tube, the frictional temperature of tube fluid is written by:

$$\left.\begin{aligned} T_{f1}(z) = & T_{f2}(z) = \theta_1\left(T_f' - T_b\right) + T_b \\ T_{f3}(z) = & T_{f4}(z) = \theta_3\left(T_f' - T_b\right) + T_b \end{aligned}\right\} \tag{71.2}$$

And then, the outlet temperature of the U-tube and the heat absorption capacity per unit depth are as follow:

$$T_{g,\text{out}} = T_{f3}(0) = T_{f4}(0) \tag{71.3}$$

$$qH = 2Mc\left[T_{f1}(0) - T_{f3}(0)\right] \tag{71.4}$$

where $T_{g,\text{in}}$, $T_{g,\text{out}}$ is inlet/outlet temperature of fluid in the U-tube, °C; q is heat transfer capacity per unit depth, W/m; θ is dimensionless temperature calculation parameter.

The heat pump unit is complexity. So it is very more difficulty to get detail model of each component. The performance of the heat pump unit is most sensitive to inlet temperature, this paper gets the fitted formula of COP under the conditions of cooling and heating according to the unit sample which provides the rule of COP going with the inlet temperature.

The water flow rate of the pump is constant in this paper and it is controlled only by the signal of on or off. The heat producing by the pump is added to the heat load of the ground heat exchanger.

The building load is simulated by DeST software according to the actual structure and size of the building.

Finally, a complete ground source heat pump system is built by mean of MATLAB.the outlet temperature of heat exchanger in GSHP calculation diagram was shown in Fig. 71.1.

71.3 Optimizing the GSHP System

The design of GCHP system was implemented by defining an objective function and using optimization techniques to find the optimum design parameters.

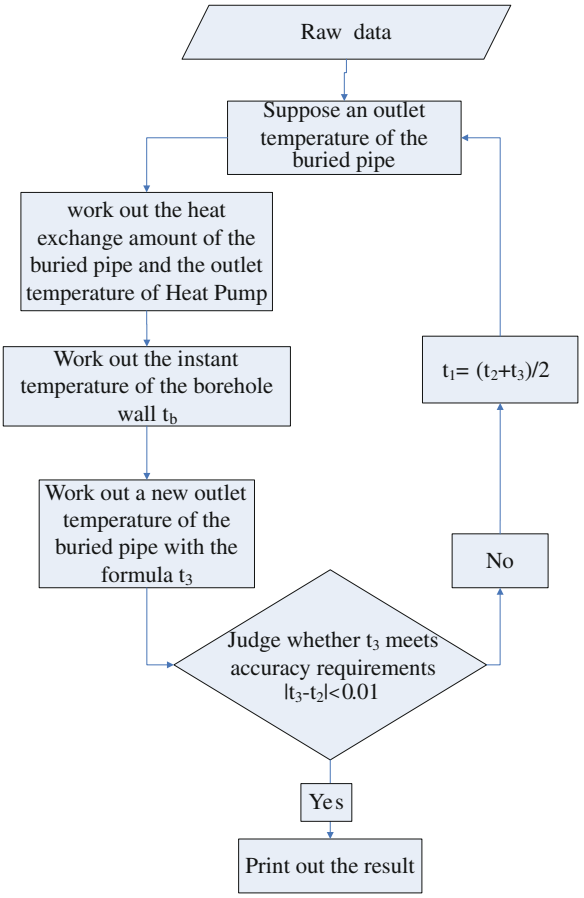

Fig. 71.1 Calculation diagram for outlet temperature of heat exchanger

71.3.1 Objective Function

The objective function of the optimal design should be judged by the result value, and be single function of optimized parameters. For the ground heat pump system with appropriate buried pipe heat exchanger size, to insure the system operating reliably and safely, the highest outlet temperature of the U-tube should lower the permit temperature of the heat pump unit in its life cycle, or the lowest temperature of it should be higher than the permit lowest inlet temperature of the heat pump unit, it can be said that cooling load determines the length of the drilling and this belongs to the cooling load dominant situation; Conversely, it belongs to heat load dominant situation. According to the literature [6], in order to ensure normal operation of the heat pump units, the inlet temperature of heat pump units should not be higher than 40 °C and less than −5 °C, in the cooling load dominant area,

the inlet temperature of heat pump unit must be less than 40 °C. Therefore the objective function is determined as follow:

$$f(\Delta t) = \left|\max T_{g,\text{out}} - T\max\right| \langle 0.1 \left(T\max \leq 40\,^{\circ}C\right) \tag{71.5}$$

71.3.2 Determination of Optimization Parameters

There are many factors that influence the GSHP system and heat exchanger, so the solution of the model will be very complex and will take a long time while considering all factors. Thus, the factors of great influential should be selected to simplify the model and save time for calculation. These facts taken together, the length and depth of the drill can be changed and effect the "hot accumulation" phenomenon through generalized analysing. So the number of the drill and depth are chosen to optimized design variables.

71.3.3 Optimization Method

The optimization by Nelder–Mead method Nelder–Mead method (NM) is one of the direct numerical search methods to find the local extermums of multivariate functions used for optimization (finding the minimum value of the objective function). For two variables, this method is a pattern search that compares function values at the three vertices of a triangle. The worst vertex, where the function is largest, is rejected and replaced with a new vertex. A new triangle is formed and the search is continued. The process generates a sequence of triangles (which might have different shapes), for which the function values at the vertices get smaller and smaller. The size of the triangle is reduced and the coordinates of the minimum point are found. The algorithm is stated using the term simplex (a generalized triangle in N dimensions) and will find the minimum of a function of N variables. This method is computationally compact and thus, had a relatively good convergence and fast run time [Nelder JA, Mead R, [11]]. The followings are implemented to optimize the objective function by NM method:

(1) Choosing n +1 initial points, each point with n components these components are in fact the independent variables of the system.
(2) Choosing the maximum number of trials to prevent the algorithm from getting involved in perpetual loop.
(3) A criterion named the tolerance which is the acceptable difference between the best and the worst points in Nelder–Mead method was considered to be 0.1.

71.4 A Case Study

According to the optimized design and analysis of GSHP system heat exchanger, once the related parameters are determined, building load and the inlet temperature of heat pump unit have the most important influence on the optimization results. A GSHP system was designed for a townhouse heating and cooling loads using GSHP heat exchanger designer. The building cooling load is 33.4 kW and heat load is 25.8 kW both of which are calculated by the DeST software, the experiment table adopts double U-tube vertical heat exchanger which made of HDPE. The parameter of the system was shown in Table 71.1:

(1) ASHRAE method uses parameters such as building design cooling and heating loads, net annual average heat transfer to the ground, effective thermal resistance of the ground in daily monthly, and annual pulses, part-load factor during design month, thermal resistance of bore, and temperature difference between ground and liquid at heat pump inlet and outlet to compute the required length of heat exchanger [12].
(2) IGSHPA method computes the bore depth based on the cooling and heating loads, thermal resistance of soil and GHX pipe, coefficient of performance (COP), part-load factor, and the temperature difference between entering water to the heat pump and the ground [13].

In this paper, a modified version of IGSHPA method was used to estimate the length of heat exchanger considering the concept of equivalent thermal circuit the calculation result of heat exchanger length is 721 m.

Base on the optimized process and IGSHPA method result, the optimized range of drill depth is 80-120 m, while the optimized range of drill number is 4–12. The initial value start with depth being 100, drill number being 6. Through optimal calculation, the result is that the number of the drill is 7 and depth is 89 m. The total length is 623 m. Compare with IGSHPA method, the total length of heat exchanger is decreased by 13.6 %. And also the inlet temperature of heat pump unit, as shown in Fig. 71.2, would be below the permit temperature of 35 °C. The GSHP system can operate safely and stably in whole life cycle.

Table 71.1 The buried pipe number for winter and summer

Parameter	Value
Equivalent diameter/m	0.15
Inner diameter/m	0.026
Outer diameter/m	0.032
Distance between leg/m	0.055
Thermal conductivity of U tube/(W m^{-1}. $°C^{-1}$)	0.44
Thermal conductivity of backfill	2.9
Thermal conductivity of soil/(W m^{-1}. $°C^{-1}$)	2.78
Volume thermal capacity (J m^{-1}. $°C^{-1}$)	2.7461×10^6
Undisturbance temperature/ °C	15.2

There are various methods to compute the required length heat exchanger

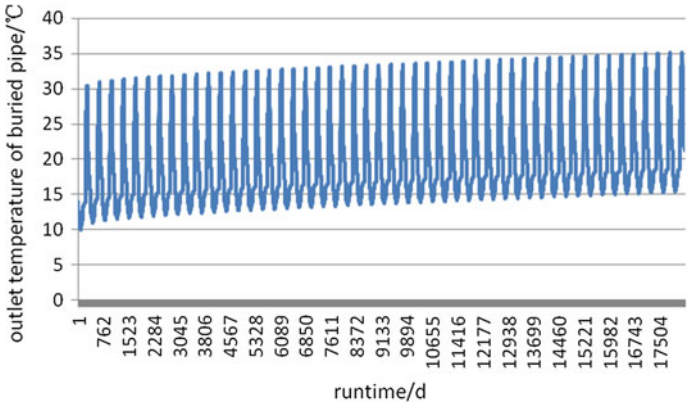

Fig. 71.2 U-tube outlet temperature (inlet temperature of heat pump unit) of optimal result

71.5 Conclusions

By using the method presented in this paper, and therefore minimizing the difference between outlet temperature of heat exchanger and permit temperature of heat pump unit, optimum u-tube length and diameter can be determined. Thus less length of heat exchanger is required for a given duty, and the GSHP system initial invest decreases. This method can also be used with available software and incorporate optimal techniques into the design of GSHP heat exchangers.

References

1. The Office of Energy Efficiency (1995) Heating and cooling with a heat pump of natural resources. Canada
2. Sanner B (2010) Description of ground source types for the heat pump. http:www.geothermie.de, Subject: geothermal networks (accessed 03.06.07)
3. Claesson J, Eskilson P (1987) Thermal analysis of heat extraction bore holes. Lund University of Technology, Sweden
4. Hepbasli A (2005) Thermodynamic analysis of a ground-source heat pump system for district heating. Int J Energ Res 29:671–687
5. Nagano K, Katsura T, Takeda S (2006) Development of a design and performance prediction tool for the ground source heat pump system. Appl Therm Eng 26:1578–1592
6. Zhao Y, Shigang Z, Xun L (2003) Cost-effective optimal design of groundwater source heat pumps. Appl Therm Eng 23:1595–1603
7. Healy PF, Ugursal VI (1997) Performance and economic feasibility of ground source heat pumps in cold climate. Int J Energy Res 21:857–870
8. Ozgener O, Hepbasli A, Ozgener L (2007) A parametric study on the exergoeconomic assessment of a vertical ground-coupled (geothermal) heat pump system. Build Environ 42:1503–1509

9. Zogou O, Stamatelos A (1998) Effect of climatic conditions on the design optimization of heat pump systems for space heating and cooling. Energy Convers manage 39:609–622
10. Ingersoll LR, Zobel OJ, Ingersoll AC (1954) Heat conduction with engineering, geological and other applications. McGraw-Hill, New York, pp 250–251
11. Nelder JA, Mead R (1965) A simplex method for function minimization. Comput J 7:308–313
12. Deng Z (2004) Modelling of standing column wells in ground source heat pump systems. Oklahoma State University, America
13. RET Screen International (2005) Ground source heat pump project analysis. Canada

Chapter 72
Positive Investigation on the Reliability of Groundwater Source Heat Pump System Usage in Yangling Normal Community

Yanzhe Chen, Zhiwei Wang and Zengfeng Yan

Abstract Groundwater source heat pump (GWSHP) as a promising renewable energy utilization technology has been widely used in building heating and cooling. But heat breakthrough and groundwater injection have become gradually revealed engineering problems in groundwater heat utilization process. Testing evaluation is an important means to understand the reliability of the practical application of GWSHP. This paper took a residential use of GWSHP system in Yangling Normal Community as study object, focusing on the analysis of "heat breakthrough," briefly illustrating the groundwater injection. Collected a year's operating data, mainly including pumping and injection wells water temperature, supply and return water temperature of water source heat pump unit's evaporator/condenser and outdoor air temperature in winter and summer. The relationship between groundwater temperature repair and heat breakthrough and injection rate were obtained through analyzing the operation test data. These operating parameters are all in the safe operation range of heat pump unit. The results show that heat transport between production water well and injection water well is not significant, and the groundwater temperature restoration is suitable, thus the GWSHP system runs normally and meets the requirement of reliability for residential building air-conditioning application in Yangling Normal Community.

Keywords Yangling Normal Community · Groundwater source heat pump · Reliability · Positive investigation

Y. Chen (✉) · Z. Wang · Z. Yan
School of Environmental and Municipal Engineering, Xi'an University of Architecture and Technology, Xi'an 710055 Shaanxi, China
e-mail: cyz_xauat@163.com

Z. Wang
e-mail: wzhiwei-atu@163.com

A. Li et al. (eds.), *Proceedings of the 8th International Symposium on Heating, Ventilation and Air Conditioning*, Lecture Notes in Electrical Engineering 262,
DOI: 10.1007/978-3-642-39581-9_72,

72.1 Introduction

GWSHP using the relatively stable groundwater resources with a higher coefficient of performance [1–3] develops very quickly in our country in recent years, but some areas do not consider their own actual situation and some blind phenomenon exists. In the deep well-pumping and injection process, the most direct impact is the temperature variation in the field of the local aquifer. If production well and injection well interact with each other, it will directly cause geothermal energy use efficiency loss and the project life reduction. Groundwater injection problem is a key technology in the shallow geothermal energy development of water source heat pump system. An unreasonable design of drilling quantity, well spacing and depth under no understanding of regional hydrogeology will lead to groundwater injection difficulty, increasing operation cost of heat pump unit and even abnormal running, etc. [4]. Therefore, whether for the purpose of GWSHP system optimization operation, or in order to strengthen the environmental protection of groundwater, it should be enhanced the scientific research on heat breakthrough and groundwater injection in the process of energy utilization of groundwater to realize the healthy and sustainable development in the field of utilization of shallow geothermal energy [5–7]. The underground heat transfer of GWSHP system is very complicated. The stability of underground directly affects the operation of heat pump unit, thus affecting the whole GWSHP system's reliability. In view of this, this paper selected the GWSHP system in Yongfengjiayuan residential area in Yangling Normal Community as study object, focusing on the analysis of "heat breakthrough," briefly illustrating the groundwater injection and judging reliability of the system usage in Yangling.

72.2 Project Description

The project is located in Yangling Normal Community, Shaanxi, China. The total area of central heating (cooling) using GWSHP is about 250,000 m^2, including residential area of about 186,400 m^2, school and office and other public construction area of about 64,000 m^2. Yangling belongs to valley terrace. This project site is level terraces of Weihe River. The compositions are the quaternary system Holocene lower alluvial sandy gravel, silty clay and clay, with good permeability. Pumping and injection are easy. Aquifer total thickness is 40–50 m. Aquifer initial temperature is 15–18 °C, relatively stable in the four seasons [8]. The development and utilization conditions are very good [9]. This project uses groundwater as heat source and heat sink of the ground source heat pump air-conditioning system. It adopts intermittent operation mode every day, pumping water from the underground and transporting the water into unit directly. Underground power station concentrated sets in the central of Yongfengjiayuan residential district. There are two sets of water source heat pump with the same type. Its heating input power is

732 kW, heating capacity is 3,171 kW. Refrigeration input power is 516 kW, refrigerating capacity is 2,868 kW. The system provides 45/40 °C heat medium water in winter to satisfy the heating requirement and 7/12 °C cold medium water to meet the refrigeration requirement. Fan coil controlled by three speed switch is used for indoor air-conditioning terminal. A total of 25 water wells are designed in this project, including 8 production wells, 16 injection wells, and 1 well for standby. The quality of single well pumping water is 100 m^3/h. The ratio of production well and injection well is 1:2. Each well is equipped with submersible pump and injection tube. Production well and injection well rotate in winter and summer regularly. Well spacing is 25 m and the distance apart from buildings is more than 10 m. In order to avoid sand deposition in long-term use, a peak shaving grit chamber has been built in the north of the power room for unit water supply. The project completed and put into use in November 2009. The usage effect is good for a few years.

72.3 Test Content and Data Processing Method

GWSHP system testing time is November 2009 to March 2010 and June 2010 to August. The system operating data is observed and recorded every 2 h every day. The main record parameters are production well and injection well temperature, supply and return water temperature and pressure of water source heat pump unit's evaporator/condenser and outdoor air temperature in winter and summer. Supply and return water temperature and pressure of water source heat pump units' evaporator/condenser are from the digital instrument display of the units. Temperature and pressure accuracy are 0.1 °C and 0.01 MPa, respectively. Outdoor temperature records by the thermometer. Its accurate is 1 °C. According to the energy conservation, heat release and heat absorption of groundwater are obtained through the water temperature difference and flow rate at underground side. The formula is shown as follows.

$$Q = \rho V c_p (t_{out} - t_{in}) \tag{72.1}$$

where,

Q heat release (absorption) at underground side, positive value is heat absorption, negative value is heat release, kW,
ρ the density of water at underground side, kg/m^3,
V the volume flux of water at underground side, m^3/s,
c_p specific heat capacity of water at underground side, kJ/(kg·°C),
t_{in}, t_{out} the inlet and outlet of water temperature at underground side, °C

72.4 Test Results and Reliability Analysis

72.4.1 Relationship between Groundwater Temperature Repair and Heat Breakthrough

In practical application of GWSHP, under the action of thermal conductivity and convection, the temperature of adjacent production well will increase or reduce in different extent, due to the difference between injection water temperature and original aquifer temperature. This phenomenon is often referred to as "heat breakthrough" [10]. The occurrence of this phenomenon and the influence range on the temperature of production well directly relate to the function of heat pump system.

Temperature change characteristic curves of outdoor air temperature, production well and injection well in the whole heating period and cooling period were obtained by means of organizing the actual measured data, respectively shown in Figs. 72.1 and 72.2. As seen from two figures, groundwater temperature variation is less than the outdoor air temperature variation in winter and summer. This is mainly because that the changes of groundwater temperature have different degree of delay and attenuation to the changes of atmospheric temperature.

In winter, the water from production well directly enters into the evaporator of water source heat pump unit. Supply water temperature change of evaporator reflects the pumping well water temperature change. As seen from Fig. 72.1, the pumping well water temperature in heating period is basically stable. But with the increasing of geothermal tail water injection amount, it tends down. Pumping well temperature change can be divided into three stages. Namely, from the early heating period to the 30th day, pumping well temperature is about 15 °C. With the increased injection amount, in the 31st day and 80th day, pumping well temperature change obviously happens twice and falls to 10.3 °C. Then as the continuous

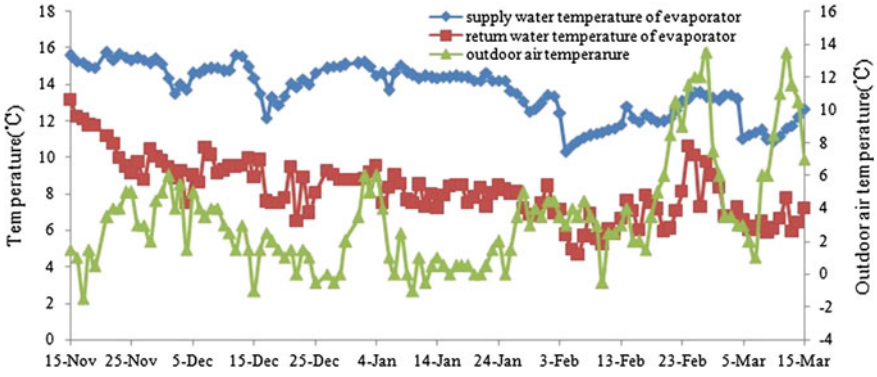

Fig. 72.1 Supply and return water temperature change characteristic curves at groundwater side in the winter of 2009–2010

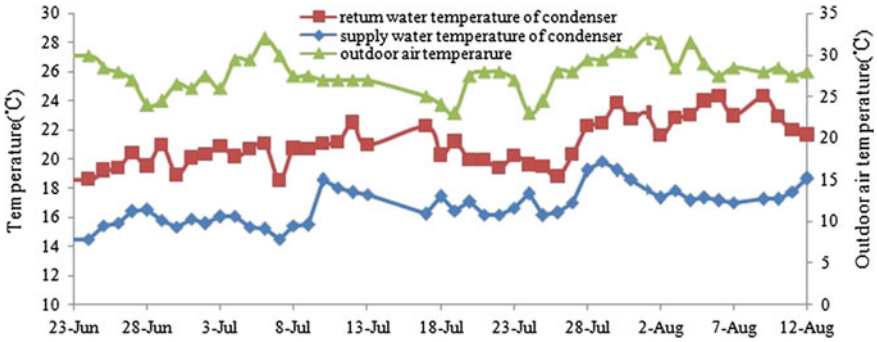

Fig. 72.2 Supply and return water temperature change characteristic curves at groundwater side in the summer of 2010

heating, the pumping well temperature is slightly rising but changes little. Because the total injection amount increases with the increase of heating days, the pumping well temperature reduces. Moreover, the change of outdoor air temperature also has certain influence on pumping well temperature. Outdoor air temperature is the lowest in January (namely in the 60–80th day of the heating period) in winter. The pumping well temperature also drops to the lowest point, only 10.3 °C. Pumping well temperature gradually rises with the outdoor temperature rising again. In the end of heating period, pumping well temperature goes up to 12.7 °C.

In the whole heating period, pumping well temperature is influenced on the return water temperature to some extent. Pumping well water temperature range is from 15.7 to 10.3 °C, falling by 5.4 °C. The average pumping temperature is 13.6 °C, which shows that that pumping well occurred heat breakthrough in the operation process in winter. This is mainly because that the underground aquifer is an open system and injection water temperature is lower than the original aquifer temperature. The injection water makes heat transfer with the surrounding environment, which results in pumping well water temperature reducing to a certain degree. After the heating period, through the spring transition period, the injection water temperature rises from 7.2 to 13.3 °C. It indicates that the ability to self-repair of groundwater temperature field is good. At the same time, it achieves cold storage across the season. That is to say, GWSHP system has the function of "use the cold of winter to summer."

In summer, the water from production well directly enters into the condenser of water source heat pump unit. Supply water temperature change of condenser reflects the pumping well water temperature change. As seen from Fig. 72.2, the pumping well water temperature in cooling period is basically stable. But with the increasing of water injection amount, it tends to rise. Pumping well temperature change can be divided into three stages. Namely, from the early cooling period to the 17th day, pumping well temperature is about 15.5 °C. With the increasing injection amount, pumping well temperature change obviously happens twice in the 18th day and 35th day and rises to 19.8 °C. Then with the continuous cooling,

the pumping well temperature changes little and was slightly declining. Because the total injection amount increases with the increase of cooling days, the pumping well temperature rises. Moreover, the change of outdoor air temperature also has certain influence on pumping well temperature. Outdoor air temperature is the highest in July (namely in the 15–35th day of the cooling period) in summer. The pumping well temperature is also up to the highest point, 19.8 °C. Pumping well temperature gradually reduces with the outdoor temperature declining. Pumping well temperature drops to 18.6 °C in the end of cooling period.

In the whole cooling period, pumping well temperature is influenced on the return water temperature to some extent. Pumping well water temperature range is from 13.3 to 19.8 °C, rising by 6.5 °C. The average pumping temperature is 16.8 °C which shows that that pumping well occurred heat breakthrough in the operation process in summer. This is mainly due to the underground aquifer is an open system and injection water temperature is higher than the original aquifer temperature. The injection water makes heat transfer with the surrounding environment, which results in pumping well water temperature rising to a certain degree. After the cooling period, the injection water temperature falls to a certain extent by self-repair of groundwater temperature field through the autumn transition period. It achieves heat storage across the season. That is to say, GWSHP system has the function of "use the heat of summer to winter."

Supply and return water temperature of water source heat pump unit at groundwater side are in normal range [11] during the whole running test stage. On the condition of certain groundwater flux, the supply water temperature of evaporator is about 13.6 °C in winter. The supply water temperature of condenser is about 16.8 °C in summer. The corresponding return water temperature fluctuates in a certain degree due to the influence of the indoor load dynamic change. Corresponding to the characteristic that heating load is greater than cooling load in Yongfengjiayuan residential area, in the same groundwater flux, the mean temperature difference between supply and return water is 5.5 °C in winter, and 4.3 °C in summer. So heat absorption in winter is 33 % more than heat release in summer.

72.4.2 Injection Problem

Groundwater injection is injecting the water which have exchanged heat in water source heat pump unit back into the underground aquifer again. Such work can supplement the groundwater sources, regulate water level, maintain reserves balance, recharge energy storage, provide heat and cold source, keep aquifer head pressure, and prevent the ground settlement. So for protecting water resources and ensuring long-term reliable operation of GWSHP system, injection measures in GWSHP system engineering is very important [12].

Injection Water Quality At present, there is no injection water quality national standard [13]. The principle that attention should be paid to is: injection water quality should be better than or equal to the original groundwater quality. Do not

cause regional groundwater water pollution after injection. In fact, groundwater through water source heat pump unit just exchanges heat. Water quality almost has no change. So injection does not cause pollution of groundwater.

Injection Quantity Injection quantity is related these factors such as hydrogeological condition, well completion technology, and injection method. The hydrogeological conditions are the main factor of all the influence factors. In the pebble aquifer, the unit injection quantity is commonly above 80 % of unit water yield. In the coarse sand aquifer, the unit injection quantity is 50–70 % of unit water yield. In the fine sand aquifer, unit injection quantity is 30–50 % of the unit water yield [14]. According to the aquifer types in Yangling and pumping and injection experiment of the project, single well injection quantity is 75 % of pumping water. So it meets the injection safety requirements.

Injection Types According to the actual situation of project site, ground infiltration recharge, induction recharge and injection recharge can be used. Injection recharge generally uses tube well. And three methods can be used in injection recharge. They are no pressure (gravity), negative pressure (vacuum), and pressure (positive pressure) injection. No pressure gravity recharge is suitable for aquifer with good permeability and the well that has water level difference between injected water level and static water level. Vacuum negative pressure recharge is suitable for buried deep groundwater level (static water level depth below 10 m) and aquifer with good permeability. Pressure recharge fits for the formation with high groundwater level and poor permeability.

Injection rate Although groundwater injection rate can reach 100 % theoretically, groundwater injection technology in most countries is not mature at present. Especially, in the fine sand aquifer, well walls can be blocked easily. Injection speed is greatly lower than pumping speed. As for the aquifer with thicker grains of sand in this project, it is relatively easier to recharge due to the large pore. Table 72.1 lists the design parameters of groundwater system under different geological conditions [15]. The single-well injection quantity is 75 % of pumping quantity in this project. The ratio of pumping well and injection well is 1:2. These parameters meet the requirements.

Table 72.1 Design parameters of groundwater system under different geological conditions

Aquifer type	Injection rate (%)	Well array	Well flux (t/h)
Gravel	>80	A pumping well with a injection well	200
Medium-coarse sand	50–70	A pumping well with two injection wells	100
Fine sand	30–50	A pumping well with three injection wells	50

72.5 Conclusions

On the basis of this study, the following conclusions can be drawn:

(1) According to pumping well water temperature change rules of GWSHP system in Yongfengjiayuan residential area, Yangling Normal Community, Shaanxi, heat breakthrough happens in heating and cooling season. But through the intermittent operation and groundwater temperature self-repair in transition season, heat breakthrough can be effectively relieved.
(2) Comprehensive consideration of hydrogeology condition and GWSHP system operation in Yangling, the single well injection quantity is 75 % of pumping water quantity, the ratio of pumping well and injection well is 1:2. The parameters meet the injection safety requirements.

Acknowledgments This study is financially supported by "Twelfth Five-Year" National Science and Technology Support Programme (2011BAJ03B06) and 2011 Shaanxi Scientific and technologic Innovation Project (2011KTCQ03-07) and 2012 Xi'an scientific and technologic project (CX12187①).

References

1. Yu M, Peng X, Fang Z et al (2007) Method for determining deep ground thermal properties accounting for water advection. Basic Sci Eng 15:196–197
2. Wang H, Zhao J, Shen L (2007) Experimental research on ground source heat pump system long-term operation characteristics. J N China Electr Power Univ 34:34–36
3. Zhang X, Liu Z, Chen B (2007) Heating performance test on a office building use of ground source heat pump and analysis of energy saving. Refrigeration and Air-conditioning and Electrical Machinery
4. Lu Y (2008) The new member of the renewable energy—shallow geothermal energy. Prospect Eng 35:1–4
5. Badruk M (2003) Environmental problems in geothermal energy applications. In: The Geothermal Energy Seminar-TESKON, pp. 345–358
6. Chao Z, Liu Y, Zhou G (2008) The environmental effect analysis of the application of ground source heat pump. Cryogenics Supercond 36:35–37
7. Wang X (2007) Refect on the development of ground source heat pump system. HV&AC 37:38–43
8. Wang Z, Liu Z, Cao X et al (2008) Feasibility analysis on the application of shallow groundwater source heat pump system for subarea cooling and heating in Yangling Normal Community. Energy Eng 61–64
9. Dao Z, Qi C (2010) Discussion hydrogeological structure of Shaanxi province and the applicable forms of GSHP. Refrig Air-conditioning 10:14–17
10. Gao Q, Zhou X et al (2012) Quantitative analysis of thermal breakthrough in pumping and injecting well group area during earth energy utilization. J Basic Sci Eng 20:447–453
11. JB/T 4329-1997.Positive displacement cold water (heat pump) unit. Mechanical Academy of Sciences Press, Beijing
12. Ni L, Ma Z (2006) Analysis of injection for groundwater source heat pump systems. HV&AC 36:84–90

13. GB50366-2005 Technical code for ground-source heat pump system. China Building Industry Press, Beijing
14. Wu X (2004) Development of groundwater loop for ATES and groundwater source heat pump systems. HV&AC 34:19–22
15. Ma Z, Lv Y (2007) Ground source heat pump system design and application. Machinery Industry Press, Beijing

Chapter 73
The Combined Operating of Radiant Floor and Fresh Air Coil in Field Experiment

Yanhong Du, Chenggong Qian and xiangzhao Fu

Abstract This paper studied the effect of the combined operating of radiant floor and fresh air coil in field experiment according to different ways of cold or hot water supply. By compared and analyzed the differences, which among indoor air temperature/humidity, radiation asymmetry, and thermal comfort in three ways of single, series, and parallel of radiant floor and fresh air coil for cold or hot water. On the basis of the analysis, this paper also discussed the risk of condensation on the surface of the floor. Experimental results showed that the indoor thermal comfort is best and the risk of floor surface condensation is least in series mode.

Keywords Radiant floor cooling · Indoor radiation environment · Condensation problems

73.1 Background

Radiant cooling has many advantages, and gets more and more attention School of Urban Construction and Environmental Engineering, Chongqing University. However, there are some problems being used. Radiant floor cooling makes the floor becomes cold radiant surface though pass into the cold water in floor radiant tube, and then relies on the cold radiant surface with the human body furniture and the rest the enclosure structure conducting radiation heat exchange, finally reaches the purpose of cooling refrigeration. Radiant floor cooling has no dehumidification function and the surface temperature is low. When the local surface air temperature is inferior to the dew point temperature, floor surface condensation is generated. Thus, it failed to be widely used, especially in high temperature and

Y. Du (✉) · C. Qian · x. Fu
School of Urban Construction and Environmental Engineering,
Chongqing University, 400045 Chongqing, China
e-mail: kuailezhoumo2012@163.com

A. Li et al. (eds.), *Proceedings of the 8th International Symposium on Heating, Ventilation and Air Conditioning*, Lecture Notes in Electrical Engineering 262,
DOI: 10.1007/978-3-642-39581-9_73,

high humidity areas (i.e., Chongqing). In recent years, scholars both at home and abroad, based on theoretical analysis and experimental research, have proposed a system form combined radiation cooling with other air supply systems, which can reduce the risk of radiation cooling condensation [1–5]. The scholars in Nanjing Normal University, such as Xian-zhong Li, Chuan-Ju Liu, Zi-Jie Wang, and so on, setted up a air conditioning test bench of radiant floor cooling and displacement ventilation load, researched the effect of the combined cooling [6]. But there is little experimental study on the practical application. We chose a villa which adopts radiation floor with fresh air coil system in a practical application to build a test bench for field study the cooling effect and the risk of floor surface condensation.

73.2 The Experimental System Introduction of the Villa

We chose a villa as the research object in Chongqing, which has three layers, two layers on the ground, and one layer on the underground, construction area of 264.2 m^2. Three layers of each room are adopted radiation floor that could realize the summer cooling and winter heating. The villa uses ground source heat pump as the cold and heat source of air conditioning, ground source heat pump and circulating pumps in underground, and the geotechnical heat exchanger is buried in the villa garden. Fresh air coil is located in the stairwell on the roof of the small villa indoor. The fresh air was collected from outdoor, it through the coil processing forcing into stairwell, which distributed from 2F to 1F and −1F in sequence from top to bottom, and then enter into each room., and finally the dirty air was exhausted to outdoor by the toilet and the ventilation system of underground into the ventilation shaft and by the exhaust shaft from the roof exhaust to outdoor. The villa of the air flow is shown in Fig. 73.1 (the research about this part will be introduced in other papers).

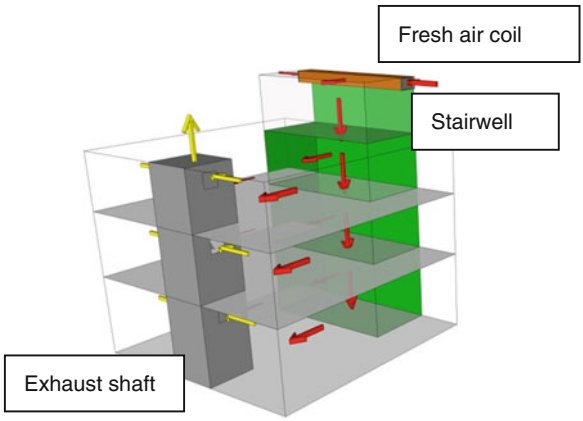

Fig. 73.1 Air flow chart of the villa

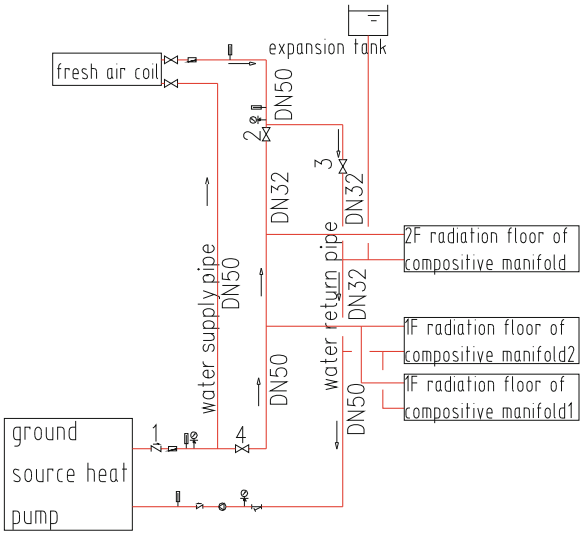

Fig. 73.2 Radiation floor and fresh air coil of hot and cold water supply system can be adjusted

It is shown in Fig. 73.2 for the villa of radiant floor and fresh air coil of hot or cold water supply system. According to different combination of open and close valves of the water supply system could be formed in series and parallel connection of two different water supply modes. When we opened the valve 2 and closed the valve 3 and valve 4, the radiant floor and fresh air coil were in series of water supplied. When we opened the valve 3 and valve 4 and closed the valve 2 those were in parallel of water supplied. Whatever the radiant floor with fresh air coil was in series or in parallel, the relationship between the radiation floor rooms were parallel.

Series water supply was that the hot or cold water making by the ground source heat pump firstly supplied fresh air coil and after heat exchange flowed into the floor radiant tube. The water flow of cold or hot is shown in Fig. 73.3. Parallel water supply was that the hot or cold water was divided into two roads, and then supplied for fresh air coil and floor radiant tubes at the same time. The water flow is shown in Fig. 73.4. The major difference between two forms is the water temperature and water flows through the heat exchange equipment. In this paper,

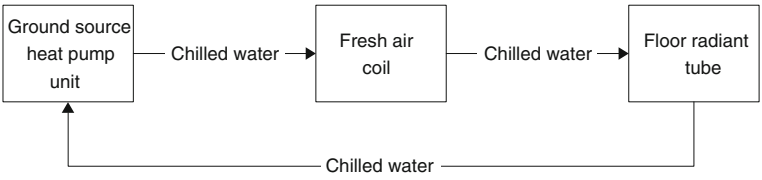

Fig. 73.3 Series form of hot and cold water flow diagram

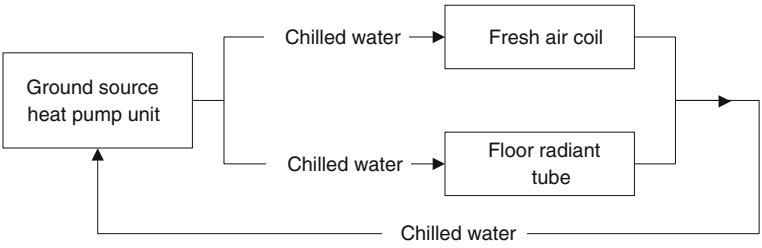

Fig. 73.4 Parallel form of hot and cold water flow diagram

we studied these influences of two parameters, which are influencing factors of the indoor thermal environment and the risk of floor surface condensation.

This paper of main experimental analysis object is floor 2 of the study whose area is 15.5 m^2 and south wall is 14.2 m^2 whose heat transfer coefficient is 1.0 W/(m^2·K). The room has a window whose area is 5.13 m^2 and heat transfer coefficient is 2.7 W/(m^2·K). All the adjacent rooms of the study are in air conditioning room.

73.3 The Design of the Test System and Experimental Condition

73.3.1 The Design of the Test System

The experiment used the copper—constantan thermocouple to test indoor wall surface and air temperatures, and the thermocouple had been in calibration with the constant temperature water bath. We used the data acquisition instrument automatically record thermocouple to test. The arrangement of thermocouple measuring points and temperature and humidity recorders are shown in Figs. 73.5 and 73.6.

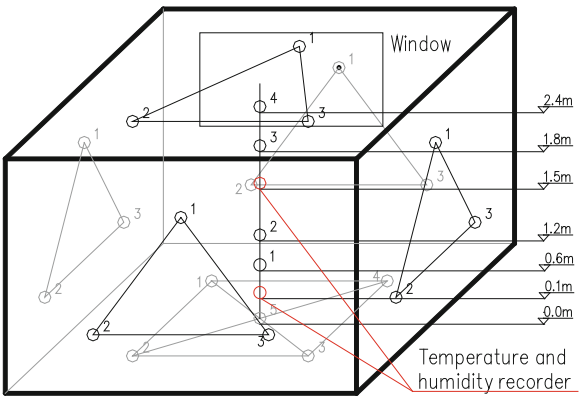

Fig. 73.5 The arrangement of thermocouple measuring points and temperature and humidity recorders in the study

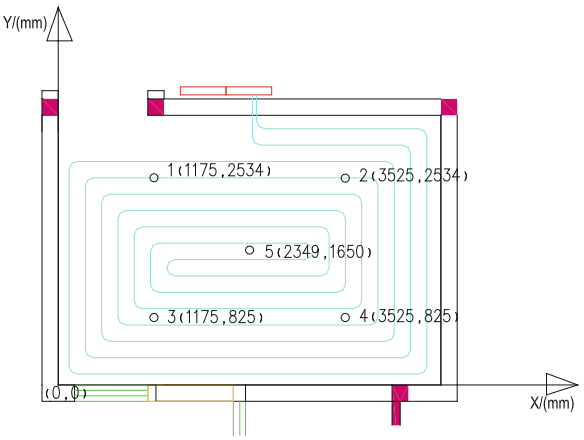

Fig. 73.6 The ground thermocouple measuring points layout plan

(1) The inner surface of walls and ceiling were laid three measuring points, and the surface of floor was laid five measuring points. Considering the ground and the south wall temperature of non-uniformity, we decorated two thermocouple measuring points (point 1 and point 2 in Fig. 73.6) above the radiant tube and arrange one point on the south wall of the window (point 1 in Fig 73.5).
(2) From the ground of 0.6, 1.2, 1.8, and 2.4 m height arranged the thermocouple measuring points to test the indoor air temperature.
(3) In order to obtain the temperature and the humidity of the air in the work zone and near the ground, we placed a temperature and humidity recorder in the middle of the room from the ground of 0.1 and 1.5 m height which could automatically records the air temperature and relative humidity.

Experimental instruments and meter accuracy in the experiment are shown in the following Table 73.1. All the instruments met the accuracy requirement. During the experiment, we record the experimental data every 10 min.

Table 73.1 Experimental instruments and the accuracy

Instrument	Model	Measuring range	Accuracy
Thermocouple	Copper—constantan thermocouple	−200–+350 °C	0.1 °C
Data acquisition instrument	A531 intelligent environment test instrument	0.0–60.0 °C	±0.5 °C
Temperature and humidity recorder	HIOKI3641	−40–85 °C, 0–100 %	±0.5 °C ±3 %
Flow meter	LZB-25 Short tube-type plastic rotor flow meter	100–1000 L/h	1.5 Level
Mercurial thermometer	50 °C	0–50 °C	0.1 °C

73.3.2 Design of Experiment Condition

It is shown in Table 73.2 which are related to the experimental conditions. In the table, the floor radiant tube flow refers to floor radiant tube return water flow rate of the testing room, and fresh air coil flow rate is the return water. In series mode, the flow of fresh air coil is equal to the sum of all the room radiant tube flow, and also equal to the ground source heat pump flow. In parallel mode, fresh air coil plus all the room of radiant tube flow is equal to the ground source heat pump flow.

73.4 Introduce of Experiment

73.4.1 The Experiment Conditions

Three kinds of working condition of the test time were on August 10, September 5, and September 6, respectively. It is shown in Table 73.3 of outdoor meteorological condition during the experiments. We seted the ground source heat pump of the return water temperature by 12 °C in the process of experiment.

73.4.2 Experimental Process

In the single cooling mode, radiation floor was cooling from 8:00 to 20:00; In Series and parallel modes, the radiation floor and fresh air coil was cooling from 9:00 to 21:00. They were not cooling at other time. They are shown in Table 73.4

Table 73.2 Design of experimental condition table

Experimental condition	The length of experimental time (h)	Floor radiant tube cold water flow of the study (L/h)	Fresh air coil cold water flow (L/h)	The return water temperature of unit(°C)
Single cooling	24	290	0	12
Series cooling	24	350	3300	12
Parallel cooling	24	220	1000	12

Table 73.3 Experimental conditions table

Order number	Test time	Mean daily temperature/°C	Mean daily relative humidity/%	Mean daily dew point temperature/°C	The supply of cold water	The return water temperature of unit/°C
NO.1	August 10	32	42	18	Single	12
NO.2	September 5	34	33	16	Series	12
NO.3	September 6	35	38	18	Parallel	12

Table 73.4 Actual flow of radiation floor and fresh air coil

Experiment condition	Single cooling	Series cooling	Parallel cooling
Floor radiant tube flow of study(L/h)	290	350	220
Fresh air coil flow(L/h)	–	3300	1060

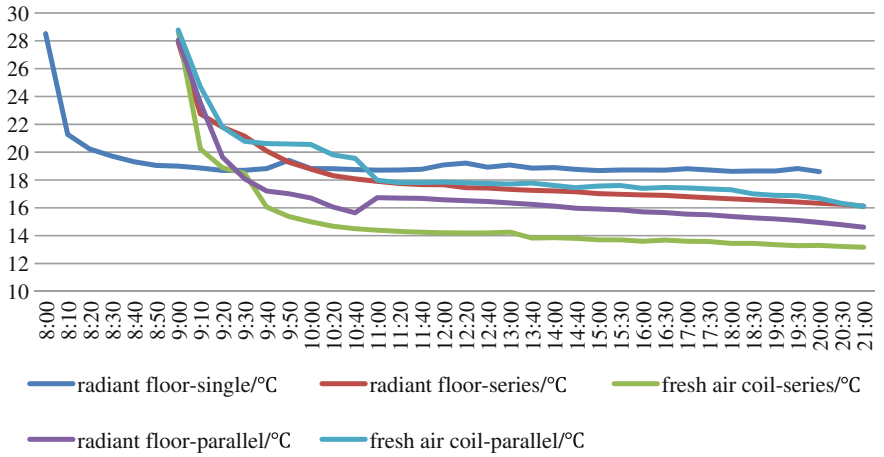

Fig. 73.7 Three experimental conditions of return water temperature changes of radiant floor and fresh air coil

of floor radiant tube flow of the study and fresh air coil actual water flow and not changed in the whole experiment process.

While we had set the return water temperature of the ground source heat pump, but in the actual operation process the temperature was always changing. The Changes of the temperature are shown in Fig. 73.7.

In these three kinds of experiment conditions, the return water temperature of the radiation floor and fresh air coil droped rapidly after opened the ground source heat pump, and the decreasing trend of the water temperature was gradually slow after opened 1 h. The return water temperature was highest at the beginning experiment. The water temperatures of the radiation floor were, respectively, 28.52 °C(single), 27.90 °C(series), 28.05 °C(parallel); of fresh air coil were 28.70 °C(series) and 28.78 °C(parallel). The return water temperature was lowest at the shutdown time. The water temperatures of the radiation floor were, respectively, 18.60 °C(single), 16.12 °C(series), 18.60 °C(parallel); of fresh air coil were 13.16 °C(series) and 13.16 °C(parallel). The lower values of water temperature of the radiation floor were, respectively, 9.92 °C(single), 11.78 °C(series), 18.60 °C(parallel); of fresh air coil were 15.54 °C(series) and 13.44 °C(parallel). Therefore, the smallest decrease of the radiant floor tube of return water temperature was single cooling, and the greatest reduction was series cooling mode. The parallel cooling return water temperature of fresh air coil was greater in reduction, and the series mode was smaller.

73.5 Thermal Comfort and Condensation Analysis

This paper studied from the three aspects of the air-conditioning system effects, which include surface condensation situations, the different height of indoor air temperature/humidity, and the radiation asymmetry.

73.5.1 The Different Height of Indoor Air Temperature/ Humidity

73.5.1.1 Data Result

(1) The different height of indoor air temperature/humidity change over time is shown in Figs. 73.8, 73.9 and 73.10.
(2) Figure 73.11 shown the air relative humidity at the height of 0.1 and 1.5 m.

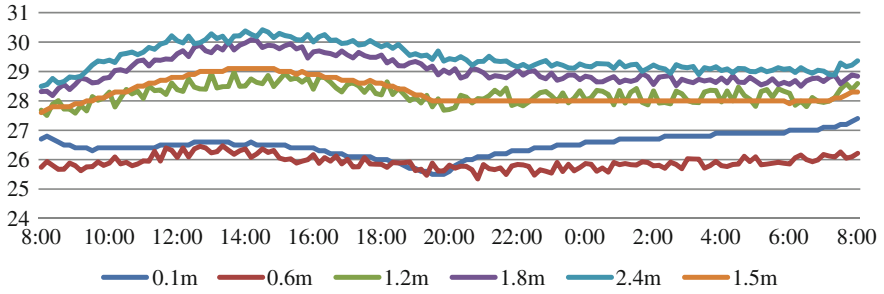

Fig. 73.8 Single for the cold air temperature change

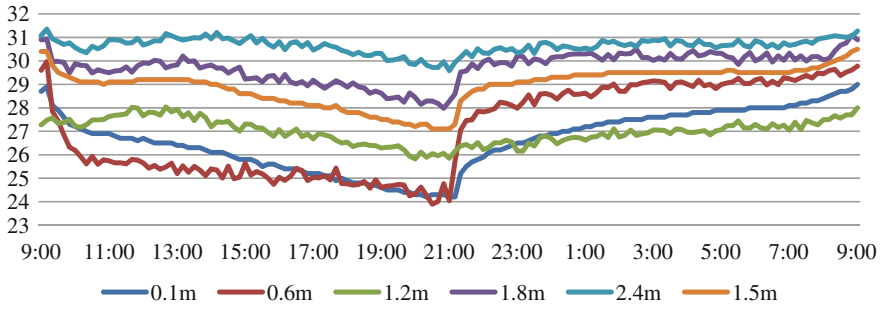

Fig. 73.9 Series for the cold air temperature change

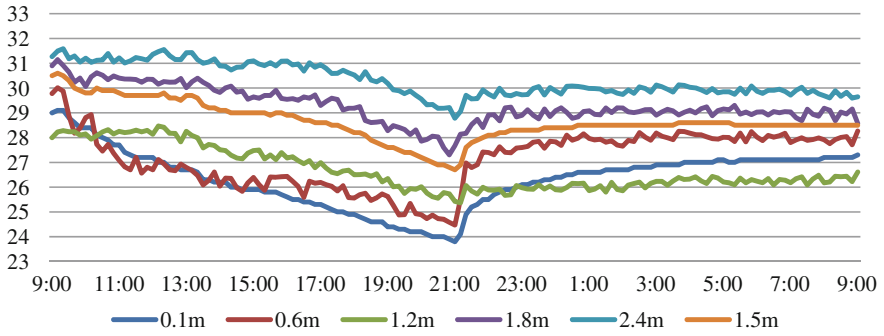

Fig. 73.10 Parallel for the cold air temperature change

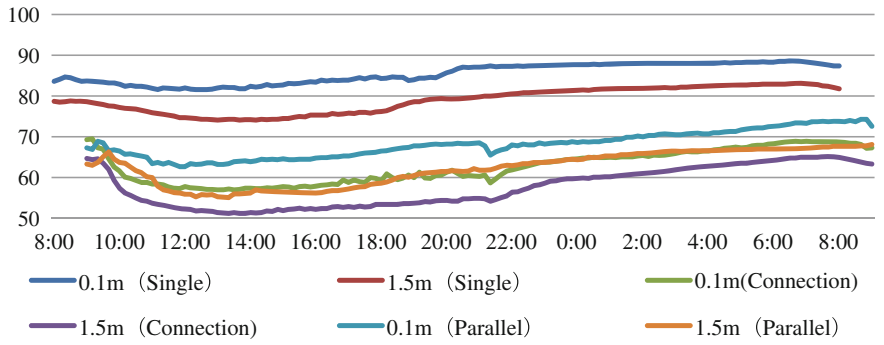

Fig. 73.11 Indoor air relative humidity change

73.5.1.2 Experimental Results Analysis

(1) We observed that the 0.1 m of air temperature for continuous reduction, the other height temperature is that the first increases, then decreases, and drops to the lowest at shutdown of the system in Figs. 73.8, 73.9 and 73.10. After shutdown, 0.1 and 0.6 m of air temperature gradually rise, and 0.1 m rises faster than 0.6 m. The other height of air temperature for a long time remains unchanged, until the next day to rise rapidly at 7:00 AM. All the height air temperature of series and parallel method drop rapidly after the experiment opened 1 or 2 h, and then remain unchanged, until 17:00 PM and then gradually reduced. After shutdown the system, it is similarity to the single method for the air temperature changing trends of series and parallel method. But after shutdown 1 or 1.5 h, the air temperature rises faster than single cooling. While during the system running 7 h, all the height of air temperature rise besides 0.1 m, and the higher the measuring points, the faster the air temperature rise, the maximum temperature to 1.9 °C. But all the height air temperature of combined cooling gradually decreases. Due to the cooling of single cooling method is less than the room heat load which does not

supply fresh air at the initial time, the indoor thermal comfort is less than the combined cooling form of supply fresh air.

(2) Compared with Figs. 73.9 and 73.10, we know that the series and parallel cooling methods of all the height of the air temperature changes are basically all the same, but during the system operation, parallel cooling air temperature of 0.1 m reduced by 5.2 °C and the lowest temperature was 23.8 °C; the series cooling decreased 4.7 °C and the lowest value is 24.05 °C; The near-surface air temperature of parallel cooling is lower than series cooling. If the temperature is too low that may cause uncomfortable. So the comfortable of series cooling form is better than parallel cooling.

(3) According to the ISO7730 standard, the temperature difference in the work area above the ground between 1.1 and 0.1 m should be less than or equal to 3 °C [8].The temperature difference of single system is 1.0 °C, series cooling system is 1.89 °C and parallel system is 1.79 °C, which are all less than 3 °C, the discomfort caused by temperature difference do not exist.

(4) As shown in Fig. 73.11, the air relative humidity of three cooling ways has the same variation tendency, which of humidity gradually reduced and then gradually increased after the 15:00 PM. But in the experimental initial time, relative humidity of combined cooling form decreased faster than single cooling form. The relative humidity of each time is that single cooling form is the largest, followed by parallel cooling form and series is minimal. Reference [8] gives the interval relative humidity range is 40–65 %, series cooling system is within the interval during the experiment period, parallel must meet while single system is on the opposite to the series. Therefore, series cooling system is most comfortable, parallel system is second, and single system is worst in the experiment.

73.5.2 Radiation Asymmetry Analysis

During the radiant cooling process, radiation uneven will bring uncomfortable feeling similar with drought. Its face mean radiant temperature of the cold surface 8 K or more lower than the mean radiant temperature of the rest of the room, the location of people would not feel comfortable [7]. It is evaluated by Eqs. 73.1.

$$T_r - T_{pr} = T_r - T_f + F_{pw}(T_f - T_w) < 8 \tag{73.1}$$

T_r The rest indoor mean radiant temperature, °C;
T_{pr} the average radiation temperature on the surface of the cold, °C;
T_f Wall temperature, °C;
F_{pw} Window to indoor plane infinitesimal Angle coefficient measurement points;
T_w The surface temperature of the window, °C.

73.5.2.1 Data Result

Tables 73.5, 73.6, and 73.7 show the three cooling mode actinomorphic calculations.

73.5.2.2 Experimental Results

The horizontal direction of the radiation asymmetry is smaller than the vertical direction. The large temperature difference between the ground and the ceiling is the main cause. Due to the strong differences of sunshine between south and north wall, the north–south inner surface wall temperature difference are larger than east–west, so do the asymmetry of the radiation.

Table 73.5 The single cooling method radiation asymmetric results

Inner surface	Temperature/ °C	Area/ m^2	The vertical direction of the radiation asymmetry/K	Horizontal direction radiation asymmetry/K
Floor	24.59	15.51	5.31	East–west direction:0.26
East wall	28.22	9.57		North–south direction:1.72
Western Wall	27.96	9.57		
South wall	29.70	13.36		
North wall	27.98	13.36		
Ceiling	29.90	15.51		

Table 73.6 The series cooling method radiation asymmetric results

Inner surface	Temperature/ °C	Area/ m^2	The vertical direction of the radiation asymmetry/K	Horizontal direction radiation asymmetry/K
Floor	24.61	15.51	6.03	East–west direction:0.69
East wall	29.20	9.57		North–south direction: 2.53
Western Wall	28.52	9.57		
South wall	30.69	13.36		
North wall	28.17	13.36		
Ceiling	30.65	15.51		

Table 73.7 The parallel cooling method radiation asymmetric results

Inner surface	Temperature/ °C	Area/ m^2	The vertical direction of the radiation asymmetry/K	Horizontal direction radiation asymmetry/K
Floor	24.23	15.51	6.31	East–west direction:0.71
East wall	29.15	9.57		North–south direction: 1.99
Western Wall	28.44	9.57		
South wall	30.11	13.36		
North wall	28.12	13.36		
Ceiling	30.54	15.51		

Single cooling system owns the smallest asymmetry of the radiation compared with the series and parallel system. The series system has a larger north–south asymmetry of the radiation than series one, while on the contrary in other directions. Therefore, Single cooling system is more comfortable, and series and parallel system are less comfortable caused by asymmetry. However, the radiation asymmetry of three cooling mode are all smaller than 8 K, within the comfort range of Ref. [4] provided.

73.5.3 Floor Surface Condensation Analysis

73.5.3.1 Data Result

(1) Figures 73.12, 73.13, and 73.14 are showing the floor surface temperature and the dew point temperature from the ground at the height of 0.1 m.

Table 73.8 shows the variation of Indoor air moisture content.

73.5.3.2 Condensation of Floor Surface Analysis

- Condensation risk analysis of the three conditions

Figure 73.12 shown that floor surface temperature is rapidly decreased within 2 h after experiment and a gentle downward trend after 2 h later. The lowest temperature appeared at the shutdown time, the value is 22.7 °C. Within the 2 h of shutdown time, floor surface temperature increased rapidly, and a gentle downward trend after 2 h later. The difference about temperature of floor surface to the air dew point at the height of 0.1 m below 0 °C first appeared at 6 h after the start of and lasted about 6.5 h. During the test period, the minus difference is −0.61 °C. Therefore, condensation is likely to occur at the floor surface.

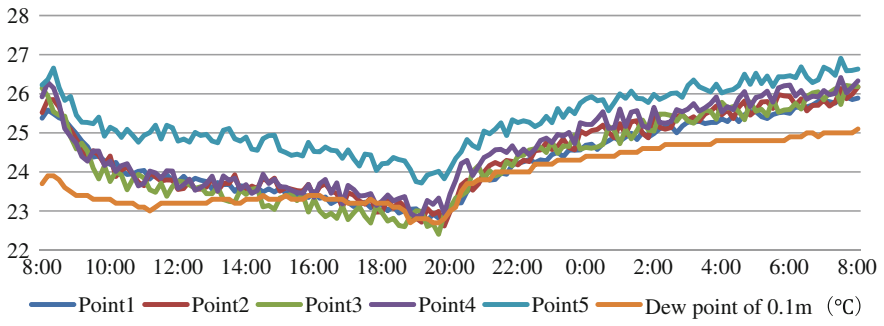

Fig. 73.12 Single connection cooling method

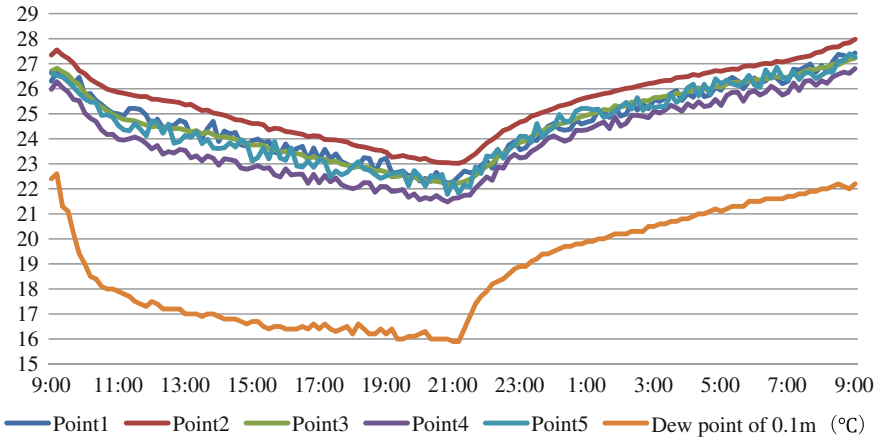

Fig. 73.13 Parallel connection cooling method

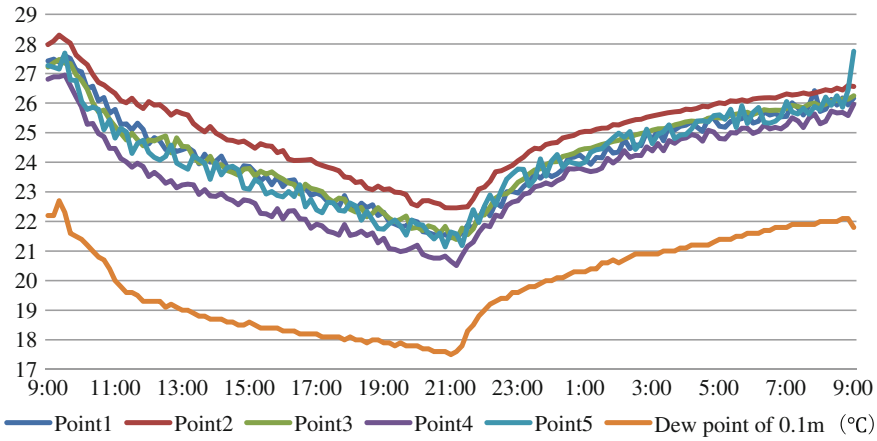

Fig. 73.14 Series connection cooling method

Table 73.8 The variation of indoor air moisture content

Experimental conditions/g/(kg·dry air)	Single method	Series method	Parallel method
Moisture content of boot	19.27	17.92	17.69
Moisture content of Shutdown	18.5	11.84	13.16
Difference	0.77	6.08	4.53

In the united system, the temperature decreased approximate liner, the lowest temperature also appeared at the shutdown time, and the value of series system and parallel connection system are 21.5 and 20.5 °C. The temperature owns the same

tendency to single system after shutdown time. Condensation risk could not appear in the united cooling system for the temperature difference of floor surface to air dew point are always greater than 0 °C. The mean temperature difference of the series and parallel are 5.89 and 4.41 °C, the minimum are 3.58 and 2.63 °C. Compared with the condensation of series connection system and parallel connection system, the former owns the less risk because the mean and the minimum temperature difference of floor surface to air dew point are all larger than the latter.

- Moisture analysis

As can be seen from the above Table 73.8, series cooling system has the largest air moisture difference change during the experiment, parallel followed and the single smallest. Series cooling system has the large water volume and small temperature difference, which enhance the fan coil dehumidification capacity and increase the air dew point, the risk of condensation eliminate.

Through the above analyze, We got a conclusion that the risk of condensation series cooling system is minimal, parallel followed, and the single largest.

73.6 Conclusion

- Under the single cooling method, there have 6.5 h long when one or more test point temperature below the air dew point temperature at the height of 0.1 m. The minimum temperature difference of floor surface to air dew point is −0.61 °C, which under 0 °C and brought about a great condensation risk. While the risk could not appeared in the united cooling system for the temperature difference always greater than 0 °C. Compared with the condensation of series connection system and parallel connection system, the former owns the less risk because the mean and the minimum temperature difference of floor surface to air dew point are all larger than the latter.
- After the system running 7 h, the high air temperature in the rooms are all rising of single cooling method, while the connection method was gradually decline during the whole system operation. From the surface air temperature, parallel cooling is lower than series cooling. Series method, the relative humidity meets the design criteria, and the single cooling method's relative humidity is much higher than the specification of the design conditions. Therefore, in the process of experiment, series cooling system is most comfortable, single system is worst comfortable and parallel system located between.
- In the single cooling method experiment, each small radiation asymmetry than the series-parallel cooling. Addition to the north and south of the radiation asymmetry, the other to the tandem cooling compared with parallel radiation asymmetry. Therefore, single cooling system is more comfortable, and series and parallel system are less comfortable caused by asymmetry.

- The shortcoming of this study is that the experiment of the villa is not normally used and there is no personnel load in the course of the experiment. In later studies, we should consider the effect of different systems for practical use.

References

1. Dongliang Z, Zijie W, Xu Z Dry—floor radiant cooling combined with displacement ventilation composite systems experimental research [J]. Build Sci 25(6):38–42
2. Zhang LZ, Niu JL (2003) Indoor humidity behaviors associated with Decoupled cooling in hot and humid climates [J]. Build Environ 38:99–107
3. Yiyun H, Ling Z, Guangming C (2003) Dehumidification for floor cooling [J] HV&AC 33(3):47–51
4. Ping Y (2004) Independent fresh air system (DOAS) study (2): design method [J] HV&AC 34(2):37–43
5. Ke Z, Zhaolin W, Zhigang Z (2009) A kind of energy-saving air-conditioning system design concept and calculation method discussed in this paper [J]. Fluid Mach 37(9):79–82
6. Xianzhong L, Chuanju L, Zijie W (2004) Displacement ventilation effect of floor radiant cooling [J]. Chinacraa 4(1):48–50
7. Yingxin Z, Yanping Z, Xianting L (2005) Building environment [M]. China Architecture & Building Press, Beijing, p 7
8. Civil building of heating ventilation and air conditioning design specification (GB50736-2012)

Chapter 74
The Complementary Heating Energy Ratio Research of Solar: Ground Source Heat Pump and Heating Network in Cold Regions

Guohui Feng, Jian Zhang, Hong Hao and Yuan Li

Abstract To propose solar—ground source heat pump and heating network complementary form of heating system, select the baseline of building in cold regions, we use Dest software for dynamic load simulation system to determine the different heating period of operating mode, according to the heating relative load ratio during the entire heating season. Taking TRNSYS transient simulation software as the platform, the complementary heating systems simulation model is established to determine the best ratio of the energy of the complementary heating system. For the benchmark construction of the cold regions, the longest time from 20 to 70 % of the design load, accounting for 63 % of the total heating time, but the time of maximum is only 1 h, and average load accounts for 25.14 % of the design load; solar energy heat can reach 89.61 % of the entire heating season and the dynamic shortest payback period is 8.77 years; solar energy as a complement thermal systems, unit air conditioning area corresponds to the collector area is 0.045 m^2, the water temperature can reach 50 °C, get the maximum cost to the present value at the same time and the economic effect is the best.

Keywords Solar energy · Ground source heat pump · Heating network · Complementary heating · Energy ratio

74.1 Introduction

At this stage, our heating areas are mainly used in conventional coal-fired energy, heating area is increasing year by year, the phenomenon of the heating network cannot meet the demand of district heating exists generally, but solar energy

G. Feng (✉) · J. Zhang · H. Hao · Y. Li
School of Municipal and Environment Engineering, Shenyang Jianzhu University, Shenyang, 110168, China
e-mail: fengguohui888@163.com

A. Li et al. (eds.), *Proceedings of the 8th International Symposium on Heating, Ventilation and Air Conditioning*, Lecture Notes in Electrical Engineering 262,
DOI: 10.1007/978-3-642-39581-9_74,

resources in these areas are very rich and the use of solar energy to meet the heating demand outlook huge. Therefore, based on the status quo of the cold northern climate characteristics and propose solar—ground source heat pump systems with thermal network combining complementary heating modes. Solar—ground source heat pump system, the initial investment is generally higher, in many cases, only a ground source heat pump system static incremental payback period is 10 years or even higher [1, 2], indicating that the ground source heat pump lower running costs must be able to compensate for the higher initial investment. Solar—ground source heat pump heating network combined heating system due to the heating network assume part of the load, there is a large extent of the savings of the initial investment, thereby improving the economics of the system.

74.2 Energy Distribution of Heat Supply Network Control Mode

In order to simulate accurately the total amount of coal during heating, we must clear load dynamic change in heating period of each time. This article utilizes Dest software to simulate dynamic thermal load of typical civil building and simulation results provide accurate data for the calculation of the quantity of the total coal during heating. I simulated dynamic load on a building of a residential district in cold region. The basic building is located in Shenyang, Liaoning province, the building is a 11 F residence building. Floor area of the building is 7730.91 m^2, the height of building is 33.2 m. According to the heat supply network control mode,

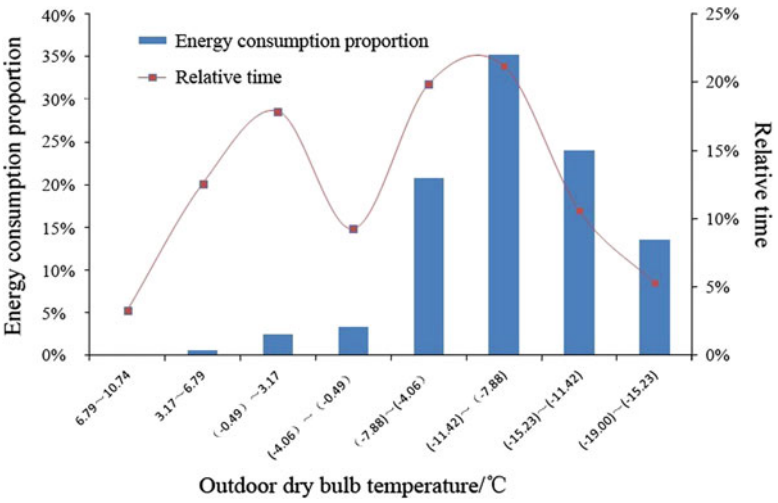

Fig. 74.1 The ratio of building energy consumption and the relative proportion of time in each interval

Fig. 74.1 shows energy consumption ratio and relative time of the building energy consumption in different outdoor temperature.

From the above we can see, the time of design heating load is very short, the vast majority of time is part of the load. For residential building, 20–70 % design load appear the longest, accounting for 63 % of the total heating time. And the biggest load appearing time is only 1 h, average load is only 25.14 % of the design load. So, hourly load is fundamental basis of the true value of fuel consumption scheme, not design load.

74.3 Fuel Consumption Calculation of Ground Source Heat Pump: Heat Supply Network System Complementary Heating

Solar energy is not stable heat source, so in order to satisfy the end of heating and cooling demand, in the design condition, the capacity allocation of ground source heat pump and heat supply network system cannot be reduced, we must take no solar system to collocate the main engine of ground source heat pump system, pump, buried pipe number. So this article given ground source heat pump—heat supply network system optimal energy matching first, then given the best solar collectors collection hot area.

Complementary heating manner, ground source heat pump system assume most of the load, heat supply network assume part load. The heating mode give full play to the heat pump energy saving and heat supply network low initial investment characteristics, do the best combinations of energy saving and economic. According to the reference architecture, ground source heat pump system for design load ratio is 40, 45, 50, 55, 60, 65, 70, 75, 80, 85, 90, 95, and 100 %. Calculated according to the 13 kinds of conditions, the result is shown in Fig. 74.2 Table 74.1 gives different scheme fuel consumption calculation results.

For reference for building, ground source heat pump system for design load ratio increased from 40 to 70 %, heat pump heating load increased from 47.80 to 89.61 %, and heat supply network of heating load accounted for only 10.40 %. Heat supply network operation time reduced from 82.50 to 37.50 %. And when design load assumed by the heat pump continue to increase, the speed of heating load increasing and heat supply network running time reducing become slow.

Table 74.1 gives different scheme fuel consumption calculation results, can be seen from the table with ground source heat pump system for design load ratio increases, the complementary of heating means standard coal consumption quantity decrease gradually. For residential building, As far as heat pump system is concerned, design load ratio assumed by ground source heat pump system increased from 70 to 100 % and the standard coal consumption quantity only reduced by 5.22 %. So for the residential building, design load assumed by ground source heat pump system is 70 %, heat supply network assumed 30 % of the design load is more energy-saving reasonable scheme.

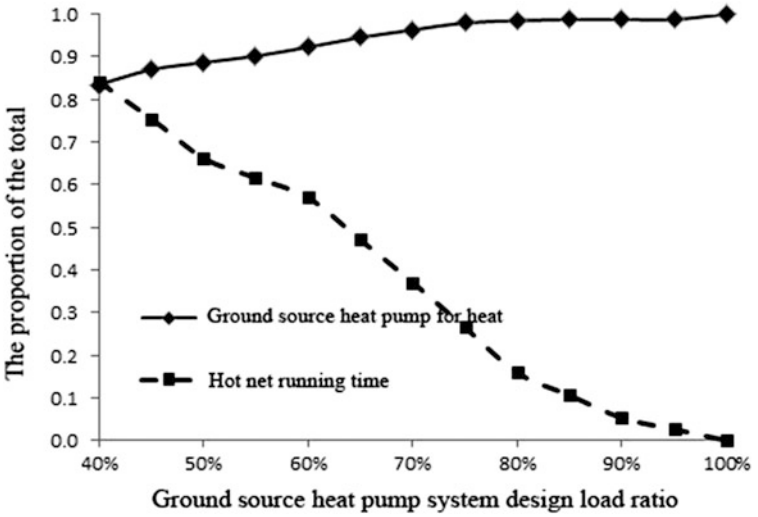

Fig. 74.2 Ground source heat pump for heat and hot net running time

Table 74.1 Standard coal consumption of fuel of different programs

Scheme heat pump + heating network	Heating network system		Ground source heat pump system		General standard coal consumption quantity/t
	Coal fired boiler/t	Auxiliary equipment/t	Heat pump host/t	Auxiliary equipment/t	
40 + 60 %	20.78	2.15	62.07	32.58	117.59
45 + 55 %	16.38	1.70	64.68	33.95	116.70
50 + 50 %	14.26	1.48	65.93	34.61	116.28
55 + 45 %	12.36	1.28	67.05	35.20	115.90
60 + 40 %	9.75	1.01	68.60	36.02	115.37
65 + 35 %	6.89	0.71	70.30	36.90	114.80
70 + 30 %	4.65	0.48	71.62	37.60	114.35
75 + 25 %	2.58	0.27	72.85	38.24	113.94
80 + 20 %	1.94	0.20	73.23	38.44	113.81
85 + 15 %	1.59	0.16	73.43	38.55	113.74
90 + 10 %	1.59	0.16	73.43	38.55	113.74
95 + 5 %	1.59	0.16	73.43	38.55	113.74
100 + 0 %	0.00	0.00	74.37	39.05	113.42

74.4 Economic Calculation of Different Program

The factors of ground source heat pump system cost mainly include three aspects: used area, building structure, function and local policies. According to the current actual engineering calculation, underground water source heat pump system initial

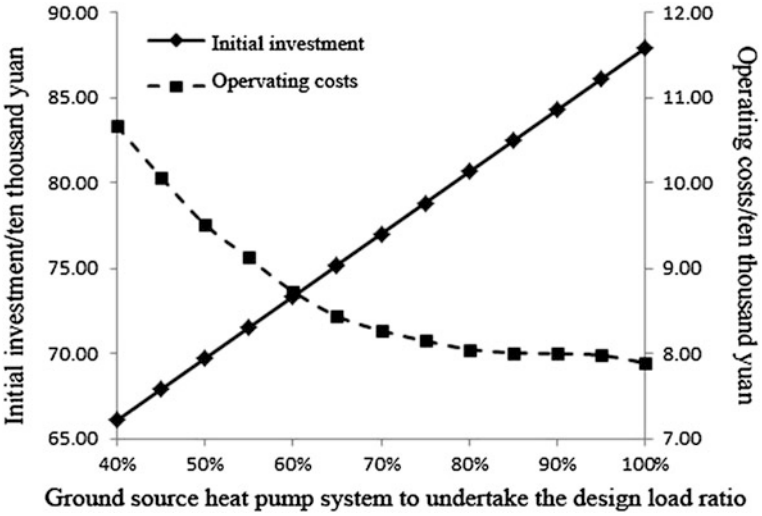

Fig. 74.3 Initial investment and operating costs of the system under different programs

investment is about 250–420 yuan/m^2, cold and heat sources of investment is about 150–220 yuan/m^2. Ground-source heat pump system initial investment is about 300–480 yuan/m^2, cold and heat sources of investment is about 200–270 yuan/m^2. Coal-fired boiler heating system investment is about 150–200 yuan/m^2; Gas dispersion boiler heating system investment is about 100–150 yuan/m^2; Cogeneration district heating system investment is about 200 yuan/m^2 [3], the initial investment of heating terminal equipment is about 40–50 yuan/m^2. According to the daily running is 24 h, rate is 0.8. For reference architecture, in different auxiliary heat source configuration cases initial investment, the running cost is as shown in Fig. 74.3 .

In order to consider the economic system under the condition of the initial investment of system and operation cost are combined, this article get economic evaluation through calculating the total cost of system in the life cycle. According to the basic principle of engineering economics, we assume that the loan to the bank annual rate (I) is 8 %, life period is 30 years, then calculate dynamic project payback period and net present value. Figure 74.4 gives the net present value of the system under different programs and dynamic payback period.

When ground source heat pump assumes 65 % of the design load, we can achieve the largest cost present value (628,200 yuan). Internal rate of return (16.12 %) 10,000 yuan is far greater than 8 % of preset bank loan interest rate), dynamic payback period is 8.77 years. We can get the best economic effect.

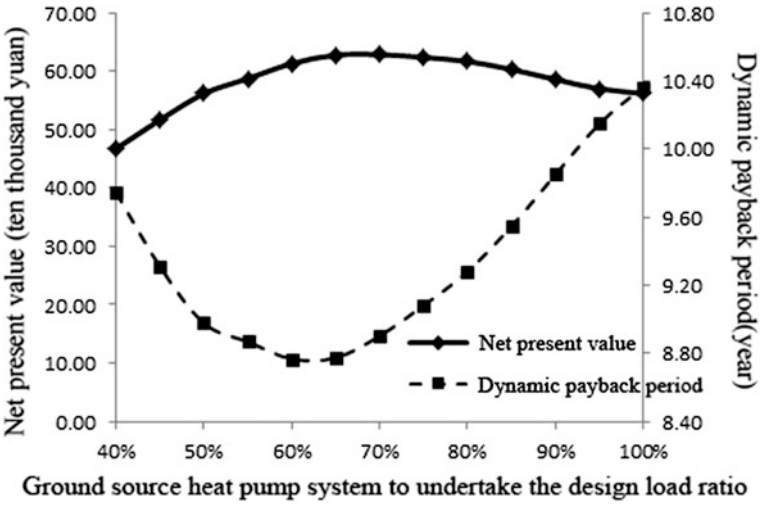

Fig. 74.4 The net present value of the system under different programs and dynamic payback period

74.5 The Simulation Analysis of Solar Collector System

The two major factors influencing complementary operation between the solar energy system and ground source heat pump system is solar collector area and terminal supply and return water temperature. Days of Shenyang heating period is 151 days, 3,624 h, in a typical meteorological year; solar irradiation time is 1,472 h, accounts for about 40.63 % of the total heating time. In order to facilitate analysis, the terminal of the supply and return water temperature about this article required the 50/40 °C.

The setting area of the collector is 180, 300, 500, and 1,000 m^2, to simulate the temperature of supplying water in heating season. Figures 74.5, 74.6, 74.7, and 74.8 show the water temperature of the solar system under four conditions in heating season, respectively.

Increase collector area from 180 to 1,000 m^2, it's small influence that the solar system water temperature is more than 40 °C, from 210 h (5.79 % of the total heating time) increase to 340 h (9.38 % of the total heating time), but it's great influence for more than 40 °C time by 0 h (0 % of the total heating time) increased to 275 h (9.02 % of the total heating time).

For the solar energy—ground source heat pump and heat supply network complementary heating system and ground source heat pump—heat supply network heating system, the cost of ground source heat pump—heat supply network system is exactly the same, so only need to consider for the increase of the initial about investment solar system. Because solar energy is clean free energy, its use can reduce the operation of the system cost. Figure 74.9 solar presents initial

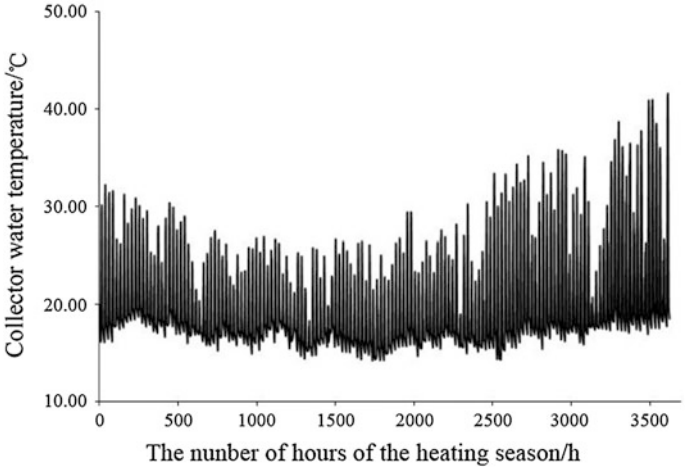

Fig. 74.5 180 m^2 collectors effluent temperature

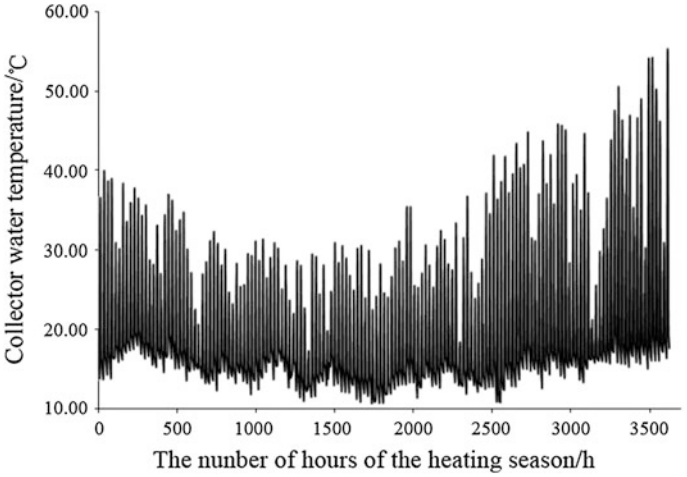

Fig. 74.6 300 m^2 collectors effluent temperature

investment and operating saving cost of energy system of different collection hot area. Assume that the loan to the annual rate I = 8 %, life period is 30 years, calculating dynamic payback period and net present value about that. Figure 74.10 shows the net present value and the investment capital is recovered under different solar system area.

Due to the increase of the system initial investment and operation cost is inversely proportional, leading the cost net present value to gradually raised, then reduce. When the solar system set hot area is more than 300 m^2, the net present

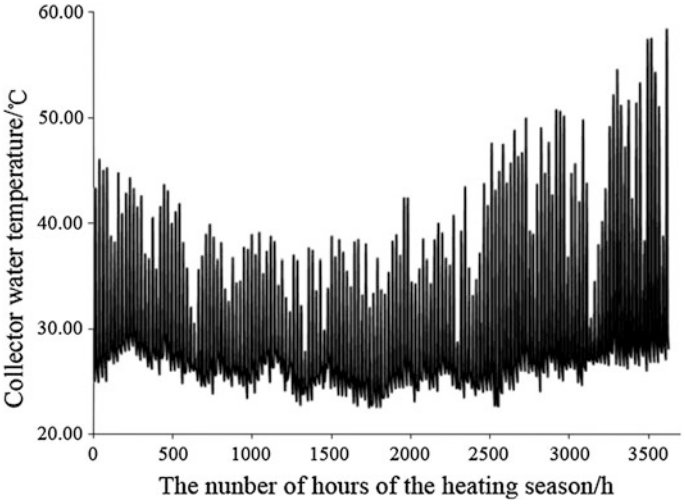

Fig. 74.7 500 m^2 collectors effluent temperature

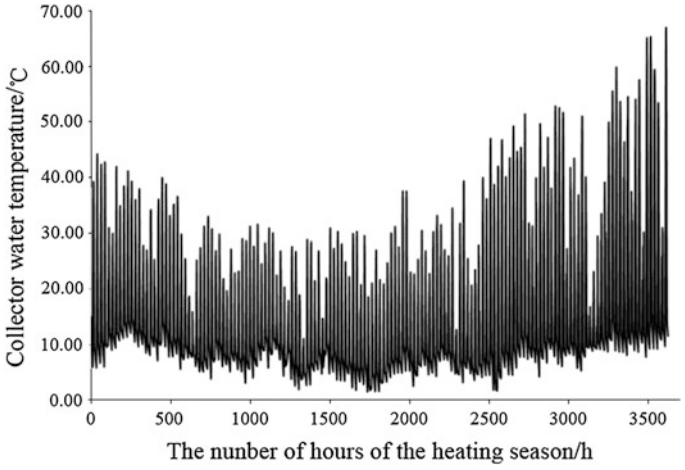

Fig. 74.8 1,000 m^2 collectors effluent temperature

value of solar system investment scheme is less than zero, it is indicated that the project has been loss, when the solar system set hot area is less than 300 m^2, scheme of net present value is greater than zero, and the project can get benefit. When the solar system set hot area is 300 m^2 (i.e., building every square meter air conditioning area need 0.045 m^2 collector areas) or so, get the biggest cost present value (27,000 yuan), the shortest investment payback period is 15.5 years. This can get the best economic effect.

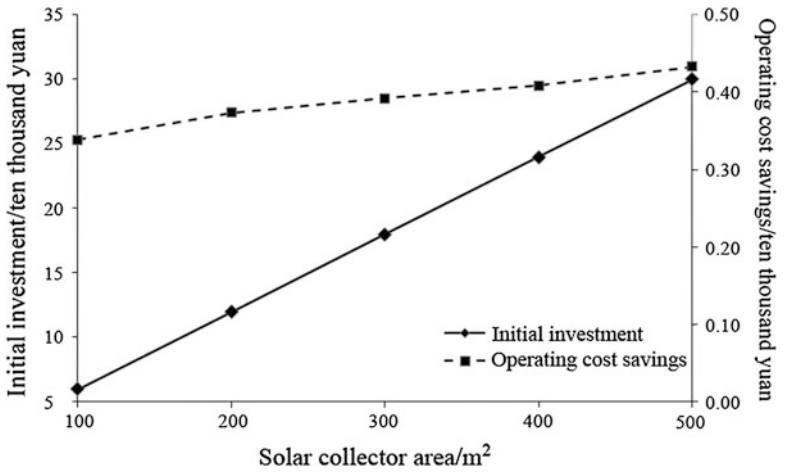

Fig. 74.9 The initial investment and operating cost savings of different collector area

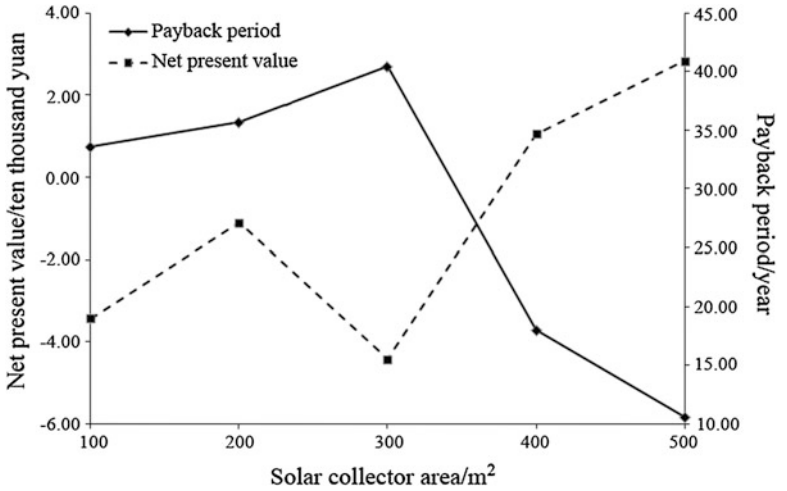

Fig. 74.10 NPV and payback period of different cost savings of different collector area collector area

74.6 Conclusion

1. For residential buildings, 20–70 % design load appear the longest time, accounting for 63 % of the total heating time, and the time of biggest appearance lord is only 1 h, average load is only 25.14 % of the design load.
2. Designing load ratio undertaken by the ground source heat pump system increased from 40–70 %, heat pump heating load increased from 47.80–89.61 %,

heat supply network of heating load only accounts for 10.40 %, heat supply network operation time reduced from 82.5 to 37.5 %, and the standard coal consumption quantity was only reduced by 5.22 %.

3. When ground heat pump undertakes 65 % of the design load, we can achieve the largest cost present value (628,200 yuan), internal rate of return is 16.12 % (it's far greater than a set of bank loan interest rate 8 %), dynamic payback period is 8.77 years. That can get the best economic effect.
4. With the increasing of solar system collection hot area, time which the supply water temperature of the system above 50 °C is gradually increasing, but to the solar energy system water temperature more than 40 °C impacts small.
5. When the solar system set hot area is more than 300 m^2, the net present value of solar system investment scheme is less than zero, it is indicated that the project has been loss, when the solar system set hot area is less than 300 m^2, scheme of net present value is greater than zero, and the project can get benefit.

Acknowledgments This study is supported by National Science and Technology Pillar Program during the 12th Five-Year Plan Period (2011BAJ05B02).

References

1. Xinguo LIN, Jun ZHAO, Qiang ZHU (2001) Economy of ground source heat pump heating air conditioning economy. J solar energy 22(4):418–421
2. Jiang B, Wang Y, Li BX (2003) Economic evaluation of ground source heat pump technology. J Harbin Ind Univ 35
3. Wei XU (2006). Economic analysis of ground source heat pump. China Constr Inf Heating Refrig 6:10

Chapter 75
Investigation and Analysis of the Heat Pump Application in Shenyang

Hongwei Wang, Jie Feng, Hui Wang, Guohui Feng and Baoling Wang

Abstract As one of the pilot cities who apply and disseminate with the renewable energy that the National Ministry of Construction has determined, Shenyang has summarized some experiences about the application and promotion of the ground source heat pump (GSHP) technology which is named "Shenyang model," and constantly expands this application model. Given this understanding, Shenyang fully extend the GSHP that apply the secondary discharge water of urban sewage plant as renewable source, and the circulating cooling water GSHP system using the waste heat of the thermal power plant, soil source heat pump system, the hybrid water source heat pump units working with the central heating system, and the other effective models. All of these systems play an important role in energy conservation and emissions reduction of our city, and also in improving the urban environment.

Keywords Underground water source heat pump · Hybrid water source heat pump · Renewable water source heat pump · Central heating system

75.1 Promotion and Application of the Heat Pump Technology in Shenyang

According to the "Ground Source Heat Pump System Engineering Technical Specifications" (GB50366-2005) regulation, GSHP system divides into ground-source heat pump system, ground-water source heat pump system and the surface

H. Wang (✉) · J. Feng · G. Feng · B. Wang
School of Municipal & Environmental Engineering, Shenyang Jianzhu University, Shenyang, China
e-mail: hj_whw@yahoo.com.cn

H. Wang
Branch Institute of Liaoning City Architectural Design, Shenyang, China

A. Li et al. (eds.), *Proceedings of the 8th International Symposium on Heating, Ventilation and Air Conditioning*, Lecture Notes in Electrical Engineering 262,
DOI: 10.1007/978-3-642-39581-9_75,

water source heat pump system which bases on the different forms of geothermal energy exchange system. In the GSHP application engineering of our country, we use shallow and deep groundwater and soil as the cold and heat sources, in addition to this, we also use the urban sewage, reservoir water, surface river water, geothermal tail water, the waste heat of the thermal power plant, waster heat from oil extraction as cold and heat sources. There are 10 % of the project using the GSHP equipped with cooling tower. A part adopt forms combined with ice storage technology, solar energy utilization, and combined heat power plant with urban other energy, etc. [1–3].

At present, Shenyang mainly popularized the application of underground water source heat pump, hybrid water source heat pump and renewable water source heat pump system. And most of these distribute in the core area within the third rode of Shenyang, where the groundwater source heat pump system accounted the most area of 2246.2×10^4 m^2, the proportion is 64.9 %; renewable water heat pump system application area is 626.15×10^4 m^2, accounting for 18.1 %; mixed water source heat pump system application area is 572.9×10^4 m^2, accounting for 16.6 %; and ground-source heat pump system application area is 13.65×10^4 m^2, accounting for 0.4 %.

75.1.1 The Groundwater Source Heat Pump System

Because of the unique hydrogeological conditions, Shenyang regards the promotion and application of ground water source heat pump (GWHP) technology as the key project, which has formed three kinds application models with its own characteristics. They are adopting water source heat pump (WSHP) system heating and refrigeration model for new buildings; transforming the existing heating and cooling mode using the WSHP technology for the original public buildings; applying WSHP and centralized heating hybrid heating mode for the original residential districts. The building area of using water heat pump technology application including both new construction projects and the transformation is 2246.2×10^4 m^2, and accounted for 64.9 % of all applications. As one of the demonstration cities who applies and disseminates with the renewable energy, Shenyang has 11 GSHP technology application projects which are identified as the demonstration projects of renewable energy of our nation, and Shenyang gets 110 million yuan financial support.

75.1.2 Renewable Water Source Heat Pump System

As we all know the heat in the secondary discharge water (recycle water) of the sewage treatment plant is difficult directly used, as an important form of GSHP, renewable water source heat pump systems extract the low grade heat energy from

the wastewater via the WSHP units for building heating. This system has simple process, stable operation, etc. Besides, it can effectively saves fossil fuels, land, water, and other scarce resources and has good economic, environmental and social benefits. Compared with the GSHP system which uses ground water as it's heat source, renewable water source heat pump system has more advantages in security and environmental protection.

Currently Shenyang has completed ten sewage treatment plants that basically distribute along the Hun He line. Of which, eight sewage treatment plants have been formally put into use. The design capacity of sewage treatment is 140×10^4 t/d, and the actual is 112.9×10^4 t/d. The dates measured in the existing seven sewage treatment plants which have perennial monitoring show that the sewage water temperature in winter is about 12 °C, which is about 20 °C above its average winter outdoor temperature; and it is about 21 °C in summer, which is 10 °C lower than the summer outdoor average temperature. In Shenyang, most of the sewage treatment plants adopt the secondary biochemical treatment technology and the effluent water quality is good. According to the calculation, energy stored in regeneration water of the eight existing sewage plants in Shenyang can meet the building heating demand of 860×10^4 m^2.

Shenyang has built three renewable water heat pump application projects, which can meet building heating demand of a total of 886×10^4 m^2. Among them, the scale of the construction of GuoHui renewable water comprehensive utilization project is three 130 t/h steam boilers, a set of 70 t/h steam boiler, a set of 70 MW hot water boiler, eight 29 MW water source heat pump units. The total installed capacity is 70 MW for water furnace, 465 t/h for steam furnace, 232 MW for the water source heat pump, and the area of heating is 1200×10^4 m^2. Among them, the eight 29 MW water source heat pump units which is drove by steam turbine, fully extract the low grade heat energy from renewable water in XianNv river sewage treatment plant that disposes 40×10^4 t renewable water every day. We adopt a mode which the steam waster heat and water source heat pump jointed for supplying to meet the heating demand of regional internal user. Water source heat pump can provide 40.2 % of the heat energy and meet 482×10^4 m^2 building heating demand. The total investment of this project is 959.92 million yuan. The scale of the construction of Shenshuiwan renewable water comprehensive utilization project is two 75 t/h steam boilers, five sets of 10 MW water source heat pump units (each source heat pump units with two Table 1.6 MW turbines). Total installed capacity is 150 t/h for boiler furnace, 50 MW for water source heat pump, and the heating area is 260×10^4 m^2. Among them, the water source heat pump units which drove by steam turbine, fully extract the low grade heat energy from renewable water in Shenshuiwan sewage treatment plant that dispose 20×10^4 t renewable water every day. The model we adopt is that steam waster heat and water source heat pump are combined to meet the heating demand of Shenshuiwan regional internal users. Water source heat pump can provide 40 % of the heat energy and meet 104×10^4 m^2 building heating demand. The total investment of this project is 247.48 million yuan. The Shenyang northern sewage treatment plant of comprehensive utilization of renewable water project, which process 40×10^4 t

recycled water every day, extract the low grade heat energy from the recycled water, to meet the surrounding buildings heating demand. The biggest characteristic of this project is "one water for three uses," recycled water can be used for heating, landscape water and daily production water for Kangping power plant.

75.1.3 Soil Source Heat Pump System (Buried Tube Ground Source Heat Pump System)

Compared with the GSHP system, the advantages of soil source heat pump are that the system is not affected by the groundwater and there is no damage or pollution to groundwater. Besides, the system runs reliability and stability. However, there are some problems such as higher initial investment, poorer unit operation conditions, great influences caused by soil properties to buried heat exchanger, larger layout area, because of these, only a few projects adopt this technology in practical application process. Here is a famous project which adopted this mode, the display greenhouse of Shenyang International Horticultural Exposition—Rose Garden.

The construction area of this project is 7,351 m^2, and the average height is 15 m, palisade structure use all vacuum glass curtain wall, and the required temperature for rose growth all the year ranges from 15 to 25 °C. But the regional geological structure and the underground water cannot meet the demand, so we adopt the GSHP technology, drill in the outdoor heat exchanger, install 286 double U type heat exchangers of 80 m depth and add 15 % glycol in medium of heat exchanger tube. So in winter we can get heat from underground; in summer cool the rose garden with central air conditioning system and at the same time absorb the indoor heat, then exhaust the heat to the underground soil via the heat pump system. By the operating of recent 2 years, the system fully meets the temperature and humidity for roses growth, and at the same time provides a good space and environment for rose visitors. The effect of this project is prominent in energy saving and environmental protection. As far as the Rose garden project is concerned, under the same energy supply, compares the yearly operation cost of soil heat pump system with the gas plus electric refrigerating system, we can save 53 and 45 % of disposable energy. According to this calculation, we can reduce 783t carbon emission and 2t oxynitride emissions a year.

75.1.4 Hybrid Water Source Heat Pump Units Combine with the Central Heating System

By the investigation from 14 heating companies such as Shenyang Huanggu thermal power plant, Shenyang Huitian thermoelectric company, Shenyang New North thermoelectric company, we get the following information: in Shenyang, the

primary circuit heating temperature ranges from 82 to 90 °C; backwater temperature is 51–56 °C; the second circuit heating temperature range is 52–57 °C, backwater temperature range is 38–42 °C. The average temperature of primary circuit heating and backwater is 85.85 and 53.90 °C, the secondary circuit is 54.35 and 39.76 °C. Although the heating temperature range which has some differences to some extent from the current national standards, we know that this survey represents the basic situation of Shenyang current heating, so hybrid water source heat pump units plus the central heating system can be properly considered during the further developing of GSHP system in Shenyang.

The municipal government promotes this technology on 10 large coal central heating enterprises of the city. And at present, the application area of hybrid water source heat pump system is 572.9×10^4 m^2, accounting for 16.6 % of the total area of the GSHP system. Due to the limitation of well arrangement site, Shenyang "Morgan Kelly" project whose construction area is 13×10^4 m^2, adopted a networking heating mode which combined with Shenyang New North thermoelectric company instead of the before design that applying WSHP heating and refrigeration system independently. Namely, the WSHP system which plans to construct in this project is purchased by the Shenyang New North thermoelectric company, and as a distribution of the company construction application of "Hybrid Water Source Heat Pump System plus Central Heating Installations." It runs unified management by the company, develops a supplementary heat source of the centralized heating, and achieves the "win–win" of heating enterprise and project construction unit. Through the popularization and application of "Hybrid Water Source Heat Pump Technology," we not only solved the problems such as water resources shortage and well limited spacing position during the popularization, but also alleviated the possible contradictions between GSHP technology application and the traditional coal enterprise, and realized the mutual complementary, greatly improved the safety and reliability of system operation.

Overall, all ground source heat pump systems applied at present in Shenyang have the following outstanding technical advantages: high efficiency, energy saving, environmental protection and no pollution. In winter heating, most of the GSHP systems do not need a boiler or increase the booster heater. And by the design, all these systems can provide heating, cooling, and the domestic hot water at the same time. Because of the dispersing heating, this greatly improves the urban energy security. We need no special person to care about or maintenance because of the lower operation and maintenance costs and simple system composition. The system has simple control equipment, agile operation, and reliable system. There is no cooling tower and other outdoor equipments, so they save the space and land, and improve the external image of the building. These equipments have long service life and usually the set life are more than 15 years; they also can provide domestic hot water during heating.

75.2 Existing Problems During the Promotion and the Application of Heat Pump Technology

1. For the actual operation of the WSHP units, the summer cooling condition is relatively good, but some problems are common in the winter heating such as mass flow, small temperature difference, low hot water outlet temperature. On one hand, these problems may be caused by low winter groundwater temperatures. On the other hand, this shows that the performance of the unit needs improving. If the WSHP can be populated, this inevitably means that we need a lot of groundwater resources. So based on the principle of water and energy saving, the WSHP should possibly adopt the technology which has big temperature differences and small flow, and also should try to enhance the outlet temperature of the winter hot water.
2. For the central air conditioning system end that adopts the WSHP units, there is no doubt that is ideal to use the fan coil as the terminal devices, but when we chose the big volume air unit or air conditioning as the terminal, especially in cold northern area, we should pay more attention that the temperature of 50–55 °C hot water provided by most manufacturers is still lower. So to meet the requirements of the winter air supply parameters, we suggest to supply additional heating measures to assist the large volume terminal equipment or divide the large volume terminal equipment into several small air terminal equipments when necessary.
3. The application of GWHP will bring groundwater mining problem, and whether it can be widely used in a city or a large area, how to solve the water balance problems between wells and recharge wells, and whether backflow speed problem of recharge well will cause problems to surrounding buildings on security and quality, all of the above need further study from the theory to practice.
4. There are also some problems such as the influence to groundwater quality and water level, corrosion and scaling problems on the equipment of pipeline caused by soil, etc.

Acknowledgments This research is funded by the National Science and Technology Support Program under grant number 2011BAJ05B01-04.

References

1. Xu W, etc. Ground source heat pump technology manual [M]. China Building Industry Press, 2011–15
2. Xu W, etc. Ground source heat pump engineering technology guide [M]. China Building Industry Press, 2011–11
3. Sun X, etc. Ground source heat pump engineering technology and management [M]. China Building Industry Press 2009–3

Chapter 76
Experimental Study on Unsteady State Properties of Ceiling Radiant Cooling Panels System

Lin Su, Nianping Li, Xuhan Zhang, Yanlin Wu, Yunsheng Jiang and Qing Huang

Abstract Ceiling radiant cooling panels (CRCP) system is more comfortable and energy-saving than the traditional convection air-conditioning system according to the research of pioneers. The former research was concentrated in the feasibility, thermal comfort, and energy saving of the CRCP system. Changes of the system parameters are not described systematically under unsteady state. There are hardly any complete and credible reference materials for engineers to design CRCP system of buildings. In this paper, the radiant thermal performance was studied in the experimental platform, and the operating data of the CRCP system was collected in the startup phase and regulating phase of the platform. The results shows that the thermal inertia of the metal radiant panel is small and the response of thermal parameters is very fast under unsteady state in the experiment. The distribution of the surface temperature is uniform on the cool ceiling, and the heat transfer resistances are basically the same among different cooling panels. Learning the changing rules of the CRCP system would provide the engineers reference materials for running control, design, and assessment of the system in the future.

Keywords Ceiling radiant cooling panels system · Radiant heat transfer · Unsteady state

76.1 Introduction

In recent years, with the development of life quality, the request for good inhabitancy condition gets higher than before. Air-condition is developing very fast as an effective means to improve the indoor thermal environment and air

L. Su · N. Li (✉) · X. Zhang · Y. Wu · Y. Jiang · Q. Huang
College of Civil Engineering, Hunan University, Changsha 410082, China
e-mail: linianping@126.com

A. Li et al. (eds.), *Proceedings of the 8th International Symposium on Heating, Ventilation and Air Conditioning*, Lecture Notes in Electrical Engineering 262,
DOI: 10.1007/978-3-642-39581-9_76,

quality of buildings. In the pursuit of a higher life quality, the demand for air-condition is not just suitable temperature and humidity. Air-condition is developed along the direction of comfortable, healthy, and energy saving.

Ceiling radiant cooling panels (CRCP) system first appeared in Europe, and the main advantages of CRCP system are the excellent thermal comfort and lower operating cost [1–3]. People complain more about the comfort problems of the traditional air-conditioning system such as draft sensation and noise [4]. These demands promote the development of CRCP system.

To evaluate the thermal comfort in air-conditioned environments, ASHRAE made rules of wind velocity and vertical temperature grade in air-conditioned workspaces [5]. People will feel uncomfortable if the wind speed and vertical temperature grade are too high. In CRCP system, the vertical temperature grade and wind velocity are reduced effectively [6, 7]. The airflow pattern without return air ensures that there is no cross contamination among rooms. CRCP system has a unique advantage in preventing the spread of disease like SARS.

The air system in CRCP system is simplified, so the operating cost is much less than that of the all-air system. The building space occupied by air pipes and air handling units is reduced greatly, and the total cost of CRCP system is reduced as well. The temperature of cold water is relatively high in CRCP system, so the ground water or cooling water in cooling tower can be used directly in CRCP system, and the energy consumption is reduced significantly due to the high-temperature cold source [8].

76.2 Radiant Heat Transfer Mechanism of CRCP

The heat transfer between the cold water and the room can be stepped with the following processes: (1) forced-convection heat transfer between the cold water in the pipe and the internal surface of the pipe; (2) heat conduction between the internal surface and the outside surface of the pipe; (3) heat transfer between the outside surface of the pipe and the cooling panel; (4) heat transfer between the cooling panel and the room. The heat transfer between the cooling panel and the room includes radiant heat transfer and heat convection. The heat transfer between the cooling panel and indoor surfaces (including wall, floor, or equipment) is radiant heat transfer, and the heat transfer between the cooling panel and the indoor air is heat convection [9–11].

76.3 Experiment Method and Instruments

The startup phase, stably running phase, and regulating running condition phase were analyzed in this experiment. Thermal parameters of different phases were recorded using paperless recording instrument. Running characteristics and laws of

CRCP system are understood and mastered through analyzing the change of these parameters, which is good for operating and regulating the CRCP system in practice.

The experiment was completed in YanTong Zhuhai Environmental Science and Technology Ltd. (Zhuhai, China). The experimental period was from November 11 to 12 in 2012. The radiant thermal performance experimental platform is made up of four parts: test chamber, cooling system, heating system and recycled-air system (in Fig. 76.1). The size of the test chamber is 2.27 × 1.68 × 1.85 m. The ceiling of the test chamber is white metal radiant panel, and the floor and wall is black metal radiant panel. In the experiment, the ceiling of the test chamber is cooled, and the floor and wall is heated. The outside surfaces of the test chamber are almost adiabatic (in Fig. 76.2). The ceiling panel of the test chamber is composed by six metal radiant panels of 1.2 m × 0.6 m each. A thermal resistance is installed on the centre of the surface of each panel (in Fig. 76.3). Six temperature changes are recorded in the experiment.

The experiment instruments include: Pt100 thermal resistance, turbine flow meter, paperless recorder, TSI temperature-humidity-wind velocity indicator and so on.

The sampling time interval is 5 s in the experiment. And the time interval in Figs. 76.4 and 76.5 are both 5 min for more clear expression.

76.4 Experimental Results

In the experiment of November 11, 2012, the water in hot water tank was heated firstly, and then the pump and valves of the heating system were opened. From the Fig. 76.4, we can see that: the hot water supply temperature is rising rapidly from 28.6 °C at 19:21. Then the hot water supply temperature reaches 42.1 °C at 19:23. The hot water return temperature rises from 23.4 to 33.8 °C with the rising of

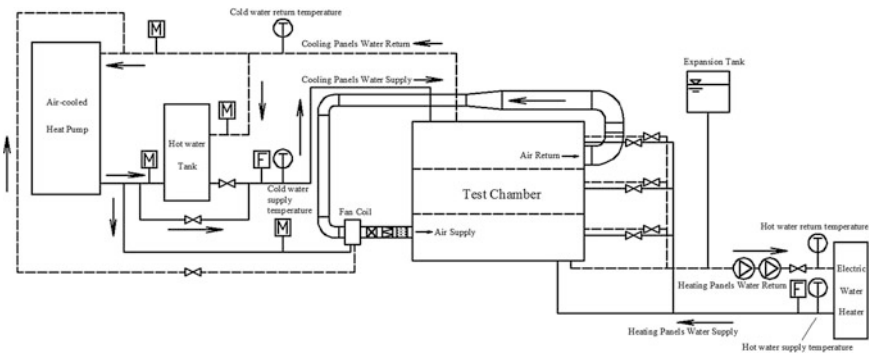

Fig. 76.1 The system chart of the experimental platform

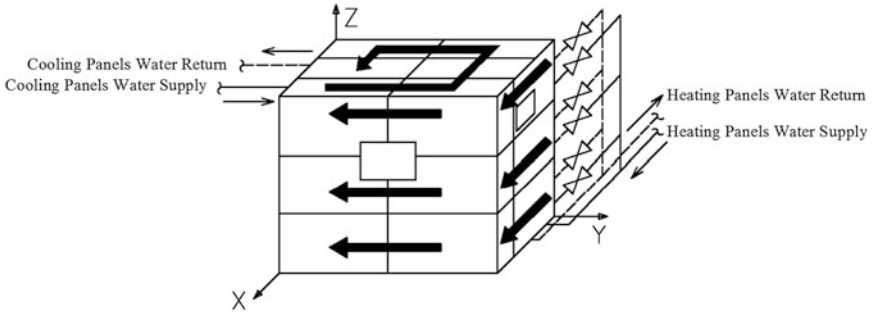

Fig. 76.2 The 3D chart of the test chamber

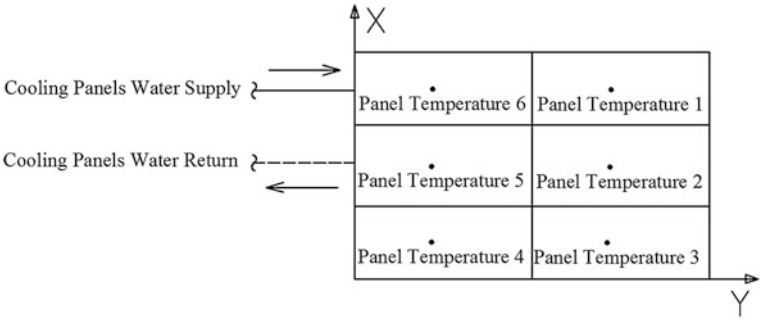

Fig. 76.3 The location of temperature measurements on the cooling panel surface

supply temperature. Then the heating power is turned down. The temperature in the hot water tank is reduced slowly because of natural cooling. The floor temperature of the chamber is rising up with the hot water. The hot floor makes the temperature of the ceiling panel rise up through radiant heat transfer and heat convection. Before the supplying of cold water, the temperatures of water supply, water return and ceiling panel all remain relatively stable and the experimental system reaches heat balance temporarily.

The pump and valves of cooling system were opened at 21:21. The temperatures of water supply and return reduce rapidly, and the temperature of ceiling panel also reduces. Under the influence of CRCP, the temperature of water supply and return reduces, but the difference of temperature between supply and return of hot water is stable and the difference is about 3 °C. The outlet water temperature of the water chilling unit is difficult to ensure stability. So the cold water supply temperature fluctuates in a range of 6.5–10 °C and the cold water return temperature fluctuates in a range of 8.4–10.7 °C.

The fluctuations of cold water supply and return temperatures are basically the same. The fluctuation of cold water return temperature delays relative to that of cold water supply temperature. In the figure, we can see that the six curves of

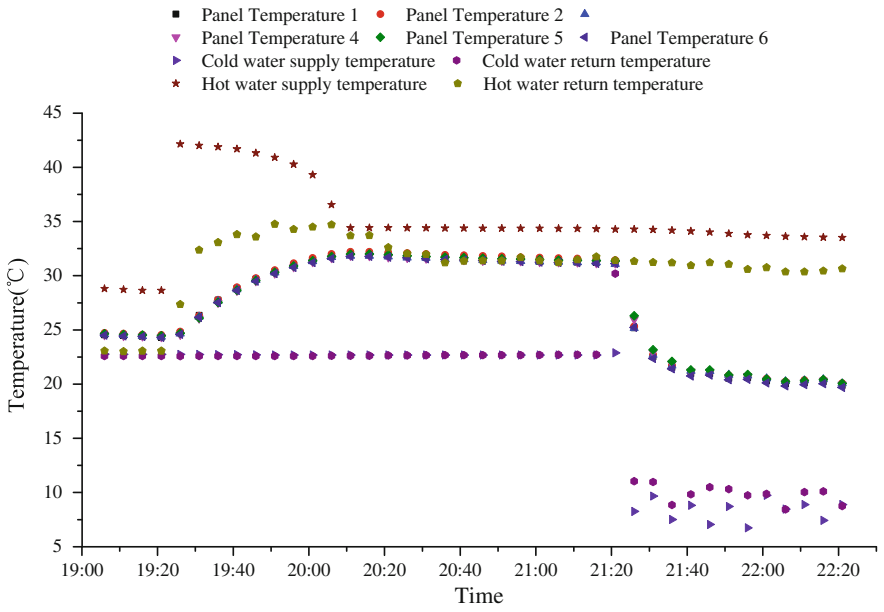

Fig. 76.4 The temperature curves at November 11, 2012

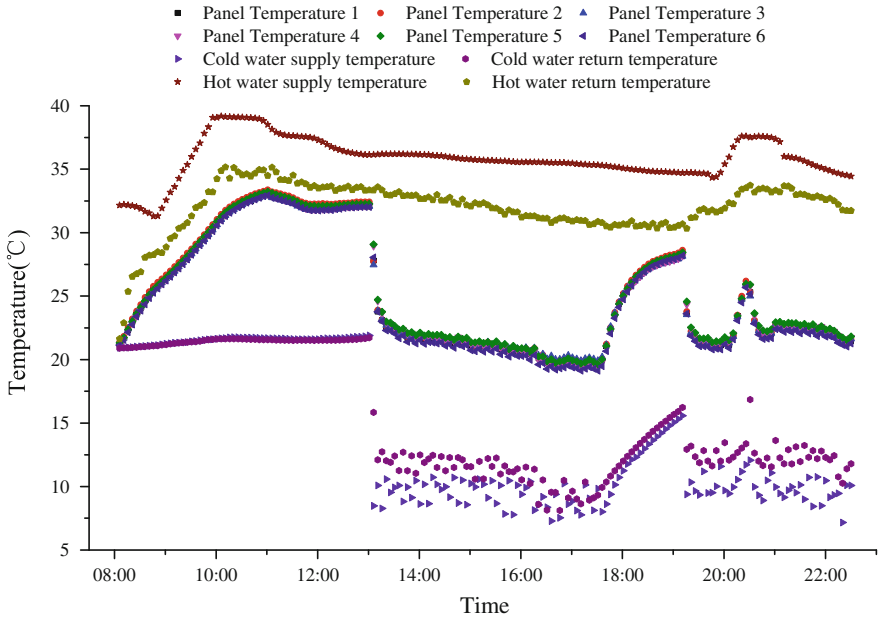

Fig. 76.5 The temperature curves at November 12, 2012

temperature changing have good overlap ratio. This means the uniformity of heat transfer of this type of metal radiant panel is very good, and the uniformity and stability of the resistance of heat transfer between the cold water and the metal panel surface are both very good in different radiant panels. There is no too big or too small local resistance in heat transfer.

Figure 76.5 shows the data of November 12, 2012. The characteristics from 13:00 to 16:00 are basically the same as the results of November 12 in CRCP system. This means the repeatability of the experiment is good and the results are accurate. At 17:30, the system is adjusted and the valve of supplying cold water is turned down, and then the flow of cold water is reduced. Because the flow of hot water is constant, the temperature of floor, wall and air rise up gradually, and the cold water supply and return temperatures are affected in turn.

76.5 Conclusions

The distribution of surface temperature is uniform, and the resistances of heat transfer are basically the same among different panels. There is no too high or too low of surface temperature in different panels. This kind of radiant metal panel is suitable for practical engineering and is good for avoiding moisture condensation on the panel surface. The changes of thermal parameters of CRCP system are showed clearly in the results. The thermal inertia of cooling panel is small and the response of the thermal parameters of the CRCP system is very fast under unsteady state. This is good for adjusting and controlling the system. This paper presents the partial properties of CRCP system under unsteady state, and this can be a reference for engineers in practice. Further study on CRCP system will be developed in the future.

Acknowledgments This study was financially supported by the National Natural Science Foundation of China (Project No. 51178169). And also express my thanks for the experimental assistance of YanTong Zhuhai Environmental Science and Technology Ltd.

References

1. Mumma SA (2001) Ceiling panel cooling systems. ASHRAE J 43(11):28–32
2. Stetiu C, Feustel HE, Nakano Y (1996) Ventilation control strategies for buildings with hydraulic radiant cooling in hot humid climates. In: Proceedings of the room vent, Japan, Yokohama, pp 1–6
3. Mumma SA, Jeong J (2007) Practical cooling capacity estimation model for a suspended metal ceiling radiant cooling panel. Build Environ 42:3176–3185
4. Fanger PO, Ipsen BM, Longkilde G et al (1985) Comfort limits for asymmetric thermal radiation. Energy Buildings 8:225–236
5. Wang ZJ (2004) Low-temperature radiant heating and radiant cooling. China Machine Press, Beijing

6. Zhang TT, Tan Y, Zhang H (2012) Experimental test on carbon crystal panel system and simulation research on its partial-heating program. Build Environ 51:263–268
7. Tian Z, Yin X, Ding Y (2012) Research on the actual cooling performance of ceiling radiant panel. Energy Buildings 47:636–642
8. Niu JL, Burnett J (1998) Integrating radiant/operative temperature controls into building energy simulations. ASHRAE Trans 104(2):210–217
9. Yang SM, Tao WQ (2006) Heat transfer theory. High Education Press, Beijing
10. Wang FJ (2004) Analysis of computational fluid dynamics- CFD software theory and application. Tsinghua University Press, Beijing
11. Sparrow EM, Cess RD (1978) Radiation heat transfer. High Education Press, Beijing

Chapter 77
Orthogonal Test and Regression Analysis on Filtration Performance of PSA/Needle-Punched PSA Filter Material

Min Fang, Henggen Shen, Tingting Xue and Libo Wang

Abstract This paper is focused on the classification filtration performance of Polysulfonamide (PSA)/needle-punched PSA filter material at room temperature. And all the experiments are handled based on the test equipment of filter materials' static characteristics. A four-level and three-factor orthogonal table was adopted in the experiment scheme and the experiment data were processed by dimensional analysis and multiple nonlinear regression method with Statistical Product and Service Solutions (SPSS). It suggests the Regression equation that analyzes the relation between classification filtration efficiency and experimental factors (like average particle diameter, dust load, filtration velocity). And the classification efficiency of the PSA/needle-punched PSA filter material varies apparently with the ranges of particle size.

Keywords PSA fibre · Filtration performance · Dimensional analysis · Orthogonal test

77.1 Introduction

Polysulfonamide fibre (short for PSA), also commercially named Tanlon, is a kind of aromatic refractory synthetic fibre co-developed by Shanghai textile science institute and Shanghai synthetic fibre institute in 1973 [1–3]. And the two enterprises own its fully independent intellectual property rights. PSA's chemical name is poly terephthaloyl amide and 3,3,4 –Diaminodiphenylsulfone, which belongs Aromatic polyamide with refractory character, its molecular structure [4] is shown in Fig. 77.1.

M. Fang · H. Shen (✉) · T. Xue · L. Wang
College of Environmental Science and Engineering, Donghua University, Shanghai 201620, China
e-mail: shenhg@126.com

A. Li et al. (eds.), *Proceedings of the 8th International Symposium on Heating, Ventilation and Air Conditioning*, Lecture Notes in Electrical Engineering 262,
DOI: 10.1007/978-3-642-39581-9_77,

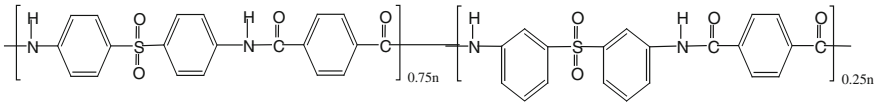

Fig. 77.1 Molecular structure of polysulfonamide fibre

As we see, its macromolecular main chain consists of p-phenylene, m-phenylene, and amide (-NHCO-) and sulfonyl (-SO_2-). Because the existence of the strong electron-drawing group, sulfonyl, and conjugated double bonds of benzene, it remarkably reduced electron density of amide, which leads extraordinary heat resistance, good stability of heat dimension, and outstanding antioxidant for PSA [5–8]. The invention of PSA fills a gap in the area of synthetic fibre with high temperature resistance (250 °C level) in China [9–11]. Therefore, PSA filter material can be used in high-temperature flue gas (≥130 °C) emitted from kiln, electric arc furnace, melter, sintering kiln and calcining kiln in asphaltum, refining aluminium, ferroalloy, cement, nonferrous metal, steel and ceramic industries. And its performance would be better if it is used in filtrating flue gas of 200–250 °C. Furthermore, PSA fibre is usually combined with other refractory fibre to achieve the compound filter material with better performance. So, its market prospect is attractive in the area of filtration at high temperature [12, 13].

Filtration efficiency is a crucial performance index of filter materials. And it can be divided into dynamic efficiency of dust removal and static efficiency of dust removal [14]. The former is the efficiency tested at the condition that the filter materials are working and then cleaning dust continuously and periodically according to the regulations. While the latter is the efficiency tested at the condition that filter materials are working continuously from clean state to the state that holding capacity approaches the set value without dust cleaning. However, it's hard to achieve dynamic efficiency of dust removal because the tests for filter materials are operated in the testing equipment for filter material's dynamic characteristics, which simulate the actual working condition of bag filter. Therefore, in this paper, we choose the static efficiency of dust removal to value the performance of filter materials. Then, the three main factors that affect the efficiency of PSA/needle-punched PSA filter material, including particle size, dust load, filtration velocity, are analyzed by orthogonal tests handled with test equipment for filter materials' static characteristics. And then, the experimental data were processed by dimensional analysis method and multiple nonlinear regression method. Finally, regression equation describing the relation between the filtration efficiency and factors are concluded.

77.2 Orthogonal Test

77.2.1 Test Equipment

The schematic of test equipment for static efficiency of dust removal is shown in Fig. 77.2. Classification efficiency of clean filter material is tested in the lab suspended with aerosols. As shown in Fig. 77.2, environmental aerosols are pumped into the PPMA duct by oilless vacuum pump, and then pass through the assigned filter material, rotameter, eventually exhausted from vacuum pump. Pressure drop through the filter material is measured by digital micro-manometer connected to two measurement ports locating at the front and the rear of the filter

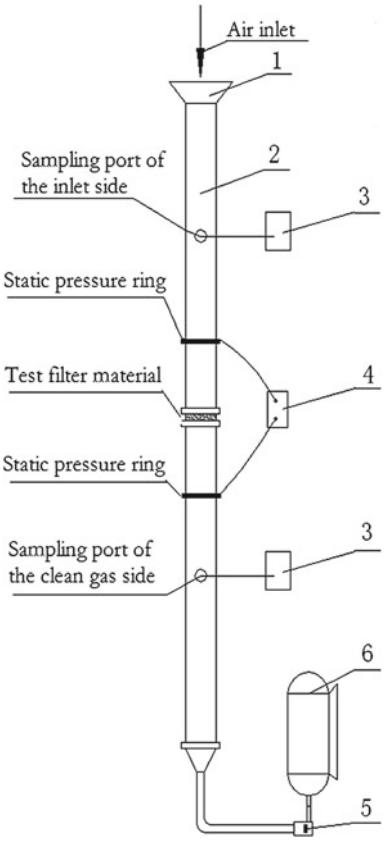

1 - inlet nozzle , 2 - PMMA duct, 3 - Grimm1.108, potable aerosol spectrometers
4 - digital micro-manometer , 5 - rotameter , 6 - oilless vacuum pump

Fig. 77.2 Test equipment of filter materials' static characteristics

Table 77.1 Technical indicators of GRIMM1.108

Technical indicator	Value
Range of particle weight	0.001–100 mg/m^3
Number of channels	15
Flow rate	72L/h
Measurable particle size	0.23–20 μm
Applicable temperature	4–45 °C

Table 77.2 Technical indicators of

Technical indicator	Value
Applicable pressure	0–2000 Pa
Maximum overload	≤200 %FS
Resolving power	1 Pa
Preheating time	15 min
Power	9 V DC or Battery

material. And mass concentrations of different particle size are measured at front and rear of the filter material by two potable aerosol spectrometers, GRIMM 1.108. Then, classification efficiency can be calculated.

The size of tested filter material is 1.66 mm of thickness and 80 m of diameter. The detailed parameters of 3 and 4 are shown in Tables 77.1 and 77.2.

77.2.2 Orthogonal Test Design

Three main factors that affect the classification efficiency of PSA/needle-punched PSA filter material, particle size (d), dust load (g), filtration velocity (v), are evaluated respectively in four levels regardless of interaction effect. Because the measuring arrange of GRIMM 1.108 starts with 0.23 μm, and the test is based on the aerosol in the common lab. And each level of particle size is the median diameter of some arrange. When the dust load is over 600, the collecting efficiency is very close to 1. And we choose the normal filtration velocity usually used in dust removing at high temperature. Table 77.1 is the orthogonal table of factors' levels (Table 77.3).

Table 77.3 The orthogonal table of factors' level

Factors' levels	Particle size d (μm)	Dust load g (g/m2)	Filtration velocity v (m/min)
1	0.265	0	0.8
2	0.350	200	1.0
3	0.450	400	1.2
4	0.575	600	1.5

The method of testing the dust collecting performance of filter material is as follow. At the airflow rate of 1.5 m/min, dust is generated uniformly every 2 min. Because of low airflow rate, the structure of dust layer doesn't change at steady-state filtration. Thus dust layer can be deemed as natural accumulation of dust, which means that thickness of dust layer increase linearly with time. With the experiment keeping on since the beginning of dust generating, the dust load of filter material reaches the set value. Then alter the filtration velocity through controlling the volume of rotameter, and get the mass concentration of particles of different size in the front and the rear of the filter material by two potable aerosol spectrometers, GRIMM 1.108. A simplified calculation of filtration efficiency rating formula is as follows [15]:

$$\eta = \left(\frac{C_2 - C_1}{C_1}\right) \times 100\,\% \tag{77.2.2.1}$$

where, C1 and C2 refer to mass concentration of some particle size in front and rear of the filter material respectively.

77.3 Regression Analysis on Tests' Result

77.3.1 Orthogonal Test's Results Table

The orthogonal test's results of the classification efficiency of PSA/PSA needle-punched filter material are shown in the Table 77.4.

Table 77.4 Design and results of the orthogonal test's results of the classification efficiency of the filter material

Test times	Particle size d(μm)	Dust load g(g/m2)	Filtration velocity v(m/min)	Classification efficiency η(%)
1	1	1	1	77.31
2	1	2	2	78.12
3	1	3	3	73.66
4	1	4	4	76.56
5	2	1	2	75.43
6	2	2	1	76.89
7	2	3	4	74.66
8	2	4	3	75.44
9	3	1	3	73.68
10	3	2	4	74.16
11	3	3	1	75.89
12	3	4	2	72.08
13	4	1	4	74.31
14	4	2	3	76.25
15	4	3	2	81.26
16	4	4	1	82.31

77.3.2 Orthogonal Design-Direct Analysis

The intuitionistic analysis on classification efficiency of the orthogonal tests is shown in Table 77.5.

where, $\overline{K_1}$–$\overline{K_4}$ refer to the mean classification efficiency of one factor in four different working conditions at the same level. It suggests that the laws, which state the correlation between three factors and the classification efficiency of PSA/needle-punched PSA filter material, are as follows: it decreases initially and rises later with the increase of particle size; rises all along with the increase of dust load; and it decrease all along with the increase of filtration velocity. Furthermore, the value of extreme difference indicates how much the factor affects the classification efficiency. The larger it is, the more it affects the classification efficiency, vice versa. The factor with large values of extreme difference is called the main factor, and the factor with small values of extreme difference is called subordinate factor. It can be seen from the table three: the order of factors that affect the classification efficiency of PSA/PSA needle-punched filter material most is particle size, then filtration, velocity, and the least dust load.

77.3.3 Regression Analysis on Tests

Through interaction analysis, assuming the interaction effect can be neglected, and then dimensional analysis is carried out to the factors that affect the classification efficiency of PSA/needle-punched PSA filter material which is described by,

$$\eta = 1 - \exp[f(d, g, v, \mu, H, \rho, c, \varepsilon)] \tag{77.3.3.1}$$

where d is particle size, μm; g is dust load attached on the filter material, g/m^2; v is filtration velocity, m/min; μ is fluid viscosity coefficient, Pa·s; H is thickness of dust load, m; ρ is fluid density, kg/m^3; c is fluid mass concentration, kg/m^3;ε is porosity of dust layer.

Change (77.3.3.1) to the power function style,

$$\eta = 1 - \exp\left[\mathrm{n0}\left(d^{\mathrm{n1}}, g^{\mathrm{n2}}, v^{\mathrm{n3}}, \mu^{\mathrm{n4}}, H^{\mathrm{n5}}, \rho^{\mathrm{n6}}, c^{\mathrm{n7}}, \varepsilon^{\mathrm{n8}}\right)\right] \tag{77.3.3.2}$$

Table 77.5 Intuitionistic analysis on classification efficiency of the orthogonal tests

Items	Particle size d(μm)	Dust load g(g/m^2)	Filtration velocity v(m/min)
Mean($\overline{K_1}$)	76.412	75.183	78.100
Mean($\overline{K_2}$)	75.605	76.355	76.722
Mean($\overline{K_3}$)	73.953	76.367	74.757
Mean($\overline{K_4}$)	78.532	76.597	74.922
Extreme difference (I)	4.579	1.414	3.343

According to Buckingham's π-theorem and dimensional harmony principle, treat (77.3.3.2) with dimensional analysis,

$$\eta = 1 - \exp\left[\mathrm{n0}\varepsilon^{\mathrm{n1}}\left(\frac{H}{d}\right)^{\mathrm{n2}}\left(\frac{vd\rho}{\mu}\right)^{\mathrm{n3}}\left(\frac{vdc}{\mu}\right)^{\mathrm{n4}}\left(\frac{vg}{\mu}\right)^{\mathrm{n5}}\right] \tag{77.3.3.3}$$

where μ, H, ρ, c, ε are known quantity. Multi-regression analysis is used to analyze the data from tests with SPSS Statistics V17.0. The equation of classification efficiency of PSA/PSA needle-punched filter material is described by,

$$\eta = 1 - \exp\left[-1.308 \times \varepsilon^{0.520}\left(\frac{H}{d}\right)^{-6.256\mathrm{E}-6}\left(\frac{vd\rho}{\mu}\right)^{-0.093}\left(\frac{vdc}{\mu}\right)^{-0.106}\left(\frac{vg}{\mu}\right)^{-0.031}\right] \tag{77.3.3.4}$$

For Reynolds number is defined,

$$\mathrm{Re} = \frac{vd\rho}{\mu} \tag{77.3.3.5}$$

Then,

$$\eta = 1 - \exp\left[-1.308 \times \varepsilon^{0.520}\left(\frac{H}{d}\right)^{-6.256\mathrm{E}-6}(\mathrm{Re})^{-0.093}\left(\frac{vdc}{\mu}\right)^{-0.106}\left(\frac{vg}{\mu}\right)^{-0.031}\right] \tag{77.3.3.6}$$

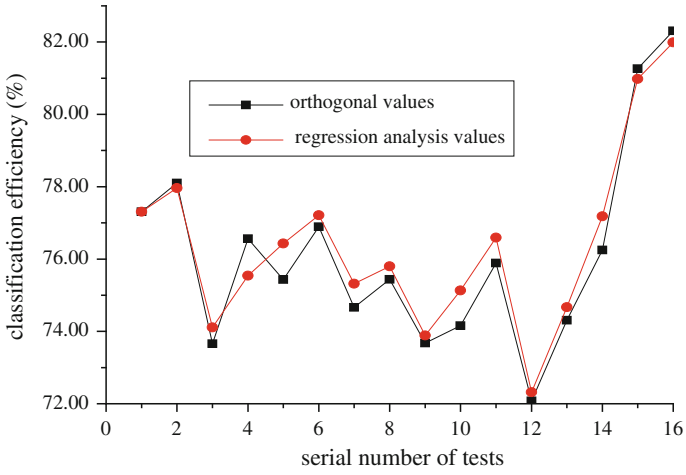

Fig. 77.3 Comparison curve between the test's value of the classification efficiency and solution of regression equation

Multi-correlation coefficient (R) is equal to 0.932, which means the effect of regression is good. The comparison curve between the test's value of the classification efficiency and solution of regression equation is shown in the Fig. 77.3.

It suggests that there is a consistent match between the test's value of the classification efficiency and solution of regression Eq. (77.3.3.1), which means that the equation is valid to express the tests.

77.4 Conclusion

(1). The classification efficiency affected most by particle size, then by filtration velocity, least by dust load. And it decreases initially and rises later with the increase of particle size; rises all along with the increase of dust load; and it also decrease all along with the increase of filtration velocity.
(2). Under the set level of one factor, the regression equation of the classification efficiency has a consistent match with orthogonal tests' results.
(3). The equation, which describes the relationship between the classification efficiency of PSA/needle-punched PSA filter material and factors including particle size, filtration velocity, and dust load, is achieved through orthogonal test and dimensional regression.

Acknowledgments This study is supported by the National "the 12th Five-Year Plan" Key Technology R&D Program of China (Grant No. 2012BAJ02B07).

References

1. McIntyre JE (2006) Synthetic fibres. China Textile and Apparel Press, China (In Chinese and English)
2. Sun JL (2007) Fibreous new material. Shanghai University Press, China (In Chinese)
3. He WY, Bao WG (2011) Study on directly converting polysulfonam ide filament into sliver. Tech Text 12(4):23–26
4. Hou WL (2010) Experimental research on the performance of PSA fibre and filtration medium for high temperature flue gas filtration. Dissertation for the Master degree. Donghua University, Shanghai (In Chinese)
5. Wang J (2008) Study of the high temperature-resistance performance of needle-punched PSA nonwovens. Dissertation for the Master degree. Donghua University, Shanghai (In Chinese)
6. Pan ZJ (2005) Modern test technology for fibrous materials. China Textile and Apparel Press, China (In Chinese)
7. Yuan XY (2010) Stability analysis of PSA fibre filter media used in the high-temperature flue gas purification. Tech Text 12(7):27–31
8. Ren JR, Wang J (2007) Thermal-mechanic Performances of PSA Fibre. Melliand China 12(11):27–34
9. Wang ZX, Mi S (1993) Fibrous paper of PSA—China Self -developed Refractory and Insulate Paper. Insulating Mater 6(3):1–13

10. Liang Z, Shen HG, Hou WL et al (2009) Test and analyses on performances of PSA medium used in baghouse. Ind text 11:17–20
11. Ye JQ, Wang XF, et al (2009) Thermal stability of PSA fibre. In: Proceedings of R&D of Refractory PSA Fibre 12–14
12. Ren JR, Wang XF, Zhang YH (2007) Application and market development of PSA material. Tech Text 12(5):1–6
13. Wang XF, Wang FH et al (2009) Performance and application of PSA fibre. In: Proceedings of R&D of refractory PSA fibre 3–7
14. Republic of China National Standard (2009) GB/T 6719-2009 Bag house technical requirements [S]. Standards Press of China, Beijing
15. Liuliu Du (2008) Experimental research on the performance of ptfe compound filtration medium of bag filter. Dissertation for the Master degree. Donghua University, Shanghai (In Chinese)

Chapter 78
Research on Condensation Pressure and Temperature of Heat Pumps Using Blends of CO_2 with Butane and Isobutane

Xianping Zhang, Xiaowei Fan, Xinli Wei, Fang Wang and Xiaojing Zhang

Abstract Based on the Thermodynamic theorem of corresponding states, the relationship between condensation pressure and temperature of subcritical heat pump systems using CO_2/R600 or CO_2/R600a as the working fluid is proposed. With the proposed correlation, the effective mass fraction range of component R600 or R600a can be readily determined according to the designed condensation pressure. Or if the condensation temperature is given, it is convenient to get the effective mass fraction scope of R600 or R600a. Within the condensation pressure range of 4.00–7.38 MPa, 36 points are calculated by the fitting formula and then checked by REFPROP8.0. The mean deviation between the fitting relationship and REFPROP8.0, below 1 %, shows that the proposed relationship can be used with satisfactory certainty under the given conditions. The research results may provide a beneficial basic data to promote the application of medium temperature heat pumps using blends of CO_2 with butane and isobutane.

Keywords CO_2/R600 · CO_2/R600a · Condensation pressure · Condensation temperature · Mass fraction

X. Zhang
School of Civil Engineering, Henan Institute of Engineering, Zhengzhou 450007, China

X. Zhang · X. Wei (✉)
School of Chemical Engineering and Energy, Zhengzhou University, Zhengzhou 450001, China
e-mail: xlwei@zzu.edu.cn

X. Fan · F. Wang · X. Zhang
School of Energy and Environment, Zhongyuan University of Technology, Zhengzhou 450007, China

A. Li et al. (eds.), *Proceedings of the 8th International Symposium on Heating, Ventilation and Air Conditioning*, Lecture Notes in Electrical Engineering 262,
DOI: 10.1007/978-3-642-39581-9_78,

78.1 Introduction

From the viewpoint of environmental protection, nowadays the widely-used working fluids, fluorocarbons, in heat pump systems will be phased out in the near future. It is ideal to utilize natural refrigerants to substitute for Freons. Therefore, over the past decades, natural refrigerants such as CO_2 (R744), HCs have been paid more and more attentions in research and practical fields [1]. CO_2, once having a widespread application in the early 20th century, has regained a new life [2]. With an ozone depletion potential (ODP) of zero and a global warmth potential (GWP) of 1.0, CO_2 present excellent eco-friendly properties. CO_2 heat pump water heater and mobile air conditioning have been successfully commercialized in developed countries as Japan and some European countries. The CO_2 heat pump systems work in the transcritical cycle, of which the heat rejection pressure, will up to 10.0 MPa or more than 10.0 MPa. For pure CO_2 transcritical cycle, the much higher working pressure than traditional system could be the main obstacle to promote CO_2 working as a refrigerant in heat pump systems because it usually results in high cost, certain technical difficulties involving with high pressure, and people's worries about safety. The potential problems resulting from high heat rejection pressure may accounts for the current research and development status for CO_2 heat pump system in China. As refrigerants, HCs (ODP = 0, GWP $\approx$ 20) are also eco-friendly. However, their obvious disadvantages are flammability and explosivity [3].

Researches have showed that on mixing of R744 and HCs, the heat rejection pressure of the system can be efficiently decreased. Kim et al. [4] present the cooling performance of several CO_2/R290 mixtures measured in air-conditioning test rig at several conditions, and the results show that adding propane to CO_2 improves the system efficiency and reduces the heat rejection pressure. They also studied the evaporative heat transfer characteristics of CO_2/R290 refrigerant mixtures [5, 6]. Sarkar et al. [7] proposed blends CO_2/R600 and CO_2/R600a as working fluids in subcritical heat pumps for medium and high temperature heating applications, and the simulation results showed that CO_2/R600a and CO_2/R600a can be efficiently employed in heat pumps for variable temperature or simultaneous cooling and heating applications at conventional high side pressure. Based on the research results by our team, under the given operation conditions, for medium temperature heat pump systems using natural zeotropic mixtures CO_2/R600a and CO_2/R600 with optimum mass fraction, component R600 or R600a accounts for a dominate percentage up to 90 % [8]. Such a mixture still belongs to the flammable and explosive working fluid. The condensation pressure will be increased as R600 or R600a is decreased for the sake of safety. It is expected to conveniently determine the effective mass fraction range of component R600 or R600a for the given condensation pressure upper limit.

Therefore, in this research, based on the Thermodynamic theorem of corresponding states, the relationship between condensation pressure and temperature of heat pump using CO_2/R600a or CO_2/R600 as the working fluid is proposed.

With the proposed correlation, the effective mass fraction range of component R600 or R600a can be easily determined according to the designed condensation pressure. On the other hand, the effective mass fraction range of component R600 or R600a can be readily gotten if the condensation temperature is given.

78.2 Methods

78.2.1 Temperature Glide

When the saturation pressure is set as 1.0 MPa, the temperature glide characteristics of CO_2/R600a and CO_2/R600 are shown in Fig. 78.1. The upper line is the dew point temperature while the lower one is the bubble point temperature. It can be seen that the dew point and bubble point constitute a shuttle shape for CO_2/R600a or CO_2/R600 mixture. If the mass fraction of CO_2 remains unchanged, CO_2/R600 presents a little larger temperature glide than that of CO_2/R600a, up to 70 °C, which means CO_2/R600a or CO_2/R600 mixture can work as a refrigerant for medium temperature heat pump systems.

78.2.2 Calculation Conditions

Based on the Chinese national standard [9], the heat sink inlet temperature is set to 17 °C, and then the mixture refrigerant outlet temperature in condenser will be 24 °C, considering the pinch point heat transfer temperature of 7 °C. Then, near 24 °C, bubble points of 15, 20, 25, and 30 °C for CO_2/R600a and CO_2/R600 mixture are calculated using REFPROP [10] according to two-parameter thermodynamic theorem of corresponding states.

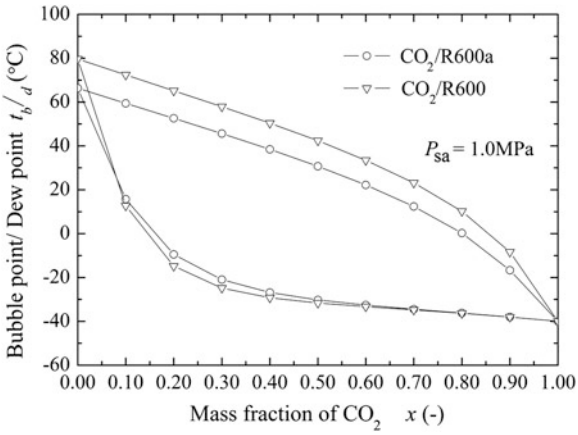

Fig. 78.1 Temperature glides of CO_2/R600 and CO_2/R600a

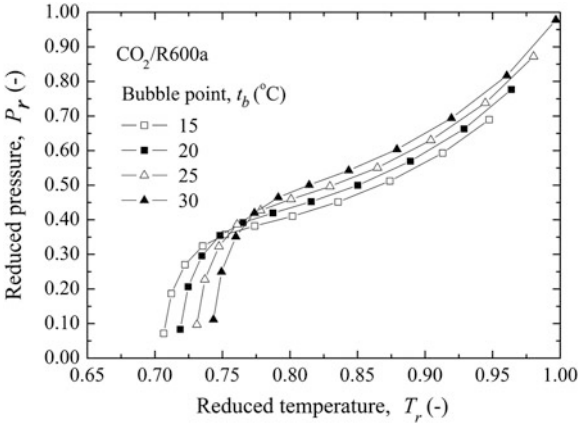

Fig. 78.2 Reduced temperature versus reduced pressure for CO_2/R600a

78.3 Results and Discussions

The calculation results are shown in Figs. 78.2, 78.3, 78.4, 78.5. It should be pointed out that the fraction of CO_2 is molar. When condensation pressure is larger than 4.0 MPa or lower than 2.0 MPa, reduced temperature and reduced pressure present a good consistency, especially for the range larger than 4.0 MPa. Therefore, for condensation pressure between 4.0 and 7.38 MPa (critical pressure of pure CO_2), a fitting formula is obtained as:

$$P_r - kT_b = aT_r^2 + bT_r + c,\ 4.00\,\text{MPa} < P_{co} < 7.38\,\text{MPa}$$

$$P_r = \frac{P_b}{P_c},\ T_r = \frac{T_b}{T_c} \tag{78.1}$$

where subscript r is reduced parameter, b bubble parameter, c critical parameter, and constants a, b, c, k are 9.685, −15, 6.128, and 0.006, respectively.

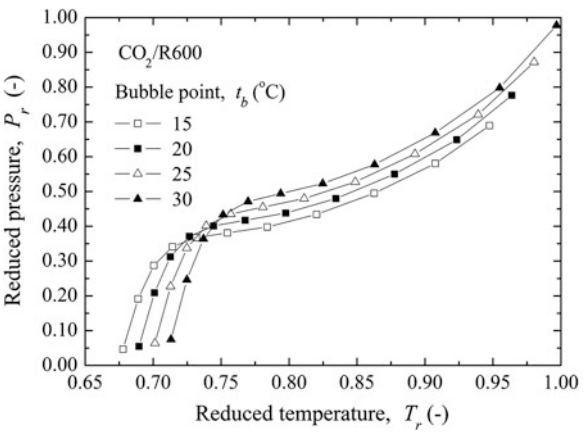

Fig. 78.3 Reduced temperature versus reduced pressure for CO_2/R600

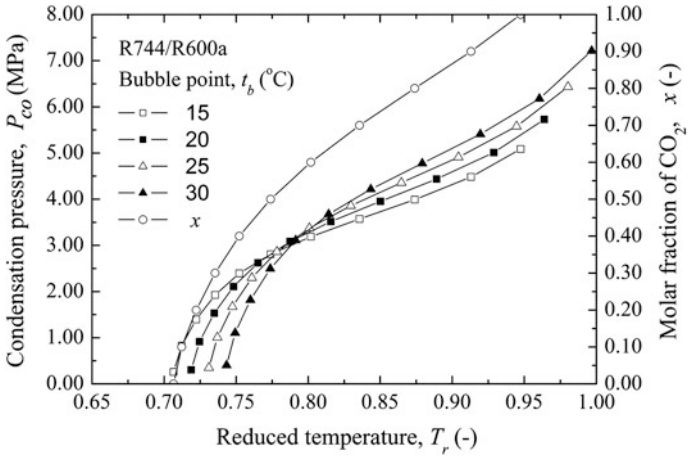

Fig. 78.4 Reduced temperature versus condensation pressure, mole fraction of CO_2 for CO_2/R600a

In order to validate the accuracy of the fitting formula, 36 points between 4.0 and 7.38 MPa of condensation pressure are calculated by the fitting formula and checked by REFPROP8.0, respectively. The mean deviation between the fitting formula and the calculation results by REFPROP8.0 is 0.58 %, while the maximum deviation is 2.98 %. The comparisons between the fitting relationship and REFPROP8.0 show that the proposed relationship can be used with satisfactory certainty under the given conditions.

According to Eq. (78.1), if condensation temperature is given, the condensation pressure can be estimated. Then from Figs. 78.4 and 78.5, the effective mass fraction range of component R600 or R600a can be readily determined. On the other hand, if the condensation pressure is designed, the condensation temperature can be estimated from Eq. (78.1), and then the effective mass fraction range of component R600 or R600a can be easily determined from Figs. 78.4 and 78.5.

78.4 Conclusion

Under the given operation conditions, for medium temperature sbucritical heat pump systems using natural zeotropic mixtures CO_2/R600a and CO_2/R600 with optimum mass fraction, component R600 or R600a accounts for the dominate percentage up to 90 %. Such a mixture still belongs to the flammable and explosive working fluid. The condensation pressure will be increased as R600a or R600 is decreased for the sake of safety. It is expected to conveniently determine the effective mass fraction range of component R600a or R600 for the given condensation pressure upper limit. Therefore, in this research, based on the

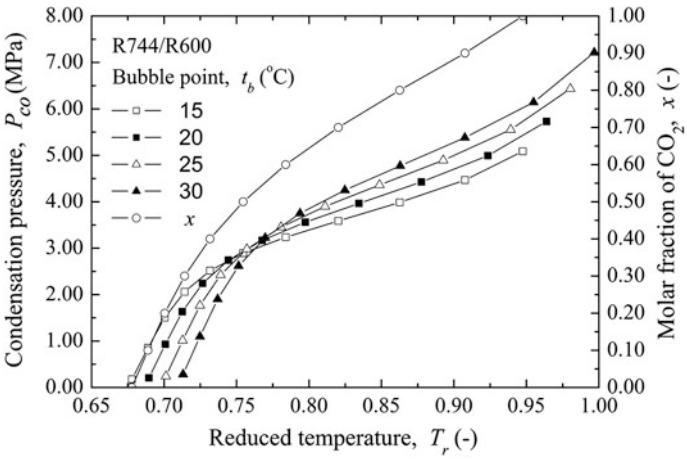

Fig. 78.5 Reduced temperature versus condensation pressure, mole fraction of CO_2 for CO_2/R600

Thermodynamic theorem of corresponding states, the relationship between condensation pressure and temperature of heat pump using CO_2/R600 or CO_2/R600a as the working fluid is proposed. With the proposed correlation, the effective mass fraction range of component R600 or R600a can be easily determined according to the designed condensation pressure or temperature. Within the condensation pressure range of 4.00–7.38 MPa, 36 points are calculated by the fitting formula and then checked by REFPROP8.0. The mean deviation between the fitting formula and the calculation results by REFPROP8.0 is 0.58 % while the maximum deviation is 2.98 %.

Acknowledgments This work was sponsored by the National Natural Science Foundation of China (No. 51176207), Henan Province Project for the Excellent Youth Scholars of Higher Education of China (No. 2012GGJS-185), Henan Province Education Department Natural Science Project (No. 2010B560003), and Zhengzhou Scientific and Technological Project (No. 121PPTGG357-7).

References

1. Lorentzen G (1995) The use of natural refrigerants: a complete solution to the CFC/HCFC predicament. Int J Refrig 18(3):190–197
2. Kim MH, Pettersen J, Bullard CW (2004) Fundamental process and system design issues in CO_2 vapor compression systems. Prog Energy Combust Sci 30(2):119–174
3. Corberán JM, Segurado J, Colbourne D et al (2008) Review of standards for the use of hydrocarbon refrigerants in A/C. heat pump and refrigeration equipment. Int J Refrig 31(4):748–756
4. Kim JH, Cho JM, Kim MS (2008) Cooling performance of several CO_2/propane mixtures and glide matching with secondary heat transfer fluid. Int J Refrig 31(5):800–806

5. Cho JM, Kim YJ, Kim MS (2010) Experimental studies on the characteristics of evaporative heat transfer and pressure drop of CO_2/propane mixtures in horizontal and vertical smooth and micro-fin tubes. Int J Refrig 33(1):170–179
6. Cho JM, Kim YJ, Kim MS (2010) Experimental studies on the evaporative heat transfer and pressure drop of CO_2 and CO_2/propane mixtures flowing upward in smooth and micro-fin tubes with outer diameter of 5 mm for an inclination angle of 45. Int J Refrig 33(5):922–931
7. Sarkar J, Bhattacharyya S (2009) Assessment of blends of CO_2 with butane and isobutane as working fluids for heat pump applications. Int J Therm Sci 48(7):1460–1465
8. Fan XW, Zhang XP, Wang FK, Shen HG, Chen SG (2011) Research on performance of heat pump systems using R744/R600 and R744/R600a mixtures as refrigerants. J Refrig 32(6):35–39 (In Chinese)
9. GB/T23137-2008 (2008) Heat pump water heater for household and similar application. (In Chinese)
10. Lemmon EW, Huber ML, McLinden MO (2010) Reference fluid thermodynamic and transport properties (REFPROP). NIST Standard Reference Database 23, Version 8.0

Chapter 79
Exergy Analysis of a Ground Source Heat Pump System Under Cooling and Heating Conditions

Lei Zhao and Chen Yuan

Abstract Energy and exergy analyses models were established to evaluate the performance of a ground source heat pump (GSHP) based on the energy conservation and the exergy destruction principles. The GSHP supplies cooling water and hot water to the air handling unit of a building air-conditioning system in cooling and heating season, respectively. It rejects and absorbs heat from the soil through borehole heat exchangers accordingly. The models were programmed and the properties of the working mediums were calculated by calling the software REFPROP. Results indicate that GSHP system operates at higher exergy efficiency in heating mode. The exergy efficiencies of the whole system are 23.07 and 34.31 % in cooling and heating modes, respectively. And the performances of every component are evaluated.

Keywords Ground source heat pump · Exergy analysis model · Exergy efficiency

79.1 Introduction

Ground source heat pump systems (GSHPs) are increasingly implemented for heating and air-conditioning in commercial and residential buildings. The efficiencies of GSHPs are inherently higher than those of the conventional air source heat pumps, because the ground maintains at a relatively stable higher/lower source/sink temperature than the ambient air [1]. The oretical and experimental researches have been accomplished based conventional energy analysis method, which cannot account for large amount of irreversible losses occurring during

L. Zhao (✉) · C. Yuan
School of Environmental and Municipal Engineering, Xi'an University of Architecture and Technology, 13 Yanta Road, Xi'an 710055, China
e-mail: leizhao0308@hotmail.com

A. Li et al. (eds.), *Proceedings of the 8th International Symposium on Heating, Ventilation and Air Conditioning*, Lecture Notes in Electrical Engineering 262,
DOI: 10.1007/978-3-642-39581-9_79,

processes, such as heat transfer process driven by finite temperature difference. It cannot evaluate the "thermodynamic perfect degree" of a process. However, exergy analysis method not only can evaluate the performance of systems, but also has the advantage of identifying the less efficient components in the system. This may be very helpful for system optimization. To this end, a set of exergy analysis model and mathematical model of a GSHP system with R-22 as the refrigerant were set up. Exergy analyses were conducted under operational conditions for both heating and cooling modes. The component which has low exergy efficiency, higher exergy destruction ratio, and low thermodynamic perfect degree was found out. And some suggestions are proposed to improve the energy and exergy performance of the GSHP system.

79.2 System Description

A refrigerating and heating systems supply chilled or hot water to a central air-conditioning system of a building with total cooling and heating load of 630.8 and 350 kW. The whole system consists of a ground source heat pump and a water chiller and two air handling units (AHU). The GSHP supplies hot water to one of the AHU to heat the air supplied to the building while operating in heating mode. But the GSHP work with the water chiller in parallel to supply chilled water to offset the building cooling load in cooling mode. It means the water chiller supplies chilled water to the other AHU as well to meet the building cooling load. The nominal cooling capacity of the GSHP is 366 kW with cooling water at 25/30 °C and chilled water at 7/12 °C. The nominal work consumption is 67.3 kW. Its nominal heating capacity is 389.9 kW with cooling water at 40 °C/45 °C and chilled water at 5 °C/10 °C. The corresponding nominal work consumption is 89.8 kW. The water chiller has nominal cooling capacity of 336 kW and work consumption of 89.6 kW with cooling water at 30/35 °C and chilled water at 7/12 °C.

It assumes that the water chiller and the GSHP share the building cooling load 50/50 %, and the exergy analyses were conducted only on the GSHP. The schematic diagram of the GSHP is illustrated in Fig. 79.1. It includes three main loops: (i) refrigerant circuit (or a vapor compression cycle), (ii) the air-handling unit (AHU) circuit for heating/cooling (water circuit), and (iii) the borehole heat exchanger (BHE) circuit (water–antifreeze solution circuit). The refrigerant circuit consists of a compressor (COM), a condenser (CON), an evaporator (EVA), and a thermal expansion valve (TXV). Conversion from the heating cycle to the cooling cycle is obtained by means of a four-way valve. The refrigerant enters the COM and is compressed to be the superheated vapor at condensation pressure. And then, it enters the EVA after throttling in the TXV. In cooling mode, the refrigerant is condensed by rejecting heat absorbed from the COM and EVA to the solution in the BHE circuit to the soil. It is evaporated by cooling the water from the AHU circuit, in which the air is handled and supplied to the building. And in heating

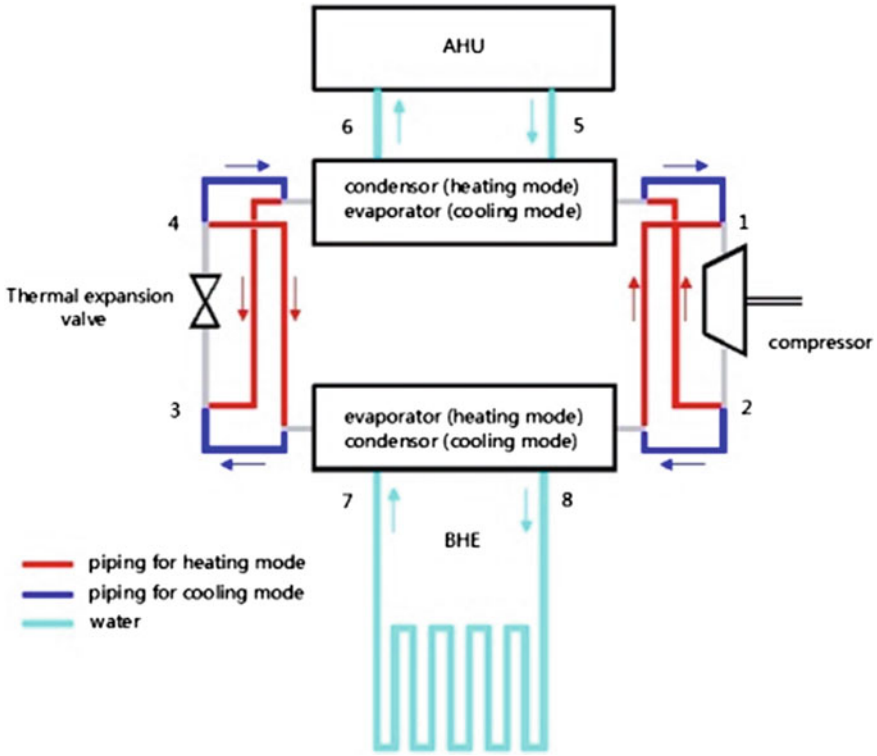

Fig. 79.1 Schematic diagram of the GSHP system

mode, the refrigerant is evaporated by absorbing heat from the water circulating in the BHE receiving heat from the soil, and condensed by rejecting heat to the water in the AHU circuit, in which air is handled to heat the building.

79.3 System Modeling and Exergy Analysis Index

The schematic diagram of the refrigeration cycle and the heating cycle is given in Fig. 79.2. The GSHP is assumed to operate steadily with negligible kinetic and potential energy [2]. Based on the mass and energy conservation principles and the exergy destruction principle, and exergy analysis models were set up for every component and the overall system, as illustrated in Table 79.1 in which, $\dot{m}$ is the mass flow rate; $\dot{Q}$ and $\dot{W}$represent rates of heat and work, respectively, and h denotes specific enthalpy. $\dot{E}x$represents exergy rate. $\dot{E}x_{\dot{Q}}$and$ex_h$are the exergy flow rate associated with heat transfer rate $\dot{Q}$ and the specific flow exergy associated with the

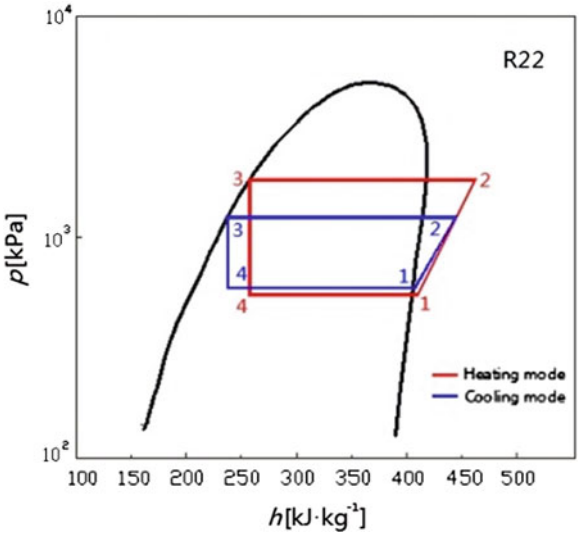

Fig. 79.2 Schematic of cooling and heating cycle

specific enthalpy, respectively$\dot{E}x_{\dot{Q}} = \dot{Q}\left(1 - \frac{T_0}{T}\right)$ and $ex_h = (h - h_0) - T_0(s - s_0)$ [3], in which T_0 is the dead-state temperature. T_{soil} is the soil temperature.η_{ex}, d andξstand for the exergy efficiency, exergy loss ratio, and thermodynamic perfect degree, respectively. In general, the exergy loss ratio of each component can be calculated by $d\_{\text{component}} = \frac{Ex_{\text{loss}\_\text{component}}}{\sum_i Ex_{\text{loss}\_\text{component}}}$ [4]. The subscripts ref and wa represent refrigerant and water streams. And the subscript loss represents loss.

79.4 Exergy Analysis Results

The exergy analyses were conducted to evaluate the GSHP performance under rated operational conditions. The parameters of the operational states under rated cooling and heating conditions are listed in Table 79.2, which is also illustrated in the *log p–h* diagram.

And the exergy analysis results are illustrated in Table 79.3 for both cooling and heating modes.

It can be found in Table 79.3 that in cooling mode the exergy efficiency of the condenser is 25.44 %, which is the lowest among all the components. However, its exergy destruction ratio is just 9.23 %. The exergy efficiencies of the BHE and the AHU are 38.37 and 47.2 %, respectively. And their exergy destruction ratios are 13.86 and 21.04 %. The exergy efficiency of the COM reaches 75.06 %, however, its exergy destruction ratio amounts to 1471 %. And the exergy efficiency of the whole system is just 11.58 %. In heating mode, the exergy efficiency of the evaporator is 38.01 %, which is the lowest among all the components. However,

Table 79.1 Exergy analysis model of each component and the overall system

	Cooling mode	Heating mode
EVA	$\dot{m}_{\mathrm{ref}}(h_4 - h_1) = \dot{m}_{\mathrm{wa\_AHU}}(h_6 - h_5)$	$\dot{m}_{\mathrm{ref}}(h_4 - h_1) = \dot{m}_{\mathrm{wa\_BHE}}(h_8 - h_7)$
	$\dot{E}x_{\mathrm{loss\_EVA}} = \dot{m}_{\mathrm{ref}}(ex_{h4} - ex_{h1}) - \dot{m}_{\mathrm{wa\_AHU}}(ex_{h6} - ex_{h5})$	$\dot{E}x_{\mathrm{loss\_EVA}} = \dot{m}_{\mathrm{ref}}(ex_{h4} - ex_{h1}) - \dot{m}_{\mathrm{wa\_BHE}}(ex_{h8} - ex_{h7})$
	$\eta_{ex_{\mathrm{EVA}}} = \dfrac{\dot{m}_{\mathrm{wa_{AHU}}}(ex_{h6} - ex_{h5})}{\dot{m}_{\mathrm{ref}}(ex_{h4} - ex_{h1})}$	$\eta_{ex\_\mathrm{EVA}} = \dfrac{\dot{m}_{\mathrm{ref}}(ex_{h1} - ex_{h4})}{\dot{m}_{\mathrm{wa\_BHE}}(ex_{h7} - ex_{h8})}$
	$\xi_{\mathrm{EVA}} = \dfrac{\dot{m}_{\mathrm{ref}} ex_{h1} + \dot{m}_{\mathrm{wa\_AHU}} ex_{h6}}{\dot{m}_{\mathrm{ref}} ex_{h4} + \dot{m}_{\mathrm{wa\_AHU}} ex_{h5}}$	$\xi_{\mathrm{EVA}} = \dfrac{\dot{m}_{\mathrm{ref}} ex_{h1} + \dot{m}_{\mathrm{wa\_BHE}} ex_{h8}}{\dot{m}_{\mathrm{ref}} ex_{h4} + \dot{m}_{\mathrm{wa\_BHE}} ex_{h7}}$
CON	$\dot{m}_{\mathrm{ref}}(h_2 - h_3) = \dot{m}_{\mathrm{wa\_BHE}}(h_8 - h_7)$	$\dot{m}_{\mathrm{ref}}(h_2 - h_3) = \dot{m}_{\mathrm{wa\_AHU}}(h_6 - h_5)$
	$\dot{E}x_{\mathrm{loss\_CON}} = \dot{m}_{\mathrm{wa\_BHE}}(ex_{h7} - ex_{h8}) - \dot{m}_{\mathrm{ref}}(ex_{h3} - ex_{h2})$	$\dot{E}x_{\mathrm{loss\_CON}} = \dot{m}_{\mathrm{ref}}(ex_{h2} - ex_{h3}) - \dot{m}_{\mathrm{wa\_AHU}}(ex_{h6} - ex_{h5})$
	$\eta_{ex\_\mathrm{CON}} = \dfrac{\dot{m}_{\mathrm{ref}}(ex_{h3} - ex_{h2})}{\dot{m}_{\mathrm{wa\_BHE}}(ex_{h7} - ex_{h8})}$	$\eta_{ex\_\mathrm{CON}} = \dfrac{\dot{m}_{\mathrm{wa\_AHU}}(ex_{h6} - ex_{h5})}{\dot{m}_{\mathrm{ref}}(ex_{h2} - ex_{h3})}$
	$\xi_{\mathrm{CON}} = \dfrac{\dot{m}_{\mathrm{ref}} ex_{h3} + \dot{m}_{\mathrm{wa\_BHE}} ex_{h8}}{\dot{m}_{\mathrm{ref}} ex_{h2} + \dot{m}_{\mathrm{wa\_BHE}} ex_{h7}}$	$\xi_{\mathrm{CON}} = \dfrac{\dot{m}_{\mathrm{ref}} ex_{h3} + \dot{m}_{\mathrm{wa\_AHU}} ex_{h6}}{\dot{m}_{\mathrm{ref}} ex_{h2} + \dot{m}_{\mathrm{wa\_AHU}} ex_{h5}}$
TXV	$\dot{m}_{\mathrm{ref}} h_3 = \dot{m}_{\mathrm{ref}} h_4;\ \dot{E}x_{\mathrm{loss\_TXV}} = \dot{m}_{\mathrm{ref}}(ex_{h3} - ex_{h4})$	
	$\eta_{ex\_\mathrm{TXV}} = \dfrac{\dot{m}_{\mathrm{ref}} ex_{h4}}{\dot{m}_{\mathrm{ref}} ex_{h3}};\ \xi_{\mathrm{TXV}} = \dfrac{\dot{m}_{\mathrm{ref}} ex_{h4}}{\dot{m}_{\mathrm{ref}} ex_{h3}}$	
COM	$\dot{m}_{\mathrm{ref}} h_2 = \dot{m}_{\mathrm{ref}} h_1 + \dot{W}_{\mathrm{COM}};\ \dot{E}x_{\mathrm{loss\_COM}} = \dot{m}_{\mathrm{ref}}(ex_{h1} - ex_{h2}) + \dot{W}_{\mathrm{COM}}$	
	$\eta_{ex\_\mathrm{COM}} = \dfrac{\dot{m}_{\mathrm{ref}}(ex_{h2} - ex_{h1})}{\dot{W}_{\mathrm{COM}}};\ \xi_{\mathrm{COM}} = \dfrac{\dot{m}_{\mathrm{ref}} ex_{h2}}{\dot{m}_{\mathrm{ref}} ex_{h1} + \dot{W}_{\mathrm{COM}}}$	
BHE	$\dot{Q}_{\mathrm{BHE}} = \dot{m}_{\mathrm{wa\_BHE}}(h_8 - h_7)$	$\dot{Q}_{\mathrm{BHE}} = \dot{m}_{\mathrm{wa\_BHE}}(h_7 - h_8);$
	$\dot{E}x_{\mathrm{loss\_BHE}} = \dot{m}_{\mathrm{wa\_BHE}}(ex_{h8} - ex_{h7}) - \dot{E}x_{\dot{Q}_{\mathrm{BHE}}}$	$\dot{E}x_{\mathrm{loss\_BHE}} = \dot{m}_{\mathrm{wa\_BHE}}(ex_{h8} - ex_{h7}) + \dot{E}x_{\dot{Q}_{\mathrm{BHE}}}$
	$\eta_{ex\_\mathrm{BHE}} = \dfrac{\dot{m}_{\mathrm{wa\_BHE}}(ex_{h8} - ex_{h7})}{\dot{E}x_{\dot{Q}_{\mathrm{BHE}}}}$	$\eta_{ex\_\mathrm{BHE}} = \frac{\dot{m}_{\mathrm{wa\_BHE}}(ex_{h7} - ex_{h8})}{\dot{E}x_{\dot{Q}_{\mathrm{BHE}}}}$
	$\xi_{\mathrm{BHE}} = \dfrac{\dot{m}_{\mathrm{wa_{BHE}}} ex_{h7}}{\dot{m}_{\mathrm{wa_{BHE}}} ex_{h8} - \dot{E}x_{\dot{Q}_{\mathrm{BHE}}}}$	$\xi_{\mathrm{BHE}} = \dfrac{\dot{m}_{\mathrm{wa\_BHE}} ex_{h7}}{\dot{m}_{\mathrm{wa\_BHE}} ex_{h8} + \dot{E}x_{\dot{Q}_{\mathrm{BHE}}}}$

(continued)

Table 79.1 (continued)

	Cooling mode	Heating mode
AHU	$\dot{Q}_{\mathrm{AHU}} = \dot{m}_{\mathrm{wa\_AHU}}(h_5 - h_6)$	$\dot{Q}_{\mathrm{AHU}} = \dot{m}_{\mathrm{wa\_AHU}}(h_6 - h_5) = \rho_a V_a (h_{10} - h_9)$;
	$\dot{E}x_{\mathrm{loss\_AHU}} = \dot{m}_{\mathrm{wa\_AHU}}(ex_{h6} - ex_{h5}) + \dot{E}x_{\dot{Q}_{\mathrm{AHU}}}$	$\dot{E}x_{\mathrm{loss\_AHU}} = \dot{m}_{\mathrm{wa\_AHU}}(ex_{h6} - ex_{h5}) - \dot{E}x_{\dot{Q}_{\mathrm{AHU}}}$
	$\eta_{ex_{\mathrm{AHU}}} = \frac{\dot{E}x_{\dot{Q}_{\mathrm{AHU}}}}{\dot{m}_{\mathrm{wa_{AHU}}}(ex_{h5} - ex_{h6})}$	$\eta_{ex\_\mathrm{AHU}} = \frac{\dot{E}x_{\dot{Q}_{\mathrm{AHU}}}}{\dot{m}_{\mathrm{wa\_AHU}}(ex_{h6} - ex_{h5})}$
	$\xi_{\mathrm{AHU}} = \frac{\dot{m}_{\mathrm{wa\_AHU}} ex_{h5} - \dot{E}x_{\dot{Q}_{\mathrm{AHU}}}}{\dot{m}_{\mathrm{wa\_AHU}} ex_{h6}}$	$\xi_{\mathrm{AHU}} = \frac{\dot{m}_{\mathrm{wa\_AHU}} ex_{h5} + \dot{E}x_{\dot{Q}_{\mathrm{AHU}}}}{\dot{m}_{\mathrm{wa\_AHU}} ex_{h6}}$
SYS	$\dot{E}x_{\mathrm{loss\_SYS}} = \sum_{i=1}^{n} \dot{E}x_{\mathrm{loss\_COMPONENT}}$	$\dot{E}x_{\mathrm{loss\_SYS}} = \sum_{i=1}^{n} \dot{E}x_{\mathrm{loss\_COMPONENT}}$
	$\mathrm{COP_{SYS}} = \frac{\dot{Q}_{\mathrm{AHU}}}{\dot{W}_{\mathrm{COM}} + \dot{W}_{\mathrm{PUMPs}} + \dot{W}_{\mathrm{AHU}}}$	$\mathrm{COP_{SYS}} = \frac{\dot{Q}_{\mathrm{AHU}}}{\dot{W}_{\mathrm{COM}} + \dot{W}_{\mathrm{PUMPs}} + \dot{W}_{\mathrm{AHU}}}$
	$\eta_{ex_{\mathrm{SYS}}} = \frac{-\dot{E}x_{\dot{Q}_{\mathrm{AHU}}}}{\dot{W}_{\mathrm{COM}} + \dot{W}_{\mathrm{PUMPs}} + \dot{W}_{\mathrm{AHU}} - \dot{E}x_{\dot{Q}_{\mathrm{BHE}}}}$	$\eta_{ex\_\mathrm{SYS}} = \frac{\dot{E}x_{\dot{Q}_{\mathrm{AHU}}}}{\dot{W}_{\mathrm{COM}} + \dot{W}_{\mathrm{PUMPs}} + \dot{W}_{\mathrm{AHU}} + \dot{E}x_{\dot{Q}_{\mathrm{BHE}}}}$
	$\xi_{\mathrm{SYS}} = \frac{-\dot{E}x_{\dot{Q}_{\mathrm{AHU}}}}{\dot{W}_{\mathrm{COM}} + \dot{W}_{\mathrm{PUMPs}} + \dot{W}_{\mathrm{AHU}} - \dot{E}x_{\dot{Q}_{\mathrm{BHE}}}}$	$\xi_{\mathrm{SYS}} = \frac{\dot{E}x_{\dot{Q}_{\mathrm{AHU}}}}{\dot{W}_{\mathrm{COM}} + \dot{W}_{\mathrm{PUMPs}} + \dot{W}_{\mathrm{AHU}} + \dot{E}x_{\dot{Q}_{\mathrm{BHE}}}}$

Table 79.2 Parameters of operational state under design conditions

		T K	p kPa	h kJ·kg^{-1}	s kJ·(kg·K)$^{-1}$	ex_h kW	$\dot{m}$ kg·s^{-1}
cooling	dead state(ref.)	308.15	101.325	435.99	2.0043		
mode	dead stat(water)	308.15	101.325	146.72	0.5051		
	ref.entering COM 1	278.15	584.1	406.85	1.7436	96.27	1.8812
	ref.leaving COM 2	325.07	1255.2	432.18	1.7641	132.05	1.8812
	ref. leaving CON 3	305.15	1255.2	239.19	1.1334	134.60	1.8812
	ref. leaving TXV 4	278.15	584.1	239.19	1.1408	130.29	1.8812
	water entering AHU 6	280.15	163	29.59	0.1064	86.16	15.019
	water leaving AHU 5	285.15	220	50.62	0.1806	58.59	15.019
	water entering BHE 8	303.15	165	125.88	0.4367	4.04	17.2886
	water leaving BHE 7	298.15	220	105.03	0.3672	14.04	17.2886
Heating	dead state(ref.)	273.16	101.325	413.09	1.9254		
mode	dead stat(water)	273.16	101.325	0.1032	6.83E − 06		
	ref.entering COM 1	276.15	548.42	406.14	1.7464	80.09	1.9092
	ref.leaving COM 2	346.24	1812.4	442.42	1.7652	139.57	1.9092
	ref. leaving CON 3	320.15	1812.4	259.09	1.1955	86.65	1.9092
	ref. leaving TXV 4	276.15	548.42	259.09	1.2139	77.05	1.9092
	water entering AHU 6	318.15	175	188.58	0.6385	234.25	16.6667
	water leaving AHU 5	313.15	220	167.72	0.5723	188.06	16.6667
	water entering BHE 8	278.15	181	21.20	0.0762	3.60	13.3681
	water leaving BHE 7	283.15	220	42.24	0.1511	11.60	13.3681

Table 79.3 Exergy efficiency, exergy destruction ratio, and thermodynamic perfect degree

	$\dot{E}x_{loss}$/ kJ s^{-1}		η_{ex}/%		d / %		λ	
	cooling	heating	Cooling	heating	cooling	Heating	cooling	heating
COM.	11.88	9.78	75.06	85.87	14.71	11.48	0.9174	0.9345
CON.	7.46	6.73	25.44	87.28	9.23	7.89	0.9489	0.9795
EVA.	6.44	4.96	81.06	38.01	7.98	5.81	0.9659	0.9441
TXV	4.30	9.61	96.8	88.91	5.33	11.27	0.968	0.8891
BHE	11.19	9.35	47.2	46.1	13.86	10.97	0.5565	0.5536
AHU	16.99	22.32	38.37	51.67	21.04	26.18	0.8028	0.9047
P & F	22.5	22.5	0	0	27.85	26.39		
SYS.	80.78	85.25	11.58	21.87	100	100	0.1158	0.2187

its exergy destruction ratio is just 5.81 %. The exergy efficiencies of the BHE and the AHU are 46.1 and 51.67 %, respectively. And their exergy destruction ratios are 10.97 and 26.18 %. The exergy efficiency of the COM reaches 85.87 %, however, its exergy destruction ratio amounts to 11.48 %. And the exergy efficiency of the whole system is just 21.87 %. In the GSHP unit, the exergy destruction ratio of the compressor is the highest. This means the irreversibility in compression process is the strongest and measures can be taken to reduce it. If it is reduced, the exergy efficiency of the GSHP unit can be improved to some extent. However, its thermodynamic perfect degrees are already approach 1. This means the room left for bettering the compressor's performance is not much.

Although the exergy efficiencies of the BHE are not high in both modes, the exergy destruction ratios are less than 20 %. However, the thermodynamic perfect degrees are about 56 % in both cooling and heating modes. This is caused by relatively larger temperature difference between the water and the soil. The temperature difference can become smaller under partial load conditions. This is being studied and will be published soon.

It can be found that the GSHP has a comparatively higher value of exergy efficiency in heating mode than it has in cooling mode. This is for reason that the GSHP was selected to satisfy the building heating load individually when it is operated in heating mode. It cannot meet the need of the building cooling load independently, but works in parallel with a water chiller to supply cooling water to the AHUs. Thus, the cooling performance of the GSHP may be restricted by the water chiller. Therefore, it is important to choose a proper design of the whole system to achieve good GSHP cooling and heating performances. Otherwise, one of the two performances will be lowered.

In addition, the exergy destruction ratios of pumps and fans reach 27.85 and 26.39 % in cooling and heating mode, respectively. Since pumps and fans of constant flow rates were used in the system, and the energy consumptions are all exergy losses and they are considerable high. Therefore, if fans and pumps of variable frequency can be used, there are still more energy and exergy saving potentials to be obtained.

79.5 Conclusion

A set of exergy analysis model was established for a GSHP serving a building. Exergy analyses were conducted under design conditions of both cooling and heating modes. It is found that the GSHP unit has higher exergy efficiency in heating mode than in cooling mode.

References

1. Bi YH, Wang XH, Liu Y, Zhang H, Chen LG (2009) Comprehensive exergy analysis of a ground-source heat pump system for both building heating and cooling modes. Appl Energy 86:2560–2565
2. Hepbasli A, Balta MT (2007) A study on modeling and performance assessment of a heat pump system for utilizing low temperature geothermal resources in buildings. Build Environ 42:3747–3756
3. Ozgener O, Hepbasli A (2007) Modeling and performance evaluation of ground source(geothermal) heat pump systems. Energ Build 39:66–75
4. Lubis LI, Kanoglu M, Dincer I, Rosen MA (2011) Thermodynamic analysis of a hybrid geothermal heat pump system. Geothermics 40:233–238

Chapter 80
Ultrasonic Vibration for Instantaneously Removing Frozen Water Droplets from Cold Vertical Surface

Dong Li and Zhenqian Chen

Abstract An experimental study concerning frozen water droplets adhered to cold surface subjected to 20 kHz ultrasonic vibration was conducted. The transient process of frozen water droplet shedding from cold surface was recorded and the simultaneous internal temperature variation of cold plate was measured. In addition, the mechanism of ultrasonic vibration for removing frozen water droplets from cold surface was qualitatively analyzed. It is found that the frozen water droplets instantaneously fall off from the vertical surface accompanying with flick phenomenon due to the combined action of interface transverse shear force induced by ultrasonic mechanical effect and impact force generated by ultrasonic cavitation. Meanwhile, an instantaneous internal temperature jump of cold flat occurs. The results indicated that the high frequency ultrasonic vibration can effectively remove the frozen water droplets adhered to cold surface which is the base for frost growth and thus it is a highly effective defrosting method.

Keywords Ultrasonic vibration · Frozen water droplets · Interface shear force · Temperature jump · Ultrasonic cavitation

D. Li
Key Laboratory of Energy Thermal Conversion and Control
of Ministry of Education, Southeast University, Nanjing, 210096, China
e-mail: lidong_0307@163.com

Z. Chen (✉)
Key Laboratory of Energy Thermal Conversion and Control of Ministry
of Education, IIUSE, School of Energy and Environment, Southeast University,
Nanjing, 210096, China
e-mail: zqchen@seu.edu.cn

A. Li et al. (eds.), *Proceedings of the 8th International Symposium on Heating, Ventilation and Air Conditioning*, Lecture Notes in Electrical Engineering 262,
DOI: 10.1007/978-3-642-39581-9_80,

80.1 Introduction

Frost phenomenon widely exists in refrigeration system and aerospace field. The deposited frost layer on the cold surfaces inevitably degrades the thermal performance of the refrigerating unit due to the increasing thermal and flow resistances. Besides, frost on aircraft wings may cause serious safety problems. Therefore, great attention has been paid to searching for the effective methods for preventing the frost formation or removing the accreted frost layer on these equipments in recent years.

Numerous studies have been performed to investigate the effect of surface energy of the cold surface or external electric field on frost nucleation and growth [1–5]. However, the publication about the effect of ultrasonic vibration on the frost suppression and defrosting is still insufficient.

Kazunari et al. [6] observed the frost accumulation on a rectangular aluminum alloy plate surface subjected to approximately 37 kHz ultrasonic vibrations. It was found that the high frequency vibration could suppress the frost accumulation by approximately 60 %. Yan et al. [7] developed a new method of ultrasonic defrost and their results showed that using more sound sources is better than using single sound source for defrosting. Wang et al. [8] experimentally studied the possibility of the frost release from a finned-tube evaporator by using ultrasonic vibrations in natural convection. The visual result shows that the frost crystals and frost branches on the ice layer can be fractured and removed effectively, but the basic ice layer on the fins cannot be removed with ultrasonic vibrations.

Therefore, the key focus of this paper is to explore the possibility of ultrasonic vibration for removing frozen water droplets, which is the substrate for frost growth, from cold vertical surface.

80.2 Basic Fundamental for Ultrasonic Defrosting

Hayashi [9] divided the entire frosting process into three stages: frost nucleation period, frost layer growth period and frost layer fully growth period. Figure 80.1 shows the schematic representation of the entire frosting process on cold surface.

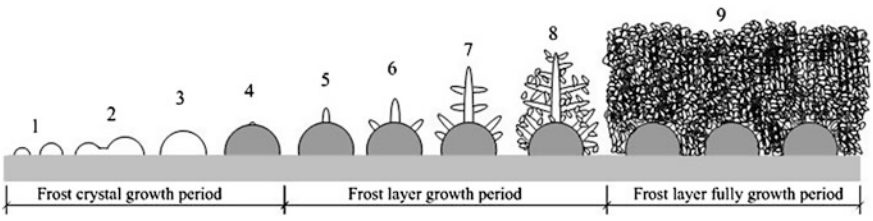

Fig. 80.1 Schematic representation of the entire frosting process on cold surface

As illustrated in [10], as soon as the necessary non-equilibrium conditions are satisfied, a heterogeneous nucleation firstly takes place and the embryo starts to grow (1). And then the adjacent embryos coalesce (2). During the process, the embryo surface temperature becomes higher than the plate temperature as its surface increases, demanding a higher amount of energy removal to maintain its growth (3). When this amount becomes higher than the energy removal required to start nucleation on a new site, the embryo stops growing and a secondary nucleation takes place (4). During the frost layer growth period, as the new embryo grows (5), so does the energy removal needed to sustain its growth and, as a result, new nucleation spots appear on the surface of the original embryo (6,7). The successive nucleation and embryo growth processes go on until the supercooling and supersaturation degrees approach zero (8). From this point on, the frost layer fully growth period starts. The frost layer behaves as a porous medium into which diffusion of water vapor leads to an increase of both thickness and density (9).

From all the above analysis, we can see that if the frozen water droplets adhered to the cold surface, as the base of frost crystal growth, could be completely removed, the subsequent frost growth process will not exist.

Accordingly, the objective of this paper is to experimentally study the effect of ultrasonic vibration on the initial frozen water droplets adhered to cold vertical surface. Detailed observations of transient process of frozen water droplets shed ding from cold surface with the presence of 20 kHz ultrasonic vibration were made with a high-speed camera to evaluate the possibility of ultrasonic vibration for the frozen water droplets removal.

80.3 Experimental Apparatus and Procedure

Figure 80.3 shows the schematic diagram of experimental apparatus used in the tests. It mainly consists of four parts: a high frequency ultrasonic vibration system, a water droplet freezing system, a high-speed image acquisition system and a data acquisition system.

The high frequency ultrasonic vibration system includes a 20 kHz ultrasonic transducer and an ultrasonic generator with the capacity of 0 to 100 W. A $70 \times 70 \times 3$ mm aluminum plate is provided as the base surface for water droplets freezing. An ultrasonic longitudinal wave probe with 10 mm in diameter is directly attached to the center of the aluminum plate by a screw bolt, as shown in Fig. 80.2. Such a relationship can get the ultrasonic transducer provide more uniform and efficient high frequency vibration to the vertical cold flat surface. In addition, a pipette that could provide the desired water droplets in different diameters and numbers on the cold surface is utilized in these tests and a commercial freezer is used to provide a cold environment to freeze the water droplets. Also, one K-type thermocouples (OMEGA) fitted the small holes which is drilled into the flat are installed to acquire the internal temperatures of the aluminum

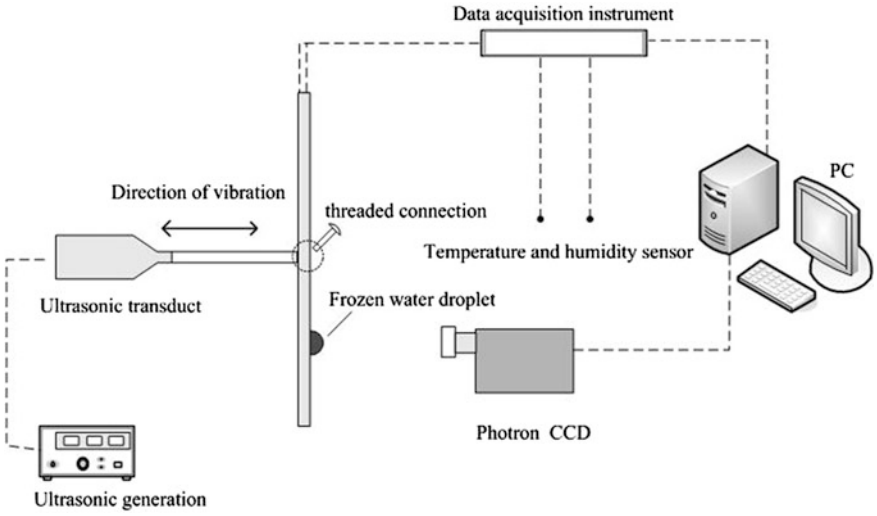

Fig. 80.2 Schematic experimental apparatus for frozen water droplets shedding from cold surface

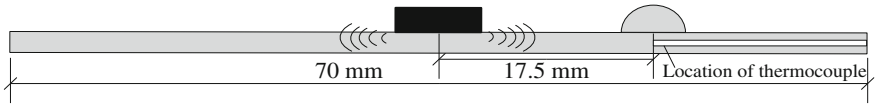

Fig. 80.3 Location of frozen water droplet on the cold surface

plate. The detailed locations of thermocouple is shown in Fig. 80.3. A thermo-hygrometer is used to measure the ambient temperature. All the temperature data are recorded by a HP34970A data acquisition system. The shedding processes of frozen water droplets from the cold vertical surface are observed by a high speed video camera (Photron SA4) and recorded by an image acquisition system connected to the computer. In all the tests, the power applied to the transducer is controlled to be 60 W.

80.4 Results and Discussion

80.4.1 Detailed Behaviour of a Frozen Water Droplet Shedding from Cold Vertical Surface Due to Ultrasonic Vibration

Figure 80.4 shows the side view of the transient process of a single frozen water droplet with approximately 12 mm in diameter shedding from the cold vertical

surface. In the test, the ambient temperature is 10.7 °C. The simultaneous falling and bouncing off of frozen water droplets from the vertical surface can be observed during the whole process. As the ultrasonic generator is turned on, the frozen water droplet subjected to the ultrasonic vibration firstly separates from the cold vertical surface (Fig. 80.4b). About 5 ms later, the whole bonding surface of frozen water droplet break away from the cold surface (Fig. 80.4d). As shown in Fig. 80.4, the frozen water droplet not only falls off but also bounces off from the cold surface (Fig. 80.4e–g). From all the pictures, it can be seen that the whole shedding process lasts only 84 ms. All the results indicate that the ultrasonic vibration can instantaneously remove frozen water droplets from the cold vertical surface with almost no time delay.

As is well-known, the ultrasound has the mechanical effect which could cause the cold flat periodic intensive vibration. Such an intensive vibration can generate sufficient transverse shear stresses at the frozen water droplets/the cold surface interface which can overcome the adhesion strength of frozen water droplets on cold surface, causing the delamination of frozen water droplets from cold surface. It is considered as the dominant reason for the shedding of frozen water droplets by Palacios [11]. However, the existence of interface transverse shear force can only explain the falling off of frozen water droplets from the vertical surface. There must be another impact force in the normal direction of vertical surface to cause the bouncing off of the frozen water droplets.

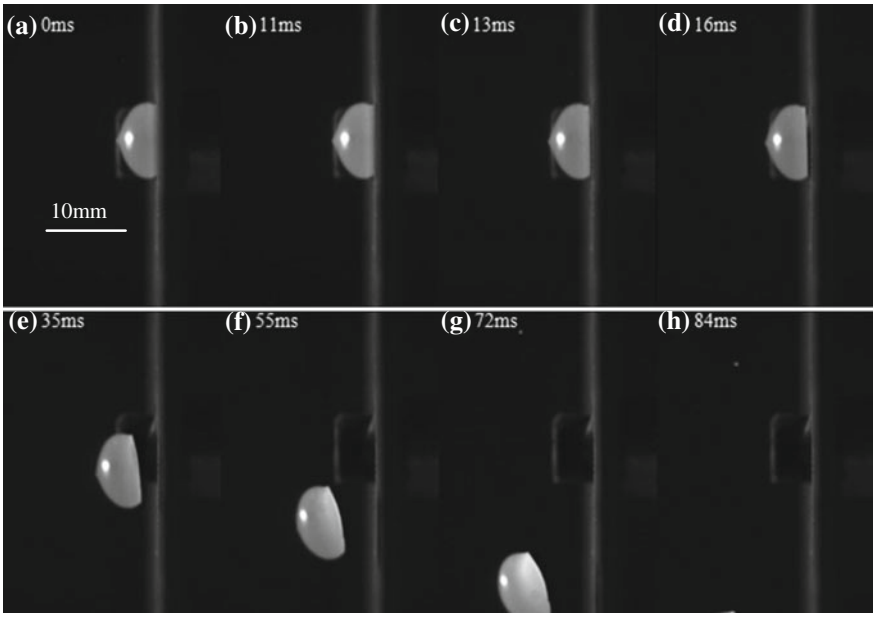

Fig. 80.4 Ultrasonic vibration for instantaneously removing frozen water droplets from cold flat surface, **a** 0 ms, **b** 11 ms, **c** 13 ms, **d** 16 ms, **e** 35 ms, **f** 55 ms, **g** 72 ms, **h** 84 ms

In order to explore the cause of impact force generated on the cold surface, the SEM image of surface topography of aluminum plate in the tests is presented. As shown in Fig. 80.5, tiny depression can be seen on the rough aluminum surface. So once the frozen water droplets adhered to the rough surface, these tiny depressions will be covered and many closed micro areas will be formed. These closed areas are most likely to induce the formation of the ultrasonic cavitations. Hence, as the ultrasonic generator is turned on, the air bubbles in the closed depressions will be compressed and stretched due to the alternated positive and negative pressure induced by ultrasonic cavitation. Ultimately, the air bubbles in the closed areas will collapse and instantaneously release enormous pressure which could even reach to 10^8 Pa. Such an enormous pressure could cause the generation of intense impact force and micro-jet which can bounce off the frozen water droplet on the cold surface.

For the purpose of exploring the effect of the heat generated by ultrasonic vibration on the frozen water droplets removal, the simultaneous internal temperatures variation of cold surface subjected to ultrasonic vibration were measured. As shown in Fig. 80.6, the instantaneous internal temperature jump of cold flat occurs due to the ultrasonic vibration which is different from that the temperature distribution on the plate after ultrasonic vibration is quite uniform which was reported by Kazunari [6]. It is found from Fig. 80.6 that the temperature variation is remarkable. Almost 5° temperature rise can be seen in a second time. With the disappearance of ultrasonic vibration, the internal temperatures of cold flat gradually decrease. However, the shedding process can not be attributable to the heat generation by ultrasonic vibration. First of all, the frozen water droplets instantaneously fall off from the cold surface in less than one second. Such a short thermal response time can not make the heat generation influence the frozen water

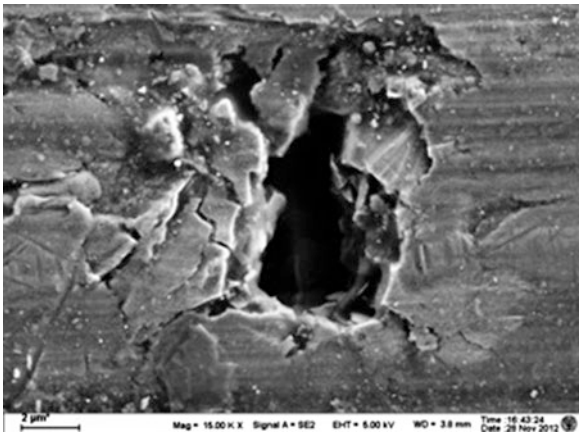

Fig. 80.5 SEM image of surface topography of aluminum plate in the tests

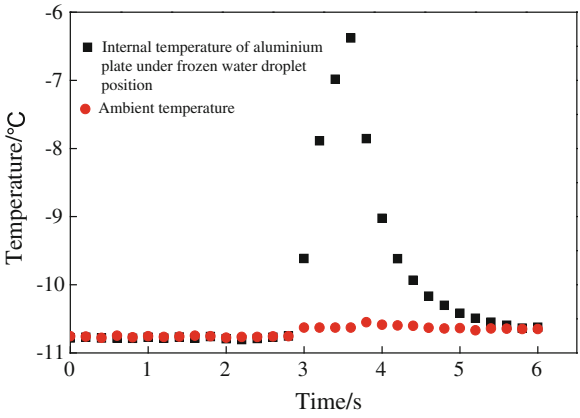

Fig. 80.6 Internal temperature variation of cold surface during the frozen water droplets shedding process

droplet. Secondly, the internal maximum temperature of cold flat after one second ultrasonic vibration is –6.4 °C, far from reaching the ice melting temperature. Hence, the phenomenon of frozen water droplets instantaneously shedding from the surface can not be ascribed directly to the heat generation caused by ultrasonic vibration.

From all the above analysis, we can draw a conclusion that the combined action of transverse shear force induced by ultrasonic mechanical effect at the interface and the intense impact force generated by ultrasonic cavitation on the depressions/cracks of rough surface maybe the main reason for frozen water droplets removal from cold aluminum surface.

80.4.2 Ultrasonic Vibration for Frozen Water Droplets Removal on Different Positions of Cold Vertical Surface

Figure 80.7 shows the effect of ultrasonic vibration on frozen water droplets in different positions on cold vertical surface. All the frozen water droplets here are 9 mm in diameter and the ambient temperature is –12 °C. As shown in Fig. 80.7, the frozen water droplets on the lower surface firstly fall and bounce off from the cold surface (Fig. 80.7c). And then the frozen water droplet on the left side separate from the surface. At 46 ms, almost all the frozen water droplets have been removed from the cold surface. It can be seen from the pictures that all the frozen water droplets in different positions in the test can be shed off in less than one second, although the shedding time of each frozen water droplet from the cold surface is different.

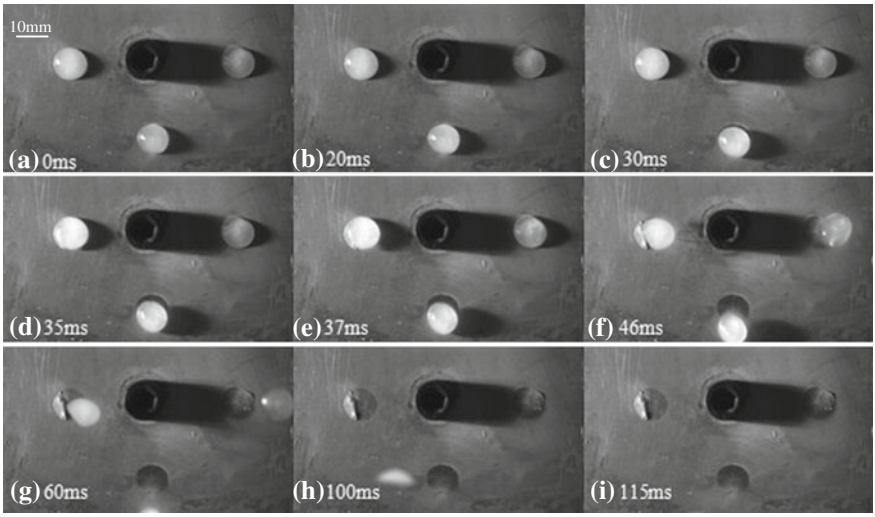

Fig. 80.7 Instantaneous shedding process of the frozen water droplets with the effect of ultrasonic vibration, **a** 0 ms, **b** 20 ms, **c** 30 ms, **d** 35 ms, **e** 37 ms, **f** 46 ms, **g** 60 ms, **h** 100 ms, **i** 115 ms

80.5 Conclusion

A series of experiments concerning frozen water droplets accreted on cold vertical surface subjected to 20 kHz and 60 W ultrasonic vibration was conducted. The visual results shows that the frozen water droplets can be instantaneously shed from the cold surface and simultaneously the internal temperatures of cold flat have an apparent rise with effect of ultrasonic vibration. The analysis about the temperature jump and surface topography of aluminum plate indicates that the shedding process can not be attributable to the heat generation by ultrasonic vibration and the joint action of the interface transverse shear force produced by ultrasonic mechanical effect and the impact force generated by the ultrasonic cavitation may be the dominant reason for the frozen droplets removal. All the experimental results presented that the ultrasonic vibration has a strong ability to remove the frozen water droplets from cold surface which is the base for frosting and thus it is a highly effective defrosting method.

Acknowledgments The authors gratefully acknowledge the support provided by Scientific Research Foundation of Graduate School of Southeast University (NO.YBJJ1203).

References

1. Liu Zhongliang, Zhang Xinghua, Wang Hongyan (2007) Influences of surface hydrophilicity on frost formation on a vertical cold plate under natural convection conditions. Exp Therm Fluid Sci 31:789–794
2. Lee Hyunuk, Shin Jongmin, Ha Samchul et al (2004) Frost formation on a plate with different surface hydrophilicity. Int J Heat Mass Tran 47:4881–4893
3. Jhee Sung, Lee Kwan-Soo, Kim Woo-Seung (2002) Effect of surface treatments on the frosting/defrosting behavior of a fin-tube heat exchanger. Int J Ref 25:1047–1053
4. Wang Chi-Chuan, Huang Ren-Tsung, Sheu Wen-Jenn et al (2004) Some observations of the frost formation in free convection: with and without the presence of electric field. Int J Heat Mass Tran 47:3491–3505
5. Joppolo Cesare Maria, Molinaroli Luca, De Antonellis Stefano (2012) Experimental analysis of frost formation with the presence of an electric field on fin and tube evaporator. Int J Ref 35:468–474
6. Adachi K, Saiki K, Sato H et al (2003) Ultrasonic frost suppression. Jpn J Appl Phys 42:682–685 Pt 1, (2A)
7. Wang Dingyuan, Tao Tangfei, Guanghua Xu, Luo Ailing, Kang Shaoying (2012) Experimental study on frosting suppression for a finned-tube evaporator using ultrasonic vibration. Exp Therm Fluid Sci 36:1–11
8. Qinlao Yan, Lin Zhu, Mi'e Zhang, Ningxi Yan, Xueying Hui (2003) Study on ultrasonic defrost technology of refrigeration fan. J Agric mach 34(3):74–75
9. Hayashi Y, Aoki A, Adachi S et al (1977) Study of frost properties correlating with frost formation types. J Heat Trans-T ASME 99(2):239–245
10. Piucco Robson O, Hermes Christian JL, Melo Cláudio et al (2008) A study of frost nucleation on flat surfaces. Exp Therm Fluid Sci 32:1710–1715
11. Palacios JL, Smith EC, Rose JL et al (2008) Investigation of an ultrasonic ice protection system for helicopter rotor blades. In: The American helicopter society 64th annual forum, April 29–May 1

Chapter 81
Experiment of a New Partitions Filler Regeneration Performance

Lining Zhou, Zhijia Huang, Liping Zhu and Ping Jiang

Abstract The filler is the important heat and mass transfer components of dehumidifier and regenerator in liquid desiccant system. The traditional gas–liquid direct contact filler meets an unfavorable factor which is gas with liquid. In this paper, a new indirect gas–liquid contact partitions filler, which has a specific surface area of 286 m^2/m^3 and a porosity of 0.86, is proposed. Both regeneration performance of the partitions filler and 5090 wet curtain has been tested on a cross-flow regeneration module laboratory. LiBr solution has been used as the desiccant and the regeneration effect is described by regeneration rate, renewable efficiency, average mass transfer coefficient, and volumetric mass transfer coefficient. The influence of the regeneration performance of the system is analyzed with solution inlet temperature. A regeneration performance comparison of the new filler and the 5090 wet curtain has been carried out. It shows the volumetric mass transfer coefficient of the filler is 7–36 % higher than the 5090 wet curtain one when the solution temperature is between 43 and 60 °C, and the quality of air with liquid of the new filler is 58–87 % lower than the 5090 wet curtain one when the face velocity is between 0.387 and 0.645 m/s.

Keywords Partitions filler · 5090 wet curtain · Cross-flow · Regeneration experiment

81.1 Introduction

As the liquid desiccant has so many advantages such as low-grade solar energy or waste heat driven, cycle working fluid is environmental friendly and so on. In recent years, the temperature and humidity independent control technology have

L. Zhou · Z. Huang (✉) · L. Zhu · P. Jiang
School of Civil Engineering and Architecture, Anhui University of Technology, Maanshan, 243002 Anhui, China
e-mail: hzj@ahut.edu.cn

A. Li et al. (eds.), *Proceedings of the 8th International Symposium on Heating, Ventilation and Air Conditioning*, Lecture Notes in Electrical Engineering 262,
DOI: 10.1007/978-3-642-39581-9_81,

been well developed in a number of public and civil buildings [1–4]. But the Liquid desiccant also has some problems such as gas with liquid, liquid has causticity, due to the gas with liquid [5, 6], when it is application in the civilian workplace, long-term inhalation of LiBr can cause skin rash and central nervous system disorders [7, 8]. On the other hand, because the liquid has causticity, when it is used in industrial sites, it will affect the quality of products. Due to the above problems this technology is limited. To solve the problem of gas with liquid from improving demister start [9–11], but install defogging device cannot fundamentally solve the issue of gas with liquid. Contact prone to the phenomenon of gas with liquid for traditional filler solution and air directly from the filler start to design a new partitions filler, in the new filler the air and the solution indirect contact, it can solve the problem of gas with liquid from the fundamental solution. Although many studies have been carried out on the regeneration performance of the regenerator at home and abroad [12–16], but there are only few studies on the performance of the regeneration for the partitions filler. In this paper experimental tests were carried out to understand the performance of the filler and a regeneration performance comparison of the new filler and the 5090 wet curtain has been carried out.

81.2 Experimental subject

The filler is important heat and mass transfer components in liquid desiccant dehumidification/regeneration process, and its performance is directly related to the performance of the system. In this paper both regeneration performance of the partitions filler and 5090 wet curtain have been tested on a cross-flow regeneration module laboratory. The air and solution are direct contact in 5090 wet curtain but indirect contact in the partitions filler. The flow channel of 5090 wet curtain is shown in Fig. 81.1a, and the flow channel of the new partitions filler is shown in Fig. 81.1b.

As is shown in Fig. 81.1 the air following as the y axis in channel 1 and the liquid following as the negative z axis in channel 2 in both 5090 wet curtain and new partitions filler. But in 5090 wet curtain the air and the solution was shared one flow channel, the air and the solution are direct contact, so the phenomenon of the gas with liquid is easy occurs. And as shown in Fig. 81.1b in the new partitions filler each layer of the filler is comprised of two pieces, the solution flows in the two pieces of the filler, and the air flows in the two layers of the filler. The solution and air flow in a different flow channel, thus achieving the indirect contact of the solution and air, so as to solve the problem of gas with liquid effectively. The performance comparison of the two fillers is shown in Table 81.1.

As shown in the Table 81.1 with the same size the performance of the 5090 wet curtain is superior than which of the new filler, but either filler air contact with solution in different ways. In the new filler air and solution are indirect contact can effectively avoid the problem of air with liquid, in order to contrast the regeneration

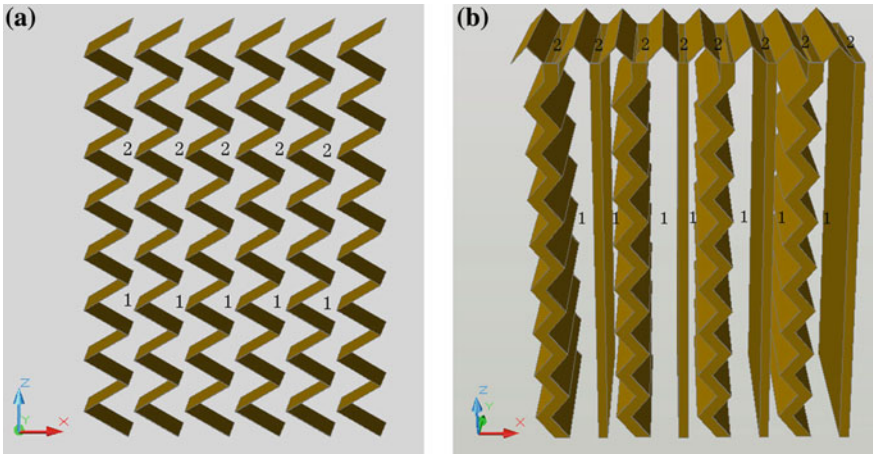

Fig. 81.1 The contrastive of the two fillers. **a** The flow channel of 5090 wet curtain. **b** The flow channel of partitions filler. *1* The flow channel of air, *2* the flow channel of solution

Table 81.1 The performance comparison of the two fillers

	Size (mm)	Porosity	Specific surface area (m^2/m^3)
5090 wet curtain	800 × 400 × 350	0.95	500
New filler	800 × 400 × 350	0.86	286

performance of the two fillers, both regeneration performance of the partitions filler and 5090 wet curtain have been tested on a cross-flow regeneration module laboratory.

81.3 Experimental Study

81.3.1 Experimental Facility

This experimental system consists regeneration module, dehumidification module, heat source, cold source, and heat exchanger five major components, which the regeneration module uses the form of a cross-flow, dehumidification module using countercurrent form, heat source using electric heaters instead of waste heat, cold source uses cooling tower, exchanger uses plate heat exchanger, both the 5090 wet curtain, and new partitions filler were used in the regeneration module, its dimensions are 780 × 400 × 350 mm. Unit flow chart shown in Fig. 81.2.

Unit processes: In dehumidifier the desiccant strong solution contact with air within the dehumidifying, then the dilute solution which after dehumidification through the dehumidification outer circulation pump exchanging heat with the hot

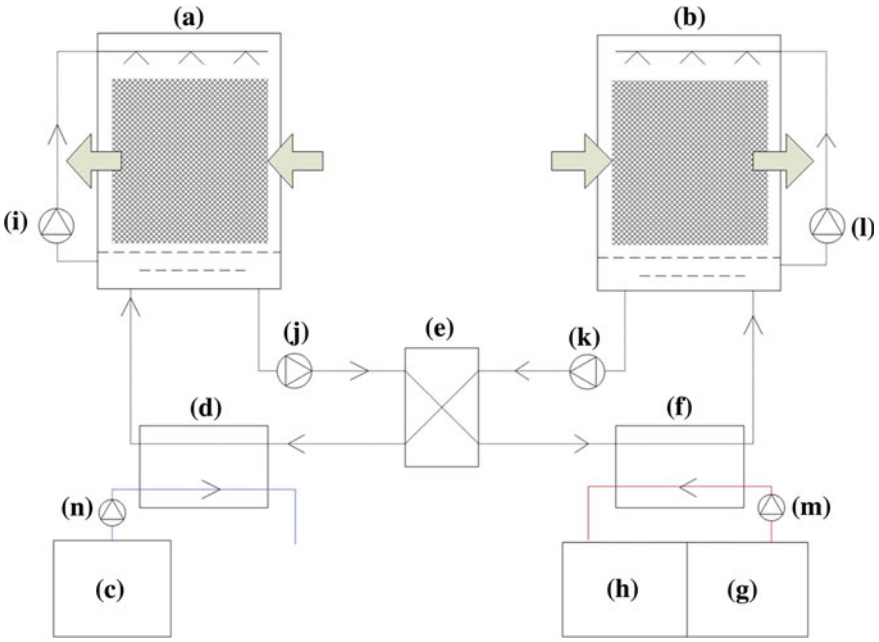

Fig. 81.2 Unit flow chart. *A* dehumidifier, *B* regenerator, *C* cooling water tank, *D* cooler, *E* economizer, *F* heater, *G* heating water tank, *H* water storage tank, *I* dehumidification internal circulation pump, *J* dehumidification outer circulation pump, *K* regeneration outer circulation pump, *L* regeneration internal circulation pump, *M* heating water pump, *N* cooling water pump

strong solution in the economizer, and then heated through the heater into the regenerator for regeneration; through a regeneration solution concentration is small changed, so part of the solution was then passed to the regeneration internal circulation pump regeneration, another portion of the solution through the regeneration internal circulation pump exchanging heat with the cold dilute solution in the economizer, and then through cooler for cooling, entering the dehumidifier be dehumidified, through a dehumidification the concentration of the solution is small changed, the portion of the solution then be dehumidified through the dehumidification internal circulation pump, so as to complete a cycle.

81.3.2 Experimental Condition

Through the fixing solution inlet flow (flow rate of 1.60 m^3/h), to change the heater heating temperature (heating temperature range of 45–75 °C), changing the face velocity (face velocity range of 0.387–0.645 m/s). The experiments were designed 18 sets to study the regeneration performance of the two fillers.

Parameters need to be measured in the experiment including: the solution flow rate, inlet and outlet temperature, the density of the solution import and export, the wet and dry bulb temperature of the air import and export.

81.4 Results and Analysis

81.4.1 Evaluation Indicators of Regeneration Performance

In the present work, some important parameters are used for evaluating the performance of the regeneration including: m_{reg} (regeneration rate), η_{reg} (regeneration efficiency), k_a (average mass transfer coefficient) and k_v (volumetric mass transfer coefficient).

m_{reg} is defined as the rate of which moisture is removed from the solution (kg/s). It can be calculated from:

$$m_{\text{reg}} = m_a(d_{a,\text{out}} - d_{a,\text{in}}) \tag{81.1}$$

where, $d_{a,\text{ in}}$ and $d_{a,\text{ out}}$ are the humidity ratio of process air at inlet and exit from the regeneration; respectively in kgv/kgda.

k_a is defined as the rate of moisture flux passing through a unit area (kg/m^{2}s). It can be obtained from the measured data as follows:

$$k_a = \frac{m_{\text{reg}}}{A(d_{\text{av}} - d_{\text{eq}})} \tag{81.2}$$

where, A is the interfacial area of contact between liquid desiccant and air inside the regeneration. If this area is assumed to be fully wetted by the solution, then $A = a_p V$ where, V is the volume of the filler in m^3, a_p is the filler density in m^2/m^3, $d_{av} = \left(d_{a,in} + d_{a,out}\right)/2$ is the average process air humidity ratio across the regeneration and d_{eq} is the humidity ratio of air in equilibrium with LiBr solution at the interfacial.

Because the constraints of the filler wetting and surface solution residence time, the filler mass transfer surface area A is often less than the filler actual surface area, the size of A is not only related to the geometric characteristics of the filler, but also with the gas–liquid two-phase flow and its physical characteristics, Thus, the mass transfer area A is difficult to measured directly. Therefore, to define the volumetric mass transfer coefficient to reflect the mass transfer of the unit volume, volumetric mass transfer coefficient is defined as the mass transfer unit volume (kg/m^{3}s). It is determined by the formula:

$$k_v = \frac{m_{\text{reg}}}{V \cdot \Delta X} \tag{81.3}$$

where: ΔX is mass transfer driving potential.

η_{reg} is defined as the actual humidity ratio drop of the process air to the maximum possible drop. It is calculated as follows:

$$\eta_{reg} = \frac{d_{a,in} - d_{a,out}}{d_{a,in} - d_{eq}} \times 100\,\% \tag{81.4}$$

The quality of air with liquid defined as the quality of solution carried by per volume air.

$$m_s = \frac{m_2 - m_1}{m_a t} \tag{81.5}$$

where:
m_s is the gas with liquid rate;
m_1, m_2 are the filter paper weight before and after the experiment respectively clicked in the regenerator outlet;
t is experiment time.

81.4.2 Effect of Solution Temperature on Regeneration Performance

The effects of the solution temperature on the rate of regeneration, volumetric mass transfer coefficient, average mass, transfer coefficient, regeneration efficiency are shown in Figs. 81.3, 81.4, 81.5, and 81.6.

As is shown in the Fig. 81.3 under the same conditions of the regenerator in the same cross-section wind speed and the same solution flows the regeneration rate increases as the solution temperature increases, this is because as the solution temperature increases the water vapor partial pressure of the solution is increases, and the mass transfer driving potential between air and solution increase, so the regeneration rate increase.

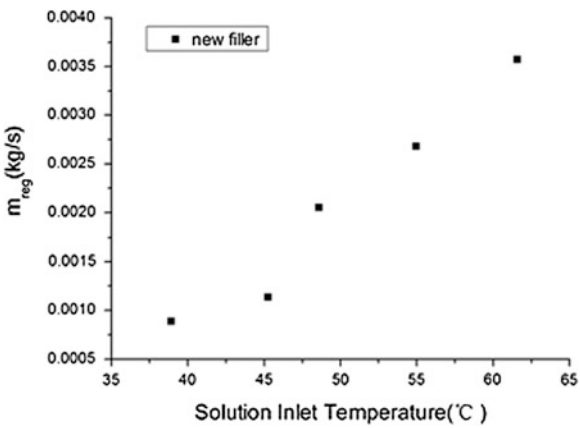

Fig. 81.3 Effect of solution temperature on m_{reg}

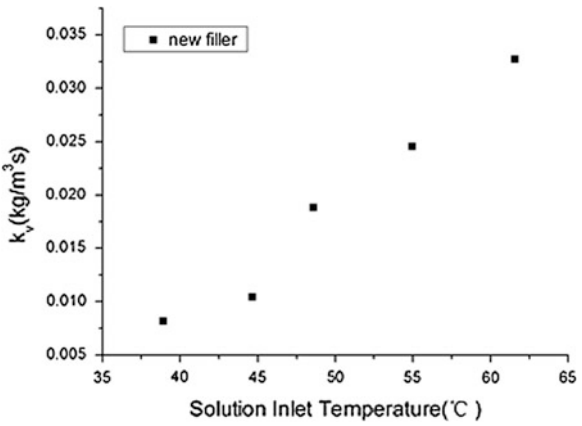

Fig. 81.4 Effect of solution temperature on k_v

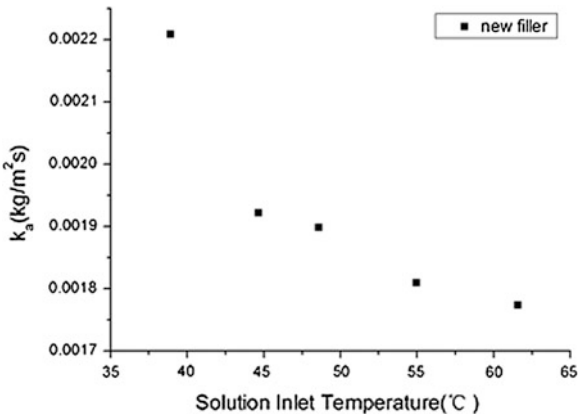

Fig. 81.5 Effect of solution temperature on k_a

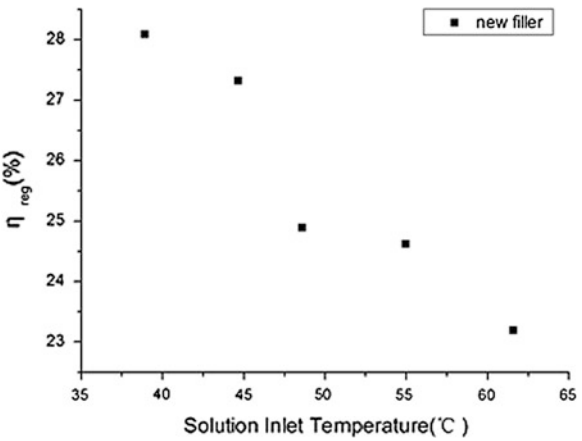

Fig. 81.6 Effect of solution temperature on η_{reg}

As is shown in the Fig. 81.4 under the same experimental conditions, the volumetric regenerator mass transfer coefficient increases as the solution temperature increases, from the above analysis we can understand the regeneration rate increases as the solution temperature increases, so as the unit volume mass transfer increase, and the volumetric mass transfer coefficient reflects per unit volume mass transfer of the packed, so the volumetric mass transfer coefficient increased with the rise of the temperature of the solution.

From Fig. 81.5 under the conditions of the same cross-section wind speed and the same solution flows, the average mass transfer coefficient of the regenerator decreases rapidly with increasing temperature of the solution, this is because as the solution inlet temperature increase its equivalent moisture decreases, and the degree of reduction is greater than the degree of increase of the regeneration rate. This resulting decline in the average mass transfer coefficient.

Figure 81.6 shows in the same experimental conditions, the regeneration efficiency decreased as the solution temperature increases, this is because the surface water vapor partial pressure of the solution and the moisture content of the outlet air increases as the solution temperature increases, and the equivalent moisture content of the solution which contact with the air increased, but the range of the latter is greater than the former, as the Eq. (81.4) shown, the regeneration efficiency decreased with increasing temperature of the solution.

81.4.3 Regeneration Performance Comparison of the Two Fillers

Figures 81.7, 81.8, and 81.9 show that in the same experimental conditions, the regeneration performance comparison of the two fillers. And the Fig. 81.10 shows the quality of air with liquid along with the change of face velocity in both the new partitions filler and 5090 wet curtain.

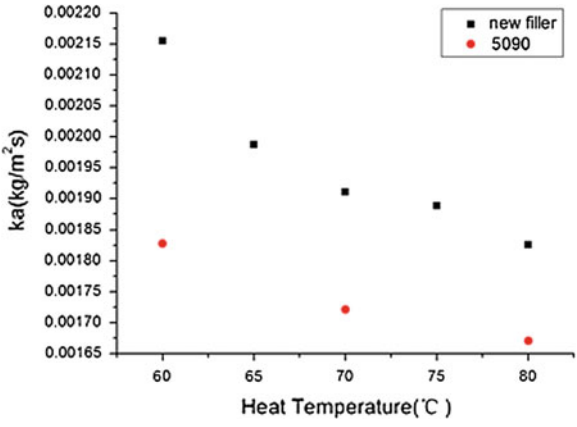

Fig. 81.7 Effect of heat temperature on k_a

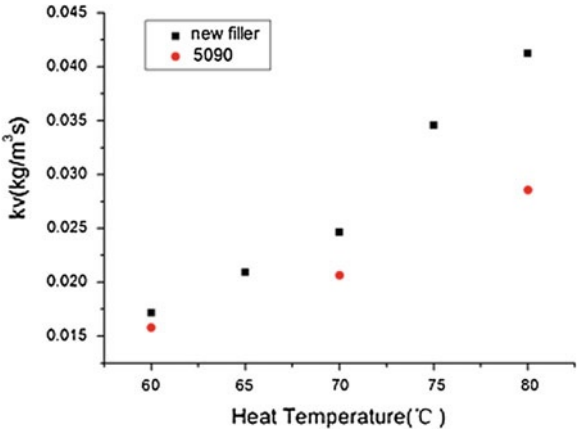

Fig. 81.8 Effect of heat temperature on k_v

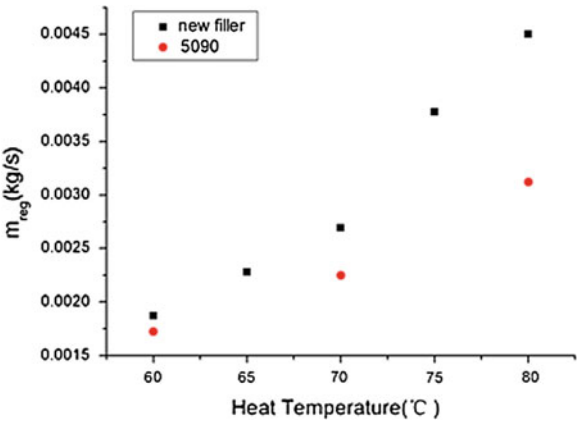

Fig. 81.9 Effect of heat temperature on m_{reg}

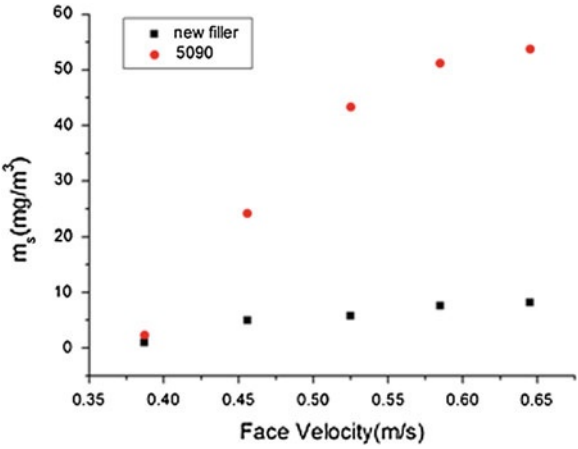

Fig. 81.10 Effect of face velocity on m_s

As is shown in the Fig. 81.7 in the same experimental conditions, although the average mass transfer coefficient of the two fillers are reduce as the inlet solution temperature increases but the average mass transfer coefficient of the new partitions filler is always higher than 5090 wet curtain.

As is shown in the Fig. 81.8 under the same experimental conditions, the volumetric mass transfer coefficient of the two fillers increases with increasing temperature, and the new partitions filler volumetric mass transfer coefficient were higher than the 5090 wet curtain and has the same trend with the regeneration rate.

Figure 81.9 shows under the same experimental conditions, the regeneration rate of the new partitions filler is higher than it for 5090, and regeneration rate of both the filler increase as the temperature increases, but as the solution temperature increases the new partitions filler regeneration rate is more higher for it compared with 5090 wet curtain, this is because the indirect contact of the solution and the air in the partitioned fillers affect the heat transfer, this could make the solution was maintained at a higher temperature, so as a higher water vapor partial pressure and mass transfer driving potential, and the temperature is the greater the more obvious advantages, and as the temperature rise the regeneration rate of the new filler is greater than it for 5090 wet curtain.

As is shown in Fig. 81.10 in 5090 wet curtain the quality of air with liquid increase as the face velocity increase, this is because with the increase of the face velocity the ability of gas with liquid increase. But in the new partitions filler the quality of air with liquid changes little with the increase of the face velocity, and in the new partitions filler the quality of air with liquid can be reduced by 58–87 %, this is mainly because indirect contact with air and solution in the new partitions filler reduces the chance of air carrying solution, so the quality of air with liquid of the new partitions filler can be significantly reduced compared with the 5090 wet curtain.

81.5 Conclusion

1. Due to the traditional filler meets an unfavorable factor which is gas with liquid. In this paper, a new partitions filler is designed, which has a specific surface area of 286 m^2/m^3 and a porosity of 0.86. Experimental study found that the regeneration rate of the new filler, volumetric mass transfer coefficient increased with the rise of the temperature of the solution, the average mass transfer coefficient, the regeneration efficiency decreases with increasing temperature of the solution.
2. Since the filler mass transfer area is difficult to directly measure, it often makes the measured average mass transfer coefficient is not accurate. And the regeneration rate and the volumetric mass transfer coefficient have the same trend, and can reflect regeneration performance of the regenerator from

macroscopic, using volumetric mass transfer coefficient evaluates the regeneration performance of the regenerator is more scientific.

3. Because the indirect contact between the solution and the air in the new partitions filler affect its heat transfer, so that the solution was maintained at a higher temperature, and the greater temperature the more obvious advantages, therefore, as the temperature increases the volumetric mass transfer coefficient of the new filler is higher than it for the 5090 wet curtain. When the temperature of the solution being heated in 60–80 °C, the volumetric mass transfer coefficient of the new partitions filler is 7–36 % higher than the one for the 5090 wet curtain.
4. Using the new partitions filler can significantly reduce the quality of air with liquid, and the quality of air with liquid of the new filler is 58–87 % lower than the 5090 wet curtain one when the face velocity is between 0.387 and 0.645 m/s. And the quality of air with liquid changes little with the increase of the face velocity in the new partitions filler.

References

1. Chen X, Cong L, Zhang T et al. (2011) Liquid desiccant air handling technology research progress. HV&AC 41(1):21–27
2. Liu S, Liu X, Jiang Y et al. (2011) Nanhai E # 3 office temperature and humidity measurement and analysis of individually controlled air conditioning system. HV&AC 41(1):55–59
3. Gu Z, Liu Y, Huang D et al. (2011) Temperature and humidity independent control air-conditioning systems in large public buildings in the Beijing area applications. HV&AC 41(1):53 –54
4. Li Y, Hu R, Feng T (2011) Temperature and humidity independent control air-conditioning system in application of the Xiangxi courtyard two villa in Qingdao. HV&AC 41(1):42–47
5. Chen Y, Pei Q, Xu G (2009) Liquid desiccant air conditioning air with liquid ion detection method and its application. Build Energy Environ 28(3):37–40
6. Wang S (2007) Preliminary study of liquid desiccant air conditioning indoor air quality. Guangzhou University, Guangzhou
7. Luo X, Li W, Cao Z (2011) The refrigerant rust change lithium bromide solution corrosive research. Light Ind Mach 29(1):104–107
8. Jiang F, Cai Z, Lu Z (1999) BTA on the corrosion of carbon steel in lithium bromide solution. The Refrigeration 18(4):29–31
9. Kumar R, Dhar PL, Jain S (2011) Development of new wire mesh packings for improving the performance of zero carryover spray tower. Energy 36:1362–1374
10. An S, Wang J, Liu I et al. (2007) Liquid desiccant packed tower liquid entrainment and pressure drop problem. HV&AC 37(4):109–112
11. Zhang L, Liu J, Zhang H (2011) Liquid desiccant screen corrugated packing application characteristics research. Fluid Mach 39(6):48–52
12. Sun J, Shi M, Zhao Y (2003) Experimental study of the performance of liquid desiccant air conditioning regeneration. Eng Thermo Phys 24(5):867–869
13. Luo L, Zhang X, Yin Y (2008) The experimental study of heat and mass transfer coefficients of Forks flow packing regenerator. J Eng Thermophys 29(7):1215–1217

14. Bassuoni MM (2011) An experimental study of structured packing dehumidifier/regenerator operating with liquid desiccant. Energy 36:2628–2638
15. Yin Y, Li S, Zhang X (2010) Adiabatic and heat- regenerative process thermal performance comparison. Chem Ind Eng 61(S2):157–162
16. Wang Q, Wang G (2010) Theoretical research and experimental analysis of the solution regeneration of liquid desiccant air conditioning system performance. Refrig Air Condition 24(4):124–128

Chapter 82
Theoretical Analysis and Numerical Simulation of Coupled Relationship of Heat and Mass Transfer between Air and Desiccant in Liquid Desiccant Dehumidification

Zhijia Huang and Ping Jiang

Abstract This dissertation presented simulation and theoretical work on disclosing the coupled relationship of heat and mass transfer between air and desiccant in dehumidifiers. The result shows that the effect of mass transfer process to the heat transfer process is mainly embodied in two aspects: one is the enthalpy carried by the mass flux, another is the water vapor turns into water release of latent heat of vaporization. The effect of heat transfer process to the mass transfer process is mainly embodied in temperature.

Keywords Liquid desiccant dehumidification · Complex heat and mass transfer · Theoretical analysis · Numerical simulation

82.1 Introduction

Dehumidification is closely related to production and life which is a process that removing or reducing the moisture in the wet air. Liquid desiccant system is widely used in the field of construction, metallurgy, chemical industry because of its advantages of the use of low-grade energy, saving energy consumption, and environmental protection [1, 2]. The mass transfer and heat transfer exist at the same time in the process of liquid desiccant dehumidification [3]. The coupled relationship has been studied by many scholars on the theoretical and experimental.

Currently, the following three methods are used to modeling and analysis, the heat and mass transfer between air and desiccant in dehumidifiers:

Z. Huang (✉) · P. Jiang
School of Civil Engineering and Architecture, Anhui University of Technology, Maanshan 243002, China
e-mail: hzj@ahut.edu.cn

A. Li et al. (eds.), *Proceedings of the 8th International Symposium on Heating, Ventilation and Air Conditioning*, Lecture Notes in Electrical Engineering 262,
DOI: 10.1007/978-3-642-39581-9_82,

(1) Experimental. This method is used for the data to develop the relational of temperature and humidity efficiency and operating parameters which is obtained by the experimental [4–7]. Although easy to analyze, this method cannot reflect the heat and mass transfer process.
(2) Finite difference model. This model is cited by many researchers because it can be very simple and intuitive to reflect the process of heat and mass transfer between air and desiccant [8–12]. But this method must get the dimensionless relational of coupled mass transfer coefficient which is based on experiments, then calculates the coupled heat transfer coefficient by assuming the number of Lewis. Therefore, this method cannot explain the coupled relationship between heat and mass transfer theoretically.
(3) Complex model that consider the resistance of both air and solution. This model is based on the Navier–Stokes equations, and is difficult to calculate, so it is not easy to design and optimize the physical structure [13–16].

However, the works are more focussed on modeling heat and mass transfer in liquid desiccant dehumidification process, instead of studying the coupled relationship of heat and mass transfer. This paper discussed the interaction of heat and mass transfer of the dehumidification process and developed the heat and mass transfer model based on the two-film theory [17].

82.2 Development of Mathematical Model of Heat and Mass Transfer

In order to analyze the coupled mechanism of heat and mass transfer, this paper will be developed as the model of heat transfer process and mass transfer process, respectively. Due to the dehumidification process and the regeneration process are the reverse processes, dehumidification process is discussed here.

When the air that the temperature is $t_{A,a}$ flowing through the phase interface, water vapor transfer through the two films and reaches the other side which the temperature is $t_{B,s}$, it is assumed that the mass flux is m. When $t_{A,a} > t_{B,s}$, the mass transfer and heat transfer are in the same direction, $m$is a positive number; When $t_{A,a} < t_{B,s}$, the mass transfer and heat transfer are in the opposite direction, m is a negative number (Fig 82.1).

82.2.1 Mass Transfer Process

According to Stephen's law [18], in the air film, the absorption rate equation is:

$$J = \frac{D_1 \cdot p_{A,a}}{R \cdot t_{A,a} \cdot \delta_1 \cdot p_{bM}} \left(p_{A,v} - p_{O,v}\right) = k_1 \cdot \left(p_{A,v} - p_{O,v}\right) \tag{82.1}$$

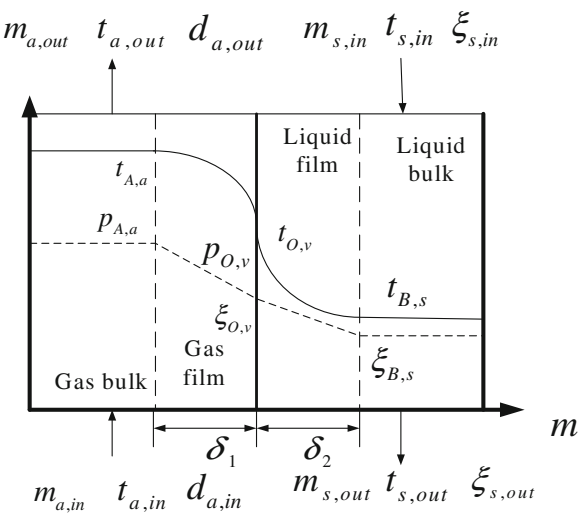

Fig. 82.1 The diagram of heat and mass transfer process

$p_{bM} = \frac{p_{O,v} - p_{A,v}}{\ln\left(p_{O,v}/p_{A,v}\right)}$ is the logarithmic average pressure of dry air.

Similarly,in the solution film, the absorption rate equation is:

$$J = \frac{D_2 \cdot \xi_{B,s}}{\delta_2 \cdot \xi_{sM}}\left(\xi_{O,v} - \xi_{B,v}\right) = k_2 \cdot \left(\xi_{O,v} - \xi_{B,v}\right) \tag{82.2}$$

$\xi_{sM} = \frac{\xi_{B,v} - \xi_{O,v}}{\ln\left(\xi_{B,v}/\xi_{O,v}\right)}$ is the logarithmic average concentration of the solution surface water vapor.

According to Henry's law [19], equation (82.2) is simplified as:

$$J = k_2 \cdot H \cdot \left(p_{O,v} - p_{B,v,e}\right) \tag{82.3}$$

Because of the absorption rate is equal at the interface, simultaneous equation (82.1) and (82.3):

$$J\left(\frac{1}{Hk_2} + \frac{1}{k_1}\right) = p_{A,v} - p_{B,v,e} \tag{82.4}$$

To the easy dissolve gas, the value of H is so big, then $1/Hk_2 \ll 1/k_1$, so mass transfer resistance only exist in the air film, the resistance in the liquid film can be ignored.

Solve the equation (82.4):

$$J = k_1 \cdot \left(p_{A,v} - p_{B,v,e}\right) \tag{82.5}$$

Generally, humidity is used to calculate the mass flux, so mass flux can be expressed as:

$$m = h \cdot \left(d_{A,v} - d_{B,v,e}\right) \tag{82.6}$$

$$h = \frac{11.2 \cdot k_1 \cdot p_{A,v}}{\left(0.622 + d_{B,v,e}\right) \cdot \left(0.622 + d_{A,v}\right)} \tag{82.7}$$

82.2.2 Heat Transfer Process

The follow model is developed when the mass transfer and heat transfer are in the same direction.

In the air film, heat flow consists of two parts [20]: thermal heat and the heat carried by the mass flux.

$$\text{Thermal heat} : q_1' = -\lambda_1 \frac{dt_{1,v}}{dx} \tag{82.8}$$

$$\text{The heat carried by the mass flux} : q_1'' = c \cdot m \cdot \left(t_{1,v} - t_0\right) \tag{82.9}$$

$$\text{Total heat flux} : \; q_1 = q_1' + q_1'' = c \cdot m \cdot \left(t_{1,v} - t_0\right) - \lambda_1 \frac{dt_{1,v}}{dx} \tag{82.10}$$

$$\text{Simplified as} : q_1 = c \cdot m \cdot \left(t_{A,a} - t_0\right) + \frac{\lambda_1}{\delta_1}\left(t_{A,a} - t_0\right) \tag{82.11}$$

Because the heat flux in two films are similar, so in the liquid film :

$$q_2 = c \cdot m \cdot \left(t_{O,v} - t_0\right) + \frac{\lambda_2}{\delta_2}\left(t_{O,v} - t_{B,s}\right) \tag{82.12}$$

In the liquid film, the vapor turns into water and release of latent heat of vaporization, according to the energy conservation law:

$$q_2 = q_1 + m \cdot r \tag{82.13}$$

Because of the latent heat of vaporization, the heat flux will no longer be the same in the heat flow field, then defined the heat flux of inflow and outflow for the system flux, taking the datum temperature $t_0 = t_{B,s}$. Then Eqs. (82.11–82.13) can be simplified as:

$$q = i \cdot \left(t_{A,a} - t_{B,s}\right) \tag{82.14}$$

$$\text{Equivalent heat transfer coefficient} : i = \frac{(1+\varphi) \cdot (c \cdot m + h_1) \cdot (c \cdot m + h_2)}{c \cdot m + h_1 + h_2} \tag{82.15}$$

Among them, $\varphi = \frac{m \cdot r}{\left(c \cdot m + h_1\right) \cdot \left(t_{A,a} - t_{B,s}\right)}$, $h_1 = \frac{\lambda_1}{\delta_1}$, $h_2 = \frac{\lambda_2}{\delta_2}$

When the mass transfer and heat transfer are in the opposite direction:

$$\text{Heat flux} : q = i \cdot \left(t_{B,s} - t_{A,a}\right) \tag{82.16}$$

$$\text{Heat transfer coefficient} : i = \frac{(1+\varphi) \cdot h_1 h_2}{c \cdot m + h_1 + h_2} \tag{82.17}$$

Among them, $\varphi = \frac{c \cdot m + h_2}{h_1 \cdot h_2} \cdot \frac{m \cdot r}{t_{A,a} - t_{B,s}}$

82.3 Simulation Results and Analysis

This paper discussed the coupled relationship of heat transfer and mass transfer for take the Lithium Bromide solution dehumidification process as an example. It can be seen in the previous theoretical analysis that the impact of mass transfer on the heat transfer is mainly reflected in the mass flux, and the impact of heat transfer on the mass transfer is mainly reflected in the temperature of air and liquid. Therefore, this paper mainly discussed how the concentration of the Lithium Bromide solution and temperature of air and the solution affect the heat and mass transfer. The relevant parameters selected in Table 82.1.

Figure 82.2 describes the mass transfer coefficient and the mass flux changes with the temperature of the air. It can be seen that, in both cases, mass transfer coefficient is increased with increasing air temperature, and the mass flux is increased slowly. The reason is that the water vapor diffusion coefficient of the air film is increased when the air temperature increases, then the mass transfer coefficient increases.

The influences of air temperature on the heat transfer coefficient and heat flux are shown in Figs. 82.3. Heat transfer coefficient is decreased and heat flux is increased with increasing temperature when the heat transfer and mass transfer are in the same direction. Heat transfer coefficient is increased and heat flux is decreased with increasing temperature when the heat transfer and mass transfer are in the opposite direction. It can be seen in the formulas (82.15) and (82.17), that the effect of mass transfer process to the heat transfer process is mainly embodied in two aspects: one is the enthalpy carried by the mass flux, and it can be considered to change the value of equivalent heat transfer coefficient; the other one is the water vapor turns into water release of latent heat of vaporization, and it can be

Table 82.1 Numeral parameter

Latent heat of vaporization/ $\text{kJ} \cdot \text{kg}^{-1}$	Thermal conductivity coefficient of air/ $\text{W} \cdot (\text{m} \cdot \text{K})^{-1}$	Thermal conductivity coefficient of LiBr/ $\text{W} \cdot (\text{m} \cdot \text{K})^{-1}$	The thickness of film/ mm	specific heat at constant pressure of Water vapor/$\text{kJ} \cdot (\text{kg} \cdot \text{K})^{-1}$
2500	0.024	0.46	0.1	1.85

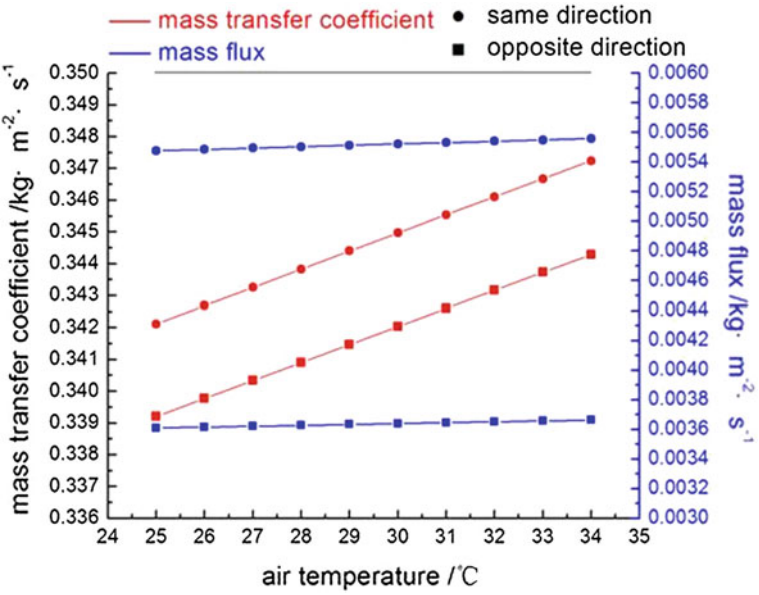

Fig. 82.2 The impact of air temperature on the mass transfer

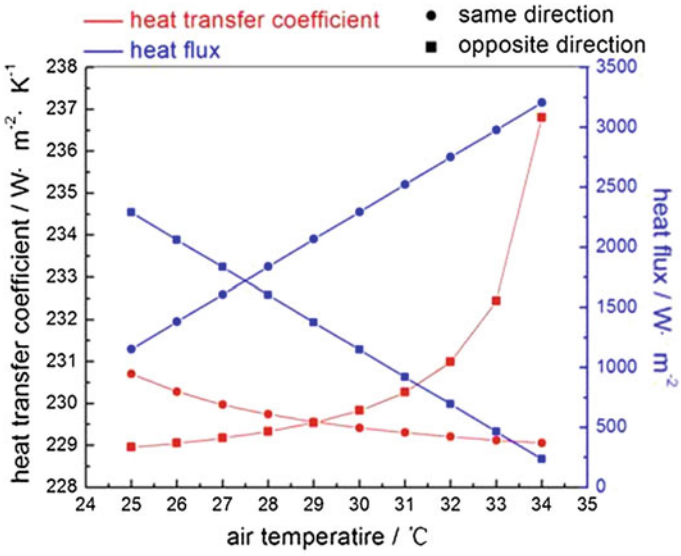

Fig. 82.3 The impact of air temperature on the heat transfer

seen as adds an additional temperature difference. The additional temperature difference is increased with increasing air temperature when the heat transfer and mass transfer are in the same direction, and the latent heat of vaporization is

impeded to the heat transfer. Therefore, as the air temperature rises, the heat transfer coefficient is decreased. Similarly the additional temperature difference is decreased with increasing air temperature when the heat transfer and mass transfer are in the opposite direction, and the latent heat of vaporization is promoted to the heat transfer. So, as the air temperature rises, the heat transfer coefficient is increased.

Figure 82.4 describes the mass transfer coefficient and the mass flux changes with the temperature of solution. It can be seen that, in both cases, mass transfer coefficient and the mass flux are decreased with increasing solution temperature. The reason is that the water vapor partial pressure of the solution surface is increased when the solution temperature increases, and impedes to the mass transfer, then the mass transfer coefficient and mass flux increases.

The influences of solution temperature on the heat transfer coefficient and heat flux are shown in Figs. 82.5. Heat transfer coefficient is increased and heat flux is decreased with increasing temperature when the heat transfer and mass transfer are in the same direction. Heat transfer coefficient is decreased and heat flux is increased with increasing temperature when the heat transfer and mass transfer are in the opposite direction.

Mass flux changes is reflected by the changes of the concentration of solution in the process of heat and mass transfer, and this paper use the concentration of solution as a factor to study the impact of the mass transfer to coupled heat and mass transfer.

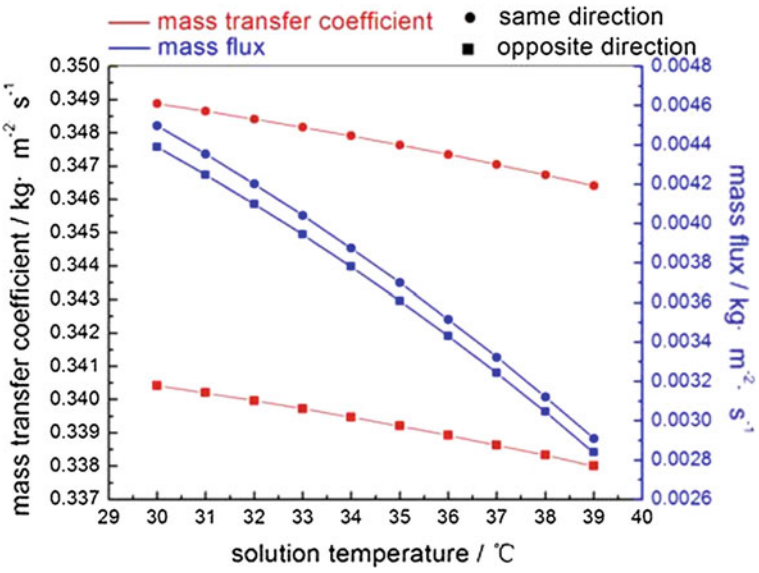

Fig. 82.4 The impact of solution temperature on the mass transfer

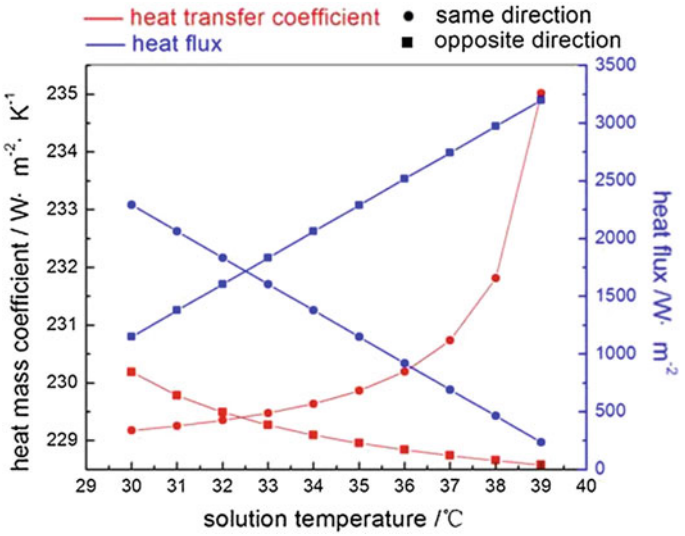

Fig. 82.5 The impact of solution temperature on the heat transfer

Figure 82.6 describes the mass transfer coefficient and the mass flux changes with the concentration of solution. It can be seen that, in both cases, mass transfer coefficient and the mass flux are decreased with decreasing concentration of solution. The reason is that the concentration of solution is decreased while the

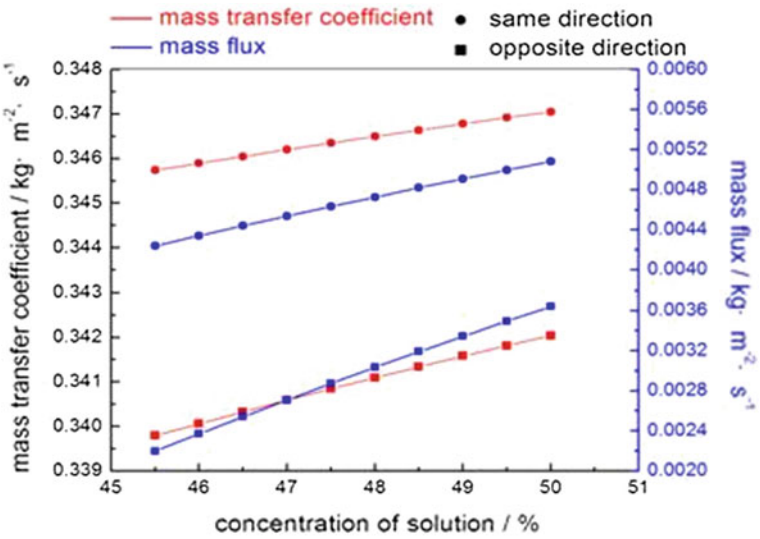

Fig. 82.6 The impact of solution concentration on the mass transfer

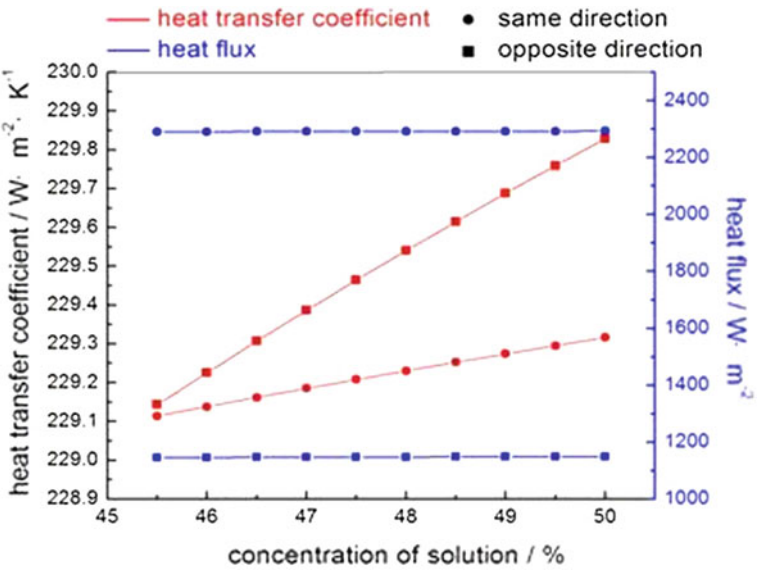

Fig. 82.7 The impact of solution concentration on the heat transfer transfer

water vapor is spread by the air to the solution. Then the water vapor partial pressure of the solution surface is increased gradually. Therefore, the mass transfer coefficient and mass flux decreases.

The influences of solution concentration on the heat transfer coefficient and heat flux are shown in Figs. 82.7. Heat transfer coefficient is decreased with increasing concentration of solution in both cases. The influence of the concentration to heat flux can be ignored.

82.4 Conclusions

1. The paper analyzes the coupled relationship of heat and mass transfer in the dehumidification process, and develops the mathematical model, then simulates. The results show that:
2. 1. The effect of mass transfer process to the heat transfer process is mainly embodied in two aspects, one is the enthalpy carried by the mass flux, and the other one is the water vapor turns into water release of latent heat of vaporization.
3. The effect of heat transfer process to the mass transfer process is mainly embodied in air temperature and solution temperature. The mass transfer coefficient is gradually increased with the increasing air temperature. The mass transfer coefficient is gradually decreased with the increasing solution temperature.

4. Heat transfer coefficient is decreased with increasing air temperature, and increased with increasing solution temperature when the heat and mass transfer are in the same direction. When the heat and mass transfer are in the opposite direction, and the conclusion is opposite.

Symbol explanation

English letters		Greek alphabet	
c	specific heat at constant pressure of Water vapor ($kJ \cdot kg^{-1} \cdot K^{-1}$)	δ	the thickness of film (m)
d	humidity ($kg \cdot kg^{-1}$)	λ	thermal conductivity coefficient ($W \cdot (m \cdot K)^{-1}$)
D	diffusion coefficient ($m^2 \cdot s^{-1}$)	ξ	concentration ($kmol \cdot m^{-3}$)
h	mass transfer coefficient ($kg \cdot m^{-2} \cdot s^{-1}$)	*Subscript*	
H	solubility coefficient ($kmol \cdot m^{-1} \cdot N^{-1}$)	a	wet air
i	heat transfer coefficient ($W \cdot m^{-2} \cdot K^{-1}$)	A	gas body
J	mole mass transfer coefficient ($kmol \cdot m^{-2} \cdot s^{-1}$)	b	dry air
k	absorption coefficient ($kmol \cdot Pa^{-1} \cdot m^{-2} \cdot s^{-1}$)	B	liquid body
m	mass flux ($kg \cdot m^{-2} \cdot s^{-1}$)	e	balanced liquid state saturated air status
p	pressure (Pa)	O	phase interface
q	heat flux ($W \cdot m^{-2}$)	s	liquid
r	latent heat of vaporization ($kJ \cdot kg^{-1}$)	v	water vapor
R	gas constant ($J \cdot (kmol \cdot K)^{-1}$)	0	standard
t	temperature (K)	1	air film
		2	liquid film

References

1. Gommed K, Grossman G (2007) Experimental investigation of a liquid desiccant system for solar cooling and dehumidification. Sol Energy 81(1):131–138
2. Gommed K, Grossman G (2004) A liquid desiccant system for solar cooling and dehumidification. Sol Energy Eng-Trans ASME 126(3):879–885
3. Xiaohua L, Yi J (2011) Match properties of heat exchange network in thermal-hygro environment building. HV & AC 41(3):29–37
4. Abdul-Wahab SA, Abu-Arabi MK, Zurigat YH (2004) Effect of structured packing density on performance of air dehumidifier. Energy Convers Manage 45(15–16):2539–2552
5. Haijiang Z, Jianhua L, Liang Z, Wenzhong G, Jianchao Y, Liwei Z (2010) Experiment on mass transfer performance of a cross-flow dehumidifier. J Refrig 31(6):21–27
6. Lei L, Xiaosong Z, Yin Y (2008) An experimental study on the heat and mass transfer coefficient in cross-flow regenerator. J Eng Thermophys 29(7):1215–1217
7. Huang Z, Lu Y, Lei B, Xu L (2010) Experiment on performance of LiBr-liquid desiccant dehumidification. CIESC J 61(S2):81–85
8. Stevens DI, Braun JE, Klein SA (1989) An effectiveness model of liquid-desiccant system heat/mass exchangers.Sol Energy 42(6):449–455
9. Factor HM, Grossman G (1980) A packed bed dehumidifier/regenerator for solar air conditioning with liquid desiccants. Sol Energy 24:541–550

10. Yonggao Y, Xiaosong Z (2008) A new method for determining coupled heat and mass transfer coefficients between air and liquid desiccant. Int J Heat Mass Transfer 51(13–14):3287–3297
11. Ren CQ, Jiang Y, Zhang YP (2006) Simplified analysis of coupled heat and mass transfer processes in packed bed liquid desiccant-air contact system. Sol Energy 80(1):121–131
12. Liu XH, Jiang Y, Xia JJ (2007) et al. Analytical solutions of coupled heat and mass transfer processes in liquid desiccant air dehumidifier/regenerator. Energy Convers Manage 48(7):2221–2232
13. Rahamah A, Elsayed MM, Al-Najem NM (1998) A numerical solution for cooling and dehumidification of air by a falling desiccant film in parallel. Renewable Energy 13(3):305–322
14. Ali A, Vafai K (2004) Analysis of heat and mass transfer between air and falling film in a cross flow configuration. Int J Heat Mass Transf 47:743–755
15. Gao W, Liu J, Wu Z, Zhang Q (2009) Study of improving heat and mass transfer performance based on coupled heat and moisture transfer characteristics. Fluid Machinery 37(3):73–77
16. Dai YJ, Zhang HF (2004) Numerical simulation and theoretical analysis of heat and mass transfer in a cross flow liquid desiccant air dehumidifier packed with honeycomb paper. Energy Convers Manage 45(9–10):1343–1356
17. Sherwood TK, Pigford RL, Wilke CR (1975) Mass transfer 1st edn. McGraw Hill, USA
18. Yan Q, Liu Y (2006) Principles of heat and mass transfer and equipment. Machinery Industry Press, Beijing, pp 15–18
19. Chen Z (2008) Advanced engineering thermodynamics. Higher Education Press, Beijing, pp 173–174
20. Teng H, Jingchun M, Yaozu S (2009) Analyses of the effects of mass transfer in the process of moisture exchange across a membrane. Chin Sci Bull 54(13):1922–1926

Chapter 83
Analysis of the Floor Heat Storage and Release During an Intermittent In-Slab Floor Heating Process

Dengjia Wang, Yanfeng Liu, Yingying Wang and Jiaping Liu

Abstract In this paper, the floor heat storage in the preheating period and the heat release in the intermittent period are studied during an Intermittent in-slab floor Heating process. The influence of design and operating parameter which are space between pipes, thickness of the filling layer, and pipe water temperature on the floor heat storage and heat release are obtained by using numerical simulation techniques. The relationship between intermittent time and preheating time is also obtained. The research results show that the biggest effect on the preheating time is the space between pipes in the preheating time. In the intermittent period, 2 h later, the two-dimensional heat transfer process can be considered as one-dimensional vertical heat transfer process, and the thickness of the filling layer has relatively big effect on the heat release time.

Keywords Intermitting heating · The floor heat storage and release · COMSOL

83.1 Introduction

In-slab floor heating system has many advantages, such as amenity, energy conservation, esthetics, and so on [1, 2]. However, considering the people's life patterns, the in-slab floor heating system is often intermittent operation, and the intermittent operation mode is determined by heat gain from floor, the floor heat storage and release. But above all, the floor heat storage and release are affected by a number of factors, including floor structure, thickness, material properties, the laying of pipe spacing, diameter, and the water temperature, which result in the difficulty in determining the heat intermittent operation mode.

D. Wang (✉) · Y. Liu · Y. Wang · J. Liu
School of Environmental and Municipal Engineering, Xi'an University of Architecture and Technology, 13 Yanta Road, Xi'an 710055, China
e-mail: wangdengjia1020@163.com

A. Li et al. (eds.), *Proceedings of the 8th International Symposium on Heating, Ventilation and Air Conditioning*, Lecture Notes in Electrical Engineering 262,
DOI: 10.1007/978-3-642-39581-9_83,

These studies are mainly focused on modeling and simulation of the floor heating systems [3–6]. Steady state computing method is a widely used computing method in in-slab heating floor transfer process [7, 8]. In 1992, Kilkis [9] introduced a steady heat transfer composite-fin model, which treated the surface between pipes as the Plate Fin heat transfer process. By introducing the efficiency of fin, he considered that indoor air temperature was not equal to mean radiant temperature and the floor surface heat transfer should contain the contributions from both convection heat between upper surface of floor and indoor air and the radiation heat with other internal surfaces. In 1995, the models mentioned above were simplified and programmed using FORTRAN language with the same procedure as the models. The calculated results were given by a series of charts, which was convenient to use [10, 11]. S. T. Hu [12] established two-dimensional floor steady state heat transfer mathematical model, in which parameters under different pipe water-supply temperature and the space between pipes, such as the highest temperature of floor surface, indoor operative temperature, heat-flow density, and preheating time, were obtained by using the dynamic simulation program based on finite element method. X. M. Feng and Y. Q. Xiao [13] established two-dimensional unsteady state floor heat transfer model, obtaining the relationship among floor surface temperature, space between pipes, thickness of the filling layer, and pipe water temperature. I. Pyeongchan [14] established two-dimensional unsteady state floor heat transfer model and used numerical simulation method to resolve it, and this model is proved to be effective by experiments. Y. F. Liu [15] established the thermal process mathematical model of the floor heating room. Based on Duhamel theorem, the solver of this model is programmed. Gilles Fraisse [16] analyzed the relationship among the needed preheating time of intermittent heating system, preheating time, thermal comfort level, and energy consumption. Other scholars [17] are mainly focused on the heat exchanges and the systems performances. Researches foresaid have some reference function to this paper.

According to above analysis, the floor heat storage in the preheating period and the heat release in the intermittent period are studied during an intermittent in-slab floor Heating process in this paper. The influence of design and operating parameter which are space between pipes, thickness of the filling layer and pipe water temperature on the floor heat storage and heat release, and the relationship between intermittent time and preheating time are obtained by using numerical simulation techniques.

83.2 Theoretical Analysis

83.2.1 Heat-Conduction Differential Equation Model

Basic assumptions

(i) The materials of each layer are homogeneous and the property parameters keep constant.

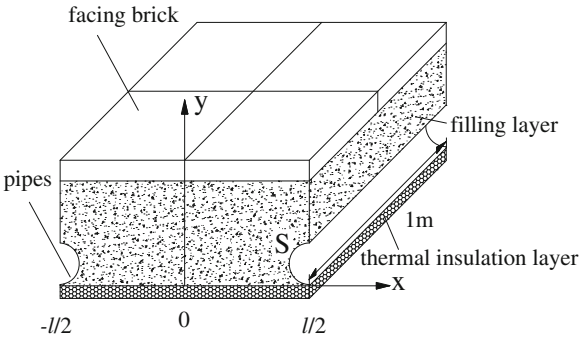

Fig. 83.1 Physical model of in-slab heating floor

(ii) The pipe surface is thought to be insulation when the heating system stops.
(iii) Heat conduction along pipe axis is ignored and the heat conduction inside floor is two-dimensional steady state [18–20].
(iv) The pipes are symmetry.
(v) The bottom of the pipe is thought to be insulation.

Two-dimensional unsteady state heat-conduction differential equation of embedded-pipe heated floor is established [21, 22], and the equation can be expressed as Eq. (83.1). The physical model of In-slab heating floor is shown in Fig. 83.1. Initial and boundary conditions are discussed respectively during preheating period and intermittent period.

$$\frac{\partial t}{\partial \tau} = a\left(\frac{\partial^2 t}{\partial x^2} + \frac{\partial^2 t}{\partial y^2}\right) \tag{83.1}$$

where a is thermal diffusion coefficient, m^2/s;

83.2.2 Soluting-Deterimining Conditions

83.2.2.1 Preheating Period

There are two cases, firstly, the intermittent time is longer enough, the temperature of the In-slab heating floor and that of the indoor air are equal approximately. Secondly, the intermittent time is short, Initial temperature of the In-slab heating floor is as the temperature field at the end time of the intermittent period.

(1) Boundary condition

① The two boundary surfaces along the x-axial direction that is adiabatic are approximately given by

$$\left.\frac{\partial t}{\partial x}\right|_{x=-\frac{l}{2}} = \left.\frac{\partial t}{\partial x}\right|_{x=\frac{l}{2}} = 0 \tag{83.2}$$

② The two boundary surfaces along the y-axial direction are given by

$$\left.\frac{\partial t}{\partial y}\right|_{y=0} = 0 \tag{83.3}$$

and

$$-\lambda \left.\frac{\partial t}{\partial y}\right|_{y=h} = (\alpha_c + \alpha_r) \times (t - t_a) \tag{83.4}$$

where λ is the thermal conductivity of the upper surface boundary layer, W/(m·K). l is the space between pipes, mm. α_c and α_r are heat convection coefficient and radiant heat transfer coefficient of floor's surface respectively, W/(m^2·K), the values are based on research results in the literature [23]. t_a is the indoor air temperature, °C.

③ the boundary of pipe surface is given by

$$t|_{(x+\frac{l}{2})^2+(y-R)^2=R^2} = t|_{(x-\frac{l}{2})^2+(y-R)^2=R^2} = t_s \tag{83.5}$$

where R is the pipe radius, m. t_s is the pipe water temperature, °C.

(2) Initial condition

In the first case, the initial condition is given as

$$t_{\tau 0} = t_a \tag{83.6}$$

In the second case, the initial condition is given as

$$t_{\tau 0} = g(x_i, y_j, n) \tag{83.7}$$

where $g(x_i, y_i, n)$ is the temperature field at the end time of the intermittent period. MATLAB is used to construct interpolating function int(x, y, n).

83.2.2.2 Intermittent Period

(1) Boundary condition

The pipe surface is of adiabatic boundary. It is shown in Eq. (83.8). Other boundary conditions are the same with those in the preheating period.

$$\left.\frac{\partial t}{\partial R}\right|_{(x+\frac{l}{2})^2+(y-R)^2=R^2} = \left.\frac{\partial t}{\partial R}\right|_{(x-\frac{l}{2})^2+(y-R)^2=R^2} = 0 \tag{83.8}$$

(2) Initial condition

The initial condition is given by.

$$t_{\tau 0} = f(x_i, y_j) \tag{83.9}$$

where $f(x_i, y_j)$ is the internal steady state temperature field of in-slab continuous heating floor. MATLAB is used to conduct interpolation processing to the simulated result of steady state. The temperature distribution law obtained is interpolating function int(x, y), which is taken as the initial condition in intermission to conduct numerical calculation.

83.3 Numerical Calculation

83.3.1 Numerical Calculation Program

COMSOL Multiphysics 4.1 numerical calculation software is used to calculate the mathematical model foresaid. The initial condition of the temperature field is conducted interpolation processing by using MATLAB, and the corresponding interpolating function int(x, y,) or int(x, y, n) is obtained.

83.3.2 Numerical Calculation Conditions

Main floor structure:

Facing brick layer: brick setting, the thickness $\delta_1 = 10\,\text{mm}$, the density $\rho_1 = 1,900\,\text{kg/m}^3$, the thermal conductivity $\lambda_1 = 1.1\,\text{W/m} \cdot \text{K}$, the specific heat $c_1 = 1.05\,\text{kJ/kg} \cdot \text{K}$, heat storage coefficient (24 h) $S_1 = 12.72\,\text{W/(m}^2 \cdot \text{K)}$.

Filling layers: crushed stone concrete, the density $\rho_2 = 2,300\,\text{kg/m}^3$, the thermal conductivity $\lambda_2 = 1.51\,\text{W/(m} \cdot \text{K)}$, the specific heat $c_2 = 0.92\,\text{kJ/(kg} \cdot \text{K)}$, heat storage coefficient (24 h) $S_2 = 15.36\,\text{W/(m}^2 \cdot \text{K)}$.

83.4 Results and Analysis

83.4.1 Intermittent Period

In the intermittent period, the floor surface temperature and heat flux density for different pipe water temperature are shown in Fig. 83.2. The average temperature of floor surface for different thicknesses of the filling layer is shown in Fig. 83.3.

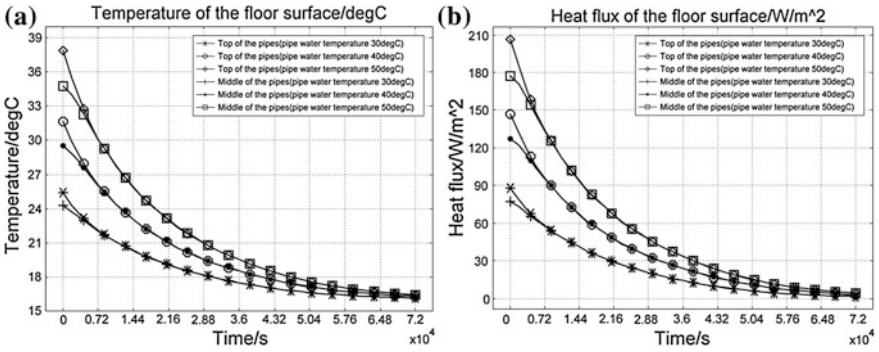

Fig. 83.2 The floor surface temperature and heat flux density for different pipe water temperature during intermittent period (Space between pipes 200 mm, thickness of filling layer 60 mm). **a** Temperature , **b** Heat flux

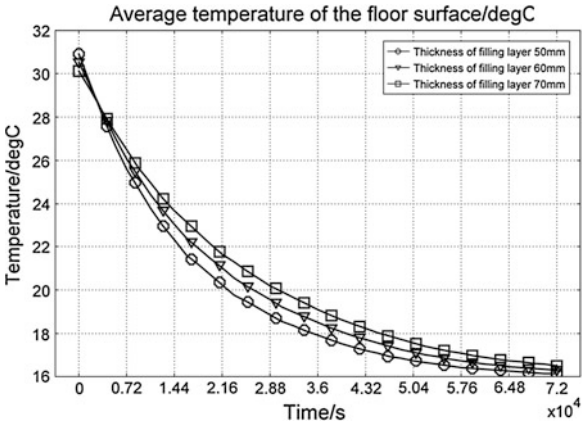

Fig. 83.3 The floor surface average temperature for different thickness of filling layer during intermittent period (Space between pipes 200 mm, pipe water temperature 40 °C)

The average temperature of floor surface for different space between pipes is shown in Fig. 83.4.

According to Fig. 83.3, the thickness of the filling layer has less effect on the floor surface average temperature. Thus, at the beginning of the intermittent period, the floor surface average temperature with different thickness of filling layers is similar to each other. But it is also clear that the smaller the thickness of filling layers is, the higher the average temperature of the floor surface is. Temperature decline during the intermittent period is relatively fast, because the smaller the filling layer is, the less the heat storage capacity is. It can be seen that 1 h later, the floor surface average temperature with thin thickness declines to be lower than that of heavy thickness. Thus, the heavier the thickness of the packing layer is, the more the heat storage capacity is. Heat releasing process during intermittent period is relatively slow.

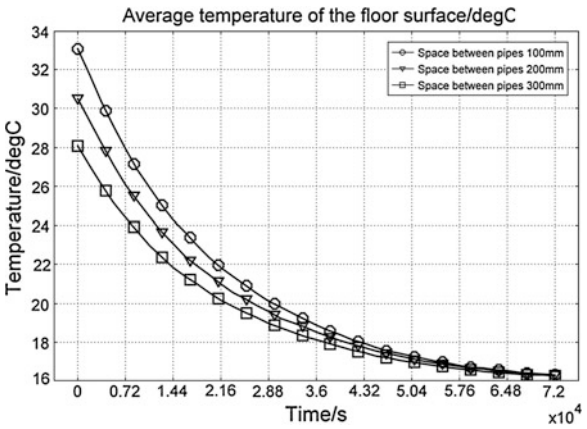

Fig. 83.4 The floor surface average temperature for different space between pipes during intermittent period (Thickness of filling layer 60 mm, pipe water temperature 40 °C)

According to Fig. 83.4, the smaller the pipe space is, the higher the average temperature of floor surface is. The temperature field is similar to the decline process for different pipe water temperature.

83.4.2 Preheating Period

The floor surface average temperature of different pipe water temperature and space between pipes as shown in Figs. 83.5 and 83.6.

According to Fig. 83.5, when the intermittent times are 2, 4, and 10 h, respectively, the corresponding preheating times are about 2, 3.5 and 4.5 h. When the intermittent time is short, the preheating time corresponds to the intermittent time. When it is long, the preheating time is shorter than the intermittent time. When the intermittent time is longer enough, it can be thought that the heat storage

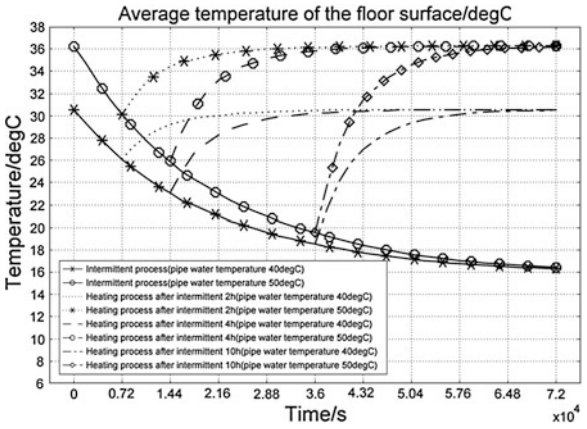

Fig. 83.5 The floor surface average temperature for different pipe water temperature and different intermittent time during preheating period (Space between pipes 200 mm, thickness of filling layer 60 mm)

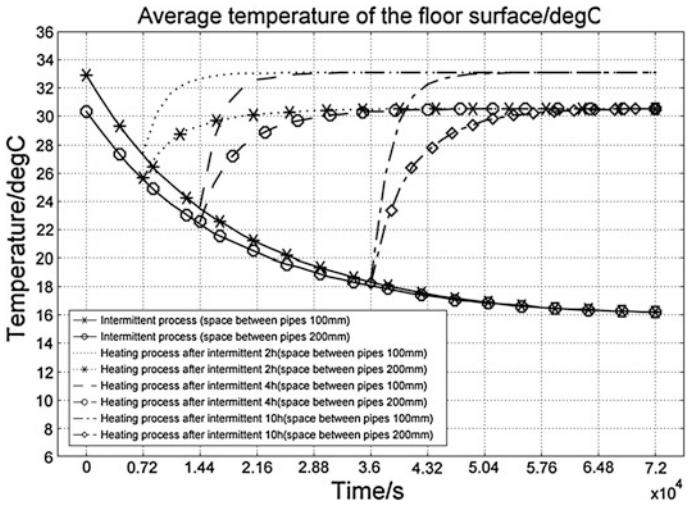

Fig. 83.6 The floor surface average temperature with different space between pipes and different intermittent time during preheating period (Thickness of filling layer 60 mm, pipe water temperature 40 °C)

Table 83.1 The relationship between intermittence and preheating time for different space between pipes (Thickness of filling layer 60 mm, pipe water temperature 40 °C)

Intermittent time/h		0.5	1	2	4	6	10	Infinite
Preheating time/h	Space between pipes 100 mm	0.5	0.7	1	1.5	1.7	2	2.5
	Space between pipes 200 mm	0.5	1	2	3.5	4	4.5	5
	Space between pipes 300 mm	0.5	1	2	3.8	5.5	7	7.5

capacity has been released fully. At this time, the preheating time is about 5 h. Pipe water temperature is only of effect on the average temperature of floor surface temperature, it has less influence on the preheating time.

According to Fig. 83.6, when the space between pipes is 100 m, the floor surface average temperature increases relatively fast. And the preheating time is relatively short. Under the condition of the same intermittent time, the smaller the space between pipes is, the shorter the preheating time is. The relationship between the intermittent time and the preheating time for different space between pipes is shown in Table 83.1.

83.5 Conclusions

The floor heat storage in the preheating period and the heat release in the intermittent period are studied during an Intermittent in-slab floor Heating process. The following conclusions are drawn.

1 During the preheating period, space between pipes is of big effect on preheating time. Pipe water temperature and the thickness of filling layers are of less effect on the preheating time. The relationship between the intermittent time and the preheating time is obtained. The heat storage characteristics of intermittent heating floor are mastered.
2 During the intermittent period, 2 h after intermittent heating, two-dimensional floor heat transfer process is approximate to be the vertical one-dimensional heat transfer process. 20 h later, it can be thought that heat release process is finished. Pipe water temperature and space between pipes are of relatively less effect on heat release time. The thickness of the filling layer is of big effect on heat release time. The heat release characteristics of intermittent heating floor are mastered.

Acknowledgments This work was financially supported by the Natural Science Foundation of China (No.51078302) and the innovation research group program of Program of NSFC(50921005).

References

1. Lihua Z (2000) Thermal performance analysis of concrete embedded plastic radiant floor heating. HV&AC 30:6–8
2. Songtao H, Huili Y, Xuquan L (1999) Dynamic simulation of operation of the radiant floor heating system. HV&AC 29:15–17
3. ASHRAE Handbook (2008) HVAC systems and equipment, panel heating and cooling. ASHRAE, Atlanta (Chap. 6.1)
4. Nonino C, Comini G (1994) Thermal analysis of floor heating panels. Numer Heat Transf 26:537–550
5. Sattari S, Farhanieh B (2006) A parametric study on radiant floor heating system performance. Renew Energy 31:1617–1626
6. Athienitis AK (1994) Numerical model of a floor heating system. ASHRAE Trans 100:1024–1030
7. Fontana L (2011) Thermal performance of radiant heating floors in furnished enclosed spaces. Appl Therm Eng 31:1547–1555
8. Yanfeng L, Dengjia W, Jiaping L (2012) Study on heat transfer process for in-slab heating floor. Build Environ 54:77–85
9. Kilkis IB (1992) Enhancement of heat pump performance using radiant floor heating systems. ASME AES 28:119–129
10. Kilkis IB, Coley M (1995) Development of a computer design software for hydronic floor heating of building. ASHREA trans CH-95-19-1:1201–1213
11. Kilkis IB, Eltez M, Sager SS (1995) A simplified model for the design of radiant in-slab heating panels. ASHREA trans 101:210–216
12. Hu ST, Yu HL, Li XQ (1999) Dynamic simulation of operation of the radiant floor heating systemHeating. Vent Air Cond 29:15–17
13. Feng XM, Xiao QY (2004) Dynamic simulation of the low temperature radiant floor heating system building. Energy Environ 34:1–4

14. Pyeongchan I (2003) Modeling and optimization in slab-on-grade radiant heating floor systems. Doctor Dissertation, University of Colorado
15. Liu YF (2004) Study on basic theory of designing and running control of imbed pipe floor heating. Doctor Dissertation, Xi'an University of Architecture and Technology
16. Fraisse G, Virgone J, Brau J (1997) An analysis of the performance of different intermittent heating controllers and an evaluation of comfort and energy consumption. Heat Vent Air cond Refrig Res 4:369–386
17. Sattari S, Farhanieh B (2006) A parametric study on radiant floor heating system performance. Renew Energy 31:1617–1626
18. Zmeureanu R (1989) Thermal performance of radiant heating panels. ASHREA trans 95:13–26
19. Dale JD (1993) The thermal performance of a radiant panel floor heating system. ASHREA trans 99:23–34
20. Peter A (1995) An evalution of themal comfort and energy consumption for a surface-mounted ceiling radiant panel heating system. ASHREA trans CH-95-19-3:1221–1236
21. Chuangchid P, Krarti M (2001) Foundation heat loss from heated concrete slab-on-grade floors. Build Environ 1(36):637–655
22. Adjali MH, Davies M, Rees SW, Littler J (2000) Temperatures in and under a slab-on-ground floor: two-and three- dimensional numerical simulations and comparison with experimental data. Build Environ 7(35):655–662
23. Chen QG (1991) Building thermal physical basis. Xi'an Jiaotong University Press, Xi'an